SCHOLARLY PUBLICATIONS

A CURRENT AWARENESS BULLETIN
OF RESEARCH OUTPUT

@DTU

(83rd Edition)

NOVEMBER 2019

BY: CENTRAL LIBRARY

DELHI TECHNOLOGICAL UNIVERSITY
(FORMERLY *DELHI COLLEGE OF ENGINEERING)*
GOVT. OF N.C.T. OF DELHI
SHAHBAD DAULATPUR, MAIN BAWANA ROAD
DELHI 110042

PREFACE

This is the **Eighty Third** Issue of Current Awareness Bulletin started by Delhi Technological University, Central Library. The aim of the bulletin is to compile, preserve and disseminate information published by the faculty, students and alumni for mutual benefits. The bulletin also aims to propagate the intellectual contribution of Delhi Technological University (DTU) as a whole to the academia.

The bulletin contains information resources available in the internet in the form of articles, reports, presentations published in international journals, websites, etc. by the faculty and students of DTU. The publications of faculty and student which are not covered in this bulletin may be because of the reason that the full text either was not accessible or could not be searched by the search engine used by the library for this purpose.

The learned faculty and students are requested to provide their uncovered publications to the library either through email or in CD, etc. to make the bulletin more comprehensive.

This issue contains the information published during **November, 2019**. The arrangement of the contents is alphabetical. The full text of the article which is either subscribed by the university or available in the web is provided in this bulletin.

Central Library

CONTENTS

1. 3 Dimensional CFD analysis of Laminar flow Natural Convection of Hollow Cylinder with Annular Fins, ***7.Gaurav Krishnayatra***, ***7.Sulekh Tokas***, ***3.Rajesh Kumar*** and ***3.Mohammad Zunaid***, Mechanical, DTU

2. A 12.08-TOPS/W All-Digital Time-Domain CNN Engine Using Bi-Directional Memory Delay Lines for Energy Efficient Edge Computing, ***8.1.Aseem Sayal***, S. S. Teja Nibhanupudi, Shirin Fathima, and Jaydeep P. Kulkarni, ECE, DTU

3. A Critique of Economic Literature on Technology and Fourth Industrial Revolution: Employment and the Nature of Jobs, ***6.Ishaan Gera*** and ***3.Seema Singh***, Humanities, DTU

4. A review on challenges and solutions in learning programming courses at undergraduate level, ***6.Massoud Massoudi***, CSE, DTU

5. A Review on Parametric Optimization of Aluminium Alloy 5754 for MIG Welding, ***7.Himanshu Yadav*** and ***3.M.S. Niranjan***, Mechanical, DTU

6. An assessment of socially responsible consciousness and multi-level integration of business morals, corporate social obligation and sustainability in higher education, ***6.Gaurav Dawar*** and ***3.Seema Singh***, Humanities, DTU

7. An Efficient Weighted Trust Method for Malicious Node Detection in Clustered Wireless Sensor Networks, ***3.Bhavnesh Jaint[1]***, ***8.Vishwamitra Singh[2]***, ***6.Lalit Kumar[2] Tanwar***, ***3.S.Indu[2]*** and ***3.Neeta Pandey[2]***, [1]Electrical and [2]Electronics, DTU

8. An integrated DEMATEL Six Sigma hybrid framework formanufacturing process improvement, ***3.Anshu Gupta***, Pallavi Sharma, Akansha Jain, Hongbo Xue, S. C. Malik and P. C. Jha, USME, DTU

9. Audio Watermarking Using Beat Detection and Pitch Estimation, ***6.Lavi Tanwar***, ***8.Radhika Dang***, ***8.Satvik Maurya*** and ***3.Jeebananda Panda***, Electronics, DTU

10. Biotechnological management of water quality: A mini review, ***7.Lakhan Kumar***, ***6.Rajkumar Bidlan***, ***3.Jai gopal Sharma*** and ***3.Navneeta Bharadvaja***, Biotech, DTU

11. Code Cloning using Abstract Syntax Tree, ***6.Gunjan Chugh***, Divya Mahajan, Nainika Sehgal, Akanksha Paul and Leena Budhiraja, Computer, DTU

12. Comparative Study and Measurement of Form Errors for the Component Printed by FDM and PolyJet Process, ***6.Nagendra Kumar Maurya***, ***3.Vikas Rastogi*** and ***3.Pushpendra Singh***, Mechanical, DTU

13. Comparing domain wall synapse with other Non Volatile Memory devices for on-chip learning in Analog Hardware Neural Network, Divya Kaushik, ***6.Utkarsh Singh***, Upasana Sahu, ***3.Indu Sreedevi*** and Debanjan Bhowmik, Electronics, DTU

14. Critically Polluted Area Analysis using Comprehensive Environmental Pollution Index, ***7.Medha Sharma*** and ***3.Dr. Geeta Singh***, Environment, DTU

15. Crowd Escape Event Detection via Pooling Features of Optical Flow for Intelligent Video Surveillance Systems, Gajendra Singh, ***6.Arun Khosla*** and ***3.Rajiv Kapoor***, Electronics, DTU

16. Design and Analysis of Thermal Therapy Pad Using Computational Fluid Dynamics – A Review, ***6.Harsh Shyam***, ***3.Amit Pal*** and Manish Jain, Mechanical, DTU

17. Design and Experimental analysis of Integer Order PID Controller for Ceramic IR heating system, ***6.Ajendra Singh*** and ***3.J. N. Rai***, Electrical, DTU

18. Detection of Angle-of-Arrival of the Laser Beam using a Cylindrical Lens and Gaussian Beam Curve Fitting, Anand Kumar Rai, Saurabh Bansod, ***8.1.Satya Prakash*** and Ajay Rathee, Electronics, DTU

19. EFFECT OF PERMANENT MAGNETIC POLE ORIENTATION ON FIELD STRENGTH IN VISCOELASTIC MAGNETIC ABRASIVE FINISHING PROCESS, ***3.K. SRINIVAS***, ***3.Q. MURTAZA*** and ***3.A. K AGGARWAL***, DTU

20. Impact of Particle Swarm Optimization parameters on its convergence, N.K.Jain, ***3.Uma Nangia*** and ***6.Jyoti Jain***, Electrical, DTU

21. Implementation and Analysis of field Control on Electric Vehicle Power Train System Employing PMSM as Traction Device, ***6.Monika Verma***, ***3.Mini Sreejeth*** and ***3.Madhusudan Singh***, Electrical, DTU

22. Improved dropClust R package with integrative analysis support for scRNA-seq data, Debajyoti Sinha, ***8.Pradyumn Sinha***, ***8.Ritwik Saha***, Sanghamitra Bandyopadhyay and Debarka Sengupta, CSE, DTU

23. Indian smart city ranking model using taxicab distance-based approach, ***3.Kapil Sharma*** and ***6.Sandeep Tayal***, IT, DTU

24. Interleukin-6 confers radio-resistance by inducing Akt mediated glycolysis and reducing mitochondrial damage in cells, ***6.Neeraj Kumari***, ***3.Asmita Das***, Anant Narayan Bhatt, Biotechnology, DTU

25. Load Flow Solution for Radial Distribution Network, ***7.Om Pathak*** and ***3.Prem Prakash***, Electrical, DTU

26. Meteorological Drought Intensity Assessment using Standardized Precipitation Index, ***7.Ashish Srivastava*** and ***3.Dr. Geeta Singh,*** Environment, DTU

27. Modeling and Simulation of Microgrid Solar Photovoltaic System with Energy Storage, ***6.Dinanath Prasad***, ***3.Narendra Kumar*** and Rakhi Sharma, Electrical, DTU

28. Modelling of vapour compression refrigeration system (VCRS) by using alternative refrigerants with TiO2 and without nano materials, ***3.R.S. Mishra***, Mechanical and Production Engineering, DTU

29. Multi-Input Multi-Level Isolated DC-DC Converter for Enhanced Reliability of Renewable Sources, ***8.Ravi Vardhan Arya,*** Amritesh Kumar and ***6.Aditya Narula***, Electrical, DTU

30. Multiple-Input Single-Output Universal Biquad Filter Using Single Output OTAs, ***7.Ajishek Raj***[1], ***3.D. R. Bhaskar***[2] and ***3.Pragati Kumar***[1], [1]Electrical and [2]Electronics, DTU

31. NAMPT, GRN, and SERPINE1 signature as predictor of disease progression and survival in gliomas, Meenakshi Vachher, ***8.Kriti Arora***, Archana Burman and Bhupender Kumar, IT, DTU

32. Nonlliinear Siignall Anallysiis Usiing Eiigen Vallue Decomposiittiion off Hankell Mattriix and Wavellett Transfform, ***3.Sudipta Majumdar*** and ***7.Charul Arora***, Electronics, DTU

33. Novel and Robust Hysteresis Current Control Strategies For a BLDC Motor : A Simulation Study and Inverter Design, ***8.Shrivatsan K Chari***, ***8.Rishav Dhiman*** and ***8.Rohit Saxena***, Electrical, DTU

34. Online or Offline Shopping: Factors that Determine Customer Behavior, ***8.Divyendu***, ***8.Siddharth Raj*** and ***8.Vivek Yadav***, DTU

35. Optimization of Process Parameters in Synergic MIG Welding of Mild Steel, ***7.Abhishek Kaushik***, Civil, DTU

36. Parameter optimization and characterization of environmental friendly aluminium hybrid metal matrix composites, ***6.Girija Moona***, ***3.R.S Walia***, ***3.Vikas Rastogi*** and Rina Sharma, DTU

37. Performance Analysis of Different Modulating Techniques for Multilevel Inverter, ***6.Allu Bhargav***, ***3.Alka Singh*** and ***3.Ankita arora***, Electrical, DTU

38. Performance Analysis of FIS and ANFIS based MPPT for Solar PV System with Boost, SEPIC and CUK Converter Topologies, ***6.Mohak Jain*** and ***3.Bharat Bhushan***, Electrical, DTU

39. PERFORMANCE EVALUATION OF ABSORPTION REFRIGERATION SYSTEMS USING INTELLIGENT OPTIMIZATION TECHNIQUES: A REVIEW, ***6.RAVINDRA KANNOJIYA*** and ***3.RAJESH KUMAR***, Mechanical, DTU

40. Performance evaluation of half effect LiBr-H2O vapour absorption systems using multi cascading of vapour compression cycles for low temperature applications, ***3.Radhey Shyam Mishra***, Mechanical, Production, Industrial and Automobiles, DTU

41. Performance measurement of flexible manufacturing system: A case study, ***3.R.S. Mishra***, ***6.Himani Saxena*** and ***3.A.K. Madan***, Mechanical Production Industrial and Automobiles, DTU

42. PermPair: Android Malware Detection using Permission Pairs, ***3.Anshul Arora***, Sateesh K Peddoju and Mauro Conti, Mathematical, DTU

43. Power Factor Correction Using APFC Panel on Different Loads, ***Vinay Sehwag***, ***8.Vaibhav Dua***, ***7.Ajendra Singh***, ***3.Jitendra Nath Rai*** and Vineet Shekhar, Electrical, DTU

44. Prediction of residual stresses in biaxial stretching of tailor welded blanks by finite element analysis, Amit Kumar, D Ravi Kumar and ***3.Vijay Gautam***, Mechanical, DTU

45. Scalable intelligent data-driven decision making for cognitive cities, ***3.Akshi Kumar*** and ***6.Arunima Jaiswal***, Computer, DTU

46. SINUSOIDAL POWER CLOCK BASED PFAL, ***8.Sagar Jain***, ***8.Shubham Garg***, ***3.Neeta Pandey*** and Kirti Gupta, Electronics, DTU

47. SLIDING MODE CRUISE CONTROL BASED ON HIGH GAIN OBSERVER, ***6.Ajit Kumar Sharma*** and ***3.Bharat Bhushan***, Electrical, DTU

48. Source Scheduling for Power Matching of Clustered Induction Generators fed VSC supported Micro grid, ***6.Peeyush Pant*** and ***3.Vishal Verma***, Electrical, DTU

49. Study of Forced Oscillations in Two Area Power System, ***7.Vertika Jain***, ***3.S.T Nagarajan*** and ***3.Rachana Garg***, Electrical, DTU

50. Suicidal - A Multipronged Approach to Identify and Explore Suicidal Ideation in Twitter, ***8.Pradyumna Prakhar Sinha***, ***8.Rohan Mishra*** and Ramit Sawhney, IT, DTU

51. Synthesis and Structural Characterization of Meso-tetrakis(3,4- dimethoxyphenyl) Porphyrin, ***3.Anil K*** and ***6.Omprakash Y*** ,Applied Chemistry, DTU

52. Taylor series based compressive approach and Firefly support vector neural network for tracking and anomaly detection in crowded videos, ***3.Avinash Ratre***, Electronics, DTU

53. The fourth industrial revolution, women engineers and SDGs: an exploratory study with special reference to India, ***3.Seema singh***, Humanities, DTU

54. Thermal modelling and optimization of four stages cascade vapor compression refrigeration systems for ultra-low temperature applications, ***3.R.S. Mishra***, Mechanical, Production, Industrial and Automobiles, DTU

55. Thermal performance of cascaded vapour compression absorption systems, ***3.R.S. Mishra***, Mechanical & Production, DTU

56. Thermal performances (first law efficiency, exergy destruction ratio & exergetic efficiency) of cascade single effect ammonia-water (NH3-H20) vapour absorption refrigeration system coupled with vapour compression refrigeration using ecofriendly refrigerants in the low temperature cycle of VCRS system, ***3.R.S. Mishra***, Mechanical & Production, DTU

57. Thermodynamic analysis of brayton cycle for power generation, ***3.R.S. Mishra*** and ***8.Manish Kumar***, Mechanical, Production, Industrial and Automobiles, DTU

58. Transformer Health Monitoring System Using Internet of Things, ***7.Divyank Srivastava*** and ***3.M. M. Tripathi***, Electrical, DTU

59. Transmission Congestion Management Considering Modeling of Solar Photovoltaic Distributed Generator in Deregulated Power System, Anu Singla, Kanwardeep Singh and ***3.Vinod Kumar Yadav***, Electrical, DTU

60. Tribological behavior of sustainable Carbon based composite coating for wear resistance applications, ***6.Ankit Tyagi***, ***3.S M Pandey***, ***6.Kalpna Gupta***, ***3.R.S. Walia***, ***3.Qasim Murtaza*** and Kumar Krishen, Mechanical, DTU

61. Wavelet Based Control of Shunt Compensator for Power Quality Enhancement, ***6.Masood Anzar***, ***3.Narendra Kumar*** and ***3.M. Rizwan***, Electrical, DTU

62. Wear Behaviour of Al/B4C Surface Composite Fabricated by Friction Stir Processing, ***3.Yuvaraj N, Mechanical***, DTU

1. *Chancellor*

2. *Pro Vice Chancellor*	***2.1.*** *Ex Pro Vice Chancellor*
3. *Faculty*	***3.1.*** *Ex Faculty*
4. *Teaching-cum-Research Fellow*	***4.1.****Asst. Librarian*
5. *Alumni*	
6. *Research Scholar*	***6.1.*** *Ex Research Scholar*
7. *PG Scholar*	***7.1.*** *Ex PG Scholar*
8. *Undergraduate Student*	***8.1.*** *Ex Undergraduate Student*

Proceedings of the 5th World Congress on Mechanical, Chemical, and Material Engineering (MCM'19)
Lisbon, Portugal – August, 2019
Paper No. HTFF 181
DOI: 10.11159/htff19.181

3 Dimensional CFD analysis of Laminar flow Natural Convection of Hollow Cylinder with Annular Fins

Gaurav Krishnayatra[1], Sulekh Tokas[2], Rajesh Kumar[3], Mohammad Zunaid[4]
[1,2,3,4]Delhi Technological University (formerly Delhi College of Engineering)
Shahbad, Daulatpur, Delhi, India
gauravkrishnayatra_mt2k18@dtu.ac.in; sulekhtokas_mt2k18@dtu.ac.in; rajeshkumar@dce.ac.in; mzunaid@dce.ac.in

Abstract **-** Natural Convection heat transfer from a horizontal hollow cylinder having annular fins on the outer surface has been studied numerically. The constant temperature boundary condition was applied at the inner surface of the hollow cylinder. Boussinesq approximation was used with steady and laminar flow. For simulation ANSYS FLUENT was used to solve the discretized system and three dimensional model was prepared in SOLIDWORKS. The present investigation showed us that the analytical solution and numerical solution for unfinned hollow cylinder are very accurate and the cases with fins from 4 to 20 were solved by simulated showing us the pictorial representation of temperature plume and velocity vectors. The plots are shown comparing different thermal parameters such has heat flux, total heat transfer, Rayleigh number, Nusselt number and effectiveness of the system with fins with respect to the number of fins attached to the hollow cylinder.

Keywords: Fins, Natural, Convection, Heat, Transfer.

1. Introduction

Convection heat transfer is complicated in itself since, it incorporates two principles i.e. heat conduction and fluid motion. Fluid motion is the key enhancement factor; higher the fluids velocity, higher the heat transfer rate. There are two type of convections : Natural Convection and Forced convection. Forced convection is one where the fluid is made to flow via some external forces and Natural convection is the one which is governed by Buoyancy forces. Natural convection plays a very important role in almost every other industry like cooling of equipment such as microprocessors, TVs, transistors and microchips, heat dissipation from cooling coils and power transmission lines etc.

In cases of natural convection in thermal systems, uses of fins is a smart method to enhance the heat transfer rate significantly, as it was studies by Welling et al. [1], Harahap et al. [2], Singh and Dash [3] and Kraus et al. [4]. The natural convection has no moving components hence, it is more feasible to use where the structural integrity of the equipment to be cooled is under consideration. There are not many significant numerical studies performed by many of the researchers all across the globe.

Senapati et al. [5] did numerical study on vertical cylinder with annular fins where they studied conjugated heat transfer characteristics for optimization of best fin spacing for the case of turbulent flow natural convection and they also derived a correlation between Nusselt number and geometrical parameters along with Rayleigh number. Senapati et al. [6] (2016) did three dimensional numerical study on the effects of shifting the annular fins on horizontal cylinder along vertical axis in certain ratios, they concluded with giving the temperature plumes and flow characteristics for laminar flow natural convection. They also derived a correlation between Nusselt number and geometrical parameters and also the Rayleigh number using regression analysis. One of the significant numerical studies was conducted by Nada et al. [7] where they analysed the effects of geometry, arrangement, dimension and number of annular and longitudinal fins on horizontal tube arrangement in an enclosure. Result showed that the heat flux increased as the Rayleigh number increase and also with increasing in annulus area, number of fins and fin width; for same area of fins longitudinal fins were more effective than annular fins. The convection heat transfer on horizontal hollow cylinder with internal axial fins was investigated by Acharya et al. [8]. They performed three dimensional numerical simulation for a short cylinder (L/D<1) where they found that the heat rejection from the surface of the cylinder can be optimized (maximized) for some level height and certain fin number after that it will reduce, for long cylinder(L/D>1) [8] the maximum value of heat transfer will vanish for all given length of

the fins and spacing between fins. Sun et al. [9] analysed very intensively the natural convection along the vertical cylinder heat sinks with longitudinal fins where they discussed the thermal boundary layer along with the flow patterns of the air,

Nomenclature

$\vec{V}$: Velocity of fluid in vector form, $\frac{m}{s}$	T : Temperature of the fluid, ℃, K
α : Thermal diffusivity, $\frac{m^2}{s}$	D_o : Outer diameter of the tube, m
ρ : Density, $\frac{kg}{m^3}$	D_i : Inner diameter of the tube, m
$\vec{g}$: Acceleration due to gravity, $\frac{m}{s^2}$	R : Specific gas constant, $\frac{J}{kgK}$
p : Free stream pressure, $\frac{N}{m^2}, Pa$	T_s : Surface temperature, ℃, K
T_f : Film temperature , ℃, K	p_{atm} : Atmospheric pressure, $\frac{N}{m^2}, Pa$
T_w : Wall temperature, ℃, K	Ra : Rayleigh number, $Ra = \frac{g\beta(T_w - T_f){L_c}^3}{\vartheta\alpha}$
Ra_i : Rayleigh number based on fin spacing, $Ra_s = \frac{g\beta(T_w - T_f)S^3}{\vartheta\alpha}\left(\frac{S}{D_o}\right)$	i : Suffix of Rayleigh number signifying the number of fins
T_∞ : Free stream temperature, ℃, K	S : Fin spacing, m
Q : Total heat transfer, W	Nu : Nusselt number, $Nu = \frac{hD_o}{k}$
h : Convective heat transfer coefficient, $\frac{W}{m^2 - K}$	μ : Dynamic Viscosity, $\frac{kg}{m-s}$
A_t : Total outer surface area of the tube, m^2	ϑ : Kinematic Viscosity, $\frac{m^2}{s}$
Pr : Prandtl Number, $Pr = \frac{\mu C_p}{K}$	N : Number of fins
D_f : Diameter of the annular fins, m	C_p : Specific heat capacity at constant pressure, $\frac{KJ}{kgK}$
L_f : Length of the fins, $L_f = \frac{D_f - D_o}{2}, m$	K : Thermal conductivity , $\frac{W}{m-K}$
q_{cfd} : Heat Flux based on CFD result, $\frac{W}{m^2}$	h_{cfd} : Convective heat transfer coefficient based on CFD result, $\frac{W}{m^2 - K}$
Nu_{cfd} : Nusselt number based on CFD result	q_{inner} : Heat flux at the inner wall based on CFD result, $\frac{W}{m^2}$
$\in$: Effectiveness of the system	β : Coefficient of thermal expansion, $\frac{1}{K}$

they also investigated the values of local Nusselt number distribution patterns along the fin length and cylinder surface[9]. They discovered that the average Nusselt number along the length of the fin is approximately proportional to the exponential function of the vertical distance with deviation of ±10%.

2. Analytical and Mathematical Modelling

A horizontal cylinder of outer diameter (D_o) 25mm and inner diameter (D_i) 20 mm with length of the fins (L_f) 10 mm is taken into analysis firstly without fins and then with a number of fins N the schematic side view of the system is shown in Fig. 1 where as the Fig. 2 shows us the three dimensional model.

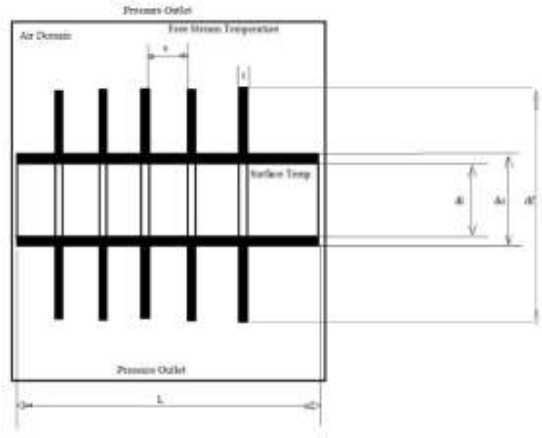


Fig. 1: Schematic Representation.

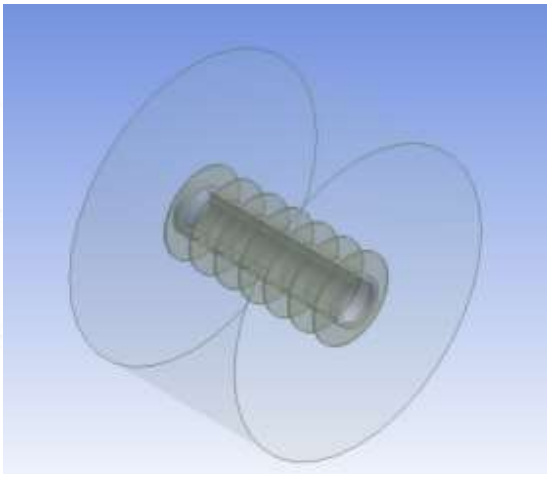


Fig. 2: Three Dimension Model Representation.

In the current study we have done the computational analysis for 10 cases with N= 0,4,6,8,10,12,14,16,18,20 along with complete analytical validation of the cases. We have selected the material of the tube i.e. Aluminium for its high thermal conductivity. The thermal parameters have been reported in their standard form. The model is in three dimensional isometric view as it is very clear from Fig. 2, the computational investigation is also done in three dimensional form.

A circular Outside air domain was chosen with a constant free stream temperature and the diameter of the domain is 150 mm. Boundary conditions employed were as follows, the temperature of inner wall of the hollow cylinder was kept constant $T_s = 398\ K$ which; is normally constant in the case of industrial application; and is fixed for all cases, As done by Senapati [6]. Since, aluminium has very high thermal conductivity the temperature drop along the radial direction of tube was ignored [8]; also with the conductive thermal resistance of the hollow cylinder.

The governing equations in differential for the analytical solution we have taken the flow to be steady, laminar and incompressible ideal gas so the assumptions are written as follows:

Energy equation :

$$\left(\vec{V}.\nabla\right)T = \alpha(\nabla^2 T) \tag{1}$$

Momentum equation :

$$\rho\left(\vec{V}.\nabla\right)\vec{V} = \rho\vec{g} - \nabla p + \mu(\nabla^2\vec{V}) \tag{2}$$

Continuity equation :

$$\nabla.\vec{V} = 0 \tag{3}$$

Equation of state :

$$p = \rho RT \tag{4}$$

Boundary conditions :
Constant temperature condition : at the inner wall of hollow cylinder

$$T = T_s \tag{5}$$

At the hollow cylinder outer wall : No Slip Condition

$$\vec{V}.\hat{n} = 0 \tag{6}$$

The cylinder wall is considered to be at a constant temperature (Fig. 1) at the inner surface since, the problem was formulated whilst taking into consideration of phase change material which takes place at constant temperature condition. Since, the cylinder has some thickness it will experience some drop in temperature as it reaches the outer surface however, the thermal conductivity is high for aluminium the temperature at outer wall was calculated to come $T_{ow} = 397.97\ K$ which is almost equal to the inner wall temperature.

At the pressure outlet, atmospheric pressure is considered and if there is any generated backflow it will have the free stream temperature.

$$p = p_{atm}\ ;\ p_{gauge} = 0\ MPa\ ;\ T = T_{\infty} \tag{7}$$

Energy equation after applying the necessary condition that will be used for conduction in the fins :

$$\nabla^2 T = 0 \tag{8}$$

Equation (8) will be solving the heat conduction for the fin. This equation requires two boundary condition one of which is the temperature at the base and other no heat conduction at the tips. However, the solution of equation for annular fins is more typical then the rectangular.

For the case of simple hollow cylinder with keeping the base temperature constant the heat transfer is calculated by empirical correlations derived by Churchill and Chu [10], equation (14). The surrounding fluid is air, the fluid properties will be taken at the film temperature T_f,

$$T_f = \frac{T_w + T_{\infty}}{2} \tag{9}$$

Rayleigh number (which is on the basis of the tube outer diameter) is calculated on the basis of the following relation:

$$Ra = \frac{g\beta(T_w - T_f){D_o}^3}{\vartheta\alpha} \tag{10}$$

The Rayleigh number on the fin spacing for the finned cylinder with fin spacing (S) is calculated by the relation :

$$Ra_s = \frac{g\beta(T_w - T_f)S^3}{\vartheta\alpha}\left(\frac{S}{D_o}\right) \tag{11}$$

From the newton's law of cooling, the total heat transfer from the outer surface is :

$$Q = hA_t(T_w - T_{\infty}) \tag{12}$$

Where, the average heat transfer coefficient (h) is calculated from the definition of Nusselt number :

$$Nu = \frac{hD_o}{k} \tag{13}$$

for the fluid and the Nusselt number is being calculated from the Churchill's relation :

$$Nu = \left[0.6 + \frac{0.387(Ra)^{1/6}}{\left\{1+\left(\frac{0.559}{Pr}\right)^{9/16}\right\}^{8/27}}\right]^2 \tag{14}$$

On solving for the case of simple tube and with the free stream temperature $T_\infty = 298K$, the Rayleigh number is $Ra = 70363.21$, which is well within the range of laminar flow natural convection ($10^4 \leq Ra \leq 10^7$). The Nusselt number using equation (14) gives the value $Nu = 7.81$. Now with use of equation (13) average heat transfer coefficient h is calculated coming out to be $h = 9.38\ \frac{W}{m^2K}$. Finally, the heat flux is calculated to be $\dot{q} = 938.11\ \frac{W}{m^2}$.

The governing equations from (1)-(5) is integrated over the control volume and then discretized by finite volume method. The computational software used is Ansys FLUENT by imposing the boundary conditions (6)&(7). The SIMPLE scheme has been used with pressure body weighted forced and second order upwind for energy. The final values obtained after the simulation for 1707k (17 lakhs) cells the heat flux was $\dot{q}_{cfd} = 936.79\ \frac{W}{m^2}$, with heat transfer coefficient $h_{cfd} = 9.36 \frac{W}{m^2K}$ and the Nusselt number $Nu_{cfd} = 7.80$. Therefore, the accuracy between the simulation and analytical calculation came out to be very high with error of only 0.14%. The grid independence test was also performed as shown in Fig. 3. The results showed us that the heat flux values coming from the solution performed by Ansys FLUENT are dropping initially and then they became steady after the 17 lakhs elements and the heat flux at the inner wall is $\dot{q}_{inner} = 1171.03\ \frac{W}{m^2}$

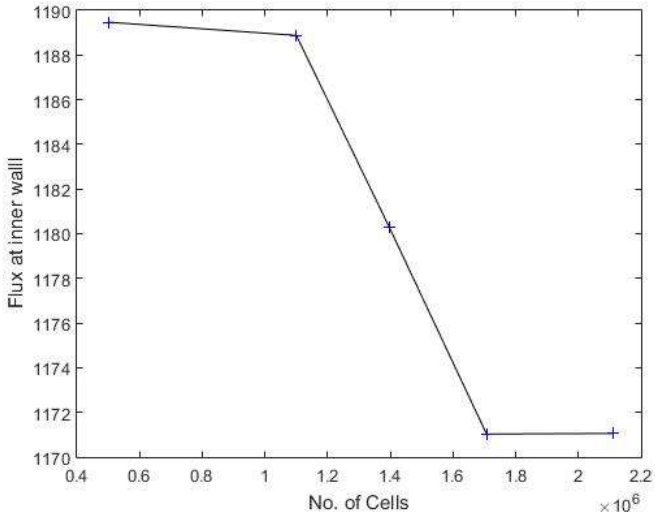


Fig. 3: Grid Independence Test.

3. Result and Discussion

After verifying the simulation for unfinned hollow cylinder we went forward with the CFD simulation for the cases of N=0,4,6,8,10,12,14,16,18,20. The temperature plume and the velocity profile for the standard unfinned cylinder case are shown in fig. 4 and fig. 5 respectively.

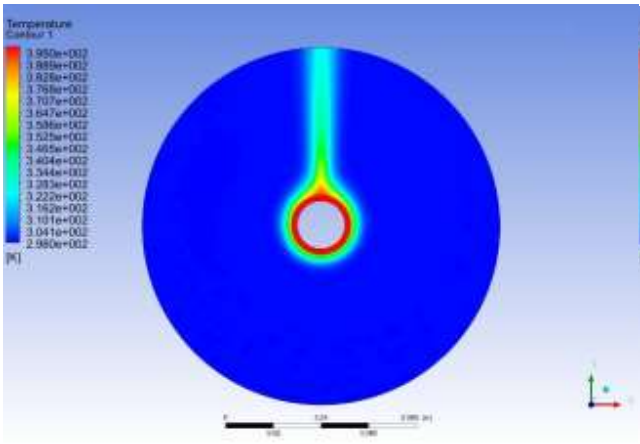


Fig. 4: Temperature Contour for Cross section.

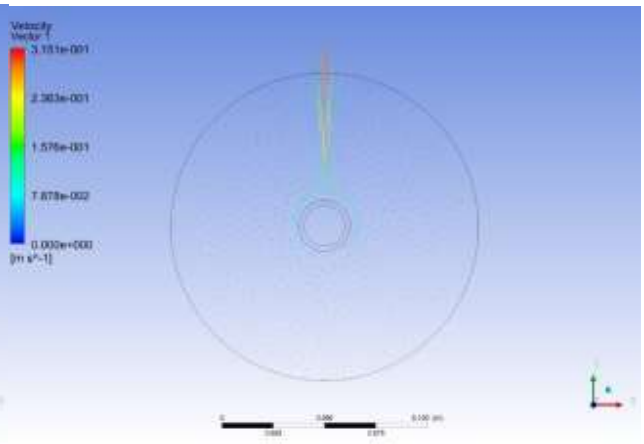


Fig. 5: Velocity Profile for cross section.

The temperature plumes for the rest of the cases are shown in table 2 containing fig. 6-14.

Table 2: Showing temperature plumes along the length for different cases.

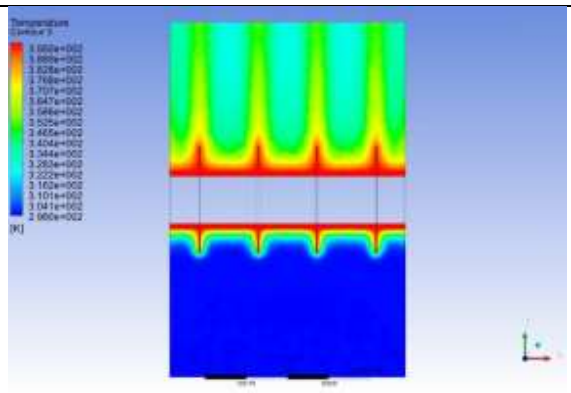


Fig. 6: Temperature Plume for 4 fin arrangement.

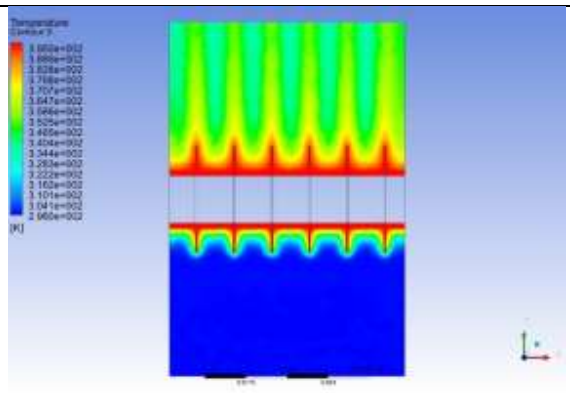


Fig. 7: Temperature Plume for 6 fin arrangement.

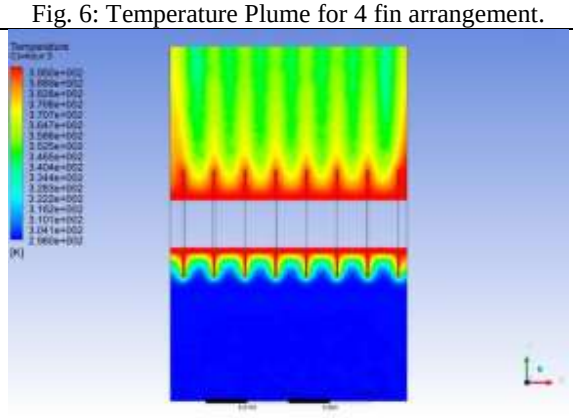


Fig. 8: Temperature Plume for 8 fin arrangement.

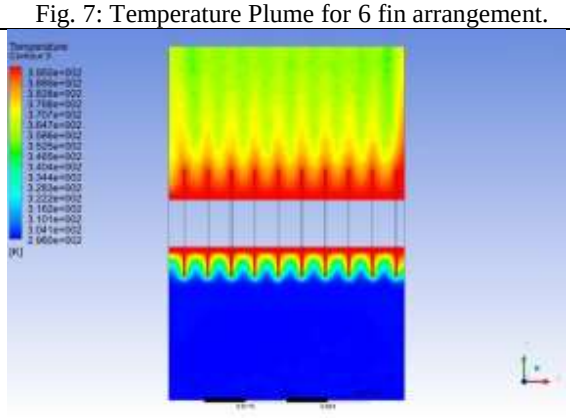


Fig. 9: Temperature Plume for 10 fin arrangement.

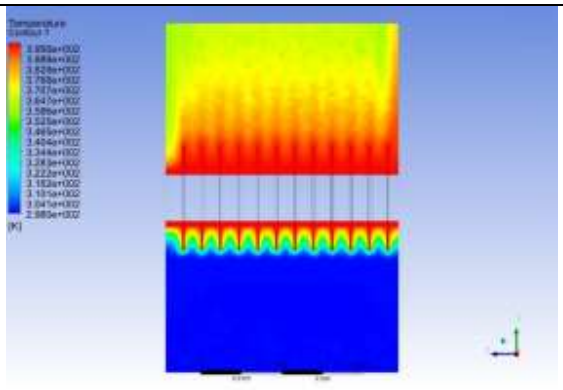


Fig. 10: Temperature Plume for 12 fin arrangement.

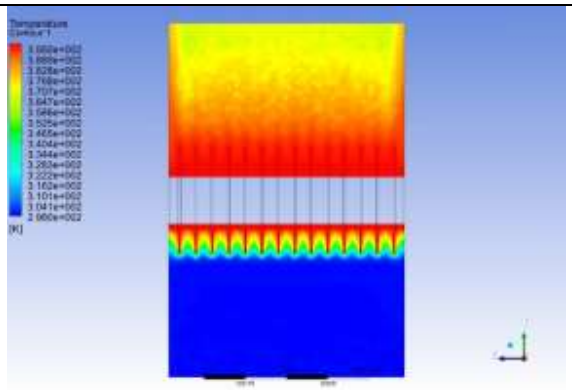


Fig. 11: Temperature Plume for 14 fin arrangement.

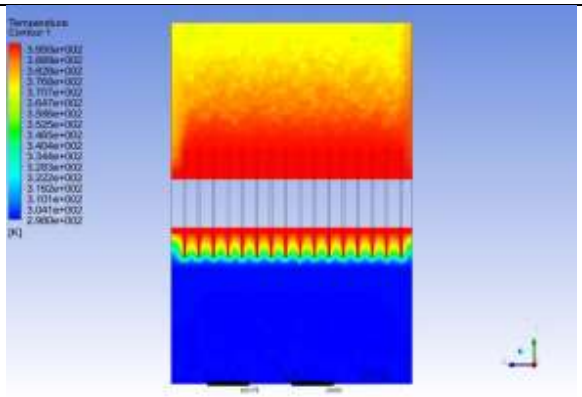


Fig. 12: Temperature Plume for 16 fin arrangement.

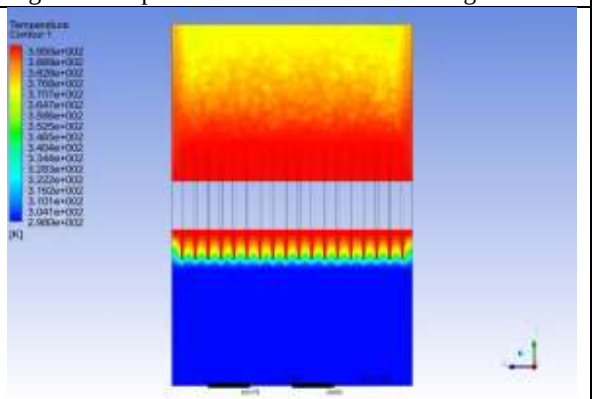


Fig. 13: Temperature Plume for 18 fin arrangement.

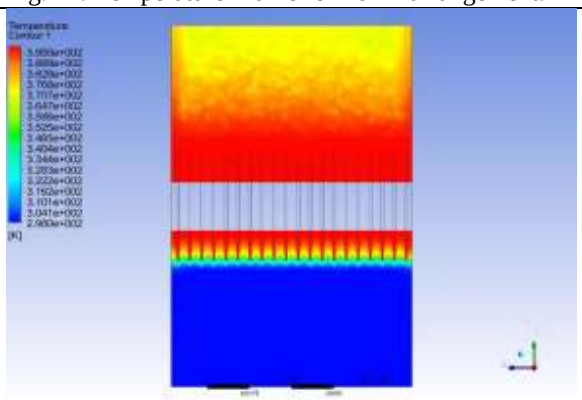


Fig. 14: Temperature Plume for 20 fin arrangement.

The Fig. 15 shows the relation between Rayleigh number and the number of fins.

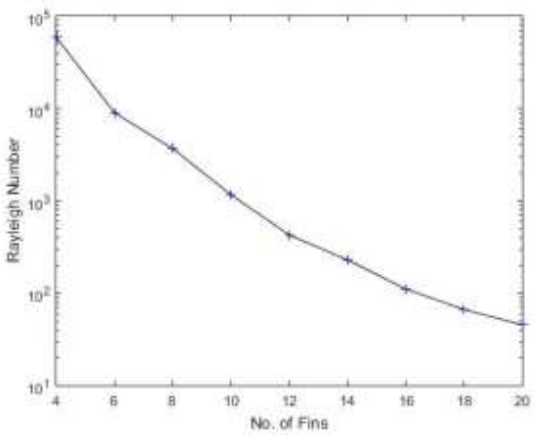


Fig. 15: Rayleigh No. vs No. of fins.

It can be deducted from the plot that for the same boundary conditions the Rayleigh number is initially dropping steadily therefore the y scale had to be taken in logarithmic scale. The Rayleigh number on the basis of fin spacing for 10 fins $Ra_{10} = 1922.97$ values going further down till Rayleigh for 20 fins $Ra_{20} = 45.479$. The following Fig. 16 shows the plot of Nusselt number and the number of fins.

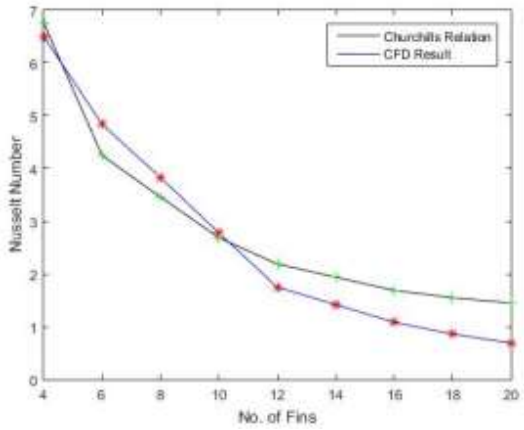


Fig. 16: Nusselt no. vs No. of fins.

There are two plots, one of the values of the Nusselt number calculated from the (Churchill's relation) equation (14) and the other plot is from the CFD data. Both the curves area showing gradual drop in the Nusselt number values. The fig. 17 and fig. 18 shows the plot for heat flux and the total heat transfer (from the cylinder to the outside air). From the plot of heat flux fig. 17 it is clear that the flux is fluctuating as the no. of fins is increasing till the number of fins are 12, then the heat flux decreased with the increase in number of fins hence, for the designing of such systems the number of fins can be selected on the basis of one's requirement of the heat flux. The fig. 18 shows us that even though heat flux is decreasing but the total heat transfer is continuously increasing, it is because the total surface area of the system is increasing even though the heat transfer coefficient is gradually decreasing as it can be deducted from the heat flux plot and equation (12).

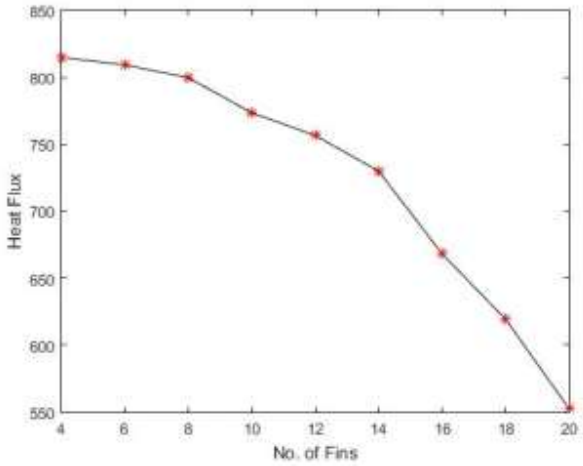


Fig. 17: Heat Flux vs No. of Fins.

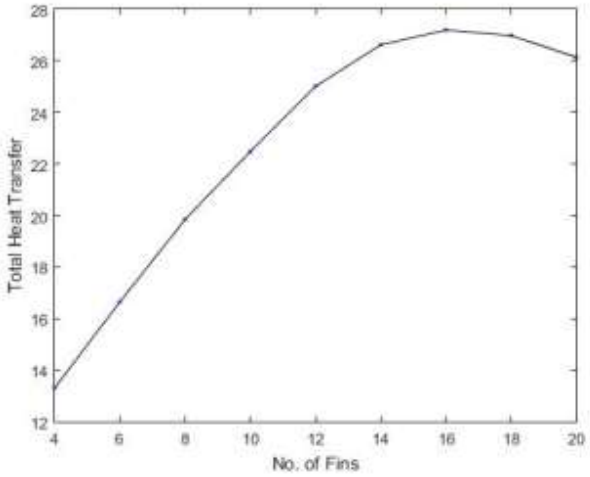


Fig. 18: Total Heat transfer vs No. of fins.

It can be inferred that the scope of optimizing is limited since, the total heat transfer is increasing with the increasing in number of fins till the 16 fins and then the total heat transfer started to decrease as we increasing the fins from 16 to 18 and 20. Moreover, the heat flux is dropping as the number of fins are increasing. The next fig. 19 is showing the most significant result of the research, the plot of effectiveness with respect to the number of fins. It can also be deduced that, as we increasing the number of fins the effectiveness is increasing at the steady rate, with maximum effectiveness $\epsilon = 3.63$ for the case of N=16 and then the effectiveness starts to decrease.

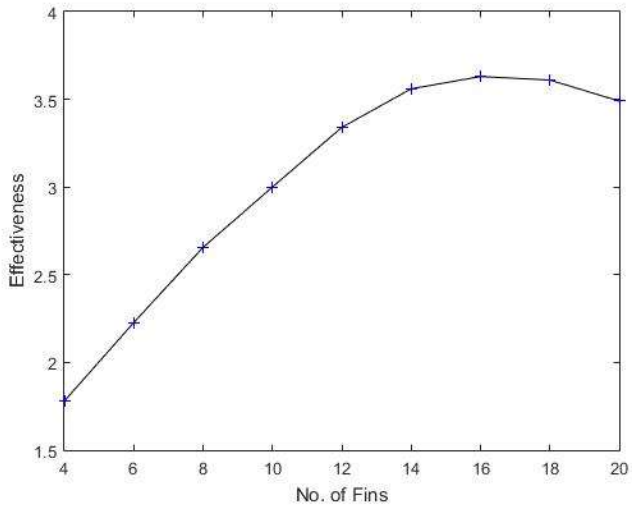


Fig. 19: Effectiveness vs No. of fins.

4. Conclusion

- From the numerical simulation of the various cases it can be concluded that the fluctuation of temperature is very gradual and slow as it should be in a laminar flow natural convection
- The analytical and numerical solution had an error of 0.14% only.
- The Rayleigh number decreases as the number of fins increases for the case of laminar flow natural convection.
- On comparing the Nusselt number values according to the Churchill's equation and from the CFD simulations, the error was only 1.74%.
- The plots of heat flux showed that optimization for the given cases is very limited.

- The overall heat transfer is increasing with number of fins up till 16 fins and then it decreases. Thus, the total heat transfer can be optimized for such natural convection cases and the maximum heat transfer is for 16 fins at this given length.
- Lastly, the variation of effectiveness concludes that the effectiveness can also be optimized for practical use and the maximum value of effectiveness is achieved in the case of 16 fins.
- The research showed us the temperature contours, heat flux, convective heat transfer coefficient and effectiveness of hollow cylinder with annular fins with constant temperature conditions and it can be stated that the values change gradually. Moreover, the total heat transfer and effectiveness can be maximized and one should keep these data in mind before designing similar thermal systems in industrial applications.

References

[1] J. R. Welling, C. B. Wooldridge, "Free convection heat transfer coefficients from rectangular vertical fins," *J Heat Transf.,* vol. 87, pp. 439-44, 1965.

[2] F. Harahap, F. McManus, "Natural convection heat transfer from horizontal rectangular fin arrays," *J Heat Transf.*, vol. 89, pp. 32-38, 1967.

[3] B. Singh, S.K. Dash, "Natural convection heat transfer from a finned sphere," *Int J Heat Mass Transf.,* vol. 81, pp. 305-24, 2015.

[4] A. D. Kraus, A. Aziz, J. Welty, *Extended surface heat transfer*. New York: John Wiley & Sons, 2001.

[5] J. R. Senapati, S. K. Dash, S. Roy, "Numerical investigation of natural convection heat transfer over annular finned horizontal cylinder," *Int J Heat Mass Transf*., vol. 111, pp. 149-59, 2016.

[6] J. R. Senapati, S. K. Dash, S. Roy, "3D numerical study of the effect of eccentricity on heat transfer characteristics over horizontal cylinder fitted with annular fins," *Int J Heat Mass Transf.,* vol. 108, pp. 28-39, 2016.

[7] S.A. Nada, M.A. Said, "Effects of fin geometries, arrangements, dimensions and numbers on natural convection heat transfer characteristics in finned-horizontal annulus," *Int J Heat Mass Transf*., vol. 137, pp. 121-37, 2019.

[8] S. Acharya, S.K. Dash, "Natural Convection heat transfer from a horizontal hollow cylinder with internal longitudinal fins," *Int J Heat Mass Transf*, vol. 134, pp. 40-53, 2018.

[9] D. Sun, Q. Shen, Y. Xu, T. Jin, X. Zhao, N. Zhang, K. Wu, Z. Huang," Natural Convection heat transfer along vertical cylinder heat sinks with longitudinal fins," *Int J Heat Mass Transf.,* vol. 100, pp 457-64, 2015.

[10] S. W. Churchill, H. H. S. Chu, "Correlating equations for laminar and turbulent free convection from a horizontal cylinder," *Int J Heat Mass Transf.,* vol. 18, pp. 1049-53, 1975.

This article has been accepted for inclusion in a future issue of this journal. Content is final as presented, with the exception of pagination.

A 12.08-TOPS/W All-Digital Time-Domain CNN Engine Using Bi-Directional Memory Delay Lines for Energy Efficient Edge Computing

Aseem Sayal, *Student Member, IEEE*, S. S. Teja Nibhanupudi, *Student Member, IEEE*, Shirin Fathima, and Jaydeep P. Kulkarni, *Senior Member, IEEE*

***Abstract*— In this article, we demonstrate an energy efficient convolutional neural network (CNN) engine by performing multiply-and-accumulate (MAC) operations in the time domain. The multi-bit inputs are compactly represented as a single pulse width encoded input. This translates into reduced switching capacitance (C_{DYN}), compared to baseline digital implementation, and can enable low power neural network computing in an edge device. The time-domain CNN engine employs a novel bi-directional memory delay line (MDL) unit to perform signed accumulation of input and weight products. The proposed MDL design leverages standard digital circuits and does not require any capacitors and complex analog-to-digital converters (ADCs) to realize the convolution operation, thereby enabling easy scaling across the process technology nodes. Four speed-up modes and a configurable MDL length are supported to address throughput versus accuracy trade-off of the time-domain computing approach. Delay calibration units have been accommodated to mitigate the process variation induced delay mismatch among concurrently operating MDL units. The proposed time-domain MDL design implements a LeNet-5 CNN engine in a commercial 40-nm CMOS process achieving an energy efficiency of 12.08 TOPS/W, a throughput of 0.365 GOPS at 537 mV in the 16× speed-up mode. 40-nm CMOS test-chip measurements over 100 MNIST images show 97% classification accuracy. Simulation results over the entire 10 000 MNIST validation dataset images taking into account the circuit non-ideal effects of the MDL-based time-domain approach show a classification accuracy of 98.42%. The test-chip is operational down to the near-threshold voltage (up to 375 mV) while maintaining the classification accuracy over 90% in the 1× speed-up mode. Furthermore, two methods of scaling MDLs to multi-bit weights are proposed. Simulation results for 1000-class AlexNet over 50 000 ImageNet validation dataset images show classification accuracy loss within 1% when compared with software implementation. The proposed MDL based time-domain approach performing 1-bit/8-bit weight and 8-bit input MAC operations when compared with the corresponding baseline digital implementations shows 2.09×-2.32× higher energy efficiency and 2.22×-3.45× smaller area.**

***Index Terms*— AlexNet, bi-directional memory delay line (MDL), binary neural network, convolutional neural network (CNN), energy efficient edge computing, ImageNet, LeNet-5, MNIST, multiply-and-accumulate (MAC), time-domain processing.**

I. Introduction

With the rapid progress in machine learning (ML) algorithms coupled with performance improvements in computing resources, there has been an unprecedented increase in the deployment of cognitive devices in various applications such as image classification, speech recognition, object localization, facial recognition, and so on [1]–[3] (see Fig. 1). In particular, convolutional neural networks (CNNs), a class of artificial neural network are extensively used for many such ML applications, due to their state-of-the-art classification accuracy at a much lesser complexity compared to their fully connected network (FCN) counterpart [4], [5]. However, the CNN inference process requires intensive compute and memory resources making it challenging to implement in energy constrained edge devices. For example, the widely known CNNs such as AlexNet [3] and VGG [6] comprise 60 million and 138 million filter weights, respectively, which are used to compute 724 million and ≈15.5 billion multiply-and-accumulate (MAC) operations [4]. Such an enormous number of MAC operations consume a significant fraction of a CNN accelerator's total power budget [7], [8]. Thus, making MAC operation energy efficient is extremely important.

In this article, a time-domain MAC computing approach is proposed by leveraging the concept of a time accumulator. The key attributes of the proposed design include: 1) bi-directional memory delay lines (MDLs) performing time-domain signed MAC operations; 2) multi-precision filter weight support (signed/unsigned 1–8 bits); 3) 16 filters each supporting 2 × 2 sub-sampling (maximum pooling) and averaging; 4) all-digital, technology scalable design without requiring any capacitors, analog-to-digital converters (ADCs), and/or frequency generators/modulators; 5) near threshold voltage operation; and 6) 4 speed-up modes supporting 1–16× throughput improvement by quantizing 4 LSBs of input activation. An energy efficient CNN engine implemented in a commercial 40-nm CMOS process (see Fig. 17) is demonstrated.

This article is organized as follows. Section II describes the background of this work and discusses the basics of CNNs and motivation for time-domain computation. Section III presents

Manuscript received April 17, 2019; revised July 5, 2019 and August 24, 2019; accepted August 26, 2019. This article was approved by Guest Editor Mingoo Seok. This work was supported in part by AMD, Austin, TX, USA, and in part by The University of Texas at Austin, USA. *(Corresponding author: Aseem Sayal.)*

A. Sayal, S. S. T. Nibhanupudi, and J. P. Kulkarni are with the Department of Electrical and Computer Engineering, The University of Texas at Austin, Austin, TX 78712 USA (e-mail: aseem.sayal@utexas.edu; subrahmanya_teja@utexas.edu; jaydeep@austin.utexas.edu).

S. Fathima was with the Department of Electrical and Computer Engineering, The University of Texas at Austin, Austin, TX 78712 USA. She is now with Apple Inc., Cupertino, CA USA (e-mail: shirin15595@gmail.com).

Color versions of one or more of the figures in this article are available online at http://ieeexplore.ieee.org.

Digital Object Identifier 10.1109/JSSC.2019.2939888

0018-9200 © 2019 IEEE. Personal use is permitted, but republication/redistribution requires IEEE permission.
See http://www.ieee.org/publications_standards/publications/rights/index.html for more information.

This article has been accepted for inclusion in a future issue of this journal. Content is final as presented, with the exception of pagination.

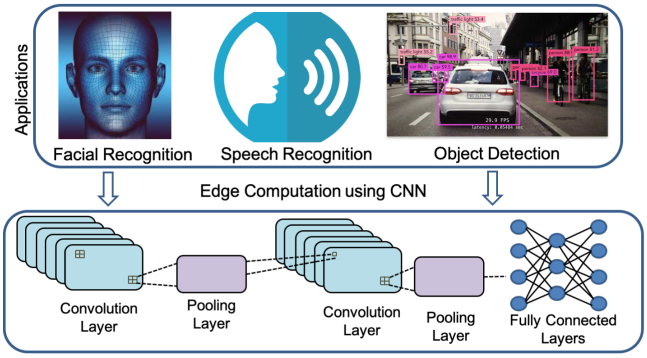


Fig. 1. Edge computation using CNN.

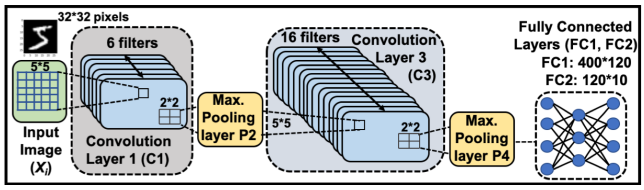


Fig. 2. LeNet-5 CNN [9] architecture.

the concept of proposed time-domain MAC computation using time accumulators, circuit design, architecture, and implementation details. Various design trade-offs along with their mitigation strategies are presented in Section IV. Section V presents the 40-nm CMOS test-chip measurement results. A case-study is also presented in this section comparing the energy efficiency of the proposed time-domain circuit with the baseline digital approach. Section VI concludes this article with the key findings.

II. Background

A. Convolutional Neural Network

A generic CNN consists of convolution layers, pooling layers, activation layers, and FCN layers. The convolution layer is the core building block of a typical CNN. Each convolution layer implements multiple trainable filters which are used to extract feature-like edges, gradients, colors, etc., in an image. Fig. 2 shows the LeNet-5 CNN [9] architecture which can be used to classify the hand-written digits (MNIST dataset [9]). During the training phase, the weights of all the filters for each layer are determined using a training algorithm (such as back-propagation [10], [11]) on the training MNIST dataset. Each filter is convolved across the width and the height of input activation, computing the dot product between the weights of the filter and the input activation, producing a 2-D output activation map for a given filter. As a result, the neural network learns to filter weights that get activated when specific types of features are detected at specific spatial positions in the input activation. During the inference phase, when the test data are presented to the CNN layers, key features (e.g., edges, gradients, color changes, orientation in a handwritten digits MNIST dataset, etc.) in the input activation are extracted at each layer. The major operation in CNNs is the MAC operation given by (1), which is computed by performing a dot product of a weight matrix and an input image matrix [4]. The MAC

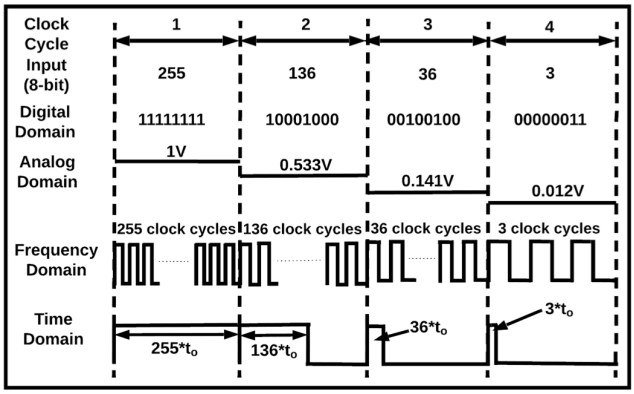


Fig. 3. Representation of 8-bit inputs in different signal domains.

value is averaged out to compute the multiply-accumulate-average (MAV) value [given by (2)], which ensures that the output value does not exceed the range

$$\text{MAC} = \sum_{i=1}^{N} (X_i \times w_i) \tag{1}$$

$$\text{MAV} = \frac{1}{N} \sum_{i=1}^{N} (X_i \times w_i) \tag{2}$$

where N is the number of products per MAC, X_i is the textitith input pixel value, and w_i is the ith weight value.

Typically, an activation layer is used between two consecutive convolutional, pooling, or fully connected layers. The purpose of this layer is to introduce nonlinearity into a neural network. The rectified linear unit (ReLU) is the most commonly used activation layer which returns 0 if it receives any negative input and returns back the same value if it is positive. Pooling (sub-sampling) is performed to reduce the data size feeding into the next layer [12], [13]. Max-pooling is typically used for the sub-sampling operation which chooses the maximum MAC value across a small output window (e.g., 2 × 2). This can reduce the memory footprint to store intermediate layer outputs by 75%, as the outputs of the pooling layers (P2 or P4) are stored instead of convolution layers (C1 or C3) [12]. Once the data size of input feature maps is reduced after passing through convolution and pooling layers, FCN layers are used. A typical FCN layer comprises a finite number of feature maps, each of size 1 × 1. Each of these feature maps is connected to all the feature maps of the previous layer. In LeNet-5 CNN, a fully connected layer (FC1) comprises 120 feature maps, each of which is connected to all the 400 nodes of the fourth layer (P4). Similarly, the last layer of LeNet-5 CNN is a fully connected layer (FC2) comprising 10 1 × 1 feature maps, each of which is connected to all 120 feature maps of FC1.

B. Motivation for Time-Domain Computing

As MAC operations constitute a significant portion of the total CNN power budget, it is worthwhile to consider various methods for compact data representation to improve the energy efficiency (see Fig. 3). The data in the digital domain are represented as a multi-bit digital vector [14], [15]

This article has been accepted for inclusion in a future issue of this journal. Content is final as presented, with the exception of pagination.

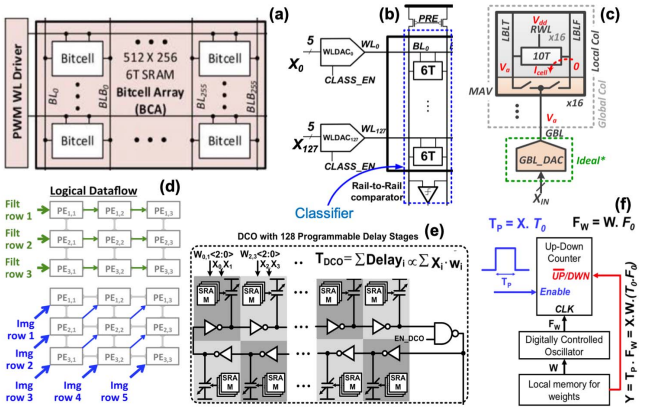


Fig. 4. Prior energy efficient ML accelerators in (a)–(c) analog voltage [16]–[18], (d) digital [4], and (e) and (f) time and frequency domains [19], [20].

[see Fig. 4(d)]. This form of data representation is implemented using higher number of nets, translating into high dynamic switching capacitance (C_{DYN}), and consequently higher power and area. A detailed case-study on the C_{DYN} comparison is presented in Section V-F.

In the analog domain approach, data are represented as a continuous varying voltage signal. Various design techniques using charge manipulation schemes and ADCs have been proposed to realize efficient MAC computations in a CNN accelerator. Analog approaches [16]–[18] compute MAC operation in the analog voltage domain using a static random access memory (SRAM) array, capacitors, and data converters [ADCs and digital-to-analog converters (DACs)]. In these approaches, input pixel data are either encoded as the pulse width modulated (PWM) signal [16] or pulse amplitude modulated (PAM) [17] signal, and applied on the wordline [see Fig. 4(a) and (b)]. The MAC operation is performed by summing up the read current of simultaneously accessed bitcells. The bitline voltage in this case represents the sum of products (SRAM bit weight $\times$ wordline input pixel). The bitline current summation approach is susceptible to: 1) process variations in the nano-scale SRAM bitcell transistors; 2) functional failures due to bit-flips as a result of long duration wordline activations and/or large bitline voltage differential; and 3) the possibility of corrupting a weak bit by shorting it to a strong bit storing opposite value due to concurrent wordline activations. In the design approach discussed in [18], the input pixel digital bit-stream is first converted into an analog voltage using DAC, and then used to precharge the bitline to compute the MAC operation [see Fig. 4(c)] using a ten-transistor SRAM bitcell. This approach mitigates the process variation induced bitcell current variation as well as bit-flip scenarios at the expense of a larger bitcell area. However, the finite voltage headroom and the sensitivity of circuit parameters to slight change in analog domain signals limit the voltage scalability, thereby degrading the MAC accuracy.

In the frequency domain approach, data are represented as signals with varying frequency using ring oscillators or *RC* loaded circuits. In [19] and [20], MAC operations are computed in the frequency domain using a digital controlled oscillator (DCO) with either resistor or capacitor loading. Various nodes of a ring oscillator are loaded with different capacitor banks to alter the *RC* time constant of the oscillator [see Fig. 4(e) and (f)]. The capacitor value is controlled by the SRAM bitcells storing the weight. This approach makes the design sensitive to parasitic diffusion capacitance of the DCO. The added *R* and *C* components need to be larger than the diffusion capacitance to linearly modulate the ring oscillator frequency in response to the weight change. In addition, adding a capacitor at every node of a continuously running ring oscillator increases the total C_{DYN}, and consequently the power dissipation. Furthermore, implementing such binary weighted capacitor banks can occupy significant area, thereby degrading the area efficiency. In [20], the MAC operation is performed in the frequency domain by counting the number of binary weighted frequency pulses (representing multi-bit weights) in a given PWM input signal. Thus, large range frequency generators/modulators limit the performance scalability of such frequency domain approaches. Moreover, larger magnitude inputs would result in higher toggle activity incurring higher switching power.

In the time-domain computing approach, data can be represented as PWM inputs or pulse position modulated inputs or a combination of thereof. In [21], the time-domain analog-to-digital mixed-signal processing (TDAMS) approach is proposed to implement time-domain binary neural networks. TDAMS uses the time difference in the rising edges to generate variable delays in order to realize the MAC operation of 1-bit input activation and weight value. This approach further employs fully spatially unrolled architecture where every memory has its dedicated processing element (PE) to increase its energy efficiency. A time-mode adder circuit is proposed in [22] to realize a trans-linear principle in time. The exponential relationship between the voltage and time in an *RC* circuit is leveraged to implement time adders.

In the proposed work, a multi-bit digital bit-stream is encoded as a single PWM signal with its pulse width representing the magnitude of the input data. This results in multi-bit data to single data-signal compaction resulting in reduced C_{DYN} compared to the conventional digital data representation. Furthermore, the time-domain computing approach can leverage standard digital gates with full rail-to-rail voltage swing outputs. This mitigates the reduced voltage headroom challenges encountered in an analog voltage domain approach enabling an ultra-low voltage operation. Additionally, the time-domain approach does not require multiple clock sources unlike frequency domain approaches which result in reduced C_{DYN}. Unlike the frequency domain, the toggle activity does not depend on the input magnitude in the proposed time-domain approach. Thus, although the time-domain approach results in slower throughput due to its sequential operation, it can be a promising approach for realizing MAC computations, especially in energy constrained edge devices.

III. Proposed Time-Domain CNN Engine Design

A. Concept of Time-Domain MAC Computation

The concept of time domain MAC computation using PWM inputs is illustrated in Fig. 5. In this example, the MAC

This article has been accepted for inclusion in a future issue of this journal. Content is final as presented, with the exception of pagination.

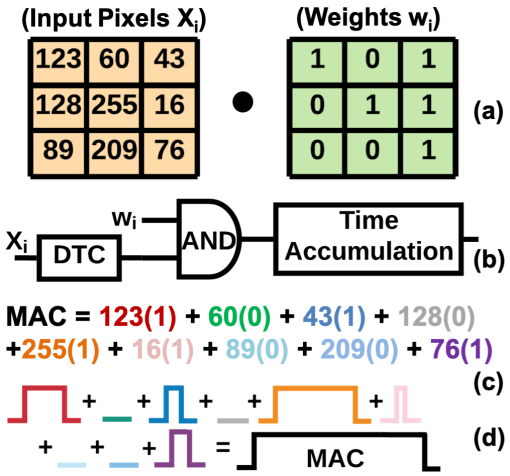


Fig. 5. Concept of time-domain MAC operation. (a) Dot product operation of the input pixel matrix and the weight matrix. (b) Time-domain MAC circuit concept. (c) MAC operation in the digital domain. (d) MAC operation in the time domain.

operation is performed by adding the products of a 3×3 weight matrix and an input pixel matrix [see Fig. 5(a) and (c)]. Binary weights [23]–[25] are used to simplify the discussion. However, the time-domain approach is scalable to multi-bit weight values. An input pixel value is encoded into a PWM signal using a digital-to-time converter (DTC). Then, the input PWM signal is multiplied by the corresponding weight bit using an AND gate. This time-encoded product signal is then passed onto the time accumulator circuit [see Fig. 5(b)] to compute the MAC operation in the time domain. Sequentially, all input pixel values are encoded as PWM signals, and its product with respective weight bit is loaded on the time accumulator circuit. Thus, all time-encoded products are applied onto the time accumulator circuit, and the width of these timing pulses gets accumulated to realize the MAC operation in the time domain [see Fig. 5(d)]. The time accumulator circuit will be discussed in detail in Section III-D4.

B. Architecture Overview

The proposed time-domain CNN architecture performing the MAC operation of 8-bit inputs with 1-bit weights is shown in Fig. 6. First, 16 PWM signals (generated using the pulse generator module) are selected based on the 8-bit input image pixel value. The pulse selector acts as a DTC, converting the digital image pixel input into a time-encoded PWM signal. The higher the pixel value, the larger the pulse width of the time-encoded input. The generated PWM signal is passed through a pulse gating logic to avoid repetitive products of same input being added to the MAC output. This ensures that the time-encoded input pixel signal is utilized only once in the time-domain MAC computation. This gated PWM signal is then multiplied by the binary weight (0 or 1 or -1) using an AND gate. Multiplication by weight bit "0" results in no toggling at the AND output, while multiplying by weight bit "± 1" results in PWM output at the AND gate which is the same as the input PWM signal. The weight bits are stored in the weight register, which is implemented as a cyclic shift register. The parallel-in

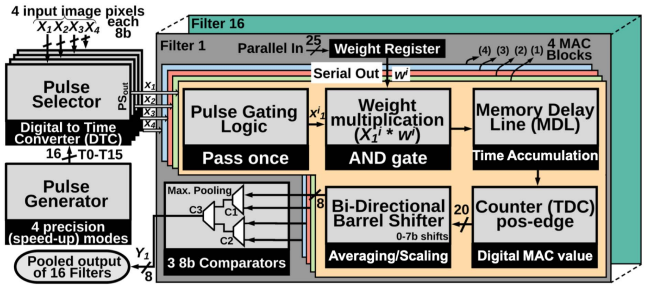


Fig. 6. Architecture of the proposed time-domain-based CNN engine.

and serial-out shift register is used to perform multiplication of the input pixel value and weight. The time-encoded product signal is then added using the proposed bi-directional MDL to perform the signed addition of the products for each MAC operation. The operation of the proposed MDL performing time-domain accumulation is discussed in detail in the next section. A 20-bit positive edge triggered up-down counter is followed by the MDL to convert the time-encoded MAC signal into digital value. It acts as a time-to-digital converter (TDC) for performing post-processing in the digital domain. This signal is right-/left-shifted using a 20-bit bi-directional barrel shifter to perform scaling and averaging after a MAC operation to compute the MAV output. The shift operation correctly scales the MAC output value before feeding it as an input to the next convolution layer. Once the shifter output value from four MDLs for each filter is obtained, the max-pooling operation (2×2 window) [12], [13] is performed using three 8-bit comparators. The pooled output from each filter is stored off-chip and reused as the input to the next convolution layer.

C. Data Flow Overview

Sixteen filters are implemented on-chip, where each filter block comprises 4 MAC blocks to perform signed time accumulation and 2×2 max-pooling. Each filter comprises a 25-bit weight register to store weights. In the C3 layer, 5×5 1-bit weights of each channel are stored in the weight register, and this process is repeated six times to perform the MAC operation. Four input pixel values encoded in the time domain are applied to these 16 filters using four pulse selector modules and a shared pulse generator module. The input activation and weight values (for all the channels) are stored off-chip and applied to the test-chip using a scan chain. The output activations (computed MAV values after pooling) from the scan out port of the scan chain are stored off-chip using the National Instruments PXIe system. Different operation modes (states) of the CNN engine such as the reset state, weight loading state, MAC computation state, shifting state, and comparison state are triggered sequentially by the top-level control logic depending upon the operating phase of the test-chip.

D. Circuit Description

1) Pulse Generator and Pulse Selector Modules: The pulse generation and selection methodology is adapted from [16].

This article has been accepted for inclusion in a future issue of this journal. Content is final as presented, with the exception of pagination.

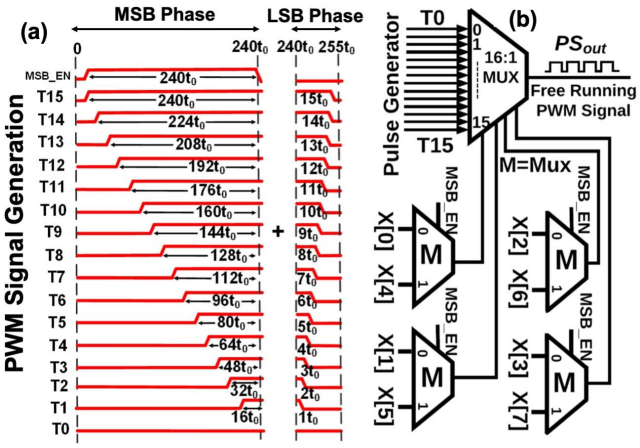


Fig. 7. (a) PWM signals generated by the pulse generator module. (b) Pulse selector circuit (adapted from [16]).

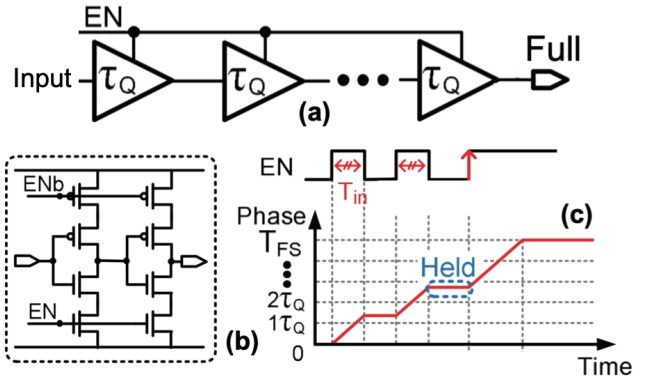


Fig. 8. (a) Time register circuit. (b) Gated delay cell. (c) Timing diagram [26].

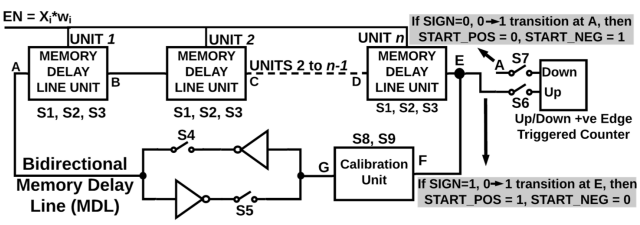


Fig. 9. Proposed bi-directional MDL performing time-domain MAC.

Sixteen free-running PWM signals (*T0–T15*) are generated in a pulse generator module such that the pulse width of each signal increments by 17 $\times$ t_o and varies in the range of 0 $\times$ t_o to 255 $\times$ t_o, as shown in Fig. 7(a). Here, t_o represents the minimum possible pulse width and equals half period of input clock (e.g., for input clock frequency of 25 MHz, t_o equals 0.5 $\times$ 40 ns = 20 ns). These pulses are generated in two phases: the MSB phase and the LSB phase. In the MSB phase, the pulse width is incremented by 16 $\times$ t_o, whereas in the LSB phase, it gets incremented by t_o. Thus, 256 $\times$ t_o or 128 input clock cycles (equals 1 *MAC_CLK* cycle) are consumed to generate these 16 PWM signals. To avoid overlapping of PWM signals between consecutive *MAC_CLK* clock cycles, an intentional delay of t_o is added at the start of each PWM signal (*T*0–*T*15). The input pixel value is then time-encoded using any of these 16 PWM signals in the MSB and LSB phases. 4 MSB bits of the input-pixel value (*X[7:4]*) select one of the 16 PWM signals for 240 $\times$ t_o duration in the MSB phase (when *MSB_EN* is held high) and 4 LSBs (*X[3:0]*) select one of the PWM signals in the remaining 15 $\times$ t_o duration in the LSB phase (when *MSB_EN* is held low). The selected PWM signals in both MSB and LSB phases are concatenated in the pulse selector module using one 16:1 multiplexer (MUX) and four 2:1 MUXes to time-encode the input pixel value *X[7:0]* as a free-running PWM signal (PS_{out}), as shown in Fig. 7(b). The pulse generation approach is not based on the logic path delay difference which is susceptible to pulse shrinking and expansion due to process variations. The proposed approach generates different PWMs based on the synchronous input clock operation. Thus, no shrinking and expansion effects are expected in the pulse generation circuit.

2) Pulse Gating Logic: As the pulse generator module operates continuously in every *MAC_CLK* period, a pulse gating logic is implemented to ensure that the product of input PWM pulse with the corresponding weight bit is applied only once to the MDL.

3) Input/Weight Product Computation: The PWM encoded pixel value is multiplied by the weight value using an AND gate. The weights are stored in a weight register, which is implemented as a 25-bit cyclic shift register. In the weight load phase, a shifter is initialized with filter weights for the convolution layer C1 or C3. In the MAC computation phase, each weight bit is serially shifted out to perform multiplication of the weight bit and the time-encoded input PWM signal using an AND gate.

4) Time Accumulation Using Bi-Directional Memory Delay Line: The proposed MDL design is derived from the concept of *time-register*, which is used in high precision TDC [26]. The property of time addition of two different input pulses is utilized to perform the accumulation operation in a MAC computation. The *time-registers* can perform the time addition and time storage using a string of gated delay cells, called the gated delay-line (GDL) which are controlled by an enable (*EN*) signal, as shown in Fig. 8(a) and (b) [26]. The phase increases when the *EN* pulse is high and held constant when *EN* is low [see Fig. 8(c)]. Hence, when an input pulse is received, the phase of the GDL is advanced by the amount of input pulse width and held when the input pulse becomes low. When the input pulse edge reaches the end of the GDL [phase equals the total full scale (TFS) value], a *Full* signal is asserted. The capacity of time-storage can be enlarged by increasing the number of gated delay cells. However, if *EN* is held low for a long duration, the gated delay cells can attain an arbitrary value due to tri-stated outputs. Thus, the *time-register* operation may pose a metastability risk when this GDL is used as a time accumulator during a MAC operation, which may often have zero product due to zero weight bit.

a) Bi-directional MDL: The time domain MAC computations are realized using the proposed Bi-directional MDL, which accumulates the product of weight bit and the time-encoded input pulse width (see Fig. 9). The MDL comprises

This article has been accepted for inclusion in a future issue of this journal. Content is final as presented, with the exception of pagination.

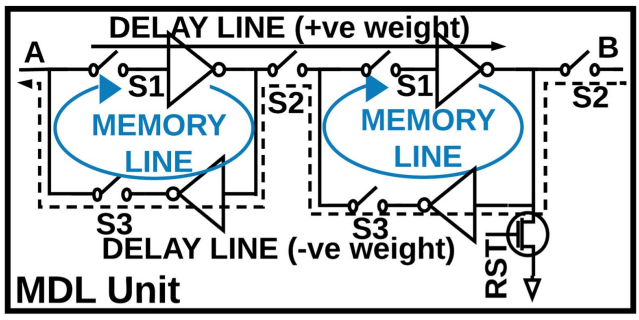


Fig. 10. Proposed MDL unit acting as a delay unit and a memory unit.

a string of delay units (MDL units) to perform signed time accumulation. The two ends of MDL (nodes A and E) are connected through an inverter. Each MDL unit comprises two cross-coupled inverter pairs, S1–S3 switches, and a reset logic (see Fig. 10). Each MDL unit is enabled by the *EN* signal. The product of time-encoded input pixel (X_i) and 1-bit weight (w_i) acts as a *EN* pulse and controls the MDL operating mode. During the time-accumulation phase, *EN* is held high and MDL acts either as a forward delay line (for positive products, S1 and S2 are ON) or a backward delay line (for negative products, S2 and S3 are ON), thus enabling bi-directional data flow emulating signed products. When *EN* becomes low, the MDL acts as a memory storage line and retains the MDL state vector using cross-coupled inverters (S1 and S3 are ON). Thus, the MDL unit can be realized as a memory or delay unit based on S1–S3 switch configurations (see Table I). The metastability risk during *EN* falling transition is resolved by the next incoming *EN* pulse, as the MDL is transformed into a chain of cascaded delay cells. In the case of positive weights (SIGN = 1), MDL state vector propagation takes place in the forward direction with switch S4 being turned on. However, in the case of negative weights (SIGN = 0), MDL state vector propagation takes place in the backward direction with switch S5 being turned on. An up-down counter is triggered (positive edge) whenever the MDL state vector string progresses towards either end of MDL (node A or node E), which translates time-domain product accumulation information into digital bits acting as a TDC. If the accumulated product pulse width exceeds the MDL full-length delay value, an overflow condition is detected, and the propagating edge is inverted (using S4 and S5, see Fig. 9) and applied at the beginning of MDL (node A). Thus, a finite length MDL can be used to perform long duration time domain accumulation using an up-down counter. The calibration unit consists of additional MDL units which can be added to the original MDL to mitigate the delay mismatch among concurrently running MDLs in the presence of process and temperature variations.

b) MDL timing diagram: Fig. 11 shows the MDL timing diagram to illustrate the MDL operation in more detail. Assuming that the initial state of MDL outputs is all "0s," and node A is held high (logic value is "1"). The first time-encoded product is loaded onto MDL and the logic value "1" at A is propagated through MDL units for the time duration when *EN*

TABLE I
SWITCH CONFIGURATIONS OF MDL, CALIBRATION UNIT, AND TDC

Switch	Logic Equation
S1	$\overline{EN} + (EN.SIGN)$
S2	EN
S3	$\overline{EN} + (EN.\overline{SIGN})$
S4, S8	SIGN
S5, S9	$\overline{SIGN}$
S6	$SIGN.\overline{START_NEG}$
S7	$\overline{SIGN}.\overline{START_POS}$

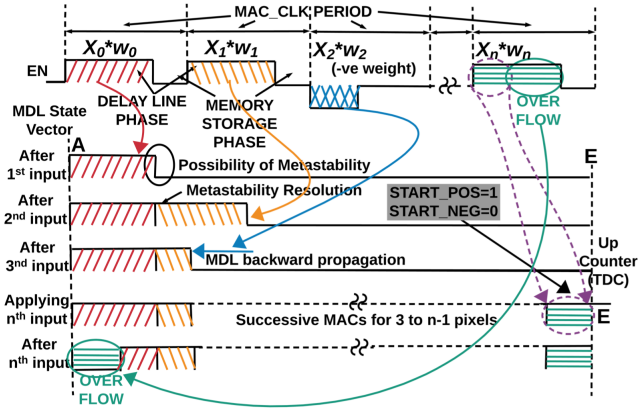


Fig. 11. Timing diagram of the proposed bi-directional MDL.

is held high. When *EN* becomes low, the logic value "1" might not get latched properly in the latest MDL unit propagating the *EN* pulse, thereby arousing a metastability issue. Since the MDL state vector is represented as a string of 1s followed by a string of 0s or vice versa, the metastability risk latching the correct value is at the transition of 1s string to 0s string. Thus, MDL may represent the input time-encoded product, which is off by 1 MDL unit delay. In the next *MAC_CLK* period, the second time-encoded product is applied by holding *EN* high and the state vector of "1s" advances through MDL for the time duration when *EN* is held high. The metastability risk (if any) from previous product accumulation gets resolved when this *EN* is applied, since MDL now acts as a delay line and the metastable node gets driven by the previous MDL unit. In the next *MAC_CLK* cycle, the third product of the time-encoded input PWM signal and the negative weight is applied. As observed in Fig. 11, state-vector propagation occurs in the reverse (backward) direction, i.e., from right to left. Once the state vector of "1s," reaches the end of MDL (node E), the 0→1 transition occurs and the counter value is incremented. The overflow value is loaded back on MDL through an inverter and a string of "0s" starts propagating through MDL. Thus, the 0→1 transition is detected at either end of MDL (node A or node E) when a string of "0s" followed by a string of "1s" is propagated. Thus, a finite MDL length along with an up-down counter can be used to perform signed time accumulation of long duration.

c) MDL design considerations for NMOS/PMOS drive strengths' mismatch and slew rate: The mismatch between the

This article has been accepted for inclusion in a future issue of this journal. Content is final as presented, with the exception of pagination.

drive strengths of NMOS and PMOS devices in the MDL units does not affect the accumulation operation. The counter value gets incremented whenever the $0 \rightarrow 1$ transition is observed at either end of MDL (node A or node E). $0 \rightarrow 1$ transition occurs at either end of MDL when a string of 0s followed by 1s is propagated through MDL. Thus, the MDL full-length delay equals the sum of fall delay (when 0s propagate through MDL) and rise delay (when 1s propagate through MDL) for all the MDL units. Since the counter gets incremented/decremented by 1 when the *EN* of pulse width equal to 1 MDL full-length delay (sum of equal number of rise and fall delays for all MDL units) is propagated, the relative difference between the rise and fall delays of individual MDL units does not affect the MDL accuracy.

All the MDL units have a fanout of 1. The layout of MDL is done using the commercial place and route (P&R) engineering design automation (EDA) tools to optimize for the timing and meet the slew rate specifications. All the MDL units are placed close to each other to optimize for the performance-power-area (PPA) metric. The optimally designed MDL block is instantiated (replicated) four times, in a filter for performing 2×2 max-pooling. The proposed time-domain CNN engine instantiates 16 such filters. Thus, all the MDLs have identical placement and routing. Thus, any potential slew rate mismatch due to random MDL unit cell placement and routing is mitigated by using identically designed and placed individual MDL blocks.

5) Time-to-Digital Converter: A 20-bit positive edge triggered, up-down counter is used to convert the time-encoded MAC value into the digital domain. The counter value is incremented when the $0 \rightarrow 1$ transition occurs at node E (if switch S6 is turned on and SIGN $= 1$) and is decremented when the $0 \rightarrow 1$ transition occurs at node A (if switch S7 is turned on and SIGN $= 0$). The configuration of switches S6 and S7 is determined based on *START_POS* and *START_NEG* signal values (see Table I). Whenever the $0 \rightarrow 1$ transition occurs at node E while accumulating negative products (SIGN $= 0$), *START_NEG* is set, whereas *START_POS* is reset. Similarly, the *START_NEG* signal is reset and the *START_POS* signal is set when the $0 \rightarrow 1$ transition occurs at node E while accumulating positive products (SIGN $= 1$), as shown in Fig. 9. If the $0 \rightarrow 1$ transition occurs at node E while accumulating positive products (SIGN $= 1$) and *START_NEG* is high, switch S6 remains turned off and the counter value is not incremented, since the negative residue loaded on MDL from the previous stage has not been fully flushed. Thus, the control logic determining the configuration of S6 and S7 switches ensures that the counter value is incremented and decremented correctly to compute signed MAC operation in the time domain.

6) Scaling and MAV Computation Using Bi-Directional Barrel Shifter: The counter output value is fed to the 20-bit bi-directional barrel shifter (supporting the left shift and the right shift up to 7 bits) to compute MAV and scaling operations.

The counter output value represents how many times the MDL full-length delay has been traversed. It does not represent the absolute MAC output value since the time-encoded input-pixel value and the counter output value are represented in different time scales. Thus, a scaling operation needs to be performed to restore the correct MAC value by incorporating the scaling factor. This scaling operation ensures that the correct MAC outputs in terms of counter values are applied as inputs to the next convolution layer. The *EN* pulse width of a unit input-pixel value is t_o, where $2 \times t_o$ is the input clock period (as discussed in Section III-D1, Fig. 7). This pulse width for a unit pixel-value can be controlled by varying the input clock frequency. The full-length delay of MDL, which is the delay between consecutive $0 \rightarrow 1$ transitions (when a string of "0s" followed by a string of "1s" propagates through MDL), is $M \times (Unit_{Rise_Delay} + Unit_{Fall_Delay})$, where M is the number of MDL units, $Unit_{Rise_Delay}$ is the rise propagation delay, and $Unit_{Fall_Delay}$ is the fall propagation delay of each MDL unit. This MDL full-length delay value can be controlled by varying the supply voltage or number of MDL units. The *EN* pulse width to increment counter by 1 is equal to the MDL full-length delay value. Thus, the scaling factor (multiple of 2^n by controlling the input clock frequency and the supply voltage) needs to be accounted to scale back the counter value, as given by (3). The counter output needs to be multiplied by this scaling factor to reflect the actual MAC output. Typically, t_o is less than the MDL full-length delay value. Thus, the shifter performs left shifts (multiplies) by n bits to restore the MAC output.

To perform the averaging operation, the right shift by appropriate number of bits is performed. It is worth mentioning that the averaging factor in the MAV computation operation is a multiple of 2^m, such that $2^m \geq N$, where N is the number of products in a MAC. For example, in the C1 layer $N = 25$, whereas averaging is performed by 32 by shifting right the scaled counter output from the above step by 5 bits. The impact of different averaging factors (25 versus 32) is mitigated by training the CNN using 2^m as the averaging factor. This step avoids any loss in the classification accuracy. Thus, the left shift and the right shift by appropriate number of bits are performed in the shifter to perform scaling and averaging operations, respectively

$$\begin{aligned}\text{ScalingFactor} &= \frac{EN \text{ pulse width of a unit counter value}}{EN \text{ pulse width of a unit input pixel value}} \\ &= \frac{M \times (\text{Unit}_{\text{Rise_Delay}} + \text{Unit}_{\text{Fall_Delay}})}{t_o} = 2^n. \end{aligned} \quad (3)$$

7) Pooling Using 8-bit Comparators: The sub-sampling operation using max-pooling across the 2×2 window is implemented to reduce the intermediate layer output memory footprint by 75%. This is achieved by four concurrent MDL operations and feeding the MDL shifter outputs to three 8-bit comparators (see Fig. 6). It should be noted that the max-pooling operation is not implemented in the time-domain since it requires MDL of very long length to accumulate pulse widths for all the products of a given MAC. Pooling in time-domain requires ORing of four long MDL state vectors to find the largest MDL state vector. Then, the largest MDL state vector needs to be converted back into the digital domain using finite length MDL and counter. Thus, the area

This article has been accepted for inclusion in a future issue of this journal. Content is final as presented, with the exception of pagination.

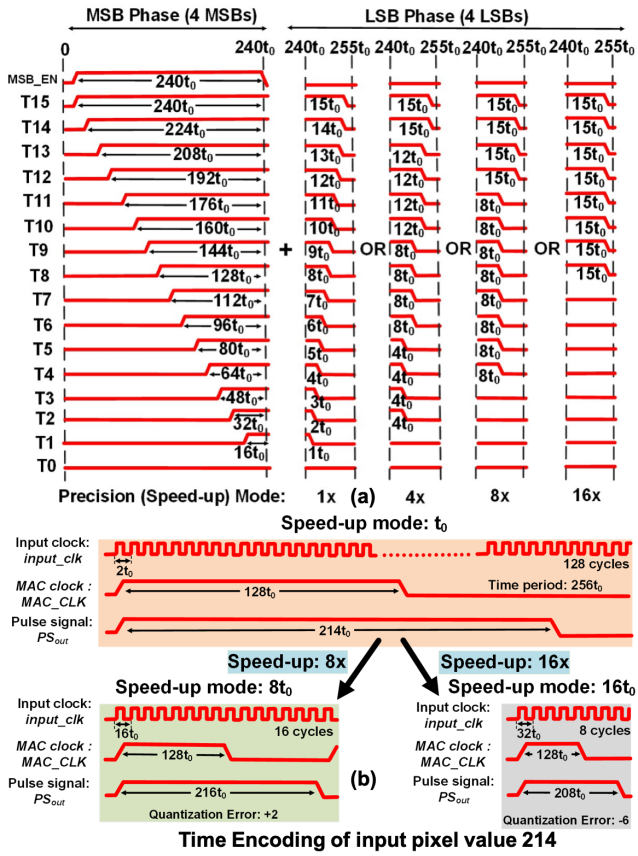


Fig. 12. (a) Quantization of input PWM signals supporting 1–16× speed-up. (b) Demonstration of 1×, 8×, and 16× speed-up modes to time-encode the input pixel value of 214.

overhead of implementing max-pooling in the time domain would be very high. In the proposed work, MDL of finite length is deployed by making use of counter which converts the partially computed time-domain MAC value to the digital domain (as discussed in Section III-D4b). The pooled output from each filter is stored off-chip and reused as the input to the next convolution layer.

IV. Design Trade-Offs and Mitigation Strategies

A. Throughput Improvement Versus Input Quantization

One of the main trade-offs of the time-domain-based MAC computation approach is the low throughput. For a n-bit input pixel value, 2^{n-1} input clock cycles are required to time-encode the input pixel value and perform its product with a weight bit. For example, for a 16-bit input pixel value, *MAC_CLK* period $= 32768 \times (2 \times t_o)$, which would require a longer duration to perform accumulation in the time domain. Hence, the throughput for larger bit-width inputs would be very small in the time-domain approach. To address the low throughput issue associated with the proposed time-domain approach, four speed-up modes are implemented to support 1–16× throughput improvement by quantizing 4-LSBs in the PWM signal. The varying pulse width pulses (*T0–T15*) are generated based on the speed-up mode in the LSB phase and concatenated with *X[7:4]* MSB pulses generated in the

Speedup Mode	1x	4x	8x	16x
Input clock period	$2t_o$	$8t_o$	$16t_o$	$32t_o$
MAC clock period	$256t_o$	$256t_o$	$256t_o$	$256t_o$
# input clock cycles/MAC clock cycle	128	32	16	8
Quantization error (input: 0-255)	0	±2	±4	±8

(a)

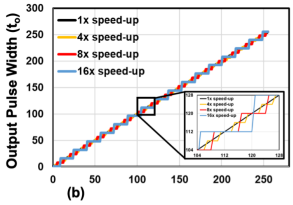


Fig. 13. (a) Throughput versus quantization error. (b) Linearity (pulse width versus input activation value) for 1–16× speed-up modes.

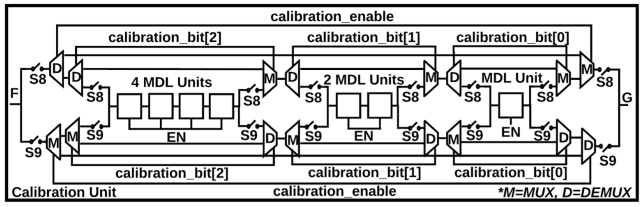


Fig. 14. Calibration unit circuit to mitigate process variations.

MSB phase [see Fig. 12(a)]. Thus, the speed-up mode results in 1–16× throughput improvement to time-encode the input pixel value, as shown in Fig. 12(a). With a higher speed-up mode, the input clock period represents a higher input magnitude. The LSB pulse width quantization steps are chosen to limit the quantization error to ± 0.5 × speed-up ratio [see Fig. 13(a)]. With a higher speed-up mode, the quantization step increases and the linearity between the pulse widths of time-encoded input and the input activation value decreases [see Fig. 13(b)].

B. Process Variation Mitigation Using Calibration Unit

To achieve correct max-pooling output due to concurrent MDL operation, the delay paths in all four MDLs need to be accurately matched for a given input PWM. However, the full-length delay value might not be the same in all four MDLs due to process mismatch or temperature variations. Therefore, a calibration unit is added to each MDL to offset the delay variations, which may exist due to process or temperature variations (see Fig. 14). Due to temperature variations, the full-length delay value of MDLs might get affected. To mitigate such delay variations (systematic delay error component) across all MDLs, the input clock frequency and the supply voltage can be tuned, to ensure that the equation (3) holds true for the same value of scaling factor n under temperature variation. The delay mismatch (random delay error component) due to random process variations among all MDLs for the same input is minimized by appropriately configuring *cal_bit[0:2]* and *cal_enable* signals to add a configurable delay of 1–7 MDL units.

C. Variable MDL Length for Residue Reduction

In the proposed CNN engine, configurable length MDLs are implemented to optimize the MDL full-length delay value. This enables controlling the residual time value in the MDL depending on the input clock frequency. Each MDL comprises 1–4 MDL blocks, where each MDL block comprises 16 MDL

This article has been accepted for inclusion in a future issue of this journal. Content is final as presented, with the exception of pagination.

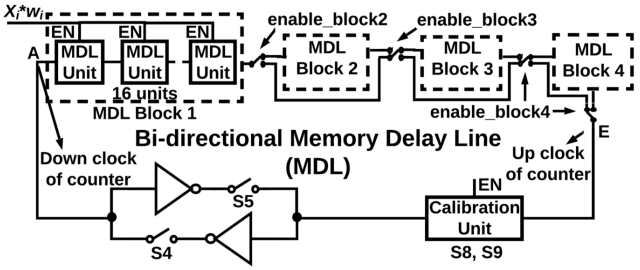


Fig. 15. Configurable MDL length (16–64 MDL units) to address accuracy versus throughput tradeoff.

units (see Fig. 15). A longer MDL results in larger time-residue, which may lower the classification accuracy of the CNN engine. The residual time loss in MDL equals the remainder of total accumulated time/MDL full-length delay. Thus, a longer MDL length implies higher residual time loss, which translates into lower classification accuracy. MDL with a longer length comprises more MDL units. Thus, it leads to more area and higher leakage power, since leakage for more number of MDL units is added.

However, longer MDL supports higher number of products per MAC for the same capacity of counter, as MDL full-length delay is increased. The dynamic power of counter decreases since it is incremented or decremented less number of times due to higher MDL full-length delay. Furthermore, longer MDL can effectively mitigate the process variations since the delay mismatch of each MDL unit gets averaged over a larger number of MDL units, resulting in a consistent full-length delay value across the MDLs. There is no effect on the dynamic power of MDL. Thus, by controlling the MDL length, the residual error can be optimized, so that classification accuracy loss is restricted to a minimal value while operating at low power.

D. MDL Half-Length Delay Offset

As discussed in Section III-D4, the initial state of each MDL unit output node value is held at the logic value "0," and node A is held at the logic value "1." Then, the first positive edge transition (0→1) at node E occurs by propagating node A value "1" for the *EN* duration until it reaches node E. Thus, the counter value gets incremented by propagating only a string of "1s" in the first round, instead of propagating "0s" followed by "1s." Thus, the intentional half of MDL full-length delay value is added upfront. For subsequent counter increments, the string of 0s followed by string of 1s needs to reach node E. This ensures that the final residual time value of the MDL is ± half of the MDL full-length delay value, instead of 1 full-length delay value.

V. Measured Results

A. Measurement Setup and Test-Chip Summary

Fig. 16 shows the overall measurement setup of the test-chip implemented using commercial 40-nm CMOS process technology [27]. The test-chip implements the LeNet-5 CNN architecture and occupies a total area of 0.124 mm^2

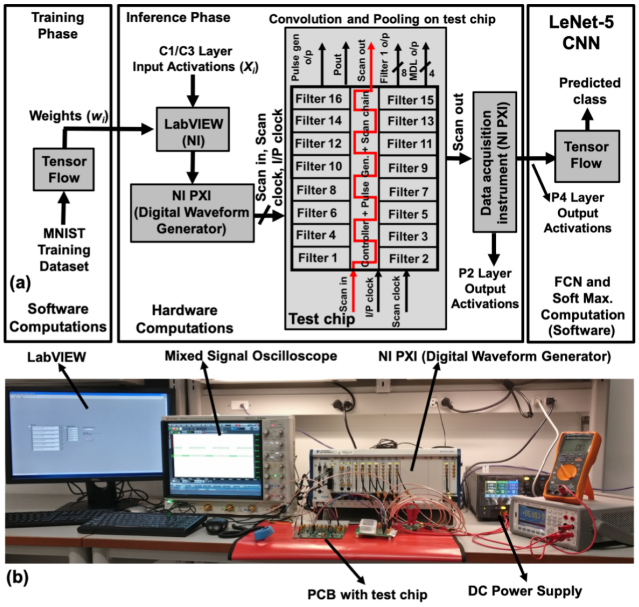
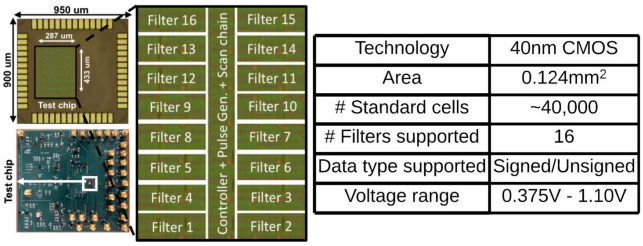


Fig. 16. (a) Block diagram of the proposed time-domain CNN engine setup. (b) Laboratory measurement setup.



Technology	40nm CMOS
Area	0.124mm^2
# Standard cells	~40,000
# Filters supported	16
Data type supported	Signed/Unsigned
Voltage range	0.375V - 1.10V

Fig. 17. Die micrograph and a summary of 40-nm test-chip implementing the time-domain CNN engine.

(see Fig. 17). The overall CNN inference and training methodology consists of: 1) training input data using the TensorFlow/Keras [28] software framework; 2) feeding trained filter weights and MNIST validation dataset image pixel values to the test-chip using LabVIEW-PXIe data acquisition instruments [29]; 3) performing on-chip MAC, averaging, and pooling operations for both C1 and C3 convolution layers; and 4) FCN layers and soft-max computation in software (TensorFlow). Due to the absence of on-chip global buffers (SRAM), the input activations, the weights, and the output activations (pooled MAV value) are applied/captured using the scan chain interface for each MAC computation. The National Instrument PXIe instrument is used to record the scan chain outputs. Each image is classified as two steps—storing output activations for layer C1 and for layer C3.

B. Test-Chip Characterization

The experimental demonstration of a 64-unit long MDL behavior under the delay phase and the memory phase is shown in Fig. 18(a). Three output node values (after 32 units, 48 units, and 64 units) are observed as shown in the oscilloscope capture. These waveforms are phase shifted in time

This article has been accepted for inclusion in a future issue of this journal. Content is final as presented, with the exception of pagination.

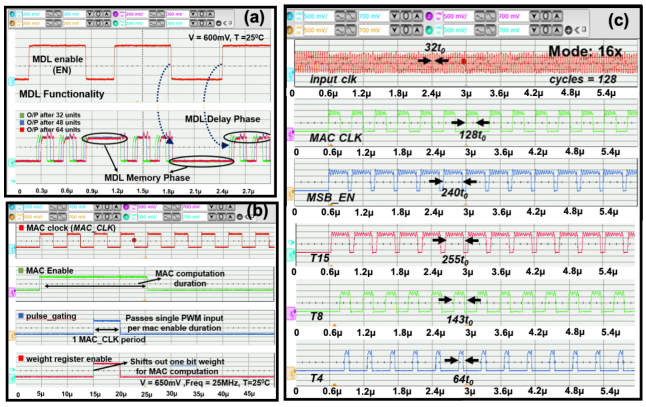


Fig. 18. Measured (a) MDL waveforms demonstrating delay and memory phases, (b) pulse gating logic module waveforms, and (c) PWM signals generated from a pulse generator module.

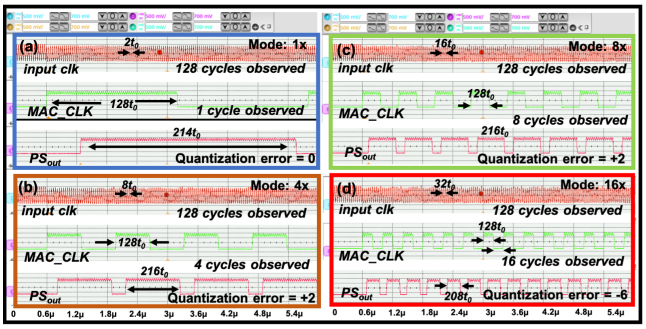


Fig. 19. Experimental demonstration of (a) 1×, (b) 4×, (c) 8×, and (d) 16× speed-up modes.

which confirms the successful operation of the proposed MDL concept. During the MDL delay phase (when *EN* is held high), the state vector on MDL is advanced, thereby resulting in transitions, whereas the MDL state is held constant during the memory phase (when *EN* is low). The pulse gating logic waveforms are shown in Fig. 18(b), confirming that the time-encoded input pixel value is used only once in the MAC computation. The pulse generator module functionality is verified with the correct toggling of *MSB_EN*, *T15*, *T8*, and *T4* outputs in the 16× speed-up mode, as shown in Fig. 18(c). 1–16× speed-up in PWM input representation is validated with multiple speed-up modes for a test-case input of 214 (see Fig. 19). In the 1× speed-up mode, 128 input clock cycles are used to time-encode the input pixel value of 214 accurately. However, the pixel value of 214 is encoded four times in 4× speed-up mode for the same number of 128 input clock cycles, thereby increasing the throughput by 4×, but with a quantization error of 2. Similarly, 16 and eight cycles of input clock are required in 8× and 16× speed-up modes to time-encode the 214-pixel value as 216 and 208, respectively. Thus, the PWM throughput increases with a higher speed-up mode at the expense of higher quantization error.

C. Accuracy, Throughput, and Energy Efficiency Results

The classification accuracy is measured for LeNet-5 CNN over 100 MNIST dataset images. Table II lists key LeNet-5 network parameters. 8-bit fixed point input pixel values and

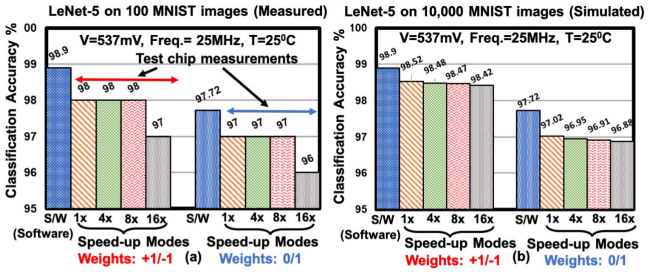


Fig. 20. Classification accuracy on LeNet-5 CNN for 4 speed-up modes using signed/unsigned weights at 537 mV (a) measured over 100 images and (b) simulated over 10 000 images accounting for MDL non-ideal effects.

TABLE II
PARAMETERS OF LENET-5 CONVOLUTION LAYERS C1 AND C3

Parameters for LeNet-5	C1	C3
Filter Size	5*5*1*6	5*5*6*16
Input/Filter Size	8bits/ 1bit	8bits/ 1bit
Input Size	32*32*1	14*14*6
Output Size	14*14*6	5*5*16
#Filters	6	16
#Operations/convolution$	(25*6*4)*2	(150*16*4)*2

$1 MAV = 2 operations: 1 multiply + 1 add/average, #MACs computed in parallel = 4

binary signed/unsigned weights are used in the convolution layers, whereas 16-bit floating point inputs and weights are used in the fully connected layer and software implementation. For signed binary weights (±1), 98% classification accuracy is obtained in 1–8× speed-up modes, whereas it is degraded by 1% in 16× speed-up mode [see Fig. 20(a)]. 16× speed-up mode resulted in lower accuracy because of input quantization and increased sensitivity of the MDL residue. For unsigned weights (0 and 1), 1% accuracy drop with respect to the signed weights case is observed. The measured accuracy values are within 1-2% of the state-of-the-art 16-bit floating point software implementation, which confirms the overall functionality of the proposed MDL based time-domain MAC computing approach.

The measurements are performed over 100 validation set MNIST images for signed and unsigned weights in all the 4 speed-up modes. In total, classification accuracy is experimentally measured for $100 \times 2 \times 4 = 800$ images. As mentioned in Section V-A, the output activations (pooled MAV value) are captured for each MAC value from the test-chip using a scan chain due to the absence of on-chip SRAM. The National Instrument PXIe instrument is used to interface with the scan chain resulting in very slow data acquisition from the test-chip.

To fully validate the effectiveness of the proposed time-domain approach, LeNet-5 simulations are performed on the entire 10 000 MNIST validation dataset images taking into account the non-ideal effects of MDL, shifter, and pulse generation circuits. The non-ideal effects modeled in the simulation are: 1) quantization of input activations in different speed-up modes; 2) addition of half-length delay value as an offset in MDL; 3) residual time loss in each MAC value depending upon the MDL full-length delay value; and 4) loss

This article has been accepted for inclusion in a future issue of this journal. Content is final as presented, with the exception of pagination.

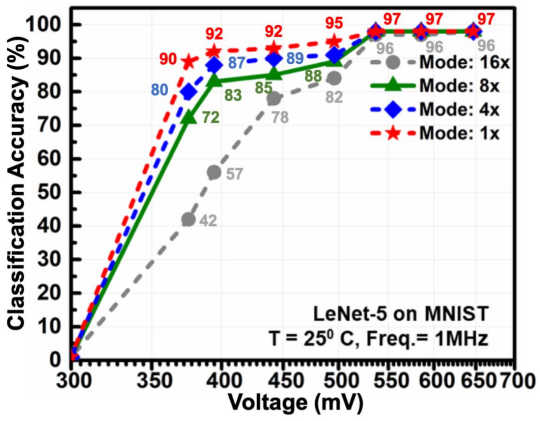


Fig. 21. Measured classification accuracy on LeNet-5 CNN over 100 MNIST dataset test images for 4 speed-up modes and signed weights for the 300–700-mV range.

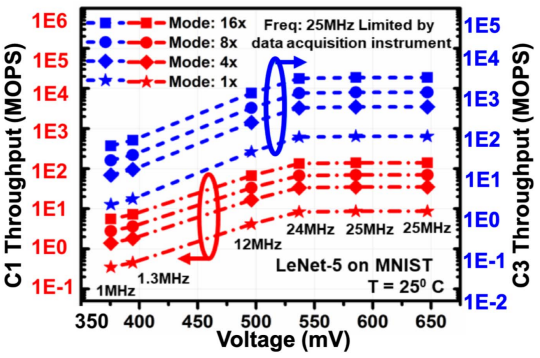


Fig. 22. Measured throughput for convolution layers C1 and C3 of LeNet-5 CNN for different voltages and speed-up modes.

of precision in averaging since it is performed by right shift operation in the bi-directional shifter. The predicted class from this simulation model matches with the experimental results obtained over 100 MNIST images. Fig. 20(b) shows the classification accuracy results obtained using a simulation model over 10 000 MNIST validation set images in all the 4 speed-up modes. 98.42% accuracy is obtained in the 16× mode, which is ≈0.5% lower than the state-of-the-art floating point software accuracy. These results confirm the overall functionality of the proposed MDL based time-domain MAC computing approach. Moreover, MDL supports the ultra-low voltage operation; is functional up to 375 mV with more than 90% accuracy in the 1× speed-up mode. 97% classification accuracy is observed at voltages down until 537 mV in 16× speed-up mode (see Fig. 21). As the supply voltage scales down and approaches the threshold voltage (V_T), increased delay variations are observed in the MDL due to: 1) intrinsic V_T variations in the NMOS and PMOS devices of the MDL unit and 2) variable and degraded input slew rate because of preceding stage MDL transitions. The increased delay variations result in variable MDL full-length delay value. Thus, MAC values are not computed accurately and the classification accuracy is degraded.

For LeNet-5 CNN, both convolution layers C1 and C3 measured throughput increases with higher speed-up mode and with increasing supply voltage, achieving a peak

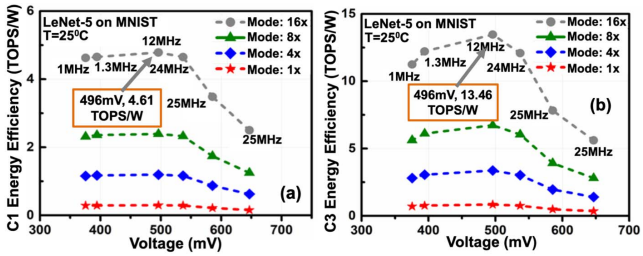


Fig. 23. Measured energy efficiency for convolution layers C1 and C3 of LeNet-5 CNN for different voltages and speed-up modes.

TABLE III

PERFORMANCE SUMMARY OF PROPOSED TIME-DOMAIN CNN ENGINE IMPLEMENTING CONVOLUTION LAYERS C1 AND C3 OF LENET-5

LeNet-5 Results/Metrics	Convolution Layer – C1				Convolution Layer – C3			
Speedup Mode	1x	4x	8x	16x	1x	4x	8x	16x
Input clock frequency (MHz)	24.0	24.0	24.0	24.0	24.0	24.0	24.0	24.0
MAC clock frequency (MHz)	0.19	0.75	1.50	3.00	0.19	0.75	1.50	3.00
Convolution Cycle Time (μs)	149.3	37.33	18.67	9.33	842.67	210.67	105.33	52.67
Operating Voltage (V)	0.537	0.537	0.537	0.537	0.537	0.537	0.537	0.537
Power (μW)	28.67	28.67	28.67	28.67	30.17	30.17	30.17	30.17
Throughput (GOPS)	0.008	0.032	0.064	0.128	0.023	0.091	0.183	0.365
Energy Efficiency (TOPS/W)	0.29	1.16	2.33	4.65	0.76	3.02	6.04	12.08

throughput of 0.38(0.128) GOPS for the C3(C1) layer at 585 mV (see Fig. 22). The maximum frequency is limited to 25 MHz due to the test equipment limitation. Thus, no increase in throughput is observed above 550 mV. The measured energy efficiency peaks with supply voltage scaling and reaches a maximum of 13.46(4.61) TOPS/W for C3(C1) layer at 496 mV (see Fig. 23). With the increase in voltage, the energy efficiency increases first until 550 mV and then decreases. This trend is observed since test equipment supports the maximum input clock frequency of 25 MHz, and thus power increases while throughput remains constant above 550 mV. Table III summarizes the test-chip performance. For a supply voltage of 537 mV and an input clock frequency of 24 MHz, an energy efficiency of 12.08 TOPS/W and a throughput of 0.365 GOPS for convolution layer C3 are observed in the 16× speed-up mode.

D. Scalability Analysis for Multi-Bit Weights

In this section, we propose two MDL design approaches to perform time-domain MAC computations for multi-bit inputs and multi-bit weights.

1) Approach 1: Using Multiple Independent MDLs: The time-accumulation of products of the m-bit weight and the time-encoded input pixel value is performed using m MDLs (1 for each weight bit). The counter values from these m MDLs are scaled appropriately (multiplied by powers of 2 depending upon weight bit position), and then added to compute the final MAC value, as shown in Fig. 24. The main limitations of using multiple independent MDLs for computing multi-bit weight/activation MAC operation are: 1) significant loss in classification accuracy due to accumulation of residual time loss across all MDLs and 2) multiple MDLs (m MDLs are required for a m-bit weight value) and an adder circuit to add

This article has been accepted for inclusion in a future issue of this journal. Content is final as presented, with the exception of pagination.

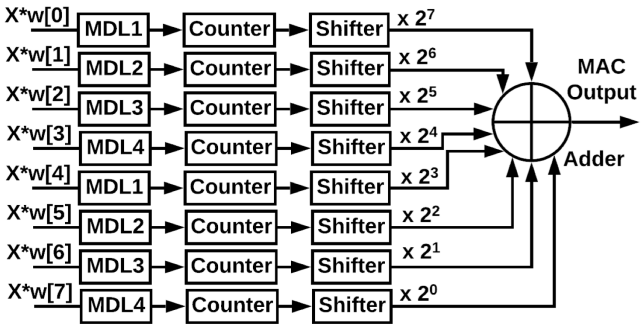


Fig. 24. Illustration of 8-bit weight and 8-bit input MAC operation using eight independent MDLs.

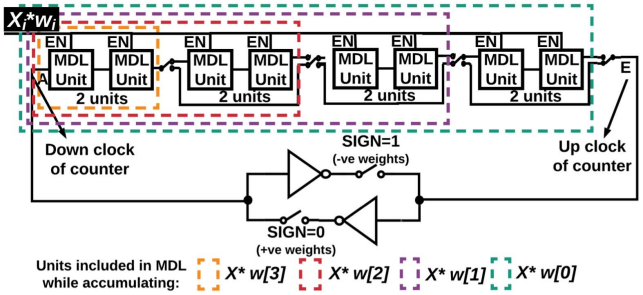


Fig. 25. Illustration of 4-bit weight and 8-bit input MAC operation using MDL with a configurable full-length delay.

the partial sums for each weight bit, thereby increasing the area and power dissipation.

2) Approach 2: Using Single MDL of Configurable Length: The limitations associated with multiple MDLs approach described above can be mitigated by designing a MDL of configurable full-length delay value, in which MDL units are dynamically added depending upon the weight-bit position. The full-length delay value of MDL is scaled by a factor of 2^{-i}, where i is the weight bit position, as shown in Fig. 25. In this approach, all the products of time-encoded input activation with MSB weight bit are first applied on the MDL (minimum MDL length). Then, the MDL length is doubled (full-length delay is doubled) and products of input activations with next significant weight bit are applied. This process is repeated until products with all the weight bits are applied on MDL. Thus, a single MDL is used to accumulate products of multi-bit input activations and weights, and the residual time loss is minimized to improve the classification accuracy. However, this approach requires a minimum of 2^{m-1} MDL units, where m is the bit-width of the weight signal. For example, a 16-bit weight value would require 32 768 MDL units, which can consume a large area and high power. Thus, this approach may pose design challenges to perform MAC operations for weight values with higher bit-widths. Moreover, careful design analysis is required to ensure that the MDL full-length delay value is scaled exactly by powers of 2 in the presence of process and temperature variations. These MDL design trade-offs for higher bit-widths inputs/weights are discussed in Section V-F3.

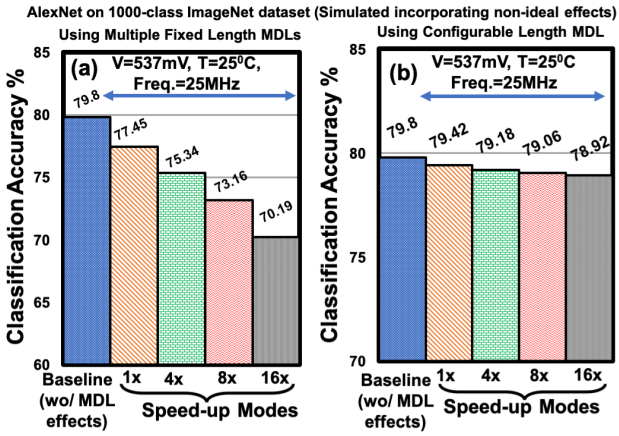


Fig. 26. Simulated classification accuracy on AlexNet CNN over 1000-class ImageNet dataset for different speed-up modes operating at 537 mV, 25 ^{o}C, and 25-MHz input clock frequency using (a) 8 independent MDLs (each 64 MDL units long) and (b) a single MDL with configurable length (1-128 MDL units).

3) Simulation Results on AlexNet CNN: The classification accuracy of the AlexNet network on the 1000-class ImageNet validation dataset (50 000 images) using the proposed multi-bit weight time-domain approaches for all the speed-up modes is evaluated by incorporating the non-ideal effects of MDL, shifter, and pulse generation circuits. The non-ideal effects modeled in the simulation are: 1) quantization of input activations in different speed-up modes; 2) addition of half-length delay value as an offset for each MDL; 3) residual time loss in all the MDLs depending upon the MDL full-length delay value and input clock frequency; and 4) loss of precision in averaging since it is performed by right shift operation in the bi-directional shifter. The full-length delay of MDL is obtained by simulating the MDL at 537 mV and 25 °C. 8-bit fixed point input and weights are used in convolution and pooling layers, whereas 16-bit floating point inputs and weights are used in FCN and soft-max layers. In approach-1, 8 independent MDLs each 64 MDL units long are used. ≈10% classification accuracy loss is observed in 16× speed-up mode when compared with the 16-bit floating point software accuracy [see Fig. 26(a)]. This loss can be attributed to the fact that residue loss in timing accumulation occurs for each weight bit and gets added since eight MDLs are used to compute each MAC value. Moreover, residual time loss is significantly high for MSB bits of weight vector. For approach-2 with configurable MDL length, less than 1% classification accuracy loss is observed using a single MDL with configurable length (1-128 MDL units) in the 16× mode when compared with the 16-bit floating point software accuracy [see Fig. 26(b)], since the residual time loss is minimized in this approach.

E. Comparison With Prior Approaches

Table IV compares the proposed time-domain approach with the earlier proposed digital [14], [15], analog [16]–[18], and frequency domain [19], [20] and time-domain [21] approaches. The comparison includes different metrics such

This article has been accepted for inclusion in a future issue of this journal. Content is final as presented, with the exception of pagination.

TABLE IV
COMPARISON OF THE PROPOSED TIME-DOMAIN CNN ENGINE WITH PRIOR ENERGY EFFICIENT ML ACCELERATORS

Reference	Tech. (nm)	Circuit Type	Input/ Weight Size	Core Size (mm^2)	Pool-ing	Low Vcc Op.	Cap. or ADCs	Accu-racy	ML/CNN Architecture	Dataset	Through put (GOPS)	Power (µW)	Energy Efficiency (TOPS/W)
ISSCC'16 [14]	65	Digital	16bits	16.00	Yes	No	No	98.3%	LeNet-5	MNIST	64	4.51E+4	1.42[α]
ISSCC'17 [15]	28	Digital	1-16bits	1.87	No	Yes	No	-	AlexNet/VGG	ImageNet	76	7.60E+3	10[α#]
ISSCC'18 [16]	65	Analog	8bits	1.44	No	No	Yes	96.0%	SVM	MIT CBCL	-	-	3.125
JSSC'17 [17]	130	Analog	5/1bits	0.267	No	No	Yes	~90%	Classifier	MNIST	-	-	-
ISSCC'18 [18]	65	Analog	6/1bits	0.067	No	No	Yes	99.0%	LeNet-5	MNIST	10.70	380.7	28.10
CICC'17 [19]	65	Frequency	8/3bits	0.24	No	Yes	Yes	91.0%	Multi-layer Perceptron	MNIST[##]	0.396	2.05E+4	0.019
ISSCC'18 [20]	55	Frequency	6/6bits	3.125	No	Yes	No	-	Reinforcement Lear.	-	2.152	690	3.12
A-SSCC'16 [21]	65	Time	1/1bit	3.61	No	No	No	98.5%	LeNet-5	MNIST	-	-	48.20**
This work (MDL CNN)	40	Time	4/1*bits	0.124	Yes	Yes	No	98.42%[$]	LeNet-5	MNIST	0.365	30.17	12.08

[α] These works focus more on data-flow (on-chip/off-chip access) optimizations. The energy efficiencies are reported at system level (including access energy)
[#] 0.8-3.8 TOPS/W for AlexNet; 2 TOPS/W on an average peaking up to 10 TOPS/W for VGG [##] MNIST image is resized from 28x28 to 22x22 pixels
** Input precision is 4bits in 16x speed-up mode, this approach is scalable to multi-bit values ** 12x higher energy efficiency due to the availability of on-chip SRAM*
[$] 97% measured over 100 images, 98.42% when simulated (incorporating non-ideal circuit effects) over 10,000 MNIST images

as the technology node, input/weight bit precision, core size, accuracy, CNN type, dataset on which classification accuracy is reported, low Vcc operation support, throughput, power, and energy efficiency. The classification accuracy of 98.42% (simulated, incorporating circuit non-ideal effects) is achieved over 10 000 MNIST images using the proposed time-domain approach in 16× speed-up mode implementing LeNet-5. This classification accuracy is comparable with the earlier proposed approaches which also perform only on-chip convolution and off-chip fully connected layer operations of LeNet-5: 98.3% in [14], 99% over 100 images in [18], and 98.5% (performing convolution layer C2) in [21]. The proposed MDL based time-domain design implements 16 filters and occupies 0.124 mm^2 in 40-nm CMOS technology. Unlike analog domain approaches [16]–[18], the proposed time-domain approach enables low voltage operation with the MDL operational down until 375 mV. The energy efficiency of the earlier proposed works [14]–[21] ranges from 0.019 to 48.20 TOPS/W. It should be noted that the energy efficiency numbers for earlier approaches as well as for the proposed MDL based time-domain approach depend upon the complexity of the implemented CNN, number of on-chip filters, on-chip global buffer (SRAM) capacity, input and weight bit-widths, operating voltage range, and CMOS technology node implementation.

F. Case Study: Time Domain Versus Digital Domain MAC

As the time-domain approach utilizes standard digital gates with sequential MAC computation, it is worthwhile to compare it with a conventional digital implementation performing sequential partial sum-based MAC computation.

1) Methodology and Design Configurations: A detailed post-PNR (P&R) analysis is performed to compare the average net length (post-Route wirelength), C_{DYN}, area, and energy efficiency of designs performing 1-bit and 8-bit weight MAC operation in conventional digital and proposed time-domain approaches. Both digital-domain and time-domain circuits are synthesized using the Cadence synthesis tool (Genus) and physically implemented using the Cadence P&R tool (Innovus) with standard cell utilization around 70% (see Table V). 40-nm commercial typical design corner libraries (nominal voltage of 1.1 V) are used in both the design approaches. The designs in both approaches are routed using metal layers M1–M4.

To perform MAC operation of 8-bit input and 1-bit weight values in the digital domain, a 15-bit sequential adder is used along with a 15-bit register to add the partial sum value and the product of 8-bit input and 1-bit weight [see Fig. 27(a)]. The input pixel values from 0 to 255 are sequentially added to perform the 1-bit weight MAC operation. The 15-bit adder and the register are used to ensure no overflow occurs when adding these 256 values. The MAC operation of the 8-bit input and 8-bit weight values is computed using a 8-bit × 8-bit multiplier, 28-bit adder, and 28-bit register in the digital domain [see Fig. 27(b)]. The input and weight values are selected randomly and the MAC operation is computed for a filter size of 3 × 3 × 256 (equals AlexNet convolution layer C3 filter size). The input and weight values are randomly selected 2304 times, and each product of input and weight value is added to compute a MAC value. Thus, 28-bit adder/register sizes are chosen to ensure no overflow occurs in adding 2304 16-bit input/weight product values. In the time-domain approach, the proposed circuit (16-unit MDL) is used along with the 15-bit counter, as shown in Fig. 27(c). Two time-domain approaches are implemented to perform the MAC operation of 8-bit input and 8-bit weight values. Eight copies of 16-unit MDL, eight copies of 28-bit counter/shifter (acts as a counter in the normal mode and a shifter in the shifting mode), and a single 20-bit adder are used to compute MAC operation using time-domain approach-1 [see Fig. 27(d)], whereas the configurable 1–128 unit MDL and 28-bit counter are used in time-domain approach-2 [see Fig. 27(e)] to compute multi-bit input/weight MAC operation in the time domain. These multi-bit weight time-domain approaches are discussed earlier in Section V-D.

2) C_{DYN}, Area, and Energy Efficiency Analysis: Table V lists the important design metrics for both these approaches using the same 40-nm CMOS standard digital gates. In the

This article has been accepted for inclusion in a future issue of this journal. Content is final as presented, with the exception of pagination.

TABLE V

AREA, C_{DYN}, AND ENERGY EFFICIENCY COMPARISON OF MAC COMPUTATION IN THE DIGITAL DOMAIN AND THE PROPOSED TIME-DOMAIN APPROACH

Metrics	MAC Computation - Inputs: 8-bit, Weight: 1-bit					MAC Computation - Inputs: 8-bit, Weight: 8-bit								
	Digital Domain	Proposed Time Domain 1-bit Weight			Comparison Digital/Time	Digital Domain	Proposed Time Domain Multi-bit Weight Approach 1			Proposed Time Domain Multi-bit Weight Approach 2			Comparison Digital/ Approach1	Comparison Digital/ Approach2
		MDL + TDC	Pulse Gen. Overhead	Total			MDL + TDC	Pulse Gen. Overhead	Total	MDL + TDC	Pulse Gen. Overhead	Total		
Number of nets	194	44	13	57	3.40	990	450	7	457	286	7	293	2.17	3.38
Average Net length (um)	6.35	5.64	8.97	6.40	0.99	7.63	7.19	8.97	7.22	7.17	8.97	7.21	1.06	1.06
Total Capacitance (pF)	0.610	0.134	0.046	0.180	3.39	5.119	2.1755	0.023	2.1985	1.4388	0.023	1.4618	2.33	3.50
Total CDYN (α∗C) (pF)	0.283	0.0799	0.0423	0.1222	2.31	1.879	0.876	0.0215	0.8975	0.779	0.0215	0.8005	2.09	2.34
Standard Cell Util. (%)	72.45%	72.08%	72.88%	-	Same (~1)	70.10	70.60	72.88	-	69.25	72.88	-	Same (~1)	Same (~1)
Area (um^2)	529.00	169.00	37.51	206.51	**2.56**	3600	1600	18.76	1618.76	1024	18.76	1042.76	**2.22**	**3.45**
Power (uW)	570.60	9.62	5.118	14.738	38.72	1516.20	105.94	2.60	108.54	11.34	2.60	13.94	13.97	108.77
F_{max} (GHz)	1.67	0.10	0.10	0.10#	16.70	0.667	0.10	0.10	0.10	0.0125	0.10	0.0125##	6.67	53.36
Energy – Power/F_{max} (pJ)	0.3417	0.0962	0.05118	0.1474	**2.32**	2.273	1.059	0.026	1.085	0.907	0.026	0.933	**2.09**	**2.29**

 # Pulse Generation and Time Accumulation are Pipelined. Hence, total time taken is 10ns. ## Pulse Generation takes 10ns, Time Accumulation takes 80ns; both are pipelined. Hence, total time taken is 80ns.

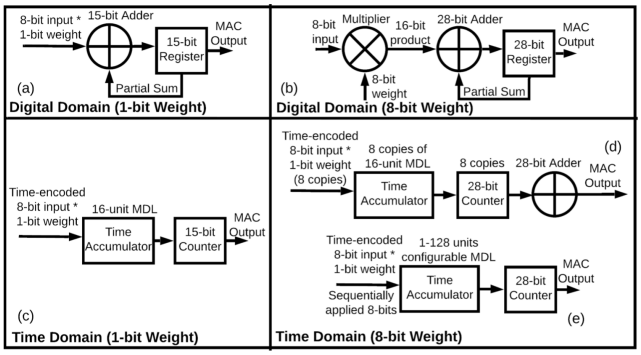


Fig. 27. Illustration of designs performing MAC operation for 8-bit inputs. (a) 1-bit weight in the digital domain. (b) 8-bit weight in the digital domain. (c) 1-bit weight in the proposed time domain. (d) 8-bit weight in the proposed time-domain approach-1. (e) 8-bit weight in the proposed time-domain approach-2.

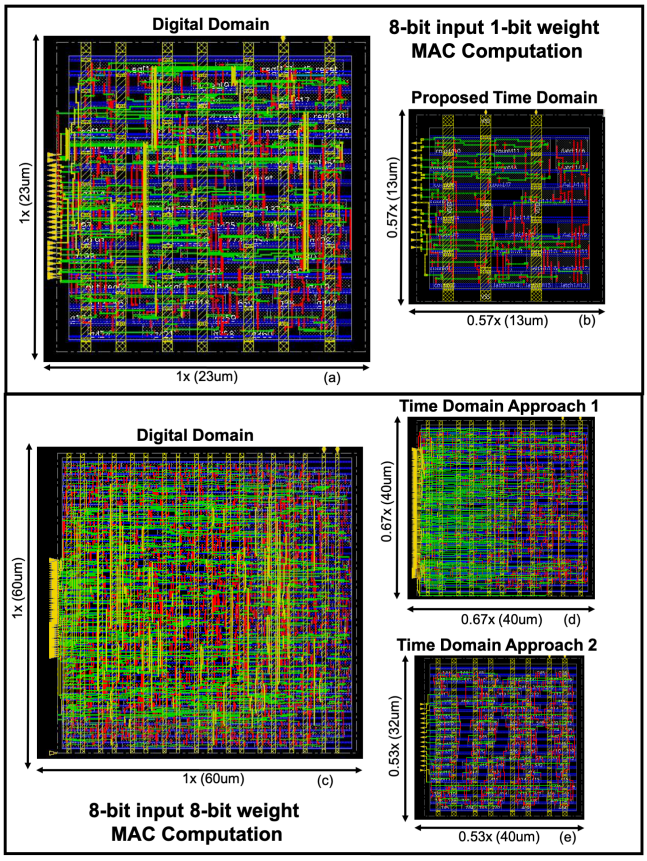


Fig. 28. Post-PNR floorplan of designs performing MAC operation for 8-bit inputs. (a) 1-bit weight in the digital domain. (b) 1-bit weight in the proposed time domain. (c) 8-bit weight in the digital domain. (d) 8-bit weight in the proposed time-domain approach-1. (e) 8-bit weight in the proposed time-domain approach-2.

proposed time-domain approach, the input pixel value in the digital domain is converted into a time-domain signal using the pulse generator and selector modules. This overhead is taken into consideration while evaluating the net length, C_{DYN}, area, power, and energy efficiency of the time-domain approach. It is assumed that 16 filters are implemented to compute MAC operation for 1-bit weight MAC operation (implementing LeNet-5), and 32 filters are implemented to compute MAC operation for 8-bit inputs and weights (implementing AlexNet). Each filter comprises four MDLs to compute four MAC values. Thus, the pulse generation overhead for each MDL is evaluated by dividing its value by 64 (16×4) and 128 (32×4) for 1-bit weight and 8-bit weight MAC computation, respectively.

The proposed time-domain implementations to compute MAC operation for 1-bit and 8-bit weight values result in 2.17–3.40× reduction in the number of nets, 2.33–3.50× reduction in total capacitance, and 2.09–2.34× reduced switching capacitance when compared with designs implemented in the digital domain (see Table V). The time-domain design implementations are compact and results in 2.22–3.45× smaller area when compared with digital design implementations, as evident in post-PNR layouts shown in Fig. 28. Since the time-domain approach operates at the *MAC_CLK* frequency which is smaller than the input clock frequency of the digital domain approach, 28-bit adder implementation in the proposed time-domain approach-1 [see Fig. 28(d)] is compact than the 28-bit adder implementation in the baseline digital approach [see Fig. 28(c)]. This translates into significant (≈2×) area benefit for the proposed time-domain approach-1 over the digital domain approach.

The vector-based power analysis using the Value Change Dump (VCD) file [30] (generated from functional simulation) is performed in the Synopsys primetime (PTPX) tool to accurately estimate the power in both digital and time-domain

This article has been accepted for inclusion in a future issue of this journal. Content is final as presented, with the exception of pagination.

approaches. For 1-bit weight MAC computation, input pixel values from 0 to 255 are sequentially applied in both digital- and time-domain approaches to estimate the power of adding an 8-bit input-pixel value to the partial sum value. The input toggle rate (including both rise and fall transitions) varies in the range of 0.0078-1 for all the input pins (1 for the LSB and decreases by a factor of 2 for the next significant bit).

For 8-bit weight MAC computation, the input and weight values are selected randomly and the MAC operation is computed for a filter size of $3 \times 3 \times 256$ (equals AlexNet convolution layer C3 filter size). The input and weight values are randomly selected 2304 times, and each input $\times$ weight product is added sequentially to compute a MAC value. The average power varies by less than 1% when estimated over 30 runs (each run with different random number generator seed values), which ensures that the reported average power in Table V is a good representation of typical power consumption. The input toggle rate varies in the range of 0.20-0.35 for all the input pins. Using these power values and the maximum clock frequency supported by these design configurations, the energy for MAC operation is quantified. The proposed MDL based time-domain circuits result in 2.09–2.32$\times$ better energy efficiency when compared with its digital design implementations at an iso-voltage (see Table V).

3) MDL Design Limitations for Higher Input/Weight Bit-Widths: The pulse generation scheme in the proposed time-domain approach requires 2^{n-1} input clock cycles to time-encode a n-bit input pixel value, thereby significantly degrading the throughput (lower *MAC_CLK* frequency) for inputs with higher bit-widths (e.g., 16 or 32 bit). The power consumption of MDL and TDC scales down appropriately at lower *MAC_CLK* frequencies such that the energy efficiency (Power/Fmax) of MDL remains the same. However, pulse generation/selection logic power consumption almost remains the same since the input clock frequency is unchanged. Thus, the power of pulse generation/selection modules starts dominating the overall time-domain CNN engine power, thereby reducing the energy efficiency of the proposed time-domain approach. Moreover, the proposed time-domain approach using multiple independent MDLs (approach-1) to perform the MAC operation of weights with higher bit-widths may result in significant classification accuracy loss, since residual loss would be accumulated for higher number of weight bits. Using a single MDL with configurable length (approach-2) requires 2^{m-1} MDL units to perform the m-bit weight MAC operation. Hence, it may lead to a significant increase in area for higher values of m (e.g., 16 or 32 bit). Thus, better MDL/pulse generation design solutions need to be devised to scale the proposed MDL based time-domain approach to larger bit-width inputs and weights.

VI. Conclusion

In this article, an energy efficient time-domain CNN engine suitable for edge computing is demonstrated. The proposed time-domain CNN engine deploys a bi-directional MDL to perform the signed accumulation of input and weight products. The fully digital and technology scaling friendly design is compact and does not use any capacitors and data converters (DACs and ADCs). It supports near-threshold voltage operation and is useful for low power edge computing applications. Four speed-up modes and a configurable MDL length are supported to address the throughput versus accuracy trade-off. The proposed design is tolerant to process variations, and the delay mismatch among MDLs are offset by the calibration unit. A 40-nm CMOS test-chip implementing the LeNet-5 CNN achieved an energy efficiency of 12.08 TOPS/W and a throughput of 0.365 GOPS at 537 mV in the 16$\times$ speed-up mode. The classification accuracy of 97% measured over 100 MNIST images and of 98.42% by simulating (incorporating circuit non-ideal effects) over 10 000 MNIST images is achieved. Furthermore, two MDL design approaches are proposed to perform MAC operations with multi-bit inputs and multi-bit weights. Simulation results taking into account MDL circuit non-idealities for 1000-class AlexNet over 50 000 ImageNet validation set images show a classification accuracy loss within 1% when compared with the 16-bit floating point software implementation. The proposed MDL based time-domain approach performing 1-bit/8-bit weight and 8-bit input MAC operations when compared with the corresponding baseline digital implementations show 2.09–2.32$\times$ higher energy efficiency and 2.22–3.45$\times$ smaller area.

Acknowledgment

The authors would like to thank V. Radhakrishnan, N. Maheshwari, and J. Rohan for helping with the test-chip measurements. They would also like to thank the Analog Circuit Research Group for helpful discussions during the test-chip implementation and AMD and TSMC University Shuttle Program for the test-chip fabrication support.

References

[1] G. Hinton *et al.*, "Deep neural networks for acoustic modeling in speech recognition: The shared views of four research groups," *IEEE Signal Process. Mag.*, vol. 29, no. 6, pp. 82–97, Nov. 2012.

[2] Y. Taigman, M. Yang, M. A. Ranzato, and L. Wolf, "DeepFace: Closing the gap to human-level performance in face verification," in *Proc. IEEE Comput. Vis. Pattern Recognit. (CVPR)*, Jun. 2014, pp. 1701–1708.

[3] A. Krizhevsky, I. Sutskever, and G. E. Hinton, "ImageNet classification with deep convolutional neural networks," in *Proc. Adv. Neural Inf. Process. Syst. (NIPS)*, vol. 2012, pp. 1097–1105.

[4] Y.-H. Chen, T. Krishna, J. S. Emer, and V. Sze, "Eyeriss: An energy-efficient reconfigurable accelerator for deep convolutional neural networks," *IEEE J. Solid-State Circuits*, vol. 52, no. 1, pp. 127–138, Jan. 2017.

[5] B. Moons and M. Verhelst, "An energy-efficient precision-scalable ConvNet processor in 40-nm CMOS," *IEEE J. Solid-State Circuits*, vol. 52, no. 4, pp. 903–914, Apr. 2017.

[6] K. Simonyan and A. Zisserman, "Very deep convolutional networks for large-scale image recognition," Sep. 2014, *arXiv:1409.1556v6*. [Online]. Available: https://arxiv.org/abs/1409.1556v6

[7] T.-J. Yang, Y.-H. Chen, and V. Sze, "Designing energy-efficient convolutional neural networks using energy-aware pruning," in *Proc. IEEE Conf. Comput. Vis. Pattern Recognit. (CVPR)*, Jul. 2017, pp. 5687–5695.

[8] M. Horowitz, "Computing's energy problem (and what we can do about it)," in *IEEE Int. Solid-State Circuits Conf. (ISSCC) Dig. Tech. Papers*, San Francisco, CA, USA, Feb. 2014, pp. 10–14.

[9] Y. LeCun, L. Bottou, Y. Bengio, and P. Haffner, "Gradient-based learning applied to document recognition," *Proc. IEEE*, vol. 86, no. 11, pp. 2278–2324, Nov. 1998.

This article has been accepted for inclusion in a future issue of this journal. Content is final as presented, with the exception of pagination.

[10] S. Pan and A. Kak, "A computational study of reconstruction algorithms for diffraction tomography: Interpolation versus filtered-backpropagation," *IEEE Trans. Acoust., Speech, Signal Process.*, vol. ASSP-31, no. 5, pp. 1262–1275, Oct. 1983.

[11] P. Koistinen and L. Holmstrom, "Kernel regression and backpropagation training with noise," in *Proc. IEEE Int. Joint Conf. Neural Netw.*, Singapore, vol. 1, Nov. 1991, pp. 367–372.

[12] J. Zhou, W. Xu, and R. Chellali, "Analysing the effects of pooling combinations on invariance to position and deformation in convolutional neural networks," in *Proc. IEEE Int. Conf. Cyborg Bionic Syst. (CBS)*, Beijing, China, Oct. 2017, pp. 226–230.

[13] C.-Y. Lee, P. Gallagher, and Z. Tu, "Generalizing pooling functions in CNNs: Mixed, gated, and tree," *IEEE Trans. Pattern Anal. Mach. Intell.*, vol. 40, no. 4, pp. 863–875, Apr. 2018.

[14] J. Sim, J.-S. Park, M. Kim, D. Bae, Y. Choi, and L.-S. Kim, "A 1.42TOPS/W deep convolutional neural network recognition processor for intelligent IoE systems," in *IEEE Int. Solid-State Circuits Conf. (ISSCC) Dig. Tech. Papers*, Jan./Feb. 2016, pp. 264–265.

[15] B. Moons, R. Uytterhoeven, W. Dehaene, and M. Verhelst, "Envision: A 0.26-to-10TOPS/W subword-parallel dynamic-voltage-accuracy-frequency-scalable convolutional neural network processor in 28 nm FDSOI," in *IEEE Int. Solid-State Circuits Conf. (ISSCC) Dig. Tech. Papers*, San Francisco, CA, USA, Feb. 2017, pp. 246–247.

[16] S. K. Gonugondla, M. Kang, and N. Shanbhag, "A 42pJ/decision 3.12TOPS/W robust in-memory machine learning classifier with on-chip training," in *IEEE Int. Solid-State Circuits Conf. (ISSCC) Dig. Tech. Papers*, San Francisco, CA, USA, Feb. 2018, pp. 490–492.

[17] J. Zhang, Z. Wang, and N. Verma, "In-memory computation of a machine-learning classifier in a standard 6T SRAM array," *IEEE J. Solid-State Circuits*, vol. 52, no. 4, pp. 915–924, Apr. 2017.

[18] A. Biswas and A. P. Chandrakasan, "Conv-RAM: An energy-efficient SRAM with embedded convolution computation for low-power CNN-based machine learning applications," in *IEEE Int. Solid-State Circuits Conf. (ISSCC) Dig. Tech. Papers*, San Francisco, CA, USA, Feb. 2018, pp. 488–490.

[19] M. Liu, L. R. Everson, and C. H. Kim, "A scalable time-based integrate-and-fire neuromorphic core with brain-inspired leak and local lateral inhibition capabilities," in *Proc. IEEE Custom Integr. Circuits Conf. (CICC)*, Austin, TX, USA, Apr./May 2017, pp. 1–4.

[20] A. Amravati, S. B. Nasir, S. Thangadurai, I. Yoon, and A. Raychowdhury, "A 55nm time-domain mixed-signal neuromorphic accelerator with stochastic synapses and embedded reinforcement learning for autonomous micro-robots," in *IEEE Int. Solid-State Circuits Conf. (ISSCC) Dig. Tech. Papers*, San Francisco, CA, USA, Feb. 2018, pp. 124–126.

[21] D. Miyashita, S. Kousai, T. Suzuki, and J. Deguchi, "Time-domain neural network: A 48.5 TSOp/s/W neuromorphic chip optimized for deep learning and CMOS technology," in *Proc. IEEE Asian Solid-State Circuits Conf. (A-SSCC)*, Toyama, Japan, Nov. 2016, pp. 25–28.

[22] R. J. D'Angelo and S. R. Sonkusale, "A time-mode translinear principle for nonlinear analog computation," *IEEE Trans. Circuits Syst. I, Reg. Papers*, vol. 62, no. 9, pp. 2187–2195, Sep. 2015.

[23] M. Rastegari, V. Ordonez, J. Redmon, and A. Farhadi, "XNOR-Net: ImageNet classification using binary convolutional neural networks," in *Proc. Eur. Conf. Comput. Vis.*, Mar. 2016, pp. 525–542.

[24] M. Courbariaux, Y. Bengio, and J.-P. David, "BinaryConnect: Training deep neural networks with binary weights during propagations," in *Proc. Adv. Neural Inf. Process. Syst. (NIPS)*, 2015, pp. 3123–3131.

[25] I. Hubara, M. Courbariaux, D. Soudry, R. El-Yaniv, and Y. Bengio, "Binarized neural networks," in *Proc. Adv. Neural Inf. Process. Syst. (NIPS)*, 2016, pp. 4107–4115.

[26] K. Kim, W. Yu, and S. Cho, "A 9 bit, 1.12 ps resolution 2.5 b/stage pipelined time-to-digital converter in 65 nm CMOS using time-register," *IEEE J. Solid-State Circuits*, vol. 49, no. 4, pp. 1007–1016, Apr. 2014.

[27] A. Sayal, S. Fathima, S. S. T. Nibhanupudi, and J. P. Kulkarni, "All-digital time-domain CNN engine using bidirectional memory delay lines for energy-efficient edge computing," in *IEEE Int. Solid-State Circuits Conf. (ISSCC) Dig. Tech. Papers*, San Francisco, CA, USA, Feb. 2019, pp. 228–230.

[28] M. Abadi *et al.*, "TensorFlow: Large-scale machine learning on heterogeneous distributed systems," Mar. 2016, *arXiv:1603.04467*. [Online]. Available: https://arxiv.org/abs/1603.04467

[29] *National Instruments LabVIEW and PXIe*. Accessed: Sep. 20, 2019. [Online]. Available: http://www.ni.com/en-us/shop/labview.html

[30] *ModelSim Command Reference Manual, Mentor Graphics*. Accessed: Sep. 20, 2019. [Online]. Available: https://www.microsemi.com/document-portal/doc_view/136660-modelsim-me-10-5c-reference-manual-for-libero-soc-v11-8



Aseem Sayal (S'18) received the bachelor's degree in electrical and electronics engineering from Delhi Technological University (formerly Delhi College of Engineering), New Delhi, India, in 2013, and the M.S. degree from the Department of Electrical and Computer Engineering, The University of Texas at Austin, Austin, TX, USA, in 2017, where he is currently pursuing the Ph.D. degree.

From 2013 to 2015, he was a Physical Design CAD Engineer with Qualcomm India Pvt., Ltd., Bengaluru, India. He was an Intern with Apple Inc., Cupertino, CA, USA, and Google LLC, Sunnyvale, CA, USA, where he was involved in developing clock tree simulation methodology and average power estimation solutions for long running arbitrary workloads. His research is focused on designing energy-efficient hardware accelerators for machine learning applications and developing engineering design automation (EDA) design methodologies for heterogeneously integrated secured application specific integrated circuits (ASICs).

Mr. Sayal was a recipient of the Chancellor Gold Medal and the Meritorious Student Award from Delhi Technological University in 2013.



S. S. Teja Nibhanupudi (S'17) received the bachelor's degree in electrical engineering from IIT Gandhinagar, Ahmedabad, India, in 2016. He is currently pursuing the Ph.D. degree with the Department of Electrical and Computer Engineering, The University of Texas at Austin, Austin, TX, USA.

From 2016 to 2017, he was a Project Associate with IIT Gandhinagar, where he was involved in the development of high-voltage process flow at the Semiconductor Laboratory. His research is focused on circuit-device co-optimization using novel materials, such as RRAM, insulator-metal transition (IMT), and STTRAM.



Shirin Fathima received the bachelor's degree in electronics and communication engineering from the Birla Institute of Technology and Science at Pilani (BITS Pilani), Pilani, India, in 2017, and the M.S. degree in electrical and computer engineering from The University of Texas at Austin, Austin, TX, USA, in 2019.

She worked on designing energy-efficient hardware accelerators for image classification in the master's thesis project. She is currently an SoC Physical Design Timing Engineer with Apple Inc., Cupertino, CA, USA.



Jaydeep P. Kulkarni (M'09–SM'15) received the B.E. degree from the University of Pune, Pune, India, in 2002, the M.Tech. degree from the Indian Institute of Science (IISc), Bengaluru, India, in 2004, and the Ph.D. degree from Purdue University, West Lafayette, IN, USA, in 2009, all in electronics/electrical engineering.

From 2009 to 2017, he was with the Intel Circuit Research Lab, Hillsboro, OR, USA, where he worked on energy-efficient integrated circuit technologies. He is currently an Assistant Professor with the Electrical and Computer Engineering Department, The University of Texas at Austin, and currently holds the AMD endowed Chair position in computer engineering. He has filed 35 patents and published 75 articles in referred journals and conferences. His research is focused on machine learning hardware accelerators, in-memory computing, emerging nano-devices, hardware security, and radiation hardened electronics.

Dr. Kulkarni was a recipient of the Best M.Tech. Student Award from IISc, the Intel Foundation Ph.D. Fellowship Award, the SRC Best Paper and Inventor Recognition Award, the Purdue Outstanding Doctoral Dissertation Award, seven Intel Divisional Recognition Awards, the 2015 IEEE TRANSACTIONS ON VERY LARGE SCALE INTEGRATION SYSTEMS Best Paper Award, and the SRC Outstanding Industrial Liaison Award. He has served as the Conference General Co-Chair for the International Symposium on Low Power Electronics Design (ISLPED) 2018. He is participating in the Technical Program Committee of Custom Integrated Circuits Conference (CICC), Design Automation Conference (DAC), International Conference on Computer Aided Design (ICCAD), and International Conference on Artificial Intelligence Circuits and Systems (AICAS) conferences. He is also serving as an Associate Editor for the IEEE SOLID-STATE CIRCUIT LETTERS and the IEEE TRANSACTIONS ON VERY LARGE SCALE INTEGRATION SYSTEMS.

The Indian Journal of Labour Economics
https://doi.org/10.1007/s41027-019-00191-8

RESEARCH NOTE

A Critique of Economic Literature on Technology and Fourth Industrial Revolution: Employment and the Nature of Jobs

Ishaan Gera[1] · **Seema Singh**[1]

© Indian Society of Labour Economics 2019

Abstract

Technology has come to the centre stage of the capitalist framework after the advent of the Fourth Industrial Revolution. Almost all schools of economic thought have realised the importance of technology in the production process. For the classical economists, technology is a tool to increase the output of the economy, ultimately leading to an increase in employment. However, Ricardo of the classical school differs in his approach from others. Despite being optimistic about the adoption of technology, he contends that labour will be worse off with the onset of technology. The issue of jobs remained the same for Marx and Keynes. For Marx, technology represents a duality which is both advantageous and disadvantageous for labour. For Keynes, it is a root for unemployment and a structural change in society and nature of work. Schumpeter, Veblen and other economists also address the issue of technology. Despite the focus, technology is not central to the theory of development or labour. However, with the Fourth Industrial Revolution, there needs to be more emphasis on the role of technology. By refining the existing literature and using anecdotal and subjective evidence, an attempt is made to put forth a modified idea of technology.

Keywords Fourth Industrial Revolution · Technology change · Job losses · Computerisation · Robotics · 3D printing · Automation · Artificial intelligence

JEL Classification B12 · B13 · B14 · B24 · B25 · B51 · B52 · O30 · O33

✉ Ishaan Gera
ishaan.gera@hotmail.com

Seema Singh
seemasinghdtu@gmail.com

[1] Department of Humanities, Delhi Technological University, Delhi, Delhi, India

Published online: 22 November 2019

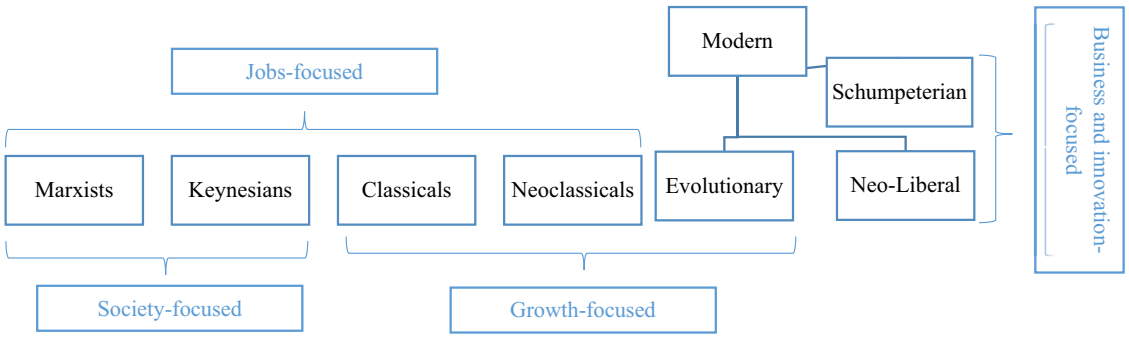


Fig. 1 Taxonomy of approaches of technology

1 Introduction

Technology has come to the centre stage of the capitalist framework after the advent of the Fourth Industrial Revolution (4th IR)[11] Technologies like artificial intelligence, 3D printing, robotics and blockchain may still be years from now, but with the likes of China stressing on robotics—the country is expected to add 134,000 industrial robots in 2018 (ABI Research 2018)—the future may not be far off. In this background, by analysing the existing literature, the paper tries to construct a theory of technology and jobs. The paper is divided into five sections. The second section reviews the discussion on technology by classical, neoclassical, Marxist, Keynesian and modern economists. The third section presents an objective for our study along with the methodology. The fourth puts light on anecdotal and subjective evidence. The last section concludes the discussion, provides suggestions for further development of economic theories and discusses limitations to the paper.

2 Critique of Economic Literature

Technology has been one of the main components of social and economic change. It has been viewed with a varied approach by each of the schools of economics, and its impact has been assessed differently (see Fig. 1).

[1] The Fourth Industrial Revolution represents a fundamental change in the way we live, work and relate to one another. It is a new chapter in human development, enabled by technology advances that are commensurate with those of the first, second and third industrial revolutions, and which are merging the physical, digital and biological worlds in ways that create both promise and peril. The speed, breadth and depth of this revolution are forcing us to rethink how countries should develop, how organisations create value and even what it means to be human; it is an opportunity to help everyone, including leaders, policy-makers and people from all income groups and nations, to harness technologies in order to create an inclusive, human-centred future (World Economic Forum).

2.1 Classical Economist

One of the first debates on technology, within the capitalist process, has been its potential to increase productivity and its ability to create or destroy jobs, while creating value for the capitalist. The manifestation of technology is clear from the writings of early inventors. One of the most significant instances comes from 1589 where the Queen of England refused to grant a patent being wary of the impact of spinning mills on jobs. The monarch argues that her subjects will become unemployed, over the long run, if such a system is deployed. Having already experienced the wrath of paper printing, invented by Guttenberg in 1436, the country tries to stop the march of technology. The view widely held—of technology being evil—does not last for long. Instead of unleashing large-scale unemployment, technology contributes to higher output, with the likes of Adam Smith (2007) and JB Say (1880) highlighting that technology can be a boon rather than a bane within a free market.

> "When printing was first brought into use, a multitude of copyists were of course immediately deprived of occupation; for it may be fairly reckoned, that one journeyman printer does the business of two hundred copyists […] Why, in a little time, the greater facility of reading printed than written books, the low price of books, the stimulus this invention gave to authorship, whether devoted to amusement or instruction, the combination, of all these causes, operated so effectually as to set at work, in a very little time, more journeymen printers, the total of other industries that the press finds occupation for, whether as type-founders and moulders, paper-makers, carriers compositors, bookbinders, booksellers, and the like, we should probably find, that the number of persons occupied in the manufacture of books is now 100 times what it was before the art of printing was invented." (Say 1880 quoted in Spithoven 1996)

Their contention revolves around the fact that with increased production technology would increase output, which even while decreasing labour in one industry would contribute to increase in labour in another, thus proving to be advantageous for labour.

The focus on technology was renewed in the writings of Ricardo (2010). While Ricardo during the early part of his writing career was enthused by the potential of technology, for the creation of value and cheapening of products and increase in demand, thereby leading to more employment, he later changed his views. The Luddite movement and protests by guilds infused pessimism in his works. Ricardo argued that technology may lead to the destruction of jobs as a capitalist would keep on innovating in order to replace workers with more and more machines. With the help of an example, he posited that if technology is allowed to run amok, it will wreak havoc on labourers as it would keep on replacing labour at a faster rate without disrupting the process of value generation. Thus, Ricardo regarded technology as the tool that can bring about a Malthusian thinning of the herd within the labour population, given its capacity to increasingly

replace labour while also adding to the growth potential of the economy (Humphrey 2004). He highlighted that with machines replacing labour, there can come a situation where even the new sectors end up employing machines rather than labour. Ricardo is the only classical to detract, and McCulloch 2005 and others support the formulation of technology creating more jobs. Ricardo and Marx both seem confounded by the impact of technology. Where Ricardo differs from Marx is the formulation of machinery. While Marx took the adoption of technology as a given phenomenon, Ricardo in his chapter 'On Machinery' went beyond a simple formulation of taking technology as given. He explains how, even if the technology is labour-saving, it is futile to ignore its use. This he does by way of using comparative advantage. Ricardo contended that even if one was to ignore technology in favour of labour, other nations or companies might adopt that innovation, ultimately leading to a pan-world adoption of it, owing to competitiveness. Thus, unlike Marx, Ricardo has a clear-cut theorisation on the adoption of technology by a capitalist, even if both end up reaching the same conclusion.

The opposition comes not from his classical peers, but many years later from the works of Wicksell. Wicksell (1981) contends that Ricardo could not see the fact that new machines would also require production at the hands of labour so that technology would lead to the generation of jobs in a different sector. While Wicksell partly agrees with Ricardo's formulation that comparative advantage would push all countries to greater adoption of technology, he does not agree with the view of decreased production and instead believes that technology can be a force multiplier, a view also supported by Paul Samuelson (1989) until he supports Ricardo's formulation (Humphrey 2004).

2.2 Marxist's View of Technology

While for classical, neoclassical and evolutionary theorists, technology represented a mode for growth, Marx's formulation for technology has differed from the beginning. Marxists have viewed technology as the driver of history and the mode of change for society. For them, technology may be exogenous or endogenous, but it has been a prime mover of the society. Although Marx's formulations are misconstrued, many of the Marxists have come out to be technological determinists, theorising that the change in systems and mechanisms can only be brought out by a change in technology (MacKenzie 1984). While Marx in his studies in Grundrisse (1973) and Capital (1990) explicitly evaluates technology relations in an automated society, Marxists ranging from Herbert Marcuse (2007) to Aleksei Gastev and Antonio Gramsci (1916) to Braverman (1998) and Harman (1979) have differed in their approach to technology adoption. Not only do they see technology as a means to an end for the capitalist, but they also see it as a means to an end for the society (Heideman 2015). However, most of this Marxist fervour of technology has also turned into ultra-left radicalism against it.

Marx does not only see technology as a mere tool, but he also envisions it as something that a capitalist can use to supplant labour. Technology, according to Marx, is neither a friend nor an enemy but contains within itself the power to

transform society. It can be an engine of social change, and not only can it drive the capitalist's objective of enslaving the labour force, it can also ultimately grant the labour the freedom to break away from the capitalist process and create a new society, where technology can serve the labour's purpose of freeing up socially necessary labour time (Marx 1990). As Marx assumes the whole capitalist process as a struggle between classes, the definition he provides to technology is no different. According to him, much like capitalism itself, there is a dichotomy to technology as well, where it becomes both an oppressor of the labour force and a liberator of the worker. Whether Marx is a technological determinist or not is a question that has been debated for long, and the open-ended writing has also left a division between his followers. While some Marxists consider technology as a messiah for the masses, there are others who think of technology as the demon destroying jobs. The likes of Lenin and others saw a great potential for technology, as force majeure to increasing productivity; Bill Haywood, on the other hand, looked at technology as a tool in the hands of capitalist which can only be used for oppression. Similarly, there has been a difference in opinion in the theory of technology within Marxists.

Although Harvey (2013) criticises the fetishism of technology of Marxists, he also contends that there is a need for a separate theory of labour value to address the issue of technology. Moreover, this theory of labour value which ultimately has to support a theory for exchange value and use value needs to be different for different countries, while Marx himself sees no need for such a theory.

2.3 Neoclassical Economists

The debate within economics has not changed much even when a theory has moved from classical and neoclassical. Wicksell, who contrary to Ricardo predicts more jobs being created with the onset of technology, belongs to this school of thought. Published seven decades later, Wicksell's contentions mostly related to technology ran contrary to Ricardo's on the level of jobs. Wicksell shows how the model Ricardo was working with was bound with contradictions and introduction of production functions brought more clarity to the issue. More critical, Wicksell's contentions include the increasing role of government in providing welfare. Thus, he believes that the thinning of the herd as predicted by Ricardo may not happen. Wicksell is trying to indicate the idea of skill enhancement sponsored by the government to tackle instances of technology.

2.4 Keynesian Theories

For Keynes (1963) much like Marx and Ricardo, theory revolves around technology and the possibility of job losses. Keynes does not link this with a crisis of capitalism as Marx does, nor expands on the production methods of Ricardo, but he does highlight a scenario closer to these economists. In positing an economy where technical efficiencies 'outrun' the pace of labour absorption, Keynes contends technological employment as labour would not be able to cope with the growth in the industries. More important, Keynes goes beyond the issue of technological unemployment and

also focuses on the issue of 'life' and 'work', a 100 years from his time. In focusing on the standard of living, Keynes in his seminal work 'The Economic Possibilities for our Grandchildren' highlights an eight to ten times rise in the standard of living. More importantly, it sheds light on the society structuring once technology starts creeping into daily life predicting a future where religion takes precedence and money loses its value. Keynes much like Wicksell has inclinations towards a universal basic income[2] in his writings.

> "If the economic problem is solved, mankind will be deprived of its traditional purpose. Thus, for the first time since his creation man will be faced with his real, his permanent problem-how to use his freedom from pressing economic cares, how to occupy the leisure, which science and compound interest will have won for him, to live wisely and agreeably and well. The strenuous purposeful money-makers may carry all of us along with them into the lap of economic abundance. But it will be those peoples, who can keep alive, and cultivate into a fuller perfection, the art of life itself and do not sell themselves for the means of life, who will be able to enjoy the abundance when it comes." (Keynes 1963)

2.5 Modern Theorists

The questions confronting technology for pre-modern theorists were very different from those that were witnessed by modern era economists. Fordism and the onset of assembly line production had provided a fresh lease of life to economic thinking. It has slowly shifted the focus on technology. Even though the technology was still not the central focus of economic theories, it did become an essential piece of the puzzle.

2.5.1 Schumpeterian View

Schumpeter (2003) looks at technology as the tool of creative destruction. For him, technology is the harbinger of a new lease of life that brings upon the destruction of old industries and replacement by new. He does not argue regarding job losses or the negative impact of technology, but instead sees it as a necessary cleansing of the system brought about disruptively by the entrepreneur to unleash changes and accord a new place for himself in the market (Gurkan 2005). More important, in Schumpeter's formulations, is his view of innovation being a sudden burst of economic activity, characterised by cost efficiency and profit drive. For Schumpeter, society and technology are disjunctive, and innovations are driven not by societal but by cost and profit considerations. Thus,

[2] 'Basic income' would be an amount sufficient to secure basic needs as a permanent earnings floor no one could fall beneath and would replace many of today's temporary benefits, which are given only in case of emergency, and/or only to those who successfully pass the applied qualification tests. UBI would be a promise of equal opportunity, not equal outcome, a new starting line set above the poverty line (Santens 2017).

Schumpeter's formulation starts and ends with businesses; he does not attach any significance to the cultural role of technology, thereby presenting a widely accepted view on creative destruction whereby businesses would only bring about such change when the cost of technology has come down. So, it is not the innovation, but the inherent pricing that innovation carries that drives change both for businesses and for the social fabric of the society (Gurkan 2005).

2.5.2 Neoliberal Economists

Veblen (1898), sticking to Marx's notion, goes in a different direction than Schumpeter. Veblen views technology as a cultural and material instrument that becomes a part of society. In placing technology as the centrepiece of his theory, Veblen argues that technology is an iconoclast, in that it can bring about change slowly and steadily. Although his ideas correspond to Schumpeter's on the view of technology as an instrument of change, he does not see it as a disruptive force. However, this change Veblen posits is only the material change that society wants to bring about and is not connected to the business's desire to adopt it. Unlike Schumpeter for whom technology has just business interest, Veblen sees technology as a cultural and social phenomenon and not just a detached economic process (Gurkan 2005).

As discussed, the approaches to technology have not only been referred to differently but are varied in themselves. These differences are a representation of different lenses used by these economists to look at the issue of technology while throwing some light on other aspects as well.

Technology has had many faces over the years, and to construct a single analysis of it would be an injustice. While the formulations related to it seem closer to Marx's assertions of having no character of itself, technology has shown the sinister side of capitalism in the hands of the capitalist. However, despite its overbearing nature, it has also become a tool for liberation of millennials (as envisioned by Hardt and Negri (2000) in their theory of Empire). To construct anyone's viewpoint as wrong would be fallacious as over the years technology has proven and disproven theories across the spectrum. Take the instance of widespread computerisation; while Samuelson had done well to side with Ricardo in his formulations, the computer phenomenon did create more jobs than possible in the history of capitalism. The destructive effects of a computer regarding loss of jobs were far lower than those of Gutenberg's printing presses. However, this hyper-connectivity coupled with the Internet and computerisation has led to more extended working hours. In a drive for profit, the home has become the workplace. Fordism created a new structure for the society, which was emulated from the factory floor. So, computerisation has created a new and a flatter structure, which has brought about a homogenisation of cultures and tastes with those without access to technology losing out on development. Moreover, as machines take more of space from humans, there is a need for a revisit to these social relations.

3 Objectives and Methodology

Thus, there is a need for a new theory of technology, as manifestations by Andrew Feenberg (1991) show a different view of technology given rapid computerisation, now that the pace of innovation has further been intensified with 4th IR, known for technologies like blockchain, artificial intelligence, full-scale automation and robotisation. A classic example of this is the use artificial intelligence for reporting company results. Computerisation did help media companies report results faster and in real time, reducing workforce, AI and machine learning have further simplified the process. As company results follow a set pattern and language, Bloomberg has deployed machines to report company results with greater accuracy and reduced overhead costs.

Marx and the likes of Harvey assume more importance, as technology becomes an entry point in a review of capitalism. In this background:

- Using contemporary studies, the paper tries to identify with the phenomenon of the Fourth Industrial Revolution.
- As the adoption of new technologies increases, it tries to put a framework to the studies by schools mentioned in the second section.
- Eventually, it will sum up a new formulation of technology which will be aligned with anecdotal and subjective evidence.

Section two presents the scrutiny of research on technology throughout the history of capitalism. To construct a new framework to fit today's time, all theories will be revisited connecting with the contemporary scenario by anecdotal evidence, Internet, newspaper articles, journals (Quarterly Journal of Economics), working papers (IZA, OECD) and World Economic Forum discussions. Using dialectics along with content analysis, a new methodology for technology is created.

4 Analysis

To construct a framework for technology, the paper has defined the Fourth Industrial Revolution, what it means for innovation and how it alters jobs in the upcoming decades in the following sections.

4.1 What is the Fourth Industrial Revolution?

The Fourth Industrial Revolution can be regarded as the era of widespread use of robots and automation on the factory floor, and artificial intelligence and machine learning for the service industries. Regarding jobs, it can correspond to a time where the dead labour takes over more work from the living labour, leaving less and less as technology progresses. This phenomenon can be represented by new modes of production, like robotics, 3D printing, full-scale automation and artificial

intelligence. One difference between this and computerisation is the increasing ability of machines to self-correct or reason. Although such a phenomenon is still far out decades, our theorisations have to take a long-term impact of such innovations.

4.2 Focus of Innovation

One of the fundamental questions of economics is 'what to produce?'. While market and factors have determined the factors concerning production, research or innovation, per se, has come from universities and institutions as well. Much of it may be market funded or business funded, but a lot of it has emerged just out of sheer innovation purposes. It can be defined as research for the sake of research, instead of profit-based innovation. This sort of activity has also attracted private investors, more importantly, crowdfunding platforms. In such scenarios, people, not businesses, decide what works and what doesn't. Many may contend that this has always been the case. Sony and Microsoft did lose out in the MP3 player market despite being first movers, while Apple capitalised on it. However, the onset of the Fourth Industrial Revolution and the availability of global finance are set to change this. People are increasingly coming together to provide products that market wants, and not what the businesses intend to pass on. Thus, Schumpeter and Veblen, in the discussion, both stand vindicated. While Schumpeter's assumption that technology is business driven is proven fallacious by the likes of 3D printer, Veblen's silence on the issue of cost considerations can also be contested. For instance, in the case of 3D printing, the technology has been present over the last two decades, but it is only due to improvements in technology and falling cost of printers that companies are increasingly adopting this phenomenon. Not only this, but it has also been true of computers where only after five decades of their existence was the case that computers became a phenomenon in society. Another expression of this can be blockchain, which after a successful stint in the world of finance and voting has become a tool in the hand of global corporations to increase profits. The formulations, unlike Schumpeter's idea, have not remained closed in the hands of capitalist or entrepreneur, but have changed the society and structures across the world. A business decision like Twitter has turned from a tool of promotion to a connection between individuals and a place of activism for today's millennial demanding for change not only in the workplace but also in the society as well. Thus, there is a need to divide the process of innovation between society focused and business focused, and not consider them as mutually exclusive events in the capitalist process. Cost considerations shall always stay an essential principle for any business, even if crowdfunding may ease some of these constraints.

4.3 Jobs

The impact of technology on jobs can be best gauged by the impact of the Internet on service companies and the process of outsourcing. Outsourcing did not lead to loss of jobs and, in fact, may have added more in the process, but the process did end up hurting some sectors more than others and created an inequity like jobs for

countries. The countries with the ready availability of resources and cheap labour did end up getting the lion's share of the market for both manufacturing and services. To understand the Fourth Industrial Revolution from the perspective of outsourcing would not be right as the dynamics of each are entirely different, but outsourcing certainly can shed light on the impact on jobs. Many claim that the pessimism surrounding the 4th IR is unfounded as studies state that more jobs have been created after computerisation, but there is also a need to consider the level of automation. A computer did require less number of people to do the same task, but it did also require a person to sit behind it and operate it.

Similarly, a machine required less number of people but nowhere was the case that it did not require any as robots could be programmed to do everything. Thus, on the question of jobs, while there was no doubt that Wicksell was right for the last half a century, the next has to go to Ricardo, Marx and Keynes. Samuelson along with many stands vindicated on their stance on technology destroying jobs. As dead labour takes over living labour and machines become smarter, only specialised workers would be required for jobs. There are only niche jobs that shall stay in the sector with a highly specialised workforce reaping the benefits of increased industrialisation. This does not mean that the future of employment is under threat, but only that niche sectors will remain. There would be no scenario where a company does not require people at all, but it would require far fewer than it did before. On the question of replacement by new sectors, these would also use new technologies as a crutch. Start-ups, in a rush to be competitive with more prominent firms, would see technology as the only mode of competition. While it is undoubtedly the age of entrepreneurs, there shall also be certain jobs that computers cannot compete with humans. Outsourcing will further increase, as companies with advanced Internet services would go one step ahead in achieving a cost advantage. A 3D printer in Germany could be fed designs from people in India, with little oversight, to produce goods that would be shipped to Britain.

4.4 Nature of Work

Where Keynes' stands confounded is the concept of time. Even if humans were not to work, he contends, there is some part of us that has been trained such to fight for basic needs, and that part would make us find work for whatever little time we can. If we are to see this phenomenon, Marx presents a similar analysis. Although Keynes is more perplexed by the idea of humans not working, Marx is welcoming of this age, as he believes that it shall leave more space for innovations. This is where Marx's theorisations take over Keynes' idea. Keynes, even though right in his manifestation of society, misses out on jobs that can derive more from a human than from a machine. Healthcare professionals, for one, can be that sector. Two, if the nature of work is considered, it is the evolution of capitalism that also corresponds with the enlightenment and age of evolution. So, it can be no surprise that people moving out of traditional jobs leave more time for people to go into literature, art and social sciences, something that has been increasingly ignored in the age of STEM fields.

However, where Marx's formulations can prove to be problematic is the fight for survival.

Moreover, this is where both Marx and Keynes can be negated. The fight for more capital and control over their time is borne not just out of necessity but greed, and greed would stay even if machines are to go out. So, we may see more jobs like data entry operators or medical transcript writers emerge, where a pennies-by-the-hour model takes over traditional roles. Instead of having more time on their hands, humans would be left with less time as they spend time searching for work and working for different companies in a race to accumulate more.

4.5 Principle of Compensation: Universal Basic Income and Robot Tax

Moreover, the cost of labour is also impacted by the fact that everybody would be guaranteed a bare minimum with the help of universal basic income. Thus, the cost of labour may even supersede the cost of innovation, with people more inclined to work in the pennies-by-the-hour model. With the issue of jobs becoming a contentious issue, there has been much debate about unemployment benefits and the nature of taxation that shall entail once companies start employing more robots than labour. Moreover, some of the countries in the name of welfare have already started contemplating the issue of universal basic income. While the idea of universal basic income precedes that of automation, it assumes much more importance in the face of growing unemployment. A basic income would provide enough for everybody to achieve necessities of life. Though the idea of basic necessity may differ from one state to another, welfare for all schemes would see the world more equitable than more. Where the real point of contention would be is the issue of taxation. With only a few finding works, income tax can become regressive rather than progressive for specific categories. Thus, the idea of robot tax can address the issue of widespread unemployment, while also sitting well with the compensation principle. What the robot tax would do is make the governments competitive on the tax policy, following a beggar-thy-neighbour approach to attract companies to set up businesses. Moreover, such a model provides more leeway for the companies to arm-twist governments in accepting their policies. An excellent example of this is the tax evasion techniques of the likes of Apple and Google across the world, where they end up setting headquarters where tax avoidance is high, and so is the government's tolerance for such activities.

Wicksell vindicates himself in proposing the idea of compensation principle, which translates into welfare from the government. Although inadvertently Wicksell becomes the first of many to come later to propose the idea of universal basic income and robot tax. This tax would be used to compensate for the loss in jobs in the form of universal basic income. Those like McCulloch contesting the rise of new products and new divisions are also limited by their knowledge of technology, and Ricardo seems to be right. Wicksell may not be dead right in predicting job losses but is right in his manifestations of welfare becoming the centre of government policy with a Kaldorian compensation (Kaldor 1939) being given to the aggrieved in

the form of universal basic income. UBI also becomes a tool for the capitalist to bargain for employing more machines and less technology.

4.6 New Formulation of Jobs and Technology

The presence of such diverse ideas stipulates the need for a sound theory of technology that can address the differing opinions while putting into context the rapid scale automation and an era of machine-to-machine interaction. On the issue of the scope of innovation, there is a need to refine the approach by looking at the product and process-based innovations as assessing which can be industry defined, while which others can come from the society. An excellent point to consider can be crowdfunded platforms; a cursory look shows that most innovations happening on such platforms are product innovations by start-ups trying to address problems of daily life. More important, even universities are more focused on ideas that can help generate a better life.

On the other hand, more of the process innovations are taking place in the industry platforms. Profit-driven innovation is also process-driven innovation in most instances. Thus, the ideas of both Schumpeter and Veblen correspond to the same society, just with a different outlook. Some of these product innovations do get the exalted status of becoming money-generating ideas, while process innovations can trickle down the society to be used by consumers in their sense. Twitter and Facebook are one such uses of the Internet, which have trickled down the public to generate conscience and action against the very companies that have started these and the very culture that supports these innovations.

In the instance of jobs, there is a clear need to define the nature of work. That jobs will be lost is an eventuality, but how much of this loss can be recouped by the governments remains to be seen. In this context, it becomes important to look at the nature of jobs and society. First, there is a need to create three-tier structures for economies. In the first tier, we put the developed countries that have borne the brunt of outsourcing. These countries are ready and have the resources to implement such mechanisms. Europe and the USA can be put into this category, and Make America Great Again can be one such initiative. The second is the transitional economies that are relatively rich and are playing catch-up with the developed economies so as not to lose out on the automation bandwagon. These economies do have a cost advantage regarding labour. So, they would like to achieve a more cost-competitive environment vis-à-vis technology and may not be so prone to the idea of mindless adoption of technology. India, China, Vietnam, Russia and Brazil can fall into this category. With a large demographic, these economies are more mindful of technology adoption as they would like to cater to the needs of their growing population and the limited availability of resources to deploy concepts like universal basic income. The third categories are developing economies or least developed economies, which do enjoy better cost advantages, but lack structures and resources to implement new technologies, and would be the last ones to innovate. This kind of hierarchy can also be placed for cities to understand the process of transition of technology. As not all processes of growth would be similar, and neither would be the job losses,

it is essential to look at all these structures as once rather than considering different theories of labour for each of the regions. Cities or countries may lie in any of these categories, but the result would be the same with specific minor cultural and social differences.

In the hypothetical case of cities, take cab aggregators like Uber and the self-driving cars. The cost-effectiveness of technology matters in this instance, but if self-driving cars are introduced cities would be the first place they would be introduced. So metropolises like Delhi, in the case of India, would see an efflux of such cars on the road, with Uber trying to cut down its overhead and regulatory costs, and it would be more than willing to take such cars on the road. For this, it can either ask owners to rent their cars for the time they are not used or better look at them as investment products raising money for each from the people. So those with resources can become rentiers. Once this happens, those with the existing stock of cars would move to peripheral towns to utilise their resource till the time these towns also adopt this innovation. Thus, there would be a flow of innovations from cities to towns to villages based on the availability of resources.

Besides, with universal basic income guaranteeing basic needs, any business model that aims to extend a person's income would flourish.

Technology has always been important within the capitalist paradigm. It is set to become more so as we enter the age of rapid scale automation and machine-to-machine interaction. However, unlike the common perception, the paper accords a neutral status to technology. Technology is both a tool in the hand of the capitalist and a means for the consumer to raise voice against the capitalist. This is evident from Twitter and Facebook.

Moreover, the paper has also tried to solve the dichotomy presented by Schumpeter and Veblen, of technology being either business driven or society driven. According to the analysis presented by the paper, it can be both, but the use case has to depend on the type of innovation. A product-driven innovation is society focused, while the process-driven innovation comes from businesses. That may not be the case, but for either of those innovations to cross to the other, they would have to achieve either cost considerations as proposed by Schumpeter or the iconoclast nature derived from scalability as suggested by Veblen.

On the issue of jobs, it would be illogical not to side with Ricardo, Marx and Keynes. That technological unemployment is a possibility cannot be denied, but the difference in approaches allows a new framework for technology coupled with the issue of jobs. For this, the paper has created three divisions to existing countries by assessing the impact of jobs on economies and also showcases the pace or adoption of technology. For the developed economies, jobs do not matter as much as the influx of companies and setting up of centres. As they are already knowledge-focused economies, they can attract companies with their infrastructure and institutions. Thus, institutions and ease of doing business assume importance in a hyper-connected and robotised world. For transitional economies, the low-cost labour still plays a part but along with education. Thus, their focus would increasingly be on education and creating niches. As these economies have a high demographic base, unemployment may have different concerns. Besides, with expansion from cities to towns and a filtration, people may not become unemployed

in one instance. For the developing economies, there is a dearth of capital, and hence there are two growth patterns. Either they can go for a direct adoption of technology leaving out their workforce, or they follow the transitional economies using a tempered approach to technology adoption. Thus, the loss of jobs, which has rarely been addressed in any of the theories, depends on the pace and type of innovation and the building of institutional structures by economies.

For UBI, there needs to be a similar division. The developed economies may be more inclined to give such benefits, but that certainly will not be the case for transitional or developing economies. Thus, the issue of what to give in conditional cash transfers and what to give as subsidies would become important.

5 Conclusion, Suggestions and Limitations

This paper attempts to revive the debate on technology and cull from the existing literature, a technique that can best fit today's time. Like 3D printing, robotics and artificial intelligence dominate the production process, the role of technology needs a review presenting regarding both its theoretical structure and its practical implications, which, even though may seem to be in conjecture, point in different directions. The paper highlights the classical's manifestation of technology and its impact on the labour. It explains the impact technology can have on the labour class either as a contributor or a destroyer of jobs. This manifestation continues in the neoclassical models as well, but with a focus towards production function and a feature of technology that is central to production, yet exogenous. Schumpeter comes closest to this formulation with a business-focused mindset for the growth of technology; this continues to the neo-Schumpeterian view, which much like neo-evolutionary theorists focuses on technology as an endogenous variable of growth. Marx and his band of followers on the other hand concentrate on the evolution of society given the efflux of technology. This formulation is also available for neoliberals like Veblen, who is focused on innovation as a society-driven process, deeming it iconoclast. Much like Keynes' formulations, the paper derives a historical viewpoint to the application of technology peeking through the history of technology and its impact on jobs.

Though technological history is proof for development of society, for the technology that is yet to come, there can be no simple formulation. So, the paper builds upon theories of all branches of economics to present a common viewpoint.

The furtherance of this type of study leaves scope for mathematical formulations for a new kind of science that goes beyond the scope of production and consumption functions. More importantly, it leaves scope for new studies detailing the society and government that growing incidence of technology will represent.

However, as any approach, in theory, this is more focused on anecdotal and subjective evidence which may change from a decade or a few years hence. There is also a need to focus on the issue of technology from a consumer or a millennial, which has not been addressed in this paper.

References

ABI Research. 2018. *The rise of Chinese robotics companies: A matter of when not if*. Retrieved from ABI Research: https://www.abiresearch.com/press/rise-chinese-robotics-companies-matter-when-not-if/. Accessed 28 Oct 2018

Braverman, H. 1998. *Labour and monopoly capital: The degradation of work in the twentieth century*. New York: Monthly Review Press.

Feenberg, A. 1991. *Critical theory of technology*. New York: Oxford University Press.

Gramsci, A. 1916. Men or Machines? Avanti!, published in http://www.marxists.org/archive/gramsci/1916/12/men_or_machines.htm. Accessed 1 Nov 2018

Gurkan, C. 2005. *A comparison of Veblen and Schumpeter on technology*. STPS working papers (509).

Hardt, M., and A. Negri. 2000. *Empire*. Cambridge, Massachusetts: Harvard University Press.

Harman, C. 1979. *Is a machine after your job?*. London: Socialist Workers Party.

Harvey, D. 2013. The fetish of technology: Causes and consequences. Macalester International, 13, Prometheus's Bequest: Technology and Change, Article 7.

Heideman, P. 2015. *Technology and socialist strategy*. Retrieved from Jacobin: https://www.jacobinmag.com/2015/04/braverman-gramsci-marx-technology/. Accessed 28 Oct 2018

Humphrey, T. 2004. Ricardo versus Wicksell on job losses and technological change. *Federal Reserve Bank of Richmond Economic Quarterly* 90 (4): 5–24.

Kaldor, N. 1939. Welfare propositions of economics and interpersonal comparisons of utility. *The Economic Journal* 49 (195): 549–552. https://doi.org/10.2307/2224835.

Keynes, J.M. 1963. *Essays in persuasion*. New York: Classic Book House.

MacKenzie, D. 1984. Marx and the machine. *Technology and Culture* 25 (3): 473–502.

Marcuse, H. 2007. *One-dimensional man*. London: Routledge Classics.

Marx, K. 1973. *Grundrisse*. London: Penguin Books in association with New Left Review.

Marx, K. 1990. *Capital volume I*. London: Penguin Classics.

McCulloch, J.R. 2005. Letter to Ricardo. In *The works and correspondence of David Ricardo, Vol. 8 Letters 1819–June 1821*, ed. P. Sraffa and M. Dobb. Indianapolis: Liberty Fund.

Ricardo, D. 2010. On the principles of political economy, and taxation. Project Gutenberg.

Samuelson, P. 1989. Ricardo was right! *Scandinavian Journal of Economics* 91: 47–62.

Santens, S. 2017. Why we should all have a basic income. Retrieved from World Economic Forum: https://www.weforum.org/agenda/2017/01/why-we-should-all-have-a-basic-income. Accessed 28 Oct 2018

Say, J.B. 1880. *A treatise on political economy*. Philadelphia: Claxton, Bemsen and Haffelfinger.

Schumpeter, J.A. 2003. *Capitalism, socialism and democracy*. London: Taylor & Francis e-Library.

Smith, A. 2007. *An inquiry into the nature and causes of the wealth of nations*. Sao Paulo: MetaLibri.

Spithoven, A. 1996. Jean-Baptiste Say (1767–1832): Between the labour theory of value and utility. *International Journal of Social Economics* 23 (7): 39–48.

Veblen, T. 1898. Why is economics not an evolutionary science? *The Quarterly Journal of Economics* 12 (4): 373–397.

Wicksell, K. 1981. Ricardo on machinery and the present unemployment. *Economic Journal* 91 (March): 199–205.

Publisher's Note Springer Nature remains neutral with regard to jurisdictional claims in published maps and institutional affiliations.



ISSN Print: 2394-7500
ISSN Online: 2394-5869
Impact Factor: 5.2
IJAR 2019; 5(8): 146-149
www.allresearchjournal.com
Received: 10-06-2019
Accepted: 13-07-2019

Massoud Massoudi
1. Assistant Professor, Faculty of Computer Science, Parwan University, Afghanistan
2. Ph.D. Scholar at CSE, Department of Delhi Technological University, New Delhi, India

Correspondence
Massoud Massoudi
1. Assistant Professor, Faculty of Computer Science, Parwan University, Afghanistan
2. Ph.D. Scholar at CSE, Department of Delhi Technological University, New Delhi, India

A review on challenges and solutions in learning programming courses at undergraduate level

Massoud Massoudi

Abstract
Taking a computer programming language course for the first time is a problematic and challenging task for most of the pupils who mostly fail or drop out of the course. In addition to this, this problem is not restricted for computer science pupils, since pupils in other engineering disciplines have to take programming courses as well.
In this paper, we review papers related to teaching approach, challenges and solutions for improving student's ability and performance in a first programming language course in undergraduate program.
One of the most well-known challenges in teaching and learning a first programming language course is that in the same course, the students must learn and get to know fundamental programming techniques, high level abstraction capabilities, the application of those tricks and techniques, notion and significance in problem solving and design.
In this paper the general trends comparing freshers and expert programmers, programming strategies and knowledge, program generation and understanding has been identified.
The main and fundamental focus and point of this review is on novice programming and concepts relating to novice learning and teaching. Different problems faced and experienced by novices are recognized, containing issues relating to core program design, to algorithmic complexity in some specific language features, to the frangibility of novice knowledge, and so on. Keep this in mind we have summarized this material and suggest some practical concepts for academicians.

Keywords: Computer programming language undergraduate

1. Introduction
The far-reaching use of programming languages commenced with the arrival of Fortran in 1957. It gave the opportunity for scientist and engineers to write different formulas using standard symbols from mathematics [8].
Coding and programming is the most interesting skill and most of the developers consider this skill as fun and can be a remunerate career. In recent years the requirement and demand for programmers, coders and pupil's interest in programming have grown quickly and rapidly, on the other hand, the introductory programming courses have become increasingly reputed. However, Learning to code and program is seems to be hard and challenging. Novice programmers mostly suffer from a vast range of difficulties and deficits. Programming subjects are mostly considered as challenging, and often have the highest drop-out rates. In general it is accepted that it takes approximately 10 years of experience to change and convert a novice programmer into an expert one [1].
The high omission and drop-out rate and failure measure in programming courses have drawn serious attention of researchers to start investigation of the causes and solutions to the drop-outs. Programming and coding is a multi-layers skill which is boring, scary and unrelated to day-to-day experiment where pupils only can learned in single context [2].
Our interest in this broad field of software engineering is focused by practical sessions and considerations. In [3] have stated that we teach the introductory programming course named as CS1, where our objective is to provide the best teaching and learning environment and experience in doing practical for our pupils. In the result, we are more eager in understanding the processes of teaching and learning programming, and come this point, Why is programming is difficult to learn? In the same [3] has been mentioned, that the only effective approach to learn a new programming language is by writing and coding the programs in it. Where the first program for all the languages is same such as print the "Hello, World"

this is the big obstacle, to bounce over it you have to be able to create the program source code somewhere in a text editor or IDEs, compile it without generating any error, run it and find out what output you will get and where your output went [3].

This paper presents a review on the challenges and difficulties where undergraduates encountered while learning programming languages and their perspectives on how learning should naturally take place. The rest of the paper is organized as follows: section II Teaching & Learning Programming Languages and Environment, III Languages Readability and Writability, IV the Role of Programming Languages, V Challenges in Learning Programming Language, VI Solutions, VII Objective Measures and Test and the conclusion is stated in section VIII.

2. Teaching & learning programming language and environments

Knowing and Understanding the learning process of any first programming language can cause an effective learning environments as much as you learn and code you will create your own appropriate learning environment. Some lecturers and systems consider the programming in an entertaining way like game playing, storytelling and fun [4-5].

Some of the most potential list of programming language advantages are state as:

- It Increased capability to express your ideas in better way, it is widely accepted that as much as at depth we can think and use our mind it causes to express the power of the language by which we communicate our thoughts and ideas.
- It can improve background for selecting appropriate languages, most of the expert programmers have had little formal education and degree in computer science, hence, they have learned programming on their own or through in-house training courses and institutions, the more you program the more you will get to know which language can help me in developing most needed applications.
- It can enlarge ability to learn new programming languages. Computer programming language is a young discipline and design methodologies, programming languages and software development tools are still trending, where this makes the software development process an exciting and interesting profession.
- Better understanding of the importance of implementation. When learning the concepts of any programming languages it is both interesting and essential to touch on the implementation issues that affect the concept. However, in some cases an understanding of implementation issues leads to an understanding of why programming languages are designed the way they are. This in turn leads to the capability to use a language more efficiently.
- It can improve the ability to design new Language. For most of the students the requirements in the future to design their own programming language seems like remote and impossible. However, most of the programming languages have been occasionally design in different sort by professional and expert programmers.
- Overall improvement in computing. As a final point, a global opinion of computing is require to rectify the study and learning of programming concepts and that is there. Although, a question may raise in your mind to determine why and how a particular language became popular and famous, this is not always vivid it is usually possible to determine why a particular programming language became popular, it is not always clear, at least in retrospect, the most popular and used programming languages are the one which are best available.

In general, if those who select languages are better informed, perhaps, that better programming languages can quickly squeeze out the poorer ones [6].

3. Languages readability and writability

Programming language is a digital device language designed to associate and communicate different instructions to a computer and device. They are used to create different programs and applications to control the behavior of a computer as well as to express algorithms. There are so many programming languages which all can do the same task but in different ways using different syntaxes. Hence, Most of the programming languages characterize computation in an imperative format and style, i.e., as a sequence of instructions and commands, however, some programming languages that support functional programming or logic programming use alternative forms of description [17].

One of the most significant criteria to judge a programming language is its simplicity and its ease, where the program can be read and understood easily, on the other hand, readability has to be considered in the context of the problem domain.

Whereas, Writability is considered as a measure of how simply a language is used to create programs for a specific problem domain. As a result, Most of the languages that affect the concept of readability also affect Writability of that language.

In view of the fact, both concept can influence reliability [6].

In addition to this, most of the developers who spend majority of their time trying to read and understand the addressed source code during the maintenance phase. This results that spending less time on reading the source code has direct impact on the amount of time for maintaining the software.

As a final point, the concept of Code readability is highly subjective and it is directly related to the level of simplicity by which a developer reads the program. It should not be unsaid, that Readers' levels mainly depend on their comprehensive and cognitive ability to process textual information [7].

4. The Role of Programming Languages

To know more the role of any programming languages, let's consider the below questions that results in recognizing the role of languages in our daily development domain.

Is a programming language a tool for guiding and instructing systems? Is it a means for communicating between programmers? Is it a device for expressing high-level designs? Is it a way of expressing relationships between concepts? Or is it a means for controlling digital devices? In My perspective a general-purpose programming language must be all of those to serve its diverse group of users. Programming languages are instructions, they are used for organizing, specifying and reasoning about computations [8].

In this digital era, it is required to everyone should learn how to program and how to code! Hence, Programming is not only designed to a specific discipline limited to computer science students. Programming is a good way of thinking where it is useful to everyone who uses digital devices for their daily communications. On the other side, Programming teaches most of the same skills as mathematics and English. Each Programs have to be designed with precision. Reading and coding them has to be done with caution. But the reward for a correct program is immediate and strong: it executes correctly and gives required and expected output and result [9].

Since the 1950s, grading and scores of different programming languages have been implemented and designed and many more will come. Those with a relevant experience in this field will agree on that concept of "the best programming language" is something meaningless. In addition to this, we need to clarify this to our pupils during teaching programming languages. In fact, some languages are better than others based on some specific purpose and indeed: (a) some languages are exclusively used for some specific purposes, and (b) people use some specific languages for specific purposes. For example, C language [7-5] is a good language for developing system software's and programs. It is a low-level and not object oriented language, as well as it is very fast language and gives programmers the opportunity to directly interact with the hardware, but it is not the best language for numerical and scientific computing now a days. In view of the fact I it is believed and accepted that C language is an inappropriate language and it is not fair to teach it as "Introduction to Programming" course. That is, because some of its characteristics are so low-level it tends to focus more on the hardware, instead of on the algorithms [10].

5. Challenges in learning programming languages

Teaching courses which have practical aspects have always formed and constituted burdens on colleges offering non-technical degrees. One of such courses is computer programming languages, especially in degrees such as: information systems, computer science, and software engineering. In such courses, pupils are expected to take between 2-5 computer programming courses during their undergraduate level. Studies show that success ratio in the first programming course is mostly low. Why is it low and how this ratio can be improved is stated in this paper [11].

Programming courses are among the main components of the curriculum to be observed, in most of the fields including mathematics, Science and Engineering at tertiary levels. But not only in the field of Information Technology. In view of the fact, the course is considered difficult, challenging and it is also categorized as part of the seven grand challenges in computing education [12].

Different research have stated regarding the struggling of the students with first steps of learning to program and code. A multi-national, multi-institutional study was conducted to dig and explore pupils' programming capabilities and skills and [13, 14, 15]. The study disclosed that pupils have mostly problems in coding [13], reading [14] as well as designing [15] a simple programming code.

Accordingly, it is necessary to interrogate the factors that guide to pupils learning difficulty in programming. The difficulties need to be rectified in order to be able to aid them learning in an effective and suitable way.

6. Solutions

Every problem comes with so many solutions. Hence, A helpful approach in learning how to code requires students to consider a real world problem and then converted it to program code to solve it. However, such methods has been difficult by students because the learning process of programming is said to be a multi-layers skill which more boring, intimidating and as well as not related to day-to-day experience where pupils mostly learned in single context [13]. Such situation often happened to a novice programming student with no experience in this field where at the starting stage they need to learn specific programming language syntax before applying their knowledge and skills in structuring and programming style.[12-16].

Since, most of the students are not able to see what is happening internally when executing a program, in addition to this, a good teaching aid is required to help them in visualizing the execution process and let them to enhance the conceptual understanding of student's in programming environment [12].

7. Objective Measures & Test

The objective measures and test which has been conducted through the Facebook social media from majority of the Afghan pupils is seemed to be more effective and are sorted out as:

a. No enough background in computer science courses in school, caused to not learn the programming languages correctly
b. Not enough practical work, no more time allocation for practicing
c. Lecturer should teach the programming course with one or two practical examples and assign some basic projects to a group of pupils as a team group or pair group
d. Most of the time problem is in both the lecturer and pupils, if lecturer is professional and hardworking, this can cause the pupils to learn more efficiently
e. The problem is more in the system and teaching methodology, the slide systems should be ban and books should be the main reference materials, pupils should be loaded with more assignments and practical projects and main point more restrictions needs to be applied on pupils during exam.
f. Lecturer plays a key role to guide the pupils and teach them how to learn not how to get.(we don't want to know how to eat fish we want to know how to get fish from the sea)
g. Having goal and interest in the course is the priority for a student second problem is the huge number of pupils in classroom and unprofessional teaching by some lecturers
h. As far as I know not paying attention of pupils to the course, however, if the lecturer is not professional still the pupils are able to solve their problem via some online resources such as YouTube, Udemy, and Kaggly and so on.
i. Lecturer is just acting as a guide this is the pupils responsibility to try more and learn more
j. Both play an important role (lecturer and student) sometimes the lecture tries more to impart the knowledge but pupils neglect and vice versa, but mostly related to pupils efforts and endeavor if a lecture teaches 20% of the course on the other side the pupils require to try 80% of the remaining course

k. In my opinion the non-availability of the facilities such as internet, equipped lab and useful curriculum
l. The main problem is with the pupils a lecturer cannot teach from A-Z this is the pupils responsibility to reach to their goals and learn the concepts
m. Both can cause the pupils to not learn the programming languages correctly first useless teaching methodologies second pupils less efforts
n. Programming languages are very tough if It is not learned step by step

8. Conclusion

Achieving the quality of teaching in introductory programming language course plays essential role, hence this course, besides its objectives, prepares the student for further courses, programming skills, problem solving skills, and orient the student attitude to computer disciplines. Unfortunately teaching this course faces a lot of challenges.

It is also been discussed about the readability and Writability of the course where the most significant part to judge a languages is the usability and ease where programs can be understood and read on the other hand Writability means how simply we can create our programs and write our source code for a specific problem, surely stated these two terms can influence reliability.

In addition to this, the challenges faced by pupils while learning programming and the solutions have been spotted, hence, student now will be able to overcome on the challenges they were faced before can easily shows interest in learning any programming languages.

In the last section of this review paper pointed about the problems while teaching this course to undergraduate pupils and the solutions and suggestions which have been given by the pupils of computer science from different universities in Afghanistan.

9. References

1. Anthony R, Janet R, Nathan R. Learning and Teaching Programming: A Review and Discussion. Computer Science Education. 2003; 13(2):137-139.
2. Phit-huan T, Choo-yee T Siew-woei L. Learning Difficulties in Programming Courses: Undergraduates' Perspective and Perception. International Conference on Computer Technology and Development. 2009; 9:3892-1.
3. Brian WK, Dennis MR. the C Programming Language. (2nd ed.). India: Pearson India Education Services, 2018.
4. Pauch R, Kelleher C. Lowering the barriers to programming: A taxonomy of programming environments and languages for novice, ACM Computing Survey 37, 2, 2005.
5. Nikolina B, Ivica B. Teaching of Novice Programmers Strategies, Programming Languages and Predictors. Conference Paper, 2015, 1-3.
6. Robert WS. Concepts of Programming Languages. (4th ed.). India: Thomson Press India, 1999.
7. Mohammad H, Bouchaib F. Application Domain and Programming Language Readability Yardstick. 7th International Conference on Computer Science and Information Technology (CSIT), 2016, 1-2.
8. Ravi S. Programming Languages Concepts & Constructs. (2nded.). India: Addison-Wesley, 2000.
9. Peter van *et al*. The Role of Language Paradigms in Teaching Programming. Computers and Education Conference. 2003; 1(3):269-270.
10. Nikolaos SP, Stathis Z. Teaching Programming through Problem Solving: The Role of the Programming Language. Federated Conference on Computer Science and Information Systems, 2013, 1545-1546.
11. Mohamed Osman H, Mohammad A. The Challenges and the Opportunities of Teaching the Introductory Computer Programming Course: Case Study. Fifth International Conference on e-Learning. 2015; 87(76):324-329.
12. Siti Rosminah D, Ahmad Zamzuri M. Difficulties in learning programming: Views of pupils. International Conference on Software Engineering Education. 2012; 76(98):1-4.
13. McCracken M *et al*, A multi-national Multiinstitutional study of assessment of programming skills of first-year CS pupils, ACM SIGCSE Bulletin, 2001; 33(4):125-180.
14. Lister R *et al*, A multi-national study of reading and tracing skills in novice programmers, in ITi CSE-WGR '04 Working group reports from ITi CSE on innovation and technology in Computer Science education, 2004, 119-150.
15. Tenenberg J, Fincher S, Blaha K, Bouvier D, Chen T, Chinn D *et al.* Vandegrift, Pupils Designing Software: a Multi-National, Multi-Institutional Study, Informatics in Education. 2005; 4(1):143-162.
16. Rudder A, Bernard M. Shareeda Mohammed, Teaching programming using visualization, in WBED'07 Proceedings of the sixth conference on IASTED International Conference Web-Based Education. 2007; 2:487-492.
17. Niyazi A, Nuraiym M. Programming Languages. IEEE Software Engineering Education, (ISSN: 4106-3), 2014, 1-3.

International Research Journal of Engineering and Technology (IRJET) e-ISSN: 2395-0056
Volume: 06 Issue: 04 | Apr 2019 www.irjet.net p-ISSN: 2395-0072

A Review on Parametric Optimization of Aluminium Alloy 5754 for MIG Welding

Himanshu Yadav[1], M.S. Niranjan[2]

[1]*M.Tech Scholar, Dept. of Mechanical Engineering, Delhi Technological University (DTU), Delhi, India*
[2]*Asstt. Professor, Dept. of Mechanical Engineering, Delhi Technological University (DTU), Delhi, India*

Abstract - Welding is the most practical and productive approach to join metals for all time. Almost everything we use today which we call them as necessities of modern life such as car which is our mode of transport, mobile phones, metal doors and all other stuff made of metal involve some sort of welding. It has been classified in number of processes and one of them is Metal Inert Gas welding(MIG) otherwise called Gas Metal Arc welding(GMAW) by American welding society. In MIG welding, welding takes place due to the melting of the wire electrode that is fed through a gun and its fusion with the base metal resulting in a bond. Shielding gas is supplied to protect the molten weld pool from reacting with oxygen and water vapour present in the surrounding. Various welding parameters govern the process. These parameters include welding current, welding voltage, welding speed, WFR and GFR. These parameters influence tensile strength, yield strength, weld bead geometry and microstructure of the weld. This paper focuses on the optimization of these parameters to obtain best parameter combination for the target quality. For optimization of these parameters, Taguchi method has emerged as the widely accepted method for optimization by the researchers across the globe. The previous work done have been discussed in this review.

Key Words: GFR, MIG Welding, Parametric optimization, Taguchi technique. UTS, WFR.

1.INTRODUCTION

In MIG, a fine wire acts as electrode and is feed by a spool bolstered on a gun through a conduit liner and outside the nozzle. The wire is feed continuously when the trigger on the gun I pulled. When the trigger is pulled it also switches on current and shielding gas that is provided from the high-pressurized cylinders through the nozzle. The protecting gas shields the weld pool from responding to oxygen and water vapour in the surrounding environment. An electric circular segment is shaped between the electrode & work piece & heats them above their melting point. These melt mix together and solidify to join the two pieces into a single piece. Since the electrode i.e. the wire in this case melts, therefore it is called as consumable electrode.

Its successful application relies upon proper determination of:

- Electrode – constitution, diameter and bundling
- Shielding Gas – type (constitution), immaculateness and flow rate
- Process Variables – current, voltage, method of metal transfer and travel speed
- Equipment – power source, welding torch and wire feeder

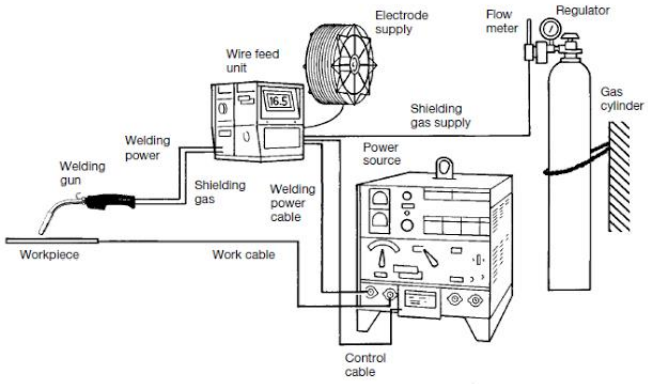


Fig -1: Diagram of MIG Welding Equipment

1.1 Advantages

- Operation can be performed in both semi-automatic as well as automatic mode.
- Welding of variety of industrial metals & alloys is achievable.
- All position welding is achievable through legitimate selection of equipment & process variables.
- Minimum after weld cleaning is needed because of the absence of a deposited slag layer over weld bead.
- Less operator expertise is required contrasted with Stick Welding.

1.2 Disadvantages

- Welding equipment is increasingly perplexing, more expensive and less convenient than that for Stick Welding.

- Welding of incredibly thin materials (<1/16") is an issue.
- The material must be free from dirt and non-corrosive.
- Welding equipment is too expensive and its complexity level is high contrasted with stick welding.

2. LITERATURE REVIEW

S. S.S. et al. [2019] carry out a comparison study of the joint of Aluminium Alloy 5052 & M.S. Plate made by MIG-brazing and Cold metal transfer with process parameters such as wire feed rate and travel speed constant. Filler wire used in the study is Al alloy BA4043 of dia. 1.3mm. Current is taken in the range 67–75 A and voltage is taken as 16.0 ± 0.2V. Torch travel velocity and WFR is 0.8 m/min and 5.8 m/min respectively, which is maintained during the process. Inert gas is used as the shielding gas with gas flow rate 20L/min. The hardness determined came out to be elevated in the toe regions when compared with CMT. In addition, zinc deposition was discovered in both the techniques. **[1]**

Vijander Kumar et al. [2018] investigates the influence of welding variables i.e. current, voltage & NPD on tensile strength of the weld. Further, the parameters are optimized using Taguchi method. The material for the study is hot die steel and copper-coated filer wire is taken as filler metal. Size of the specimen is 200*100*5mm^3. Welding is carried out in presence of inert gas. Values of current taken are 180, 190, 200A, Voltage taken is 21, 24, 27V and NPD as 12, 16, 20mm. The optimal set of parameters obtained are current as 200A, voltage as 27V and NPD is 16mm. **[2]**

Vijaya sankar et al. [2018] focusses on the effect of input variables i.e. current, GFR & potential difference on weld robustness of AISI 310 stainless steel and optimization of the variables by Taguchi method. The substrate material stainless steel AISI 310 and the filler metal AISI steel wire of dia. 0.8mm is chosen for the study. Current varies from 130-170A, voltage varies from 23-27V and GFR 13-17L/min. The optimum parameters obtained are Weld current 130A, Voltage 27V and Gas flow rate is 17L/min. The weld strength shows improvement for increasing value of voltage and GFR and decreasing value of current. **[3]**

Pavan G. Chaudhari et al. [2018] investigates the effect of single component oxide flux on the AISI 316L S.S. and MOORA technique is used for optimization. SiO_2 & Cr_2O_3 fluxes are used. Current varies from 150-180A, voltage 20-24V, welding speed is 150-180mm/min. Mixture of argon & carbon dioxide with a GFR of 15l/min is used to protect the weld pool. The technique for optimization used by them is simple, operation is carried out with lesser calculations, and overall computational time is less. **[4]**

C. Chen et al. [2018] utilized an optical magnifying lens and rapid imaging to demonstrate the impact of continuous & beat ultrasonic on weld appearance and molten metal drop movement in ultrasonic MIG. Used an optical microscope and high speed imaging to show the influence of continuous & pulsed ultrasonic on weld appearance and droplet transfer in ultrasonic assisted MIG welding. The substrate material is pure aluminium 1060 with aluminium 1003 as filler metal. Welding parameters taken are as follows: voltage-22V, WFR-5.5m/min, GFR-15l/min and welding speed -4.5m/min. Necking is observed in case of conventional MIG that is reduced in case of ultrasonic assisted MIG. The penetration of continuous ultrasonic MIG is1.68 times and of pulsed ultrasonic MIG is 1.3-1.8 times when compared to that of conventional process. **[5]**

Patil et al. [2017] shows the influence of process variables such as current, torch travel velocity & voltage on UTS of mild steel grade AISI 1030 and optimization of the variables by Taguchi method. The filler metal used is Carbon steel wire ER70S-6. Shielding gas used is argon. Current 200-240A, voltage is 23-27V and welding speed is 250-450mm/min. Argon gas is used with a flow rate of 17L/min. Ultimate tensile strength varies linearly with speed and inversely with the welding current. The parameter that has a significant influence on weld strength is welding speed. **[6]**

X. Zhan et al. [2017] discusses about the porosity formation in weld of invar alloy done by laser metal multi-layer hybrid MIG weld. Invar M93 is the filler metal. The power (laser), current and torch travel velocity are set to be 2–6 kW, 220–320 A and 0.35–1 m/s resp... The -ve clearance came out to be 0.2 mm. Gas flow rate of 20L/min is taken. Shielding gas used is argon. Conditions involving low capacity of laser in root & less current in cover pass results in porosity generation. The inner side of porosity wall has high oxygen concentration & nickel oxide, iron oxide and manganese oxide react with carbon when the weld cools to generate carbon dioxide leading to porosity. **[7]**

C. Labesh kumar et al. [2017] investigates the variation of process variables. Variables that were singled out for the study were welding current expressed in ampere, travel speed expressed in mm/min and potential difference expressed in volts. They also optimize the process variables. Optimization of these variables was carried out by DOE method. HDS steel is the test specimen and the filler metal is copper-coated mild steel wire. Inert gas is used for purpose of shielding. Three values of welding current chosen: 190, 195 and 200 amps. Three values of voltage chosen: 20, 23 and 26 V. welding speed are 0.037, 0.042, 0.048 mm/min. The optimum parameters are welding speed-0.051mm/min, voltage 26V and current 200A. **[8]**

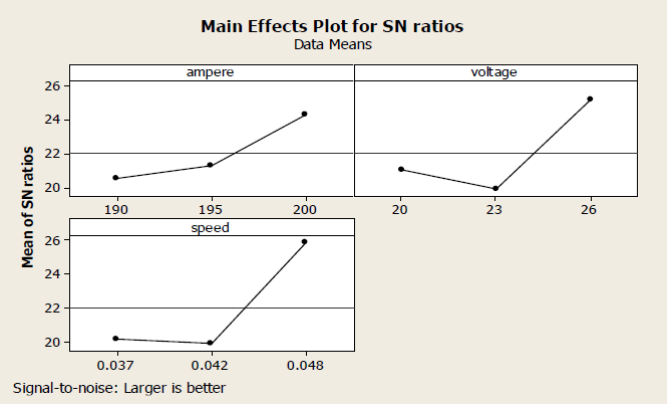


Chart -1: Plot for Parameter VS S/N ratio [8]

X. Zhan et al. [2016] focuses his attention to overcome the poor weld ability of the Invar 36 alloy by comparing MIG and laser-MIG welding. Current values are 250 & 200A, voltage is 22-20V and welding speed is 6-3 mm/sec. The maximum residual deformation of hybrid laser-MIG and MIG are 0.7 mm and 2.3 mm respectively. Welding of invar plates occurred in 4 passes in case of MIG and 3 passes in hybrid laser-MIG and time taken in welding for MIG is equal to 8 times of time taken by hybrid laser-MIG. **[9]**

Nabendu Ghosh et al. [2016] focusses on process variable variation and their effect on weld quality measured in respect of yield strength, UTS and % elongation of 316L stainless steel. Filler metal taken is 316L S.S. Current values are 100,112,124A, GFR is 10, 15, 20L/min and NPD is 9-12-15mm. The best weld quality is achieved when current is 100 A, GFR is 20 l/min and NPD 15mm and worst for sample with settings equal to 124 A as current, 10 l/min GFR and NPD 15mm. The significance of current on strength of joint is found to be more when compared to remaining variables. Optimum set of parameters obtained are welding current-100A, GFR-20L/min & NPD-15mm. **[10]**

Pappu kumar et al. [2016] focusses on the consequence of variation of process variables i.e. current (A), welding voltage expressed in volt & WFR expressed in m/min on Tensile strength of mild steel and optimization of these variables done by Taguchi method. Carbon dioxide is used for shielding the weld. The values of welding current chosen are 50, 100 and 150 amps. Three values of arc voltage chosen: 15, 19 and 23 V & wire feed rate is 3, 4, 5 m/min. Among the set of process variables, the variables that has larger influence on tensile strength are voltage and current. Optimum set of variables determined are 150A (current), 19V (voltage) & WFR-5m/min corresponds to maximum value of tensile strength. **[11]**

Prasenjit Mondal et al. [2015] emphasises on optimisation of process variables such as welding current, voltage & welding speed for maximum value of hardness and tensile strength and their effect on them. The substrate material is S.S. AISI-304 & Mild steel plate IS 1079. Current values taken are 130-135-140A, voltage is 22-24-26V and welding speed is 25-30-35cm/min. Optimum values of welding current, voltage & welding speed are 135A, 22V & 35 cm/min respectively. The effect of parameters on the MRPI is as follows: voltage > current >speed. **[12]**

K. Sivasakthivel et al. [2015] investigates the variation of process variables. The selected variables are welding current expressed in ampere, voltage expressed in volts & travel speed expressed in cm/min and their consequence on material properties of titanium i.e. tensile strength, impact strength, hardness and to optimise the above parameters by ANOVA. Shielding gas is argon. Three values of welding current are chosen: 250, 280 and 300 amps. Three values of arc voltage are chosen : 20, 25 and 30 V. welding speed are 55, 60, 65 cm/min. Acc. to S/N ratio analysis and ANOVA, the process variables affecting the Tensile Strength were speed, current and Voltage. The effect of parameters on penetration is as follows: voltage> current>speed. **[13]**

Vikas Mukhraiya et al. [2014] studies the influence of process variables on torsional rigidity of welded rod of steel ST-37 of 20mm dia. Argon and carbon dioxide concoction was used to shield the weld pool combined in ratio 4:1 respectively. Three values of welding current are chosen: 340, 350 and 360 amps. Three values of arc voltage are chosen: 350, 360 and 370 V. wire feed rate are 80, 100, 120 m/min. The welding voltage shows greater effect than wire feed rate on torsional rigidity. An optimum parameter combination is obtained by Taguchi method for maximum torsional rigidity. **[14]**

Mohd. Shoeb et al. [2013] worked to determine the consequence of variation of input variables (singled out are welding speed (mm/sec), voltage (volts) and GFR (l/min)) on weld bead geometry i.e. penetration, width & height of HSLA steel IS 304. The filler metal is OK Autrod 13.14 Cu based alloy. Mixture of 80% Argon, 18%, CO_2 & 2% O_2 is used for shielding the weld pool. Voltage is varying from 26-32V, GFR is varying from 20-25L/min and welding speed varies 2.7-3.6mm/sec. No effect of welding speed has been observed on penetration. Also for any value of current, bead width varies inversely to the welding speed. No significant effect of gas flow rate variation on penetration has been observed. The penetration is proportional to increase in voltage and the height varies inversely with voltage. **[15]**

Izzatul Aini Ibrahim et al. [2012] discusses the consequence of welding parameter variation. Welding current (A), voltage (V) and torch travel (cm/min) are singled out to carry out the research. By varying these variables, influence of these variables on properties of the weld of mild steel material is determined. Filler metal used is ER 70S-6. Shielding gas is carbon dioxide. Three values chosen for the welding voltage are 22, 26 and 30 V. Three values of welding current chosen are 90A, 150A and 210 A respectively. The welding speed values selected for the research are 20cm/min, 40cm/min and 60 cm/min. The value of hardness is higher at 90A and decreased a little at 150A and at 210A it increased by a little than 150A and maximum value is obtained when voltage corresponds to 26 V, current corresponds to 90 ampere & welding speed corresponds to 60 cm/min. The grain boundary size is affected when process variables are varied as per DOE. The penetration increases with increasing value of welding current and is maximum for

welding speed 60 cm/min, voltage 26 V & welding current 210 A. **[16]**

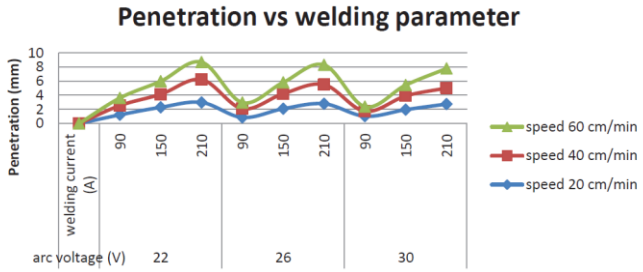


Chart -2: Penetration VS process parameters [16]

Ajit Hooda et al. [2012] determines the consequence of process parameters variation such as welding current, voltage, wire feed rate & gas flow rate on tensile strength of AISI 1040 medium carbon steel joint and an optimum set of parameters is obtained using Taguchi technique. Filler metal used is ER 70S-6. Values of Welding Voltage (V), Current (A), Wire Speed (m/min), and Gas Flow Rate (l/min) Values taken are 23-25V, 200-220A, 2.4-3.2m/min, and 12-16l/min respectively. Optimum values of process variables i.e. welding voltage- 22.5V, current- 190A for transverse & 210A for longitudinal, wire feed rate- 2.4m/min and gas flow rate- 12l/min corresponds to maximum yield strength of AISI 1040 medium carbon steel joint. **[17]**

S. V. Sapakal et al. [2012] shows the effect of various process variables such as welding current, voltage and welding speed on penetration depth in MS C20 material. Shielding gas used is carbon dioxide. Three values of welding current chosen: 60, 90 and 120 amps. Three values of arc voltage chosen: 15, 22.5 and 30 V. welding speed are 2, 4, 6 m/min. The value that has been obtained experimentally from optimum parameters is 5.25mm for penetration and 14.4 as S/N ratio. **[18]**

H.T. Zhang, J.Q. Song [2011] discusses of the welding of two dissimilar metals AZ31 Magnesium & 2B50 Aluminium using MIG with layer of zinc foil between the two metal layers. The filler metal taken for the welding is ER4043 Al-Si wire. Welding is done on CLOOS GLC403/603 QUINTO Welding machine. Welding current is 20A, voltage is 22.5V, WFR is 3.1m/min and welding speed is 185cm/min. Use of zinc foil as the inter layer between the metals made the welding of these metals possible without burn through and cracking. An Al–Si hypoeutectic structure and an Al–Zn eutectic structure is observed in the fusion zone of the weld. **[19]**

BAI Yan, et al. [2010] uses an orthogonal experimental design to study the influence of plasma-MIG welding parameters on the weld porosity of 5A06 aluminium alloy. Argon serves the purpose of shielding gas. Values of wire feed rate (m·min−1) are 9.0-10.1-11.2-12.3. MIG welding Voltages are 26.4-28.5-30.2-32.0V. Shielding gas flow rate (L·min−1) 20.0 & 25.0. Welding speed (mm·min−1) 400.0 & 600.0. Plasma current is 95-110-125-140A and Plasma gas flow rate (L·min−1) 8.0 &10.0. The effect of plasma gas flow rate is more dominant than other factors. The secondary factors are welding voltage, welding speed, wire feed rate and plasma current. Optimum parameters obtained are wire feed rate as 10.1 m/min, voltage as 28.5V, welding speed as 400 mm/min and current is ranging from95A to 140A with GFR corresponding to 20-25l/min. From this hybrid method joint with great mechanical performance were acquired, which achieved excellent rigidity of 92%.**20]**

3. CONCLUSIONS

From this review, it has been concluded that very less research has been done on Aluminium alloy 5754 that offers excellent weld ability and machinability among 5*** series of aluminium alloys. It has a wide range of applications that includes shipbuilding, vehicle bodies, rivets, nuclear structure and food processing industry. It has excellent corrosion resistance.

REFERENCES

[1] S.S. Sravanthi, Swati Ghosh Acharyya, K.V. Phani Prabhakar, G. Padmanabham, "Integrity of 5052 Al-mild steel dissimilar welds fabricated using MIG-brazing and cold metal transfer in nitric acid medium," Journal of Materials Processing Tech. 268 (2019), Science Direct, 97–106.

[2] Vijander Kumar, Navneet Goyal, "Parametric Optimization of Metal Inert Gas Welding for Hot Die Steel by using Taguchi Approach" Material Science Research India, ISSN: 0973-3469, Vol.15, No.(1) 2018, Pg. 100-106.

[3] Vijaya Sankar, Daniel Lawrence, Jayabal, "Experimental Study and Analysis of Weld Parameters by GRA on MIG Welding" Materials Today: Proceedings 5 (2018), Science Direct, 14309–14316.

[4] Pavan G. Chaudhari, Priyank B. Patel, Jaksan D. Patel, "Evaluation of MIG welding process parameter using Activated Flux on SS316L by AHP-MOORA method" Materials Today: Proceedings 5 (2018), Science Direct, 5208–5220.

[5] Chao Chen, Chenglei Fan, Sanbao Lin, Xiaoyu Cai, Lei Zhou, Sanfeng Ye, Chunli Yang, "Effect of ultrasonic pattern on weld appearance and droplet transfer in ultrasonic assisted MIG welding process" Journal of Manufacturing Processes 35 (2018), Science Direct, 368–372.

[6] S. R. Patil, C. A. Waghmare, "Optimization Of Mig Welding Parameters For Improving Strength Of Welded Joints" International Journal of Advanced Engineering Research and Studies, ISSN: 2249–8974, July-Sept., 2013/14-16.

[7] Xiaohong Zhan, Qiyu Gao, Cheng Gu, Weihua Sun, Jicheng Chen, Yanhong Wei, "The porosity formation mechanism in the laser-MIG hybrid welded joint of Invar alloy" Optics and Laser Technology 95 (2017), Science Direct, 86–93.

[8] C. Labesh kumar, T. Vanaja, Dr. KGK Murti, VVSH Prasad. "Optimization of Mig Welding Process Parameters for Improving Welding Strength of Steel" International

Journal of Engineering Trends and Technology, ISSN: 2231-5381, Volume 50 Number 1 August 2017.

[9] Xiaohong Zhan, Yubo Li, Wenmin Ou, Fengyi Yu, Jie Chen, Yanhong Wei, "Comparison between hybrid laser-MIG welding and MIG welding for the invar36 alloy" Optics & Laser Technology 85 (2016), Science Direct, 75–84.

[10] Nabendu Ghosh, Pradip Kumar Pal, Goutam Nandi, "Parametric Optimization of MIG Welding on 316L Austenitic Stainless Steel by Grey-Based Taguchi Method" 2212-0173, Procedia Technology 25 (2016) 1038 – 1048.

[11] Pappu Kumar, Prakash Kumar, "Optimization of Welding Parameter (MIG Welding) Using Taguchi Method" International Journal of Scientific Research and Education, ISSN:2321-7545, Vol. 4, Issue 11, November-2016, Pg-6053-6058.

[12] Prasenjit Mondal, Dipankar Bose, "Optimization Of The Process Parameters For MIG Welding Of AISI 304 And Is 1079 Using Fuzzy Logic Method" International Research Journal of Engineering and Technology, ISSN: 2395-0072, Volume: 02 Issue: 08, Nov-2015.

[13] K.Sivasakthivel, K.Janarthanan, R.Rajkumar, "Optimization of Welding Parameter in MIG Welding by Taguchi Method" International Journal of Advanced Research in Mechanical Engineering & Technology" ISSN : 2454-4736, Vol. 1, Issue 1 (Apr. - Jun. 2015).

[14] Vikas Mukhraiya, Raj Kumar Yadav, Sanjay Jathar. "Parametric Optimisation of MIG Welding Process with the Help of Taguchi Method" International Journal of Engineering Research & Technology, Vol. 3 Issue 1, January – 2014.

[15] Mohd. Shoeb, Mohd. Parvez, Pratibha Kumari, "Effect Of Mig Welding Input Process Parameters On Weld Bead Geometry On Hsla Steel" International Journal of Engineering Science and Technology, ISSN : 0975-5462, Vol. 5, No.01, January 2013.

[16] Izzatul Aini Ibrahim, Syarul Asraf Mohamat, Amalina Amir, Abdul Ghalib, "The Effect of Gas Metal Arc Welding (GMAW) processes on different welding parameters" Procedia Engineering 41 (2012), Science Direct, 1502 – 1506

[17] Ajit Hooda, Ashwani Dhingra, Satpal Sharma. "Optimization Of MIG Welding Process Parameters To Predict Maximum Yield Strength In AISI 1040" International journal of mechanical engineering and robotics Research, ISSN 2278 – 0149 Vol. 1, No. 3, October 2012.

[18] S. V. Sapakal, M. T. Telsang, "Parametric Optimization Of MIG Welding Using Taguchi Design Method" International Journal of Advanced Engineering Research and Studies, ISSN2249–8974, Vol. I, Issue IV, July-Sept., 2012, 28-30.

[19] H.T. Zhang , J.Q. Song, "Microstructural evolution of aluminum/magnesium lap joints welded using MIG process with zinc foil as an interlayer" Materials Letters 65 (2011), Science Direct, 3292–3294.

[20] BAI Yan, GAO Hong-ming, WU Lin, MA Zhao-hui, CAO Neng, "Influence of plasma-MIG welding parameters on aluminum weld porosity by orthogonal test" Trans. Nonferrous Met. Soc. China 20(2010) Science Direct, 1392-1396

BIOGRAPHIES



Himanshu Yadav
M.tech Scholar
(Production Engineering)
DELHI TECHNOLOGICAL UNIVERSITY(FORMERLY DCE)

Dr. M.S. Niranjan
Asstt. Professor
DELHI TECHNOLOGICAL UNIVERSITY(FORMERLY DCE)

ResearchGate

See discussions, stats, and author profiles for this publication at: https://www.researchgate.net/publication/336824913

An assessment of socially responsible consciousness and multi-level integration of business morals, corporate social obligation and sustainability in higher educ....

Article · January 2019

DOI: 10.1504/IJHES.2019.10025062

CITATIONS
0

READS
5

2 authors:



Gaurav Dawar
Delhi Technological University
8 PUBLICATIONS **10** CITATIONS
SEE PROFILE



Seema Singh
Delhi Technological University
37 PUBLICATIONS **32** CITATIONS
SEE PROFILE

Some of the authors of this publication are also working on these related projects:



AICTE sponsored project on Indian Continuing Engineering Education System in context of Globalisation View project



Agricultural Technology Adoption, Poverty and Income Inequality in Ethiopia View project

All content following this page was uploaded by Gaurav Dawar on 26 October 2019.

The user has requested enhancement of the downloaded file.

An assessment of socially responsible consciousness and multi-level integration of business morals, corporate social obligation and sustainability in higher education

Gaurav Dawar*

IMS Ghaziabad,
UP 201009, India
and
Department of Humanities,
Delhi Technological University,
Delhi – 110042, India
Email: gauravdawar@gmail.com
*Corresponding author

Seema Singh

Department of Humanities,
Delhi Technological University, India
Email: seemahumanitiesdtu@gmail.com

Abstract: The recent developments have generated the need for sense of community building, social apprehension and inculcation of social-consciousness in the young managers and achieving this requires being a part of curriculum. The current article aims to explore the integration of business morals, corporate social obligations and sustainability principles in B-schools of NCR in India and its impact on social consciousness of budding managers. We propose an integrative and holistic framework to brief the coordination of morals, corporate social responsibility and sustainability in management education through three independent analyses – institutional level, curriculum level and pupil level learning analysis. Our findings reveal that government universities are imparting both compulsory as well as CSR-embedded courses yet it fails to moderate the perception of budding managers. The current article points towards the new paradigm of CSR education in academic institutes and suggestions are made to enhance it further.

Keywords: CSR; management education; CSR in management education; sustainable development; morals; social obligation.

Reference to this paper should be made as follows: Dawar, G. and Singh, S. (2019) 'An assessment of socially responsible consciousness and multi-level integration of business morals, corporate social obligation and sustainability in higher education', *Int. J. Higher Education and Sustainability*, Vol. 2, No. 4, pp.303–326.

Biographical notes: Gaurav Dawar is a Research Scholar in Delhi Technological University and working in the area of corporate social responsibility.

Copyright © 2019 Inderscience Enterprises Ltd.

Seema Singh is a Professor of Economics at the Delhi Technological University since 2008. She is largely, interested in the issues related to gender, higher education, employment and labour market, she has presented, published several papers and conducted successfully several research projects. She received AICTE Career Award for Young Teachers in 2000. Now, she has been elected Vice President (Education and Research) and Board Member (South Asia) of International Network of Women Engineers and Scientists (INWES) for 2018–2020. She is a member of the editorial team of many journals.

This paper is a revised and expanded version of a paper entitled 'Perspectives of corporate social responsibility in technical education: a study of developing country' presented at ICBESD – 2018, Delhi, 22–23 February 2018.

1 Introduction

The financial, economic and political emergencies of recent years feature that proceeding business by seeking a conventional economic growth paradigm, does not bode well with long-term sustainability in future (WEC, 2016). The policymakers today recognise today's global imperative is to maintain health, eradicate poverty and maintain the planet's balance. The global financial crisis has enlarged the stakeholder pressure for cognisant corporate conduct enhancing the significance of CSR, SD and business ethics in directing the behaviour of future leaders and this expectation of stakeholders can be met through the transfer of responsible knowledge.

In December 2002, United Nations General Assembly announced 2005 to 2014 as decade of education for sustainable development (ESD) and point was to create and advance education and training as a basis for responsible society and imbibing the principles of sustainability at all the level of education framework (Grindsted and Holm, 2012; Baltic 21E, 2002; Nordic Council of Ministers, 2009, 2011; Holm et al., 2012; Renmin Educational institution of China UNDP, 2010; UN DESD, 2011). This recent development has put enormous pressure on educational institutions for their significant role in addressing the critical issue of sustainability among future managers.

Educational institutions have a primary responsibility to equip the coming generation with the required skill set to cope-up with globalisation, create economic development and a future viable for both individuals and planet (Ethical Corporation, 2006). Therefore to comprehend this sense of equalisation, essentialness of integrity and genuineness in future managers imparting knowledge related to morals, corporate social obligation and environmental protectionism is a crucial step (Kolodinsky et al., 2010).

Recently, the discipline of sustainability has demonstrated the growing dimension in the scholarly field with an increase in conferences, dedicated departments, educational projects and journals (O'Byrne et al., 2015). Despite the accretion of scholarly work in the field of teaching sustainability and a related concept, less work has been done to assess the outcome of these instructions for sustainability. A comprehensive multi-level analysis has been done by Setó-Pamies and Papaoikonomou (2016) evaluate the higher education program for sustainability.

The current paper is an endeavour to investigate the learnings from the combination of business morals, corporate social obligation and sustainability (BMCSOS) in the

management programs towards socially responsible consciousness of future managers in higher education institutions in the national capital region in India. Along these lines, the paper delivers the need to build up a more comprehensive and integrative model to guide the training of BMCSOS to add more meaningful and enduring learning and conduct of future managers. The paper has organised a review of the previous writings on the combination of BMCSOS in the management education; the multi-level framework for the evaluation of the involvement of BMCSOS, discussion and implications.

2 Literature review

According to the world council for economic development (WCED), sustainable development is meeting the present need without compromising the ability for future generations to meet their needs. At the prominent stage, it implies addressing the issues related to the problems identified with monetary effectiveness, social value and environmental responsibility. As per UNESCO "education for sustainable development learns to take informed decisions and responsible actions for environmental integrity, economic viability and just society, for present and future generations while respecting cultural diversity." Thus ESD is a broad subject with differentiated objectives focusing on addressing the needs of present and future generations. Consequently, issues like social value and environmental obligation are becoming the primary social foundation of advanced education.

Table 1 Studies on the teaching of ethics, CSR and SD

Authors	*Country*	*Findings*
Mahoney (1990)	USA, UK, Europe	Compared course structures and concluded that there is an increase in business ethics course in USA, UK and Europe.
Cummins (1999)	UK	A reported detailed critical development in the arrangement of business ethics.
Macfarlane and Otterwill (2004)	UK	Business ethics occupied a marginal position in management programs in UK.
McKenna (1995)	Australia	Has surveyed and reported that teaching business ethics in Australian business academics is a priority and little has been done for its promotion in curricula.
Barkhuysen and Rossouw (2000)	Africa	Reported business ethics are taught in 77 courses and mostly in South Africa and business schools are leading in its delivery.
Bampton and Cowton (2002)	UK	Established minority of lectures in management accounting explicitly and implicitly dealt with ethics.
Pesonen (2003)	Finland	Expostulated issues in integration of sustainability in b-school curricula faced by University of Jyväskylä.
Matten and Moon (2004)	Europe	Analysed and highlighted the avenues of imparting CSR education and methodology to bring it into mainstream teaching.
Tilbury et al. (2005)	Australia	Analysed and highlighted Australian business programs limited in scope while dealing with multidisciplinary challenges of introducing sustainability at workplace.

Table 1 Studies on the teaching of ethics, CSR and SD (continued)

Authors	*Country*	*Findings*
Cornelius et al. (2007)	Worldwide	Evaluated the level of integration of ethics in the curricula of top 25 b-school as per FT and noted that business ethics are either taught as a stand along or as a part of general management business module.
Benn and Dunphy (2009)	Australia	Explored and identified the facilitators and impediments for integration of sustainability issues in Australian MBA core courses.
Wu et al. (2010)	Worldwide	Explored the b-schools of Europe and USA and highlighted the b-schools in later used compulsory-oriented approach, whereas in b-schools in earlier used elective-oriented approach for teaching sustainability issues.
Fernández Fernández and Sanjuán (2010)	Spain	Examined the study patterns of executives and businessmen in academic year 2009–2010 and found CSR courses are offered in minority at postgraduate level and barely existed at graduate level.
Stubbs and Schapper (2011)	Australia	Has worked and suggested a curriculum for sustainability and corporate social responsibility in the b-school at Monash University.
Lambrechts et al. (2013)	Belgium	Identified the competencies related to sustainable development and highlighted that competency related to emotional intelligence and responsibility are widely integrated in curricula.
O'Byrne et al. (2015)	Worldwide	Examined the institutes grating degree at both graduate and post-graduate level and results have highlighted that 85% of such programs cover issues related to sustainability and 2% of masters' program have compulsory natural science course besides wide diversion in the content of programs.
Rutherford and Scullion (2017)	Worldwide	Brought-out the opportunities and challenges of embedding CSR principles in marketing communication program for working individuals focusing on administrative and economic constraints post 2008 financial crisis.
Beitelspacher and Rodgers (2018)	USA	Designed project involving students undertaking buying decisions based on corporate social responsibility issues and it resulted an effective way to engage them in learning about CSR.

The education for BMCSOS has pulled significant attention in academic writing and has become a growing part of interest to scholarly practitioners (Turker et al., 2016). The main explanation for the said improvement is higher in-depth education on social issues that can positively lead to the subtlety of the organisation towards such topics in future. The quality and quantity of BMCSOS instructions in the present could be a distinguishing factor for the attention of executives towards the social issues in future. There are a remarkable number of both qualitative and quantitative studies that have attempted to investigate how and to what degree BMCSOS are effective in moulding the attitude of future managers (Table 1). The management education over the years has realised the importance of CSR, SD and business ethics at both undergraduate and post-graduate level (Christensen et al., 2007; Orlitzky and Moon, 2011). In order to

translate the complex issues in to a common sense dimension BMCSOS are explored heuristically through various themes like enhancing social consciousness (Markley Rountree and Koernig, 2015); developing socially conscious entrepreneur (Parris and McInnis-Bowers, 2017); sustainable development goals and business education (Kolb et al., 2017); developing a socially influential curriculum (Horng et al., 2019).

Currently a significant number of higher education institutions are offering courses dealing with CSR, SD and business ethics (Evans and Marcal, 2005; May et al., 2014; Rasche et al., 2013) and the themes of these courses deal with sustainability, corporate social reporting, sustainable finance, responsible investment (Christensen et al., 2007; Paine, 1988; Van Liedekerke and Demuijnck, 2012). These courses are expected to develop future managers towards the inculcation of ethical and social thinking aspect in their decision-making process (Carroll, 1991; Adler, 2002; Gautschi and Jones, 1998; Treviño et al., 2006; Hemingway and Maclagan, 2004). Though, in Indian higher education institutions courses with a focus on sustainable outlook is work in progress. We can categories the Indian institutions are still in stage 2 as per the Leal Filho (2011).

The work of Srinivasan et al. (2012) brought out the current state of ethics and CSR courses taught in Indian universities. Though to date, no investigation has been undertaken to evaluate the impact of BMCSOS education in Indian universities. India in Asian countries is growing in favour of corporate social responsibility after the recent amendments made to Companies Act, 2013, making CSR an integral part of corporate activities. The associations and forums are bringing together top executives of major companies, academicians and NGO's for promoting CSR.

Corporations in India have become very sensitive to CSR post-amendment and planned to implement it effectively. It implies that new advancements and execution of CSR are to be expected in India. Hence the teaching of ethics and CSR at a different level has increased. Some academic institutes have also signed up for *'principles of responsible management education' (PRME)* an initiative of United Nations Global Compact (UNGC) (2007) that aims to improve awareness of future business leaders for economic efficiency, social equity and environmental accountability. Thus there is a need to understand the current practices of Indian universities to make future managers ready for meeting the challenges arising out of CSR and SD practices in corporations.

The principal aim of the current study is to investigate the level of inculcation and impact of BMCSOS courses in the management program offered by higher education institutes in Delhi and NCR Region. This study can act as a point of starting a further discussion about leading and implementing ESD in Indian universities.

2.1 Hypothesis development

Few previous studies have inspected explicitly a variety of factors that may influence the incorporation of BMCSOS in higher education. Through we found work by Srinivasan et al. (2012) focusing only on the current state of ethics and CSR courses taught in Indian universities. No study has been found focusing on the impact of these courses on the future manager, especially in Indian universities. Therefore, it is considered an eclectic approach and use of the multi-theoretical framework to evaluate the impact of BMCSOS education on responsible behaviour of future managers by following factors: higher education institution and responsible education intervention.

2.1.1 Higher education institution

Sustainable thinking can be inculcated if it is applied not just in teaching but also in campus operations (Leal Filho, 2011). Higher education institutions are regarded as a critical driver for the development of sustainable societies (Findler et al., 2019), and stakeholders expect them to be a change agent transforming the mindset of future leaders in academia. The current higher education framework in India, especially in the case of management education, institutes are organised at three levels; the first is institutes established by special act of Indian parliament offers two year management programs; the second category is the business school affiliated to central or state universities; the third category is the business schools set up by private foundations and societies. The content and pedagogy of the programs shift widely between institutes imparting business education (Srinivasan et al., 2012). The approach has been that faculties at government-funded institutes develop the courses depending on their interest and institutional support. Though such initiatives are also influenced by higher education regulatory agencies and judiciary. Environmental knowledge was permeating at all level of education by the Supreme Court in, 1991 and directed the apex body UGC to design the syllabus and textbook for the courses. The sustainability-related courses were first introduced by IIM at Ahmedabad and Calcutta first during the early nineties and later adopted by various institutes. The government also mandated environmental education in rural higher education institutions to meet challenges they may arise in future professional lives (Chhokar, 2010). Students in government-funded institutions have a higher exposure to environmental and sustainability-related issues. Thus it will be interesting to explore if the sensitivity of future managers to BMCSOS related issues is influenced by category of the educational institution.

H1 Managers studying in public university have more responsible consciousness.

2.1.2 Responsible education intervention

Active education systems broaden access to opportunities and fuelling economic growth. ESD aims at providing the skill set people to need to survive in a sustainable economy, smart agriculture, forest rehabilitation, working with renewable energy and efficient ecosystem management (Bokova, 2015). It aims at bringing a fundamental shift on how managers may think, act and discharge responsibilities effectively. Thus, to increase the spirit of sustainability b-schools are sensitising professionals towards BMCSOS issues developing individual competencies among the new breed of professional and cater to the future needs of corporations. These competencies can be improved by imparting greater responsible knowledge and skills without which an expert may not be able to function effectively (Mulder, 2014). Institutions offering higher courses in sustainability shall be able to provide the right skill needed for responsible leaders and tune with the future of business and consumer behaviour (Lykkegaard, 2018). It forms the basis for our second hypothesis that studying a higher number of BMCSOS related courses are more sensitive towards related issues.

H2 Managers undergoing higher BMCSOS courses have more responsible consciousness.

The next section presents the methodology used for the study.

3 Methodology

The universities are considered as a multi-level learning environment where the students undergo learning and socialisation through various sites (Blasco, 2012). With this in mind, we use a multi-level evaluation system proposed by Setó-Pamies and Papaoikonomou (2016) and Setó-Pamies et al. (2011) and modified to test the integration of BMCSOS issues in institutions providing management courses at three levels, i.e., institutional level, curriculum level and pupil level to evaluate its impact.

The study has been conducted in three phases: in phase 1 – institutional level analysis is undertaken on the basis of their mission, vision and strategic plan and web-content analysis has been considered as an appropriate methodology; in phase 2 – curriculum level analysis is done through web-content analysis aiming to expedite on the basis of concentration or dispersion, single discipline or multiple discipline approach and compulsory or elective-based courses; finally in phase 3 – pupil level analysis is conducted to test the learning for knowledge, skill, competency and attitude for BMCSOS through questionnaire. The budding managers undergoing business program at appropriate B-schools are randomly selected for the study. Most of the previous investigations were survey-based, and web-content examination shall be able to mitigate the shortcoming of the questionnaire. The survey was administered among the management institutes teaching MBA program in the National Capital Region, India.

The questionnaire has been divided into two parts: part 1 is for evaluation of attitude towards social initiatives and part 2 involves the questions related to CSR and SD dimension for evaluation of responsible consciousness. For part 1, a brief description of the case was presented from the work of Rosario et al. (2014) to test the attitude of students towards social initiatives. The case is shown in Appendix B. The opinions of the respondents were measured on seven-point rating scale from "I don't like it at all" to "I like it at all." The attitude of respondents was measured through the questions to evaluate the degree of acceptance of social initiatives; assess the value aspect; the degree of support for the effort and the perceived utility of the action.

Part 2 of the questionnaire is related to the measurement of socially responsible consciousness of budding managers. The questionnaire has been adapted for the purpose based on the work of Boehm (2002) which is developed on the literary work (Besser, 1999; Shai et al., 1999; Etheredge, 1999) and has been further edited and modified as per the author's perspective building. The dimension of the questionnaire not relevant for the study was removed, i.e., the reason for not undertaking CSR. The opinions of the budding manager are recorded on seven-point scale for various parameters. A summarised value of an overall parameter is calculated, and it is further verified by ANOVA considering learning of BMCSOS courses as the independent variable. Finally, the last step independent sample t-test is performed to investigate the students' perception by educational institutions, to test more significant intervention of responsible courses and gender.

The study was conducted during the academic session 2017–2018 using educational institution's website and related document as primary data sources. The database of all the courses offered in the academic year 2017–2018 was created and teaching of management program of all educational institutions, i.e., state government funded, central government funded, and private funded were analysed as per the issues relating to BMCSOS.

4 Analysis and results

The results are presented as per three levels proposed in the section above.

4.1 Phase 1 – institutional level analysis

The analysis of the educational institutions for BMCSOS education has been adapted from the methodology suggested by Kolb et al. (2017). There are more than 14 educational institutions currently supported by government and privately held in the National Capital Region in India. Out of these 80%, educational institutions are offering management programs. For phase 1, only those educational institutions are selected who have published detailed curriculum on their websites. Finally, a total of five institutions are selected for analysis. Namely, CU is a central government-funded educational institution, SU 1 and SU 2 is state government funded educational institutions, and PV 1 and PV 2 are privately funded educational institutions.

4.1.1 Analysis of educational institutions' approach towards sustainability, CSR and ethics

The vision statement is the first level of integration of responsible management practices in educational institutions. The vision statements provide an opportunity for the educational institution to establish a strategic position. In the first step, the vision statements are taken from the website of the department of management of all selected institutions and analysed with the help of an extensive list of keywords based on Wals (2009). The keywords (Appendix A) are matched with the mission and vision statements, and the amalgamation of responsibility and sustainability in strategic direction of educational institutions are analysed. B-schools should follow a systematised and comprehensive approach while incorporating sustainability in its mission. An effective BMCSOS education requires systematic reasoning and an interdisciplinary approach (Geli de Ciurana and Leal Filho, 2006). Despite a holistic approach to deal with sustainability is frequently pronounced; a limited execution is directed; generally concentrating on the environmental aspects of campus (Leal Filho, 2009). Many scholars have advocated that ESD should be integrated in the practice of educational institution and should be integrated into all the areas like education, research, outreach and operations (Kolb et al., 2017). Table 2 presents the analysis of mission and vision statements of educational institutions, and the keywords are highlighted. It is observed that the mission and vision statement of PV 1, SU 1 and PV 2 contains relevant keywords related to sustainability. The vision statements bring out the words like 'inclusive', 'social transformation', 'socially responsible', 'business and society', 'sustainable', etc., which reflects the direction of these institutions in imparting the knowledge towards building a socially responsible nation.

To evaluate the requirements to integrate sustainability in education, the institutions need to integrate 'responsibility' in their actions and engagements. Educational institution's association or engagements with international organisations like Academy for Business in Society (ABIS), Principle of Responsible Management Education (PRME), Central and Eastern European Management Development Association (CEEMAN), etc., are focusing on implementation of quality standards and imparting of education as per international standard in the area of management. It has been observed

from the websites of the institutions that only PV 2 is accredited with one of the international body and is one of the signatories of PRME, a initiative of UN that seeks to continuously improve management education in order to educate "a new generation of business leaders capable of managing the complex challenges faced by business and society in the 21st century" (PRME, 2015). Thus in the initial exploration private institution appears to have more inclination towards BMCSOS issues.

Table 2 Mission and vision of educational institutions

Institute name	*Mission*	*Vision*
PV 1	"To impart borderless inclusive, absolute ingress to management and technical education based on excellence."	"To be a world class management institute for social transformation through dynamic education."
SU 1	"To develop socially responsible and technology driven innovative managers and future leaders equipped with knowledge and professional ethics."	"To be the epitome of world class management education and research for meeting the contemporary challenges of business and society."
CU 1	"Academic excellence and leadership in educational institution based management education in India through high quality teaching, research, case development, innovative courses and pedagogy of learning."	"To develop CU 1 as a world class educational institution based institution which strives for academic excellence and thought leadership in management education."
PV 2	"Our mission is to impart vibrant, innovative and global education and to make PV 2 the world leader regarding excellence in education, research and to serve the nation in the 21st century."	"Top create an understanding and regard amongst our students for human values, pride in their heritage and culture besides a keen sense of right and wrong."
SU 2	"To develop managers with the capability to understand and analyze the dynamic business environment for effective decision-making while maintaining higher domains of professionalism."	"The educational institution will stimulate both the hearts and minds of scholars, empower them to contribute to the welfare of society at large; train them to adopt themselves to the changing needs of the economy; advocate them for cultural leadership to ensure peace, harmony and prosperity for all."

4.2 Phase 2 – curriculum level analysis

The second step is an evaluation of the inculcation of knowledge related to BMCSOS in business schools. It requires nurturing graduates to develop appropriate skills and competencies (Matten and Moon, 2004). Competencies are developed from knowledge, and so it is imperative to impart the understanding of CSR, SD and business ethics to students (Wascher and Theis, 2015; Shephard, 2008). Therefore the re-orientation of the curriculum is essential for managers to become accountable administrators who are intended to develop an alternative perspective on management (Wals, 2009; Læssøe et al., 2009). In line with this notion, the author's objective in this step is to inspect the

content of the curriculum of master's program in general management at Department of Management in Educational institutions to impart socially responsible and sustainable education. Although it may be challenging to observe the extent of knowledge transfer on BMCSOS through the course content of syllabi (Rasche et al., 2013) and in-depth qualitative analysis is better suited as instructors like the high degree of autonomy while delivering in classrooms (McLaughlin and Talbert, 2001). However, it is considered that curriculum change regarding BMCSOS is a necessary precondition for nurturing responsible management education. The program structure of general management programs has been reviewed and used as a basis of comparison for the different educational institution.

Matten and Moon (2004) have contended that B-schools have the responsibility to provide CSR education to practitioners to develop more unique synergies for imparting of sustainable management education. Thus, to evaluate the extent of transformation of BMCSOS, the featured topics related to CSR, business ethics and sustainability and using the keywords from Appendix A is matched with the contents of the curriculum. Table 3 shows the percentage of courses having CSR embedded contents, the percentage of compulsory or elective course related to BMCSOS and the overall percentage of such courses to the total number of courses. From Table 3 it is observed that the government funded institutions like central and state educational institutions are offering more contents related to BMCSOS in comparison to private counterparts as more than 40% of their overall curriculum is focusing on responsible education and contains keywords like business ethics, sustainable, ethics, society, corporate social responsibility, e-governance, corporate governance, stakeholder involvement and responsibility. This method of screening the curriculum from keywords has also been used by Matten and Moon (2004). This method helps in analysing the transferability of desired knowledge objectively.

Table 3 Integration of sustainability, CSR and business ethics in management program

Educational institutions	*Percentage of courses embedding sustainability, CSR and ethics of total course in management program*	*Percentage courses focusing on sustainability, CSR and ethics of total course in management program*	*Percentage of courses concentrate on sustainability, CSR and ethics to total courses in management program*
PU 1	42	4	46
SU 1	34	6	40
CU 1	37.5	9	46.5
PU 2	20	4.5	24.5
SU 2	53	5	58

4.3 Phase 3 – student learning analysis

The survey was conducted from mid of semester of the academic year 2017–2018. The sample of managers was chosen from the eight educational institutions from the capital out of which two institutions were funded by central government; Delhi state government supported three institutions and rest were private institutions offering

management programs. The scale developed by Boehm (2002) based on his work, tested and pretested, has identified different dimension from literature for evaluating the perspective of managers for socially responsible consciousness. His work has also been examined by Majumdar and Saini (2016) to assess the perception of people in Goa towards CSR efforts of companies. The dimensions on *reason not to undertake CSR* was not relevant for the study and was removed. The aspects were beforehand explained to the respondents so that they can easily comprehend the statements while answering. The opinions of the respondents on different dimensions were measured on a seven-point scale from "I like it" to "I don't like it." Table 4 reports multiple dimension of CSR on which the perception of managers' was measured along with the various statements in it. All aspects have shown adequate reliability with Cronbach alpha values in the range of 0.867 to 0.965. There were six dimension and total 34 statements in the questionnaire.

Table 4 Items and reliability statistics

Socially responsible dimension	*No. of items*	*Reliability statistics (Cronbach alpha)*
Company's commitment to the community	4	0.867
Areas for company's support	7	0.921
Company involvement with stakeholders	5	0.935
Community's commitment to the company	5	0.923
Using media to promote CSR activity	8	0.965
CSR as benefiting to the company	5	0.931

Through the first section of the questionnaire collected information about the demographic profile of respondents like gender, stage in the program, association with the type of educational institutions and courses studied on BMCSOS. In total, the perception data of 2050 respondents were collected from business educational institutions, but out of it, ten responses were rejected due to incomplete information and hence our final sample for the study is 2040, with a response rate of 99% of total responses.

The responses are balanced regarding gender as 60% of the samples is male, and 40% are females (Table 5). The respondents from 1st year participating in the survey are 58% and from the 2nd year is 42%. The respondents participating in the study from various educational institutions are 27% from state educational institutions, 24% from central educational institutions and 49% from private educational institutions. Regarding BMCSOS courses studied by respondents about 8% have reviewed it as elective, 16% have studied it as compulsory courses, 46% of respondents have considered as a part of existing courses, and 15% of them have involved themselves in the social project during the program. 15% of the respondents has reported that they have not studied any course related to BMCSOS. The respondents were further asked to rank the most critical factor that is responsible for the integration of BMCSOS in their program and responses were recorded on five-points Likert scale and in their opinion industry's requirement, government recommendation and other institute CSR initiatives practices were most influential factors whereas the least important factors were recommendations of accreditation bodies and recommendation by the individual department (Table 6).

Table 5 Composition of respondents as per university, courses studied, gender and stage in program

Gender	*1st year*	*2nd year*	*Total*	*%*
Male	560	670	1,230	60
Female	620	190	810	40
Total	1,180	860	2,040	100
%	58	42		

Educational institutions\ type of courses	*Elective course*	*Compulsory course*	*Part of existing course*	*Involved in social projects*	*Not studied*	*Total*	*%*
State educational institution	100	170	100	130	60	560	27
Central educational institution	20	80	240	100	40	480	24
Private educational institution	40	70	600	80	210	1,000	49
Total	160	320	940	310	310	2,040	100
%	8	16	46	15	15		

Table 6 Ranking of drivers for integration of CSR in their program

Factors	*Ranking*
Industry's requirement	1
Government	2
CSR initiatives of other institutes	3
Student's requirements	4
CSR related network and associations	5
NGO's	6
Business support organisation recommendation	7
Head of institute	8
Accreditation bodies	9
Recommended by department	10

4.3.1 Attitude towards social initiative

This section examines the attitude of budding managers towards social initiatives. The evaluation of attitude social initiatives has been categorised into four aspects namely degree of acceptance, perceived value, the degree of support and perceived usefulness of efforts as shown in Table 7.

An independent sample t-test was conducted to determine the difference in the attitude of male and female for analysing their attitude towards social initiatives. The results reveal that there is no impact of gender on the attitude of female and male towards acceptance of initiatives, perceived value and support initiatives. The perceived usefulness of social efforts is statistically significant for gender and females to have a positive outlook in comparison to male respondents. The perception towards social initiatives was further analysed based on courses studied, education institution and exposure to BMCSOS and there is no significant difference towards social efforts.

Table 7 T-test scores of managers' attitude towards social initiatives

Dependent variables	*Gender*	*Courses studied*	*Educational institution*	*Intervention of BMCSOS*
Like initiatives	0.339	0.208	0.640	0.913
Initiative goodness	0.466	0.227	0.676	0.436
Support initiative	0.987	0.157	0.714	0.521
Usefulness initiative	0.034*	0.687	0.853	0.666

Notes: *P-value significant < 0.05 and **P-value significant < 0.10.

4.3.2 Evaluation of socially responsible consciousness

This section aims to assess the budding managers' sentiments about CSR and SD issues in the business setting. The aspiring managers were asked to give their opinion about the different variable measured in seven-point rating scale from 'strongly agree' to 'strongly disagree'. The views of respondents were then analysed through independent sample t-test. Company commitment, company support, stakeholder involvement, community commitment, media, CSR benefiting and CSR dimensions are tested variable, and gender is grouping variable for the test. The respondents not studying BMCSOS subjects have been dropped, and 1,730 responses were considered for further analysis. Results tested at 95% confidence interval reveals that there is no statistical difference between the perception of male and female respondents for CSR and SD issues. This concludes that gender is not an influential factor for CSR and SD dimension. Table 8 has displayed the result for t-test statistics to test the equality of mean of respondents with high exposure to in-depth BMCSOS course for CSR and SD dimension. This concludes that there is no statistical impact of the intervention of BMCSOS courses in the management program towards CSR and SD dimensions.

Table 8 Test statistics for manager's perception for social consciousness dimensions

DV/IV	*Gender*	*Exposure of BMCSOS*	*Type of course*	*Type of institution*	*Type of courses * type of institutions*
Company commitment	0.830	0.248	0.504	0.926	0.766
Company support	0.965	0.302	0.516	0.667	0.654
Stakeholder involvement	0.292	0.329	0.337	0.863	0.589
Community commitment	0.519	0.293	0.120	0.971	0.175
Media	0.612	0.647	0.255	0.925	0.247
CSR benefiting	0.806	0.653	0.044*	0.954	0.055**

Notes: *P-value significant < 0.05 and **P-value significant < 0.10.

A one-way ANOVA was conducted to compare the impact of sustainability education and the perception of the budding manager towards socially responsible dimension. The CSR education had four levels, i.e., study BMCSOS as a part of course, as a compulsory course, as an elective course and involved in the social project. Whereas, CSR and SD dimensions are company commitment, company support, the involvement of stakeholder, community commitment, the role of media and CSR is benefiting the society. The results

are statistically not significant, i.e., there is no impact of BMCSOS courses on CSR and SD dimensions.

Table 9 Mean and standard deviation of CSR dimensions

CSR dimensions	*Statements*	*Mean*	*Std. deviation*
Corporate commitment to community	Commitment to community is an important thing for a company.	1.4913	0.91891
	Company should do their best to source supplies needed to produce output (including workers) locally in the community.	1.7168	1.03182
	There is a need to spend company resources to help the community.	1.8555	1.14979
	Managers of company should take a leadership role in the community.	1.95954	1.282069
Area for company support	Companies' direct involvement in social projects (e.g., education, health, youth development) can make their social responsibility effective.	1.5491	.97299
	Companies' direct involvement in projects for people/community in distress (e.g., situations of flood, epidemic, communal violence, etc.) can make their social responsibility effective.	1.7919	1.18741
	Companies' personal help (e.g., helping individually to elderly, sick persons through monetary or non-monetary support) can make their social responsibility effective.	1.9480	1.43164
	Care for the quality of community physical environment (road, bridges, community hall, environment, etc.) can make their social responsibility effective.	1.8266	1.21233
	Capacity building of community through training (e.g., vocational training) and other required support (e.g., machines) can make their social responsibility effective.	1.8382	1.23766
	Monetary donations can make their social responsibility effective.	2.1792	1.42944
	Donations of resources in kind can make their social responsibility effective.	2.0058	1.29173
Stakeholder involvement	Company's involvement with community leaders (local leaders and representatives) can make their social responsibility effective.	1.7549	1.48514
	Company's involvement with representatives of government departments (such as collector, DRDA, BDO office, Gram Panchayat, etc.) in community can make their social responsibility effective.	1.7549	1.45498
	Company's involvement with NGOs and people from development agencies in society can make their social responsibility effective.	1.8324	1.15673

Table 9 Mean and standard deviation of CSR dimensions (continued)

CSR dimensions	*Statements*	*Mean*	*Std. deviation*
Stakeholder involvement	Company's involvement with politicians and decision makers in community can make their social responsibility effective.	2.2370	1.53123
	Company's involvement with any other professional (s)/institution (s) outside community can make their social responsibility effective.	2.2486	1.52558
Community's commitment to the company	People in community should care about the fate of company in their community.	2.0751	1.26220
	People in community should value company contributions to the community.	1.8786	1.30841
	Community should give support to company when they (company) have problems.	1.9942	1.40389
	There is a need to expand community resources to help the local company.	2.0925	1.51066
	Community leadership is important in corporate leadership.	2.1156	1.36332
Using media to promote CSR activity	The local newspaper should be used to encourage CSR activity.	1.9364	1.19179
	Local radio should be used to promote CSR activity.	1.9595	1.24526
	Local television should be used to promote CSR activity.	1.9306	1.21800
	National newspaper should be used to promote CSR activity.	2.0000	1.26675
	National radio should be used to promote CSR activity.	1.7108	1.37166
	National television should be used to promote CSR activity.	1.9480	1.19235
	Social media should be used to promote CSR activity.	1.8092	1.18298
	Bill boards, Nukad Naatak, puppet shows, etc., should be used to promote CSR activity.	2.0000	1.35544
CSR as benefiting to the company	CSR is an important factor for the company's corporate business management.	1.7688	1.17817
	CSR contributes to the company's net benefit (benefits-CSR cost).	1.8324	1.13132
	General corporate success is highly influenced by CSR.	1.9133	1.13019
	CSR is important for a company's market share.	1.8613	1.21203
	Social responsibility must continue even when a company has monetary problems.	2.1792	1.44159

Further, we attempted to explore if the perception of managers undergoing BMCSOS courses towards CSR and SD dimension is influenced by the type of educational institution through which they are pursuing their program. The relationship is tested taking the interaction between educational institutions and BMCSOS courses. It was found that managers studying of various CSR courses across the different educational institution as an indifferent social consciousness as $p > 0.05$. Hence the managers' perception towards social consciousness is not influenced by educational institutions.

5 Discussion

Sustainability learning is thematic, introduces diverse and non-dominant perspectives and is experiential (Burns, 2013). Thus organisations require professionals undertaking the task of CSR are expected to comply with moral and humanitarian obligations in addition to meeting a reasonable return for owners and comply with the law. The recent corporate debacles and global financial crisis have enhanced the awareness for ethical and responsible management education in managing the conduct of future business pioneer (Davis et al., 2003). There is a widespread growth regarding importance of awareness for corporate social responsibility and business moral education, at higher education level (Moon et al., 2006; Van Liedekerke and Demuijnck, 2012) as most of the institutes believe in the need for serving the environment and people for their upliftment and at the same time, they understand how CSR is also one of the key contributing factors for their growth (Taneja, 2016). Teaching BMCSOS to budding managers and inculcating the value system for Sustainability in an integral part of educational institution framework contribute to shaping the future of managers to become better leaders (Lozano et al., 2013). Therefore, to make it impactful, CSR and business ethics should be mainstreamed into the educational modules in the degree rather than isolated courses (Doh and Tashman, 2014; Moon et al., 2006; Sims, 2002; Thomas, 2005). Some authors even argue that teaching BMCSOS at postgraduate level are too late to be useful as by this time students have already established their thoughts and opinions, and it is difficult to change through educational institution's education (Glavas and Kelley, 2014; Hartman, 1998; Low et al., 2008; Ritter, 2006; Chirieleison and Scrucca, 2017).

In the current research framework, concerning the minimal studied Indian context, the result provides the following contribution.

Firstly about the knowledge of social responsibility and examination of curricula of the educational institution, the empirical data analysed to demonstrate that budding managers' fail to recognise the topics related to BMCSOS which are embedded in courses focusing different areas. This fact indeed proposes the presence of threshold of effective teaching of such issues.

Secondly, as emerging from the academic research and analysing the perception of managers', the finding supports the concept that BMCSOS course is useful in moulding budding managers' opinion but only to a certain extent in context to different courses studied. As per our analysis, there is no difference in the perception of managers studying a course embedded with CSR and the isolated course like the compulsory or elective course. Therefore isolated courses focusing on issues related to BMCSOS and fragmented programs have demonstrated to have insignificant effectiveness in its execution.

6 Conclusions

Our aim from this paper was to explore the perception of manager' studying different BMCSOS courses towards CSR and SD dimensions across various educational institutions and study was conducted in three phases namely: phase 1, the evaluation of educational institutions on its strategic mission and objectives; phase 2 evaluation of its curricula on the ground for courses related to BMCSOS and phase 3 empirically testing the students' perception, and the significant findings show that BMCSOS education has no impact on the CSR and SD dimensions.

The value structures of life are adapted from the experiences and circumstances of life, and also the value structures are affected by value priorities (Yao et al., 2009). The results about the relationship between gender, educational institutions, courses studied and intervention of BMCSOS in higher education institutions towards social initiatives are in line with previous research on this issue. The sample under study reveals that female managers have developed self-transcendence values higher than male managers. The results also suggest that despite the groups have maintained a favourable attitude towards CSR dimensions yet gender and stage in the program are not significantly different from each other.

6.1 Challenges in management education

Using the results of the study undertaken author has attempted to highlight the challenges faced by the management program in higher education in India. The first challenge is related to awareness and understanding of BMCOS related issues as 15% of the respondents have expressed of not been exposed to such topics. In contrast, the examinations of the curriculum of management institutions have revealed that on average of 43% of courses are either standalone or embedded the issues related to BMCSOS. This is a serious concern as managers who shall be dealing with such matter in future are unable to comprehend with them today. These challenges can be overcome by strengthening the base of BMCSOS related topics in the subjects and introducing programs related such issues; one the learning by doing a platform for management graduates is internships during programs and promoting internship in CSR projects can certainly make sustainable education more impactful.

The second major challenge is managers have an indifferent attitude towards issues related to BMCSOS. The author attempts to highlight here that a high quantity of BMCSOS associated topics in education is ineffective in reshaping the behavioural pattern of future managers. Therefore it generates the opportunity to further carefully design the curricula for efficient learning in future from the Indian perspective. For sustainable development, the committed managers are so crucial that indifferent attitude would not be understood by societal stakeholders. This does not imply that managers should simply learn 'sustainable development'; instead it should be the core principle of the program. It can be achieved by mandate training of academic workforce towards the important BMCSOS issues so that it becomes the DNA of the program. Culture plays a crucial role in enabling sustainable orientation at an early age (Verma and Petersen, 2018). Hence, it is always advantageous to teach these concepts before higher education, i.e., maybe during high school or primary school with a keen involvement in a community development program at large like *Kar Seva* and *Shramdaan*, meaning

selflessly working towards serving humanity, regarded the most humbled form of a community development program as per Indian ethos. Authors affirm here that CSR education in educational institutions, not just need a long-term perspective while defining its objective but also need to play an overall supportive role in the local development. Since CSR is becoming a professional field where managers shall be hiring the employees requiring CSR and ethics competencies, educational institutions have a critical role in training professionals in this field (Majumdar and Saini, 2016).

The third challenge is a disconnection in the strategic vision of private HEI and its execution. These institutions pretend to have a responsible outlook and offering fewer BMCSOS issues in their program. This approach immediately creates a zero-sum problem creating private benefits that defy the objective of ESD. Thus, it can be overcome by the adoption of practices by institutions to create an environment of innovation and collaboration focusing on teacher development and evaluation systems.

Thus, it is inferred from above that sustainable thinking cannot just be taught by application of BMCSOS topics in the management program but also making it a part of its campus framework and operations.

7 Limitation of study and scope for future research

The current study is one the initial attempt to explore the Indian education system contribution to sustainability development. The national and international administration, faculty and leaders in educational institutions can use the results of the study, for the task of enhancing BMCSOS education. The results of the current research can be used to establish a better SD education system in Indian educational institutions. The paper provides a fruitful insight into the education of sustainability in Indian educational institutions, and it does have some shortcomings. Firstly, the findings stem from the examination of a similar department of different educational institutions. Hence the results cannot be generalised as the generalisation is a significant disadvantage in action research, although the aim here is not to generalise but to lay the ground for further investigations and the current study might be considered as a representative in the Indian context. In context to the education of BMCSOS, only the contents of syllabi had been evaluated, while the quality of education regarding academic delivery by faculties and pedagogy followed can have a strong influence on its effectiveness. Moreover, the dimensions used to measure CSR and SD, a more extensive range of aspects can be used to measure the perception of future managers.

There is a scope of further investigation as the current one is an exploratory study evaluating the impact of BMCSOS and further investigations can be done in exploring the effect of BMCSOS in context to a specific program offered by an institution. Moreover, new research is required to examine if some different set of variables can be used as CSR dimensions.

References

Adenipekun, M., Ibiyemi, A., Adnan, Y.M. and Daud, M.N. (2015) 'Comparative analysis of sustainable facilities planning and users' satisfaction in Nigerian universities – a standardised residuals approach', *Int. J. Higher Education and Sustainability*, Vol. 1, No. 1, pp.40–65.

Adler, P.S. (2002) 'Corporate scandals: it's time for reflection in business schools', *The Academy of Management Executive*, Vol. 16, No. 3, pp.148–149.

Alcaraz, J.M. and Fotaki, M. (2018) 'Teaching sustainability and management critically: 'expectation failures' as a powerful pedagogical tool', in *Disciplining the Undisciplined?*, pp.225–242, Springer, Cham.

Annan, K.A. (2002) 'Towards a sustainable future', *Environment: Science and Policy for Sustainable Development*, Vol. 44, No. 7, pp.10–15.

Baltic 21E (2002) *Agenda 21 for the Baltic Sea Region Sector Report e-Education (Baltic 21E)*, Stockholm [online] http://www.hu2.se/hu2old/Baltic21E.pdf (accessed 23 November 2018).

Bampton, R. and Cowton, C.J. (2002) 'Pioneering in ethics teaching: the case of management accounting in universities in the British Usles', *Teaching Business Ethics*, Vol. 6, No. 3, pp.279–295.

Barkhuysen, B. and Rossouw, G. (2000) 'Business ethics as academic field in Africa: its current status', *Business Ethics: A European Review*, Vol. 9, No. 4, pp.229–235.

Beitelspacher, L. and Rodgers, V.L. (2018) 'Integrating corporate social responsibility awareness into a retail management course', *Journal of Marketing Education*, Vol. 40, No. 1, pp.66–75.

Benn, S. and Dunphy, D. (2009) 'Action research as an approach to integrating sustainability into MBA programs: an exploratory study', *Journal of Management Education*, Vol. 33, No. 3, pp.276–295.

Berman, S. (1990) 'Educating for social responsibility', *Educational Leadership*, Vol. 48, No. 3, pp.75–80.

Besser, T.L. (1999) 'The significance of community to business social responsibility', *Rural Sociology*, Vol. 633, No. 8, pp.412–431.

Blasco, M. (2012) 'Aligning the hidden curriculum of management education with PRME. An inquiry based framework', *Journal of Management Education*, Vol. 36, No. 3, pp.364–388.

Boehm, A. (2002) 'Corporate social responsibility: a complementary perspective of community and corporate leaders', *Business and Society Review*, Vol. 107, No. 2, pp.171–194.

Bokova, I. (2015) *Why Education is the Key to Sustainable Development* [online] https://www.weforum.org/agenda/2015/05/why-education-is-the-key-to-sustainable-development/ (accessed 26 July 2018).

Bruch, H. (2005) 'The keys to rethinking corporate philanthropy', *MIT Sloan Management Review*, Vol. 47, No. 1, pp.49–59.

Burns, H. (2013) 'Meaningful sustainability learning: a study of sustainability pedagogy in two university courses', *International Journal of Teaching and Learning in Higher Education*, Vol. 25, No. 2, pp.166–175.

Carroll, A.B. (1991) 'The pyramid of corporate social responsibility: toward the moral management of organizational stakeholders', *Business Horizons*, Vol. 34, No. 4, pp.39–48.

Chhokar, K.B. (2010) 'Higher education and curriculum innovation for sustainable development in India', *International Journal of Sustainability in Higher Education*, Vol. 11, No. 2, pp.141–152.

Chirieleison, C. and Scrucca, L. (2017) 'Shaping students' attitudes towards business ethics and corporate social responsibility: education versus personal perspectives', *Education*, Vol. 7, No. 5, pp.83–95, DOI: 10.5923/j.edu.20170705.01.

Christensen, L.J., Peirce, E., Hartman, L.P., Hoffman, W.M. and Carrier, J. (2007) 'Ethics, CSR, and sustainability education in the Financial Times top 50 global business schools: baseline data and future research directions', *Journal of Business Ethics*, Vol. 73, No. 4, pp.347–368.

Corcoran, P.B., Walker, K.E. and Wals, A.E. (2004) 'Case studies, make-your-case studies, and case stories: a critique of case-study methodology in sustainability in higher education', *Environmental Education Research*, Vol. 10, No. 1, pp.7–21.

Cornelius, N., Wallace, J. and Tassabehji, R. (2007) 'An analysis of corporate social responsibility, corporate identity and ethics teaching in business schools', *Journal of Business Ethics*, Vol. 76, No. 1, pp.117–135, DOI: 10.1007/s10551-006-9271-6.

Cummins, J. (1999) *The Teaching of Business Ethics: at Undergraduate, Postgraduate & Professional Levels in the UK: a Survey & Report*, Institute of Business Ethics, London.

Davis, S.A., Edmister, J.H., Sullivan, K. and West, C.K. (2003) 'Educating sustainable societies for the twenty-first century', *International Journal of Sustainability in Higher Education*, Vol. 4, No. 2, pp.169–179.

Deshpande, S.P. (1997) 'Managers' perception of proper ethical conduct: the effect of sex, age, and level of education', *Journal of Business Ethics*, Vol. 16, No. 1, pp.79–85.

Doh, J.P. and Tashman, P. (2014) 'Half a world away: the integration and assimilation of corporate social responsibility, sustainability, and sustainable development in business school curricula', *Corporate Social Responsibility and Environmental Management*, Vol. 21, No. 3, pp.131–142.

Etheredge, J.M. (1999) 'The perceived role of ethics and social responsibility: an alternative scale structure', *Journal of Business Ethics*, Vol. 18, No. 1, pp.51–64.

Ethical Corporation (2006) *Corporate Responsibility and Education* [online] http://www.ethicalcorp.com.

Evans, F.J. and Marcal, L.E. (2005) 'Educating for ethics: business deans' perspectives', *Business and Society Review*, Vol. 110, No. 3, pp.233–248.

Falkenstein, M. (2014) *Ethics, Sustainability and Responsibility in Business and Management Education* [online] https://www.eaie.org/blog/ethical-business-and-management-education/ (accessed 20 June 2018).

Fernández Fernández, J.L. and Sanjuán, A.B. (2010) 'The presence of business ethics and CSR in the higher education curricula for executives: the case of Spain', *Journal of Business Ethics Education*, Vol. 7, pp.25–38.

Findler, F., Schönherr, N., Lozano, R. and Stacherl, B. (2019) 'Assessing the impacts of higher education institutions on sustainable development – an analysis of tools and indicators', *Sustainability*, Vol. 11, No. 1, p.59.

Gautschi, F.H. and Jones, T.M. (1998) 'Enhancing the ability of business students to recognize ethical issues: an empirical assessment of the effectiveness of a course in business ethics', *Journal of Business Ethics*, Vol. 17, No. 2, pp.205–216.

Geli de Ciurana, A.M. and Leal Filho, W. (2006) 'Education for sustainability in educational institution studies: experiences from a project involving European and Latin American educational institutions', *International Journal of Sustainability in Higher Education*, Vol. 7, No. 1, pp.81–93.

Giacalone, R.A. and Wargo, D.T. (2009) 'The roots of the global financial crisis are in our business schools', *Journal of Business Ethics Education*, Vol. 6, pp.147–168.

Glavas, A. and Kelley, K. (2014) 'The effects of perceived corporate social responsibility on employee attitudes', *Business Ethics Quarterly*, Vol. 24, No. 2, pp.165–202, DOI: 10.5840/beq20143206

Grindsted, T.S. and Holm, T. (2012) 'Thematic development of declarations on sustainability in higher education', *Environ. Econ.*, Vol. 3, No. 1, pp.32–40.

Hartman, E.M. (1998) 'The role of character in business ethics', *Business Ethics Quarterly*, Vol. 8, No. 3, pp.547–559, DOI: 10.2307/3857437.

Haski-Leventhal, D., Pournader, M. and McKinnon, A. (2017) 'The role of gender and age in business students' values, CSR attitudes, and responsible management education: learnings from the PRME international survey', *Journal of Business Ethics*, Vol. 146, No. 1, pp.219–239.

Hemingway, C.A. and Maclagan, P.W. (2004) 'Managers' personal values as drivers of corporate social responsibility', *Journal of Business Ethics*, Vol. 50, No. 1, pp.33–44.

Holm, T., Sammalisto, K., Vuorisalo, T. and Grindsted, T.S. (2012) 'A model for enhancing education for sustainable development with management systems: experiences from the Nordic countries', in Leal Filho, W. (Ed.): *Sustainable Development at Educational Institutions: New Horizons*, pp.261–272, Peter Lang Scientific Publishers, Frankfurt am Main.

Horng, J.S., Hsu, H. and Tsai, C.Y. (2019) 'Learning corporate ethics and social responsibility: developing an influential curriculum for undergraduate tourism and hospitality students', *Journal of Hospitality, Leisure, Sport & Tourism Education*, Vol. 24, pp.100–109.

Kolb, M., Fröhlich, L. and Schmidpeter, R. (2017) 'Implementing sustainability as the new normal: responsible management education – from a private business school's perspective', *The International Journal of Management Education*, Vol. 15, No. 2, pp.280–292.

Kolodinsky, R.W., Madden, T.M., Zisk, D.S. and Henkel, E.T. (2010) 'Attitudes about corporate social responsibility: business student predictors', *Journal of Business Ethics*, Vol. 91, No. 2, pp.167–181.

Læssøe, J., Schnack, K., Breiting, S., Rolls, S., Feinstein, N. and Goh, K.C. (2009) *Climate Change and Sustainable Development: the Response from Education. A Cross-National Report*, International Alliance of Leading Education Institutes, Denmark.

Lambrechts, W., Mulà, I., Ceulemans, K., Molderez, I. and Gaeremynck, V. (2013) 'The integration of competences for sustainable development in higher education: an analysis of bachelor programs in management', *Journal of Cleaner Production*, Vol. 48, pp.65–73.

Lau, C.L. (2010) 'A step forward: ethics education matters!', *Journal of Business Ethics*, Vol. 92, No. 4, pp.565–584.

Leal Filho, W. (2009) *Sustainability at Educational Institutions Opportunities, Challenges and Trends*, Peter Lang, Frankfurt.

Leal Filho, W. (2011) 'About the role of universities and their contribution to sustainable development', *Higher Education Policy*, Vol. 24, No. 4, pp.427–438.

Low, M., Davey, H. and Hooper, K. (2008) 'Accounting scandals, ethical dilemmas and educational challenges [abstract]', *Critical Perspectives on Accounting*, Vol. 19, No. 2, pp.222–254, DOI: 10.1016/j.cpa.2006.05.010.

Lozano, R., Lukman, R., Lozano, F.J., Huisingh, D. and Lambrechts, W. (2013) 'Declarations for sustainability in higher education: becoming better leaders, through addressing the educational institution system', *Journal of Cleaner Production*, Vol. 48, pp.10–19, DOI: 10.1016/j.jclepro. 2011.10.006.

Lykkegaard, A.M. (2018) *CBS Students Demand More Teaching in Sustainability* [online] https://cbswire.dk/cbs-students-demand-more-sustainability/ (accessed 15 June 2018).

Macfarlane, B. and Ottewill, R. (2004) 'Business ethics in the curriculum: assessing the evidence from UK subject review', *Journal of Business Ethics*, Vol. 54, No. 4, pp.339–347.

Mahoney, J. (1990) *Teaching Business Ethics in the UK, Europe and the USA: a Comparative Study*, Athlone Press, London.

Majluf, N. (2016) 'Teaching human centered management to engineering students: a personal account', in *Human Centered Management in Executive Education. Humanism in Business Series*, Palgrave Macmillan, London.

Majumdar, S. and Saini, G.K. (2016) 'CSR in India: critical review and exploring entrepreneurial opportunities', *Journal of Entrepreneurship and Innovation in Emerging Economies*, Vol. 2, No. 1, pp.56–79.

Markley Rountree, M. and Koernig, S.K. (2015) 'Values-based education for sustainability marketers: two approaches for enhancing student social consciousness', *Journal of Marketing Education*, Vol. 37, No. 1, pp.5–24.

Matten, D. and Moon, J. (2004) 'Corporate social responsibility', *Journal of business Ethics*, Vol. 54, No. 4, pp.323–337.

Matten, D. and Moon, J. (2004) 'Corporate social responsibility', *Journal of business Ethics*, Vol. 54, No. 4, pp.323–337.

May, D.R., Luth, M.T. and Schwoerer, C.E. (2014) 'The influence of business ethics education on moral efficacy, moral meaningfulness, and moral courage: a quasi-experimental study', *Journal of Business Ethics*, Vol. 124, No. 1, pp.67–80.

McKenna, R.J. (1995) 'Business ethics education: should we? Can we?', *Journal of Management & Organization*, Vol. 1, No. 2, pp.44–63.

McLaughlin, M.W. and Talbert, J.E. (2001) *Professional Communities and the Work of High School Teaching*, Educational institution of Chicago Press.

Moon, J., Crane, A. and Matten, D. (2006) 'Corporate power and responsibility: a citizenship perspective', *Revue de lorganisation responsable*, Vol. 1, No. 1, pp.82–92.

Moratis, L. and Jezrawi, M. (2016) 'Responsible management education in the Netherlands: to what extent have Dutch business schools integrated CSR into their MBA programs?', in *Social Responsibility Education Across Europe*, pp.49–70, Springer, Cham.

Mulder, M. (2014) 'Organised of professional competence', in *International Handbook of Research in Professional and Practice-Based Learning*, pp.107–137, Springer, Dordrecht.

Nordic Council of Ministers (2009) *Sustainable Development e New Bearings for the Nordic Countries*, in Revised Edition with Goals and Priorities 2009e2012, Scanprint a/s, Copenhagen.

Nordic Council of Ministers (2011) *Knowledge for Green Growth and Welfare*, Arco Grafisk A/S, Skive.

O'Byrne, D., Dripps, W. and Nicholas, K.A. (2015) 'Teaching and learning sustainability: an assessment of the curriculum content and structure of sustainability degree programs in higher education', *Sustainability Science*, Vol. 10, No. 1, pp.43–59.

O'Byrne, D., Dripps, W. and Nicholas, K.A. (2015) 'Teaching and learning sustainability: an assessment of the curriculum content and structure of sustainability degree programs in higher education', *Sustainability Science*, Vol. 10, No. 1, pp.43–59.

Orlitzky, M. and Moon, J. (2011) 'Assessing corporate social responsibility education in Europe: trends and comparisons', in Fisher, D.G. and Swanson, D.L. (Eds.): *Toward Assessing Business Ethics Education*, pp.143–175, Information Age Publication, Charlotte, NC.

Paine, L.S. (1988) *Ethics Education in American Business Schools*, Ethics Resource Centre, Washington, DC.

Parris, D.L. and McInnis-Bowers, C. (2017) 'Business not as usual: developing socially conscious entrepreneurs and intrapreneurs', *Journal of Management Education*, Vol. 41, No. 5, pp.687–726.

Pesonen, H.L. (2003) 'Challenges of integrating environmental sustainability issues into business school curriculum: a case study from the University of Jyväskylä, Finland', *Journal of Management Education*, Vol. 27, No. 2, pp.158–171.

PRME (2015) [online] http://www.unprme.org/participation/search-participants.php?nameparent=&country%5B%5D=India&from=&to=&utype=sig&search=Search (accessed 30 May 2018).

Rasche, A. and Gilbert, D.U. (2013) 'What drives ethics education in business schools? Influences on ethics in the MBA curriculum', *Academy of Management Proceedings*, No. 1, p.11704, DOI: 10.5465/AMBPP.2013.11704abstract.

Rasche, A., Gilbert, D.U. and Schedel, I. (2013) 'Cross-disciplinary ethics education in MBA programs: rhetoric or reality?', *Academy of Management Learning & Education*, Vol. 12, No. 1, pp.71–85.

Renmin Educational institution of China UNDP (2010) *China Human Development Report 2009/10: China and a Sustainable Future: towards a Low Carbon Economy and Society*, Beijing [online] http://planipolis.iiep.unesco.org/format_liste1_en.php?Chp2¼China (accessed 18 January 2018).

Ritter, B.A. (2006) 'Can business ethics be trained? A study of the ethical decision-making process in business students', *Journal of Business Ethics*, Vol. 68, No. 2, pp.153–164.

Rosario, G.R.M., Carmen, D.F.M. and Biagio, S. (2014) 'Values and corporate social initiative: an approach through Schwartz theory', *International Journal of Business and Society*, Vol. 15, No. 1, p.19.

Rutherford and Scullion R. (2017) 'Embedding social responsibility in HE corporate communications degrees. The place of CSR in teaching corporate communications programs (advertising, branding and public relations)', in Theofilou, A., Grigore, G. and Stancu, A. (Eds.): *Corporate Social Responsibility in the Post-Financial Crisis Era. Palgrave Studies in Governance, Leadership and Responsibility*, Palgrave Macmillan, Cham.

Saat, M.M., Porter, S. and Woodbine, G. (2010) 'An exploratory study of the impact of Malaysian ethics education on ethical sensitivity', *Journal of Business Ethics Education*, Vol. 7, pp.39–62.

Scullion, R. (2017) 'Embedding social responsibility in HE corporate communications degrees. The place of CSR in teaching corporate communications programs (advertising, branding and public relations)', in *Corporate Social Responsibility in the Post-Financial Crisis Era*, pp.3–23, Palgrave Macmillan, Cham.

Setó-Pamies, D. and Papaoikonomou, E. (2016) 'A multi-level perspective for the integration of ethics, corporate social responsibility and sustainability (ECSRS) in management education', *Journal of Business Ethics*, Vol. 136, No. 3, pp.523–538.

Setó-Pamies, D., Domingo-Vernis, M. and Rabassa-Figueras, N. (2011) 'Corporate social responsibility in management education: current status in Spanish educational institutions', *Journal of Management & Organization*, Vol. 17, No. 5, pp.604–620.

Shai, S., Lazar, A., Duchin, R. and Gidron, B. (1999) *Philanthropy in Israel: Contribution and Voluntary Patterns. Ben-Gurion Educational Institution*, Israeli Center for Third Sector Research, Hebrew, Beer Sheva.

Shephard, K. (2008) 'Higher education for sustainability: seeking affective learning outcomes', *International Journal of Sustainability in Higher Education*, Vol. 9, No. 1, pp.87–98.

Sims, R.R. (2002) 'Business ethics teaching: using conversational learning to build an effective classroom learning environment', *Teaching Business Ethics*, Vol. 6, No. 4, pp.393–410, DOI: 10.1023/b:busi.0000015782.99051.d4.

Srinivasan, P., Srinivasan, V. and Anand, R. (2012) *Status of ethics, corporate governance, CSR and environment education in business schools in India: An exploratory study. Corporate Governance, CSR and Environment Education in Business Schools in India: An Exploratory Study*, 15 April, p.362, IIM Bangalore Research Paper.

Stubbs, W. and Schapper, J. (2011) 'Two approaches to curriculum development for educating for sustainability and CSR', *International Journal of Sustainability in Higher Education*, Vol. 12, No. 3, pp.259–268.

Taneja, J. (2016) *Indian Education Sector and CSR: the Collaborative Path to Growth* [online] https://www.franchiseindia.com/education/Indian-education-sector-and-CSR-The-collaborative-path-to-growth.8754 (accessed 12 April 2018).

Thomas, T.E. (2005) 'Are business students buying it? A theoretical framework for measuring attitudes toward the legitimacy of environmental sustainability', *Business Strategy and the Environment*, Vol. 14, No. 3, pp.186–197, DOI: 10.1002/bse.446.

Tilbury, D., Crawley, C. and Berry, F. (2005) *Education About and for Sustainability in Australian Business Schools: Stage 1*, Australian Research Institute for Environment and Sustainability (ARIES) and Arup Sustainability.

Treviño, L.K., Weaver, G.R. and Reynolds, S.J. (2006) 'Behavioral ethics in organizations: a review', *Journal of Management*, Vol. 32, No. 6, pp.951–990.

Turker, D., Altuntas, C. and Idowu, S.O. (2016) *Social Responsibility Education across Europe. A Comparative Approach*, Springer International Publishing, New York.

UN DESD (2011) *United Nations Decade for Sustainable Development 2005, 2014*, Paris [online] http://portal.unesco.org/en/ev.php-URL_ID¼47100&URL_DO¼DO_TOPIC&URL_SECTION¼201.html (accessed 4 December 2018).

UNGC (2007) *The Principles for Responsible Management Education*, New York.

United Nations Educational Scientific and Cultural Organisation (UNESCO) (2005) *United Nations Decade of Education for Sustainable Development, 2005–2014* [online] http://unesdoc.unesco.org/images/0014/001416/141629e.pdf (accessed 14 April 2018).

Van Liedekerke, L. and Demuijnck, G. (2012) 'Business ethics as a field of training, teaching and research in Europe', *Journal of Business Ethics*, Vol. 104, No. S1, pp.29–41.

Verma, S. and Petersen, A.C. (2018) 'Developmental science and pathways to sustainable development for children and youth', *Social Indicators Research Series*, pp.1–35, DOI: 10.1007/978-3-319-96592-5_1

Wals, A. (2009) *United Nations Decade of Education for Sustainable Development (DESD, 2005–2014) – Review of Contexts and Structures for Education for Sustainable Development 2009*.

Wascher, E. and Theis, F. (2015) 'Competence development in the field of sustainability', *Journal of Economic and Business Ethics*, Vol. 16, No. 1.

WEC (2016) *Business as Usual' Is Not An Option Anymore* [online] https://www.weforum.org/agenda/2016/01/why-do-we-need-a-multistakeholder-approach-to-sustainable-development/ (accessed 26 April 2018).

Wu, Y.C.J., Huang, S., Kuo, L. and Wu, W.H. (2010) 'Management education for sustainability: a web-based content analysis', *Academy of Management Learning & Education*, Vol. 9, No. 3, pp.520–531.

Yao, G., Cheng, Y.P. and Cheng, C.P. (2009) 'The quality of life in Taiwan', *Social Indicators Research*, Vol. 92, No. 2, pp.377–404.

Appendix A

List of keywords based on Wals (2009) (adapted from Kolb et al., 2017)

> "Corporate social responsibility; business ethics; corporate citizenship; sustainability; corporate environmental management; business & society; business & governance; business & globalization; stakeholder management; governance; responsibility; critical thinking; local and global vision; learning to change, interdisciplinary; problem-solving; lifelong learning."

Appendix B

The case adopted from the work of Rosario et al. (2014)

> "Company A initiates a 3-year social initiative, the aim of which is to combat the undernourishment problem among children. The program will entail, in particular, the assistance provided to primary school canteens in town B. Apart from the financial support, this shall include supplies of food products, as well as the voluntary work by the company's employees whose task will be to advise on the menu, and to assist on the canteen renovation works. The amount to be donated to all canteens in total shall be equivalent to around Rs 19, 50,000. The program implemented shall have the following features: (a) the support shall be provided for three years. (b) The subject matter is the undernourishment problem among children and youth. (c) The support shall both financial and in-kind, as well as in the form of voluntary work."

View publication stats

An Efficient Weighted Trust Method for Malicious Node Detection in Clustered Wireless Sensor Networks

Bhavnesh Jaint
Department of Electrical Engineering
Delhi Technological University
Delhi, India
bhavneshmk@gmail.com

Vishwamitra Singh
Department of Electronics and Communication Engineering
Delhi Technological University
Delhi, India
vishwamitra_bt2k15@dtu.ac.in

Lalit Kumar Tanwar
Department of Electronics and Communication Engineering
Delhi Technological University
Delhi, India
lalittanwar55@yahoo.com

S.Indu
Department of Electronics and Communication Engineering
Delhi Technological University
Delhi, India
s.indu@dce.ac.in

Neeta Pandey
Department of Electronics and Communication Engineering
Delhi Technological University
Delhi, India
neetapandey@dce.ac.in

***Abstract*—In this paper, we consider a wireless sensor network (WSN) that consists of sensor nodes (SN), cluster head (CH), forward node (FN) and a base station (BS). The information acquired by the sensor node is sent to the CH, all the CH's send the information to a FN which forwards it to the BS. Fast detection of malicious nodes is imperative to the performance of a WSN and therefore we study the weighted trust method for malicious node detection. We have considered two scenarios one with single cluster head without grid and other with multiple cluster head with non-overlapping grid. The results indicates that the scenario with multiple cluster heads with non-overlapping grid requires less time for malicious node detection with better accuracy as compared to the scenario with single cluster head without grid.**

***Keywords*—weighted trust, sensor nodes, malicious nodes, cluster cased WSN,**

I. INTRODUCTION

Wireless Sensor Network (WSN) have a huge domain in applications varying from emergency response system, energy management, medical monitoring, logistics management, inventory management, and battlefield management [11]. WSN consists of a group of small devices which are called sensor nodes. These nodes are portable devices equipped with sensors, processing unit, memory unit, transceiver and power supply as shown in Fig.1. The sensor nodes are application specific and are intended to monitor specific parameters like temperature, pollutant levels at various locations, particle concentration in chemicals, pressure, intensity of sound/light, etc. These sensors are deployed randomly in a geographical region of interest. The sensor nodes collects information and send it to base station (BS) with the help of cluster head (CH) node and forward node (FN). The sensor nodes have limited power supply, usually a battery and therefore possess limited capabilities. The forwarding nodes are assumed to have high power and it collects and processes the data from lower level sensor nodes (SNs) and Base Stations (BSs) that act as media between Wireless Sensor Network (WSN) and wired network. The clusters are formed by equipartitioning the area under operation in four clusters. Each cluster head processes the data from all sensor points under it and pass the result to forwarding node. This scheme is based on assumptions that the forwarding node and base stations are not malicious and thus are always trusted.

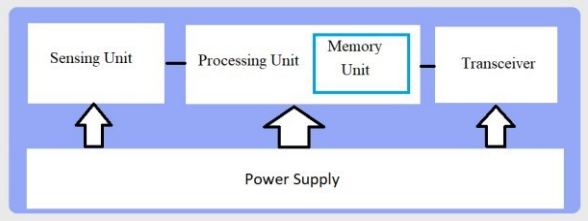


Figure 1. WSN Sensor Node Components

Due to unattended nature of the sensor networks, an attacker could launch various attacks and compromise sensor nodes. The network should be robust against these attacks, and if an attack succeeds, its impact should be minimized. Compromising of one or few sensor node should not crash the entire network. Therefore the critical issues of security and performance have to be studied for wireless sensor networks.

There have been many techniques presented in literature for detection of malicious node in wireless sensor networks.

There have been many techniques presented in literature for detection of malicious node in the wireless sensor networks. Wireless Sensor Networks can be compromised due to many reasons such as finite battery life, finite memory space, and finite computing capabilities [1], [2], [3]. It is very essential to detect the malicious node and isolate it to prevent it from generating wrong results. Ad hoc networks without a definite structure are rarely good against any types of attacks, which can lead to a node being compromised easily [4]. They presented a method that if a node is treated as trusty by its neighboring, then the node will be declared fault free, and is not a malicious node. However, for it to work it must have a minimum number of nodes nearby, which is not guaranteed in sensor networks.

So the better idea as proposed by W. Du, L. Fang and P. Ning [6] to get the node to compare the data from the other nodes nearby around it with the data generated by the node itself. If the difference between the data is marginal, then the nodes are said to be trusty. This method gave a better result for the localized detection of malicious node.

978-1-5386-6625-8/18/$31.00 ©2018 IEEE

Weighted Trust Evaluation, used primarily for the detection of the malicious node is quite reliable. The entire sensor nodes are assigned a weight or amount of trust that is evaluated frequently. The trust decreasing every time the node provides wrong information. Once the trust decreases below the fixed threshold, the node is declared malicious and isolated [5] [7] [8] demonstrated the method by using a three-level hierarchical network with components as: Sensor Nodes (SN) whose function is to sense the parameter. SNs sends its data to Forwarding Node. Forwarding nodes are high powered that collects data from SNs and processes it and transmits to base station.

This scheme is based on one critical assumption, the forwarding nodes and Base station are never faulty as once a faulty forwarding node is entered it can launch attack in network [9] [10] [7]. [15] Presents extensive simulation in MATLAB for Extensive weighted trust evaluation emphasizing on response time and detection ratio [13] [14]. Focused on the security issues in WSN and described the various kinds of attacks [17] described various clustering algorithms in the network, these clustering algorithms describes a power efficient way to localize sensor nodes and increase reliability.

In this paper we study the propagation time required to detect the malicious sensor nodes using weighted trust evaluation scheme. We compare the time taken by a traditional weighted trust evaluation scheme [5] (one with three level hierarchical network consisting of Sensor Nodes, Forwarding Node and Base Stations) with time taken by one proposed cluster based weighted trust evaluation (one with hybrid topology sensing nodes, cluster head, forward node and base station).

The rest of the paper is organized as follows. Section II describes the security in WSN and related work. Network model and architecture to be used throughout the paper is presented in Section III. In Section IV Cluster based weighted trust evaluation scheme is presented. Simulation results are shown in Section V. This paper concludes in Section VI.

II. Security in WSN

Security in WSN is paramount importance and the following are the challenges faced while designing WSN:

Unfavorable harsh environment: Sensor nodes faces extremely harsh environmental conditions and are susceptible to damage through it or capture by attackers as the sensor nodes are exposed in an open area. The attackers can capture a sensor node and access to data or transmit false data through them.

Unattended operations: The sensor nodes are deployed in a hostile area which expose them to physical tempering and attacks.

Limited resources: The security of sensor nodes requires resources like energy, memory and storage capacity as the data are constantly monitored and/or recorded the shortage of resources of sensors brings out challenges to resource-intensive security mechanisms. These resources are very limited in a small sensor node.

Reliability in Wireless Communication: In WSN the sensor data may be distorted due to channel errors which may lead to conflicts, and at highly busy node the data may also be and thus Denial-of Service (DoS) attack can be easily launched. Due to the greater congestion at a single node the overload results in increasing the latency in the sensor network thus causing synchronization errors and lag in the system, including sensor nodes. Attackers can launch an attack in sensor network through malicious nodes. These attacks are broadly classified as Passive attack and Active attack. The passive attack is easier to analyze and is difficult to detect. In passive attack, attacker does not modify or exchange information, this type of attack is basically for finding the knowledge of some classified information [12].

In an active attack the attacker tries to alter the data transferred by the sensor node or overload the sensor by inserting the traffic to start denial of service attack.

III. Network Model And Architecture

There are basically two components of network model i.e. WSN components and WSN networking topology. The components are explained as follows:

A. Components of WSN

Wireless Senor Network for environment monitoring for air pollution system consists of the sensor points or sensor nodes that are spread over the field. These sensor nodes consist of sensors that detects and monitors the concentration of pollutants in the environment. These sensor nodes are connected together through a wireless link to the cluster head that processes the collected readings from every individual node and forwards these data to the forwarding node that again processes the collected readings from individual cluster heads and propagates it to a base station shown in Fig.2.

B. Network Topology

In Wireless Sensor Network we present a clustered WSN architecture that uses a hybrid network topology which combines star, mesh and ring topologies together. These three topologies are used to increase the versatility of the system while maintaining reliability taking into account the available resources as following [16]:

- A group of the sensing nodes are connected to a central node i.e. cluster head that has other abilities like connectivity and data exchange from other cluster heads this includes the star topology thus resulting is a set of clusters. Star topology has advantages over other topologies that includes its scalability and power usage reduction.
- Cluster heads are connected together as a mesh to provide a reliable communication, clusters heads had additional resources that facilitate the use of such topology. All clusters heads are connected directly to the forwarding node which acts as a path from wireless to wired network i.e. to the outside world. Fig.2 depicts the overall architecture of WSN using hybrid network topology.

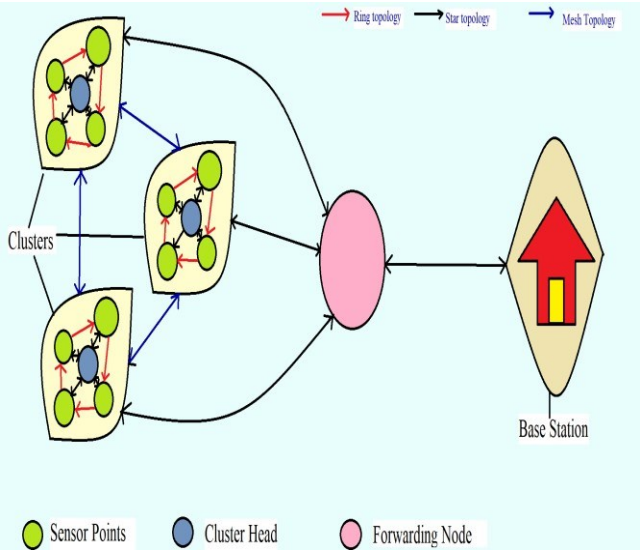


Figure 2. System Architecture

C. *Error Detection and Weight Reduction Formula*

In detecting malicious nodes, we employ trust values of sensor node to reflect their track record in decision making process. Each cluster head maintains trust values of its associated sensor nodes. The trust value (V_w) lies in the range (0,1) and is initialized to 1 for each sensor node. The weight represents the sensor node dependability and the sensor node with a higher weight is more trustworthy. Updating the trust values is important to maintain the fidelity of the readings obtained from the sensors. To determine the non-erroneous node the weighted threshold value should be greater than the minimum threshold value.

$$V_{th} \leq V_w$$

$$V_w = \frac{M - |D|}{M}$$

Where, V_{th} is the minimum threshold weight and V_w is the weighted threshold. M is the Average or mean value of the sensor at a point. (M is the user defined value). D is the deviation from the M. D is dependent on sensor input value and can be calculated as ($M - I$). Where I is the Input value from the sensor.

For example in a tropical rainforest thee temperature varies from 21 to 30 degrees then the value of mean (M) would be 25.5 degrees. If a particular sensor detects the temperature at that time the detected value would be I. Let the detected value be 34 degrees. Now the calculated threshold value would be

$$V_w = \frac{25.5 - |25.5 - 34|}{25.5}$$

Thus, V_w is calculated to be 0.67. Assuming the minimum threshold to be set to 0.7, the equation $V_{th} \leq V_w$ is not satisfied. Thus the corresponding sensor node is an erroneous node.

Weight Modification

If the sensor node is found as erroneous then the weight is reduced according to following formula.

$$W' = W + F \times W$$

Where W' Is the modified weight, W is the current weight and F is weight penalty factor.

IV. Cluster Based Weighted Trust Evaluation

The goal was to come up with a prototype of the enhanced weighted trust evaluation scheme that detect malicious Sensor Nodes and Cluster Heads. The performance requirements that the scheme should meet are short response time, high detection ratio and low misdetection ratio. Response time refers to the average number of cycles required by the scheme to correctly detect malicious nodes, detection ratio refers to the ratio of malicious nodes correctly detected by the scheme to the total number of malicious sensor nodes present in the WSN. Several sensor nodes "n" are deployed randomly in the field, a subset of them are elected as the forwarding nodes whereas the rest become the ordinary sensor node (SN). The sensor nodes organize themselves to form a clustered operational network.

V. Simulation Results

The WTE based detection algorithm was installed in the cluster node for monitoring of all the member sensor nodes.

TABLE I. Simulation Parameters

Minimum threshold weight	0.7
Number of clusters	4
Number of repetitions of samples	5
Network field dimension	100x100
Sensor Nodes in field	100
Weight Penalty Factor	20%
Malicious nodes at deployment	20%

Though the field parameters are user inputs but heterogeneous network of hundred sensor nodes are deployed randomly in the area with a dimension of [100x100] the simulation is as shown in Fig.4

The Sensors are grouped in clusters and the weighted trust evaluation algorithm performs over it. As shown in figure 5 the malicious nodes are displayed in respective clusters. This method is performed for 5 times and the propagation time is compared in figure 6. It is shown that the propagation time decreases with clustering and increases without clustering as the number of samples increases.

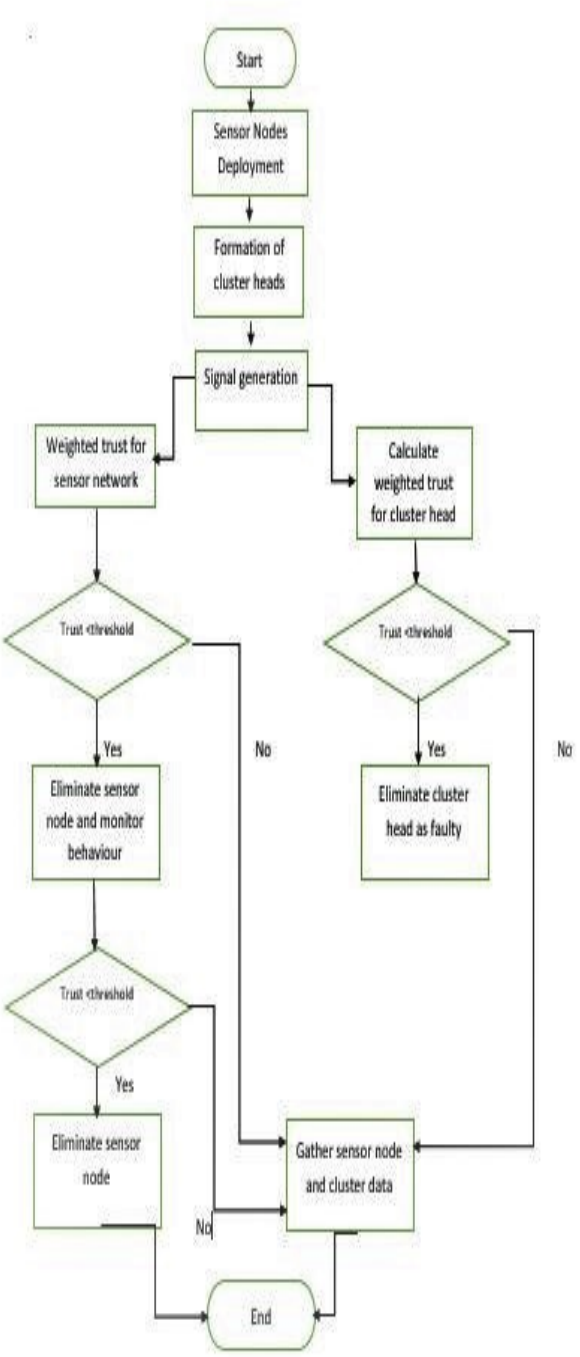


Figure 3. Algorithm for Weighted Trust Evaluation

Though the field parameters are user inputs but heterogeneous network of hundred sensor nodes are deployed randomly in the area with a dimension of [100x100] the simulation is as shown in Fig.4

The Sensors are grouped in clusters and the weighted trust evaluation algorithm performs over it. As shown in figure 5 the malicious nodes are displayed in respective clusters. This method is performed for 5 times and the propagation time is compared in figure 6. It is shown that the propagation time decreases with clustering and increases without clustering as the number of samples increases.

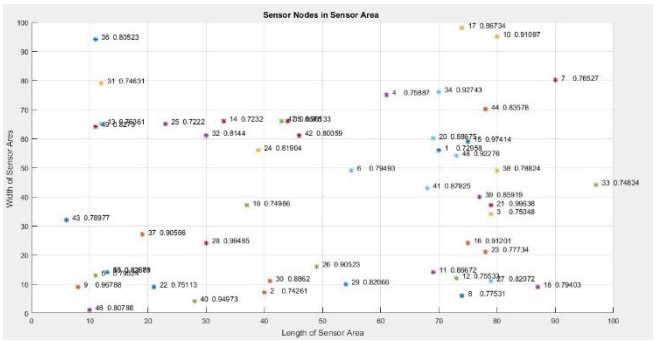


Figure 4. Plot of all the Sensor Nodes in an area

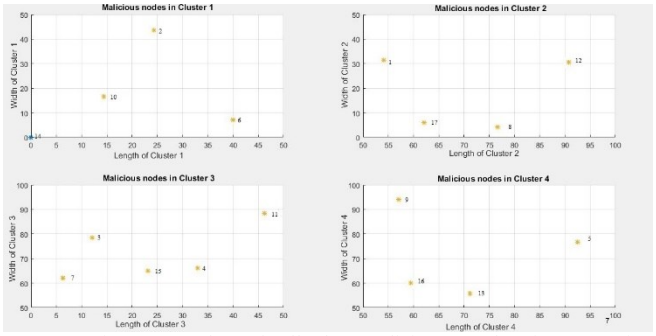


Figure 5. Plot of all the Malicious Nodes in respective forwarding node

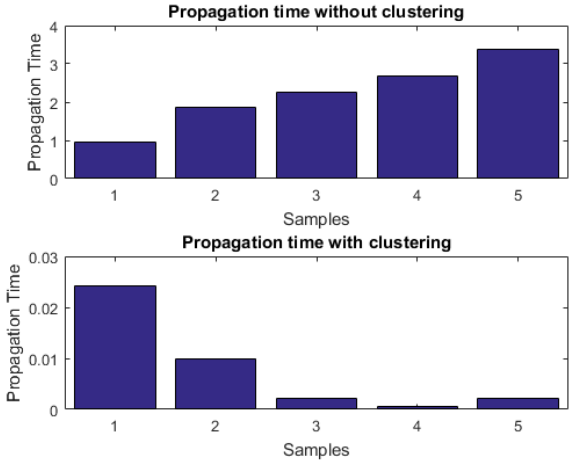


Figure 6. Time taken to find malicious nodes in

i. Whole area at once and then find propagation time.
ii. Considering individual clusters and then find propagation time including all forwarding nodes.

Detection Ratio:

Detection Ratio (DR) is the ratio between the number of malicious nodes detected and the total number of malicious nodes in the network (set at the time of deployment). In one of the simulation runs, the percentage of malicious nodes, is set to 20% (m = 0.2). This means that:

Malicious nodes = 20/100 * n

Where n = number of deployed sensor nodes i.e. =100.

Malicious nodes =20

There is one more set of malicious nodes that is cluster head

Malicious cluster head = m *(p*n)

=20/100 *(4/100 * 100) = 0.8=1

Where p= percentage of cluster head in the network =4/100.

TABLE II. Parameter Vs Nodes

Total Malicious Nodes (At Deployment)	20	40	60	80
Detected Malicious Nodes (Simulation)	18	33	38	29
Detection Ratio (DR)	0.9	0.83	0.63	0.36

Malicious ordinary sensor nodes = m *(n- (p*n))
=20/100 * (100 – (4/100* 100)) = 19.2= 19
The number of detected malicious ordinary sensor nodes is 17 out of the 19 (Through Simulation) that had been set as malicious whereas all the malicious cluster heads are detected by the method.
Detection Ratio = No. of correctly detected malicious nodes/Total no. of malicious nodes in the network.
DR = (17 + 1) / 20 = 0.90
In figure 7, we plot the number of malicious nodes vs detection ratio. It is observed that the detection ratio decreases with the increase in malicious nodes.

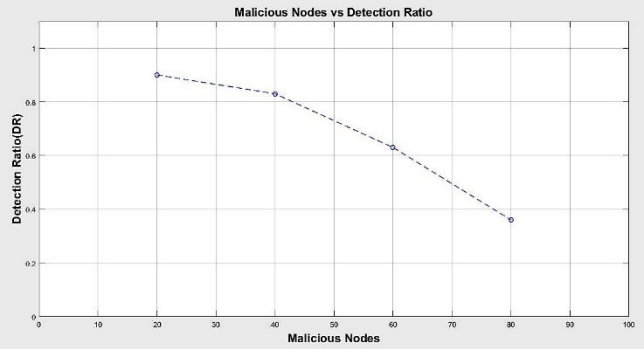


Figure 7. Malicious Nodes vs Detection Ratio

VI. CONCLUSION

The simulation clearly shows that the propagation time in second case (when individual clusters are considered independently instead of whole area at once) is much smaller (nearly1times less).Also 90% malicious nodes are detected when 20 malicious nodes at deployment are considered. If the number of clusters are increased then the Detection Ratio would increase.

In this paper simulation results are being reported and they shows that algorithm can be applied to a flexible number of sensor nodes that operate under a cluster head, it thus has achieved better scalability with a considerable detection rate and less propagation time.

REFERENCES

[1] E. Ayday, F. Delgosha, and F. Fekri, “Location-Aware Security Services for Wireless Sensor Networks using Network Coding,” *Infocom*, May 2007.

[2] S. Zhu, S. Setia, and S. Jajodia, “LEAP: Efficient Security Mechanisms for Large-Scale Distributed Sensor Networks,” *CCS'03*, October 2003.

[3] C. Karlof, N. Sastry, and D. Wagner, “TinySec: A Link Layer Security Architecture for Wireless Sensor Networks,” *ACM Sensys*, November 2004.

[4] Haiyun Luo, Petros Zerfos, Jiejun Kong, Songwu Lu, Lixia Zhang, “Self-securing Ad Hoc Wireless Networks,” IEEE ISCC (IEEE Symposium on Computers and Communications) 2002, Italy.

[5] Idris M. Atakli, Hongbing Hu, Yu Chen, Wei-Shinn Ku and Zhou Su, "Malicious Node Detection in Wireless Sensor Networks using Weighted Trust Evaluation", SpringSem, pp. 836-843, 2008.

[6] W. Du, L. Fang, and P. Ning, “LAD: Localization Anomaly Detection for Wireless Sensor Networks,” the 19th International Parallel and Distributed Priocessing Symposium (IPDPS’05), April 3 – 8, 2005, Denver, Colorado, USA.

[7] I. M. Atakli, H. Hu, Y. Chen, W. S. Ku and Z. Su, Malicious Node Detection in Wireless Sensor Networks, The Symposium on Simulation of Systems Security (SSSS‟08), Ottawa, Canada, p. 838, 2008.

[8] S. Zhao, K. Tepe, I. Seskar and D. Raychaudhuri, Routing Protocols for Self-Organizing Hierarchical Ad-Hoc Wireless Networks, Proceedings of the IEEE Sarnoff Symposium, Trenton, NJ,, March 2013.

[9] K. Sumathi and D. M. Venkatesan, A Survey on Detecting Compromised Nodes in Wireless Sensor Networks, (IJCSIT) International Journal of Computer Science and Information Technologies, vol. 5, pp. 7720-7722, 2014.H. Hu, Y. Chen, W.-S. Ku, Z. Su and C.-H. J. Chen, Weighted trust evaluation-based malicious node detection for wireless sensor networks, Int. J. Information and Computer Security, vol. 3, no. 2, p. 148, 2009.

[10] R. Sharma and N. Tripathi, Comprehensive Review on Wireless Sensor Networks, Oriental Journal of Computer Science & Technology, Vol. 8, No. 1, pp. 59-64, April 2015.

[11] D. G. Padmavathi and M. D. Shanmugapriya, A Survey of Attacks, Security Mechanisms and Challenges in Wireless Sensor Networks, International Journal of Computer Science and Information Security,, vol. 4, 2009.

[12] Rajkumar, Vani B. A., G. Rajaraman, Dr. H. G. Chandrakanth, “Security Attacks and its Countermeasures in Wireless Sensor Networks”, Int. Journal of Engineering Research and Applications, Vol. 4, Issue 10 (Part-1), pp. 04-15, October 2014.

[13] Mohamed-Lamine Messai” Classification of Attacks in Wireless Sensor Networks” International Congress on Telecommunication and Application’14University of A.MIRA Bejaia, Algeria, 23-24 APRIL 2014.

[14] Koriata P. Tuyaa and W.Okelo-Odongo, “Enhanced weighted Trust Scheme for detection of malicious nodes in Wireless Sensor Networks”, International journal of computer applications (0975-8777), Vol 155-No.4, December 2016.

[15] T. Sathyamoorthi, D. Vijayachakaravarthy, R. Divya And M. Nandhini, A Simple and Effective Scheme To Find Malicious Node In Wireless Sensor Network, International Journal of Research In Engineering And Technology, Vol. 03, No. 02, 2014.

[16] X. liu and J. Shi, “Clustering Routing Algorithms in Wireless Sensor networks: an overview”,KSII Transactions on Internet and Information Systems, Vol 6, No.7, 2012 :pp.1735-1755.

Annals of Operations Research
https://doi.org/10.1007/s10479-019-03341-9

S.I.: OR FOR SUSTAINABILITY IN SUPPLY CHAIN MANAGEMENT

An integrated DEMATEL Six Sigma hybrid framework for manufacturing process improvement

Anshu Gupta[1] · Pallavi Sharma[2] · Akansha Jain[3] · Hongbo Xue[4] · S. C. Malik[2] · P. C. Jha[3]

© Springer Science+Business Media, LLC, part of Springer Nature 2019

Abstract
Six Sigma is a widely practiced, systematic, and structured methodology embedded with statistical methods and managerial philosophies for quality improvement by large firms along with small firms in the industrialized economies. Application of Six Sigma in Micro Small Medium Enterprises (MSMEs) in developing economies is limited due to several barriers these firms face. In academic literature, there is unavailability of sufficient evidence of successful implementation of the practice in these firms to encourage and provide a roadmap for its implementation. Thus, there is a need for studies that presents frameworks with illustrative case studies demonstrating the implementation of Six Sigma in MSMEs. In the present times, MSME firms in developing economies are facing competition from world leaders, and thus it has become essential for them to focus on the quality of their manufacturing products and at the same time being productive and efficient. Moreover, in the literature, it is observed that the potential of operations research (OR) methods is not sufficiently explored in Six Sigma studies. OR-based methods and tools should be integrated into Six Sigma implementation frameworks as these methods expand the application portfolio and tackle some of the barriers that limit the application of Six Sigma in small-scale firms. In this paper, a Six Sigma implementation framework for an MSME organization is developed incorporating Multi Criteria Decision Making (MCDM) tool Decision-Making Trial and Evaluation Laboratory, apart from other conventional tools like cause and effect analysis, benefit effort analysis, Pareto analysis, control charts, etc. The proposed framework is illustrated in detail with the help of a real-life case study of an MSME in India. The results obtained after the implementation of this framework signify that the incorporation of MCDM in Six Sigma lead to a significant improvement in the sigma level of the firm despite of unavailability of sufficient resources.

Keywords Six Sigma · Micro Small Medium Enterprises · Multi-Criteria Decision Making · Operations research · Cause and effect matrix

✉ Hongbo Xue
hongbo.xue@mail.nankai.edu.cn

Extended author information available on the last page of the article

Published online: 04 November 2019

1 Introduction

1.1 Research background and motivation

Small & Medium Enterprises (SMEs) are an integral part of developing economies owing to their contribution to industrial and economic growth. They play an important role in employment generation, value creation in domestic supply chains and Gross Domestic Product (GDP) contribution in developing economies (Singh et al. 2006; Lande et al. 2016). A similar trend has been observed in the Indian economy. In the Indian context, the Micro, Small and Medium Enterprise (MSME) Development Act of 2016 classifies organizations based on investments in plant and machinery, and they term SMEs as MSMEs (MoMSME 2017). (Now onwards, both MSME and SME are used interchangeably in this study.) 40% of total manufacturing output of India comes from the MSME sector. The sector is generating more than 117 million employment opportunities in the country, especially for suburban and rural populations. In terms of total exports, the MSME sector's contribution is 45% in the Indian economy (FICCI and PwC 2017). In India, 31% of the MSMEs are engaged in manufacturing activities with Engineering and Capital Goods manufacturing sector is a major contributor to the manufacturing output. Within the Engineering and Capital Goods sector, electrical equipment production accounted for $27.3 billion in 2017–2018, which is expected to reach $100 billion by 2022 (IBEF report 2017–2018). In recent years, to fuel the country's economic growth, Indian Government has initiated several schemes and supporting policies like Make in India, Startup India, and Skill India to strengthen the manufacturing sector of which MSME sector is the major beneficiary (Tripathi and Singh 2018). On the other hand, globalization and open trade have brought challenges of meeting global standards of quality in products and services and shrinking profit margins (Ihua 2009).

To position Indian manufacturing to produce in the global marketplace and continue to survive in the growing competitive environment, MSME organizations have to prioritize their efforts towards quality improvement of their product, processes, and services (Herzallah et al. 2014). Their focus should be on meeting the global quality standards by improving the quality of their products and processes (Sharma et al. 2018). Further, they have to deal with shrinking profit margins by increasing efforts in inventory management, productivity improvement, waste reduction, and value addition through product variety and after-sales services (MoMSME 2017; Prashar 2018). These efforts can be best implemented through Quality Management (QM) and improvement programs (Tang et al. 2007). With the support of the various schemes and policies by the Indian Government, several organizations in MSME sector of the country have started focusing on building competitive advantage through quality improvement initiatives, upgrading the technology, building a skilled manpower base and required infrastructure such that their manufacturing output matches the global standards (IBEF report 2017–2018). However, the efforts are still in the infancy stage both in practice as well as in academic research. The thrust to gain competitive advantage requires continuous QM efforts following structured QM frameworks with visible returns, keeping customer satisfaction in the center (Chakraborty et al. 2019). Our study contributes significantly by developing a Six Sigma (SS) based framework for the deployment of a quality improvement project in an Indian MSME manufacturing firm.

1.2 Need of the study

In developing countries, the non-standardize output is one of the major problems that MSMEs face (Prashar 2018; Chakraborty et al. 2019). Shortage of skilled labor, limited financial support, conventional machinery, and production process are some of the causes for variation in the output in such organizations (Garza-Reyes et al. 2018). Variation in output leads to higher waste generation in terms of rejections and repairs, leading to financial and goodwill losses. Dealing with process variation requires dedicated QM efforts, targeting the elimination of causes of variations following robust methods of QM (Antony 2008; Singh et al. 2008). The popular QM frameworks developed in the literature and practiced by practitioners include statistical control of quality, quality circles, SS, lean methods, benchmarking and total quality control and management (Lakhal et al. 2006; Sahoo and Yadav 2018).

Sufficient literature is available to support the application of all of these methodologies. Amongst all, SS has evolved as a successful methodology for manufacturing as well as service organizations suitable for both large- and small-scale organizations in the literature of QM (Snee 2004; Shafer and Moeller 2012). Success of SS methodology for QM follows from its structured approach that is customer focused and is built on data driven tools and techniques (Chakravorty 2009; Jin et al. 2011). Several frameworks for QM based on SS methodology majorly following the DMAIC model (Gupta et al. 2016) of SS are discussed in the literature that serve as a roadmap for implementation of QM projects in similar organizations (Gijo et al. 2011; Prashar 2016a, b). Nevertheless, existing studies in the literature of SS mostly concentrate on large organizations (Drohomeretski et al. 2014). While a good number of studies also discuss the SS QM project deployment for small organizations in industrialized countries, but those for the developing economies are limiting (Antony 2008). Within the limiting successful illustrations of SS implementation available in the literature for small-scale organizations in the developing economies, full potential of SS methodology is yet to be realized (Chakraborty et al. 2019).

The implementation of a quality improvement program in large scale firm is not replicable in small scale organizations. Targeting structured and continuous improvement endeavors for quality improvement is strenuous for small organizations due to lack of awareness, required skill and resources, use of conventional processes and methods of data collection and ownership of employees (Chakravorty 2009). Given this backdrop, our study focuses on bridging this gap and proposes a SS DMAIC framework that effectively harnesses the power of SS project implementation in small scale industries (Deshmukh and Chavan 2012). The purpose of our study is to propose a SS DMAIC framework that serves as a roadmap for SS practitioners in SME organizations for implementation of an effective quality improvement endeavor.

Further, large organizations that practice scientific and continuous approach to strategic QM have robust methods of data collection and have well established capabilities to channelize the power of data to unfold the areas and dimensions within (Kumar et al. 2011; Drohomeretski et al. 2014). While in case of small-scale organizations (as also seen in the case organization), the methods of data collection, analysis and tools are mostly conventional leading to incomplete and inappropriate availability of information. In such cases, it becomes difficult to identify the dimension(s) that is most Critical To Quality (CTQ) to target the improvement efforts (Basu and Bhola 2015). In most of the studies discussed in the literature, a single dimension is clearly known to target the improvement efforts. For example, Gijo et al. (2011) applied SS methodology for improving first pass yield of a grinding process in an automotive products manufacturing unit, Prashar (2018) discussed DMAIC model implementation for reducing the cycle time of the production process in an SME manufac-

turing firm. On the other hand, when more than one CTQ dimensions are identified, they are prioritized based on frequency using Pareto analysis (Soković et al. 2009). The existing literature ignores the scenario when multiple dimensions are observed wherein the improvement efforts can be targeted but the available information is not sufficient to prioritize the key dimensions. Our study in addition to the above mentioned purpose, also provides an analytical framework and illustrates the application of a Multi-Criteria Decision Making (MCDM) method, Decision Making Trial and Evaluation Laboratory (DEMATEL), for prioritization of key defects in the define phase of the DMAIC model and thereby expands the SS toolkit in terms of application of operations research (OR) based methods.

The applicability of the proposed framework is illustrated through an application experience in a small-scale Indian manufacturing firm facing rejections and repairs in the screen-printing process of an amplifier production process. The management realized the significant cost of waste due to rejects and repairs and also increasing complaints from customers. In thrust of improving the firm's productivity through waste minimization and increased customer satisfaction, the management called for this quality improvement project. The results presented in this study are the result of study undertaken during the implementation of the project.

1.3 Research objectives

The objective of this study is to develop an effective framework integrating appropriate statistical, OR and managerial methods and tools for SS implementation in a small-scale manufacturing firm operating in a developing economy. This objective is met through the following specific sub-objectives:

- To understand the status of research relating to the deployment of QM programs in small-scale manufacturing organizations, particularly in context to India.
- To identify the challenges and limitations a small-scale manufacturing enterprise faces in implementing a QM project.
- To develop and illustrate the application experience of an effective DMAIC SS implementation framework for a small-scale Indian manufacturing firm.
- To illustrate the application of an MCDM model to prioritize the key dimensions (defects in case of our study) to be addressed through the quality improvement project when prioritization purely based on Pareto analysis is not applicable due to unavailability of sufficient data.

1.4 Research contributions

Given the limiting availability of literature and the use cases for SS implementation in small-scale manufacturing organizations for developing economies, this paper contributes by developing a SS DMAIC framework for implementation of a QM project in small-scale manufacturing organizations. The proposed SS DMAIC framework is supported and hence validated with the observations, analysis and results obtained during its real life implementation for an MSME organization in India involved in the manufacturing of portable amplifiers.

As concluded from the literature review by Tang et al. (2007), most of the methods and tools integrated in different stages of DMAIC and other SS models are drawn from the discipline of statistics or are developed as part of the theoretical developments in QM (Hillier and Lieberman 2001; Snee 2000). Apart from these tools and methods, few studies

have attempted to integrate OR, and managerial methods with SS methodology (Tang and Paoli 2004; Kumar et al. 2008; Sharma et al. 2018). However, the attempts are still at an infancy stage. As reported in Tang et al. (2007), for the SS methodology to remain effective, it is important to expand the toolset. OR methods provide great potential in increasing the effectiveness and broadening the application of SS frameworks. With this perspective, our study provides a major contribution by illustrating the application of an MCDM method, DEMATEL, for defect prioritization in the measure phase of the DMAIC model.

1.5 Organization of paper

The manuscript is organized into the following sections. Section 2 discusses the literature review and highlights the research gap. Section 3 describes the research methodology and highlights the various techniques used in each phase of the DMAIC methodology. In Sect. 4 the case illustration is discussed and execution of the DMAIC SS model is demonstrated following a step by step approach. Insights and managerial implications are drawn in Sect. 5. Section 6 concludes the study indicating limitations and future scope of the research.

2 Literature review

In order to meet the first two sub-objectives of the study mentioned in the introduction section, i.e., to understand the status of SS literature, to overcome the challenges SME organizations face in SS implementation and to explore the appropriate methods and tools to apply in the DMAIC stages, a detailed Review Of Literature (ROL) is conducted and the research gap is identified in this section. The ROL is organised into three subsections: an overview of SS and its applications, integration of SS with OR tools and techniques and application of SS in SMEs. The identified research gap is elaborated in detail in the fourth subsection.

2.1 Overview of SS and its applications

Over the years theoretical developments and applications of QM projects in different industries with diverse objectives have gained the interest of the academic researchers and practitioners (Tang et al. 2007; Kumar et al. 2008; Veena and Prabhushankar 2019). One of the major methodologies widely discussed and practiced for quality improvement is the SS methodology (Kumar et al. 2008). SS is a customer-focused, structured, and data and outcome driven strategic business improvement initiative. Many of the globally known companies such as General Electric (GE), DuPont, Honeywell, Samsung, and IBM have adopted this approach since its inception by Motorola in the 1980s (Nonthaleerak and Hendry 2008; Wang and Chen 2010). Despite of the development of various new quality philosophies and strategic approaches, SS still remained a very powerful approach for quality improvement (Zhang et al. 2015). By the end of the 20th century, several other companies, whether large or small have adopted SS as it provides irreplaceable powers for continuous improvements by rigorously focusing on processes (Augusto et al. 2012). SS initiatives are commonly based on the identification and elimination causes of variations in the process, improving the precision and thereby increasing the market value and gaining consumers' loyalty towards the company and its products (Arturo Garza-Reyes et al. 2014). The goal of SS is to reduce the rejection rate to almost zero, that is, to achieve a level of 0.0003% rejections (Prashar 2016a, b).

One of the most popular ways of implementing SS is by using the DMAIC model (Montgomery and Woodall 2008). The DMAIC methodology is implemented in five phases namely, (1) D: defining the objective, (2) M: measuring the current performance of the process, (3) A: analyzing the key defects to identify root causes, (4) I: improving the performance of the process and (5) C: controlling the improved performance of the process. Initially, the DMAIC method of SS was used in the manufacturing sector (Gijo et al. 2011) for continuous improvement. For instance, Anand et al. (2007) used the DMAIC methodology to optimize deep drawing operation variables, Gijo et al. (2011) applied the same for improving first pass yield of a grinding process in an automotive products manufacturing unit, Southard et al. (2012) examined the effect of implementing Radio Frequency Identification (RFID) technology on improving effectiveness and efficiency of outpatient surgical processes in hospitals using DMAIC, Zhang et al. (2015) used DMAIC methodology for the processes in a stainless steel cold rolling mill and so on. Later it gained popularity, and the application of DMAIC methodology did not remain limited to the manufacturing sector, various researchers applied this methodology in the service sector (Prashar 2016a, b), transactional environment (Antony et al. 2012a, b), the health sector (Southard et al. 2012) and many more.

Several statistical, mathematical, QM, operations research, and managerial methods are integrated into the DMAIC stages to develop an appropriate frame for SS implementation (Brady and Allen 2006; Tang et al. 2007). As mentioned earlier, statistical methods such as statistical quality control, Analysis Of Variance (ANOVA), Design Of Experiments (DOE), hypothesis testing, regression analysis and the like (Elshennawy 2004) and methods developed as part of the theoretical and methodological developments in QM such as Quality Function Deployment (QFD), Failure Mode and Effect Analysis (FMEA), Cause and Effect (C&E) analysis and Supplier-Input-Process-Output-Customer (SIPOC) have gained popularity and are widely practiced in the QM literature (Montgomery 2007). Due to these wider and diverse applications, new methods and tools have been continuously integrated within the DMAIC stages. Table 1 tabulates some of the selected studies from the literature listing their objective and the tools integrated in the different stages of DMAIC model. Though methods from OR and other analytical disciplines are also being considered in the SS implementation, the full potentials of these method is yet to be harnessed (De Mast 2004; Tang et al. 2007; Sanchez-Diaz et al. 2018).

2.2 SS and OR

The objective of SS is not just to target a single CTQ characteristic; rather it is a continuous business-improvement approach (Harry and Schroeder 2000). It focuses upon all those dimensions of the business processes that are of high significance to customers and tries to identify and eliminate causes of defects in these dimensions (Snee 2000). Through SS implementation, companies strive to achieve improvements in their business processes such that enhancement in the bottom-line is realized with higher customer satisfaction and expanded market reach (Tang et al. 2007). As mentioned earlier, OR based methods and tools have been limitedly explored in the SS literature (Hoerl 2001; Elshennawy 2004) while OR methods have found extensive applications in diverse areas including financial services, healthcare, logistics and supply chain management, manufacturing and service operations and the like (Brady and Allen 2006).

Since its inception, SS has been widely recognized as a statistical approach incorporating application of QM tools. Due to its data driven orientation, these tools have been widely discussed in a number of SS implementation frameworks. But, statistical and QM methods

Table 1 SS studies with different tools/techniques

Citations	Objective/focus	Tools/technique used
Anand et al. (2007)	SS-based approach to optimize deep drawing operation variables	D: Identify CTQs M: C&E diagram, QFD, *X* bar chart A: DOE I: Response Surface Methodology (RSM) C: Process improvement
Gijo et al. (2011)	An application of SS methodology for improving the first pass yield of a grinding process in the manufacturing of automotive products	D: SIPOC, Project Charter M: Guage RR, Kappa statistics A: C&E diagram, Gemba analysis I: DOE, ANOVA C: *X* bar and *R* chart
Southard et al. (2012)	To examine the effect of implementing Radio Frequency Identification (RFID) technology on improving effectiveness and efficiency of outpatient surgical processes in hospitals	D: Identify CTQs M: Value stream map A: Poke-Yoke I: Simulation C: Process improvement
Jirasukprasert et al. (2014)	Manufacturing process of rubber gloves by reducing defects and process improvement	D: Identify CTQs, Project charter M: Pareto analysis, defects per million opportunities (DPMO) A: C&E diagram I: DOE, ANOVA C: Box plot and line chart
Zhang et al. (2015)	Comprehensive SS application: a case study in stainless steel cold rolling mill	D: Identify CTQs, M: Measurement system analysis (MSA), Process map, C&E diagram A: FMEA, ANOVA, C&E matrix, Regression analysis, ANOVA I: DOE C: Process improvement
Prashar (2016a, b)	A conceptual hybrid framework for industrial process improvement: integrating Taguchi methods, Shainin system and SS	D: Project charter, SIPOC, Control charts, CTQs M: Process capability analysis, MSA A: Multi-variate chart, Paired comparison, Component search technique I: Orthogonal arrays, ANOVA C: Process improvement
Sharma et al. (2018)	An application of DMAIC SS methodology to identify and eliminate the sources of variations and improve the process productivity	D: Project charter, SIPOC M: Check sheet, *p*-chart, Pareto analysis A: C&E diagram, current reality tree (CRT) I: Process improvement C: *p*-chart, Pareto analysis

Table 1 continued

Citations	Objective/focus	Tools/technique used
Proposed paper	An integrated DEMATEL Six Sigma hybrid framework for manufacturing process improvement	D: Project charter, SIPOC M: DEMATEL, check sheet, *p*-chart, Pareto analysis A: Fishbone diagram, C&E matrix I: Process improvement, benefit-effort matrix, AHP, Gemba C: *p*-chart, Pareto analysis, Check sheet

are often not sufficient for some of the problems encountered during the implementation of SS like unavailability of past data, irregular and inappropriate methods for data collection and recording, lack of appropriate information and inadequate rate of production in small-scale operations (Brady and Allen 2006; Kumar et al. 2008). These problems can be efficiently and effectively tackled with the help of OR techniques. The primary goal of OR techniques is to determine the most efficient and effective course of action/decision that the company should take to manage its day to day operations which is also the prime focus of SS studies (Tang et al. 2007). Therefore, it is crucial for SS practitioners to integrate OR tools and techniques into SS applications to enhance the analysis conducted during these studies and sustain the value of SS for business process improvements (Brady and Allen 2006; Tang et al. 2007).

Understanding the importance of integration of SS and OR tools, many researchers have tried to incorporate OR tools like goal programming (Kahraman and Büyüközkan 2008), Analytical Hierarchy Process (Rathi et al. 2015), Analytical Network Process and DEMETAL (Ortíz et al. 2015) and so on in SS framework, but the application of these tools is limited mostly to SS project selection. Organizations usually have several areas in their operations with a scope for improvements which are to be weighted on cost of implementations, benefit realized and other evaluation criteria and accordingly a SS project is selected. The full potential of OR methods is yet to be established in the execution of the DMAIC and other SS frameworks. For instance, problems like defect prioritization based on multiple dimensions, production and service planning, training of semi and unskilled operators, resource allocation, waste management and investment decision encountered during the measure phase of SS methodology can be handled with the help of OR tools (Schouten and Tapiero 1995; Tang et al. 2007). But, due to unavailability of the literature that establishes the integration of OR methods in DMAIC phases the practitioners' acceptability of these methods is low and limits the ability of SS practice in strategic decisions making. This problem magnifies in case of SMEs as they don't have trained personnel to solve these problems due to unavailability of resources, information required and required skill to deal with these methods.

2.3 SS and SMEs

Since more than past 30 years, large organizations are concentrating on QM in their organizations. Small sized industries were of the opinion that SS implementation is beneficial only for large industries or SMEs in industrialized economies as the cost incurred in its implementation is not much for large organization due to economies of scale (Deshmukh and Chavan 2012). To check the appropriateness of this assumption, Antony (2008) conducted a study on the

topic "Can SS be effectively implemented in small and medium-sized enterprises (SMEs)?". As part of this study the author organized a pilot survey to interview various academicians, researchers and practitioners to collate their opinions and views on the practice of SS in small scale industry. Research outcomes of this pilot survey clearly specified that SS is appropriate for both large and small organizations. In fact, the improvements are quite visible in Small and Medium sized Enterprises (SMEs) as compared to large enterprises if implemented successfully. The study conducted by Antony (2008) was able to remove a misleading and common myth that SS is primarily designed and applicable only for large enterprises. Later, we could find many studies in the literature focusing on implementing quality improvement efforts in SME organizations. The study presented by Kumar et al. (2011) discussed a framework for deployment of SS in SMEs based on a survey in which case studies were conducted in ten SMEs located in Scotland and England. A five-phase framework for SS was developed by them based on this survey: (1) readiness, (2) preparing, (3) initializing, (4) institutionalizing and (5) sustaining. But in developing countries like India, the situation remained the same; SMEs were reluctant in incorporating these principles. Deshmukh and Lakhe (2010) presented a study which was aimed at identifying the extent of awareness regarding SS in small scale industries of central India. The outcome of this survey showed that only 67.5% of SMEs in central India were aware of the SS methodology, but not a single one was practicing it in their respective organizations. They were sceptical about the applicability of these efforts for them. Apart from the lack of top management's commitment, the unavailability of resources, convention and inappropriate methods of data collection, and unavailability of skilled labour were identified as the main barriers to the implementation of QM efforts (Tang et al. 2007; Kumar et al. 2008). Internal resistance, temporary employment, lack of knowledge and poor training acted as additional barriers in the implementation of SS in SMEs (Chakraborty et al. 2019).

Understanding these limitations for implementing SS in the SMEs in developing countries, some researchers took initiatives to help them in implementing improvement efforts. For instance, in the research presented by Kaushik et al. (2012), SS methodology was adopted for an SME. The methodology was executed to improve the productivity of a bicycle chain manufacturing unit of an SME. Later, Gijo et al. (2014) presented a roadmap for application of SS DMAIC model for improving leaf spring manufacturing process of a small-scale foundry industry to reduce the rejections and rework in one of its processes. Parsana and Desai (2016) applied SS quality improvement methodology to identify, quantify and abolish sources of variation in the manufacturing production process of cylinder head in a manufacturing SME in India. Prashar (2018) presented an exploratory SS case study for a small-scale engineering enterprise located in north India, facing chronic delays in the delivery. A Lean SS (LSS) deployment roadmap was conceptualized and validated for manufacturing SMEs in the research presented in this study. The academic research and practice are yet to fully establish the applicability of SS frameworks for quality improvement in the SME organizations in developing economies (Zhou 2016). Such studies are required to not only fully explore the application of conventional SS tools and methods but should also focus on harnessing the applicability of OR and analytical methods like MCDM, mathematical programming etc. to fully establish the SS implementation and overcome the barriers in context to SME organizations.

2.4 Research gap

From the ROL discussed above it is clear that several authors have contributed in the field of SS implementation for process improvement. But, still there are clear research gap in the existing literature. Firstly, in terms of limited focus of SS implementation in SMEs, particularly, those in developing countries like India. Secondly, in terms of development of SS frameworks expanding the implementation toolsets integrating methods from disciplines such as operations research.

Chakraborty et al. (2019) while conducting a study to understand the status of implementation of SS in SMEs concluded that a significant number of researchers have paid attention towards the implementation of SS in SMEs in industrialized economies. However, the scope still remains limited for SS implementation in the SME organizations in developing economies like India. For achieving sustainable benefits through such efforts, it is imperative for researchers to understand critical success factors and barriers in the implementation of such initiatives (Antony 2008; Yusof and Aspinwasll 2000). Antony (2008) in a comparative study of SS in SMEs in UK found that lack of knowledge and limited resource availability were the main barriers for the implementation of SS. Further, Ihua (2009) stated that most significant barriers in the implementation of SS in SMEs are lack of top management's commitment, unavailability of resources and information, inadequate staff training and lack of technical competencies. In the Indian context, Majumdar (2016) argued that though a number of Indian manufacturing SMEs have adopted SS but they are still reluctant to embed SS with their business philosophies. Chakraborty et al. (2019) emphasized on the need to carry out research describing the SS implementation and publishing use cases to help practitioners in providing a roadmap for further use of the methodology in SMEs in developing countries despite of these barriers and also provide a means to tackle these barriers.

In accordance with the gaps highlighted above, the work presented in this paper develops a SS implementation framework for SME organizations in developing countries and illustrates its application for an Indian SME firm involved in the manufacturing of portable amplifiers. Further, as discussed in the ROL, development of SS DMAIC frameworks has remained as a focal point of study in the QM literature. Their applications are discussed in diverse areas with objectives centred on improving dimensions of the business processes. Based on the appropriateness of methods, knowledge and available literature support, primarily statistical and QM methods were integrated in different stages of DMAIC execution (Prashar 2016a, b). OR methods and tools offer great potential in expanding the horizon of SS applications as they provide efficient and effective solutions to problems related to unavailability of appropriate and complete data required for implementation of the conventional methods used in DMAIC implementation (Andersson et al. 2006). However, there is little awareness and focus on the usability of OR and other analytical methods in SS project execution (Yousefi and Hadi-Vencheh 2016). Brady and Allen (2006) in their literature review paper concluded that integration of these methods with SS will lead to improved performance of SS projects in comparison to other time-tested methods. The authors stated that a significant amount of research in the field of SS that integrates these methods is concentrated on macro level of decision making related to the overall quality performance of the company. Goh et al. (2003) claimed that the benefits obtained after such level of decision making are short lived and their long-term effects were largely inconclusive. Snee (1999, 2001) concluded that there is a need for research to help SS practitioners in identifying a robust set of micro level improvement tools that can be used in accordance of the DMAIC methodology.

On this backdrop, the SS implementation framework proposed in this study explores the application of DEMATEL method from the class of MDCM methods developed in the OR

literature for prioritisation of defects in the measure phase of the DMAIC model integrating several other methods and tools such as SIPOC, C&E analysis and a number of Statistical Quality Control (SQC) methods to achieve the desired objective of reduction in process variation. The proposed framework is tested through an illustrative application for a small-scale Indian manufacturing firm facing the problem of low productivity and higher cost due to rejections and repairs in the screen-printing process of an amplifier production process.

3 Research methodology

The study conducted in this paper is aimed at the development of a hybrid SS implementation framework on DMAIC model effectively integrating DEMATEL method along with other statistical and QM tools. The application of the proposed DMAIC framework is validated through a case illustration for the quality improvement of the screen printing process of an amplifier manufacturing process of an Indian MSME firm (Fig. 1). Stages of DMAIC method are planned following a well-defined Plan-Do-Check-Act (PDCA) structure (Montgomery 2007; Prashar 2017). Appropriate statistical, OR and managerial tools and techniques are embedded in each of stage of DMAIC to derive the required output (Hagemeyer et al. 2006). The literature provides theoretical and practical foundations of the methods enabling selection of suitable methods. The methods and tools used in the study include project charter, SIPOC analysis, *p*-chart, C&E analysis (fishbone analysis), C&E matrix, DEMATEL and Analytical Hieratical Process (AHP). The following paragraphs describe the methodology in detail.

Define phase of the DMAIC methodology helps the decision makers in clearly understanding and formulating the problem. In the early literature, definition of the problem was often based on the results of the brainstorming sessions conducted to determine the CTQ dimensions and process flow diagrams were prepared through observations (Anand et al. 2007; Southard et al. 2012; Zhang et al. 2015). Gijo et al. (2011), Mitchell and Kovach (2016), Prashar (2016a, b), Sharma et al. (2018) highlighted the subjectivity in the problem definition in these studies and proposed application of QM tools such as project charter, SIPOC analysis and affinity diagram to understand the problem under consideration and tackle this limitation. In this study we have integrated project charter and SIPOC diagram for problem definition and process mapping. Project charter explains the details of the problem under consideration. It defines the objectives and goals of the project along with various other factors like project team, project timeline, expected benefits, etc. (Sharma et al. 2018). Problem definition is based on process mapping. It is an essential activity of problem definition as it enables the project team in learning the process wherein the improvement efforts are targeted. SIPOC analysis used in our study helps in documenting the suppliers, inputs, outputs and customers of the process (Gijo et al. 2011). It also lists down each of the steps of the process. Thus, a complete understanding of the process under study is developed in this phase with the help of these two tools.

In the *measure* phase of the DMAIC methodology the objective is to identify the key dimension(s) to analyse and improve and to establish the baseline process performance on the basis these dimensions. In the literature, process performance is commonly defined in terms of matrices such as process control and fraction defectives, process capability, DPMO and sigma level (Montgomery 2007). Further, studies in the literature either consider a single known dimension for process improvement (Gijo et al. 2011; Prashar 2018) or prioritize key dimensions (defects in our case) from multiple dimensions to target improvements using Pareto principle (Jirasukprasert et al. 2014; Sharma et al. 2018). This prioritization

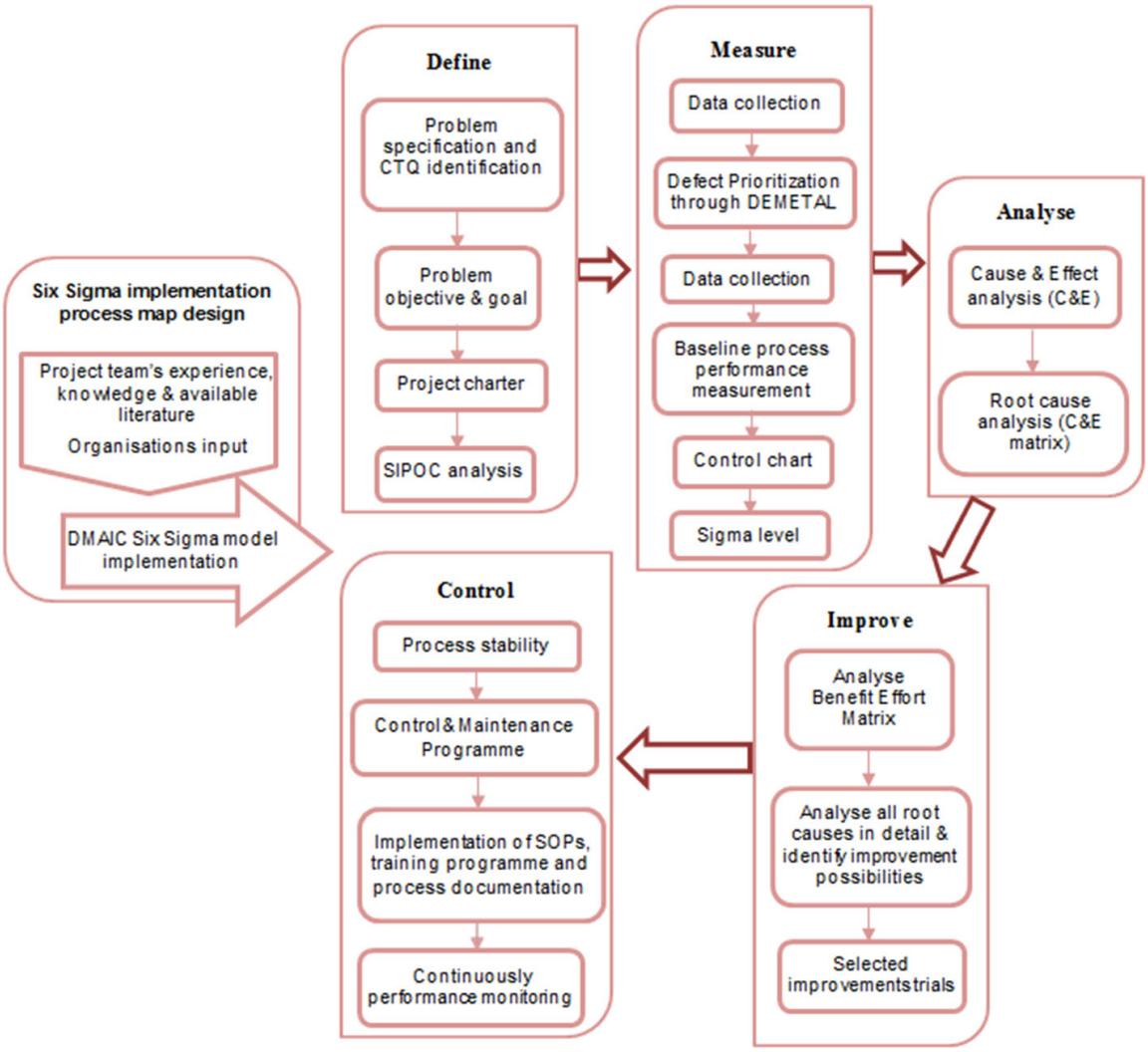


Fig. 1 Proposed hybrid DMAIC implementation framework

is important especially for small-scale organisations because multiple improvement dimensions cannot be considered simultaneously as it may require multiple parallel changes and improvements in the process that limits the realization of desired results, receives resistance from employees and leads to instability in the process (Kumar et al. 2011). Prioritization of defects using Pareto principle requires sampling data of the process output. It prioritizes the defects based on the 80–20 rule, which states that 80% of the problems are due to 20% of the errors (Jirasukprasert et al. 2014). But when a large number of defects are observed, prioritizing them using Pareto principle requires significant amount of data. But due to the small-scale of production in MSMEs, obtaining this data through sampling becomes costly as well as time consuming. To overcome this limitation, DEMATEL, an OR based method, is integrated in the measure phase to segregate the defects into cause group and effect group using which the key defects are identified. The data for required for the application of DEMATEL is collected from experts' opinions which is not affected by the small-scale of operations and thus helps in dealing with the limitation of unavailability of data for defect prioritization. DEMATEL is an MCDM method, which is useful in analysing the co-relationships amongst the attributes (Soheilirad et al. 2018). It builds a map to reflect cause and effect relationships within these attributes. This methodology not only maps the co-relationship between the attributes but also measures the strength of interdependency between them (Tzeng and Huang 2012). The detailed steps of the DEMATEL approach are given in "Appendix A". Once the key defects

are identified process performance is established using *p*-chart for fraction defective (Gupta et al. 2016) to check the process control and based on the obtained results, the baseline sigma level is computed (Gijo and Sarkar 2013).

Analyse phase of DMAIC methodology is aimed at identifying the causes and root causes of the key defects. In this study, C&E (fishbone) analysis and C&E matrix (Jirasukprasert et al. 2014; Lee et al. 2009) have been used to uncover the potential causes and root causes of the screen-printing process. In C&E analysis, potential causes of the problem are classified into: Material, Manpower, Maintenance, Method, Machine and Environment (5M&1E) and are represented in the form of a fishbone diagram. This classification is arrived at through brainstorming sessions, 5-why method, process observations and interactions with shop floor operators (Cherrafi et al. 2017). C&E matrix has been used in the study to isolate the root causes of the problem. C&E matrix is used to understand the interrelationships between the potential causes, their undesirable defects and the core problem. It relates the process steps to Key Process Input Variables (KPIVs) and correlates these KPIVs to Key Process Output Variables (KPOVs) and computes the importance ratings of each of the KPIVs (Rajagopalan et al. 2004). The detailed steps of formulating a C&E matrix are given in "Appendix B". The root causes revealed by C&E matrix have been diagnosed to identify the potential solutions for process improvement (Lee et al. 2009).

The aim of *improve* phase of DMAIC methodology is to identify potential corrective measures and to investigate the feasibility of these potential solutions for elimination of the root causes considering the requirement of time and monetary resources, manpower, skills, and expected results. In the improve phase of this study, benefit-effort matrix has been used (Gijo and Sarkar 2013). Given the several barriers in the implementation of QM efforts in MSME organizations, benefit-effort matrix analysis is conducted to prioritize the corrective measures based on their impact and the effort needed to implement those measures. Benefit-effort matrix helps in performing a risk analysis, which classifies the actions to be taken to eradicate these root causes into four quadrants viz. high impact with low effort, high impact with high effort, low impact with low effort and low impact with high effort (Gijo and Sarkar 2013). The result of this analysis facilitates in the identification of corrective measures that are likely to result in major benefits. Further, the improvement actions could be implemented sequentially in subsequent trials resulting in much stable improvements. The detailed steps of constructing a benefit-effort matrix are given in "Appendix C". Once the corrective actions have been prioritized, tools like Gemba and AHP have been used to implement the identified corrective measures. a management tool, has been used for determining the potential solutions (Gijo et al. 2011; Govindan et al. 2017).

In the *control* phase of the methodology, control mechanisms are established to sustain the improvements realised through the implementation of correct actions. Given the limitations of the SS implementation in SMEs, this phase also focused on conducting training programs for the employees and helping in proper documentation of each step. The implementation of the proposed DMAIC framework is illustrated through a real life case illustration.

4 Case illustration

To examine the effectiveness of the proposed SS DMAIC framework a single case study design is selected due to its ability to provide a systematic and holistic view of the context (Yin 2014).

4.1 Case background

The case study is presented on the basis of experience from an academic research conducted for quality improvement in a small-scale manufacturing firm in India. The firm was facing the problems of low productivity and heightened cost due to high rate of rejections and repairs leading to productivity and financial losses. The study aims at reducing the variations in the output of the screen-printing stage of a portable amplifier production process such that productivity and production cost is optimized. Identity of the firm is protected due to commercial confidentiality.

The firm is involved in the production of a variety of public address systems like megaphones, portable amplifiers, speakers and microphones. The manufacturing process of portable amplifier is designed in seven sequential stages, namely; chassis preparation, anodizing, powder coating, printing, fitting, final fitting and packaging and dispatch (Gupta et al. 2016; Sharma et al. 2018). The scope of this case is limited to variation minimization in the screen-printing stage of the manufacturing process. Screen-printing is one of the most versatile, durable, economical and high-quality graphic resolution processes having a variety of commercial and retail applications (Foster et al. 2016). An important factor that makes screen-printing so popular is the fact that it allows one to use a wide variety of printing materials like plastic labels, powder coated metal plates, resistor or circuit boards, cylindrical containers and so on as a surface for printing (Phillips et al. 2014). Despite these wider applications, screen-printing is still considered as a secondary process in any manufacturing firm. The same problems were faced by the firm under consideration. They were getting a lot of customer complaints because of low quality, transient and improper printing. The firm realized productivity and financial losses in fixing the repairs in the rejects. To control these customer complaints, the firm wanted to identify and remove the problems in its screen-printing process. The study presented here assisted the firm in improving the capability of its screen printing process through systematic implementation of the proposed DMAIC framework.

The SS's DMAIC phases for the improvement of screen-printing process of the firm are elaborated in the following sections.

4.2 Define

The objective of the define phase of DMAIC model is to clearly understand and formulate the problem of study. In this phase one needs to understand the CTQs which are directly related to the quality of the process and are crucial to the customers. Proper problem definition is a vital step before any quality improvement project can actually be put into action. The first step of the DMAIC project is to discuss the problems that hinder the growth of the enterprise and scar its reputation with various decision makers like field operators, managers and customers.

After understanding the problems on the lines of the proposed DMAIC framework, the project objective and goals were defined by discussions with the quality head, research advisor and floor operators and by observing the process. These objectives and goals along with various other factors like project team, project timeline, expected benefits, etc. are illustrated with the help of a project charter (Fig. 2) (Cherrafi et al. 2017). The project goal was set to reduce the top two defects by 50% to be completed over a 6 months' timeframe.

To develop a clear understanding of the activities involved in the screen-printing process, SIPOC analysis was conducted and SIPOC diagram was prepared. This helps in further

Project Charter	
Project title : Defect reduction in screen printing process	
Project objective and goal: To reduce the uneven ink deposits and maligned print defects by 50%	
Project location : An Amplifier Production facility in Delhi NCR, India	
Background and Rational for project selection :	
In the baseline process, uneven ink deposits and misaligned print have been identified as the key defects based on factors like cost, time, quality improvement, etc.	
Project team:	Quality Head
	Managers from Production, Purchasing and Maintenance Departments
	Quality control inspector
	Research advisor and associates
	Floor operator
Expected benefits: Reduction in the defects due to uneven ink deposits and misaligned print	
Project plan : Application of DMAIC model of Six-Sigma	
Project timeline : Six months	

Fig. 2 Project charter

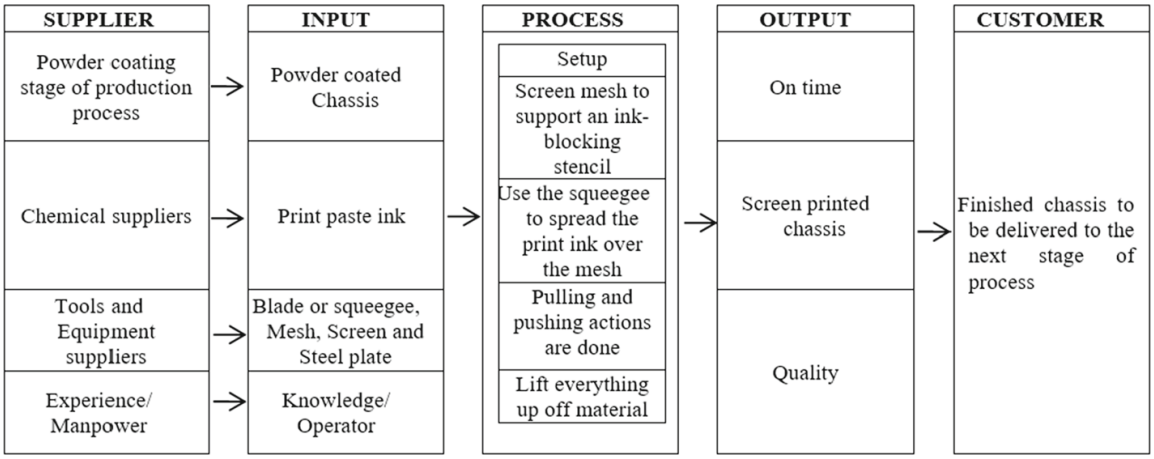


Fig. 3 SIPOC diagram of the final fitting process

investigation of the problem (Yeung 2009). The SIPOC diagram for the screen-printing process is shown in Fig. 3.

As can be seen from this diagram, the screen printing process is a five-step process. The first step is to set up the area for the printing process by cleaning and organizing the area along with the powder coated plate so that it is balanced and free from any dust. After that, a mesh is mounted on the wooden frame which supports the ink blocking stencil. This mesh mounted wooden frame is known as a screen. Next, the screen is placed over the powder coated plate and a printing tool called squeegee is used to spread the ink over it. In the next step, a fixed amount of pressure is applied on the screen by pulling and pushing the squeegee over it. Due to this pressure, the screen comes in contact with the power coated plate which leads to the printing of the desired content. In the last step, the screen is carefully lifted off the powder coated plate to avoid any spill overs of ink (shown in Fig. 4) (Foster et al. 2016). The output of this stage is a screen-printed powder coated plate that goes to the fitting stage (Fig. 5). Based on past customer complaints, consulting with the process operators and quality inspectors and inspection of the defective pieces available in the inventory; the team was able to identify ten types of defects in the screen-printing process (Phillips et al. 2014). These defects were

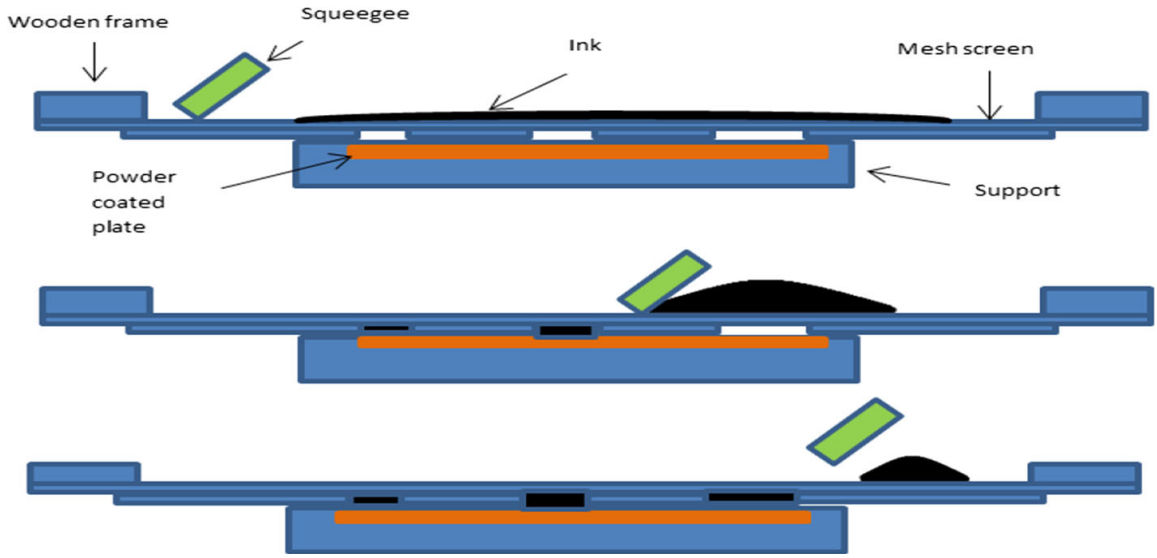


Fig. 4 Schematic representation of the screen printing process

Fig. 5 Screen printed plate



Table 2 Types of defects and their consequences

No.	Type of defects	Consequences
D1	Stringing	
D2	Scratches/pinholes	
D3	Smudged paint	Smashed print
D4	Uneven ink deposits	Vagueness of print
D5	Bad registration	Fuzzy print
D6	Incomplete print	Communication of partial information
D7	Misaligned print	Communication of wrong information
D8	Double/blurry image	Violation of printing standard
D9	Poor adhesion	Violation of printing standard
D10	Mottle	Spotty or blotchy print

further deliberated upon and the consequences of these defects were identified (as given in Table 2).

On the basis of the above analysis, the objective of the study was defined as to identify the key defects in the process output and to recommend process improvement measures by analysing the causes and root causes of these defects. The improvement was to be established

in terms of the Sigma level of the process. The timeline for collecting and analysing the data in this study was set to 3 months.

4.3 Measure

The diagnosis of problem begins with measuring the baseline sigma level performance of the current process. For the quality characteristics under consideration, it was important to take sample observations of each and every defect identified in the define phase in order to prioritize the key defects. Define phase resulted in the identification of 10 defects of different types and the MSME firm under consideration had low rate of production and appropriate past data was not available to identify the top defects. Identification of top defects could be done through process sampling but as large sampling data was required to conclude the top defects, sampling was found to be infeasible at this stage as it was estimated that this method will increase the cost and time of implementation of the project (Drohomeretski et al. 2014). Further, in the define phase during the identification of defects, the firm's quality inspectors pointed out the fact that the identified defects are interdependent and have a cause and effect type of relationship between them. However, there was no clarity on the exact interdependencies. Keeping this indication in reference, to tackle this situation, the literature was explored to identify another method that can be applied here to prioritize the ten defects. As discussed in the ROL, DEMATEL method (explained in detail in "Appendix A") from the OR discipline was identified to ease the decision making and to uncover the cause and effect relation between the defects (Agarwal et al. 2016).

Using DEMATEL technique, the ten defects highlighted in Table 2 were prioritized on the basis of interdependencies between them using the direct relation matrix obtained from experts (including six internal customers of the process: Quality head, Maintenance manager, Research advisor, Quality control inspector, Financial head and Shop floor operator). The defects were divided into cause group and effect group based on the degree by which they affect or are affected, respectively (Zhou et al. 2018). The list of defects along with the group they belong to is provided in Table 3. The responses of the project team and interaction matrices are given in Tables 9, 10, 11 and 12 in "Appendix D". It can be seen from Table 3 that four defects, namely; smudged paint, uneven ink deposits, incomplete print and misaligned print were identified as part of the cause group. These are the defects whose occurrences were causing other defects. Therefore, the reduction of these defects is likely to reduce the occurrence of other defects as well which in turn will lead to increased process performance.

As mentioned previously, the primary aim of measure phase of DMAIC methodology is to measure the current level of process performance (in terms of sigma level). The performance of screen-printing process, now, is measured based on the four defects identified in the cause group. Further, the data for these defects was collected by observing the output of the screen-printing process for 20 days with 100% product inspection (Montgomery 2007). The sampling data were recorded using check sheets (shown in Fig. 6). Process standard specifications were followed to scrutinise the items for each defect. Sampling resulted in the inspection of 5924 production units in 20 days. Out of these, 94 defective units were identified.

For measuring the performance of the screen-printing process; fraction defective, DPMO and sigma level were used as the performance matrices. To check whether the process was in controlled state or not, p-chart for fraction defectives (Gijo et al. 2011) was constructed for the 20 samples with process average fraction defective of 0.0158 as shown in Fig. 7. Based on this analysis, the base line process performance level was estimated to be 3.64 corresponding to 15,867.65 defective Parts Per Million (PPM) (Jirasukprasert et al. 2014).

Table 3 Classification of defects into cause and effect groups

No.	Defect	R_i	C_i	$R_i + C_i$	$R_i - C_i$	Group
D1	Stringing	4.8529	6.0538	10.9067	−1.2010	Effect
D2	Scratches/pinholes	5.0056	5.1938	10.1993	−0.1882	Effect
D3	Smudged paint	5.4213	4.9796	10.4009	0.4417	Cause
D4	Uneven ink deposits	5.8448	4.4120	10.2568	1.4328	Cause
D5	Bad registration	4.4645	4.5222	8.9867	−0.0577	Effect
D6	Incomplete print	5.4866	5.0936	10.5802	0.3930	Cause
D7	Misaligned print	5.0207	4.3786	9.3993	0.6421	Cause
D8	Double/blurry image	5.0183	5.1719	10.1902	−0.1535	Effect
D9	Poor adhesion	4.6501	5.6192	10.2693	−0.9690	Effect
D10	Mottle	5.6599	6.0000	11.6598	−0.3401	Effect

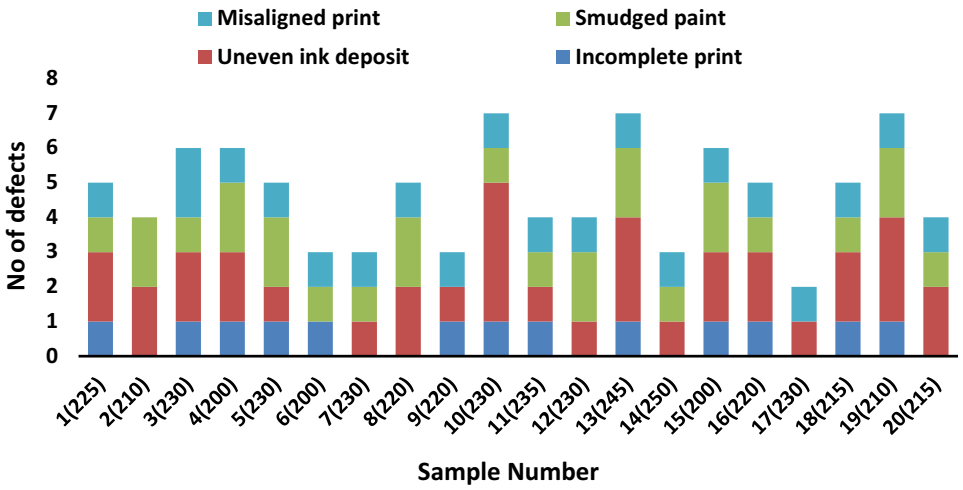


Fig. 6 Sampling data (measure phase)

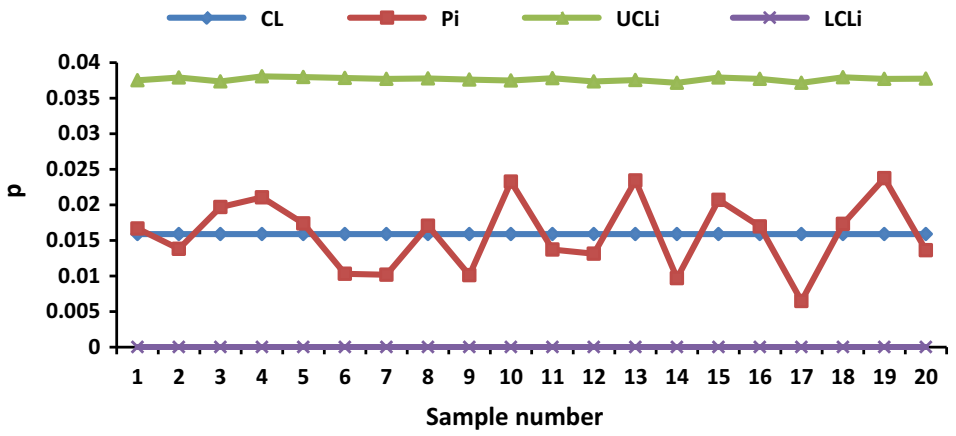


Fig. 7 *P*-chart (measure phase)

Check sheet for sampling data was further analysed using Pareto rule to identify the key defects on the basis of frequency of occurrence of defects. The Pareto analysis depicted the 64.89% of defectives in the process were due to uneven ink deposits and smudged paint, while the other two defects, namely; misaligned print and incomplete print accounted for 35.10%

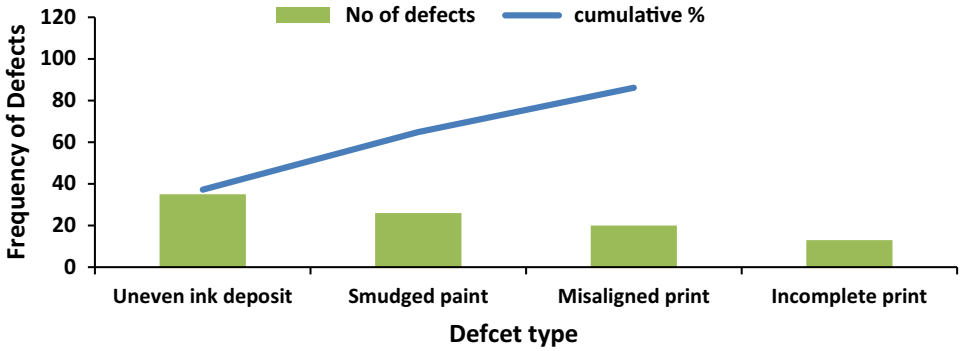


Fig. 8 Pareto analysis (measure phase)

of defectives jointly (Fig. 8). As defined in the project charter, decision was taken to target the improvement efforts only in the top two defects in the cause group. However, the results of top defect prioritization based on DEMATEL analysis were different from Pareto analysis. The project team discussed these results with the top management and decision was taken to deal with the top defects identified through DEMATEL analysis and thus, uneven ink deposits and misaligned print were identified as more critical defects. Further, the improvement efforts ware targeted to achieve 50% reduction in the defectives due to uneven ink deposits and misaligned print.

4.4 Analyse

Analyse phase of SS study is aimed at identifying the root causes of the problem that involves an in-depth analysis of the screen-printing process with respect to the two key defects identified in the measure phase. Inappropriate viscosity of ink was identified as the primary reason behind uneven ink deposits. There may be two types of problems with the viscosity of ink, that is, it may be too thin or too thick. If the ink is thick it leads to incomplete print image. On the other hand, if it is too thin the paint may spread outside the screen. As a result, when the screen is lifted off the powder coated plate, the print is not uniform. Sometimes, it may also lead to no print or wrong print. Another major defect under consideration, misalignment of print leads to portrayal of wrong information due to which customer is not able to use the product properly.

In contemporary situations, the project quality head arranges a meeting with the higher management and the team members to brainstorm the causes and root causes of the defects (Gijo et al. 2011; Prashar 2016a, b). Another objective of this meeting is to determine the potential solution alternatives to narrow down the gap between baseline performance and the aspiration drawn (Gijo and Scaria 2010). The session resulted in the identification of potential causes of the problem which were classified into six generic categories: Material, Manpower, Maintenance, Method, Machine and Environment (5 M&1E), represented with the help of fishbone diagram (Gupta et al. 2016). Each of the potential causes listed in the fishbone diagram (Fig. 9 and Fig. 10) are studied in detail using the available information, floor observations and discussions with operators and engineers to diagnose the root causes.

For identifying these root causes, various techniques like Interrelationship Diagram (ID) (Doggett 2005), C&E matrix (Lee et al. 2009) and CRT (Sharma et al. 2018) have been discussed in the literature. In this study, C&E matrix is used to understand the interrelationships between the potential causes, their undesirable defects and the core problem (Rajagopalan et al. 2004). As discussed earlier, it relates the process steps to KPIVs and correlates these

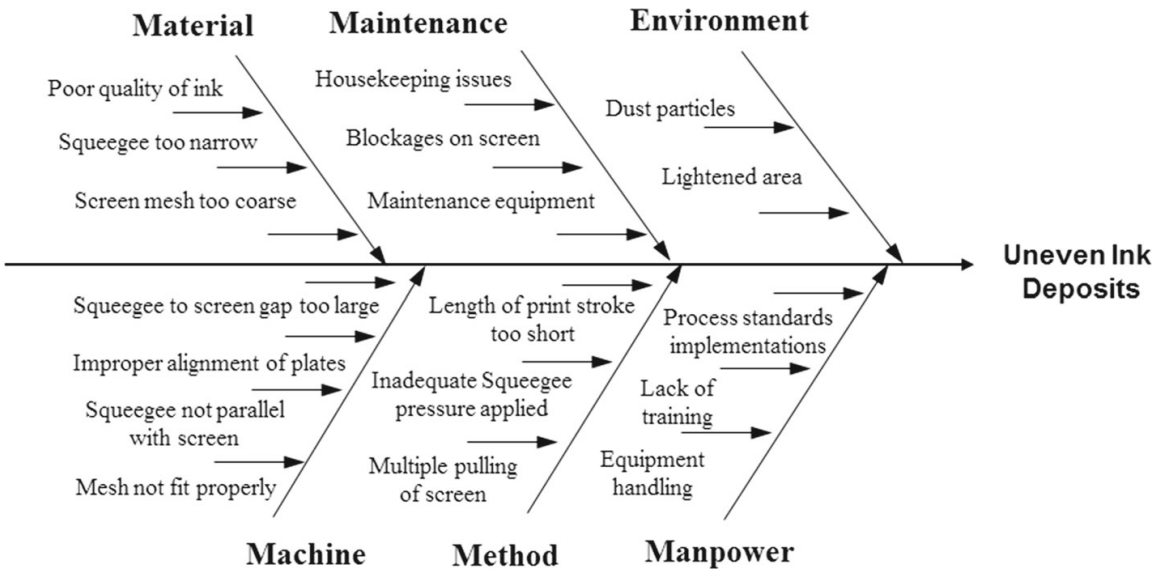


Fig. 9 Cause and effect diagram for uneven ink deposits

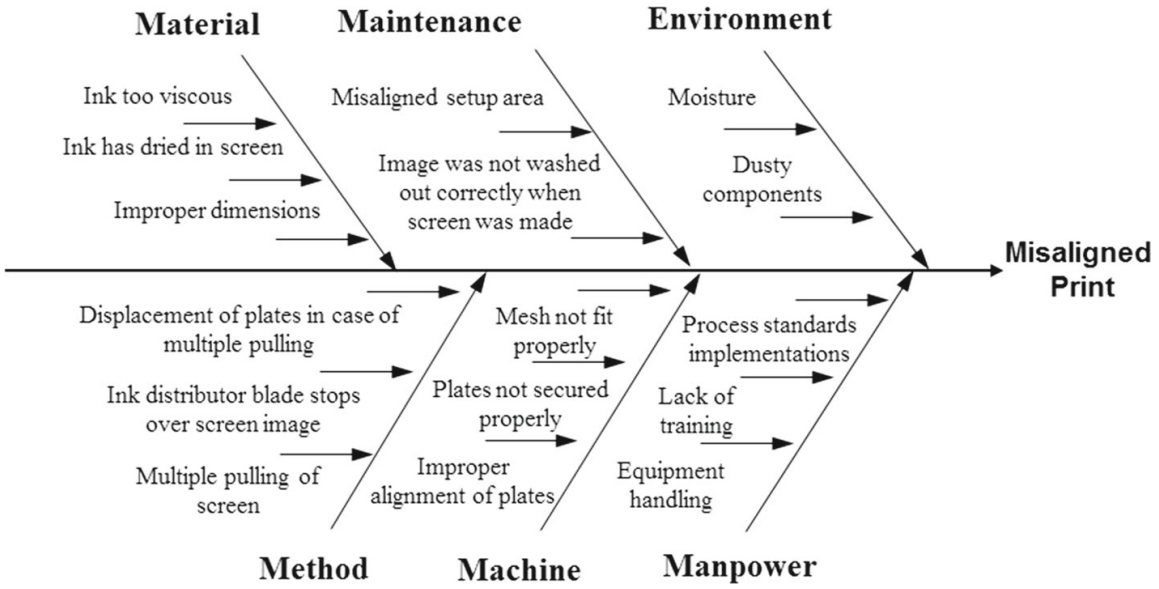


Fig. 10 Cause and effect diagram for misaligned print

KPIVs to KPOVs. For understanding these relationships, a score is attached to each KPOV with respect to customers' opinion using Likert scale (varying from 1 to 10, 1 defines least important and 10 defines most important). Further, correlation scores are assigned between each KPIV and KPOV based on the scale defined by Sokovic et al. (2005) (given in Table 8 Appendix B). With the help of these scores the importance ratings of each of the KPIVs are calculated. The complete C&E matrices for uneven ink deposits and misaligned print are given in Tables 4 and 5. KPIVs for both top defects were then prioritized in accordance to their importance ratings. KPIVs having highest ratings are concluded as root causes which the team dwelled upon in the improve phase of DMAIC methodology (Sokovic et al. 2005). Ratings greater than the threshold value of 150 (as suggested by the decision maker) are concluded as root cause as highlighted by bold values in column 6 of Tables 4 and 5. The analysis of C&E matrix resulted in the identification of five major root causes leading to the two key defects, namely, *poor quality of ink, improper technique for squeegee pressure, poor process standards implementations, misaligned setup area and training.*

Table 4 C&E matrix for uneven ink deposits

Rating of importance to customer →		6	9	8	Total
Process step	Process inputs	On time	Finished screen printed chassis	Quality	
Setup	Process standards implementations	9	3	3	105
Setup	Cleaned area	3	1	3	51
Setup	Alignment of plates	0	9	9	153
Screen is prepared by fixing the mesh on the wooden frame to support the ink blocking stencil	Screen mesh fitting	0	9	9	153
Screen is prepared by fixing the mesh on the wooden frame to support the ink blocking stencil	Maintenance equipment	3	3	9	117
Squeegee to spread the print ink over the mesh	Ink	3	9	9	**171**
Squeegee to spread the print ink over the mesh	Steel plates	0	9	3	105
Squeegee to spread the print ink over the mesh	Proper alignment of squeegee and screen	0	9	9	153
Squeegee to spread the print ink over the mesh	Process standards implementations	9	9	9	**207**
Pulling and pushing actions of squeegee	Length of print stroke	1	3	9	105
Pulling and pushing actions of squeegee	Proper technique for squeegee pressure	3	9	9	**171**
Pulling and pushing actions of squeegee	Cleaned area	9	9	3	159
Pulling and pushing actions of squeegee	Training	9	9	9	**207**

4.5 Improve

In this phase of the DMAIC methodology, solutions to eliminate the root causes were identified. As described in the analyse phase, five major root causes were identified for the two key defects and listed in column 1 of Table 6. The improve phase first focused on finding the corrective measures to eliminate the root causes and investigating the feasibility of implementing these measures based on expected time, efforts and cost required for implementation. Further, given the barriers of limited resources, availability of skills, small scale of operation, internal resistance, lack of ownership especially from temporary employees, lack of knowledge and poor training methods; it was realised that multiple corrective actions couldn't be implemented simultaneously and multiple changes are also likely to bring process instability. To tackle these issues, based on literature support and previous experience of the firm, after discussion with the top management, it was decided to implement corrective measures sequentially instead of parallelly. Further, before implementing corrective measures for these

Table 5 C&E matrix for misaligned print

Rating of importance to customer →		6	9	8	Total
Process step	Process inputs	On time	Finished screen printed chassis	Quality	
Setup	Process standards implementations	9	3	3	105
Setup	Misaligned setup area	3	9	9	**171**
Setup	Dusty components	3	3	9	117
Screen is prepared by fixing the mesh on the wooden frame to support the ink blocking stencil	Mesh fitting	1	9	3	111
Screen is prepared by fixing the mesh on the wooden frame to support the ink blocking stencil	Washed/cleaned image	1	3	3	57
Squeegee to spread the print ink over the mesh	Alignment of plates	1	9	3	111
Squeegee to spread the print ink over the mesh	Plates not secured properly	1	9	3	111
Squeegee to spread the print ink over the mesh	Gap measurement between squeegee and screen	1	9	3	111
Squeegee to spread the print ink over the mesh	Ink	3	9	9	**171**
Squeegee to spread the print ink over the mesh	Process standards implementations	9	9	9	**207**
Pulling and pushing actions of squeegee	Multiple pulling of screen	1	9	3	111
Pulling and pushing actions of squeegee	Training	3	9	9	**171**

root causes, they were first prioritized using benefit-effort matrix on the basis of time, effort and cost incurred and the impact of these corrective actions once they are implemented (Gijo and Sarkar 2013). Detailed description of conducting the analysis using benefit-effort matrix is given in "Appendix C". Based on the results of the benefit-effort analysis, the improvement is implemented in three trials. The corrective actions identified to deal with root causes are summarized in Column 2 of Table 6. Details of analysis for corrective measures identification and improvements undertaken are described in the trials below.

As per the results of benefit-effort matrix, correct actions for RC1 were a part of second quadrant which belongs to high impact and low effort group, corrective actions for RC3 and RC5 were a part of the third quadrant which is high impact, high effort group and lastly, corrective actions for RC2 and RC4 were a part of the fourth quadrant with low impact and high effort (as shown Fig. 11). Given the low impact and high effort required to deal with RC2 and RC4, these root causes were eliminated from further considerations and corrective measures for RC1, RC3 and RC5 were implemented in two improvement trails as they had high impact. Figure 11 describes the benefit effort matrix results for all the root causes.

Table 6 Root causes and summary of corrective actions undertaken in improvement trials

Root causes	Corrective actions
RC1: Poor quality of ink	CM1: Choose the best supplier based on the criteria's responsible for performance of print paste
RC2: Proper technique for squeegee pressure not followed	CM2: A person should be hired and trained for observing and collecting data regarding the pressure applied on squeeze by each operator
RC3: Standard specifications not followed	CM3: A pictorial representation of manuals specifications required in the process should be introduced
RC4: Misaligned setup area	CM3: Setup area should be clean and organised
RC5: Training issues	CM4: Training programmes and workshops should be organised for unskilled operators

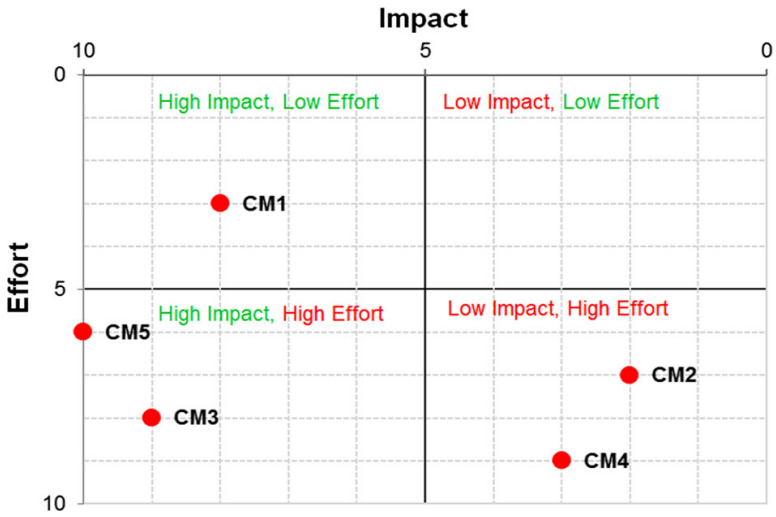


Fig. 11 Benefit-effort matrix

4.5.1 Improvement Trial 1

In the first improvement trial, the root cause: poor quality of ink (RC1) was selected and corrective actions corresponding to this root cause were implemented. A that time, the ink for screen-printing was being sourced from a single supplier. The first step was to check the current level of quality of the ink being used for the screen-printing process in terms of viscosity, pH-value, resistivity and solid contents. For quality check, a sample was collected and tested under laboratory conditions. It was found that the ink was not as per the required standard which was affecting the printing process. The team discussed this problem with the supplier and they were able to gather that the current supplier was reluctant to supply a better quality ink given the cost implications on both parties and transactional relations with the supplier. The matter was discussed further and it was concluded with the suggestion that a new supplier for ink should be selected.

To eradicate the root cause under consideration, seven potential suppliers were identified who were willing to supply ink with the desired quality. However, the challenge here was to select a supplier in such a way that the ink of required quality is procured at best prices considering other important criteria the supplier should meet such that the overall procurement

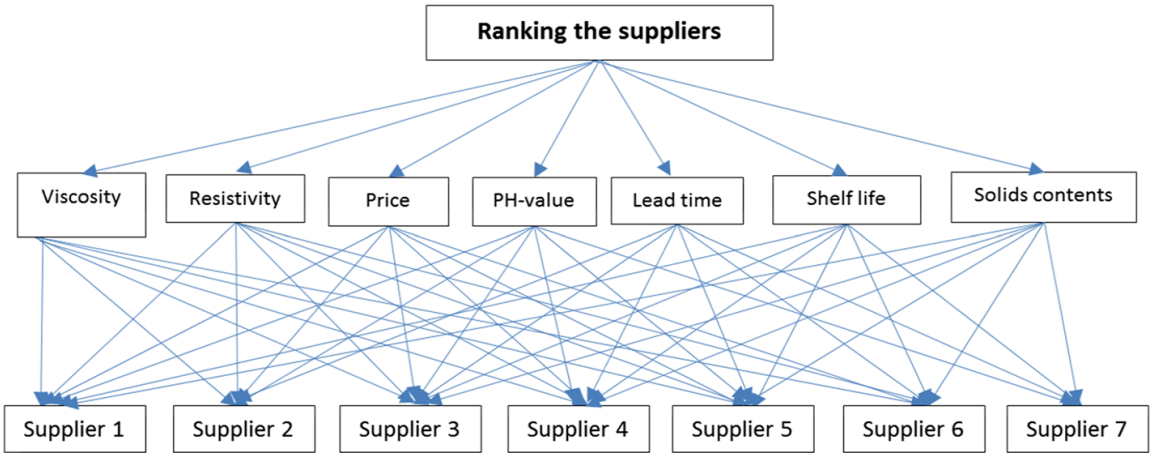


Fig. 12 Conceptual framework for AHP

of the ink is profitable. Top management suggested comparative evaluation of the alternatives to determine the best suitable suppliers. Seven criteria were identified by the project team on the basis of which this selection should be carried out. These criteria included: viscosity of ink, resistivity, price, pH value, lead time, shelf life and solids content (Krebs 2009). The suppliers were, therefore, evaluated using Analytical Hierarchy Process (AHP) discussed widely in the literature for supplier selection. Figure 12 describes the conceptual framework of AHP used to evaluate the suppliers and the detailed steps of the methodology is given in "Appendix E" (Pan et al. 2018).

A questionnaire was prepared for determining the weights of importance of the criteria and the responses of the project team were recorded. For example, the pairwise comparison matrix for the criteria under consideration as obtained from the responses of the quality head is given in Table 14 in "Appendix F". The final weights of each criterion were calculated using hierarchical additive weighting method based on the importance of each member in the project team (given in Tables 15 and 16 in "Appendix F"). Next, the suppliers were evaluated on the basis of each criterion. The pairwise comparison matrix with respect to viscosity criterion is given in Table 17 in "Appendix F". Table 7 below, provides the evaluation scores for each supplier with respect to each criterion. The aggregated weights for each supplier were calculated using the weights of criterion obtained in the previous step (Govindan and Sivakumar 2016). Table 7 also lists the weights of each supplier and their corresponding ranks. It can be inferred from column 10 of Table 7 that supplier S_6 is the most preferred supplier with preference weight of 0.196 and thus was selected for sourcing ink for the printing process.

After implementing corrective actions for RC1, that is, changing the supplier, the process was closely monitored for 20 days. The process output was sampled for 20 days following 100% sampling and the sampled pieces were inspected for all the four types of defects under consideration. It was observed that there was an improvement in the process sigma level from 3.64 (baseline sigma level) to 4.07. The percentage defective of the key defects, uneven ink deposits and misaligned print was estimated to be 36.66%, i.e., a reduction of 37.33% from the baseline fraction defective was observed for these two defects. The total fraction defective of the process reduced to 0.50% from the baseline level of 1.58%. The project was started with the aim of reducing the percentage of key defects by 50%. In the first improvement trial 37.33% reduction was achieved.

Table 7 AHP results

Criteria	Viscosity (Pas.)	pH-value	Shelf life	Price (1 k/bottle 250 g)	Lead time (no. of days)	Resistivity (ohm/sq)	Solids content (%)	Preference weights	Rank
Weights of criteria	0.148	0.178	0.154	0.115	0.079	0.022	0.105		
Alternatives									
S1	0.034	0.223	0.034	0.035	0.110	0.398	0.391	0.113	3
S2	0.382	0.153	0.142	0.389	0.031	0.067	0.053	0.160	2
S3	0.054	0.022	0.074	0.059	0.404	0.157	0.251	0.092	4
S4	0.098	0.057	0.034	0.095	0.257	0.235	0.099	0.077	7
S5	0.022	0.107	0.327	0.020	0.031	0.024	0.027	0.081	6
S6	0.151	0.403	0.356	0.154	0.135	0.083	0.158	0.196	1
S7	0.259	0.035	0.034	0.247	0.031	0.036	0.022	0.084	5

4.5.2 Improvement Trial 2

Root causes: standard specifications not followed (RC3) and training issues (RC5) were selected for the second improvement trial. It was observed that mostly semi-skilled and contractual operators were employed on the shop floor. After discussions with the team members and shop floor operators, issues related to improper instructions manual and lack of training of employees were identified (Gijo and Sarkar 2013). It was observed that although measurement specifications and instructions were listed correctly in the manuals; but the language used was too technical for the floor operators to understand and they were not adequately trained to follow these standards. Due to which the operators were not able follow the process standards well. The project team concluded that each step of the screen printing process should be pictorially represented in the manuals highlighting the precautions and Standard Operating Procedures (SOPs) that the operators should follow. Henderson and Evans (2000) stated "training is a cornerstone and that improved human input is critical in the productivity equation", therefore, special training routines should be deigned and executed for the employees to provide them the required training of technical as well as organizational skills. The project team worked with a documentation expert to design the first set of SOPs as recommended and some of the important SOPs were also demonstrated pictorially in the workshop. Further, the shop floor operators were given short trainings of the SOPs including organizational skills with special focus on importance of involvement of all stakeholders in continuous quality improvement.

After implementing the corrective actions for RC3 and RC5, the process was again monitored for 20 days. The process output was sampled for 20 days following 100% sampling and the sampled pieces were inspected for all the four types of defects under consideration. The data collected after implementing second improvement trial was recorded using check sheets as shown in Fig. 13. To check whether the process was in control or not, *p*-chart for fraction defective was drawn (shown in Fig. 14). The *p*-chart showed the process was still in control even when the improvements have been implemented. Increase in the process sigma level was observed from 4.07 (achieved after first improvement trial) to 4.54. The percentage defective of the key defects: uneven ink deposits and misaligned print was estimated to be 28.57%, i.e., a reduction of 22% was observed from the one observed after the implemen-

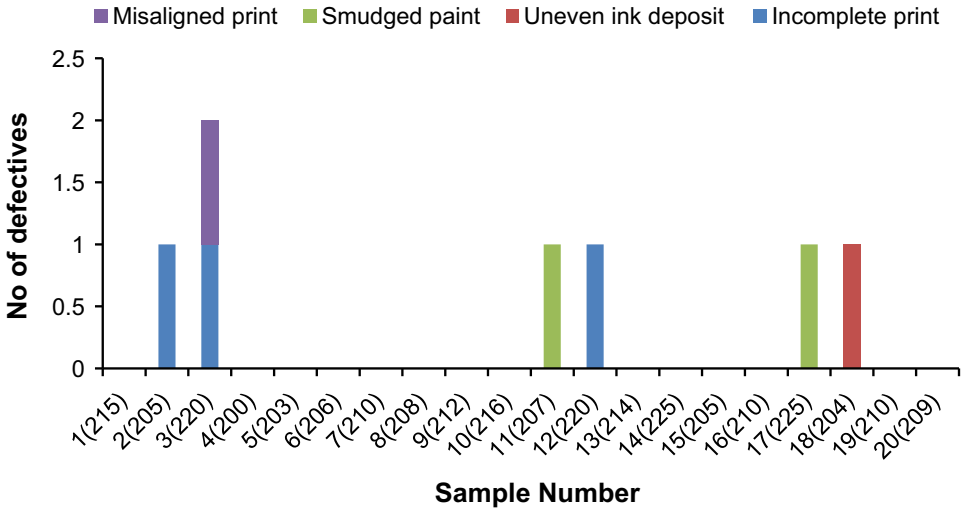


Fig. 13 Sampling data (Improve phase)

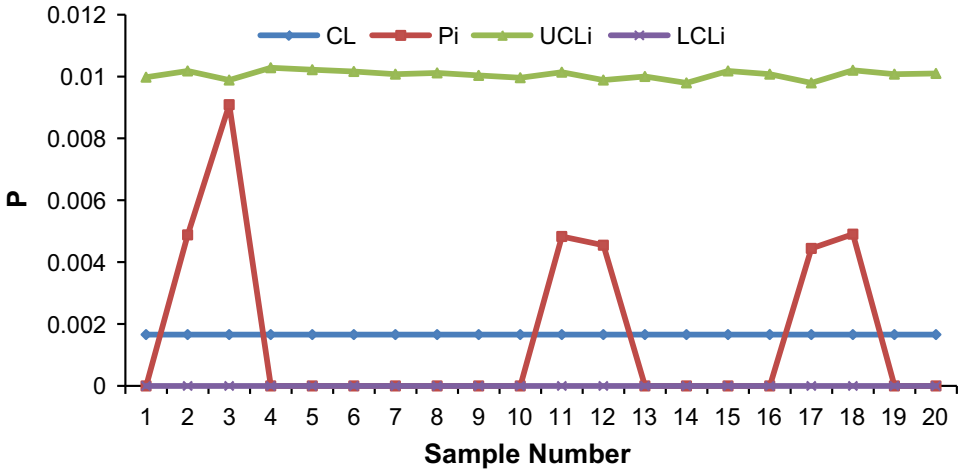


Fig. 14 *P*-chart (Improve phase)

tation of the first improvement trial. The total fraction defective of the process reduced to 0.11% from 0.50%.

4.6 Control

The control phase of the DMAIC model aims to bring the process to stable operations after the improvement cycles have been implemented. This stage of the model plays a very important role in sustaining the improvements achieved by implementing the corrective actions. Through the improvement efforts the short-term sigma level of the improved process was observed to be 4.54 compared to the baseline sigma level 3.64. After the improvement phase of the DMAIC methodology, 51% reduction was achieved in the two key defects: uneven ink deposits and misaligned print (shown in Fig. 15).

The project concluded with the recommendation that sampling and monitoring of the process should be done regularly for continuous monitoring of the process performance. The team recommended maintaining regular record of data at different levels to facilitate continuous QM activities, data driven decision making and to facilitate quick rectification of problems whenever there is a signal for process variations.

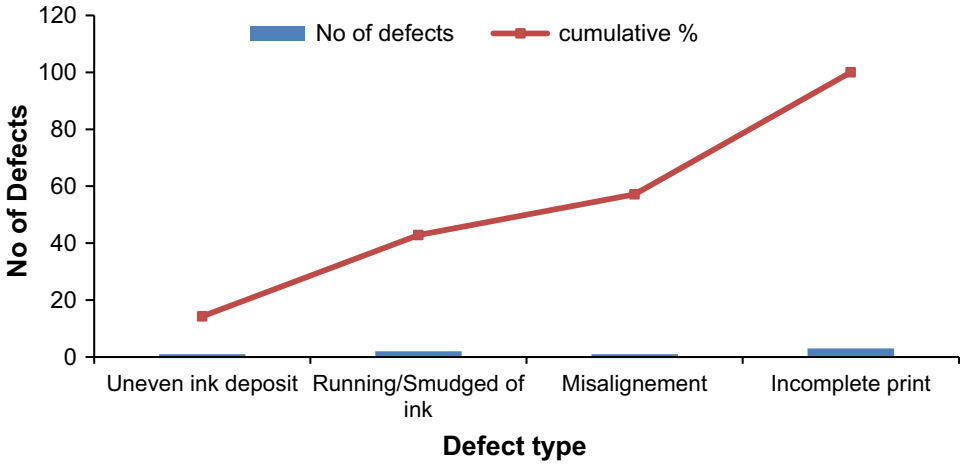


Fig. 15 Pareto analysis (Improve phase)

Further, it was proposed to build a culture of regular training programs for its employees focusing on technical as well as organisational skill development at all levels of organisational hierarchy to upscale the skills available in the firm. Given the limitations of organising such training programmes in-house, the firm can explore the options for training partners.

5 Theoretical and managerial implications

The focal point of this research is on the development of a hybrid DMAIC SS framework with specific focus on MSME manufacturing firms in developing economies integrating MCDM tools to enable effective decision making. An enormous amount of academic literature of SS discusses theoretical developments in terms of (1) QM methods and tools and (2) case studies illustrating real life applications providing roadmaps for future applications (Kumar et al. 2011). However, the scope of most of the applications discussed in the literature has remained limited either to large-scale organisations or small-scale organisations in industrialised economies (Drohomeretski et al. 2014). Small-scale organizations, especially in developing economies are aware of the need of diverting their focus on QM initiatives to survive in the globalised and liberalised economies and proper positioning their products in global markets (Prashar 2018). Further, Tang et al. (2007) and Chakraborty et al. (2019) highlighted that though these firms appreciate the effectiveness of the SS methodology for QM, they are hesitant to put efforts in this direction given several barriers in implementing these efforts. The limiting discussions on the successful applications and real-life illustrations of SS implementation for these organisations act as an additional barrier for adoption of the practice in these organisations. In the literature authors have mentioned (also revealed by the ROL in this study) extension of the scope of SS applications not only requires dealing with these barriers but also to extend the toolset of SS from the existing one limited mostly to statistical, QM and managerial philosophies to effective and efficient OR methods, analytical methods and many more.

On the background of the above requirements our study explores the status of SS implementation in small scale firms in developing counties, barriers they face and proposes a hybrid DMAIC framework for SS implementation in MSME firms integrating MCDM methods. The suitability of the proposed framework is tested with a real-life case illustration. The following implications can be drawn from the result findings of this study:

- MSMEs play an important role in developing economies like India, and due to globalization, the MSMEs in these countries are facing competition from market leaders imposing the need for these firms to prioritize their efforts towards quality improvement of their product, processes, and services. The SS implementation framework proposed and validated with a single comprehensive case study in this paper is suitable to guide the management in MSME organizations through the implementation of quality improvement efforts subjugating their challenges.
- Through exploration of the literature (Brady and Allen 2006; Kumar et al. 2008) limited resources, unavailability of skills, improper and little recording of data, high cost of data collection, small-scale of operations, internal resistance, lack of ownership especially from temporary employees, lack of knowledge and poor training methods are identified as some of the barriers for implementation of QM initiates in MSME firms. These barriers are the primary reason for the low level of adoption of this practice in the MSME sector and hence the limiting existing literature in this area. The study integrates MCDM method in the DMAIC methodology by illustrating the effective use of DEMATEL technique to prioritize the key defects in the define phase. It helps in prioritizing the defects when there is unavailability of dat, and conventional techniques like Pareto analysis cannot be applied. The defects are prioritized by understanding the interrelationships between them and classifying defects in cause and effect groups. This helps in understanding the actual cause of a particular defect. This technique gives mathematical rigour and objectivity to the methodology for quality improvement which was earlier only carried out subjectively.
- This study shows that the integration of techniques from other disciplines like OR can be productive for SS practitioners as such techniques help in overcoming some of the shortcomings of SS approach. For instance, Antony (2004) criticised that SS is not backed by proper theoretical foundation and has a strategic disconnect. The use of OR tools and techniques can remove these barriers in the implementation of SS. The use of DEMATEL during the measure phase is an attempt in this direction. Hence, opens up an area for consideration for academic researchers and practitioners in the field to propose and embed the applicability of OR and other contemporary methods in SS implementation framework to achieve enhanced results.
- Another important implication of the study lies in the proposed application of benefit effort analysis for classifying the corrective measures for eliminating the identified root causes of variations based on their impact and cost. Thus, it helps in evaluating the effectiveness of the corrective measures before implementation and prioritizing the improvements. The improvement efforts can be implemented in multiple subsequent trials measuring the performance improvement in each trial and enabling steady improvements. This approach is also helpful in dealing with the resistance of internal employees to sudden parallel changes in work practices and stable process improvements.

6 Conclusion

The research presented in this paper proposes a hybrid DMIAC Six Sigma framework integrating MCDM methods to guide the adoption and implementation of SS keeping MSME firms in developing economies in focus. The study contributes to enriching the limited literature of SS referring to small scale manufacturing firms in developing countries. The proposed framework is adaptable to other generic applications also. While attempting to eliminate the barriers of limited resources and unavailability of required data during SS implementation

(as also experienced in the case situation) for using statistical methods in DMAIC stages, usability of MCDM methods from the OR discipline is explored and the efforts resulted in proposing the application of DEMATEL for defect prioritization in the measure phase of the DMAIC model. In the literature, researchers have highlighted the limited exploration of the use of sound OR methods in SS implementation, that is well taken in our study. The suitability of the proposed framework for MSME firms also follows from the proposed application of the benefit effort analysis of the corrective actions in the improve phase of the DMAIC model. The method weights the impact and effort required for the implementation of corrective actions and helps in evaluating the benefits that could be realised from the corrective actions. Based on this evaluation, the corrective actions which are likely to have the highest impact within minimum efforts could be implemented first, followed by other corrective actions in a sequential order to realize steady and stable process improvements. The approach is beneficial for small firms to tackle some of the barriers to quality management effort implementation.

The proposed SS framework is tested through a comprehensive single case illustration of quality management efforts through DMIAC SS methodology implemented in an MSME manufacturing firm in India involved in the production of portable amplifiers. The study is conducted with an objective to improve the quality of the screen-printing process in the manufacturing of the portable amplifier through variation reduction to minimize the repairs and rejections. Several appropriate statistical, OR, quality management and managerial methods are integrated in the DMAIC model. Analysis, results and findings are elaborated in the paper for the methods used in the DMAIC model execution providing theoretical foundations of new methods integrated in the proposed framework. Uneven ink deposits and misalignment of print were the two key defects identified using DEMATEL methodology for improvement. The root causes for these defects were identified with the help of Ishikawa diagram and C&E matrix. C&E matrix helps in reducing the subjectivity and identification of root causes. Corrective measures identified for the four root causes are prioritized following the Benefit-Effort analysis and improvements are deployed in two improvement trails. The project resulted in the improvement of the short-term sigma level of the process from the base level of 3.64–4.54. Also, after improvement the target reduction of over 50% was achieved in the top two defects viz. uneven ink deposits and misaligned prints. The limitations of the study include unavailability of data to measure the financial gains achieved through the adopted DMAIC model and short time frame for the study that offered limitation in providing sufficient training to shop floor workers. As the future scope of the research, three important dimensions of research came out that need attention, first to test and validate the suitability of the proposed framework for different applications, second exploration of new methods from different disciplines to expand the application of SS for business process improvements and third to identify the skills that should be focused upon during the training programmes of the employees of the MSME firms adopting SS strategy for quality management and development of suitable programs for the same. The proposed methodology could be expanded in the grey environment (Govindan et al. 2016).

Appendix A

DEMATEL methodology

DEMATEL, an MCDM approach is utilized to classify the defects identified in the define phase into cause group and effect group based on whether they affect or are affected by others respectively (Govindan and Chaudhuri 2016). The detailed steps of the DEMATEL approach are given below (Zhou et al. 2018):

Step 1 Define quality feature and establish measurement scale.

The quality feature is a set of influential characteristics that impact the sophisticated system, which can be determined by literature review, brainstorming, and expert evaluation. After defining the influential characteristics in researching system, establish the measurement scale for the causal relationships and pairwise comparisons among influential characteristics. Four levels 0, 1, 2, 3 are suggested, respectively meaning "no impact", "low impact", "high impact," and "extreme high impact". In this step, factors and their direct relations are displayed by a weighted and directed graph.

Step 2 Extract the Direct Relation Matrix (DRM) of influential factors.

In this step, the transformation from the weighted and directed graph into DRM has been carried out. For n influential characteristics $F_1, F_2, \ldots, F_n$, DRM is denoted as

$$D = \left(d_{ij}\right)_{n\times n} (i, j = 1, 2, \ldots, n),$$

where d_{ij} is the direct relation of F_i over F_j based on the measurement scale.

Step 3 Normalize the DRM.

Normalized direct relations of factors are a mapping from d_{ij} to [0, 1], which is calculated as follows:

$$N = \frac{D}{\max\left(\sum_j d_{ij}, \sum_i d_{ij}\right)}$$

Step 4 Calculate the Total Relations Matrix (TRM).

TRM contains direct and indirect relations among factors. The calculation of TRM through the normalized DRM can be done as follows:

$$T = N(E - N)^{-1}$$

where E is $n \times n$ identity matrix.

Step 5 Classify influential factors.

Based on the sum of each row R_i ($i = 1, 2, \ldots, n$) and column C_i ($i = 1, 2, \ldots, n$) of the TRM $T_{n\times n}$, $R_i + C_i$ and $R_i - C_i$ can be obtained. $R_i + C_i$ is defined as the prominence, indicating the importance of the ith influential factor. $R_i - C_i$ classifies the ith influential factor as the cause ($R_i - C_i > 0$) or effect ($R_i - C_i < 0$) factor in researching system.

Appendix B

Construction of C&E Matrix

Cause and Effect matrix is a quality tool which helps the decision makers in identifying the causes and root causes of the problem based on customers' preferences. The detailed steps for constructing a C&E matrix are given below (Lee et al. 2009):

Table 8 Scale for correlation scores

Scores	Relationship between KPIVs and KPOVs
0	No relationship
1	Slight relationship
3	Average relationship
9	Direct relationship

Step 1 List down the outputs identified during SIPOC. These are our Key Process Output Variables (KPOVs). There should be no less than three outputs under O in SIPOC. Therefore, there will be no less than three outputs in C&E matrix.

Step 2 Rate these KPOVs according to customers' preferences (X_i) using a scale from 1 to 10 with 1 representing least important and 10 representing most important.

Step 3 List the steps of the process as listed in SIPOC.

Step 4 List the Key Process Input Variables (KPIVs) for all the steps in the process found using fishbone diagram.

Step 5 Determine the correlation scores between KPOVs and KPIVs based on the scale defined in Table 8 (Y_{ij}).

Step 6 Calculate the total score of each KPIV as given below

$$Z_j = \sum_i X_i Y_{ij}$$

and select top four as root causes for further improvements.

Appendix C

Construction of Benefit Effort Matrix

The benefit-effort matrix was designed specifically for the purpose of deciding which of the many suggested solutions to implement. It provides answers to the question of which solutions seem easiest to achieve with the most effects (Gijo and Sarkar 2013). The steps of construction of a benefit effort matrix are as follows:

Step 1 Retrieve suggested solutions through barnstorming or discussions.

Step 2 Ask the decision makers to rate each of the solution using a scale from 1 to 10 with 1 representing least important and 10 representing most important based on two factors, the benefit that can be obtained after the implementation of that solution and the cost that will be incurred during its implementation.

Step 3 Construct the benefit effort matrix by plotting effort rating on the horizontal axis and benefit ratings of the solution on the vertical axis and divide it into four quadrants namely, high effort-high benefit, high effort-lo benefit, low effort-high benefit and low effort-low benefit.

Appendix D

See the Tables 9, 10, 11 and 12.

Table 9 Direct relation matrix given by quality head

Quality head	D1	D2	D3	D4	D5	D6	D7	D8	D9	D10
D1	0	1	3	3	0	3	2	1	2	0
D2	2	0	2	1	1	1	1	2	1	3
D3	2	3	0	3	1	3	2	3	0	2
D4	3	2	3	0	1	2	3	2	2	1
D5	1	1	2	3	0	2	3	0	1	0
D6	3	2	3	3	2	0	3	1	2	3
D7	2	3	3	3	3	2	0	3	3	1
D8	2	1	2	2	0	1	3	0	1	2
D9	3	0	1	2	3	2	0	2	0	3
D10	1	1	0	1	0	1	2	1	2	0

Table 10 Average direct relation matrix

	D1	D2	D3	D4	D5	D6	D7	D8	D9	D10
D1	0.0000	1.3333	2.0000	1.0000	1.0000	2.1667	1.1667	1.3333	1.8333	2.3333
D2	2.0000	0.0000	1.8333	1.1667	1.0000	1.5000	1.0000	1.5000	1.8333	2.8333
D3	2.3333	2.0000	0.0000	1.8333	1.3333	1.6667	1.0000	2.0000	2.5000	1.5000
D4	2.8333	1.5000	2.0000	0.0000	1.0000	2.1667	1.5000	1.5000	2.0000	2.8333
D5	1.5000	1.0000	1.5000	1.6667	0.0000	1.3333	1.8333	1.0000	1.5000	1.6667
D6	2.8333	2.0000	1.8333	1.8333	1.3333	0.0000	1.1667	1.8333	1.8333	1.6600
D7	1.6667	1.8333	1.5000	1.3333	2.5000	1.3333	0.0000	1.5000	1.8333	1.5000
D8	1.0000	2.1667	1.1667	1.3333	1.8333	2.0000	1.0000	0.0000	2.1667	2.1667
D9	1.0000	1.5000	1.0000	1.8330	1.8333	1.1667	1.0000	2.8333	0.0000	1.5000
D10	3.0000	2.0000	1.8333	1.0000	1.5000	1.6667	3.0000	1.6667	1.3333	0.0000

Table 11 Normal direct relation matrix

	D1	D2	D3	D4	D5	D6	D7	D8	D9	D10
D1	0.0000	0.0734	0.1101	0.0550	0.0550	0.1193	0.0642	0.0734	0.1009	0.1284
D2	0.1101	0.0000	0.1009	0.0642	0.0550	0.0826	0.0550	0.0826	0.1009	0.1560
D3	0.1284	0.1101	0.0000	0.1009	0.0734	0.0917	0.0550	0.1101	0.1376	0.0826
D4	0.1560	0.0826	0.1101	0.0000	0.0550	0.1193	0.0826	0.0826	0.1101	0.1560
D5	0.0826	0.0550	0.0826	0.0917	0.0000	0.0734	0.1009	0.0550	0.0826	0.0917
D6	0.1560	0.1101	0.1009	0.1009	0.0734	0.0000	0.0642	0.1009	0.1009	0.0914
D7	0.0917	0.1009	0.0826	0.0734	0.1376	0.0734	0.0000	0.0826	0.1009	0.0826
D8	0.0550	0.1193	0.0642	0.0734	0.1009	0.1101	0.0550	0.0000	0.1193	0.1193
D9	0.0550	0.0826	0.0550	0.1009	0.1009	0.0642	0.0550	0.1560	0.0000	0.0826
D10	0.1651	0.1101	0.1009	0.0550	0.0826	0.0917	0.1651	0.0917	0.0734	0.0000

Table 12 Total relation matrix

	D1	D2	D3	D4	D5	D6	D7	D8	D9	D10
D1	0.4890	0.4877	0.4997	0.4075	0.4157	0.5161	0.4135	0.4865	0.5429	0.5944
D2	0.6034	0.4317	0.5049	0.4245	0.4263	0.4988	0.4187	0.5065	0.5564	0.6343
D3	0.6557	0.5651	0.4462	0.4876	0.4722	0.5420	0.4430	0.5659	0.6270	0.6165
D4	0.7268	0.5799	0.5828	0.4252	0.4888	0.6014	0.5020	0.5781	0.6423	0.7174
D5	0.5248	0.4362	0.4445	0.4101	0.3350	0.4446	0.4172	0.4350	0.4910	0.5261
D6	0.6873	0.5707	0.5451	0.4912	0.4762	0.4645	0.4565	0.5617	0.6025	0.6309
D7	0.5843	0.5213	0.4893	0.4354	0.4991	0.4904	0.3643	0.5050	0.5576	0.5742
D8	0.5564	0.5387	0.4737	0.4352	0.4669	0.5210	0.4182	0.4310	0.5720	0.6053
D9	0.5159	0.4764	0.4344	0.4312	0.4404	0.4536	0.3900	0.5358	0.4324	0.5399
D10	0.7103	0.5860	0.5590	0.4641	0.5016	0.5611	0.5553	0.5665	0.5950	0.5610

Appendix E

AHP Methodology

AHP is a powerful MCDM approach which is used to prioritize the alternatives based on some selected criteria. The detailed steps of the AHP approach is given below (Darbari et al. 2019):

Suppose there are n alternatives $A_1, A_2, \ldots, A_n$ and m criteria $C_1, C_2, \ldots, C_m$ whose importance weights need to be calculated with respect to a given goal 'g'. The AHP method is employed as per the sequential steps given below:

Step 1 Pairwise-comparison.

The criteria are compared pair-wise on a scale of 1–9 representing subjective judgements for the levels of importance. The numeric values '1–3–5–7–9' represent the "equally important-moderately important–important-very important–extremely important", with the intermediate subjectivities represented by 2, 4, 6 and 8. This leads to construction of *mxm* matrix $A = (a_{ij})$ where a_{ij} is the numeric value of the pair-wise comparison of the ith and jth criteria in terms of how much criteria i dominates criteria j, following the mathematical rule

$$a_{ij} = \frac{1}{a_{ji}}, \quad a_{ii} = 1, \quad a_{ij} = \frac{a_{ik}}{a_{jk}}$$

Step 2 Normalization.

Normalize the matrix A by dividing each (i, j)th element (a_{ij}) by the jth column sum a_j to derive the matrix A^* as shown below:

$$A^* = \left[a^*_{ij}\right] = \begin{array}{c} \\ C_1 \\ C_2 \\ . \\ . \\ . \\ C_m \end{array} \begin{array}{c} \begin{array}{cccc} C_1 & C_2 & & C_m \end{array} \\ \begin{bmatrix} a_{11}/a_1 & a_{12}/a_2 & \ldots & a_{1m}/a_m \\ a_{21}/a_1 & a_{22}/a_2 & \ldots & a_{2m}/a_m \\ . & . & . & . \\ . & . & . & . \\ . & . & . & . \\ a_{m1}/a_1 & a_{m2}/a_2 & \ldots & a_{mm}/a_m \end{bmatrix} \end{array}$$

Step 3 Generate principal eigen vector.

Table 13 Random index

n	1	2	3	4	5	6	7	8	9
RI	0	0	0.52	0.89	1.11	1.25	1.35	1.40	1.45

Calculate the average a_i* of rows of the matrix A* to generate the priority vector (a_1*, a_2*,.... a_m*) which is the principal eigenvector of A. Since the priority vector is unique up to positive scalar multiplication, therefore the normalization of A is done to ensure the uniqueness of the vector of priorities. The principal eigen vector $y \in R^n$ corresponding to the maximum eigen value $\lambda_{\max}$ is generated using the following equation: $A^*\lambda_{\max} = \lambda y$.

Step 4 Check consistency.

The judgment must be checked for its consistency by utilizing the following equations:

$$CI = \frac{\lambda_{\max} - n}{n-1}, \quad CR = \frac{CI}{RI}$$

where CI is the Consistency Index, CR is the Consistency Ratio and RI is the Random Index whose value is taken as per the Table 13.

The matrix with CR < 0.1 is acceptable, which implies that the overall inconsistency less than 10% is acceptable. Else, the judgment is reviewed and the steps are repeated till an acceptable consistency ratio is derived.

Step 5 Generate weights of alternatives.

The priorities of the criteria so obtained are used in the calculation of the weight of priorities of sub-criteria in the next level. This continues till the priority weights of alternatives are calculated. The rating of the alternatives is obtained by aggregating the relative priorities using the hierarchical additive weighting method.

Appendix F

See the Tables 14, 15, 16 and 17.

Table 14 Pairwise comparison matrix given by quality head

Quality head	Viscosity	pH-value	Shelf life	Price	Lead time	Resistivity	Solid contents	Weights
Viscosity	1	2	7	5	3	1/3	6	0.223
pH-value	1/2	1	6	4	2	1/4	5	0.153
Shelf life	1/7	1/6	1	1/4	1/5	1/9	1/3	0.022
Price	1/5	1/4	4	1	1/3	1/7	3	0.057
Lead time	1/3	1/2	5	3	1	1/5	5	0.107
Resistivity	3	4	9	7	5	1	7	0.403
Solid contents	1/6	1/5	3	1/3	1/5	1/7	1	0.035

Table 15 Priority weights for each member

Project team members	Financial Head	Quality head	Purchase Manager	Maintenance manager	Quality control inspector	Floor operator	Research advisor	Research associates
Weights	4	5	4	5	4	3	3	2
	0.133	0.167	0.133	0.167	0.133	0.100	0.100	0.067

Table 16 Comparison matrix

	Financial head	Quality head	Purchase manager	Maintenance manager	Quality control inspector	Floor operator	Research advisor	Research associates	Calculated weights of criteria
Vicosity	0.034	0.223	0.034	0.035	0.110	0.398	0.391	0.033	0.148
PH-value	0.382	0.153	0.142	0.389	0.031	0.067	0.053	0.033	0.178
Shelf life	0.054	0.022	0.074	0.059	0.404	0.157	0.251	0.437	0.154
Price	0.098	0.057	0.034	0.095	0.257	0.235	0.099	0.072	0.115
Lead time	0.022	0.107	0.327	0.020	0.031	0.024	0.027	0.033	0.079
Resistivity	0.151	0.403	0.356	0.154	0.135	0.083	0.158	0.254	0.219
Solid contents	0.259	0.035	0.034	0.247	0.031	0.036	0.022	0.139	0.105
Weights of stakeholder	0.133	0.167	0.133	0.167	0.133	0.100	0.100	0.067	

Table 17 Pairwise comparison matrix with respect to viscosity

Viscosity	S1	S2	S3	S4	S5	S6	S7	Weights
S1	1	5	1/5	1/3	5	1/2	5	0.110
S2	1/5	1	1/9	1/7	1	1/5	1	0.031
S3	5	9	1	2	9	5	9	0.404
S4	3	7	1/2	1	7	3	7	0.257
S5	1/5	1	1/9	1/7	1	1/5	1	0.031
S6	2	5	1/5	1/3	5	1	5	0.135
S7	1/5	1	1/9	1/7	1	1/5	1	0.031

References

Agarwal, V., Govindan, K., Darbari, J. D., & Jha, P. C. (2016). An optimization model for sustainable solutions towards implementation of reverse logistics under collaborative framework. *International Journal of System Assurance Engineering and Management, 7*(4), 480–487.

Anand, R. B., Shukla, S. K., Ghorpade, A., Tiwari, M. K., & Shankar, R. (2007). Six sigma-based approach to optimize deep drawing operation variables. *International Journal of Production Research, 45*(10), 2365–2385.

Andersson, R., Eriksson, H., & Torstensson, H. (2006). Similarities and differences between TQM, six sigma and lean. *The TQM Magazine, 18*(3), 282–296.

Antony, J. (2004). Six Sigma in the UK service organisations: Results from a pilot survey. *Managerial Auditing Journal, 19*(8), 1006–1013.

Antony, J. (2008). Can Six Sigma be effectively implemented in SMEs? *International Journal of Productivity and Performance Management, 57*(5), 420–423.

Antony, J., Gijo, E. V., & Childe, S. J. (2012a). Case study in Six Sigma methodology: Manufacturing quality improvement and guidance for managers. *Production Planning and Control, 23*(8), 624–640.

Antony, J., Singh Bhuller, A., Kumar, M., Mendibil, K., & Montgomery, D. C. (2012b). Application of Six Sigma DMAIC methodology in a transactional environment. *International Journal of Quality and Reliability Management, 29*(1), 31–53.

Arturo Garza-Reyes, J., Flint, A., Kumar, V., Antony, J., & Soriano-Meier, H. (2014). A DMAIRC approach to lead time reduction in an aerospace engine assembly process. *Journal of Manufacturing Technology Management, 25*(1), 27–48.

Augusto Cauchick Miguel, P., Satolo, E., Marcos Andrietta, J., & Araújo Calarge, F. (2012). Benchmarking the use of tools and techniques in the Six Sigma programme based on a survey conducted in a developing country. *Benchmarking: An International Journal, 19*(6), 690–708.

Basu, R., & Bhola, P. (2015). Exploring quality management practices and its pattern analysis in Indian service SMEs. *Journal of Enterprising Culture, 23*(2), 199–235.

Brady, J. E., & Allen, T. T. (2006). Six Sigma literature: A review and agenda for future research. *Quality and reliability engineering International*, *22*(3), 335–367.

Chakraborty, A., Mutingi, M., & Vashishth, A. (2019). Quality management practices in SMEs: A comparative study between India and Namibia. *Benchmarking: An International Journal*, *26*(5), 1499–1516.

Chakravorty, S. S. (2009). Six Sigma programs: An implementation model. *International Journal of Production Economics, 119*(1), 1–16.

Cherrafi, A., Elfezazi, S., Govindan, K., Garza-Reyes, J. A., Benhida, K., & Mokhlis, A. (2017). A framework for the integration of Green and Lean Six Sigma for superior sustainability performance. *International Journal of Production Research, 55*(15), 4481–4515.

Darbari, J. D., Kannan, D., Agarwal, V., & Jha, P. C. (2019). Fuzzy criteria programming approach for optimising the TBL performance of closed loop supply chain network design problem. *Annals of Operations Research*, *273*(1–2), 693–738.

De Mast, J. (2004). A methodological comparison of three strategies for quality improvement. *International Journal of Quality & Reliability Management*, *21*(2), 198–213.

Deshmukh, S. V., & Chavan, A. (2012). Six Sigma and SMEs: a critical review of literature. *International Journal of Lean Six Sigma, 3*(2), 157–167.

Deshmukh, S. V., & Lakhe, R. R. (2010). Six sigma awareness in central Indian SMEs. *International Journal of Productivity and Quality Management*, *5*(2), 200–212.
Doggett, A. M. (2005). Root cause analysis: A framework for tool selection. *Quality Management Journal, 12*(4), 34–45.
Drohomeretski, E., Gouvea da Costa, S. E., Pinheiro de Lima, E., & Garbuio, P. A. D. R. (2014). Lean, Six Sigma and Lean Six Sigma: An analysis based on operations strategy. *International Journal of Production Research, 52*(3), 804–824.
Elshennawy, A. K. (2004). Quality in the new age and the body of knowledge for quality engineers. *Total Quality Management, 15*(5–6), 603–614.
FICCI and PwC, India. (2017). *India manufacturing barometer: Standing strong*. http://www.ficci.in/India-Manufacturing-Barometer.pdf. Accessed 02 February 2019.
Foster, C. W., Kadara, R. O., & Banks, C. E. (2016). Fundamentals of screen-printing electrochemical architectures. In *Screen-printing electrochemical architectures* (pp. 13–23). Cham: Springer.
Garza-Reyes, J. A., Salomé Valls, A., Peter Nadeem, S., Anosike, A., & Kumar, V. (2018). A circularity measurement toolkit for manufacturing SMEs. *International Journal of Production Research*. https://doi.org/10.1080/00207543.2018.1559961.
Gijo, E. V., Bhat, S., & Jnanesh, N. A. (2014). Application of Six Sigma methodology in a small-scale foundry industry. *International Journal of Lean Six Sigma*, *5*(2), 193–211.
Gijo, E. V., & Sarkar, A. (2013). Application of Six Sigma to improve the quality of the road for wind turbine installation. *The TQM Journal, 25*(3), 244–258.
Gijo, E. V., & Scaria, J. (2010). Reducing rejection and rework by application of Six Sigma methodology in the manufacturing process. *International Journal of Six Sigma and Competitive Advantage, 6*(1–2), 77–90.
Gijo, E. V., Scaria, J., & Antony, J. (2011). Application of Six Sigma methodology to reduce defects of a grinding process. *Quality and Reliability Engineering International, 27*(8), 1221–1234.
Goh, T. N., Low, P. C., Tsui, K. L., & Xie, M. (2003). Impact of Six Sigma implementation on stock price performance. *Total Quality Management & Business Excellence*, *14*(7), 753–763.
Govindan, K., Agarwal, V., Darbari, J. D., & Jha, P. C. (2017). An integrated making model for the selection of sustainable forward and reverse logistic providers. *Annals of Operations Research, 273,* 607–650.
Govindan, K., & Chaudhuri, A. (2016). Interrelationships of risks faced by third party logistics service providers: A DEMATEL based approach. *Transportation Research Part E: Logistics and Transportation Review, 90,* 177–195.
Govindan, K., Khodaverdi, R., & Vafadarnikjoo, A. (2016). A grey DEMATEL approach to develop third-party logistics provider selection criteria. *Industrial Management and Data Systems, 116*(4), 690–722.
Govindan, K., & Sivakumar, R. (2016). Green supplier selection and order allocation in low-carbon paper industry: Integrated multi-criteria heterogeneous decision-making and multi-objective linear programming approaches. *Annals of Operations Research, 238*(1–2), 243–276.
Gupta, A., Sharma, P., Malik, S. C., Agarwal, N., & Jha, P. C. (2016). Productivity improvement in the chassis preparation stage of the amplifier production process: A DMAIC Six Sigma methodology. *International Journal of Reliability, Quality and Safety Engineering, 23*(06), 1640012.
Hagemeyer, C., Gershenson, J. K., & Johnson, D. M. (2006). Classification and application of solving quality tools: A manufacturing case study. *The TQM Magazine, 18*(5), 455–483.
Harry, M. J., & Schroeder, R. (2000). *Six Sigma: The breakthrough management strategy revolutionizing the World's Top corporations*. New York: Doubleday.
Henderson, K. M., & Evans, J. R. (2000). Successful implementation of Six Sigma: benchmarking general electric company. *Benchmarking: An International Journal, 7*(4), 260–282.
Herzallah, A. M., Gutierrez, L. G., & Rosas, J. F. M. (2014). Total quality management practices, competitive strategies and financial performance: The case of the Palestinian industrial SMEs. *Total Quality Management, 25*(6), 635–649.
Hillier, F. S., & Lieberman, G. J. (2001). *Introduction to operations research* (7th ed.). New York: McGraw-Hill.
Hoerl, R. W. (2001). Six Sigma black belts: What do they need to know? (with discussion). *Journal of Quality Technology, 33*(4), 391–417.
IBEF. (2017). The best of India in engineering. In *India Brand Equity Foundation*. https://www.ibef.org/the-best-of-india-in-engineering-2017.pdf. Accessed 02 February 2019.
Ihua, U. B. (2009). SMEs key failure-factors: A comparison between the United Kingdom and Nigeria. *Journal of Social Sciences, 18*(3), 199–207.
Jin, T., Janamanchi, B., & Feng, Q. (2011). Reliability deployment in distributed manufacturing chains via closed-loop Six Sigma methodology. *International Journal of Production Economics, 130*(1), 96–103.

Jirasukprasert, P., Arturo Garza-Reyes, J., Kumar, V., & Lim, K. M. (2014). A Six Sigma and DMAIC application for the reduction of defects in a rubber gloves manufacturing process. *International Journal of Lean Six Sigma, 5*(1), 2–21.

Kahraman, C., & Büyüközkan, G. (2008). A combined fuzzy AHP and fuzzy goal programming approach for effective Six-Sigma project selection. *Journal of Multiple-Valued Logic and Soft Computing*, *14*(6), 599–615.

Kaushik, P., Khanduja, D., Mittal, K., & Jaglan, P. (2012). A case study: Application of Six Sigma methodology in a small and medium-sized manufacturing enterprise. *The TQM Journal*, *24*(1), 4–16.

Krebs, F. C. (2009). Fabrication and processing of polymer solar cells: A review of printing and coating techniques. *Solar Energy Materials and Solar Cells, 93*(4), 394–412.

Kumar, M., Antony, J., & Tiwari, M. K. (2011). Six Sigma implementation framework for SMEs: A roadmap to manage and sustain the change. *International Journal of Production Research, 49*(18), 5449–5467.

Kumar, U. D., Nowicki, D., Ramírez-Márquez, J. E., & Verma, D. (2008). On the optimal selection of process alternatives in a Six Sigma implementation. *International Journal of Production Economics, 111*(2), 456–467.

Lakhal, L., Pasin, F., & Limam, M. (2006). Quality management practices and their impact on performance. *International Journal of Quality and Reliability Management, 23*(6), 625–646.

Lande, M., Shrivastava, R. L., & Seth, D. (2016). Critical success factors for Lean Six Sigma in SMEs (small and medium enterprises). *The TQM Journal*, *28*(4), 613–635.

Lee, K. L., Wei, C. C., & Lee, H. H. (2009). Reducing exposed copper on annular rings in a PCB factory through implementation of a Six Sigma project. *Total Quality Management, 20*(8), 863–876.

Majumdar, J. P. (2016). Causes of reluctance of Indian manufacturing SMEs to implement. Total quality management. *International Journal of Applied Research*, *2*(2), 126–134.

Mitchell, E. M., & Kovach, J. V. (2016). Improving supply chain information sharing using design for Six Sigma. *European Research on Management and Business Economics, 22*(3), 147–154.

MoMSME. (2017). Annual report 2016–17. In *Ministry of micro, small and medium enterprises*. http://msme.gov.in/sites/default/files/MSME%20ANNUAL%20REPORT%202016-17%20ENGLISH.pdf. Accessed 02 February 2019.

Montgomery, D. C. (2007). *Introduction to statistical quality control*. New York: Wiley.

Montgomery, D. C., & Woodall, W. H. (2008). An overview of six sigma. *International Statistical Review, 76*(3), 329–346.

Nonthaleerak, P., & Hendry, L. (2008). Exploring the six sigma phenomenon using multiple case study evidence. *International Journal of Operations and Production Management, 28*(3), 279–303.

Ortíz, M. A., Felizzola, H. A., & Isaza, S. N. (2015). A contrast between DEMATEL-ANP and ANP methods for six sigma project selection: a case study in healthcare industry. *BMC Medical Informatics and Decision Making, 15*(3), S3.

Pan, X., Han, C., Lu, X., Jiao, Z., & Ming, Y. (2018). Green innovation ability evaluation of manufacturing enterprises based on AHP–OVP model. *Annals of Operations Research*. https://doi.org/10.1007/s10479-018-3094-6.

Parsana, T. S., & Desai, D. A. (2016). A case study: to reduce process variability of valve seat depth in cylinder head using Six Sigma methodology. *International Journal of Productivity and Quality Management*, *17*(4), 474–506.

Phillips, C. O., Beynon, D. G., Hamblyn, S. M., Davies, G. R., Gethin, D. T., & Claypole, T. C. (2014). A study of the abrasion of squeegees used in screen printing and its effect on performance with application in printed electronics. *Coatings, 4*(2), 356–379.

Prashar, A. (2016a). A conceptual hybrid framework for industrial process improvement: Integrating Taguchi methods, Shainin System and Six Sigma. *Production Planning and Control, 27*(16), 1389–1404.

Prashar, A. (2016b). Six Sigma adoption in public utilities: A case study. *Total Quality Management and Business Excellence, 27*(5–6), 479–506.

Prashar, A. (2017). Adopting PDCA (Plan-Do-Check-Act) cycle for energy optimization in energy-intensive SMEs. *Journal of Cleaner Production, 145,* 277–293.

Prashar, A. (2018). Towards cycle time reduction in manufacturing SMEs: Proposal and evaluation. *Quality Engineering, 30,* 469–484.

Rajagopalan, R., Francis, M., & Suárez, W. (2004). Managers at work: Developing novel catalysts with Six Sigma. *Research-Technology Management, 47*(1), 13–16.

Rathi, R., Khanduja, D., & Sharma, S. (2015). Synergy of fuzzy AHP and Six Sigma for capacity waste management in Indian automotive industry. *Decision Science Letters, 4*(3), 441–452.

Sahoo, S., & Yadav, S. (2018). Lean implementation in small- and medium-sized enterprises: an empirical study of Indian manufacturing organizations. *Benchmarking: An International Journal, 25*(4), 1121–1147.

Sanchez-Ruiz, L., Blanco, B., & Diaz, E. (2019). Difficulty in implementing continuous improvement–Rasch measurement analysis. *Business Process Management Journal*, *25*(6), 1228–1250.
Schouten, F. A., & Tapiero, C. S. (1995). OR models for maintenance management and quality control. *European Journal of Operational Research, 82*(5), 211–213.
Shafer, S. M., & Moeller, S. B. (2012). The effects of Six Sigma on corporate performance: An empirical investigation. *Journal of Operations Management, 30*(7–8), 521–532.
Sharma, P., Malik, S. C., Gupta, A., & Jha, P. C. (2018). A DMAIC Six Sigma approach to quality improvement in the anodising stage of the amplifier production process. *International Journal of Quality and Reliability Management, 35*(9), 1868–1880.
Singh, L. P., Bhardwaj, A., & Sachdeva, A. (2006). Quality management practices vs. performance of SMEs: An empirical study of Indian industries. In *PICMET Proceedings*, Istanbul, July 9–13 (pp. 2393–2399).
Singh, R. K., Garg, S. K., & Deshmukh, S. G. (2008). Strategy development by SMEs for competitiveness: A review. *Benchmarking: An International Journal, 15*(5), 525–547.
Snee, R. D. (1999). Why should statisticians pay attention to Six Sigma? *Quality Progress*, *32*(9), 100.
Snee, R. D. (2000). Guest editorial: Impact of Six Sigma on quality engineering. *Quality Engineering, 12*(3), 9–14.
Snee, R. D. (2001). Dealing with the Achilles heel of Six Sigma initiatives. *Quality Progress*, *34*(3), 66–72.
Snee, R. D. (2004). Six Sigma: The evolution of 100 years of business improvement methodology. *International Journal of Six Sigma and Competitive Advantage, 1*(1), 4–20.
Soheilirad, S., Govindan, K., Mardani, A., Zavadskas, E. K., Nilashi, M., & Zakuan, N. (2018). Application of data envelopment analysis models in supply chain management: A systematic review and meta-analysis. *Annals of Operations Research, 271*(2), 915–969.
Soković, M., Jovanović, J., Krivokapić, Z., & Vujović, A. (2009). Basic quality tools in continuous improvement process. *Journal of Mechanical Engineering, 55*(5), 1–9.
Sokovic, M., Pavletic, D., & Fakin, S. (2005). Application of Six Sigma methodology for process design. *Journal of Materials Processing Technology, 162,* 777–783.
Southard, P. B., Chandra, C., & Kumar, S. (2012). RFID in healthcare: A Six Sigma DMAIC and simulation case study. *International Journal of Health Care Quality Assurance, 25*(4), 291–321.
Tang, L. C., Goh, T. N., Lam, S. W., & Zhang, C. W. (2007). Fortification of Six Sigma: Expanding the DMAIC toolset. *Quality and Reliability Engineering International, 23*(1), 3–18.
Tang, L. C., & Paoli, P. M. (2004). A spreadsheet-based multiple criteria optimization framework for Quality Function Deployment. *International Journal of Quality and Reliability Management, 21*(3), 329–347.
Tripathi, K. A., & Singh, S. (2018). Analysis of barriers to women entrepreneurship through ISM and MICMAC: A case of Indian MSMEs. *Journal of Enterprising Communities: People and Places in the Global Economy, 12*(3), 346–373.
Tzeng, G. H., & Huang, C. Y. (2012). Combined DEMATEL technique with hybrid MCDM methods for creating the aspired intelligent global manufacturing and logistics systems. *Annals of Operations Research, 197*(1), 159–190.
Veena, T. R., & Prabhushankar, G. V. (2019). A literature review on lean, Six Sigma and ISO 9001: 2015 in manufacturing industry to improve process performance. *International Journal of Business and Systems Research, 13*(2), 162–180.
Wang, F. K., & Chen, K. S. (2010). Applying Lean Six Sigma and TRIZ methodology in banking services. *Total Quality Management, 21*(3), 301–315.
Yeung, S. M. C. (2009). Using Six Sigma-SIPOC for customer satisfaction. *International Journal of Six Sigma and Competitive Advantage, 5*(4), 312–324.
Yin, R. K. (2014). *Case study research: Design and methods* (5th ed.). Thousand Oaks, CA: Sage.
Yousefi, A., & Hadi-Vencheh, A. (2016). Selecting six sigma projects: MCDM or DEA? *Journal of Modelling in Management, 11*(1), 309–325.
Yusof, S. R. M., & Aspinwall, E. M. (2000). Critical success factors in small and medium enterprises: survey results. *Total quality management*, *11*(4–6), 448–462.
Zhang, M., Wang, W., Goh, T. N., & He, Z. (2015). Comprehensive Six Sigma application: A case study. *Production Planning and Control, 26*(3), 219–234.
Zhou, B. (2016). Lean principles, practices, and impacts: a study on small and medium-sized enterprises (SMEs). *Annals of Operations Research, 241*(1–2), 457–474.
Zhou, X., Hu, Y., Deng, Y., Chan, F. T., & Ishizaka, A. (2018). A DEMATEL-based completion method for incomplete pairwise comparison matrix in AHP. *Annals of Operations Research, 27,* 1045–1066.

Publisher's Note Springer Nature remains neutral with regard to jurisdictional claims in published maps and institutional affiliations.

Affiliations

Anshu Gupta[1] · Pallavi Sharma[2] · Akansha Jain[3] · Hongbo Xue[4] · S. C. Malik[2] · P. C. Jha[3]

1 University School of Management and Entrepreneurship, Delhi Technological University, Delhi, India

2 Department of Statistics, M.D. University, Rohtak, India

3 Department of Operational Research, University of Delhi, Delhi, India

4 Business School, Nankai University, Tianjin 300071, P.R. China

Audio Watermarking Using Beat Detection and Pitch Estimation

Lavi Tanwar
Department of Electronics & Communication Engineering Delhi Technological University
Delhi, India
lavi.tanwar02@gmail.com

Radhika Dang
Department of Electronics & Communication Engineering Delhi Technological University
Delhi, India
radhika_bt2k14@dtu.ac.in

Satvik Maurya
Department of Electronics & Communication Engineering Delhi Technological University
Delhi, India
satvik_bt2k14@dtu.ac.in

Jeebananda Panda
Department of Electronics & Communication Engineering Delhi Technological University
Delhi, India
jpanda@dce.ac.in

***Abstract*- This paper presents a novel semi-blind Audio Watermarking Algorithm in the Time Domain with the use of Beat detection and Pitch Estimation. Using the estimated values of the beat locations and their respective pitch or fundamental frequencies, a watermark is generated from the binary information that is to be hidden, which is then embedded in the audio file. The robustness of this algorithm has been gauged using standard audio processing attacks such as Resampling, Re-quantisation and Noise attack using AWGN. Apart from these, the watermarked audio file has been subjected to equalisation attacks which are prevalent in the music industry today, using equalisation modes such as Jazz, Rock, Classical and Bass. The performance of the algorithm has been proved to be satisfactory against all such attacks.**

Keywords- Objective Differential Grade, Beat Detection, Pitch Estimation, Audio Equalisation.

I. INTRODUCTION

With the continuous growth of the internet, it is becoming increasingly easier to obtain pirated versions of various types of intellectual property which include Books, Software, Music and even Publications. It has thus become imperative to provide such properties with some form of protection against illegal reproduction.

Digital Audio Watermarking has thus received great interest in recent years because of the lack of means to provide copyright protection of audio content. The watermarking of audio signals is thus characterised by the need to keep the watermark imperceptible i.e., it should not be audible and robust against various malicious and non – malicious attacks. These requirements have resulted in a wide variety of time domain and transform domain watermarking algorithms which can be used effectively for copyright protection of audio content [1], [2]. Other approaches include the use of both time and transform domains and compressed domain watermarking. As mentioned in [1], the use of transform domain algorithms is preferred by researchers even though no conclusive evidence of the superiority of the transform domain approach over other approaches has been found.

Time domain algorithms for audio watermarking primarily exploit the principle that the Human Auditory System (HAS) cannot detect slight changes in time varying regions of an audio signal [3]. Some noteworthy time domain approaches as mentioned in [4] include the one proposed by Lie et. Al. in [5] in which the amplitudes are varied for embedding the watermark. This method fulfils the imperceptibility criteria for a good watermarking scheme but was shown to exhibit poor robustness as the watermark could easily be removed by using a suitable attenuator. Van Schyndel et. Al. proposed the elementary method of digital watermarking i.e., the Least Significant Bit (LSB) method [6]. In this approach, the watermark is embedded in the LSB of the host signal. A major drawback of this method was the lack of robustness against noise. The use of Empirical Mode Decomposition (EMD) for watermarking has been mentioned in [7] in which the watermark is embedded in the lower order IMFs. However, this scheme was computationally complex. In [13], S. Xiang et. Al. modified the statistical features in time domain and shifted the histogram to embed the watermark. This method is robust to MP3 compression and can embed large number of bits but its imperceptibility is poor than the existing methods. K. Gopalan presented a fragile technique in [14] by modifying the bits of the audio signal. The bit values at selected indices are used to choose the watermark key. This technique is fragile and robust to noise but the careful selection of key is required as wrong key selection may result in loss of information and false detection. D. Bratic et. Al. proposed an algorithm in [15] which generates a support function using spectrogram and that support function is used to create the watermark. The gradient algorithm is used for reconstruction. The perceptuality of this technique is good but its computational complexity is high.

In this paper, a novel watermarking method in the time domain has been presented, which has then been proven imperceptible and robust to a wide range of signal processing attacks. The algorithm proposed here makes use of the estimated values of the beat locations and the fundamental frequencies for the generation of a watermark from a binary image which is then embedded in the audio file. The proposed

978-1-5386-6625-8/18/$31.00 ©2018 IEEE

algorithm is semi-blind in nature and thus the original audio file is not required for the successful recovery of the binary image from the watermarked audio file. To determine the robustness of the watermarking procedure, the watermarked audio file has been subjected to signal processing attacks such as addition of AWGN, Re-quantisation and Resampling, and to several popular Audio Equalisation modes wherein particular frequency components of the audio signal are amplified or attenuated. With the help of readily available audio processing software, Equalisation can be applied easily on an audio file using various pre-determined settings which define different genres such as 'Jazz', 'Rock', 'Classical', 'Pop' and 'Bass'. Thus, to gauge the performance of the algorithm proposed in this paper against such attacks, the watermarked audio was equalised into different modes and the reconstruction of the binary information was performed for each case. The paper thus proceeds to elaborate the process of beat detection and pitch estimation in Section II. Then in Sections III and IV, the watermark embedding and reconstruction algorithms have been presented, followed by the results and performance analysis in Section V. The conclusions have been presented in Section VI.

II. BEAT DETECTION AND PITCH ESTIMATION

A. Beat Detection

A beat, in the simplest of terms, is an instant in the audio file when the listener will tap his foot, and thus it represents the rhythmic nature of an audio file. The domain beat tracking and detection has been researched upon for quite a few years and many efficient algorithms have been formulated including the one proposed by Fillon et. Al. in [8] which used Conditional Random Field (CRF) framework for the efficient detection of beats. Zapata et. Al. proposed a in [9] a beat tracker modelled with multiple input features. Their implementation was shown to be highly accurate and was better than most state-of-the-art beat detectors at the time. In this paper, however, a simple beat detection algorithm proposed by Daniel P.W. Ellis in [10] has been implemented which used dynamic programming for a simple beat detector.

Ellis' system first estimates a global tempo. Then, using dynamic programming, the prospective beat times are evaluated which match the chosen tempo and the best matches are retained. This approach was shown to be simple and computationally efficient and performed satisfactorily. Further elaboration of the algorithm is beyond the scope of this paper.

B. Pitch Estimation

The term 'Pitch Estimation' is most commonly used for the estimation of the Fundamental frequency or the Formant frequency of a periodic waveform. The Fundamental frequency for a periodic waveform can be defined as the lowest frequency component present in that waveform. The Formant frequency on the other hand is defined as the resonant frequency of the waveform and there can be more than one Formant in an audio file. In music, the Fundamental frequency, or Pitch, is the lowest tone present. As this paper deals with music, the terms fundamental frequency and pitch have been used interchangeably.

There are many pitch estimation algorithms that have been devised in recent years for various uses such as pitch scaling, intonation scoring etc. Some of the common methods for extracting the pitch from an audio file are explained briefly below:

1) *Using Auto-Correlation Function:* The auto-correlation of a signal $x(m)$ with a window function $w(m)$ with a lag parameter 'k' is given by-

$$R_n(k) = \sum_{m=-\infty}^{+\infty} x(m)w(n-m)x(m+k)w\big(n-(m+k)\big) \quad (1)$$

This method uses the property that the auto-correlation function is a measure of self-similarity. Thus, when the auto-correlation of an audio file is taken which has a repeating pattern, it will yield maximum values when the entire periodic sequence is overlapped with itself. Hence, by using these local maxima, the period and hence fundamental frequency can be calculated for a sequence of samples.

2) *Using Cepstral Analysis:* The real – cepstrum of a frame of audio $x(m)$ using a window $w(m)$ at a sample n can be defined by-

$$c_s(n) = F^{-1}\big(\log\big(\big|F\big(x(m)\big)\big|\big)\big) \quad (2)$$

Where F is the DTFT operator and F^{-1} is the inverse DTFT operator. In the cepstral domain, the pitch can be calculated by taking the frequency in the cepstral domain which has the highest energy. This frequency is thus the fundamental frequency of the set of samples.

Apart from these methods, there are several other ways to estimate the pitch of an audio file such as the use of Harmonic Product Spectrum, the Average Magnitude Difference Function (AMDF) and Maximum Likelihood estimation. For this paper, the cepstral analysis method for pitch estimation has been used.

III. THE EMBEDDING ALGORITHM

Kirovski and Attias introduced beat detection and block redundant coding for nullifying the effects of desynchronization [11]. Teleşpan et. Al. proposed a watermarking scheme which employed Empirical Mode Decomposition and Beat Detection for the watermark embedding process [12]. Their primary aim was to perform the watermark embedding at locations that are least susceptible to various audio compression techniques, which they successfully executed with the help of beat detection. The proposed approach towards the watermark embedding process is based on the same principle.

It should be noted here that the watermarking procedure has been performed on audio which has a stereo output. Thus, throughout the embedding and reconstruction processes, two distinct sets of sampled data corresponding to two distinct channels will be considered. A flowchart showing the embedding process is shown in Figure 2 followed by a description of all the steps involved.

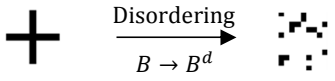


Fig. 1. Disordering of the Binary Image

1) Beat Detection: Using the beat detection functions, the beat locations are computed for both channels. Let the number of beats be 'c_1' and 'c_2' for the two channels.

2) Disordering of Binary Information: For additional security in the watermarking procedure, the binary image of size m × n is used for generation of watermark. It is disordered to obtain B^d using Key 1 as shown in Figure 1, which will be used as side information for extraction of watermark.

3) Pitch Estimation: Taking windows of length 'L', where L is the number of samples between the last beat location and the end of the audio file, the fundamental frequencies are calculated for a window starting at every beat location and are stored in vectors f_1 and f_2 of lengths c_1 and c_2 respectively.

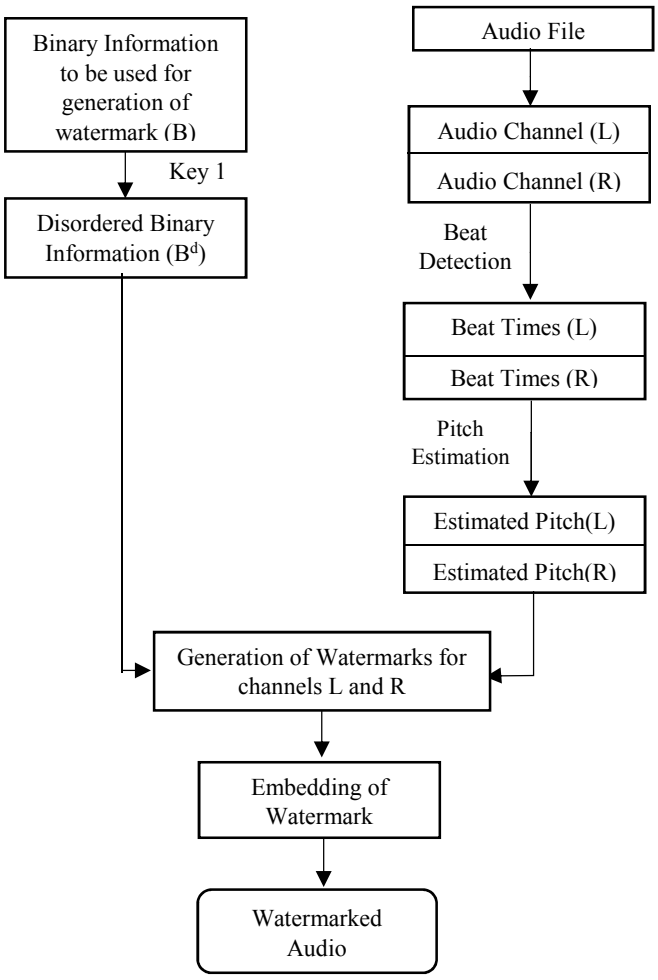


Fig. 2. Flowchart for the embedding algorithm

4) Generation of the Watermarks: To provide redundancy to the watermarking procedure to further improve its security and invisibility, two different watermarks, W_L^M and W_R^M are generated for the two channels, as per the following comparisons:

$$W_L^M(i,j) = \begin{cases} -1, if\ f_L(i \times j) < f_0\ and\ B^d(i,j) = 0 \\ 1, if\ f_L(i \times j) > f_0\ and\ B^d(i,j) = 1 \\ -2, if\ f_L(i \times j) < f_0\ and\ B^d(i,j) = 1 \\ 2, if\ f_L(i \times j) > f_0\ and\ B^d(i,j) = 0 \end{cases} \quad (3)$$

$$W_R^M(i,j) = \begin{cases} -1, if\ f_R(i \times j) < f_0\ and\ B^d(i,j) = 0 \\ 1, if\ f_R(i \times j) > f_0\ and\ B^d(i,j) = 1 \\ -2, if\ f_R(i \times j) < f_0\ and\ B^d(i,j) = 1 \\ 2, if\ f_R(i \times j) > f_0\ and\ B^d(i,j) = 0 \end{cases} \quad (4)$$

Where, f_L and f_R represent the set of fundamental frequencies corresponding to the two channels (L and R) and f_0 is a pre-defined reference frequency. This Non-Return to Zero (NRZ) scheme was chosen because embedding zero as binary watermark will not cause any change to the sample magnitude of the audio file and this will affect the robustness of the watermarking scheme.

5) Embedding of the Watermarks: W_L^M and W_R^M are embedded in the original audio file to obtain the watermarked audio file. First, a window of length L is taken at every beat location of the two audio channels. In that window, the corresponding Watermark generated by using (3) and (4) is embedded using the relation –

$$x_1(wn: wn + L) = x_1(wn: wn + L)\big(1 + \alpha \times W_L^M(i,j)\big) \quad (5)$$

Where, wn is n^{th} beat location and $(wn: wn + L)$ represents a window starting from wn up to a length L, 'α' represents the strength of watermarking and x_1 represents the set of sample values corresponding to audio channel (L) and x_2 represents the set of sample values corresponding to audio channel (R). The same relation as shown in (5) is applied for the audio channel(R). Thus, the watermarked audio file will contain both watermarked channels, x_1 and x_2.

The value of the reference frequency f_0 is calculated as follows: The fundamental frequency is obtained from L samples of the audio file starting at every beat location. If the mean of all the fundamental frequencies that have been obtained for the two channels are represented as M_L and M_R and the highest fundamental frequencies that have been obtained for both channels are given by P_L and P_R, then the reference frequency f_0 is given by–

$$f_0 = mean(P_L - M_L, P_R - M_R) \quad (6)$$

IV. THE RECONSTRUCTION ALGORITHM

As the watermarking procedure is semi-blind in nature, the original audio file is not required for the reconstruction of the binary image from the watermarked audio file. However, the reference frequency f_0 and the original watermark information derived in (3) and (4) are necessary for the proper reconstruction of the binary image B. The steps are shown in Figure 3 and are explained below:

1) Beat Detection: The beat locations are first calculated for the watermarked audio file (again, the file will contain two data sets for the two channels). Let the sets of beat locations have lengths 'rc_1' and 'rc_2'.

2) Pitch Estimation: Now, for the first channel, at every beat location, a window of length 'L' is taken, where

'L' is the number of samples between the last beat location and the last sample of the audio file, and the fundamental frequency is calculated for that window. This process is repeated for the second channel as well resulting in two sets of data fr_1 and fr_2 of lengths rc_1 and rc_2 respectively containing pitch information.

3) Retrieval of Disordered Binary Image B^d: The modified watermarks W_L^M and W_R^M of the two channels are used for the retrieval of the disordered binary image B^d as per the following comparisons:

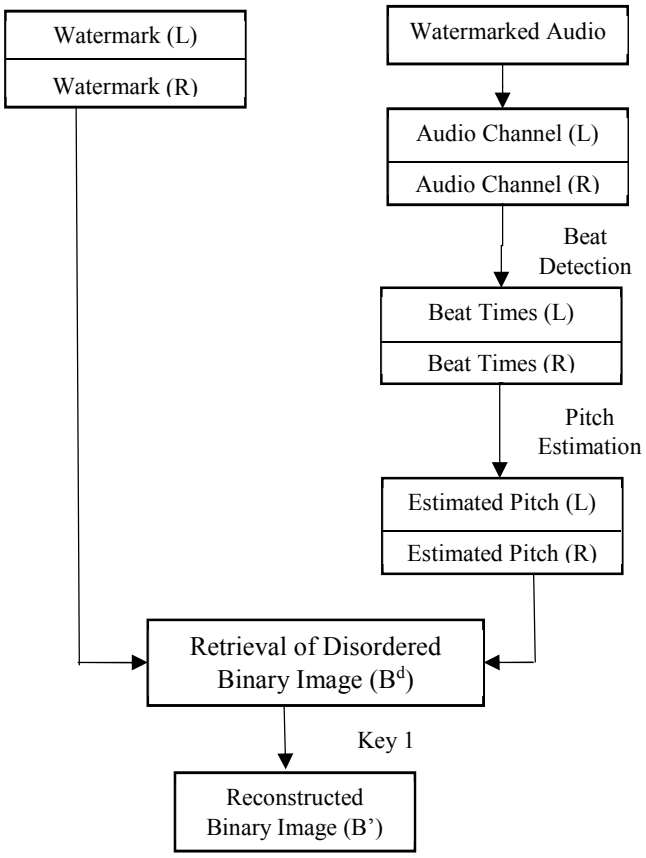


Fig. 3. Flowchart for the reconstruction algorithm

$$B_1^d(i,j) = \begin{cases} 0, if\ fr_L(i \times j) < f_0\ and\ W_L^M(i,j) = -1 \\ 1, if\ fr_L(i \times j) < f_0\ and\ W_L^M(i,j) = -2 \\ 0, if\ fr_L(i \times j) > f_0\ and\ W_L^M(i,j) = 1 \\ 1, if\ fr_L(i \times j) > f_0\ and\ W_L^M(i,j) = 2 \end{cases} \quad (7)$$

$$B_2^d(i,j) = \begin{cases} 0, if\ fr_R(i \times j) < f_0\ and\ W_R^M(i,j) = -1 \\ 1, if\ fr_R(i \times j) < f_0\ and\ W_R^M(i,j) = -2 \\ 0, if\ fr_R(i \times j) > f_0\ and\ W_R^M(i,j) = 1 \\ 1, if\ fr_R(i \times j) > f_0\ and\ W_R^M(i,j) = 2 \end{cases} \quad (8)$$

$$B^d = B_1^d \wedge B_2^d \quad (9)$$

As is apparent from the above relations, the disordered binary image is reconstructed from a logical OR of the disordered binary images obtained from both the channels. As mentioned before, both channels are used to add redundancy to the watermarking procedure.

4) Reordering of the Disordered Binary Image: After obtaining the disordered binary image from (7), (8) and (9), the final binary image is reconstructed by reordering the disordered binary image using Key 1.

V. RESULTS

A binary image of size 11 × 11 pixels, as shown in Figure 4, has been used here for the watermarking procedure described in section III. The implementation of the embedding and reconstruction algorithm was performed in a MATLAB 2015a environment and the equalisation attacks were performed using Simulink models. The algorithm has been implemented on audio files of three distinct genres of music, namely, Rock, Pop and EDM (Electronic Dance Music) of different lengths and tempo sampled at 44.1 kHz with 16-bit quantisation. The reference frequency f_0, as obtained from (8), for the Rock genre was 147.5424 Hz, for the Pop genre, it was 157.8009 Hz and for the EDM genre, it was 164.1590 Hz. Table 1 shows the number of detected beats for the three audio files.

The Rock audio file the window lengths for both channels was 58984 samples and 58278 samples respectively. For the Pop audio file, the window lengths for pitch estimation for the two channels were 326490 samples and 310260 samples while for the EDM audio file, they were 340400 samples and 347980 samples for the two channels.

To measure the robustness of our algorithm, various attacks on the watermarked audio were performed, and the values of the Bit Error Rate (BER) and Normalised Cross-Correlation (NC) as defined in (9) and (10) were analysed for all the cases with attacks [12]. Reconstruction of the binary information without any attacks resulted in a Signal to Noise Ratio (SNR) of infinity, which signifies that the watermark was perfectly retrieved.

$$BER(B,B') = \frac{\sum_{i=0}^{N} B(i) * B'(i)}{N} \quad (10)$$

$$NC(B,B') = \frac{\sum_{i=0}^{N} B(i) * B'(i)}{\sqrt[2]{\sum_{i=0}^{N} B(i)^2} * \sqrt[2]{\sum_{i=0}^{N} B'(i)^2}} \quad (11)$$

Where, B and B' represent the original and reconstructed binary images respectively with length N. To assess the quality and imperceptibility of the watermarked audio, 15 human subjects were asked to use the Objective Differential Grade (ODG) scale (Table 2) to rate a thirty second sample of the watermarked audio file based on the perceptibility of the watermark. Table 3 shows the ODG values obtained for the three genres that have been watermarked.

It can be seen from Table 3 that the watermark has a satisfactory level of imperceptibility. The performance of the watermarking algorithm has been thoroughly analyzed by determining the values of BER and NC of the reconstructed binary image after the watermarked audio is attacked as shown in Table 4.



Fig. 4. Original Binary Image

TABLE 1. NUMBER OF BEATS FOR AUDIO FILES

Channel	Rock	Pop	EDM
L	500	1190	1071
R	501	596	1070

TABLE 2. ODG SCALE

Perception	ODG
Imperceptible	0
Perceptible, but not annoying	-1
Slightly annoying	-2
Annoying	-3
Very Annoying	-4

TABLE 3. ODG VALUES OBTAINED FROM HUMAN SUBJECTS

	Rock	Pop	EDM
ODG	-0.06	-0.13	-0.40

TABLE 4. PERFORMANCE OF THE ALGORITHM

GENRE	ROCK		POP		EDM	
AUDIO TYPE	SNR (dB)					
Original	Inf		Inf		Inf	
ATTACK PERFORMANCE						
ATTACK	BER (%)	NC	BER (%)	NC	BER (%)	NC
Cropping	0.826	0.995	0.826	0.995	0.826	0.995
AWGN	4.959	0.972	0.000	1.000	1.653	0.991
Re-Quantisation (8 bits)	2.479	0.986	0.826	0.995	0.000	1.000
Re-Sampling	0.826	0.995	0.000	1.000	0.000	1.000
MP3 Compression (128 bits)	2.479	0.986	0.000	1.000	0.826	0.995
MP3 Compression (96 bits)	0.826	0.995	0.000	1.000	0.000	1.000
Jazz Equalisation	4.959	0.972	2.479	0.986	0.000	1.000
Bass Equalisation	3.306	0.981	0.000	1.000	0.826	0.995
Treble Equalisation	2.479	0.986	0.000	1.000	0.000	1.000
Rock Equalisation	4.959	0.972	0.000	1.000	0.000	1.000
Classical Equalisation	4.959	0.972	0.000	1.000	0.826	0.995
Pop Equalisation	3.306	0.981	0.000	1.000	3.306	0.981

The binary image 'B' can be reconstructed perfectly when the watermarked audio file is not attacked. In this paper, attacks such as cropping, addition of WGN, Re-quantisation and Re-sampling as well as MP3 compression and equalisation, have been used.

For the cropping attack, the watermarked audio file was cropped to 60% of its original length and then the binary image B was reconstructed. This attack reported similar values of BER and NC for all three genres.

For the AWGN attack, WGN was added to the watermarked audio file till the SNR of the audio file was 30 decibels. This attack had maximum effect on the Rock genre while it didn't have any effect on the Pop genre. Thus, on average, the BER for this attack was about 2.2%.

The watermarked audio file was re-quantised to 8 bits and 24 bits. Re-quantisation to 24 bits resulted in perfect reconstruction of the watermark and hence we refrain from listing those results. Re-quantisation to 8 bits had no effect on the EDM genre and thus the average BER for this attack was about 1%.

For the Re-sampling attack, the watermarked audio file was down-sampled to 22.05 kHz and then re-sampled back to the original sampling frequency of 44.1 kHz. In this case, the genres Pop and EDM were unaffected by the attack and thus, the average BER was about 0.27%.

MP3 compression at 96 kbps resulted in perfect reconstruction of the binary image B for the Pop and EDM genres while Rock was slightly affected, thus giving an average BER of around 0.27%. MP3 compression at 128 kbps did not affect the Pop genre thus yielding an average BER of 1.1%.

The following equalisation attacks have been performed on the watermarked audio file: Jazz, bass, treble, classical, pop and rock equalisation. These modes were chosen because they are generally the most popular and most widely used equalisation modes among average users today. The equalisation attacks had maximum effect on the rock genre while Pop and EDM were relatively unaffected.

VI. CONCLUSION

In this paper, a novel time domain watermarking algorithm has been proposed which makes use of both pitch estimation as well as beat detection. An interesting aspect of this algorithm is that the binary information that is to be hidden is not embedded directly in the audio. Instead, two watermarks are generated using this information which are then embedded in the audio file. These watermarks are then used for the reconstruction of the binary information. The proposed algorithm is semi-blind in nature and is quite imperceptible as indicated by the ODG values. Considerably good results were obtained for the BER and NC, when the watermark was retrieved from a corrupted watermarked audio file, which are also significantly better than the ones reported in [12] which reported an average BER of 7.7% for addition of WGN to the watermarked audio file, and an average BER of 7.5% against re-sampling. Furthermore, it shows better robustness against MP3 compression (both 96 and 128 kbps). The proposed algorithm is computationally efficient as it is a time domain approach without use of any complex mathematical operations.

REFERENCES

[1] G. Hua, J. Huang, Y. Q. Shi, J. Goh and V. L. Thing, "Twenty Years of Digital Audio Watermarking – A Comprehensive Review," Signal Processing, vol. 128, pp. 222-242, 2016.

[2] K. V. Goenka and P. K. Patil, "Overview of Audio Watermarking Techniques," International J. of Emerging Technology and Advanced Engineering , vol. 2, pp. 67-70, 2012.

[3] P. Bassia, I. Pitas and N. Nikolaidis, "Robust audio watermarking in the time domain," IEEE Trans. on Multimedia, vol. 3, pp. 232-241, 2001.

[4] R. Shahriar, S. Cho and U. Chong, "Time-domain audio watermarking using multiple marking spaces," International Conf. on Informatics, Electronics and Vision, 2012.

[5] W. N. Lie and L.-C. Chang, "Robust and high-quality time-domain audio watermarking based on low-frequency amplitude modification," IEEE Trans. on Multimedia, vol. 8, pp. 46-59, 2006.

[6] V. Schyndel, R. G. Tirkel, A. G. and C. F. Osborne, "A Digital Watermark," in IEEE International Conf. on Image Processing, Austin, 1994.

[7] J. Panda, K. R. Gera and A. Bhattacharyya, "Non-Blind Audio Watermarking Scheme Based on Empirical Mode," International J. of Advanced Science, Engineering and Technology, vol. 3, pp. 38-43, 2014.

[8] T. Fillon, C. Joder, S. Durand and S. Essid, "A Conditional Random Field System for Beat Tracking," in IEEE International Conf. on Acoustics, Speech and Signal Processing, 2015.

[9] J. R. Zapata, M. E. P. Davies and E. Gomez, "Multi-feature beat tracking," IEEE/ACM Trans. on Audio, Speech and Signal Processing, vol. 22, pp. 816-825, 2014.

[10] D. P. Ellis, "Beat Tracking by Dynamic Programming," J. of New Music Research, vol. 36, pp. 51-60, 2007.

[11] D. Kirovski and H. Attias, “Audio Watermark Robustness to Desynchronization via Beat Detection,” Information Hiding, Springer, pp. 160-176, 2003.

[12] M. Teleşpan and B. M. Schuller, “Audio Watermarking Based on Empirical Mode Decomposition and Beat Detection,” IEEE International Conf. on Acoustics, Speech and Signal Processing, Shanghai, 2016.

[13] S. Xiang, L. Yang and Y. Wang, “Robust and Reversible Audio Watermarking by Modifying Statistical Features in Time Domain,” Advances in Multimedia, vol. 2017, pp. 1-10, 2017.

[14] K. Gopalan, “An algorithm for fragile audio watermarking by bit modification,” IEEE Int. Conf. on Industrial Informatics, France, 2016.

[15] D. Bratic, F. Vesovic and V. Mijanovic, “Audio Watermarking under gradient-based reconstruction attack,” IEEE Meditearanean Conf. on Embedded Computing, Montenegro, 2016.

Biotechnological Communication

Biosci. Biotech. Res. Comm. 12(1): 140-146 (2019)

BBRC
Bioscience Biotechnology Research Communications

Biotechnological management of water quality: A mini review

Lakhan Kumar, Rajkumar Bidlan, Jaigopal Sharma and Navneeta Bharadvaja*

Department of Biotechnology, Delhi Technological University, Shahbad Daulatpur, Delhi-110042, India

ABSTRACT

Since eighteenth century onwards, with the advent of industrial revolution, petrochemical and chemical industries have seen tremendous growth. Wastewater is an essential raw material as well as a by-product of modern day industries and the magnitude of wastewater generation depends upon the level of technological progress of the particular industry of a particular country. It has been observed that least developed and developing countries generate a huge volume of wastewater as compared to the developed ones. This paper discusses the chemistry of water and wastewater, parameters of water for application in drinking water, wildlife and fisheries, irrigation and industrial cooling purpose. Various methods based on physical, chemical and biological treatment available for treatment of wastewater to make it reusable and less harmful to the environment on discharge. Several biological methods of waste treatment and treatment process including trickling filter, activated sludge, aerated lagoon, and waste stabilisation ponds to reduce or degrade some pollutants have been presented in this study. New approaches incorporate natural processes instead of conventional chemical treatment. The role of various microbes has been also discussed to treat various organic pollutants present in wastewater. Applications of genetic engineered microbes as well as certain metabolic engineering mediated interventions have shown significant degradation and reduction of pollutants concentration. Research on wastewater treatment suggests treatment of wastewater must be designed specifically for the particular type of effluent produced. Nevertheless, strategies can be developed for multipollutant targets using biotechnological approaches.

KEY WORDS: BIOLOGICAL TREATMENT, DDT, METABOLIC ENGINEERING, ORGANOCHLORINE, WASTEWATER

ARTICLE INFORMATION:

Corresponding Author: navneetab@dce.ac.in
Received 15th Dec, 2018
Accepted after revision 21st March, 2019
BBRC Print ISSN: 0974-6455
Online ISSN: 2321-4007 CODEN: USA BBRCBA
Thomson Reuters ISI ESC / Clarivate Analytics USA
Crossref Clarivate Analytics
NAAS Journal Score 2019: 4.31 SJIF: 4.196
© A Society of Science and Nature Publication, Bhopal India 2019. All rights reserved.
Online Contents Available at: http//www.bbrc.in/
DOI: 10.21786/bbrc/12.1/18

INTRODUCTION

Waste is defined as the unwanted or the discarded material which has no further known application and can be divided into three categories-solid, liquid and gaseous. When any undesired agent mixes with water it makes it impure and unacceptable for further use. Wastewater has been defined as water which has some impurities. Generally, it is pure water and various polluting agents in different proportion. Chemistry of pure water elaborating the physical and chemical properties of water and how its peculiar structure makes it a universal solvent has been discussed in detail later section. Wastewater is an essential a by-product of modern day industries (Buljan & Kral 2011, Shi Hanchang 2011, Miksch et al., 2015, González-Camejo et al., 2017).

From agriculture to domestic to anindustrial level, water is extensively used as a raw material. Agriculture and public health practices add many pesticides to the water making it unfit for use. From oil, food, dairy& beverages to textile & leather to pharmaceutical & chemical to paper & pulp to metal and power generating industries, each and every industry needs ahuge amount of water for its operation and is a major contributor of wastewater production. Nuclear, mining and quarries also produce agreat volume of wastewater as a by-product. For example, agricultural nitrate is one of the major reasons for groundwater pollution, (Shukla et al. 2013) (Miksch et al., 2015) (González-Camejo et al., 2017). After use of water, it is discharged as wastewater. Composition of wastewater varies to reference to its production site. Major characteristics include total organic content, solid content present in it, pH, temperature, colour, presence of heavy metals and their concentration, presence of microbes and their population etc. For reuse of this water, government agencies and various international bodies dealing with water and health have graded water into different categories. In India, Central Pollution Control Board has classified water into five classes depending upon their end use and passing the standards set by it. It is very important to know the standard parameters of water quality before its application towards human and animal consumption and for watering plants. Scientific progress in each sector contributed to exhaustion of water resources and waste generation. The amount of wastewater generation depends on the level of technological process development to the particular industry in a particular country and it will be reduced with the improvement of industrial technology. (Hammer 2001, Gogate and Pandit, 2004, Rastogi, 2010 Shi, Hanchang 2011 Rawat et al., 2011, Veerakumari, 2015, Ansari et al., 2017).

It has been observed that least developed and developing countries generate a huge volume of wastewater as compared to the developed ones. In the present review, a detailed account of water chemistry, wastewater characteristics, and wastewater treatment methods has been summarized. Also, the role of various biological methods in the treatment of a range of organic pollutants has been discussed.

Chemistry of water

Water is composed of one oxygen atom and two hydrogen atoms that form covalent bonds with the unpaired electrons of oxygen. The hydrogen atoms are placed at 0.958Å from oxygen. The angle between the two hydrogen (bond angle) is 104.5° making it a bent molecule with partial positive charges on each hydrogen and a partial negative charge on the oxygen atom. Thus, it is a polar molecule. This helps water molecules to form hydrogen bonds with other molecules, including water, (Némethy et al., 1962, Devangee Shukla, et al 2013, Veerakumari, 2015, Emiliano et al. 2017).

It is termed as a universal solvent for the ability to effect many chemical reactions and facilitating the hydrolysis, breaking the bigger molecules into their simpler forms. It possesses certain peculiar and unique physiochemical properties vital for the maintenance of life activities. It solubilises a large number of organic and inorganic compounds. Therefore, it might have been the primary resource for the origin of life. Almost all living organisms possess >70% of their mass comprising water. It is important for many biochemical reactions. It has a high affinity for salts. Physical properties of water are as follows: heat capacity 1 cal/g, heat of vaporization 540 cal/g at 0°C, latent heat of fusion 97.7 cal/g at 0°C, surface tension 76 erg/cm^2, dielectric constant 79, melting point 0°C, boiling point 100°C and viscosity 1.14 x 10^{-3} g/cm-s (Rastogi Smita, 2010 Devangee Shukla, et al 2013, Veerakumari 2015).

Parameters of water for various uses

Central Pollution Control Board (CPCB) of India has proposed various classes of water as 'A to E' about their end use. Drinking Water Source without conventional treatment but after disinfection has been categorised under Class "A" of water and possess the following characteristics: i) Total Coliforms Organisms MPN/100mL shall be 50 or less ii) pH between 6.5 and 8.5 iii) Dissolved Oxygen 6mg/L or more and iv) Biochemical Oxygen Demand (BOD_5^{20}) of 5 days at 20°C 2mg/L or less. Bureau of Indian Standards has defined Indian Standard Specifications for Drinking Water, under IS: 10500, 1992. This report provides information on the permissible and desirable limits of various parameters in drinking water. Rahmanian et al. (2015) have discussed the determination of parameters for drinking water. Class B water is designated best for organised outdoor bathing. The coli-

forms MPN/100 mL in this class is ≤500 and pH 6.5-8.5. The dissolved oxygen and the BOD_5^{20} levels are set at ≥5 ppm and ≤3 ppm respectively. Class C water is a drinking water source that is available after conventional treatment and disinfection process. The MPN for coliforms is set at ≤5000 per mL with pH 6-9 and dissolved oxygen level of ≥ 4 ppm while the BOD_5^{20} is recommended at ≤ 5 ppm. Class D water is useful for wildlife and fisheries. Its free ammonia -N is ≤ 1.2 ppm. The pH ranges between 6.5-8.5 while the dissolved oxygen is ≥ 4 ppm. Water for Irrigation, Industrial Cooling, Controlled Waste disposal comes under class "E" of water and it shall have the pH between 6 and 8.5. Additionally, the boron content shall not be more than 2mg/L and maximum Electrical Conductivity at 25°C (mhos/cm) is capped on 2250 (Ansari et al., 2009) for the purpose of proper treatment and dilution of effluent before discharge in water stream or on land. Physico-chemical characteristics of distillery effluent samples such as colour, odour, Total Solids, Total dissolved solids, Total Suspended Solids, pH, Electrical Conductivity, Total hardness, Calcium, Magnesium, Alkalinity, Chloride, Dissolved Oxygen, Biological Oxygen Demand, Chemical Oxygen Demand, Ammonical Nitrogen, Total Phosphorus, and Total Potassium were analysed and it was observed that the characteristics of spent wash and PTDE (primary treated distillery effluent.

The composition of wastewater

Wastewater is simply that part of the water supply to the community or to the industry which has been used for different purposes and has been mixed with solids, either suspended or dissolved. Wastewater is 99.9% water and 0.1% solids. The main task of treating the wastewater is to remove most or all of this 0.1% of solids (Spellman, 2013) toxic chemical products formed as secondary metabolites by a few fungal species that readily colonise crops and contaminate them with toxins in the field or after harvest. Ochratoxins and Aflatoxins are mycotoxins of major significance and hence there has been significant research on broad range of analytical and detection techniques that could be useful and practical. Due to the variety of structures of these toxins, it is impossible to use one standard technique for analysis and/or detection. Practical requirements for high-sensitivity analysis and the need for a specialist laboratory setting create challenges for routine analysis. Several existing analytical techniques, which offer flexible and broad-based methods of analysis and in some cases detection, have been discussed in this manuscript. There are a number of methods used, of which many are lab-based, but to our knowledge there seems to be no single technique that stands out above the rest, although analytical liquid chromatography, commonly linked with mass spectroscopy is likely to be popular. This review manuscript discusses (a.The composition of wastewater varies according to the primary use of water. It gives a reflection of the lifestyle and technologies enjoyed by this progressive world. Two major constituents are organic and inorganic compounds, (Rastogi, 2010, Ansari et al., 2017).

Carbohydrate, protein, fats, amino acids and volatile acids etc. come under the organic compounds while sodium, calcium, chlorine, potassium, sulphur, magnesium, bicarbonate ammonium salts and heavy metals etc. are listed as inorganic compounds by various researchers (Abdel-Raouf et al., 2012). Hydrocarbons, fats, oils, waxes and high molecular weight fatty acids are collectively referred to as oil and grease come under organic substances (Hammer 2001). Biological components constitute bacteria, fungi, virus and algae etc. Eutrophication is a common phenomenon worldwide due to the discharge of industrial wastes into open water resources which includes vast amounts of nitrogen and-phosphorous (Rawat et al., 2011, González-Camejo et al., 2017). Characteristics of wastewater from various industries

Characteristics and compositions of wastewater vary from industry to industry. Wastewater characterisation depends upon changes in colour, odour, total dissolved solids (TDS), total suspended solids (TSS), pH, conductivity, temperature, biochemical oxygen demand (BOD), chemical oxygen demand (COD) and volatile organic compounds (VOCs)etc. The physical characteristics of distillery effluent samples and observed spent wash colour to be dark brown, odour unpleasant, total solids 42400.2 ± 6.4 (CPCB: 90000-120000), total dissolve solids 38200.2 ± 4.8, total suspended solids 4200.0 ± 0.0, pH 4.2 ± 1.2 (CPCB: 3.7-4.5), electrical conductivity (µmho/cm) 16450.8 ± 8.2, total hardness 2432.4 ± 5.4 calcium 2070.0 ± 2.6 (CPCB: 2000-3500), magnesium 2260.5 ± 6.7, alkalinity 2864.5 ± 8.0, chloride 8530.2 ± 8.3(CPCB: 5000-6000), dissolve oxygen Nil, biochemical oxygen demand 32300.8 ± 10.8 (CPCB: 45000-50000), chemical oxygen demand 57164.6 ± 12.9 (CPCB: 80000-100000), ammonical nitrogen 1254.4 ± 2.4 (CPCB: 1000-2000), total phosphorus 44.4 ± 5.6 (CPCB: 200-300), total potassium 7440.2 ± 3.8 (CPCB: 8000-12000). All values given here are in mg/litre(Central Pollution Control Board, 2008) (Ansari et al., 2009)for the purpose of proper treatment and dilution of effluent before discharge in water stream or on land. Physico-chemical characteristics of distillery effluent samples such as colour, odour, Total Solids, Total dissolved solids, Total Suspended Solids, pH, Electrical Conductivity, Total hardness, Calcium, Magnesium, Alkalinity, Chloride, Dissolved Oxygen, Biological Oxygen Demand, Chemical Oxygen Demand, Ammonical Nitrogen, Total Phosphorus, and Total Potassium were analysed and it was

Table 1. Various methods of biological treatment. (Cheremisinoff, 1996) (Hoffmann, 1998) (Tchobanoglous et al., 2003) (Von Sperling, 2007) (Mara, 2009) (Butler et al., 2017)

S. No.	Process	Treatment Agents	Waste treated
1	Trickling filters (attached growth)	Packed bed covered by the microbial film	Acetaldehyde, benzene, chlorinated hydrocarbons, nylon, rocket fuel
2	Activated sludge (suspended growth)	Aerobic microorganisms suspended in wastewater	Refinery, petrochemical and biodegradable organic wastewaters
3	Aerated lagoon	Surface impoundment plus mechanical agitation	Biodegradable organic chemicals
4	Waste stabilization ponds	Shallow surface impoundments plus aeration to promote the growth of algae and bacteria and algae symbiosis	Biodegradable organic chemicals

observed that the characteristics of spent wash and PTDE (primary treated distillery effluent (Devangee Shukla, et al. 2013).

Wastewater treatment

Wastewater treatment refers to the application of various treatment methods on wastewater to make it reusable or less harmful to the environment when discharged. Methods of treatment used for removal of contaminants using physical, chemical and biological reactions are known as unit operations, and they are categorized as primary, secondary and tertiary treatment methods. Primary treatments involve physical operations such as screening and sedimentation for removal of floating and settle able solids found in wastewater. Secondary treatments involve chemical and biological processes to remove most of the organic and inorganic matters present in the wastewater. Then comes the tertiary treatment methods or advanced techniques. Treatment of wastewater must be designed specifically for the specific effluent produced (Gogate and Pandit, 2004, a review of oxidation processes operating at ambient conditions was presented. It has been observed that none of the methods can be used individually in wastewater treatment applications with good economics and high degree of energy efficiency. Moreover, the knowledge required for the large-scale design and application is perhaps lacking. In the present work, an overview of hybrid methods (the majority are a combination of advanced oxidation processes Central Pollution Control Board, 2008, Shi, Hanchang 2011).

Biological treatments of wastewater

Biological treatments of wastewater facilitate the removal of all the settleable colloidal solids and degrade or reduce the present organic as well as inorganic matters (Rawat et al., 2011). Microorganisms utilize the organic/inorganic sources present in the wastewater as a nutrient or food for growth. The process of nutrient utilisation significantly reduces the organic and inorganic loads of the wastewater. Several microorganisms including bacteria, fungus and algae (Table-2) or symposium of algae and bacteria or fungal and bacterial have been explored for wastewater remediation across the globe, (Cheremisinoff, 1996, Butler et al., 2017). Various methods have been devised to date for remediation of wastewater and they include aerobic, anaerobic and the combination of both. They are further subdivided as per their growth system into attached or suspended growth systems. Some of them are listed in Table 1 & 2.

Metabolic engineering to treat wastewater

Metabolic engineering stands for a branch of molecular biology where alternation in the genome of an organism is carried out to achieve a specific purpose of bringing specific genotypic or phenotypic changes in the concerned microorganism. Metabolic engineering is exercised to achieve many objectives such as to reduce or stop the production of by-products to optimise the yield, to increase the rate of thebiochemical process, reduce the energy consumption and ultimately to develop a strain with resistance to biotic as well abiotic stress (Yang & Liu, 2007) (Kumar and Prasad, 2011). The purpose of metabolic engineering is to obtain a robust strain of microorganism to gain optimum productivity, in the case of wastewater remediation, optimum nutrient removal to decrease the organic and inorganic loads. Mutant bacteria have also been introduced for wastewater treatment (Ostergaard et al., 2000) (Siejen & Macro 2008) (Naidoo & Adimola 2014).

Although for metabolic overproduction, very often the strains of the microorganisms are subjected to mutation and selection for yield improvement, the prospect to introduce heterologous genes and regulatory elements makes metabolic engineering, a promising area of research (Soda et al., 1999). The use of a floc-forming bacterium as the host for a recombinant plasmid was proposed. The floc-forming and phenol-degrading GEM Sphingomonas paucimobilis 551 (pS10-45. Bioaugmentation engineered bacteria have a unique position

Table 2. Microbial degradation of various organic pollutants. (Bush et al., 1961) (McCLURE et al., 1991) (Rochkind et al., 1986) (Cheremisinoff, 1996) (Smidt et al., 2000) (Wang et al., 2000) (Tchobanoglous et al., 2003) (Bidlan R, Manonmani H. K., 2007) (Seo et al., 2009) (Mandal and Mallick, 2011) (Renuka et al., 2013) (Saxena et al., 2016) (Gong et al., 2017) (Kumar et al., 2017) (Singh et al., 2017)

S. No.	Organic Pollutant	Microbes involved
1	Petroleum hydrocarbons,	*Acinetobacter, Arthrobacter, Mycobacteria, Actinomycetes, Pseudomonas etcamongbacteria; Scolecobasidium and Cladosporium among yeasts.*
2	Pesticides,herbicides, like Aldrin, Dieldrin and organophosphates like Parathion and Malathion	*Zylerionxylestrix (fungus)*
3	2, 4-D, 1,2,3-trichloropropane (TCP)	*Pseudomonas, Arthrobacter*
4	Diichlorodiphenyltrichloro ethane(DDT)	*Penicillium (fungus), Serratia marcescens (Bacteria)*
5	Kepone, piperonylic acid, Lignocellulosic wastes, Pentachlorophenol	*Pseudomonas*
6	Ethyl benzene	*Nocardiatartaricans (Bacteria)*
	Wastewater	*Calothrix sp., Lyngbya sp., Ulothrix sp, and Chlorella sp. Chlamydomonasrenhardtii, Parachlorellakessleri-I, Nannochloropsisgaditana Scenedesmussp.(Algae)*
7	Heavy metals like cadmium	*Genetically modified E. coli*
8	Chlorinated aromatic compounds	*Desulfomonile tiedjei (bacteria)*
9	Lignins from Paper mills	*Aspergillustrichosporon (Yeast), arthrobacter, Chromobacter, Pseudomonas, Xanthomonas (Bacteria)*

in the treatment of effluent from printing and dyeing industries because of its various advantages, including powerful treatment capability, good decolourisation effect, and modest impact on the surrounding of the original processing system and so on (Xie et al., 2014). McClure *et al*. discussed the role of genetic engineering in improving wastewater treatment with a focus on the degradation of recalcitrant compounds especially chlorinated aromatic compounds. They also investigated the survival and function of natural and genetically modified bacteria when inoculated into laboratory-scale activated sludge units, (McClure et al., 1991). Research on wastewater treatment suggests treatment of wastewater must be explicitly designed for the particular type of effluent produced. Banerjee *et al*. studied various aspects to increase the lipid accumulation in microalgae *Chlamydomonas reinhardtii* and stressed on metabolic engineering associated with other factors to get the desired result (Banerjee et al., 2016).

Trained microorganisms to treat wastewater

Raju *et al*. investigated the role of a consortium of microorganisms to degrade or reduce the concentration of lindane and DDT present in pesticide water. They reported enhanced green gram seed germination upon reduction of Lindane and DDT concentration when the microbial consortium was used (Raju et al., 2017). The strain of *Serratia marcescens* was found to have profound DDT degrading potential Organochlorine which was considered recalcitrant compounds were shown to degrade at enhanced rates in the presence of non-ionic surfactants such as tweens and specificdead-end metabolites of Dichlorodiphenyltrichloroethane (DDT) like Dichlorodiphenyldichloroethylene (DDE) and Dichlorodiphenyldichloroethane (DDD) have also been shown to get metabolised by indeed trained microbes (Bidlan 2007a) (Bidlan 2007b) (Bidlan 2009) (Bharadvaja et al., 2016).

CONCLUSION

Wastewater is generated from various activities in the community and also through natural processes. There are various strategies developed to reduce the levels of various contaminants in the wastewater. Most of the treatment plants use microbial remediation from the microbes already exixtinng in the sludge. Latest trend is to shift from the conventional chemical treatments to the biological treatments as these are more ecofriendly. Research is being carried out around the globe by various groups and a lot of funds are being pushed into this by many countries so that the best possible treatment methods can be implemented for facilitating clean and healthy water for a better, green and robust environment.

REFERENCES

Abdel-Raouf, N., Al-Homaidan, A.A. and Ibraheem, I.B.M. (2012), Microalgae and wastewater treatment Saudi Journal of Biological Sciences, Elsevier, 1 July.

Ansari, A.A., Khoja, A.H., Nawar, A., Qayyum, M. and Ali, E. (2017), Wastewater treatment by local microalgae strains for CO2 sequestration and biofuel production Applied Water Science, Springer Berlin Heidelberg, Vol. 7 No. 7, pp. 4151–4158.

Ansari, F., Awasthi, A.K. and Srivastava, B.P. (2009), Physicochemical Characterization of Distillery Effluent and its Dilution Effect at Different Levels Archives of Applied Science Research, Scholars Research Library, Vol. 4 No. 4, pp. 1705–1715.

Banerjee, C., Dubey, K.K. and Shukla, P. (2016), Metabolic Engineering of Microalgal Based Biofuel Production: Prospects and Challenges, Frontiers in Microbiology, Vol. 7, p. 432.

Bidlan R, Manonmani HK, Kunhi AAM. (2007) Indian Patents. 209454:A Process For Degration Of Dichloro Dipheny Ltrichloro Ethane (Ddt) Using An Improved Strain Of *Serratia marcescens*.

Bidlan R., Manonmani HK. (2007a), A Process For Enhanced Degradation Of Dichloro-Dip Henyl-Trichloroethane (DDT) Indian patent.

Bidlan R., Manonmani HK. (2007b), A Process For The Preparation Of Biocatalysts Useful For The Degradation Of Dichlorodiphenyldichloroethylene (Dde) Indian patent.

Bidlan Rajkumar, Manonmani HK. (2009), A Process For The Preparation Of Biocatalysts For The Remediation Of Dichlorodiphenyldichlo Roethane (Ddd /Tde) Containing Industrial Effluents Indian patent.

Brini, Emiliano, Brini, E., Fennell, C.J., Fernandez-Serra, M., Hribar-Lee et al (2017) How water's properties are encoded in its molecular structure and energies Chemical reviews, Vol. 117, No. 19, pp. 12385-12414.

Buljan J. and I. Kral (2011), Introduction To Treatment of Tannery Effluents United Nations Industrial Development Organization, p. 10.

Bush, A.F., Isherwood, J.D. and Rodgi, S. (1961) Dissolved Solids Removal from Waste Water by Algae Journal of the Sanitary Engineering Division, ASCE, Vol. 87 No. 3, pp. 39–60.

Butler, E., Hung, Y.-T., Suleiman Al Ahmad, M., Yeh, R.Y.-L., Liu, R.L.-H. and Fu, Y.-P. (2017), Oxidation pond for municipal wastewater treatment Applied Water Science, Springer Berlin Heidelberg, Vol. 7 No. 1, pp. 31–51.

Central Pollution Control Board. (2008), Guidelines for Water Quality Management CPCB, available at:https://doi.org/10.1074/jbc.M002965200.

Cheremisinoff, N.P. (1996), Biotechnology for Waste and Wastewater Treatment, Noyes Publications.

Devangee Shukla, et al (2013) Physicochemical Analysis of Water from Various Sources and Their Comparative Studies IOSR Journal of Environmental Science, Toxicology, and Food Technology , Vol. 5, No. 3, pp. 2319-2402.

Gogate, P.R. and Pandit, A.B. (2004) A review of imperative technologies for wastewater treatment II: hybrid methods Advances in Environmental Research, Pergamon, Vol. 8 No. 3–4, pp. 553–597.

Gong, T., Xu, X., Che, Y., Liu, R., Gao, W., Zhao, F., Yu, H., et al. (2017), Combinatorial metabolic engineering of *Pseudomonas putida* KT2440 for efficient mineralization of 1,2,3-trichloropropane Scientific Reports, Vol. 7 No. 1, p. 7064.

González-Camejo, J., Serna-García, R., Viruela, A., Pachés, M., Durán, F., Robles, A., Ruano, M.V., et al. (2017), Short and long-term experiments on the effect of sulphide on microalgae cultivation in tertiary sewage treatment Bioresource Technology, Vol. 244 No. Pt 1, pp. 15–22.

Hammer MJ, J.H.M. (2001), Water and Wastewater Technology / Mark J. Hammer, Mark J. Hammer, Jr. - Version Details - Trove.

Hoffmann, J.P. (1998) Wastewater Treatment With Suspended And Nonsuspended Algae Journal of Phycology, Vol. 34 No. 5, pp. 757–763.

Indian Standard Specifications for Drinking Water, under IS: 10500, 1992 by Bureau of Indian Standards.

Kumar L, Roy A, Saxena G, Kundu K, Bharadvaja N. (2017) Isolation , Identification and biomass productivity analysis of microalga *Scenedesmus rubescens* from DTU Lake Vol. 8 No. July, pp. 56–67.

Kumar, R.R. and Prasad, S. (2011) Metabolic Engineering of Bacteria Indian Journal of Microbiology, Springer, July.

Mandal, S. and Mallick, N. (2011) Utilization and biodiesel production by the green microalga *Scenedesmus obliquus* Applied and Environmental Microbiology, Vol. 77 No. 1, pp. 374–377.

Mara, D. (2009) Waste stabilization ponds: Past, present and future Desalination and Water Treatment, Taylor & Francis Group, Vol. 4 No. 1–3, pp. 85–88.

McClure, N.C., Fry, J.C. and Weightman, A.J. (1991) Genetic Engineering for Wastewater Treatment Water and Environment Journal, John Wiley & Sons, Ltd, Vol. 5 No. 6, pp. 608–616.

Miksch, K., Cema, G., Corvini, P.F.-X., Felis, E., Sochacki, A., Surmacz-Górska, J., Wiszniowski, J., et al. (2015) R&D priorities in the field of sustainable remediation and purification of agro-industrial and municipal wastewater New Biotechnology, Vol. 32 No. 1, pp. 128–132.

Naidoo Shalinee and Ademola Olaniran (2014) Treated wastewater effluent as a source of microbial pollution of surface water resources International journal of environmental research and public health, Vol. 11, No.1, pp. 249-270.

Némethy, George, and Harold A. Scheraga (1962) Structure of water and hydrophobic bonding in proteins. I. A model for the thermodynamic properties of liquid water The Journal of Chemical Physics , Vol. 36, No. 12, pp. 3382-3400.

Ostergaard, S., Olsson, L. and Nielsen, J. (2000) Metabolic engineering of Saccharomyces cerevisiae. Microbiology and Molecular Biology Reviews : MMBR, American Society for Microbiology (ASM), Vol. 64 No. 1, pp. 34–50.

Raju, S.M., Bashambu, D., Bidlan, R., Sharma, J.G. and Kumar, S. (2017), Enhancement In Seed Germination Through Simultaneous Degradation Of Organochlorine Pesticides (Lindane And Ddt) By A Novel Microbial Consortium International

Journal of Advance Research in Science and Engineering, Vol. 6, pp. 707–13.

Rahmanian, Nejat, et al. (2015), Analysis of physiochemical parameters to evaluate the drinking water quality in the State of Perak, Malaysia Journal of Chemistry, Hindawi publications, pp. 1-10.

Rastogi, S.C. (2010), Biochemistry, 3rd ed., Tata McGraw-Hill Education.

Rawat, I., Ranjith Kumar, R., Mutanda, T. and Bux, F. (2011), Dual role of microalgae: Phycoremediation of domestic wastewater and biomass production for sustainable biofuels production Applied Energy, Elsevier, Vol. 88 No. 10, pp. 3411–3424.

Renuka, N., Sood, A., Ratha, S.K., Prasanna, R. and Ahluwalia, A.S. (2013), "Nutrient Sequestration, Biomass Production By Microalgae And Phytoremediation Of Sewage Water International Journal of Phytoremediation, Vol. 15 No. 8, pp. 789–800.

Rochkind, M.L., Blackburn, J.W. and Sayler, G.S. (1986), Microbial decomposition of chlorinates aromatic compounds.

Saxena G, Kumar L, Hariri SM, Bhardvaja N (2016) Identification of Potential Culture Conditions for Enhancing the Biomass Production of Microalga *Chlorella minutissima* Expert Opinion on Environmental Biology, SciTechnol, Vol. s1.

Seo, J.-S., Keum, Y.-S. and Li, Q.X. (2009) Bacterial Degradation of Aromatic Hydrocarbons Int. J. Environ. Res. Public Health, Multidisciplinary Digital Publishing Institute (MDPI), Vol. 6 No. 1, pp. 278–309.

Shi, Hanchang (2011) Industrial wastewater-types, amounts and effects Encyclopedia of Life Support Systems, Vol. 1, pp. 191–204.

Siezen, RJ, and Marco Galardini (2008) Genomics of biological wastewater treatment Microbial biotechnology, Vol. 1, No. 5, pp. 333.

Singh, A.K., Sharma, N., Farooqi, H., Abdin, M.Z., Mock, T. and Kumar, S. (2017), Phycoremediation of municipal wastewater by microalgae to produce biofuel International Journal of Phytoremediation, Vol. 19 No. 9, pp. 805–812.

Smidt, H., Akkermans, A.D.., Van Der Oost, J. and De Vos, W.M. (2000) Halorespiring bacteria-molecular characterization and detection Enzyme and Microbial Technology, Vol. 27, Elsevier, pp. 812–820.

Soda, S., Uesugi, K., Ike, M. and Fujita, M. (1999) Application of a floc-forming genetically engineered microorganism to a sequencing batch reactor for phenolic wastewater treatment Journal of Bioscience and Bioengineering, Elsevier, Vol. 88 No. 1, pp. 85–91.

Spellman, F.R. (2013), Handbook of Water and Wastewater Treatment Plant Operations, Springer, Vol. 23, CRC Press, available at:https://doi.org/10.1007/s13398-014-0173-7.2.

von Sperling, M. (2007), Wastewater Characteristics, Treatment and Disposal, Iwa Publishing. London.

Tchobanoglous, G., Burton, F.L. (Franklin L., Stensel, H.D. and Metcalf & Eddy. (2003), Wastewater Engineering : Treatment and Reuse, McGraw-Hill. Veerakumari, L. (2015), Biochemistry, MJP Publ.

Wang, C.L., Maratukulam, P.D., Lum, A.M., Clark, D.S. and Keasling, J.D. (2000), "Metabolic engineering of an aerobic sulfate reduction pathway and its application to precipitation of cadmium on the cell surface", Applied and Environmental Microbiology, Vol. 66 No. 10, pp. 4497–4502.

Xie, X.H., Liu, N., Jiang, H. and Zhu, L.Y. (2014) Construction and Application of Engineered Bacteria for Bioaugmentation Decolorization of Dyeing Wastewater: A Review Journal of Geoscience and Environment Protection, Scientific Research Publishing, Vol. 02 No. 02, pp. 84–88.

Yang ST, Liu X, Z.Y. (2007) Metabolic Engineering - Applications, Methods, and Challenges Bioprocessing for Value-Added Products from Renewable Resources - New Technologies and Applications - Elsevier Publications.

International Research Journal of Engineering and Technology (IRJET) e-ISSN: 2395-0056
Volume: 06 Issue: 04 | Apr 2019 www.irjet.net p-ISSN: 2395-0072

Code Cloning using Abstract Syntax Tree

Gunjan Chugh[1], Divya Mahajan[2], Nainika Sehgal[3], Akanksha Paul[4], Leena Budhiraja[5]

[1]*Assistant Professor, Department of Information Technology, Dr. Akhilesh Das Gupta Institute of Technology & Management, New Delhi, India*
[2,3,4,5]*Student, Dr. Akhilesh Das Gupta Institute of Technology & Management, New Delhi, India*

Abstract - *Today, most of the software that are being developed by the developers consists of code clones in it. Although it is sometimes necessary to meet deadlines, to save time but in the long run it always emerge as the source of bad design. It increases maintenance cost which is one of the important phases the of software development life cycle. Not only this, it sometimes becomes the source of defects in our code which results in the huge demand for resource utilization thereby increasing the cost for both development and maintenance phase of the software development the life cycle. In order to detect those clones, a number of detection techniques have been presented so far. In this paper, an approach to detect code clones from the software is presented using Abstract Syntax Tree(AST). The aim of proposing this approach is to provide a solution to these code clones by an approach that is simple yet powerful enough to easily detect the code clones present in the software.*

Key Words: **clone detection; code cloning; clone class; clone pair; code clones.**

1. INTRODUCTION

A clone is a code segment that has been created through duplication of another piece of code [4]. Code cloning is the practice of duplicating existing source code for use elsewhere within a software system [7]. It is a process of replicating code blocks by doing copy-and-paste in order to save time and meet deadlines. Doing copy and paste proves to be a better solution in the short term to meet the deadlines but in the long run it results in the huge amount of cost that the organization have to spent in order to maintain the software not only this but also it results in the increase in amount of resource utilization. If faults found in one code block, then the entire cloned blocks need modification and it becomes more difficult tasks to maintain if the system becomes big.

For detecting these code clone's numerous techniques have been proposed. Text based techniques are the earliest and provide the easiest way of clone detection. In these techniques, code is compared line by line in the form of simple strings.[9] Then token based technique was proposed which is also the primary step for abstract syntax tree approach that is presented in this paper. In this techniques, the code is first transformed into tokens before comparing. In abstract syntax tree approach, lexical analyzer is used to transform the code into tokens then source code is transformed into AST using the required language parser and then code clones are detected by finding similar sub trees from the AST. [8] This method determines exact tree matches; a number of adjustments are needed to detect equivalent statement sequences, commutative operands, and nearly exact matches. We additionally suggest that clone detection could also be useful in producing more structured code, and in reverse engineering to discover domain concepts and their implementation [6].

2. RELATED TERMINOLOGY

Clone Pair

Two code segments form a clone pair, if they are related to each other by an equivalence relation [3]. An equivalence relation holds all reflexive, symmetric and transitive relations. A clone try is outlined as a try of matching code segments.

Clone Class

Clone class is defined as a set of code segments with similar code portions. Each code segment in a clone class forms a clone pair with other code segments of that class.

Classifications of Class

Code segments can be identical in two ways. Either they can be identical on the basis of their program text or they can be functionally identical. They are classified as follows: -

i. On the basis of Program text

On the basis of Program text these clones are classified in three ways namely: -

1) **Type-1 Clones**

If a code segment is copied as it is with some minor amendments in whitespaces, layout and comments then it comes under type-1 or exact clones [5]. In figure 2.1, code segment 2 is an exact copy of code segment 1.

Code1:-	Code 2:-

int s=0, p=1, n=5;
while (n > 0)
{
s= s+n;
p=p* n;
n= n-1;
}
	int s=0, p=1, n=5;
	while (n > 0)
	{
	s= s+n;
	p=p* n;
	n= n-1;
	}

Fig-2.1 Exact Clones

2) **Type-2 Clones**

If a code segment is copied with some amendments in name of the variables, functions, types and identifiers as shown in figure 2.1 then it comes under type-2 or renamed clones.

Code1:-	Code 2:-

int s=0, p=1, n=5;
while (n > 0)
{
s= s+n;
p=p* n;
n= n-1;
}
	int a=0, b=1, c=5;
	while (c > 0)
	{
	a=a+c;
	b=b*c;
	c=c-1;
	}

Fig-2.2 Renamed Clones

3) **Type-3 Clones**

If a code segment is copied with some changes like insertion or deletion of statements along with change in name of variables, functions and type, then it comes under type-3 or near miss clones.

Code 2:-	Code 3:-

int a=0, b=1, c=5;
while (c > 0)
{
a=a+c;
b=b*c;
c=c-1;
}
	int a=0, b=1, c=5,s=0;
	while (c > 0)
	{
	a=a+c;
	b=b*c;
	s= a+b;
	c=c-1;
	}

Fig -2.3: Near- miss Clones

ii. On the basis of Functional Similarity

4) On the basis of Functional Similarity, clones are classified as follows: -

If two code segments perform the same functionality but they are having different syntax, then they are said to be type-4 or semantic clones [5]. These clones are the most difficult to detect.

Code 1:-	Code 2:-

int num1=2, num2=6, i, prod=0;
for(i=1; i<= num2; i++)
{
prod+= num1;
}
	int num1=2, num2=6, prod;
	prod= num1 * num2;

Fig -2.4: Semantic Clones

3. OCCURRENCE OF CODE CLONES

Software clones appear for many reasons:
1.Code reuse by copying existing codes.
2.Programming styles of the programmers.
3.Instantiation of definitional computations.
4. Failure to identify/use abstract data types.
5. Enhancement in the performance.
6. Shortage of time or other resources. [8]

4. METHODOLOGY OF PROPOSED WORK

4.1. Clone Detection Using ASTs

To find the code fragments which yields similar result or are similar in syntax are the main problem in clone detection. So for this, first the program or the file in which we are trying to find clones is fragmented into parts before comparison. Then, it has to be determined as impossible, two arbitrary program fragments halting under the same circumstance is not determined. Hence, it is impossible theoretically to finalize that they compute identical results. [8]

There are some steps in the process of clone detection: -

i. The code is first parsed and then an AST is produced for it using the lexical analyzer for parsing.

ii. Then algorithms are applied to find clones.

a. The purpose of the basic algorithm, which is the first algorithm, is to detect sub –tree clones.

b. The second algorithm is sequence detection algorithm. This is helpful in the detection of statement and in the declaration of sequence clones.

c. The third algorithm attempts to generalize combinations of other clones and looks for more complex near miss-clones.

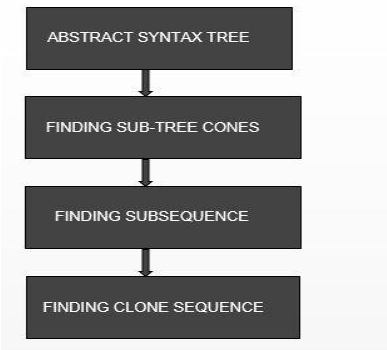


Fig 4.1: Methodology

4.2. Finding sub-tree clones

For finding sub-tree clones compare every subtree to every other sub-tree for equality. Though it seems easy in theory but in practice there are many problems associated with it like: near-miss clone detection, sub-clones, and scale. Near misses can be handled by comparing trees for similarity rather than exact equality whereas the scale problem is harder.

In order to handle this problem associated with practical implementation of finding sub-cones we generally partition the sets of comparisons by categorizing sub-trees with hash values. The approach is based on the tree matching technique for building DAGs for expressions in compiler construction [2]. This allows the easy detection of actual subtree clones. But this approach works well only when we are trying to find exact clones but when we are trying to locate near-miss clones hashing on complete subtrees fails because for a good hash function, it must include all elements of the tree, thus sorts trees with minor differences into different buckets.

This problem can be solved by choosing an artificially bad hash function. This bad hash function should be characterized in such a way that the main properties one wants to find on near-miss clones that are preserved. A hash function that ignores small subtrees is a good choice. [9]

4.3. Finding clone sequences

Finding clone sequences means to detect statement sequence clones in ASTs. And for that we are using the Basic algorithm as a foundation. Sequences of subtrees appear in AST as a consequence of the occurrence in the dialect grammar of rules encapsulating sequences of zero or more syntactic constructs. These sequence rules are typically expressed by the use of left or right recursion on production rules [2].

4.4. Generalization

This method consists of visiting the parents of the already-detected clones and check if the parent is a near miss clone too. An advantage of this method is that any near miss clones must be assembled from some set of exact sub clones, and therefore no near miss clones will be missed. [9]

5. BENEFITS OF CODE CLONING

Detection and removal of code clones promises decreased software maintenance costs of possibly the same magnitude. There are variety of benefits provided by code cloning detection and they are as follows: -

- **Reduced Probability of Defects** :-Detection of the code clones in the source code may also reduce the probability of bug propagation in the system.
- **Low Resource Requirement**: -Code cloning detection results in reducing the system size due to which compilation time as well as memory requirements for the system also get reduced. It may also result in less expensive software and hardware upgrades than the one having code clones in it. [9]
- **Reduced Maintenance Work and Cost: -**Code cloning may result in reduced maintenance effort because during the maintenance phase if an error or bug is found in one code fragment, then all its corresponding clones should be find out to detect the same error or bug. This makes maintenance a complex and time consuming task. Code cloning multiplies the effort required during maintenance. Hence detecting code clones helps to reduce the maintenance work and cost.
- **Reduced Chances of Bad Design: -**Code duplication also causes unfavourable effects on the system's design. It results in poor abstraction and raises difficulty in reusing the code in future projects. [2]
- **Inconsistent Updates:** -Code cloning may result in inconsistent updates because if there is a need to modify a piece of code, one needs to modify all clone segments of that piece of code. This can be avoided by code clone detection and removal.
- **Helps in Reducing Code Size :-**If the detected code clones are replaced by function calls to a generic code segment performing the same functionality as that of the code clone, then it results in reducing the complexity and size of software system. It also improves maintainability and readability of code. [1]
- **Better Understanding of Problem :-**If working of a cloned segment is apprehended, one is able to understand the working of all duplicate code segments of the cloned segment.
- **Helps in Reducing Code Size :-**If the detected code clones are replaced by function calls to a generic code segment performing the same functionality as that of the code clone, then it results in reducing the complexity and size of software system. It also improves maintainability and readability of code.

- **Discovering Domain: -**Clone detection is not only helpful in producing more structured code but also in discovering domain concepts and their idiomatic implementations. [8]

6. CONCLUSION

The code clone detection is an issue in the software system which decrease the software's comprehensibility as well as maintainability. Therefore, its analysis and detection is necessary for improving the quality, maintenance and design of the software system. In this paper, discussion in terms of attributes based on code clone detection is presented. The clone detection method is implemented using abstract syntax trees (ASTs), which for finding exact and near miss clones for arbitrary fragments in the source code [2]. Since detection done in the program structure. clones can be factored in the source using standard transformational methods. The approach is based on variations of methods for compiler to find common subtree on elimination using hashing and then we find subsequence. The method is straightforward to implement using parsing technology.

REFERENCES

[1] Lee, Y. J., Lim, J. S., Ji, J. H., Cho, H. G., & Woo, G. (2012). Plagiarism detection among source codes using adaptive methods. *KSII Transactions on Internet and Information Systems (TIIS)*, *6*(6), 1627-1648.

[2] Baxter, I. D., Yahin, A., Moura, L., Sant'Anna, M., & Bier, L. (1998, November). Clone detection using abstract syntax trees. In *Proceedings. International Conference on Software Maintenance (Cat. No. 98CB36272)* (pp. 368-377). IEEE.

[3] Morshed, M., Rahman, M., & Ahmed, S. U. (2012). A literature review of code clone analysis to improve software maintenance process. *arXiv preprint arXiv:1205.5615*.

[4] Jiang, Z. M., & Hassan, A. E. (2007, September). A framework for studying clones in large software systems. In Seventh IEEE International Working Conference on Source Code Analysis and Manipulation (SCAM 2007) (pp. 203-212). IEEE.

[5] Roy, C. K., & Cordy, J. R. (2007). A survey on software clone detection research. *Queen's School of Computing TR*, *541*(115), 64-68.

[6] Baxter, I. D., Yahin, A., Moura, L., Sant'Anna, M., & Bier, L. (1998, November). Clone detection using abstract syntax trees. In *Proceedings. International Conference on Software Maintenance (Cat. No. 98CB36272)* (pp. 368-377). IEEE.

[7] Kapser, C. (2009). Toward an understanding of software code cloning as a development practice.

[8] Ijptjournal.org. (2019). *Code Cloning Detection using Abstract Syntax Tree*. [online] Available at: http://www.ijpttjournal.org/volume-9/IJPTT-V9P407.pdf [Accessed 17 Apr. 2019].

[9] Baxter, I., Yahin, A., Moura, L. and Bier, L. (2019). Code Cloning Using Abstract Syntax Tree. *www.eecs.yorku.c*, [online] p.2. Available at: http://www.eecs.yorku.c [Accessed 17 Apr. 2019].

BIOGRAPHIES



Gunjan Chugh, she is currently pursuing PhD with specialization in Computer Science from Delhi Technological University, New Delhi. She received her M. Tech degree in Computer Science from Banasthali University, Rajasthan in 2013 & is currently working in Department of Information Technology, at Dr. Akhilesh Das Gupta Institute of Technology and Management, New Delhi. Her research interest includes Artificial Intelligence, Machine Learning and Information Security.



Divya Mahajan, she is currently pursuing Bachelor of Technology with specialization in Information Technology from Guru Gobind Singh Indraprastha University, New Delhi. Her research interest lies in software engineering, data mining and Machine learning.



Nainika Sehgal, she is currently a student who is pursuing Btech in Information Technology from IP university. She has searched and made a research paper on Code detection using an abstract syntax tree. The main motive was to study about clones and different techniques and how to detect it. Her career objective is to continuously enhance her knowledge, skills and experience by getting involved in challenging work environment and utilize them for personal and organizational growth to the best of her ability.



Akanksha Paul, currently she is a student in Guru Gobind Singh Indraprastha University, New Delhi pursuing her B. Tech in Information Technology. She made a research paper on Code Cloning for better understanding of clones and code reuse.



Leena Budhiraja, currently she is pursuing B. Tech in Guru Gobind Singh Indraprastha University, New Delhi in Information Technology. Her objective of life is to pursue a challenging career in life and enhance her knowledge.

ResearchGate

See discussions, stats, and author profiles for this publication at: https://www.researchgate.net/publication/336796193

Comparative Study and Measurement of Form Errors for the Component Printed by FDM and PolyJet Process

Article · October 2019

DOI: 10.18280/i2m.180404

CITATIONS
0

READS
3

3 authors, including:



Nagendra Kumar Maurya
GL Bajaj Institute of Technology and Management
20 PUBLICATIONS **5** CITATIONS

SEE PROFILE

Some of the authors of this publication are also working on these related projects:

conferance paper View project

All content following this page was uploaded by Nagendra Kumar Maurya on 25 October 2019.

The user has requested enhancement of the downloaded file.

IIETA International Information and Engineering Technology Association
Advancing the World of Information and Engineering

Instrumentation Mesure Métrologie
Vol. 18, No. 4, August, 2019, pp. 353-359
Journal homepage: http://iieta.org/journals/i2m

Comparative Study and Measurement of Form Errors for the Component Printed by FDM and PolyJet Process

Nagendra Kumar Maurya[1,2*], Vikas Rastogi[1], Pushpendra Singh[1]

[1] Department of Mechanical Engineering, Delhi Technological University, Delhi 110042, India
[2] Department of Mechanical Engineering, G.L Bajaj Institute of Technology & Management, Gr. Noida 201310, India

Corresponding Author Email: nagendramnnit@gmail.com

https://doi.org/10.18280/i2m.180404

Received: 17 April 2019
Accepted: 26 July 2019

Keywords:
rapid prototyping, dimensional accuracy, flatness analysis, IT grades, surface roughness, cylindricity analysis, analysis of roundness

ABSTRACT

In Rapid Prototyping (RP) parts are manufactured layer-upon-layer. The part accuracy primarily influenced by process parameters, material, geometry of parts and types of RP technology used. This work presents the comparative study of dimensional accuracy, form error (roundness, flatness and cylindricity), surface roughness, cost analysis and tolerance grade of a automotive parts (connecting rod) generated through fused deposition modeling system (Ultimaker-2, MakerBot Replector-2) and polyjet 3D printing system (Objet30). CATIA-V6 was used for the 3D modeling and coordinate measuring machine (CMM) was employed for the measurements of dimensions. Optical profilometer was considered to measure the surface roughness of component. ISO UNI EN 20286-I (1995) and DIN 16901 standards was used for the evaluating IT grades for each selected dimension. Total cost of prototype generated by different 3D printers was calculated on the basis of cost of build material, cost of support material, labour cost and machine cost. The results of measurement show that quality of prototype fabricated by Objet30 is better than Ultimaker and MakerBot. Form error and surface roughness of objet30 printer was good enough to produce industrial grade prototype. The novel contribution of this work lies in the fact that no such studies was conducted using complex shape geometry in the archival literature.

1. INTRODUCTION

Prototypes are the most important for the realization of concepts in design analysis and manufacturing [1]. Prototyping is the first steps in product development and manufacturing. Rapid Prototyping has becoming as a solution to manufacturing industry globally [2]. Rapid prototyping (RP) is a technology that can fabricate prototype rapidly and efficiently any three-dimensional (3D) physical model without the restrictions of geometric complexities. Many of the RP technologies have been developed over the past several decades [3]. Some of the techniques being commonly used for the prototyping are stereo-lithography apparatus (SLA), fused deposition modeling (FDM), selective laser sintering (SLS), poly-jet amongst many other processes [4]. In 1983 Charles (Chuck) has invented the first stereo-lithography (SLA) machine, patented in 1986 and commercial available in 1988, which is a form of additive manufacturing (AM) technology used for creating models, pattern making, scaled model etc. in layer by layer fashion using photo-polymerization process. RP is also applied to direct manufacture of components in small to medium sized batches [5]. RP has potential to reduce the manufacturing lead time of the product up to 50 %, even when the relative part complexity is very high [6]. Poly-jet technology is an RP technology that utilizes a high precision 3D printing process. The poly-jet process utilized ink-jet technology combined with ultraviolet (UV) light for the curable materials (photo-polymers) to produce accurate physical prototypes with small layer thicknesses [7].

Dimensional accuracy and surface quality of objets fabricated using many RP processes is generally poor due to the staircase effect., 2015 [8]. Dimensional accuracy is primarily influenced by the process parameters and types of material. Garrett et al., 2015 [9] have carried out experimental investigation using design of experiments (DOE) testing protocol to evaluate dimensional accuracy of FDM part. The process parameters used in FDM process during fabrication is dominant factors which define the quality and functionality of any manufactured part. Owing to this reason, several studies have carried out to develop a statistical model between the processing conditions and dimensional accuracy of parts built by FDM process [10-12]. Selective laser sintering is also very popular RP techniques sued for the prototyping. Several studies have conducted to develop optimum process parameters for the SLS [13-15]. Stereolithography is one of the oldest rapid prototyping techniques, still frequently used due to its better Nizam et al. [16]; Onuh and Hon [17]; Zhou et al. [18] have attempted to optimizing the process parameters for improving the DA and quality of surface manufactured by stereolithography. Vacuum casting is very popular for the investment casting and pattern making for the mold design. For this resign good DA, shape and surface quality become primary importance. Several attempts have made to optimize process parameters [19-20].

In this work, automotive component (connecting rod) was considered to compare the process capabilities of three 3D printers namely Objet30 (polyjet), Ultimaker (FDM) and MakerBot (FDM). Comparative studies were carried out on the basis of DA, form error (flatness, cylindricity and circularity), cost of the prototype and international tolerance

(IT) grades.

2. DETAILS OF THE EXPERIMENTS AND DATA ANALYSIS

2.1 Details of FDM machine

Fused Deposition Modeling (FDM) is the second most widely used rapid prototyping technology, developed in 1988 and commercially available in 1992. A plastic filament is unwound from a coil and supplies material to an extrusion nozzle. Nozzle is heated to melt the plastic has a mechanism which allows the flow of the melted plastic to be turned on and off [21]. The nozzle is mounted to an X-Y plotter type mechanism to trace out the part contours. There is a second extrusion nozzle for the support material (different from the model material). Nozzle is moved over the table in the required geometry, it deposits a thin bead of extruded plastic to form each layer and plastic hardens immediately after being squirted from the nozzle and bonds to the layer below. This process continued and part is buildup layer by layer. The schematic diagram of the FDM machine used in the experimentation is shown in Figure 1. A CAD model, created in CATIA V6, is first tessellated and sliced into layers of 0.1mm thickness to get contour information of each layer. In this study PLA plastic material is used for both build as well as support material.

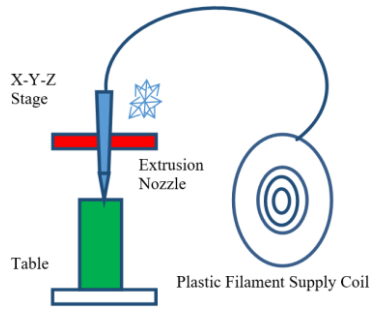


Figure 1. Fused deposition modelling system

2.2 Details of PolyJet machine

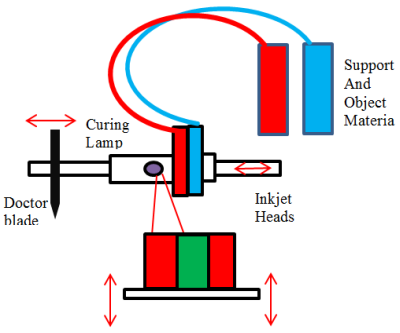


Figure 2. PolyJet 3D Printing system

PolyJet 3D printing technology is developed by Israeli company Objet Geometries Ltd in 2000. It is a potentially encouraging replacement for stereolithography. In this method photopolymers are used for both build as well as support material. Inkjet head is use to layer wise deposition for both builds and support materials. It subsequently completely cures each layer after it is deposited with a UV flood lamp mounted on the print head. The support material which is removed by washing it away with pressurized water in a secondary operation. In this work RGD-840 was used as build material and SUP705 for support materials. Thickness of each layer is around 28 µm. The schematic diagram of the polyjet machine used in the experimentation is shown in Figure 2.

2.3 3-D modelling of the scaled model radial engine connecting rod

In the recent years, digital fabrication has slowly infiltrated the field of prototype making. At present there are more than twenty different types of 3D printers are available for the rapid prototyping. In order to analyze the effect of DA, shape error, surface roughness, cost of prototype and tolerance grade scaled model of radial engine connecting rod was consider as a case study. For creating the geometry 3D CAD software CATIVA V6 was used. Figure 3 shows the dimensions of the selected component. The 3D CAD model of the specimen used in the experiment is as shown in Figure-4(a). RP used standard .STL file format only. The sliced model is as shown in Figure 4(b).

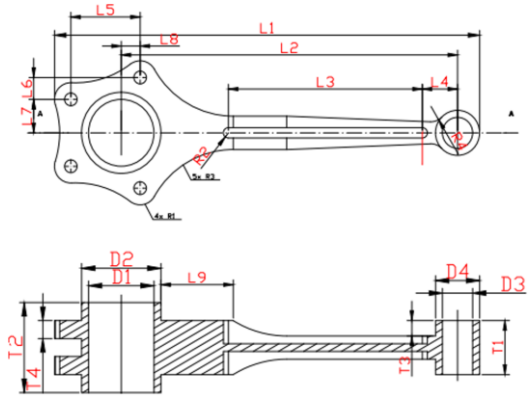


Figure 3. Dimension of the component

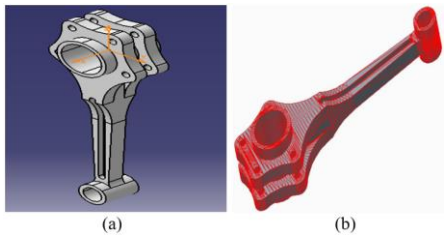


Figure 4. (a): 3D CAD Model of Connecting Rod; (b): Sliced Model of Connecting Rod

2.4 Digital fabrication of the component

For comparing the process capability of the selected RP technology (Objet30, Ultimaker and MakerBot) component fabricated at the optimum process parameters conditions of each printer. VeroBlue840 was used as the build material and SUP705 as support material for the Objet30 printer. For Ultimaker and MakerBot, polylactic acid (PLA) was used as build and support material both. Figure 5 shows the printing of automotive component through Objet30. Figure 6(a) shows the fabricate component by Objet30, Figure 6(b) shows the fabricated component through MakerBot and Figure 6(c) shows the generated component by Ultimaker.

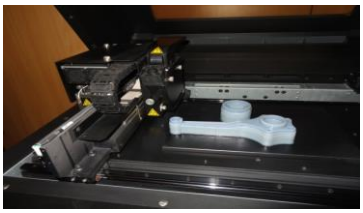


Figure 5. Printing of automotive part by Objet30



Figure 6. (a) Connecting rod printed by Objet360 (polyjet) printer; (b) Connecting rod printed by MakerBot (FDM) printer; (c) Connecting rod printed by Ultimaker (FDM) printer

2.5 Measurement of dimension

The coordinate measuring machine (CMM) as shown in Figure 7, was used for the measurement of linear as well as radial dimension of the automotive component (connecting rod and piston). For connecting rod total 12 linear dimension, 4 radial dimension and 4 circular dimensions were measured. Total 9 linear dimensions were measured along the print bed (X-Y axis) and 3linear dimension were measured perpendicular to the print bed (Y-Z axis) as shown in Table 1 and Table 2 respectively. Table 3 shows the measured radial dimensions for the connecting rods and Table 4 shows the circular dimensions.

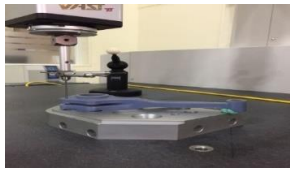


Figure 7. Measurement of the dimensions of connecting rod

Table 1. Linear dimension along XY plane

Dimension	CAD Dimension	Objet 30	Ultimaker	MakerBot	%error Objet 30	%error Ultimaker	%error MakerBot
L1	202.56	200.75	200.69	200.09	0.89	0.92	1.22
L2	160.26	160.10	160.30	159.03	0.10	0.02	0.77
L3	92.40	92.07	92.00	91.38	0.36	0.43	1.10
L4	16.80	16.91	17.15	16.81	0.64	2.10	0.03
L5	33.00	32.21	33.25	32.35	2.41	0.77	1.97
L6	10.20	10.27	10.12	9.69	0.65	0.82	5.05
L7	15.60	15.26	15.30	16.00	2.18	1.93	2.55
L8	9.00	8.89	8.86	9.17	1.25	1.58	1.91
L9	33.00	32.86	30.82	32.98	0.43	6.61	0.06
		Average % error			0.99	1.69	1.63
		Maximum % error			2.41	6.61	5.05
		STDEV			0.81	1.97	1.54

Table 2. Linear dimension along YZ plan

Dimension	CAD Dimension	Objet 30	Ultimaker	MakerBot	%error Objet 30	%error Ultimaker	%error MakerBot
T1	25.2	26.156	25.341	25.37	3.79	0.56	0.67
T2	42	42.36	41.564	41.79	0.86	1.04	0.50
T3	9.7	9.9	9.4	9.49	2.06	3.09	2.16
		Average			2.24	1.56	1.11
		Maximum			3.79	3.09	2.16
		STDEV			1.48	1.35	0.92

Table 3. Circular dimension of connecting rod.

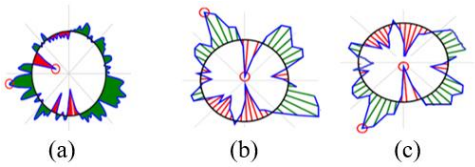
Dimension	CAD Dimension	Objet 30	Ultimaker	MakerBot	%error Objet 30	%error Ultimaker	%error MakerBot
D1	14.4	14.62	13.887	14.02	1.53	3.56	2.64
D2	21	21.1	20.657	20.71	0.48	1.63	1.38
D3	31.2	31.39	30.373	30.64	0.61	2.65	1.79
D4	37.8	37.67	37.233	37.19	0.34	1.5	1.61
		Average			0.74	2.34	1.86
		Maximum			1.53	3.56	2.64
		STDEV			0.54	0.97	0.54

Table 4. Radial dimension of connecting rod

Dimension	CAD Dimension	Objet 30	Ultimaker	MakerBot	%error Objet 30	%error Ultimaker	% error MakerBot
R1	21.00	20.96	20.88	20.95	0.19	0.60	0.24
R2	2.50	2.46	2.45	2.44	1.68	1.98	2.40
R3	43.20	43.23	42.94	44.04	0.07	0.60	1.94
R4	7.80	7.79	7.76	7.99	0.19	0.52	2.44
		Average			0.53	0.92	1.75
		Maximum			1.68	1.98	2.44
		STDEV			0.77	0.70	1.04

2.6 Measurement of roundness, cylindricity and flatness

For checking the circularity of cylindrical portion (big end), roundness was measured by using coordinate measuring machine (CMM). Table 5 shows the measured value of form error (roundness, cylindricity and flatness) in the selected component. Figure 8 (a) shows the graphical representation of roundness in big end of the connecting rod of Objet30. Figure 8(b) and Figure 8(c) shows roundness in the component printed by Ultimaker and MakerBot respectively.



(a) (b) (c)

Figure 8. (a) Roundness of big end of the connecting rod of Objet 30; (b) Roundness of big end of the connecting rod of Ultimake; (c) Roundness of big end of the connecting rod of MakerBot

Table 5. Measurement of roundness, cylindricity and flatness.

S.N	Measurement	Objet30 (polyjet)	MakerBot (FDM)	Ultimaker (FDM)
1	Roundness (mm)	0.0686	0.1673	0.2917
2	Cylindricity (mm)	0.0001	0.3426	0.0330
3	Flatness (mm)	0.1630	0.3692	0.1678

2.7 Measurement of surface roughness

The measurement of surface roughness was performed by using optical profilometer as shown in Figure 9. Surface roughness of connecting rod was measured on top surface only. All the surface roughness parameters Ra, Rz and Rq were measured for both polyjet and FDM printed component. Table 6 shows the measured value of surface roughness. Figure 10 (a-c) shows the variation of surface roughness and 3D surface of SR for the printed component along the length.

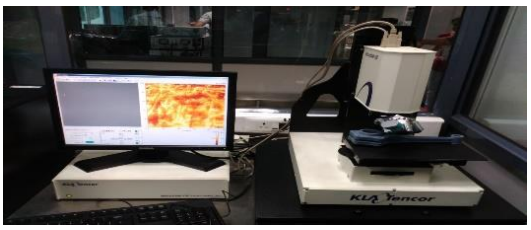
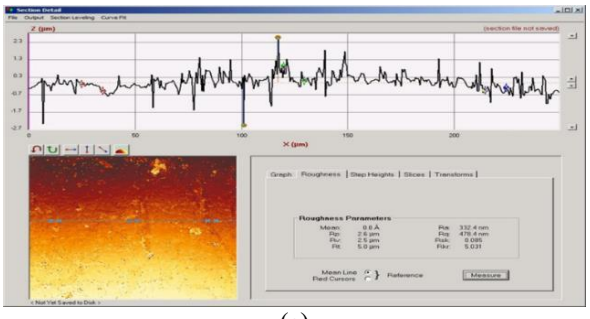
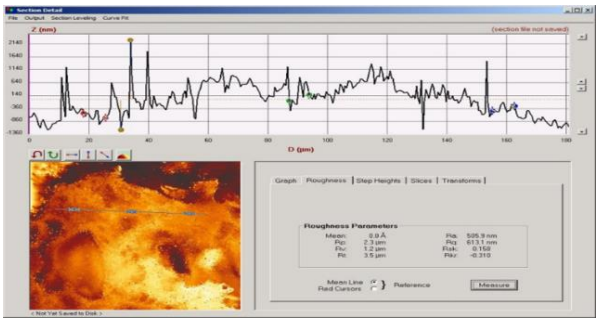


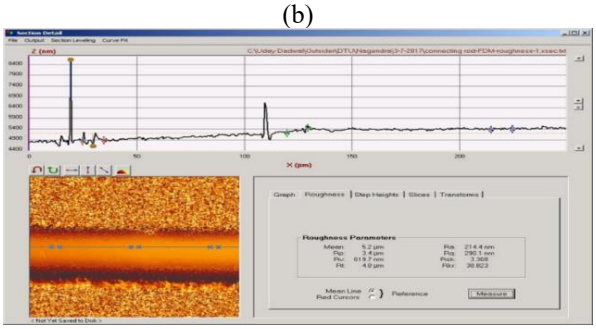
Figure 9. Optical profilometer setup for the measurement of surface roughness



(a)



(b)



(c)

Figure 10. (a) surface roughness of MakerBot component; (b) Surface roughness of Ultimaker component; (c) Surface roughness of Objet30 component

Table 6. Measured surface roughness parameters

S.N	Roughness Parameters	Objet 30	MakerBot	Ultimaker
1	Average roughness height Ra (nm)	214.4	332.4	505.9
2	Mean roughness height Rq (nm)	290.1	478.3	613.1
3	Average peak to valley height Rz nm)	1043.3	2304.2	2600.7
4	Peak roughness height Rp (nm)	3423.3	2634.6	2331.3
5	Peak valley height Rv (nm)	619.7	2530.7	1241.3
6	Peak height to peak valley height Rt nm)	4043.0	5165.3	3572.6

3. RESULTS AND DISCUSSION

3.1 Analysis of dimensional accuracy

Figure 11 shows the comparative analysis of average percentage error in DA of polyjet and FDM technology. Four different types of dimensions were selected for the analysis i.e. linear dimension in X-Y plane, linear dimension Y-Z plane, radial dimension and circular dimension. Table (1-4) shows the measured dimension in terms of average percentage error. It is observed that the dimensional accuracy of polyjet is better than the FDM components except along the Y-Z plane. It was also noticed that most of the dimensions are smaller than the CAD model dimension due to the shrinkage occurs during the sintering of component. In FDM shrinkage was found more as compared to polyjet technology. In FDM process there are always present air gapes which lead to the shrinkage. Along the Y-Z plane polyjet always produce dimension greater than the actual dimension because it forms a base on platform which yields the large size. The average percentage error in radial and circular dimension in the component produced by

Objet30 was very less as compared to Ultimaker and MakerBot

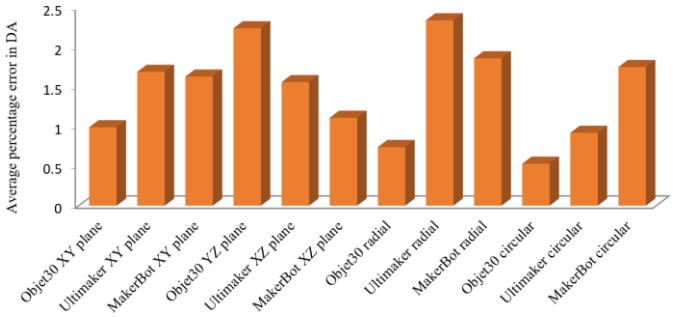


Figure 11. Comparison of average percentage error in dimensions of polyjet and FDM

3.2 Analysis of form error

Figure12 highlights the comparison of form error (circularity, cylindricity and flatness) in the selected component generated by Objet30, Ultimaker and MakerBot printer. Experimental results raveled that polyjet technology have minimum form error as compared to the FDM. The measured value of form error is as reported in Table 5. For perfect cylinder the value of cylindricity is '0'. In our analysis it was found that cylindricity in the component fabricated by objet 30 is 0.0001, which is close to '0'.

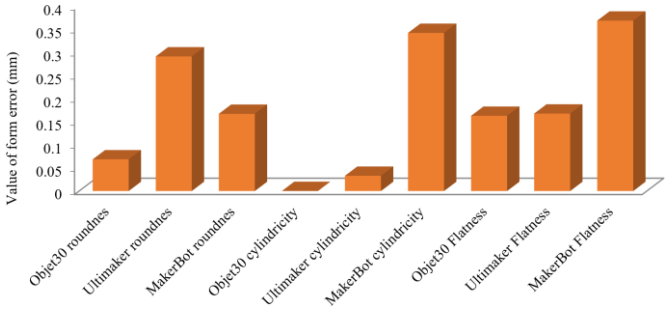


Figure 12. Form error comparison of polyjet and FDM technology

3.3 Analysis of surface roughness parameters

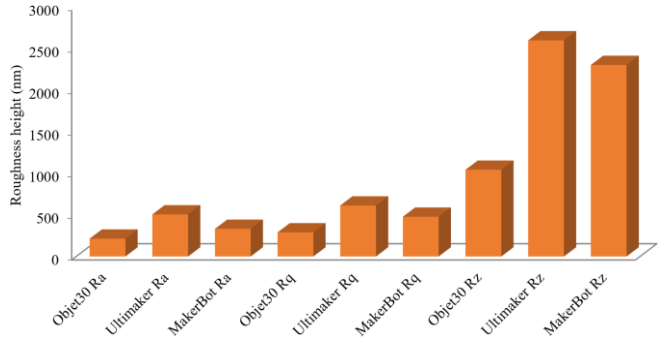


Figure 13. Roughness parameters comparison of polyjet and FDM technology

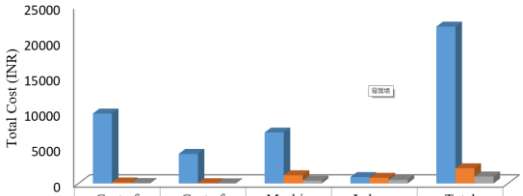
Table 6, shows the measured value of various surface roughness parameters namely; average surface roughness (R_a), mean average surface roughness height (R_q) and average peak to valley height (R_z). The variation of surface roughness and 3D plots of the surface roughness parameters are as shown in Figure 10 (a-c) The completive analysis of the measured surface roughness is as shown in Figure 13. The experimental results revealed that component generated through polyjet technology have superior surface quality than FDM components. The roughness parameter R_z is much greater than Ra and R_z value, it implies that the surface irregularities is high in the components fabricated by using additive manufacturig technology.

3.4 Cost analysis

Cost analysis of additive manufacturing is important parameters for the designers while selecting the RP technology for printing the components. Cost analysis is very difficult for any RP technology because it depends on the number of factors which are locally vary place to place. However in this paper cost analysis was calculated as per the Indian scenario. The factors which are mainly influence the cost are amount of materials (build and support) consume, machine cost and labors cost. Total cost was calculated by using Eq. (1). Figure 14 show the summary of cost analysis report of this study.

$$T_c = C_b*A_b+C_s*A_s+ (t_{pre} + t_{post}) C_{lc} +t_{pre}* C_m \quad (1)$$

where, (Tc) is the total cost in (INR), C_b is the unit cost per kg of build material in (INR), C_s is the unit cost per kg of support material in (INR), A_b is the amount of build material consumed in (Kg), A_s is the amount of support material consumed in (Kg), t_{pre} is the preprocessing time in (hrs), t_{post} is the post processing time in (hrs), C_{lc} is the labour cost and C_m is the machine cost in (hrs).



	Cost of Build materia l	Cost of support materia l	Machin e Cost	Labour Cost	Total Cost
Objet 30	9828	4160	7160	900	22048
MakerBot Replicator 2	147	37.5	1150	800	2134.5
Ultimaker	60.5	14.1	406	500	980.6

Figure 14. Cost comparison of prototype fabricated by different 3D printers

3.5 Calculation of tolerance IT grade

For checking the tolerance grade of fabricated component ISO UNI EN 20286-I (1995) and DIN 16901 standard was considered. The measured dimension was used to evaluate tolerance unit 'n' derived from the fundamental tolerance 'i'. The fundamental tolerance 'i' is used for the range of nominal dimension. The fundamental tolerance 'i' and tolerance unit 'n' can be expressed by using the following Equation 2 and Equation 3 respectively Maurya et al. [22].

$$i = 0.45\sqrt[3]{D} + 0.001D \quad (2)$$

$$n = 1000\left(\frac{|Dn-Dm|}{i}\right) \quad (3)$$

where, 'D' is the geometric mean diameter, Dn is the nominal dimension and Dm is the measured dimension. Table 7 shows the IT grades for each linear dimension of the component

fabricated by Objet30, Ultimaker and MakerBot 3D printers. Results revealed that tolerance in the linear dimension depends on the size and orientation of the component. Within the same component different dimension have different tolerance grade in each selected technology. The lower value of IT grade implies that better dimensional accuracy. Table 8 shows the IT grade of radial dimension. Likewise linear dimension radial dimension also have different IT grade for the different size. Most of the radial dimension generated through Objet30 have lower IT grade.

Table 7. IT grade for linear dimension as per the DIN 16901 standards

Dimension	Objet 30 (polyjet)			Ultimaker (FDM)			MakerBot (FDM)		
	LD	n	IT grade	LD	n	IT grade	LD	n	IT grade
L1	200.75	267.5	IT11	200	276.4	IT11	200	97.5	IT9
L2	160.1	28.6	IT7	160	7.1	IT3	159	191.0	IT11
L3	92.07	72.5	IT9	92	87.9	IT10	91.3	151.6	IT11
L4	16.91	66.2	IT10	17.1	210.7	IT13	16.8	60.2	IT10
L5	32.21	279.3	IT13	33.2	88.4	IT10	32.3	49.5	IT9
L6	10.27	42.1	IT9	10.1	48.2	IT10	9.69	349.2	IT14
L7	15.26	204.7	IT13	15.3	180.6	IT13	16	445.5	IT15
L8	8.89	87.3	IT11	8.86	111.1	IT12	9.17	222.2	IT14
L9	32.86	49.5	IT9	30.8	770.6	IT15	32.9	42.4	IT9
T1	26.156	436.1	IT14	25.3	64.3	IT11	25.3	358.6	IT14
T2	42.36	127.3	IT11	41.5	154.1	IT11	41.7	201.5	IT12
T3	9.9	158.7	IT13	9.4	238.1	IT14	9.49	325.4	IT14

Table 8. IT grade for Radial dimension as per the ISO standards for plastic component

Dimension	Objet 30 (polyjet)			Ultimaker (FDM)			MakerBot (FDM)		
	RD	(n)	IT grade	RD	(n)	IT grade	RD	(n)	IT grade
D1	31.39	67.2	IT10	30.373	292.3	IT13	30.64	265.1	IT13
D2	37.67	46.0	IT9	37.233	200.4	IT12	37.19	169.7	IT12
D3	14.62	132.5	IT12	13.887	308.9	IT14	14.02	361.2	IT14
D4	21.1	45.6	IT9	20.657	156.5	IT12	20.71	177.9	IT12
R1	20.96	18.2	IT7	20.88	54.7	IT11	20.95	22.8	IT8
R2	2.46	67.5	IT12	2.45	84.3	IT12	2.44	101.2	IT13
R3	43.23	10.6	IT5	42.94	91.9	IT10	44.04	296.9	IT13
R4	7.79	7.9	IT6	7.76	31.7	IT9	7.99	150.0	IT12

4. CONCLUSIONS

In this paper comparative study of process capability of three different 3D printers namely Objet30, Ultimaker and MakerBot have been evaluated. For the purpose of analyzing this technology automotive component (connecting rod) was selected. comparison was carried out on the basis of linear DA, radial DA, circular DA form error (circularity, cylindricity and flatness), surface roughness, cost of the component and IT tolerance grade. ISO UNI EN 20286-I (1995) and DIN 16901 standards was used for the evaluating IT grades for each selected dimension. The major finding of this research work was highlighted as:

(1) The average percentage error in DA along XY plane (build platform) for Objet30 (0.99 %), Ultimaker (1.69 %) and Makerbot (1.63 %) were found. Objet30 has minimum percentage error along the XY plane.

(2) The average percentage error in DA along YZ plane (perpendicular to build platform) for Objet30 (2.24 %), Ultimaker (1.56 %) and Makerbot (1.11 %) were found. MakerBot have minimum percentage error along the YZ plane.

(3) In case of radial dimension average percentage of DA of objet30 (0.53 %), Ultimaker (0.92 %), MakerBot (1.75 %) were found.

(4) Average percentage error in circular dimension of Objet30 (0.74 %), Ultimaker (2.34 %) and MakerBot (1.86) were found.

(5) Component generated through polyjet technology (objet30) have minimum form error. The measured value of form error for Objeted-30 was roundness (0.0686 mm), cylindricity (0.0001 mm) and flatness (0.1630 mm).

(6) All the surface roughness parameters Ra, Rq, Rt, Rv, Rz and Rv was measured by using optical profilometer. Table shows the measured value of surface roughness in (nm). Component fabricated through Objet30 have minimum surface roughness.

(7) Cost analysis of the component was calculated based on the build material, support material, labour cost and machine cost. Table shows the Summary of cost report of three different technologies for our selected component. Total cost prototype generated through Objet 30 is very high as compared to Ultimaker and MakerBot.

(8) Within the same component different dimension have different tolerance for each printer. Comparatively IT grade of the dimensions in the part fabricated by Objet30 have lower IT grade which implies that better DA.

REFERENCES

[1] Jaina, P., Kuthe, A.M. (2013). Feasibility study of manufacturing using rapid prototyping: FDM approach. Procedia Engineering, 63: 4-11. https://doi.org/10.1016/j.proeng.2013.08.275

[2] Maurya, N.K., Rastogi, V., Singh, P. (2018). Experimental investigations for improving part strength in fused deposition modeling. International Journal of Engineering & Technology, 7(4.39): 457-461.

https://doi.org/10.14419/ijet.v7i4.39.24124
[3] Kumar, K., Kumar, G.S. (2015). An experimental and theoretical investigation of surface roughness of poly-jet printed parts. Virtual and Physical Prototyping, 10(1): 23-34. https://doi.org/10.1080/17452759.2014.999218
[4] Maurya, N.K., Rastogi, V., Singh, P. (2019). Experimental and computational investigation on mechanical properties of reinforced additive manufactured component. EVERGREEN Joint Journal of Novel Carbon Resource Sciences & Green Asia Strategy, 6(3): 207-214.
[5] Senthilkumaran, K., Pandey, P.M., Rao, P.V.M. (2012). Statistical modeling and minimization of form error in SLS prototyping, Rapid Prototyping Journal, 18(1): 38-48. https://doi.org/10.1108/13552541211193485
[6] Melenka, G.W., Schofield, J.S. (2015). Evaluation of dimensional accuracy and material properties of the MakerBot 3D desktop printer. Rapid Prototyping Journal, 21(5): 556-571. https://doi.org/10.1108/RPJ-09-2013-0093
[7] Sood, A.K., Ohdar, R.K., Mahapatra, S.S. (2009). Improving dimensional accuracy of fused deposition modelling processed part using grey Taguchi method. Materials and Design, 30: 4243-4252. https://doi.org/10.1016/j.matdes.2009.04.030
[8] Singh, J., Singh, R., Singh, H. (2017). Experimental investigations for dimensional accuracy and surface finish of polyurethane prototypes fabricated by indirect rapid tooling: a case study. Prog Addit Manuf, 2(1-2): 85-97. https://doi.org/10.1007/s40964-017-0024-0
[9] Singh, R. (2011). Process capability study of polyjet printing for plastic components. Journal of Mechanical Science and Technology, 25(4): 1011-1015. https://doi.org/10.1007/s12206-011-0203-8
[10] Senthilkumaran, K., Pandey, P.M., Rao, P.V.M. (2009). Influence of building strategies on the accuracy of parts in selective laser sintering. Materials and Design, 30: 2946-2954. https://doi.org/10.1016/j.matdes.2009.01.009
[11] Nizam, A., Gopal, R.N., Naing, L., Hakim, A.B., Samsudin, A.R. (2006). Dimensional accuracy of the skull models produced by rapid prototyping technology using stereolithography apparatus. Archives of Orofacial Sciences, 1; 60-66.
[12] https://www.semanticscholar.org/paper/Dimensional-Accuracy-of-the-Skull-Models-Produced-Nizam-Naing/028d696644f241534b0ebd211a9c84e9789877a3#citing-papers, accessed on 16 December 2018.
[13] Pennington, R.C., Hoekstra, N.L., Newcomer, J.L. (2004). Significant factors in the dimensional accuracy of fused deposition modelling. Institution of Mechanical Engineers, 219(1): 89-92. https://doi.org/10.1243/095440805X6964
[14] Mohamed, O.A., Masood, S.H., Bhowmik, J.L. (2017). Experimental investigation for dynamic stiffness and dimensional accuracy of FDM manufactured part using IV-Optimal response surface design. Rapid Prototyping Journal, 23(4): 736-749. https://doi.org/10.1108/RPJ-10-2015-0137
[15] Onuh, S.O., Hon, K.K.B. (2011). Improving stereolithography part accuracy for industrial applications. The International Journal of Advanced Manufacturing Technology, 17(1): 61-68. https://doi.org/10.1007/s001700170210
[16] Gibson, I.R., Brent, D.S. (2015). 3D Printing, Rapid Prototyping, and Direct Digital Manufacturing. Additive Manufacturing Technology. Springer Science and Business Media, New York.
[17] Onuh, S.O., Hon, K.K.B. (2011). Integration of rapid prototyping technology into FMS for agile manufacturing. Integrated Manufacturing Systems, 12(3): 179-186. https://doi.org/10.1108/09576060110391138
[18] Zhou, J.G., Herscovici, D., Chen, C.C. (2000). Parametric process optimization to improve the accuracy of rapid prototyped stereolithography parts. International Journal of Machine Tools & Manufacture, 40(3): 363-379. https://doi.org/10.1016/S0890-6955(99)00068-1
[19] Farzadi, A., Waran, V., Solati-Hashjin, M., Rahman, Z.A.A., AsadiM., Osman, N.A.A. (2015). Effect of layer printing delay on mechanical properties and dimensional accuracy of 3D printed porous prototypes in bone tissue engineering. Ceramics International, 41(7): 8320-8330. https://doi.org/10.1016/j.ceramint.2015.03.004
[20] Stevinson, B., Bourell, D.L., Joseph, J.B. (2006). Dimensional stability during post-processing of selective laser sintered ceramic performs. Virtual and Physical Prototyping, 1(4): 209-216. https://doi.org/10.1080/17452750601107003
[21] Cho, U., Wood, K.L., Crawford, R.H. (1998). Online functional testing with rapid prototypes: A novel empirical similarity method. Rapid Prototyping Journal 4(3): 128-138. https://doi.org/10.1108/13552549810223000
[22] Chang, D.Y., Huang, B.H., (2010). parts using the fused deposition modeling process. The International Journal of Advanced Manufacturing Technology, 53(9-12): 1027-1037. https://doi.org/10.1007/s00170-010-2882-1
[23] Maurya, N.K., Rastogi, V., Singh, P. (2019). Investigation of dimensional accuracy and international tolerance grades of 3D printed polycarbonate parts. Materials Today: Proceedings. https://doi.org/10.1016/j.matpr.2019.06.007

View publication stats

arXiv:1910.12919v1 [physics.app-ph] 28 Oct 2019

Comparing domain wall synapse with other Non Volatile Memory devices for on-chip learning in Analog Hardware Neural Network

Divya Kaushik*[1], Utkarsh Singh*[2], Upasana Sahu[1],
Indu Sreedevi[2] and Debanjan Bhowmik[1]
*These authors contributed equally to the work.
[1]Department of Electrical Engineering,
Indian Institute of Technology Delhi, New Delhi-110016, India
[2]Department of Electronics and Communication Engineering,
Delhi Technological University, Delhi-110042, India
E-mail: debanjan@ee.iitd.ac.in

Abstract

Resistive Random Access Memory (RRAM) and Phase Change Memory (PCM) devices have been popularly used as synapses in crossbar array based analog Neural Network (NN) circuit to achieve more energy and time efficient data classification compared to conventional computers. Here we demonstrate the advantages of recently proposed spin orbit torque driven Domain Wall (DW) device as synapse compared to the RRAM and PCM devices with respect to on-chip learning (training in hardware) in such NN. Synaptic characteristic of DW synapse, obtained by us from micromagnetic modeling, turns out to be much more linear and symmetric (between positive and negative update) than that of RRAM and PCM synapse. This makes design of peripheral analog circuits for on-chip learning much easier in DW synapse based NN compared to that for RRAM and PCM synapses. We next incorporate the DW synapse as a Verilog-A model in the crossbar array based NN circuit we design on SPICE circuit simulator. Successful on-chip learning is demonstrated through SPICE simulations on the popular Fisher's Iris dataset. Time and energy required for learning turn out to be orders of magnitude lower for DW synapse based NN circuit compared to that for RRAM and PCM synapse based NN circuits.

1 Introduction

Crossbar array based analog hardware Neural Network (NN) is considered to be extremely time and energy efficient in executing NN algorithms for data classification applications because it computes at the location of memory itself unlike CPU, GPU and even the recent digital neuromorphic chips which all have memory and computing separate at their

smallest cores [1, 2, 3, 4, 5, 6]. Such crossbar based NN needs an analog Non Volatile Memory (NVM) device, also known as synapse, at each of the intersection points of the crossbars. Typically a Resistive Random Access Memory (RRAM) or a Phase Change Memory (PCM) device is used as synapse [1, 7, 8, 9, 10]. Training the NN in hardware (on-chip learning) is achieved by modulating the conductances of the synapses, corresponding to weights stored in synapses, with electrical programming pulses at every iteration. Though the conductance of RRAM and PCM synapses changes by orders of magnitude due to programming pulses, conductance response characteristic is highly non-linear and asymmetric (between positive and negative conductance update) [1, 11, 12, 13]. This leads to issues with design of peripheral circuits for on-chip learning. Learning accuracy suffers. Time and energy consumed in the learning process are also very high [1, 11, 12, 13, 9].

Spin orbit torque driven Domain Wall (DW) device based on heavy metal-ferromagnet hetero-structure has been recently proposed and experimentally demonstrated to exhibit synaptic behaviour [3, 14, 15, 16, 17, 18, 19, 20]. In Section II of this paper, we simulate such DW synapse based on experimentally calibrated micromagnetic model. We show that though the range of conductance variation is much smaller for DW synapse than RRAM and PCM synapse, the conductance response of DW synapse to programming current pulse is linear and symmetric unlike RRAM and PCM synapse. In Section III, we design crossbar array of DW synapses in SPICE circuit simulator, with the synapses being Verilog-A models developed from our micromagnetic simulation results. Fully Connected Neural Network (FCNN) algorithm, with Stochastic Gradient Descent (SGD) based weight/ conductance update, has been used here for on-chip learning [17, 21]. Conductance of DW synapse has been quantized here unlike in Bhowmik *et al.* [17] to take the effect of DW pinning by defects into account [22, 23, 24]. Despite the quantization, high accuracy is obtained on a popular machine learning dataset- Fisher's Iris [25], in our circuit simulations. We next show that the time taken and energy consumed for on-chip learning of the DW synapse based NN circuit are orders of magnitude lower than RRAM and PCM synapse based NN circuit. Section IV concludes the paper. To the best of our knowledge, this is the first comparison study between a spintronic synapse and RRAM/ PCM synapse, with respect to on-chip learning in NN hardware.

2 Device Level Comparison

Schematic of our heavy metal/ ferromagnetic metal hetero-structure based domain wall based synapse is shown in Fig. 1. The operating physics of the device has been discussed extensively in [3, 14, 15, 17]. The core physics is that of spin orbit torque driven DW motion, which has been extensively studied through simulations and experiments in the past[26, 27, 28, 29]. When in-plane current ("write" current) flows through the heavy metal layer ("write" path), a DW in the ferromagnetic layer above the it experiences spin orbit torque. If the DW is of Neel type due to presence of Dzyaloshinskii Moriya Interaction

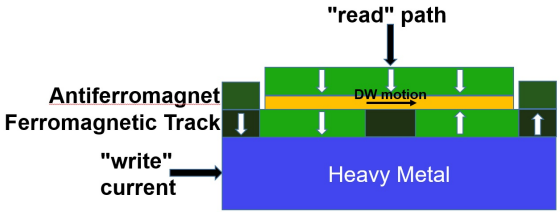


Figure 1: Schematic of Domain Wall (DW) synapse.

(DMI) [26, 27, 30, 31] at the interface, it moves even in the absence of magnetic field,as observed in several experiments[26, 27, 30] and also our micromagnetic simulations (Fig. 2).

In this paper, we consider a device with lateral dimensions 1000 nm × 50 nm. Thickness of the heavy metal (Pt) layer is taken to be 10 nm, which is greater than the spin diffusion length. Hence, we can consider the vertical spin current density injected by the heavy metal layer on the ferromagnetic layer above it (J_s) = in-plane charge current density (J_c) × spin Hall angle (0.07 here, considering Pt) [37, 38, 39]. Thickness of the ferromagnetic layer above the heavy metal layer is taken to be 1 nm. Dynamics of the moments of this layer under the influence of this spin current is simulated using micromagnetic simulation package "mumax3" [36] to model such spin current driven DW motion inside it. We choose micro-magnetic simulation parameters for the ferromagnetic layer based on that used for Pt(heavy metal)/ CoFe (ferromagnet)/ MgO devices in the simulation study of Emori *et al.* [30], which is based on experimentally observed spin orbit torque driven DW motion in the same devices. The parameters can also be found in Supplementary Material (Section 1) accompanying this paper.

Since the DW is of Neel type (DMI = 1.2×10^{-3} J/m^2), average magnetization inside the wall ($\vec{M_{avg}}$) and direction of spin polarization of the electrons at the interface of heavy metal and ferromagnet due to current flowing through heavy metal ($\vec{\sigma}$) form a non-zero cross product (Fig. 2). The effective magnetic field experienced by DW is equal to that cross-product [26, 28, 30]. As a result, DW moves as seen in our micro-magnetic simulations (Fig. 2). Triangular notch regions with Perpendicular Magnetic Anisotropy (PMA) constant = 9×10^5 J/m^3 are present on the edges of the simulated ferromagnetic layer in our simulations. PMA in rest of the layer = 8×10^5 J/m^3. These notch regions mimic defects, which pin the domain wall for in-plane charge current lower than a certain threshold value [15, 22, 23, 24, 31]. Hence, our micro-magnetic simulation Fig.(3(a)) shows that only above a certain threshold value of current density ($\approx 5 \times 10^6$ A/cm^2), velocity of the domain wall is linearly proportional to the current density [32]. Hence in our device we have only moved the domain wall with a current pulse (3 ns long) of fixed magnitude (25 μA)(Fig. 2),corresponding to a current density of 5×10^6 A/cm^2 (Fig. 2) so that the domain wall is never pinned by defects [22, 23, 24]. Pinned ferromagnetic regions are present at

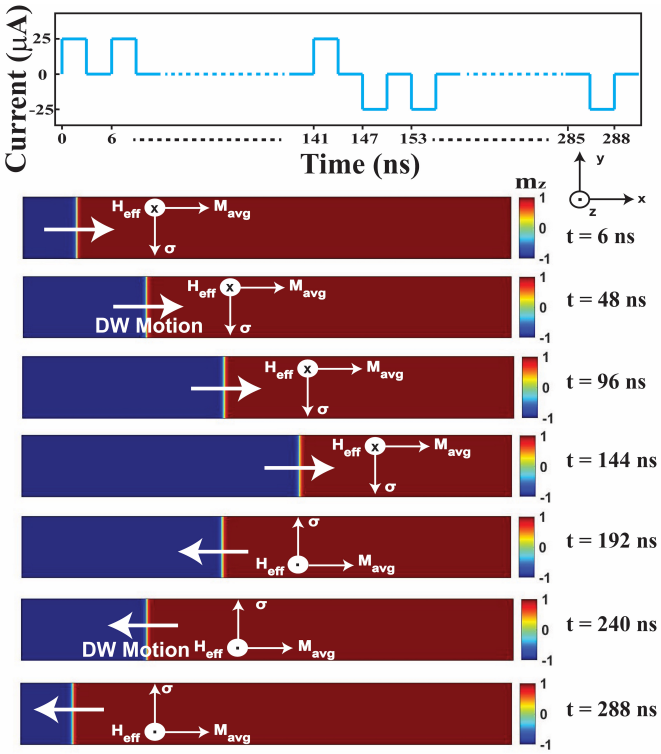


Figure 2: (a) "Write" current pulses applied on the heavy metal layer of constant magnitude (25 μA) and opposite polarities as a function of time. (b) DW motion in the ferromagnetic layer, above the heavy metal layer, shown for different time instants corresponding to different current pulses in (a).

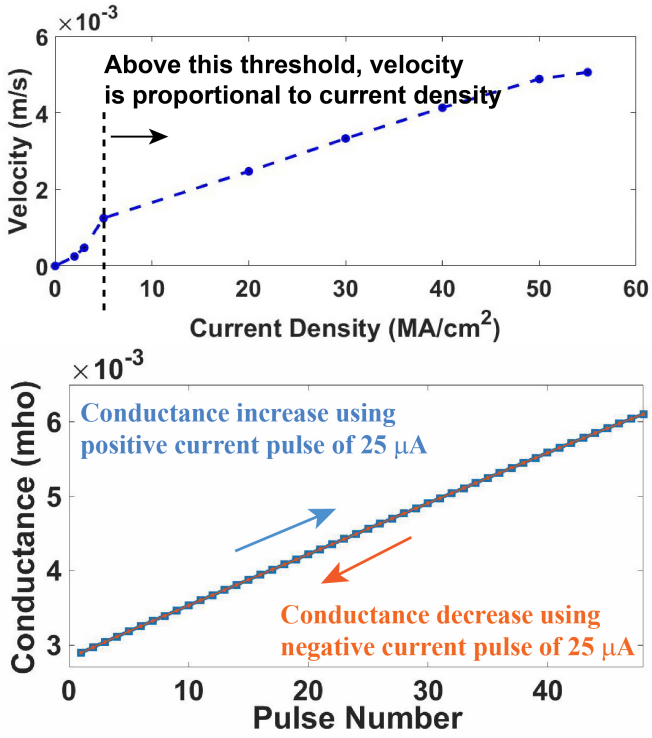


Figure 3: (a) Velocity vs. in-plane charge current density, obtained from micro-magnetic simulation of the ferromagnetic free layer of the DW synapse device in which the DW moves. (b) Conductance response of DW synapse as a function of programming "write" current pulse.

each edge of the free layer to stabilize the DW at the edge and prevent it from getting destroyed[3, 14, 33].

Following [14] conductance of the "read" path (vertical tunnel junction structure in Fig. 1) of the synapse is given by,

$$G^{synapse} = (G_{max} + G_{min})/2 - ((G_{max} - G_{min}) < m_z > /2) \quad (1)$$

where $< m_z >$ represents the average out of plane magnetization component of the free layer ($< m_z > = 1$ corresponds to up and $< m_z > =$ -1 corresponds to down), G_{max} is maximum conductance of MTJ and G_{min} is minimum conductance of MTJ. Taking the Resistance-Area product of the MTJ to be [34] 4.04×10^{-12} ohm/m^2 and TMR ratio of 120 % [35], $G_{min} \approx 2.9 \times 10^{-3}$ mho and $G_{max} \approx 6.1 \times 10^{-3}$ mho. Moment of the fixed layer is in down direction (Fig. 1).

As observed from our micromagnetic simulation, "write" current pulse of magnitude 25 μA and positive polarity always moves DW to the right by a fixed distance of $\approx$ 20 nm (Fig.

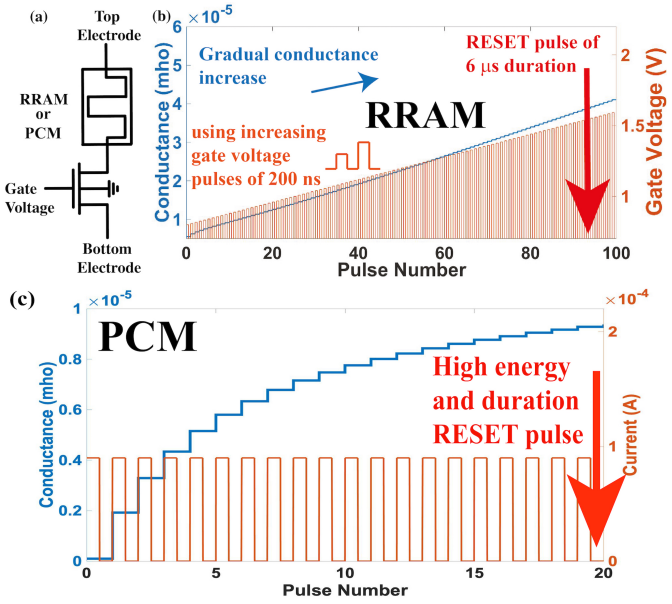


Figure 4: (a) Schematic of RRAM device connected to transistor. (b) Conductance increase in RRAM by applying gate voltage pulses of increasing magnitude at the transistor of in (c) Conductance increase in PCM device by application of constant magnitude gate voltage pulses at the transistor.

2). Hence $< m_z >$ decreases and following equation (1) conductance increases by a step of 0.071×10^{-3} mho (Fig. 3(b)). Current pulse of same magnitude and negative polarity moves DW to the left, $< m_z >$ increases and conductance decreases by the same step of 0.071×10^{-3} mho (Fig. 3(b)). Hence conductance response to a series of programming "write" current pulses of equal magnitude (25 μA) is linear and is also symmetric between positive and negative pulses. Also conductance of DW synapse and hence the corresponding weight of the synapse only takes quantized values and thus we take defect pinning into account. Energy consumed through Joule heating per programming pulse of 25 μA for conductance increase/ decrease by a single step is calculated to be 0.18 fJ (Table I).

Next we compare the conductance response of this DW synapse with that of typical RRAM and PCM synapse. Verilog-A model provided by [40], experimentally benchmarked against [41], has been used for RRAM modeling. Following the 1T1M (one transistor, one memristor) configuration [42, 43, 44] we connect this RRAM device with a 65 nm technology node transistor (from UMC library) in Cadence Virtuoso circuit simulator (Fig. 4(a)). We observe that when gate voltage pulses of fixed magnitude and duration (200 ns) are applied at the gate of the transistor for conductance increase (voltage of top electrode kept higher than that of bottom electrode for that purpose) (Check Supplementary Material- Section

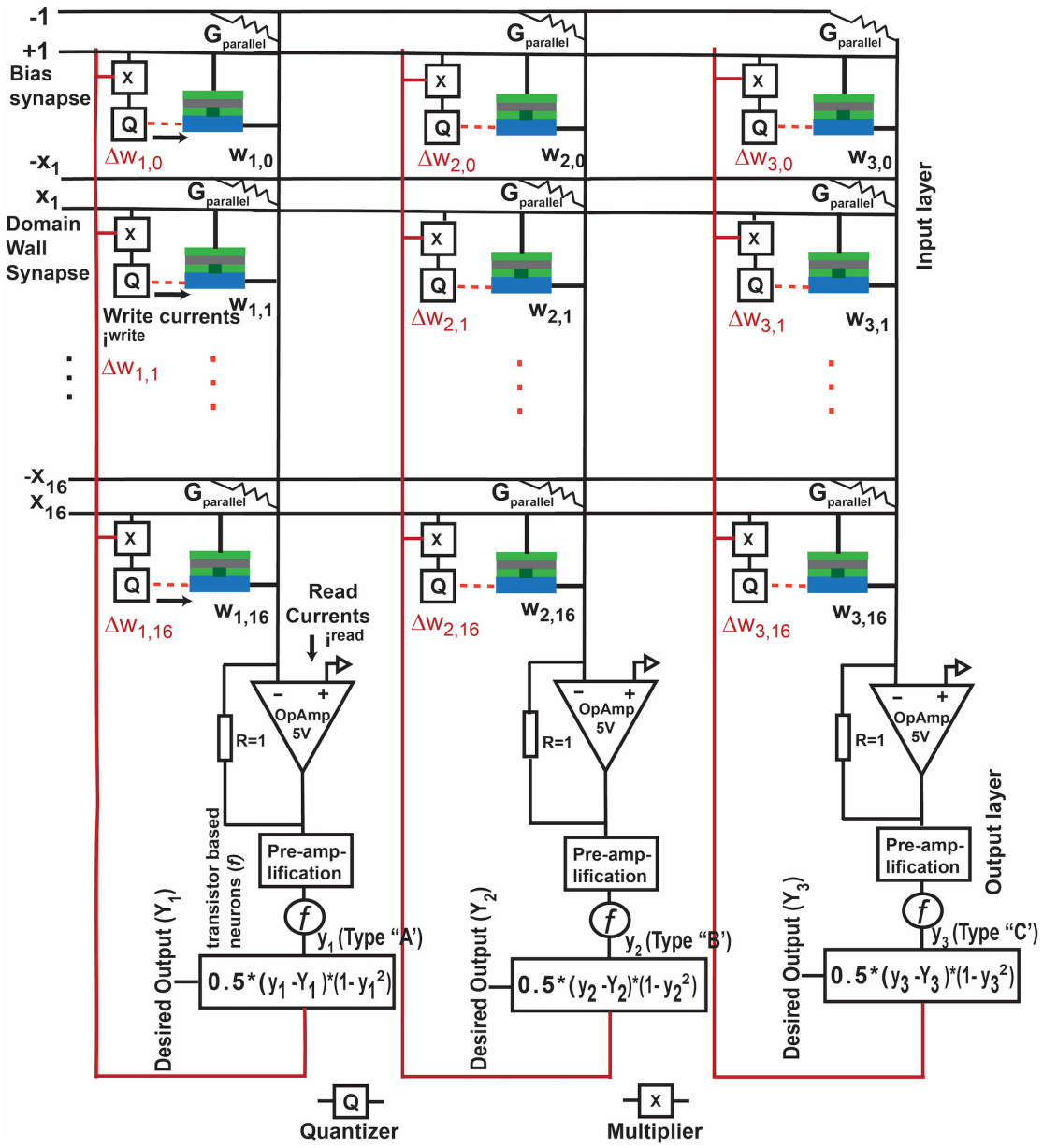


Figure 5: Schematic of designed DW synapse based crossbar array along with analog peripheral circuits for on-chip learning

2), the conductance of the RRAM synapse does not go up linearly unlike the domain wall synapse. In fact the conductance just saturates to a fixed value (Check Supplementary

Material- Section 2). To achieve a linear increase in conductance gate voltage pulses of increasing magnitude (SET pulses) need to be applied (Fig. 4(b)). This has been observed experimentally in the RRAM devices of [42, 44, 45]. Thus, though the conductance varies over a much wider range for RRAM synapse than DW synapse (Table I), the conductance response is inherently non-linear in nature. As a result, if a certain value of weight update is needed for any synapse for an iteration during on-chip, different magnitude of voltage pulses may need to be applied to bring about the same weight update, depending on what weight/ conductance value of the RRAM synapse is before that iteration. This makes designing the analog peripheral circuit for weight update very complicated. In fact, the demonstrations of on-chip learning in RRAM based crossbar NN array so far use a digital FPGA unit or an on-chip CMOS based digital processor, connected to the analog crossbar array, for weight update[44, 46]. ADC-s and DAC-s needed as a result, which can potentially consume a lot of energy and slow down the circuit. Energy consumed in the 1T1M circuit of Fig. 4(a) ranges between 12 pJ (minimum gate voltage) and 51 pJ (maximum gate voltage), which is much larger than energy consumed for weight/ conductance update by a single step in a domain wall synapse (Fig. 3(b)) (Table I). Apart from non-linearity, another issue with conductance response of RRAM synapse is asymmetry between positive and negative update of conductance. If we apply the same gate voltage pulses as in Fig. 4(b) in the reverse order in order to decrease the conductance of the synapse (bottom electrode at higher voltage than top for that purpose), we see that the conductance hardly decreases (Check Supplementary Material- Section 2). Rather in order to decrease conductance by a certain step, long duration (6 μs) and high magnitude (2.5 V) voltage pulse (hence high energy consuming), known as RESET pulse, needs to be applied at the gate of the transistor for abrupt conductance decrease to the smallest value. It is followed by pulses of gradually increasing voltage pulses (SET pulses) to then increase the conductance.

Synaptic devices	**Conductance range (mho)**	**Number of conductance states**	**Energy per pulse (conductance increase)**	**Energy per pulse (conductance decrease)**	**Train accuracy for on-chip learning (%)**	**Test accuracy for on-chip learning (%)**	**Total energy consumed in all synapses for on-chip learning**
Domain Wall	2.9m - 6.1m	48	0.18 fJ	0.18 fJ	89	90	9 fJ
RRAM	3μ - 30μ	100	12 pJ - 51 pJ	2.28 nJ (abrupt Reset)	93	94	1 μJ
PCM	0.1μ - 9.3 μ	20	5 pJ	30 pJ (abrupt Reset)	89	92	1.1 μJ

Table 1: Performance comparison between Domain Wall, RRAM and PCM based fully connected neural networks for on-chip learning.

Conductance response characteristic of PCM synapse we simulated, based on model developed in Nandakumar *et al.* [48] (See Supplementary Material- Section 3 for more details), is more linear than RRAM i.e. programming current pulse of fixed magnitude 90 μA and duration 50 ns increase the conductance of the PCM synapse fairly linearly for a larger number of pulses (≈ 12) (Fig. 4(c)). Energy associated with each such pulse is 5 pJ

[48, 2], still much higher than that for domain wall synapse (Table I). Conductance decrease on the other hand is carried out by an abrupt RESET pulse that consumes 30pJ energy each [2], followed by a series of SET pulses much like RRAM synapse. Thus the conductance response characteristic of PCM synapse is still asymmetric like RRAM synapse.

3 Network Level Comparison

Next we design crossbar array based Fully Connected Neural Network (FCNN) with domain wall synapses [17] and compare the energy and speed performance for on-chip learning with that for equivalent FCNN designed with RRAM and PCM synapses. It is to be noted that this NN is of the second generation non-spiking type [49] and uses standard Stochastic Gradient Descent (SGD) algorithm for weight update [21]. Verilog-A model of domain wall synapse is designed, based on its conductance response obtained from micromagnetic physics as shown in Fig. 3(b)) and inserted in crossbar schematic designed on Cadence Virtuoso circuit simulator (Fig. 5).

Fisher's Iris dataset, a popular machine learning dataset, is used for the training [25]. Since the dataset is not completely linearly separable, in order to carry out accurate classification on it with a FCNN without a hidden layer which we design here, the 4 input features corresponding to each sample are passed through some basic filters first to convert to 16 features [50]. Input voltages, proportional to these 16 input features, are applied on the crossbar as shown in (Fig. 5). Read currents, proportional to product of weight of the synapse and each input feature, add up following Kirchhoff's current law and enter the neuron/ activation function circuit at each output node. Thus the input Vector-weight Matrix Multiplication (VMM) is carried out in the crossbar array. [1, 17]."tanh" neuron/activation function (f) acts on the read current at each output node. This function has been designed with transistors in differential amplifier configuration, as shown in Bhowmik *et al.* [17]. A weight update circuit follows which calculates the common part of weight update at each output node, using the same SGD method and circuit described in Bhowmik *et al.* [17]. The common part of weight update computed at each output node is next multiplied with the inputs using the multiplier circuit (x) as shown in(Fig. 5). In Bhowmik *et al.* [17], write current proportional to the output of the multiplier (x) at each synapse acts on the DW synapse and updates its weight. However, since conductance of the DW synapse here takes only quantized values and is updated by write current pulses of fixed magnitude (25 μA) only (Fig. 3(b)), an additional quantizer circuit (Q) is present after the multiplier circuit here unlike in Bhowmik *et al.* [17]. Design and typical output of the quantizer circuit can be found in Supplementary Material (Section 4), accompanying this paper. Despite the fact that conductance and hence weight of each synapse takes only quantized value, on-chip learning is achieved with 89 % train and 92 % test accuracy on the Fisher's Iris dataset (Table I). Test accuracy turns out to be slightly higher than train accuracy because the number of samples available in the dataset is low (100 train, 50

test), so a correct or wrong result just with respect to 1 or 2 samples changes the accuracy number by a few percent.
Similar crossbar based FCNN is designed next with RRAM and PCM synapses, with conductance response as shown in Fig. 4. Similar accuracy for on-chip learning is achieved on Fisher's Iris dataset (Table I). However, net energy consumed in the synapses for on-chip learning is several orders of magnitude higher for RRAM/PCM synapse than DW synapse (Table I). This is expected because we already showed in Section II that energy consumed for each programming pulse that causes increase of conductance by a step (SET pulse) is orders of magnitude higher for RRAM/PCM synapse than DW synapse. Also, high energy consuming RESET pulses are still needed even though the need for decreasing conductance of a synapse is reduced by using 2 RRAM or 2 PCM per synapse [9, 44] (Check Supplementary Material- Section 5). Also, training takes much longer for RRAM/ PCM synapse based FCNN compared to DW synapse based FCNN because of the need of occasional long duration RESET pulses (in microseconds). Since at each iteration (each sample in the training set) weights of all synapses need to be updated simultaneously, even if one synapse needs a RESET pulse of microsecond duration, time needed to carry out that iteration is in microseconds. Since DW synapse does not have this issue, time taken for each iteration during learning is 3 ns only (duration of each programming pulse for DW synapse in Fig. 3(b))

4 Conclusion

Thus in this paper we have shown through device and network level simulations that on-chip learning in DW synapse based NN circuit can consume much less time and energy than RRAM and PCM synapse based NN circuit.

Supplementary Material

1 Simulation of domain wall synapse

The lateral dimensions of the device are taken to be 1000 nm $\times$ 50 nm. Thickness of the ferromagnetic layer above the heavy metal layer is 1 nm. Thickness of heavy metal layer is 10 nm.

Magnetization dynamics of the moments in this ferromagnetic layer is simulated in micromagnetic package "mumax3" with the following parameters: saturation magnetization (M_s) = 7×10^5 A/m, Perpendicular Magnetic Anisotropy (PMA) constant (K) = 8×10^5 J/m^3, exchange correlation constant (A) =1×10^{-11} J/m and damping factor = 0.3 [30]. Also, from [30], Dzyalonshinskii Moriya Interaction (DMI) is taken to be 1.2×10^{-3} J/m^2 and hence DW acquires Neel type chirality.

Triangular notch regions with Perpendicular Magnetic Anisotropy (PMA) constant = 9×10^5 J/m^3 are present on the edges of the simulated ferromagnetic layer in order to mimic defects, which can pin the domain wall if the driving current pulse magnitude is below a certain threshold.

Verilog-A model provided by [40], experimentally benchmarked against [41], has been used for RRAM modeling. Following the 1T1M (one transistor,one memristor) configuration [42, 43, 44] we connect this RRAM device with a 65 nm technology node transistor (from UMC library) in Cadence Virtuoso circuit simulator.

2 Simulation of RRAM synapse

Scheme for conductance increase-

1. Voltage at the Top Electrode is 2V and Bottom Electrode is 0V, to enable conductance increase. When gate voltage pulses of fixed magnitude and duration (200 ns) are applied at the gate of the transistor , conductance increases and then saturates to a fixed value. When gate voltage pulses of fixed but larger magnitude are applied, conductance saturates to a higher final value (Fig. 6(a) of Supplementary Material).

2. Voltage at the Top Electrode is again 2V and Bottom Electrode is again 0V, to enable conductance increase. If gate voltage pulses of fixed duration (200 ns) but increasing magnitude are applied at the gate of the transistor, the conductance goes up linearly (Fig. 4(b) of main manuscript).

Scheme for conductance decrease-

1. Voltage at Top Electrode = 0 V and voltage at Bottom Electrode = 4.8 V, to enable conductance decrease. If we apply the same gate voltage pulses as in Fig. 4(b) of main manuscript in the reverse order in order to decrease the conductance of the synapse, we see that the conductance hardly decreases (Fig. 6(b) of Supplementary Material).

2. With voltage at Top Electrode being 0 V and Bottom Electrode being 3.5 V, when a long duration (6 μs) and high magnitude (2.5 V) voltage pulse, known as RESET pulse,

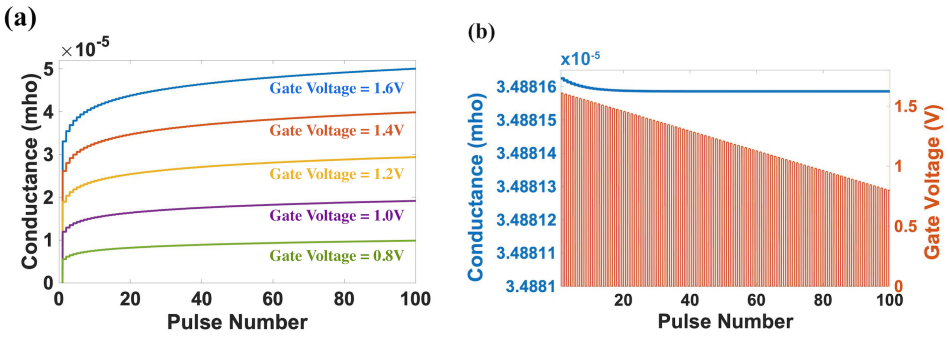


Figure 6: (a) Non-linear increase and saturation of conductance of the 1T1M device when fixed gate voltage pulses are applied. (b) No appreciable change in conductance is seen by applying decreasing gate voltage pulses.

is applied at the gate of the transistor, conductance abruptly decreases from maximum to minimum value.

3 Simulation of PCM synapse

To model the conductance response of the Phase Change Memory (PCM) synapse, the model developed in [48], based on the experiments conducted on $Ge_2Sb_2Te_5$ devices, has been used by us. By averaging the different conductance response curves generated by the model due to the stochasticity inherent in it, we have obtained the conductance response of the PCM synapse as shown in Fig. 4(c) of main manuscript.

Scheme for conductance increase-

The conductance increase characteristic is found to be more linear for PCM synapse than the case of RRAM synapse. For RRAM synapse, applying programming pulse of same magnitude led to saturation of conductance within first $\approx$ 5 pulses (Fig. 1(a) of Supplementary Material). Hence programming pulses of linearly increasing magnitude are needed to increase the conductance linearly for a wide range of pulses and hence obtain many more conductance/ weight states (Fig. 4(b) of main manuscript). However, as observed in Fig.4(c) of main manuscript, programming current pulses (SET pulses) of magnitude 90 μA and duration 50 ns increase the conductance of the PCM synapse fairly linearly for a larger number of pulses ($\approx$ 12) [48]. The energy associated with each such pulse is 5 pJ [48, 2].

Scheme for conductance decrease-

Conductance decrease is carried out by an abrupt RESET pulse that consumes 30pJ energy each [2], followed by a series of SET pulses (for conductance increase in small steps) much like RRAM synapse.

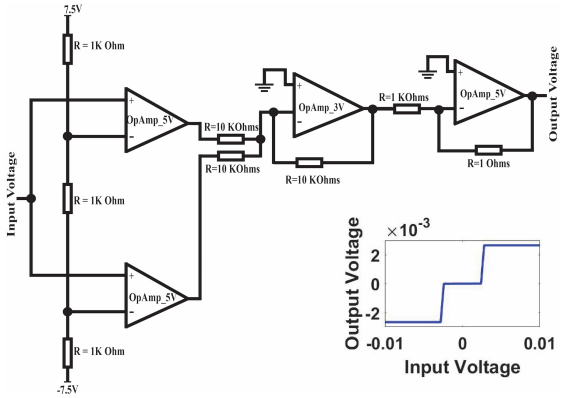


Figure 7: (a) Operational amplifier based implementation of quantizer circuit we design here. (b) Input-output characteristics of the circuit.

4 Quantizer Circuit for Domain Wall based Spintronic NN

To limit our "write" current to a magnitude of 25μA for either polarity, an additional "quantizer" circuit is added after the multiplier circuit which multiplies common part of weight update with the input (Fig. 7 of Supplementary Material). The quantizer circuit consists of a couple of op-amps working in "Comparator" configuration, which compare the input voltage with voltages at two different points in a potential divider circuit, followed by an op-amp in "Summing amplifier" configuration which adds the output voltages of the two comparator circuits (Fig. 7 of Supplementary Material). The output of the overall quantizer circuit is hence either $\approx 2.5 \times 10^{-3}$ V, 0 or $\approx 2.5 \times 10^{-3}$ V. When this output voltage is applied on the "write" terminal/ "write" path of the domain wall synapse, "write" current of three possible values ($\approx -25\mu$A, 0 ,$\approx 25\mu$A) flows through the domain wall synapse. As a result conductance of the synapse goes up or down by a fixed step ($\approx 0.071 \times 10^{-3}$ mho) or stays unchanged (Fig. 8 of Supplementary Material).

5 RRAM/PCM synapse based NN

Fig. 9 of Supplementary Material shows the variation of conductance values of a randomly chosen synapse in the RRAM based FCNN for 50 epochs during on-chip learning on the Fisher's Iris dataset. Under the two RRAM or PCM devices per synapse scheme [44, 9] used here ,in order to increase the net conductance of the synapse, conductance of one device (positive synapse) is increased. In order to decrease the net conductance of the synapse, conductance of the other device (negative synapse) is increased. But this way, during the course of the learning, conductance of either or both synapses reaches the maximum and then Reset pulses are needed to lower the conductance to the minimum value. Frequent use of Reset pulses increases the overall energy consumption in the scheme.

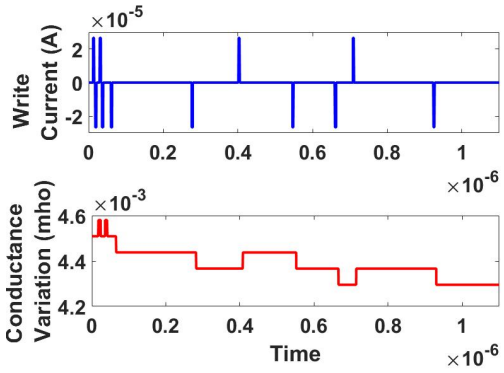


Figure 8: (a) Write current pulse (quantized) applied on a particular domain wall synapse during the course of on-chip learning of the overall domain wall synapse based neural network circuit on the Fisher's Iris dataset. (b) Corresponding change in conductance of the domain wall synapse. Since write current is quantized, conductance increases of decreases in steps of fixed magnitude.

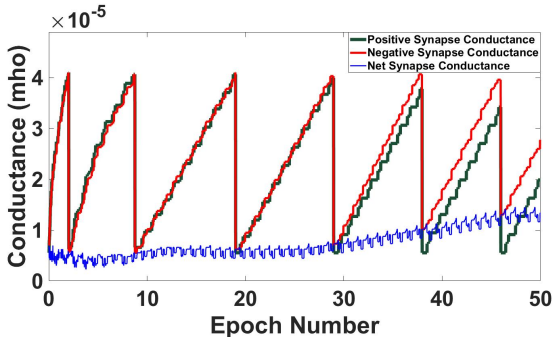


Figure 9: Conductance variation of a 2-RRAM synapse showing the need of multiple RESETs needed during on-chip training of the neural network. It can be seen that both the positive and negative synapse saturate due to conductance increase and decrease and need RESETs during training.

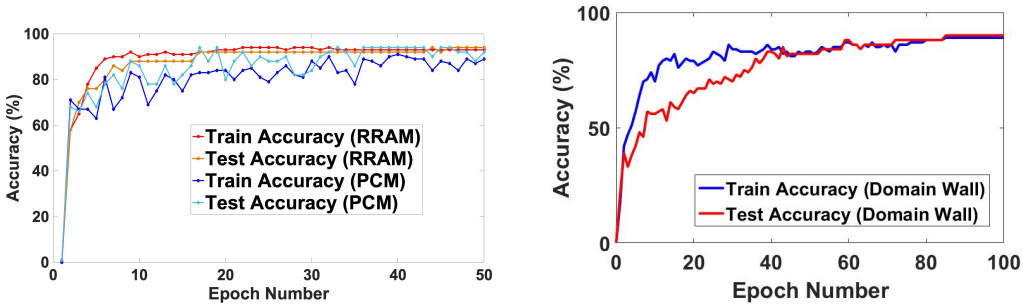


Figure 10: (a) Train and test accuracy of RRAM and PCM synapse based neural network circuit as a function of epochs during on-chip learning on Fisher's Iris dataset. (b) Train and test accuracy of domain wall synapse based neural network circuit for the same.

6 Classification accuracy of designed Domain wall, RRAM and PCM synapse based Neural Network

Fig. 10 of Supplementary Material shows the train and test accuracies of of the RRAM, PCM and spintronic (Domain wall synapse) based neural network circuits as a function of epochs for on-chip learning on the Fisher's Iris dataset.

References

[1] H. Tsai, S. Ambrogio, P. Narayanan, R.M. Shelby, and G.W. Burr, Journal of Physics D: Applied Physics 51, 283001 (2018).

[2] A. Sebastian, M.L. Gallo, G.W. Burr, S. Kim, M. BrightSky et al., Journal of Applied Physics 124, 111101 (2018).

[3] A. Sengupta, and K. Roy, IEEE Transactions on Circuits and Systems I: Regular Papers 63, 2267 (2016).

[4] P.A. Merolla, J.V. Arthur, R. Alvarez-Icaza, A.S. Cassidy, J. Sawada et al., Science 345, 668 (2014).

[5] M. Davies, N. Srinivasa, T.H. Lin, G. Chinya, Y. Cao et al., IEEE Micro 38, 82 (2018).

[6] G.W. Burr, P. Narayanan, R.M. Shelby, S. Sidler, I. Boybat, IEEE International Electron Devices Meeting, 4.4.1 (2015).

[7] I. Boybat, M.L. Gallo, S.R. Nandakumar, T. Moraitis, T. Parnell et al., Nature Communications 9, 1 (2018).

[8] Y. Li, Z. Wang, R. Midya, Q. Xia, and J.J. Yang, Journal of Physics D: Applied Physics 51, 503002 (2018).

[9] M. Suri, O. Bichler, D. Querlioz, O. Cueto, L. Perniola et al., IEEE International Electron Devices Meeting, 4.4.1 (2011).

[10] M. Suri ed., Cognitive Systems Monographs, Springer, 2017.

[11] G.W. Burr, R.M. Shelby, S. Sidler, C.D. Nolfo, J. Jang et al., IEEE Transactions on Electron Devices 62, 3498 (2015).

[12] P.Y. Chen, X. Peng, and S. Yu, IEEE International Electron Devices Meeting, 6.1.1 (2017).

[13] T. Gokmen and Y. Vlasov, Frontiers in Neuroscience 10, 333 (2016).

[14] A. Sengupta, Y. Shim and K. Roy, IEEE Transactions on Biomedical Circuits and Systems 10, 1152 (2016).

[15] U. Saxena, D. Kaushik, M. Bansal, U. Sahu and D. Bhowmik, IEEE Transactions on Magnetics 54, 1 (2018).

[16] S. Zhang, S. Luo, N. Xu, Q. Zou, M. Song et al., Advanced Electronic Materials 5, 1800782 (2019).

[17] D. Bhowmik, U. Saxena, A. Dankar, A. Verma, D. Kaushik et al., Journal of Magnetism and Magnetic Materials 489, 165271 (2019).

[18] N. Hassan, X. Hu, L. Jiang-Wei, W.H. Brigner, O.G. Akinola et al., Journal of Applied Physics 124, 152127 (2018).

[19] K. Yue, Y. Liu, R. K. Lake and A. C. Parker, Science Advances 5, eaau8170 (2019).

[20] S. Li, W. Kang, Y. Huang, X. Zhang, Y. Zhou et al., Nanotechnology 28, 31LT01 (2017).

[21] Y. LeCun, Y. Bengio, and G. Hinton, Nature 521, 436 (2015).

[22] S. Dutta, S. A. Siddiqui, J. A. Currivan-Incorvia, C. A. Ross and M. A. Baldo, AIP Advances 5, 127206 (2015).

[23] Y. Nakatani, A. Thiaville, and J. Miltat, Nature Materials 2, 521 (2003).

[24] E. Martinez, Advances in Condensed Matter Physics, 1 (2012).

[25] R. A. Fisher, Annual Eugenics 7, 179 (1936).

[26] S. Emori, U. Bauer, S.M. Ahn, E. Martinez and G.S.D. Beach, Nature Materials 12, 611 (2013).

[27] K.S. Ryu, L. Thomas, S.H. Yang and S. Parkin, Nature Nanotechnology 8, 527 (2013).

[28] D. Bhowmik, M.E. Nowakowski, L. You, O. Lee, D. Keating et al., Scientific Reports 5, 11823, (2015).

[29] I.M. Miron, T. Moore, H. Szambolics, L.D. Buda-Prejbeanu, S. Auffret et al., Nature materials 10, 419 (2011).

[30] S. Emori, E. Martinez, K.J. Lee, H.W. Lee, U. Bauer et al., Physical Review B 90, 184427, 2014.

[31] J. Sampaio, V. Cros, S. Rohart, A. Thiaville and A. Fert, Nature Nanotechnology 8, 839 (2013).

[32] E. Martinez, S. Emori, N. Perez, L. Torres and G. S. D. Beach, Journal of Applied Physics 115, 213909 (2014).

[33] D. M. Bromberg, M. T. Moneck, V. M. Sokalski, J. Zhu, L. Pileggi et al., IEEE International Electron Devices Meeting, 33.1.1 (2014).

[34] J.-G. Zhu and C. Park, Materials Today 9, 36 (2006).

[35] S. Ikeda, K. Miura, H. Yamamoto, K. Mizunama, H.D. Gan et al., Nature Materials 9, 721 (2010).

[36] A. Vansteenkiste, J. Leliaert, M. Dvornik, M. Helsen, F. Garcia-Sanchez et al., AIP Advances 4, 107133 (2014).

[37] L. Liu, C.F. Pai, Y. Li, H.W. Tseng, D.C. Ralph et al., Science 336, 555 (2012).

[38] L. Q. Liu, T. Moriyama, D. C. Ralph and R. A. Buhrman, Physical Review Letters 106, 036601 (2011).

[39] L. Q. Liu, O. J. Lee, T. J. Gudmundsen, D. C. Ralph and R. A. Buhrman, Physical Review Letters 109, 096602 (2012).

[40] X. Guan, S. Yu and H.S.P. Wong, IEEE Electron Device Letters 33, 1405 (2012).

[41] S. Yu, Y. Wu, and H.S.P. Wong., Applied Physics Letters 98, 103514 (2011).

[42] F. Miao, W. Yi, I. Goldfarb, J.J. Yang, M.X. Zhang et al., ACS Nano 6, 2312 (2012).

[43] H. Jiang, L. Han, P. Lin, Z. Wang, M.H. Jang et al., Scientific Reports 6, 28525 (2016).

[44] C. Li, D. Belkin, Y. Li, P. Yan, M. Hu et al., Nature Communications 9, 2385 (2018).

[45] J. Woo, K. Moon, J. Song, M. Kwak, J. Park et al., IEEE Transactions on Electron Devices 63, 5064 (2016).

[46] F. Cai, J.M. Correll, S.H. Lee, Y. Lim, V. Bothra et al., Nature Electronics 2, 290 (2019).

[47] O. Bichler, M. Suri, D. Querlioz, D. Vuillaume, B. DeSalvo et al., IEEE Transactions on Electron Devices 59, 2206 (2012).

[48] S. R.Nandakumar, M. Le Gallo, I. Boybat, B. Rajendran, A. Sebastian et al., Journal of Applied Physics 124, 152135 (2018).

[49] A. Sengupta, and K. Roy, Applied Physics Reviews 4, 041105 (2017).

[50] A. Biswas, S. Prasad, S. Lashkare and U. Ganguly, arXiv preprint arXiv:1612.02233 (2016).

International Research Journal of Engineering and Technology (IRJET) e-ISSN: 2395-0056
Volume: 06 Issue: 10 | Oct 2019 www.irjet.net p-ISSN: 2395-0072

Critically Polluted Area Analysis using Comprehensive Environmental Pollution Index

Medha Sharma[1], Dr. Geeta Singh[2]

[1]M. Tech Scholar, Delhi Technological University, Delhi
[2]Assistant Professor, Delhi Technological University, Delhi

---

Abstract *Environmental pollution has been a challenging issue for the past few decades which have been aggravated by industrialization across the country. Industrial developments could not be ignored as they are backbone of economics of a country. To address problem, the Study is done which is typically based on usage of data measuring ambient air, Groundwater and Surface water quality from various point locations in study area. This study focused on the Ghaziabad District of Uttar Pradesh, India. Study area is highly industrialized. Environmental pollution index (EPI) is calculated by selecting three most critical pollutants for Air, Surface water and Groundwater. Thereafter, Comprehensive Environmental Pollution Index (CEPI) is calculated by selecting three most critical parameters for air, water and Groundwater in 16, 06, and 16 monitoring locations respectively. In industrialized urban areas, this approach may present critical issues due to the spatial complexities of air pollutants which are emitted by different sources. The objectives of study is to show variability of pollutants in Air, Surface water and Groundwater and to interpret the results in relation to the applicability of data in assessing population exposure. Relative and absolute spatial concentration variations were investigated by means of Inverse distance weighting (IDW) tool in GIS, which is a kind of approach for multivariate interpolation taking a known scattered set of points. Results suggest evaluating the population exposure to pollutants in study area by taking into account the possible zones of influence of different emission sources.*

Key Words: *Geographical Information System, IDW, deterministic approach, CPA, Ghaziabad*

1. INTRODUCTION

Environmental pollution has been a challenging issue for the past few decades and it endangers the health of livings. The problem of pollution and its corresponding harmful ecological impacts have been increased by industrialization across the country and affecting the life of billions of people, other living creatures and damaging the natural resources locating nearby. Industrial developments could not be ignored as they are backbone of economics of a country. The micro, small and medium enterprises sector has emerged as a highly vibrant and dynamic sector of the Indian economy over the last five decades and most of them are concentrated in Industrial areas. Industrial areas specifically concentrated with large, medium and small scale industries with different category are in alarming condition and there is a need to restore the quality of the environment. There is an urgent need to identify critically polluted areas and their problematic dimensions. The Government shall take measure to the purpose of protecting and improvement in quality of the environment. The quality of the environment is studied by monitoring the environmental components such as water, air and land and health of human and other living creatures. The monitoring data does not help the policy makers and other public to understand the quality of environment system. A weighted measurement of environmental performance or sustainability, in form of comprehensive environmental pollution index (CEPI) is very useful. CEPI gives the idea about how much an industrial area is environmentally sound by using information on status of environment provided with quantity data.

Environmental quality assessment, in the form of index is a complex process which has limited study. As the present method of assessment of pollution studies does not give clear picture on the quality of environment to the public and policy makers, there is a need to form a common code/number/description. In view of this, an index with description was needed and an innovative concept of CEPI has been developed by Central Pollution Control Board, Government of India. The index value will be derived based on the available sources of pollution, presence of the pollution, level of the pollution and number of exceedance of the pollution, impact on health of human, ecosystem and the preventive action taken in controlling the environmental pollution are playing important role in establishment of the quality index value. To evaluate the CEPI scores of polluted industrial areas, a project on 'Monitoring, sampling and analysis for ambient air quality, surface water quality and ground water quality in 100 polluted industrial areas' has been carried out in 2018. The outcome of the project studies is presented in this paper.

1.1 Comprehensive Environmental Pollution Index

Comprehensive Environmental Pollution Index (CEPI) is a rational number to characterize the environmental quality at a given location following the algorithm of source, pathway and receptor. The concept of CEPI was developed by IIT Delhi, CPCB and many other organization like NEERI, TERI and DTU. CEPI was calculated on basis of various factors and three rounds of monitoring have been undertaken by CPCB in 2009, 2011, 2013 and 2018 on basis of which, CEPI assessment has been done periodically. CEPI is calculated by using the following formula

$CEPI = i_{max} + [(100 - i_{max}) \times (i_2/100) \times (i_3/100)]$

Where, imax is maximum index (which may be Air EPI or Surface Water EPI or Ground Water EPI);
and i2, and i3 are indices for other media
EPI of surface water, air and groundwater are evaluated on a scale of 1-100 using the formula
EPI = A+B+C+D
Where A-source, B- pathway, C-receptor and D- additional high risk elements.

1.2 Elements of CEPI

Three criteria pollutants are selected for air, water and land based on the pollutants relevant with the Area depending on the nature of industrial activity (preferable option /method) or depending on the concentration and exceedance. For selected criteria pollutants, scoring is done for A, B, C and D element for EPI calculation of air, water and land. Scoring methodology is described as below:

- A - Source: factor 'A' comprise of A_1 and A_2 as sub components. A_1 is based on the data on presence of toxins with maximum value 5. A_1 score for selected one primary and two secondary pollutants is given as per the group in which the pollutant lies.

Table-1: Source factor score for criteria pollutants

Group of toxicity	Property for pollutants in respective group	Contribution Value for Primary pollutant	Contribution Value for each of the Secondary pollutant
Group A	Pollutants not classified as acute or systematic	1	0.25
Group B	Pollutants/organics that are probable carcinogens or with systematic toxicity.	2	0.50
Group C	Known carcinogens or chemicals with significant systemic or organ system toxicity	3	1.00

Source: cpcb.nic.in

Component A_2 is based on the scale of industrial activities as no. of small scale, medium scale and large scale industrial units in given industrial cluster with maximum achievable score of 4. Large = 4 (if there are > 10 R17 per 10 sq km area or fraction OR > 2 R17 + 10 R54 per 10 sq km area or fraction OR > 100 R54 per 10 sq km area or fraction. Moderate = 2.5 (if there are 2 to 10 R17 per 10 sq km area or fraction OR 10-100 R54 per 10 sq km area or fraction. Limited = 1 (else there is any industry within 10 sq km area or fraction). This is how the 'A' score is calculated by multiplying A_1 and A_2.

- B - Pathway Factor: pathway factor is based on the level of exposure which is calculated by the Surrogate Number Level Factor (SNLF). SNLF is calculated using % violation of ambient pollutant concentration and ratio of no. Of samples exceeding prescribed standard value to the total no. of samples collected.

Table-2: Category classification on SNLF basis

Range of SNLF	Category	Contribution Value for Primary pollutants	Contribution Value for each of the secondary pollutants
(For EF > 0.75)	Low	0	2.5
7.5 < 0.50	Moderate	15	5.0
0.5 to < 1.0	High	22.5	7.5
1.0 and above	Critical	30	10.0

Source: cpcb.nic.in

- C - Receptor Factor: Percent increase is evaluated based on the total no. of cases recorded during two consecutive years. For Air Environment, total no. of case related to Asthma, Bronchitis, Cancer, Acute respiratory infections etc. are to be considered. For surface water / ground water Environment, cases related to Gastroenteritis, Diarrhea, renal (kidney) malfunction, cancer etc. are to be considered. For the above evaluation, the previous 5 years' records of 3-5 major hospitals of the area shall be considered.

Table-3: Health impact score

C (Impact on Human Health) = 10	
Increase in cases	Marks
<5%	0
5-10%	5
>10%	10

Source: cpcb.nic.in

- D – Additional high risk element factor: scoring of 'D' element is based on the adequacy status industries and common facilities like Common effluent treatment plant (CETP), Final effluent treatment plant (FETP) and Common hazardous waste.

Table-4: Score for Additional High Risk Element: Factor D

Large Scale Industries	Small/ Medium Scale Industries	Common Facilities for Pollution Control	Score
Adequate	Adequate	Adequate	0
Adequate	Inadequate	Adequate	5
Adequate	Adequate	Inadequate	10
Adequate	Inadequate	Inadequate	15
Inadequate	Inadequate	Inadequate	20

Source: cpcb.nic.in

2. STUDY AREA AND METHODOLOGY

Study area includes industrial area of Mohan nagar/Mohan Meakin Industrial area, Rajender nagar Industrial area, Sahibabad Industrial area, South side of Grand trunk road industrial area, Sahibabad, Sahibabad industrial area Site-4, Pandav nagar Industrial area, Kavi nagar industrial area, Bulandshahar road industrial area, Amrit nagar, Arya nagar industrial area, Meerut road industrial area, Loni industrial area, Loni road industrial area, Roop nagar industrial area,

Hapur road industrial area, Dasna, Philkua, South side of GT road, Kavi nagar, Tronica city, Anand nagar, Jindal nagar, Prakash nagar, Rural Industrial estate in Ghaziabad, Uttar Pradesh state of India.



Fig-1: Study Area

2.1 Methodology Involved

The aggregated CEPI Score can be calculated as.
$CEPI = i_m + \{(100 - i_m)*(i_2/100)*(i_3/100)\}$
Where, i_m: maximum sub index; and
i_2, and i_3 are sub-indices for other media.
To study the spatial variation of pollutant over the area, GIS is used.
Steps involved in creating the GIS images of spatial variation of pollutants over the study area are:
1. Creating the Base map of Study area (here, Ghaziabad) by Geo-referencing in GIS.
2. Adding base map in blank sheet.
3. Adding X-Y coordinates as respective latitudes and longitudes of the study area over its base map.
4. Exporting data of Ambient air pollutants, Surface water pollutants and groundwater pollutants one at a time over the base map.
5. Using Inverse Distance weighing tool to calculate the assigned value to unknown points with a weighted average of the values available at the known points.

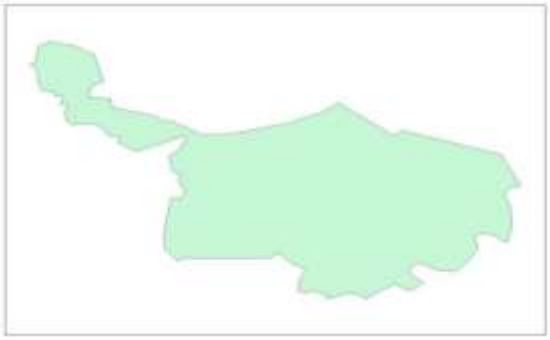


Fig-2: Basemap of Ghaziabad

3. RESULTS AND DISCUSSION

3.1 Air Quality Analysis

Available data of year 2018 of air pollutants from sixteen monitoring locations is assessed and analyzed over whole study area. Discrete data is used to create continuous variation of pollutants over basemap. IDW interpolation technique is used to map the spatial extent of pollutants to show the desired variation in simple and intuitive manner.

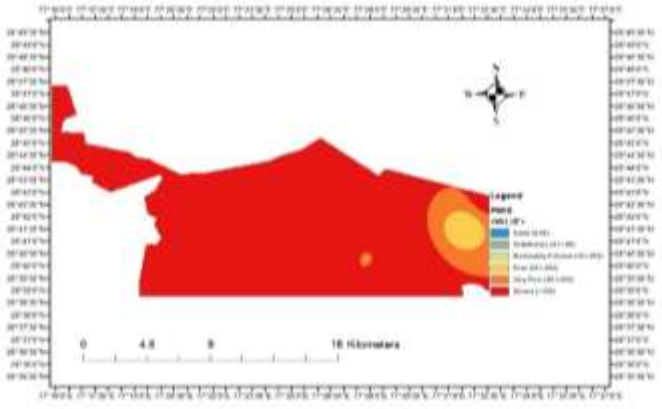


Chart-1: Spatial variation of PM_{10}

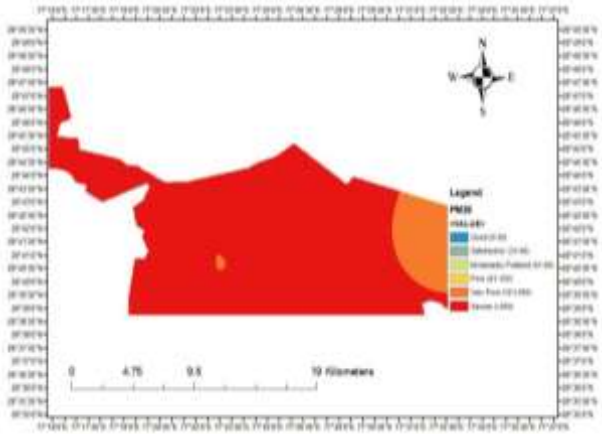


Chart-2: Spatial variation of $PM_{2.5}$

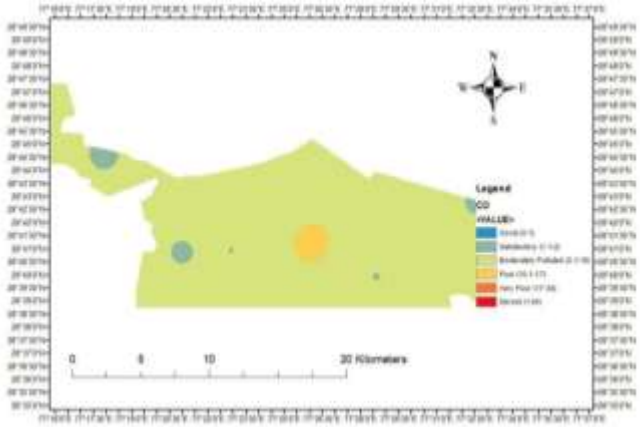


Chart-3: Spatial variation of CO

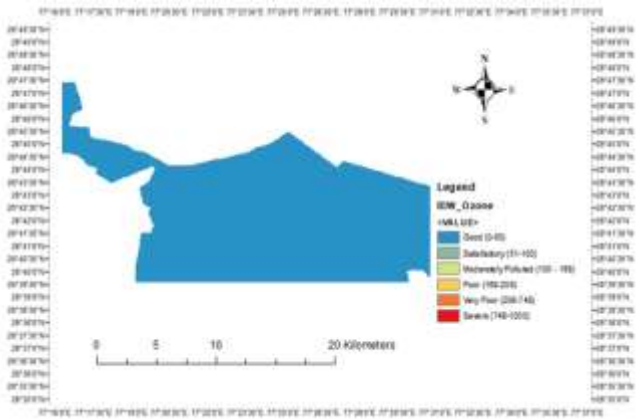


Chart-4: Spatial variation of O_3

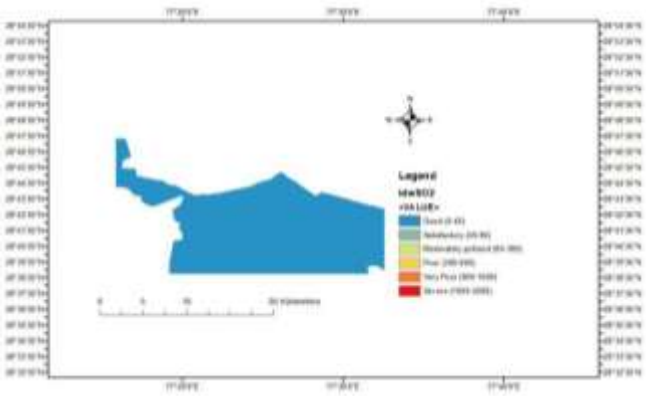


Chart-5: Spatial variation of SO_2

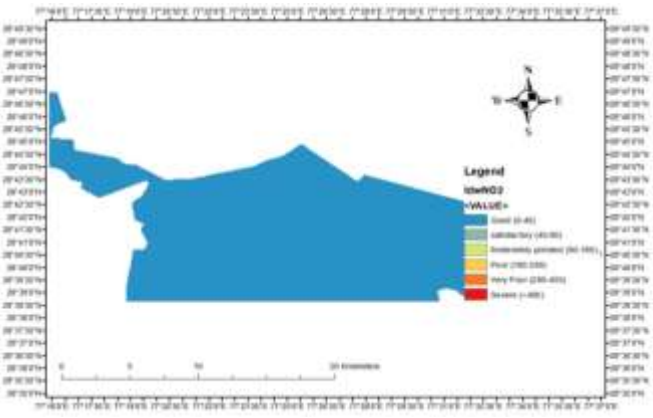


Chart-6: Spatial variation of NO_2

3.2 Surface Water Quality Analysis

Available data of year 2018 of surface water pollutants from six monitoring locations is assessed and analyzed over whole study area.

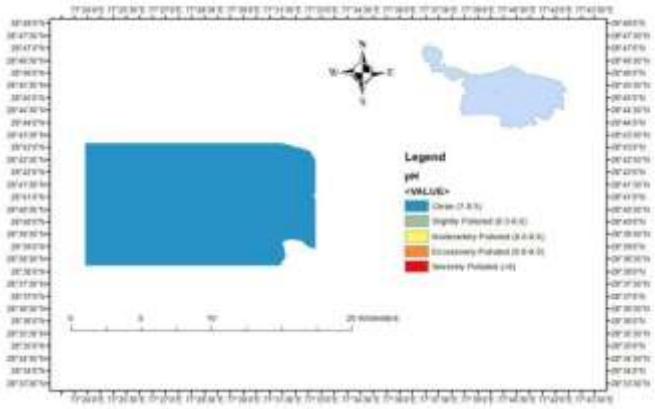


Chart-7: Spatial variation of pH

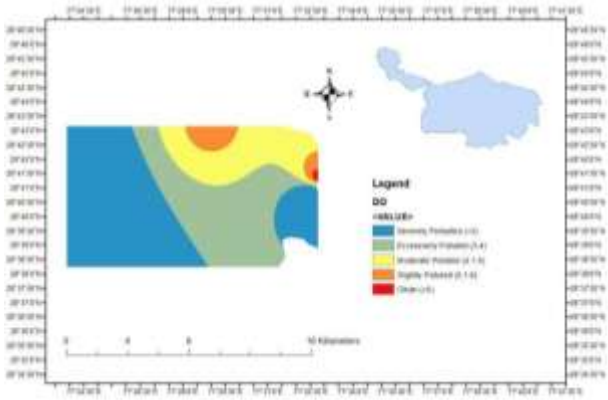


Chart-8: Spatial variation of DO

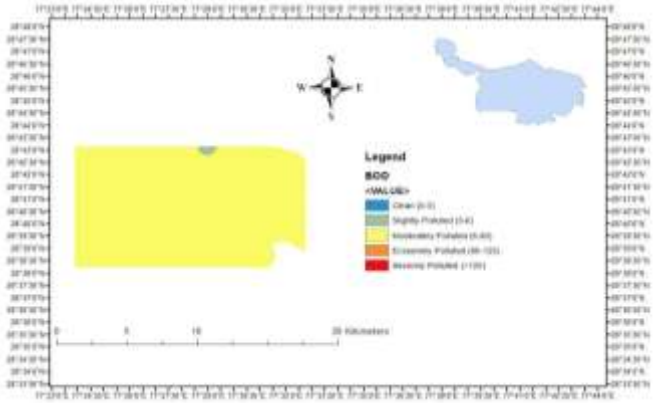


Chart-9: Spatial variation of BOD

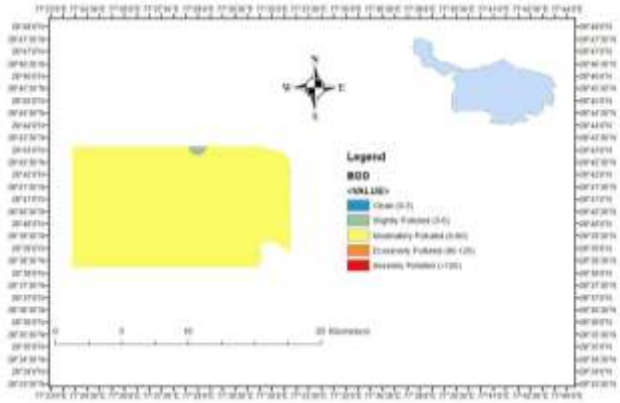


Chart-10: Spatial variation of $_{Sodium}$ Absorption ratio

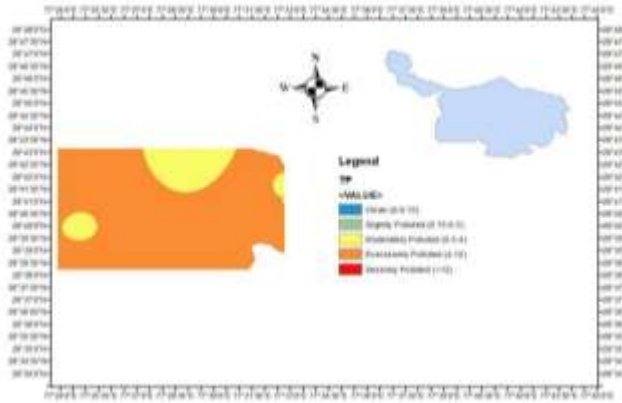


Chart-11: Spatial variation of Total Phosphate

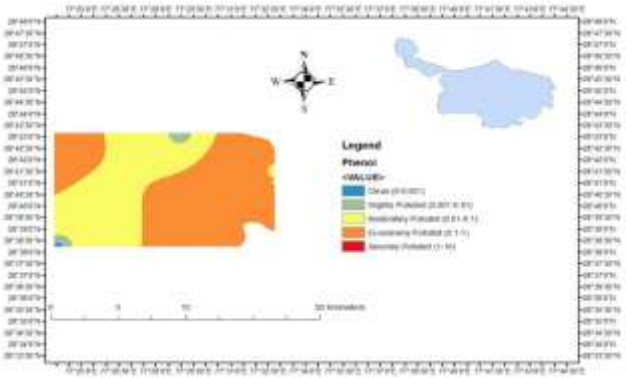


Chart-12: Spatial variation of $_{Phenolic}$ Compounds

3.3 Ground Water Quality Analysis

Available data of year 2018 of surface water pollutants from sixteen monitoring locations is assessed and analyzed over whole study area

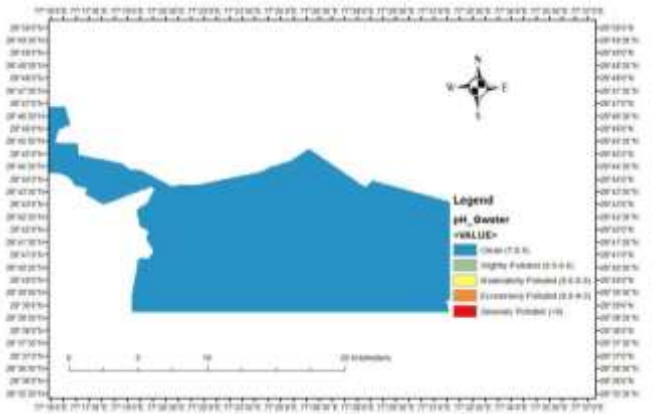


Chart-13: Spatial variation of pH

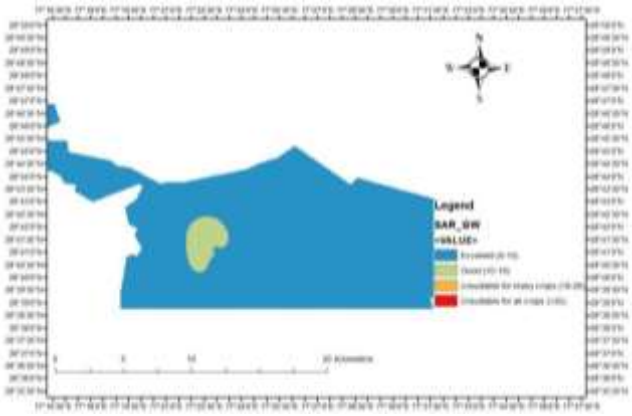


Chart-14: Spatial variation of $_{Sodium}$ Absorption ratio

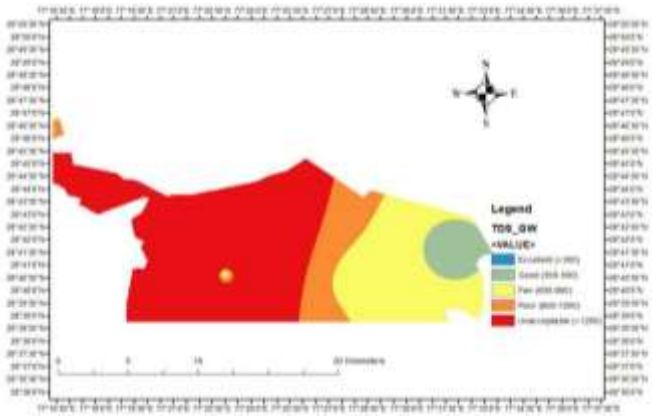


Chart-15: Spatial variation of Total Dissolved Solids

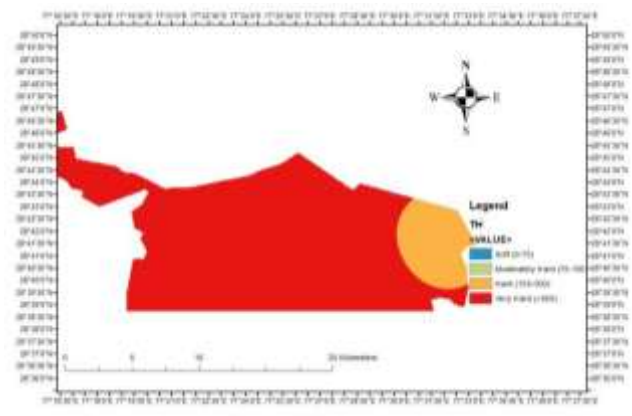


Chart-16: Spatial variation of Total Hardness

3.4 Air EPI Calculation

For Ambient air quality analysis in Ghazibad area, PM_{10} is exceeding the standard of PM_{10} (80µg/m3 for 24-Hr average) prescribed by CPCB in all 36 samples out of 36 ambient air samples analyzed at 16 ambient air quality monitoring locations and considered as primary critical pollutant.

In similar fashion $PM_{2.5}$ is exceeding the standard of $PM_{2.5}$ (80µg/m^3 for 24-Hr average) prescribed by CPCB in all 36 samples out of 36 ambient air samples and Carbon Monoxide (CO) is exceeding in 20 samples out of 36 ambient air samples collected by the standard fixed by CPCB for CO (2mg/m^3 for 8-Hr, average). Since PM_{10} categorized as group B pollutant i.e., Probable carcinogen and thus scored 2 points in industrial activity calculation and $PM_{2.5}$ and CO being Secondary critical pollutant and categorized as Group B pollutant thus scored 0.5-0.5. As per the data collected, there are more than ten R17 category industries in Ghaziabad per 10 KM^2 area under the polluted industrial area considered. Thus Ghaziabad PIA categorized as Large on scale of industrial activities

Surrogate Number Level factor (SNLF) is a function of Exceedance factor and ratio of no. Of samples exceeding the standard to total no. Of samples analyzed. It is calculated as described in methodology giving B score as 45.5 with PM_{10} scored 30 as primary critical pollutants and $PM_{2.5}$ scored 10 as secondary critical pollutant SNLF is > 1 and CO being secondary critical pollutant with SNLF 0.56 scores 5.5 giving collective value of B as 45.5.

Score C corresponds to the health data received from at least major three to five hospitals situated in PIA. For Air EPI calculation, annual percent increment in the patients suffering from air Borne diseases like Asthma and Bronchitis received by hospital is calculated for past five years. Here for Air EPI calculation in year 2018, annual percent increment in no. of patients are less than 5% hence the Receptor score is given as 0.

For D score, the adequacy of large/medium/small scale industries and Compliance of CETP/STP/ETP/CHWTSDF and MSW management facilities is observed. For Ghaziabad, in the demarcated PIA, industries as well as waste management facilities are complying thus resulting in D score as zero.

3.5 Water EPI Calculation

Phenolic compounds, Total Phosphorus and BOD are taken as primary, secondary and secondary critical parameters respectively according to the surface water samples collected and tested further. BOD is exceeding the standard (5 mg/l) given by CPCB in 14 samples out of 27 samples collected from monitoring locations. Total Phosphorus is exceeding at all 27 locations and being a probable carcinogen it lies in group B scoring 0.5 points. Phenolic compounds exceeding the standard of Phenolic Compounds (0.01 mg/l) for surface water prescribed by BIS. Phenolic compound being the Carcinogenic compound lies in group C and scores 3 giving total score of A1 as 4 and A as 16.

For B score calculation, SNLF calculated is highest for Total Phosphorus and thus TP is taken as primary critical pollutant giving B1 score 30 (as SNLF is above 1) and marked as critical. Two runner ups with highest SNLF next to TP is considered as secondary critical pollutant and scored 10 points for having SNLF greater than 1 for each of them. B2 and B3 score for BOD and Phenolic compound is calculated in similar manner giving total B score as summation of B1, B2, and B3 as 50. Thus, total water EPI came out as 66 categorizing water in PIA as critical.

3.6 Land EPI Calculation

Out of total 23 parameters tested for groundwater sample collected from 17 monitoring locations in demarcated PIA, three most critical parameters are selected on basis of exceedance. For A score calculation mercury is found exceeding the standard prescribed by BIS for Mercury (0.001 mg/l) in groundwater and since C lies in group C category and is a known carcinogen thus it is considered ass primary critical pollutant and scored 3 points. For other two parameters Total Hardness and Total Dissolved Oxygen as group A parameter scored 0.25 points each. For B score calculation SNLF calculated is highest for Total Hardness among three critical pollutants selected and considered for Primary critical pollutant and scored accordingly 11.25 points with Moderate label giving total B score of 18.25. Other two secondary critical pollutants scored 3.5 score with moderate label and since health related and adequacy score were zero thus total Land EPI came out as 32.25. Land is categorized as Normal.

$$CEPI = imax + \{(100-i_{max}) \times (i_2/100) \times (i_3/100)\}$$

$$= 66+34 \times (57.5/100) \times (32.25/100)$$

$$=72.3$$

4. CONCLUSIONS

In the study area, Ambient air quality of samples are analyzed for all the 12 notified parameters however the predominant pollutants identified were PM_{10}, $PM_{2.5}$ and CO as critical pollutants. At some locations benzene and heavy metals were also identified. It is interpreted that majorly vehicular movement and vehicular emission due to burning of fuel is responsible for $PM_{2.5}$ and PM_{10} and Recessively, emissions of SO_2, NO_2, ammonia and VOCs is a reason in formation of the inhalable particulate matter ($PM_{2.5}$) by photochemical reactions. Ambient air component has been observed severe in Ghaziabad Industrial area. Similarly, in terms of water quality, the BOD, Phenolic Compounds, TP, Total Hardness, TDS and Hg are predominant parameters and most of the other parameters were not significant. The specific pollutants such as PAH and Hg are reported in some locations. Surface water is observed critical in Ghaziabad industrial areas with BOD, TP and Phenolic compounds as critical parameters. Whereas, ground water is in normal condition.

The CEPI analysis helps to categorize industrial areas/clusters into critically polluted area, severely polluted are and other polluted area with respect to one or more environmental component. The areas having aggregated CEPI scores of 70 and above are considered as critically polluted industrial clusters/ areas, whereas the areas having CEPI between 60-70 are considered as severely polluted areas and they are kept under surveillance and pollution control measures, whereas, for the critically polluted industrial clusters/ areas further detailed investigations in terms of the extent of damage and a formulation of appropriate remedial action plan. It is recommended that as the step II a comprehensive analysis of spatial and temporal data shall be done for the identified critical polluted industrial clusters/ areas so as to define the spatial boundaries and extent of damage to the eco-geological features.

REFERENCES

[1] CPCB, 2009. Criteria for Comprehensive Environmental Assessment Industrial Clusters, Series EIAS/4/2009–10, December 2009.http://cpcb.nic. in/divisions of head office/ess/New Item_151_Final_ Book1.pdf

[2] CPCB, 2016. Final Document on Revised CEPI Version – 2016', No. B-29012/ESS(CPA)/2015–16/ April 26, 2016.http://www.cpcb.nic.in/upload/Latest/Latest_120_Directions_on_Revised_CEPI.pdf

[3] CPCB, 2010. Pollution Control Acts, Rules and Notifications Issued Thereunder, Series PCLS/02/2010 (Sixth Edition), June 2010.

[4] The World Bank Group, 1998. Pollution Prevention and Abatement Handbook – Towards Cleaner Production, the World Bank Group, Washington, D.C.

[5] MoEF, GOI, 2010. Office Memorandum J-11013/5/2010-IA.II(I) Dated 13th January, 2010. www.moef.nic.in

[6] MoEF, GOI, 2010. Office Memorandum J-11013/5/2010-IA.II(I) Dated 26th October, 2010. www.moef.nic.in

[7] Rajamanickam R. and Nagan S., 2014. Evaluation of Environmental Quality of SIPCOT Industrial Complex, Cuddalore, Tamil Nadu through CEPI, J. Environ. Science & Engin. 56(4), 383–398.

BIOGRAPHIES



Medha Sharma
M. Tech Scholar,
Delhi Technological University, Delhi



Dr. Geeta Singh,
Assistant Professor,
Delhi Technological University, Delhi

I.J. Image, Graphics and Signal Processing, **2019, 10, 40-49**
Published Online October 2019 in MECS (http://www.mecs-press.org/)
DOI: 10.5815/ijigsp.2019.10.06

Crowd Escape Event Detection via Pooling Features of Optical Flow for Intelligent Video Surveillance Systems

Gajendra Singh[1]
[1] Dr. B R Ambedkar National Institute of Technology, Jalandhar, Punjab, India
Email: singhgajendra87@gmail.com

Arun Khosla [1], **Rajiv Kapoor**[2]
[2] Delhi Technological University, Delhi, India
Email: khoslaak@nitj.ac.in, rajivkapoor@dce.ac.in

Received: 30 May 2019; Accepted: 26 June 2019; Published: 08 October 2019

Abstract—In this paper we propose a method for automatic detection of crowd escape behaviour. Motion features are extracted by optical flow using Lucas-Kanade derivative of Gaussian method (LKDoG) followed by robust probabilistic weighted feature pooling operation. Probabilistic feature polling chooses the most descriptive features in the sub-block and summarizes the joint representation of the selected features by Probabilistic Weighted Optical Flow Magnitude Histogram (PWOFMH) and Probabilistic Weighted Optical Flow Direction Histogram (PWOFDH). One class Extreme Learning Machine (OC-ELM) is used to train and test our proposed algorithm. The accuracy of our proposed method is evaluated on UMN, PETS 2009 and AVANUE datasets and correlations with the best in class techniques approves the upsides of our proposed method.

Index Terms—Crowd escape, Probabilistic weighted feature Probabilistic Weighted Optical Flow Magnitude Probabilistic Weighted Optical Flow Direction, One-Class ELM

I. Introduction

Video surveillance systems for indoor and outdoor environments, such as metro stations, intersection at roads, fun-fairs etc., where a large number of people gather, play vital role both in the assurance of safety conditions for the persons and managing the road transport. But the scientific challenge in crowd image analysis is to observe and analyze this huge amount of data generated by these cameras network, which may contain hundreds of cameras and monitors. Human interaction based surveillance systems are more prone to errors because abnormal events take place after a long period. In such situations human attention may wander and abnormal situation may be more challenging to get noted. So, to avoid such situations an automated system is needed that can analyze such huge amount of data and trigger alarm in abnormal events. Now a days, automation of surveillance systems is a major research area for researchers. The use of computer vision algorithms in surveillance systems, which can automatically detect adverse situations such as violence, accidents or defacement of public property etc., at an early stage will make these environments safer for public and issuing timely warning will minimize the loss of life and public property. Abnormal event detection framework consists of two components viz. feature extraction and pattern identification. Feature extraction is arrangement of low-level data into different primitives that describes the scene characteristics in a compact way. Feature extraction methods are mainly classified into two categories: object based and pixel based. Object based methods extract geo- spatial information of objects and one sort of methods are trajectory based [1, 2, 3], where anomalous events are detected based on object trajectory. These methods track each object in the scene and make model based on the object trajectory statistics of each object. Efficiency of these methods is mainly dependent on the extraction of objects. But there are too many objects in the scene and tracking of each object is difficult due to occlusion in crowed scene and it takes lot of time for tracking multiple objects [3]. On the other hand, pixel-based methods [4, 5] describe the scene by low level features. One such approach is based on flow of crowd which uses motion statistics of scene. In [4], abnormal event detection is carried out by modelling change in each pixel value and this method uses optical flow that models the crowd movement through motion statistics. Optical flow methods are capable of easily and accurately modeling densely crowded scenes. Feature extraction is followed by pattern identification for differentiation between normal and abnormal events. Pattern identification is broadly classified into supervised, semi-supervised and unsupervised techniques.

In this paper, a new anomaly detection framework is proposed for video surveillance systems using semi

Copyright © 2019 MECS

supervised learning process. For feature extraction optical flow is used. Feature vector consists of both magnitude and direction information about the objects in the scene. This is followed by robust pooling operation, which robustly describe even small change in movement or in direction and the distribution of activity is modelled by OC-ELM. Due to robust features and robust classifier our method works well in challenging conditions (e.g. camera shake and varying crowd density) with respect to other state of the art methods. Rest of the paper is organized as follows; Section 2 provides an overview of related work on abnormality detection in video surveillance systems. Section 3 gives an overview of proposed method. Sections 3 describes the process of robust feature extraction from the scene and feature modelling process for the detection of abnormal events from normal events. The performance results of our proposed method are described in Section 4. In section 5 finally the paper is concluded.

II. Related Work

Abnormal event detection is application specific task and depends on situation in the scene. One thing that is normal at some places, may not be normal at other places e.g. running at racing track is normal task while running in the mall or running at the railway track is abnormal situation. So abnormal event detection techniques generally learn from its environment, where they are being deployed. First thing in anomalous event detection is to abstract the features which can describe the scene statics i.e. low level features, high level features. After abstraction of features, event modelling or classification is done. Event modelling is formal way to designate and classify whether scene comprises an anomalous event or not. Event modeling techniques are generally classified into three categories: supervised, semi supervised and unsupervised techniques. The anomaly detection based on supervised technique requires the labeling of samples for both normal samples and abnormal samples to train the model. These methods are usually modelled for specific abnormal situation whose characteristics are previously defined, such as 'U' turn detection in traffic surveillance scene [6, 7]. Semi supervised approaches require only normal samples for training and these approaches can be further categorized into two sub-approaches, rule-based and model-based. In rule-based approach, some rule are created according to the scene features [8, 9]. Samples not following a pre-defined rule would be classified/labelled as abnormal/irregular. Sparse coding [8], Online dictionary updating [10] and sparse combination learning [9] are widely rule-based methods. In [8], author proposed a method based on reconstruction cost criterion, if the reconstruction cost of a sample is high then the sample is labelled as abnormal sample. In [11, 12, 13], similarity-based methods were proposed, where abnormal score of a test data is measured by its similarity to the training sample. While model-based methods [2, 14] attempts to build a model only for normal scene data and calculate the probability of test sample from the model learned. Test sample which is similar to the learned data gives high probability and labelled as normal, while low probability test samples with respect to the train model will be considered as anomalous samples. The commonly used model-based techniques are Hidden Markov Model (HMM) [2, 15, 16] and Markov Random Field (MRF) model [14, 17], which are used in a wide variety of applications. Kim et al. [14] proposed a Space Time Markov Random Field (STMRF) approach illustrating distribution of regular motion behavior. Kratz et al. [2] proposed a model based on the local spatial and temporal motion behavior using distribution-based HMM. Andrade et al. [16] proposed a model-based grouping of video into different cluster using spectral clustering and trained the model for each cluster using Multiple Observation Hidden Markov Model (MOHMM). Mehran et al. [18] proposed Social Force Model (SFM) for detection and localization of abnormal behavior of crowd based on interaction forces. Adam et al. [19] presented a method for abnormal behavior detection by observing histogram statistics of optical flow for normal behavior at several fixed-location monitors. While Wu et al. [20] modelled chaotic invariants of Lagrangian particle trajectories for normal events to characterize crowded scene.

Cui et al. [21] proposed a model based on interaction energy potential function describing the action and spatial arrangement with the surroundings of normal objects changing over time, and events with abrupt fluctuations in functions are likely to be uncommon. M.H.Sharif et al. [22] proposed a method based on entropy of the spatio-temporal information of the interest points to measure randomness in video frame. Kwon et al. [23] proposed predefined energy model whose parameters reflect frequency, causality, and significance of events, which can be used for abnormal event detection. Xuxin Gu et.al [24] proposed a method for detection of abnormal event based on particle entropy which describes the distribution information of crowded scenes. The energy-based algorithms are generally sensitive to various parameters, and a particular energy function can perform well only for specific scenes. Unsupervised methods do not require normal or abnormal data samples in advance and abnormal event detection is done based on the fact that abnormalities are rare with respect to normal situation. Several proposed techniques categorize an event as anomalous if the distance between the test data point and the nearest cluster center is greater than the predefined threshold, that may be adaptive, or user specified. The Battacharyya distance is a commonly used for distance calculation [25]. In many techniques, threshold is not directly a distance measure. Goshorn et al. [26] used the number of fluctuations essential to cause the test data point to fit into a trained cluster. Each fluctuation is given a cost and if the total cost surpasses a predefined threshold, then the action/event is labelled as abnormal.

Copyright © 2019 MECS

III. Proposed Algorithm

This section presents our anomaly detection framework for surveillance systems at crowded places. Our proposed algorithm is based on extraction of motion information and concrete representation of extracted features followed by machine learning for classifying normal/abnormal events. Block diagram of the proposed algorithm is shown in Fig 1.

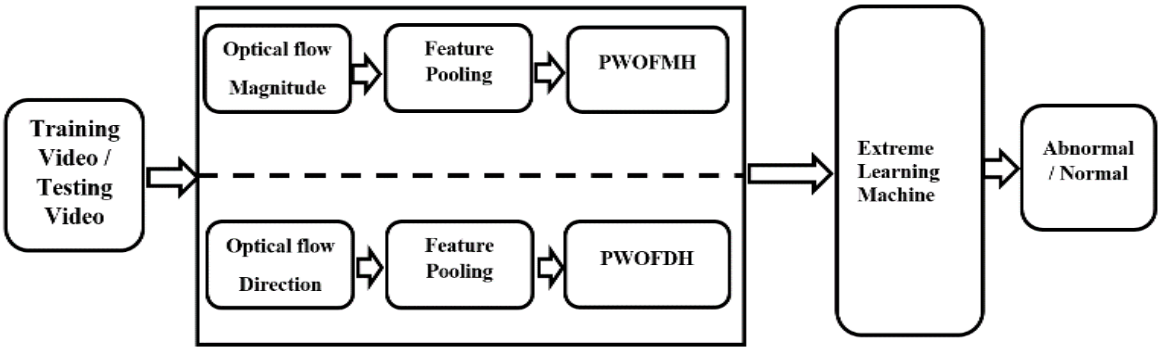


Fig.1. Block diagram of our proposed algorithm

A. Feature Extraction

When some abnormal event occurs in crowded area e.g. market, mall, playground etc., crowd disperse from that location speedily. So for such situations, information about motion of crowd plays crucial role for the detection of abnormal events. Motion information is extracted using optical flow that represents the apparent movement of objects, surface and edges due to relative movement between observer and objects. Optical flow magnitude and direction provides the information about the velocity and direction of movement of object(s) and motion information is described by Probabilistic Weighted Optical Flow Magnitude Histogram (PWOFMH) and Probabilistic Weighted Optical Flow Direction Histogram (PWOFDH). Probabilistic weights are obtained by pooling operation, which uses probability for finding weights. After feature extraction, feature vectors are fed into OC-ELM to learn model parameters for classification. After training, same process is followed for test frames to detect whether the given frames belong to normal or abnormal situation. Motion information for each frame of video is extracted by using Lucas-Kanade derivative of Gaussian method (LKDoG) [27] in the form of optical flow that estimates the speed and direction of object(s) in video. It assumes that the flow is essentially constant in a local neighborhood of the pixel under observation. To estimate the optical flow between two frames, the following optical flow constraint equation for all the pixels in that neighborhood is solved by the weighted least squares criterion.

$$E_x u + E_y v + E_t = 0 \tag{1}$$

Where E_x, E_y and E_t are image intensity derivatives in spatial as well as temporal dimension of a video and u, v are optical flow vector in horizontal and vertical directions respectively.

Before calculation of spatial derivatives and temporal derivatives (Ex, Ey and Et) gaussian smoothing is performed and then derivative of gaussian filter are used for derivative calculation. To solve the optical flow constraint equation (1) for u and v, this method divides the original frame into small blocks and assumes a constant velocity in each block. Then, it performs a weighted least-square criterion of equation (1) for calculating $[u\ v]^T$ in each block. The method attains this by minimizing the following equation:

$$\sum_k W^2 \left[E_x u + E_y v + E_t\right]^2 \tag{2}$$

Where k is kth block of original frame and W is a window function. Solution of the minimization problem is given as

$$\begin{bmatrix} \sum W^2 E_x^2 & \sum W^2 E_x E_y \\ \sum W^2 E_y E_x & \sum W^2 E_y^2 \end{bmatrix} \begin{bmatrix} u \\ v \end{bmatrix} = - \begin{bmatrix} \sum W^2 E_x E_t \\ \sum W^2 E_y E_t \end{bmatrix} \tag{3}$$

After obtaining optical flow (u, v) using LKDoG [27], motion features (velocity magnitude and movement direction) at every pixel location of each frame can be calculated as

$$M(x, y, t) = \sqrt{u_{x,y,t}^2 + v_{x,y,t}^2} \tag{4}$$

$$D(x, y, t) = atan2\left(\frac{u_{x,y,t}}{v_{x,y,t}}\right) \tag{5}$$

Where $M(x, y, t)$ and $D(x, y, t)$ are magnitude and direction of optical flow at (x, y) pixel location in t^{th} frame of video respectively. Optical flow magnitude and direction matrix after extraction from each frame is divided into smaller sub blocks with 50 percent of overlapping. Strong feature points are pooled from each sub block form optical flow magnitude matrix and final feature vector of frame is concatenated vector of pooled features from optical flow magnitude and direction matrices as shown in Fig 2.

Copyright © 2019 MECS

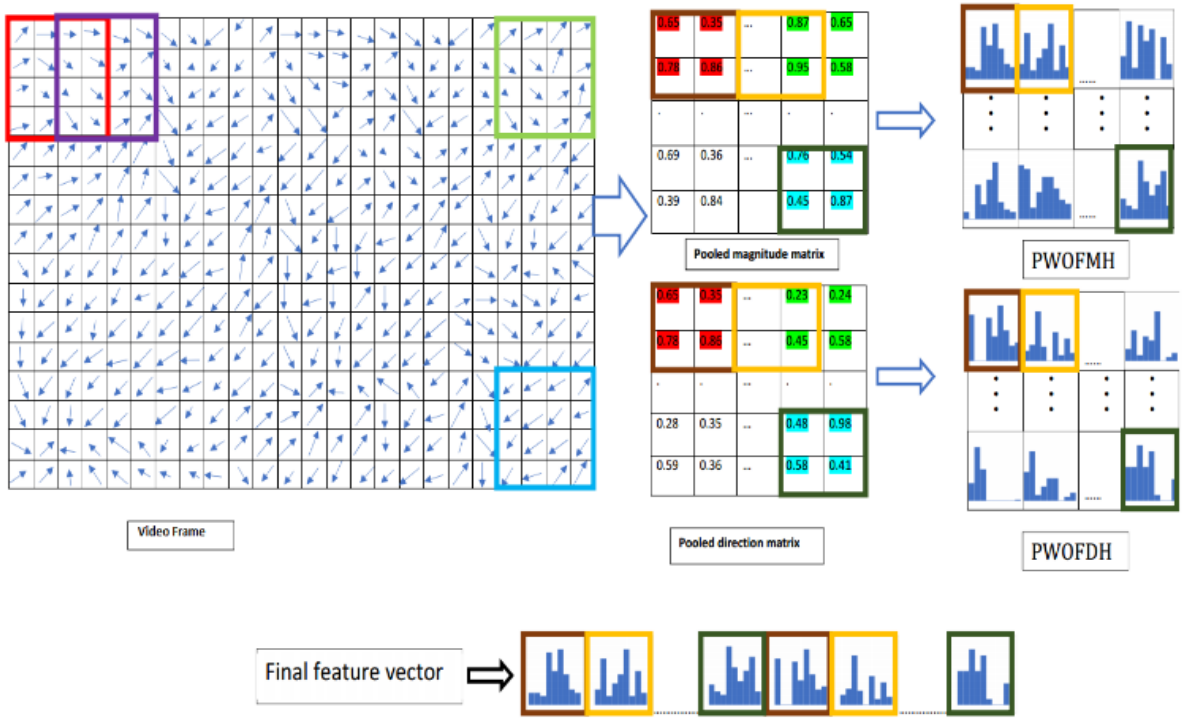


Fig.2. Illustration of Feature extraction for a video frame based on proposed algorithm

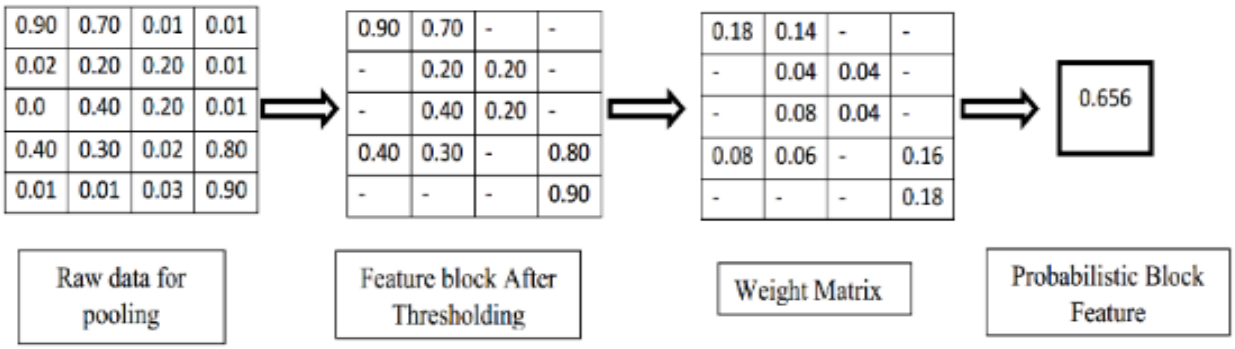


Fig.3. Illustration of Pooling Operation

Robust features are pooled from optical flow magnitude obtained by using rich and robust feature pooling (R2FP) method proposed by Xiong et.al [28]. Fig 3 illustrates the feature pooling process. For obtaining PWOFMH, optical flow magnitude matrix is first divided into *K* blocks and each block is further sub divided into *c* cells with 50 percent overlapping and magnitude value for each cell is firstly sorted in decreased order, the resulting vector for c^{th} cell of K^{th} block is $V_{K_c} \in R^{1*N}$, where *N* is the number of pixels in the cell. After sorting, feature selection is done based on the fact that feature that are more indicative are retained, while less indicative features are discarded. So feature value close to zero contain less important information [28] so these values are discarded. This feature selection gives more concrete representation compared to raw features. Finally the selected features of cell are pooled according to Eq. (6) [28] given as:

$$f(K_c) = w_{K_c}^T . V_{K_c} \quad (6)$$

Where $f(K_c)$ is pooled value of c^{th} cell of K^{th} sub Block, $w^T K_c$ is probabilistic weight matrix of c^{th} cell of K^{th} sub-block and V_{K_c} raw optical flow magnitude vector of c^{th} cell of K^{th} sub-block. After obtaining pooled value for each cell in a block, each block is represented by a histogram having 9 bins. The PWOFMH for a frame can be represented as $Fmi = [M_1, M_2 \ldots, M_K]$, where $M_1, M_2 \ldots, M_K$ are pooled magnitude values for *K* number of block in i^{th} frame of a video. Same procedure is followed for PWOFDH and represented as $Fdi = [D_1, D_2 \ldots, D_K]$, where $D_1, D_2 \ldots, D_K$ are pooled directional values from optical flow direction matrix for *K* number of blocks in i^{th} frame. Final feature vector for i^{th} frame of a video is concatenated histogram of PWOFMH and PWOFDH and can be represented as

$Fi = [Fmi\ Fdi]$. Final feature vector length for a frame will be equal to $2 * 9 * K * c$. Number of blocks and number of cells within a block depends upon the frame size of a video, as in our case each standard dataset having different frame size e.g. UMN dataset having frame size of 320*240 pixels, PETS 2009 dataset having frame size of 728*576 and Avanue dataset having frame size of 640*360. Subsequently those features are fed to classifier to obtain prediction on frames whether the given frame presents normal or abnormal situation and this process is described in the section below.

B. Training And Classification

Features obtained as explained in the previous section, is fed to OC-ELM that tries to find the smallest training error as well as the smallest norm of output weights [29] between the output layer and the hidden layer. As per Bartlett's theory [19], the network having smaller norm of weights, tends to have the better generalization performance. Thus, OC-ELM networks can give better generalization performance. In [17], equality constraints are used in ELM, which yields a unified solution for regression, binary, and multiclass classifications. For given N training samples (x_i, y_i), where i varies from$1\ to\ N$, $x_i = [x_{i1}, \dots x_{in}]^T \in R^n$ is the individual n dimensional feature vector and $y_i \in R^k$ is the desired output. In case of one-class classification problem, single output node is required. The ELM output function can be given as

$$f(x) = \sum_{j=1}^{L} \beta_j G(w_j, b_j, x) \tag{7}$$

where $\beta = [\beta_1, \dots \beta_L]^T$ is the weights vector connecting the output layer and the hidden layer, $w_j = [w_{j1}, \dots w_{jn}]^T$ is the vector of input weights between input nodes and the j^{th} hidden node, b_j is the bias of the j^{th} hidden node, and $G(w, b, x)$ is the activation function (e.g., sigmoid function) satisfying ELM universal approximation capability theorems [20, 21]. Actually, $G(w, b, x)$ is a nonlinear mapping function which maps the feature data x from the n-dimensional input space to the L-dimensional ELM feature space [17]. The objective of ELM is to minimize the training errors and the norm of output weights, which is equivalent to

$$\text{MIN}\ L_{ELM} = \frac{1}{2}\|\beta\|^2 + C\frac{1}{2}\sum_{i=1}^{N}\|\xi_i\|^2 \tag{8}$$

$$s.t \sum_{j=1}^{L} \beta_j G(w_j, b_j, x) = t_i - \xi_i; i = 1,2, \dots N$$

Where ξ_i is the slack variable of the training sample x_i and C controls the tradeoff between the errors and the output weights. When only normal or target class data is available for training purpose, the one-class classifier is trained to accept normal class objects and discard objects that deviate significantly from the normal class. In the training phase, the one-class classifier, which defines a distance function d between the objects and the target class, takes in the training set X to build the classification model. In general, the classification model contains two important parameters to be determined: threshold θ and modal parameter λ. A generic test sample z is accepted by the classifier if $d(z|X, \lambda) < \theta$.

The fundamental theory behind object recognition is that similar objects have to be close in the feature space and for similar objects, the target outputs should be the same:

$$t_i = a;\ \forall x_i \in X \tag{9}$$

Where a is class number (real number). All the training samples target outputs are set to the same value a. Then, the desired target output vector is $T = [t1, t2, \dots tn]^T = [a, a, \dots a]^T$. Training the samples from the target class can directly use the optimization function Eq. (8). For a new test sample z , the distance function between the sample object and the target class is defined as

$$\mathrm{d}_{ELM}(z|X, \lambda) = \left|\beta_j G\left(w_j, b_j, z\right) - a\right| \tag{10}$$

Threshold decides whether a test sample z belongs to the target class or outlier. It is optimized to reject a small fraction of training samples to avoid overfitting. The distances of the training samples to the target class can be directly determined using Eq. (10) and the constraint of Eq. (8)

$$\mathrm{d}_{ELM}(x_i|X, \lambda) = \left|\beta_j G\left(w_j, b_j, x_i\right) - a\right| = |\xi_i| \tag{11}$$

From Eq. (11), larger the value of $|\xi_i|$ means the training sample xi is more deviant from the target class. Hence, threshold is derived based on θ, a quantile function to reject the most aberrant training samples. The sorted sequence of the distances of training samples are denoted by $d = [d1, d2 \dots, dN]$. Here, $d1$ represents the most deviant samples and dN represents the least deviant samples. The function determining θ can be given as

$$\theta = \mathrm{d}_{floor(\mu, N)} \tag{12}$$

Where $floor(k)$ returns the largest integer not greater than k. Then, we can get the decision function for z to the target class:

$$\xi_{Elm}(z) = sign\left(\theta - \mathrm{d}_{ELM}(z|X, \lambda)\right) \tag{13}$$

When $\xi_{Elm}(z) = 1$, z is classified as target otherwise labeled as outlier.

IV. Experiment Simulation and Result Analysis

To demonstrate the effectiveness of our proposed algorithm, experiments were performed on three publicly available datasets: the UMN dataset [30], the PETS2009 dataset [31] and AVANUE dataset [32]. Our proposed method is compared against the state-of-the-art methods. The Receiver Operator Characteristics (ROC) plot and

Area Under the Curve (AUC) are being used as performance evaluation parameters. In a Receiver Operating Characteristic (ROC) curve is plotted between the true positive rate (Sensitivity) the false positive rate (100-Specificity) for different cut-off values. Each point on the ROC plot shows a sensitivity/specificity pair corresponding to a fixed threshold. A test with ideal segregation (no overlapping between two distributions) has a ROC curve that passes 100% sensitivity and 100 specificity.

THE UMN DATASET: The UMN dataset [30] were recorded by a stationary camera located at some elevation at three different locations (Lawn, Indoor, and Plaza). This dataset contains normal (walking) as well as abnormal behavior (running). Lawn scene contains total 1452 frames out of which 296 frames shows crowd escape behavior. Indoor scene and Plaza scene contains 4144 and 2142 frames respectively. The original resolution images are of 320 * 240 pixels. Some of the detected results of our proposed algorithm on UMN dataset (lawn scene) are shown in Fig 4, 5 and 6.



Fig.4. Detected results on UMN dataset (Lawn Scene)



Fig.5. Detected results on UMN dataset (Indoor Scene)



Fig.6. Detected results on UMN dataset (Plaza Scene)

Our proposed algorithm is compared with [4, 33] and [34], comparison results are given in Table 1. Our method achieve higher AUC value over state of the arts methods. ROC curve for all three different scenes are shown in Fig. 7, 8, 9.

Table 1. Comparison results of our proposed method with state-of-the-art methods (AUC performance of anomaly detection on the UMN dataset)

S.No	Dataset	HOFO [4]	HOS [33]	STCOG [34]	PROPOSED METHOD
1	Lawn Scene	0.9845	**0.9950**	0.9362	0.9910
2	Indoor Scene	0.9037	0.9330	0.7759	**0.9859**
3	Plaza Scene	0.9815	0.9800	0.9661	**0.9982**

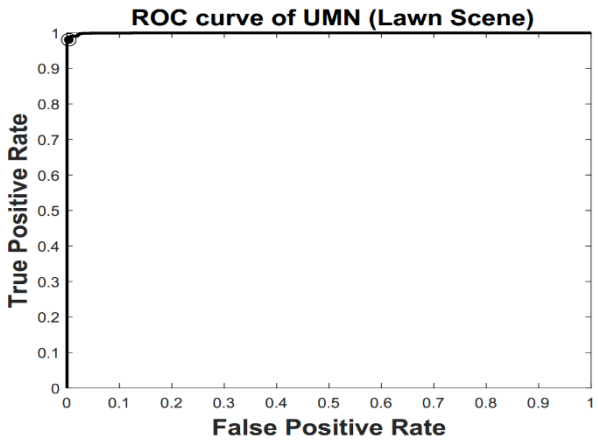


Fig.7. ROC curve for UMN lawn scene

THE PETS2009 DATASET: The PETS2009 datasets [31] contain three different sequences encompassing crowd situations with increasing complexity of scene. The resolution of the PETS2009 dataset images are 728 x 576 pixels. Dataset S0 contains training data. Dataset S1 is

mainly for person count and density estimation. Dataset S2 involves people tracking. Dataset S3 addresses crowd flow analysis and abnormal event detection. Some frames of PETS2009 dataset are shown in Fig 10.

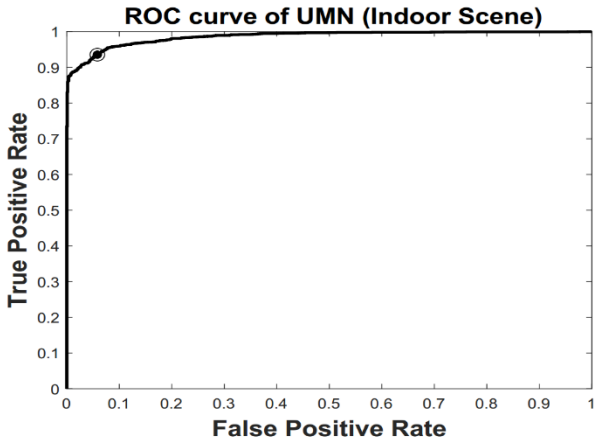


Fig.8. ROC curve for UMN Indoor scene

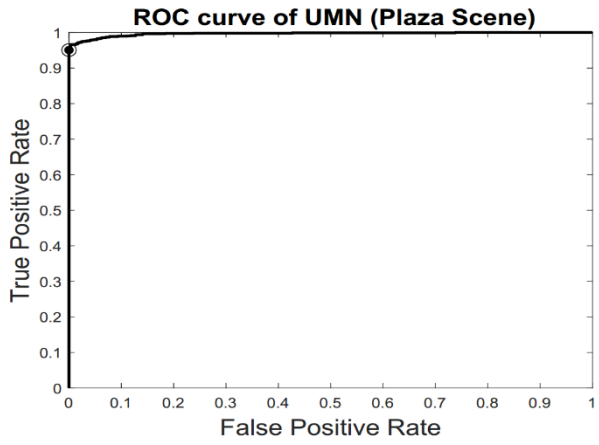


Fig.9. ROC curve for UMN Plaza scene

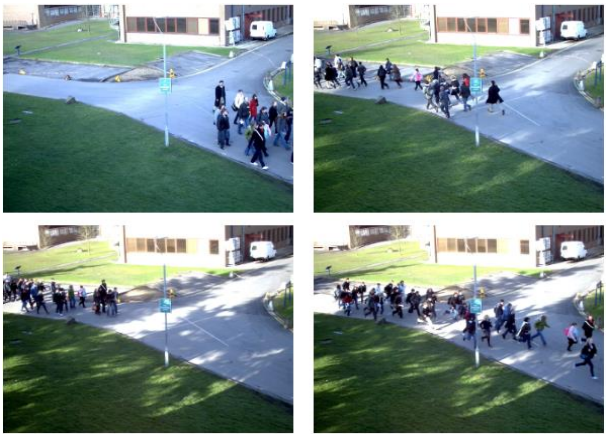


Fig.10. PETS2009 dataset :(left column: normal situation, right column: abnormal situation)

The experiments are performed on view 1 [31] for time sequence 14-17, 14-16, 14-06 and 14-55. The detection results on PETS2009 (time sequence 14-16) are shown in Fig 11. Where persons are running or walking from left to right or right to left direction. A normal situation corresponds to individuals walking at normal speed. While aberrant situation corresponds to the persons started running.



Fig.11. Detected results on PETS2009 (Time 14-16)

Classifier is trained only for normal situation where individuals are walking, training frames are chosen form time sequence 14-16 and 14-06. By our proposed method 95.27% detection accuracy is achieved. ROC curve for detection result on Time 14-16 is shown in Fig 12, AUC value for roc curve of time 14-16 is 0.9874.

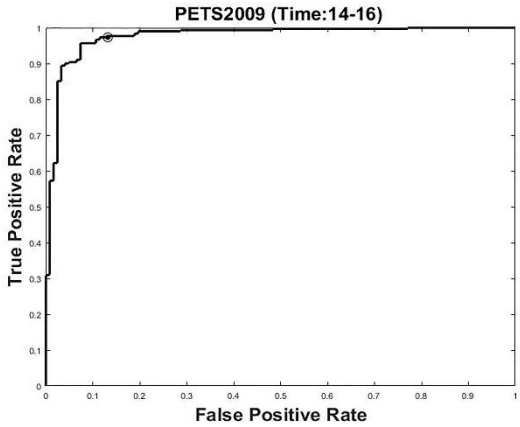


Fig.12. ROC curve for PETS2009 (Time 14-16)



Fig.13. Detected results on PETS2009 (Time 14-17)

The detection result on PETS2009 (time sequence 14-17) are shown in Fig 13, where walking is taken as normal situation and running is taken as abnormal situation. Detection accuracy for time 14-17 is 92.28% and AUC value is 0.9558. ROC curve is shown in Fig 14.

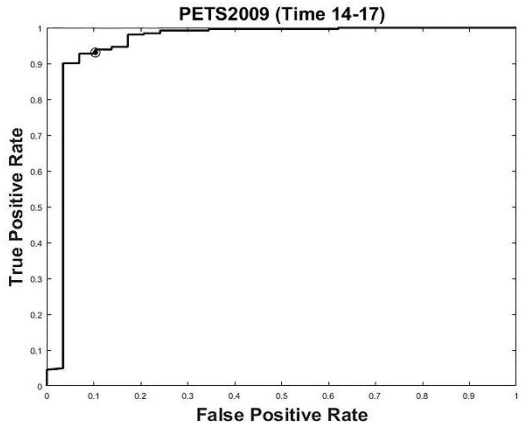


Fig.14. ROC curve for PETS2009 (Time 14-17)

THE AVANUE DATASET: The Avenue dataset [32] contains 16 training videos and 21 videos for testing, the videos include a total of 15183 frames for training and 15324 frames for testing. The resolution of video is 640*360. The training videos capture normal situations. Testing videos include both normal and abnormal events. This dataset contains abnormalities like running, wrong direction movement, jumping and throwing object. Some frames, where abnormalities are detected are shown in Fig 15.



Fig.15. Detected results on AVANUE dataset

This dataset contains the challenges like minor camera shake (testing video 2, frame 1051- 1100) presents, a few outliers are included in training data and some normal patterns seldom appear in training data. ROC Curve of detection result on Avanue dataset are shown in Fig.16 and comparison result of our method with method presented [35] in Table 2.

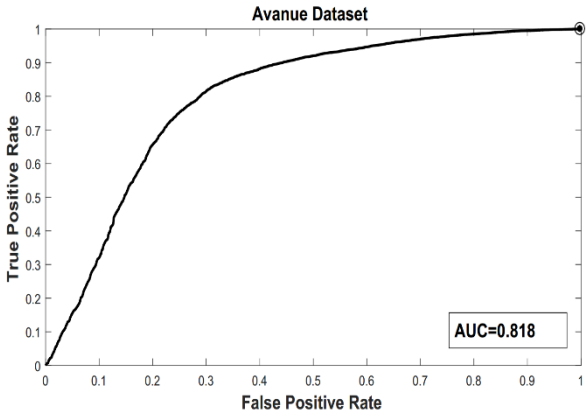


Fig.16. ROC curve for AVANUE dataset

Table 2. Comparison results of our Proposed method with state-of-the-art methods (AUC performance of anomaly detection on the AVANUE dataset)

S.No	Method	AUC	Accuracy
1	[36]	0.809	-
2	Proposed Method	0.818	88.10

V. CONCLUSION

In this paper, an effective algorithm for crowd escape or stampede event detection based on crowd motion modelling is proposed. Crowd movement information is represented by movement direction and speed model is trained on One Class Extreme Learning Machine (OC-ELM), which outperform for anomaly detection. In this algorithm, pooling operation is used which gives sparse representation of features and reduces the computational load of machine learner. ROC curve and high value of AUC of our model on different datasets show good performance of proposed algorithm over state-of-the-art methods. High detection rate on UMN, PETS2009 datasets and AVANUE dataset demonstrate that our proposed algorithm can be used in challenging conditions specially in little bit noisy conditions. It's effectiveness in challenging crowed scenes, make our method very suitable for a wide variety of video surveillance applications. Our proposed method achieve good accuracy over different crowd datasets, however our algorithm is not applicable for real time application because optical flow calculation of each frame consumes a lot of time of this algorithm. So some different approach to obtain motion information can be used in future to make this algorithm work in real time. So in future, some other addition information can also be utilize e.g. deep learning, shape information etc., to make this algorithm work more efficiently and effectively in more challenging conditions.

Copyright © 2019 MECS

ACKNOWLEDGMENT

We would like to thanks unknown reviewers for their valuable suggestions. This research work is fully supported by Dr. B R Ambedkar National Institute of Technology, Jalandhar, Punjab, India.

REFERENCES

[1] M. Heikkila, M. Pietikainen, "A texture-based method for modeling the background and detecting moving objects" *IEEE transactions on pattern analysis and machine intelligence* 28 (4) (2006) 657–662.

[2] L. Kratz, K. Nishino," Anomaly detection in extremely crowded scenes using spatio-temporal motion pattern models", *Computer Vision and Pattern Recognition, 2009. CVPR 2009. IEEE Conference on, IEEE, 2009*, pp. 1446–1453.

[3] Y. Yuan, J. Fang, Q. Wang, "Online anomaly detection in crowd scenes via structure analysis", *IEEE Transactions on Cybernetics* 45 (3) (2015) 548–561.

[4] T. Wang, H. Snoussi, "Detection of abnormal visual events via global optical flow orientation histogram", *IEEE Transactions on Information Forensics and Security* 9 (6) (2014) 988–998.

[5] N. Dalal, B. Triggs, "Histograms of oriented gradients for human detection", Computer *Vision and Pattern Recognition, 2005. CVPR 2005. IEEE Computer Society Conference on, Vol. 1*, (2005), pp. 886–893.

[6] G. Zen, E. Ricci, 'Earth mover's prototypes: A convex learning approach for discovering activity patterns in dynamic scenes", *Computer Vision and Pattern Recognition (CVPR), 2011 IEEE Conference on, IEEE*, 2011, pp. 3225–3232.

[7] Z. Fu, W. Hu, T. Tan, "Similarity based vehicle trajectory clustering and anomaly detection", *Image Processing, 2005. ICIP 2005. IEEE International Conference*, Vol. 2, IEEE, 2005, pp. II–602.

[8] Y. Cong, J. Yuan, J. Liu, "Sparse reconstruction cost for abnormal event detection", *Computer Vision and Pattern Recognition (CVPR), 2011 IEEE Conference on, IEEE*, 2011, pp. 3449– 3456.

[9] C. Lu, J. Shi, J. Jia, "Abnormal event detection at 150 fps in matlab", *Proceedings of the IEEE International Conference on Computer Vision*, 2013, pp. 2720–2727.

[10] B. Zhao, L. Fei-Fei, E. P. Xing, "Online detection of unusual events in videos via dynamic sparse coding", *Computer Vision and Pattern Recognition (CVPR), 2011 IEEE Conference on, IEEE*, 2011, pp. 3313–3320.

[11] O. Boiman, M. Irani, "Detecting irregularities in images and in video", *Computer Vision, 2005. ICCV 2005. Tenth IEEE International Conference on*, Vol. 1, IEEE, 2005, pp. 462–469.

[12] V. Saligrama, Z. Chen, "Video anomaly detection based on local statistical aggregates", *Computer Vision and Pattern Recognition (CVPR), 2012 IEEE Conference on, IEEE*, 2012, pp. 2112– 2119.

[13] R. Hamid, A. Johnson, S. Batta, A. Bobick, C. Isbell, G. Coleman, "Detection and explanation of anomalous activities: Representing activities as bags of event n-grams", *Computer Vision and Pattern Recognition, 2005. CVPR 2005. IEEE Computer Society Conference on, Vol. 1, IEEE*, 2005, pp. 1031–1038.

[14] J. Kim, K. Grauman, "Observe locally, infer globally: a space time mrf for detecting abnormal activities with incremental updates", *Computer Vision and Pattern Recognition, 2009. CVPR 2009. IEEE Conference on, IEEE*, 2009, pp. 2921–2928.

[15] D. Zhang, D. Gatica-Perez, S. Bengio, I. "McCowan, Semisupervised adapted hmms for unusual event detection", *Computer Vision and Pattern Recognition, 2005. CVPR 2005. IEEE Computer Society Conference on*, Vol. 1, 2005, pp. 611– 618.

[16] E. L. Andrade, S. Blunsden, R. B. Fisher, "Modelling crowd scenes for event detection", *Pattern Recognition, 2006. ICPR 2006. 18th International Conference on*, Vol. 1, IEEE, 2006, pp. 175–178.

[17] Y. Benezeth, P.-M. Jodoin, V. Saligrama, C. Rosenberger, "Abnormal events detection based on spatio-temporal cooccurences", *Computer Vision and Pattern Recognition, 2009. CVPR 2009. IEEE Conference on, IEEE*, 2009, pp. 2458–2465.

[18] R. Mehran, A. Oyama, M. Shah, "Abnormal crowd behavior detection using social force model", *Computer Vision and Pattern Recognition, 2009. CVPR 2009. IEEE Conference on, IEEE*, 2009, pp. 935–942.

[19] A. Adam, E. Rivlin, I. Shimshoni, D. Reinitz, "Robust real-time unusual event detection using multiple fixed-location monitors", *IEEE transactions on pattern analysis and machine intelligence* 30 (3) (2008) 555–560.

[20] S. Wu, B. E. Moore, M. Shah, "Chaotic invariants of lagrangian particle trajectories for anomaly detection in crowded scenes", *Computer Vision and Pattern Recognition (CVPR), 2010 IEEE Conference on, IEEE*, 2010, pp. 2054–2060.

[21] X. Cui, Q. Liu, M. Gao, D. N. Metaxas, "Abnormal detection using interaction energy potentials", *Computer Vision and Pattern Recognition (CVPR), 2011 IEEE Conference on, IEEE*, 2011, pp. 3161–3167.

[22] M. H. Sharif, C. Djeraba, "An entropy approach for abnormal activities detection in video streams", *Pattern recognition* 45 (7) (2012) 2543–2561.

[23] J. Kwon, K. M. Lee, "A unified framework for event summarization and rare event detection from multiple views", *IEEE transactions on pattern analysis and machine intelligence* 37 (9) (2015) 1737–1750.

[24] X. Gu, J. Cui, Q. Zhu, "Abnormal crowd behavior detection by using the particle entropy", *Optik-International Journal for Light and Electron Optics* 125 (14) (2014) 3428–3433.

[25] M. H. Sharif, S. Uyaver, C. Djeraba, "Crowd behavior surveillance using bhattacharyya distance metric", *International Symposium Computational Modeling of Objects Represented in Images, Springer*, 2010, pp. 311–323.

[26] R. Goshorn, D. Goshorn, J. Goshorn, L. Goshorn, "Abnormal behavior-detection using sequential syntactical classification in a network of clustered cameras", *Distributed Smart Cameras, 2008. ICDSC 2008. Second ACM/IEEE International Conference on, IEEE*, 2008, pp. 1–10.

[27] J. L. Barron, D. J. Fleet, S. S. Beauchemin, T. Burkitt, "Performance of optical flow techniques", *Computer Vision and Pattern Recognition*, 1992. *Proceedings CVPR'92., 1992 IEEE Computer Society Conference on, IEEE*, 1992, pp. 236–242.

[28] W. Xiong, L. Zhang, B. Du, D. Tao, "Combining local and global: Rich and robust feature pooling for visual recognition", *Pattern Recognition* 62 (2017) 225–235.

[29] Q. Leng, H. Qi, J. Miao, W. Zhu, G. Su, "One-class classification with extreme learning machine", *Mathematical problems in engineering* 2015.

[30] UMN, Unusual event datasets of university of minesota. URL http://mha.cs.umn.edu/Movies/Crowd-Activity-All.avi.
[31] PETS, Pets2009 benchmark dataset. URL http://cs.binghamton.edu/~mrldata/pets2009
[32] C. Lu, J. Shi, J. Jia, Abnormal event detection at 150 fps in matlab, in: *Proceedings of the IEEE international conference on computer vision*, 2013, pp. 2720–2727. URL http://www.cse.cuhk.edu.hk/leojia/projects/detect abnormal/dataset.html
[33] V. Kaltsa, A. Briassouli, I. Kompatsiaris, L. J. Hadjileontiadis, M. G. Strintzis, "Swarm intelligence for detecting interesting events in crowded environments", *IEEE transactions on image processing* 24 (7) (2015) 2153–2166.
[34] Y. Shi, Y. Gao, R. Wang, "Real-time abnormal event detection in complicated scenes", *Pattern Recognition (ICPR), 2010 20th International Conference on, IEEE*, 2010, pp. 3653–3656.

Authors' Profiles



Mr Gajendra Singh, received the Bachelor degree in Electronics and communication engineering from GLAITM, Mathura and his post-graduation degree in Electronics and communication engineering from NIT, Jalandhar. His research interests are Image Processing, Deep Learning and Machine Learning.



Prof. Arun Khosla is professor at NIT jalandhar, He has published hundreds of research papers on Image, fuzzy systems and wireless communication in journal and conferences. His research interest includes Image Processing, Internet of Things (IoT) and Wireless Communication.



Prof Rajiv Kapoor is professor at Delhi Technological University, Delhi. He was also Principle of AIACT&R, Delhi. He has published hundreds of research papers on Image and signal analysis in journal and conferences. His research interest includes Vision/Speech based Tracking, Activity Recognition Vision/Speech based, Signal Processing, Pattern Recognition, Cognitive Radio.

How to cite this paper: Gajendra Singh, Arun Khosla, Rajiv Kapoor, "Crowd Escape Event Detection via Pooling Features of Optical Flow for Intelligent Video Surveillance Systems", International Journal of Image, Graphics and Signal Processing(IJIGSP), Vol.11, No.10, pp. 40-49, 2019.DOI: 10.5815/ijigsp.2019.10.06

Journal of The Gujarat Research Society

ISSN: 0374-8588
Volume 21 Issue 11, November 2019

Design and Analysis of Thermal Therapy Pad Using Computational Fluid Dynamics – A Review

Harsh Shyam[1], Amit Pal[2], Manish Jain[3]

[1]P.G. Scholar, [2]Professor
Department of Mechanical Engineering, Delhi Technological University, Delhi, 110042
[3]Asstt. Professor, RJIT BSF Tekanpur, Gwalior

Abstract

In medical technology, the advancement of thermal therapy of either heating or cooling gives an extra edge that are intended to improve the quality of healthcare. Thermal therapy pad is a device which can influence blood circulation at an injured site, to a specific area of the body and increase the comfort of the patient. The main purpose of thermal therapy pad is to enhance the heeling process. Localized thermal transfer helps to provide one or more of the therapeutic effects. These effect refers to the acknowledgement after a treatment of any kind, the results of which are judged to be indispensable and effective.

In medical industry, thermal therapy has emerged as an effective and reliable treatment to make the patient feel good and acts as a catalyst in healing process. The forms of using of thermal therapy has a wide range. Some of the household application are using a moist hot cloth during fever, using hot water bottle for pain relief, manicure & pedicure, bonfire. This is not the limit of its application, these being the domestic application, now-a-days this therapy is being used by medical persons to cure cancer, keep the exposed tissues of patients in required surrounding so that the tissue does not get affected, keep the newly born infant warm.

The Mul-T-Pads are disposable thermal transfer devices for use in a Localized Temperature Therapy system. The Mul-T-Pad, disposable pads are intended as thermal transfer devices for use with a Temp Pump Localized Therapy Pump, which supplies warm or cold water at controlled temperatures for the application of localized therapy in situations where a physician determines that temperature therapy is necessary or desirable.

Keywords- *CFD;heattherapy;thermal therapy pad; heat transfer.*

1. INTRODUCTION

In medical technology, it is a common practice to treat the injured areas of the patient using thermal therapy pad. This practice involves the application of cold or heat locally to the specified area to heel the injured or operated part. The main purpose of thermal therapy pad is to provide uniform temperature to the assigned body parts to get the effective and efficient result. For this even distribution of temperature is important at each point of the thermal pad. Moreover, the thermal pad may be used in folded state so the uniform circulation of the fluid is also a desired factor for the effective result.

Localized thermal transfer involves the application of cold or heat, either dry or moist, to a specific area of the body to provide one or more of the following therapeutic effects [1]:

ISSN: 0374-8588
Volume 21 Issue 11, November 2019

Table 1 : Thermal Therapy and their therapeutic effects

Cold Therapy	Heat Therapy
Decrease Blood Flow	Increase Blood Flow
Decrease Edema	Decrease Swelling
Decrease Hemorrhage	Prevent Tissue Encrustation
Decrease Inflammation	Promote Wound Drainage
Decrease Muscle Spasm	Decrease Muscle Spasm
Decrease Pain	Decrease Pain
Provide Patient Comfort	Provide Patient Comfort

As seen in Table , these therapeutic indications for localized cold or heat therapy are broad. Many conditions demand for application of either modality depending on how soon the treatment is initiated. For example, in orthopedic cases, if treatment commences within the first 48 hours after the injury occurs, cold therapy is usually instituted. Thereafter, heat therapy is the desired mode of treatment. Thermal therapy comprising applications of cold, heat or some combination of the two is useful for a variety of cellulitis, chronic pain, low back pain, muscle spasm, post-op, sprains, strains, wounds, alopecia, abscesses, headaches, nose bleeds, burns, circulatory disorders, infections, neuritis, phlebitis, and tendonitis [1].

Having so much of diversified application, there is a need to optimize the circulation of fluid inside thermal therapy pad and uniform temperature distribution is of high concern. Developments has helped to process this therapy using a fluid-circulating thermal therapy systems in which the therapy pad is connected with this system. After feeding the desired input data in the system like pressure, temperature and cycle time, the system is switch on and the fluid starts circulating in the thermal pad. Within a time span of 5 min a steady state can be observe on the thermal pad.

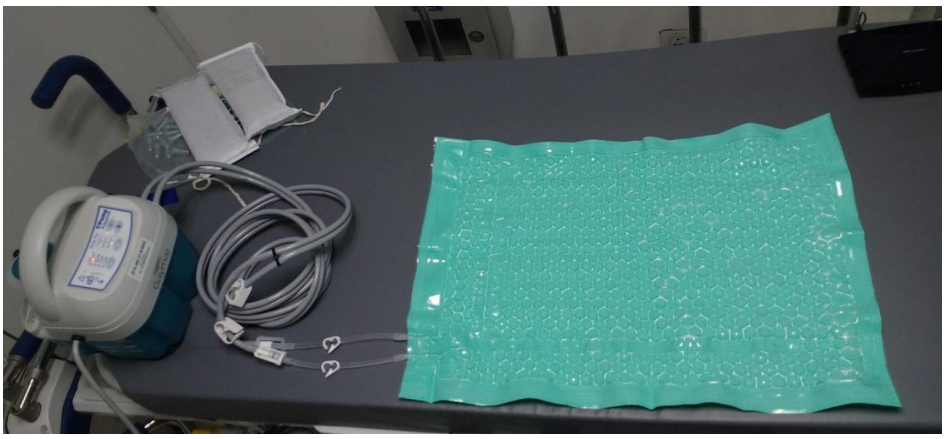


Fig. 1. Thermal Therapy System with Mul T Pad

2. THERMAL THERAPY SYSTEMS AND DEVELOPMENTS

Living in 21st century one cannot guess the actual evolution of thermal therapy. But one can surely assist that this was being used from AD (Anno Domini - Latin for The Year of the Lord) or even BC (Before Christ).

G.P. Herndon (1889) was the one whose model of water bandage was first patented in field. Herndon invented some new design and techniques to make the bandage more helpful and efficient by providing different arrangements of tubes i.e. a coiled flexible tube to hold the surface intact, numbers of short tubes being secured to the inner surface and thus hold the surface intact. These improvements also prevent the inflation of the bag or covering [1].

J. Holland (1903) proposed a hot water bottle design that prevents the accumulation of fluid at some points which was leading to unexpected expansion. He suggested to sandwich the tube of same material between the two surfaces of the bottle at different points and place it in a vulcanizing heat. Vulcanization process unite the short tubes with the bottle surfaces. This makes the bottle more serviceable, serves well even if the bottle is not full as the small pockets thus formed restrict the movement of fluid [2].

R. E. Coleman (1963) proposed a personal thermal device comprising of flexible heat exchanger with inbuilt passages to circulate the liquid by means of thermopump. This thermopump may consists of electrical heater or some other heat source to heat the liquid and the pump play the role in circulating the heated liquid through the passages provided between the two fabrics of the blanket, garments, mattress cover, or similar items of personal use. Coleman suggested to use the tube of small diameter and connect this to the small junction units rather than using large diameter tubes which may arises problems when the blanket gets folded in operating condition [3].

Gammons et al. (1979) gave a design of a flexible fluid circulating pad having interconnecting internal passages for circulating desired liquid i.e. hot or cold. In this design, there are set of partitions that enables the continuous flow of the fluid to all the areas even if the pad is in folded condition. This is possible because the liquid can flow randomly in any direction. Suppose the pad gets crimp at any particular area then the liquid will deviate its direction through the most possible passage thus avoiding the accumulation or discontinuity in the flow. This patient treatment pad was named, the Gaymar T-pad. Major concept in designing this pad was to provide a narrow inlet and outlet channel along two adjacent edges by providing row of closely spaced seal button pattern and the remaining circulating area was covered by randomly placing the round seal buttons to provide random passage to the entire area. This reduces the fluid restriction during the folded condition and fluid will take the path of least resistance and there might be a possibility of no circulation region or little circulation region when pad is folded but this will not restrict the flow as it will deviate the flow [4].

Ronald et al. (1989) build a liquid circulating thermal therapy system which includes flexible thermal pad and a pump assembly. Pump assembly consist of heater, thermostat, reservoir. A honeycomb like passage was provided inside the thermal therapy pad. This reduces the fluid's blocking problem even in folded condition. The system had a function to control the temperature so that the user gets the desired therapy environment. Thermal pad surface was built with a foam having cushion surface to reduce the risk of ischemia and enhance patient comfort[5].

A. K. Bhaskar (1975)invented fluid heating and temperature control unit for a system utilizing a circulating fluid type heating pad or thermal blanket. The unit comprises a bulkhead with a fluid reservoir mounted below and a cover mounted above including means for directing the flow of ventilating air. The bulkhead carries a heater extending into the reservoir, a fluid circulator and a thermostatic temperature control device including a sensor having channels, one of which carries in flowing fluid and the other of which carries outgoing fluid so that the control of temperature is responsive to both inflowing and outflowing fluids, substantially to the average temperature thereof. In this manner a more satisfactory control of temperature of the heating pad is achieved than if the control were made responsive either to the temperature of the hotter fluid flowing into the pad or the cooler fluid returning therefrom [10].

Moore et al. (1975)designed a temperature controlled applicator or pad which may be applied to a selected area of application of the body as a covering or dressing; or in the treatment of a wound, incision, bruise, burn or sprain; or as a covering for an organ either in situ or after removal, as in a transplant, to induce hypothermia in the organ. In this pad, a continuous fluid conduit is formed by heat sealing sheets of thermoplastic material together so as to form a conduit layer having a continuous serpentine or meandering flexible tubular conduit for conducting the hot or cold fluid, such as water. Earlier pads are especially designed for use with a companion heating and cooling unit, and the same pad is used over and over again until it is either damaged or wears out. Hence, in order to prevent cross-contamination, the pad must be sterilized. These pads are difficult to sterilize and they may become contaminated during storage between use. So, the inventor designed a disposable pad which may be made of low-cost materials to reduce the overall cost, and it is easily sterilized during manufacture according to conventional technique [11].

Gammons et al. (1979**)** gave a design of a flexible fluid circulating pad having interconnecting internal passages for circulating desired liquid i.e. hot or cold. In this design, there are set of partitions that enables the continuous flow of the fluid to all the areas even if the pad is in folded condition. This is possible because the liquid can flow randomly in any direction. Suppose the pad gets crimp at any particular area then the liquid will deviate its direction through the most possible passage thus avoiding the accumulation or discontinuity in the flow. This patient treatment pad was named, the Gaymar T-pad. Major concept in designing this pad was to provide a narrow inlet and outlet channel along two adjacent edges by providing row of closely spaced seal button pattern and the remaining circulating area was covered by randomly placing the round seal buttons to provide random passage to the entire area. This reduces the fluid restriction during the folded condition and fluid will take the path of least

resistance and there might be a possibility of no circulation region or little circulation region when pad is folded but this will not restrict the flow as it will deviate the flow [4].

Ronald et al. (1989)build a liquid circulating thermal therapy system which includes flexible thermal pad and a pump assembly. Pump assembly consist of heater, thermostat, reservoir. A honeycomb like passage was provided inside the thermal therapy pad. This reduces the fluid's blocking problem even in folded condition. The system had a function to control the temperature so that the user gets the desired therapy environment. Thermal pad surface was built with a foam having cushion surface to reduce the risk of ischemia and enhance patient comfort. [5] .

Kelly et al. (1995) designed a device that enables application of continuous passive motion therapy and thermal therapy simultaneously. In doing so, the therapy pad may face the blockage problems. To overcome this the easiest option is to provide a parallel circuit from inlet to outlet to maintain continuity of flow, but the heat transfer rate would get affected. So, Inventors provided a spiral cut on the internal conduit. Thus, on action of radial compression these spiral cuts get elongated and makes a passage for the fluid to escape. This gave the possibility to use thermal pad in folded condition, which has increased reliability and improved continuity of flow [6].

Agarwal et al. (2005)designed a new thermal therapy pad having removable layers. The pad has a plurality of layers that may be removed. In a heating pad, this exposes the reactive material in the pad core to more oxygen while simultaneously removing insulation from the pad. In a cooling pad, this removes insulation between the reactive material and the user. The user may thus tailor the rate of heat delivery or removal to his/ her skin to the rate he/she desires. The removal of layers results in increased heat removal or delivery to the skin. The removed layer may be reapplied on the same side from which it was removed or on the side opposite, or discarded. The pad may use an iron powder reactive core which reacts exothermically with air to provide heating or water and other reactants that react endothermically. More than one core may be used to further tailor the amount and rapidity of the temperature change [12].

Flick et al. (2005)invented afirst conformable material having a three-dimensional shape and a first hypothermia (reduction of the core temperature) and/or hyperthermia (increase in the body core temperature) device [14]. This invention is used as a pad for sleeping, lying down, or sitting, to maintain a desired temperature to the contacting surface of a body to the pad. This pad comprises of pad cover and is a first gelatinous elastomeric material having a three-dimensional shape with a top surface, a bottom surface and at least one side surface and a plurality of apertures positioned on the exterior of the top surface, the bottom surface or the at least one side surface and interspaced throughout the first gelatinous elastomeric material. It is a first convective hypothermia and/or hyperthermiadevice positioned near the first gelatinous elastomeric material to allow the pad to have a desired temperature [13].

Mohn Louise (2011)gave a new thermosimulation method using multilayer pads with integrated temperature regulation. the therapeutic method is thermostimulation and includes the steps of applying heat and stimulation via the pad, sensing temperature at the pad with an embedded temperature sensor and regulating the heat current at the pad via the inline control system in response to the output of the temperature sensor. In an alternative embodiment, the embedded sensor is a galvanic skin response sensor for measuring skin conductivity and having output is used by the inline controller in the treatment of dermatological conditions, relaxation treatment, desensitization training or other purposes. In any case, useful data with respect to the performance of and conditions at each pad is displayed either on the inline controller and/ or at the console. In addition, the inline controllers may be adapted to communicate with each other and/ or with other external devices [21].

Kelner et al. (2012)invented a thermal pump for controlling air bubbles, thermal therapy to allow the patient to perceive that thermal therapy is constantly being applied, and ensure the appropriate amount of water flows through the thermal pump. This thermal pump system comprises of a pump container having a dry compartment that contains a motor, a wet compartment that contains a propeller, and a shaft system that interconnects the motor to the propeller. The wet compartment has a water inlet, the propeller pulls water from a water bath into the wet compartment through the water inlet and pushes the water into a conduit toward a heating block and to a patient application device, the heating block has a heating pad and/or a cooling pad; and a therapy management device that controls the thermal energy provided by the heating pad and/or the cooling pad to direct the water's temperature [15].

3. PROBLEM IDENTIFICATION AND OBJECTIVES

The primary function of heat therapy primarily for relaxation, comfort, and reassurance, and taking the edge off of several kinds of body pain, mostly duller and persistent pains associated with stiffness, cramping, and/or sensitivity, which can be loosely categorized [8]:

I. Acute soreness from over-exertion: the pain we get after the first ski trip of the season.

II. Stiffness and pain in specific areas related to osteoarthritis, muscle "knots" or trigger points, and most kinds of cramping/spasm (menstrual, neuropathic, restless leg syndrome, for example, or even just stiffness from postural strain)

III. "Hurts all over" pain and sensitivity. There are many kinds, but primarily: fibromyalgia, the rheumatic diseases, drug (Several drugs make muscles hurt, but the most notorious are the statins (cholesterol-reducing drugs) and bisphosphonates (for osteoporosis). In some people, these act like muscle poisons) side effects, vitamin D deficiency, and sleep deprivation.

Heat will make some conditions much worse. Heat is never applied to an infection or fresh injury, or any other acutely inflammation, like a flare-up of arthritis. In these cases, ice is used for: soothing inflamed tissue [8].

The primary function of heat therapy system is to transfer temperature to the desired body parts. Specifically, the primary design goal is to distribute the fluid and maintain required temperature evenly to the entire surface area, as doing so improve the therapy system ability to efficiently produce uniform temperature and therapeutic effects. The geometric design of the thermal therapy pad affects the efficiency of the therapy system, and thus directly affects the level of comfort [9]. The construction of the passage in thermal pad has a major influence on how the therapy performs at various condition [10]. The challenge, therefore, was to optimize the design of the intake passage system and remap the thermal therapy system. To achieve primary design goal of distributing equivalent amount of heat to entire surface area, there are several objectives to consider when designing a thermal pad:

i. Minimize pressure loss, as pressure loss results in a discontinuity.

ii. Maximize fluid velocity into the pad, as this provides a better result by providing a uniform temperature distribution in minimum possible time.

iii. Provide uniform warming/cooling. The difference between the supply line temperature and the return line temperature must not exceed 4 ºF. The difference between the temperature at any point on the product must not exceed 4 ºF.

iv. Minimize fluid spillage when disconnecting. So, there shall be no flow of water through the product once the connectors are disengaged.

v. Resistant to Bio fluids.

vi. Pad may be used with X-ray, MRI and CT imaging procedures and equipment. So, material should be compatible with X-ray, MRI, and CT imaging procedures and equipment.

4. CONCLUSION

In medical technology, the advancement of thermal therapy of either heating or cooling gives an extra edge that are intended to improve the quality of healthcare. Thermal therapy pad is a device which can influence blood circulation at an injured site, to a specific area of the body and increase the comfort of the patient. The main purpose of thermal therapy pad is to enhance the heeling process. Localized thermal transfer helps to provide one or more of the therapeutic effects. These effect refers to the acknowledgement after a treatment of any kind, the results of which are judged to be indispensable and effective.In medical industry, thermal therapy has emerged as an effective and reliable treatment to make the patient feel good and acts as a catalyst in healing process. The forms of using of thermal therapy has a wide range. Some of the household application are using a moist hot cloth during fever, using hot water bottle for pain relief, manicure & pedicure, bonfire. This is not the limit of its application, these being the domestic application, now-a-days this therapy is being used by medical persons to cure cancer, keep the exposed tissues of patients in required surrounding so that the tissue does not get affected, keep the newly born infant warm.The thermal pad model was made in CREO PARAMETRIC and analysis will be done in ANSYS 18.1(FLUENT).

REFERENCES

[1] GEORGE P. HERNDON (1889). *Water Bandage.* Available:www.google.tl/ patents/US396208. Last accessed September 11, 2017

[2] JOSEPH HOLLAND (1903). *Hot-Water Bottle*. Available:www.google.ch/patents/US735876. Last accessed September 12, 2017

[3] R. E. COLEMAN (1963). *Personal Thermal Device*. Available:www.google.com/patents/US3112792. Last accessed September 13, 2017

[4] Clifford E. Gammons, Francis C. Moore, Leon R. Perkinson (1979). *Fluid Circulating Pad*. Available: www.google.tl/patents/US4149541. Last accessed September 13, 2017.

[5] Ronald L. French, Ronald E. Smith, Mark J. Buch (1989). Liquid-Circulating Thermal Therapy System. Available: www.google.co.in/patents/US4844072. Last accessed September 11, 2017

[6] Kevin A. Kelly, Roman Szpur (1995). *Thermal Therapy Pad*. Available: www.google.tl/patents/US5383919.

[7] Heat Treatments. (n.d.) Gale Encyclopedia of Medicine. (2008). Retrieved November 12 2017 from https://medicaldictionary.thefreedictionary.com/Heat+Treatment

[8] Garra G, Singer AJ, Leno R, et al. *Heat or cold packs for neck and back strain: a randomized controlled trial of efficacy.*AcadEmerg Med. 2010 May;17(5):484–9.

[9] Kenneth R. Diller (2015). Heat Transfer in Health and Healing. Journal of Heat Transfer. OCTOBER 2015, Vol. 137 / 103001-1, 1-12.

[10] Bhaskar Kumar Agarwala (1975). *Fluid Circulating Pad*. Available: www.google.com/patents/US3894213.

[11] Francis C. Moore, Leon R. Perkinson (1975). *Disposable, Sterile Temperature Control Applicator Pad for Medical Application*. Available: www.google.si/patents/US3867939.

[12] Naveen Agarwal, Jeffrey Eldon Fish (2005). *Thermal Therapy Pad with Variable Heat Control*. Available: www.google.com/patents/US6893453.

[13] Roland E. Flick, T.Jusiak (2005). *Hypo/Hyperthermia Pad*. Available:www.google.com/patents/US6871365.

[14] Deussen, A. Anaesthesist (2007) 56: 907. https://doi.org/10.1007/s00101-007-1219-4.

[15] William J. Kelner, Thomas P. Stewart (2012). *Thermal Pumps with Features*. Available: http://www.google.tl/patents/US8257414

[16] Furlan RM, Giovanardi RS, Britto AT, Oliveira e Britto DB (2015). *The use of superficial heat for treatment of temporomandibular disorders: an integrative review*. 2015 Mar-Apr;27(2):207-12. doi: 10.1590/2317-1782/20152014148.

[17] Guy L. Clifton, Emmy R. Miller (2004). *Heat Transfer Blanket for and Method of Controlling a Patient's Temperature.* Available: www.google.com/patents/US6682550.

[18] Richard D. Grant, Shaker Heights (1965). *Air Mattress.* Available: https://www.google.com/patents/US3199324

[19] Aziz Belmiloudi (2011). *Thermal Therapy: Stabilization and Identification, Heat Transfer – Mathematical Modelling, Numerical Methods and Information Technology*, Prof. Aziz Belmiloudi (Ed.), ISBN: 978-953-307-550-1, InTech, Available from: http://www.intechopen.com/books/heat-transfer-mathematical-modellingnumerical-methods-and-information-technology/thermal-therapy-stabilization-and-identification.

[20] ANSYS® Academic Research, Release 18.1, Help System, Fluent User's and Theory Guide, ANSYS, Inc

[21] Mohn Louise (2011). *Thermosimulation Methods using multilayer Pads with Integrated Temperature Regulation*. Available: www.google.ch/patents/US20110130796.

[22] Clinton 0. Fruitman (2012). *High Comfort Hot or Cold Thermal Therapy Pad*. Available: www.google.com/patents/US20120215293.

[23] John L. Woods (2013). *Multi-Layered Heat Therapy and Electrotherapy Back Pad Device*. Available: www.google.ch/patents/US20130345778.

2nd IEEE International Conference on Power Electronics, Intelligent Control and Energy Systems (ICPEICES-2018)

Design and Experimental analysis of Integer Order PID Controller for Ceramic IR heating system

Vineet Shekher
Department of Electrical Engineering,
Noida Institute of Engineering and Technology, Greater Noida, Utter Pradesh,201306, India
vshekher2407@gmail.com

Ajendra Singh
Department of Electrical Engineering
Delhi Technological University Delhi-110042, India
ajendrasingh25@gmail.com

J. N. Rai
Department of Electrical Engineering
Delhi Technological University Delhi-110042, India
jnrai@dce.ac.in

***Abstract* -This paper shows the tuning methods for determination of parameters of proportional-integral- derivative (PID) controllers with reference to fractional order model with unity power function. The study focused to the step response of real time hardware in loop of ceramic temperature control to the response of a MATLAB Simulink of the reference model for the precise and smoother control experience. This is much benefited when worked with model and uncertain parameters in real time control application. Real time Experimental study shows that the reference model driven by auto-tuning of the HIL temperature loop.**

Keywords -Integer Order PID Controller, Ceramic Infrared heater, First Order plus Time Delay System, Data Acquisition

I. INTRODUCTION

Due to having simple tuning rules and design, standard PID controller has great success. In literature, several schemes and design methods were presented. Zeigler-Nichols, Cohen-Coon and Åström-Hugglund tuning method for PID being proposed in [1, 4, 5]. The main module available in MATLAB, for the usage information for the users in [1, 4, 8]. Fractional calculus introduced for differentiation and integration of non-integer orders. Podlubny introduced the basics of fractional controller having generalized PI Dμ controller, in which and μ are the order of integrator and differentiator. Using integer order PID controllers, which have five tuning parameters, in which differentiation and integration parameters are taken as unity whereas fractional order controller provides flexibility in the design process, being based on five tuning parameters (Kp, Ki, Kd, ,μ), but the calculation and setting of these parameter are more complex Over the last few decades, theoretical research on fractional order integration and derivative for many application proposed based on fractional calculus based controller in various fields such as transmission lines, modelling of thermal system, signal processing, system identification and control system[6,7].

In this section of the paper a short review of fractional calculus based IOPID controllers, as presented in the literature is presented. In chapter 2, the concepts related to the fractional calculus and IOPID controllers are presented. In chapter 3, simulation and real time implementation of various PID controlled systems, tuned by Zeigler-Nichols method, Cohen Coon, Åström-Hugglund and IOPID method are tested and final result are considered and include in conclusion section.

II. FRACTIONAL CALCULUS

The fractional order calculus (FOC) deals with the branch of mathematics, in which differentiation and Integration work under real or even complex number, not only the integer one. The FOC has great consequences in modern research and real-world applications.

The fractional order differential equation for the continuous time or time invariant system shown by the equation (1)

$$a_n D^{\alpha_n} y(t) + a_{n-1} D^{\alpha_{n-1}} y(t) + \cdots + a_0 D^{\alpha_0} y(t) = b_m D^{\beta_m} u(t) + b_{m-1} D^{\beta_{m-1}} u(t) + \cdots + \beta_0 D^{\beta_0} u(t) \quad (1)$$

Where input signal is $u(t)$, output signal is y (t) , fractional derivative represented as $D^{\gamma} \equiv {}_0D_t^{\gamma}$, constants are denoted as a^K where (K=0,----n) and b^K where (K=0,-----,m) and α_K with (k=0,-----,n) and β_K with (K=0,-----,m) are arbitrary real numbers.

Stability is very fundamental and critical requirement for control system design. The stability of an integer order continuous time linear time invariant system is stable if and only if all roots of its characteristics equation have negative real parts.

The differ-integral operator, denoted by ${}_aD_t^q$, commonly used in fractional calculus and expressed in single notation by (2)

$${}_aD_t^q = \begin{cases} \dfrac{d^q}{dt^q} & q > 0 \\ 1 & q = 0 \\ \displaystyle\int_a^t (de)^{-q} & q < 0 \end{cases} \quad (2)$$

Where q is the fractional order and a and t are the limits of operation. The Grunwald- Letnikov (G-L) definition [18] is given as:

$${}_aD_t^q f(t) = \frac{d^q f(t)}{d(t-a)^q} = \lim_{N\to\infty}\left[\frac{t-a}{N}\right]^{-q} \sum_{j=0}^{n-1} (-1)^j \binom{q}{j} f\left(t - j\left[\frac{t-a}{N}\right]\right)$$

978-1-5386-6625-8/18/$31.00©2018IEEE

The Riemann- Lowville (R-L) definition is the simplest and easiest definition to use. This definition is given as (3):

$$ {}_a D_t^q f(t) = \frac{d^q f(t)}{d(t-a)^q} = \frac{1}{\Gamma(n-q)} \frac{d^n}{dt^n} \int_0^t (t-z)^{n-q-1} f(z)\, dz \quad (3) $$

Where, 'n' is the integer which is not less than q i.e. $n-1 \le q < n$ and Γ is the gamma function.

$$ \Gamma(z) = \int_0^\infty t^{z-1} e^{-t}\, dt $$

For function $f(t)$ having n continuous derivative for $t \ge 0$ where $n-1 < q < n$, the G-L and R-L definitions are equivalent. The Laplace transform of the Riemann- Lowville fractional integral and derivative are given as follow (4):

$$ L\left\{ {}_0 D_t^q f(t) \right\} = s^q F(s) - \sum_{k=0}^{n-1} s^k \, {}_0 D_t^{q-k-1} f(0) \quad n-1 < q \le n \in N \quad (4) $$

It is observed that transform technique is not suitable for R-L fractional derivative because it should have the knowledge of the non-integer derivatives of the functions at t=0..

The equations with R-L operators are equivalent to Caputo operator with homogeneous initial conditions assumptions and Laplace transform of the Caputo fractional derivative is given as (5)

$$ L\left\{ {}_0 D_t^q f(t) \right\} = s^q F(s) - \sum_{k=0}^{n-1} s^{q-k-1} f^{(k)}(o) \quad n-1 < q \le n \in N \quad (5) $$

The Caputo fractional derivative in the form of Laplace transform for zero initial condition, above equation takes the form as below:

$$ L\left[{}_0 D_t^q f(t) \right] = s^q F(s) $$

The Fractional Order differentiation has the following properties

a. $ {}_0 D_t^\alpha f(t) = f(t) $

b. $ {}_0 D_t^\alpha [af(t) + bg(t)] = a \, {}_0 D_t^\alpha f(t) + b \, {}_0 D_t^\alpha g(t) $

c. $ {}_0 D_t^\alpha [{}_0 D_t^\beta f(t)] = {}_0 D_t^\beta [{}_0 D_t^\alpha f(t)] = {}_0 D_t^{\alpha+\beta} f(t) $

d. $ L[{}_0 D_t^\alpha f(t)] = s^\alpha L[f(t)] - \sum_{k=1}^{n-1} s^k [{}_0 D_t^{\alpha-k-1} f(t)]_{t=0} $

In particular, if the derivatives of the function $f(t)$ are all equal to 0 at t = 0, so laplace transform of the fractional derivative is given as follow (6)

$$ L[{}_0 D_t^\alpha f(t)] = s^\alpha L[f(t)] \quad (6) $$

III. INTEGER ORDER PID CONTROLLER

The differential equation of Fractional PID is represented by

$$ u(t) = K_p e(t) + K_i ({}_a D_t^\lambda e(t)) + K_d ({}_a D_t^\mu e(t)) \quad (7) $$

The continuous transfer function of fractional PID controller is obtained through the properties used in equation (7) , which is given by

$$ \frac{U(s)}{E(s)} = C_{FOPID}(s) = K_p + \frac{K_i}{s^\lambda} + K_d s^\mu \ , (\lambda, \mu > 0) \quad (8) $$

Figure 1(a) shows the block diagram of FOPID having =1 and μ=1, and takes an form of an integer order Proportional-I and Derivative (PID) Controller as shown in figure 1(b).

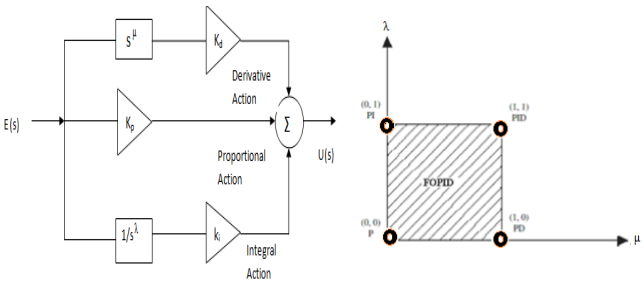


Fig: 1(a) FOPID Block Diagram

Fig. 1(b) Expansion of FOPID in Plane

From the figure1 (b), the fractional order PID controller generalizes the integer order PID controller and expands it from point to plane which shows the flexibility in the Integer order PID control design.

Design Specification:

1. Phase Margin & Gain Crossover frequency

$$ \left| G(j\omega_{cp}) \right| = \left| C(j\omega_{cp}) P(j\omega_{cp}) \right|_{dB} = 0 \ dB $$

$$ Arg[G(j\omega_{cp})] = Arg[C(j\omega_{cp}) P(j\omega_{cp})] = -\pi + \phi_{pm} \quad (9) $$

Where cp is gain crossover frequency, •pm is phase margin, $C(j\omega_{cp})$ is the PID Controller in frequency domain with crossover frequency and $P(j\omega_{cp})$ is the IR plant (FOPID) in frequency domain with crossover frequency.

2. Robustness to gain variation in the gain of the plant

$$ \left(\frac{d(Arg(G(j\omega))}{d\omega} \right)_{\omega=\omega_c} = 0 \quad (10) $$

The variation in gain of the plant shows that the phase order with respect to the frequency is zero i.e. the bode plot of phase is flat at a certain gain crossover frequency.

IV. SIMULATION EXPERIMENT WITH CONTROLLER

In recent era an increasing interest by researcher for the integration of controllers in industrial application are been observed .For closed loop system, four tuning methods are studied and compare with real time implementation, as follows;

- FOPTD plant with ZN Controller;
- FOPTD plant with Åström - Hägglund Controller;

- FOPTD plant with Coon-Cohen Controller;
- FOPTD plant with IOPID Controller.

Using the Zeigler- Nichols process reaction method, the plant (infrared heater, 400watt) was found to have an approximately transfer function by open loop experiment data (reaction curve method) expressed by equation (11)

$$G_{IR}(s)=\frac{[2.6770]e^{-46s}}{262s+1} \quad (11)$$

Case 1. Zeigler Nichols Closed loop Controller

A ZN-PID tuning rule is the classical tuning rules for closed loop, in which the gain (Kcr) that will cause the closed loop output to oscillate at constant amplitude. Corresponding to the Ultimate gain (Kcr), oscillation ultimate period (Pcr) can be determined. Zeigler – Nichols recommended the following ZN-PID tuning rule presented in the table (I)

Table I. Zeigler Nichols closed loop tuning rule

Controller	Gain (Kp)	Integral Gain(Ki)	Derivative Gain(Kd)
PID	0.6 Kcr	2/Pcr	Pcr/8

Case 2. Åström- Hägglund tuning

A little improvement of the Zeigler- Nichols closed loop method is provided by Åström- Hägglund method having relay feedback system. Åström- Hägglund recognized that the Zeigler- Nichols continuous cycling method actually identifies the point $\left(-1/K_u, 0\right)$ on the nyquist curve, and moves it to a predefined point.

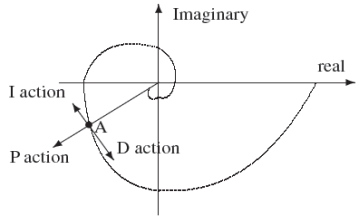


Fig.2 Effect of Changing the PID parameter on Nyquist plot

To move an arbitrary point A to a predefined position B, a convenient choice for point A is the ultimate point. Point B can be determined by a desired gain margin and phase margin, and is written in polar co-ordinates as $B=r_b e^{j(\pi+\phi_b)}$. Assuming that the PID controller at frequency ω_0 is $G_c(s)=r_c e^{j(\phi_c)}$.Then,

$$r_b e^{j(\pi+\phi_b)} = r_a.r_c e^{j(\pi+\phi_c+\phi_a)} \quad (12)$$

Therefore, $r_c = r_b / r_a$ and $\phi_c = \phi_b - \phi_a$

PID Controller	Gain(Kp)	Integral Time(Ti)	Derivative Time(Td)
PID	$k_u r_b \cos(\phi_b)$	$\frac{-Tu}{\pi}\left(\frac{1+\sin(\phi_b)}{\cos(\phi_b)}\right)$	$\frac{-Tu}{4\pi}\left(\frac{1+\sin(\phi_b)}{\cos(\phi_b)}\right)$

Table II. Åström-Hägglund Tuning values

This method identifies only one point on the Nyquist curve and moves to a desired position.

Case 3. COHEN- COON METHOD

The Cohen- Coon method used for the First Order plus Delay time (FOPDT) model to develop the tuning parameters and it is similar to Zeigler-Nichols reaction method. The parameters involved have more mathematical operations.

Table III. Cohen-Coon Tuning values

PID Controller	Gain(Kp)	Integral Time(Ti)	Derivative Time(Td)
PID	$\frac{1}{K}*\left(\frac{T}{L}\right)\left(\frac{4}{3}+\frac{L}{4T}\right)$	$L\left(\frac{32+6(L/T)}{13+8(L/T)}\right)$	$L\left(\frac{4}{11+((2*L)/T)}\right)$

Case 4. IOPID Method

The phase margin and gain margin of the process plant as per Bode as shown in figure 3and the value of ω_{cg} and ϕ_{pm} as 0.008 rad/sec and 80^0 respectively.

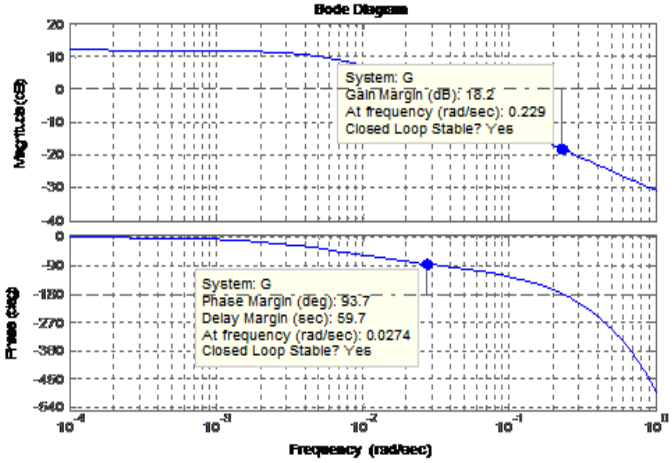


Fig.3 Bode plot of FOPTD transfer function of Ceramic IR heater

Åström-Hägglund	0.5184	0.0038	17.7915
Cohen-Coon	2.8593	0.0271	46.3487
IOPID	0.9768	0.0063	25.6246

V. RESULTS AND SIMULATION

4.1 Simulation studies

The simulation runs are carried out with ZNC-PID, AH-PID, CC-PID and IOPID controllers in Matlab Simulink. The performance indices calculated in terms of error (ISE and IAE) and performance parameters (Tr, Tp, %Mp and Ts) and are reported in table (V). From the result table, IOPID yield a fair response with minimum error values, acceptable overshoot and settling time.

Table IV. IOPID Parameters

PID Controller parameter	IOPID Parameters
Kp	$K_p = \frac{1}{K}\sqrt{\frac{B_1}{1+A_1^2}}$
Ki	$K_i = \frac{1}{2K}\sqrt{\frac{1+A_1^2}{B_1}}\left(T\omega_{cp}^2 + LB_1\omega_{cp}^2\right) - A_1\omega_{cp}\sqrt{\frac{B_1}{1+A_1^2}}$
Kd	$K_d = \frac{1}{2K}\left[\sqrt{\frac{1+A_1^2}{B_1}}\left(T+LB_1\right) + A_1\omega_{cp}^{-1}\sqrt{\frac{B_1}{1+A_1^2}}\right]$

Where $\frac{K_d\omega_{cp}^2 - K_i}{K_p\omega_{cp}} = A_1$ and $B_1 = 1+\omega_{cp}^2 T^2$

The PID controller setting (Kp,Ki,Kd) for the above said controllers and worked out based on FOPTD system is provided in table (IV).

Table IV. Calculated PID Controlling parameter for FOPTD

Controller Tuning	Kp	Ki	Kd
ZN-Closed loop	2.15	0.027389	42.193

Table V. Performance parameter using controller tuning

Performance	Rise Time (T_r)	Peak Overshoot(M_p)	Peak Time (T_p)	Settling Time(T_s)	ISE	IAE
ZNC-PID	25.39	74.70	116.93	389.36	80.55	116.4
CC-PID	21.10	103.57	105.07	1270	143.8	269.8
AH-PID	207.91	11.82	504.27	850.55	96.58	183.2
IOPID	112.41	9.8	341.91	613.86	66.92	114.8

4.2 Real time experiment studies

In this section, experiments made it possible and the performance of ZNC-PID, AH-PID, CC-PID and IOPID controller is tested in hardware in loop for ceramic IR heater. A ceramic infrared heater plate temperature shown in figure (4) is controlled using analog power controller made by Libratherm LTC-16 shown in figure (4), having variable control signal range of 0-5v,4-20mA or 10K potentiometer. The output voltage varies proportionally to the input variable signal. LTC-16 has back-back connected SCR to control load of 2kW, 10A, 230V. The firing phase angle controls the gradual and smooth voltage control for the load.

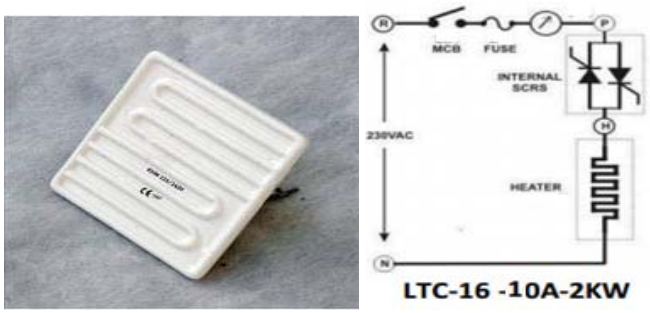


Fig.4 Ceramic IR Heater Plate and LTC 16 wiring diagram

The laboratory setup and wiring diagram as shown in Figure (5) consists of Ceramic IR heater, DAQ card, Analog power controller and temperature sensor (K-type thermocouple). The power delivered to the IR heater is controlled by an analog signal using analog power controller. DAQ card is used for the analog signal generation, where output is 0-5 V DC and it provides to analog power controller which get in firm of fixing angle to back to back SCR of analog power controller to maintain the desired analog power or voltage to IR Heater.

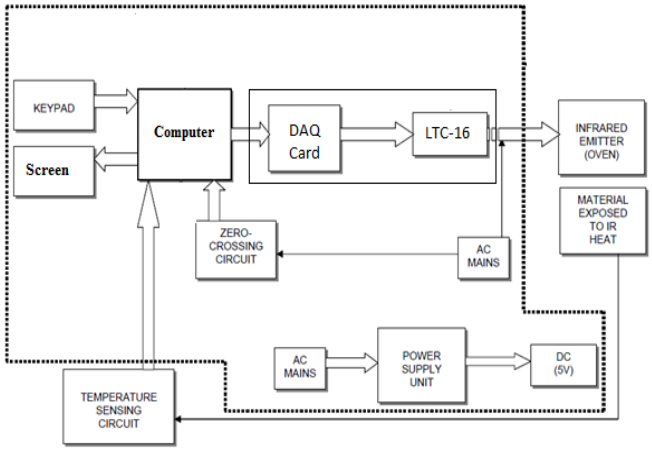


Fig.5 Block Diagram of the temperature control of ceramic IR heating System

Block diagram shown in figure (5) consists of Ceramic IR heater, DAQ card, Analog power controller and temperature sensor (K-type thermocouple). The power delivered to the IR heater is controlled using an analog signal using analog power controller. For the analog signal generation, we use DAQ Card, where output is 0-5 V DC and it provides to analog power controller which get in firm of fixing angle to back to back SCR of analog power controller to maintain the desired analog power or voltage to IR Heater.

Simulation Conducted on Infrared heater to show warm up temperature shown in figure (6) with respect to time was conducted. The type of heater used in the study was 400 watt and has a maximum operating temperature of 1200^0C.

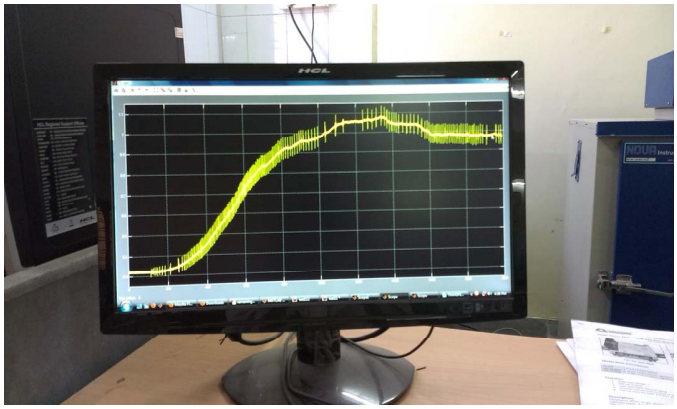
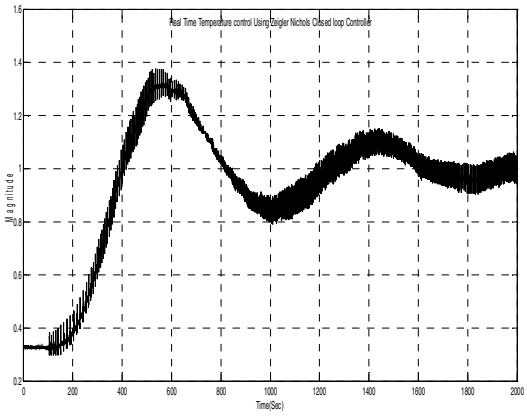
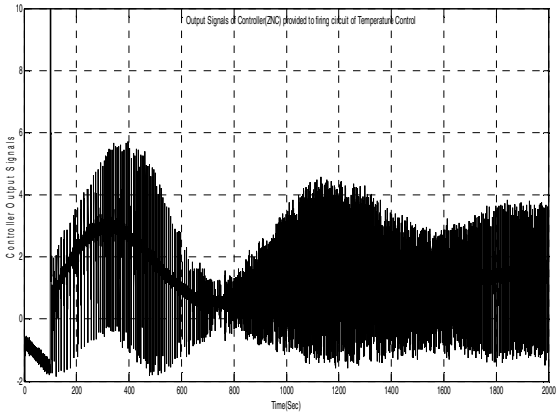


Fig. 6 Experimental output step response

Real time experimental performance of Zeigler Nichols closed loop, Åström-Hägglund loop, Coon-Cohen and IOPID method and their Controller output as shown in figure (7).





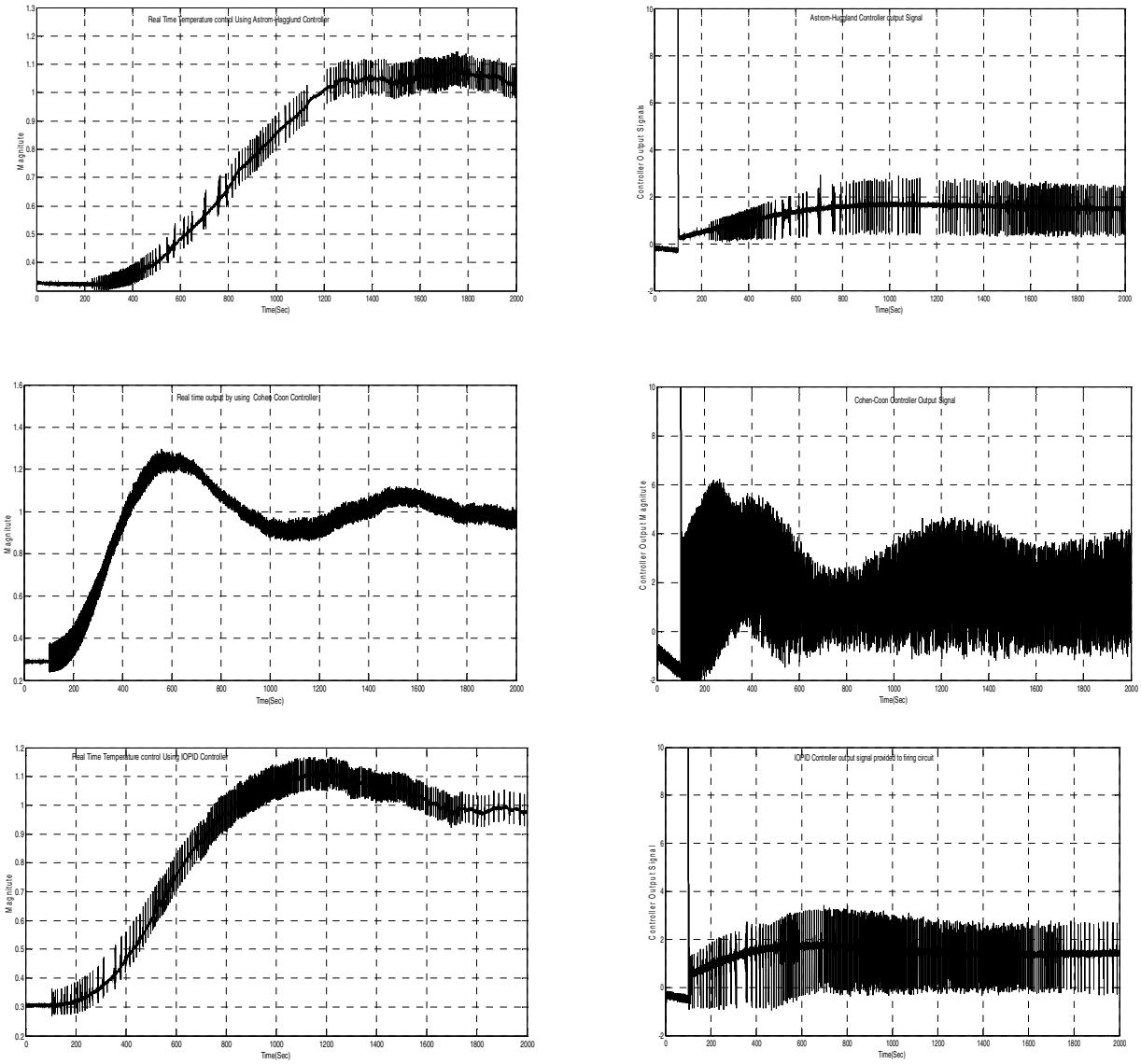


Fig. 7 Real Time Temperature control and Output Signal generate by using ZN, AH, CC and IOPID Controller

The comparative analysis of the temperature control of ceramic Infrared HFE system

Table VI. Performance parameter of different Controller

Performance Parameter	ZNO	ZNC	AH-PID	CC-PID	IOPID
Rise Time	241.3	226.16	632.06	259.2	484.47
Settling Time	1997	1999	1997	1993	1989
Peak Time	538.7	536.3	1749	559	1129
Peak Overshoot	34.72	38.15	11.25	34.6	20.07

VI. CONCLUSION

By observing the result in Table, it is found that the IOPID method is generally better than other conventional tuning method controllers. In the experimental set up the process control includes the time required by the heater to be settled on the initial set up temperature. The real time controller includes

the signal transfer from the temperature sensor for the real time action. The temperature warm up is slow due the resistance heating element used in ceramic infrared heater. So the settling time is very high in comparison with the simulation result.

REFERENCES

[1] C. A. Monje, Y. Q. Chen, B. M. Vinagre, D. Xue and V. Feliu, Fractional-order systems and controls: fundamentals and applications,Springer,2010.

[2] H. S. Ahn, V. Bhambhani and Y. Q. Chen, Fractional-order integral and derivative controller design for temperature profile control,Control and Decision Conference, 2008, CCDC 2008, Chinese, IEEE, 4766-4771 (2008).

[3] A. Tepljakov, E. Petlenkov, J. Belikov and S. Astapov, Tuning and digital implementation of a fractional-order PD controller for a position servo, Int. J. Micr. Comput. Sci. 4(3), 116-123 (2014).

[4] C. A. Monje, B. M. Vinagre, Y. Q. Chen, V. Feliu, P. Lanusse and J. Sabatier, Proposals for fractional PIl Dm tuning, Proceedings of The First IFAC Symposium on Fractional Differentiation and its Applications (FDA04), 115-120 (2004).

[5] S. Das, S. Saha, S. Das and A. Gupta, On the selection of tuning methodology of FOPID controllers for the control of higher order processes, ISA Transact. 50(3), 376-388 (2011).

[6] V. Bhambhani, Y. Han, S. Mukhopadhyay, Y. Luo and Y. Q. Chen, Hardware-in-the-loop experimental study on a fractional order networked control system testbed, Commun. Nonlin. Sci. Numer. Simul. 15(9), 2486-2496 (2010).

[7] I. Podlubny, Fractional differential equations: an introduction to fractional derivatives, fractional differential equations, to methods of their solution and some of their applications, vol. 198, Academic Press, 1998.

[8] K. H. Ang, G. Chong and Y. Li, PID control system analysis, design, and technology, Control Systems Technology, IEEE Transactions 13(4), 559-576 (2005).

[9] C. A Monje, B. M. Vinagre, V. Feliu and Y. Q. Chen, Tuning and auto-tuning of fractional order controllers for industry applications, Contr. Engin. Pract. 16(7), 798-812 (2008).

[10] D. Valerio and J. Sa da Costa, A review of tuning methods for fractional PIDs, 4th IFAC Workshop on Fractional Differentiation and its Applications, FDA, vol. 10, 2010.

[11] I. Petras, The fractional-order controllers: Methods for their synthesis and application, arXiv preprint math/0004064 (2000).

[12] Y. Q. Chen, I. Petras and D. Xue, Fractional order control-a tutorial, American Control Conference, 2009 ACC09, IEEE, 1397-1411 (2009).

[13] I. Podlubny, Fractional-order systems and fractional-order controllers, Institute of Experimental Physics, Slovak Academy of Sciences, Kosice 12 (1994).

[14] I. Podlubny, L. Dorcak and I. Kostial, On fractional derivatives, fractional-order dynamic systems and PIl Dmcontrollers, Proceedings of the 36th Conference on Decision & Control, 5, 4985-4990 (1997).

[15] K. J. Astrom, PID controllers: theory, design and tuning, Instrument Society of America (1995).

[16] Z. Li, L. Lu, S. Dehg, Y. Q. Chen and X. Ding, A review and evaluation of numerical tools for fractional calculus and fractional order controls, Int. J. Contr.1-17(2016).

[17] H. Panagopoulos, K. J. Astrom and T. Hagglund, Design of PID controllers based on constrained optimisation, IEE Proceedings- Control Theory and Applications 149(1), 32-40 (2002).

[18] D. Valerio and J. S da Costa, Time-domain implementation of fractional order controllers, IEE Proc. Contr. Theor. Appl.152, 539-552 (2005).

[19] B. M. Vinagre, I. Podlubny, A. Hernandez and V. Feliu, Some approximations of fractional order operators used in control theory and applications, Fract. Calc. Appl. Anal. 3 3, 231-248 (2000).

[20]. A. Oustaloup, F. Levron, B. Mathieu and F. M. Nanot, Frequency-band complex noninteger differentiator: characterization and synthesis, Circuits and Systems I: Fundamental Theory and Applications, IEEE Transactions 47(1), 25-39 (2000).

[21]. A. Tepljakov, E. Petlenkov and J. Belikov, FOMCON: Fractional-order modeling and control toolbox for MATLAB, Proc. 18th Int Mixed Design of Integrated Circuits and Systems (MIXDES) Conference, 684-689 (2011).

[22]. A. Tepljakov, E. Petlenkov, J. Belikov and M. Halas, Design and implementation of fractional-order PID controllers for a fluid tank system, American Control Conference (ACC), 2013, IEEE, 1777-1782 (2013).

[23]. A. Tepljakov, E. Petlenkov and J. Belikov, A flexible MATLAB tool for optimal fractional-order PID controller design subject to specifications, Control Conference (CCC), 2012, 31st Chinese, IEEE, 4698-4703 (2012).

International Research Journal of Engineering and Technology (IRJET) e-ISSN: 2395-0056
Volume: 06 Issue: 07 | July 2019 www.irjet.net p-ISSN: 2395-0072

Detection of Angle-of-Arrival of the Laser Beam using a Cylindrical Lens and Gaussian Beam Curve Fitting

Anand Kumar Rai[1], Saurabh Bansod[2], Satya Prakash[3], Ajay Rathee[4*]

[1]M. Tech in Electronics Design Technology, National Institute of Electronics & Information technology Aurangabad, Maharashtra
[2]Scientist 'B', National Institute of Electronics & Information technology Aurangabad, Maharashtra
[3]Scientist 'F', Laser Science and Technology Centre (LASTEC), Defence Research& Development Organization (DRDO)
[4]Scientist 'E', Laser Science and Technology Centre (LASTEC), Defence Research& Development Organization (DRDO)

Abstract – *This paper presents a simple approach for finding the direction of incoming laser radiation on combat vehicles. This finds application in warning the crew of combat vehicles about incoming laser threats. The design is based on a linear array of photo-detectors and a Plano-convex cylindrical lens. The incoming laser radiation is focused by the lens on to linear array of photo-detectors and Gaussian curve fitting is used to find the position of center or peak of Gaussian, which in turn is calibrated to calculate the Angle of Arrival (A-o-A). Basic idea behind the design is the displacement of centroid of Gaussian beam with the change in angle-of-arrival. The system is able to measure the angle-of-arrival with the very high angular resolution, depending upon the number of sampling instants in the Gaussian fitted curve. The designing of the cylindrical lens and its simulation with laser beam is performed, at different angle-of-arrival using OSLO designer. The curve fitting and error analysis of the samples collected by the detector on being illuminated by the laser beam is performed using MATLAB curve fitting tool.*

Key Words*: *Cylindrical lens; Gaussian curve fitting; angle-of-arrival (A-o-A); Laser Warning Receivers.

1. INTRODUCTION

The detection of angle-of-arrival (A-o-A) is a technique used to detect the direction of the incident laser beam. The detection of A-o-A is useful in the functioning of the laser-based 3D scanners, and laser warning receivers.

1.1 Previous work

Researchers have proposed many schemes for detection of the angle-of-arrival of the incident beam of radiation, some of which employ the linear array of photo-detectors along with the coded mask or shadow mask techniques [1,2,3,4,5]. Later an improved method uses a cylindrical lens along with the top mask for focusing the laser radiation in the space between the cylindrical lens and the detector array which is concentric about the backside of the lens [1]. The top mask or coded mask with one slit or many parallel slits through it serves the purpose of encoding. The encoding schemes such as binary encoding using gray code is used to position slits on the top mask [2]. Each of these slots or rows of slots is positioned centrally directly above active area of photo-detectors [3]. The detector array is so arranged in rows that the radiation bars created by the slits of the mask are perpendicular to the detector row. The aperture of the slits is kept equal to the active area aperture of the used photo-detector [4]. When the radiation directed towards the device and falls on the detector plate, the radiation bars are created by slits above the few detectors, generating the electrical response for each detector. The generation of radiation bars depends on both the positions of slits in the encoded mask and the angle-of-arrival of radiation [3]. The electrical signal generated in photo-detectors is converted into digital by using reference signal and analog-to-digital converters which are then decoded to give the angle-of-arrival of the laser beam entering to the photo-detector. This scheme depends upon the use of coded mask and isolated channels, which is difficult to assemble. However, some proprietary solutions are available

Another kind of technology to serve the similar purpose makes use of the four-quadrant detector associated with a diaphragm formed by the central transparent zone of an opaque mask. These are kept in parallel with a transparent window and a circuit to measure deviation to process the detected Laser beam. This setup measures the angular deviation of a pinpoint radiation source. With two sensors of this kind, the locus of the radiating source can be ascertained [5].

1.2 Theoretical framework

The Laser beam is a coherent monochromatic electromagnetic radiation. Most of the Lasers follow the fundamental TEM_{00} Gaussian mode [6].

The mathematical expression for Gaussian function is:

$$f(x) = ae^{\frac{-(x-b)^2}{2c^2}} = \left(\frac{1}{\sigma\sqrt{2\pi}}\right) e^{\left(\frac{-1}{2}\right)\left(\frac{x-\mu}{\sigma}\right)^2} \quad (1)$$

The fundamental transverse mode, TEM_{00} is of the lowest order and has a Gaussian intensity profile

$$I(r,z) = I_0 \left[\frac{\omega_0}{\omega(z)}\right]^2 e^{\frac{-2r^2}{\omega(z)^2}} \quad (2)$$

The power contained in a Gaussian beam is

$$P = \int_0^\infty I(r,z) 2\pi r dr = \frac{1}{2} I_0 \pi {\omega_0}^2 \quad (3)$$

In order to understand the intensity and power distribution, there is a need to know the beamwidth or beam diameter. The beamwidth is the diameter of the Laser beam at which its intensity is decremented to a $1/e^2$ value of its peak or axial value. FWHM (full width at half maximum) is the diameter of a Laser beam at which its intensity is decremented to 50% of its peak value [7]. The figure 1 below, describes both definitions graphically.

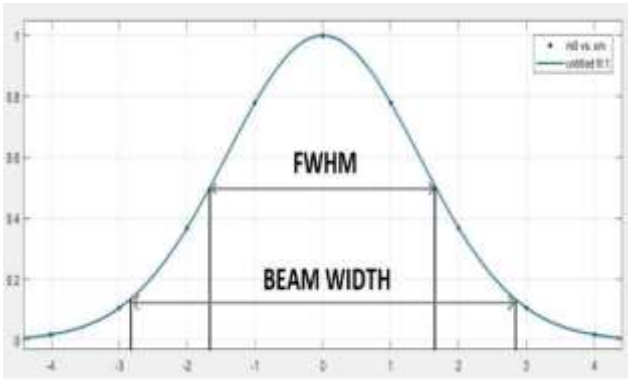


Fig - 1: Gaussian function curve showing FWHM and beamwidth at $1/e^2$ intensity.

Diffraction leads to the transverse spreading of light waves while propagation, due to which, it is impossible to acquire a perfectly collimated beam. Even if a TEM00 Laser beam wavefront is perfectly flat, the beam while propagation, quickly acquires curvature and spread [7] in accordance with

$$R(z) = z\left[1 + \left(\frac{\pi {\omega_0}^2}{\lambda z}\right)^2\right] \quad (4)$$

And

$$w(z) = w_0\left[1 + \left(\frac{\lambda z}{\pi {\omega_0}^2}\right)^2\right]^{1/2} \quad (5)$$

Where z denotes the distance propagated by the wave from the plane where the wavefront is found to be flat, λ denotes the wavelength of Laser beam, $w0$ denotes the beamwidth radius i.e. radius at $1/e^2$ intensity contour at the plane where the flat wavefront achieved, $w(z)$ represents the radius of the $1/e^2$ contour at distance z, and $R(z)$ represents the radius of curvature of the wavefront at distance z. Plano-convex cylindrical lenses are the Aspheric lens and are curved only in one direction. Therefore, they focus or defocus light in the plane parallel to the Plano axis of the lens, into a line. It compresses the image along the power axis, which is perpendicular to the focal line, without altering it in a plane parallel to the Plano axis [8]. Their focusing behavior can be characterized by an effective focal length [9]. The same is represented in figure 2.

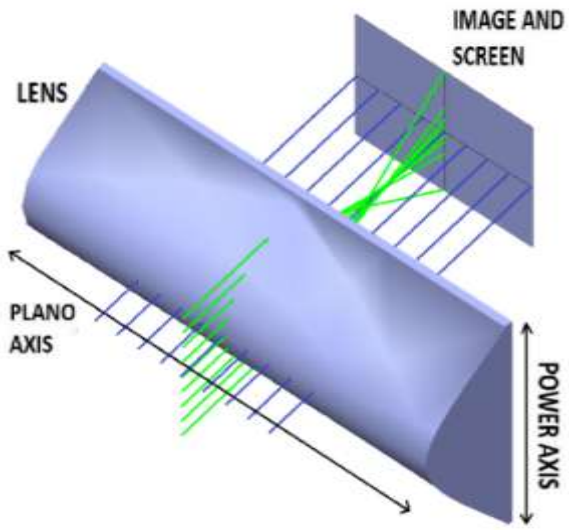


Fig - 2: Cylindrical lens showing focusing of light along Plano axis and Power axis.

The curve fitting tool is used to find a curve that best fits the data. Interpolation and smoothing are the two possible ways for curve fitting. There are several algorithms and method available that serves the purpose of curve fitting. Few of these methods are iterative method, nonlinear least square estimation, weighted least square estimation, and algorithms are Trust-Region algorithm, Caruana's algorithm, Guos algorithm, and Levenberg-Marquardt algorithm. Gaussian curve fitting fits the Gaussian function on to the given data points. Out of all methods, the Guos algorithm is the most appropriate method as it is least sensitive to the random noise [10].

1.3 Problem statement

To develop a simple and cost-effective method for the measurement of the angle-of-arrival of incident laser beam, with very high resolution by ascertaining the centroid of the beam using Gaussian curve fitting.

2. EXPERIMENTAL SETUP

The setup consists of three units, a Gaussian laser source, detection unit, and a processing unit. The laser source fires the laser beam towards the cylindrical lens at a specific angle. The beam suffers turbulence and also gets dispersed while propagating through the atmosphere. This effect is simulated in this work by adding white Gaussian noise to the signal. A cylindrical lens is used to focus the beam of laser, at the detector plane. The detector samples the wave and transfers it to the processing unit where Gaussian curve fitting, error analysis and calculation of angle-of-arrival is performed. The block diagram of the working experimental setup is explained in Figure 3 below.

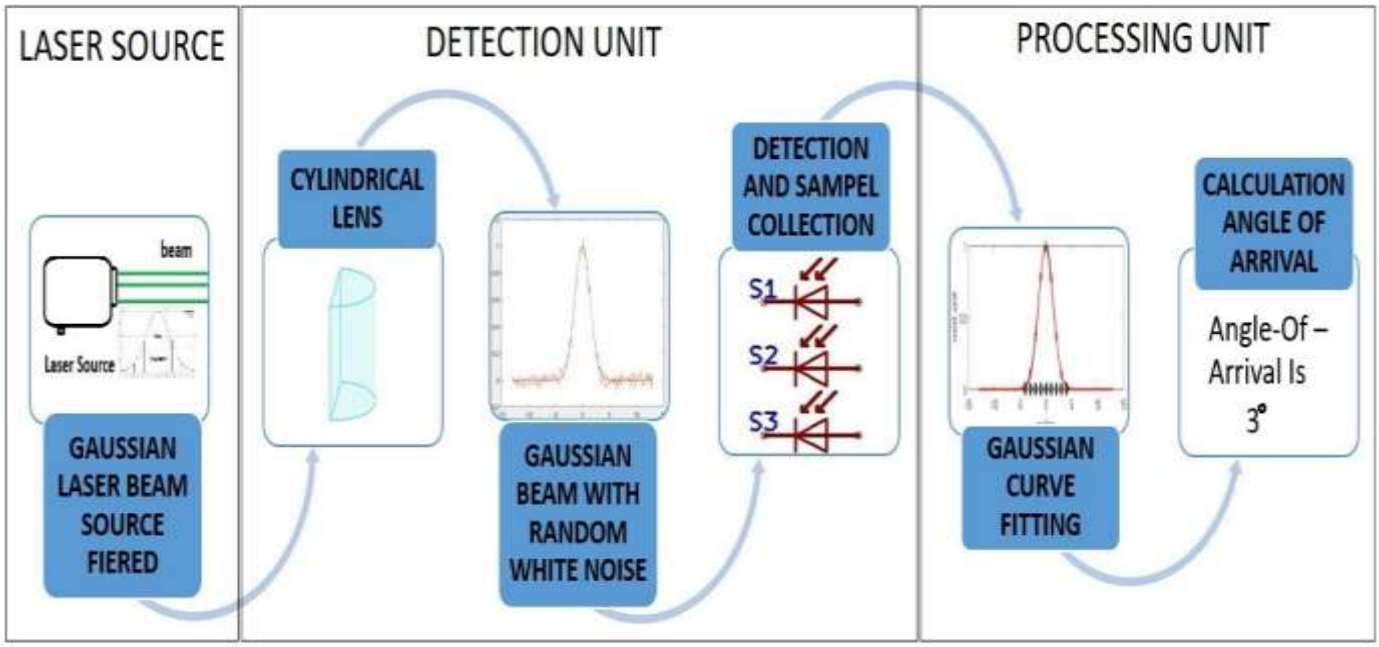


Fig - 3: Block diagram of the experimental setup for Gaussian curve fitting based angle-of-arrival detector.

3. METHODOLOGY

The Gaussian beam (wave) is generated using Gaussian function in MATLAB and different intensity of white Gaussian noise is added to the generated wave for achieving different signal to noise ratios as per experimental requirements. The Laser beam with a Gaussian profile is made to pass through a cylindrical lens. The beam, after propagating through the cylindrical lens remains Gaussian only at one axis i.e. at Plano axis. This beam falls on the linear detector array having nine photo-detectors each working as fixed sampling points or fixed sampling locations.

The central photo-detector is set to serve as a zero-point photo-detector which corresponds to the 0^{o} (angle-of-arrival) of the incident beam at the photo-detector array. In this case, all nine photo-detectors are illuminated.

As the incident beam changes its angle-of-arrival (A-o-A) other than 0^{o}, the spot at the detectors and the centroid of the spot shifts away from the central detector in the direction of propagation of the refracted beam namely; positive angle-of-arrival (+A-o-A) and negative angle-of-arrival (-A-o-A), as the A-o-A increases the beam falls on a lesser number of detectors i.e. Fewer detectors are illuminated by beam spot. For both positive and negative A-o-A at a maximum value of A-o-A, a minimum of three photo-detectors is needed to be illuminated. This limitation comes into the picture because minimum three data points are required for single term Gaussian curve plotting using a nonlinear least square method using Trust-Region algorithm by Matlab curve plotting tool. As the beam falls on photo-detectors and the illuminated photo-detectors set the data value corresponding to the Gaussian power and intensity falling on the detectors and are fed to processing unit as a numerical value for curve fitting while data value corresponding to non-illuminated photo-detectors are set to not-a-number (NaN) state. NaN state is ignored automatically while plotting the curve and the detectors are treated as no signal or off. The Gaussian model that fits the intensity peaks of the received Laser beam and is given by the equation

$$y = \sum_{i=1}^{n} a_i e^{\left[\frac{-(x-b)^2}{c_i^2}\right]} \quad (6)$$

Where *a* denotes the amplitude, *b* denotes the centroid of the Gaussian curve (location of the peak) while *c* is related to the FWHM beamwidth. Once the curve is plotted the system returns the value for three entities, namely *a, b* and *c*. Comparing them to mathematical expression for Gaussian function, we get

$$peakamplitude = a = \frac{1}{\sigma\sqrt{2\pi}} \quad (7)$$

$$mean = b = \mu \quad (8)$$

$$standarddeviation = c = \sigma = w0 \quad (9)$$

Using the values of a, b and c the errors related to noise and angle-of-arrival can be calculated. Using the locus of centroid related to the maximum and minimum A-o-A formula for calculation angle-of-arrival can be computed as the distance of the centroid increases proportionally to the increase in angle-of-arrival of the Laser beam.

4. SIMULATION AND RESULT

Using the Oslo designer, a rectangular Plano-convex cylindrical lens is designed with a radius of curvature 25mm, aperture radius 28mm, length 100mm, width 50mm, thickness 27mm. The 'BK7' material with a reflective index of 1.517 is selected for the lens. The effective focal length of the lens is 48.639mm.

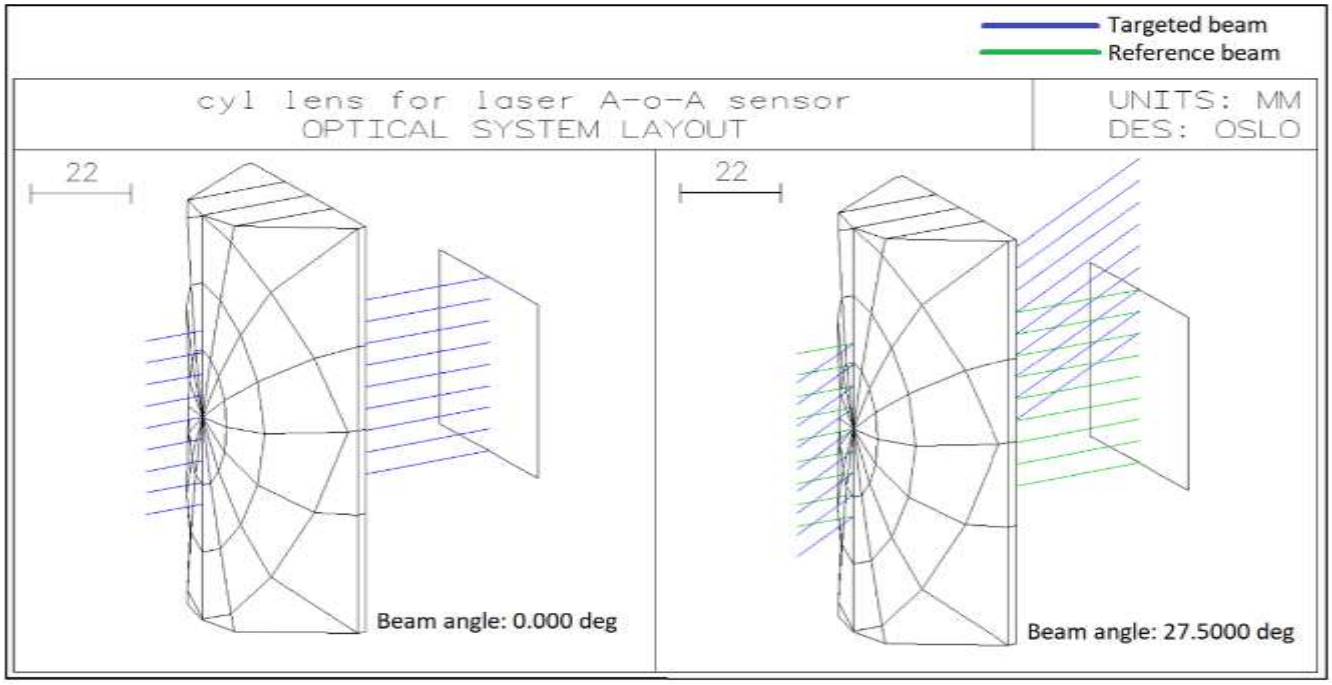


Fig - 4: Cylindrical lens showing the beam tilt and focusing of the beam at 0° angle-of-arrival (left) and at 27.5° angle-of-arrival (right) of the incident Laser beam

Described above in figure 4, the cylindrical lens projecting the image on the detector surface i.e. screen plane, at two different angle-of-arrival. The lens at left shows an image projection for 0°A-o-A while the one at right shows an image projection for +27.5°A-o-A.

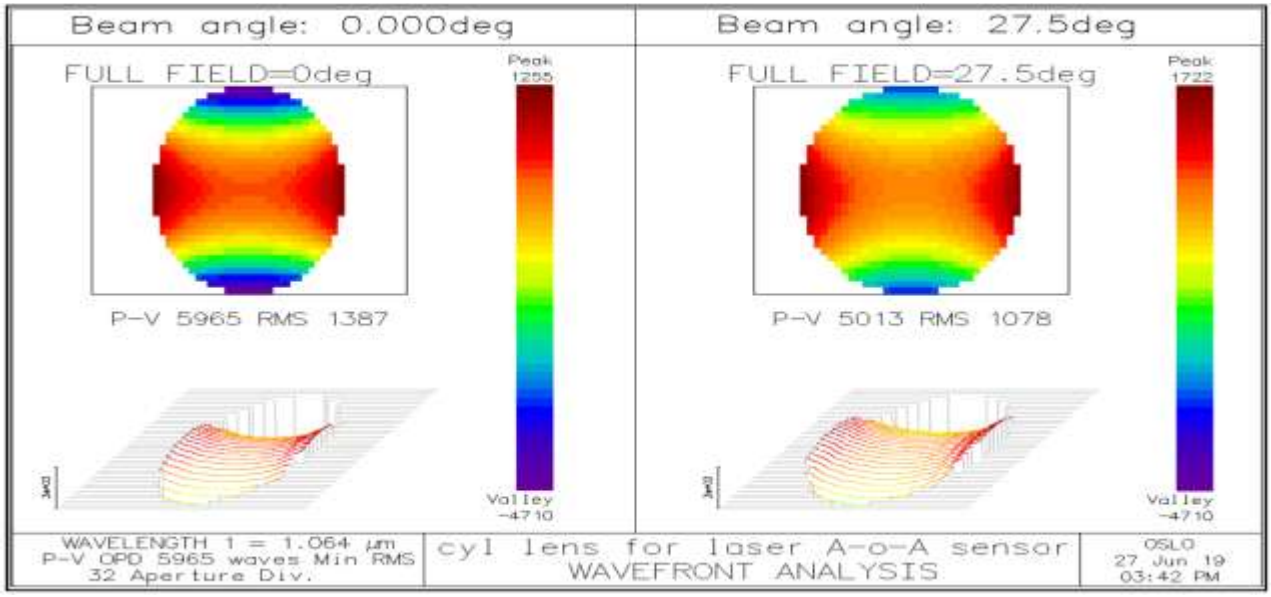


Fig - 5: Wavefront analysis of the focused beam showing Gaussian intensity distribution at the detector plane beam at 0° angle-of-arrival (left) and at 27.5° angle-of-arrival (right) of the incident Laser beam.

Figure 5 describes the wavefront analysis of the beam spot formed at detector surface i.e. screen plane by the cylindrical lens for two different angle-of-arrival. The plot at left shows wavefront and intensity distribution for 0° A-o-A while the plot at right shows wavefront and intensity distribution for +27.5° A-o-A. The diagram describes the intensity distribution follows the Gaussian profile along the planar axis of the cylindrical lens and is compressed along power axis i.e. the beam is no more Gaussian in a plane along the power axis of the lens.

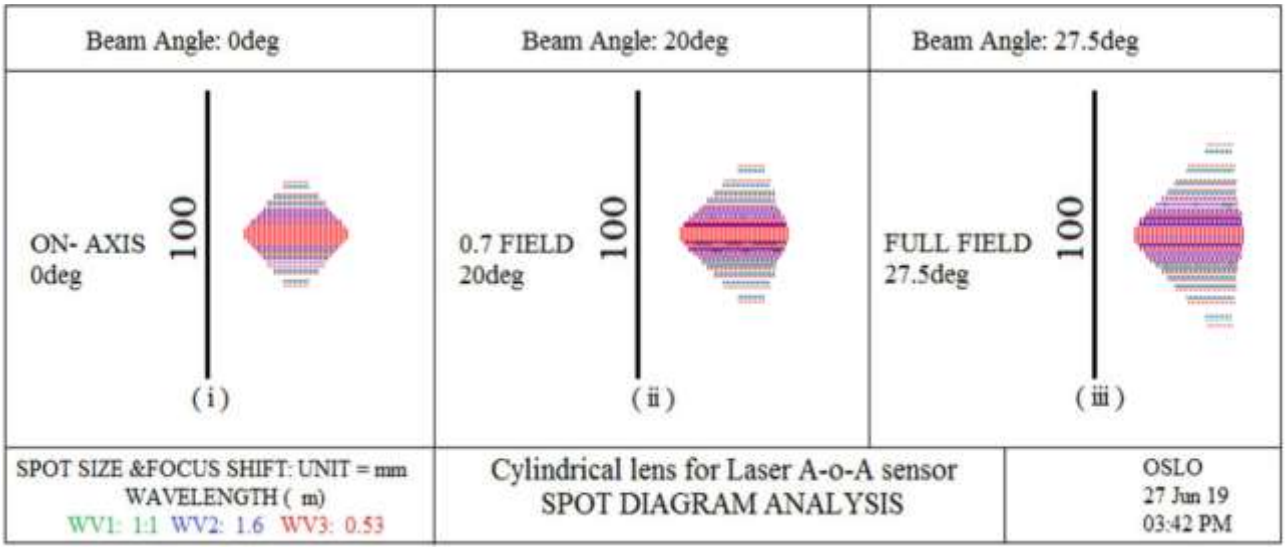


Fig - 6: Spot diagram showing size and shape of the spot formed at detector plane at 0 focal shift beam (i) at 0° angle-of-arrival, (ii) at 20° angle-of-arrival and (iii) at 27.5° angle-of-arrival of the incident Laser beam.

Figure 6 describes the spot diagram analysis of the beam spot formed at detector surface i.e. screen plane by the cylindrical lens for three different angle-of-arrival. The 6(i) shows a spot diagram for 0°A-o-A. The 6(ii) shows a spot diagram for 20°A-o-A while the 6(iii) shows a spot diagram for +27.5°A-o-A. The diagram describes the shape, size and the focal shift for the beam passing through the lens at some particular A-o-A.

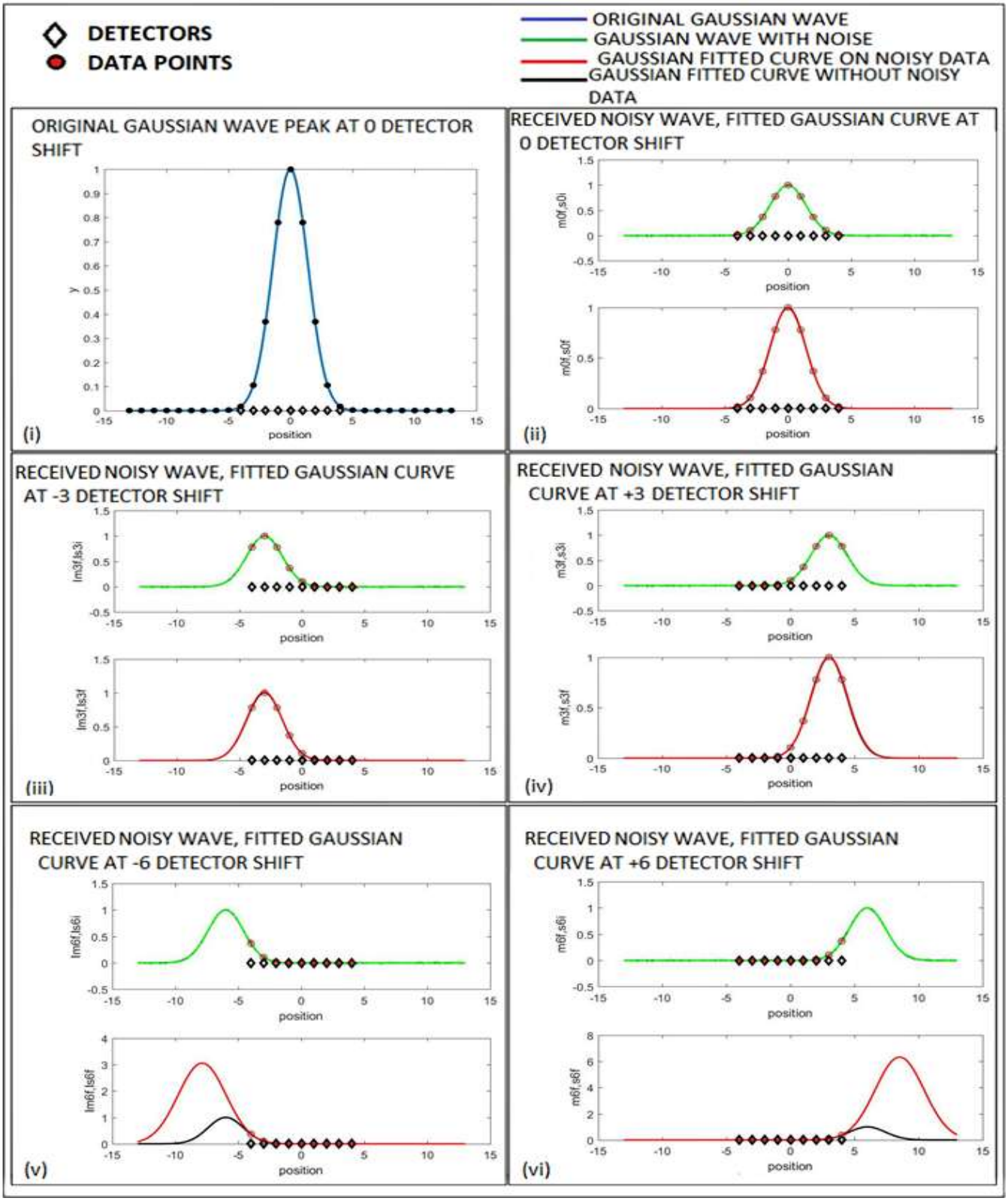


Fig - 7: Gaussian curve fitting of the detected signal and comparison with originally received noisy Gaussian signal.

Figure 7 graphs Gaussian curve of the noisy beam (green) that illuminate the detectors, and the plotted Gaussian curve (red) using samples received at the detectors. The figure 7(iii) describes the curve of wave at for -3 detector shift indicating that the image is shifted till 3 photo-detectors towards left (if the lens and detector are placed horizontally) or downward (if the lens and detector are placed vertically) and 3 detectors from right or upward

are not getting illuminated and their response is considered as NaN state. While the figure 7(iv) describes the curve of wave at +3 detector shift indicating that the image is shifted till 3 photo-detectors towards right (if the lens and detector are placed horizontally) or upward (if the lens and detector are placed vertically) and 3 detectors from left or downward are not getting illuminated and their response is considered as NaN state. The same applies for -6 to 0 and 0 to +6 detector shifts respectively. The distance corresponding to each detector can be calculated by multiplying the number of the detector with 5.36mm

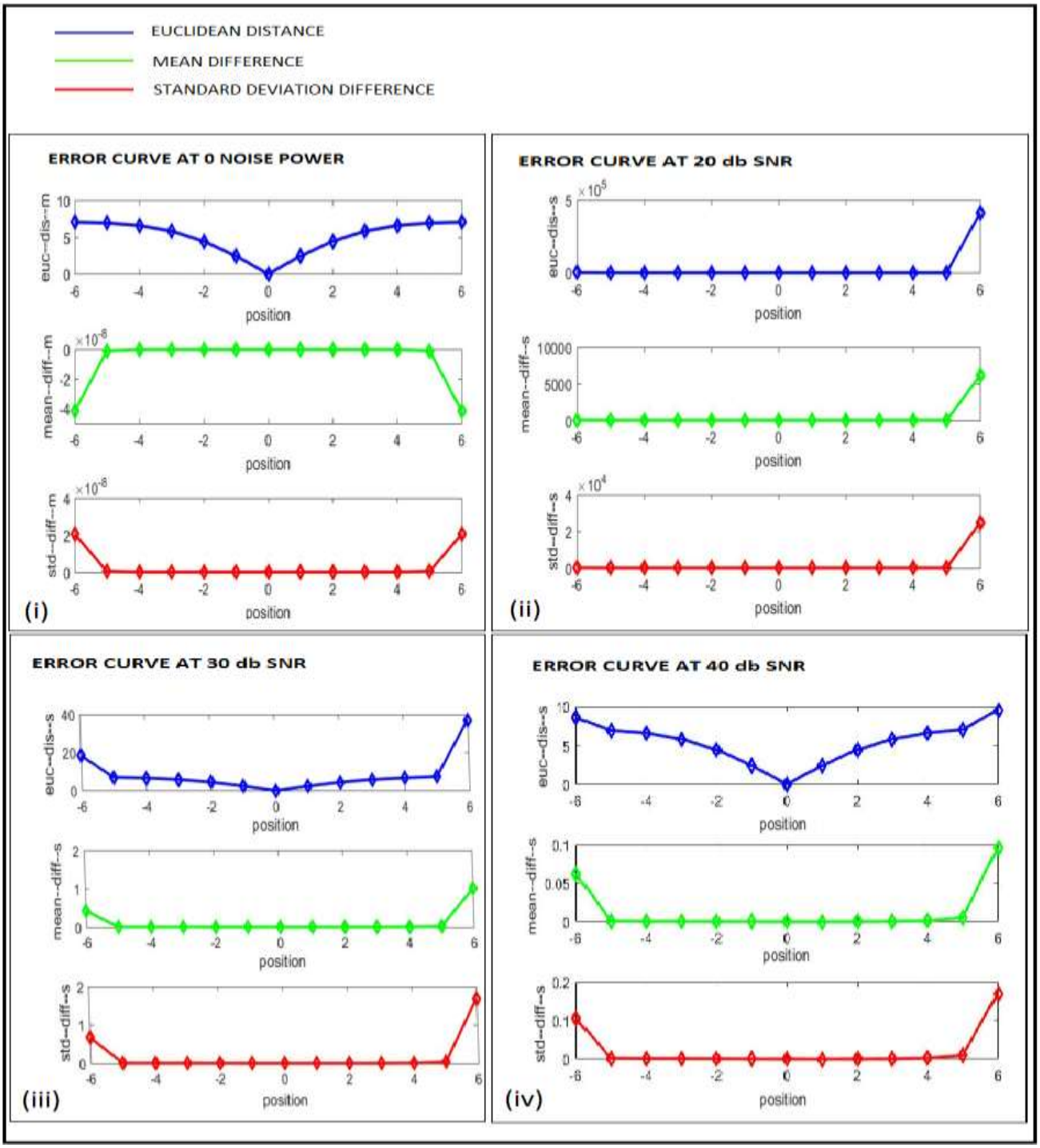


Fig - 8: Error analysis of Gaussian fitted curves at showing the performance of the system at different SNRs.

Figure 8 graphs the analysis of the errors in curve fitting and centroid detection capability of the system for different signal-to-noise ratios. The figure 8(i) shows the expected error in curve fitting when there is no noise in

system, and figure 8(ii), figure 8(iii) and figure 8(iv) shows the error curves at 20db, 30db, 40db of SNR respectively. The error curves are generated by determining the total Euclidian distance, mean difference and standard deviation of the curve plotted for beam with noise at different SNRs and comparing it to Euclidian distance, mean difference and standard deviation of the curve plotted for beam without noise.

The angle-of-arrival can be computed using formula

$$A - o - A = F_o_V_{MAX} \frac{L}{L_{MAX}} \quad (10)$$

Where *A-o-A* is the angle-of-arrival, $F_o_V_{MAX}$ is the maximum field of view, L is the distance of the centroid from the origin and L_{MAX} is the maximum possible distance of the centroid from the origin.

Further, it is found that the maximum entrance angle for the setup is ±27. 5° i.e. maximum angle-of-arrival possible is ±27. 5°. The maximum possible centroid distance from origin L_{MAX} increases when SNRs decreases for both +A-o-A and –A-o-A. The system takes samples at nine points using nine photo-detectors having 5.36 mm pitch between centers of active areas of two consecutive photo-detectors.

Table - 1: L_{MAX} at different SNRs for given $F_o_V_{MAX}$

$F_o_V_{MAX}$	SNR 20db	SNR 30db	SNR 40db
-27.5°	104.252mm	42.210mm	34.711mm
+27.5°	224.905mm	45.64576mm	35.531mm

Therefore, at an SNR of 40db angle-of-arrival is

$$A - o - A = 27.5^{\circ} \frac{L}{35.531mm} \quad (11)$$

The angular resolution of the system can be computed by using the formula

$$R_\theta = \frac{F_o_V_{MAX}}{S} \quad (12)$$

Where R_θ denotes the angular resolution and S denotes the number sampling instants in the Gaussian fitted curve. The sampling rate used in the experiment is 261, and the angular resolution of the system is 0.105°.

5. CONCLUSION

With the fitting of Gaussian curves at different signal-to-noise ratio for the incident laser beam, it is found that the location of centroid shifts away from mean position as the SNR decreases. This results in the different position of the centroid for maximum and minimum A-o-A at different SNRs. It is found that the position of centroid of the Laser beam is different at different angle-of-arrival and moves correspondingly with the change in angle-of-arrival. The system works with the assumption that laser beam has a Gaussian intensity profile. Theoretically, the system is able to measure the angle-of-arrival with the very high angular resolution, depending upon the number of sampling instants in the Gaussian fitted curve. The resolution can be increased by increasing the sampling instants in the Gaussian fitted curve. With 261 sampling points the resolution of the system is 0.105°. Since minimum three detectors are to be illuminated for Gaussian curve fitting, total field of view achieved is 55°. This is less than other techniques mentioned in introduction section. The minimum SNR required for the operation of system is 30db as below this the errors in curve plotting increase drastically. This technique can be used as a simple approach for designing angle-of-arrival sensors for finding the direction of incoming laser radiation on combat vehicles.

ACKNOWLEDGEMENT

The Laser Science and Technology Centre (LASTEC), Defence Research & Development Organization (DRDO) is the rightful owner of the work, and the work is also supported by National Institute of Electronics & Information technology (NIELIT) Aurangabad. The authors are grateful to the institutions to provide us with all the necessary facilities, instruments, and materials required to conduct the experiment.

The authors express their gratitude to Shri Hari Babu Srivastava, OS & Director, LASTEC, DRDO for his constant encouragement & support. We are thankful to Shri Deepak Kumar, Scientist 'E', LASTEC, DRDO for his kind guidance in designing cylindrical lens for this work.

The authors are also grateful to Dr. Sanjeev Kumar Gupta, Director NIELIT Aurangabad, for his constant encouragement & support.

REFERENCES

[1] David S.Dunavan & Richard babish (Feb. 21, 1989), "optical direction of arrival sensor with cylindrical lens". Us4806747

[2] David S.Dunavan, Rene Abren, Stephen Messelt & Edward Slebert (aug.15, 1989), "optical direction sensor having grey code mask spaced from a plurality of interdigitated detectors". Us4857721

[3] Jacques Dubois, André Cantin & Maurice gravel (Jun. 27, 1995), "digital high angular resolution laser irradiation detector (HARLID)". Us5428215

[4] Jacques Dubois, André Cantin & Maurice gravel (Feb. 18, 1997), "analog high-resolution laser irradiation detector (HARLID)". Us5604695

[5] Patrice Marquet, Jean-Mare Lemaire & Philippe Dunouvion (aug.7, 1990), "optoelectronic device for detecting and locating a radiant source". Us4946277

[6] Bandres Miguel a., Gutierrez-Vega & Julio c. (2004). "Ince Gaussian beams". Opt. Lett. Osa. 144–146. Bibcode:2004optl...29..144b. Doi:10.1364/ol.29.000144. Pmid 14743992.

[7] https://www.academia.edu/15180935/optical_specifications_gaussian_beam_propagation_material_properties_optical_coatings.

[8] Jacobs Donald h. Fundamentals of optical engineering. Mc Graw-hill book co., 1943

[9] R. Paschotta, article on 'cylindrical lenses' in the encyclopedia of laser physics and technology, 1. Edition October 2008, Wiley-vch, ISBN 978-3-527-40828-3

[10] Pastuchová Elena & Zákopčan Michal. (2015), "Comparison of Algorithms for Fitting a Gaussian Function Used in Testing Smart Sensors". Journal of Electrical Engineering. 66. 178-181. 10.2478/jee-2015-0029.

BIOGRAPHIES



Anand Kumar Rai
M.Tech Electronics Design Technology (pursuing), NIELIT Aurangabad.
B.Tech Dr. A.P.J. Abdul Kalam Technical University, Lucknow.



Saurabh Bansod
Scientist 'B', NIELIT Aurangabad.
M.Tech in Electronics & Instrumentation, N.I.T. Rourkela.
B.E. in Electronics



Satya Prakash
Scientist 'F', LASTEC, DRDO.
B.tech in Electronics Communication Engineering, Delhi College of Engineering.



Ajay Rathee
Scientist 'E', LASTEC, DRDO.
M.Tech in Computer Technology, IIT Delhi.
B.Tech, M.D.U Rohtak, Haryana.

Impact of Particle Swarm Optimization Parameters on its Convergence

N.K.Jain
Electrical Engineering Dept.
Delhi Technological University
Delhi,INDIA
uma.nangia62@gmail.com

Uma Nangia
Electrical Engineering Dept.
Delhi Technological University
Delhi,INDIA
uma_nangia@rediffmail.com

Jyoti Jain
Electrical and Electronics Engineering Dept.
Maharaja Surajmal Institute of Technology
Delhi, INDIA
jyotijain_in@yahoo.com

***Abstract* - Particle swarm optimization algorithm is an intelligent optimization technique applied to solve optimization problem in the field of Engineering, optimization design of electrical networks, aircraft, control systems, optimum design of chemical processing equipment, design of civil engineering structure, economic load dispatch, load flow, management system, medical etc. Various parameters of PSO are : population size(P), inertia weight, acceleration constants random number, Maximum number of iteration. In this paper an attempt is made to understand the PSO algorithm by solving Rosenbrock benchmark function manually. The impact of variations of parameters on PSO convergence has been studied. Each parameters is varied systematically keeping all other parameters fixed to some value. Rosenbrock benchmark function has been used to study the impact of parameters variations. It was found that PSO is sensitive to the values of these parameters, combination of various parameters for best accuracy and faster convergence has been determined.**

Keywords— convergence, optimization, iteration, Inertia weight

I. INTRODUCTION

Intelligent search methods such as Genetic Algorithm [1-2], Particle Swarm Optimization [3-4] and Ant Colony Optimization [5] etc. have been employed to solve various optimization problems.

Wei-bing Liu and Xian-Jia Wang [6] presented a new particle swarm optimizer based on evolutionary game (EGPSO). Ying-Ping Chen and Wen-Chih Peng [7] suggested to improve the performance of the particle swarm optimizer by incorporate the linkage concept, which is an essential mechanism in Genetic Algorithms and design a new linkage identification technique called dynamic linkage discovery to address the linkage problem in real-parameter optimization problems. Tao Gongand Andrew L. Tuson [8] presented the working mechanism of PSO in a principled manner with forma analysis and investigates the applicability of PSO on the quadratic assignment problem.

Narender Kumar Jain et al. [9-11] developed improved PSO algorithm to reduce the number of function evaluations required to optimize the function. Recently PSO has been applied to solve various power system problems ELD [12], MELD [13] and Load flow [14] problem etc. Review of particle swarm optimization is presented in [15].

In this paper, the working of PSO algorithm has been studied in detail by solving the Rosenbrock function manually for a fixed set of parameters for ten iterations. Also, the effect of parameters of PSO: population size, inertia weight maximum number of iterations on convergence has been studied.

II. PARTICLE SWARM OPTIMIZATION

Particle Swarm Optimization is a self adaptive, population based technique. Initially Population and their velocities are randomly generated. According to mathematical model fitness function is evaluated. Then personal best values and global best value are searched, this process is repeated until all the function values converge at single point. This convergence depends on stopping criteria number of iterations, function value, difference between the function values of consecutive iterations etc. In an n-dimensional search space, position and velocity of particle j is represented by vectors $X_j=(Xj1,Xj2,\ldots\ldots Xjn)$ and $V_j=(Vj1,Vij2,\ldots\ldots Vjn)$ respectively.

Let X_{pbest} and X_{gbest} be the personal and global best position of particle j. The modified velocity of each particle can be calculated using current velocity and distance from Xpbest and Xgbest as follows:

$$V_{ij}^{k+1} = W*V_{ij}^{k} + C_p*r_p\,(X_{pbestij}^{k} - X_{ij}^{k}) + C_g*r_g\,(Xg_{bestj}^{k} - X_{ij}^{k})$$

$$j=1,2\ldots..P \quad i=1,2,3\ldots N \quad \ldots \qquad (1)$$

Velocities of particles are updated using (1)

Where
k is iteration count.

N	Number of variables
P	Number of Particles
V_{ij}^{k+1}	is velocity of j^{th} particle of i^{th} variable at k^{th} iteration.
X_{ij}^{k}	is the value of position of j^{th} particle of i^{th} variable at k^{th} iteration.
C_p, C_g	are acceleration coefficients.
$Xpbesti_j^{k}$	is the value of i^{th} variable of Personal best position of j^{th} particle in k^{th} iteration.
$Xgbesti^{k}$	is the value of i^{th} variable of global best particle until k^{th} iteration.
N	is the total number of variables.
P	is Number of particles in swarm.
rp, rg	are two separately generated uniformly distributed random numbers.
W	Inertia weight

978-1-5386-6625-8/18/$31.00 ©2018 IEEE

ITmax Maximum number of iteration
Wmax Maximum value of inertia weight
Wmin Minimum value of inertia weight

Position of each particle is updated using. (2):

$$X^{k+1} = X^{k} + V_{ij}^{k+1}$$

$$i = 1,2\ldots.N; \quad j=1,2\ldots..P \qquad (2)$$

In this paper two types of Inertia weight Linearly decreasing using (3) and Simulated annealing inertia weight using (4) have been used to observe the effect of Inertia weight on convergence using Matlab programme.

$$W=Wmax-[(Wmax-Wmin)*k/ITmax \qquad (3)$$

$$W=W+(W_{max}-W_{min})*\lambda^{(k-1)} \qquad \lambda=0.95 \qquad (4)$$

Flow Chart of Particle Swarm Optimization Technique is shown in Fig.1.

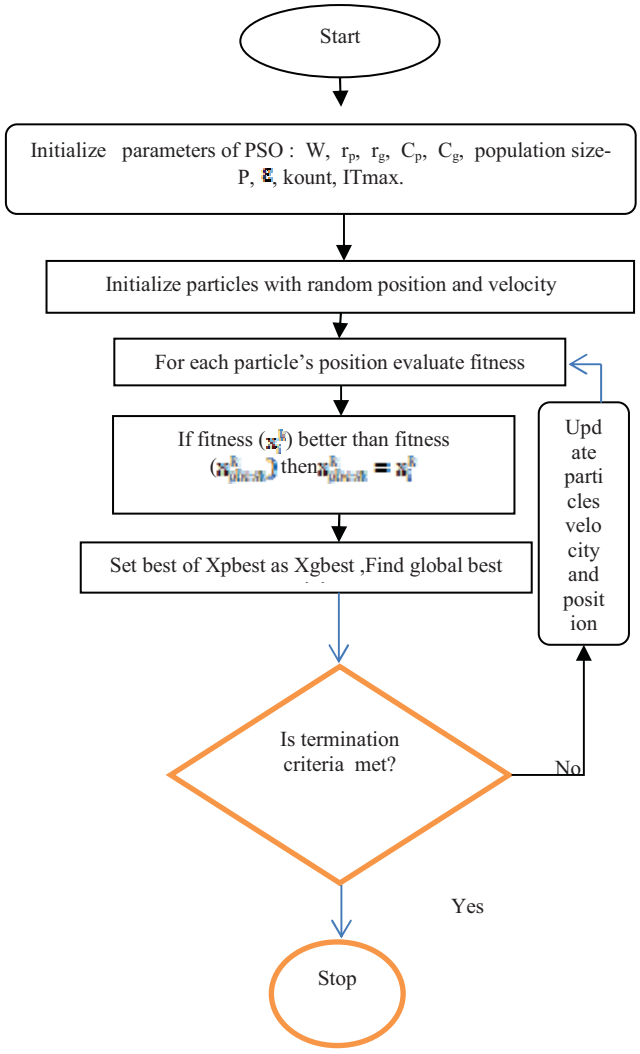


Fig. 1 Flow Chart of Basic PSO

III. MATHEMATICAL REPRESENTATION OF ROSENBROCK FUNCTION

In mathematical optimization, the Rosenbrock function is a non-convex function used to check the performance of test maintaining the integrity of the specifications problem for optimization algorithm. Mathematically, it is defined as:

$$f=100*(x_1^2 - x_2)^2+(1-x_1)^2$$

f (1,1)=0 Range: $x_1 \geq 0, x_2 \leq 2$ (5)

It has global minimum at (1,1) where $f(x_1, x_2)=0$.

IV. COMPUTATIONAL PROCEDURE

The PSO algorithm is applied to optimize the Rosenbrock function. Initially following parameters are considered for PSO algorithm to optimize the function manually as shown in Table 1.

Table 1: Parameters for PSO algorithm

P	rp	rg	Cp	Cg	ITmax	Wmax	Wmin
10	0.4	0.5	2	2	10	0.9	0.4

V. COMPUTATIONAL RESULTS

Initially population size of 10 particles and their velocities are generated randomly and PSO algorithm is applied to Rosenbrock function. The calculations have been done manually to understand the working of PSO.

Results of function value at position of particles X1 and X2 for zeroth iteration is shown in Table 2.

Table 2: Result of Rosenbrock function at Zeroth Iteration

S. No.	X1	X2	V1	V2	function value
1	1.2886	0.4155	0.3111	0.5949	155.08329
2	0.7572	0.6025	0.9234	0.2622	0.143913363
3	1.6232	0.9418	0.4302	0.6028	287.0059104
4	1.0657	0.461	0.1848	0.7112	45.52855068
5	0.7015	1.6886	0.9049	0.2217	143.2497888
6	1.878	0.3895	0.9797	0.1174	985.0887203
7	1.7519	0.4518	0.4389	0.2967	685.6193456
8	1.1003	0.3414	0.1111	0.3188	75.5713705
9	1.245	0.4553	0.2581	0.4242	119.9023076
10	1.1741	0.8714	0.4087	0.5079	25.74644817

Results are graphically represented by Fig.2 for zeroth iteration as shown in Table 2. The position of particles at Zeroth Iteration is shown in Fig.2.

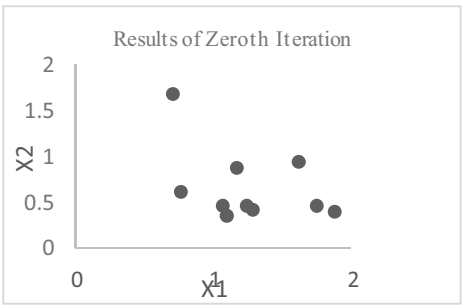


Fig.2 position of particles at Zeroth Iteration

Results of function value for position of particles X1 and X2 for First iteration is shown in Table 3.

Table 3: Result of Rosenbrock function at First Iteration

S. No.	X_1	X_2	V_1	V_2	function value
1	1.0216	1.1065	-0.26697	0.692665	0.41555
2	1.5420	0.8253	0.78489	0.22287	241.3727
3	1.1228	1.1148	-0.50033	0.17308	2.14544
4	0.9142	1.2070	-0.15142	0.74602	13.7797
5	1.5263	0.7909	0.824865	-0.89766	237.0814
6	1.5899	0.7022	-0.28806	0.31279	333.6423
7	1.1302	0.8546	-0.62164	0.402895	17.8932
8	0.8516	0.8738	-0.24867	0.53208	2.21821
9	0.9765	0.9630	-0.26842	0.50777	0.00929
10	1.1045	1.0342	-0.0695	0.162815	3.4673

The position of particles X_1 and X_2 for First Iteration is shown in Fig.3.

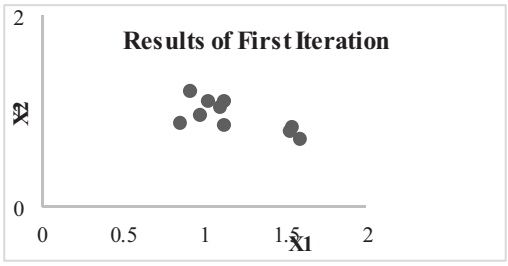


Fig. 3. position of particles at First Iteration

Results of function value and position of particles X_1 and X_2 for Second Iteration is shown in Table 4.

Table 4: Result of Rosenbrock function at Second Iteration

S. No.	X_1	X_2	V_1	V_2	function value
1	0.7630	1.5172	-0.2586	0.409037	87.4811
2	0.9765	0.9630	-0.5655	0.1377	0.0092
3	0.5763	1.1015	-0.5465	-0.01335	59.3753
4	0.8554	1.5598	-0.05883	0.3528	68.5946
5	0.9765	0.9630	-0.54978	0.172125	0.00929
6	0.7461	1.2133	-0.8438	0.511012	43.17359
7	0.4792	1.2853	-0.65099	0.430691	111.7170
8	0.7776	1.3887	-0.07398	0.515254	61.51340
9	0.7618	1.3692	-0.21473	0.406216	62.28767
10	0.9209	1.0933	-0.18361	0.059107	6.014429

Fig.4 shows results for Second Iteration.

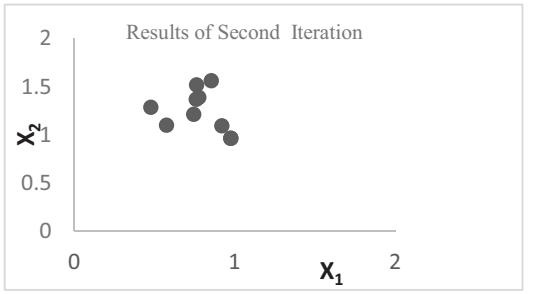


Fig.4. position of particles at Second Iteration

Results for position of particles X_1 and X_2 for Third Iteration is shown in Table 5.

Table 5: Result of Rosenbrock function at Third Iteration

S.No.	X_1	X_2	V_1	V_2	function value
1	0.989516	0.942618	0.226503	-0.57458	0.13351
2	0.552456	1.066345	-0.42413	0.103275	58.1333
3	1.003912	0.963737	0.427591	-0.1378	0.19452
4	0.979527	0.945427	0.124078	-0.61446	0.02015
5	0.56425	1.092164	-0.41234	0.129094	60.0643
6	0.343732	1.346329	-0.40241	0.133027	151.273
7	1.009134	0.941535	0.529857	-0.34385	0.59017
8	0.980284	0.937307	0.202631	-0.45143	0.05632
9	0.987322	0.942759	0.225469	-0.42653	0.013703
10	0.985766	0.960115	0.064785	-0.13321	0.013703

Results of Table 5 are graphically represented in Fig.5. for position of particles for Third Iteration .

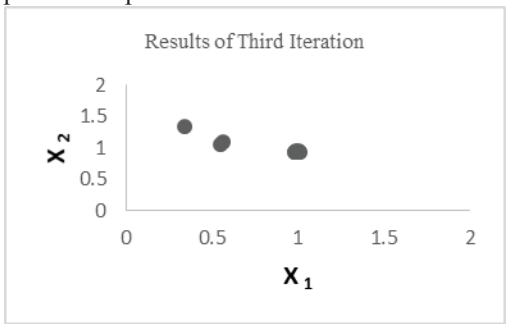


Fig.5. position of particles at Third Iteration

Results of function value at position of particles X_1 and X_2 for Forth Iterationis shown in Table 6.

Table 6: Result of Rosenbrock function at Fourth Iteration

S. No.	X_1	X_2	V_1	V_2	function value
1	1.01899	0.952743	0.466542	-0.1136	0.73333
2	1.27589	0.866612	0.271987	-0.09712	58.0348
3	1.06343	0.532948	0.083913	-0.41248	35.7589
4	0.68795	1.053436	0.123701	-0.03873	33.7559
5	1.01682	0.949767	0.673094	-0.39656	0.7087
6	1.34748	0.722375	0.338351	-0.21916	119.660
7	1.11842	0.647071	0.138143	-0.29024	36.4723
8	1.13441	0.664501	0.147091	-0.27826	38.755

9	1.02193	0.869825	0.036169	-0.09029	3.0463
10	1.16441	0.654501	0.17091	-0.28826	37.7552

Results of Table 6 are graphically represented in Fig.6. for position of particles for Forth Iteration .

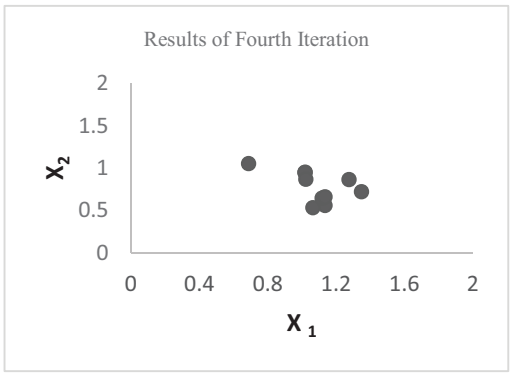


Fig.6. position of particles at Fourth Iteration

Similarly results for Fifth, Sixth, Seventh, Eighth , Ninth and Tenth Iterations are shown in Fig.7,8,9,10, 11 and 12.

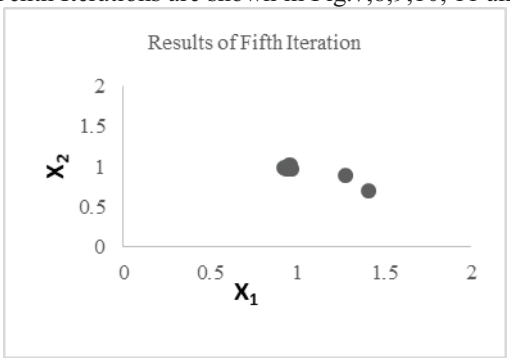


Fig.7. position of particles at Fifth Iteration



Fig.8. position of particles at Sixth Iteration

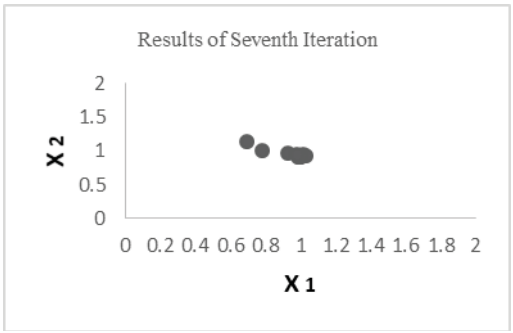


Fig.9. position of particles at Seventh Iteration

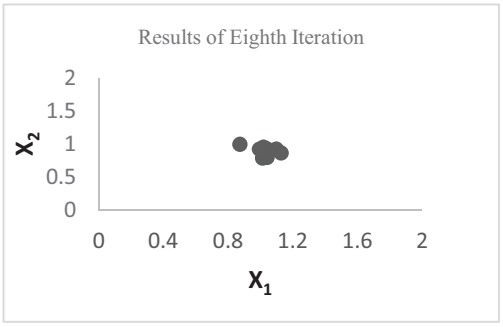


Fig.10. position of particles at Eighth Iteration

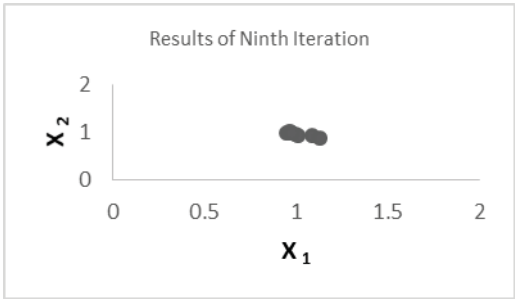


Fig.11. position of particles at Ninth Iteration

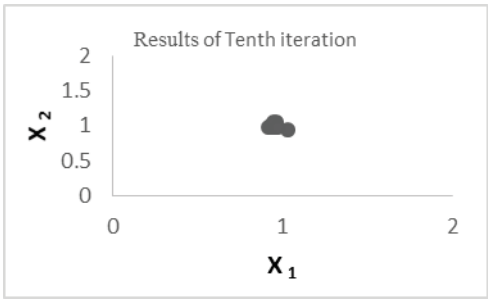


Fig.12. position of particles at Tenth Iteration

Position of particles in each iteration represented by Figures 2-12 shows that initially particles have large search area, when iteration increases search area reduces and at 10^{th} iteration all particles converged in small area between 0.92923676 and 1.050355942. In this paper results were graphically presented for small populations because calculations are done manually. When population size increases, convergence occurred at exact position (1,1) for Rosenbrock function. Same is true for others functions [10].

VI. VARIATIONS Of PARAMETERS OF PSO

Population Size (P), maximum iteration (ITmax), Inertia weight (W) on convergence has been studied. One of the parameters is varied while all other are kept fixed. This study has been conducted with the help of Matlab programme in which r_p and r_g are fixed to 0.4 and 0.5 respectively while C_p and C_g are fixed to two(2).

A. Population Size (P):

In this case, linearly decreasing Inertia weight and ITmax of 1000 has been considered. The population size is varied from 10 to 60.The results are shown in Table 7.

Table 7 : Effect of Population Size

P	k	x1	x2	function value
10	56	1.220362	1.489734	4.85797e-002
20	40	9.53764e-001	9.080800e-001	2.39098e-003
30	62	1	1	3.989808e-020
40	51	1	1	1.828370e-022
50	60	1	1	1.828370e-022
60	58	1	1	8.692590e-020

From Table 7, it is observed that the function does not get optimimized for population size of 10 and 20. Howere,it gets optimized accurately for 30 particle size. It is further observed that for a particle size of 40, maximum accuracy is achieved in minimum number of iteration.

B. Maximum Iteration (ITmax):

In this study, for each fixed value of particle size, Maximum number of iteration (ITmax) is varied from 30 to 200. The particle size has been fixed to 30, 40, 50 and 100. The results are shown in Table 8.

In the table 9, Column (2) and (3) represents particles size and maximum number of iteration for a particle swarm optimization algorithm. Column (4) represents number of iterations required to optimize the function. Column (5) and (6) represents the value of variables X_1 and X_2 at which function is optimized. Columns (7) represents the function value.

Table 8: Effect of ITmax

S.No.	P	ITmax	k	X1	X2	Function value
(1)	(2)	(3)	(4)	(5)	(6)	(7)
1	30	30	30	1	1	1.145576e-011
2	30	40	32	1	1	1.375645e-011
3	30	50	40	1	1	2.5987932e-013
4	30	60	41	1	1	6.940071e-015
5	30	70	39	1	1	1.216929e-013
6	30	80	41	1	1	2.343508e-014
7	**30**	**110**	**55**	**1**	**1**	**4.763705e-020**
8	30	140	50	1	1	1.675177e-019
9	30	200	53	1	1	1.821156e-018
10	40	90	48	1	1	9.198076e-018
11	40	100	45	1	1	1.944461e-017
12	40	120	48	1	1	1.149075e-017
13	40	140	53	1	1	1.216215e-019
14	40	160	52	1	1	2.827675e-019
15	**40**	**180**	**57**	**1**	**1**	**1.093662e-020**
16	40	200	54	1	1	2.085538e-018
17	50	30	30	1	1	1.415376e-012
18	50	50	36	1	1	3.085142e-014
19	50	60	41	1	1	6.603557e-016
20	50	70	41	1	1	1.532676e-014
21	50	80	47	1	1	1.308451e-015
22	50	100	50	1	1	4.974816e-018
23	50	120	47	1	1	5.543777e-017
24	**50**	**140**	**57**	**1**	**1**	**2.060528e-021**
25	50	160	48	1	1	1.193581e-017
26	50	180	58	1	1	5.891339e-021
27	50	200	56	1	1	2.357654e-019
28	50	220	51	1	1	9.522462e-018
29	100	50	40	1	1	2.65228e-015
30	100	60	45	1	1	3.845000e-019
31	100	70	48	1	1	4.959005e-018
32	100	80	49	1	1	5.829558e-020
33	100	90	49	1	1	9.005843e-019
34	100	100	57	1	1	30268523e-021
35	100	110	43	1	1	2.1000047e-016
36	100	120	57	1	1	3.910962e-020
37	100	140	51	1	1	4.449501e-019
38	100	160	50	1	1	2.142912e-018
39	100	180	53	1	1	1.868118e-019
40	**100**	**200**	**58**	**1**	**1**	**6.037815e-022**
41	100	220	59	1	1	2.402596e-020

From Table 8 it is observed that accuracy is obtained for the following combinations of particle size (P) and ITmax which are shown in Table 9.

Table 9: Best combination of P and ITmax

P	ITmax	k	X_1	X_2	Function value
30	110	55	1	1	4.763705e-020
40	180	57	1	1	1.093662e-020
50	140	57	1	1	2.060528e-021
100	200	58	1	1	6.037815e-022

C. Inertia Weight:

In this paper, a study has been conducted by an PSO algorithm in which, two types of Inertia weight have been considered :Linearely decreasing Inertia weight given by (3) and simulated annealing inertia weight as given by (4).

The other parameters have been fixed to the values shown in Table 10.

Table 10:Parameters of PSO

P	rp	rg	Cp	Cg	ITmax	Wmax	Wmin
10-1000	0.4	0.5	2	2	10-120	0.9	0.4

For both types of Weights, population size is varied from 10 to 1000 and ITmax has been fixed to the corresponding value for which the function got optimized with maximum accuracy. Results for Linearely decreasing weight is shown in the Table 11.

Table 11: Results of Linearly Decreasing Inertia weight

P	k	IT_{max}	X_1	X_2	function value
10	71	200	1	1	3.7e-11
20	74	200	0.99	0.99	3.5e-09
30	80	160	1	1	3.9e-015
40	63	90	1.0	1.0	9.8e-019
50	74	140	1.00	1.00	9.87e-021
100	48	50	1.00	1.00	8.31e-018
200	96	220	1.00	1.00	2.71e-023
1000	54	60	1.00	1.00	4.93e-129

Results of Simulated annealing inertia weight is shown in Table 12.

Table 12: Results of simulated annealing Inertia weight

P	k	IT_{max}	X_1	X_2	function value
10	10	10	0.99	0.99	3.66e-08
20	51	110	1.000	1.0	3.6e-017
30	55	110	0.99	0.99	4.7e-020
40	57	180	1.0	1.0	1.09e-020
50	57	140	1.00	1.00	2.06e-021
100	58	200	1.00	1.00	6.03e-022
200	59	110	1.00	1.00	5.38e-023
1000	60	220	1.00	1.00	1.33e-025

VII. CONCLUSION

The Calculations have been done manually as well as by Matlab Programme to understand the variation of PSO parameters on convergence. Following are the results:

(1) Particles size should not be less than 20 to optimize the function accurately.
(2) For small size of Particles less number of maximum iteration required.
(3) Simulated annealing Inertia weight optimized the function accurately in minimum number of iteration in comparison to Linearly decreasing Inertia weight.
(4) For better accuracy particle size should be less than maximum number of iteration

REFERENCES

[1] N.K.Jain, Uma Nangia, Jyoti Jain,"Effect of Population and Bit Size on optimization of Function by Genetic Algorithm", International Conference on Computing for Sustainable Global Development March, 2016 .

[2] N.K.Jain, Uma Nangia, Jyoti Jain, "GA based Multi-objective Economic Load Dispatch by Maximization Of Minimum Relative Attainments", IEEE 5th India International Conference on Power Electronics (IICPE 2012), December 2012.

[3] J. Kennedy and R. Eberhart, "Particle Swarm Optimization, " in Proc. IEEE Int. Conf. Neural Networks, 1995, pp. 19942-1948.

[4] James Kennedy and Russell Eberhart, "A New Optimizer Using Particle Swarm Theory." Proceeding of sixth International Symposium on Micro Machine and Human Science,1995,pp. 39-43. 0-7803-2676-8/95 IEEE.

[5] Musirin I., Ismail N.H.F., Kalil M. R. et al.: 'Ant Colony Optimization (ACO) Technique in Economic Power Dispatch Problems' Trends in Communication Technologies and Engineering Science. Lecture Notes in Electrical Engineering, vol 33. Springer, Dordrecht pp. 191-203.

[6] Liu Weibing and Wang Xianjia "An evolutionary game based particle swarm optimization algorithm." Journal of computational and Applied Mathematics,2008 (214)4,30-35.

[7] Ying-Ping Chen and Wen-ChihPeng, "Particle Swarm Optimization With Recombination and Dynamic Linkage Discovery."IEEE transaction on systems, man, and cybernetics-Part B:cybernetics, vol. 37, no.6, December 2007.

[8] Tao Gong and Andrew L.Tuson, "Particle Swarm Optimization For Quadratic Assignment Problems –A Forma Analysis Approach" International journal of computational Intelligence Research ,ISSN 09731-1873 Vol.2,No.X(2007).

[9] N.K.Jain, Uma Nangia, Jyoti Jain, "An improved PSO Based On Initial Selection of particles (ISBPSO) for Economic Load Dispatch", IEEE first *International Conference on Power*Electronics, Intelligent Control and Energy (PIECES 2016).

[10] N.K.Jain, Uma Nangia, Jyoti Jain, "An improved PSO Based On Initial Selection of particles (ISBPSO)", IEEE first *International Conference on Power*Electronics, Intelligent Control and Energy (PIECES 2016).

[11] N.K.Jain, Uma Nangia, Jyoti Jain ,"Economic Load Dispatch using Social acceleration Constant based PSO", J.Inst.Eng. India ser.B (2018).

[12] PulkitJain,PranjalBhatia,Rashika Mann, Nidhikumari andJyotijain, "Economic Load Dispatch using PSO", International journal of Technology and science,Vol. 5, issue 2, 2018.

[13] Narender Kumar Jain, Uma Nangia, Aishwary Jain , "PSO for multiobjective Economic Load Dispatch (MELD) for Minimizing Generation Coast and Transmission losses", J.Inst.Eng. India ser.B (2015).

[14] U. Nangia, N.K. Jain, C.L. Wadhwa, "Multiobjective optimal load flow based on ideal distance minimization in 3D space", Electr. Power Energy Syst. **23**, 847–855 (2001).

[15] N.K.Jain, Uma Nangia, JyotiJain ,"Review of particle swarm optimization", J.Inst.Eng. Indiaser.B, August (2018),Vol.99, Issue 4, pp. 407-411.

Implementation and Analysis of field Control on Electric Vehicle Power Train System Employing PMSM as Traction Device

Monika Verma
Electrical Engineering Department
Delhi Technological University
New Delhi, India
monikaverma_phd2k17@dtu.ac.in

Mini Sreejeth
Electrical Engineering Department
Delhi Technological University
New Delhi, India
minisreejeth@dce.ac.in

Madhusudan Singh
Electrical Engineering Department
Delhi Technological University
New Delhi, India
madhusudan@dce.ac.in

***Abstract*— Traction system in the electric powertrain (PT) plays the crucial role of transmitting energy from battery to the wheels of electric vehicle (EV). Various motors have been employed for such transmission in the system but the most efficient one is permanent magnet synchronous motor (PMSM) because of its elevated torque and power density. The PMSM has comparatively high efficiency due to the absence of windings on the rotor. In this paper a MATLAB/Simulink model of the complete EVPT is developed and analyzed under different operating condition. A Voltage Source Inverter (VSI) is used to feed PMSM for variable speed operation. The speed of the system is regulated via field control of the electric motor. The simulation results are presented and verified under different operating conditions to the system. This analysis is helpful for understanding and developing advanced controls in electric PT system.**

Keywords*— *Electric vehicle powertrain, PMSM, power electronics, VSI, powertrain modelling, Field control.

I. INTRODUCTION

The electric vehicle industry in India has tremendously developed during last few decades. At global level among the largest vehicle manufacturers, India has reached at the sixth position. The automotive industry contributes about 21% to India's excise duty collection. 'National Electric Mobility Mission Plan 2020' was launched in 2013 by the Indian government to address various issues like pollution caused by vehicles, national energy security and boost in country's manufacturing capabilities [1], [2].

Various types of electric vehicles are being manufactured and launched in India such as hybrid cars, motorcycles, scooters, bicycles, buses, mini pick-up trucks, semi-trailer and tractor trucks, rickshaws, railways and solar electric boats etc. Automobile related pollution, greenhouse gas emissions, dependency on fossil fuel based economy, noise pollution etc. are some of the reasons for the shift to clean mobility which is effectively addressed by the use of electric vehicles.

An electric vehicle which utilizes electric motors and motor controllers in place of internal combustion engine (ICEs) for propulsion and uses stored chemical energy of rechargeable battery packs is termed as battery electric vehicle. This paper shows the usage of PMSM as traction device in EVPT system and explores its future potential in this area [3]. An electrical vehicle means the commercial electric cars developed by different original equipment manufacturers (OEMs). For thorough understanding of vehicle dynamics, modeling of traction system is necessary. The dynamic model of PMSM under load conditions is developed and simulated in MATLAB. The controller in EV provides wide range of speed for traction motor and it is developed on the principle of field oriented control. The proposed system is validated for different modes of operation.

II. FEATURES OF ELECTRIC MOTORS FOR EVPT SYSTEMS

Specifications of electric motor used by different OEMs include drivetrain configuration, cooling methodology, output power from motor, torque developed by motor, battery type used and top speed achievable by the motor [4]. OEMs like Audi, Ford, Honda, Toyota and others use permanent magnet AC machine as integrated system with or without internal combustion engines. The basic requirements for electric motor performance currently being used by OEMs in the market are shown in Table I.

TABLE I. ELECTRIC MOTOR SPECIFICATIONS USED BY OEMS

OEMs	Output Power (kW)	Maximum Torque (Nm)	Li-Ion Battery Capacity (kWh)	Cooling Methodology
Audi	75	330	8.8	Liquid cooled
Ford	35	243	1.4	Liquid cooled
Toyota Prius	60	207	4.4	Water cooled
Nissan Leaf	90	210	24	Air cooled
Renault Zoe	90	350	22	Air cooled
Honda	135	490	4.7	Oil cooled
Volvo	150	1200	76	Air cooled

III. ANALYSIS OF EVPT SYSTEM

A. A Typical EVPT System

The conventional PT system uses internal combustion engine as propulsion system. The high oscillations and ripples are observed in torque and speed response of a conventional PT, which can be easily controlled in electrical PT system via integrated power electronics [5]. EVPT

978-1-5386-6625-8/18/$31.00 © 2018 IEEE

system consists of a battery supplying energy to the traction motor via VSI motor is connected to the transmission system, which transfer the mechanical energy to the wheels of the vehicle. The schematic diagram of typical EVPT system is shown in Fig. 1.

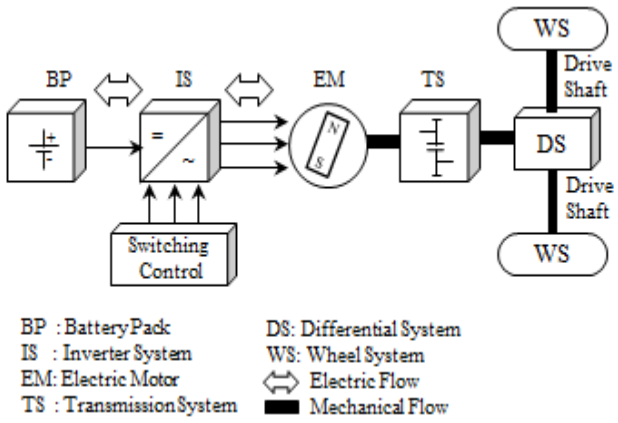


Fig. 1. Typical EVPT schematic diagram

B. Dynamic Modeling of Traction Motor

The traction motor is modeled in synchronously rotating frame to avoid the difficulty in calculation of quantities due to variations in the machine parameters [6]. Three phase to two phase transformation is carried out using Park's transformation. The stator voltages in direct and quadrature axes are given by equations (1-2).

$$V_q = R_s i_q + p\lambda_q + \omega_r \lambda_d \quad (1)$$

$$V_d = R_s i_d + p\lambda_d - \omega_r \lambda_q \quad (2)$$

Stator fluxes in two axes are:

$$\lambda_q = L_q i_q \quad (3)$$

$$\lambda_d = L_d i_d + \lambda_{af} \quad (4)$$

The electromagnetic torque developed by PMSM is given by following equations:

$$T_e = \frac{3}{2}\frac{P}{2}(\lambda_d i_q - \lambda_q i_d) \quad (5)$$

$$T_e = \frac{3}{2}\frac{P}{2}(\lambda_m i_q^* - (L_d - L_q) i_d^* i_q^*) \quad (6)$$

Where R_s is stator resistance; $p = d/dt$ is the differential operator; ω_r is the rotor speed; L_q, L_d, i_q, i_d are quadrature and direct axes inductances and currents respectively.

The mechanical equation for P pole motor having flux density B and motor inertia J with load torque T_l is given in equation (7):

$$T_e = \frac{J}{p} p\omega_r + \frac{B}{p}\omega_r + T_l \quad (7)$$

C. Field Control of EVPT system

There are two different terms in the electromagnetic torque equation (6); first one is due to permanent magnet λ_m and q axis current component i_q, known as magnetic torque and the second one is due to difference in direct and quadrature axes interaction, known as reluctance torque. For field oriented control, magnetic torque component is utilized. Reluctance torque component is utilized for flux weakening operation beyond base speed which is a critical affair for normal operation of electric motor. Hence, by maintaining i_d equal to zero and controlling i_q component of stator current, the speed control strategy can be applied over the PT system. However, the d axis flux linkage being dependent only on the permanent magnet, it is not a sufficient condition for a motor to operate above rated speed at voltage and current ratings of the motor and inverter configuration. So, for high speed operations and flux weakening regions, the i_d component is maintained at proper non-zero value [7].

Equation (8) gives analogous torque equation of DC machine when the direct axis current component is kept zero in equation (6). Rotor flux due to permanent magnet λ_m is constant in this motor. The required torque equation is obtained as follows:

$$T_e = \frac{3}{2}\frac{P}{2}\lambda_m i_q^* \quad (8)$$

IV. Results and Discussions

A MATLAB/Simulink model of overall PT system is developed and analyzed under different operating conditions. The detailed block diagram of implemented field oriented control strategy over complete PT system is shown in shown in Fig. 2.

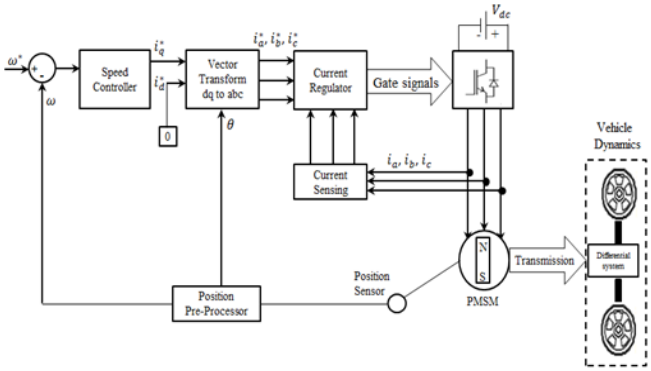


Fig. 2. Schematic Diagram for control of EVPT system

The dynamic model of traction motor is implemented, simulated and tested under varying load. The nominal rating of the motor used for Simulink model is listed in Table II. The developed electromagnetic torque and speed of PMSM are shown in Fig. 3. The performance based parameters of vehicle used for testing the Simulink model are listed in Table III.

TABLE II. PMSM Motor Specifications Used in Simulink Model

Motor Specifications			
Rated Power	9 kW	Stator resistance	1.2 ohm

978-1-5386-6625-8/18/$31.00 © 2018 IEEE

Motor Specifications			
Rated Torque	60 Nm	d, q axes inductance	5.7 mH, 12.5 mH
Rated Voltage	300 V	Magnetic flux	0.07145 V-sec
Poles	4	Moment of inertia	1.584×10^{-4} kg-m^2
Phases	3	Field intensity	3.035×10^{-3}Nm-sec

TABLE III. VEHICLE PARAMETERS

Parameter	Value	Parameter	Value
Mass	1200 kg	Wheel velocity threshold	0.1 m/s
Frontal Area	3 m^2	Vertical load on wheels	3000 N
Drag Coefficient	0.4	Peak longitudinal force	3500 N
Rolling radius	3 m	Carrier to drive teeth ratio	4
Slip at peak load	10	Follower to base teeth ratio	2

Initially the motor is running at no load condition. A sudden load disturbance of 20 Nm is applied at t=1 sec. The traction motor develops torque to adjust to the new load and track the system load torque approximately.

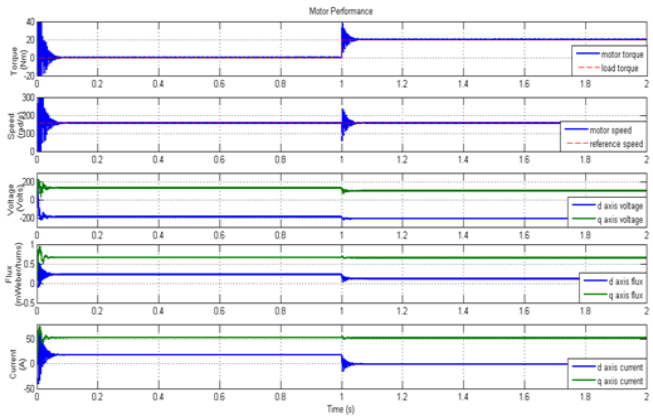


Fig. 3. Dynamic Response of traction motor under load variation

The Simulink model for overall EVPT system is shown in Fig. 4. The field control is implemented for both modes of operation; traction and braking mode. In order to check the performance of the controller, simulations are performed for four different cases. The controller gains are taken as: K_p =1000 and K_I = 5 respectively. The initial conditions of all the estimated parameters are assumed to be zero in order to monitor exact vehicle performance.

A. *Constant speed operation:*

The reference speed is chosen as a constant value of 150 rad/sec. The speed tracking capability of the system is analyzed under load torque variations. Fig. 5 represents the actual and reference torque, motor and vehicle speed, stator reference abc and dq currents under the disturbance caused to the system due to load variation applied at t=1 sec.

As soon as the load demand from the motor increases, the vehicle accelerates since the controller generates the required quadrature axis current i_q in order to control the motor speed and thus the system tracks the variation in the load torque.

B. *Variable speed operation:*

Initially the motor reference speed is 0 rad/sec. At t=0.5 sec, a step variation of speed from 150 rad/sec to 300 rad/sec is applied. Moreover at t=1 sec, a step load torque variation from no load to 10 Nm is applied. As the load fluctuates, the necessary q axis current i_q is generated by the controller for providing the required acceleration to EVPT system. The speeds, torques and currents are shown in Fig. 6.

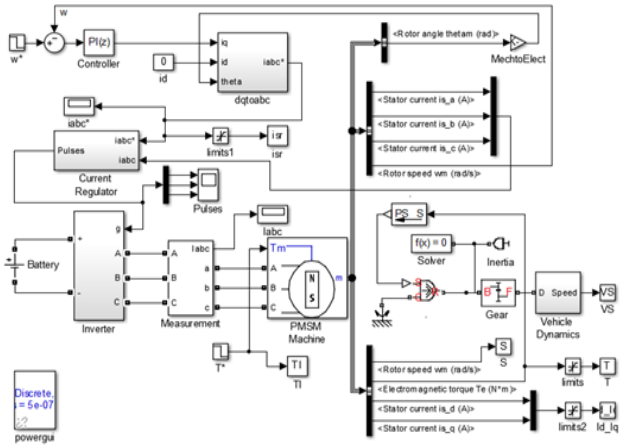


Fig. 4. MATLAB/Simulink Model of controlled EVPT system

C. *Ramp speed operation:*

The reference speed is a time varying ramp function with respect to time with the slope of 1 rad/sec2. With the change in load torque of 10 Nm from no load condition, the controller performs the action of producing the required quadrature current for regulating motor and vehicle speed. The performance of controller applied to the EVPT system is shown in Fig. 7. The three mentioned case studies cover the traction mode of PT system.

D. *Braking mode of operation of EVPT system:*

For braking mode of operation, the proposed PT system is tested with stepped varied speed profile from 150 rad/sec to 0 rad/sec at t=0.5 sec and the load torque is varied from 10 Nm to no load condition at t=1 sec. The controlled motor and vehicle speeds, torques and stator dq and abc currents are shown in Fig. 8. The system responds in accordance with the load variations. The field control is easier and advantageous to maintain the required vehicle speed.

978-1-5386-6625-8/18/$31.00 © 2018 IEEE

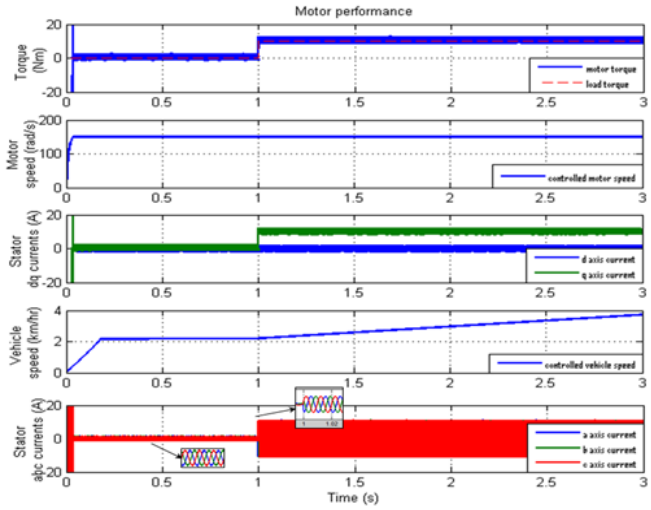


Fig. 5. System response under load disturbance for constant speed profile

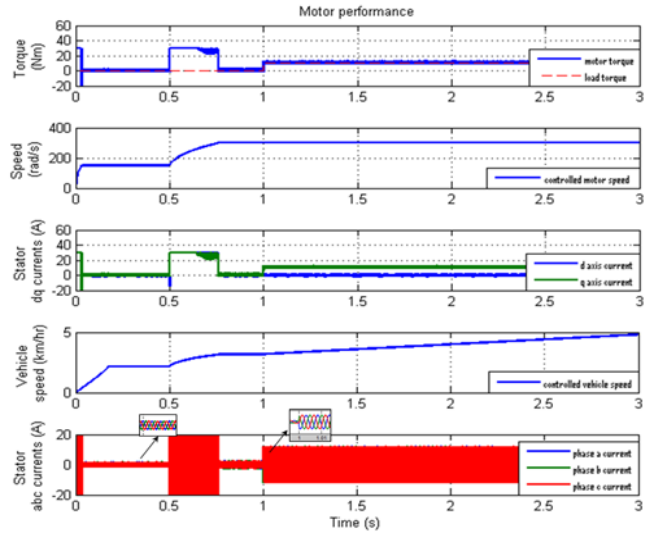


Fig. 6. System response under load disturbance for variable speed profile

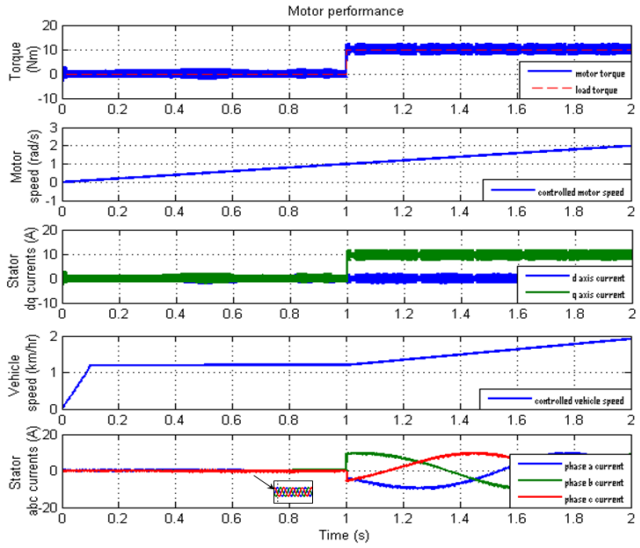


Fig. 7. System response under load disturbance for ramp speed profile

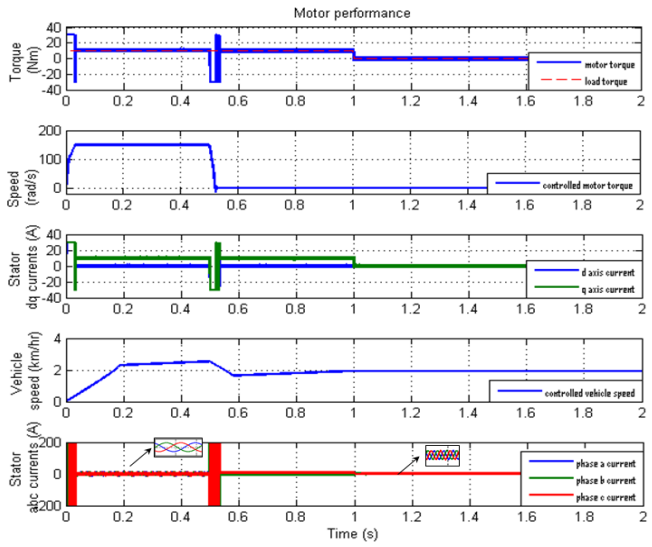


Fig. 8. System response under load disturbance for braking mode

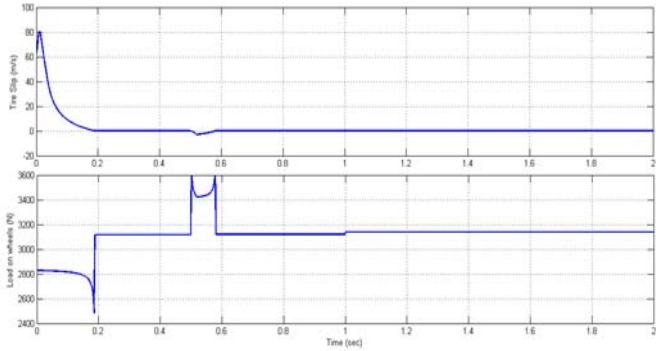


Fig. 9. Tire Slip and normal force characteristics

In an EVPT system, the tire in contact with the road is subjected to slip. When the traction device applies torque to axle of the wheel, tire due to contact friction shoves on the ground and transfers back the resultant reactive force on the wheel due to which it is pushed forward or backward [8].

In case of absence of slip, the translational motion of tire is given in equation (9):

$$v = r.\omega \quad (9)$$

Here v is linear velocity, r is radius and ω is angular velocity of wheel. But practically tire slips and produces a longitudinal force in response to slip.

Fig. 9 shows the tire slip characteristics and normal force characteristics which represents load on wheels during movement of EVPT system. Tire deformity is ignored in this analysis.

The tire slip is nearly zero for perfect rolling [9]. From the tire slip characteristics, it is observed that the slip is approaching zero in less than 0.2 sec.

Also PMSM used as traction motor in the proposed EVPT system is providing the necessary tractive force in accordance with the load variation.

The net effect of all the forces and acting torque

978-1-5386-6625-8/18/$31.00 © 2018 IEEE

Downloaded from https://academic.oup.com/bioinformatics/advance-article-abstract/doi/10.1093/bioinformatics/btz823/5613889 by Delhi Technological University user on 11 November 2019

Gene expression

Improved *dropClust* R package with integrative analysis support for scRNA-seq data

Debajyoti Sinha [1,2], Pradyumn Sinha [3,+], Ritwik Saha [3,+], Sanghamitra Bandyopadhyay [1,*] and Debarka Sengupta [4,*]

[1] SyMeC Data Center, Indian Statistical Institute, Kolkata, 700108, India,
[2] Department of Computer Science & Engineering, University of Calcutta, Kolkata, 700098, India,
[3] Department of Computer Science & Engineering, Delhi Technological University, Delhi, 110042, India and
[4] Department of Computer Science & Engineering, Department of Computational Biology, Center for Artificial Intelligence, Indraprastha Institute of Information Technology, New Delhi, 110020, India.

*To whom correspondence should be addressed.
+These authors contributed equally to this work.

Associate Editor: XXXXXXX

Abstract

Summary: DropClust leverages Locality Sensitive Hashing (LSH) to speed up clustering of large scale single cell expression data. Here we present the improved dropClust, a complete R package that is, fast, interoperable and minimally resource intensive. The new dropClust features a novel batch effect removal algorithm that allows integrative analysis of single cell RNA-seq (scRNA-seq) datasets.
Availability and implementation: dropClust is freely available at https://github.com/debsin/dropClust as an R package. A lightweight online version of the dropClust is available at https://debsinha.shinyapps.io/dropClust/.
Contact: debarka@iiitd.ac.in; sanghami@isical.ac.in
Supplementary information: Supplementary data are available at *Bioinformatics* online.

Introduction

With the advent of single cell transcriptomics, it is now possible to discern phenotypic diversity among seemingly similar cells in complex tissues (Tanay and Regev, 2017). A large pool of cells presents the opportunity of identifying cell types which are previously unseen due to their limited presence or rarity (Jindal *et al.*, 2018). The observed exponentiation of single cell data dimensions demands high performance data analytics capabilities. DropClust R package is one of the speediest clustering algorithms for large scale scRNA-seq data (Sinha *et al.*, 2018). However, the existing implementation requires interfacing with multiple programming languages *viz.* R, python and C. This, hinders seamless installation experience on the user end. Also, it's unfit for personal computer use, due to its memory requirements.

Here, we present an upgraded version of the dropClust pipeline (Sinha *et al.*, 2018) with substantially improved execution time and memory efficiency. The current dropClust R package also enables integrative analysis (Haghverdi *et al.*, 2018) of scRNA-seq datasets obtained from independent experiments. The current implementation adopts the widely used *SingleCellExperiment* container R class (Lun *et al.*, 2018) thereby enhancing its interoperability with other tools.

Improvements and new features

Selection of Principal Components: In the existing version of dropClust, principal components are rank-ordered based on the number of Gaussian mixtures detected from projection of single cells on individual components. We replaced the Gaussian Mixture Model (GMM) by the Gaussian Kernel Density estimator to identify the number of modes in a distribution (More details in Supplementary Information). This improvement led to a 3.5X speed-up over the GMM based approach.
Integrative analysis: A simple, rank based method has been introduced to mitigate batch-effect during clustering. The algorithm takes a merged expression matrix as input. As features, it selects, the union of cluster-specific differentially up-regulated genes obtained from batch-wise dropClust analyses. As part of an additional gene filtering step, some more genes are dropped to ensure that the remaining genes do not display similar expression levels in a large fraction of the cells under study. Cell-wise

© The Author(s) (2019). Published by Oxford University Press. All rights reserved. For Permissions, please email: journals.permissions@oup.com

expression ranks are then used for the final clustering (Supplementary Information).

Disambiguation of post-hoc cluster assignment: When presented with large scale scRNA-seq data, dropClust clusters only a subset of the cells. Each remaining cell is assigned to one of its closest clusters based on the most frequently observed cluster identities, among its nearest neighbours. Clustering outcomes improved significantly upon the introduction of an acceptance threshold to discard ambiguous cluster assignments. This is illustrated in the Supplementary material.

Resolving software dependencies: Existing dropClust uses python module `LSHForest` and C module `Louvain` for nearest neighbour search and community detection respectively. We replaced `LSHForest` with `RcppAnnoy`, which implements a significantly faster version of LSH (Andoni *et al.*, 2017). C implementation of Louvain was replaced by its R equivalent, as part of the popular `igraph` R package. DropClust pipeline performs dispersion based gene selection at an early stage. This step uses R function `var` through `apply`, which creates multiple copies of the expression matrix, thereby incurring significant memory footprint. We implemented a custom function called `ColDispersion` in Rcpp that operates on a single copy of the matrix, which reduces both memory usage and execution time.

Addressing software adaptability: To increase modularity and cross package interaction, the latest implementation of dropClust adopts the widely used `SingleCellExperiment` container class (Lun *et al.*, 2018). The container class allows the user to store raw and the normalised single-cell expression profiles along with multiple layers of information (annotations) regarding individual cells and genes, accessible via the `rowData`/`colData` modules. The use of SingleCellExperiment enables seamless interaction with other best practice software utilities.

Key steps involved in dropClust analysis

Pre-processing: The modules `FilterCells()` and `FilterGenes()` return filtered raw counts that can be accessed using `count()`. Total count normalization is performed using `CountNormalize()`. The normalized count matrix can be accessed using `normcounts()` of the `SingleCellExperiment` class.

Selecting highly variable genes: The normalized expression count values are used to rank the genes by their dispersion scores. The dispersion score associated with each gene can be accessed using `rowData(.)$dispersion_norm`. The top `ngenes_keep` genes are flagged as TRUE in the `rowData(.)$HVG` vector.

Sampling: To expedite clustering dropClust allows the user to perform cell sub-sampling using `Sampling()`. The user can choose SPS or random sampling by setting the value of `use.method` as "sps" or "random" respectively. The sampled single cells are marked `TRUE` in the `colData(.)$Sampling` vector.

Clustering The previous dropClust version had hierarchical clustering as the only option for single cell clustering. In the current implementation, `Cluster()` allows the users to choose from three alternative approaches: topological clustering using Louvian (Blondel *et al.*, 2008), agglomerative hierarchical clustering and k-means. For this, user argument `method` can be assigned an appropriate value from "louvian", "hclust", and "kmeans". `Cluster()` also allows the passing of method-specific arguments. Cluster identities are accessible via `colData(.)$ClusterIDs`. In case of prior cell sub-sampling, the same can be retrieved using `colData(.)$Sample_ClusterIDs`.

Marker Identification: `FindMarkers()` returns cluster specific deferentially up-regulated genes using one-vs-rest strategy. Output of the differential expression (DE) analysis is stored in a list consisting of `DE_up`, a vector of unique DE gene names and `DE_res`, a list of data frames for respective cluster specific DE genes, supplemented with corrected and raw *P*-values along with the log fold change (LFC) information.

Batch effect removal The batch effect removal is carried out in two steps. In the first step, individual expression matrices are merged using the `Merge` module. The union of DE genes retrieved independently on each data are used as feature genes subsequently, for integrative clustering and low dimensional embedding of single cells. `Correction()` function of the dropClust package can be used for this step. `Correction()` facilitates integrative analysis using our newly proposed rank-based integrative analysis strategy, as discussed above. As an alternative method, the user can also use `mnnCorrect` (Haghverdi *et al.*, 2018). `Correction()` can be instructed the same by setting `method` as `fastmnn`. Post-integration low dimensional embeddings and rank-transformed expression matrix are stored in the `"CComponents"` and `"RankMat"` elements respectively in the `reducedDim` list.

Comparative results

We used a large scRNA-seq dataset containing about 68,000 peripheral blood mononuclear cell (PBMC) transcriptomes (Zheng *et al.*, 2017) to benchmark various methods. Unsupervised clusters obtained using Seurat (Stuart *et al.*, 2019), Scanpy (Wolf *et al.*, 2018), and dropClust offered ARI of 0.33, 0.34 and 0.40, respectively. The current dropClust attained a 4.5X speedup as compared to the original implementation of the software, whereas 1.3X and 26X speedup over Scanpy and Seurat respectively. The latest implementation of the software consumed 8.3 times less memory compared to the original version (Supplementary Table 1, Figure S7). We also compared dropClust integrative analysis pipeline with three recently published batch-correction methods on two gold-standard datasets. Visual inspection clearly reveals the superior performance of dropClust (Supplementary Figures S3 and S4).

Funding

This work is supported by INSPIRE Faculty grant (DST/INSPIRE/04/2015/003068) awarded to Debarka Sengupta, J. C. Bose Fellowship (SB/S1/JCB-033/2016) awarded to Sanghamitra Bandyopadhyay by the Dept. of Sci. and Tech., Govt. of India and the SyMeC Project grant (BT/Med-II/NIBMG/SyMeC/2014/Vol. II), Dept. of BioTech., Govt. of India.

References

Andoni, A. *et al.* (2017). Lsh forest: Practical algorithms made theoretical. In *Proceedings of the Twenty-Eighth Annual ACM-SIAM Symposium on Discrete Algorithms*, pages 67–78. SIAM.

Blondel, V. D. *et al.* (2008). Fast unfolding of communities in large networks. *Journal of Statistical Mechanics: Theory and Experiment*, **2008**(10), P10008.

Haghverdi, L. *et al.* (2018). Batch effects in single-cell rna-sequencing data are corrected by matching mutual nearest neighbors. *Nature Biotechnology*, **36**(5), 421.

Jindal, A. *et al.* (2018). Discovery of rare cells from voluminous single cell expression data. *Nature Communications*, **9**(1), 4719.

Lun, A. *et al.* (2018). Singlecellexperiment: S4 classes for single cell data. *R package version*, **1**(0).

Sinha, D. *et al.* (2018). dropclust: efficient clustering of ultra-large scrna-seq data. *Nucleic Acids Research*, **46**(6), e36.

Stuart, T. *et al.* (2019). Comprehensive integration of single-cell data. *Cell*.

Tanay, A. and Regev, A. (2017). Scaling single-cell genomics from phenomenology to mechanism. *Nature*, **541**(7637), 331.

Wolf, F. A. *et al.* (2018). Scanpy: large-scale single-cell gene expression data analysis. *Genome Biology*, **19**(1), 15.

Zheng, G. X. *et al.* (2017). Massively parallel digital transcriptional profiling of single cells. *Nature Communications*, **8**, 14049.

Downloaded from https://academic.oup.com/bioinformatics/advance-article-abstract/doi/10.1093/bioinformatics/btz823/5613889 by Delhi Technological University user on 11 November 2019

Energy Systems
https://doi.org/10.1007/s12667-019-00365-9

ORIGINAL PAPER

Indian smart city ranking model using taxicab distance-based approach

Kapil Sharma[1] · **Sandeep Tayal**[1,2]

Received: 26 June 2019 / Accepted: 28 October 2019
© Springer-Verlag GmbH Germany, part of Springer Nature 2019

Abstract

The smart urbanization is getting popular in international urban planning for the last decade. The smart city word is to combine information and communication technology to define smart living. A smart city has an infrastructure to provide life quality, a safe and clean environment to its citizens by smart technology. These days people want to live a smart life. So, the urban planner/researcher is evolving "smart city models" based on the following six dimensions, economy, environment, people, governance, mobility, and living. This model was developed based on "American" and "European" cities. In the Indian smart city development scheme taken by India in 2014 to urbanized 100 smart cities. So, the requirement to developed "Indian smart city model" arises. This paper used the "Indian smart city model" define with eight dimensions matching to cities of India. The model takes a smart data-driven decision based on 80 indicators of the city. The "Indian smart cities" are ranking according to the calculated distance of optimal indicators values. The Taxicab Distance-Based Approach (TDBA) is purposed to ranking the "Indian smart city." The TDBA find the optimal solution on the bases of "Indian smart city" indicators multiple values. The approach calculates the optimal distance solution to find the best result. The result shows the ranking of "Indian smart cities" on the bases of a defined model using TDBA. The ranking gives a status of growth by comparing the cities' rank. The cities can change and update their planning according to cities rank. The data gathering from different departments and surveys of the cities. This information used for evaluation of city rank using the TDBA approach. TDBA is a mathematical tool that has been used to aggregate and convert data into a standard form that is used to rank "Indian smart cities". The result clarifies cities vision and makes a blueprint of the cities it wants to be in the future.

Keywords Distance-based approach · Smart city · Ranking model

✉ Kapil Sharma
kapil@ieee.org

[1] Delhi Technological University, Delhi, India

[2] Maharaja Agrasen Institute of Technology, Delhi, India

Published online: 22 November 2019

1 Introduction

The Indian cities are moving towards smart urban planning for the last decades. The Indian urban population is improved from 62.4 to 377.1 million in 60 years from 1951 to 2011 [1]. This information shows that 30% of the urban population increased in India. The 97 million population increased in the urban area. The global population increased by 4.3 times [2] in the last 60 years, from seven hundred fifty million to four billion approx [3]. World development is the growth of every county of the world. Some countries are developing at a very higher rate, and some are not developing because all the countries are not developing at the same rate [4]. Smart city means altered equipment to altered people. Smart cities have the most vital part in modifying diverse areas of mortal life, moving sectors like transportation, energy, health, and education [5]. Efficiently to create statistics to enrich different smart city services systems are stored, processed, and extracted in smart cities for an aggressive rise in data by numerous orders of magnitude is the security of a smart city [6]. To get a correct comprehension from a huge amount of data composed through different sources. To improve the customer experience and services [7] The Indian growth of urbanization is rapid in respect of the world. India has more area to develop as only 31% of the population is in urban area [4]. In the coming decades, India will develop a more urban area. The nonstop forecast of Indian growth is six hundred million in the year 2031 [6]. For the development in India, the concept of smart cities was initiated by India in 2014 to developed 100 smart cities [6]. To achieve the goal of "Indian smart cities" [8] subsequent mission has started by the "MINISTRY OF URBAN DEVELOPMENT" Programs since 2014, (AMRUT)," [7] "(SBM)," [7] "(SPUHS)" [9], "(HRIDAY)" [10]." (ICT) Play a leading role in these respects. This target to progress urban life concerning the "economy," "government," "living," "people," "environment," and "mobility." Ruddolf Giffinger [11] specified a ranking model for calculating European Smart cities ranking based on the European medium-sized cities using six dimensions. [15] Boyd Cohen Dr. Cohen [11] provided a model based on North America, the Asia Pacific, and Latin America cities using six dimensions. IESE CITIES IN MOTION INDEX(ICMI) [12] evaluate cities based on nine dimensions. The models have dimension and indicators according to their continent's information urban planning. [13] So, the model for "Indian smart city" proposed with eight dimension and eighty indicators according to information of Indian sub-continent. India has different indicators from the rest of the countries. The building of the Indian dimension is different from the rest of the cities. So, the paper defines an "Indian smart city model" with dimension according to Indian sub-continental for ranking the twenty "Indian smart cities" using a taxicab distance-based approach. The paper organized a follow. Section 2 shows the existing literature for a different type of smart cities model including their dimensions and indicators. In Sect. 3, the "Indian smart city model" explained, including all dimensions. The TDBA approach explained in Sect. 4. The evaluation of "Indian smart cities" rank using TDBA is defined in Sect. 5. Finally, Sect. 6 explain the conclusion.

2 Literature review

The growth of the smart city from the last decades rapidly increasing. The researcher has proposed smart city models, which have different dimensions and indicators for defining the smart city. The Boyd Cohen Dr. Cohen [11] defines the cities using the six factors and 62 indicators. The model based on Europe, North America, Latin America. [14] This model is not including the progress tracking and security aspect of the smart cities. Edvinsson [15] defines the city based on the City as a knowledge tool model in the six dimensions and 11 indicators [16]. Shapiro [17] define the city based on Neoclassical city growth model with three dimensions and nine indicators. [18] This considers only Employment growth sources, productivity, quality of life. Innovation Cities Index [19] is finding the index of a global city by 2thinknow. The model index on the bases of three dimensions and 162 indicators. ISO 37120 and Global City Indicators Facility [20] gives a standard definition for the smart cities. This model has the individual scale for calculation, so the optimal comparison within indicators has not done [21]. ITU FG-SSC [22] used the six dimension and 88 indicators. In the model, the scale 0–100 score assign to rank the city. IUME Integrated Urban Monitoring in Europe [23] defines a city using four dimensions, 56 indicators. The calculation based on the average value of all dimensions. Networked Society City Index [24] define the city based on two perspectives, six dimensions, 15 variables, 35 indicators represented by 41 proxies. The model used a Hierarchic structure by using a geometric mean considering. [25] In this model, the value is assigned from 1 to 100 to calculate the rank of city. Siemens Green City Index [26] used 30 indicators in eight subthemes. In this 0–10 per indicator, 0–100 overall value assign for average calculation. The all the model assigns a numeric value for calculation. The model does not work on actual value of indicators. Shakti Sustainable Energy Foundation with ISB [1] with six dimension and 58 indicators as an act in the European ranking model. [27].

All these models used the traditional techniques for calculation like average and giving score. The models are given the ranking of cities not based on the actual quotative value of the indicators.

The literature analysis gives detail of models proposed by researchers that all the defined model ranks the cities based on different indicators of related cities. The all the smart city model is based on their area related indicators. The calculation method of ranking is different in several models. The model is not considered the normalization of indicators to avoid the influence of measurement units. The collection of information is difficult for all indicators of cities. The TDBA solve all these issues to calculate optimal solution ranking.

3 Indian smart city model

The smart city model defines eight dimensions and 80 indicators. Here the model is used for calculating Indian smart city rank. [28] In the last decade's 100 of the definition has been proposed in the literature some standard is ISO/TC and TMB smart city definitions defined in ISO/IEC JTC 1 report given in 2014 [27] and 2018 [28]. ITU-T Group provides smart city definition in FG-SSC report 2014 and 2015 [29]. All the stated definitions are around in six dimensions. [29] The all the definition is focused based on European and American cities. So, this Indian smart city model is used to rank Indian smart cities. The "Indian smart city model" is based on information based on Indian sub-continent [30].

Consequently, it is said to be an extremely complex zone. All the more regularly, the urban communities, likewise named as the appealing spots for individuals looking for business and are engines of financial advancement. The necessities utilized as a part of the smart cities are E-governance and computerization, finance, environmental, progress tracking, and security—Fig. 1 shown the system model for the smart city. As examined in over, a smart subsystem of city framework is a smart city. The change of a framework characterized as the change of a city framework into a smart city framework [31]. It requires to change as a framework. This work is planned with a change approach to upgrade the learning of city frameworks change. A city regularly considered as one entire element and a framework in the outlined model. Here, one model is displayed, in which the smart city work considered as the smart structure. How the smart subsystems of a city structure get the information from various sources, at that point procedure it, and furthermore share the data on a coordinated stage is appeared in the city subsystems.

The model is used demographic profile to focus on the population and type of population, which is measure criteria in the context of Indian cities. The model defines the economic profile to find the status of employability of the cities. The infrastructure is an important role in the development of building growth. The e-Governance and Computerization provide smart services valuable in the cities to

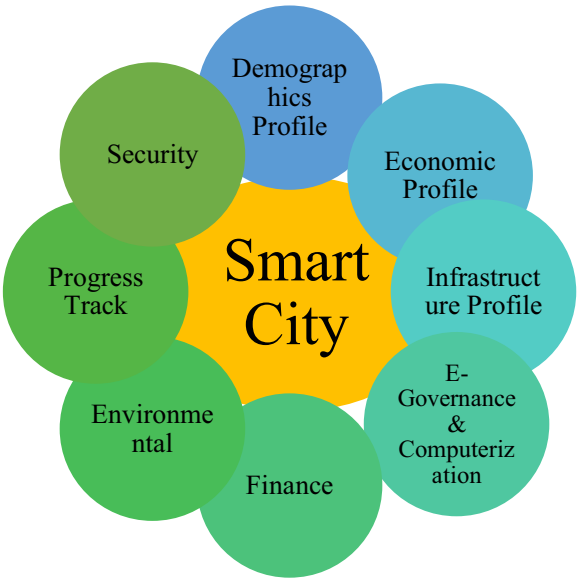


Fig. 1 Indian smart city model [8]

make a smart living. Finance is the financial sources having in the cities for better growth.

The clean and safe environment is essential for smart living; this model also considered the cleanness of environments. The work progress is also including in the model to track the working of smart cities. The last dimension is security to make important in techno word. This model covers all the aspect of smart living, so this model used for ranking the smart Indian cities. The next section gives the technique using for evaluation for the rank using this model.

4 Taxicab distance based smart city ranking (tdba)

The TDBA operational standard is to specify the optimum objective spot identifies within the optimum model as criteria of cities and the noblest value in each criterion of the cities having in the computation action.

The cities ranking criteria indicators are quality value set which represented a vector (C_1, C_2, … C_N) in n-dimensional area optimum spot. In the approach, the optimum quality value evaluated through all the criteria indicators noblest value. So, OPTI represents to the alternate Cities taking the noblest value for each criteria indicators computed. The chance of the presence of several alternate cities is very fewer that results in respect of several alternates to advise the cities. In this case, OPTI works as a suggestion spot to compare every alternate. The optimum spot, i.e., OPTI fitness value evaluated by the likely comparison of alternate's cities. Therefore, here need to find an answer nearby to OPTI to resolve this decision-based problem. The objective function formulated to obtain a solution as:

$$\text{Min}\delta\{Alt(y), OPTI\} \tag{1}$$

Subject to y ς Y

Here, $\{Alt(y)\}$, and δ indicate cities in an n-dimensional area, and the distance from OPTI, correspondingly. The result is conditional on the two objectives, OPTI and δ. The result demonstration in the 2D area provided in Fig. 2. Here possible region is R, and OPTI is the optimum spot.

The TDBA finds the spot in the possible region 'R' nearby to the OPTI, and this appears in Fig. 3. In the figure, axis E1 and E2 have a parallel line $(Alt - OPTI)_{E1}$ and $(Alt - OPTI)_{E2}$ respectively. So, $(Alt - OPTI)_{E1} = |OPTI_{E1} - Alt_{E1}|$, and $(Alt - OPTI)_{E2} = |OPTI_{E2} - Alt_{E2}|$. In 2-D, δ is given by

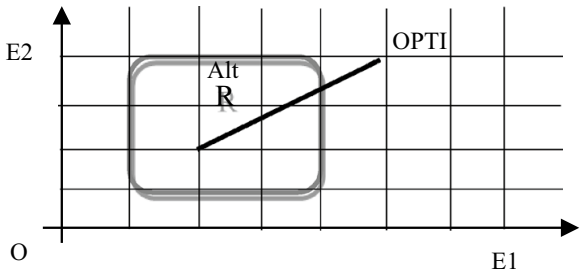


Fig. 2 Distance approach

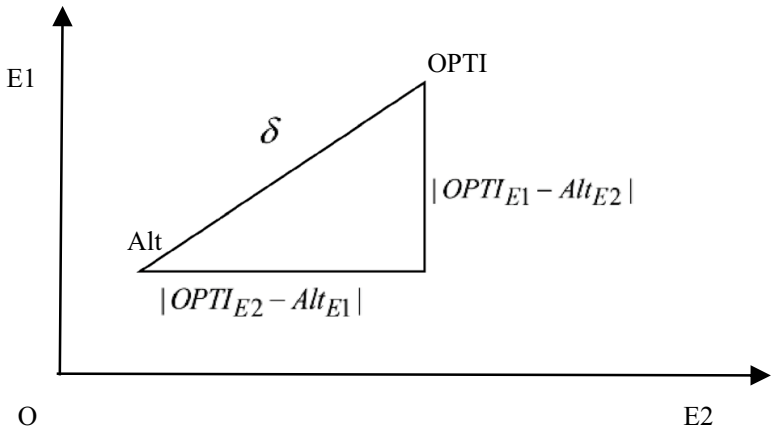


Fig. 3 Taxicab distance

$$\delta = |OPTI_{E1} - Alt_{E1}| + |OPTI_{E2} - Alt_{E2}| \tag{2}$$

In specific terms, the "distance δ" taxicab distance use to frame as

$$\delta = \sum |OPTI_{xy} - Alt_{xy}| \tag{3}$$

Here $x = 1$ to n = alternate cities and $y = 1$ to m ranking criteria.

To implement TDBA requirement to signify 'n' Cities and 'm' criteria for ranking associated with every City, e.g.$Alt_1(C_{11}, C_{12}, \ldots, C_{1m})$, $Alt_2(C_{21}, C_{22}, \ldots, C_{2m})$, $Alt_n(C_{n1}, C_{n2}, \ldots, C_{nm})$, and the cities $(C_{b1}, C_{b2}, \ldots, C_{bm})$ where C_{bm} = the ranking criteria quality value 'm.'

So, the whole set of cities can be appeared by the values of every given ranking criteria indicators in this matrix:

$$[C] = \begin{bmatrix} C_{11} & C_{12} & \ldots & C_{1m} \\ C_{21} & C_{22} & \ldots & C_{2m} \\ \vdots & \vdots & \vdots & \vdots \\ C_{n1} & C_{n2} & \ldots & C_{nm} \\ C_{b1} & C_{b2} & \ldots & C_{bm} \end{bmatrix}. \tag{4}$$

Now eliminated the quantity units influence by standard matrix using the formula:

$$Z_{xy} = \frac{C_{xy} - \overline{C_y}}{S_y} \tag{5}$$

$$\text{Here, } \overline{C}_y = \frac{1}{n} \sum_{x=1}^{n} C_{xy}, \text{ and} \tag{6}$$

$$S_y = \left[\frac{1}{n} \sum_{x=1}^{n} (C_{xy} - \overline{C}_y)^2 \right]^{1/2} \tag{7}$$

Here x = 1 to n, and y = 1 to m.

For every ranking criteria, indicators of all alternate cities evaluate $\overline{C}_y$ donates the average value and S_y donates the standard deviation. The matrix for standardized framed as:

$$[Z_s] = \begin{bmatrix} Z_{11} & Z_{12} & \cdots & Z_{1m} \\ Z_{21} & Z_{22} & \cdots & Z_{2m} \\ \vdots & \vdots & \vdots & \vdots \\ Z_{n1} & Z_{n2} & \cdots & Z_{nm} \\ Z_{OPTI1} & Z_{OPTI2} & \cdots & Z_{OPTIm} \end{bmatrix} \tag{8}$$

Here $Z_{11} = \frac{C_{11}-\overline{C}_1}{S_1}$, $Z_{12} = \frac{C_{12}-\overline{C}_2}{S_2}$, $Z_{1m} = \frac{C_{1m}-\overline{C}_m}{S_m}$.

After this evaluation, the distance matrix [z_d] by deducting the value of the optimum set by the following value in the alt set. The OPTI is the difference between cities and alternate.

$$[Z_d] = \begin{bmatrix} Z_{\mathrm{OPTI1}} - Z_{11} & Z_{OPTI2} - Z_{12} & \cdots & Z_{OPTIm} - Z_{1m} \\ Z_{\mathrm{OPTI1}} - Z_{21} & Z_{OPTI2} - Z_{22} & \cdots & Z_{OPTIm} - Z_{2m} \\ \cdots & \cdots & \cdots & \cdots \\ Z_{\mathrm{OPTI1}} - Z_{n1} & Z_{OPTI2} - Z_{n2} & \cdots & Z_{OPTIm} - Z_{nm} \end{bmatrix} \tag{9}$$

Now at finishing the distance, TCD evaluated in every alternate city to the OPTI using:

$$TCD_{OPTI-Alt} = \sum_{y=1}^{m} |Z_{OPTIy} - Z_{xy}| \tag{10}$$

This taxicab distance is measured conclusion to evaluate many distances on every rank criteria indicators of cities are valued and lastly given a ranking. TDBA flow chart is shown in Fig. 4.

5 "Indian smart cities" ranking evaluation

The data set Tables 1, 2, 3 and 4 has depicted from the published report by the government of India. ("http://smartcities.gov.in/content/innerpage/cities-profile-of-20-smart-cities.php"). The eight criteria have 80 indicators/sub-criteria. All eight criteria are having the same wattage of their 80 indicators. Among the 80 indicators, 59 indicators having high value as optimal/noblest and 21 indicators having low value as optimal/noblest. So, the 59 indicators values calculated in case 1 and 21 values calculated in case 2.

The data set of 20 cities name mentioned in Table 5 has ranked based on 80 indicators of eight criteria. The Ligated values in the data set have converted into 0 and 1 for criteria E-Governance and Computerization. The symbolic orientations of cities as is given in Table 6 and the criteria and sub-criteria represented, as shown in Tables 5 and 7. The information about indicators, as explained in

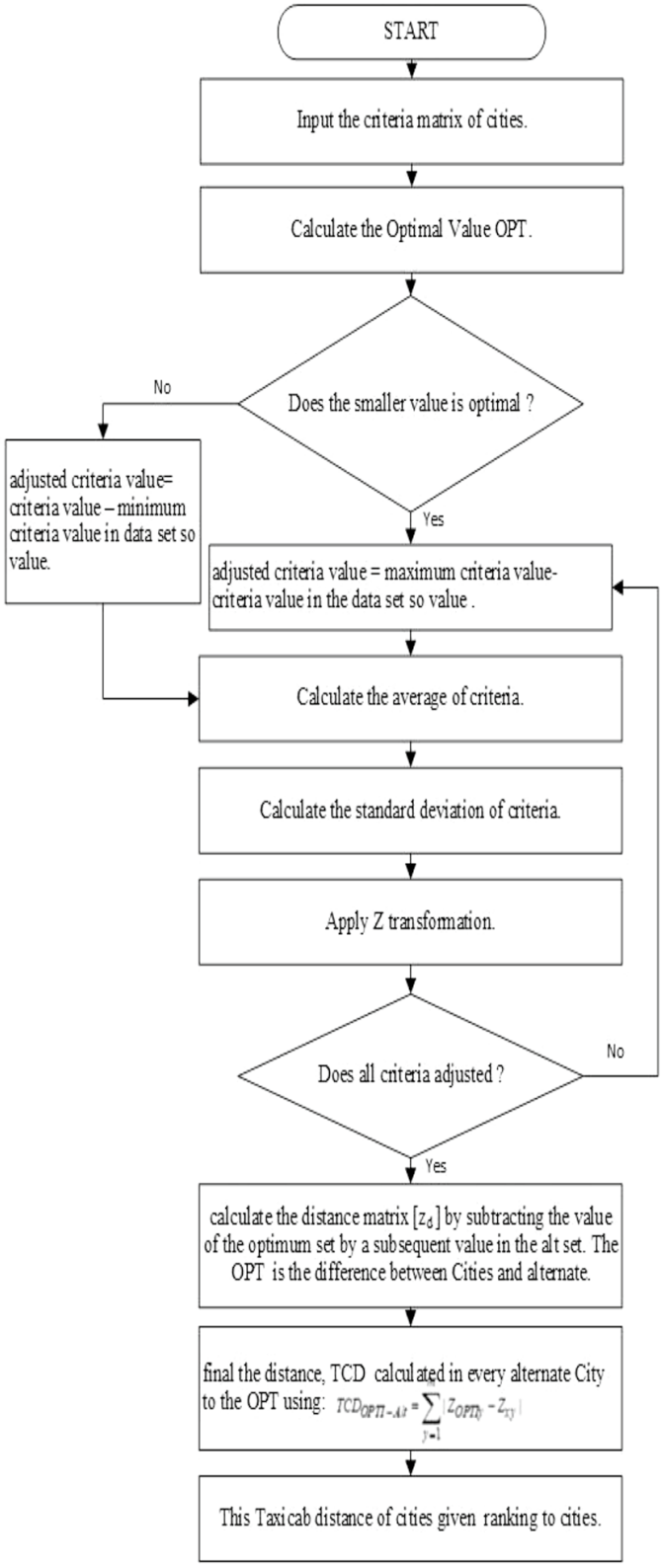


Fig. 4 Taxicab distance based approach (TDBA)

Table 7 As data set the input matrix having 20 rows shows the candidates cite for ranking and 80 columns of indicators are using for evaluating the ranking of 20 cities. The input matrix is now calculating the optimal value for each criteria's indicators the 59 indicators having high value as optimal/noblest and 21 indicators having low value as optimal/noblest. So, the following cases are:

Table 1 Data set part 1

City	A1	A2	A3	A4	A5	A6	A7	A8	A9	A10	A11	A12	A13	B1	B2	B3	B4	B5
C1	312,538	443,028	24	1	57	1	5449	81	9	1	20	36	68	37,712	5	5	37	45
C2	1,728,128	1,728,128	85	6	514	5	3365	82	8	1	19	45	68	50,580	6	4	37	26
C3	957,352	962,334	92	2	219	23	4370	91	6	5	19	3	71	43,278	9	4	32	47
C4	257,803	16,349,831	0	2	43	0	6032	90	19	0	22	8	74	112,510	1	2	37	19
C5	5,577,940	6,357,693	92	5	469	6	11,895	88	11	1	19	4	67	0	7	1	37	51
C6	4,467,797	4,591,246	92	6	336	7	13,304	88	2	3	22	10	68	0	6	0	42	37
C7	488,157	610,350	40	2	100	1	4901	90	8	3	18	11	66	28,856	32	7	35	48
C8	434,971	0	69	2	77	1	5640	85	12	6	21	14	67	30,219	24	4	32	47
C9	602,046	2,119,724	27	0	107	0	5620	97	3	0	15	1	66	63599	4	4	42	32
C10	1,798,218	1,886,100	94	2	286	10	6290	83	13	3	21	27	65	47,214	10	2	36	33
C11	1,964,086	2,170,295	81	3	172	4	11,393	86	15	3	20	30	65	52,501	3	2	29	56
C12	1,055,525	1,268,848	73	1	153	3	6920	87	14	4	20	46	67	38,968	17	0	33	40
C13	951,558	0	68	1	179	1	5329	83	15	2	21	18	64	45,859	19	2	41	45
C14	3,124,458	5,057,709	54	2	276	2	11,304	90	13	1	19	22	67	88,341	3	3	35	28
C15	840,834	885,363	78	3	135	5	6228	92	8	5	20	20	70	33,312	5	4	36	40
C16	1,618,879	0	78	1	159	4	10,158	86	14	0	20	15	67	51,633	10	0	38	34
C17	3,046,163	0	88	3	485	4	6285	83	13	4	21	11	65	3,046,163	6	4	35	42
C18	451,100	474,531	74	1	57	0	7925	90	10	5	19	14	67	24,135	16	0	39	46
C19	4,646,732	8,653,521	100	1	175	100	26,553	90	17	0	17	29	69	57,706	2	2	41	26
C20	1,050,721	2,136,916	40	1	106	2	9950	91	10	0	16	12	68	65,781	4	3	41	33
Optimal	257,803	16,349,831	100	0	514	100	3365	97	2	0	22	1	74	3,046,163	32	0	42	56

Table 2 Data set part 2

City	B6	B7	B8	B9	B10	B11	B12	B13	B14	B15	B16	B17	B18	B19	B20	B21	C1	C2	C3	C4	C5	C6	C7
C1	44	11	10	28	62	18	10	6	6	10	5	18	10	17	0	4	83	97	83	84	6	9	57
C2	55	19	2	33	65	11	7	10	4	17	2	24	11	15	0	11	71	97	84	92	9	11	67
C3	48	4	16	19	65	1	15	5	4	19	6	28	3	15	4	0	33	93	85	77	12	22	79
C4	77	3	0	41	59	16	0	6	12	9	0	17	25	15	0	1	98	99	85	97	28	16	63
C5	46	4	2	48	50	16	5	6	6	17	1	22	19	7	0	7	80	99	92	93	10	11	63
C6	57	6	0	66	34	28	2	6	1	6	0	14	34	8	0	1	81	99	94	96	5	8	71
C7	34	18	26	24	50	19	5	9	10	7	20	13	4	13	0	1	90	98	91	89	9	13	62
C8	40	12	15	22	63	28	8	3	4	15	14	13	4	11	0	0	82	97	82	95	5	13	65
C9	45	23	5	31	64	16	12	9	9	14	3	14	7	15	0	14	96	99	95	87	21	15	54
C10	53	14	5	25	70	30	10	9	15	7	0	9	3	17	0	1	79	97	82	92	10	13	61
C11	40	4	1	26	73	39	9	3	9	9	1	15	11	4	0	7	74	98	90	92	11	13	63
C12	49	11	1	25	74	17	3	7	2	28	0	18	16	9	0	3	70	96	81	91	8	12	57
C13	28	27	21	27	51	19	5	5	2	8	14	23	11	13	0	0	97	94	59	91	5	9	61
C14	66	6	0	32	68	21	19	6	8	12	0	13	12	10	0	20	99	98	76	98	22	17	64
C15	45	15	1	28	71	15	10	12	4	25	0	29	3	2	0	3	63	87	72	69	16	15	65
C16	64	3	1	51	48	8	5	9	1	15	1	20	18	22	0	0	81	99	93	89	12	11	65
C17	47	11	6	45	49	13	12	6	3	13	7	22	9	15	0	8	89	98	89	91	12	14	66
C18	47	7	8	29	64	13	10	10	5	21	2	19	8	11	0	1	83	97	83	84	6	9	57
C19	66	9	1	27	71	19	13	10	3	11	1	16	13	14	0	12	71	97	84	92	9	11	67
C20	55	11	9	45	46	24	7	6	5	10	4	26	8	10	0	4	33	93	85	77	12	22	79
Optimal	77	3	26	19	34	39	19	12	15	28	20	29	34	22	0	20	99	99	95	98	28	8	79

Table 3 Data set part 3

City	C8	C9	C10	C11	C12	C13	C14	C15	D1	D2	D3	D4	D5	D6	D7	D8	D9	D10	D11	D12	E1
C1	53	46	31	0	65	42	27	9	0	0	0	0	1	0	0	0	0	1	0	1	54
C2	51	47	33	3	8	7	12	2	1	1	1	1	1	1	1	1	1	1	1	0	64
C3	54	41	23	1	27	11	15	14	1	0	0	0	0	0	0	0	0	0	0	1	84
C4	12	68	37	0	0	0	0	0	1	1	1	1	1	1	1	1	1	1	0	1	89
C5	77	21	36	0	24	0	9	0	1	1	1	1	1	1	1	1	1	1	0	1	71
C6	55	43	49	0	19	0	10	2	1	1	1	1	1	1	1	1	1	1	0	1	54
C7	62	35	28	0	41	33	23	13	0	1	0	1	1	0	0	0	0	1	0	1	71
C8	52	45	34	0	51	45	37	16	1	1	1	1	1	1	1	1	0	1	0	1	53
C9	75	22	6	0	0	0	0	0	1	1	1	1	1	1	1	1	0	1	0	1	83
C10	68	27	31	1	43	8	15	12	1	1	1	1	1	1	1	1	0	1	0	1	68
C11	69	28	25	1	25	14	12	5	1	1	1	1	1	1	1	1	1	1	0	1	68
C12	75	22	19	0	21	19	14	4	1	1	1	1	1	1	1	1	1	1	0	1	65
C13	70	29	45	2	29	25	20	15	1	0	1	1	1	0	0	1	0	1	0	1	63
C14	67	31	40	0	32	28	21	9	1	1	1	1	1	1	1	1	0	1	0	1	86
C15	47	43	33	1	31	15	11	9	1	1	1	1	1	0	1	1	1	1	0	1	73
C16	69	28	31	0	15	3	10	5	1	1	1	1	1	1	1	1	0	0	0	1	65
C17	78	20	25	1	59	57	49	12	1	1	1	1	1	1	1	1	1	1	0	1	73
C18	53	46	31	0	65	42	27	9	1	1	0	1	1	1	1	1	0	1	0	1	83
C19	51	47	33	3	8	7	12	2	1	1	1	1	1	1	1	1	1	1	0	1	71
C20	54	41	23	1	27	11	15	14	1	1	1	1	1	1	1	1	1	1	0	1	70
Optimal	78	20	6	3	75	59	56	16	1	1	1	1	1	1	1	1	1	1	1	1	89

Table 4 Data set part 4

City	E2	E3	E4	E5	E6	E7	E8	E9	E10	E11	F1	F2	G1	G2	G3	G4	H1	H2
C1	0	1	34	6932	7239	0	6530	6787	0	0	0	0	0	0	0	0	48	52
C2	1	1	0	0	0	131,899	0	0	129,990	0	5	71	154,677	87	69	80	42	58
C3	95	79	0	0	0	0	0	0	0	0	50	0	31,611	87	76	107	56	44
C4	85	82	300	194,461	169,119	137,720	193,570	152,336	130,056	0	16	0	0	0	0	0	60	40
C5	1	1	322	161,600	189,900	223,900	115,500	132,200	160,600	0	14	75	257,380	85	27	90	40	60
C6	1	1	356	147,951	159,532	187,027	173,618	172,113	163,676	0	6	58	200,533	86	55	90	42	58
C7	0	0	16	7467	7702	0	6401	5884	0	0	0	0	0	0	0	0	44	56
C8	0	0	0	44,083	35,087	33,120	47,633	36,308	33,841	33	0	0	3464	98	81	104	42	58
C9	90	86	57	1652	1235	1093	1435	966	809	25	55	75	48712	49	49	0	34	66
C10	1	1	23	100,033	0	0	114,247	0	0	0	21	0	119431	74	37	63	38	62
C11	1	1	40	116,187	151,709	134,054	117,762	151,714	134340	0	25	71	68,981	77	56	111	60	40
C12	1	1	13	184	272	275	163	236	320	0	63	0	48,937	82	58	70	25	75
C13	0	0	0	1626	2004	1584	1626	2004	2584	0	0	0	7199	100	82	0	44	56
C14	0	0	0	324,700	233,521	203,164	324,700	184,143	219,085	25	11	0	390,667	81	52	90	44	56
C15	1	1	20	33	37	38	33	38	37	0	24	0	57,326	62	17	47	29	71
C16	57	68	61	41,364	55,512	58,078	35,803	56,818	59,743	0	34	82	33,924	48	26	50	58	42
C17	17	0	27	39,227	36,929	42,441	0	34,224	43,193	0	29	67	57,808	64	59	104	31	69
C18	0	0	0	7246	5409	7069	6992	5090	5399	0	0	0	0	0	0	0	40	60
C19	1	1	495	94,004	102,258	136,838	82,219	99,738	85,623	0	36	0	388,302	79	40	62	43	57
C20	1	1	103	34,669	35,983	39,551	26,176	27,985	30,811	0	18	72	127,787	67	63	49	42	58
Optimal	95	86	0	324,700	233,521	223,900	0	0	0	33	63	82	390,667	100	82	111	25	75

Table 5 City symbol

S. no	Criteria	Symbol
1	Demographics profile	A
2	Economic profile	B
3	Infrastructure profile	C
4	E-governance and computerization	D
5	Finance	E
6	Environmental	F
7	Progress track	G
8	Security	H

Table 6 Criteria symbol

S. no	City	Symbol
1	Kakinada	C1
2	Vishakhapatnam	C2
3	Guwahati	C3
4	Delhi	C4
5	Ahmadabad	C5
6	Surat	C6
7	Belgaum	C7
8	Davanagere	C8
9	Kochi	C9
10	Bhopal	C10
11	Indore	C11
12	Jabalpur	C12
13	Solapur	C13
14	Pune	C14
15	Bhubaneswar	C15
16	Ludhiana	C16
17	Jaipur	C17
18	Udaipur	C18
19	Chennai (M. Corp)	C19
20	Coimbatore	C20

Case-1 The first case the lower value is noblest to real value then $\left(c = c_{max} - c_i\right)$.

Case-2 The second case the higher value is noblest to real value then $\left(c = c_i - c_{min}\right)$.

c = adjusted criteria value, c_{max} = maximum criteria value, c_{min} = minimum criteria value, c_i = criteria value in the data set so value.

Now calculate the standard matrix by using Eq. (5) the distance matrix calculated with the help of equation number 9. The Eq. (10) is used to calculate the TCD "Taxicab Composite Distance" between every alternate city to the optimum spot, OPTI.

Table 7 Indicators/sub-criteria symbol

S. no	Indicators/sub-criteria	Symbol
1	"Total population"	A1
2	"Total population of UA" (if)	A2
3	"Share of ULB population in district urban population" (%)	A3
4	"Population growth rate" (AEGR) 2001–11	A4
5	"Area" (sq. km)	A5
6	"Share of ULB area in the district" (%)	A6
7	"The density of population" (person per sq. km)	A7
8	"Literacy rate" (%)	A8
9	"Scheduled caste" (%)	A9
10	"Scheduled tribes" (%)	A10
11	"Youth, 15–24 years" (%)	A11
12	"Slum population" (%)	A12
13	"Working age group, 15–59 years (%)"	A13
14	"Per Capita Income (Rs.) at 2004–05 constant price "	B1
15	"Urban Poverty Ratio" (% of urban population)	B2
16	"Unemployment rate", 2011–12	B3
17	"Work participation rate", 2011–12	B4
18	"Work status, 2011–12 (%) self-employed"	B5
19	"Work status, 2011–12 (%) regular/wage salaried employees"	B6
20	"Work status, 2011–12 (%)" casual labor:	B7
21	"Sectoral distribution of workers, 2011–12 (%) primary"	B8
22	"Sectoral distribution of workers, 2011–12 (%) secondary"	B9
23	"Sectoral distribution of workers, 2011–12 (%) tertiary"	B10
24	"Legislators, senior officials and managers"	B11
25	"Professionals"	B12
26	"Technicians and associate professionals"	B13
27	"Clerks"	B14
28	"Service workers and shop and market sales workers"	B15
29	"Skilled agricultural and fishery workers"	B16
30	"Craft and related trades workers"	B17
31	"Plant and machine operators and assemblers"	B18
32	"Elementary occupations"	B19
33	"Workers not classified by occupation"	B20
34	"no. of sanctioned SEZ"	B21
35	"% of households with access to tap water (from treated source) within Premises"	C1
36	"% of households with access to electricity"	C2
37	"% of households having toilet facilities within premises"	C3
38	"% of household Waste water outlet connected to the drainage"	C4
39	"% of households with access to computer/laptop with internet"	C5
40	"% of households with access to computer/laptop without internet"	C6
41	"% of households with access to mobile phones"	C7
42	"Ownership pattern of housing (%) owned"	C8

Table 7 (continued)

S. no	Indicators/sub-criteria	Symbol
43	"Ownership pattern of housing (%) rented"	C9
44	"% of households living in congested houses"	C10
45	"No. of hospitals per 1,00,000 people "	C11
46	"No of schools per 1,00,000 people primary"	C12
47	"No of schools per 1,00,000 people middle"	C13
48	"No of schools per 1,00,000 people secondary"	C14
49	"No of SCHOOLS per 1,00,000 people college"	C15
50	"Property tax"	D1
51	"Accounting"	D2
52	"Water supply and other utilities"	D3
53	"Birth and death registration and health programs"	D4
54	"Citizens' grievance monitoring"	D5
55	"Personnel management system"	D6
56	"Building plan approval"	D7
57	"e-Procurement"	D8
58	"Does ULB has the facility to accept online payments"	D9
59	"Are ULB offices connected with each other through local area network (LAN)/ wide area network (WAN) "	D10
60	"Do you have access to the state data centre (SDC)? "	D11
61	"Does the ULB have their own website#"	D12
62	"% of households with access to banking facilities "	E1
63	'Property tax coverage (%)"	E2
64	"Property tax collection efficiency (%) "	E3
65	"Property tax amount (Rs.)"	E4
66	"Details of municipal income (Rs. Lakhs) 2009–10"	E5
67	"Details of municipal income (Rs. Lakhs) 2010–11"	E6
68	"Details of municipal income (Rs. Lakhs) 2011–12"	E7
69	"Details of municipal expenditure (Rs. Lakhs) 2009–10"	E8
70	"Details of municipal expenditure (Rs. Lakhs) 2010–11"	E9
71	"Details of municipal expenditure (Rs. Lakhs) 2011–12"	E10
72	"% of municipal Budget reserved for urban poor"	E11
73	"Swachh Sarvekshan was conducted between 5 January 2016"	F1
74	"Comprehensive environmental assessment for available cities"	F2
75	"Total approved cost of projects (Rs. Lakhs)"	G1
76	"Share of central assistance released (%)"	G2
77	"% of work completed (physical progress)"	G3
78	"Funds utilised (%)"	G4
79	Crime index	H1
80	Safety index	H2

Table 8 Result showing TCD and rank

City	TCD	Rank
Kakinada	199.8288	20
Vishakhapatnam	153.3956	7
Guwahati	176.2668	17
Delhi	149.8682	6
Ahmadabad	144.4897	4
Surat	145.5258	5
Belgaum	183.074	19
Davanagere	158.2838	9
Kochi	166.1073	13
Bhopal	162.7193	10
Indore	154.2875	8
Jabalpur	169.6948	15
Solapur	178.7641	18
Pune	131.4859	1
Bhubaneswar	172.8226	16
Ludhiana	168.1034	14
Jaipur	142.7679	3
Udaipur	165.5154	12
Chennai	131.6461	2
Coimbatore	163.8349	11

This TCD gives the optimal result for ranking the cities. The result show TCD and rank in Table 8. The result calculated based on 80 indicators of the criteria. The influence of all optimal criteria in the rank. The rank 1 allotted to the smallest TCD value and next to allotted rank 2 and so on.

The result indications that the Pune has attained the rank number one after evaluation 80 indicators of criteria and next order is Jaipur, Ahmadabad, Surat, Delhi, Vishakhapatnam, Indore, Davanagere, Bhopal, Coimbatore, Udaipur, Kochi, Ludhiana, Jabalpur, Bhubaneswar, Guwahati, Solapur, Belgaum, Kakinada correspondingly.

6 Conclusion

The paper has designed the Indian smart cites model on the bases of evaluation of eight dimensions/criteria as defined in Fig. 1. The eight criteria have 80 indicators for the Indian smart cities model. All eight dimensions optimal indicators values show any energy-efficient systems in smart cities that also include energy-saving building concession free roads and renewable energy harvesting. The paper has used the Taxicab Distance-Based Approach (TDBA) which evaluate all the 80 indicators of eight dimensions to calculate the ranking of Indian smart cities. TDBA is a mathematical tool that has been used to aggregate and convert data into a model form that is used to ranking "Indian smart cities." The experiment result represents that the

Pune has attained the ranking number one after assessment criteria and next order is Jaipur, Ahmadabad, Surat, Delhi, Vishakhapatnam, Indore, Davanagere, Bhopal, Coimbatore, Udaipur, Kochi, Ludhiana, Jabalpur, Bhubaneswar, Guwahati, Solapur, Belgaum, Kakinada correspondingly. This evaluation is the smart data-driven decision making for the Indian smart cities. The data gathering from different departments and surveys of the cities. The cities can change update their planning according to cities rank. The future planning of the Indian cities can be decided based on the rank evaluated. The result clarifies cities vision and makes a blueprint of the cities it wants to be in the future.

References

1. Smart cities index: a tool for evaluating. Cities—shakti sustainable energy foundation. [Online]. Available: https://shaktifoundation.in/report/smart-cities-index-a-tool-for-evaluating-cities/. Accessed 12 June 2019
2. Clean and sustainable energy policy—Shakti sustainable energy foundation". https://shaktifoundation.in/. Accessed 18 Jun 2019
3. Vuelvas, J., Ruiz, F.: A novel incentive-based demand response model for Cournot competition in electricity markets. Energy Syst. **10**(1), 95–112 (2019)
4. Aketi, P., Sen, S.: Modeling demand response and economic impact of advanced and smart metering. Energy Syst. **5**(3), 583–606 (2014)
5. Agrawal, S.K., Sharma, K.: 5th generation millimeter wave wireless communication propagation losses dataset for Indian metro cities based on corresponding weather conditions. Data Br. **23**, 103564 (2019)
6. Padode, P., Padode, F., Mali, D., Gawde, S., Yadav, S., Smart Cities India Readiness Guide: The planning manual for building tomorrow's cities today. Smart Cities Council **7**, 1–404 (2016)
7. Goyal S.P.: Press Information Bureau Government of India Ministry of Power. Gov. India, Minist. Road Transp. Highw, pp. 1–3 (2015)
8. Sharma, K., Tayal, S.: Indian smart city ranking model. Int. J. Recent Technol. Eng. **8**(2), 4820–4832 (2019). **(ISSN2277-3878)**
9. Bhattacharya S., Rathi S.: Reconceptualising smart cities: a reference framework for India. Cent. Study Sci. Technol. Policy, vol. September (2015)
10. M.U.D.G. India, Ministry of Urban Development Government of India Smart Cities Mission Statement & Guidelines. Government of India Ministry of Urban Development (2015)
11. Benamrou B., Mohamed B., Bernoussi A., Mustapha O.: Ranking models of smart cities. In: 2016 4th IEEE International Colloquium on Information Science and Technology (CiSt), pp. 872–879. Tangier (2016). https://doi.org/10.1109/CIST.2016.7805011
12. J.E.R. Pascual Berrone; (Schneider Electric Sustainability and Strategy Chair) and Carl; (Carl Schroeder Chair of Strategic Management), "IESE Cities in Motion Index 2017," Univ. Navarra, no. IESE Business School-IESE Cities in Motion Index (ST-442-E), 2017
13. Tayal, S., Sharma, K.: The recommender systems model for smart cities. Int. J. Recent Technol. Eng. **8**(2S7), 451–456 (2019)
14. Yin, X., Zhang, J., Wang, X.: Sequential injection analysis system for the determination of arsenic by hydride generation atomic absorption spectrometry. Fenxi Huaxue **32**(10), 1365–1367 (2004)
15. Mahizhnan, A.: Smart cities. Cities **16**(1), 13–18 (1999)
16. Tayal, S., Goel, S.K., Sharma, K.: A comparative study of various text mining techniques. In: 2015 international conference on computing for sustainable global development, INDIACom 2015, vol. 11, no. 5, pp. 76–81 (2015)
17. Garg, R., Sharma, R.K., Sharma, K.: Ranking and selection of commercial off-the-shelf using fuzzy distance-based approach. Decis. Sci. Lett. **5**(2), 201–210 (2016)
18. John Batten (Global Cities Director), Citizen Centric Cities The Sustainable Cities Index (2018)

19. Innovation Cities™ index 2018—global city ranking by 2thinknow". https://www.innovation-cities.com/innovation-cities-index-2018-global/13935/. Accessed: 19 Jun 2019
20. How ISO standardized city indicators could change the way we design | DeepRoot Blog. http://www.deeproot.com/blog/blog-entries/how-iso-standardized-city-indicators-could-change-the-way-we-design. Accessed 02 Apr 2019
21. Caragliu, A., Del Bo, C., Nijkamp, P.: Smart cities in Europe. J. Urban Technol. **18**(2), 65–82 (2011)
22. Sang, Z.: Vice-chairman of ITU-T Focus Group on Smart Sustainable Cities Fiberhome Technologies Group China, standard\ITUT\ITU-T S,Sept 2014\Bangkok training\Ziqinsmart city KPIs and monitoring V2, China (2014)
23. Minx, J., Creutzig, F., Medinger, V. et al.: Climatecon working paper series developing a pragmatic approach to assess urban metabolism in Europe, vol. 240, Department of Climate Change Economics Technische Universität Berlin (2011). https://www.climatecon.tu. Accessed 2 Apr 2019
24. Network Society City Index 2014 Appendix 1-Methodology. Ericsson Stockholm, Sweden (2014). https://www.ericsson.com/assets/local/trends-and-insights/consumer-insights/reports/city-index/networked-society-city-index-2014-appendix1-methodology.pdf. Accessed 2 Apr 2019
25. Dominguez, O.D.M., Kasmaei, M.P., Lavorato, M., Mantovani, J.R.S.: Optimal siting and sizing of renewable energy sources, storage devices, and reactive support devices to obtain a sustainable electrical distribution systems. Energy Syst. **9**(3), 529–550 (2018)
26. Castro, T., Quartin, M.: A summary of the Green City Index research series. Mon. Not. R. Astron. Soc. Lett. **443**(1), 25 (2014)
27. Kambatla, K., Kollias, G., Kumar, V., Grama, A.: Trends in big data analytics. J. Parallel Distrib. Comput. **74**(7), 2561–2573 (2014)
28. Marek, L., Campbell, M., Bui, L.: Shaking for innovation: the (re)building of a (smart) city in a post-disaster environment. Cities **63**, 41–50 (2017)
29. Sharma, K., Garg, R., Nagpal, C.K., Garg, R.K.: Selection of optimal software reliability growth models using a distance-based approach. IEEE Trans. Reliab. **59**(2), 266–276 (2010)
30. Tayal, S., Nagwal, N., Sharma, K.: Role of big data in make in India. Adv. Intell. Syst. Comput. **564**, 431–437 (2018)
31. Agrawal, S.K.: 5G millimeter wave (mmWave) communication system with software-defined radio (SDR). Int. J. Inov. Res. Sci. Eng. **2**(09), 263–270 (2016)

Publisher's Note Springer Nature remains neutral with regard to jurisdictional claims in published maps and institutional affiliations.

Regular Paper

Topics - Metabolism and Bioenergetics < BIOCHEMISTRY, Cell General < CELL

Title: Interleukin-6 confers radio-resistance by inducing Akt mediated glycolysis and reducing mitochondrial damage in cells

Neeraj Kumari[1,2], Asmita Das[2], Anant Narayan Bhatt[1]

[1]Institute of Nuclear Medicine and Allied Sciences, Delhi 110 054
[2]Department of Biotechnology, Delhi Technological University, Delhi 110042

Short Title: Role of Glycolysis in IL-6 induced radio-resistance

Correspondence:
Dr. Anant Narayan Bhatt
Institute of Nuclear Medicine and Allied Sciences
Brig S K Mazumdar Marg
Delhi-110 054
INDIA
Telephone: (+91) 11 2390-5138
Fax: (+91) 11 2391-9509
E-mail: anant@inmas.drdo.in, anbhatt@yahoo.com

Abbreviations: Interleukin-6 (IL-6), Hexokinase-2 (HK-2), Pyruvate kinase M2 (PKM2), 6-phosphofructo-2-kinase/fructose-2,6-bisphosphatase 3 (PFKFB3), Phosphofructokinase 1 (PFK-1)

© The Author(s) 2019. Published by Oxford University Press on behalf of the Japanese Biochemical Society. All rights reserved.

Downloaded from https://academic.oup.com/jb/advance-article-abstract/doi/10.1093/jb/mvz091/5610530 by Delhi Technological University user on 06 November 2019

Abstract

Interleukin-6 (IL-6) induced glycolysis and therapeutic resistance is reported in some cell systems; however the mechanism of IL-6 induced glycolysis in radio-resistance is un-explored. Therefore to investigate, we treated Raw264.7 cells with IL-6 (1hr prior to irradiation) and examined the glycolytic flux. Increased expression of mRNA and protein levels of key glycolytic enzymes was observed after IL-6 treatment, which conferred glycolysis dependent resistance from radiation induced cell death. We further established that IL-6 induced glycolysis is activated by Akt signaling and knocking down Akt or inhibition of pan Akt phosphorylation significantly abrogated the IL-6 induced radio-resistance. Moreover, reduction of IL-6 induced pAkt level suppressed the expression of Hexokinase-2 and its translocation to the mitochondria, thereby inhibiting the glycolysis induced resistance to radiation. IL-6 induced glycolysis also minimized the radiation induced mitochondrial damage. These results suggest that IL-6 induced glycolysis observed in cells may be responsible for IL-6 mediated therapeutic radio-resistance in cancer cells, partly by activation of Akt signaling.

Key words: IL-6, Glycolysis, Radio-resistance, Hexokinase-2, PKM2, Akt signaling

Downloaded from https://academic.oup.com/jb/advance-article-abstract/doi/10.1093/jb/mvz091/5610530 by Delhi Technological University user on 06 November 2019

1. Introduction

Interleukin-6 (IL-6) is a cytokine synthesized and secreted by various types of human body cells like monocytes, adipocytes, fibroblasts, vascular endothelial cells and tumour cells of different types of cancers[1]. It was primarily known as pro-inflammatory cytokine for decades however many recent evidences demonstrated its role in tissue remodelling and as anti-inflammatory cytokine[1,2]. IL-6 is also known as myokine as it is secreted by muscle cells during exercise and acts on skeletal muscles to promote myogenesis, regulate energy metabolism and protect them from physical exercise induced ischemic reperfusion injury[3]. It also protects cardiomyocytes and lung cells from ischemic reperfusion injury and oxidative stress induced cell death[4,5]. Besides this, IL-6 plays an important role during differentiation and tumour progression in majority of cancers. Increased IL-6 secretion in serum and tumour tissues is one of the key factors that promote rapid growth rate and resulted in aggressive phenotypes of cancer [1,6]. An adaptive consequence of chemo and radiotherapy resulted in elevated levels of IL-6 in tumor microenvironment through NF-kB signaling that impose the major limitation to therapies [7–9]. The cytoprotective role of IL-6 is beneficial in normal physiological conditions however; it brings in an additional challenge in therapeutic management of tumors with high IL-6 levels.

The cancer cells and also the normal cells during various types of stress primarily depends on glycolysis for energy production even in the presence of oxygen, due to faster rate of ATP synthesis, this phenomenon is known as Warburg effect [10]. Moreover, glycolysis over the oxidative phosphorylation is predominant pathway of energy metabolism in all the cells involved in inflammatory response [11]. Hence, it is clear that this phenomenon of aerobic glycolysis, which was originally discovered in cancer cells, is not restricted to cancer cells only [12]. It has been recently reported that pro-inflammatory cytokine IL-6 increases the availability of substrates such as glucose and lipids by promoting

Downloaded from https://academic.oup.com/jb/advance-article-abstract/doi/10.1093/jb/mvz091/5610530 by Delhi Technological University user on 06 November 2019

glycogenolysis and lipolysis in skeletal muscles in an autocrine manner and its deficiency suppresses the key genes of glycolysis pathway [6,13]. These studies suggest that aerobic glycolysis is a common phenomenon among many proliferating cells, which provides advantage during proliferation in terms of faster ATP production to meet the high demand of rapidly dividing cells and cells recovering from injury.

It has been demonstrated earlier that IL-6 can induce glycolysis in various types of cell like mouse embryonic fibroblasts, human skeletal muscles etc [14,15]. However, the molecular mechanism of IL-6 induced glycolysis is poorly understood. Recent studies have demonstrated that the IL-6 mediated activation of cellular antioxidant pathway is implicated in the radio-resistance of cancer cells [16–18]. Accumulating evidences indicate that induced glycolysis confers radio-resistance in various cancers [6,7,19,20]. Although, various mechanisms of IL-6 induced radio-resistance is known but, the role of IL-6 induced glycolysis in radio-resistance remains unclear. In the present study, we therefore investigated the mechanism of IL-6 induced glycolysis in Raw 264.7 cells and tested the hypothesis, if IL-6 can protect normal cells from ionizing radiation by inducing glycolysis mediated radio-resistance. In this study, we have shown that IL-6 treatment induces glycolysis in relatively radio-sensitive Raw 264.7 (murine monocytic) cells [21,22], which protects it from ionizing radiation (IR) induced cell death. Results obtained clearly showed that IL-6 induced Akt signaling plays an important role in stimulating glycolysis and protect the cells by conferring glycolysis mediated radio-resistance.

Downloaded from https://academic.oup.com/jb/advance-article-abstract/doi/10.1093/jb/mvz091/5610530 by Delhi Technological University user on 06 November 2019

Materials and methods

2.1 Materials

High glucose Dulbecco's Minimum Essential Medium (HGD), Penicillin G, streptomycin, nystatin, dimethyl sulfoxide (DMSO), Sulforhodamine B (SRB)3-4,5-dimethylthiazol-2-yl)-2,5-diphenyltetrazolium bromide(MTT) were purchased from Sigma Chemicals Co. (St Louis, USA), whereas mouse IL-6 was purchased from Merck Millipore (Burlington, USA). MK2206 (Akt inhibitor) and Akt1/2 siRNA was purchased from selleckchem (Houston, TX, USA) and Santacruz Biotechnology (Dallas, TX, USA) respectively.

2.2 Sources of cell line

The mouse normal monocyte macrophage (Raw 264.7) was obtained from NCCS, Pune, India and cultured in their respective media containing 10% heat inactivated foetal bovine serum and antibiotics. Stock culture was maintained in the exponential growth phase by passaging them every 3 days with their respective growth medium supplemented with 10% foetal bovine serum and antibiotics in 60mm tissue culture petri dish (BD Falcon, USA).

2.3 Radiation treatment

All the experiments were carried out using 96, 24 and6 well plates, 35mm and 60mm tissue culture dishes. Exponentially growing cells were treated with 1ng/ml IL-6 followed by γ-radiation (2Gy) and kept for overnight incubation at 37°C in 5% CO_2 incubator. All experiments were carried out at a single dose of gamma radiation (2Gy), cells were irradiated using ^{60}Cobalt-Teletherapy Unit (Bhabhatron-II, Panacea Medical Technologies, Bangalore, India) at a source to sample distance of 80 cm and a field size of 35x35 cm^2 with dose rate of 1.05 Gy/ min. The treatment schedule and concentration of other drug/ inhibitors are mention in respective figure legends.

2.4 Glucose uptake and lactate production assay

Downloaded from https://academic.oup.com/jb/advance-article-abstract/doi/10.1093/jb/mvz091/5610530 by Delhi Technological University user on 06 November 2019

Raw264.7 cells were incubated in HGD before IL-6 treatment and irradiation. Cells were treated with IL-6, 1 hours prior to irradiation. Subsequently cell medium was removed and cells were incubated with 2NBDG (50uM, 2-(*N*-(7-Nitrobenz-2-oxa-1,3-diazol-4-yl)Amino)-2-Deoxyglucose) prepared in Phosphate Buffered Saline (PBS) for 30 minutes (Fig 1A). Further the cells were harvested and washed twice with cold PBS to analyze on flow cytometer. Lactate production was estimated in the growth medium using enzymatic assays (Fig1B). Lactate was estimated using lactate oxidase method using kit (Randox; Cat. No.-LC2389). Glucose uptake and lactate production was normalized with number of viable cell in respected wells.

2.5 Immuno-blot for Protein levels

The protein level of hexokinase 2, PFK-1, PKM2, GLUT4, phospho Akt, Akt and loading control β-Actin were determined in control and irradiated cells (Raw264.7) by immuno-blot analysis (Fig 1C &4A). Cells were cultured in PD60 incubated in CO_2 incubator before treatment. Further cells were harvested post irradiation at various time points and lysed in ice cold RIPA lysis buffer (Tris–HCl: 50mM, pH 7.4, NP-40: 1%, NaCl: 150 mM, EDTA: 1 mM, PMSF: 2 mM, protease inhibitor cocktail, Na3VO4: 1 mM, NaF: 1 mM) containing protease inhibitors. The protein concentration in cell lysates was determined using BCA protein assay kit. Protein (40µg) was resolved on 10–12% SDS–PAGE (depending on the molecular weight) and electroblotted onto PVDF membrane (MDI). The membrane was then incubated in 4% BSA for 2 h followed by primary antibody incubation HK-2 (1:1000), PKM2 (1:500), PFK-1 (1:500), GLUT4 (1:500) and β-Actin (1:3000) from Santa Cruz Biotechnology and pAkt (1:1000), Akt (1:1000) and SDH (1:1000) from Cell Signaling Technology. Membrane was washed followed by incubation with the appropriate HRP conjugated secondary antibody (1:5000, Santa Cruz Biotechnology) for 2h. After washing, the blots were developed using Luminata Forte Western HRP substarte (Millipore) The signal

Downloaded from https://academic.oup.com/jb/advance-article-abstract/doi/10.1093/jb/mvz091/5610530 by Delhi Technological University user on 06 November 2019

was captured by Chemidoc system (Bio-Rad, CA, USA) and band intensities for each individual protein were quantified by densitometry, corrected for background staining, and normalized to the signal for β-Actin.

2.6 Quantitative PCR for mRNA levels

Total RNA was isolated from cells by qiagen RNA isolation kit according to the manufactures instructions (Qiagen RNeasy mini kit). Further RNA was dissolved in nuclease-free water (Thermo Scientific, USA) and quantified with Nanodrop (Thermo Scientific, USA). 1ug of RNA was used for cDNA synthesis via First-strand cDNA synthesis kit (Thermo Scientific, USA) in thermal cycler (Applied Biosystems, CA, USA). Kick start ready to use primers were purchased from Sigma Aldrich (St.Louis, USA). For real time PCR, 25ng of cDNA was added to 100nM gene specific primers and 1x Sybr Green supermix (Bio-Rad, CA, USA). The amplification program consisted of a hot start at 95°C for 3 min, followed by 40 cycles of denaturation at 95°C for 15 s, annealing at 60°C for 30 s, and extension at 72°C for 15s. The amount of target gene was normalized by β-Actin (Fig 1D).

2.7 Growth Kinetics/Cell number

Cells were seeded in PD35. After IL-6 and radiation treatment cells were kept at 37°C in 5% CO_2 incubator for doublings (Fig 2A). At respective time points cell numbers were counted with a Neubauer-improved counting chamber (Paul Marienfeld GmbH & Co. KG, Germany) under 10 X objective, and 10X eye piece magnification with compound light microscope (Olympus CH30, Japan).

2.8 Clonogenic cell survival assay

Macro colony assay was performed using pre plating method of macro colony assay. Cells were plated at a low density of 100-3200 cells in triplicates in 60mm Petri dishes. After IL-6 and radiation treatment (0-8Gy), cells were incubated at 37°C in a humidified CO2 (5%) incubator for 7-10 days. Colonies of at least 50 cells (5 to 6

Downloaded from https://academic.oup.com/jb/advance-article-abstract/doi/10.1093/jb/mvz091/5610530 by Delhi Technological University user on 06 November 2019

generations of proliferation) were scored as survivors. Colonies were washed once with PBS to remove media, fixed with methanol and then stained with 1% crystal violet (dissolved in 7% methanol in PBS). Plating efficiency was calculated as PE = (Number of colonies counted / Number of cells plated) X 100. The Surviving Fraction (S.F.) was calculated as: $SF = PE_T / PE_C$ Where, PE_T is the plating efficiency of the treated group and PE_C is the value of the control.

2.9 ATP measurement

ATP was measured using ATP bioluminescent assay kit (Sigma Aldrich (St.Louis, USA)) following manufacturer's protocol. Briefly, cells were treated with IL-6 followed by irradiation at 1hr. At 4 and 24 hour post irradiation cells were washed and scraped in cold PBS and pelleted at 1000 rpm for 10 min. Cells were lysed in 350 µl of lysis buffer (4mM EDTA and 0.2% Triton X-100). 100 µl of this lysate was loaded per well in triplicates with 100 µl of ATP mix in a 96-well white luminescence measuring plate. Luminescence of samples along with standards was read at 562 nm and normalized with the cell number (Fig 3D). ATP concentration is depicted as pg/cell.

2.10 Acridine Orange-Ethidium Bromide staining

Raw 264.7 cells were seeded in 96 well and stained with acridine orange-ethidium bromide according to Deborah Ribble protocol [23] with minimal modifications (Fig 3G). Images were captured under fluorescence microscope using 10X objective, and 10X eye piece magnification with fluorescence microscope (Olympus IX51 Fluorescence Microscope, Japan).

2.11 Formazan quantification

The cells were plated in 24 well culture plates (40,000 cells/well) and incubated in CO2 incubator. Next day, treatment was given according to the experimental requirement. Further,

Downloaded from https://academic.oup.com/jb/advance-article-abstract/doi/10.1093/jb/mvz091/5610530 by Delhi Technological University user on 06 November 2019

at respective time points, 50 µl MTT solutions from the stock (5 mg/ml) was added and cells were incubated in CO2 incubator in the dark for 2 hrs. The medium was removed and Formazan crystals formed by the cells were dissolved using 500 µl of DMSO followed by transfer in 96 well plate. The absorbance was read at 570 nm using 630 nm as reference wavelength on a Multiwell plate reader (Biotech Instruments, USA). Reduced formazan quantification was done with Formazan standard. At each respective time points cell numbers were counted with a Neubauer-improved counting chamber (Paul Marienfeld GmbH & Co. KG, Germany) under 10X objective, and 10X eye piece magnification with compound light microscope (Olympus CH30, Japan).

2.12 Measurement of mitochondrial Mass and mitochondrial Calcium

Quantitative analysis of mitochondrial content was carried out using Mitotracker Green (at respective time points, post irradiation), Cells were incubated with mitotracker green (100 nM; 15 min; 37 °C), in PBS, then washed with PBS and resuspended in PBS before analysis. The signals were recorded using BD FACSAria™ III cell sorter. (BD Biosciences, USA). Images of Calcium loaded mitochondria was captured by staining cells with A23187 (6uM, 20min). Briefly Raw264.7 cells were grown in PD-35 having cover slip. At 4hr post irradiation medium was removed and stained for 20min in dark. Stain was removed and cells washed with cold PBS. Images were captured under fluorescence microscope with 40X objective.

2.13 Mitochondrial Membrane potential

Quantitative and qualitative analysis of mitochondrial membrane potential was carried out using TMRM and JC-1 dyes respectively, Cells were incubated with TMRM (50 nM; 30 min; 37 °C) in PBS, then washed and resuspended in PBS for analysis. Fluorescence signals were measured by flow cytometer (BD FACSAria™ III cell sorter). For microscopy, cells were stained with JC-1 dye (10ug/ml; 30 min; 37 °C). After staining cells were washed with PBS

Downloaded from https://academic.oup.com/jb/advance-article-abstract/doi/10.1093/jb/mvz091/5610530 by Delhi Technological University user on 06 November 2019

and observed at 40X magnification under fluorescence microscope (Olympus IX51 Fluorescence Microscope, Japan). JC-1 accumulates in mitochondria as monomer or J-aggregates depending on the membrane potential. The monomeric form is predominately present in depolarized mitochondria and emits green fluorescence (~530 nm), whereas the oligomeric (J-aggregate) form in mitochondria with more potentials and emits red fluorescence (~590 nm).

2.14 siRNA transfection

The control siRNA and Mouse Akt1/2 siRNA pool was purchased from Santacruz Biotechnology (Dallas, Texas, USA) to knock down gene expression. siRNA transfection was performed using Lipofectamine 2000 (Invitrogen, Carlsbad, USA), according to the manufacturer's instructions, briefly 0.1 x106 cells were seeded in 6-well plate a day before transfection. Next day transfection was done in Opti-MEM (serum and antibiotic free medium) for 4hr followed by 24hr recovery in 2x serum containing medium. Pilot experiments were performed to optimize the amount and time of maximal protein knockdown.

2.15 Statistical analysis

All the experiments were carried out in triplicates or quadruplicates. Means and standard errors were computed. Student's t test and one-way ANOVA test was performed for comparisons between two groups and multiple groups respectively. P-values <0.05 were considered statistically significant.

3. Results:

3.1 ***IL-6 induces Glycolysis:*** We first tested if IL-6 can induce glycolysis in Raw 264.7 cells. Thus we measured glucose uptake using non metabolizing, fluorescent glucose analogue 2-

Downloaded from https://academic.oup.com/jb/advance-article-abstract/doi/10.1093/jb/mvz091/5610530 by Delhi Technological University user on 06 November 2019

NBDG (2-(*N*-(7-Nitrobenz-2-oxa-1,3-diazol-4-yl)Amino)-2-Deoxyglucose) in Raw264.7 cells. IL-6 treatment showed significant increase in glucose consumption at both 1 and 10 ng/ml IL-6 with highest 1.5 fold consumption at 1ng/ml (Fig. 1A). Therefore, we used 1ng/ml concentration of IL-6 for all the further experiments. Consequently, lactate production, which is the end product of glycolysis was also increased by 1.65 fold after IL-6 treatment (Fig 1B). Further to understand if the high rate of glycolysis is achieved by IL-6 induced enhanced levels of glycolytic enzymes, we checked the levels of key glycolytic enzymes HK-1, HK-2, PFK-1 and PKM2 after IL-6 treatment. We found nearly 1.3 to 2 fold time dependent increase in the protein levels of HK-2, PFK-1, and PKM2, while the protein level of HK-1 was found unchanged (Fig. 1C). Enhanced levels of HK-2 and PKM2 protein was further supported by the time dependent increase in HK-2 and PKM2 mRNA levels (Fig. 1D).We also checked the IL-6 induced gene expression of PFKFB3 gene, which produces Glucose 2,6 bis phosphate (G2,6BP) for allosteric activation of PFK-1 enzyme [24] We found, IL-6 induced the mRNA levels of PFKFB3 gene also, suggesting it regulates the flow of glucose through glycolysis (Fig. 1D). These findings suggest that IL-6 induces glycolysis by inducing the expression of glycolytic regulatory enzymes in Raw264.7 cells.

3.2 ***IL-6 protects Raw264.7 cells from radiation induced cell death:*** Our Previous studies suggest that transient elevation of glycolysis confers radio-resistance [20]. Therefore in order to check the correlation between IL-6 induced glycolysis and radio-resistance, we further carried out SRB assay and growth kinetics in Raw264.7 cells to test the effects of IL-6 on radiation induced cell death. SRB assay was performed at same concentration range of IL-6 0.1 to 10 ng/ml as used in glucose uptake and we found significant protection of 45 to 50% at 1 and 10 ng/ml (Fig. 2A). Growth kinetic assay was also performed under similar experimental conditions and nearly 45% reduction in radiation induced cell death was observed in IL-6 treated cells as compared to irradiated cells (Fig. 2B). The marginal increase

Downloaded from https://academic.oup.com/jb/advance-article-abstract/doi/10.1093/jb/mvz091/5610530 by Delhi Technological University user on 06 November 2019

in protection, observed at 10 ng/ml with respect to 1ng/ml IL-6 in SRB assay (Fig. 2A) and marginally low cell count at 10ng/ml (Fig. 2B inset) was statistically insignificant; Since, significant and nearly equal increase in glucose consumption and radioprotection were observed at both 1ng/ml and 10 ng/ml doses of IL-6, therefore we used 1 ng/ml concentration for all further experiments. Further, to validate IL-6 treatment induced radio-resistance; we irradiated the IL-6 pre-treated cells and then analyzed the clonogenicity using macro-colony assay. Indeed a significant increase in survival was evident in IL-6 pre-treated cells as compared to radiation alone on all radiation dose between 0 to 8Gy[Fig. 2C]. Together, these findings suggest that IL-6 induced glycolysis confers radio-resistance in monocytic Raw264.7 cells.

3.3 ***IL-6 induced radio-resistance is glycolysis dependent:*** Further, to validate the correlation between IL-6 induced glycolysis and radio-resistance; we analyzed the levels of glucose uptake and lactate production after radiation exposure in IL-6 pre-treated samples. Radiation alone group also showed increase in glucose uptake, however it was significantly less (~1.5 fold) as compared to IL-6 alone and combined (IL-6 pre-treatment followed by irradiation) treatment groups (~2 fold) (Fig. 3A). Similarly, the lactate production was also found significantly higher in IL-6 and radiation combined treatment as compared to radiation exposed cells (Fig. 3A). This result is substantiated by several fold increased protein levels of glycolytic enzymes (HK-2, PFK-1, PKM2), glucose transporter GLUT4 (Fig 3B) and mRNA expression of HK-2, PKM2 and PFKFB3 gene (Fig. 3C) in cells co-treated with IL-6 and radiation as compared to radiation alone. We also found about 1.9 fold increased ATP level at 4 hours post irradiation in IL-6 pre-treated cells with respect to control and radiation alone (Fig. 3D).

We further inhibited the glycolysis using non-toxic concentrations of 2-dexoy-D-Glucose (2-DG) and 3-bromo pyruvate (3-BP) in IL-6 pre-treated cells before exposing to radiation

Downloaded from https://academic.oup.com/jb/advance-article-abstract/doi/10.1093/jb/mvz091/5610530 by Delhi Technological University user on 06 November 2019

and performed growth kinetics. Both the glycolytic inhibitors 2-DG and 3-BP reversed the IL-6 induced protection from radiation induced cell death (Fig. 3E&F). This observation from growth kinetics assay was correlated with qualitative imaging of ethidium bromide and acridine orange (apoptosis assay) at 24 hours. Radiation alone and in combination with glycolytic inhibitors (2-DG and 3-BP) in IL-6 pre-treated group showed nearly similar number of apoptotic and necrotic cell population, which was significantly higher as compared to IL-6 pre-treated and radiation exposed treatment group (Fig. 3G&H).Therefore, these findings evidently validate our earlier observation that induced glycolysis confers radio-resistance. It also suggests that IL-6 induced radio-resistance in Raw264.7 cells is glycolysis dependent.

3.4 ***IL-6 protects from radiation induced mitochondrial damage:*** Ionizing radiation is known to damage mitochondria and affect its energy metabolism [25,26]. Therefore, we tested if IL-6 protects from radiation induced mitochondrial damage also. To test the mitochondrial energy metabolism, we analyzed complex II activity of mitochondrial respiratory chain by monitoring formazan formation. We found, radiation induces nearly 2.5 fold increased formazan formation in IL-6 untreated and treated cells at early time point (4h), which comes down to normal at later time point (24h, Fig 4A). Mitochondrial enzymatic activity depends on the mitochondrial mass in cells and we have shown in our earlier study that radiation induced mitochondrial damage can induce mitochondrial biogenesis and thereby increases the mitochondrial mass and formazan formation in cells [25]. Interestingly, we noted nearly similar formazan formation in IL-6 untreated and treated cells after radiation exposure from 1.8 and 1.25 fold increased mitochondrial mass respectively (Fig. 4B). This observation shows that radiation exposed cells have 80% more mitochondrial mass, but all may not be contributing to enhanced complex II activity. However, similar formazan formation from

Downloaded from https://academic.oup.com/jb/advance-article-abstract/doi/10.1093/jb/mvz091/5610530 by Delhi Technological University user on 06 November 2019

only 25% increased mitochondrial mass and nearly similar SDH level (Fig. 4C, D) after radiation exposures in IL-6 pre-treated cells as compared to radiation alone exposed cells suggest reduced mitochondrial damage and higher efficiency of mitochondrial respiration in IL-6 pre-treated cells. Subsequently, we also analyzed the mitochondrial membrane potential (MMP) under similar experimental conditions to analyze the mitochondrial status in radiation exposed cells using fluorescent potentiometric dyes JC-1 and TMRM (Fig 4E & F). We observed radiation induced increased MMP in IL-6 and radiation treated cells (Fig. 4E), however radiation induced hyperpolarized mitochondria and increased mitochondrial mass (Fig. 4B) can also show higher dyes uptake in cells giving false information of higher MMP [25]. Therefore, we normalized the MMP values with mitochondrial mass of the respective sample to obtain the accurate MMP of the cells. When radiation induced increased MMP was normalized with enhanced mitochondrial mass, it showed significant 30% decrease in MMP, which was restored in IL-6 pre-treated and radiation exposed samples both at 4 and 24 hours (Fig. 4F). This was further validated by microscopic observation of radiation induced damaged mitochondria using A23187 dye [26]. We found highly reduced numbers of A23187 puncta positive cells and much smaller intracellular bodies (showing damaged mitochondria) in IL-6 pre-treated cells as compared to radiation alone (Fig. 4G & H). Interestingly, glycolysis inhibition using 2-DG in IL-6 pre-treated cells reverses the protective effects of IL-6 from radiation induced mitochondrial damage (Fig. 4G & H). These observations suggest that IL-6 protects from radiation induced mitochondrial damage and this protective effect is also linked with IL-6 induced glycolysis.

3.5 ***IL-6 induced Akt signaling promotes glycolysis and confers radio-resistance:*** Enhanced glycolytic metabolism is known to be regulated by two main signaling pathways in normal cells namely, HIF1α and Akt. IL-6 activates both HIF1α and Akt signaling pathway [1,27]. Whereas, we found that IL-6 at 1ng/ml concentration does not induce detectable levels

Downloaded from https://academic.oup.com/jb/advance-article-abstract/doi/10.1093/jb/mvz091/5610530 by Delhi Technological University user on 06 November 2019

HIF1α in Raw264.7 cells. Therefore, we tested Akt pathway by estimating the time dependent protein levels of pAkt (active form) in IL-6 treated cells. We found more than 2 fold increase in pAkt levels as early as 1 hr. of IL-6 treatment (Fig 5A). Further, to authenticate if IL-6 induced radio-resistance is dependent on Akt signaling and enhanced glycolysis mediated by it; we inhibited Akt signaling using pan Akt inhibitor MK2206 [28] and also knock down the Akt expression (53% depletion in Akt1/2 level) using Akt1/2 siRNA. Downregulation of Akt signaling not only reduced the IL-6 induced pAkt levels to un-induced basal level (Fig 5B) but also significantly brought down the level of IL-6 induced glucose uptake, and lactate production to the basal level (Fig 5C). Further, low pAkt level reduced the IL-6 induced total and mitochondrial bound fraction of HK-2 (Fig. 5D &F) and reversed the IL-6 induced radio-resistance, indicated by significant reduction in cell number of IL-6 pre-treatment combined with Akt1/2 siRNA and MK2206 in irradiated cells nearly to the level of radiation control (Fig. 5E). These results suggest that IL-6 induced Akt signaling upregulate the levels of glycolytic enzymes, which leads to enhanced glycolysis and radio-resistance in Raw264.7 cells.

4. Discussion:

IL-6, which is known to be a cytoprotective cytokine in normal physiological conditions, also protects tumor cells from radiotherapy and chemotherapeutic agents posing major limitation in therapeutic gain in cancer treatment [1]. IL-6 protects the cells from therapeutic stress induced cell death by inducing various pro-survival signaling namely inhibition of apoptosis, induce survival and proliferation [1,6,14]. Therefore, IL-6 induced cellular defense to therapeutic stress causes therapeutic resistance [1,6,16–19]. It is known that IL-6 can induce aerobic glycolysis in cells [12,15], and we have demonstrated earlier that induced glycolysis caused radio-resistance in cells [20]. IL-6 mediated radio-resistance in

Downloaded from https://academic.oup.com/jb/advance-article-abstract/doi/10.1093/jb/mvz091/5610530 by Delhi Technological University user on 06 November 2019

cells has been attributed to IL-6 induced anti-oxidant defense system and STAT-3 mediated pro-survival signaling [14,18]; however, the role of IL-6 induced energy metabolism mainly glycolysis in radio-resistance is not known. Therefore, we tested the hypothesis, if IL-6 induced glycolysis plays any role in cellular radio-resistance, which may be diminishing the therapeutic gain in cancer treatment. IL-6 induced radio-resistance can also be exploited in protecting the normal tissues from radiation hazards. We selected murine monocytic cell line Raw264.7 to test the IL-6 induced radio-resistance because hematopoietic cells are relatively more sensitive to radiation [21,22].

The data presented above demonstrate the potential of IL-6 to induce glycolysis in hematopoietic Raw264.7 cells. It induced the glycolysis by increasing the levels of many regulatory glycolytic enzymes viz. HK-2, PFK-1 and PKM2 (Fig. 1C & D). Enhanced expression of HK-2 and its association with mitochondria ensures rapid phosphorylation of glucose using mitochondrial ATP [29]. The PFK-1 is the first critical and irreversible step of glycolysis which diverts the glucose through glycolysis (catabolic pathway) and ensures that glucose should not enter to pentose phosphate pathway or gluconeogenesis, both anabolic pathways. At the time of stress or cellular injury, ATP generated from catabolic pathways is required for macromolecular repair and cell survival therefore, diverting glucose towards glycolysis for more ATP production is vital and decisive for cell survival [24]. We found higher ATP levels in IL-6 treated cells (Fig 3D), which acts as inhibitor of PFK-1, however increased expression of PFKFB3 (Fig. 1D) produces fructose 2,6bisphosphate (F2,6BP), which acts as allosteric activator of PFK-1 and ensures the continuous activation of PFK-1, even in the presence of high ATP [15,24]. Further, IL-6 induced higher protein levels of PKM2 (Fig. 1C & D) maintains the smooth running of glucose through glycolysis by reducing the level of its substrate Phosphoenolpyruvate (PEP), which can inhibit the PFK-1

Downloaded from https://academic.oup.com/jb/advance-article-abstract/doi/10.1093/jb/mvz091/5610530 by Delhi Technological University user on 06 November 2019

and stop the flow of glucose towards glycolysis. These results suggest that IL-6 induces the glycolysis by elevating the levels of all the crucial regulatory enzymes of this pathway.

Interestingly, IL-6 pre-treatment to induce glycolysis could protect the radio-sensitive Raw264.7 cells from radiation induced cell death (Fig. 2). The protein levels of glucose transporter and glycolytic enzymes, which was decreased after radiation exposure was found high in IL-6 alone and combined treatment group, suggesting that IL-6 induced the glycolysis in radiation exposed cells also. Radiation is also known to induce the glycolysis [30], which can be observed by enhanced glucose uptake, lactate production and higher levels of glycolytic enzymes, HK-2, PFK-1 and PKM2 in radiation exposed sample as compared to control (Fig. 3A, B & C). However, these levels were found further increased in IL-6 pretreated and radiation exposed (combined treatment) sample. These findings suggest that radiation induced glycolysis, which is marginally higher than the control cannot meet the requirement of energy to rescue the cells from radiation induced cell death however, IL-6 can induce the glycolysis at sufficiently higher level to accomplish the requirement of energy for repair and survival of cells battling with radiation induced damage. This proposition is further confirmed by significantly higher levels of ATP in radiation exposed cells pretreated with IL-6 as compared to control and radiation alone (Fig. 3D). The IL-6 induced high levels of ATP in IL-6 alone and combined treatment was noted at early time point (4 hrs.), when it was obligatory to rescue the cells, as ATP is essentially required for energy consuming processes like macromolecular repair, mainly DNA [20]. The reversal of IL-6 induced radio-resistance by glycolytic inhibitors 3-BP and 2-DG (Fig. 3E to H) authenticated the role of glycolysis in IL-6 induced radio-resistance. Radiation induced mitochondrial damage also contributes in radiation induced cell death; we observed that IL-6 reduced the mitochondrial damage in IL-6 pretreated cells. Interestingly, inhibition of IL-6 induced glycolysis also reverses the protective effect of IL-6 from radiation induced mitochondrial damage (Fig. 4).

Downloaded from https://academic.oup.com/jb/advance-article-abstract/doi/10.1093/jb/mvz091/5610530 by Delhi Technological University user on 06 November 2019

IL-6 after binding to its receptor on the cell surface induces the phosphorylation of STAT-3 and PI3K (Phosphoinositol-3-kinase), which further phosphorylates the Akt [1]. Increased Akt phosphorylation is found to be associated with increased rates of glucose metabolism in cells [31]. Akt signaling influence the glycolysis directly by regulating the localization of the GLUT to the plasma membrane [32], HK-2 expression and mitochondrial interaction [33], and expression of PFK-1 and PFKFB3 [34]. Since, we found the expression levels of all these genes were increased by IL-6 treatment in Raw264.7 cells; we envisaged that IL-6 induced glycolysis in Raw264.7 cells could be mediated by Akt pathway. IL-6 induced Akt phosphorylation suggested the involvement of Akt signaling in IL-6 induced enhanced glycolysis, which was further verified by knocking down the Akt expression and inhibition of Akt signaling under similar experimental settings (Fig.5). Downregulation of Akt signaling in IL-6 pre-treated samples not only reduced the glycolysis (glucose uptake and lactate production) but also the expression level of key glycolytic enzyme HK-2 and its association with mitochondria, which resulted in reversal of IL-6 induced radio-resistance (Fig. 5). HK-2 association with mitochondrial outer membrane not only facilitates the quick phosphorylation of glucose using mitochondrial ATP but also prevents the cytochrome C release from mitochondria thereby inhibiting the apoptosis [35]. Therefore, IL-6 induced and Akt mediated translocation of HK-2 to mitochondrial membrane may cause radio-resistance besides glycolysis also. Moreover, besides the direct role of PKM2 in glucose catabolism, it was demonstrated to facilitate the homologous recombination of DNA repair in nucleus [36]. Hence, we can assume that IL-6 induced high levels of PKM2 and HK-2 may be causing radio-resistance through glycolysis as well as other moonlighting functions. It will be pertinent to see the role of IL-6 induced glycolytic enzymes in DNA repair and other moonlighting functions. Pending this insight to be unravelled, results of the present studies lend support to our hypothesis that IL-6 induced glycolysis is a favourable metabolic change

Downloaded from https://academic.oup.com/jb/advance-article-abstract/doi/10.1093/jb/mvz091/5610530 by Delhi Technological University user on 06 November 2019

partly responsible for radio-resistance. This study adds induced glycolysis also as one of the factor among the list of various causes responsible for IL-6 induced radio-resistance.

5. Conclusion:

In conclusion, the results of this study suggest that IL-6 induced the glycolysis in Raw264.7 cells by activating Akt signaling, which further induced the expression of key regulatory glycolytic enzymes and glucose transporters. The IL-6 induced aerobic glycolysis and reduced mitochondrial damage at the time of radiation exposure ensures continuous and sufficient supply of energy for repair of radiation induced macro-molecular and cellular damages, thereby causing radio-resistance (Fig.6). The moonlighting functions of IL-6 induced glycolytic enzymes also need to be understood to know their role in IL-6 induced radio-resistance. Further, understanding the mechanisms underlying IL-6 induced Glycolysis may help in unraveling critical molecular targets responsible for therapeutic resistance and facilitate the design and/or identification of molecules/agents that specifically overcome resistance linked to enhanced glycolysis, thereby enhancing the efficacy of radio- and chemotherapies. Clinical use of costly anti-IL-6 or anti IL-6 receptor antibodies in combination with therapies in IL-6 over-expressing tumors is challenging. Instead, use of metabolic inhibitors will be economical in achieving the similar level of therapeutic gain; however more research is required to validate this proposition. This study also throws the light that IL-6 can protect the normal cells from radiation induced cell death and it has potential to be developed as radio-protector.

Downloaded from https://academic.oup.com/jb/advance-article-abstract/doi/10.1093/jb/mvz091/5610530 by Delhi Technological University user on 06 November 2019

Author Contribution:

Anant N Bhatt: Conceptualization, Writing-Reviewing and Editing, Supervision. **Neeraj Kumari**: Data curation, Investigation, Writing- Original Draft. **Asmita Das**: Writing-Reviewing and Editing. All authors reviewed and approved the final version of the manuscript for submission.

Acknowledgments

NK thanks the Defence Research and Development Organisation, Government of India, for fellowship support. We acknowledge Director INMAS for constant support and encouragement. We also acknowledge Yogesh Rai, Dhananjay Sah and Ankit Chauhan for support during experiments. We extend our sincere thanks to Dr. Ravi Soni and the staff of the institutional Central Instrument Facility.

6. References:

1 Kumari, N., Dwarakanath, B. S., Das, A. and Bhatt, A. N. (2016) Role of interleukin-6 in cancer progression and therapeutic resistance. Tumour Biol. **37**, 11553–11572.

2 Scheller, J., Chalaris, A., Schmidt-Arras, D. and Rose-John, S. (2011, May) The pro- and anti-inflammatory properties of the cytokine interleukin-6. Biochim. Biophys. Acta - Mol. Cell Res.

3 Muñoz-Cánoves, P., Scheele, C., Pedersen, B. K. and Serrano, A. L. (2013) Interleukin-6 myokine signaling in skeletal muscle: a double-edged sword? FEBS J. **280**, 4131–48.

4 Smart, N., Mojet, M. H., Latchman, D. S., Marber, M. S., Duchen, M. R. and Heads, R. J. (2006) IL-6 induces PI 3-kinase and nitric oxide-dependent protection and

Downloaded from https://academic.oup.com/jb/advance-article-abstract/doi/10.1093/jb/mvz091/5610530 by Delhi Technological University user on 06 November 2019

preserves mitochondrial function in cardiomyocytes. Cardiovasc. Res. **69**, 164–77.

5 Kolliputi, N. and Waxman, A. B. (2009) IL-6 cytoprotection in hyperoxic acute lung injury occurs via suppressor of cytokine signaling-1-induced apoptosis signal-regulating kinase-1 degradation. Am. J. Respir. Cell Mol. Biol. **40**, 314–24.

6 Mauer, J., Denson, J. L. and Brüning, J. C. (2015) Versatile functions for IL-6 in metabolism and cancer. Trends Immunol. **36**, 92–101.

7 Ishibashi, K., Koguchi, T., Matsuoka, K., Onagi, A., Tanji, R., Takinami-Honda, R., Hoshi, S., Onoda, M., Kurimura, Y., Hata, J., et al. (2018) Interleukin-6 induces drug resistance in renal cell carcinoma. Fukushima J. Med. Sci. **64**, 103–110.

8 Ahmed, K. M. and Li, J. J. (2008) NF-kappa B-mediated adaptive resistance to ionizing radiation. Free Radic. Biol. Med. **44**, 1–13.

9 Yoon, S., Woo, S. U., Kang, J. H., Kim, K., Shin, H.-J., Gwak, H.-S., Park, S. and Chwae, Y.-J. (2012) NF-κB and STAT3 cooperatively induce IL6 in starved cancer cells. Oncogene **31**, 3467–81.

10 Warburg, O. (1956) On the origin of cancer cells. Science (80-.). **123**, 309–314.

11 Wang, T., Liu, H., Lian, G., Zhang, S.-Y., Wang, X. and Jiang, C. (2017) HIF1α-Induced Glycolysis Metabolism Is Essential to the Activation of Inflammatory Macrophages. Mediators Inflamm. **2017**, 9029327.

12 Wang, T., Marquardt, C. and Foker, J. (1976) Aerobic glycolysis during lymphocyte proliferation. Nature **261**, 702–5.

13 Inoue, H., Ogawa, W., Asakawa, A., Okamoto, Y., Nishizawa, A., Matsumoto, M., Teshigawara, K., Matsuki, Y., Watanabe, E., Hiramatsu, R., et al. (2006) Role of

Downloaded from https://academic.oup.com/jb/advance-article-abstract/doi/10.1093/jb/mvz091/5610530 by Delhi Technological University user on 06 November 2019

hepatic STAT3 in brain-insulin action on hepatic glucose production. Cell Metab. **3**, 267–75.

14 Chen, X., Wei, J., Li, C., Pierson, C. R., Finlay, J. L. and Lin, J. (2018) Blocking interleukin-6 signaling inhibits cell viability/proliferation, glycolysis, and colony forming activity of human medulloblastoma cells. Int. J. Oncol. **52**, 571–578.

15 Ando, M., Uehara, I., Kogure, K., Asano, Y., Nakajima, W., Abe, Y., Kawauchi, K. and Tanaka, N. (2010) Interleukin 6 enhances glycolysis through expression of the glycolytic enzymes hexokinase 2 and 6-phosphofructo-2-kinase/fructose-2,6-bisphosphatase-3. J. Nippon Med. Sch. **77**, 97–105.

16 Matsuoka, Y., Nakayama, H., Yoshida, R., Hirosue, A., Nagata, M., Tanaka, T., Kawahara, K., Sakata, J., Arita, H., Nakashima, H., et al. (2016) IL-6 controls resistance to radiation by suppressing oxidative stress via the Nrf2-antioxidant pathway in oral squamous cell carcinoma. Br. J. Cancer **115**, 1234–1244.

17 Tamari, Y., Kashino, G. and Mori, H. (2017) Acquisition of radioresistance by IL-6 treatment is caused by suppression of oxidative stress derived from mitochondria after γ-irradiation. J. Radiat. Res. **58**, 412–420.

18 Brown, C. O., Salem, K., Wagner, B. A., Bera, S., Singh, N., Tiwari, A., Choudhury, A., Buettner, G. R. and Goel, A. (2012) Interleukin-6 counteracts therapy-induced cellular oxidative stress in multiple myeloma by up-regulating manganese superoxide dismutase. Biochem. J. **444**, 515–27.

19 Wang, T., Ning, K., Sun, X., Zhang, C., Jin, L. fang and Hua, D. (2018) Glycolysis is essential for chemoresistance induced by transient receptor potential channel C5 in colorectal cancer. BMC Cancer, BioMed Central Ltd. **18**.

Downloaded from https://academic.oup.com/jb/advance-article-abstract/doi/10.1093/jb/mvz091/5610530 by Delhi Technological University user on 06 November 2019

20 Bhatt, A. N., Chauhan, A., Khanna, S., Rai, Y., Singh, S., Soni, R., Kalra, N. and Dwarakanath, B. S. (2015) Transient elevation of glycolysis confers radio-resistance by facilitating DNA repair in cells. BMC Cancer **15**, 335.

21 Huang, B., Zhang, Q., Yuan, Y., Xin, N., He, K., Huang, Y., Tang, H. and Gong, P. (2018) Sema3a inhibits the differentiation of Raw264.7 cells to osteoclasts under 2Gy radiation by reducing inflammation. PLoS One **13**, e0200000.

22 Kato, K., Omori, A. and Kashiwakura, I. (2013) Radiosensitivity of human haematopoietic stem/progenitor cells. J. Radiol. Prot. **33**, 71–80.

23 Deborah Ribble, Nathaniel B Goldstein, D. A. N. and and Shellman, Y. G. (2005) A simple technique for quantifying apoptosis in 96-well plates. BMC Biotechnol. **5**.

24 Berg JM, Tymoczko JL, S. L. (2002) The Glycolytic Pathway Is Tightly Controlled. In Biochemistry 5th ed., W H Freeman, New York.

25 Rai, Y., Pathak, R., Kumari, N., Sah, D. K., Pandey, S., Kalra, N., Soni, R., Dwarakanath, B. S. and Bhatt, A. N. (2018) Mitochondrial biogenesis and metabolic hyperactivation limits the application of MTT assay in the estimation of radiation induced growth inhibition. Sci. Rep., Nature Publishing Group **8**.

26 Verma, A., Bhatt, A. N., Farooque, A., Khanna, S., Singh, S. and Dwarakanath, B. S. (2011) Calcium ionophore A23187 reveals calcium related cellular stress as "I-Bodies": An old actor in a new role. Cell Calcium, Elsevier Ltd **50**, 510–522.

27 Zhang, F., Duan, S., Tsai, Y., Keng, P. C., Chen, Y., Lee, S. O. and Chen, Y. (2016) Cisplatin treatment increases stemness through upregulation of hypoxia-inducible factors by interleukin-6 in non-small cell lung cancer. Cancer Sci. **107**, 746–54.

Downloaded from https://academic.oup.com/jb/advance-article-abstract/doi/10.1093/jb/mvz091/5610530 by Delhi Technological University user on 06 November 2019

28 Oki, Y., Fanale, M., Romaguera, J., Fayad, L., Fowler, N., Copeland, A., Samaniego, F., Kwak, L. W., Neelapu, S., Wang, M., et al. (2015) Phase II study of an AKT inhibitor MK2206 in patients with relapsed or refractory lymphoma. Br. J. Haematol., Blackwell Publishing Ltd **171**, 463–470.

29 Chen, Z., Zhang, H., Lu, W. and Huang, P. (2009) Role of mitochondria-associated hexokinase II in cancer cell death induced by 3-bromopyruvate. Biochim. Biophys. Acta **1787**, 553–60.

30 Zhong, J., Rajaram, N., Brizel, D. M., Frees, A. E., Ramanujam, N., Batinic-Haberle, I. and Dewhirst, M. W. (2013) Radiation induces aerobic glycolysis through reactive oxygen species. Radiother. Oncol. **106**, 390–6.

31 Elstrom, R. L., Bauer, D. E., Buzzai, M., Karnauskas, R., Harris, M. H., Plas, D. R., Zhuang, H., Cinalli, R. M., Alavi, A., Rudin, C. M., et al. (2004) Akt stimulates aerobic glycolysis in cancer cells. Cancer Res. **64**, 3892–3899.

32 Barthel, A., Okino, S. T., Liao, J., Nakatani, K., Li, J., Whitlock, J. P. and Roth, R. A. (1999) Regulation of GLUT1 gene transcription by the serine/threonine kinase Akt1. J. Biol. Chem. **274**, 20281–6.

33 Miyamoto, S., Murphy, A. N. and Brown, J. H. (2008) Akt mediates mitochondrial protection in cardiomyocytes through phosphorylation of mitochondrial hexokinase-II. Cell Death Differ. **15**, 521–9.

34 Deprez, J., Vertommen, D., Alessi, D. R., Hue, L. and Rider, M. H. (1997) Phosphorylation and activation of heart 6-phosphofructo-2-kinase by protein kinase B and other protein kinases of the insulin signaling cascades. J. Biol. Chem. **272**, 17269–75.

Downloaded from https://academic.oup.com/jb/advance-article-abstract/doi/10.1093/jb/mvz091/5610530 by Delhi Technological University user on 06 November 2019

35 Pastorino, J. G., Shulga, N. and Hoek, J. B. (2002) Mitochondrial binding of hexokinase II inhibits Bax-induced cytochrome c release and apoptosis. J. Biol. Chem. **277**, 7610–8.

36 Sizemore, S. T., Zhang, M., Cho, J. H., Sizemore, G. M., Hurwitz, B., Kaur, B., Lehman, N. L., Ostrowski, M. C., Robe, P. A., Miao, W., et al. (2018) Pyruvate kinase M2 regulates homologous recombination-mediated DNA double-strand break repair. Cell Res. **28**, 1090–1102.

Downloaded from https://academic.oup.com/jb/advance-article-abstract/doi/10.1093/jb/mvz091/5610530 by Delhi Technological University user on 06 November 2019

7. Figure Legends:

Figure 1: IL-6 induced rate of glycolysis was measured by observing glucose uptake and lactate production in cells after IL-6 treatment. Glucose uptake **(A)** and lactate production **(B)** was measured in culture media, 2 hours after IL-6 treatment. **(C)** Protein levels of various glycolytic regulatory enzymes (indicated in figure) were measured in untreated and IL-6 (1ng/ml) treated cells at given time points. β-Actin was used as loading control. Values shown in between the blots are the average fold change value of densitometric analysis of 3 blots, normalized with respective β-Actin. **(D)** The mRNA levels of HK-2, PKM2 and PFKFB3 genes at indicated time points after IL-6 (1ng/ml) treatment. Statistical significance calculated by one way ANOVA and Student's t test between the groups. Data are expressed as mean ± SD (n = 4) *p <0.05

Figure 2: IL-6 confers radio-resistance **(A)** SRB assay carried out at 48h post irradiation using different concentrations of IL-6 (0.1 to 10ng/ml). Graph (ΔOD 340nm) plotted and treatment groups were compared with their respective control. **(B)** The cell number in control and treatment group was quantified at 0 to 48h post irradiation and graph presented on log scale against time at single concentration of IL-6 (1ng/ml). Inset graph presents the cell number at 48 hours on two different concentrations of IL-6. **(C)** Dose response curve of Raw264.7 cells with or without IL-6 treatment. Surviving fraction was plotted against increasing radiation doses (0 to 8 Gy). Star shows the statistical significance of change between the groups calculated by one way ANOVA and Student's t test. Data are expressed as mean ± SD (n = 4) *p <0.05

Downloaded from https://academic.oup.com/jb/advance-article-abstract/doi/10.1093/jb/mvz091/5610530 by Delhi Technological University user on 06 November 2019

Figure 3: IL-6 induced radio-resistance is glycolysis dependent; **(A)** Glucose uptake and lactate production measured 2 hours post irradiation, as described **(B)** Immuno-blotting of key regulatory glycolytic enzymes was performed at 24 hours post irradiation. β-Actin was used as loading control. Values shown in between the blots are the average fold change value of densitometric analysis of 3 blots, normalized with respective β-Actin. **(C)** The mRNA levels of HK-2, PKM2 and PFKFB3 with respect to control were observed after 12 hours post irradiation **(D)** ATP levels in cells was measured by bioluminescence ATP assay kit at indicated time points and represented as ATP concentration per cell calculated from standard. **(E & F)** Cell number was quantified at 48 hrs. post irradiation in various treatment groups and plotted as bar graph with cell number on Y axis. **(G & H)** Cells were stained with AO/EtBr 24 h post irradiation and examined under a fluorescent microscope at 10x magnification. Zoomed images of dying cells are shown in inset for improved view. Dead cells (red) were counted from multiple images and the mean of dead cells per group was plotted as bar graph. Star shows the statistical significance of change between the groups calculated by Student's t test. Data are expressed as mean ± SD (n = 4) *p <0.05

Figure 4: IL-6 prevents mitochondrial damage from radiation **(A)** The Formazan formed per cell was quantified spectro-photometrically and presented as bar graph at indicated time points. **(B)** The mitochondrial mass was analyzed by staining cells with MitoTracker Green FM (100 nM; 20 min) at indicated time points. Graph showing mean fluorescence intensity (MFI), presented as fold change with respect to control. **(C&D)** Immunoblot showing protein expression of mitochondrial complex-II subunit SDH-A presented in Raw264.7 cells. The bar graph represents the fold increase in SDH levels quantified by densitometry and normalized with β-Actin. **(E)** Microscopic evaluation of mitochondrial membrane potential shown by distribution of JC-1-loaded mitochondria in response to radiation, the retention of green

Downloaded from https://academic.oup.com/jb/advance-article-abstract/doi/10.1093/jb/mvz091/5610530 by Delhi Technological University user on 06 November 2019

(monomer) and orange/yellow (aggregates) color represents the shift in mitochondrial membrane potential. Images were captures at 40x (objective) and 10x (eye piece) magnification. **(F)** Quantitative estimation of MMP by TMRM and normalized with respective mitochondrial content (data obtained from mitotracker green, fig;4B) at 4 and 24h post irradiation. **(G)** Photomicrograph shows the radiation change in mitochondrial calcium by staining the cells with A23187 (6 μM, 30 mins). Images were captured under fluorescence microscope with 40X objective. **(H)** Graph representing quantification of I-bodies formation per cell in different treatment groups. Data obtained from n=10 fields per group. Star shows the statistical significance of change between the groups calculated by Student's t test. Data are expressed as mean ± SD (n = 4) *p <0.05, # represents the significance with respect to the MMP/ mitochondrial mass of control group.

Figure 5: IL-6 induced glycolysis is Akt dependent **(A)** Phosphorylation of Akt at ser473 was detected at indicated time points after IL-6 treatment. **(B)** Cells treated with MK2206 (2.5uM) 15 min prior to IL-6 treatment followed by irradiation were harvested 1hr post irradiation for Western blotting. Akt1/2 siRNA (100nM) and Control (scramble) siRNA transfected cells were also treated with IL-6 followed by irradiation and harvested for Western blotting of pAkt and Akt levels. Total Akt levels was normalized with the values of beta actin (loading control). **(C)** Graph represents fold change in glucose uptake and lactate production per cell respectively in various treatment groups at 2hr. post irradiation. **(D)** Immuno-blot of total HK-2 protein with MK2206 and Akt siRNA. β-Actin used as loading control and (E) Cell number quantified at 48 hr. post irradiation in various treatment groups is presented as bar diagram. (F) Showing immunoblot of mitochondrial bound fraction of HK-2 where VDAC used as loading control. Values shown in between the blots are the average fold change value of densitometric analysis of 3 blots, normalized with respective β-Actin. Star shows the statistical significance of change between the groups calculated by one way

Downloaded from https://academic.oup.com/jb/advance-article-abstract/doi/10.1093/jb/mvz091/5610530 by Delhi Technological University user on 06 November 2019

ANOVA and Student's t test. # represents the statistical significance between siRNA or MK2206 group with respect to IL-6 pre-treated irradiated group. Data are expressed as mean ± SD (n = 4) *p <0.05

Figure 6: The picture illustrates that IL-6 treatment before irradiation activates PI3K-Akt pathway which resulted in the upregulation of important regulatory genes of Glycolysis. Akt also phosphorylates HK-2, which allows its binding to outer membrane of mitochondria where it facilitates efficient glucose phoshphorylation using mitochondrial ATP and ensures rapid rate of glycolysis. Efficient supply of energy (ATP) for repair of radiation induced macro-molecular and cellular damages and moonlighting functions of glycolytic enzymes like prevention of cytochrome C release from mitochondria by HK-2 resulted in IL-6 induced radio-resistance.

Conflict of Interest

We wish to confirm that there are no known conflicts of interest associated with this publication. We confirm that the manuscript has been read and approved by all named authors and that there are no other persons who satisfied the criteria for authorship but are not listed. We further confirm that the order of authors listed in the manuscript has been approved by all co-authors.

Funding

This work was supported by grant (INM 311/1.4) funded by Defence Research and Development Organisation, Government of India. The funders had no role in study design, data collection and analysis, decision to publish, or preparation of the manuscript.

Downloaded from https://academic.oup.com/jb/advance-article-abstract/doi/10.1093/jb/mvz091/5610530 by Delhi Technological University user on 06 November 2019

Downloaded from https://academic.oup.com/jb/advance-article-abstract/doi/10.1093/jb/mvz091/5610530 by Delhi Technological University user on 06 November 2019

Figure 1

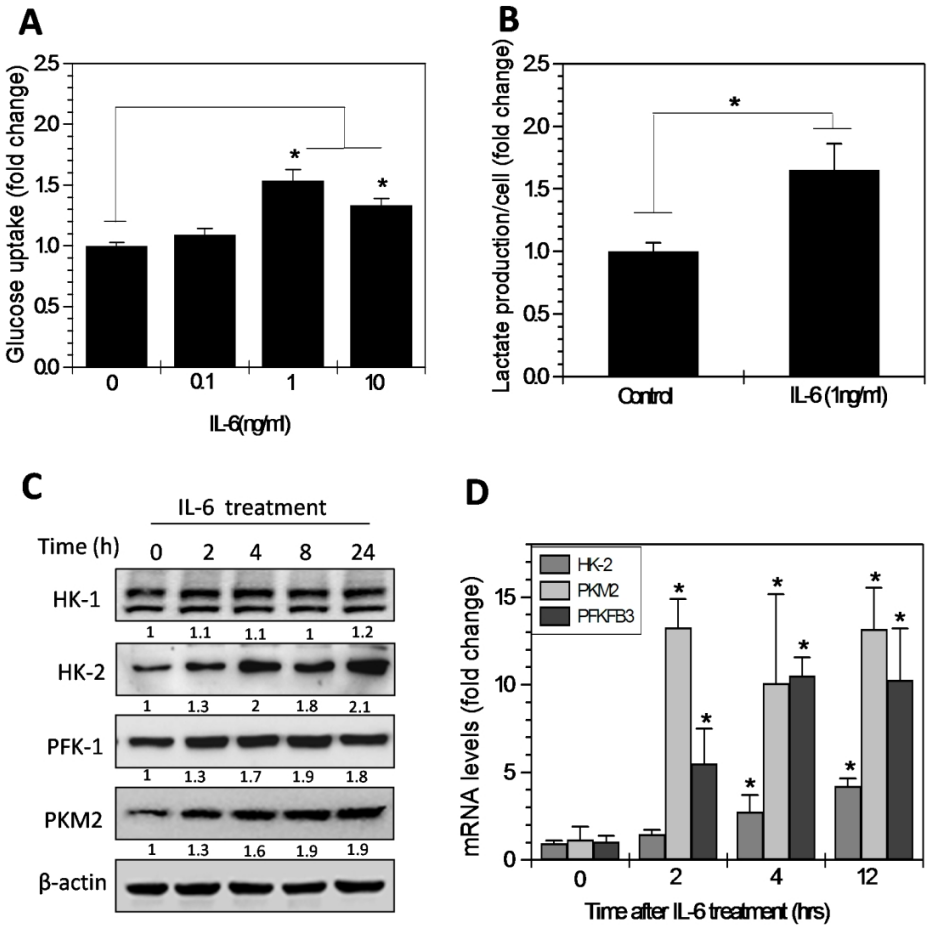


Figure 1: IL-6 induced rate of glycolysis was measured by observing glucose uptake and lactate production in cells after IL-6 treatment. Glucose uptake (A) and lactate production (B) was measured in culture media, 2 hours after IL-6 treatment. (C) Protein levels of various glycolytic regulatory enzymes (indicated in figure) were measured in untreated and IL-6 (1ng/ml) treated cells at given time points. β-Actin was used as loading control. Values shown in between the blots are the average fold change value of densitometric analysis of 3 blots, normalized with respective β-Actin. (D) The mRNA levels of HK-2, PKM2 and PFKFB3 genes at indicated time points after IL-6 (1ng/ml) treatment. Statistical significance calculated by one way ANOVA and Student's t test between the groups. Data are expressed as mean ± SD (n = 4) *p <0.05

481x545mm (96 x 96 DPI)

Downloaded from https://academic.oup.com/jb/advance-article-abstract/doi/10.1093/jb/mvz091/5610530 by Delhi Technological University user on 06 November 2019

Figure 2

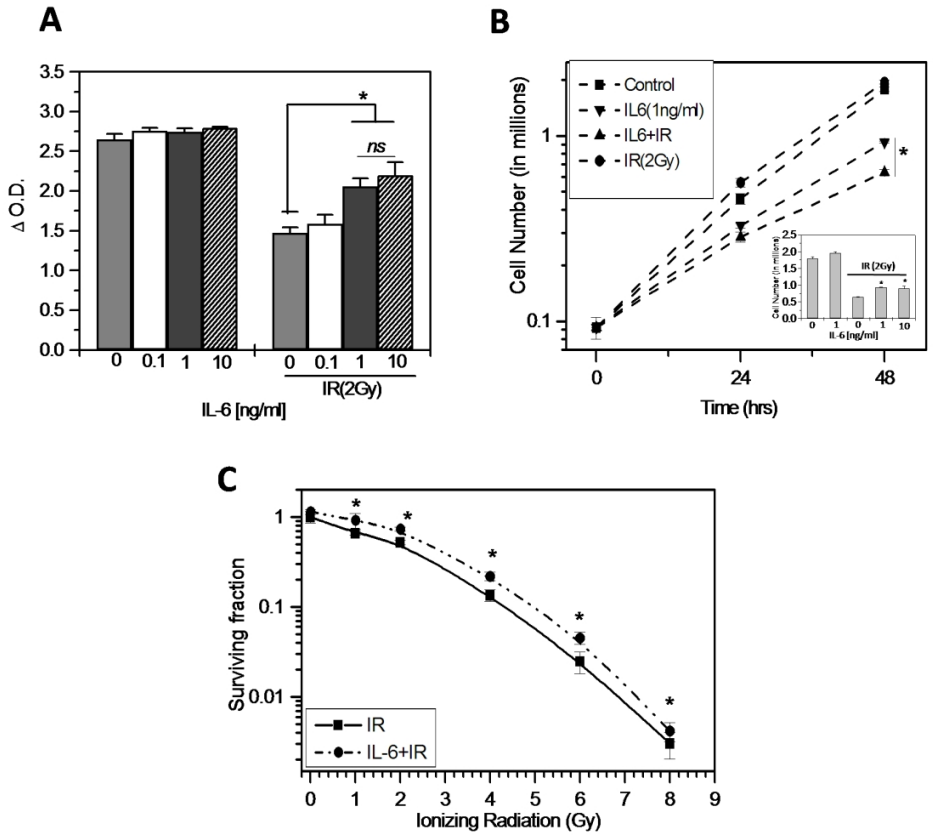


Figure 2: IL-6 confers radio-resistance (A) SRB assay carried out at 48h post irradiation using different concentrations of IL-6 (0.1 to 10ng/ml). Graph (ΔOD 340nm) plotted and treatment groups were compared with their respective control. (B) The cell number in control and treatment group was quantified at 0 to 48h post irradiation and graph presented on log scale against time at single concentration of IL-6 (1ng/ml). Inset graph presents the cell number at 48 hours on two different concentrations of IL-6. (C) Dose response curve of Raw264.7 cells with or without IL-6 treatment. Surviving fraction was plotted against increasing radiation doses (0 to 8 Gy). Star shows the statistical significance of change between the groups calculated by one way ANOVA and Student's t test. Data are expressed as mean ± SD (n = 4) *p <0.05

509x524mm (96 x 96 DPI)

Downloaded from https://academic.oup.com/jb/advance-article-abstract/doi/10.1093/jb/mvz091/5610530 by Delhi Technological University user on 06 November 2019

Figure 3

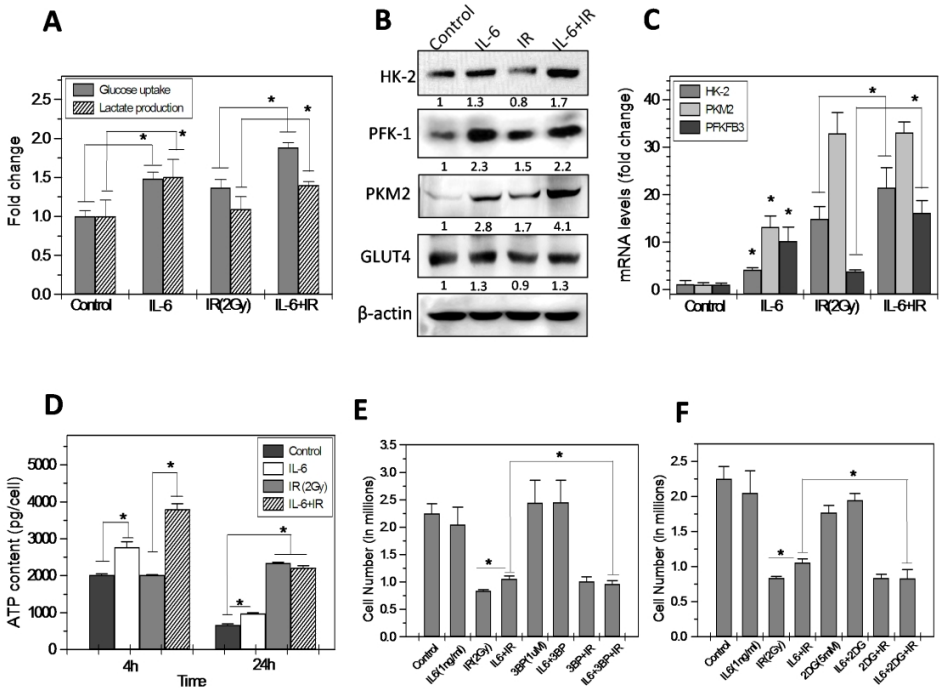


Figure 3: IL-6 induced radio-resistance is glycolysis dependent; (A) Glucose uptake and lactate production measured 2 hours post irradiation, as described (B) Immuno-blotting of key regulatory glycolytic enzymes was performed at 24 hours post irradiation. β-Actin was used as loading control. Values shown in between the blots are the average fold change value of densitometric analysis of 3 blots, normalized with respective β-Actin. (C) The mRNA levels of HK-2, PKM2 and PFKFB3 with respect to control were observed after 12 hours post irradiation (D) ATP levels in cells was measured by bioluminescence ATP assay kit at indicated time points and represented as ATP concentration per cell calculated from standard. (E & F) Cell number was quantified at 48 hrs. post irradiation in various treatment groups and plotted as bar graph with cell number on Y axis.

601x507mm (96 x 96 DPI)

Downloaded from https://academic.oup.com/jb/advance-article-abstract/doi/10.1093/jb/mvz091/5610530 by Delhi Technological University user on 06 November 2019

Figure 3

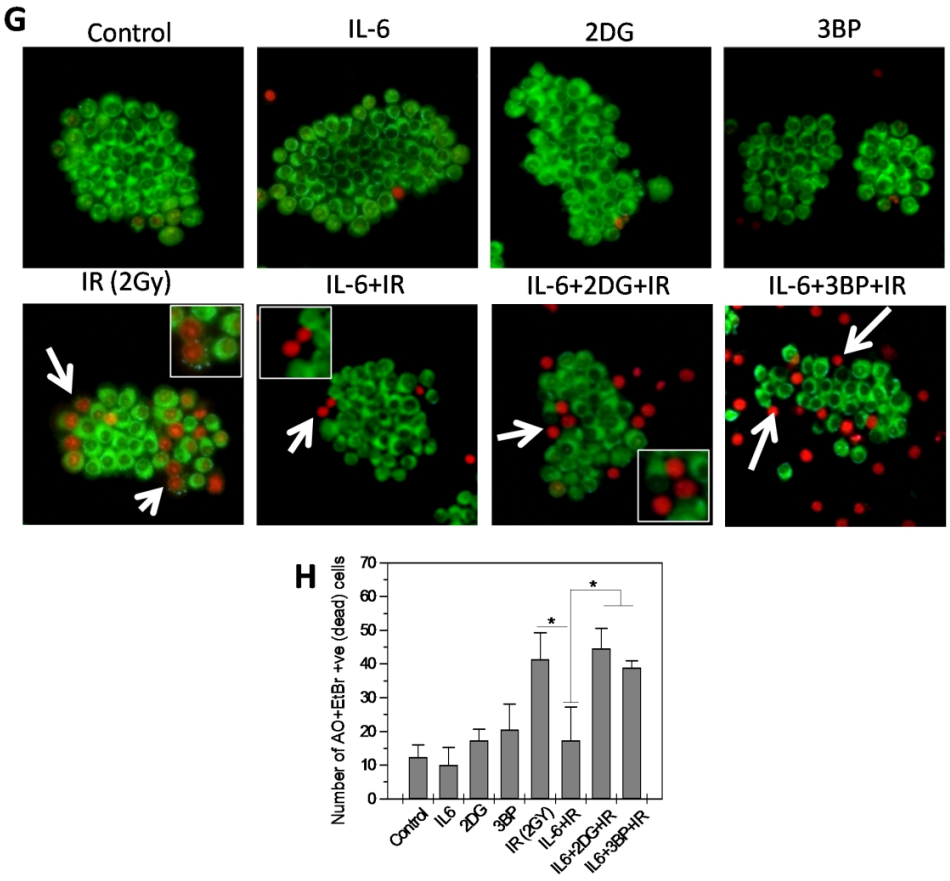


Figure 3 Continued(G & H) Cells were stained with AO/EtBr 24 h post irradiation and examined under a fluorescent microscope at 10x magnification. Zoomed images of dying cells are shown in inset for improved view. Dead cells (red) were counted from multiple images and the mean of dead cells per group was plotted as bar graph. Star shows the statistical significance of change between the groups calculated by Student's t test. Data are expressed as mean ± SD (n = 4) *p <0.05

523x545mm (96 x 96 DPI)

Downloaded from https://academic.oup.com/jb/advance-article-abstract/doi/10.1093/jb/mvz091/5610530 by Delhi Technological University user on 06 November 2019

Figure 4

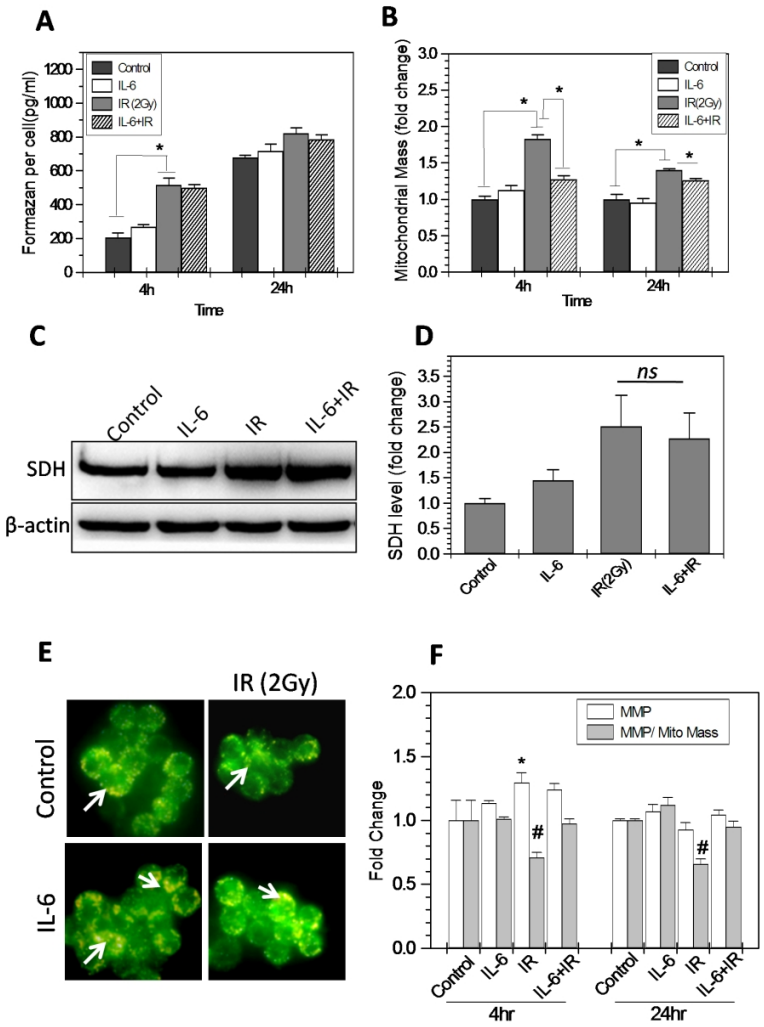
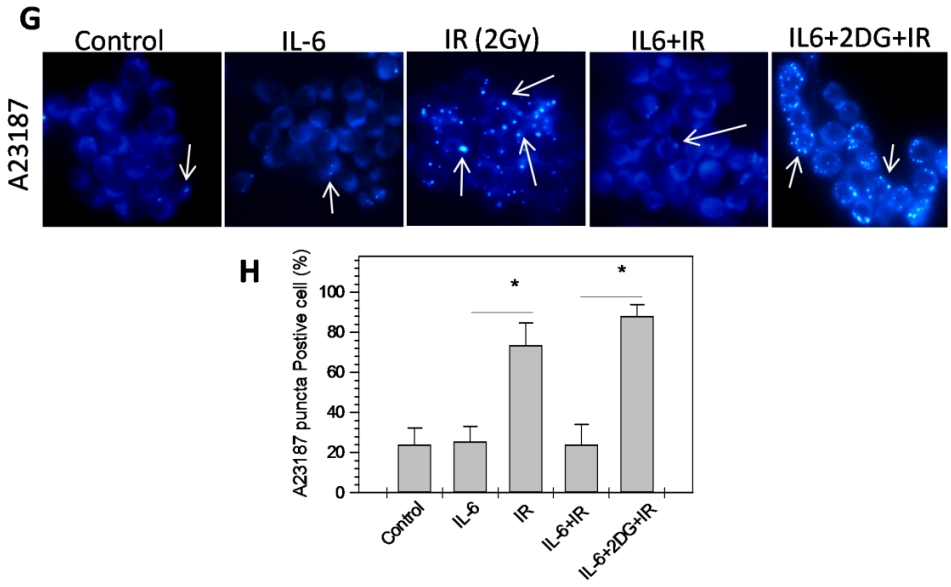


Figure 4: IL-6 prevents mitochondrial damage from radiation (A) The Formazan formed per cell was quantified spectro-photometrically and presented as bar graph at indicated time points. (B) The mitochondrial mass was analyzed by staining cells with MitoTracker Green FM (100 nM; 20 min) at indicated time points. Graph showing mean fluorescence intensity (MFI), presented as fold change with respect to control. (C&D) Immunoblot showing protein expression of mitochondrial complex-II subunit SDH-A presented in Raw264.7 cells. The bar graph represents the fold increase in SDH levels quantified by densitometry and normalized with β-Actin. (E) Microscopic evaluation of mitochondrial membrane potential shown by distribution of JC-1-loaded mitochondria in response to radiation, the retention of green (monomer) and orange/yellow (aggregates) color represents the shift in mitochondrial membrane potential. Images were captures at 40x (objective) and 10x (eye piece) magnification. (F) Quantitative estimation of MMP by TMRM and normalized with respective mitochondrial content (data obtained from mitotracker green, fig;4B) at 4 and 24h post irradiation.

456x664mm (96 x 96 DPI)

Downloaded from https://academic.oup.com/jb/advance-article-abstract/doi/10.1093/jb/mvz091/5610530 by Delhi Technological University user on 06 November 2019

Figure 4



(G) Photomicrograph shows the radiation change in mitochondrial calcium by staining the cells with A23187 (6 μM, 30 mins). Images were captured under fluorescence microscope with 40X objective. (H) Graph representing quantification of I-bodies formation per cell in different treatment groups. Data obtained from n=10 fields per group. Star shows the statistical significance of change between the groups calculated by Student's t test. Data are expressed as mean ± SD (n = 4) *p <0.05, # represents the significance with respect to the MMP/ mitochondrial mass of control group.

495x402mm (96 x 96 DPI)

Downloaded from https://academic.oup.com/jb/advance-article-abstract/doi/10.1093/jb/mvz091/5610530 by Delhi Technological University user on 06 November 2019

Figure 5

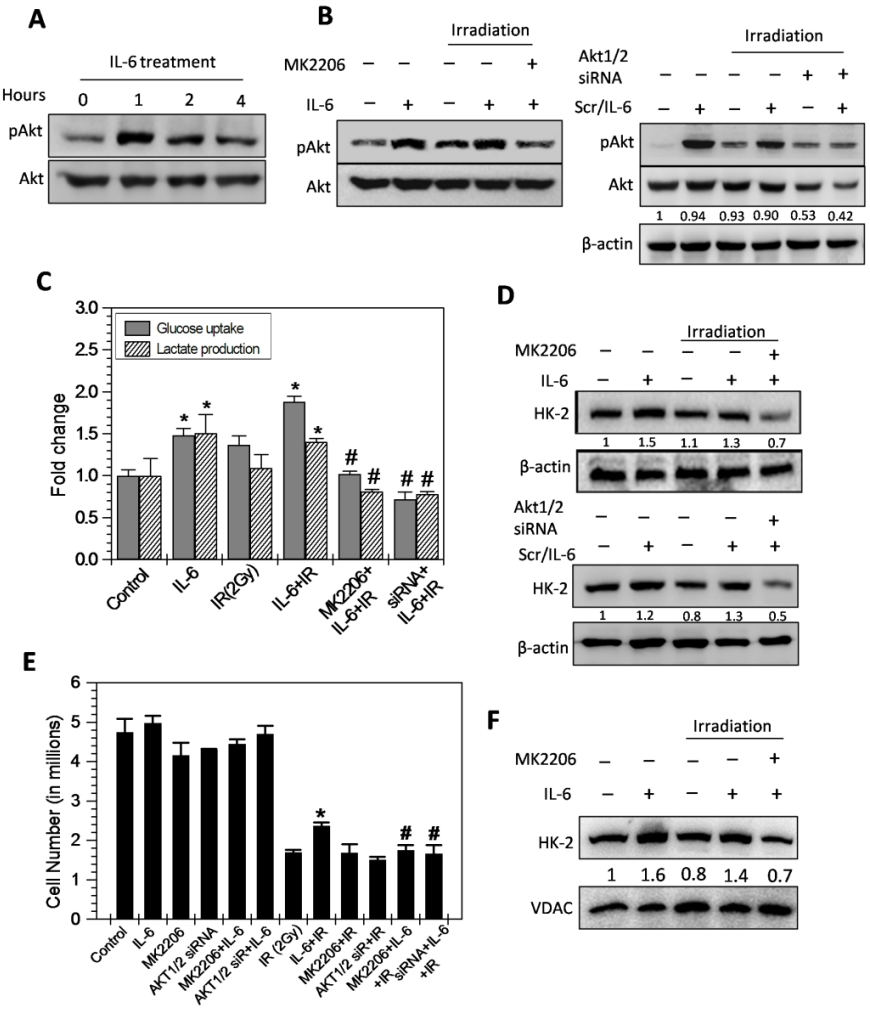


Figure 5: IL-6 induced glycolysis is Akt dependent (A) Phosphorylation of Akt at ser473 was detected at indicated time points after IL-6 treatment. (B) Cells treated with MK2206 (2.5uM) 15 min prior to IL-6 treatment followed by irradiation were harvested 1hr post irradiation for Western blotting. Akt1/2 siRNA (100nM) and Control (scramble) siRNA transfected cells were also treated with IL-6 followed by irradiation and harvested for Western blotting of pAkt and Akt levels. Total Akt levels was normalized with the values of beta actin (loading control). (C) Graph represents fold change in glucose uptake and lactate production per cell respectively in various treatment groups at 2hr. post irradiation. (D) Immuno-blot of total HK-2 protein with MK2206 and Akt siRNA. β-Actin used as loading control and (E) Cell number quantified at 48 hr. post irradiation in various treatment groups is presented as bar diagram. (F) Showing immunoblot of mitochondrial bound fraction of HK-2 where VDAC used as loading control. Values shown in between the blots are the average fold change value of densitometric analysis of 3 blots, normalized with respective β-Actin. Star shows the statistical significance of change between the groups calculated by one way ANOVA and Student's t test. # represents the statistical significance between siRNA or MK2206 group with respect to IL-6 pre-treated irradiated group. Data are expressed as mean ± SD (n = 4) *p <0.05

Downloaded from https://academic.oup.com/jb/advance-article-abstract/doi/10.1093/jb/mvz091/5610530 by Delhi Technological University user on 06 November 2019

537x709mm (96 x 96 DPI)

Downloaded from https://academic.oup.com/jb/advance-article-abstract/doi/10.1093/jb/mvz091/5610530 by Delhi Technological University user on 06 November 2019

Figure 6

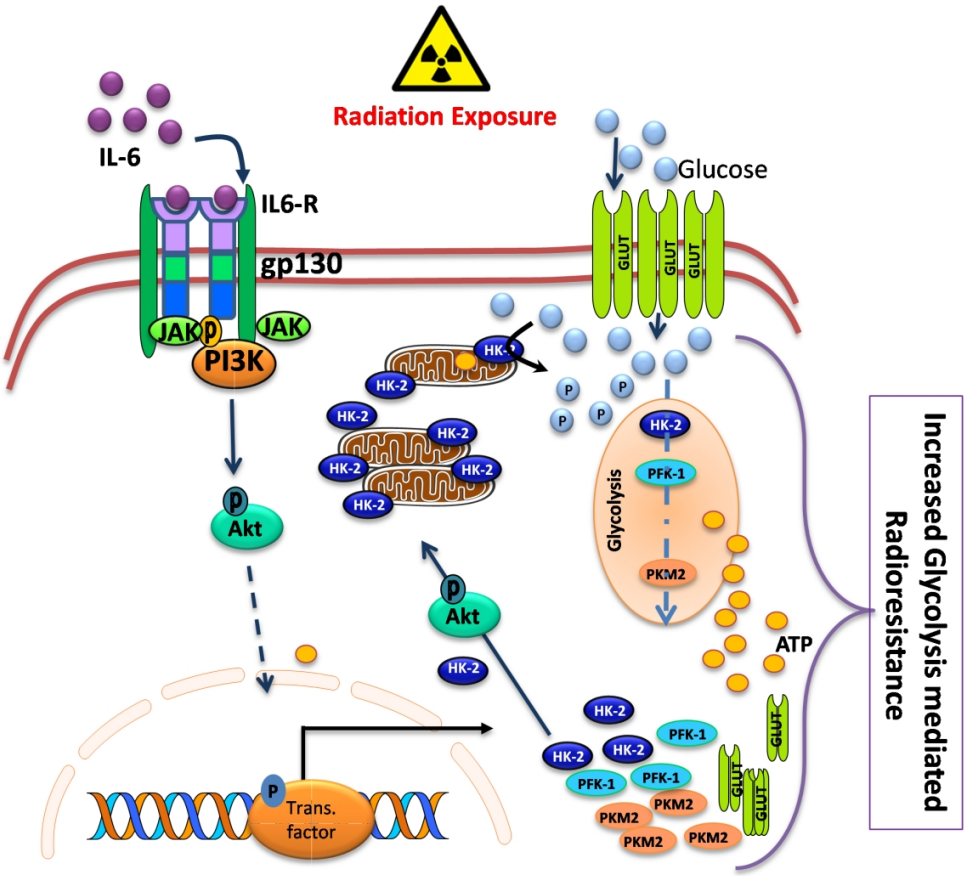


Figure 6: The picture illustrates that IL-6 treatment before irradiation activates PI3K-Akt pathway which resulted in the upregulation of important regulatory genes of Glycolysis. Akt also phosphorylates HK-2, which allows its binding to outer membrane of mitochondria where it facilitates efficient glucose phoshphorylation using mitochondrial ATP and ensures rapid rate of glycolysis. Efficient supply of energy (ATP) for repair of radiation induced macro-molecular and cellular damages and moonlighting functions of glycolytic enzymes like prevention of cytochrome C release from mitochondria by HK-2 resulted in IL-6 induced radio-resistance.

533x598mm (96 x 96 DPI)

Downloaded from https://academic.oup.com/jb/advance-article-abstract/doi/10.1093/jb/mvz091/5610530 by Delhi Technological University user on 06 November 2019

Load Flow Solution for Radial Distribution Network

Om Pathak
Department Of Electrical Engineering
Delhi Technological university
Delhi,India
ompathak95@gmail.com

Prem Prakash
Department Of Electrical Engineering
Delhi Technological University
Delhi,India
ppyadav1974@gmail.com

***Abstract*—The paper proposes an elementary and straightforward approach for load flow evaluation for radial distribution networks. Two developed matrices – BIBC and BCBV (the bus injection to branch current matrix and the branch current to bus voltage matrix) and an easy matrix multiplication are applied to get load flow results. The developed matrices are formed with help of backward and forward sweep (BFS method) using KCL and KVL (Kirchhoff's current law and Kirchhoff's voltage law respectively). This approach can be enforced to the solution for three-phase and for single-phase configuration of the system. The considered method finds the array of branches for feeders, laterals and sub laterals. The presented algorithm has been tested for IEEE 85 bus system without tie lines. The algorithm converged well for constant power, constant current, constant impedance and composite load modeling.**

Keywords — radial distribution system, load-flow, BIBC and BCBV matrix, backward forward sweep method, load models.

I. INTRODUCTION

The Load Flow Analysis is an essential requirement for power system studies as the flow of power from generators to loads should be balanced, reliable and economical. The Load flow information is useful for analysis of the normal operating mode and contingency analysis, outage security appraisal, dispatching and stability [1]-[2][14]. Various approaches for solution of load flow problem like Gauss-Seidel, Newton-Raphson and Fast Decoupled load flow have been studied and extensively used in power system operation, control, and planning. These techniques are not appropriate in case of distribution systems due to their special characteristics such as radial and weak structure, multiphase operation, unbalancing, continuous load fluctuation, extensive branch network and higher number of nodes, higher resistance and reactance values in comparison with transmission networks. Methods developed for the radial distribution systems may be studied into two sections, one is forward-backward sweep process to solve ladder networks and the other is by rectifying the existing methods such as Newton-Raphson.

BFS methodology is the most suitable process for calculations of distribution load flow. The first version of this method was developed using a radial system model and considering only constant complex power nodes. Several corrections are made since it was firstly proposed [3]; these modifications can solve systems with a weakly meshed topology [4], [5], voltage dependent loads systems [7], systems with DG (distributed generation) [15], three-phase systems [6], or three-phase star systems, including neutral grounding [10]. An approach for weakly meshed systems in which the loops are broken and the network is converted into radial was given in [4]; calculation of the breakpoint currents with the help of multi-port compensation. The approach was later improved in [5]. A further expansion of this solution method included some important features, such as three-phase systems, PV node, distributed generation, distributed loads, or voltage regulators [6]. Reference [11] proposed an approach to solve radial and meshed systems in which only a backward sweep method is required. A thorough comparison and analysis of backward forward sweep methods is presented in [12]. Data for IEEE 85 bus are taken from [13]. The base values are considered as 100 MVA and 12.66 kV.

Conducting load flow evaluation for multiple scenarios ensures that the system is appropriately designed to meet the performance criteria. A perfect drafted system provides calculation for initial capital investments and future operating costs. Load flow analysis is required when:

- Significant plant or load expansion occurs
- Local generation is proposed to be added
- New utility feed installation
- Large motor is added to the system
- New transformer installation etc.

Normally prior to the analysis, we need three phase voltage at sub-station and complex power of all the loads and load models.

A power flow analysis of a feeder can determine the following by phase and total three phase:

- Magnitude of voltage and angles at each buses
- Power flow in each section having units as kW and kVAr, ampere and degrees.
- Line loss in all line section.
- Total feeder input in kW and kVAr.
- Total power loss in feeder.

II. .LOAD MODELING

Loads modeling developed is to be used in the process of iteration of a power flow program where the initial values of node voltage are assumed. Load on a feeder can be modeled as wye-connected or delta connected. The modeling of load can be done as :

- Constant complex power(constant PQ)
- Constant current (constant I)
- Constant impedance (constant Z)
- Composite (ZIP)

978-1-5386-6625-8/18/$31.00 ©2018 IEEE

All models are initially defined by a complex power per phase and an assumed line to neutral voltage (wye load) or an assumed line to line voltage (delta load).

The notation for the complex powers and voltage are as :

$$S = P + j * Q = |S| \angle \theta$$

$$V = |V| \angle \delta$$

i) CONSTANT PQ LOADS :-

The line currents for constant complex power loads are given by

$$IL_{PQ} = \left[\frac{|S|}{|V|} \right] \angle (\delta - \theta) \quad (1)$$

In this modeling, the value of load voltage will change in each iteration to achieve convergence.

ii) CONSTANT IMPEDANCE (Z) LOADS :-

In this model, the constant load impedance is determined first. The calculation is based upon the complex power and assumed voltages, given as

$$Z = \left[\frac{|V|^2}{|S|} \right] \angle \theta \quad (2)$$

Load currents as a function of the constant load impedance are given by

$$IL_Z = \left[\frac{|V|}{|Z|} \right] \angle (\delta - \theta) \quad (3)$$

iii) CONSTANT CURRENT LOADS:-

In this modeling the magnitudes of the currents are calculated according to Equation (1) and are then held constant while the angle of the voltage (delta) changes, resulting in a changing angle of the current such that the load power factor remains constant.

$$IL_I = (S/V)^* = \left[\frac{|S|}{|V|} \right] \angle (\delta - \theta) \quad (4)$$

Where δ = voltage angle

θ = power factor angle

iv) COMPOSITE LOAD (ZIP LOADS):-

ZIP loads are modeled by assigning a percentage of the total load to the three above load models. The total line current entering the load is the addition of the three load current components. The values of ZIP coefficients can be changed according to system specification.

ZIP COEFFICIENTS:-

- ZP = percentage of constant Z-type load
- IP = percentage of constant I-type load
- SP = percentage of constant PQ-type loads

Here we have taken, ZP=0.30, IP=0.10, SP=0.60

As $ZP + IP + SP = 1$

$$IL_{ZIP} = I_Z + I_I + I_{PQ} \quad (5)$$

Thus $I_Z = ZP * IL_Z$

$$I_I = IP * IL_I$$

$$I_{PQ} = SP * IL_{PQ}$$

III. BIBC AND BCBV MATRIX.

A. BIBC MATRIX

It explains a direct correlation of the node current injection with branch current. The power injections at every node might be transformed into the equivalent current injection using (1), (3), (4) and (5). The relation of node current with branch current can be easily obtain by applying KCL (Kirchhoff's current law) with backward sweep. Now each the branch current can be shaped as a function of the equivalent current injection (ECI) [9].For example, in fig. 1, branch currents IB1, IB2 and IB3 can be expressed by ECI as

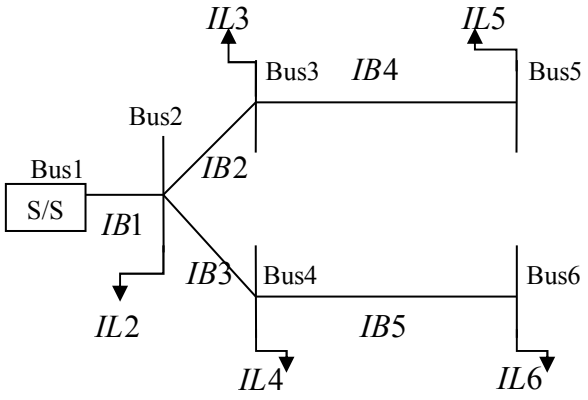


Fig.1. Simple distribution system

$$IB1 = IL2 + IL3 + IL4 + IL5 + IL6$$
$$IB2 = IL3 + IL5 \quad (6)$$
$$IB3 = IL4 + IL6$$

$$\begin{bmatrix} IB1 \\ IB2 \\ IB3 \\ IB4 \\ IB5 \end{bmatrix} = \begin{bmatrix} 1 & 1 & 1 & 1 & 1 \\ 0 & 1 & 0 & 1 & 0 \\ 0 & 0 & 1 & 0 & 1 \\ 0 & 0 & 0 & 1 & 0 \\ 0 & 0 & 0 & 0 & 1 \end{bmatrix} \begin{bmatrix} IL2 \\ IL3 \\ IL4 \\ IL5 \\ IL6 \end{bmatrix}$$

$$[IB_i] = [BIBC][IL_{i+1}] \quad (7)$$

B. BCBV MATRIX

It builds a direct correlation of branch current with node voltage. This relation can be achieved easily by applying

KVL (Kirchhoff's voltage law) with forward sweep. It can be calculated using $[BIBC]$ and diagonal impedance matrix $[ZD]$ as given in step-IV of algorithm.

IV. ALGORITHM FOR LOAD FLOW OF DISTRIBUTION NETWORKS

- Step-I: Read the input line and bus data.
- Step-II: Determine the each node current or node current injection matrix using (1), (3), (4), (5), (6) and (7).
- Step-III: Calculate BIBC matrix as shown.
- Step-IV: Calculate the $[BCBV]$ matrix using $[BIBC]$ and diagonal impedance matrix $[ZD]$

$$[BCBV] = [BIBC]^T [ZD]$$

- Step-V: Calculate $[DLF]$ with simple multiplication of $[BCBV]$ and $[BIBC]$

$$[DLF] = [BCBV][BIBC]$$

- Step-VI: Evaluate the branch currents by using $[BIBC]$ matrix and equivalent current injections for their respective load models,

$$[IB] = [BIBC][IL]$$
$$[\nabla V] = [DLF][IL]$$

- Step-VII: Set iteration, $K = 0$
- Step-VIII: Iteration, $K = K + 1$
- Step-IX: Update voltage by using specified load models

$$[\nabla V^{K+1}] = [DLF][IL^K]$$
$$[V^{K+1}] = [V^0] + [\nabla V^{K+1}]$$

- Step-X: If max $[|V(K+1)| - |V(K)|]$ > tolerance, go to step VIII for next iteration.
- Step-XI: Calculate branch currents and losses from final node voltage.
- Step-XII: Display the magnitudes of node voltage and losses
- Step-XIII: Stop.

V. RESULT AND ANALYSIS

The bus voltage of 85 bus system is given in tables (1)-(4) for specific load modeling. Depending upon tolerance value, number of iterations may vary. The convergence tolerance is set at 0.0001. The proposed method took five iterations to give converged solution. The comparison of load models with minimum bus voltage value is given in table (5) that clearly shows that power loss decreases after including the voltage dependent loads than voltage independent loads in the system although the fraction of ZIP constant may vary according to given system.

Voltage profile for various load modeling is given in fig. (2),that clearly shows the effect of voltage dependency in voltage profile of system. The time consuming algorithms, such as the forward/backward substitution of the Jacobian matrix or Y matrix and LU factorization are not required in the proposed method. Thus, the proposed method is robust and efficient. As in the proposed method we require relation matrices (i.e. BIBC and BCBV) for load flow solutions.

Table 1: VOLTAGE FOR CONSTANT POWER LOAD

Bus Number	Voltage Magnitude	Bus Number	Voltage magnitude
1	1	43	0.913163473
2	0.996763383	44	0.909191564
3	0.991961686	45	0.90843817
4	0.985832424	46	0.907999055
5	0.982850117	47	0.907924347
6	0.972131486	48	0.907123738
7	0.965541085	49	0.906934619
8	0.937001954	50	0.906605549
9	0.935621435	51	0.906355812
10	0.932751977	52	0.905304842
11	0.930488718	53	0.904897
12	0.928573183	**54**	**0.904597046**
13	0.927849578	55	0.905067263
14	0.927630399	56	0.906859823
15	0.927499026	57	0.933794547
16	0.996534503	58	0.928748696
17	0.991505099	59	0.928651431
18	0.980813633	60	0.925682417
19	0.979555154	61	0.92489928
20	0.97911792	62	0.924360475
21	0.978593215	63	0.924955006
22	0.978097384	64	0.922138455
23	0.979462936	65	0.922015988
24	0.965245594	66	0.921918013
25	0.932915472	67	0.920685002
26	0.929771661	68	0.918580545
27	0.925645237	69	0.917022113
28	0.923729682	70	0.916619451
29	0.920193906	71	0.916432911
30	0.916954953	72	0.920586885
31	0.915429298	73	0.917534278
32	0.914475823	74	0.917386394
33	0.9137094	75	0.917191917
34	0.910365918	76	0.916323337
35	0.908634867	77	0.922003791
36	0.908572232	78	0.932412342
37	0.92957694	79	0.920499286
38	0.925106482	80	0.927242516
39	0.919898942	81	0.92677273
40	0.914007403	82	0.926724189
41	0.913319643	83	0.925950077
42	0.913226046	84	0.92553474
		85	0.927572884

Table 2: VOLTAGE FOR CONSTANT Z MODEL

Bus Number	Voltage Magnitude	Bus Number	Voltage magnitude
1	1	43	0.925561241
2	0.997155242	44	0.922257358
3	0.992941904	45	0.92162694
4	0.987591283	46	0.921259638
5	0.984994341	47	0.921197154
6	0.975777411	48	0.920540746
7	0.970119388	49	0.920383022
8	0.945651463	50	0.920108606
9	0.944458592	51	0.919900387
10	0.941961471	52	0.919028909
11	0.939994497	53	0.918689992
12	0.938331588	**54**	**0.918440786**
13	0.937702377	55	0.918831337
14	0.937511789	56	0.920320597
15	0.937397569	57	0.942887055
16	0.996927856	58	0.938554881
17	0.992492594	59	0.938470114
18	0.983036289	60	0.935925758
19	0.98182713	61	0.935248714
20	0.98140742	62	0.93478315
21	0.980904004	63	0.935304265
22	0.980428526	64	0.932898749
23	0.981738454	65	0.932793438
24	0.969842768	66	0.932709191
25	0.942186042	67	0.931659108
26	0.939523567	68	0.929867837
27	0.936044034	69	0.928541974
28	0.934431907	70	0.928199567
29	0.93146232	71	0.928040917
30	0.928746704	72	0.931574964
31	0.927468704	73	0.928976452
32	0.926670682	74	0.928850439
33	0.926030827	75	0.928684837
34	0.923240595	76	0.927947782
35	0.921798606	77	0.932782948
36	0.921746151	78	0.941663267
37	0.939353537	79	0.931499867
38	0.93557774	80	0.937177296
39	0.93120965	81	0.936770036
40	0.926274548	82	0.936727898
41	0.925693234	83	0.936057474
42	0.925614117	84	0.935697819
		85	0.937461774

Table 3: VOLTAGE FOR CONSTANT I LOAD MODEL

Bus Number	Voltage Magnitude	Bus Number	Voltage magnitude
1	1	43	0.920096843
2	0.996981778	44	0.91650148
3	0.992508005	45	0.915817279
4	0.986812819	46	0.915418574
5	0.984045379	47	0.915350745
6	0.974165187	48	0.914631755
7	0.968095437	49	0.914460319
8	0.941830056	50	0.914162034
9	0.940553976	51	0.913935684
10	0.937891249	52	0.91298599
11	0.93579254	53	0.912617013
12	0.934017341	**54**	**0.912345677**
13	0.93334615	55	0.912770965
14	0.933142847	56	0.91439249
15	0.933020999	57	0.938869411
16	0.996753692	58	0.934221503
17	0.992055296	59	0.934131178
18	0.982050816	60	0.931399053
19	0.980818685	61	0.930674948
20	0.980390808	62	0.930176901
21	0.979877466	63	0.930730773
22	0.979392495	64	0.928143713
23	0.98072836	65	0.928030806
24	0.967810216	66	0.927940481
25	0.938091854	67	0.926809678
26	0.935218053	68	0.924880234
27	0.931454905	69	0.923451781
28	0.929709834	70	0.923082799
29	0.926492345	71	0.922911847
30	0.923547725	72	0.926719353
31	0.922161388	73	0.923920494
32	0.921295385	74	0.923784828
33	0.920600232	75	0.923606484
34	0.917568318	76	0.922811463
35	0.916000144	77	0.928019561
36	0.915943236	78	0.93757457
37	0.935037045	79	0.926638727
38	0.930956502	80	0.932784671
39	0.926221009	81	0.93234963
40	0.920867505	82	0.932304646
41	0.920239452	83	0.931588166
42	0.920153977	84	0.931203778
		85	0.933089497

Table 4: VOLTAGE FOR COMPOSITE LOAD MODEL

Bus Number	Voltage Magnitude	Bus Number	Voltage Magnitude
1	1	43	0.9179885
2	0.99691558	44	0.91427772
3	0.992342407	45	0.91357234
4	0.986515611	46	0.91316127
5	0.983683012	47	0.91309134
6	0.97354827	48	0.91234722
7	0.967320415	49	0.91217037
8	0.940364377	50	0.91186266
9	0.939056653	51	0.91162914
10	0.936331455	52	0.91064837

11	0.934182994	53	0.91026747
12	0.932365344	**54**	**0.90998736**
13	0.931678308	55	0.91042643
14	0.931470205	56	0.91210041
15	0.931345477	57	0.9373289
16	0.996687266	58	0.93256017
17	0.991888579	59	0.93246775
18	0.981676186	60	0.92966364
19	0.980436342	61	0.92892166
20	0.980005722	62	0.92841127
21	0.979489048	63	0.92897738
22	0.979000891	64	0.9263205
23	0.980345463	65	0.92620469
24	0.96703218	66	0.92611204
25	0.936520065	67	0.92495011
26	0.933563965	68	0.92296735
27	0.929689949	69	0.9214993
28	0.927892816	70	0.92112005
29	0.924578067	71	0.92094435
30	0.921543454	72	0.92485742
31	0.920114508	73	0.92198126
32	0.919221744	74	0.92184187
33	0.91850477	75	0.92165862
34	0.915377445	76	0.92084116
35	0.913759363	77	0.92619315
36	0.913700703	78	0.93600787
37	0.933378822	79	0.92477467
38	0.929179342	80	0.93110302
39	0.924299559	81	0.93065747
40	0.918781504	82	0.93061141
41	0.918135243	83	0.92987748
42	0.918047292	84	0.92948372
		85	0.9314156

TABLE 5: TOTAL POWER LOSS AND MINIMUM OF BUS VOLTAGE VALUE

Types of Load	**Total real Power loss(kW)**	**Total reactive Power loss (kVAr)**	**Node No.**	**Minimum Voltage value (per unit)**
Constant Power	234.4670	147.8563	54	0.904597
Constant Z	173.9550	109.9251	54	0.918440
Constant I	199.5502	125.9818	54	0.912345
Composite (ZIP)	209.8584	132.4394	54	0.909987

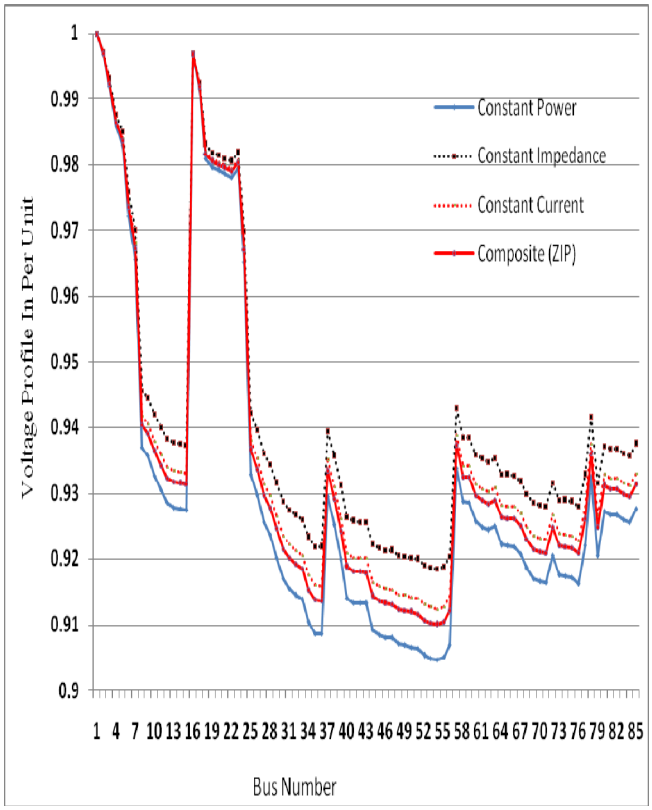


Figure 2: Voltage profile for 85 bus system for specified loads

VI. CONCLUSION

An efficient and decent method for load flow calculation is presented in the paper named forward backward sweep method with the help of BIBC matrix and BCBV matrix. The presented methodology converges for complex power modeling, constant impedance modeling, constant current modeling and composite load modeling. This methodology has been tested for IEEE 85 bus system without tie lines. From the results it is observed that the power loss decreases after including the voltage dependent loads than the voltage independent loads. After this loss evaluation, the various loss minimizing methods and improvement in voltage profile can be applied.

REFERENCES

[1] IEEE Tutorial Course on 'Distribution Automation'.

[2] IEEE Tutorial Course on 'Power Distribution Planning'.

[3] R. Berg et al, "Mechanized calculation of unbalanced load flow on radial distribution circuits," IEEE Transactions On Power Apparatus and Systems, vol. 86, no.4, pp. 415-421, April 1967.

[4] D. Shirmohammadi et al, "A compensation based power flow method for weakly meshed distribution networks," IEEE Transaction on Power Systems, vol. 3, no. 2, pp. 753-762, May 1988.

[5] Luo and Semlyen, "Efficient load flow for large weakly meshed networks," IEEE Trans. on Power Systems, vol. 5, no. 4, pp. 1309-1316, November 1990.

[6] C.S. Cheng and Shirmohammadi, "A three phase power flow method for real time distribution system analysis," IEEE Trans. on Power Systems, vol. 10, no. 2, pp. 671–679, May 1995.

[7] M.H. Haque, "Load flow solution of distribution systems with voltage dependent load models," Electric Power System Research, vol. 36, pp. 151-156, 1996.

[8] Y. Zhu and Tomsovic, “Adaptive power flow method for distribution systems with dispersed generation,” IEEE Transactions on Power Delivery, vol. 17, no. 3, pp. 822–827, July 2002.

[9] Jen-Hao Teng ,” A direct approach for distribution system load flow solutions” IEEE transactions on power delivery, vol. 18, no. 3,pp. 882-887,July 2003.

[10] R.M. Ciric et al,, “Power flow in fourwire distribution networks – General approach,” IEEE Trans. on Power Systems, vol. 18, no. 4, pp. 1283-1290, November 2003.

[11] A. Augugliaro et al., “A backward sweep method for power flow solution in distribution networks,” Electrical Power and Energy System, vol. 32, pp. 271-280, 2010.

[12] Eminoglu and Hocaoglu, “Distribution systems forward/ backward sweep based power flow algorithms: A review and comparison study,” *Electric Power Components and Systems*, vol. 37, pp. 91-110, 2009.

[13] D. Das et al. “Simple and efficient method for load flow solution of radial distribution system” Electrical Power and Energy Systems, vol. 17, no. 5, pp. 335-346, 1995.

[14] Kersting, William. (2007). Distribution System Modeling and Analysis. 10.1201/9781420009255.book

[15] Tanveer Husain, Muqueem Khan, Mujtahid Ansari, “Power flow analysis of radial distribution system” IJAREEIE, vol. 5, 2016.

Meteorological Drought Intensity Assessment using Standardized Precipitation Index

Ashish Srivastava[1], Dr. Geeta Singh[2]

[1]M. Tech Scholar, Delhi Technological University, Delhi
[2]Assistant Professor, Delhi Technological University, Delhi

---

Abstract - *Drought is a condition which due to deficiency of moisture in a region due to uneven rainfall, drying up of rivers and loss of ground water. It is estimated that droughts effects around 200 million people are affected from drought every year in India. In 2019, 42% of the country's area is under drought with almost 500 million people severely affected in some ways. The study focuses on the Uttar Pradesh region of Bundelkhand Plateau, which faces continuous droughts every year. The study is carried out for six districts of Uttar Pradesh viz. Auraiya, Banda, Jalaun, Jhansi, Hamirpur and Lalitpur. To identify drought conditions and classify it Standard Precipitation Index (SPI) was computed. The monthly rainfall data from 1988 to 2018 was collected from various sources. The 3-Month SPI(April-June), 3-Month SPI (July-September) and 6-Month SPI (Oct-Mar) were computed using DrinC software and MS excel. The SPI values were used to categorise drought under four groups based on its severity namely mild, moderate, severe and extreme from 1988 to 2018. The IMD classification of rainfall involves categorizing drought by computing the percentage deviation of the current rainfall from normal rainfall. The SPI values of thirty years are compared with actual rainfall and deviation from normal rainfall. The aim is to assess if SPI can provide better drought analysis in comparison to rainfall deviation method which is conventionally used.*

Key Words*: *Drought, Standardized Precipitation Index, DrinC, IMD, Rainfall

1. INTRODUCTION

Droughts are natural disasters related to water deficiency which has an impact on various activities related to environment such as vegetation, agriculture, wildlife, humanity and economy. Drought is one of the most significant natural disaster associated to weather which is often intensified by human activities, since its impacts affect greater areas for time ranging from months to years, thus it has a stern effect on life expectancy, food and grain production for entire population. In recent times large-scale severe droughts have been noticed across the globe leading to starvation due to restricted food supply and shortage among millions, destruction of ecological resources and heavy losses is economy.

The disaster management actions are organized into following:

a. Preparedness stage in which prediction of disaster and the zone of risk are identified well in advance before the occurrence of event;

b. Prevention stage during which early forecasting and warning, monitoring and preparation of emergency plans are easily executed before or during the occurrence of event;

c. Mitigation and Action stage where actions are taken just after the occurrence which comprise damage valuation and mitigation.

The statistics of the disaster events show the alarming trend (Manikiam, 2003). One of the worst natural catastrophes that distress India is the occurrence of drought on large-scale during the (June to September) south-west monsoon season. Semi-arid region faces the greatest drought hazard and is characterized by low and uncertain crop yields, mostly rainfed. For most of dry crops, the yields are invariably dependent on residual soil moisture storage (Dhopte, 2002).

1.1 Drought definitions

Drought is an event when the rainfall for a week is less than fifty percent of the normal, when the weekly normal rainfall is more than or equal to 5 mm. Drought is a period when dry conditions than normal are seen which results in water-scarcity.

According to the Indian Meteorological Department (IMD) drought occurs in an area when the deviation from normal or precipitation deficiency is more than or equal to 26 percent of long-term normal rainfall of that area. Further it is classified in to moderate and severe drought based on the rainfall. A drought incident is well-defined as a year or a period of time during which the total rainfall is less than 75% of the normal rainfall. If the deficit of rainfall lies between 26 percent to 50 percent it is classified as a moderate drought and when it is more than 50 percent it is classified under severe category.

1.2 Drought Classification

a. **Meteorological drought**: It is a condition during which a substantial (more than 25%) deficiency from normal precipitation occurs over a region.

b. **Hydrological drought**: Longer duration meteorological drought results in hydrological drought. It also results in drying up of rivers, streams, lakes, reservoir and decreasing levels of underground water. Hydrological drought impacts agriculture and industries as it causes scarcity of water.

c. **Agricultural drought**: If there is not sufficient rainfall to retain enough moisture levels in soil which result in reduced plant growth or no growth at all and also wilting of crops then a situation of agricultural drought is marked.

d. **Socio-Economic drought**: When there is such scarcity in precipitation that it affects the growth of the country economically it marks socio-economic drought.

1.3 Drought Impacts

Drought can be referred to as a prominent moderate catastrophe as compared to other normal disasters. It negatively impacts life, economy, horticulture, animals, water bodies, small insects etc.

a. **Economic Impacts of Drought**

Areas like agriculture and fish culture or aqua culture, may affect economy of the country. These jobs require water in considerable amount whether it is ground water or surface water.

b. **Environmental Impacts**

Drought impacts on the environment can be interpreted by evaluating the loss in green cover, loss of bio-diversity, drying up of wetlands further resulting in restriction on coming migratory birds, loss of various species and extreme drying up of land which leads to cracking and disintegration of soil.

c. **Impact on society**

Drought has huge impacts on society during the time period through which it lasts and also after it. Lack of harvests, increasing loans which result in debts, bring about suicides of farmers which is a major cause of concern in India.

1.4 Meteorological drought indices and drought detection

Drought indices are frequently applied to measure the possible danger of incidence and drought severity. They also are used to assess spatial–temporal behaviour. A number of the indices have been used for sensing magnitude and variability of the drought temporally across different areas. Few extensively used drought indices include Crop Moisture Index (CMI), Palmer Drought Severity Index (PDSI), Standardized Precipitation Index (SPI), and Surface Water Supply Index (SWSI).

a. Standardized Precipitation Index (SPI)

Even though there are many indices present to compute drought related parameters, assess its severity and classify it, the SPI is the most extensively used index according to Jain(2010). The SPI was computed by Tom McKee, Nolan Doesken, and John Kleist of the Colorado Climatic Centre in 1993. Its computation can be done at different periods and time scales and therefore it can measure water deficiency of different duration. The design of SPI is such that it makes possible to concurrently monitor dry conditions on a specific time scale and wet conditions on a different time-scale. The rainfall difference from the mean of an equal normally distributed function with a mean 0 and a standard deviation of 1 then gives the SPI. The soul premise of the current effort is that using a drought index, such as SPI, leads to more suitable understanding of drought duration, magnitude, and spatial reach in semiarid regions (Karavitis et al. 2011). The SPI is a tool for measuring drought that differs from the PDI. Like the PDI, this index is positive for wet conditions and negative for drought. But the SPI only considers precipitation and is a probability index, while Palmer's indices uses precipitation, evapotranspiration, and loss due to runoff and are water balance indices.

Table 1: SPI based Classification

SPI VALUES	CLASSIFICATION
2.0+	extremely wet
1.5 to 1.99	very wet
1.0 to 1.49	moderately wet
-.99 to .99	near normal
-1.0 to -1.49	moderately dry
-1.5 to -1.99	severely dry
-2 and less	extremely dry

2. STUDY REGION AND METHODOLOGY

The study area includes the districts of Lalitpur, Banda, Auraiya, Jhansi, Jalan and Hamirpur in Uttar Pradesh State of India.

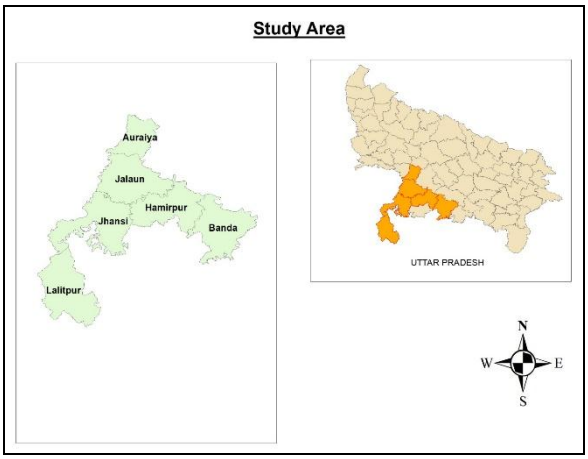
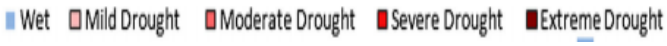


Fig-1: Study Area

3. RESULTS AND DISSCUSSIONS

3.1 Drought Classification Using SPI

The results and discussions in this study, are based on the 3-month SPI (April-May-June) and 3-month SPI (July-Aug-Sept) used to signify short-term and is also used seasonally drought during the summer season and the 6-month SPI (Oct-Mar) is used for intermediate-term drought during the winters in the region.



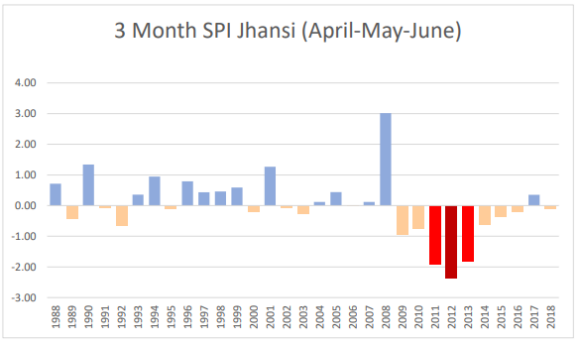


Chart-1: 3-Month SPI Jhansi (April-May-June)

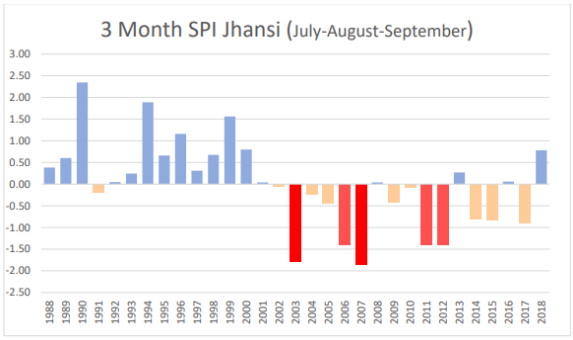


Chart-2: 3-Month SPI Jhansi (July-Aug-Sep)

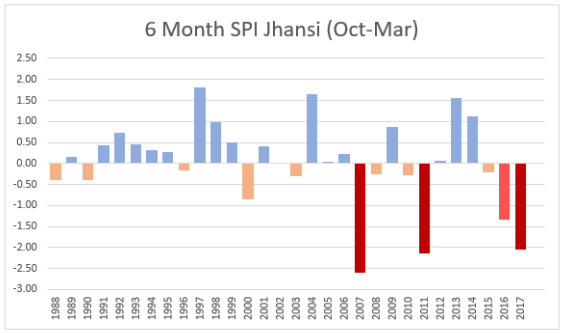


Chart-3: 6-Month SPI Jhansi (Oct-Mar)

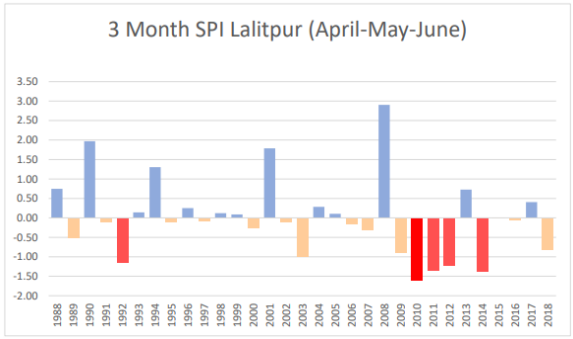


Chart-4: 3-Month SPI Lalitpur (April-May-June)

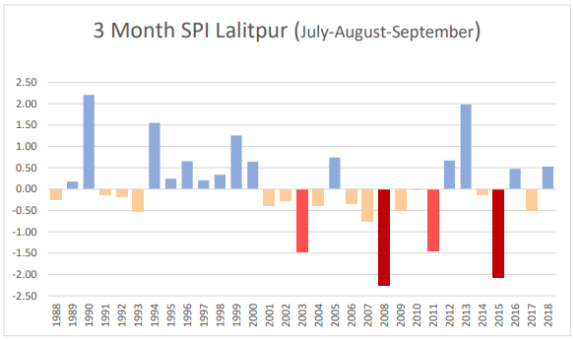


Chart-5: 3-Month SPI Lalitpur (July-Aug-Sep)

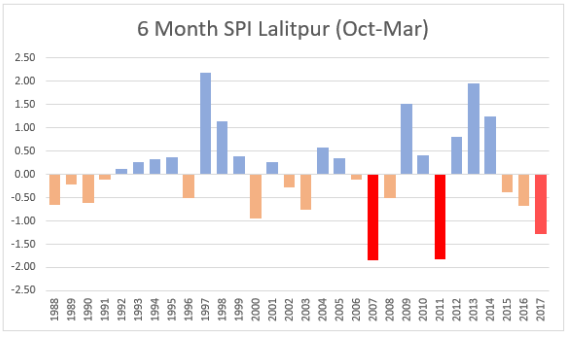


Chart-6: 6-Month SPI Lalitpur (Oct-Mar)

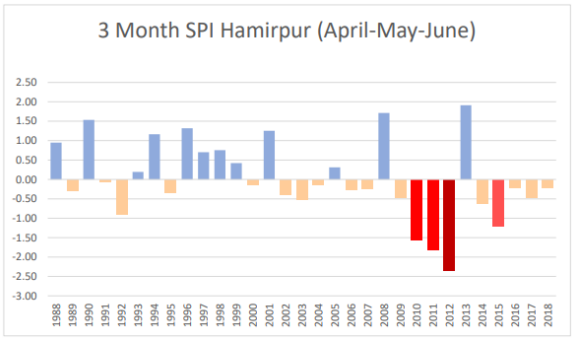


Chart-7: 3-Month SPI Hamirpur (April-May-June)

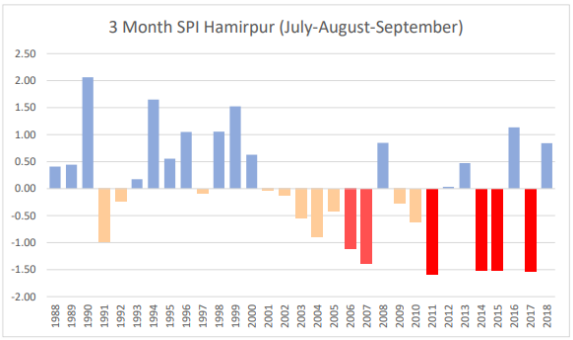


Chart-8: 3-Month SPI Hamirpur (July-Aug-Sep)

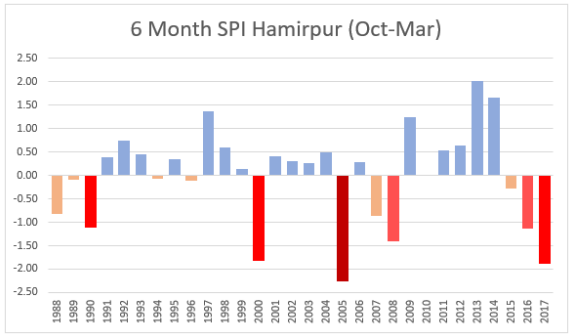


Chart-9: 6-Month SPI Hamirpur (Oct-Mar)

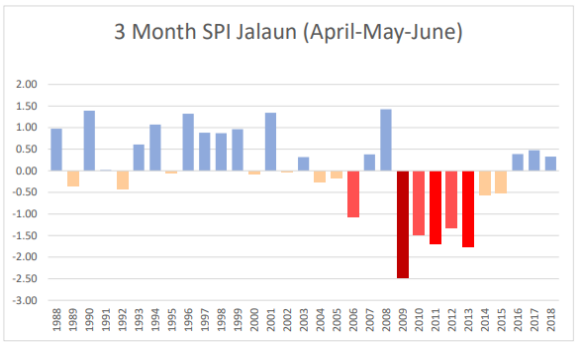


Chart-10: 3-Month SPI Jalaun (April-May-June)

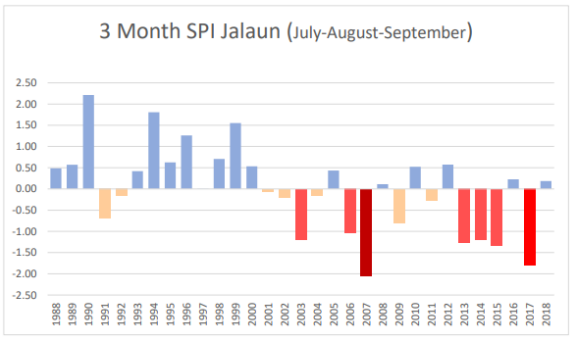


Chart-11: 3-Month SPI Jalaun (July-Aug-Sep)

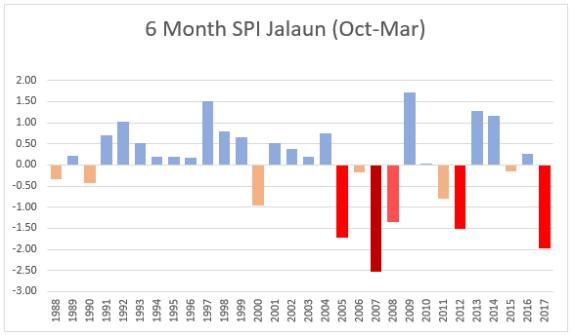


Chart-12: 6-Month SPI Jalaun (Oct-Mar)

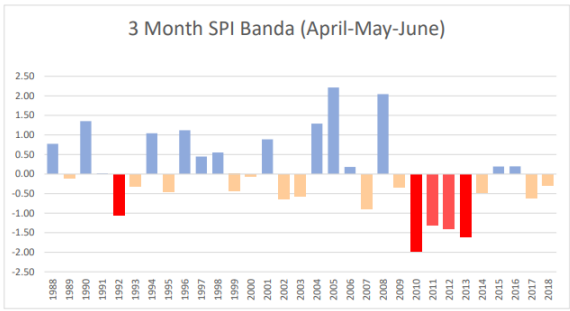


Chart-13: 3-Month SPI Banda (April-May-June)

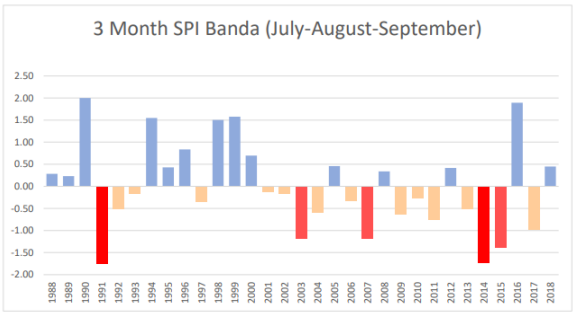


Chart-14: 3-Month SPI Banda (Jul-Aug-Sep)

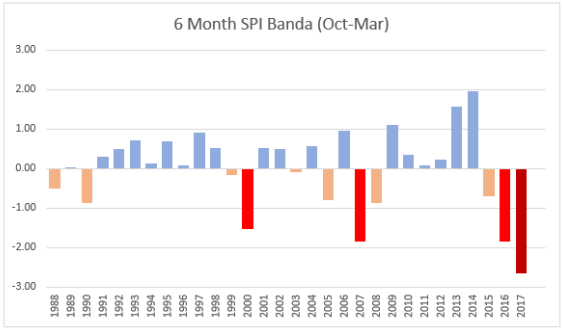


Chart-15: 6-Month SPI Banda (Oct-Mar)

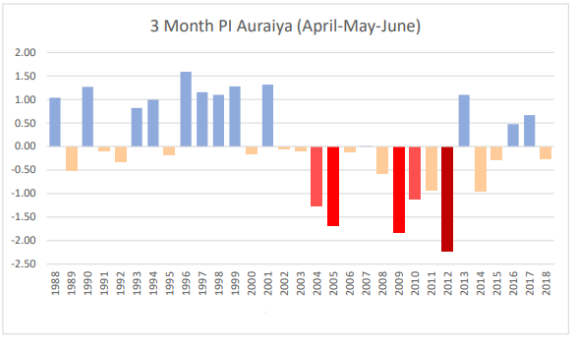


Chart-16: 3-Month SPI Auraiya (April-May-June)

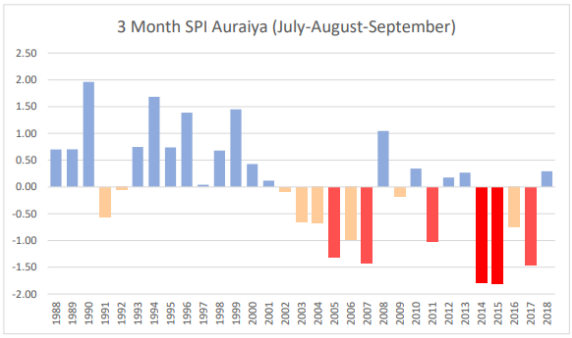


Chart-17: 3-Month SPI Auraiya (July-Aug-Sep)

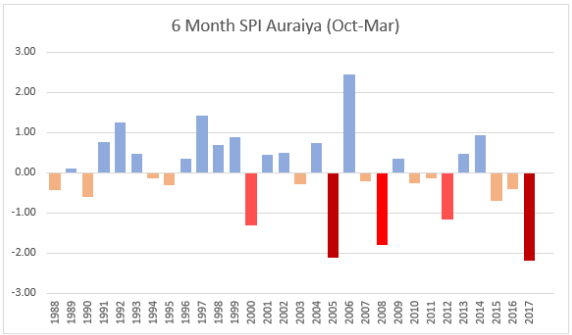


Chart-18: 6-Month SPI Auraiya (Oct-Mar)

3.2 Scatter Plots between SPI and Rain fall Deviation

Scatter charts of 3-Month SPI vs. Rainfall Deviation from average for 2009-2018 using excel for both positive and negative rainfall deviations as shown in the Figure 2 and Figure 3.

It is clear from Figure 2 for Auraiya district that even at negative rainfall deviations of -30% to -40% as shown the SPI values incline to be very negative around -2.0 which represent severe to extreme drought condition. Where as in the same area from Figure 3 in which SPI is plotted during a wetter period, the SPI values are found to be more in accordance but still negative rainfall deviations of around -60% to -80% which represent extreme drought conditions correspond to a lower SPI of around -1.5 to -1.8 rather it should be near -2.0 and above.

Negative rainfall deviations in Hamirpur district (-75% to -95%) represent extreme dryness, but the SPI values corresponding to -70% and -80% represent only a severe case of drought and at -92% SPI drops to -2.35 correctly depicting an extreme drought as shown from Figure 2. The 3-month SPI (July-Aug) from Figure 3 for Hamirpur represent the values of SPI in better agreement with Negative Rainfall Deviations.

Similar observations can be made from for Jalaun where negative rainfall deviations of above -80% which otherwise represent very dry conditions and extreme drought are only once indicated under the same. Similar analysis can be made through Figures 2 and 3 for Jhansi, Lalitpur and Banda where also very high negative deviation from rainfall greater than -70% are not exactly referred under extreme condition but under severe condition with values less than -1.5.

In the case of positive deviations from rainfall which indicates that actual rainfall is more than the normal rainfall with the positive values of SPI representing wet condition, the degree of positive SPI did not correspond with the range of the positive deviation. The rainfall deviations of 100 to 400% which represent fairly wet conditions are only shown by SPI values of 1.5-3 a particular case being the year 2008 when during April-June good rainfall can be seen which otherwise correspond to the drier months.

On the other hand, during periods of high rainfall in the area from July-August the SPI values are better distributed and stretched between +2.5 to -2.5 correctly representing the drought conditions reported by both positive and negative rainfall deviation .The SPI values for all the districts during this period for most of the year can be seen in accordance.

Hence, even the very less amount of precipitation which is surely not enough for keeping moisture of optimum level in soil have led to the SPI values around -1.5 which otherwise must have represented very high level of dryness with SPI of less than and near -2.0. In the same way, excess

rainfall events are represented by SPI near 1.5. This tendency of extreme high rainfall not representing a greater SPI and less rainfall not representing less SPI and can be seen in all the districts during all the time scale of SPI calculation.

Hence, from this analysis we can infer that values of SPI are under-valued during high rainfall and over-valued during less rainfall particularly during dry spells of April-June. Whereas, during the period of ample rainfall the SPI values give a fair representation in agreement to the deviations from normal.

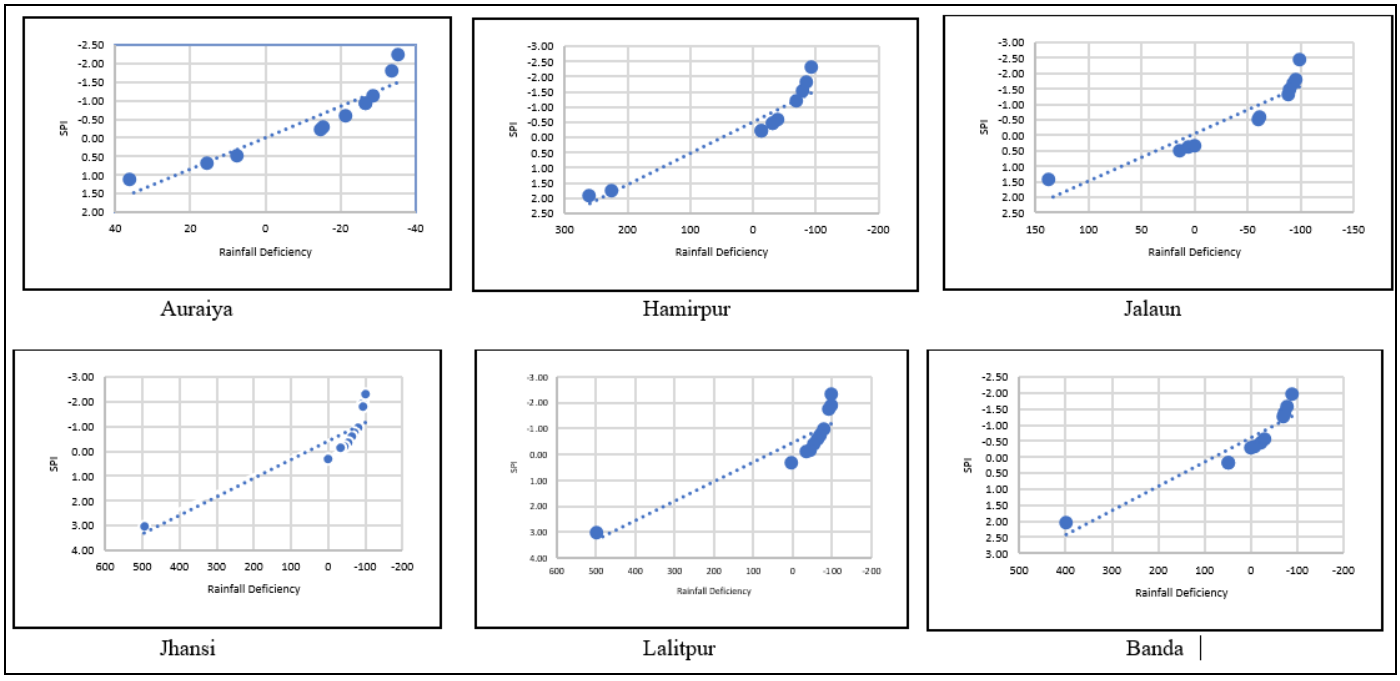


Figure-2: 3-Month SPI(April-May-June) vs. Rainfal deviation Scatter Plots

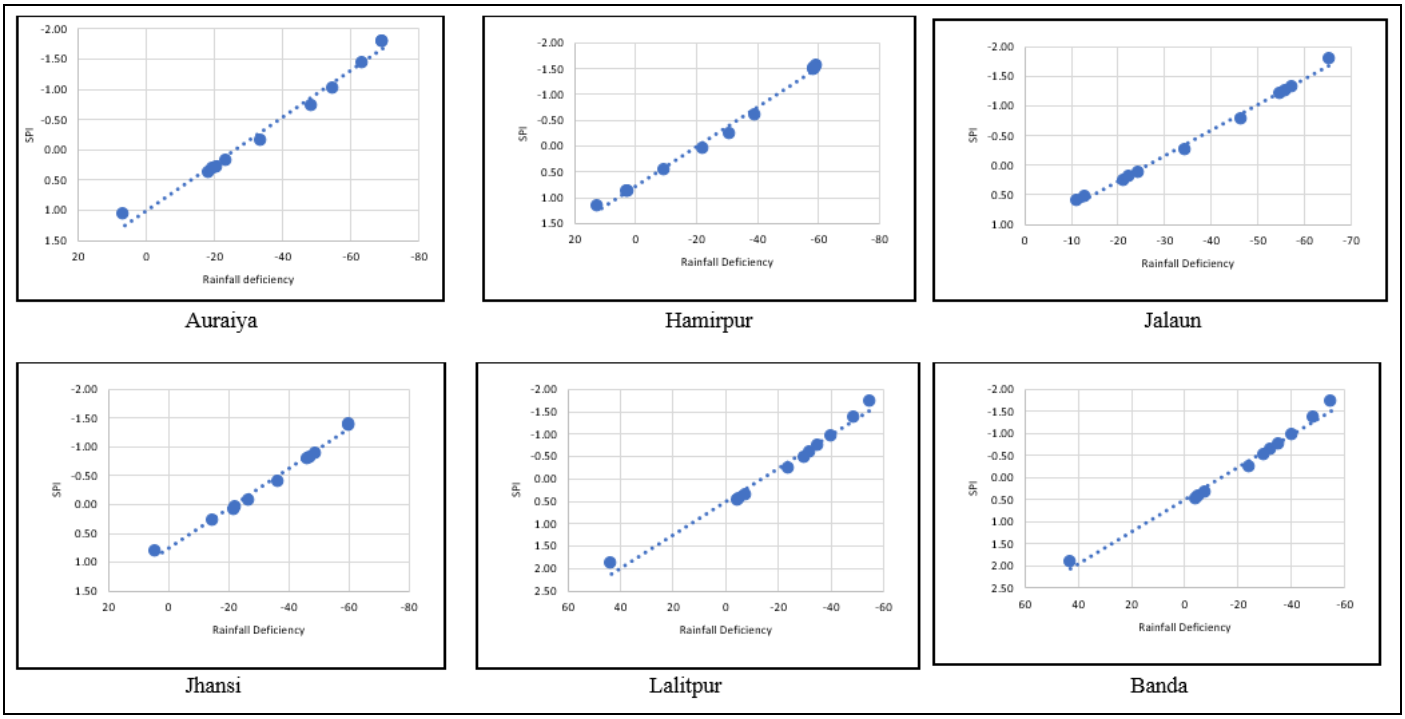


Figure-3: 3-Month SPI(July-Aug-Sep) vs. Rainfal deviation Scatter Plots

4. CONCLUSIONS

1. It is found that the during years 2009,2010,2011,2012,2013 almost all the districts are severely and extremely affected by drought with 2012 being the worst year with SPI values below -2 and less based on 3-Month SPI (April-June).

2. In the years 2007,2011,2014,2015 and 2017 severe and extreme drought has affected all the districts as classified by 3-Month SPI (July-Sep) with 2014 and 2015 being the worst affected years having SPI values in Range of -1.5 to -3.

3. The drought in the 6-month period is due to less rainfall during receding south-west monsoon and the region depends on winter agriculture but as can be seen from the results that most of the past ten years have been drought affected. 2008, 2012 and 2018 have seen extreme drought events based on 6-Month SPI (Oct-Mar).

4. To ascertain the validity of SPI in the region, the SPI values for the last ten years for April-June and July-September are compared with the rainfall deviation from mean. Scatter plots are plotted to see the variation in SPI and Rainfall deficiency.

5. It is found that when there is very low rainfall the SPI values under-estimate the drought situation like in 2010,2011 and 2013 for Hamirpur, Jalaun, Jhansi, Lalitpur and Banda rainfall deviations of -60% to -90% are only represented by SPI values of severe drought stations with values lying between -1 to -2.

REFERENCES

1) Abdel-Aziz Belal & Hassan R. El-Ramady & Elsayed S. Mohamed & Ahmed M. Saleh, "Drought risk assessment using remote sensing and GIS techniques". DOI 10.1007/s12517-012-0707-2

2) Anil Kumar Gupta (PI) Sreeja S. Nair (Co-PI) Oishanee Ghosh Anjali Singh Sunanda Dey "Bundelkhand Drought Retrospective Analysis and Way Ahead".

3) Dhopte M. ARVIND (2002), "Agrotechnology for dry land farming", Scientific Publishers, Jodhpur, India.

4) Dipanwita Dutta, Arnab Kundu & N.R. Patel, 2012. "Predicting agricultural drought in eastern Rajasthan of India using NDVI and standardized precipitation index".

5) Diwan P.L (2002), "Water environment and drought, Proceedings: All India seminar on "Water and Environment-Issues and Challenges" October 2002, IIT, Roorkee, India, 21-185.

6) Herbst, P.H., Bradenkamp, D.B., and Barker, H.M.G., (1966). "A technique for evaluation of drought from rainfall data", Journal of Hydrology, 4, pp 246-272.

7) Jain SK, Keshri R, Goswami A, Sarkar A (2010) "Application of meteorological and vegetation indices for evaluation of drought impact: a case study for Rajasthan, India". Nat Hazards 54:643–656. doi:10.1007/s11069-009-9493-x.

8) Karavitis CA, Alexandris S, Tsesmelis DE, Athanasopoulos G (2011) "Application of the Standardized Precipitation Index (SPI) in Greece. Water J" 3:787–805. doi:10.3390/w3030787.

9) Manikiam B. (2003), "Remote sensing applications in disaster management, Mausam", 54, 1, 73-18.

10) McKee TB, Doesken NJ, Kleist J (1993) "The relationship of drought frequency and duration to time scales". Preprints, 8th Conference on Applied Climatology, 17–22 January, Anaheim, CA, pp. 179–184.

11) Morid Saeid, Smakhtin Vladimir and Moghaddasi Mahnosh, 2006, Comparison of seven meteorological indices for drought monitoring in Iran, International Journal of Climatology, 26, 7, pp971-985

12) Moumita Palchaudhuri, Sujata Biswas ,"Analysis of Meteorological Drought Using Standardized Precipitation Index – A Case Study of Puruliya District, West Bengal, India". World Academy of Science, Engineering and Technology International Journal of Environmental and Ecological Engineering Vol:7, No:3, 2013.

13) NDMA (2009). "National Policy on Disaster Management, 2009". National Disaster Management Authority,. New Delhi: Magnum Custom Publishing.

14) P. V. Aswathi, Bhaskar Ramchandra Nikam, +1 author Shiv Prashad Aggarwal "Assessment and monitoring of agricultural droughts in maharashtra using meteorological and remote sensing based indices Published 2018, DOI:10.5194/isprs-annals-IV-5-253-2018.

15) P.H. Shiva Prakash, P.K. Garg and S.K. Ghosh GIS based modelling for drought assessment Geomatics Engineering Section Department of Civil Engineering Indian Institute opf Technology, Roorkee Roorkee 247667, India.

BIOGRAPHIES



Ashish Srivastava,
M. Tech Scholar, Delhi
Technological University, Delhi



Dr. Geeta Singh,
Assistant Professor, Delhi
Technological University, Delhi

2nd IEEE International conference on power Electronics, Intelligent Control and Energy systems (ICPEICES-22018)

Modeling and Simulation of Microgrid Solar Photovoltaic System with Energy Storage

Dinanath Prasad
Dept.of Electrical Engineering
Delhi Technological University
Delhi, India
dinanath6@gmail.com

Narendra Kumar
Dept. of Electrical Engineering
Delhi Technological University
Delhi, India
dnk_1963@yahoo.com

Rakhi Sharma
Dept. of Electrical Engineering
Indira Gandhi National Open University Delhi, India
rakhis_ignou@rediffmail.com

***Abstract*— This paper highlights the integrated operations of the photovoltaic system with energy storage device. The variations in the energy produced and the variations in the load, the DC link voltage does vary, which has to be tackled using an energy storage device so as to maintain the DC link voltage. The battery is used as a storage device which is connected to a bidirectional converter and switching of the bidirectional converter has to be done in such a way that it either charges or discharges the battery depending upon the load conditions. The DC bus is connected to the utility grid, the power sharing and transfer should be in such a way to maximize the efficiency. An efficient algorithm is to be used to attain maximum efficiency through an interactive inverter. The SPV generating system with MPPT and boost converter is accomplished with a storage unit, and simulations are performed and the results are analyzed.**

Keywords*— Microgrid, SPV, MPPT, PVSC, Grid integration, SOC

I. INTRODUCTION

With technological advancement and extensive R & D in the power electronics field very sophisticated and advanced microgrid have been developed. As the conventional sources are running out at a very fast rate distributed generators (DG) including renewable sources, within microgrids can help to overcome the power system limitations to efficiency improvement, reduction in emissions and manage the variability of renewable sources [1]. Nowadays small generators and the energy storage devices are being used with power electronics to control the flow of energy within the system.The non conventional energy sources with these devices can be efficiently used to meet the increase in load demand. The use of Microgrid with solar array acts as an energy source has also emerged as an efficient alternative to meet the increase in load demand. Since the solar energy is the best and cheapest source of energy, we can use their energy for power generation when they connected to grid. This incredible renewable source of energy having numbers of advantages like it neither pollutes the environment not destroy the forest cover, harnessing of energy is absolutely free, there is no need of maintenance, there are multiple other uses such as heating of water, keeping the house warm, also used in many more applications [1, 2].

The main problem is to design a suitable energy balance of microgrid and its integration with the utility grid. Energy generation by the solar photovoltaic source is highly fluctuating and the maintenance of the DC bus voltage at a constant value is one of the major problems. With the variety of loads the maintenance of the voltage is much difficult. The effective utilization of the renewable energy by the loads and its integration to the utility grid is the major concerns.

This paper presents modeling of the PV array, with MPPT to utilize the maximum power from the PV array. Energy storage unit is used with PV array for the maintaining the DC link voltage using a control strategy. The importance of the storage unit in Microgrid emphasized where the power is either injected or absorbed by the storage unit in order to maintain the voltage at a constant value [3]. To connect the microgrid to the utility grid an energy management algorithm is proposed. The simulation is carried out and the results are analyzed in Matlab/ Simulink environment.

II. GRID-CONNECTED MICROGRID SYSTEM

Fig.1, shows the main circuit topology for grid-connected microgrid system. This system consist of the PV array and the battery storage system which is connected to the DC bus and then utility grid using an inverter. The DC bus is connected to the utility grid, for the power sharing and transfer that should be in such a way to maximize the efficiency. An efficient algorithm is to be used to attain maximum efficiency through interactive inverter. The grid-connected mode is carried out using a 3 leg 3 phase inverter and the switching to the inverter is done with the help of a droop control technique to generate reference current. PV array is connected through boost converter are used, to fulfill the objective is to produce reference current by MPPT algorithm. The battery is connected with the help of bi-directional, which can either charge the battery by absorbing the energy from the grid or by discharging the battery by injecting the power into the grid. Bi-directional converter is used for achieving the following, for which the switching has to be in such a way that it either charges or discharges the battery depending on the load condition. From the fig.1, we can observe that solar as a renewable energy source and

978-1-5386-6625-8/18/$31.00 ©2018 IEEE

battery as an energy storage device is connected to the DC bus by which, they are connected to the DC to AC converter [4-5].

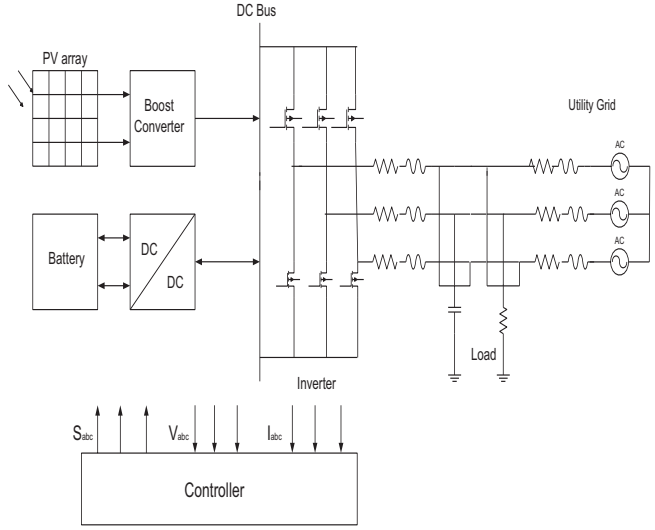


Fig.1. Schematic diagram of grid connected system

III. MODELING OF MICROGRID COMPONENTS

A. Modeling and Analysis of PV cell

PV cell is a solid state device which converts solar energy into electrical energy using photovoltaic effect. Model of Photo Voltaic cell is developed by analyzing the properties using Matlab/Simulink.

B. Equivalent circuit of PV cell

Fig. 2, shows the equivalent circuit of a PV cell, a current source represented by I_{ph} indicates the current caused by movement of electron and holes due to the incident light called photons. A diode current I_d , is represented parallel to the current source, a shunt resistance R_{sh} ,represents the leakage of current due to the presence of impurities in the junction diode, and series resistance R_s , due to the metallic contacts of the semiconductor [6, 7].

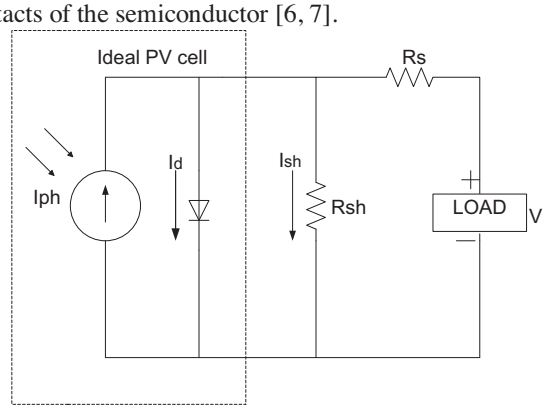


Fig.2. Equivalent circuit diagram of PV cell

V_{oc} is the open circuit voltage which is the voltage produced by the P-N junction diode. I_{sc} is the short circuit current, which is the photon current during short circuit condition.
From the figure (2) ,using Kirchhoff's law

$$I_{pv} = I_{ph} - I_d \qquad (1)$$

The photon current (I_{ph}) *is,*

$$I_{ph} = [(I_{sc} + \alpha(T - T_{ref})]\frac{\beta}{\beta_{ref}} \qquad (2)$$

Where,

I_{ph} is the photon current (A)

I_{sc} Is the photon current at standard conditions (=298K,

β_{ref} *= 1000W/m²)*

α is temperature coefficient

The diode current $I_d = I_s(e^{\frac{qV}{nkT}} - 1)$ *(3)*

Where I_s represents saturation current of the diode (A), q represents charge of an electron ($1.6*10^{-19}$ C), *n* represents the ideality factor, k is Boltzmann constant ($1.381*10^{-23}$ J/K) and T is the absolute temperature (K).
The saturation current of the diode varies with temperature as

$$\mathrm{I}_s = I_0(\frac{T}{T_{ref}})^3 e^{\frac{qv_g}{nk}(\frac{1}{T_{ref}} - \frac{1}{T})} \qquad (4)$$

Where I_0 is the reverse saturation current, T_{ref} is the reference Temperature (298 K), v_g is the bandgap voltage of the semiconductor (V).

By using initial conditions, I_{pv} =0 on the open circuit condition and the constant temperature. Equation (1) can be transformed into

$$0 = I_{sc} - I_d$$

$$I_{sc} = I_s(e^{\frac{qV}{nkT}} - 1)$$

$$I_s = I_0 \, at \, T = T_{ref}$$

$$I_{sc} = I_0(e^{\frac{qV}{nkT}} - 1)$$

$$I_0 = \frac{I_{sc}}{(e^{\frac{qV}{nkT}} - 1)}$$

From equation (1) the PV current can be expressed by

$$I_{pv} = I_{ph} - I_s(e^{\frac{qV}{nkT}} - 1)$$

Since the voltage across the diode itself is the voltage across the PV cell $\mathrm{V}_d = V_{pv}$

$$I_{pv} = I_{ph} - I_s(e^{\frac{qV_{pv}}{nkT}} - 1) \qquad (5)$$

So, the output current can be expressed as

$$I_{pv} = [I_{sc} + \alpha(T - T_{ref})]\frac{\beta}{\beta_{ref}} - I_s(e^{\frac{qV_{pv}}{nkT}} - 1) \qquad (6)$$

By using the above equations a model which fits the configuration is simulated in the Matlab Simulink environment. The following parameters are used for the simulation is tabulated in the table.

Table I. PARAMETERS FOR PV CELL SIMULATION

Parameters	*Value*
Open circuit Voltage (Voc)	0.6 V
Short circuit Current (Isc)	1.8 A
Band Gap Voltage (VG)	1.12 V
Diode Ideality Factor	1.24
Short circuit current temeperature coefficient	2.47*10^3

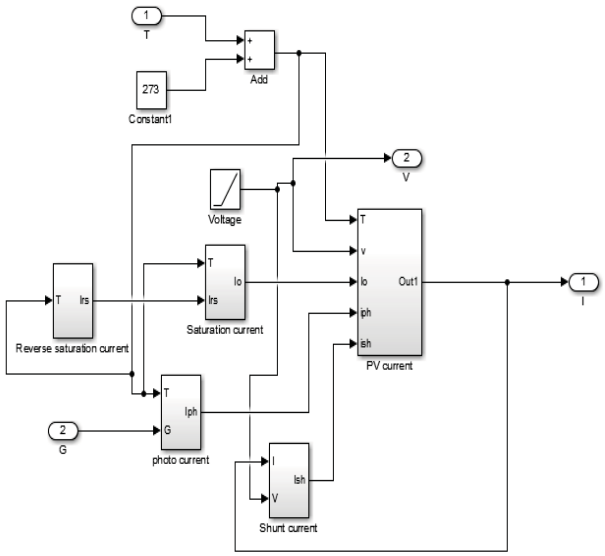


Fig.3. PV cell simulink model

The simulation of the PV array is similar to that of the PV cell, but instead of current being calculated, from the equation (6) and operating at reference temperature

$$Ipv - I_{sc}\frac{\beta}{\beta_{ref}} - I_s(e^{\frac{qVpv}{nkT}} - 1) = 0 \qquad (7)$$

Solving the following equation, Vpv can be calculated, which should be the voltage across the PV cell. For the consideration of an array, the equation (7) can be transformed in to equation (8)

$$\frac{Ipv}{N_p} - I_{sc}\frac{\beta}{\beta_{ref}} - I_s(e^{\frac{qVpv}{nkTNs}} - 1) = 0 \qquad (8)$$

The following simulations are carried out for Ns=100 and Np=10.

IV. MAXIMUM POWER POINT TRACKING TECHNIQUES

Maximum power point tracking (MPPT) plays a significant role in renewable energy sources, in this paper focuses on PV system as a source because of its intermittent nature with the changes in solar irradiance level, ambient temperature, and load the output of the PV array is nonlinear. For the determination of efficient PV output continuously adjust the operating point of the PV array to be around the maximum power point. This process is called MPPT. The available MPPT techniques are perturbed and observe (P&O), Incremental conductance (IC), fractional

Voltage, fractional current, fuzzy logic, feedback control, neural network. The MPPT classifications could be made on the basis of control strategies. Direct, indirect and probabilistic are three different types that are in use. Perturb and observe (P&O), incremental conductance (IC), fuzzy logic, and neural network are considered as direct methods. For estimating the Maximum Power Point (MPP), the indirect method is also used. Indirect methods include the look-up table, curve fitting, open circuit and short circuit methods [8].

In this paper perturb and observe (P&O) / Hill-climbing/ true seeking method is modeled for the determination of MPP. Because this algorithm could be easily implemented, and the accuracy of the sensors is not needed very high. The disadvantage of this method is that it may result in oscillations of power output near the MPP. The perturbance steps are used for the determination of the oscillation amplitude. The larger the perturbance step , faster the tracking is, but it serves the fluctuations. Also, if the solar irradiance changes suddenly, the P&O method may become invalid.

V. PV SIDE CONVERTER

For the PV side converter (PVSC) a boost converter is used. The main objective is that the I_{ref} (reference current) produced by the MPPT algorithm is tracked, for that by varying the duty cycle of the boost converter, the maximum power is transmitted and I_{ref} is to be tracked by the PV array.

TABLE II. PARAMETERS OF BOOST CONVERTER

Parameter	**Value**
Input value	200 V
Output value	600 V
Frequency	20 KHZ
Maximum Power	3 KW

The value of the inductor and capacitor are calculated from the following equations (9) and (10). The value of ripple is taken as 5% of the nominal value.

$$L = \frac{V_{pv} * d}{\Delta I * f} \quad (9)$$

$$C = \frac{I_o * d}{\Delta V * f} \quad (10)$$

The simulation is carried out with the following values, for the duty cycle input is analyzed in the next section.

The control circuit of the boost converter is shown below

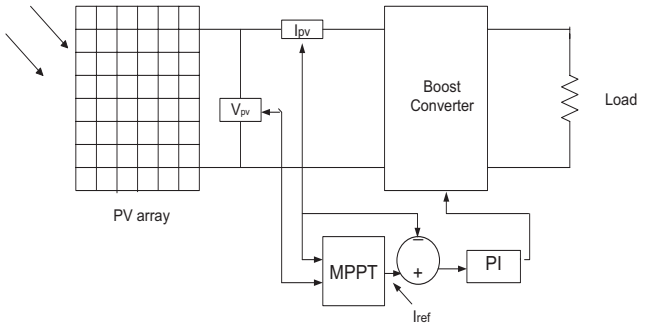


Fig.4. Control of boost converter

The control of boost converter is done for the tracking the reference current. The reference current is compared in between the MPPT with the actual current into the boost converter; the error is processed by PI controller. The output of the PI controller is further processed to generate PWM signals to the boost converter, by which the current is tracked [9].

VI. MICROGRID WITH STORAGE

It is essential for maintaining the DC grid voltage constant by injecting power if required in the system or conserving the energy by storing the excess amount of energy produced by the PV array. In this section, the operation of the Microgrid is carried out with a storage unit and simulations are carried out and analyzed. Since the battery is to be charged or discharged, depending on whether the power is to be injected or ejected from the DC grid, an algorithm is proposed for effective maintenance of DC grid voltage.

A. Storage connected to DC grid

In DC grid storage i.e. battery is not directly connected. The function of the battery is to inject the power or absorb the power from the grid. So, the battery is connected via bidirectional converter which can either be injecting the power into the grid by discharging the battery or either absorbing the energy from the grid to charge the battery. To fulfill the above requirements, switching of bidirectional converter has to be in such a way that it either charges or discharges the battery depending upon the load condition**.** Figure (5) shows the block diagram of the Microgrid with storage connected to the DC bus. The PV array is connected to the grid directly using the boost converter and the battery is connected to the grid using the bidirectional converter. The major bidirectional converter which is commonly used is the Buck-Boost converter. There are many bi-directional converters, but buck-boost is usually selected with the simplicity of its operation and implementation. Using the buck-boost converter, the battery is either charged or discharged, depending on the switching to the converter.

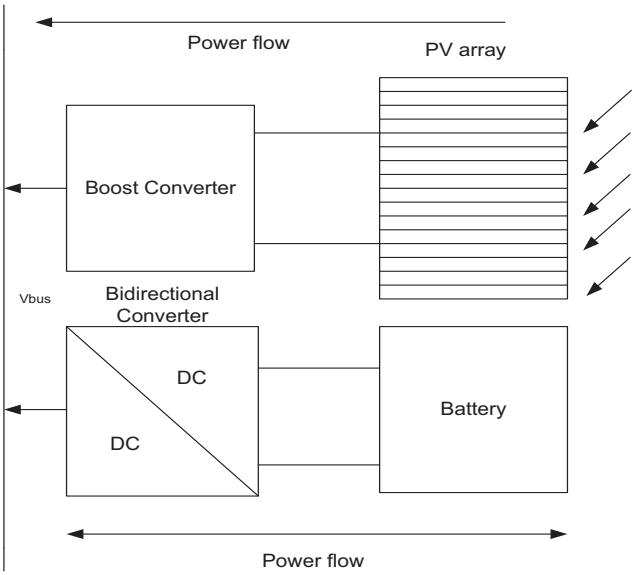


Fig.5. Microgrid with storage

B. Buck-Boost Converter

The Buck-Boost converter is very useful in real-time battery powered applications, as the name suggests it can act as a buck converter or it can act as a boost converter, that all depends upon the switched to the converter. For the buck operation or the step-down operation the power flow from the high voltage side to the low voltage side and for the boost operation or the step-up operation the power flow from the low voltage side to the high voltage side. The power flow can be controlled by suitably choosing the switching to either charge or discharge the battery [10].

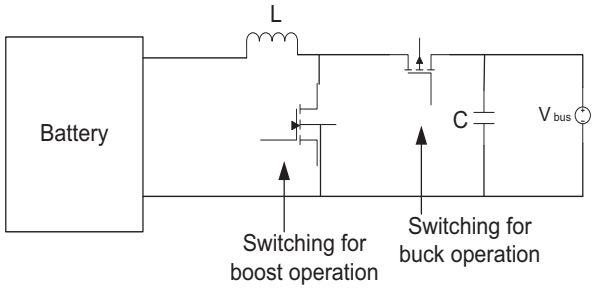


Fig.6. Buck-Boost circuit diagram

In the specified region of operation, the buck-boost converter parameters are so chosen in such a way that it can get both as buck and boost converter. The analysis of buck-boost converter can be done into buck operation and boost operation as the value of inductor and capacitor are calculated and selected for the lowest ripple value.

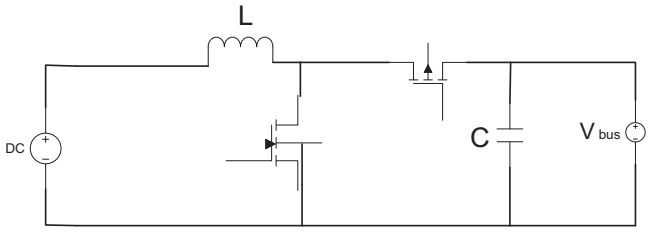


Fig.7. Bi-directional converter

$$(V_{bus} - V_{Battery})T_{ON} = V_{Battery}(T - T_{ON}) \quad (11)$$

$$D_1 = \frac{V_{Battery}}{V_{bus}} \quad (12)$$

$$D_1 = \frac{T_{ON}}{T} \quad (13)$$

The value of inductance (L) can be calculated as follows

$$L = \frac{(V_{bus} - V_{Battery})D_1}{\Delta I * \mathrm{f}} \quad (14)$$

The value of capacitance (C) can be calculated as follows

$$\mathrm{C} = \frac{\Delta I}{8 * \Delta V * f} \quad (15)$$

For good estimation the ripple current is 20% to 40% of the output current or $0.2 < \Delta I < 0.4$. The parameters of the boost converter are calculated from the equation, the value for which the lowest ripple of current and voltage is obtained is selected.

TABLE III. PARAMETERS OF THE BUCK-BOOST CONVERTER

PARAMETERS	VALUE
V_{BUS}	600 V
$V_{BATTERY}$	240 V
SWITCHING FREQUENCY	20 KHZ
INDUCTANCE (L)	14 MH
CAPACITANCE (C)	100 μ F

The power is to be injected or to be absorbed from the grid is decided from the selection of Buck/Boost converter which is very important for the following a selection mechanism is required. If it is to be noted that solar PV power is greater than the load, then the voltage of the DC bus increases above the desired value, hence to maintain the DC voltage steady at required voltage should be absorbed. And when solar PV power is less than the load, then the voltage of the DC bus decreases from the required voltage, hence to maintain the DC voltage steady at required voltage power should be injected [11- 14] .

C. Control of switching for the Buck-Boost converter

The switching for the buck-boost converter should be done so that the voltage reference is maintained at the DC voltage bus. To acquire the above, the voltage of the DC bus is sensed and the error in voltage between the DC grid voltage and the reference voltage is fed to a PI controller from which a reference current (Iref) is generated.

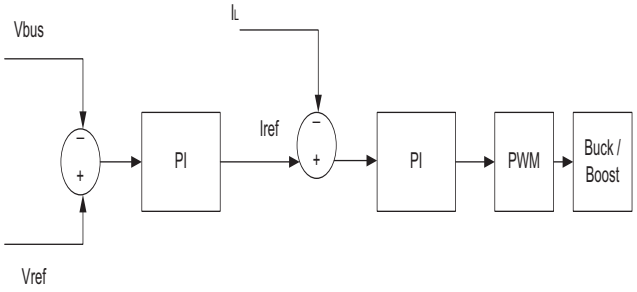


Fig.8. Control diagram for a buck - boost converter

VII. SIMULATION RESULTS

The Simulations are carried out for different cases when microgrid system connected to the DC link with and without storage unit. Microgrid without storage unit can also be classified into two different sections; either the load power at 600V is greater than the power produced by the PV array or when the load power at 600V is less than the PV array. So for the case when power required by the load at 600V is more than power by PV array with the maximum rated power at around 3KW, the load resistance is taken 120 ohms, for that load resistance at which the nominal value of about 600V is reached. Now for the load less than 120 ohms, to maintain the voltage of 600V, additional power is to be injected into the DC grid, but due to the lack of storage unit connected to the grid, the bus lack power and the voltage drops from the nominal value. The following simulation is carried out a load of 60 ohms for which to maintain the 600V nominal value of the DC bus, 6KW of power should be transmitted by the PV array. The maximum power from the PV array is around 3KW, so the DC bus voltage drops below 600V mark. It settles around 400V. This is the very unsuitable case without the storage unit system in the DC bus.

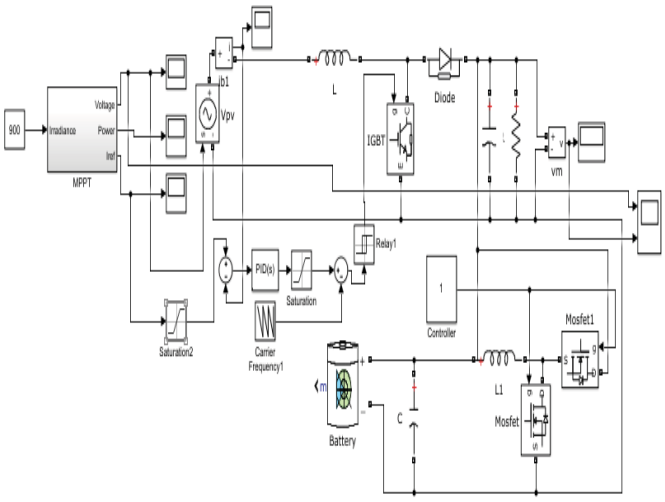


Fig.9. Matlab/Simulink diagram for PV, battery connected to DC link

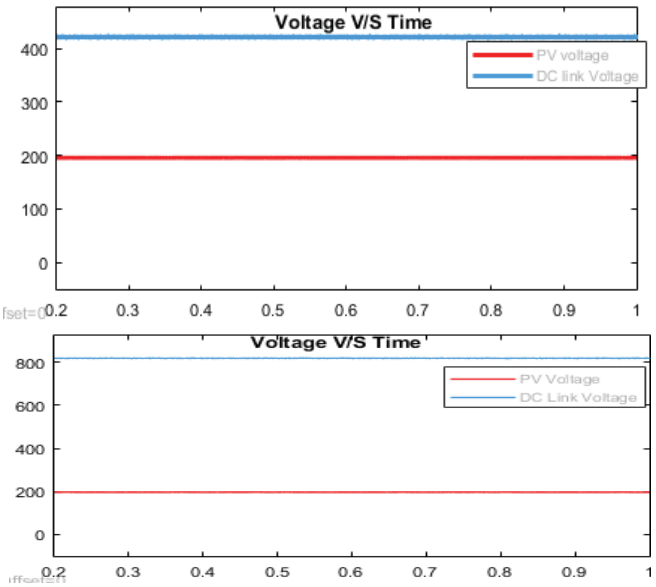


Fig.10(a). PV voltage and DC link Voltage when R_{load} = 60 ohm (b) PV voltage and DC link Voltage when R_{load} = 240ohm.

The DC link grid voltage has to be maintained at about 600V, but from the figure 10(a), the DC grid voltage is approx. 400V. The same situation is carried out a load of 240 ohms, and since the load power at 600V is 1.5KW but the power generated by the PV array is around 3KW. Since there is an excess generation of power than the load power, the voltage instead of maintaining at 600V will increase and reach a voltage around 850V which is shown in figure 10(b).

From the following, we can conclude that an energy source is essential for the maintenance of the DC link grid at a constant voltage. If the following DC bus is connected to the energy source, which can inject/eject the remaining power to maintain the voltage level at 600V. The other simulation is carried out where the PV array and the storage device is connected to the utility grid using an inverter and the switching to the inverter is executed by droop control method. The inverter is connected to the grid and the required power is transmitted to the grid.

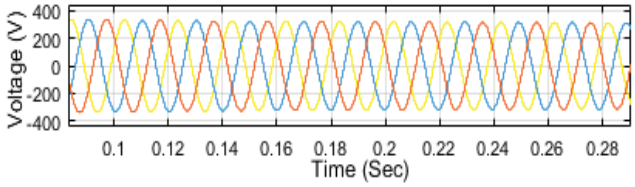


Fig.11. Grid Voltage

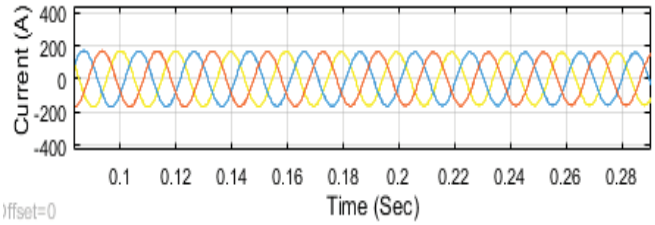


Fig.12. Grid Current

The following system was tested under the following conditions: Vs= 415 V, switching frequency = 10 kHz, Vdc= 600 V, line impedance Ls= 2.6 MH, Rs= 0.6 ohms, filter inductance L_L = 0.6 MH, filter capacitance = 1500μF, a linear load of 75 KW.

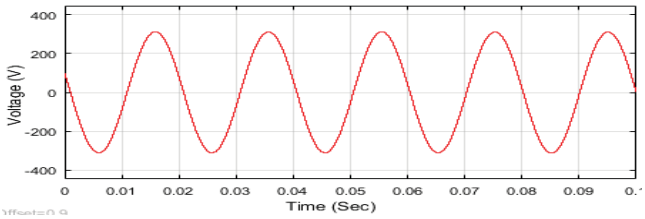


Fig.13. Line to line voltage during grid connected mode

Grid voltage and grid current in the respected figure 11 and 12 demonstrate system performance, and figure 13 shows the line to line voltage during grid-connected mode.

VIII. CONCLUSION

The Microgrid integration with the utility grid will help in the effective utilization of the renewable sources for improving the quality of the grid. Through this paper, explains the modeling of the components of the PV array, and uses Maximum Power Point Tracking to utilize the maximum power from the PV array and the is connected to an energy storage so as to maintain the DC link voltage using a control strategy. Algorithm for energy management is proposed to connect the Microgrid to the utility grid. The simulations are carried out, and the results are analyzed in Matlab/Simulink environment.

REFERENCES

[1] K. Venkateswarlu and J. Krishna Kishore, "Modeling and simulation of micro grid system based on renewable power generation units by using multilevel converter,'' in International Journal of Engineering Research & Technology (IJERT), ISSN: 2278-0181, Vol. 1 Issue 6, August – 2012.

[2] Juan Manuel Carrasco, Leopoldo Garcia Franquelo, Jan T. Bialasiewicz, Eduardo Galván, Ramón C. Portillo Guisado, Ma. Ángeles Martín Prats, José Ignacio León and Narciso Moreno-Alfonso, "Power-Electronic Systems for the Grid Integration of Renewable Energy Sources: A Survey,'' IEEE transactions on industrial electronics, vol. 53, no. 4, august 2006.

[3] Hamid R. Teymour, Danny Sutanto, Kashem M. Muttaqi and P. Ciufo, "Solar PV and battery storage integration using a new configuration of a three-level NPC inverter with advanced control strategy," IEEE transactions on energy conversion, 2014.

[4] Irvin J. Balaguer, Qin Lei, Shuitao Yang and Athena Supatti, "Control for grid-connected and intentional islanding operations of distributed power generation," IEEE transactions on industrial electronics, vol. 58, no. 1, January 2011.

[5] Amir Khaledian and Masoud Aliakbar Golkar, "Analysis of droop control method in an autonomous microgrid," Journal of Applied Research and Technology 15 (2017) 371–377.

[6] Ba'amani beams, Dr. Iliya Tithe Thuku and Simon Samuel, "Design of a grid connected solar system for yola north and south, adamawa state ," International Journal of Science and Engineering Applications, Volume 6 Issue 10, 2017, ISSN-2319-7560.

[7] Cemal Keles, B. Baykant Alagoz, Murat Akcin, Asim Kaygusuz and Abdulkerim Karabiber, "A photovoltaic system model for Matlab/Simulink simulations," 4th International Conference on Power Engineering, Energy and Electrical Drives, Istanbul, Turkey, 13-17 May 2013.

[8] Bidyadhar Subudhi and Raseswari Pradhan, "A comparative study on maximum power point tracking techniques for photovoltaic power systems," IEEE transactions on sustainable energy, vol. 4, no. 1, January 2013.

[9] Bhim Singh, Shailendra Dwivedi, Ikhlaq Hussain and Arun Kumar Verma, "Grid integration of solar pv power generating system using a couple based control algorithm," IEEE. India International Conference (PIICON), Dec. 2014.

[10] Nupur Saxena, Ikhlaq Hussain, Member, Bhim Singh and A. L. Vyas, "Implementation of grid integrated pv-battery system for residential and electrical vehicle applications," IEEE transactions on industrial electronics, Volume: 65, Issue: 8, Aug. 2018.

[11] David Velasco de la Fuente, César L. Trujillo Rodríguez, Gabriel Garcerá, Emilio Figueres and Rubén Ortega González, "Photovoltaic power system with battery backup grid-connected and island operation capabilities," IEEE transactions on industrial electronics, vol. 60, no. 4, April 2013.

[12] Ya-Xiong Wang, Fei-Fei Qin, and Young-Bae Kim, "Bidirectional DC-DC converter design and implementation for lithium-ion battery application," IEEE PES Asia-Pacific Power and Energy Engineering Conference (APPEEC), Dec. 2014.

[13] Cody A. Hill, Matthew Clayton Such, Dongmei Chen, Juan Gonzalez, Student Member and W.Mack Grady, "Battery energy storage for enabling integration of distributed solar power generation" IEEE transactions on smart grid, vol. 3, no. 2, June 2012.

[14] Sathish Kumar Kollimalla, Mahesh Kumar Mishra, and N. Lakshmi Narasamma, "Design and analysis of novel control strategy for battery and supercapacitor storage system," IEEE transactions on sustainable energy, vol. 5, no. 4, October 2014.

International Journal of Research in Engineering and Innovation (IJREI)
journal home page: http://www.ijrei.com
ISSN (Online): 2456-6934

Modelling of vapour compression refrigeration system (VCRS) by using alternative refrigerants with TiO_2 and without nano materials

R.S. Mishra

Department of Mechanical & Production Engineering, Delhi Technological University Delhi, India

Abstract

Application of Nano particles in refrigerants has been identified as a better way of enhancing the thermal performance of the vapour compression refrigeration system (VCRS) without modification the system design. When nano particles are dispersed in a refrigerant, they are regarded as nano refrigerants. The improvement in evaporator and condenser heat transfer coefficient are responsible for the enhancement of VCRS performance.

In this paper, the effect of TiO_2 (nano particles) on the first law efficiency in terms of coefficient of performance (COP), exergetic efficiency (second law efficiency0 and system exergy destruction ratio (EDR) based on exergy of fuel / exergy of product) using alternative refrigerants are discussed. It is shown that the application of Nano particles as additives in refrigerant and lubricant in VCRS is favorable and promising. Therefore, Nano refrigerants are expected to be the future refrigerants for improving thermal performances of vapour compression refrigeration systems.

© 2018 ijrei.com. All rights reserved

Keywords: Thermodynamic performance improvements, Mixing Nano materials, Vapour Compression Refrigeration System

1. Introduction

Refrigeration systems have become one of the most important utilities for people's daily lives. With the advancement and technological developments in the field of refrigeration new methods are developed to increase the COP of the systems. Traditional methods for exchanging heat from the system involves increment in the surface area but this leads to the increase in the size of the system, so there was need of some efficient way that can enhance the heat transfer. The inventive idea of using nanofluids, fluids which consist of suspended nanoparticles are used to remove such kind of barriers. The nano refrigerant is used to improve system performance, and it is decreased energy consumption of the system (viz. enhance heat transfer rate in cooling coil). Nano particles of Al_2O_3, TiO_2 and CuO are used due to their higher thermal conductivity to achieve better efficiency. Mishra et al. [1] experimentally evaluated the performance of a vapour compression refrigeration system by using Cu, Al_2O_3,CuO and TiO_2 based nano refrigerants in the primary circuit. The experimental results showed that the C.O.P of the system using Al_2O_3/R134a nano refrigerant was enhanced by 35% which was highest among all other nanorefrigerant. Sabareesh et al. [2] experimentally investigated 17% increase in COP by using 0.01% by volume concentration TiO2 nano fluid in VCRS as a lubricant additive.. Shengshan Bi et al. [3] found performance improvement reduction in power consumption upto 25% by mixed mineral oil TiO2 as the lubricant with refrigerant R600a

Subramani & Prakash [4] found improvement in performance by using Al_2O_3 at 0.06% weight in the mineral oil. Kumar et al. [5] found improvement in COP by 19.6% and reduction in power consumption by 11.5%. Due to enhancement in heat transfer coefficient using nanofluid Al_2O_3 & R600a/mineral oil as working fluid in a domestic refrigerator. Abbas et al. [6] performed the analysis of an air conditioning system by using a concentration of 0.01-0.1wt% of CNT Polyester oil with refrigerant R134a and found 4.2% enhancement in the COP was enhanced by using CNT particles concentration of 0.1% by weight. Hussen [7] showed the conventional

Corresponding author: R. S. Mishra
Email Address: hod.mechanical.rsm@dtu.ac.in

refrigeration system performance improved with nano refrigerant. Compressor work decreases by about 13.3% and system C.O.P. increases by about 12%.

2. Results and Discussion

The numerical computation was carried out for finding thermal performance of vapour compression refrigeration from developed model, the following input data have been assumed.

Condenser temperature=48^{0}C, Evaporator temperature-5^{0}C, mixing of nano particles =5% by volume.

2.1 Effect of refrigerants with mixing TiO_2 nano particles

Table-1 shows the variation of thermal performances with titanium di oxide in the different ecofriendly refrigerants and it was found that by using nano in the R410a gives worst thermal performance in terms of first law efficiency, second law efficiency and exergetic efficiency. The best thermal performance in terms of first law efficiency is found by using R152a. By using hydrocarbons mixed TiO_2 nano the thermal performance of R600a hydrocarbon is lower than by using TiO_2 in the R290a. By comparing R134a and R407C, R404a, R507a and R125, it is observed that R407c gives better performance when TiO_2 is used in these refrigerants. With comparing thermal performances from Table-1, without nano by using R134a, the first law performance (COP) and second law performance (exergetic efficiency) increased significantly. Two types of EDR were computed. EDR computed based on exergy of product i.e. in terms of exergy of fuel in terms of total power utilized for running compressor for finding the components defects (Exergy losses) in the system as shown in Table-1 and effective utilization of cooling load (Q_Eva*(1-(T_Dead_State/T_eva)) in Table-1 respectively.

Table-1: Variation of thermal performances (First law efficiency (COP) and Exergetic efficiency) with ecofriendly refrigerants using TiO_2 nano material mixing

Refrigerants	First law COP	EDR	Exergetic Efficiency
R134a	4.36	1.659	0.3761
R404a	4.303	1.704	0.3698
R407c	4.634	1.458	0.4068
R125	4.044	1.935	0.3407
R507a	4.328	1.685	0.3725
R290	4.826	1.335	0.4282
R600a	4.009	1.969	0.3368
R152a	5.169	1.143	0.4666
R410a	2.138	6.847	0.1274
R502	4.671	1.433	0.4110
R134a without nano	2.978	2.44	0.2904

2.2 Effect of Thermal performances first law Performance (COP) on VCRS using TiO_2 Nano Material

The variation of evaporator temperature with variation of first law thermal performances in terms of COP and second law efficiency (exergetic efficiency) for different ecofriendly refrigerants withTiO_2 nano particles and without nano by using R134a is shown in Table-2 (a) and table-3(a) respectively. It was found that by increasing evaporator temperature the first law performance (COP) increases. And best first law performance (COP) was found by using R152a since R152a and hydrocarbon are flammable, therefore R134a gives better first law performance (COP). Similarly by increasing condenser temperature, the first law thermal performance (COP) decreases as shown in table-2(b) and table-3(b) respectively.

Table-2(a) Variation of COP with Evaporator temperature of Vapour compression using TiO_2 nano materials

T_Evaporator (K)	R134a	R404a	R125	R290	R600a	R410a	R507a	R152a	R502
283	7.932	7.12	6.715	7.802	6.866	2.557	7.09	9.273	7.645
278	6.595	5.942	5.595	6.548	5.751	2.416	5.945	7.734	6.396
273	5.517	5.048	4.746	5.599	4.873	2.282	5.06	6.493	5.448
268	4.36	4.303	4.044	4.826	4.009	2.138	4.328	5.166	4.671
263	2,182	3.525	3.327	4.086	2.588	1.932	3.58	2.70	3.908
258	--------	2.242	2.192	3.043	---------	1.466	2.399	-------	2.769

Table-2(b) Variation of COP with condenser temperature of Vapour compression using TiO_2 nano materials

T_Condenser (K)	R134a	R404a	R125	R290	R600	R410a	R507a	R152a	R502
329	1.992	3.591	3.025	3.768	1.484	1.99	3.249	2.434	3.591
325	3.342	4.118	3.532	4.281	2.323	2.087	3.785	3.99	4.118
321	4.36	4.671	4.044	4.826	3.605	2.138	4.328	5.169	4.671
317	5.229	5.294	4.605	5.444	4.578	2.166	4.924	6.185	5.294
313	6.096	6.035	5.26	6.18	5.446	2.183	5.62	7.207	6.035

Table-3(a) Variation of Exergetic Efficiency with evaporator temperature of Vapour compression using TiO_2 nano materials

T_EVA (K)	R134a	R404a	R125	R290	R600a	R410a	R507c	R152a	R502
283	0.3674	0.3556	0.3029	0.3605	0.3639	0.08253	0.3557	0.4385	0.3522
278	0.4025	0.3707	0.3306	0.3991	0.4137	0.1019	0.3718	0.4845	0.3882
273	0.4136	0.3698	0.3430	0.4211	0.4462	0.1174	0.3725	0.497	0.4073
268	0.3761	0.3360	0.3407	0.4282	0.4488	0.1274	0.3434	0.4666	0.4110
263	0.1573	0.1926	0.3049	0.4107	0.3444	0.124	0.2169	0.2262	0.4387

Table-3(b) Variation of COP with condenser temperature of Vapour compression using TiO_2 nano materials

T_EVA (K)	R134a	R404a	R125	R290	R600a	R410a	R507c	R152a	R502
329	0.1111	0.2469	0.2267	0.3099	0.1593	0.2228	0.2517	0.1606	0.290
325	0.2622	0.3083	0.2834	0.3673	0.2571	0.2337	0.3117	0.3348	0.3491
321	0.3761	0.3648	0.3407	0.4282	0.3368	0.2394	0.3725	0.4666	0.5890
317	0.4734	0.4369	0.4036	0.4975	0.4110	0.2425	0.4392	0.5804	0.4807
313	0.5704	0.5152	0.4769	0.5798	0.490	0.2443	0.4828	0.6948	0.5634

3. Conclusion

Following conclusions were drawn from present investigation.

(i) By using nano in the R410a gives worst thermal performance in terms of first law efficiency, second law efficiency and exergetic efficiency.

(ii) The best thermal performance in terms of first law efficiency is found by using R152a.

(iii) By increasing evaporator temperature the first law performance (COP) increases and best first law performance (COP) was found by using R152a

(iv) R152a and hydrocarbon are flammable, therefore R134a gives better first law performance (COP) and second law performances.

(v) By increasing condenser temperature, the first law thermal performance (COP) decreases.

References

[1] Mishra R S and Jaiswal Rahul Kumar [2015] Thermal Performance Improvements of Vapour Compression Refrigeration System Using Eco-Friendly Based Nanorefrigerants in Primary Circuit, International Journal of Advance Research and Innovation **3,** page-524-535.

[2] Sabareesh R K, Gobinath N, Sajith V, Das S and Sobhan C B 2012 Application of TiO 2 nanoparticles as a lubricant-additive _ for vapor compression refrigeration systems–An experimental investigation International journal of refrigeration 35, page-1989-1996.

[3] Bi Shengshan, [2011] Performance of a domestic refrigerator using TiO 2-R600a nano-refrigerant as working fluid Energy Conversion and Management **52** 733-737

[4] Bandgar M S, Ragit S S, Kolhe K P and Biradar N S 2016 Effect of Nano Lubricant on the Performance of Vapour Compression Refrigeration System: A Review JETIR **3,** page- 2349-5162.

[5] Subramani N and Prakash M J 2011 Experimental studies on a vapour compression system using nanorefrigerants International Journal of Engineering, Scie-nce and Technology ,3, page- 95-102.

[6] Kumar R R, Sridhar K and Narasimha M 2013 Heat transfer enhancement in the domestic refrigerator using *R600a/mineral* oil/nano-Al_2O_3 as working fluid International Journal of Computational Engineering Research **3,** page-42-50.

[7] Abbas M, [2013] Efficient Air—Condition Unit By Using Nano—Refrigerant 1st Engineering undergraduate research catalyst conference.

[8] H.A. Hussen [2014] Experimental investigation for TiO2 nanoparticles as a lubricant- Additive for a compressor of window type air-conditioner system **J.** Eng., 20 (2014), pp. 61-72

2nd IEEE International Conference on Power Electronics, Intelligent Control and Energy systems (ICPEICES-2018)

Multi-Input Multi-Level Isolated DC-DC Converter for Enhanced Reliability of Renewable Sources

Ravi Vardhan Arya
Department of Electrical Engineering
Delhi Technological University, Delhi

Amritesh Kumar
Department of Electrical Engineering
National Institute of Technology, Silchar,

Aditya Narula
Department of Electrical Engineering
*Delhi Technological University,*Delhi

***Abstract* –This paper proposes an isolated multi-input multi-output power electronics converter for interfacing with multiple renewable energy sources. The converter provides the capability of multi-level output based upon the secondary side series-parallel configuration. The modular architecture of the converter enable plug and play operation. In Control algorithm proposed for the converter ensures equal load sharing between the inputs during continuous and discontinuous operating modes while maintaining the output voltage during load perturbations. The system is modeled and simulated under MATLAB Simulink environment with the presented results verifying the performance of the proposed converter.**

Keywords - Multi-Input converter, Multi-Level converter, switched capacitor, close loop control.

I. INTRODUCTION

Renewable energy sources (RES) have gained great attention due to its advantages of rich reserve and environment-friendly nature. It is regarded as the best alternative to fossil energy. However, these energy sources are easily gets perturbed by climatic conditions and these are unpredictable to provide continuous and reliable power supply.

In order to address the issue, it is preferred to integrate RES with conventional sources to form a hybrid configuration to get a stable and continuous power supply. To support such architecture Power Electronics based converter-inverter system becomes an integral for these RES for maximum power extraction and feeding power to load/grid. With this, the concept of Multi-Input Converter (MIC) has been proposed to accommodate multiple sources i.e. renewable and conventional sources [1-8]. Recently researchers have tried to integrate multiple batteries through a MIC to get a reliable output for Electric Vehicles [1]. Others have proposed PV-Wind-Battery based MIC to get a reliable dc supply which is further inverted to feed it to grid [2-3].

In literature, several topologies of MICs with resonant, non-resonant, isolated, non-isolated has been reported to combine different types of DC input sources to obtain single DC output [1-8]. In [4-5], a systematic approach for designing MIC is reported using a multi-winding transformer for renewable energy application.

In [1],[6], a non-isolated MIC with Modular Parallel topology is employed to get a single DC output. In this only one input transfers power to the load, at a time. If more than one sources are used to transfer power to the load at a time, then this increases the problem of circulating current. In [7], a non-isolated MIC based on switched capacitor is proposed with very simple control circuitry. Author has employed the concept of LC oscillator, for improvement in output waveform and reducing the stress on the capacitor.

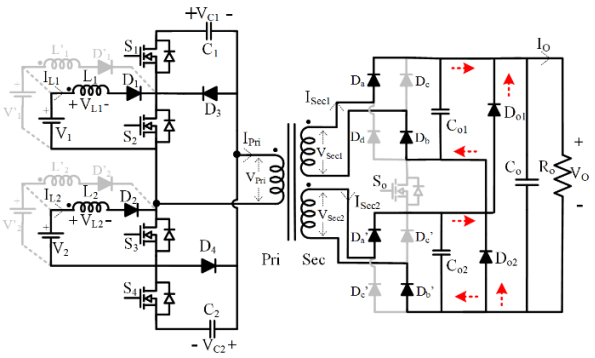


Fig. 1 Proposed Isolated Multi-Input Multi-Level Output DC-DC Converter

MIC provides a simple circuit, reduced number of components, centralized control, high reliability and decreased size/cost [8]. Most of these MIC topologies are confined to single output only. But in many application, variable output voltages are also requisite. This basically opens the avenue for isolated MIC topology capable of having multi-level output with multiple inputs to avoid multiplicity of converters. Though non-isolated topology is having low cost and less circuitry but lacks in safety and hazards protection. Isolated topology credits in terms of isolation, protection, and also avoid leakage/circulating current.

The authors have proposed single-input multi-level dc-dc converters for variable output [9]. But things are scarcely discussed on isolated multi-input multi-level dc-dc converter.

In this paper, an isolated multi-input multi-level dc-dc converter is proposed for variable output as shown in Fig. 1. For maintaining variable controlled output voltage irrespective of perturbation in loading, a close loop control strategy is designed. The proposed converter uses two distinct dc-dc converters on either side of a high-frequency transformer. Switching sequence of multiple switches is maintained in a way to provide continuous energizing to primary winding with proper boost. The primary side of the converter provides a base for integrating multiple inputs and secondary side of converter enables to get multi-level output. To verify the working operation of the proposed multi-input system, two uniform battery sources of 48V is used at each input. The effectiveness of the proposed topology and control logic is verified using MATLAB Simulink.

978-1-5386-6625-8/18/$31.00 ©2018 IEEE

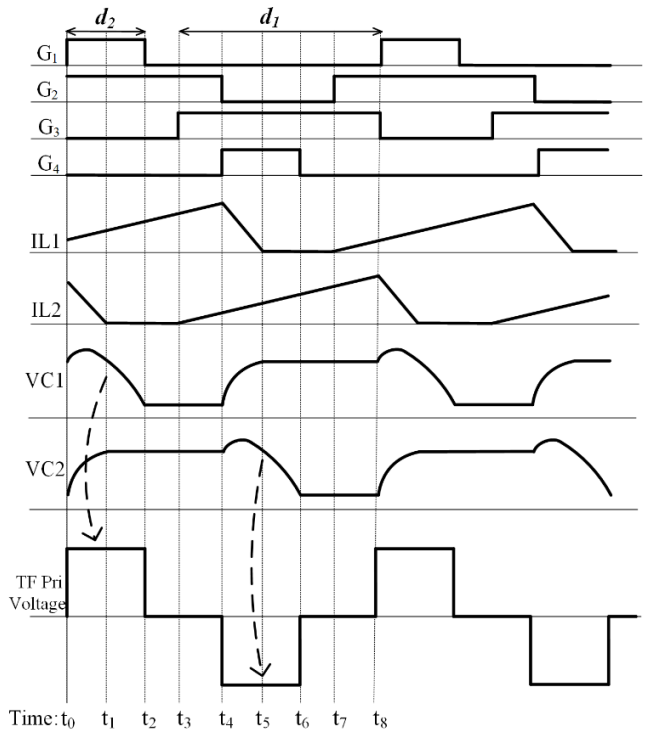


Fig.2: Gating Scheme and key waveforms

II. TOPOLOGY DESCRIPTION

Fig.1 shows the schematic of the proposed isolated Multi-input Multi-level (MI-ML) dc-dc converter. In the proposed structure two input sources in the form of battery stack of 48V each are integrated with the converter. The close loop operation of the converter is performed to have equal load sharing between the battery stack even in CCM. Switched capacitors (C_1, C_2) are also utilized in converter for efficiently absorbing and releasing excess energy from the input sources.

Input boost inductors (L_1, L_2) stores energy when switch S_2 and S_3 are turned ON respectively. When these switches are turned OFF the stored energy is transferred to the load and excess energy is stored in Capacitors C_1 and C_2. Switches S_1 and S_4 are switched to release or absorb excess energy in the capacitor. When S_1 (or S_4) is switched ON, then energy is released from Capacitor C_1 (or C_2). When these switches are turned OFF, input sources and stored energy in the inductor deliver power to the load and charges respective capacitor.

Gating scheme of all the switches is shown in Fig. 2. d_1 denotes the duty ratio of S_2 and S_3, and d_2 denotes the duty ratio of S_1 and S_4. Switching pulses of S_2 & S_3 are phase-shifted by 180° with respect to each other. Similarly, pulses of S1 & S4 are phase shifted by 180°. The duty ratio of middle switches (S_2 and S_3) is maintained greater than 0.5 to allow a freewheeling path for the transformer primary side current, and a limit is set around 0.72 for proper close loop operation under perturbing load condition. S_1 is switched ON just after the S_3 is OFF, and similarly, S_4 switched ON after the S_2 is OFF with proper dead band.

III. OPERATING PRINCIPLE

In this section operating modes of the converter is explained which are shown in Fig. 3 and Fig. 4. First, the operation of the secondary side is discussed. Owing the switching of S_o , the secondary side circuit form a multi-level dc output. When S_o is OFF, output terminals of both the full wave rectifiers which are connected to secondary windings of the transformer will make parallel connections through diodes D_{o1} and D_{o2} to feed the load. And when S_o is turned ON, the output terminals of both rectifiers will cascade (connect in series) as shown in Fig. 3(a-b).

Operation of primary side converter is divided into 8 various intervals discussed below without dead band consideration. All the operation interval of primary are shown in Fig. 2 & 4. Before the first interval, S_3 is ON and S_1 is OFF. Energy in L_2 stored to its peak. C_1 is fully charged and C_2 is discharged and L_1 starts storing energy from input-1.

Interval A (t_0-t_1): During this interval, S_3 is switched OFF and S_1 is Switched ON, due to which energy stored in L_2 and C_1 was transferred to the primary winding of transformer and excess energy get stored in C_2 and Inductor L_2 become fully discharged and enters DCM. And L_1 continues in storing energy.
Interval B (t_1-t_2): In this interval load is solely powered by C_1.
Interval C (t_2-t_3): In this interval S_1 is turned OFF, applying a zero voltage at the primary winding of Transformer, and a freewheeling path is made through diode D_3 and S_2.
Interval D (t_3-t_4): Till this interval, S_2 is turned ON and S_1, S_3, S_4 are turned OFF. Now S_3 is switched ON and L_2 starts storing energy from input 2. And Primary winding continues to freewheeling through D_3 and S_2. Also, the energy in L_1 is about to reaches its peak.

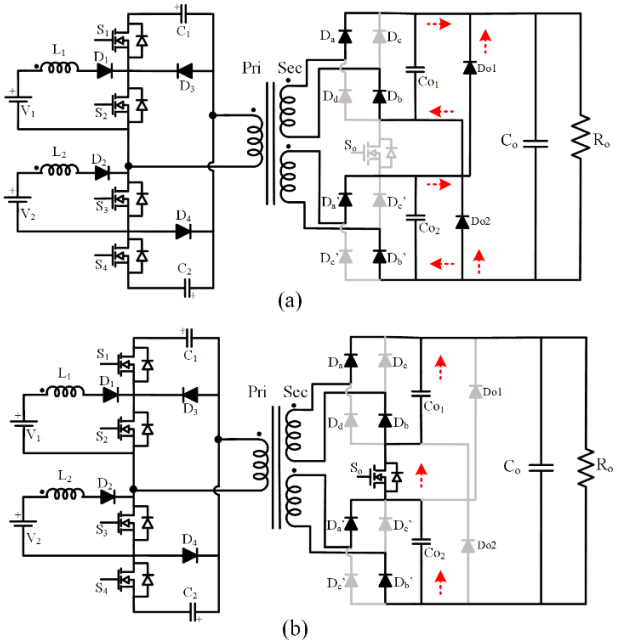


Fig.3 Secondary Windings connected in: (a) Parallel (S_o is OFF); (b) Series (S_o is ON)

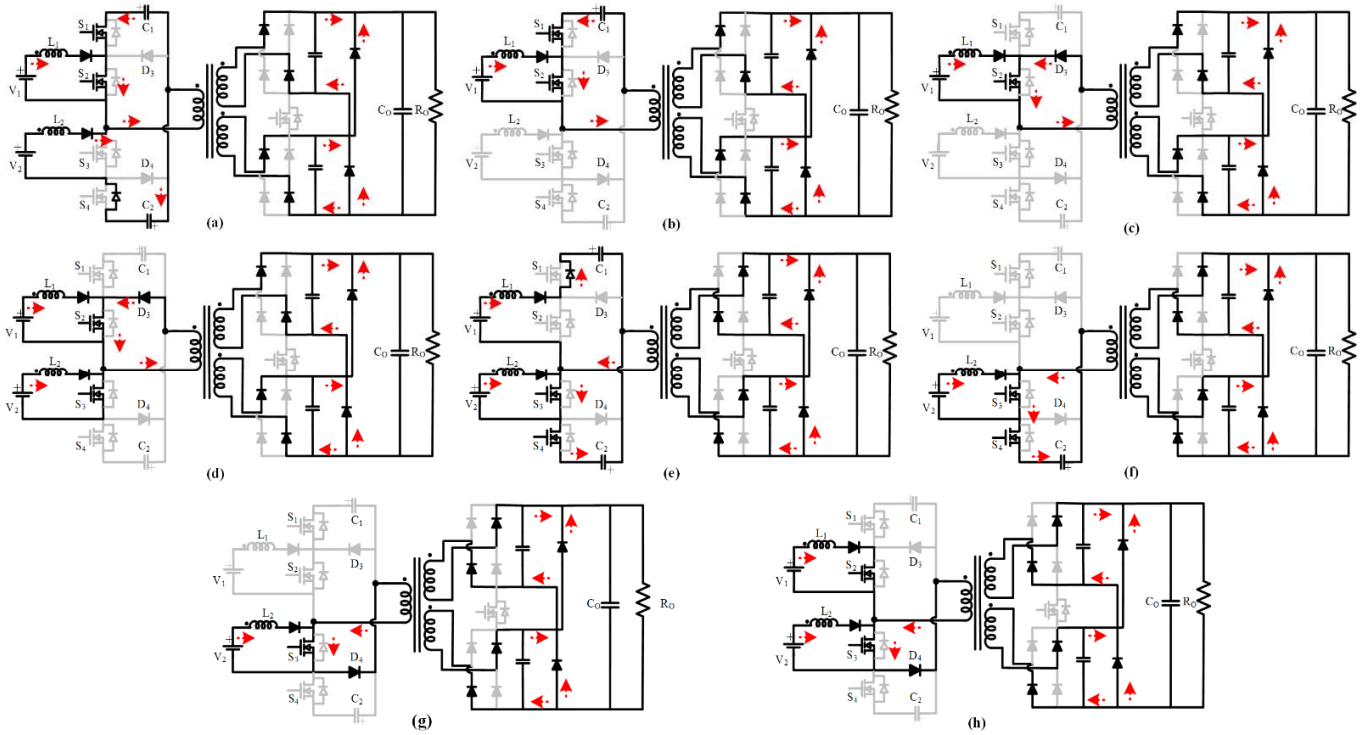


Fig.4: Operation intervals of converter: (a) Interval A(t_0-t_1), (b) Interval B(t_1-t_2), (c) Interval C(t_2-t_3), (d) Interval D(t_3-t_4), (e) Interval E(t_4-t_5), (f) Interval F(t_5-t_6), (g) Interval G(t_6-t_7), (h) Interval H(t_7-t_8)

Interval E (t_4-t_5): At this point of time S_2 is OFF and S_4 is ON. Stored energy in L_1 and C_2 is transferred to the load via primary having negative voltage and causing a reverse current in primary circuitry. Excess energy is absorbed by C_1. In this interval, L_1 is fully discharged and enters DCM. And L_2 continues to store energy form input-2.

Interval F (t_5-t_6): During this interval, the primary winding is solely energized by C_2.

Interval G (t_6-t_7): At this time, S_4 is OFF, applying a zero voltage at the primary winding of transformer, and a freewheeling path is made through diode D_4 and S_3.

Interval H (t_7-t_8): Before t_7, S_3 is ON and S_1, S_2, S_4 are turned OFF. Now at t_7 S_2 is ON, resulting in the increase in I_{L1} and L_1 starts storing energy from input-1. And primary winding continues to freewheeling through D_4 and S_3. Also, the energy in L_2 is about to reaches its peak.

IV. CONTROL STRUCTURE

A constant output voltage control is implemented in this converter, by regulating the duty cycle of S_1, S_2, S_3, and S_4. The close loop control strategy for the converter is shown in Fig. 5. Close loop control initializes with comparing of output DC-link voltage (V_o) with the reference voltage (V_{ref}) to generate the error signal. This error signal is fed to the PI Controller. Now from the output of the PI controller, 4 different gating pulses G_1, G_2, G_3 and G_4 for all the switches has to be generated by comparing it with Saw-tooth (carrier) signal. G_3 and G_2 are generated by directly comparing the PI output with 0° and 180° phase shifted Saw-tooth signals of 20 kHz respectively as shown in fig.2. A D flip-flop is used in control circuitry to provide an initial delay for G_1 and G_4. On feeding the PI output, flip-flop result and both saw-tooth signals to Dead band controller (DBC), the dead band between the switching of S_1-S_3 and S_2-S_4 is being controlled and appropriate Saw-tooth signals are generated. K_a is used to provide dead band when middle switches (S_2, S_3) is switched OFF and outer switches (S_1, S_4) are turned ON. And similarly, K_b provide dead band when outer switches are switched OFF and middle switches are turned ON. After that, DBC output is compared with 0° and 180° phase shifted Saw-tooth signals to generate G_1 and G_4.

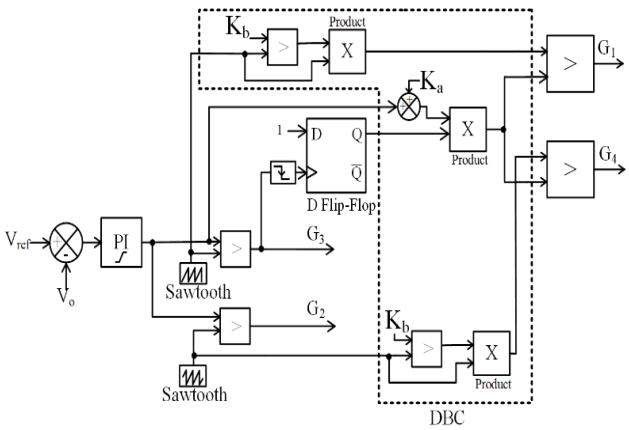


Fig.5: Close loop Control Logic for gating structure with proper dead band.

V. TOPOLOGY ANALYSIS

To understand the input-output relation of the proposed converter, it is necessary to analyze the steady state behavior of various storing elements like L_1, L_2, C_1, and C_2. Capacitors are switched at a proper time to power up the primary of the transformer and apply positive and negative voltages to get the required output. Similarly, L_1 and L_2 are properly switched ON and OFF for requisite power transfer in the secondary.

As discussed in the previous section, the duty of middle switches (S_2, S_3) is maintained greater than 0.5 to apply zero voltage at the primary of transformer. The relation between d_1 (duty ratio of G_2, G_3) and d_2 (duty ratio of G_1, G_4) is given as:

d_1=1- d_2 -DB (1)

Where, DB is the dead band and must be considered between switching of S_1-S_3 and S_2-S_4 for providing proper freewheeling path and reversal of polarity without overshoot due to switching.

For the proposed isolated converter consisting of a high-frequency transformer having m no. of secondary windings, with turns ratio 1: n, then-

$V_{Pri}=V_o/n$ & $I_{Pri}=nI_o$ (S_o=OFF), (2)

$V_{Pri}=V_o/nm$ & $I_{Pri}=nmI_o$ (S_o=ON), (3)

For the steady-state operation of the converter, the net change in inductor current is zero, i.e. inductors should follow volt-second balance. Also, net change in capacitor voltage should be zero and hence it must follow ampere-second balance.

Considering the converter operating in continuous conduction mode, the following analysis is done.

Applying volt-sec balance across L_1 (as represented in Fig. 1-2):

$$V_1 d_1 + (1-d_1)(V_1 - V_{Pri} - V_{c1}) = 0 \quad (4)$$

i.e., $$V_{Pri} = \frac{V_1}{(1-d_1)} - V_{c1} = V_{c2} \quad (5)$$

Similarly, volt-sec balance across L_2 gives:

$$V_{Pri} = \frac{V_2}{(1-d_1)} - V_{c2} = V_{c1} \quad (6)$$

Therefore, $$V_O = nxV_{Pri} = \frac{n}{2}\left(\frac{V_1+V_2}{(1-d_1)} - (V_{c1}+V_{c2})\right) \quad (7)$$

And, $$d_1 = \left(1 - \frac{V_1}{(V_{Pri}+V_{c1})}\right) = \left(1 - \frac{V_2}{(V_{Pri}+V_{c2})}\right) \quad (8)$$

Now by Amp-sec balance in C_1:

$$-d_2(I_{Pri} - I_{L1}) + (1-d_1)(I_{L2}) = 0 \quad (9)$$

i.e., $$-d_2(I_{Pri} - I_{L1}) + (d_2 + DB)(I_{L2}) = 0 \quad (10)$$

$$I_{Pri} = \frac{I_{L2}(d_2+DB)}{d_2} + I_{L1} \quad (11)$$

Similarly, Amp-sec balance in C_2:

$$I_{Pri} = \frac{I_{L1}(d_2+DB)}{d_2} + I_{L2} \quad (12)$$

Therefore, $$I_O = \frac{I_{Pri}}{n} = \frac{1}{2n}\left(\frac{(I_{L1}+I_{L2})(d_2+DB)}{d_2} + I_{L1} + I_{L2}\right) \quad (13)$$

And, $$d_2 = \left(\frac{DBxI_{L1}}{(I_{Pri}-I_{L1}-I_{L2})}\right) = \left(\frac{DBxI_{L2}}{(I_{Pri}-I_{L1}-I_{L2})}\right) \quad (14)$$

From (11-12), it can be seen that input currents I_{L1} and I_{L2} are controlled by d_1 and d_2 in the PWM which is necessary for some applications such as renewable energy resources to extract maximum power.

Eq. (5-6) and (11-12) clearly shows that the load is equally power by both the input in DCM as well as CCM.

From the above analysis, the relation between Input voltages and Output voltage can be synthesized by averaging which is shown in Eq. (7) and (13).

According to (5), when source-1 is powering the load then at that point of time C_2 is also discharging and C_1 is getting charged by I_{L1}. And (6), clearly shows when source-2 is powering the load then at that time C_1 is discharging and C_2 is getting charged by I_{L2}.

Eq. (5-6) can be easily verified by the simulation results shown in Fig. 6. It can be seen clearly when C_1 is discharging then a positive voltage is applied on the primary winding of transformer (TF Voltage), I_{L2} is decreasing and C_2 is charging. And when C_2 is discharging then a negative voltage is applied on primary winding, I_{L1} is decreasing and C_1 is charging.

VI. SIMULATION RESULTS

The close loop operation of proposed topology is modeled and verified by simulation in MATLAB Simulink environment. Simulation results of both cascaded and parallel modes of the secondary side of transformer are observed under steady and dynamic conditions. Simulation results are obtained using two 48V battery sources as input to this MIC with the following parameter: V_1=V_2=48V, L_1=L_2=200µH, C_1=C_2=100µF, f_{sw}=20 kHz, 1:2 (4.5kVA) high-frequency transformer and C_o=220µF. Fig. 7 shows response of isolated MIC under the load variation from 130Ω to 90Ω with switch S_o OFF, i.e. secondary windings are connected in parallel, output voltage is maintained at 170V as shown in Fig. 7(b). To satisfy the load requirement, 1.3 A of

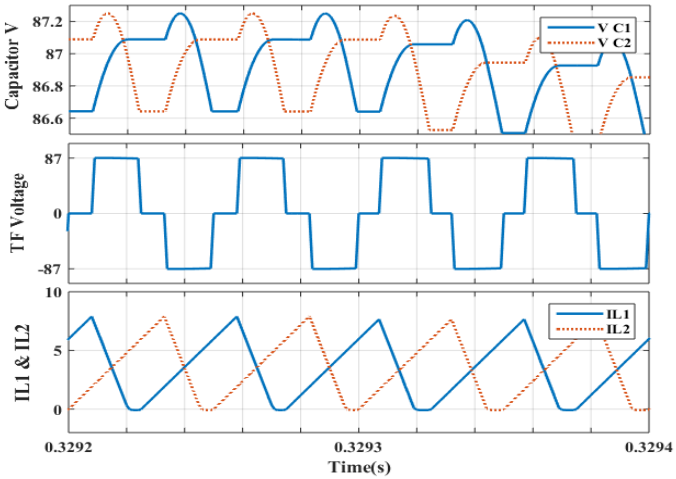


Fig.6: Capacitor Voltage Ripple and Transformer Primary Voltage

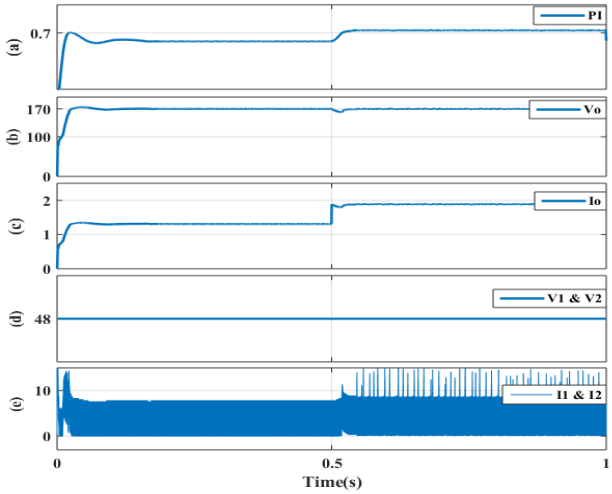


Fig. 7 Simulation Results with S_o is OFF showing: (a) PI output, (b)Output voltage, (c) Output current, (d) Input voltage V_1 and V_2, (e) Input inductor currents I_{L1} and I_{L2}

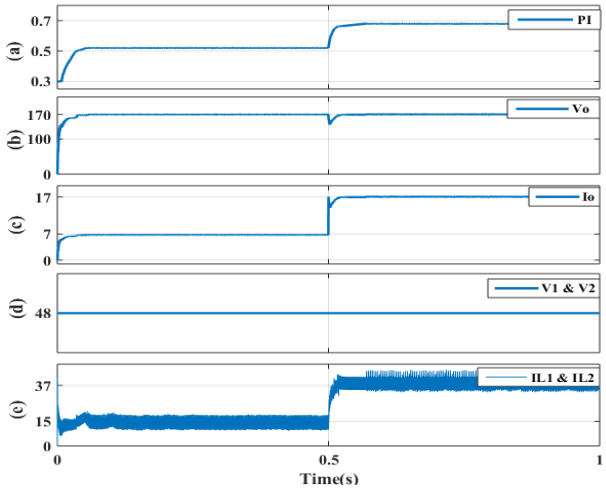


Fig. 9 Simulation Results with S_o is ON showing: (a) PI output, (b)Output voltage, (c) Output current, (d) Input voltage V_1 and V_2, (e) Input inductor currents I_{L1} and I_{L2}

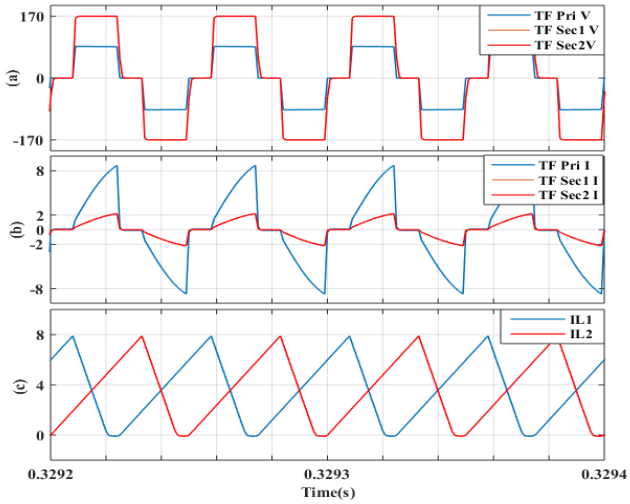


Fig. 8 Simulation Results with S_o is OFF showing: (a) Transformer Voltages across Primary and both secondary windings, (b) Transformer Current in Primary and both secondary windings, (c) Magnified waveforms of I_{L1} and I_{L2} in DCM

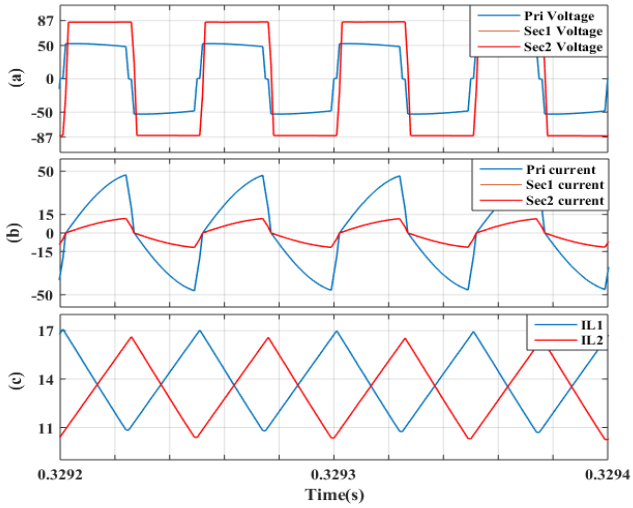


Fig. 10 Simulation Results with S_o is ON showing: (a) Transformer Voltages across Primary and both secondary windings, (b) Transformer Current in Primary and both secondary windings, (c) Magnified waveforms of I_{L1} and I_{L2} in CCM

current is drawn from the secondary terminals as shown in Fig. 7(c). At t=0.5s, a load perturbation command is initiated causing a step change in load current from 1.3A to 1.9A as shown in Fig. 7(c). With a change in load current output voltage is regulated at 170V as in Fig. 7(b). Variation in loading also changes the PI output from 0.65 to 0.71 as shown in Fig. 7(a), which control the duty of switches and stabilizes the output voltage to V_{ref}.

Fig. 8 shows the magnified waveform of transformer voltages, currents, and input inductor currents. Fig. 8(a) shows the transformer terminals input-output voltage resembling chopped square waveform. With the turns ratio of primary to secondary 1:2, for a peak primary voltage of 87V, a voltage 170V peak is observed at the secondary side. From Fig.8(c) it is clear that both I_{L1} and I_{L2} (input inductor current) operates in discontinuous mode (DCM).

Fig. 9 shows another mode of operation with S_o ON, giving a cascade connection of secondary windings. Dynamic response of the converter under the load perturbation from 25Ω to 10Ω is shown in Fig. 9. With the initial load of 25Ω connected on output, 7A of output current is drawn as in Fig. 9(c). With the same input voltage of 48V a load perturbation is initiated at 0.5s. It results in the increase in output current 7A to 17A, in a small time. Meanwhile, a steady reference voltage of 170V is maintained at the output as in Fig. 9(b).

Fig. 10(a-c) shows the magnified response of transformer winding currents, voltages and input inductor currents. Due to high current demanded at the output, input currents enter into CCM as clearly shown in Fig. 10(c).

CONCLUSION

The isolated Multi-Input Multi-level output DC-DC Converter presented in this paper with close loop control strategy can be exploited as DC-link with the storage system for the generation of AC Power with various standard voltages. In this paper, the output voltage is referenced to 170V with two 48V batteries as input sources. Modular-structure enables multiplication of output voltages by adding the desired no. of inputs. Having the advantages of the centralized control scheme and high reliability the proposed converter credits with very good Voltage regulation.

REFERENCES

[1] Furkan Akar et al., ''A Bidirectional Non-isolated Multi-Input DC–DC Converter for Hybrid Energy Storage Systems in Electric Vehicles", IEEE Trans. Veh. Tech., vol. 65, no. 10, pp.7944-7955, October 2016.

[2] V. Karthikeyan and Rajesh Gupta, "Multiple-Input Configuration of Isolated Bidirectional DC–DC Converter for Power Flow Control in Combinational Battery Storage", IEEE Trans Ind. Info, Vol. 14, No. 1, January 2018.

[3] B. Mangu et al. ,"Grid-Connected PV-Wind-Battery-Based Multi-Input Transformer-Coupled Bidirectional DC-DC Converter for Household Applications", IEEE Journal Of Emerging And Selected Topics In Power Electronics, Vol. 4, No. 3, September 2016

[4] Yuan-Chuan Liu and Yaow-Ming Chen,'' A Systematic Approach to Synthesizing Multi-Input DC–DC Converters'', IEEE Trans. Power Electron. , vol. 24, no. 1, pp.116-127, January 2009.

[5] Yuan-Chuan Liu and Yaow-Ming Chen, ''Multi-Input DC/DC Converter Based on the Multi winding Transformer for Renewable Energy Applications'', IEEE Trans. Ind. App, vol. 38, no. 4, pp.1096-1104, July/August 2002

[6] Ebrahim Babaei and Okhtay Abbasi, ''Structure for multi-input multi-output dc–dc boost converter'', IET Power Electron., vol. 9, no. 1, pp.1–11, May 2015.

[7] Ye Yuan-mao and Ka Wai Eric Cheng, ''Multi-input voltage-summation converter based on switched-capacitor'', IET Power Electron., 2013, Vol. 6, Iss. 9, pp. 1909–1916.

[8] Serkan Dusmez, IEEE, Xiong Li and Bilal Akin, ''A New Multi-Input Three-Level DC/DC Converter'', IEEE Trans Power Electron. , vol.31, no.7, pp. 1230-1240, 2016.

[9] Hurng-Liahng Jou et al., ''Novel Isolated Multi-level DC-DC Power Converter'', IEEE Trans. on Power Electron. , vol. 31, no. 4, pp. 2690-2694, 2016.

Multiple-Input Single-Output Universal Biquad Filter Using Single Output OTAs

Ajishek Raj
Department of Electrical Engineering
Delhi Technological University
New Delhi, India
ajishekaerotek@gmail.com

D. R. Bhaskar
Department of Electronics and Communication Engineering
Delhi Technological University
New Delhi, India
drbhaskar@dtu.ac.in

Pragati Kumar
Department of Electrical Engineering
Delhi Technological University
New Delhi, India
pragati_1964@yahoo.co.in

***Abstract*— A new voltage-mode multi-input single-output(MISO) universal biquad filter configuration employing five single output operational transconductance amplifiers (OTAs), two grounded capacitors (ideal for integrated circuit implementation) with three input voltage signals has been proposed. The circuit has versatility to realize all five second-order filter responses namely, low pass (LPF), high pass (HPF), band pass (BPF), band reject (BRF) and all pass (APF) using appropriate selection(s) of three inputs. The biquad enjoys low active and passive sensitivities. The workability of this multifunctional biquad filter topology has been established through SPICE simulation results.**

Keywords—Operational Transconductance Amplifier (OTA), Analog Circuit Design, Voltage Mode Filters.

I. INTRODUCTION

Operational transconductance amplifiers (OTAs) based analog filters (used for continuous-time signal processing) have exhibited some advantages due to their structural simplicity, high frequency capability, electronic controllability and monolithic integrability both in Bipolar and CMOS technologies. MISO-type multifunction biquad filters are especially versatile due to the fact that the same topology may be used to describe various filter responses by the appropriate choice of input signal(s). In reference [1] advantages and applications of such filters have been reported. Number of voltage-mode (VM) MISO-type OTA-C universal biquad filter topologies have been presented in [2-7] using multiple-output OTAs. VM MISO-type filter structures presented in [8-16] use only single output OTAs which are commercially available as off-the self ICs.

Recently, Psychalinos, Kasimis and Khateb [16] presented an OTA-C universal biquad filter employing six single output OTAs, two grounded capacitors with four input voltage signals for use in discrete applications since commercially available OTAs are only single output type. This filter configuration is capable of realizing all the standard second-order filter responses by proper selection of four input voltage signals therein. In this communication we propose a new circuit structure which by contrast, employs only five OTAs and two grounded capacitors, to realize all the five filter functions with appropriate choice of only three input voltage signals. Workability of this biquad filter has been verified through SPICE simulations and some sample results have been presented.

II. THE PROPOSED VOLTAGE-MODE FILTER CONFIGURATION

The proposed new MISO-type VM universal biquad filter structure for realizing low pass (LPF), high pass (HPF), band pass (BPF), band reject (BRF) and all pass (APF) using appropriate selection(s) of three inputs is shown in Fig. 1. A routine analysis of the circuit of Fig. 1 with ideal OTAs yields the expression for the output voltage in terms of the three input voltages as:

$$V_0(s)=\frac{AV_{in1}(s)+BV_{in2}(s)+s^2V_{in3}(s)}{s^2+s\frac{g_{m2}g_{m3}}{C_2g_{m4}}+\frac{g_{m1}g_{m2}g_{m3}}{C_1C_2g_{m4}}} \quad (1)$$

Where

$$A=\left(s^2\frac{g_{m3}}{g_{m4}}-s\frac{g_{m3}g_{m5}}{C_2g_{m4}}+\frac{g_{m1}g_{m2}g_{m3}}{C_1C_2g_{m4}}\right)$$

$$B=s\left(\frac{g_{m3}g_{m5}}{C_2g_{m4}}\right)$$

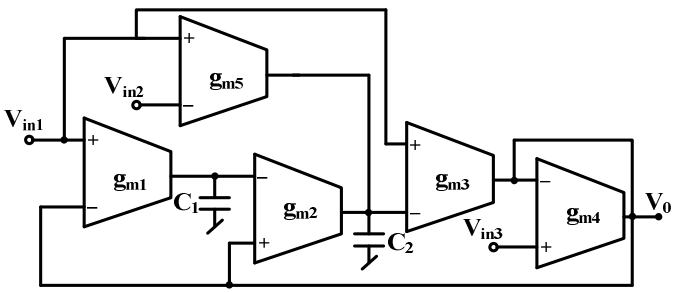


Fig. 1. Proposed Biquad Filter Configuration

Thus, the various second-order filter functions can be derived from equation (1) by proper selection of input voltages as follows:

(i) LPF: if $V_{in1}=V_{in2}=-V_{in3}=V_{in}$ (input voltage signal), and $g_{m3}=g_{m4}$,

$$\frac{V_0(s)}{V_{in}(s)}=\frac{\left(\frac{g_{m1}g_{m2}}{C_1C_2}\right)}{D(s)} \quad (2)$$

(ii) BPF: if $V_{in1}=V_{in3}=0$ and $V_{in2}=V_{in}$,

978-1-5386-6625-8/18/$31.00 ©2018 IEEE

$$\frac{V_0(s)}{V_{in}(s)} = \frac{s\left(\frac{g_{m3}g_{m5}}{C_2 g_{m4}}\right)}{D(s)}; g_{m2} = g_{m5} \quad (3)$$

(iii) HPF: if $V_{in1} = V_{in2} = 0$ and $V_{in3} = V_{in}$,

$$\frac{V_0(s)}{V_{in}(s)} = \frac{s^2}{D(s)} \quad (4)$$

(iv) BRF: if $V_{in3} = 0$ and $V_{in1} = V_{in} = V_{in2}$,

$$\frac{V_0(s)}{V_{in}(s)} = \frac{(s^2 + \frac{g_{m1}g_{m2}}{C_1C_2})}{D(s)}; g_{m3} = g_{m4} \quad (5)$$

(v) APF: if $V_{in1} = V_{in}, V_{in3} = V_{in2} = 0$,

$$\frac{V_0(s)}{V_{in}(s)} = \frac{s^2 - s(\frac{g_{m5}}{C_2}) + (\frac{g_{m1}g_{m2}}{C_1C_2})}{D(s)}; g_{m3} = g_{m4} \quad (6)$$

where

$$D(s) = s^2 + s(\frac{g_{m2}g_{m3}}{C_2 g_{m4}}) + \frac{g_{m1}g_{m2}g_{m3}}{C_1C_2g_{m4}} \quad (7)$$

The various filter parameters namely, resonance frequency (ω_o) bandwidth (BW) and quality factor (Q_o) of the proposed filter configuration can be obtained as:

$$\omega_o = \sqrt{\frac{g_{m1}g_{m2}g_{m3}}{g_{m4}C_1C_2}} \quad (8)$$

$$Q_o = \sqrt{\frac{C_2 g_{m1}g_{m4}}{C_1 g_{m2}g_{m3}}} \quad (9)$$

$$BW = \frac{g_{m2}g_{m3}}{C_2 g_{m4}} (for\ BPF\ and\ BRF) \quad (10)$$

From equations (8) and (10), it is evident that ω_o and BW are orthogonally programmable through the transconductance g_{m1} (i.e., after fixing the value of BW, the ω_o can be controlled with g_{m1}).

The sensitivities of ω_o, and Q_o can be determined as:

$$S_{gm1}^{\omega o} = S_{gm2}^{\omega o} = S_{gm3}^{\omega o} = S_{gm1}^{Qo} = S_{gm4}^{Qo} = S_{C_2}^{Qo} = 0.5$$

$$S_{gm4}^{\omega o} = S_{C_1}^{\omega o} = S_{C_2}^{\omega o} = S_{gm2}^{Qo} = S_{gm3}^{Qo} = S_{C_1}^{Qo} = -0.5$$

Thus, all active and passive sensitivities are small.

III. Simulation Results

The workability of the proposed configuration has been verified through SPICE simulations using the macro model of the OTAs in the IC LM13700 [17]. The DC power supplies of ±15V were used to bias the OTAs and equal bias currents $I_{bias1} = I_{bias2} = I_{bias3} = I_{bias4} = I_{bias5} = 548\mu A$ ($g_{mi} = 10.5mS$) $(i = 1-5)$ were used to simulate the circuit of Fig. 1. The capacitors used were of values C_1 = 47 nF and C_2 = 23.45 nF for the cut-off frequency f_o = 50 kHz and quality factor Q_o = 0.707. Fig. 2 shows the simulated magnitude responses of all the filters. Transient response and phase response of APF at cut-off frequency 50 kHz are shown in Fig. 3 and Fig. 4 respectively.

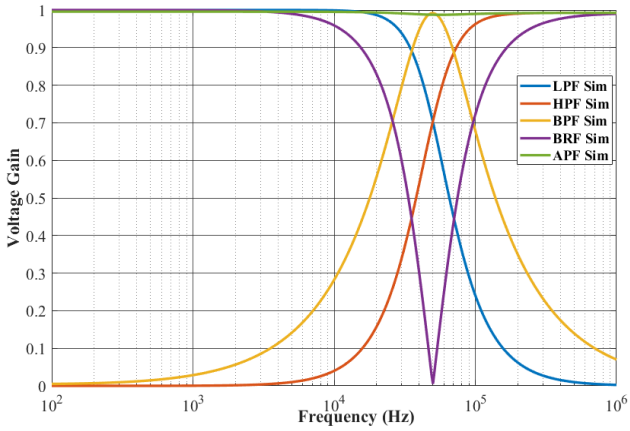


Fig. 2 Frequency responses of the proposed configuration

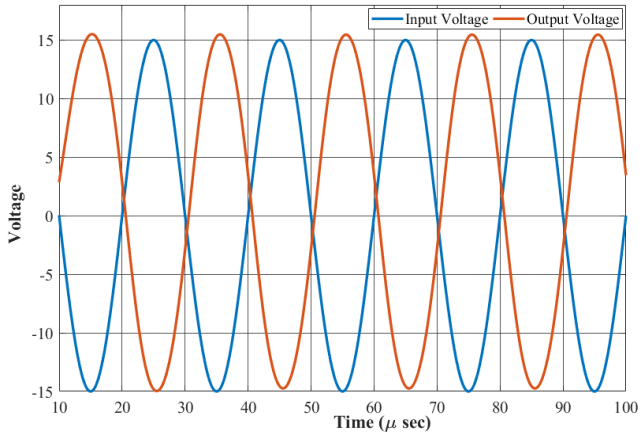


Fig. 3 Simulated transient response of APF

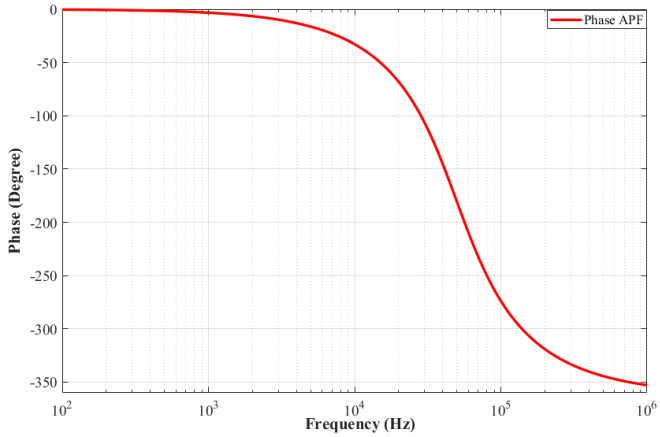


Fig. 4 Simulated phase response of APF

IV. Orthogonal Tuning of Resonant Frequency and Bandwidth

It is observed from equations (8) and (10) that the BW and the resonant frequency are orthogonally tunable, i.e., the resonant frequency can be tuned without changing the BW

by varying g_{m1}. The biquad filter with the nominal value of the cut-off frequency f_o = 50 kHz, BW = 71.49 kHz, quality factor = 0.707 and gain = 1 was designed by taking g_{mi} (i=1-5) = 10.5mS, C_1 = 47 nF and C_2 = 23.45 nF. I_{bias} of 548 µA (for all the OTAs) results in fixing this value of g_m for all the OTAs.

To confirm the controllability of f_o without changing the bandwidth, we have used I_{bias1} = 276 µA, 368 µA, 552 µA and 1.104mA to get the variations in cut-off frequencies 36.76 kHz, 41.12 kHz, 50.429 kHz and 69.589 kHz respectively for the BPF and BRF. These results have been shown in Fig. 5 and Fig. 6 for BPF and BRF respectively. It may be noted that the BW remained constant at 71.3 kHz for both BPF and BRF. A comparison with previously published MISO type OTA-C biquads has also been presented in Table 1.

TABLE I. COMPARISION RESULTS OF PROPOSED FILTER

Features	Circuit Reference					
	[4]	[5]	[8]	[9]	[16]	Fig. 1
Numbers of OTAs	7	6	6	7	6	5
Number of resistors and capacitors	2 C	2C	2C+ 2R	2C	2C	2C
Grounded passive components	Y	Y	Y	Y	Y	Y
High impedance at the inputs	Y	Y	Y	Y	Y	Y
Availability of orthogonal tunability of ω_o and BW	N	N	Y	Y	Y	Y

From the Table 1, it is observed that the proposed circuit uses minimum number of single output OTAs while providing tunability of ω_o and BW for BPF and BRF.

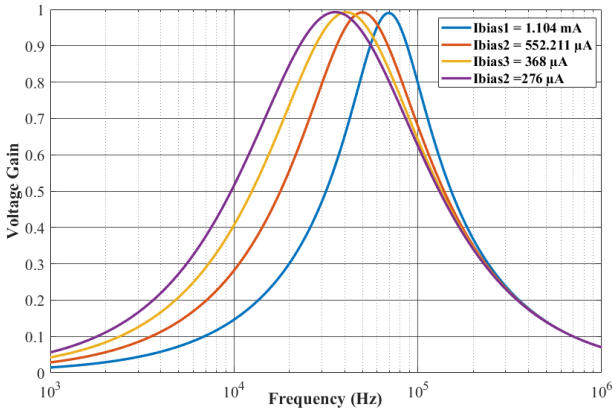


Fig. 5 Electronic tunability of BPF

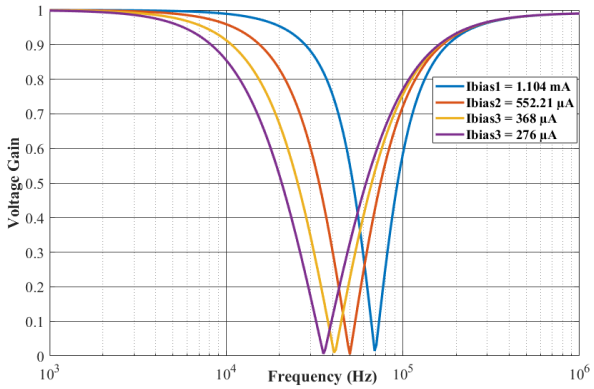


Fig. 6 Electronic tunability of BRF

V. CONCLUSION

In this paper, a new voltage-mode electronically controllable three input, one output universal biquadratic filter configuration using five single output OTAs and two grounded capacitors has been presented. The LPF, BPF, HPF, BRF and APF can be realised by appropriate choice(s) of the input signals from the same topology. The input terminals of the OTAs offer high input impedance level which enables easy cascadability of the voltage-mode operation. The cut-off frequency (f_o) and bandwidth are orthogonally tunable through bias current of the OTA1 for BPF and BRF.

REFERENCES

[1] Horng JW. Voltage-mode universal biquadratic filter with one input and five outputs using OTAs. International Journal of Electronics. vol. 89, no. 9, 2002, pp. 729-37.

[2] Horng, JW. "Voltage-mode universal biquadratic filter using two OTAs." *Active and Passive Electronic Components* vol. 27, no. 2, 2004, pp. 85-89.

[3] Chang, Chun-Ming. "New multifunction OTA-C biquads." *IEEE Transactions on Circuits and Systems II: Analog and Digital Signal Processing* vol. 46, no. 6, 1999, pp. 820-824.

[4] Lee, Chen-Nong. "Multiple-mode OTA-C universal biquad filters." *Circuits, Systems and Signal Processing* vol. 29, no. 2, 2010, pp. 263-274.

[5] Kumngern, Montree, Boonying Knobnob, and Kobchai Dejhan. "Electronically tunable high-input impedance voltage-mode universal biquadratic filter based on simple CMOS OTAs." *AEU-International Journal of Electronics and Communications,* vol. 64, no. 10, 2010, pp. 934-939.

[6] Wu, Jie, and Chang-Yan Xie. "New multifunction active filter using OTAs." *International Journal of Electronics* vol. 74, no. 2, 1993, pp. 235-239.

[7] Chen, Hua-Pin, Yi-Zhen Liao, and Wen-Ta Lee. "Tunable mixed-mode OTA-C universal filter." *Analog Integrated Circuits and Signal Processing* vol. 58, no. 2, 2009, pp. 135-141.

[8] Kumngern, Montree, Pichai Suksaibul, and Boonying Knobnob. "High-input impedance four-input one-output voltage-mode universal filter using OTAs." In *Information and Communication Technology, Electronic and Electrical Engineering (JICTEE), 2014 4th Joint International Conference on*, pp. 1-4. IEEE, 2014

[9] Abuelma'atti*, Muhammad Taher, and Abdulwahab Bentrcia. "A novel mixed-mode OTA-C universal filter." *International Journal of Electronics* vol. 92, no. 7, 2005, pp. 375-383.

[10] Lee, Chen-Nong, and Chun-Ming Chang. "High-order mixed-mode OTA-C universal filter." *AEU-International Journal of Electronics and Communications* vol. 63, no. 6, 2009, pp. 517-521.

[11] JIE, WU EZZ I. "Universal voltage-and current-mode OTAs based biquads." *International Journal of Electronics* vol. 85, no. 5, 1998, pp. 553-560.

[12] Sanchez-Sinencio, Edgar, Randall L. Geiger, and H. Nevarez-Lozano. "Generation of continuous-time two integrator loop OTA filter structures." *IEEE Transactions on Circuits and Systems* vol. 35, no. 8, 1988, pp. 936-946.

[13] Sun, Yichuang. "Second-order OTA-C filters derived from Nawrocki-Klein biquad." *Electronics letters* vol. 34, no. 15, 1998, pp. 1449-1450.

[14] Wattikornsirikul, Natchayathorn, and Montree Kumngern. "Three-input one-output voltage-mode universal filter using simple OTAs." In *ICT and Knowledge Engineering (ICT and Knowledge Engineering), 2014 12th International Conference on*, pp. 28-31. IEEE, 2014.

[15] Safari, Leila, Shahram Minaei, and Bilgin Metin. "A low power current controllable single-input three-output current-mode filter using MOS transistors only." *AEU-International Journal of Electronics and Communications* vol. 68, no. 12, 2014, pp. 1205-1213.

[16] Psychalinos, Costas, Chrysostomos Kasimis, and Fabian Khateb. "Multiple-input single-output universal biquad filter using single output operational transconductance amplifiers." *AEU-International Journal of Electronics and Communications* vol. 93, 2018, pp. 360-367.

[17] Texas Instruments, LM13700: Dual Operational Transconductance Amplifier with Linearizing Diodes and Buffers, URL http://www.ti.com/product/LM13700; 2015.

Received: 4 June 2019 | Accepted: 10 October 2019

DOI: 10.1002/jcb.29560

Check for updates

Journal of Cellular Biochemistry WILEY

RESEARCH ARTICLE

NAMPT, GRN, and SERPINE1 signature as predictor of disease progression and survival in gliomas

Meenakshi Vachher[1] | **Kriti Arora**[2] | **Archana Burman**[1] | **Bhupender Kumar**[1]

[1]Department of Biochemistry, Institute of Home Economics, University of Delhi, New Delhi, India

[2]Department of Information Technology, Delhi Technological University, New Delhi, India

Correspondence
Bhupender Kumar, Department of Biochemistry, Institute of Home Economics, University of Delhi, F-4, Hauz Khas Enclave, New Delhi 110016, India.
Email: bhupender19@ihe.du.ac.in and bhupender19@gmail.com

Abstract

Adipose tissue is an important source of adipokines involved in anti- and pro-inflammatory effects. Their involvement in certain cancers such as breast and colon cancer is known but in gliomas it remains unexplored till date. The aim of this study was to assess the status of adipokines as prognostic markers of gliomas (low grade gliomas [LGG] and glioblastoma mutiforme [GBM]). Expression status (messenger RNA [mRNA]), overall survival (OS) and disease-free survival (DFS) was identified using gene expression profiling interactive analysis server. Clinicopathological analysis and correlation between different adipokines was performed using Xena server. Protein expression status was analyzed using tissue sections from the Human Protein Atlas. Out of 11 adipokines studied visfatin (NAMPT), apelin (APLN), granulin (GRN), serpin peptidase inhibitor/plasminogen activator inhibitor type 1 (PAI-1) member 1 (SERPINE1), and chemokine (C-C motif) ligand 2 (CCL2) mRNA levels were significantly upregulated in both LGG and GBM. Interleukin 6 (IL6) mRNA was found be significantly upregulated only in GBM. NAMPT, GRN, SERPINE1, and IL6 showed reduced OS as well as worst DFS for patients having higher mRNA expression in LGG. Increased expression of CCL2 showed worst OS in LGG patients while resistin (RETN) and GRN showed the worst OS in GBM patients. Higher expression of RETN, GRN, IL6, SERPINE1, and CCL2 were found to be positively correlated with shorter DFS in GBM. In the clinicopathological analysis, NAMPT, GRN, IL6, SERPINE1, and CCL2 expressions were significantly associated between the neoplasm histological G2 and G3 grades. Furthermore, expression of NAMPT, GRN, tumor necrosis factor, IL6, SERPINE1, and CCL2 were significantly associated with histological type in LGG patients. NAMPT, GRN, SERPINE1, CCL2, and RETN expression were found to be correlated with each other in gliomas. Finally, NAMPT, GRN, and SERPINE1 were also found to be upregulated using immunohistochemistry in a lower grade and high grade gliomas as compared to normal cells. In conclusion, we have identified key adipokines, namely NAMPT, GRN, and SERPINE1 as potential diagnostic and prognostic markers that might be instrumental in the development and progression of gliomas.

KEYWORDS

adipokines, GBM, gliomas, GRN, LGG, NAMPT, prognosis, SERPINE1, TCGA

 © 2019 Wiley Periodicals, Inc.

1 | INTRODUCTION

Adipokines constitute a family of factors produced by white adipose tissue (WAT) that acts as autocrine, paracrine, and endocrine hormones.[1] These are essential molecules involved in the regulation of varied processes inclusive of appetite, satiety, fat distribution, inflammation, homeostasis, cell proliferation, apoptosis, endothelial function, and other crucial cell processes. They act in different organs including adipose tissue itself, brain, liver, muscle, and vessels.[2-4] These adipokines include mainly adiponectin, leptin, tumor necrosis factor-alpha (TNF-α), interleukin 6 (IL6), resistin, apelin, visfatin, monocyte chemotactic protein-1, plasminogen activator inhibitor-1 (SERPINE1), and others.[1,4]

Cancer is a complex and multifactorial disease. Over the past decade the associations between adipokines and cancer have been increasingly recognized.[5] Obesity is an established risk factor for the development of various carcinomas. A state of chronic inflammation in adipose tissue, resulting in genotoxic stress, might contribute to tumorogenesis. Evidence that adipokines play a role in cancer establishment and aggressiveness is mounting. Overall research suggests that adipokines promote cancer cell progression via enhancement of cell proliferation and proinflammatory pathways. During cancer progression, tumor cells engage in a metabolic symbiosis with adjacent adipose tissue. Mature adipocytes provide adipokines and lipids to cancer cells, while stromal and immune cells from adipose tissue infiltrate carcinomas and locally secrete paracrine factors within the tumor microenvironment.[6] Further research and longitudinal studies are warranted to define the specific independent and additive roles of adipokines in cancer progression and reoccurrence.

There are more than 100 histologically distinct types of primary brain and central nervous system (CNS) tumors. While primary CNS tumors account for only 2% of all primary cancers, they cause 7% of deaths from cancer for those younger than age 70.[7,8] Glioma is a broad term describing neuroepithelial tumors originating from the glial or supporting cells of the CNS. Gliomas account for 24% of all primary brain and CNS tumors; these tumors vary greatly in histology from low grade gliomas (LGG) to the most aggressive and deadly grade IV glioblastoma multiforme (GBM). Although reasonable progress has been made in identifying risk factors for gliomas, most tumors arise beyond the scope of these exposures and genetic conditions, more research is needed to explore causal relationships with occupational, environmental, and lifestyle risk factors. Greater insight and identification of specific predictive prognostic biomarkers is warranted to improve diagnosis and prognosis of gliomas.

Keeping this in view, the aim of the present study was to explore the expression status of 11 adipokines in LGG and GBM. The 11 adipokines included in the present study were leptin (LEP), visfatin (NAMPT), apelin (APLN), adiponectin (ADIPOQ), plasminogen activator inhibitor type 1 (PAI-1/SERPINE1), resistin (RETN), granulin (GRN), TNF, IL6, intelectin 1 (ITLN1), and chemokine (C-C motif) ligand 2 (CCL2). These adipokines were selected as they are known to play vital role during the process of inflammation where most of these are proinflammatory except adiponectin which is an important anti-inflammatory molecule. The difference in the messenger RNA (mRNA) expression and survival analysis, both overall survival (OS) and disease-free survival (DFS) was identified in The Cancer Genome Atlas (TCGA) and Genotype Tissue Expression (GTEx) dataset using gene expression profiling interactive analysis (GEPIA) server. Moreover, clinicopathological analysis and correlation between adipokines was performed using Xena server. Lastly, protein expression of various adipokines was studied using the Human Protein Atlas.

2 | MATERIAL AND METHODS

Expression and prognostic values of 11 members of adipokines family were analyzed with the help of an online server, GEPIA. GEPIA is an interactive web server for estimating the mRNA expression data from 9736 tumors and 8587 normal samples in TCGA and GTEx dataset projects.[9] The [Log2FC] cut-off of the expression of the proposed biomarker was 1. All boxplot analysis used log2 (TPM+1) for log scale. GEPIA server was used to analyze prognostic significance of gene mRNA expression in LGG and GBM patients. *P* value and Hazard's ratio (HR) were carefully noted. A *P* value less than .05 was considered to be statistically significant. The UCSC Xena (http://xena.ucsc.edu) is a functional genomics browser that provides visualization and integration for analyzing and viewing public data hubs was used for this investigation. For LGG, 530 patients were studied and the age of the patients at the initial pathological diagnosis ranged from 14 to 87 years. For GBM, 631 samples were studied and the age at initial pathological diagnosis ranged from 21 to 89 years. The clinicopathological analysis and correlation among various adipokines in LGG alone and in LGG plus GBM together were performed using the UCSC Xena browser having TCGA datasets. The expression of various adipokines at the protein level from immunohistochemical analysis data was studied using the Human Protein Atlas (http://proteinatlas.org).

TABLE 1 Expression of 11 adipokines in the TCGA dataset in LGG and GBM using http://gepia.cancer-pku.cn/

	Boxplot data: matched TCGA normal to GTEx data		Overall survival		Disease-free survival	
Type adipokine	**LGG**	**GBM**	**LGG**	**GBM**	**LGG**	**GBM**
LEP	–	–	–	*P* = .67 HR(high) = 1.1 p(HR) = 0.68 n(high) = 76 n(low) = 57	–	***P* = .062** HR(high) = 1.5 p(HR) = 0.071 n(high) = 76 n(low) = 57
NAMPT	Upregulated T = 518, N = 207	Upregulated T = 163, N = 207	***P* = 9.5e−07** HR(high) = 2.6 p(HR)=2.3e−06 n(high) = 257 n(low) = 257	*P* = .099 HR(high) = 1.4 p(HR) = 0.098 n(high) = 81 n(low) = 81	***P* = 7.1e−05** HR(high) = 1.9 p(HR)=9.1e−05 n(high) = 257 n(low) = 257	*P* = .1 HR(high) = 1.4 p(HR) = 0.1 n(high) = 81 n(low) = 81
APLN	Upregulated T = 518, N = 207	Upregulated T = 163, N = 207	*P* = .15 HR(high) = 1.3 p(HR) = 0.15 n(high) = 256 n(low) = 256	*P* = .8 HR(high) = 0.96 p(HR) = 0.8 n(high) = 81 n(low) = 81	*P* = .56 HR(high) = 1.1 p(HR) = 0.55 n(high) = 256 n(low) = 256	*P* = .98 HR(high) = 1 p(HR) = 1 n(high) = 81 n(low) = 81
ADIPOQ	–	–	–	–	–	–
RETN	–	–	–	***P* = .00034** HR(high) = 2 p(HR) = 0.00043 n(high) = 80 n(low) = 81	–	***P* = .0065** HR(high) = 1.8 p(HR) = 0.0079 n(high) = 80 n(low) = 81
GRN	Upregulated T = 518, N = 207	Upregulated T = 163, N = 207	***P* = 6.3e−06** HR(high) = 2.3 p(HR)=1.1e−05 n(high) = 257 n(low) = 257	***P* = .013** HR(high) = 1.6 p(HR) = 0.013 n(high) = 81 n(low) = 81	***P* = .0052** HR(high) = 1.6 p(HR) = 0.0054 n(high) = 257 n(low) = 257	***P* = .032** HR(high) = 1.6 p(HR) = 0.033 n(high) = 81 n(low) = 81
TNF	–	–	*P* = .27 HR(high) = 0.82 p(HR) = 0.27 n(high) = 257 n(low) = 257	*P* = 0.66 HR(high) = 1.1 p(HR) = 0.69 n(high) = 81 n(low) = 81	*P* = .45 HR(high) = 0.89 p(HR) = 0.46 n(high) = 257 n(low) = 257	*P* = .5 HR(high) = 0.86 p(HR) = 0.49 n(high) = 81 n(low) = 81
IL6	–	Upregulated T = 163, N = 207	***P* = .00068** HR(high) = 1.9 p(HR) = 0.00082 n(high) = 255 n(low) = 254	***P* = .074** HR(high) = 1.4 p(HR) = 0.074 n(high) = 81 n(low) = 81	***P* = .028** HR(high) = 1.4 p(HR) = 0.028 n(high) = 255 n(low) = 254	*P* = **.0077** HR(high) = 1.8 p(HR) = 0.0085 n(high) = 81 n(low) = 81
SERPINE1	Upregulated T = 518, N = 207	Upregulated T = 163, N = 207	*P* = **3.6e−07** HR(high) = 2.6 p(HR)=9.5e−07 n(high) = 257 n(low) = 257	*P* = .12 HR(high) = 1.3 p(HR) = 0.12 n(high) = 81 n(low) = 81	*P* = **.0014** HR(high) = 1.7 p(HR) = 0.0015 n(high) = 257 n(low) = 257	***P* = .0084** HR(high) = 1.7 p(HR) = 0.01 n(high) = 81 n(low) = 81
ITLN1	–	–	–	–	–	–
CCL-2	Upregulated T = 518, N = 207	Upregulated T = 163, N = 207	***P* = .051** HR(high) = 1.4 p(HR) = 0.052 n(high) = 257 n(low) = 257	***P* = .07** HR(high) = 1.4 p(HR) = 0.071 n(high) = 81 n(low) = 81	*P* = .96 HR(high) = 1 p(HR) = 0.94 n(high) = 257 n(low) = 257	***P* = .0023** HR(high) = 1.9 p(HR) = 0.0027 n(high) = 81 n(low) = 81

Abbreviations: ADIPQ, adiponectin; APLN, apelin; CCL2, chemokine (C-C motif) ligand 2; GBM, glioblastoma multiforme; GRN, granulin; GTEx, Genotype Tissue Expression; IL6, interleukin 6; ITLN1, intelectin 1/ omentin; LEP, leptin; LGG, low grade glioma; NAMPT, visfatin/nicotinamide phosphoribosyltransferase; RETN, resistin; SERPINE1, serpin peptidase inhibitor/plasminogen activator inhibitor type 1 (PAI-1) member 1; TCGA, The Cancer Genome Atlas; TNF, tumor necrosis factor.

Bold values represent significant differences for Hazard ratio obtained.

3 | RESULTS

3.1 | Expression status of 11 adipokines between normal and tumor tissues in LGG and GBM

This study was designed to assess the status of various adipokines in gliomas. TCGA and GTEx dataset for transcript analysis was used to study mRNA expression levels of 11 members of the adipokine family in gliomas using GEPIA server. The differential expression levels of these adipokines are depicted in Table 1 and Figure 1. The results of the present analysis showed that the levels of mRNA of NAMPT, APLN, GRN, SERPINE1, and CCL2 were significantly upregulated in both LGG and GBM (Figures 1A-F, 1 H,I and 1 L,M). The levels of IL6 mRNAs were also found to be significantly upregulated in GBM alone (Figure 1G).

3.2 | Prognostic assessment of various adipokines in LGG and GBM

Prognostic value of 11 adipokines was assessed in both LGG and GBM using GEPIA server (Table 1). Out of 11 adipokines studied, five adipokines namely NAMPT ($P = 9.5e{-}07$; HR, 2.6), GRN ($P = 6.3e{-}06$; HR, 2.3), SERPINE1 ($P = 3.6e{-}07$, HR, 2.6), IL6 ($P = .00068$; HR, 1.9), and CCL2 ($P = .05$; HR, 1.4) showed reduced OS for patients having higher mRNA expression in LGG (Figure 2A-E). On the other hand, RETN ($P = .0034$; HR, 2.0) and GRN ($P = .013$; HR, 1.6) showed the worst OS for increased expression in GBM patients (Figure 2F,G). Higher mRNA expression of NAMPT ($P = 7.1e{-}05$; HR, 1.9), GRN ($P = .0052$; HR, 1.6), IL6 ($P = .028$; HR, 1.4), and SERPINE1 ($P = .0014$; HR, 1.7) was also found to be significantly associated with worst DFS in LGG patients (Figure 3A-D). Whereas increased expression of RETN

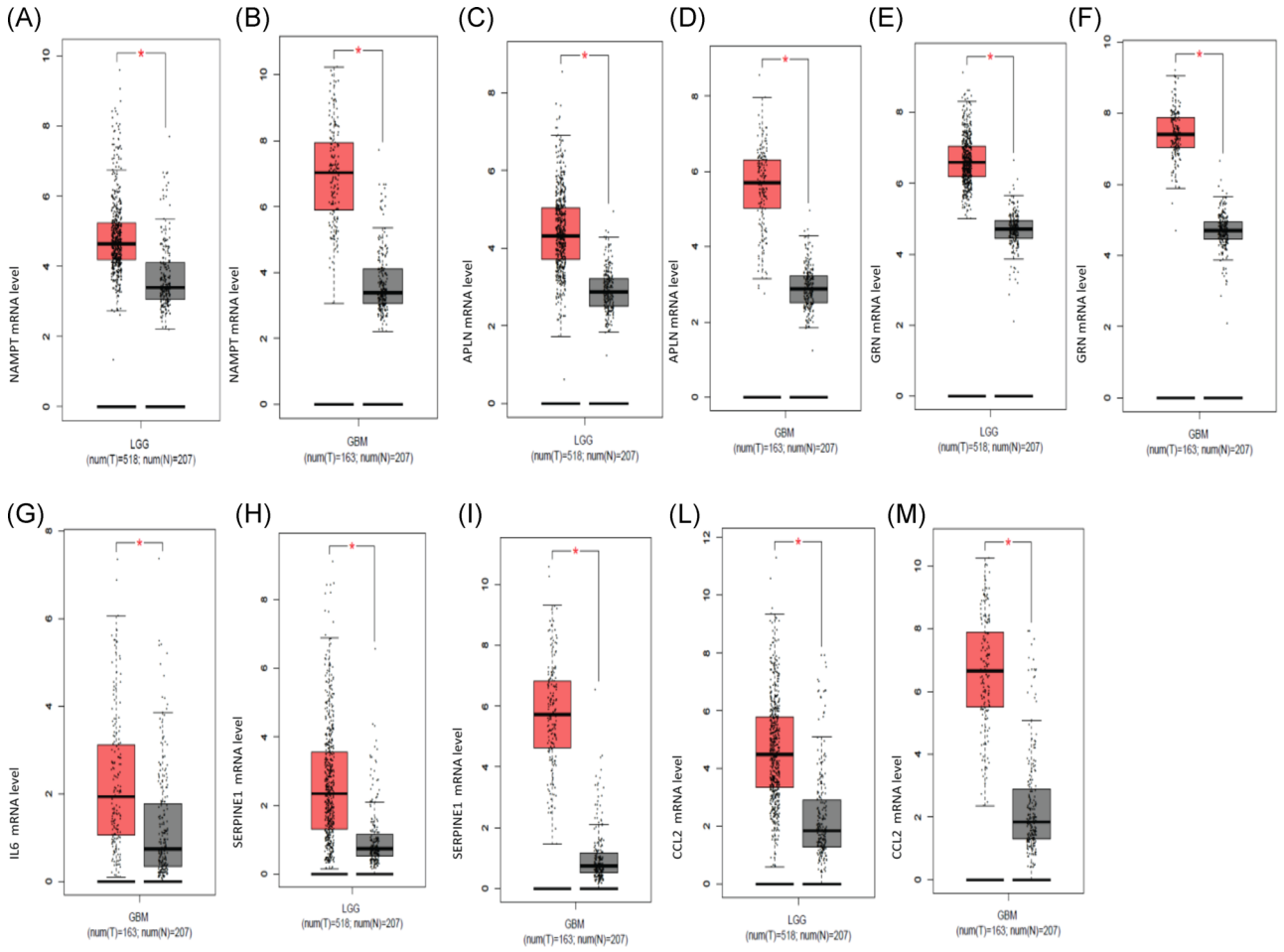


FIGURE 1 Analysis of various adipokine mRNA levels in human LGG and GBM. Compared to normal tissues the expression of NAMPT (A,B), APLN (C,D), GRN (E,F), SERPINE1 (H,I), and CCL2 (L,M) mRNA levels increase in LGG and GBM both; IL6 (G) mRNA levels were also higher compared to normal tissues in GBM. The red and gray boxes represent cancer and normal tissues respectively. Only statistically significant differences in the mRNA profile are shown. (*$P < .01$). APLN, apelin; CCL2, chemokine (C-C motif) ligand 2; GBM, glioblastoma mutiforme; GRN, granulin; IL6, Interleukin 6; LGG, low grade gliomas; mRNA, messenger RNA; NAMPT, visfatin/nicotinamide phosphoribosyltransferase; SERPINE1, serpin peptidase inhibitor/plasminogen activator inhibitor type 1 (PAI-1) member 1

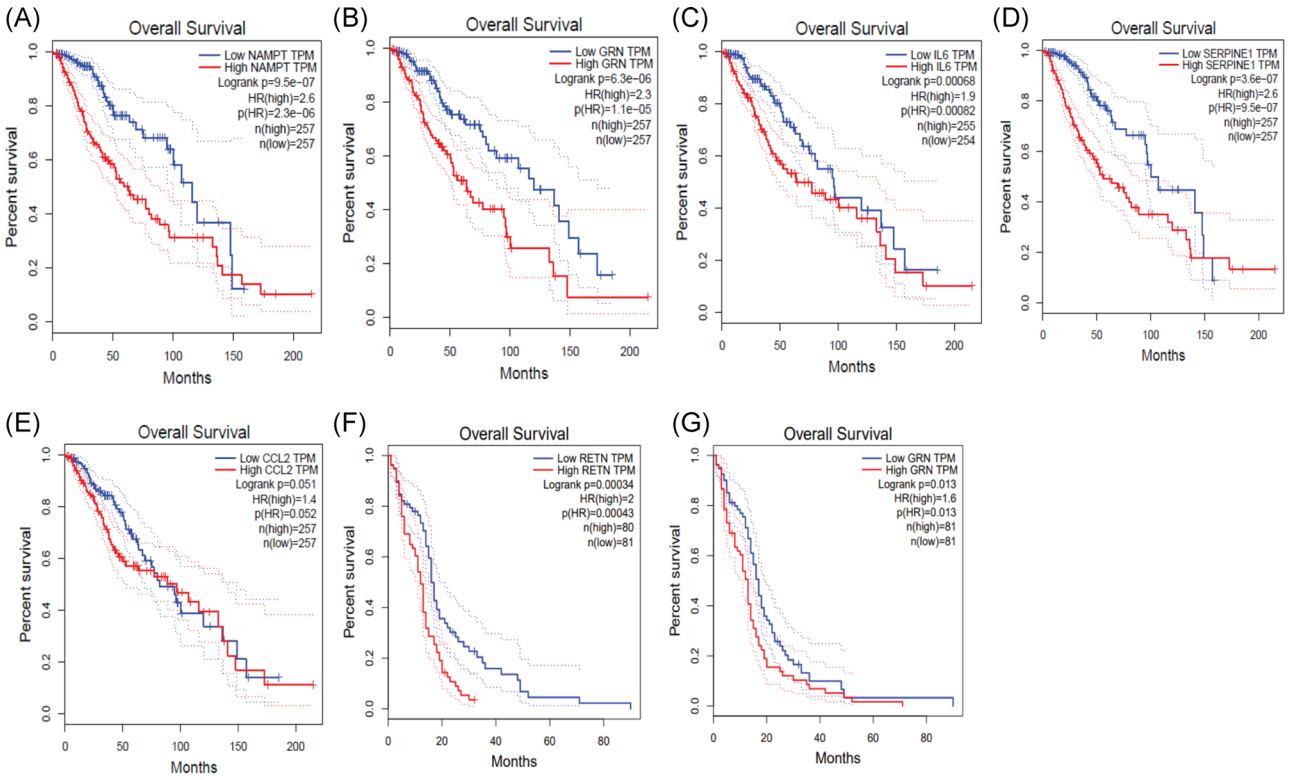


FIGURE 2 Prognostic role (overall survival [OS]) of adipokines in LGG using gepia.cancer-pku.cn. A, depicts OS curve for NAMPT, (B) for GRN, (C) for IL6, (D) for SERPINE1, (E) for CCL2 in LGG. F, depicts OS curve for RETN and (G) for GRN in GBM. Only statistically significant differences in the mRNA profile are shown (*$P < .01$). CCL2, chemokine (C-C motif) ligand 2; GBM, glioblastoma multiforme; GRN, granulin; IL6, interleukin 6; LEP, leptin; mRNA, messenger RNA; NAMPT, visfatin/nicotinamide phosphoribosyltransferase; RETN, resistin; SERPINE1, serpin peptidase inhibitor/plasminogen activator inhibitor type 1 (PAI-1) member 1

($P = .0065$; HR, 1.8), GRN ($P = .0032$; HR, 1.6), IL6 ($P = .0077$; HR, 1.8), SERPINE1 ($P = .0084$; HR, 1.7), and CCL2 ($P = .0023$; HR, 1.9) was found to be positively correlated with shorter DFS in GBM (Figure 3E-I). Therefore, NAMPT, GRN, IL6, and SERPINE1 emerged as suitable candidates for prognosis in LGG patients whereas; RETN and GRN emerged as important prognosticators for GBM. Importantly, GRN emerged as a significant prognostic factor for both OS and DFS in both LGG and GBM patients.

3.3 | Correlation of adipokines levels in LGG and GBM with clinicopathological parameters

The clinicopathological analysis was carried out for 11 adipokines in LGG and LGG and GBM patients using Xena server. The results are summarized in Table 2 and Figures 4, 5, and 6. In the clinicopathological analysis, mRNA expression status of five adipokines, namely NAMPT ($P = 2.664e{-}11$), GRN ($P = 1.209e{-}7$), IL6 ($P = .000003781$), SERPINE1 ($P = 3.551e{-}12$), and CCL2 ($P = .01008$) was significantly associated with the neoplasm histological G2 and G3 grade in LGG patients. Furthermore, six adipokines, that is, NAMPT ($P = .000003259$), GRN ($P = 4.676e{-}8$), TNF ($P = .000002939$), IL6 ($P = .00002188$), SERPINE1 ($P = .0002749$), and CCL2 ($P = 1.565e{-}9$) mRNA expression was significantly associated with histological type in LGG patients. Importantly, the mRNA expression of these six adipokines was significantly associated with histological type in LGG and GBM patients studied together also ($P = .0001$). Besides LEP, APLN and RETN also significantly associated with histological type in pooled LGG and GBM patients ($P = .0001$). It is also noteworthy that LEP ($P = .04025$), NAMPT ($P = .0007039$) and SERPINE1 ($P = .01062$) mRNA expression was significantly associated with IDH1 wild type status in LGG samples.

3.4 | Correlation between various adipokines using Pearson's rho correlation in LGG and GBM patients

Statistically significant correlation for simultaneous mRNA expression among different combinations of 11 adipokines analyzed was determined using Pearson's rho (r) correlation coefficient with the help of Xena browser

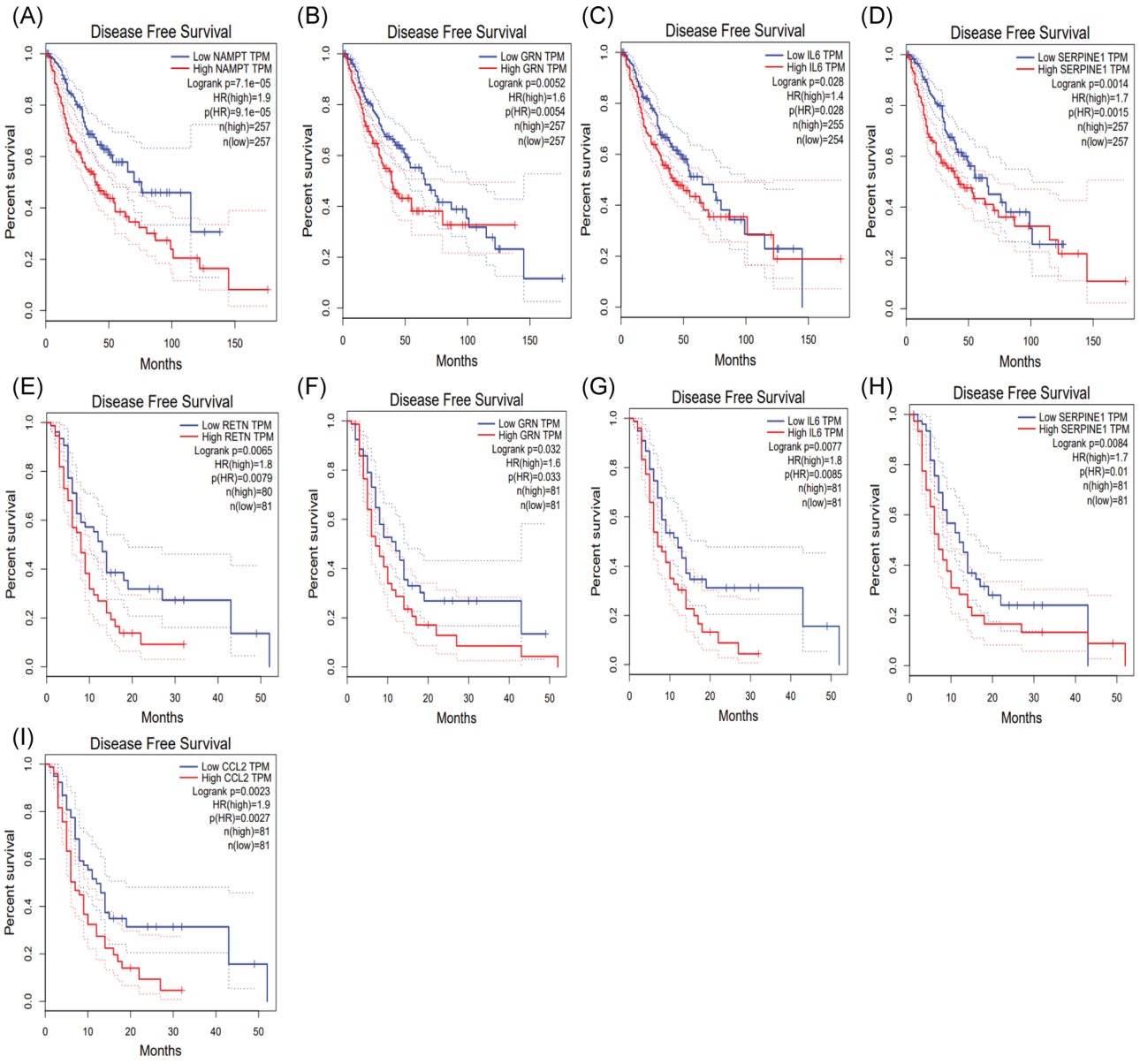


FIGURE 3 Prognostic role (disease-free survival) of adipokines in LGG and GBM using gepia.cancer-pku.cn. A, depicts DFS curve for NAMPT, (B) for GRN, (C) for IL6, (D) for SERPINE1 in LGG. E, depicts DFS curve for RETN, F for GRN, G for IL6, (H) for SERPINE1, and I for CCL2 in GBM. Only statistically significant differences in the mRNA profile are shown (*$P < .01$). CCL2, chemokine (C-C motif) ligand 2; GBM, glioblastoma multiforme; GRN, granulin; IL6, interleukin 6; LEP, leptin; mRNA, messenger RNA; NAMPT, visfatin/nicotinamide phosphoribosyltransferase; RETN, resistin; SERPINE1, serpin peptidase inhibitor/plasminogen activator inhibitor type 1 (PAI-1) member 1

in LGG and GBM patients together (Table 3). NAMPT was significantly correlated with RETN (r = 0.5669), GRN (r = 0.54534), IL6 (r = 0.6429), SERPINE1 (0.7548), and CCL2 (r = 0.6800). RETN was associated with GRN (r = 0.5098), IL6 (r = 0.4969), SERPINE1 (r = 0.5146), and CCL2 (r = 0.4843). GRN was significantly correlated with IL6 (r = 0.4969), SERPINE1 (r = 0.5720), and CCL2 (r = 0.5110). IL6 was found to be associated with SERPINE1 (r = 0.6150) and CCL2 (r = 0.7574). Furthermore, SERPINE1 was significantly correlated with CCL2 (r = 0.4469). Therefore, it seemed that these adipokines are expressed in a grouped pattern in gliomas.

3.5 | Immunohistochemical analysis of various adipokines in normal brain glial cells, LGG, and high grade gliomas

Immunohistochemical analysis of various adipokines in normal brain glial cells, LGG, and high grade gliomas was studied using Human Protein Atlas and the results are summarized in Table 4 and Figure 7. No detectable immunostaining of NAMPT was observed in normal brain tissues whereas low immunostaining was observed in lower grade and medium immunostaining was observed in high grade gliomas (Figure 4A). GRN showed no

TABLE 2 Correlation of eleven Adipokines mRNA levels with the clinicopathological features of LGG patients and LGG and GBM patients together using Xena.ucsc

Clinicopathological features	No.	LEP	NAMPT	APLN	ADIPQ	GRN	RETN	TNF	IL6	SERPINE1	ITLN1	CCL2
Clinicopathological features of LGG patients												
Gender												
Female	238	[a]*P* = .1432 (t = −1.466)	[a]*P* = .6303 (t = −0.4816)	[a]***P* = .02034** (t = −2.328)	[a]*P* = .08771 (t = −1.711)	[a]*P* = .6752 (t = −0.4192)	[a]*P* = .5249 (t = −0.6362)	[a]*P* = .06703 (t = −1.835	[a]*P* = .1926 (t = −1.305)	[a]*P* = .4955 (t = −0.6820)	[a]*P* = .5816 (t = 0.5515)	[a]***P* = .01084** **(t = −2.557)**
Male	291											
Neoplasm histological grade (LGG)												
G2 (WHO grade 2)	258	[b]*P* = .1418 (f = 1.961)	[b]***P* = 2.664e−11** **(f = 25.51)**	[b]*P* = .1082 (f = 2.233)	[b]*P* = .6933 (f = 0.3665)	[b]***P* = 1.209e−7** **(f = 16.42)**	[b]*P* = .1140 (f = 2.180)	[b]*P* = .9719 (f = 0.02852)	[b]***P* = .000003781** **(f = 12.79)**	[b]***P* = 3.551e−12** **(f = 27.73)**	[b]*P* = .9553 (f = 0.04572)	[b]***P* = .01008** **(f = 4.637)**
G3 (WHO grade 3)	270											
Discrepancy	1											
Histological type (LGG)												
Oligodendroglioma	198	[b]*P* = .9813 (f = 0.01888)	[b]***P* = .000003259** (f = 12.94)	[b]*P* = .06828 (f = 2.698)	[b]*P* = .1686 (f = 1.786)	[b]***P* = 4.676e-8** **(f = 17.43)**	[b]*P* = .9191 (f = 0.08436)	[b]***P* = .000002939** **(f = 13.05)**	[b]***P* = .00002188** **(f = 10.95)**	[b]***P* = .0002749** **(f = 8.328)**	[b]*P* = .7138 (f = 0.3373)	[b]***P* = 1.565e−9** **(f = 21.08)**
Oilgoastrocytoma	134											
Astrocytoma	197											
IDH1 mutation		[a]***P* = .04025** **(t = −2.111)**	[a]***P* = .0007039** (t = −3.671)	[a]*P* = .06119 (t = −1.920)	[a]*P* = .1477 (t = −1.473)	[a]*P* = .1610 (t = −1.425)	[a]*P* = .5142 (t = −0.6554)	[a]*P* = .1325 (t = −1.522)	[a]*P* = .1079 (t = −1.632)	[a]***P* = .01062** **(t = −2.653)**	[a]*P* = .9094 (t = 0.1144)	[a]*P* = .1564 (t = −1.439)
No	34											
Yes	91											
Histological type studied in LGG and GBM patients combined together												
Histological type												
Oligodendroglioma	198	[b]***P* = .000** **(f = 28.28)**	[b]***P* = .000** **(f = 104.1)**	[b]***P* = .000** **(f = 38.11)**	[b]*P* = .1639 (f = 1.578)	[b]***P* = .000** **(f = 55.13)**	[b]***P* = .000** **(f = 47.58)**	[b]***P* = .000005508** **(f = 6.571)**	[b]***P* = .000** **(f = 42.72)**	[b]***P* = .000** **(f = 86.84)**	[b]*P* = .9566 (f = 0.2140)	[b]***P* = .000** **(f = 45.25)**
Oilgoastrocytoma	134											
Astrocytoma	197											
GBM	1											
Treated primary GBM	1											
Untreated primary (de novo) GBM	164											

Abbreviations: ADIPQ, adiponectin; APLN, apelin; CCL2, chemokine (C-C motif) ligand 2; GBM, glioblastoma multiforme; GRN, granulin; IL-6, interleukin-6; ITLN1, intelectin 1/ omentin; LEP, leptin; LGG, low grade glioma; mRNA, messenger RNA; NAMPT, visfatin/nicotinamide phosphoribosyltransferase; RETN, resistin; SERPINE1, serpin peptidase inhibitor/plasminogen activator inhibitor type 1 (PAI-1) member 1; TNF, tumor necrosis factor.

Bold values represent significant differences for Hazard ratio obtained.

[a]Welch's *t*-test OR.

[b]One way ANOVA.

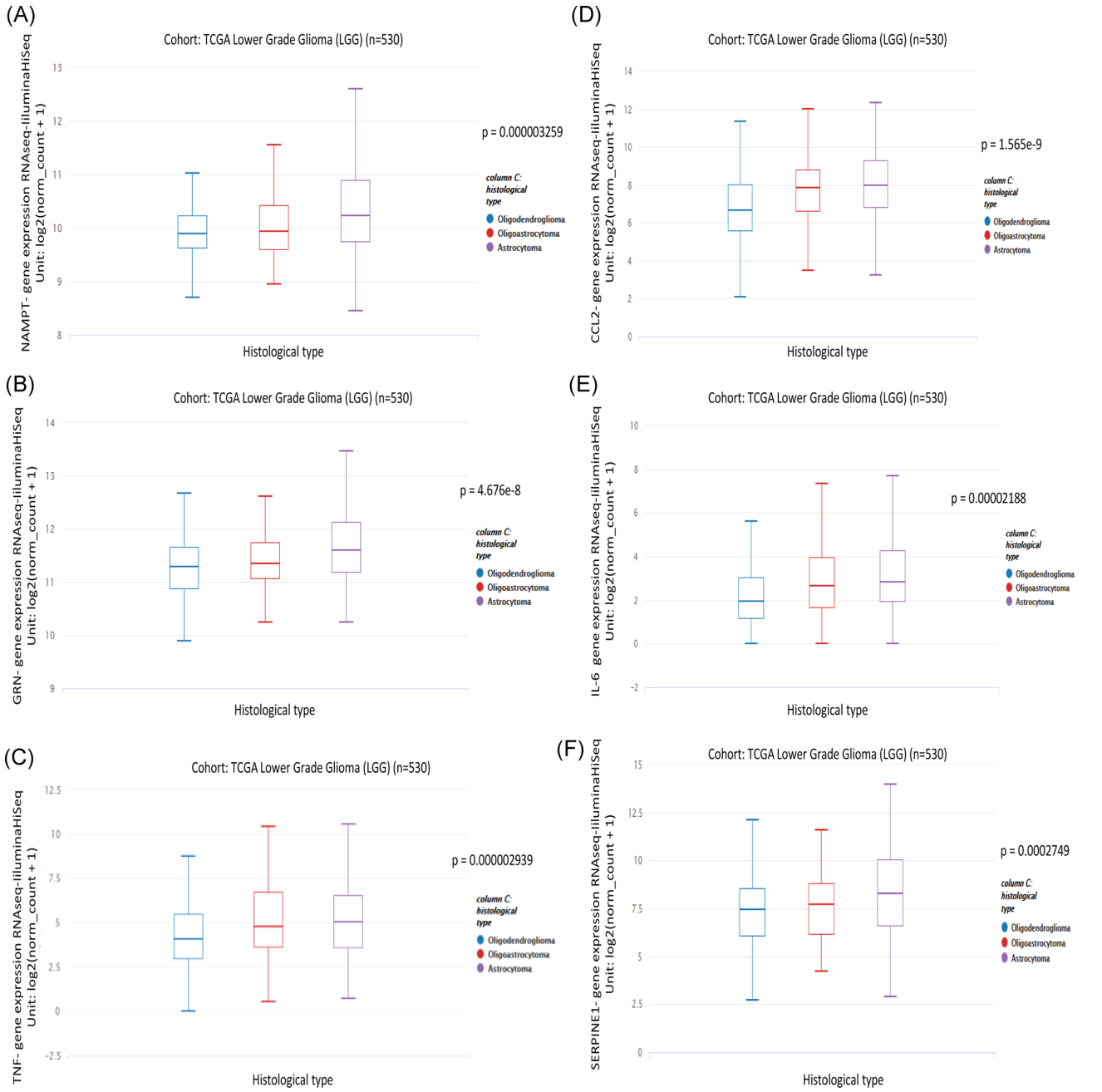


FIGURE 4 Association of various adipokines mRNA levels with the histological type in LGG patients (n = 530) using Xena. A, depicts NAMPT expression, (B) depicts GRN, (C) depicts TNF, (D) depicts CCL2, (E) depicts IL6 and (F) depicts SERPINE1 expression with various histological types (oligodendroglioma, oligoastrocytoma, and astrocytoma) in LGG. CCL2, chemokine (C-C motif) ligand 2; GRN, granulin; IL6, interleukin 6; LGG, low grade glioma; mRNA, messenger RNA; NAMPT, visfatin/nicotinamide phosphoribosyltransferase; SERPINE1, serpin peptidase inhibitor/plasminogen activator inhibitor type 1 (PAI-1) member 1; TNF, tumor necrosis factor

immunostaining in normal brain tissues whereas low immunopositivity was observed in lower grade and high immunopositivity was observed in high grade gliomas (Figure 4B). SERPINE1 exhibited low immunostaining in normal brain tissues whereas medium immunopositivity in lower grade and high immunopositivity high grade gliomas was observed (Figure 4C). Finally, NAMPT, GRN, and SERPINE1 emerged as the most important adipokine candidates that might be playing a functional role in the biology of glioma development and progression.

4 | DISCUSSION

Gliomas are the most prevalent primary brain tumors that are typically associated with a dismal prognosis and

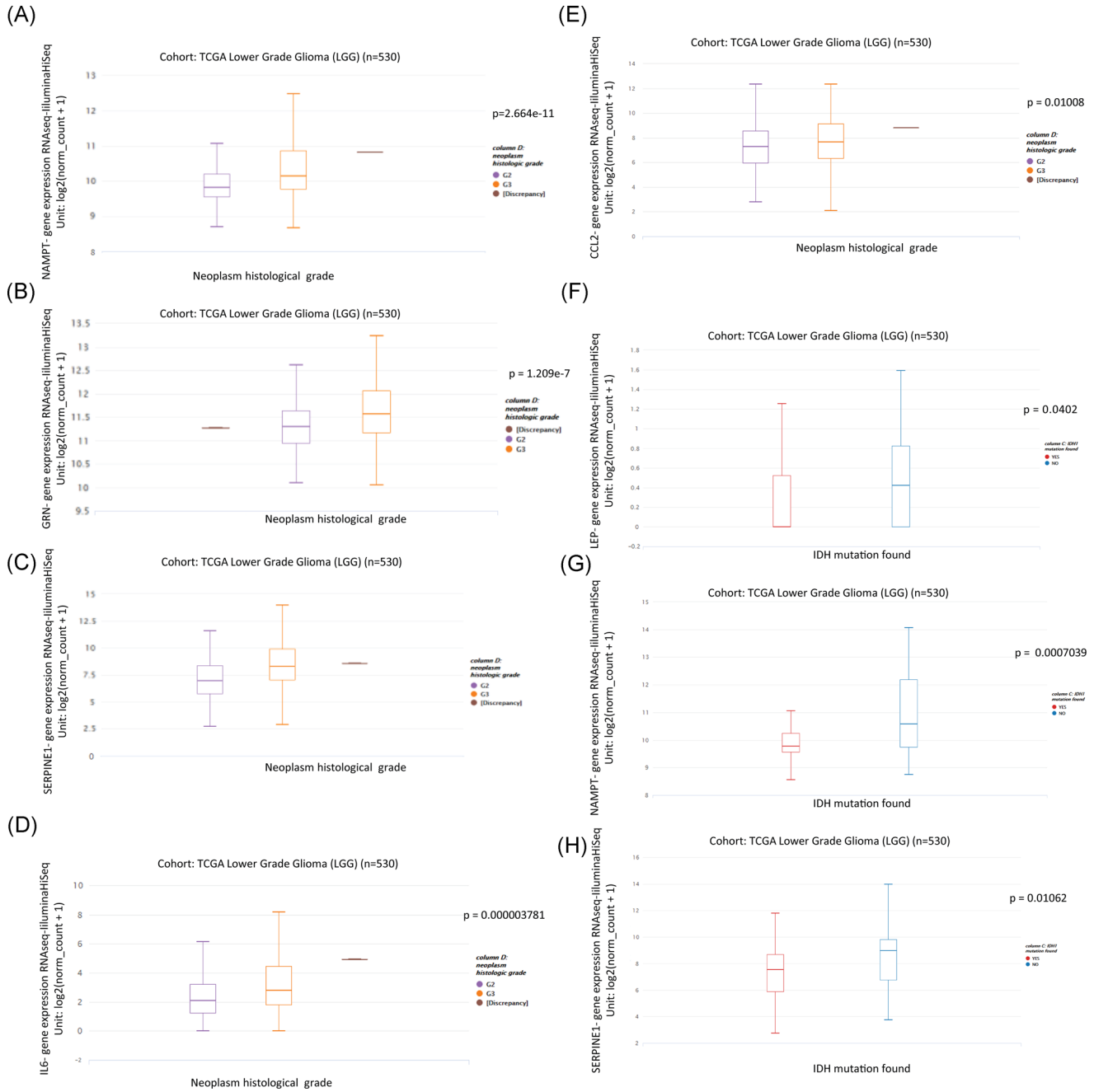


FIGURE 5 Association of various Adipokines mRNA levels with the increased histological grade and IDH1 mutation in LGG patients (n = 530) using Xena.ucsc. A, depicts NAMPT expression, (B) depicts GRN, (C) depicts SERPINE1, (D) depicts IL6 and (E) depicts CCL2 expression with increased histological grade (G2, G3) in LGG. F, depicts LEP expression, (G) depicts NAMPT, (H) depicts SERPINE1 expression with IDH1 mutation found or not in LGG patients. CCL2, chemokine (C-C motif) ligand 2; GRN, granulin; IL6, interleukin 6; LEP, leptin; LGG, low grade glioma; mRNA, messenger RNA; NAMPT, visfatin/nicotinamide phosphoribosyltransferase; SERPINE1, serpin peptidase inhibitor/plasminogen activator inhibitor type 1 (PAI-1) member 1

inferior quality of life.[10] These are a challenging area of research owing to the heterogeneity of gliomas and difficulty to access brain tissue owing to the presence of blood-brain barrier (BBB) that makes glioma treatment even more arduous. The difficulties are further built owing to the lack of knowledge regarding the mechanisms underlying the development and progression of gliomas.[11] Comprehensive research indicates that adipokines act in autocrine, paracrine and endocrine manner, and aggrandize cancer progression through enhancement of cell proliferation, migration, inflammation, and anti-apoptotic pathways, eventually leading to metastasis.[12,13] highlighted that adipokines have an extensive influence and function on brain health and form prospective

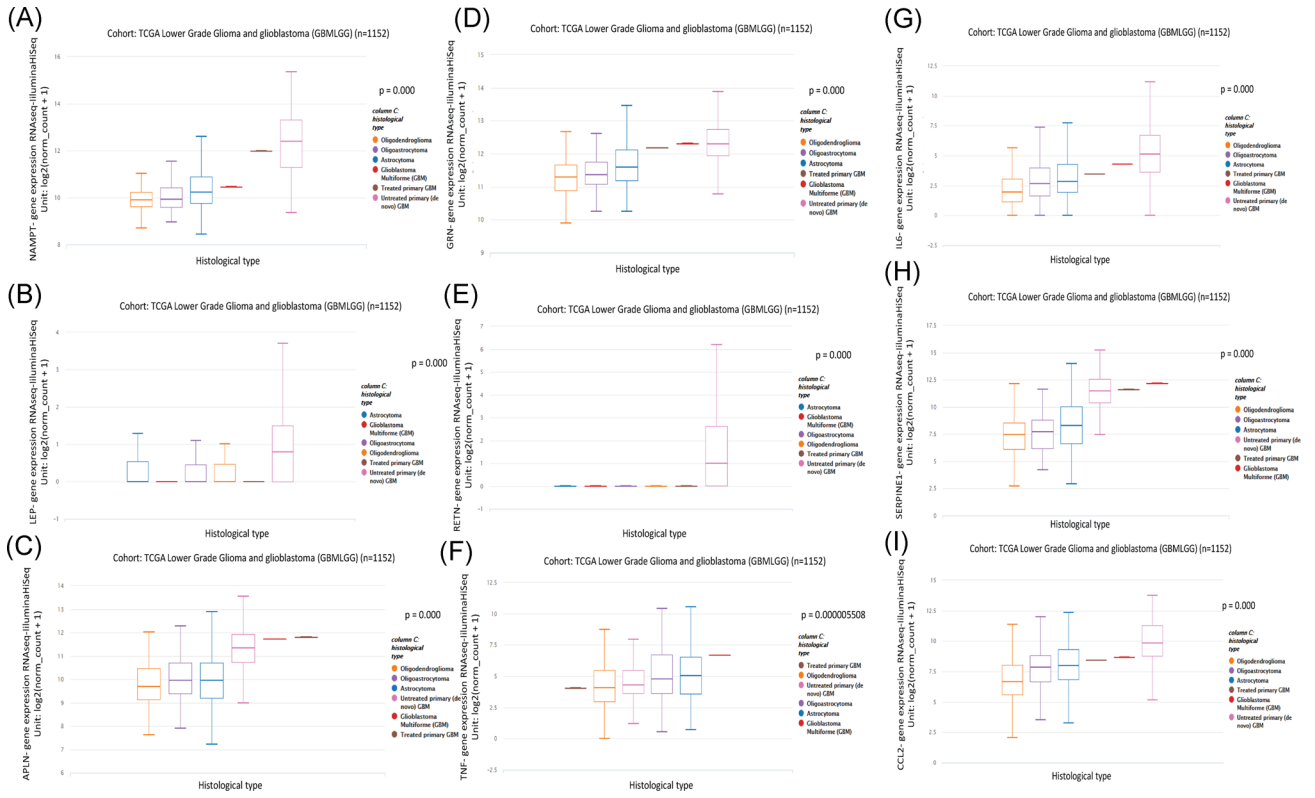


FIGURE 6 Association of various adipokines mRNA levels with the histological type in LGG and GBM patients (n = 1152) using Xena. A, depicts NAMPT expression, (B) depicts LEP, (C) depicts APLN, (D) depicts GRN, (E) depicts RETN, (F) depicts TNF, (G) depicts IL6, (H) depicts SERPINE1 and I depicts CCL2 expression with various histological types (oligodendroglioma, oligoastrocytoma, astrocytoma) treated primary GBM, GBM, and untreated primary GBM in LGG and GBM patients together. APLN, apelin; CCL2, chemokine (C-C motif) ligand 2; GBM, glioblastoma multiforme; GRN, granulin; IL6, interleukin 6; LEP, leptin; LGG, low grade glioma; mRNA, messenger RNA; NAMPT, visfatin/nicotinamide phosphoribosyltransferase; RETN, resistin; SERPINE1, serpin peptidase inhibitor/plasminogen activator inhibitor type 1 (PAI-1) member 1; TNF, tumor necrosis factor

TABLE 3 Correlation among 11 adipokines using Pearson's correlation coefficient (r) using xenabrowser.net in LGG and GBM patients

Adipokine mRNA	NAMPT	LEP	APLN	ADIPOQ	RETN	GRN	TNF	IL6	SERPINE1	ITLN1	CCL2
NAMPT	1.000										
LEP	0.4332	1.000									
APLN	0.5508	0.2210	1.000								
ADIPOQ	−0.02229	0.0605	0.02463	1.000							
RETN	**0.5669**	0.5537	0.3137	−0.01785	1.000						
GRN	**0.5434**	0.3843	0.4216	−0.06010	**0.5098**	1.000					
TNF	0.002165	0.0510	-0.0204	0.0153	0.03255	0.1072	1.000				
IL6	**0.6429**	0.4023	0.3430	0.04555	**0.4969**	**0.4321**	0.3046	1.000			
SERPINE1	**0.7548**	0.4180	0.4649	0.02235	**0.5146**	**0.5720**	−0.004341	**0.6150**	1.000		
ITLN1	0.002628	0.1419	0.06759	0.03867	0.06905	0.05553	−0.05975	0.0195	0.03375	1.000	
CCL2	**0.6800**	0.3322	0.4392	−0.01667	**0.4843**	**0.5110**	0.3913	**0.7574**	**0.6120**	−0.004294	1.00

Abbreviations: ADIPQ, adiponectin; APLN, apelin; CCL2, chemokine (C-C motif) ligand 2; GBM, glioblastoma multiforme; GRN, granulin; IL6, interleukin 6; ITLN1, intelectin 1/omentin; LEP, leptin; LGG, low grade glioma; mRNA, messenger RNA; NAMPT, visfatin/nicotinamide phosphoribosyltransferase; RETN, resistin; SERPINE1, serpin peptidase inhibitor/plasminogen activator inhibitor type 1 (PAI-1) member 1; TNF, tumor necrosis factor.
Bold values represent significant differences for Hazard ratio obtained.

TABLE 4 The protein expression of 11 adipokines in normal, lower grade and high grade gliomas using immunohistochemistry data from the Human Protein Atlas database; www.proteinatlas.org

Type of tissue adipokine	Normal	Lower grade glioma	High grade glioma
LEP (CAB010490)	Low	Not detected	Not detected
NAMPT (HPA047776)	Not detected	Low	Medium
APLN	NA	NA	NA
ADIPOQ (HPA051767)	Not detected	Not detected	Not detected
RETN	NA	NA	NA
GRN (HPA028747)	Not detected	low	High
TNF	NA	NA	NA
IL6 (CAB023406)	Not detected	Not detected	Not detected
SERPINE1 (HPA050039)	Low	Medium	High
ITLN1 (CAB012652)	Not detected	High nuclear	High nuclear
CCL-2 (HPA019163)	Not detected	Not detected	Not detected

Note: Bracket depicts the antibody used.
Abbreviations: ADIPQ, adiponectin; APLN, apelin; CCL2, chemokine (C-C motif) ligand 2; GBM, glioblastoma multiforme; GRN, granulin; IL6, interleukin 6; ITLN1, intelectin 1/ omentin; LEP, leptin; LGG, low grade glioma; NAMPT, visfatin/nicotinamide phosphoribosyltransferase; RETN, resistin; SERPINE1, serpin peptidase inhibitor/plasminogen activator inhibitor type 1 (PAI-1) member 1; TNF, tumor necrosis factor.

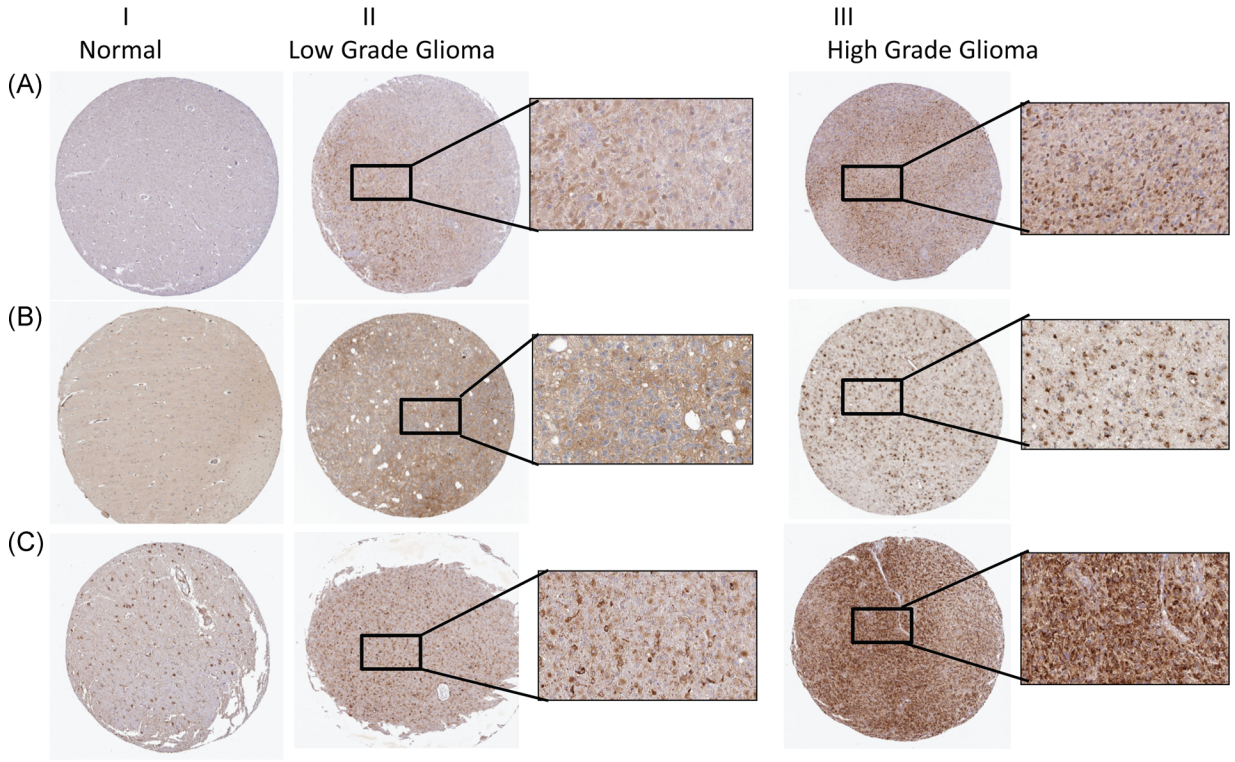


FIGURE 7 Immunohistochemical analysis of NAMPT, GRN, and SERPINE1 in normal brain tissue, low grade glioma, and high grade glioma using Human Protein Atlas, www.proteinatlas.org. I depict normal brain tissue, II depicts low grade glioma, and III depicts high grade glioma. Insets show high resolution images (microscope view). A, depicts NAMPT expression using HPA047776 antibody. I A shows NAMPT expression was not detected in normal glial cells, II A depicts low immunostaining in low grade glioma tumor cells, III A depicts medium immnunostaining in high grade glioma cells; (B) depicts GRN expression using HPA028747 antibody, I B shows GRN expression was not detected in normal glial cells, II B depicts low immunostaining in low grade glioma tumor cells, III B depicts high immnunostaining in high grade glioma cells; (C) depicts SERPINE1 expression using HPA050039 antibody; I C shows SERPINE1 expression was low in normal glial cells, II C depicts medium immunostaining in low grade glioma tumor cells, III C depicts high immnunostaining in high grade glioma cells. GRN, granulin; NAMPT, visfatin/nicotinamide phosphoribosyltransferase; SERPINE1, serpin peptidase inhibitor/plasminogen activator inhibitor type 1 (PAI-1) member 1

mechanisms that links obesity with brain health.[13] The paucity of research and longitudinal studies associating gliomas and adipokines prompted us to study the independent and additive roles of 11 adipokines in gliomas. The main aim in this study sought to determine which adipokines show positive expressions and could act as prognosticators in LGG and GBM.

Previous reports have indicated a positive correlation between NAMPT levels and cancer risk.[14,15] Reddy et al[15] identified NAMPT as a potential malignant astrocytoma serum marker and prognostic indicator among GBMs. Our results are consistent with their findings suggesting increased NAMPT levels as the worst prognosticator in GBM samples. NAMPT has been suggested to act as a dedifferentiation inducer gene controlling energy core axis for glioma cancer stem like cells maintenance.[16,17] Liu et al[17] reported that elevated levels of NAMPT in the serum of small cell lung cancer (SCLC) patients were associated with brain metastasis and CCL2 was involved in transendothelial migration of tumor cells across the BBB. Our results also indicated upregulation of CCL2 and association with adverse prognosis in LGG and GBM. Accumulating evidence suggests NAMPT to upregulate inflammatory cytokines like IL6, TNF, and CCL2 in rheumatoid arthritis synovial fibroblasts and monocytes in response to inflammatory stimuli.[18] In our study, NAMPT was significantly correlated with CCL2 and IL6 suggesting that NAMPT might serve in autocrine regulation of inflammatory response and exert a permissive role for the activity of other adipocytokines like CCL2 and IL6 leading to transendoethlial migration of the BBB and assumes a dark visage that leads to the establishment of neuroinflammation and gliomas.

GRN is also reported to promote tumor growth and it has been implicated in many forms of cancer like breast, skin, lung, astrocytoma, ovarian, cervical, liver, head and neck, lymphoma, multiple myeloma, and leukemia.[19,20] Wang et al[20] suggested that GRN is involved in astrocytoma progression and may serve as a prognostic marker for glioblastoma. Our results go hand in hand with these studies and demonstrate association between increased GRN expression in GBM as compared to normal samples and with poor prognosis. Our results also demonstrate association of IL6 in glioma prognosis along with higher expression with increasing tumor grade and aggressive type. IL6 is considered to be proinflammatory and promotes tumorigenesis by affecting multiple pathways like apoptosis, survival, proliferation, angiogenesis, and metabolism.[21] IL6 is secreted by glioma cells and Shan et al.[22] demonstrated its role in the prognosis of glioma. Our results further strengthen the vital role played by IL6 in glioma progression and prognosis.

Previous investigations have demonstrated that overexpression of SERPINE1 in GBM is associated with shorter survival[23] and its serum levels were shown to be predictive for glioma grade.[24,25] Roy et al[25] studied the role of SERPINE1 on the mast cells recruitment in gliomas. Deepak[26] suggested heterogeneous activation of TGFβ and increased SERPINE1 expression in GBM.[26,27] Rowlinson et al[27] also identified SERPINE1 as a potential therapeutic target in clinically relevant invasive glioblastoma cells isolated from patients. Our results clearly demonstrate association of increased expression of SERPINE1 with poor prognosis in LGG and go hand in hand with other reports for GBM. RETN is another adipokine implicated in inflammation.[28,29] Pariisetty et al[29] suggested that RETN could participate in acute response to cerebral damage through inflammatory mechanisms. RETN is implicated in the synthesis and secretion of the proinflammatory cytokines TNF-α and IL6 through NF-κB-dependent pathway in macrophage.[30] Our results clearly suggest RETN as an important prognosticator for GBM and for aggressive histological type.[31] Vokuda et al[31] reported LEP expression in diffuse gliomas. Porcile et al[32] reported ADIPOQ as a novel regulator of cell proliferation in glioblastoma. However, no association in the TCGA and GTEx dataset was found with prognosis for LEP and ADIPOQ. Interestingly we did observe that LEP expression was correlated with aggressive histological type in LGG and GBM patients.

IDH mutation has been proposed to be a favorable prognosticator in LGGs and GBMs.[33,34] We analyzed the correlation of adipokines expression in LGG samples with IDH1 mutation status. For GBM samples IDH1 mutation status was not available in the Xena server. We report LEP, NAMPT, and SERPINE1 overexpression correlates with IDH1 wild type status in LGG patients. Lucena-Cacace et al suggested that high expression of NAMPT and SERPINE1 correlated with IDH1 wild type GBM tumors leading to the worst prognosis. They also proposed that NAMPT overexpression in glioma cell lines increases the tumorogenic properties.[16] IDH wild type LGG vessels are molecularly distinct from the IDH1 mutated, therefore indicative of vascular remodeling and angiogenesis.[35] We believe more studies with large number of samples of multiple ethnicities are warranted before establishing NAMPT and SERPINE1 overexpression as a surrogate biomarker for adverse prognosis within IDH1 wild type LGG subgroup.

At present, there very few reports on the mechanism of action of adipokines in gliomas.[36] We report coexpression of NAMPT, GRN, RETN, IL6, SERPINE1, and CCL2 in LGG and GBM and it seems that they are coexpressed in gliomas playing significant roles in glioma establishment and progression.[37] Mohammadi et al[37] reported

synergistic effects of RETN and NAMPT on telomerase gene expression and acceleration of tumor growth in gastric cancer cells. Comprehension and disruption of tumor mechanisms in the gliomas microenvironment could improve therapeutic intervention for these lethal tumors.

In conclusion, the present study establishes abnormal expressions and prognostic values of adipokines in gliomas. The findings of our study concluded that NAMPT, GRN, and SERPINE1 were found to be overexpressed in LGG and GBM, both at the mRNA and protein level and were found to be associated with poor prognosis. Clinicopathologically they are also associated with the higher grade and type of gliomas. Also, they are expressed simultaneously in LGG and GBM. RETN was found to be an important prognosticator for GBM. Therefore, we conclude that NAMPT, GRN, and SERPINE1 as potential biomarkers of gliomas, and may contribute to tumor progression. However, there is limited information on physiological significance of these in gliomas, their specific function, mechanism, and crosstalk among them needs to be further elucidated.

CONFLICT OF INTERESTS

The authors declare that the research was conducted in the absence of any commercial or financial relationships that could be construed as a potential conflict of interest.

AUTHOR CONTRIBUTIONS

All authors participated in the design of the manuscript, drafted the manuscript, revised the manuscript critically, and approved the final version.

ETHICS STATEMENT

Since this study was conducted using data freely available in the public domains, ethical clearance was not required.

ORCID

Bhupender Kumar http://orcid.org/0000-0003-3887-5040

REFERENCES

1. Bluher M. Adipokines - removing road blocks to obesity and diabetes therapy. [Review]. *Mol Metab*. 2014;3(3):230-240. https://doi.org/10.1016/j.molmet.2014.01.005
2. Bluher M. Adipose tissue dysfunction in obesity. [Review]. *Exp Clin Endocrinol Diabetes*. 2009;117(6):241-250. https://doi.org/10.1055/s-0029-1192044
3. Lehr S, Hartwig S, Sell H. Adipokines: a treasure trove for the discovery of biomarkers for metabolic disorders. [Review]. *Proteomics Clin Appl*. 2012;6(1-2):91-101. https://doi.org/10.1002/prca.201100052
4. Van de Voorde J, Pauwels B, Boydens C, Decaluwe K. Adipocytokines in relation to cardiovascular disease. [Research Support, Non-U.S. Gov't Review]. *Metabolism*. 2013;62(11):1513-1521. https://doi.org/10.1016/j.metabol.2013.06.004
5. Lee CH, Woo YC, Wang Y, Yeung CY, Xu A, Lam KS. Obesity, adipokines and cancer: an update. [Review]. *Clin Endocrinol*. 2015;83(2):147-156. https://doi.org/10.1111/cen.12667
6. Lengyel E, Makowski L, DiGiovanni J, Kolonin MG. Cancer as a matter of fat: the crosstalk between adipose tissue and tumors. [Research Support, N.I.H., Extramural Research Support, Non-U.S. Gov't Review]. *Trends Cancer*. 2018;4(5):374-384. https://doi.org/10.1016/j.trecan.2018.03.004
7. Davis ME. Epidemiology and overview of gliomas. [Review]. *Semin Oncol Nurs*. 2018;34(5):420-429. https://doi.org/10.1016/j.soncn.2018.10.001
8. Vigneswaran K, Neill S, Hadjipanayis CG. Beyond the World Health Organization grading of infiltrating gliomas: advances in the molecular genetics of glioma classification. [Review]. *Ann Transl Med*. 2015;3(7):95. https://doi.org/10.3978/j.issn.2305-5839.2015.03.57
9. Tang Z, Li C, Kang B, Gao G, Zhang Z. GEPIA: a web server for cancer and normal gene expression profiling and interactive analyses. *Nucleic Acids Res*. 2017;45(W1):W98-W102. https://doi.org/10.1093/nar/gkx247
10. Omuro A, DeAngelis LM. Glioblastoma and other malignant gliomas: a clinical review. [Review]. *JAMA*. 2013;310(17):1842-1850. https://doi.org/10.1001/jama.2013.280319
11. Jovcevska I, Kocevar N, Komel R. Glioma and glioblastoma—how much do we (not) know? [Review]. *Mol Clin Oncol*. 2013;1(6):935-941. https://doi.org/10.3892/mco.2013.172
12. Booth A, Magnuson A, Fouts J, Foster M. Adipose tissue, obesity and adipokines: role in cancer promotion. [Review]. *Horm Mol Biol Clin Investig*. 2015;21(1):57-74. https://doi.org/10.1515/hmbci-2014-0037
13. Arnoldussen IA, Kiliaan AJ, Gustafson DR. Obesity and dementia: adipokines interact with the brain. [Research Support, N.I.H., Extramural Research Support, Non-U.S. Gov't Review]. *Eur Neuropsychopharmacol*. 2014;24(12):1982-1999. https://doi.org/10.1016/j.euroneuro.2014.03.002
14. Mohammadi M, Mianabadi F, Mehrad-Majd H. Circulating visfatin levels and cancers risk: a systematic review and meta-analysis. *J Cell Physiol*. 2019;234(4):5011-5022. https://doi.org/10.1002/jcp.27302
15. Reddy PS, Umesh S, Thota B, et al. PBEF1/NAmPRTase/Visfatin: a potential malignant astrocytoma/glioblastoma serum marker with prognostic value. [Research Support, Non-U.S. Gov't]. *Cancer Biol Ther*. 2008;7(5):663-668. https://doi.org/10.4161/cbt.7.5.5663
16. Lucena-Cacace A, Otero-Albiol D, Jimenez-Garcia MP, Peinado-Serrano J, Carnero A. NAMPT overexpression induces cancer stemness and defines a novel tumor signature for glioma prognosis. *Oncotarget*. 2017;8(59):99514-99530. https://doi.org/10.18632/oncotarget.20577
17. Liu T, Miao Z, Jiang J, et al. Visfatin Mediates SCLC Cells Migration across Brain Endothelial Cells through Upregulation

of CCL2. [Research Support, Non-U.S. Gov't]. *Int J Mol Sci*. 2015;16(5):11439-11451. https://doi.org/10.3390/ijms160511439
18. Brentano F, Schorr O, Ospelt C, et al. Pre-B cell colony-enhancing factor/visfatin, a new marker of inflammation in rheumatoid arthritis with pro-inflammatory and matrix-degrading activities. [Research Support, Non-U.S. Gov't]. *Arthritis Rheum*. 2007;56(9):2829-2839. https://doi.org/10.1002/art.22833
19. Arechavaleta-Velasco F, Perez-Juarez CE, Gerton GL, Diaz-Cueto L. Progranulin and its biological effects in cancer. [Review]. *Med Oncol*. 2017;34(12):194. https://doi.org/10.1007/s12032-017-1054-7
20. Wang M, Li G, Yin J, Lin T, Zhang J. Progranulin overexpression predicts overall survival in patients with glioblastoma. [Research Support, Non-U.S. Gov't]. *Med Oncol*. 2012;29(4):2423-2431. https://doi.org/10.1007/s12032-011-0131-6
21. Kumari N, Dwarakanath BS, Das A, Bhatt AN. Role of interleukin-6 in cancer progression and therapeutic resistance. [Review]. *Tumour Biol*. 2016;37(9):11553-11572. https://doi.org/10.1007/s13277-016-5098-7
22. Shan Y, He X, Song W, Han D, Niu J, Wang J. Role of IL-6 in the invasiveness and prognosis of glioma. *Int J Clin Exp Med*. 2015;8(6):9114-9120.
23. Colin C, Voutsinos-Porche B, Nanni I, et al. High expression of cathepsin B and plasminogen activator inhibitor type-1 are strong predictors of survival in glioblastomas. [Research Support, Non-U.S. Gov't]. *Acta Neuropathol*. 2009;118(6):745-754. https://doi.org/10.1007/s00401-009-0592-2
24. Iwadate Y, Hayama M, Adachi A, et al. High serum level of plasminogen activator inhibitor-1 predicts histological grade of intracerebral gliomas. *Anticancer Res*. 2008;28(1B):415-418.
25. Roy A, Coum A, Marinescu VD, et al. Glioma-derived plasminogen activator inhibitor-1 (PAI-1) regulates the recruitment of LRP1 positive mast cells. [Research Support, Non-U.S. Gov't]. *Oncotarget*. 2015;6(27):23647-23661. https://doi.org/10.18632/oncotarget.4640
26. Xu XL, Kapoun AM. Heterogeneous activation of the TGFbeta pathway in glioblastomas identified by gene expression-based classification using TGFbeta-responsive genes. *J Transl Med*. 2009;7:12. https://doi.org/10.1186/1479-5876-7-12
27. Rowlinson J, Estevez-Cebrero MDLA, Lourdusamy A, Rahman R, Smith S. SERPINE1 identified as potential therapeutic target through rna-seq of clinically relevant invasive glioblastoma cells isolated from patients by 5-ala based methodology. *Neuro Oncology*. 2018;20(5):v348-v349. https://doi.org/10.1093/neuonc/noy129.020
28. Ouchi N, Parker JL, Lugus JJ, Walsh K. Adipokines in inflammation and metabolic disease. [Research Support, N.I.H., Extramural Review]. *Nat Rev Immunol*. 2011;11(2):85-97. https://doi.org/10.1038/nri2921
29. Parimisetty A, Dorsemans AC, Awada R, Ravanan P, Diotel N, Lefebvre d'Hellencourt C. Secret talk between adipose tissue and central nervous system via secreted factors-an emerging frontier in the neurodegenerative research. [Research Support, Non-U.S. Gov't Review]. *J Neuroinflammation*. 2016;13(1):67. https://doi.org/10.1186/s12974-016-0530-x
30. Silswal N, Singh AK, Aruna B, Mukhopadhyay S, Ghosh S, Ehtesham NZ. Human resistin stimulates the pro-inflammatory cytokines TNF-alpha and IL-12 in macrophages by NF-kappaB-dependent pathway. [Research Support, Non-U.S. Gov't]. *Biochem Biophys Res Commun*. 2005;334(4):1092-1101. https://doi.org/10.1016/j.bbrc.2005.06.202
31. Vokuda RS, B HS, Madhugiri VS, Velusamy SK, Verma SK. The expression of leptin and its receptor during tumorigenesis of diffuse gliomas such as astrocytoma and oligodendroglioma-Grade II, III and IV (NOS). *Asian Pac J Cancer Prev*. 2019;20(2):479-485. https://doi.org/10.31557/APJCP.2019.20.2.479
32. Porcile C, Di Zazzo E, Monaco ML, et al. Adiponectin as novel regulator of cell proliferation in human glioblastoma. [Research Support, Non-U.S. Gov't]. *J Cell Physiol*. 2014;229(10):1444-1454. https://doi.org/10.1002/jcp.24582
33. Ohgaki H, Kleihues P. The definition of primary and secondary glioblastoma. [Review]. *Clin Cancer Res*. 2013;19(4):764-772. https://doi.org/10.1158/1078-0432.CCR-12-3002
34. Xia L, Wu B, Fu Z, et al. Prognostic role of IDH mutations in gliomas: a meta-analysis of 55 observational studies. [Meta-Analysis Research Support, Non-U.S. Gov't]. *Oncotarget*. 2015;6(19):17354-17365. https://doi.org/10.18632/oncotarget.4008
35. Zhang L, He L, Lugano R, et al. IDH mutation status is associated with distinct vascular gene expression signatures in lower-grade gliomas. [Research Support, Non-U.S. Gov't]. *Neuro Oncol*. 2018;20(11):1505-1516. https://doi.org/10.1093/neuonc/noy088
36. Almeida J, Costa J, Coelho P, et al. Adipocyte proteome and secretome influence inflammatory and hormone pathways in glioma. [Research Support, Non-U.S. Gov't]. *Metab Brain Dis*. 2019;34(1):141-152. https://doi.org/10.1007/s11011-018-0327-y
37. Mohammadi M, Zarghami N, Hedayati M, Ghaemmaghami S. Synergistic effects of resistin and visfatin as adipocyte derived hormones on telomerase gene expression in AGS gastric cancer cell line. *Acta Med Iran*. 2017;55(10):621-627.

How to cite this article: Vachher M, Arora K, Burman A, Kumar B. NAMPT, GRN, and SERPINE1 signature as predictor of disease progression and survival in gliomas. *J Cell Biochem*. 2019;1–14. https://doi.org/10.1002/jcb.29560

International Journal of Electronics Engineering (ISSN: 0973-7383)
Volume 11 • Issue 2 June - Dec 2019 pp. 68-72 www.csjournals.com

Nonlinear Signal Analysis Using Eigen Value Decomposition of Hankel Matrix and Wavelet Transform

Sudipta Majumdar[1], Charul Arora
[1]Department of Electronics and Comm. Engg, Delhi Technological University, Delhi, India

Abstract: This paper presents the time-frequency analysis of multi-component non-stationary signal. The method uses the iterative eigen value decomposition of Hankel matrix and wavelet transform (IEVD HM WT). The proposed work uses the wavelet transform to obtain the analytic signal. This analytic signal is used to find out the instantaneous parameters. The proposed method compares the time frequency representation with iterative eigen value decomposition of Hankel matrix and Hilbert transform (IEVD HM HT) and spectrogram method. Simulation results show the effectiveness of time frequency representation of the proposed method.
Keywords: Eigenvalue decomposition, wavelet transform, Hilbert transform, spectrogram.

1.Introduction

The time frequency (TF) illustration of signal presents the signal characteristics over the time domain and frequency domain. The methods use both, the time and frequency domain analysis to present the temporal localization of spectral components of a signal. The illustration of non-stationary signals in both, the time domain and frequency domain is useful as it is used in various applications such as for target localization by radars [1] [2], instantaneous frequency analysis [3], design of optimal filters for signal estimation [4], for seismic data analysis [5], fault diagnosis of wind turbine[6]. It has been also used to study beat variations occuring in cardiac rhythm [7], to study the current collection quality of electric locomotives [8] and motion estimates of time varying objects [9].

Various techniques have been used for time frequency representation of nonstationary signals. In [10], bilinear time-frequency representation is used. In [11], Cohen's class of time-frequency representation is used that uses both, spectrogram and Wigher-Ville distribution. The commonly used method of time-frequency representation is STFT method [12]. [12] presents the instantaneous frequency representation of signal using energy density domain method, namely, the Wigner distribution. In [13], Yang*et al.* proposed time-frequency representation for multicomponent frequency modulated signal that uses parameterized time-frequency transform. In [14], Belouchraniet al. proposed time-frequency signal representation for blind source separation that uses joint diagonalization of a t-1 distribution. In [15], Hlawatsch*et al.* used time-frequency representation for signal estimation purpose that uses time varying Weiner filter and time varying filter. In [16], Liu *et al.* used empirical WT for TF representation of seismic signal to obtain the geographical structure information hidden in seismic data. In [17], Sattar *et al.* presented combination of filter bank and Wiener-Ville distribution for time-frequency representation. The advantage of this method is the reduction in cross terms and noise. In [18], Hlawatsch*et al.* used quadratic TF representation. In [19], Aysin*et al.* presented time-frequency representation for heart rate variability to detect abrupt changes in HRV and for segmentation of nonstationary signals in less nonstationary parts.

In [20], Sharma *et al.* proposed the time frequency representation using IEVD-HM and Hilbert transform (IEVD HM HT). Hilbert transform has been used to obtain the analytic signal to derive the instantaneous parameters. We used IEV HM WT method for time frequency representation of signal.

2.Hilbert Transform

Hilbert transform (HT) is a linear operator. It takes a function, $y(t)$ of a real variable and produces another function of a real variable $H(y)(t)$. The convolution of the function $u(t)$ with $\frac{1}{\pi t}$, gives the HT of the function. $\frac{1}{\pi t}$ is called the Cauchy kernel.

$$H(y)(t) = \frac{1}{\pi}\int \frac{y(\tau)}{t-\tau} d\tau \tag{1}$$

International Journal of Electronics Engineering (ISSN: 0973-7383)
Volume 11 • Issue 2 June - Dec 2019 pp. 68-72 www.csjournals.com

HT produce phase shift of 90^o to every Fourier component of function. The real function and its HT function are combined to produce a strong analytic function.

3. Component Extraction from Multi-Component Signal

Representing the square Hankel matrix by [21] H_N^x, of size $N \times N$ having $2N-1$ elements as

$$\mathrm{H}_N^x = \begin{bmatrix} x[0] & x[1] & \dots & x[N-1] \\ x[1] & x[2] & \dots & x[N] \\ . & . & \dots & . \\ x[N-1] & x[N] & \dots & x[2N-2] \end{bmatrix} \tag{2}$$

where $n = 0,1,\dots,Q$. N denotes an even integer. The H_N^x is obtained from $x[n]$. $x[n]$ is a real signal.

The H_N^x having interesting properties due to its unique structure. The symmetric characteristic of this matrix is as follows:

$$\mathrm{H}_N^x = (\mathrm{H}_N^x)^T \tag{3}$$

where T denotes the transpose operator. The eigen value decomposition (EVD) of the square matrix H_N^x is given by

$$\mathrm{H}_N^x = V_x \Lambda_x V_x^T \tag{4}$$

The diagonal matrix Λ_x having N eigenvalues which are real values. $\lambda_{x,i}, i = 1,2,\dots,N$. V_x is an orthogonal matrix and contains real valued eigenvectors.

Columns of V_x having N elements as $\vec{v}_{x,i}$.

The components of a multicomponent signal $x[n]$ can be extracted by iterative EVD of Hankel matrix H_N^x, formed by $x[n]$ i.e.

$$\mathrm{H}_N^x = \sum_{l=0}^{L} \mathrm{H}_N^{x_l} \tag{5}$$

where $\mathrm{H}_N^{x_l} = (\mathrm{H}_N^{x_l})^T$.

H_N^x characteristic equation is

$$det(\mathrm{H}_N^x - \lambda I) = \lambda^N - Tr(\mathrm{H}_N^x)\lambda^{N-1} + \dots + det(\mathrm{H}_N^x) \tag{6}$$

where $Tr(.)$ represents the trace of a matrix and $det(.)$ represents the determinant of a matrix. The trace of a matrix is represented using its nonzero eigenvalues as

$$Tr(\mathrm{H}_N^x) = \sum_{i=1}^{2L} \lambda_{x,i} \tag{7}$$

$$Tr(\mathrm{H}_N^{x_l}) = \sum_{i=1}^{2} \lambda_{x_l,i} \qquad N \geq 2L \tag{8}$$

4. Wavelet Transform Based Time Frequency Representation

To obtain the instantaneous parameters (instantaneous amplitude, phase and frequency), we obtain the analytic signal using wavelet transform method. To obtain the analytic signal using wavelet transform we used the method proposed by Gao [22].

Gao proved that with analytic wavelet $g(t)$ and for any $s(t) \in L^2(R, dt)$,

$$\frac{1}{C_g} \int_0^\infty S(t,a) \frac{da}{a} = s(t) + jH[s(t)] \tag{9}$$

where $H[s(t)]$ is the Hilbert transform of $s(t)$. $S(t,a)$ is defined as

International Journal of Electronics Engineering (ISSN: 0973-7383)
Volume 11 • Issue 2 June - Dec 2019 pp. 68-72 www.csjournals.com

$$S(b,a)=\frac{1}{a}\int_{-\infty}^{\infty}s(t)\bar{g}(\frac{t-b}{a})dt \tag{10}$$

where,

$$C_g=\int_0^{\infty}(\hat{g}_R(\omega)/\omega)d\omega \tag{11}$$

$g_R(t)$ is real and even. $g(t)$ and $s(t)$ has to satisfy the conditions given in [22].

Using this analytic signal the instantaneous parameters are defined as:The instantaneous amplitude, instantaneous phase, and instantaneous frequency

$$A(t)=\sqrt{y^2(t)+(\mathrm{H}[y(t)])^2} \tag{12}$$

$$\theta(t)=arctan\left(\frac{\mathrm{H}[y(t)]}{y(t)}\right) \tag{13}$$

$$\omega(t)=\frac{d\theta(t)}{dt} \tag{14}$$

The presentation of instantaneous frequency and squared instantaneous amplitude of monocomponents present the TF representation of the signal [20].

5. Simulations

This method is implemented in MATLAB. The analytic wavelet $g(t)$ used is the Morlet wavelet [22].The modified Morlet wavelet is defined as

$$g_\tau(t)=e^{imt}e^{(-1/2)}[\sqrt{2}\sigma m/(2\pi\tau)t]^2 \tag{15}$$

where m denotes the angular frequency. τ denotes the carrier wave cycles in an envelope. σ is related to precision.

For wavelet method, $\sigma=5$, $\tau=4$, $m=28.28$. To implement the proposed method, we used summation of three sinusoids of different frequencies and amplitude as given by equation (17). Fig 1 shows the multi component signal and three individual signals. Fig. 2 presents the time frequency representation using the proposed method and compares the proposed method using IEV-HM HT method and the spectrogram method as shown in Fig 3 and Fig. 4. respectively.

$$s1[n]=\sum_{i=1}^{3}A_i\cos\left(\frac{2\pi f_i n}{F_s}\right) \tag{16}$$

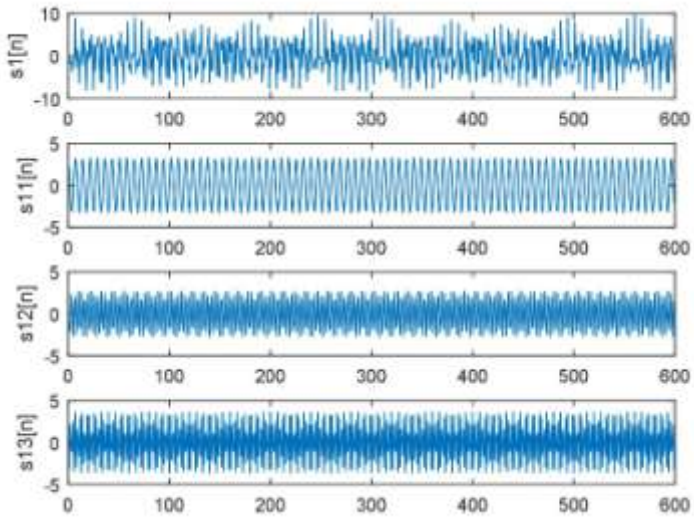


Figure 1: Multicomponent and individual signals.

International Journal of Electronics Engineering (ISSN: 0973-7383)
Volume 11 • Issue 2 June - Dec 2019 pp. 68-72 www.csjournals.com

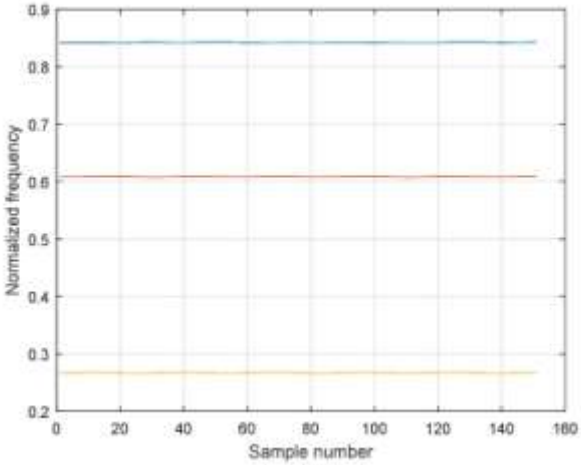


Figure 2: Time frequency representation using the proposed method.

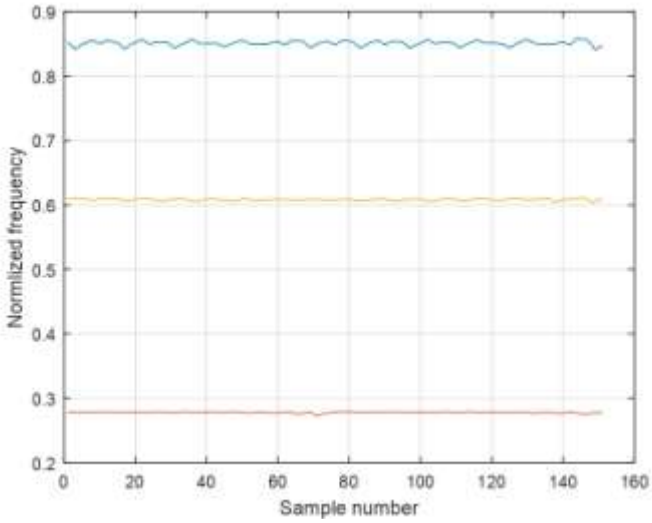


Figure 3: Time frequency representation using the IEVD -HM HT method.

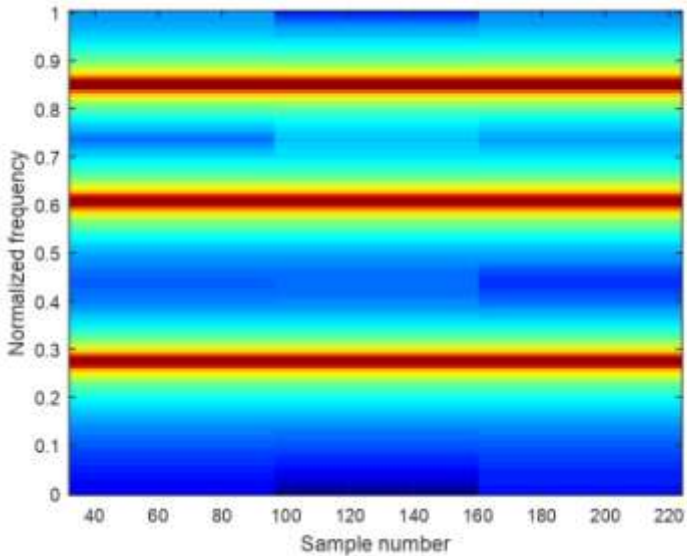


Figure 4: Time frequency representation using spectrogram method.

6. Conclusions

The proposed method uses the iterative eigen value decomposition of Hankel matrix and wavelet transform (IEVD HM WT)for time frequency representation of non stationary signal and compares the method with IEVD HM HT method and the spectrogram method. The simulation results show the effectiveness of the proposed method, which is due to time frequency localization characteristic of the wavelet transform.

References

[1]. Y. Zhang, M. Amin and F. Ahmad, "Time-frequency analysis for the localization of multiple moving targets using dual-frequency radars", IEEE Signal Processing Letters, 15, pp. 777-780, 2008.

[2]. B. Jokanovic, M. Amin and T. Dogaru, "Time-frequency signal representations using interpolations in joint-variable domains", IEEE Geoscience and Remote Sensing Letters, vol. 12, no. 1, pp. 204-208, 2015.

[3]. L. Stankovic and S. Stankovic, "An analysis of instantaneous frequency representation using time-frequency distributions-generalized Wigner distribution", IEEE Transactions on Signal Processing, vol. 43, no. 2, pp. 549-552, 1995.

[4]. F. Hlawatsch, G. Matz, H. Kirchauer and W. Kozek, "Time-frequency formulation, design, and implementation of time-varying optimal filters for signal estimation", IEEE Transactions on signal processing, vol. 48, no. 5, pp.1417-1432, 2000.

[5]. W. Liu, S. Cao, and Y. Chen, "Seismic Time-Frequency Analysis via Empirical Wavelet Transform", \emph{IEEE Geosci. Remote Sensing Lett., vol. 13, no. 1, pp. 28-32, 2016.

[6]. B. Yang, R. Liu, and X. Chen, Sparse time-frequency representation for incipient fault diagnosis of wind turbine drive train. IEEE Transactions on Instrumentation and Measurement, vol. 67, no. 11, pp. 2616-2627, 2018.

[7]. B. Aysin, L.F. Chaparro, I. Grave and V. Shusterman, "Orthonormal-basis partitioning and time-frequency representation of cardiac rhythm dynamics", IEEE Transactions on Biomedical Engineering, vol. 52, no. 5, pp.878-889, 2005.

[8]. H. Wang, Z. Liu, Y. Song, X. Lu, Z. Han, J. Zhang and Y. Wang, "Detection of contact wire irregularities using a quadratic time–frequency representation of the pantograph–catenary contact force", IEEE Transactions on Instrumentation and Measurement, vol. 65, no. 6, pp.1385-1397, 2016.

[9]. D.S. Alexiadis and G.D. Sergiadis, "Estimation of multiple, time-varying motions using time-frequency representations and moving-objects segmentation", IEEE Transactions on Image Processing, vol. 17, no. 6, pp. 982-990, 2008.

[10].A.M. Sayeed and D.L. Jones, "Optimal detection using bilinear time-frequency and time-scale representations", IEEE transactions on signal processing, vol. 43, no. 12, pp. 2872-2883, 1995.

[11].C. Richard and R. Lengelle, Recursive implementation of some time-frequency representations. In time-frequency and time-scale analysis, Proceedings of the IEEE-SP International Symposium, pp. 313-316, 1996.

[12].L. Stankovic and S. Stankovic, "An analysis of instantaneous frequency representation using time-frequency distributions-generalized Wigner distribution", IEEE Transactions on Signal Processing, vol 43, no. 2, pp.549-552, 1995.

[13].Y. Yang, Z. Peng, X. Dong, W. Zhang and G. Meng, "Application of parameterized time-frequency analysis on multicomponent frequency modulated signals", IEEE Transactions on Instrumentation and Measurement, vol. 63, no. 12, pp. 3169-3180, 2014.

[14].Belouchrani, A. and Amin, M.G., "Blind source separation based on time-frequency signal representations", \emph{IEEE Transactions on Signal Processing}, vol. 46, no. 11, pp. 2888-2897, 1998.

[15].F. Hlawatsch, G. Matz, H. Kirchauer and W. Kozek, "Time-frequency formulation, design, and implementation of time-varying optimal filters for signal estimation", IEEE Transactions on signal processing, vol. 48, no. 5, pp. 1417-1432, 2000.

[16]. W. Liu, S. Cao and Y. Chen, "Seismic time-frequency analysis via empirical wavelet transform", IEEE Geosci. Remote Sensing Lett., vol. 13, no. 1, pp. 28-32, 2016.

[17].F. Sattar, and G. Salomonsson, "The use of a filter bank and the Wigner-Ville distribution for time-frequency representation", \emph{IEEE transactions on Signal Processing}, vol. 47, no. 6, pp. 1776-1783, 1999.

[18].F. Hlawatsch, A. Papandreou-Suppappola and G.F. Boudreaux-Bartels, "The hyperbolic class of quadratic time-frequency representations. II. Subclasses, intersection with the affine and power classes, regularity, and unitarity", IEEE Transactions on Signal Processing, vol. 45, no. 2, pp. 303-315, 1997.

[19].B. Aysin, L.F. Chaparro, I. Grave and V. Shusterman, Orthonormal-basis partitioning and time-frequency representation of cardiac rhythm dynamics", IEEE Transactions on Biomedical Engineering, vol. 52, no. 5, pp. 878-889, 2005.

[20].R.R. Sharma and R.B. Pachori, "A new method for non-stationary signal analysis using eigenvalue decomposition of the Hankel matrix and Hilbert transform", Signal Processing and Integrated Networks (SPIN-2017), IEEE 4th International Conference, pp. 484-488, 2017.

[21].P. Jain, and R.B. Pachori, "An iterative approach for decomposition of multi-component non-stationary signals based on eigenvalue decomposition of the Hankel matrix", Journal of the Franklin Institute, vol. 352, no. 10, pp. 4017-4044, 2015.

[22].J. Gao, X. Dong, W.B. Wang, Y. Li and C. Pan, Instantaneous parameters extraction via wavelet transform. IEEE Transactions on Geoscience and Remote Sensing, vol. 37, no. 2, pp. 867-870, 1999.

Novel and Robust Hysteresis Current Control Strategies For a BLDC Motor : A Simulation Study and Inverter Design

Shrivatsan K Chari
Department of Elecctrical Engineering
Delhi Technological University New Delhi, India
shrivatsan3@gmail.com

Rishav Dhiman
Department of Electrical Engineering
Delhi Technological University, New Delhi, India
dhiman.rishav97@gmail.com

Rohit Saxena
Department of Elecctrical Engineering
Delhi Technological University, New Delhi, India
rohit.saxena17.1.96@gmail.com

***Abstract* – The major objective of the present study is to control the torque of the BLDC motor through hysteresis current control for electric vehicle applications. In this regard, we have proposed two strategies. In the case of small machines due to their low inductance values, a buck-boost circuit is implemented using a three-phase inverter configuration with a novel sensing algorithm. Speed control is implemented using a PI controller which generates the reference current signal. For machines with higher inductance value, a novel topology has been suggested to control the current using a single current sensor, thereby decreasing sensor costs by one third. Also the strategies presented are robust as they are minimally dependent on motor parameters.**

Keywords— BLDC motor, Buck-Boost circuits, Hysteresis current control, torque control, speed control, PI controller, Current sensor

I. INTRODUCTION

Products powered by alternative energy are being thrust into the market because of the ill effects of non-renewable energy sources. Due to latest developments in Electrical Engineering technologies, reliability and sustainability of renewable sources such as solar power have improved leaps and bounds [1]. Electrical Vehicles have no gaseous emissions and when combined with a grid powered by renewable energy, have a negligible carbon footprint. Hence, there has been an avid interest in electric vehicle research and development to have a greener future. Brushless Direct Current motors are used in low power electric vehicles because of their reliability, efficiency and high power-to-volume ratio [2]. They have similar torque and speed characteristics to a traditional brushed DC motor. Because of the electronic commutation and absence of brushes, BLDC motors require lower maintenance and have longer lifetimes than brushed DC motors. Hall sensor feedback is often employed to govern the commutation. When the accelerator pedal is pressed in a gasoline powered vehicle, reference acceleration is commanded by the driver. To get the same feel and ride in an electric car, it requires torque control. This method has the advantages of being able to scale inclines from a stationary position and start the motor with higher payload (passengers). Also, the ride would be smoother. Hysteresis current control keeps the current within a tolerance band, and the average value of current is used to control the torque [3]. In a BLDC motor, the torque developed is directly proportional to the phase current [4].

II. CONTROL STRATEGIES

We propose two different methods to carry out the intended result. First method is suitable for smaller machines with lower inductances. The second method utilizes reversal of voltage polarity to reduce current in machines with large inductances. Both strategies utilize a 3-phase inverter bridge.

A. For smaller machines

Consider the inverter structure Fig 1.a. The leg which has to be fired is determined through the hall sensor data coming from the motor. At a time only one MOSFET of a leg conducts otherwise it would lead to short circuiting of power supply. The phase through which current enters the motor is connected through the MOSFETs in the upper row and the phase through which current exits is connected through the MOSFETs in the bottom row.

Boost mode

In Fig 1.a, let the phases which are conducting be R and Y. In order to operate the inverter in Boost mode, it follows from switching scheme that MOSFET 1 and 4 conduct. This leads to an increase in motor current with the inductance of the motor acting as inductor present in a boost circuit. Hence the conducting sequence is:

Battery → mosfet 1 → motor → mosfet 4 → Battery

Buck mode

In Fig 1.b, in order to decrease the current, we switch OFF MOSFET 1 and let the current decrease by free-wheeling through the internal diode of MOSFET 2. Hence the conducting sequence is:

Internal diode 2 → motor → mosfet 4 → internal diode 2

Current Sensing

In our approach, we were keen to compute a single value which would be compared to the reference current irrespective of which phase is conducting. For the same reason, we arrived at the following formulation:-

$$I = \frac{|I_R| + |I_Y| + |I_B|}{2} \quad (1)$$

978-1-5386-6625-8/18/$31.00 ©2018 IEEE

Let the motor be operating in boost mode as in Fig 1.a. This would mean that phase B current, $I_B = 0$. R phase current, I_R and Y phase current, I_Y are opposite to each other because the current enters through phase R and leaves through phase Y. Hence, sum of the absolute values of I_R and I_Y will give twice the DC link current. When finally divided by 2, we arrive at our intended current value to be sent into the relay. Same line of reasoning applies to buck mode as well.

B. For large machines

Large machines have higher inductances than their smaller counterpart. Hence the current may not decrease fast enough in the free-wheeling mode as desired for hysteresis control. We utilized a strategy where the boost mode remains same as in the case of small machines (Fig 1.a) and buck mode is replaced by a technique where the source voltage polarity is reversed to drive down the current (Fig 1.c). One significant advantage of this implementation is the requirement of only one current sensor, thereby decreasing sensor costs by order of one-third. However, this method would lead to more switching losses [5].

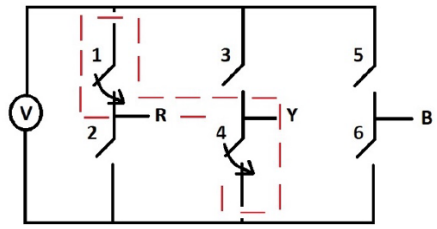


Figure 1.a. Boost mode operation

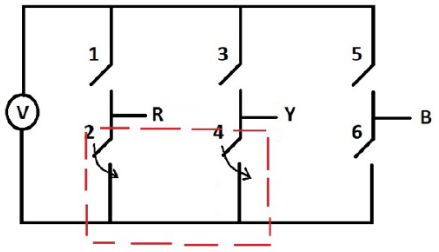


Figure 1.b. Buck mode operation

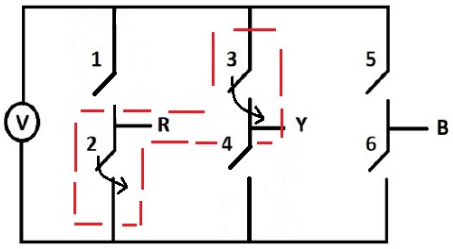


Figure 1.c Voltage polarity reversal for large machines

III. SIMULATION

For the purpose of simulation, we used Simulink software developed by MathWorks. The test setup was based on the block diagram given in Fig 2.a and Fig 2.b. As explained in the next section, hall sensor feedback decides which leg to switch. A relay is used to compare the phase current (DC link current for Fig 2.b) to a reference current. The relay then actuates the switches in upper and bottom row accordingly to increase or decrease the current.

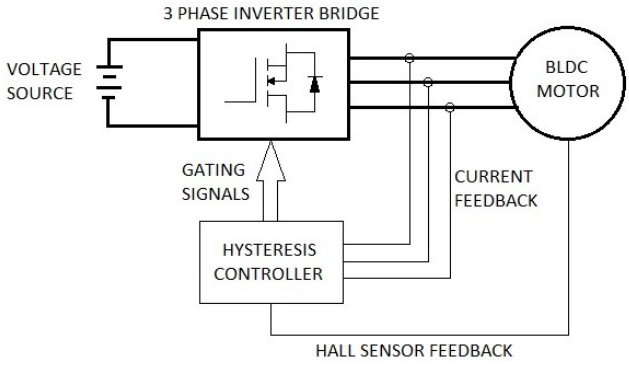


Figure 2.a. Control topology block diagram for small machines

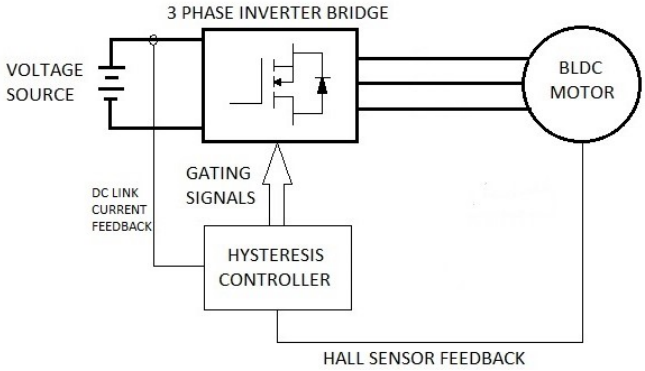


Figure 2.b. Control topology block diagram for large machines

We have used a Permanent Magnet Synchronous Machine model to represent our BLDC motor as it has the same construction and the required trapezoidal back electromotive force, EMF profile. The machine parameters were set corresponding to the specifications of the chosen BLDC motor. The exact value of parameters only influences the hardware components to be used, and not the control strategy thereby rendering our methodology robust. Hall sensor gives output as per the position of the rotor. Table 1 shows how the hall sensor output encodes the maximum positive and maximum negative phase back EMF (Fig 3.a). Current enters through the phase which has maximum positive back EMF and exits through the one with maximum negative back EMF. Using this data, we constructed the Switches Section of Table 1 to generate the necessary gating pulses.

A. Simulink modeling for small machines

It is to be noted that the output labels A, B and C shown in simulation is same as labels R, Y and B in Fig.1. Since the rating of our motor is 3300 revolutions per minute, rpm we simulated different reference speeds ranging from low to high. The reference speed is compared to rotor speed to generate a speed error. This error is then sent into the

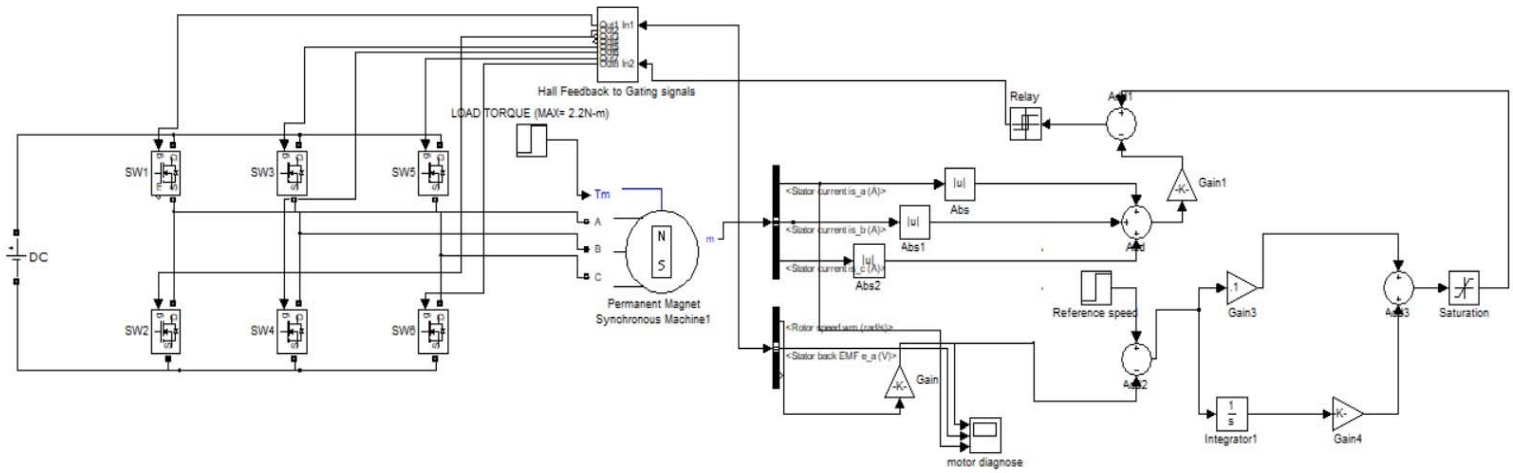


Fig 4.a Simulink model for small machines

proportional integral controller, which produces the current reference. The maximum phase current is limited to 20 Amperes, the rating of our BLDC motor. The reference current is then compared to I (computed from (1)), and their difference is fed to the relay (Fig 3.b). The relay increases phase current by sending gating signals for boost mode operation and decreases the same using buck mode described earlier. Overall, the relay switches such that the phase current is within a band 0.5 Amperes above and below the reference current. The final simulation model of hysteresis current control for small machines has been depicted in Fig 4.a.

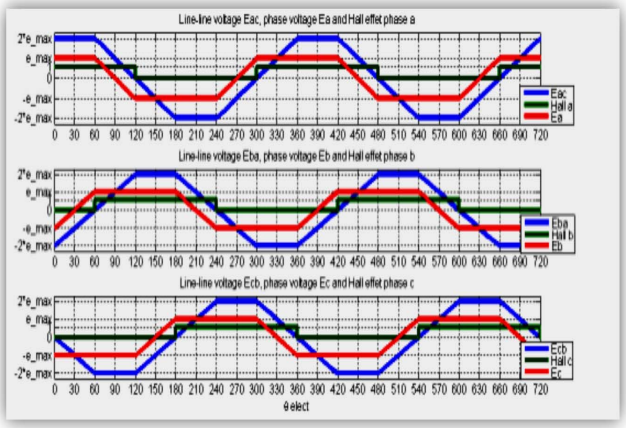


Figure 3.a. back EMF waveforms with Hall sensor outputs. To be read with table 1.a.

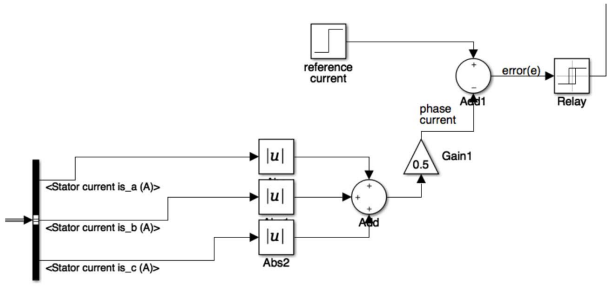


Figure 3.b. current sensing and relay output

HALL OUTPUTS			EMF			SWITCHES					
0	0	1	E_A	E_B	E_C	1	2	3	4	5	6
0	1	0	0	-1	+1	0	0	0	1	1	0
0	1	1	-1	+1	0	0	1	1	0	0	0
1	0	0	-1	0	+1	0	1	0	0	1	0
1	0	1	+1	-1	0	1	0	0	1	0	0
1	1	0	0	+1	-1	0	0	1	0	0	1

Table 1.Cell value with +1 indicates the phase with maximum positive back EMF. -1 indicates the phase with maximum negative back EMF. Switches with value are 1 are to be turned on and those with value 0 are to be switched off.

B. Simulink modeling for large machines

In this strategy we measure the DC current and directly compare that to the reference current. From thereon, the relay outputs gating signals on the same basis as described for small machines. The difference comes when current has to be decreased. Voltage polarity to the motor is reversed rather than operating in buck mode. Fig 4.b shows the model.

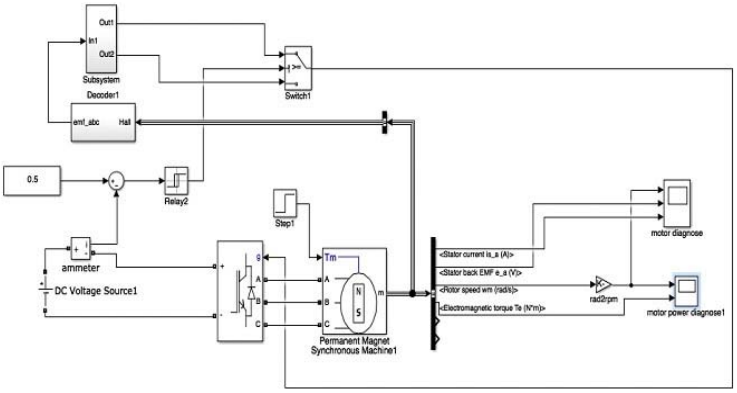


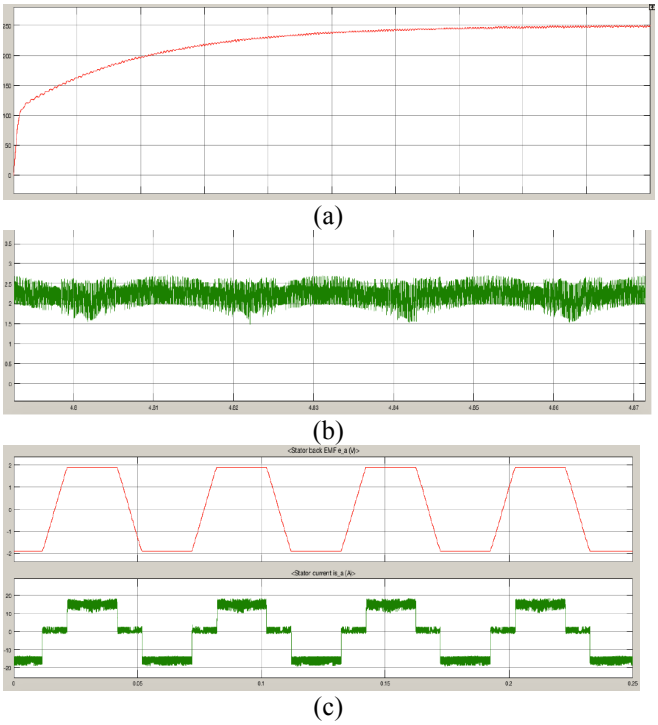
Fig.4.b Simulink model for large machines

IV. PERFORMANCE AND RESULTS

A. For small machines

Our model was simulated for two different speed references, i.e., at 2000 rpm (high) and 250rpm (low). In both cases, a load torque of 2.2 Newton-meter was applied. The controller showed good tracking ability as in both instances steady state was reached. The motor each time generated the required electromagnetic torque equal to the load torque, rendering our design as competent. Fig 5 shows the corresponding speed, torque, current and back EMF waveforms for 250 rpm and Fig. 6 is for 2000rpm, with current nicely following a hysteresis profile.

Also, it is essential to focus on the MOSFET switching profile. Fig.7 shows the MOSFET current and Voltage waveforms when the particular switch in a leg is to be actuated (governed by Hall sensor feedback). It depicts the extra power losses that will we have to incur. However, switching frequency of the MOSFET is variable that depends upon the width of the hysteresis band, DC voltage applied and the motor's speed. Also, amount of harmonics on the DC side has increased due to hysteresis current control.



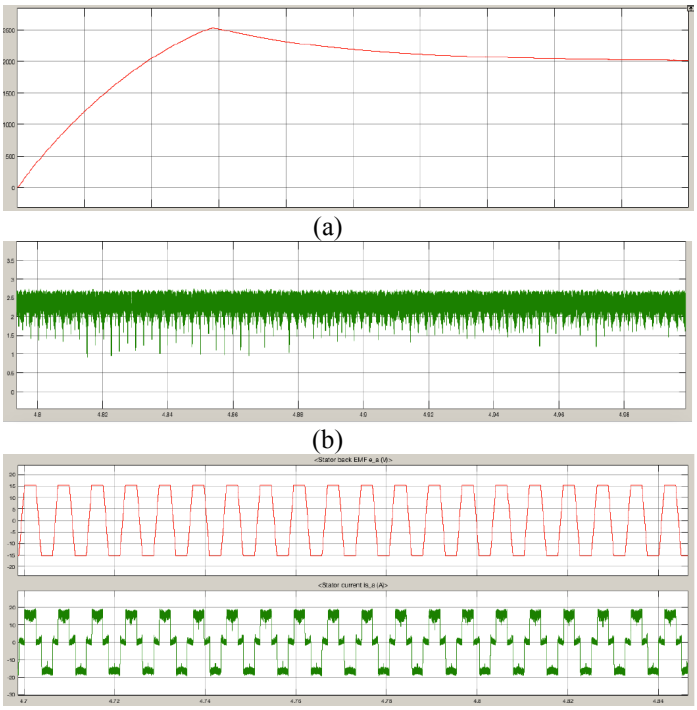
(a)

(b)

(c)

Fig.5

a. Speed profile for 250 rpm reference
b. Steady state electromagnetic Torque
c. Steady state back EMF
d. Steady state phase current



(a)

(b)

(c)

Fig.6

a. Speed profile for 2000 rpm reference
b. Steady state electromagnetic Torque
c. Steady state back EMF
d. Steady state phase current

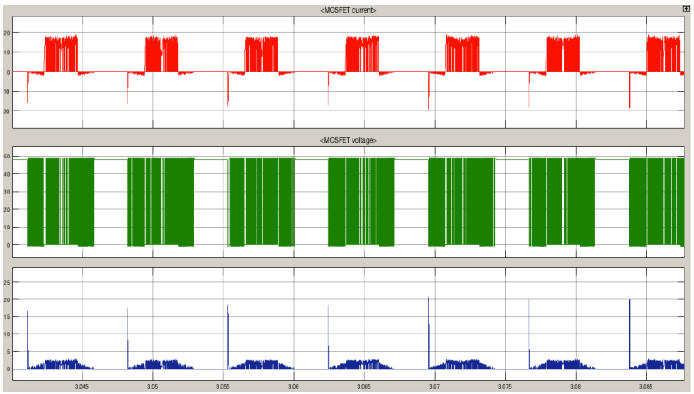


Fig. 7 Mosfet switching characteristics: - the first row scope being current, second being voltage, and third shows power loss.

B. For large machines

For this simulation we applied a load torque of 1 Newton-meter on the motor. Also the tolerance wass set to be 0.25 Amperes above and below the reference current. Satisfactory current waveform and torque control was achieved (Fig.8). Another external loop for speed control can be added as demosntrated in the strategy for small machines.

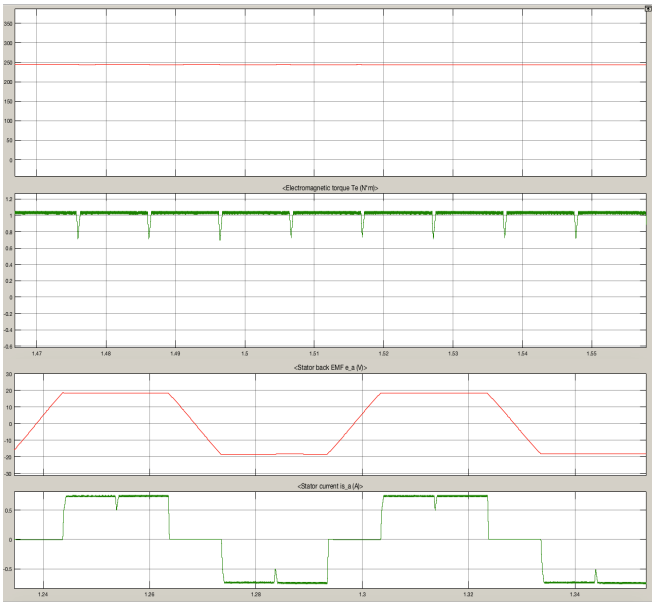


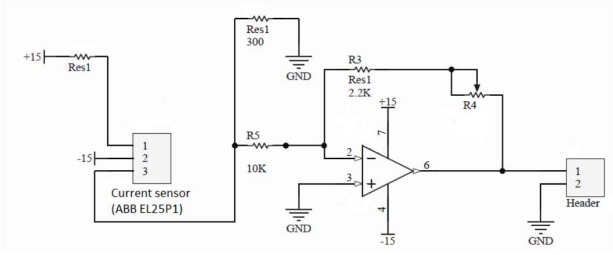
Fig. 8 From top to below :- steady state speed, electromagnetic torque, back EMF and phase current.

V. INVERTER DESIGN

The current sensor and 3-phase Inverter Bridge are essential hardware components for the implementation of our control strategy. Following section provides brief introduction to their design.

A. Current Sensor

Current sensor (suggested: ABB-EL25P1) generates a voltage signal proportional to the current using closed loop hall-effect technology. This voltage is then amplified by an op-amp (OP07) to a desired output voltage level. Fig 9 shows our circuit, and the PCB design for a three phase current sensor.



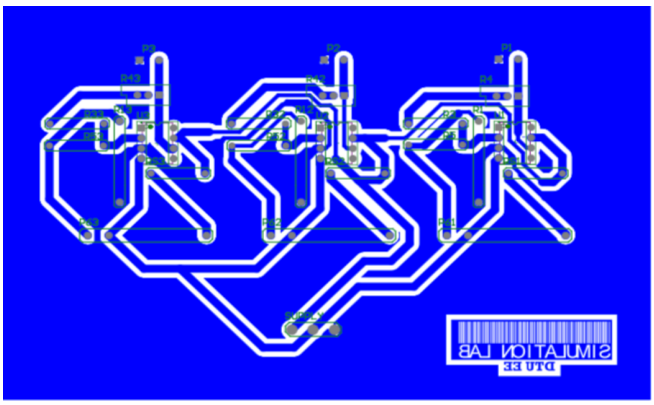


Fig.9 From top to bottom:- Circuit and PCB design for a three phase current sensor.

B. 3-phase Inverter Bridge

For the purpose of this project, a three legged inverter has been designed which uses six MOSFETs. Gating Signals have been provided via the gate Driver ADUM 4223. For MOSFETs, we suggest the use of CSD19531KCS n-channel MOSFETs made by Texas Instruments. The voltage rating of the same is 100V and it can carry a drain current of 100A.

Gate Driver Design

The gate driving circuit is made using ADUM 4223 (in Bootstrapping mode). Bootstrapping allows us to provide sufficient voltage between gate and source for the top row MOSFET, as its source is floating (not connected to ground). The optimum value of the capacitor is calculated using the MOSFET specifications (comes out to be 100 nF). 10K resistors have been used to for current and voltage rate limiting purposes. Fig.10 shows the schematic and PCB design.

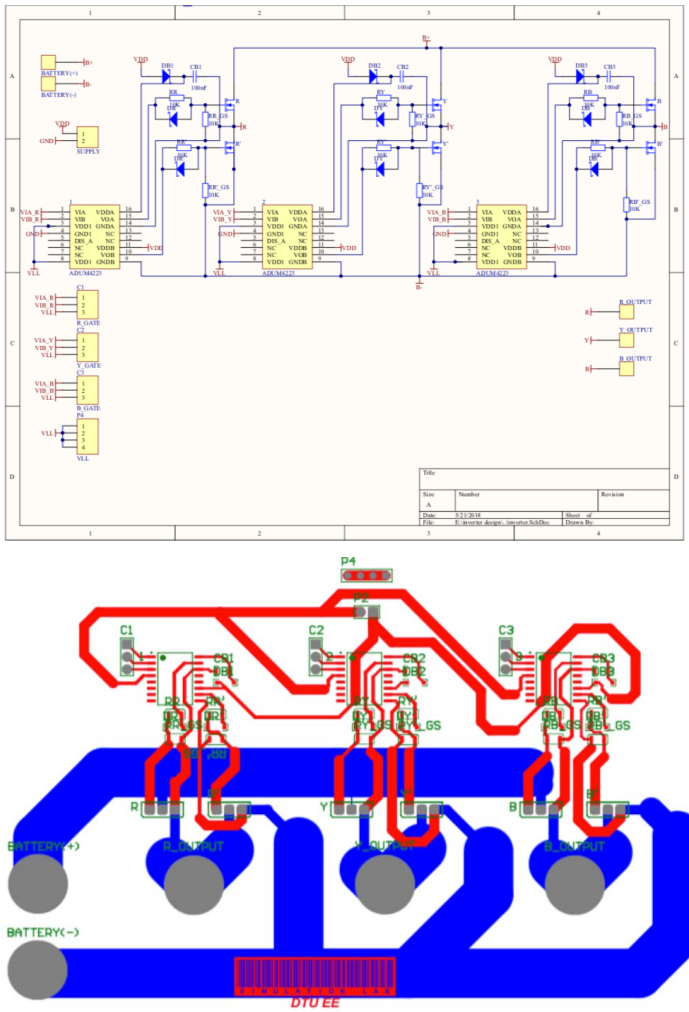


Fig.10 From top to bottom: - Schematic and PCB design

VI. CONCLUSION

The impetus is being given to renewable energy especially for assisting mobility. Naturally electric vehicles have become an active area of research and development. BLDC motors form one of the critical components of the said vehicles and hence designing an appropriate control mechanism needs attention [6]. This relevant because low

power vehicles will be used extensively in rural settings and thus any improvement in model design is useful [7]. Keeping this in mind, we have proposed two strategies which make use of hysteresis control mechanism and tested its feasibility using computer-based simulation studies. The control methodology is novel, robust and the cost is comparatively much less than commercially available controllers.

REFERENCES

[1]. S. Faddel, T. Youssef, A. Elsayed and O. Mohammed, "An Automated Charger for Large Scale Adoption of Electric Vehicles," in IEEE Transactions on Transportation Electrification, 2018.

[2]. J.C. Gamazo-Real, E.V. Sanchez, J.G. Gil, "Position and Speed Control of Brushless DC Motors Using Sensor-less Techniques and Application Trends", Sensors 2010.

[3]. Jianwei Zhang, Haitao Yang, Tianshi Wang, Li Li, David G. Dorrell, Dylan Dah-Chuan Lu, "Field-oriented control based on hysteresis band current controller for a permanent magnet synchronous motor driven by a direct matrix converter", IET Power Electronics, 2018, Vol. 11 Iss. 7, pp. 1277-1285.

[4]. K. V. P. Kumar and T. V. Kumar, "Direct torque control of brush less DC motor drive with modified switching algorithm", IEEE International Conference on Power Electronics, Drives and Energy Systems (PEDES), 2016.

[5]. W. Han, T. Y. Lee, Y. J. Kim and S. Y. Jung, "Comparative analysis on efficiency of brushless DC motor considering harmonic component of phase current and iron loss," *2015 18th International Conference on Electrical Machines and Systems* (ICEMS), Pattaya, 2015, pp. 1575-1579.

[6]. A. F. Noor Azam et al., "Current control of BLDC drives for EV application," *2013 IEEE 7th International Power Engineering and Optimization Conference* (PEOCO), Langkawi, 2013, pp. 411-416.

[7]. A. Karthikeyan, K. K. Prabhakaran and C. Nagamani, "Four quardrant operation of direct torque controlled PMSM drive using speed loop PDFF controller," *2018 International Conference on Power, Instrumentation, Control and Computing* (PICC), Thrissur, India, 2018, pp. 1-6.

International Research Journal of Engineering and Technology (IRJET) e-ISSN: 2395-0056
Volume: 06 Issue: 11 | Nov 2019 www.irjet.net p-ISSN: 2395-0072

Online or Offline Shopping: Factors that Determine Customer Behavior

Divyendu[1], Siddharth Raj[2], Vivek Yadav[3]

[1,2,3]B. Tech Undergraduates, Delhi Technological University, New Delhi, India

---

Abstract - *In this paper, the objective is to study the preference of online/offline shopping by consumers based on a plurality of factors, such as, geography, app/webpage, developed/developing/underdeveloped countries, urgency of delivery. The online/offline shopping behaviour by consumers based on geographical factor includes various land forms and climatic conditions. The online/offline shopping behaviour by consumers based on app/webpage includes a study of an e-commerce giant's user data usage. The online/offline shopping behaviour by consumers based on the type of country includes a case study comparing three countries, one each in developed, underdeveloped, and underdeveloped. The online/offline shopping behaviour by consumers based on the urgency of delivery is classified on the basis of product type.*

Key Words: **Online, Offline, Geography, Webpage, App, Developed, Developing, E-Commerce, Delivery, Underdeveloped, Land Forms, Climate**

1. INTRODUCTION

The growth of internet in the past two decades has been insurmountable, catalyzing digital economy driven by information technology. This growth in internet technology marks an increased user base and improved internet speed. Today, the growth of internet has most predominantly been capitalized by companies to widen its consumer base, through the use of web development. Apropos, the companies promote, advertise, sell, and display images of their products and services on the internet through their website/application. Furthermore, the company website entails all the relevant details pertaining the product that a user would desire to know from a seller. This is slowly embarking a shift in consumers' behavior from the traditional style of shipping by visiting shops to the easily accessible online shopping. Moreover, this paradigm shift in internet access and technology now means that the beneficiaries of the internet are also a contributor to the development of online shopping. Keeping up with the change in consumers' behavior, most companies have now revamped their marketing strategy to best suit their consumers and not fall behind in changing demands. On the other hand, the consumers gain a clear advantage when the Internet gives them an access to the best of global market, through which they get to compare prices across regions, assess the fragmentation of prices by order, and also be informed of better alternatives.

To sum up, the growth of the e-commerce industry today seems a promising story. In the past however, capturing this growth typically meant the transactional elements of activating online channels, optimizing merchandising, and investing in traffic generation. On the basis of the consumers' behavior, it is required to follow some considerations, such as, value proposition, market, competition, human resources, inventory control, financing, pricing, technology, trend and legislations. In order to draft a business plan involving e-commerce activity, studying consumer behavior is most indispensable. This behavior may include chasing quick and easy ways, high quality and inexpensive product, personality, consumption experiences, enforced requirements and loyalty (secured in terms of transactions and desired product).

2. Literature Review

Shopping in any country is directly influenced by the needs and demands of a customer. Good customer research helps in planning on how to convince the customers, that they need your products and services. The shopping behaviour of customers depend on different factors in both online as well as offline means.

(Arjun Mittal, November 2013): A study shows that web consumer's trust and risk factor drastically affects their online shopping choices. The trust of a consumer on an e-commerce company affects the acquiring choice of a buyer.

(Abdul Gaffar Khan, 2016): Online shopping has a plurality of factors that increases a consumers' loyalty towards online shopping and empowers the organization to acquire upper hand over different rivals in a developing economy.

(Mohammad Ahmad Al-hawari, Auguat 2012): Different factors have been analyzed and studies have shown that online shopping depends on many factors. However, there is also a need to consider the influence of offline factors on customer's trust for online services use. Results shows that any employee-based service quality don't have any relationship with online mode and completely has a positive relationship with existing offline mode

(Cherukuri Jayasankara Prasad, February 2011): According to a study shoppers' age, gender, occupation, education, monthly household income, family size and distance travelled to store has significant impact on offline shopping behaviour. However, in some conditions the offline buying behaviour to some extent may depend upon shoppers' demographic attributes.

(Jin Zhang, April 2014): Also O2O e-commerce has open new doors to consumers to have an offline trust for any product and then use online services to buy the same. However, this has created more difficulties for the traditional online as well as offline shopping mode

Although, various factors have been analyzed in the past for prediction of customer behavior, multiple other factors that are less addressed should not be neglected during customer research for any business idea or model.

3. Methodology

HYPOTHESIS 1: GEOGRAPHY

1. Study location: Researcher was surveying the factors influencing consumers‟ attitude and perception to make e-commerce purchase through online shopping from range of age in every selected location/area.

2. Sampling Method: This study was conducted by convenience sampling method because of the unavailability of the list online consumer that involved in online purchases. There were 100 respondents in this research study. The respondents were drawn from different occupational categories, education, age, gender or ethnic categories but all of them fulfilled the basic condition mentioned earlier.

3. Instruments the main instrument for this study was a questionnaire. The questionnaire aimed to gather information about respondents‟ socio-demographic background, behaviour towards online shopping and purchase perception towards online shopping.

4. Pre-test: Pre-test was done prior to the actual research. This pre-test is involved 10 respondents in order to ensure that the questions are understandable by the actual respondents.

5. Data collection/analysis: The data were analysed and the main statistical analysis was descriptive statistics such as frequency, percentage and mean were calculated to describe respondents‟ background behaviour and patterns of using internet and buying online.

E -commerce, even under the most radical scenarios, will not make geography irrelevant. So long as goods must be delivered and complementary face-to-face interactions are stimulated by online interactions, distance will still matter. E-commerce may, however, have a significant effect on the spatial distribution of economic activities. Broadly speaking, the locational choices of firms and households depend on spatial patterns of accessibility that at the end depends upon consumer’s behaviour. To the extent that e-commerce alters patterns of accessibility it will affect location choices.

1. Industrial impacts.

The term “industrial impacts” refers to changes in the location of facilities directly involved in the shift from offline retailing to e-retailing. This has significant implications since retail is one of the largest categories of employment, especially in metropolitan areas. The spatial distribution of this employment decline will depend on two things: first, which segments of the consumer market behaviour or experience the highest rate of e-retailing penetration, and second, which segments of the retail industry will suffer the most direct competition from e-retail.

One can make two plausible hypotheses. First, that urban populations are most likely to adopt e-retail because they are better educated and more likely to use the Internet actively for other purposes, and second, that people in non-metropolitan counties will adopt most rapidly because they have the most to gain from access to the wide variety of goods provided on the Internet. If the first hypothesis is correct, offline retailers in urban areas will suffer the greatest decline, while if the second is true, the greatest decline will occur in rural areas or in towns with rural service areas. Perhaps the first hypothesis will prove true in the short run while the second will prove true in the long run.

2. Transportation impacts

Outside the retail sector itself, the most obvious impacts of growth in e-retailing will be on transportation. Put simply, substitution of e-retail for offline retail entails a substitution of personal transportation (almost exclusively by car) for

freight transportation of the package delivery variety. A relatively small number of delivery firms with prior experience in this type of service (in the U.S., UPS, U.S. Postal Service, and FedEx are the dominant players) have benefited from the rapid growth in e-commerce. And, this likely to have faster accordingly and appreciated by every consumer. Even not only has the volume of goods they handle increased, but the range of services they provide to the e-retailer has expanded as well. Many failures in e-retail over the last few years have been in large part the outcome of the fact that e-retail site developers have placed too much emphasis on site design and marketing and not enough on the more mundane order fulfilment process with correct geographical approaches.

3. Pervasive impacts

From the customer's perspective, the attraction that some locations have over others based on accessibility to offline shopping facilities. This is not an inconsequential point since 12 percent of the average U.S. household's budget is spent on transportation 7 and 8 percent of the vehicle miles travelled is for shopping purposes. Since this is roughly comparable to the 10 percent of miles travelled for journey-to-work, 8 e-commerce in principle has a potential to affect residential decisions roughly equivalent to that of telecommuting. Note that despite the pricing regimes, it will still be more expensive to deliver goods to households who opt for more remote residential locations. Therefore those consumers will enjoy a cross-subsidy from more centrally located consumers. The possible hypothesis on this factor can be stated as the consumer choices and behavioural aspects acknowledges through the ease in availability of the desired product. This may not depends upon the e-retailing with any e-commerce website or doing offline shopping. But prior potential will change these factors to tend the choices over internet product choices at every location indeed, immersed and brutally impacted every consumer brain via socialized advertisements.

Specific Objective	Hypotheses	Statistical Test	Discussion
To investigate how socio-demographic (age, income and occupation) affect consumers‟ attitude towards online shopping.	Ho1: There is no significant difference between age and attitude towards online shopping.	One-way ANOVA	Fail to reject
	Ho2: There is no significant difference between income and attitude towards online shopping.	One-way ANOVA	Rejected
	Ho3: There is no significant difference between occupation and attitude towards online shopping.	One-way ANOVA	Fail to reject
To probe how the pattern of online buying (types of goods, e-commerce experience and hours use on internet) influence consumers‟ attitude towards online shopping.	Ho4: There is no significant difference between pattern of online buying (types of goods) and attitude towards online shopping.	One-way ANOVA	Fail to reject
	Ho5: There is no significant relationship between e-commerce experience and attitude towards online shopping.	Pearson Correlation Test	Rejected
	Ho6: There is no significant relationship between hours spent on internet and attitude towards online shopping.	Pearson Correlation Test	Fail to reject
To examine how purchase perception (product perception, customer service and consumer risk) influence consumers‟ attitude towards online shopping.	Ho7: There is no significant relationship between product perception and attitude towards online shopping.	Pearson Correlation Test	Rejected
	Ho8: There is no significant relationship between customer service and attitude towards online shopping.	Pearson Correlation Test	Rejected
	Ho9: There is no significant relationship between consumer‟ risk and attitude towards online shopping.	Pearson Correlation Test	Fail to reject

HYPOTHESIS 2: TYPE OF COUNTRY (DEVELOPED, DEVELOPING, UNDERDEVELOPED)

Based on the availability of the product, internet access, product affordability, awareness of online shopping, logistics, market, government stability, threats of terrorism, discount offers, delivery period, brand loyality. In Bbenkele (1986), a study on less developed countries discusses impact of multiple factors and presents an investigation of brand loyality in Zambia.

Based on an example of Amazon's operation in three different countries US (developed), India (developing), Bangladesh (Underdeveloped). The countries are selected based on Human Development Index data 2019.

Amazon US: It should come as no surprise that Amazon.com is one of the most successful eCommerce retailers in the US, but what may be a little more surprising is just how much the marketplace dominates the eCommerce market in America. In 2016, Amazon accounted for 43% of all US online retail sales. While that alone should be enough of a reason to consider Amazon as part of your US expansion plans, there are several other benefits as well. To start with, Amazon invest a lot into developing their US offering, arguably more so than in any of their other global markets. Amazon Prime Now (delivery within an hour) is just one example of their services being developed in the US. With regards to sheer potential though, it can't be ignored that Amazon.com also has over 95 million unique visitors to their site every month. That's a lot of potential customers. Despite there being no language barriers between the UK and the US, there are variations on spellings which should be reflected in your US listings. Let's assume you sell jewellery, for example. If you're not optimizing your Amazon listings for the US spelling of 'jewlery', you could be significantly reducing your visibility, reach and more importantly, sales. Language variations aside, there are of course other barriers that come with selling into the US, largely requirements regarding tax, customs and even having a physical presence. We would urge you to seek advice from lawyers to discuss these requirements.

Amazon India:

With an annual growth rate of 51% (the highest in the world) and as many as 83% of the population now shopping online, there's no denying the Indian eCommerce market is one to watch. What's perhaps more interesting is that 25% of the consumers have shopped internationally in the last year alone, highlighting the demand for international products. That in itself opens up a huge opportunity for your business. Despite there being several marketplaces available to sell on in India, however, Amazon's Indian site - Amazon.in - is in fact growing in popularity, particularly following the launch of Prime in 2016. As if that isn't enough of a reason to consider Amazon.in, the marketplace further dominated eCommerce mobile search in India last year, accounting for 46% of all eCommerce related searches in the country. As with any international market, there are of course advantages and disadvantages to consider. To start with, the logistics landscape in India is still relatively undeveloped, which should be a something to bear in mind if you're not using a fulfillment service. In order to sell in India (on Amazon or any other marketplace), you will also need to appoint a third-party service provider to represent you in the country. More specifically, they will need to provide the legal and financial entity for Amazon to trade with. Logistics challenges and entry requirements aside, there are plenty of benefits, including the fact that English is one of the official languages of India - eliminating any language barriers - and there is a growing appetite for international brands and higher quality foreign products, thanks to the rising income levels and increased awareness

Amazon Bangladesh: Amazon operates in 12 online marketplaces across the globe with most countries being developed or developing.

However, Amazon, global e-commerce giants, have planned to enter the Bangladeshi market by 2020, said Rezwanul Haque Jami, vice -president of the e-Commerce association of Bangladesh (e-CAB). "On the other hand, Amazon has come to Bangladesh and held meetings with the government and the authorities concerned. They are planning to start operating here by 2020," said Rezwanul. Underdeveloped countries which are expected to grow, have a stable government, market and decent logistics, will flourish in upcoming times.

Hypothesis suggests that the Amazon qualitatively operates best in US, quantitatively in India and has a future in Bangladesh. For countries similar to the countries researched upon, the data would should or less hold true.

HYPOTHESIS 3: APP VS WEBPAGE

The rate of online shopping by a person is much more in case of mobile app as compared to the webpage. The use of mobile phones has increased dramatically in the past few years. The increased number of smartphone users has effectively increased the online shopping behavior from 2015 to 2019. In the current scenario, about 77% of the population of USA owns a smartphone, which is about 230 million of consumers. Apart from smartphone about 100 million of US consumers

have a tablet. The number of US smartphone users will reach an approximate value of 232.8 million in 2019, surpassing desktop/laptop internet users (228.9 million) for the first time. Till January 2019, 53.60 million active mobile users are among the population of UK. Talking about India, currently, there are about 515.2 million active mobile internet users and about 765.1 million active mobile internet users in China. An estimated 10 billion mobile connected devices are currently in use. About 79% of smartphone users in US have made a purchase online using their mobile device in the last 6 months about 40% of all ecommerce purchases during the 2018 holiday season were made on a smartphone in US. Interestingly a fact concluded that about 80% of shoppers compared the product with the mobile devices in the stores to find a better alternative product or physical shop (Jason Chow, August 2019).

Looking at the stats according to the time spent by an amazon app user with respect to an Amazon web user is much higher. Amazon app users on average per month spend 12.843 billion minutes in app versus mobile web visitors who spend on an average 2.352 billion minutes per month on Amazon's mobile site. So, on an average per month, of all the time consumers spend shopping on Amazon, 84.5% of that time is in app versus 15.5% on the mobile web. Same is the case with Alibaba and other shopping sites (April Berthene, Mar 25, 2019).

Thus, online shopping behavior of the consumer is more inclined towards shopping on an app as compared to a webpage.

HYPOTHESIS 4: URGENCY OF PRODUCT

Online shopping behavior of the consumers highly depend on the urgency of product and delivery system of any company. The big giants including Amazon and Alibaba are trying to reduce the delivery time by various methods.

Prime by Amazon is an annually or monthly paid membership, which is part of the company's subscription service segment. Amazon prime offers customers with exclusive offers, free one day or two-day shipping in the United States. However, apart from the big offers and exclusive deals, the main reason for accepting a high number of prime users is free one day or two-day shipping. As of March 2019, there were approximately 103 million Amazon Prime members in US. Industry sources estimates that 62 percent of Amazon customers in the United States are Amazon Prime members. (J. Clement, Jul 12, 2019)

Talking about the consumer satisfaction on the product delivery, most of the consumer are disappointed with only one-day late delivery. 33 percent of the online shoppers contact customer service regarding an urgent or time-sensitive item when it arrives just one day late. One third of online shoppers contact customer service when a non-urgent item arrives just one day late, and 79 percent claim that they would contact customer service when a non-urgent item arrives two to three days late. With the growth of the mobile phones, it is seen that a consumer tracks a product delivery and is growingly more disappointed when the product is not delivered in a given time. Also, the product delivery depends on the type of product needed. Household items including grocery are considered of urgent requirement by the consumers. These items are preferred to be delivered within one day. On the other hand, some products such as, furniture or electronic product are expected to be delivered in 2-3 working days.

Furthermore, Amazon pantry and grocery service has been started, through which products get delivered in a whopping two hours. This is attracting the customers to new aspect of buying their daily needs online.

The above stats show that the delivery time is one of the most important factors for consumer's trust and satisfaction for online shopping. The business growth in amazon to this level is because of its product delivery and time which satisfies consumer according to the expectations.

SURVEY:

A survey was performed by the team in which a sample of 536 people were asked to fill a questionnaire asking about their online shopping preferences based on the factors covered in the hypotheses. These people were from different countries including India, China, Sri lanka, USA, Canada, Bangladesh etc. The people in the survey were both men and women from diverse economic, social, academic and cultural backgrounds.

The results of the survey were analyzed, and it was concluded that, about 76.39% of the people surveyed who were analyzed, had shopped online within 3-6 months. Further, 8% of the people surveyed bought a product online in last 9 months. In addition, 69.43% of the people surveyed suggested that they would like to shop on websites such as, Amazon using their mobile app and not on the webpage. However, 18.22% of the people surveyed suggested that they would prefer webpage over an app. Apart from this most of the people from countries like India and USA were inclined towards buying product from amazon prime due to its one-day delivery. Talking about the time of delivery, about 85.53% of the people

surveyed suggested that they would buy a product of their need from an option which provides fast delivery and about 38.66% of people were ready to give extra money for a single day delivery. Based on the portion of the population from different countries, the result showed that most of the buyers are from developed countries including USA, however the number of buyers is exponentially improving in developing countries as well. Further, in the survey conducted on American, Indian, and Bangladeshi citizens, it was found that 76.32% people were satisfied with online shopping services in US, while 54.23% people were satisfied with online shopping services in India. This number was at 12.7% in Bangladesh but is expected to go up in coming times.

5. Conclusions

The paper talks about various factors of online and offline shopping based on a plurality of factors.

What we conclude from our study and survey is discussed below:

1. In types of countries, divided into developed, developing and underdeveloped, countries which are developed and have a decent sized market are most effectively operating online, some developing countries with a decent sized market are quantitatively operating at best and underdeveloped countries with decent sized market are an interesting place for e-commerce companies to invest in the future. They currently mostly prefer offline mode of shopping.

2. Shopping behavior of an individual based on their mode of operation is much more inclined towards app based operation as compared to webpage. The use of smartphones by an individual has drastically increased from a decade which has an immense impact on the mode of shopping. The survey also concluded that a large section of the potential consumer of any product is more incline towards shopping a product based on the app rather than the website.

3. The shopping behavior and more importantly the trust of a consumer highly depends on the need of a product and the delivery time of that particular product. It is shown that an individual want to buy a product from a place from where his or her product is delivered with minimum time. Therefore, the delivery system of any product highly influence consumers and it is clear that any potential consumer of online product is more inclined toward a company which provides a lesser time in delivering their product.

4. Based on the results obtained from the questionnaire, there was no clear trend indicating the preference for online/offline shopping behavior based on geography. However, it was observed that regions with better infrastructure and connectivity had a rise in preference for online shopping in most cases.

REFERENCES

[1] Arjun Mittal (2013) E-commerce: It's Impact on consumer Behavior, ISSN 2248-9878 Volume 3, Number 2 (2013), pp. 131-138
[2] Abdul Gaffar Khan (2016) Electronic Commerce: A Study on Benefits and Challenges in an Emerging Economy, ISSN: 2249-4588 & Print ISSN: 0975-5853
[3] Mohammad Ahmad Al-hawari, Samar Mouakket (2012) Do offline factors trigger customers' appetite for online continual usage? ISSN: 1355-5855
[4] Cherukuri Jayasankara Prasad, Ankisetti Ramachandra Aryasri (2011) Effect of shopper attributes on retail format choice behaviour for food and grocery retailing in India, ISSN: 0959-0552
[5] Jin Zhang (2014) Customer' Loyalty Forming Mechanism of O2O E-Commerce, Vol. 5, No. 5(1); April 2014
[6] Jason Chow (2019) Online Shopping, eCommerce, and Internet Statistics (2019) You Should Know
[7] April Berthene (2019) Mobile shopping trends in 2018 for Amazon
[8] J. Clement (2019) Amazon Prime - Statistics & Facts
[9] The State of Online shopper delivery expectations and actions, how to please consumers in today's rapidly evolving e-commerce shipping landscape

Published by :
http://www.ijert.org

International Journal of Engineering Research & Technology (IJERT)
ISSN: 2278-0181
Vol. 6 Issue 11, November - 2017

Optimization of Process Parameters in Synergic MIG Welding of Mild Steel

Abhishek Kaushik
[a] Currently pursuing MBA at NMIMS, Mumbai
b Conducted under Department of Production and Industrial Engineering,
Delhi College of Engineering, Delhi

Abstract **— MIG Welding is compatible with continuous welding of all commercial metals and it can be adapted in mechanized as well as robotic applications. Therefore efficient optimization of machining parameters can produce high-quality products with low cost and high productivity. The experimental study is carried out to optimize various control factors to achieve the best results of Synergic MIG welding on Mild Steel. Design of Experiment, which is an orthogonal array, is formed using Minitab 16.0. Using Taguchi's parameter design, three control parameters affecting the desired weld quality viz. traverse speed (Vt), welding voltage (V) and wire feed rate (F) were selected with three levels selected for each factor. The process' output characteristics include bead width (W), bead height (H), penetration (P), heat affected zone (HAZ) and hardness (HRB). Observed weld bead features are useful in deciding the strength of the bead formed. Based on the mathematical values of these an optimum combination of welding parameters is found. Finally, Grey relational analysis, a popular evolutionary approach to uncertainty, multi-input, discrete data problem, is applied to determine the suitable selection of machining parameters for MIG process. The effect of each control factor on the performance measure is studied individually using various plots.**

The study demonstrates that the combination of welding parameters can be optimized so as to achieve better metal deposition rate, bead geometry, Shape factor, Form factor using Taguchi design optimization and Grey relational analysis.

Keywords: Synergic MIG, Traverse speed, Welding Voltage, Wire Feed Rate, Bead geometry, Design of Experiment, Taguchi method, Grey Relational analysis

1. INTRODUCTION

Metal Inert Gas Welding of mild steel is a process in which the source of heat is an arc formed between consumable metal electrode and the work piece, and the arc and the molten puddle are protected from contamination by the atmosphere (i.e. oxygen and nitrogen) with an externally supplied gaseous shield of active gases such as carbon dioxide, argon-carbon dioxide mixture, which is chemically active or not inert.
Synergic MIG, an advanced welding system, incorporates both Spray and pulse transfer and provides complete range of high technology digital microprocessor controlled equipment.

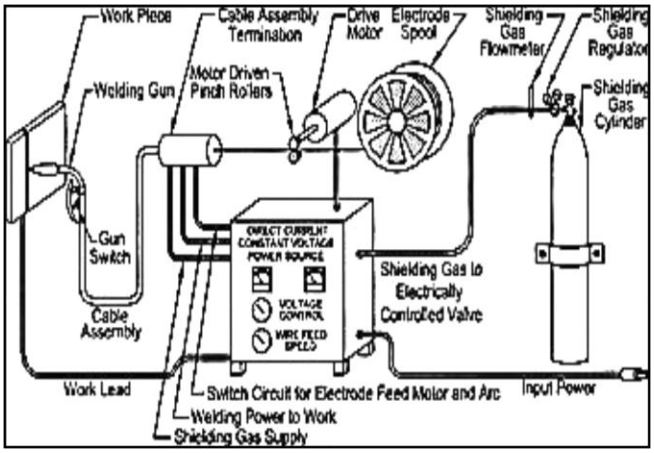


Fig. 1: Schematic diagram of Experimental setup

This welding process overcomes the restriction of using small lengths of electrodes to overcome the inability of the submerged-arc process of welding in various positions. By suitably adjusting the process parameters, it is possible to weld joints in the thickness range of 1-13 mm in all welding positions.

The quality of any weld process is characterized by the weld bead distortion, mechanical properties and weld bead geometry (as shown in fig. 2). Out of these factors, the weld bead geometry is the easiest to measure and control. Thus by controlling the weld bead geometry we can successfully control the weld quality. Therefore, the complex relationship between the process variables and the weld bead geometry necessitates a robust mathematical approach i.e. Taguchi method to quantify the relationship between them.
Optimum conditions can be established for a range of applications which are readily reproduced by the welder. However, certain important points must be considered in order to enhance the working accuracy. Researchers have many attempts to predict the process parameters of submerged arc welding to get smooth quality of weld.

(This work is licensed under a Creative Commons Attribution 4.0 International License.)

International Journal of Engineering Research & Technology (IJERT)
ISSN: 2278-0181
Vol. 6 Issue 11, November - 2017

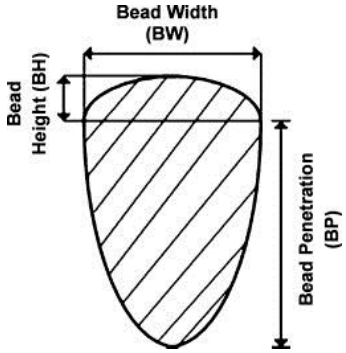


Fig. 2: Bead Geometry

ManiharSingh, AbhijitSaha [1] worked on optimization of welding parameters for maximization of weld bead widths for submerged arc welding of mild steel plates. Taguchi's philosophy has been applied for obtaining optimal parametric combinations to achieve desired weld bead geometry and dimensions related to heat affected zone. H.J. Park, D.C. Kim,M.J. Kang, S. Rhee [2] worked on optimization of the wire feed rate during pulse MIG welding of Al sheets. Welding experiments were conducted with various wire feed speeds of 0.5 m/min, 1.0 m/min, and 1.5 m/min, and the bead characteristics were evaluated along with shape factors for the weld bead, the bead width was measured. It concluded that with the increase of the welding speed (on aluminum sheet) the corresponding wire feed speed should increase as well. SauravDatta, Asish Bandyopadhyay, Pradip Kumar Pal [3] used Grey-based taguchi method for optimization of bead geometry in submerged arc bead-on-plate welding. A multi-response optimization problem has been developed in search of an optimal parametric combination to yield favorable bead geometry of submerged arc bead-on-plate weld.K. Abbasi, S. Alam, Dr. M.I. Khan [4] studied the effect of MIG welding parameters on the Weld-Bead shape characteristics. The depth of penetration and weld width were measured for each specimen after the welding operation. Effect of welding speed and heat input rate on depth of penetration and weld width were also investigated.

The most important performance parameters in Synergic MIG welding are metal deposition rate (MDR), bead height (BH), bead width (BW) and weld zones hardness (HRB). The other dependent parameters include penetration shape factor (PSF), Heat affected zone and reinforcement form factor (RFF).
In Synergic MIG operations, material deposition rate determines the economies of machining and rate of production whereas bead geometry denotes quality of the weld. In setting the machining parameters, the goal is: the maximization of MDR, maximization of HRB, maximization of PSF, maximization of RFF, minimization of BH.

2. EXPERIMENTAL SETUP

The experiments were performed on PHOENIX 521 EXPERT PLUS force arc welding machine, which is manufactured by EWM high-tech welding technologies. Welding machine is capable of choosing the current curve when the welder has set the wire speed, the metal alloy, the wire diameter and the shielding gas. That is the welding equipment controls the base current, the form and number of the current pulsations. The synergic capability enables all of the welding parameters to be controlled from a signal dial control which optimizes the current peak pulse and background values, the voltage, wire feed speed. It has also become possible to reprogram the power source instantly when wire size, shield gas, filler metal composition, etc. are changed simply by dialing in a program number. These programs have been established by the equipment manufacturer with the optimum parameters for the application.

3. PLAN OF INVESTIGATION

The main aim of the project is investigation and statistical analysis of process variables on the bead geometry of Synergic MIG Welding and to find out the optimum combination of process parameters. To achieve the above mentioned objectives, following are the sequence of steps which are carried out:

1. Identification of important process parameters.
2. Deciding the working range of the process parameters, viz. wire feed rate (f), welding voltage (V), and Traverse Speed (V_T).
3. Developing the L_9 design matrix.
4. Conducting the experiments as per the design matrix.
5. Recording the responses viz. bead height (BH), bead width (BW) and bead penetration (P) and calculating penetration shape factor and reinforcement form factor.
6. Identification of the optimum values of the process parameters.
7. Plotting the graphs and drawing conclusions.
8. Discussion of the results.

3.1 Identification of important process parameters

Based on the effect on weld bead geometry, ease of control and capability of being maintained at the desired level, three independently controllable process parameters were identified namely, the welding Voltage (V), the traverse speed (V_t), and wire feed rate (F) at constant nozzle to plate distance.

3.2 Selection of working range of design parameters

Trial runs were conducted by varying the process parameters at a time. The working range was fixed by literature review, some experience and some preliminary investigations. The upper and lower levels were decided based on trial runs conducted at extreme limits and an intermediate level was selected where better results were obtained.

Table 1: Selection of levels of Process Parameters

Levels	L1	L2	L3
VOLTAGE	21.1	23.2	24.3
FEED RATE	2.2	3.4	4.2
TRAVERSE SPEED	5.93	7.75	9.15

3.3 Developing the design of experiment

Generally, the machine tool builder provides machine parameter table to be used for setting input parameters. This process relies heavily on the experience of the operators. In practice, it makes very difficult to utilize the optimal functions of a machine owing to there being too many adjustable process parameters. With an objective to alleviate this difficulty, a simple but reliable method based on statistically designed

(This work is licensed under a Creative Commons Attribution 4.0 International License.)

International Journal of Engineering Research & Technology (IJERT)
ISSN: 2278-0181
Vol. 6 Issue 11, November - 2017

experiments is suggested for investigating the effects of various process parameters on MDR, HRB, bead Geometry and determines optimal process settings. The Taguchi method, a powerful experimental design tool, uses simple, effective, systematic approach for deriving of the optimal process parameters. Further this approach requires minimum experimental cost and efficiently reduces the effect of source of variation. However, this optimization should be performed in such a way that all the objectives are fulfilled simultaneously. Such an optimization technique is called multi-response optimization.

Table 2: Input Values for Taguchi Design of Experiments

Exp. No.	Voltage (Volts)	Feed Rate (mm/s)	Traverse Speed (mm/s)
1	21.1	2.2	5.93
2	21.1	3.4	7.75
3	21.1	4.2	9.15
4	23.2	2.2	7.75
5	23.2	3.4	7.75
6	23.2	4.2	5.93
7	24.3	2.2	9.15
8	24.3	3.4	5.93
9	24.3	4.2	7.75

The method utilizes a well-balanced experimental design which allows a limited number of experimental runs called as Orthogonal array design and signal-to-noise ratio (S/N ratio/ SNR), which serves the objective function to be optimized (maximized) within experimental domain. The control factors are used to select the best conditions for stability in design of manufacturing process, whereas noise factors denote all factors that cause vibrations. In this study we applied a Taguchi L_9 orthogonal array to plan the experiments on MIG welding process. Three controlling factors viz. traverse speed (V_T), welding voltage (V) and wire feed rate (F) with three levels for each factor were selected.

However, traditional Taguchi method cannot solve multi-objective optimization problem. To overcome this, the Taguchi method was coupled with Grey relational analysis. This approach can solve multi-response optimization problem simultaneously.

3.4 Conducting the Experiment

Various welding parameters throughout the experiment are as follows:

Table 3: Parameters of the setting

Control Factors	Fixed Parameters	
Welding Voltage(V)	NTD (mm)	17.5 mm
	Stick Out (mm)	16 mm
	Wire Diameter (mm)	1.2 mm
Wire feed rate(F)	Shielding gas	CO_2
	Angle of welding gun	60-70 degree
Traverse Speed(V_T)	Shape of w/pc	Rectangular
	Thickness of w/pc	5 mm

The Grey relational analysis is then applied to examine how the welding process factors influence the bead width (BW), reinforcement height (BH), penetration (P) and HAZ, as well as weld hardness (HRB). The Grey theory can provide solution to a system in which the model is unsure or the information is incomplete. Besides, it provides an efficient solution to the uncertainty, multi-input and discrete data problem. According to the Taguchi quality design concept, a L9 mixed-orthogonal-array table was chosen for the experiments. With Grey relational analysis, it is found that the wire feed rate has a significant influence on the machining speed. Moreover, the optimal machining parameters setting for maximum MDR and minimum PSF, RFF can be obtained. The process called as Grey relational generating is next followed to find the grey relational grade for each performance characteristic. Using grey relational grades for each characteristic, we found the rank of our output from optimum to less considerable.

4. EXPERIMENTAL PROCEDURE

Bead on plate technique was employed for depositing the weld beads on mild steel plate using semi mechanized welding station. For the experiment, three different parameters were taken; they are welding voltage, traverse speed and wire feed rate. By using Taguchi technique, 9 run orders were computed for three different levels. Correspondingly 9 plates cut each of dimensions 6 inch in length were cut. After cutting all plates, welding was carried out as per specified parameters for all plates individually. All experiments were carried out with a a contact-tip to work piece distance of 17.5 mm using the mixture of CO_2 as shielded gas. A DC power source was used to perform the bead on plate by means of synergic MIG process.

4.1 Optimization Using Grey Based Taguchi Method

- Metal Deposition Rate

Table 4: Response table for MDR's SNR

Level	Voltage (Volts)	Feed Rate (mm/s)	Traverse Speed(mm/s)
1	52.83	49.76	52.96
2	52.52	53.14	52.41
3	52.61	55.07	52.70
Delta	0.31	5.31	0.55
Rank	3	1	2

The response table and corresponding response graphs are shown for S/N ratio for MDR in table 4 and Fig. 3. The ranks obtained from the response table show that feed rates have the maximum effect on the MDR. The factors' levels viz. V(1), V_t(1), F(3) have the maximum S/N ratio.

(This work is licensed under a Creative Commons Attribution 4.0 International License.)

International Journal of Engineering Research & Technology (IJERT)
ISSN: 2278-0181
Vol. 6 Issue 11, November - 2017

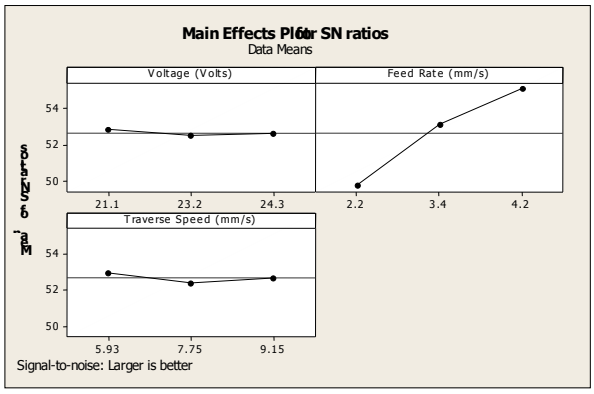


Fig. 3: SN Ratio of MDR for process parameters independently

Table 5: Grey Relational analysis for MDR

Exp.	MDR(mg/s)	x_i*(k)	Δ_0i(k)	γ(k)
1	314.7	0.0804	0.9196	0.3522
2	457.6	0.5467	0.4533	0.5245
3	584.2	0.9599	0.0401	0.9258
4	290.1	0.0000	1.000	0.3333
5	436.7	0.4785	0.5215	0.4895
6	596.5	1.0000	0.0000	1.000
7	318.8	0.0936	0.9064	0.3555
8	467.4	0.5787	0.4213	0.5427
9	522.9	0.7596	0.2404	0.6754

From the above graphs and rank obtained from response table it can be observed that the feed rate has the most significant effect on the MDR's SNR.

- Heat Affected Zone

Table 6: Response Table for HAZ's SNR

Level	Voltage (Volts)	Feed Rate (mm/s)	Traverse Speed(mm/s)
1	2.5830	4.6363	2.4580
2	0.2142	1.9475	1.1198
3	4.3013	0.5147	4.7213
Delta	4.0871	4.1216	3.6015
Rank	2	1	3

The response table and corresponding response graphs are shown for S/N ratio for HAZ in table 6 and Fig.5. The ranks obtained from the response table show that feed rates have the maximum effect on the HAZ .The factors' levels viz. V(3), V_t(3), F(1) have the maximum S/N ratio.

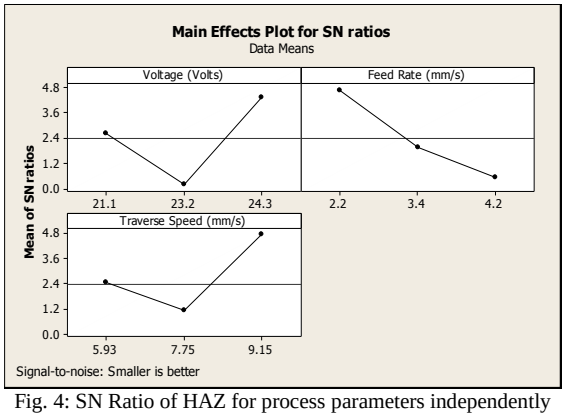


Fig. 4: SN Ratio of HAZ for process parameters independently

Table 7: Grey Relational analysis for HAZ

Exp. No.	HAZ			x_i*(k)	Δ_0i(k)	γ(k)
	B1	B2	Mean			
1	0.445	0.659	0.552	0.763	0.237	0.679
2	0.839	0.832	0.8355	0.373	0.627	0.444
3	0.769	1.008	0.8885	0.301	0.699	0.417
4	0.896	1.029	0.9625	0.199	0.801	0.384
5	0.703	1.041	0.872	0.323	0.677	0.425
6	1.129	1.084	1.1065	0.000	1.00	0.333
7	0.25	0.509	0.3795	1.00	0.000	1.00
8	0.698	0.703	0.7005	0.559	0.441	0.531
9	0.769	0.934	0.8515	0.351	0.649	0.435

- Bead Height

Table 8: Response Table for BH's SNR

Level	Voltage (Volts)	Feed Rate (mm/s)	Traverse Speed (mm/s)
1	-6.838	-4.641	-6.688
2	-6.903	-6.686	-6.566
3	-5.326	-7.740	-5.436
Delta	1.577	3.099	1.252
Rank	2	1	3

The response table and corresponding response graphs are shown for S/N ratio for BH in table 9 and Fig. 5. The ranks obtained from the response table show that feed rate has the maximum effect on the BH The factors' levels viz. V(3), V_t(3), F(1) have the maximum S/N ratio.

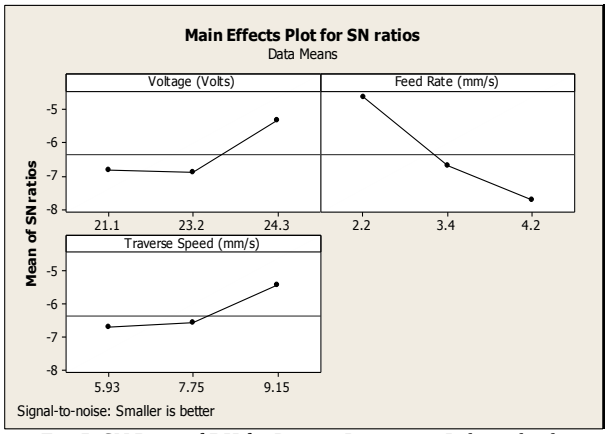


Fig. 5: SN Ratio of BH for Process Parameters Independently

Table 9: Grey Relational analysis for BH

Exp. No.	Bead Height			x_i*(k)	Δ_0i(k)	γ(k)
	B1	B2	Mean			
1	1.874	2.017	1.945	0.5525	0.4475	0.5277
2	2.178	2.223	2.201	0.3391	0.6609	0.4307
3	2.429	2.527	2.478	0.1067	0.8933	0.3589
4	1.744	1.875	1.809	0.6664	0.3336	0.5998
5	2.157	2.446	2.301	0.2545	0.7455	0.4014
6	2.603	2.608	2.605	0.0000	1.000	0.3333
7	1.688	1.134	1.411	1.000	0.0000	1.000
8	2.221	1.754	1.987	0.5174	0.4826	0.5089
9	2.338	2.15	2.244	0.3026	0.6974	0.4176

(This work is licensed under a Creative Commons Attribution 4.0 International License.)

International Journal of Engineering Research & Technology (IJERT)
ISSN: 2278-0181
Vol. 6 Issue 11, November - 2017

- Penetration

Table 10: Response Table for Penetration's SNR

Level	Voltage (Volts)	Feed Rate (mm/s)	Traverse Speed(mm/s)
1	4.0902	0.2577	2.9817
2	3.3242	3.3257	3.7354
3	2.3065	6.1375	2.6381
Delta	1.7836	5.8798	1.0973
Rank	2	1	3

The response table and corresponding response graphs are shown for S/N ratio for Penetration in table 10 and Fig. 6. The ranks obtained from the response table shows that feed rate has the maximum effect on the Penetration. The factors' levels viz. V(3), V_t(2), F(3) have the maximum S/N ratio.

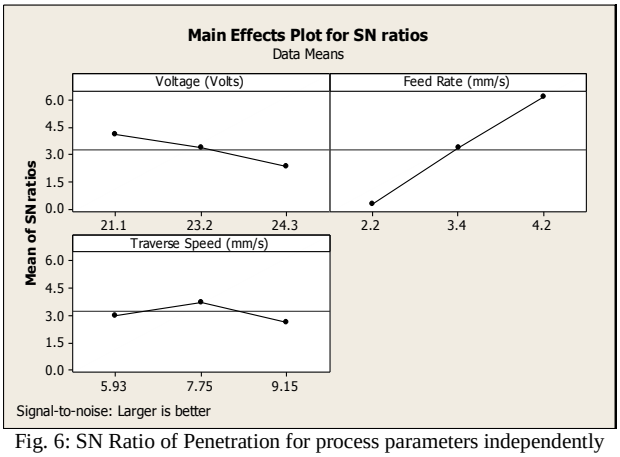


Fig. 6: SN Ratio of Penetration for process parameters independently

Table 11: Grey Relational analysis for Penetration

Exp No	Penetration			x_i*(k)	Δ_0i(k)	γ (k)
	B1	B2	Mean			
1	1.228	1.026	1.127	0.1911	0.8088	0.3820
2	1.824	1.785	1.804	0.7852	0.2148	0.6994
3	1.977	2.062	2.019	0.9737	0.0263	0.9500
4	1.183	0.951	1.067	0.1385	0.8614	0.3672
5	1.425	1.458	1.441	0.4669	0.5330	0.4840
6	1.699	2.400	2.049	1.000	0.0000	1.000
7	0.7680	1.050	0.909	0.0000	1.0000	0.3333
8	1.303	1.122	1.212	0.2661	0.7339	0.4052
9	2.182	1.843	2.012	0.9676	0.0324	0.9391

- Penetration Shape Factor

Table 12: Response Table for PSF's SNR

Level	Voltage (Volts)	Feed Rate (mm/s)	Traverse Speed(mm/s)
1	-7.963	-9.515	-9.911
2	-9.197	-9.417	-8.751
3	-10.349	-8.576	-8.894
Delta	2.385	0.939	1.161
Rank	1	3	2

The response table and corresponding response graphs are shown for S/N ratio for PSF in table 12 and Fig. 7. The ranks obtained from the response table shows that the voltage has the maximum effect on the PSF. The factors' levels viz. V(1), V_t(2), F(3) have the maximum S/N ratio.

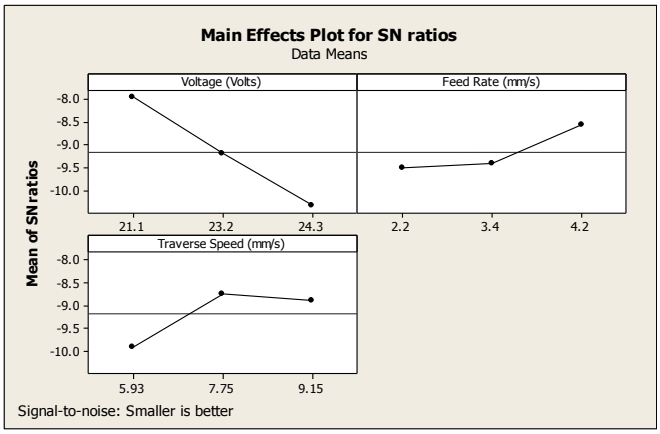


Fig. 7: SN Ratio of PSF for process parameters independently

Table 13: Grey Relational analysis for PSF

Exp. No.	W (mm)	P (mm)	PSF	x_i*(k)	Δ_0i(k)	γ (k)
1	5.167	1.127	4.585	0.4186	0.5814	0.4623
2	5.919	1.804	3.280	0.8183	0.1817	0.7334
3	5.427	2.019	2.688	1.000	0.0000	1.000
4	5.149	1.067	4.826	0.3448	0.6552	0.4328
5	6.093	1.441	4.227	0.5283	0.4717	0.5146
6	8.287	2.049	4.044	0.5844	0.4156	0.5461
7	4.994	0.909	5.494	0.1400	0.8600	0.3677
8	7.215	1.212	5.951	0.0000	1.000	0.3333
9	6.229	2.012	3.095	0.8751	0.1249	0.8001

- Reinforcement Form Factor

Table 14: Response Table for RFF's SNR

Level	Voltage (Volts)	Feed Rate (mm/s)	Traverse Speed(mm/s)
1	-7.963	-9.515	-9.911
2	-9.197	-9.417	-8.751
3	-10.349	-8.576	-8.894
Delta	2.385	0.939	1.161
Rank	1	3	2

The response table and corresponding response graphs are shown for S/N ratio for RFF in table 14 and Fig. 8. The ranks obtained from the response table shows that the voltage has the maximum effect on the RFF. The factors' levels viz. V(1), V_t(2), F(3) have the maximum S/N ratio.

(This work is licensed under a Creative Commons Attribution 4.0 International License.)

International Journal of Engineering Research & Technology (IJERT)
ISSN: 2278-0181
Vol. 6 Issue 11, November - 2017

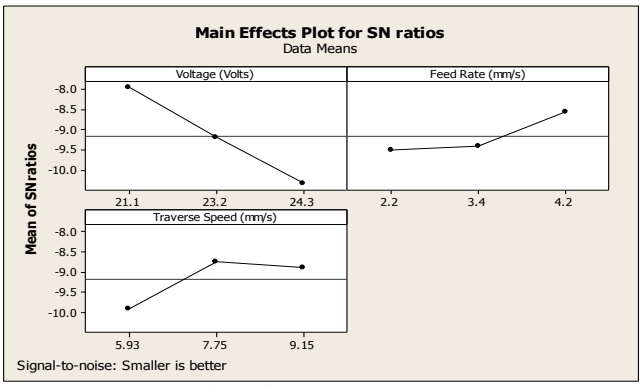


Fig.8: SN Ratio of RFF for Process Parameters independently

Table 15: Grey Relational analysis for RFF

Exp. No.	W (mm)	H (mm)	RFF	x_i*(k)	Δ_0i(k)	γ (k)
1	5.167	1.945	2.656	0.6767	0.3233	0.6073
2	5.919	2.201	2.690	0.6529	0.3470	0.5903
3	5.427	2.478	2.190	1.000	0.0000	1.000
4	5.149	1.809	2.846	0.5450	0.4550	0.5236
5	6.093	2.301	2.647	0.6826	0.3174	0.6117
6	8.287	2.605	3.180	0.3122	0.6878	0.4210
7	4.994	1.411	3.539	0.0633	0.9367	0.3480
8	7.215	1.987	3.630	0.0000	1.000	0.3333
9	6.229	2.244	2.776	0.5934	0.4066	0.5515

- Hardness of Weld Zone

Table 16: Response Table for Hardness's SNR

Level	Voltage (Volts)	Feed Rate (mm/s)	Traverse Speed(mm/s)
1	38.69	38.92	38.55
2	38.58	38.55	38.71
3	38.85	38.65	38.94
Delta	0.27	0.37	0.39
Rank	3	2	1

The response table and corresponding response graphs are shown for S/N ratio for hardness in table 16 and Fig. 9. The ranks obtained from the response table shows that the voltage has the maximum effect on the PSF. The factors' levels viz. V(1), V_t(2), F(3) have the maximum S/N ratio.

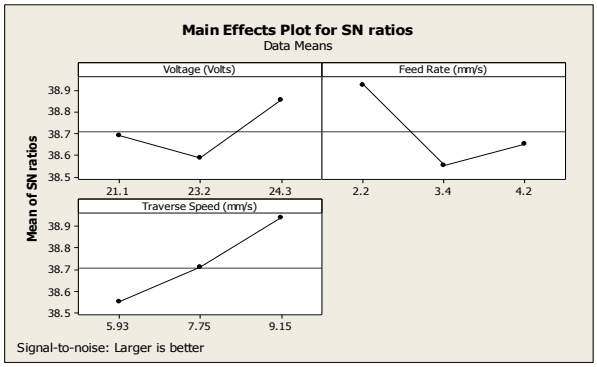


Fig. 9: SN Ratio of Hardness for process parameters independently

Exp. No.	HRB Weld Zone	x_i*(k)	Δ_0i(K)	γ (k)
1	87	0.63	0.38	0.57
2	84	0.25	0.75	0.40
3	87	0.63	0.38	0.57
4	88	0.75	0.25	0.67
5	85	0.38	0.63	0.44
6	82	0.00	1.0	0.33
7	90	1.0	0.00	1.0
8	85	0.38	0.62	0.44
9	88	0.75	0.25	0.67

Table 17: Grey Relational Analysis for HRB Number

GREY'S RELATIONAL GRADE is calculated by taking the mean of all the grey relational coefficients. Correspondingly, rank or order of the all experiments is calculated.

Table 18: Grey Relational Grade for all experiments

MDR γ (k)	H γ (k)	PSF γ (k)	HAZ γ (k)	P γ (k)	RFF γ (k)	HRB γ (k)	Grade	Order
0.352	0.527	0.462	0.678	0.382	0.607	0.571	0.512	6
0.524	0.430	0.733	0.443	0.699	0.590	0.400	0.546	5
0.925	0.359	1.000	0.416	0.949	1.000	0.571	0.746	1
0.333	0.599	0.432	0.384	0.367	0.523	0.667	0.473	8
0.489	0.401	0.514	0.424	0.483	0.611	0.444	0.481	7
1.000	0.333	0.546	0.333	1.000	0.420	0.333	0.567	4
0.355	1.000	0.367	1.00	0.333	0.347	1.00	0.629	3
0.542	0.508	0.333	0.531	0.405	0.333	0.444	0.443	9
0.675	0.417	0.800	0.435	0.938	0.551	0.667	0.641	2

5. RESULTS AND DISCUSSIONS

5.1 Prediction using Taguchi method

The Values of the output parameters is then predicted using MINITAB 16.0 to obtain values for the remaining 18 experiments. The accuracy obtained from this method is verified from the already available values to be as close to 95% and as precise as 99%. The obtained values (shown in table 19) are used to plot surface charts for the output parameters against other two control factors.

The following observations have been made about Metal Deposition Rate, Bead Height, Penetration, Penetration Shape Factor, Reinforcement Form Factor and Weld Zone Hardness.

(This work is licensed under a Creative Commons Attribution 4.0 International License.)

International Journal of Engineering Research & Technology (IJERT)
ISSN: 2278-0181
Vol. 6 Issue 11, November - 2017

1) Metal Deposition Rate (MDR)

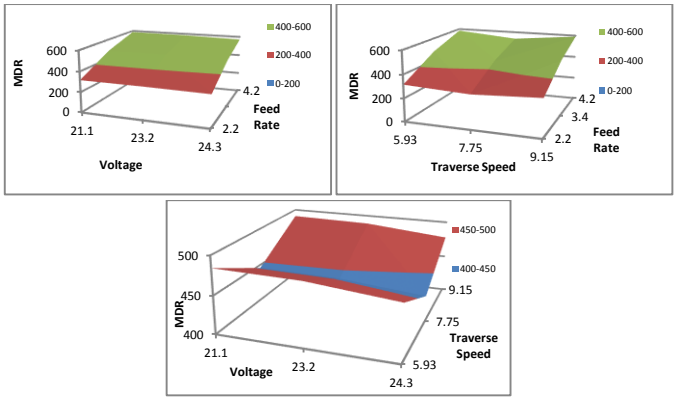


Fig. 10: Variation in MDR

MDR increases with increase in feed rate. It remains constant with Voltage and with Increase in Traverse Speed it decreases earlier but then shows an increasing trend.

Table 19: Prediction table for output parameters using Taguchi method

Voltage	Feed Rate	Traverse Speed	Predicted MDR	Predicted Bead Height	Predicted Penetration Shape Factor	Predicted Penetration	Predicted Reinforcement Form Factor	Predicted HRB
21.1	2.2	5.93	318.2	1.908	4.664	1.145	2.797	86.48
21.1	2.2	7.75	292.6	1.851	3.528	1.266	2.412	88.80
21.1	2.2	9.15	322.0	1.707	4.085	1.070	2.562	89.02
21.1	3.4	5.93	484.5	2.350	4.304	1.541	2.822	82.97
21.1	3.4	7.75	445.7	2.280	3.256	1.704	2.433	85.19
21.1	3.4	9.15	490.3	2.102	3.770	1.441	2.584	85.40
21.1	4.2	5.93	586.4	2.726	3.039	2.252	2.510	83.84
21.1	4.2	7.75	539.4	2.645	2.299	2.490	2.165	86.08
21.1	4.2	9.15	593.5	2.438	2.662	2.106	2.299	86.30
23.2	2.2	5.93	316.9	1.871	6.212	0.9910	3.290	85.53
23.2	2.2	7.75	291.5	1.815	4.699	1.096	2.836	87.81
23.2	2.2	9.15	320.7	1.673	5.441	0.9267	3.013	88.03
23.2	3.4	5.93	482.6	2.305	5.733	1.334	3.319	82.05
23.2	3.4	7.75	443.9	2.236	4.337	1.475	2.861	84.24
23.2	3.4	9.15	488.4	2.061	5.021	1.248	3.039	84.46
23.2	4.2	5.93	584.1	2.674	4.048	1.950	2.952	82.91
23.2	4.2	7.75	537.2	2.594	3.062	2.156	2.546	85.13
23.2	4.2	9.15	591.1	2.391	3.545	1.824	2.704	85.34
24.3	2.2	5.93	310.1	1.603	6.333	0.932	3.681	88.15
24.3	2.2	7.75	285.2	1.555	4.790	1.031	3.174	90.50
24.3	2.2	9.15	313.8	1.434	5.547	0.871	3.371	90.73
24.3	3.4	5.93	472.2	1.975	5.844	1.255	3.714	84.57
24.3	3.4	7.75	434.3	1.916	4.421	1.388	3.202	86.83
24.3	3.4	9.15	477.9	1.766	5.119	1.173	3.401	87.05
24.3	4.2	5.93	571.6	2.291	4.127	1.834	3.304	85.45
24.3	4.2	7.75	525.7	2.222	3.122	2.028	2.849	87.74
24.3	4.2	9.15	578.4	2.049	3.615	1.715	3.026	87.96

With increase in feed rate more metal is deposited and as a result metal deposition rate increases. It is expected that with increase in traverse speed MDR should increase but this negative effect of speed is due to the fact that when speed increases, the thermal energy transmitted to the base plate from the arc or line power per unit length of the weld bead decreases and less filler metal is deposited per unit length of weld bead, resulting in thinner and narrower weld bead.

2) Bead Height (BH)

This is consistent with the fact that on increasing the voltage the weld beads become more flatter, which in turn decreases the bead height. The reason for decrease in reinforcement height has been discussed in previous paragraph. As with increase in feed rate more amount of metal is deposited therefore bead height increases.

(This work is licensed under a Creative Commons Attribution 4.0 International License.)

International Journal of Engineering Research & Technology (IJERT)
ISSN: 2278-0181
Vol. 6 Issue 11, November - 2017

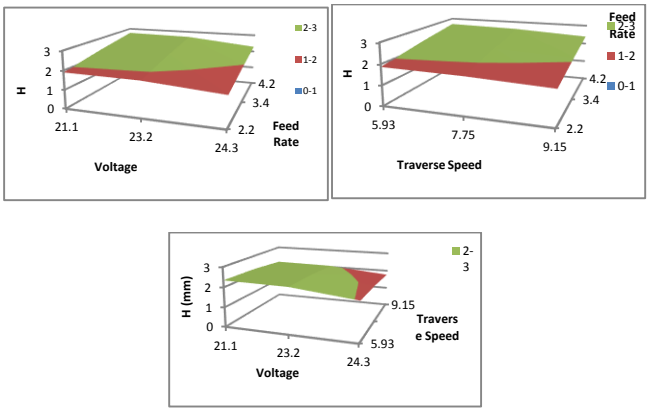


Fig. 11: Variation in Bead Height

Bead Height decreases with increase in Voltage and Traverse speed while it increases with increase in Feed Rate.

3) Penetration Shape Factor(PSF) and Reinforcement Form Factor(RFF)

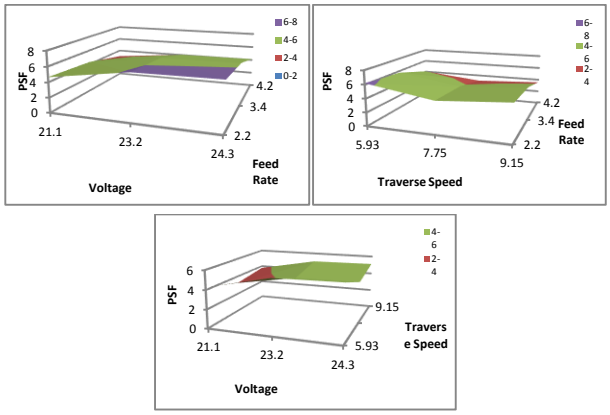


Fig. 12: Variation in PSF

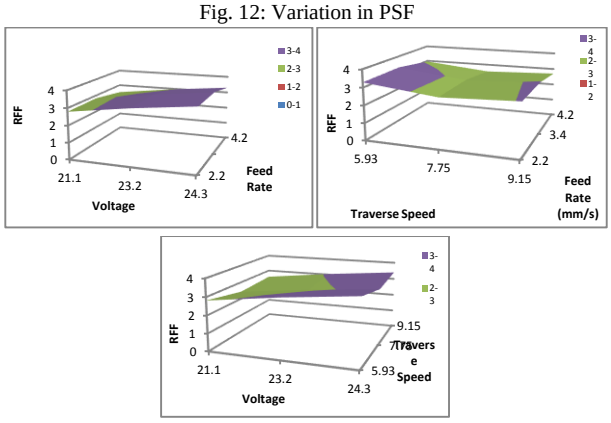


Fig. 13: Variation in RFF

As with increase in voltage the bead becomes flatter, i.e., bead width increases but reinforcement height and penetration decrease therefore both RFF & PSF increase. With increase in traverse speed, both factors should follow a trend similar to be bead width and inverse to bead height and penetration respectively. But, Form Factor follows a trend similar to Bead height despite the fact that bead height is inversely proportional to RFF. It is due to the presence of bead width as a factor. RFF decreases initially because bead width decreases but after a certain value bead height decreases at a higher rate therefore form factor starts increasing. With increase in feed rate all the parameters including bead width, bead height and penetration increase but bead width increase at a higher rate, therefore both RFF & PSF increase initially but when feed rate reach a higher value, but start decreasing.

4) HRB

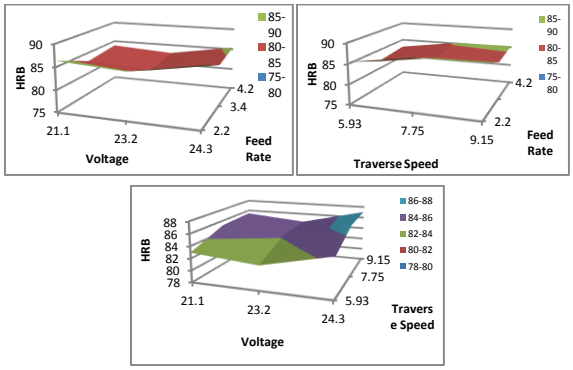


Fig. 14: Variation in HRB

Hardness of the weld zone firstly decreases slightly with increase in voltage and then increases continuously. It increases with traverse speed and then remains constant.

5) Bead Height (H)

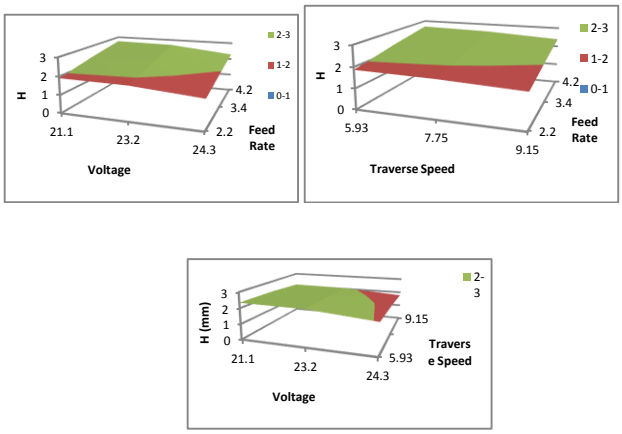


Fig. 11: Variation in Bead Height

Bead Height decreases with increase in Voltage and Traverse speed while it increases with increase in Feed Rate.

This is consistent with the fact that on increasing the voltage the weld beads become more flatter, which in turn decreases the bead height. The reason for decrease in reinforcement height has been discussed in previous paragraph. As with increase in feed rate more amount of metal is deposited therefore bead height increases.

5.2 Conclusions

It has been observed that the wire feed rate has the maximum effect on output parameters in most cases as it has been ranked 1 for most of the output parameters. Also based on the

(This work is licensed under a Creative Commons Attribution 4.0 International License.)

International Journal of Engineering Research & Technology (IJERT)
ISSN: 2278-0181
Vol. 6 Issue 11, November - 2017

Grey Relational Methodology, experiment number 3 is considered to be the most optimum combination of process parameters. The observation set is as follows: Experiment Number 3 has the highest value of current and the largest wire feed rate, therefore, it results in higher penetration and reinforcement height and also fine welds are formed more commonly. As with increase in Voltage, Penetration Shape factor and Reinforcement form factor also increases therefore, lower value of Voltage is preferred to have more penetration and reinforcement height making the weld stronger.

Table 20: Order for grey based Taguchi method

Order	Exp. No.	Current (Amp)	Voltage (Volts)	Feed Rate (mm/s)	Traverse Speed (mm/s)
1	3	159	21.1	4.2	9.15
2	9	159	24.3	4.2	7.75
3	7	89	24.3	2.2	9.15
4	6	159	23.2	4.2	5.93
5	2	137	21.1	3.4	7.75
6	1	89	21.1	2.2	5.93
7	5	137	23.2	3.4	7.75
8	4	89	23.2	2.2	7.75
9	8	137	24.3	3.4	5.93

5. REFERENCES

[1] Manihar Singh, AbhijitSaha; optimization of welding parameters for maximization of weld bead widths for submerged arc welding of mild steel, *International Journal of Engineering Research & Technology (IJERT)* , ISSN: 2278-0181 Vol. 1 Issue 4, June - 2012.

[2] H.J. Park, D.C. Kim, M.J. Kang, S. Rhee; Optimization of the wire feed rate during pulse MIG welding of Al sheets.

[3] SauravDatta, AsishBandyopadhyay, Pradip Kumar Pal; Grey-based taguchi method for optimization of bead geometry in SAW, *International Journal of Advanced Manufacturing Research*, Volume 39, no. 11-12, pp. 1136-1143.

[4] K. Abbasi, S. Alam, Dr. M.I. Khan; An Experimental Study on the effect of MIG welding parameters on the Weld-Bead shape characteristics, *International Journal* for *Engineering Science and Technology(ESTIJ)*,ISSN: 2250-3498,2012, Vol.2, No. 4, pp. 599-602

[5] Minnick, William H.; *Gas Metal Arc Welding Handbook Textbook*, Tinley Park: Goodheart–Willcox, ISBN 978-1-59070-866-8.

[6] Parmar, R.S., Welding process and technology, Khanna Publishers, Delhi.

[7] Blunt, Jane, Balchin, Nigel C.; *Health and Safety in Welding and Allied Processes*, 2002, UK: Woodhead, ISBN 1-85573-538-5.

[8] Wadsworth, Harrison M; *Handbook of statistical methods for engineers and scientist*, 2nd edition, McGraw-Hill Professional, New York, 1997.

[9] Liu S. & Lin Y.; Grey information: Theory and practical applications, 1st edition, 2006.

[10] P. Kumari, K. Archna and R.S. Parmar; Effect of Welding Parameters on Weld Bead Geometry in MIG Welding of Low Carbon Steel, *International Journal of Applied Engineering Research*, ISSN 0973-4562 Volume 6, No. 2 (2011), pp. 249–258.

[11] S. Alam Khan, M.I.Khan; Prediction of Weld Bead Reinforcement Height for Steel using SAW Process Parameters, *International Journal Of Applied Engineering Research*, ISSN 0973-4562, Volume 6, No 15,2011, pp. 1857-1871.

[12] Kumanan S, Edwin J, Dhas Raj & Gothman K.; Determination of submerged arc welding process parameters using Taguchi method and regression analysis, *Indian Journal of Engineering & Materials Sciences*,2007, Vol. pp.177-183.

[13] Jiju Antony, Frenie Antony; Teaching the taguchi method to the industrial engineers, 2001, Work study, Volume 50, No. 4, pp. 141-149.

[14] Roy R. K. Design of experiments using Taguchi approach, John Wiley & sons Inc., New York

(This work is licensed under a Creative Commons Attribution 4.0 International License.)

IJERT

ISSN : 2278 - 0181

Call for Papers 2018

OPEN ACCESS

Click Here for more details

International Journal of Engineering Research & Technology

☑ Fast, Easy, Transparent Publication

☑ More than 50000 Satisfied Authors

☑ Free Hard Copies of Certificates & Paper

Publication of Paper : Immediately after Online Peer Review

Why publish in IJERT ?

✓ Broad Scope : high standards

✓ Fully Open Access: high visibility, high impact

✓ High quality: rigorous online peer review

✓ International readership

✓ Retain copyright of your article

✓ No Space constraints (any no. of pages)

Submit your Article

www.ijert.org

Materials Research Express

PAPER

Parameter optimization and characterization of environmental friendly aluminium hybrid metal matrix composites

To cite this article: Girija Moona *et al* 2019 *Mater. Res. Express* **6** 1165d5

View the article online for updates and enhancements.



IOP ebooks™

Bringing you innovative digital publishing with leading voices to create your essential collection of books in STEM research.

Start exploring the collection - download the first chapter of every title for free.

This content was downloaded from IP address 14.139.251.100 on 06/11/2019 at 04:57

Materials Research Express

PAPER

Parameter optimization and characterization of environmental friendly aluminium hybrid metal matrix composites

RECEIVED
28 June 2019

REVISED
4 October 2019

ACCEPTED FOR PUBLICATION
21 October 2019

PUBLISHED
1 November 2019

Girija Moona[1,3], **R S Walia**[1,2], **Vikas Rastogi**[1] and **Rina Sharma**[3]

[1] Delhi Technological University, New Delhi-110042, India
[2] Punjab Engineering College, Chandigarh, India
[3] CSIR- National Physical Laboratory, Dr K. S. Krishnan Marg, New Delhi-110012, India

E-mail: moonag@nplindia.org

Keywords: Hybrid composites, Reinforcement, Electromagnetic stirring, Metal matrix composites, Optimization

Abstract

The present experimental investigation was carried out to fabricate environmental friendly hybrid aluminium metal matrix composites with three reinforcements in minimal amount through electromagnetic stir casting: an uncommon fabrication technique. Al 7075-T6 alloy was infused with three reinforcements; eggshell particles (wt% 0.5, 1 and 1.5, particle size ~60 μm), SiC particles (wt% 1, 1.5 and 2, particle size ~65 μm) and Al_2O_3 particles (wt% 1.5, 2 and 2.5, particle size ~90 μm) with variable mechanical stirring time (2, 4 and 6 min). Composite fabrication experiments were run in accordance with Taguchi's orthogonal array L9 and analysis of variance (ANOVA) was conducted to optimize process parameters and to observe their influence on quality characteristics. Developed composites were characterized for various physical and mechanical properties such as density, porosity, residual stress, micro hardness and tensile strength. Investigation outcomes show that synthesized hybrid composite specimen S8 with a total reinforcement content of 4.5% only, demonstrated no significant change in density (only upto 2.2%) whereas the maximum reduction in percentage porosity was 75%. Additionally, maximum abatement in residual stress of hybrid composite specimen S8 was 76% as compared to their unreinforced counterpart specimen S0, there was a maximum enhancement of 83% in microhardness and 107% in tensile strength of fabricated hybrid aluminium metal matrix composite specimen S8 in comparison of as-cast Al 7075-T6 specimen S0. Disposal of eggshells is a serious threat to environment, thus more focus was put on recycling them and using them for development of environmental friendly and cost effective hybrid composites with enhanced properties for numerous engineering applications.

1. Introduction

In present scenario, metal matrix composites are replacing their conventional counter parts in a flashing way in most of the advanced engineering applications due to their augmented mechanical properties [1]. Aluminium alloys as base metals can be infused using fibers, whiskers and particulate reinforcements [2]. A wide range of particulate reinforcements such as TiB_2, B_4C, SiC, Al_2O_3, TiC, TiO_2, WC, graphite, fly ash, red mud, rice husk ash, bamboo leaf ash and bagasse ash etc have been used to develop aluminium metal matrix composites with enhanced properties [3]. Al 7075 mixed with B_4C particles through stir casting route showed increased hardness and wear resistance, whereas Al 7075 infused with TiB_2 particles displayed increased micro hardness, tensile strength and yield strength [4]. In another study Al 7075 alloy with SiC particles was analyzed for wear behavior and surface finish and it was observed that for higher content of reinforcement the tool wear was increased and surface finish became inferior [5]. Established AMMCs with single reinforcement exhibit enhanced characteristics but often compromise with other crucial properties, hence hybrid composites have been developed keeping in view the reasonable enhancement in properties by exploiting different virtues of various reinforcements without any noticeable deterioration in composite attributes [6]. Addition of SiC particles into

© 2019 IOP Publishing Ltd

aluminium alloys increases mechanical strength and wear resistance but at the cost of ease of machining. Whereas Al-SiC-Gr hybrid composites possess improved wear resistance and machinability both [7]. Hybrid composites of aluminium alloy with SiC and B_4C particles fabricated through ultrasonic cavitation based solidification process exhibited enhanced hardness and higher tensile strength. Aluminium composite with SiC and bamboo leaf ash, developed by two step stir casting method showed decreased density and improved corrosion resistance [8]. Al 2219/B_4C/MoS_2 hybrid composites showed decreased densities, increased microhardness and better wear resistance. With enhanced thermal stability, Al/Zn/Al_2O_3 stir casted hybrid composites have wide utilizations in precision applications and thermal packaging [9].

Among various fabrication techniques for development of particulate reinforced aluminium metal matrix composites, stir casting is considered to be the most advantageous due to its cost effectiveness, ability to handle large volume, simplicity and capacity to control metal matrix structure. In stir casting process composites are produced by continuous stirring of base metal melt followed by infusion of reinforcements [10, 11]. The desired particulate reinforcements with reasonable wettability are incorporated into molten aluminium matrix and the mixture is solidified. Composites developed by stir casting technique demonstrate modifiable properties depending upon distinct process parameters such as reinforcement content, reinforcement preheat temperature, stirring temperature, stirring time, stirring speed and stirrer position etc [12]. Fundamental complications experienced during stir casting are improper wetting due to poor interfacial bonding between reinforcement & metal matrix and non-uniform distribution of reinforcement particles due to agglomeration [13]. To improve interfacial bonding of filler and metal matrix, various surface treatments were performed including ultrasonic cavitation effect and inclusion of nanostructures into composites while for enhanced wettability, either alloying elements were added to molten metal matrix or coating of reinforcements was carried out [14, 15]. Even with such critical corrective actions, sometimes in stir casting process the reinforcement particles get repelled away from the mechanical stirrer due to the centrifugal force of rotating melt resulting into non uniform dispersion [16]. To overcome this complication, in current study, modifications were implemented to existing mechanical stir casting setup in form of electromagnetic stirrer. In electromagnetic stirrer, a three phase motor with the help of alternating current generated rotational motion and applied rotational force on reinforcement particles infused in molten metal resulting into uniform dispersion of particulate reinforcements in metal matrix. In order to enhance mechanical attributes of developed hybrid composites and avert agglomeration, hard particles of comparable sizes (eggshell particles with particle size ~60 μm, SiC particles with average particle size ~65 μm and Al_2O_3 particles with average particle size ~90 μm) were used as reinforcements. Hybrid aluminum metal matrix composites prepared using electromagnetic stirring were evaluated for porosity, as porosity is a defect caused by interfacial reactions of preform and metal matrix inducing decline in mechanical characteristics of composites. Hence investigations for density and percentage porosity of fabricated hybrid aluminium composites were important measures [17]. Also the analysis of residual stress of hybrid composites was extremely momentous as they cause dimensional distortions and diminished mechanical characteristics [18]. Sequentially, fabricated hybrid aluminium composites were evaluated for microhardness, tensile strength and fractographic studies. Developed hybrid composites with light weight and enhanced strength may replace conventional alloys in aerospace and automobile industry for manufacturing of specific parts such as wing slat tracks, bulkheads, landing gears, wheels, piston cylinder liners, transmission housings, connecting rods, suspension components and brakes etc and also for fabrication of numerous structural components likewise platforms, bridges, power plant structures, offshore structures and roof structures.

In present industrial scenario, a humongous research gap can be observed for development of eco-friendly materials with distinctive mechanical attributes to cater specialized needs. In reference to hybrid aluminium metal matrix composites, literature on few conventional fabrication methods, with limited reinforcement combinations (utmost two reinforcements) and higher filler contents is available. Also detailed influence of various reinforcements on a wider range of mechanical traits of developed composites such as percentage porosity and residual stress has not been reported so far. In this backdrop, there is an enormous scope for current research work for development of ecodesigned hybrid aluminium metal matrix composites with upgraded mechanical properties using three reinforcements through electromagnetic stir casting route.

2. Experimental procedure

2.1. Setup design

The present experiment for fabrication of aluminium hybrid metal matrix composites was conducted using a combined setup of conventional stir casting system and electromagnetic stirrer. The conventional stir casting setup included a furnace, stirrer impeller (rotating at 150 rpm), temperature sensors and control panel etc. An electromagnetic stirrer originally was an electric motor using a rotating magnetic field causing whirling motion

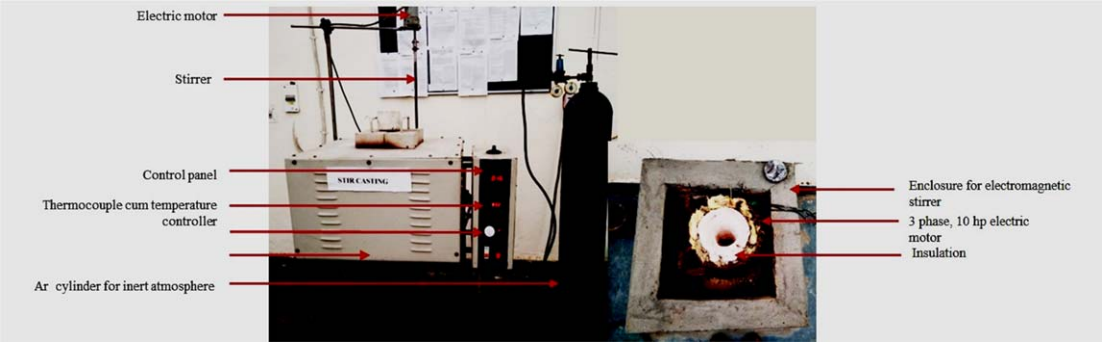


Figure 1. Electromagnetic Stir casting setup.

Table 1. Composition of Al 7075-T6 [19].

Component	Al	Cr	Cu	Fe	Mg	Mn	Si	Ti	Zn	Others
Wt%	87–91	0.18–0.28	1.2–2	>0.5	2.1–2.9	>0.3	>0.4	>0.2	6	Balance

Table 2. Reinforcement details.

Reinforcement	Average particle size (μm)
Egg shell powder	60
Cleaned Hen Eggshells → Sundried → Ball milled at 200 rpm with ball to powder ratio 5:1 → Sieved for require particle size → Carburized at 500^0C for 2 hours	
SiC powder	65
Al_2O_3 powder	90

in molten metal. When a three phase AC voltage was applied to the motor, its magnetic coil generated a moving magnetic field and electromagnetic force was developed in the metal melt causing its stirring. In current investigation a three phase 10 hp motor rotating at 960 rpm used as electromagnetic stirrer was combined with mechanical stir casting setup (figure 1).

2.2. Details of selected base metal matrix and reinforcements

2.2.1. Base metal matrix

Previous series of aluminium alloys have already been explored extensively for numerous experimental investigations. The metal matrix used for current study was Al 7075-T6 alloy due to superior physical properties. Synthesized Al 7075-T6 hybrid composites with their ameliorated traits may have extensive spectrum of state-of-the-art applications including high strength structural applications, thermally modifiable & light weight aerospace applications, automotive applications due to better tribological & fatigue properties, electronics applications due to higher specific strength for power electronics & packaging materials and numerous defence applications due to low density, high thermal conductivity, high heat capacity & dimensional stability at higher temperatures. Chemical compositions of Al 7075-T6 alloy is given in table 1 [19].

2.2.2. Reinforcements

Each reinforcement used for current investigation had specific characteristics, thus when mixed with molten metal, they contributed towards enhancement of distinct properties of synthesized composites as compared to the unreinforced metal. Disposal of certain natural waste matter such as eggshells is extremely harmful for our environment, hence after recycling; these can be used as natural reinforcements to develop composites. In

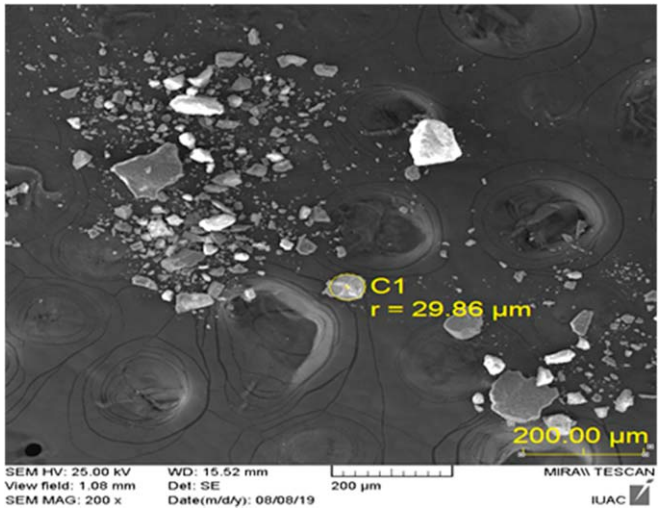


Figure 2. SEM micrograph of eggshell particles.

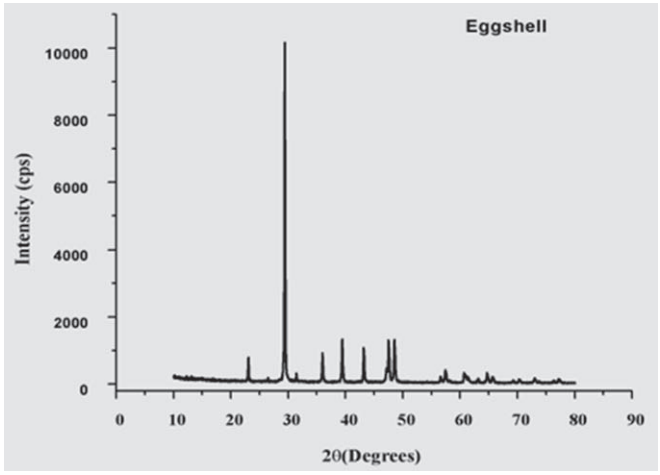


Figure 3. XRD pattern of eggshell particles.

present experiment, hybrid aluminium metal matrix composites were prepared by infusing three fillers in order to tailor the properties of fabricated composites as per desired applications. Details of reinforcements used in the experiment are given in table 2.

Microstructural and elemental analysis of reinforcement particles using field emission scanning electron microscope (Make: OXFORD Instruments, Model: 7718) and x ray diffractometer (Make: Rigaku Japan, Model-Miniflex-II) are illustrated in figures 2 to 7. Reinforcement particle sizes were determined by SEM micrographs obtained at 200X magnification. Avergae size of eggshell particles was observed to be ≈60 μm, of SiC particles ≈65 μm and of Al_2O_3 particles ≈90 μm as show in figures 2, 4 and 6. XRD intensity data for all the reinforcements were taken for 2θ range of 10°–100°. For eggshell particles the diffraction peaks are located at 23.58°, 30°, 37.76°, 40°, 44.89° and 50° as shown in figure 3, whereas for silicon carbide particles the intensity peaks occur at 38.52°, 41.96°, 60° and 73.84° as shown in figure 5. In figure 7, the spectrogram of aluminium oxide particles displays distinctive peaks at 25.9°, 35.41°, 37°, 44.25°, 52.72°, 57°, 68.78° and 77°.

2.3. Composite preparation

Here, 9 hybrid aluminium composites were fabricated using Al 7075-T6 as metal matrix infused with variable weight percentage of three reinforcements (eggshell particles weight percentage 0.5%, 1%, 1.5%, average particle size ~60 μm, SiC particles weight percentage 1%, 1.5% and 2%, average particle size ~65 μm and Al_2O_3 particles weight percentage 1.5%, 2% and 2.5%, average particle size ~90 μm) with varied mechanical stirring time

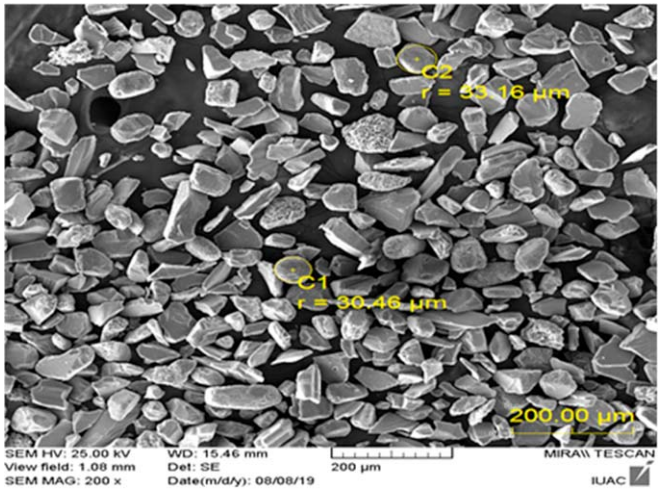


Figure 4. SEM micrograph of SiC particles.

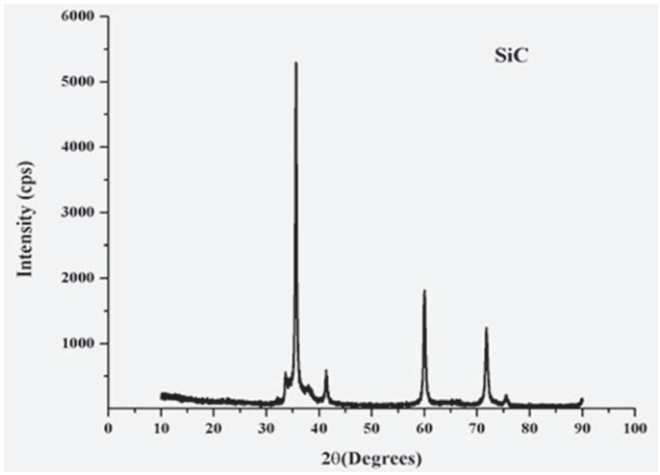


Figure 5. XRD pattern of SiC particles.

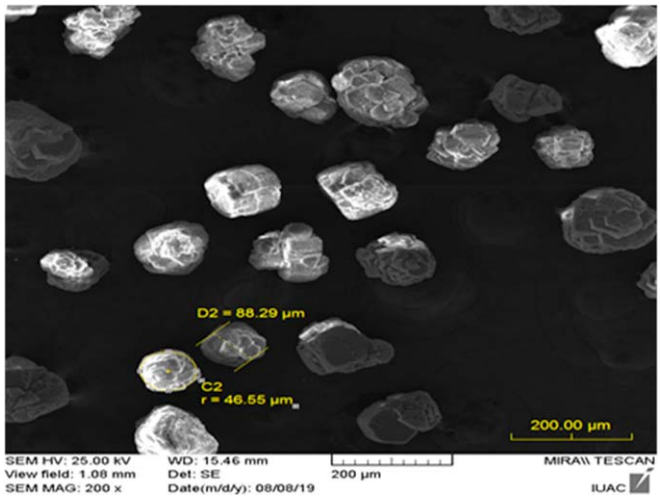


Figure 6. SEM micrograph of Al_2O_3 particles.

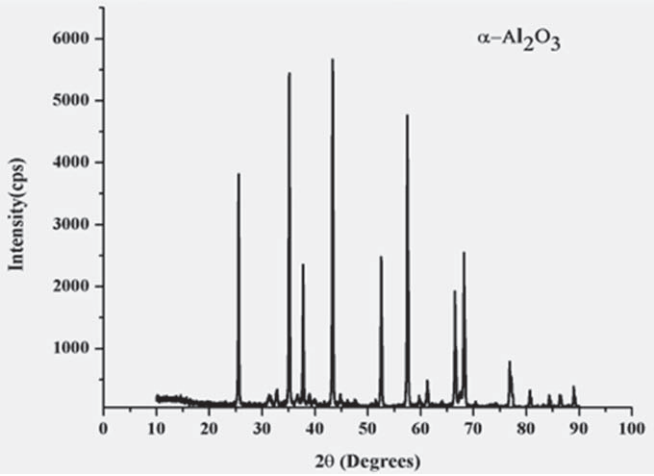


Figure 7. XRD pattern of Al_2O_3 particles.

Table 3. Design of experiment layout.

Hybrid composite specimen number	Eggshell wt%	SiC wt%	Al_2O_3 wt%	Mechanical stirring time (minutes)
S1	0.5	1	1.5	2
S2	0.5	1.5	2	4
S3	0.5	2	2.5	6
S4	1	1	2	6
S5	1	1.5	2.5	2
S6	1	2	1.5	4
S7	1.5	1	2.5	4
S8	1.5	1.5	1.5	6
S9	1.5	2	2	2
S0			As-cast Al 7075-T6	
Mechanical stirring speed			150 rpm	
Stirring temperature			850 °C	
Reinforcement preheat temperature			500 °C	
Electromagnetic stirring speed			960 rpm	
Electromagnetic stirring time (minutes)			0.5	

(2 min, 4 min and 6 min) in accordance with the design matrix using Taguchi L9 orthogonal array as shown in table 3. An L9 orthogonal array was appropriate for this experiment as it was conducted to figure out the effect of four independent factors (eggshell particles wt%, SiC particles wt%, Al_2O_3 particles wt% and mechanical stirring time) with three different factor level values assuming that there is no cross product effect between any two factors [20].

To fabricate composites, aluminium ingots were cleaned and melted in crucible in an electric furnace at 900 °C. Meanwhile required amount of reinforcements were wrapped in aluminium foil and preheated in a muffle furnace up to 500 °C for 1 h in order to remove absorbed gases from reinforcements surface, avoid temperature drop on infusion of reinforcement particles into molten metal and obtain improved wettability. The temperature of metal melt was slightly reduced and reinforcements were added in 3 steps. A preheated stirrer was used to stir the mixture in inert atmosphere at 150 rpm for variable time intervals as per the design of experiment. After mechanical stirring, the crucible was placed on electromagnetic stirrer rotating at 960 rpm for 30 s for electromagnetic stirring in inert atmosphere. The composite castings (figure 8) were allowed to solidify and various test specimens were prepared as per standard sizes for mechanical testing.

In order to evaluate mechanical and physical characteristics of composites, ten specimens (one as-cast Al 7075-T6 and nine Al 7075-T6/egg shell/SiC/Al_2O_3 hybrid composites, in three replications) for each characterization were prepared. For density, porosity, residual stress and micro hardness testing, specimen palates (conventionally polished up to Ra $\sim$ 0.1 μm) of size $10 \times 10 \times 5$ mm^3 were prepared (figure 9), whereas for tensile testing the sub-size dog bone plate type specimens were prepared as per ASTM E8-M11 (figure 10).



Figure 8. Composite castings.

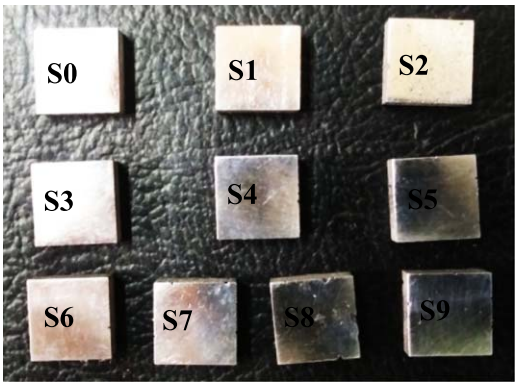


Figure 9. Specimens for density, porosity, micro hardness and residual stress testing.

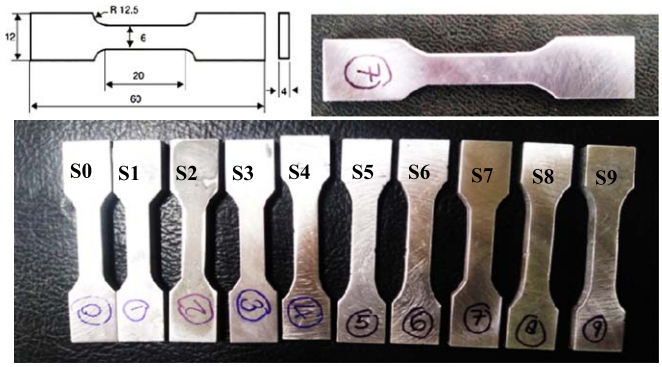


Figure 10. Specimens for tensile testing (all the dimensions are in mm).

3. Results and discussions

Taguchi method is based on predefined instructions and uses a set of arrays to designate a procedure for carrying out minimum number of experiments being able to provide complete information related to the performance parameters. In Taguchi approach, for an orthogonal experimental design the influence of control factors can be segregated in terms of S/N ratio and mean response [20, 21]. Mean objectives/response functions were analysed using data from designed experiments in order to calculate signal to noise (S/N) ratio. Analysis of variance (ANOVA) was conducted to investigate the influence of process parameters on specific quality characteristics in

Table 4. Factors and their levels.

Control factors	Factors designation	Level 1	Level 2	Level 3
Eggshell weight %	A	0.5	1	1.5
SiC weight %	B	1	1.5	2
Al_2O_3 weight %	C	1.5	2	2.5
Mechanical stirring time (minutes)	D	2	4	6

terms of F-ratio and percentage contribution. All the four control factors with three levels (because they may affect the performance attributes nonlinearly) are shown table 4.

3.1. Prediction of optimum Porosity in fabricated hybrid composites

Density measurement was done using gravimetric method/hydrostatic weighing method as per standard OIML-r111 on a Mettler Toledo weighing balance. At recorded temperature, each specimen was first weighed in air and then weighed in distilled water. Density of distilled water is calculated by an empirical formula given in equation (1).

$$\rho_l = 0.99997495\left[1 - \frac{(t - 3.983035)^2(t + 301.797)}{522528.9X(t + 69.348.81)}\right] \quad (1)$$

Where t: Recorded temperature

Density of each test specimen was obtained by equation (2).

$$\rho_t = \frac{(I_{ta} \times \rho_l) - (I_{tl} \times \rho_a)}{I_{ta} - I_{tl}} \quad (2)$$

Where ρ_t: Density of test specimen at recorded temperature

ρ_l: Density of distilled water at recorded temperature

ρ_a: Density of air at recorded temperature

I_{ta}: Weight of specimen in air at recorded temperature

I_{tl}: Weight of specimen in distilled water at recorded temperature

Theoretical values of density for hybrid composites were calculated by using rule of mixtures [22], explained by equation (3).

$$\frac{1}{\rho_c} = \frac{1}{\rho_{f1}}\left(\frac{w_{f1}}{w_c}\right) + \frac{1}{\rho_{f2}}\left(\frac{w_{f2}}{w_c}\right) + \frac{1}{\rho_{f3}}\left(\frac{w_f 3}{w_c}\right) + \frac{1}{\rho_m}\left(\frac{w_m}{w_c}\right) \quad (3)$$

Where ρ_c and w_c: Density and weight of composite

ρ_{f1} and w_{f1} : Density and weight of eggshell powder

ρ_{f2} and w_{f2}: Density and weight of Silicon carbide

ρ_{f3} and w_{f3}: Density and weight of Aluminium Oxide

ρ_m and w_m: Density and weight of Al 7057-T6 alloy used as metal matrix

Percentage porosity of developed composites was calculated by expression given in equation (4) [22].

$$\%\ \text{Porosity} = \left\{\left(\frac{\rho_T - \rho_{EX}}{\rho_t}\right)\right\} \times 100\% \quad (4)$$

Here ρ_T: Theoretical density of composite

ρ_{EX}: Experimental density of composite

Experimentally obtained and theoretically calculated mean values of density for as-cast Al 7075-T6 specimen and 9 composites specimens (in three replications) are shown in figure 11. It was observed that there was no significant change in density of composites as compared to the base metal (only upto 2.2%) due to comparable densities of infused reinforcements.

Table 5 shows three readings corresponding to three raplications for percentage porosity measurement of developed hybrid composite specimens with respective S/N ratio for 'smaller the better' type of quality characteristic. Plots in figure 12 demonstrate the effect of different process parameters on S/N ratio and percentage porosity. It is displayed that for increased reinforcements content (figures 12(a)–(c)) and longer mechanical stirring time (figure 12(d)) percentage porosity of developed hybrid aluminium metal matrix

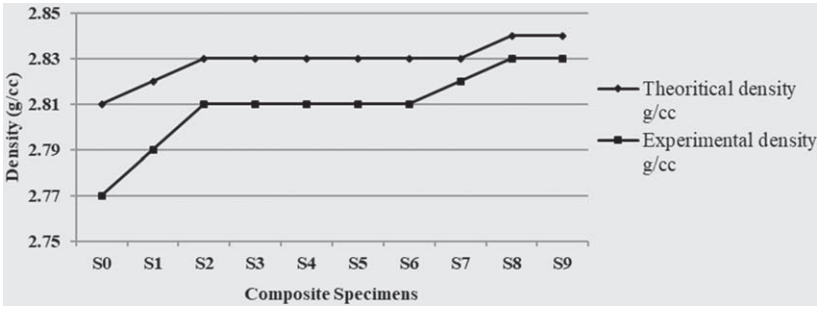


Figure 11. Density of composites.

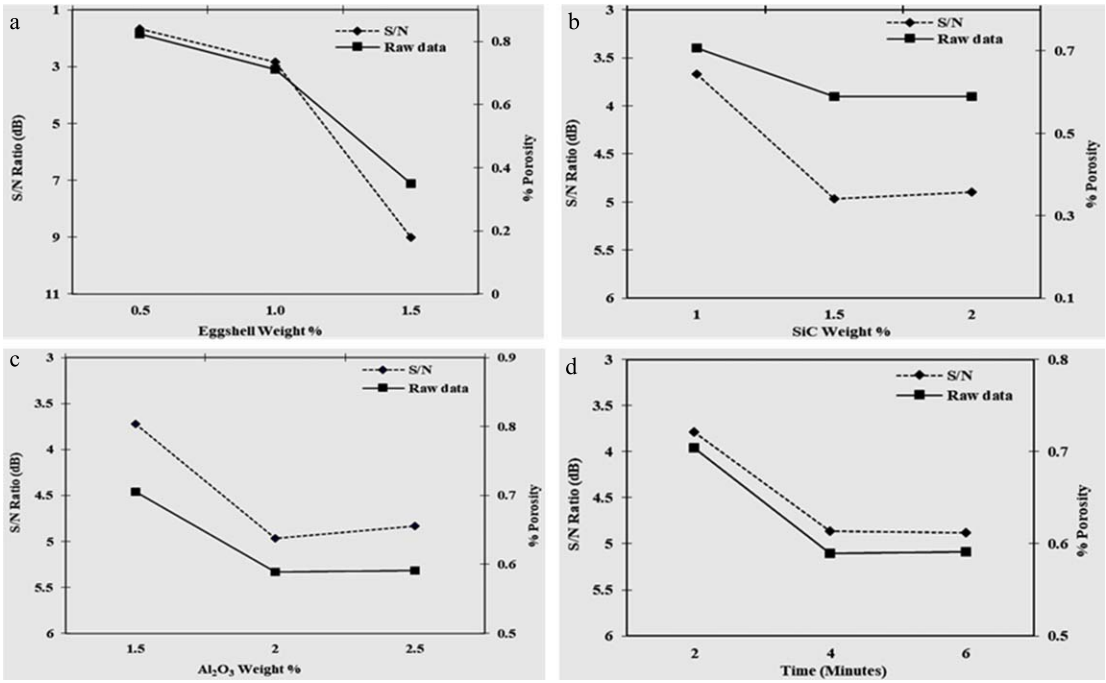


Figure 12. Effect of (a) Eggshell wt% (b) SiC wt% (c) Al_2O_3 wt% (d) mechanical stirring time on percentage porosity and S/N ratio.

Table 5. Observations for percentage porosity and S/N ratio.

Percentage porosity					
Average percentage porosity of as-cast Al7075-T6 Specimen S0: 1.42					
Composite specimen	Reading 1	Reading 2	Reading 3	Mean	S/N ratio (dB)
S1	1.35	1.03	0.79	1.06	−0.67
S2	0.83	0.67	0.62	0.71	2.94
S3	0.7	0.91	0.52	0.71	2.76
S4	0.86	0.6	0.68	0.71	2.83
S5	0.61	0.84	0.68	0.71	2.89
S6	0.88	0.73	0.52	0.71	2.79
S7	0.45	0.27	0.34	0.35	8.84
S8	0.29	0.37	0.39	0.35	9.05
S9	0.35	0.4	0.29	0.35	9.12

composites was decreased. It was inferred that for minimum percentage porosity and S/N ratio, 3rd level of eggshell content (A_3), 2nd level of SiC content (B_2), 2nd level of Al_2O_3 content (C_2) and 2nd level of mechanical stirring time (D_2) were optimum levels. ANOVA is a statistical technique that is capable of analysing any

Table 6. Analysis of variance (ANOVA) for percentage porosity.

Factor	Sum of squares (SS)	Degrees of freedom	Variance (V)	Percentage contribution (P)	F-Ratio
Eggshell Wt%	1.11	2	0.55	54.32	46.27
SiC Wt%	0.17	2	0.08	8.26	7.04
Al_2O_3 Wt%	0.17	2	0.09	8.62	7.34
Stirring time	0.37	2	0.19	18.23	15.53
Others/errors	0.21	18	0.01	10.57	—
Total	2.03	26	—	100	—

Table 7. Confirmation experiment for percentage porosity.

Quality characteristic	Replications			
Percentage porosity of composites	Replication 1	Replication 2	Replication 3	Mean
	0.57	0.29	0.32	0.39

experimental data and drawing significant conclusions in terms of F ratio, percentage contribution and error variance [23, 24]. Table 6 shows ANOVA results computed at 95% confidence level, it demonstrates F-ratio and percentage contribution of various factors toward quality characteristic. It was noticed that eggshell wt% (P = 54.32%) had significant effect and mechanical stirring time (P = 18.23%) had moderate influence on porosity of synthesized hybrid composites where as other control factors were insignificant.

In can be observed from graphs in figure 12 that the insignificant control factors had almost horizontal lines while the significant control factors had lines with higher inclinations [25, 26]. After analysing S/N ratio and mean response characteristic, optimum levels of physically and statistically significant factors were determined to be A_3 and D_2. The predicted mean of percentage porosity at optimal level of process parameters was enumerated using equation (5) [27, 28].

$$X_{mp} = \overline{G} + (\overline{A_3} - \overline{G}) + (\overline{D_2} - \overline{G}) \quad (5)$$

Here X_{mp} denoted the predicted mean of percentage porosity at optimum condition and $\overline{G}$ was the grand average of all 27 observations of utility characteristics from table 5. $\overline{A_3}$ and $\overline{D_2}$ represented the average values of percentage porosity at optimal level of significant process parameters. On submitting estimated values of various response averages as $\overline{G} = 0.63$, $\overline{A_3} = 0.35$ and $\overline{D_2} = 0.59$ in equation (5), predicted mean optimum value of percentage porosity was realized to be 0.311. From table 6 the values were obtained for error variance (0.01) and degree of freedom (DOF) for error (18) whereas F-ratio value at 95% confidence interval was determined from standard statistical table. Further, confidence interval (CI) was calculated to be ± 0.19. Hence confidence interval with respect to 95% confidence level of predicted optimum percentage porosity was 0.121 < percentage porosity (PP) < 0.5. In accordance with Taguchi's optimization approach, a confirmation experiment was conducted by running three more replications for percentage porosity of developed hybrid composites at optimal levels of process parameters as given in table 7 in order to authenticate the predicted results. It is realized from table 7 that confirmation experiment result obtained for percentage porosity of composites was covered within the predicted confidence interval $0.121 < PP < 0.5$.

3.2. Prediction of optimum Residual Stress in fabricated hybrid composites

Residual stress might occur in fabricated hybrid composite specimens due to temperature gradients and machining forces resulting into premature failure. Measurements of residual stresses in specimens were carried out by x-ray diffraction technique using a non-destructive x-ray analyser (μ-X360) as shown in figure 13(a). It consists of a position sensitive detector unit with scintillation counter for measuring the residual stress in metallic surfaces by detecting and comparing the full Debye ring data (figures 13(b)–(e)) from a single incident x-ray angle with non-stressed state. X ray diffraction method determined the residual stress by measuring the distance between crystallographic planes using the angles at which maximum intensity takes place when a sample was subjected to x-ray exposure. From these angles we could find out changed spacing between diffraction planes due to any kind of deformation, which corresponds to the magnitude of residual stress [29]. The measurement conditions for residual stress were as given below:

Pitch: 50 μm.

X-ray incidence angle: 25.0 deg

X-ray irradiation time (Setup): 90 s.

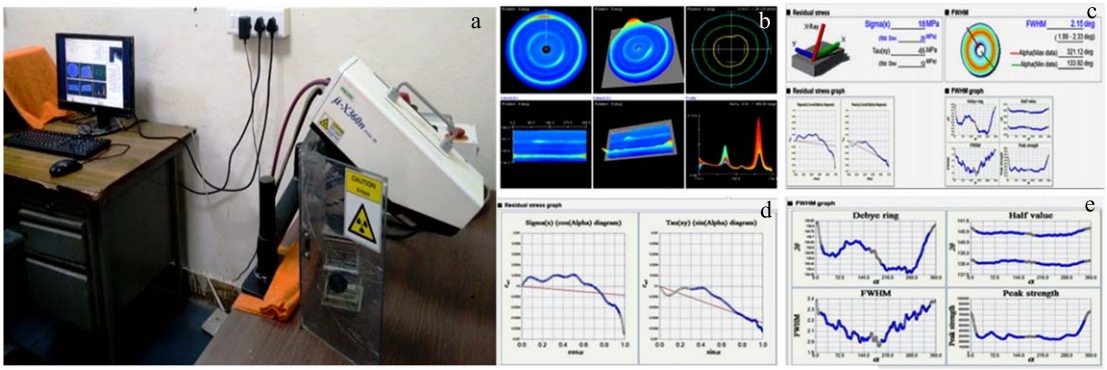


Figure 13. (a)–(e): Residual stress measurement using X-ray diffraction.

Table 8. Observations for residual stress and S/N ratio.

Residual stress (Mpa)					
Average residual stress in as-cast Al7075-T6 Specimen S0: 89					
Composite specimen	Reading 1	Reading 2	Reading 3	Mean	S/N ratio (dB)
S1	97	99	89	95	−39.56
S2	105	84	109	99.33	−39.99
S3	115	105	118	112.67	−41.05
S4	58	51	32	47	−33.67
S5	18	84	18	40	−34.10
S6	42	36	58	45.33	−33.31
S7	42	14	54	36.67	−32.11
S8	36	13	14	21	−27.431
S9	65	55	85	68.33	−36.831

X-ray wavelength (K-Alpha): 2.29093 A.
X-ray irradiation time (Meas.): 47 s.
X-ray irradiation time (Max): 82 s.
Sample distance (Monitor): 29.000 mm
Total measurement count: 7498
Sample distance (Analysis): 29.611/30.304 mm
Detection sensitivity: 52.8%
Temperature: 35.88 deg Centigrade
Peak analysis method: Fitting Lorentz

In this experimental work, as-cast Al 7075-T6 specimen and hybrid composite specimens (all in three replications) were characterized for residual stresses. Table 8 shows signal to noise ratio calculation from experimental data (three set of observations for three replications) for residual stress as 'smaller the better' type of quality characteristic of developed composites. In current investigation, all the residual stresses were found to be compressive in nature and it was noticed that generally residual stresses are lower for composites with higher reinforcement content.

Effects of all the process parameters considered during composite fabrication on S/N ratio and residual stress were studied and plotted as in figure 14. Graph in figure 14(a) displays that on increasing wt% of eggshell, residual stress in composites was decreased whereas from figures 14(b)–(d) it can be observed that on increasing SiC wt%, Al_2O_3 wt% and mechanical stirring time residual stress in composites was increased. Various graphs from figure 14 explain that for minimum residual stress in synthesized hybrid aluminium composites and S/N ratio optimum process parameter levels were 3rd level of eggshell content (A_3), 1st level of SiC content (B_1), 1st level of Al_2O_3 content (C_1) and 2nd level of mechanical stirring time (D_2). ANOVA at 95% confidence level was carried out to study effect of process parameters on utility function. Table 9 shows percentage contribution and F-ratio of different factors affecting the residual stress. It was realized from table 9 that eggshell wt% with percentage contribution P = 64.66% and SiC wt% with percentage contribution P = 28.42% influence the residual stressses significatly whereas Al_2O_3 wt% with percentage contribution P = 6.30% had moderate effect on residual stresses induced in synthesized hybrid composites. On the other hand, mechaincal stirring time had

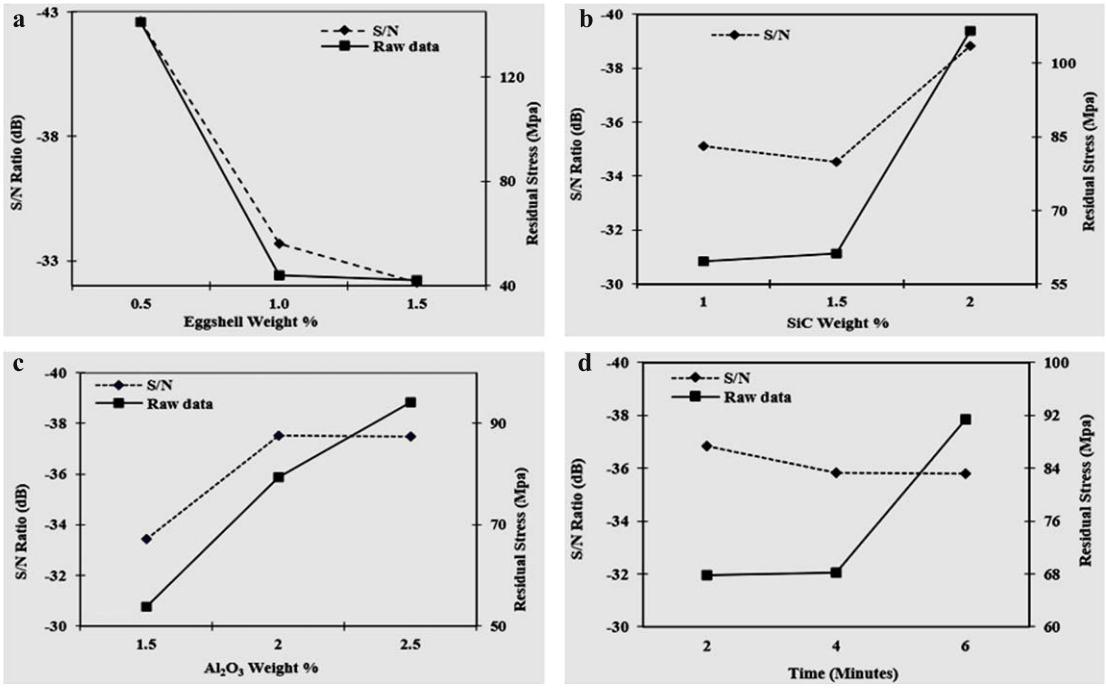


Figure 14. Effect of (a) Eggshell wt% (b) SiC wt% (c) Al_2O_3 wt% (d) mechanical stirring time on residual stress and S/N ratio.

Table 9. Analysis of variance (ANOVA) for residual stress.

Factor	Sum of squares (SS)	Degrees of freedom	Variance (V)	Percentage contribution (P)	F-Ratio
Eggshell Wt%	57840.22	2	28920.11	64.66	2266.52
SiC Wt%	25422.35	2	12711.18	28.42	996.2
Al_2O_3 Wt%	5635.65	2	2817.83	6.30	220.84
Stirring time	326.77	2	163.36	0.37	12.80
Others/errors	229.67	18	12.76	0.26	—
Total	89454.67	26	—	100	—

negligible influence on residual stresses. The main effect plots shown in figure 14 display that predominent control factors (eggshell wt%, SiC wt% and Al_2O_3 wt%) had highly inclined lines as compared to the insignifcant control factor. S/N ratio and mean response characteristics analysis was conducted followed by realization of optimum levels of significant factors as A_3, B_1 and C_1 for prediction of mean residual stress (X_{mp}). Following response average components were evaluated using experimental data from table 8.

$$\overline{G} = 62.81,\ \overline{A_3} = 42.0,\ \overline{B_1} = 59.56 \text{ and } \overline{C_1} = 53.78$$

$$X_{mp} = \overline{G} + (\overline{A_3} - \overline{G}) + (\overline{B_1} - \overline{G}) + (\overline{C_1} - \overline{G}) \quad (6)$$

Predicted mean optimum value of residual stress $X_{mp} = 29.70$ Mpa was calculated form equation (6). From table 9, error variance $= 12.76$ and DOF for error $= 18$ were obtained. F-ratio value at 95% confidence interval was determined from standard statistical table. The confidence interval (CI) calculated was ± 6.13. Confidence interval with respect to 95% confidence level of predicted optimum residual stress was 23.57< Residual Stress (RS in Mpa) <35.83. Additionally a confirmation experiment was carried out by running three more replications for residual stress in developed hybrid composites at optimal levels of process parameters. Results of confirmation experiment were reported in table 10 and it was realized that mean value of residual stress 31.5 Mpa fell within the confidence interval 23.57< RS (Mpa) <35.83.

3.3. Prediction of optimum Microhardness in fabricated hybrid composites

Each of the specimens (one as-cast Al 7075-T6 specimen and nine hybrid specimens, in three replications) was tested for microhardness (on Fischer HM 2000S). During microhardness test a load of 300 mN was applied for 20 seconds keeping creep time 5 seconds and load release time 20 seconds. The microhardness of as-cast Al 7075-T6 specimen and composite specimens (in three replications) with varying reinforcement ratios along

Table 10. Confirmation experiment for residual stress.

Quality characteristic	Replications			
Residual stress in composites	Replication 1	Replication 2	Replication 3	Mean
	37.1	29.9	27.5	31.5

Table 11. Observations for microhardness and S/N ratio.

Microhardness (VHN)					
Average microhardness of as-cast Al7075-T6 Specimen S0: 167.5					
Composite specimen	Reading 1	Reading 2	Reading 3	Mean	S/N ratio (dB)
S1	196.5	197.7	196.5	196.9	44.12
S2	205.55	212.55	207.55	208.55	44.62
S3	215.5	218.6	217.8	217.3	44.97
S4	212.29	210.29	211.39	211.32	44.73
S5	229.01	229.01	230.01	229.34	45.44
S6	277.52	278.52	280.52	278.85	47.14
S7	226.34	228.34	238.34	231.00	45.50
S8	303.25	309.25	307.25	306.58	47.96
S9	286.4	286.4	288.4	287.06	47.39

Table 12. Analysis of variance (ANOVA) for microhardness.

Factor	Sum of squares (SS)	Degrees of freedom	Variance (V)	Percentage contribution (P)	F-Ratio
Eggshell Wt%	20394.81	2	10197.40	54.38	1279.29
SiC Wt%	11103.67	2	5551.83	29.44	696.49
Al_2O_3 Wt%	5833.95	2	2916.97	15.49	365.94
Stirring time	262.53	2	131.26	0.69	16.46
Others/errors	143.48	18	7.97	0.38	—
Total	37738.46	26	—	100	—

with S/N ratio calculation for 'larger the better' type of quality characteristic are given in table 11. Simultaneously, effects of various process parameters on S/N ratio and mean response were investigated and plotted as in figure 15. Figures 15(a)–(d) display that on increasing wt% of eggshell, wt% of SiC particles and mechanical stirring time, hardness of composites was increased. Whereas plot in figure 15(c) exhibits that composites hardness was decreased with increasing wt% of Al_2O_3 particles. It was observed from figure 15 that for maximum microhardness and S/N ratio, 3rd level of eggshell content (A_3), 3rd level of SiC content (B_3), 1st level of Al_2O_3 content (C_1) and 3rd level of mechanical stirring time (D_3) were optimum levels.

Table 12 represents ANOVA results for microhardness measurements performed at 95% confidence level in terms of F-ratio and percentage contribution of various factors. Microhardness of synthesized hybrid composites appeared to be influenced significantly by two control factors i.e. eggshell wt% (P = 54.38%) and SiC wt% (P = 29.44%) while the third control factor Al_2O_3 wt% (P = 15.49%) had moderate effect on it. The fourth control factor mechanical stirring time could maginally affect the microhardness of composites. The graphs in figure 15 demonstrate that momentous control factor lines (eggshell wt%, SiC wt% and Al_2O_3 wt%) had elevated slopes whereas the insignifcant control factor mechanical stirring time had almost horizontal line. To compute predicted mean of microhardness (X_{mp}), S/N ratio and mean response characteristics analysis was conducted followed by realization of optimum levels of significant factors as A_3, B_3 and C_1. In current study for microhardness of developed hybrid composites following response average components were evaluated using experimental data from table 11.

$$\overline{G} = 240.77,\ \overline{A_3} = 274.89,\ \overline{B_3} = 261.07\ ,\ \overline{C_1} = 260.78$$

$$X_{mp} = \overline{G} + (\overline{A_3} - \overline{G}) + (\overline{B_3} - \overline{G}) + (\overline{C_1} - \overline{G}) \quad (7)$$

From equation (7) predicted mean optimum value of microhardness X_{mp} was observed to be 315.20. Table 12 demonstrates values of error variance (7.97) and DOF for error (18). F-ratio value at 95% confidence

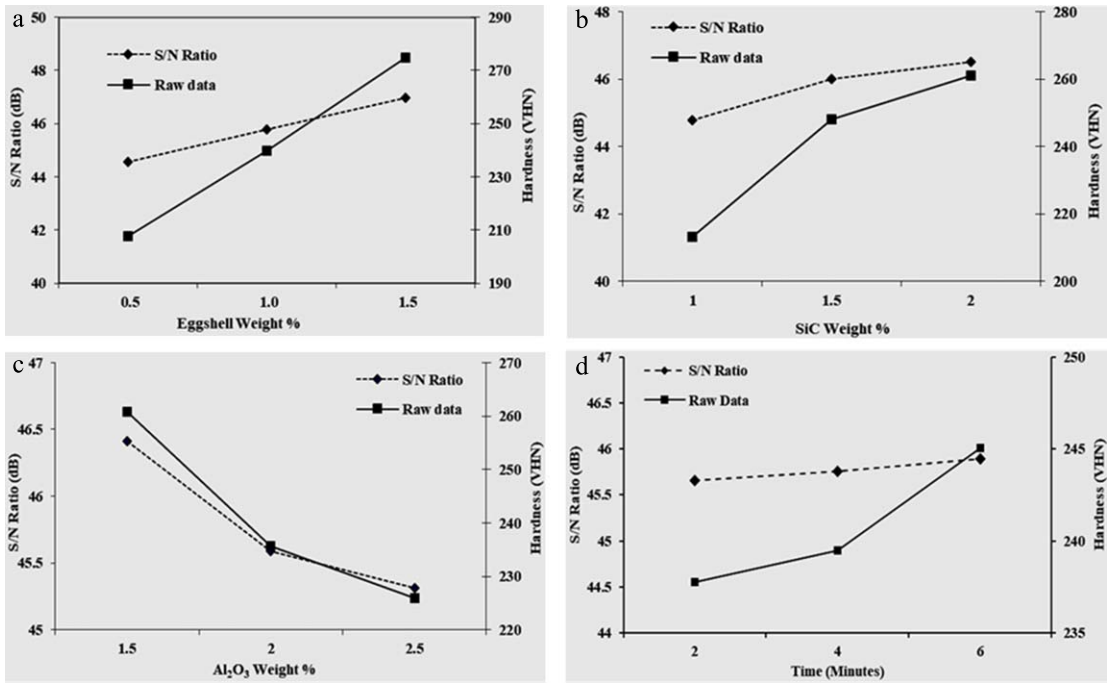


Figure 15. Effect of (a) Eggshell wt% (b) SiC wt% (c) Al_2O_3 wt% (d) mechanical stirring time on microhardness and S/N ratio.

Table 13. Confirmation experiment for microhardness.

Quality characteristic	Replications			
Microhardness of composites	Replication 1	Replication 2	Replication 3	Mean
	309.43	297.55	329.85	312.28

interval was determined from standard statistical table. The computed confidence interval (CI) was ±4.84. Therefore the confidence interval with respect to 95% confidence level of predicted optimum microhardness was 310.36 < H (Vickers Hardness Number) < 320.04. The confirmation experiment was done by running three more replications for microhardness of developed hybrid composites at optimal levels of process parameters and it was noticed that mean value of microhardness 312.28 as reported in table 13 was lying within the confidence interval 310.36 < H (VHN) < 320.04.

3.4. Prediction of optimum tensile strength of fabricated hybrid composites

In order to investigate the tensile behaviour of developed hybrid aluminium composites, specimens (in three replications) were characterized as per ASTM E8-M11 for ultimate tensile strength on universal testing machine (Tinius Olsen, H 50 K-S, Cross head speed: 2.5 mm min^{-1}, Strain rate : 0.002 s^{-1}). Each specimen was subjected to axial tensile load and the ultimate tensile strength value was observed, one of the fractured specimens is shown in figure 16. The ultimate force ranged from 876 N to 1520 N and the ultimate tensile strength was observed to be improving with infusion of reinforcement particles. Stress-strain diagrams of as-cast Al 7075-T6 alloy and composites are shown in figure 17. To analyse mean response function, signal to noise ratios ('larger the better' type of quality attribute) calculated from designed experimental data are expressed in table 14. Analysis of variance was performed to observe the impact of control factors on quality attribute. The effects of process parameters on tensile strength and S/N ratio have been plotted in figure 18. Figures 18(a)–(d) display that on increasing wt% of eggshell, wt% of SiC particles and mechanical stirring time, tensile strength of composites was increased. Whereas plot in figure 18(c) exhibits that composites tensile strength was decreased with increasing wt% of Al_2O_3 particles.

It was experienced that all the process parameters have a significant effect on utility function and the optimum levels are 3rd level of eggshell content (A_3), 2nd level of SiC content (B_2), 1st level of Al_2O_3 content (C_1) and 3rd level of mechanical stirring time (D_3). Table 15 demonstrates ANOVA results at 95% confidence level in



Figure 16. Fractured tensile test specimen.

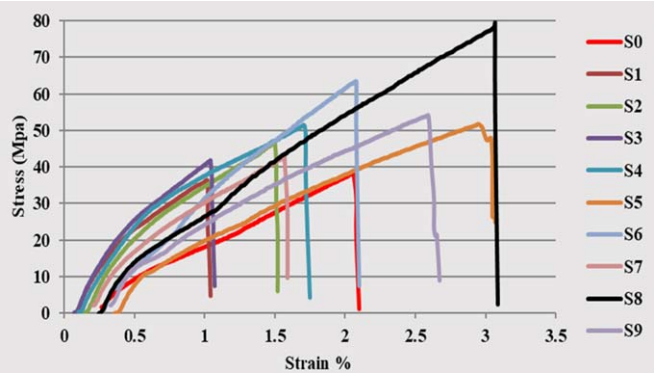


Figure 17. Stress-Strain diagram.

Table 14. Observations for tensile strength and S/N ratio.

Tensile strength (Mpa)					
Average tensile strength of as-cast Al7075-T6 Specimen S0: 38.3					
Composite specimen	Reading 1	Reading 2	Reading 3	Mean	S/N ratio (dB)
S1	36.7	34.6	38.3	36.5	30.73
S2	47.5	45.6	47.2	46.7	31.67
S3	40.9	42.9	41.9	41.9	31.08
S4	55.4	46.2	51.9	51.3	28.25
S5	44.3	56.1	54.9	51.8	31.55
S6	70.3	63.8	55.7	63.3	32.59
S7	43.1	50.1	34.7	42.6	30.70
S8	84.1	82.1	72.4	79.5	37.54
S9	49.7	54.6	58.1	54.1	33.70

terms of F-ratio and percentage contribution of process parameters. By analyzing S/N ratio and mean response characteristic, significant control value optimum levels were identified as A_3, B_2 and C_1.

Control factors eggshell content with percentage contribution P = 27.22%, Silicon Carbide content with percentage contribution P = 25.81% and Aluminium Oxide content with percentage contribution P = 21.36% had impactful influence on tensile strength of hybrid composites while mechaincal stirring time had imperceptible effect on it. The plots shown in figure 18 demonstrate that dominating control factors (eggshell wt%, SiC wt% and Al_2O_3 wt%) had lines with higher inclinations in comparison of the insignifcant control factor. For estimation of predicted mean of tensile strength (X_{mp}), equation (8) is used after putting the values of following response average components from table 14:

$$\overline{G} = 51.97,\ \overline{A_3} = 58.8,\ \overline{B_2} = 59.4\ ,\ \overline{C_1} = 59.8$$

$$X_{mp} = \overline{G} + (\overline{A_3} - \overline{G}) + (\overline{B_2} - \overline{G}) + (\overline{C_1} - \overline{G}) \quad (8)$$

From equation (6), predicted mean optimum value of tensile strength X_{mp} was computed to be 74.0 Mpa. Table 15 shows error variance = 79.80 and DOF for error = 18. For F-ratio evaluation at 95% confidence interval standard statistical table was used. The calculated confidence interval (CI) obtained was ±15.32. Hence the confidence interval with respect to 95% confidence level of predicted optimum tensile strength was 58.68<

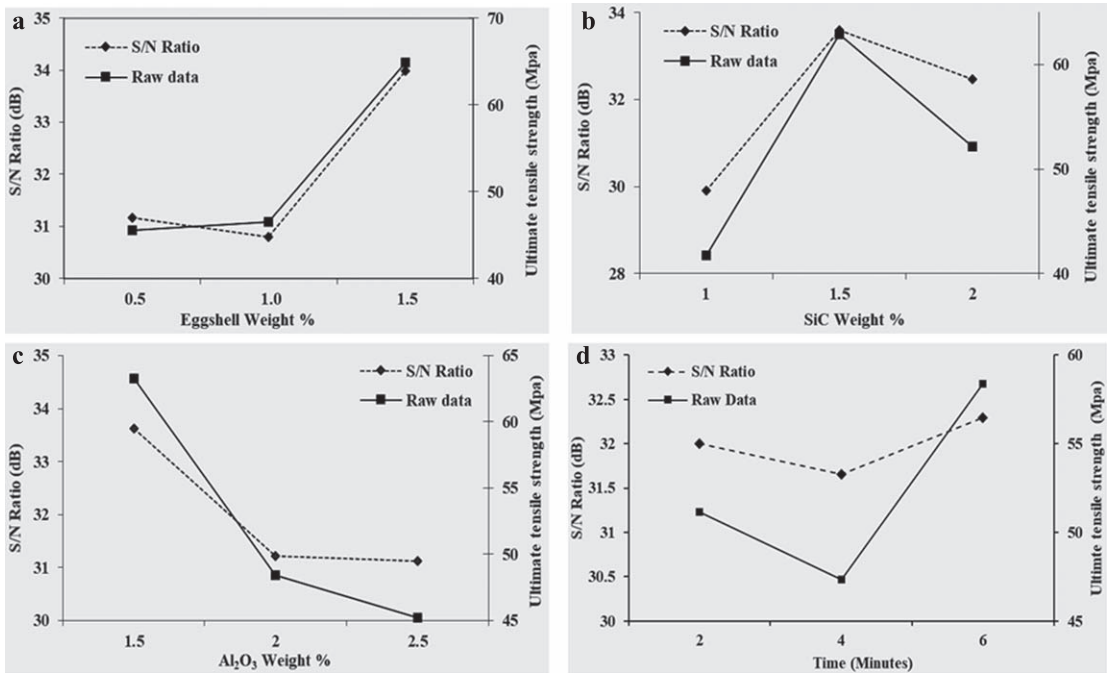


Figure 18. Effect of (a) Eggshell wt% (b) SiC wt% (c) Al_2O_3 wt% (d) mechanical stirring time on tensile strength and S/N ratio.

Table 15. Analysis of variance (ANOVA) for tensile strength.

Factor	Sum of squares (SS)	Degrees of freedom	Variance (V)	Percentage contribution (P)	F-Ratio
Eggshell Wt%	2133.43	2	1066.71	27.22	13.37
SiC Wt%	2022.66	2	1011.33	25.81	12.67
Al_2O_3 Wt%	1674.40	2	837.20	21.36	10.49
Stirring time	570.90	2	285.45	7.28	3.58
Others/errors	1436.48	18	79.80	18.33	—
Total	7837.89	26	—	100	—

Table 16. Confirmation experiment for tensile strength.

Quality characteristic	Replications			
Tensile strength of composites	Replication 1	Replication 2	Replication 3	Mean
	68.26	75.32	60.25	67.94

Tensile Strength (TS in Mpa) < 89.32. It was followed by a confirmation experiment by running three more replications for tensile strength of developed hybrid composites at optimal levels of process parameters and it was observed that mean value of tensile strength 67.94 Mpa as reported in table 16 was lying within the confidence interval 58.68< TS (Mpa) < 89.32.

3.5. Metallographic analysis

Among fabricated composites, composite specimen S8 (Al 7075-T6/1.5 wt% eggshell/1.5 wt% SiC/1.5 wt% Al_2O_3/Mechanical stirring time 6 min) exhibited outstandingly enhanced mechanical properties in terms of lowest percentage porosity, lowest residual stress, highest micro-hardness and highest tensile strength. For comparative studies, XRD plots, EDS profiles and Raman spectra of as-cast Al 7075-T6 specimen S0 and hybrid composite specimen S8 demonstrating their elemental composition without any oxygen and carbon content are shown in figures 19–21. FESEM images of as-cast Al 7075-T6 specimen S0 and hybrid composite specimen S8 are shown in figure 22. The micrograph of base alloy displayed uniform fine grain sizes whereas in composite along with reinforcement traces, occurrence of some uneven grains may be associated with infusion of reinforcement particles. From figure 22, composite microstructure appeared to have homogenous distribution

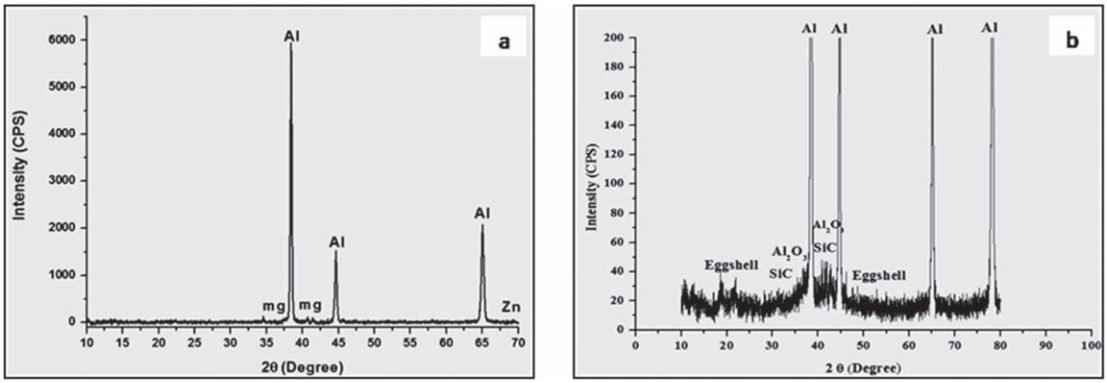


Figure 19. XRD patterns of (a) As-cast Al 7075-T6 specimen S0 (b) Composite specimen S8.

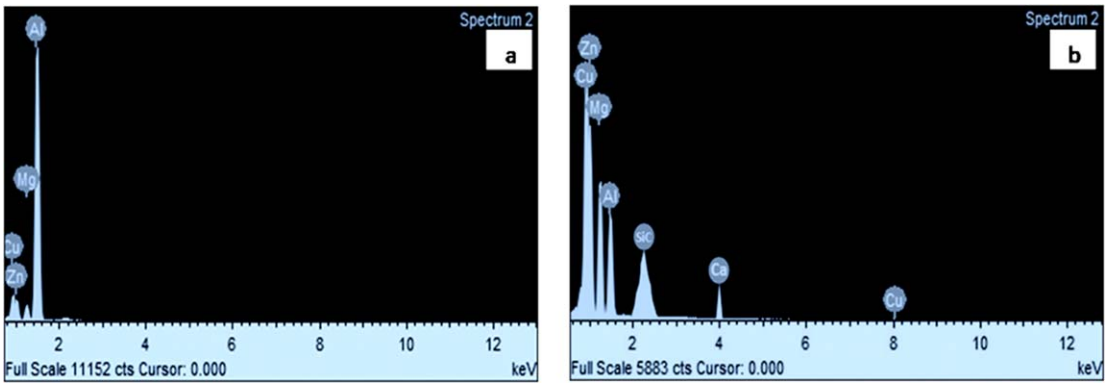


Figure 20. EDS profiles of (a) As-cast Al 7075-T6 specimen S0 (b) Composite specimen S8.

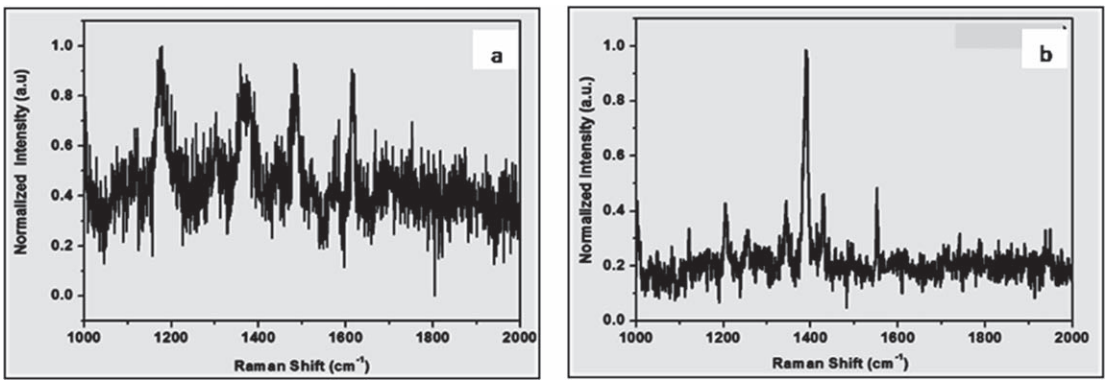


Figure 21. Raman spectra of (a) As-cast Al 7075-T6 specimen S0 (b) Composite specimen S8.

of filler particles, but the occurrence of particle clusters could not be ignored due to agglomeration. Synthesized composites also exhibited some traces of porosity due to various process induced effects such as gas trapped in metal melt during mixing, shrinkage due to composites solidification, presence of moisture on reinforcement particles surfaces, evolution of hydrogen and inappropriate casting parameters during fabrication creating isolated areas in composites which get solidify at last and generate voids. Porosity reduces the mechanical attributes of composites due to occurrence of stress concentration in proximity of voids [30]. To reduce porosity, a balance is necessary between void sources (trapped air and moistures layers etc) and voids sink (vacuum evacuation and bubble mobility etc). Comparative reduction in porosity with reinforcement addition to metal matrix is shown in figure 23. In general, residual stresses or strain fields are developed within the

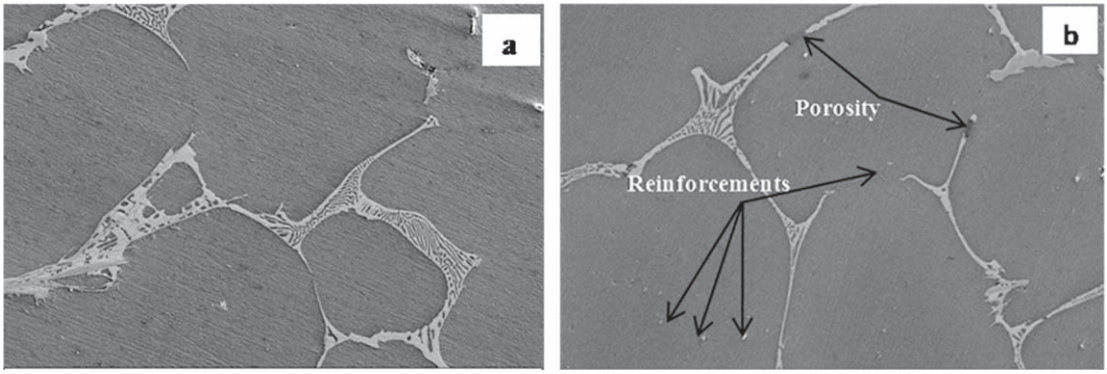


Figure 22. FESEM images of (a) As-cast Al7075-T6 specimen S0 (b) composite specimen S8.

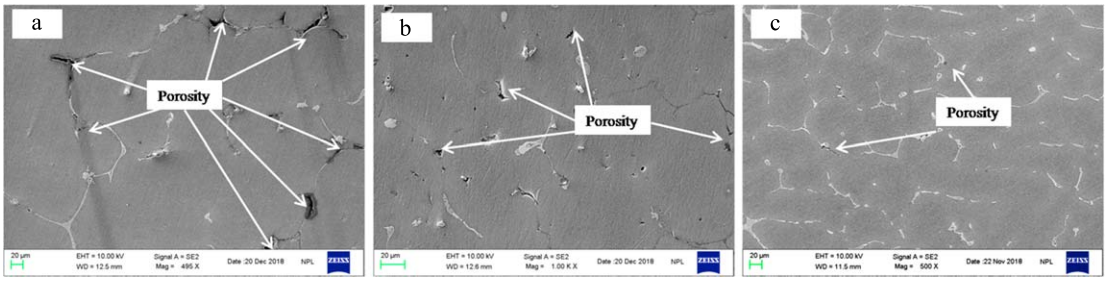


Figure 23. Porosity in microstructure (a) As-cast Al 7075-T6 specimen S0 (b) Hybrid composite specimen S5 (c) Hybrid composite specimen S8.

composites because of thermomechanical mismatch in the characteristics of metal matrix and reinforcement during cooling from fabrication temperature, presence of moisture, fluctuation in material properties, difference in amount of reinforcement and tool-part interaction during machining [31]. Variations in residual stresses of fabricated hybrid composites may primarily be associated with thermal residual stresses during electromagnetic stir casting process, distinct weight percentage of reinforcements infused and residual stresses developed during machining of hybrid composites. Lower values of residual stress in hybrid composites may be because of increased dislocation density due to higher reinforcement content [32]. Specimens S0 was subjected to higher residual stresses while specimens S8 with higher filler content exhibited lower residual stresses. Specimen S3 was an exception with higher reinforcement content and higher residual stress and this possibility may be attributed to the phenomenon of plastic deformation which got enhanced with reduced dislocation density. As compared to the unreinforced metal matrix, the presence of reinforcement particles in base metal restrains mechanical dislocations within the composites [33, 34] causing enhanced strength and hardness. All the composite specimens showed improved microhardness as compared to the unreinforced base metal specimen S0, due to the hardness properties of incorporated reinforcement particles (predominantly eggshell and SiC particles). It was ascertained from current experimental data that as percentage porosity increased, hardness and tensile strength of fabricated hybrid composites decreased due to failure inception from voids within composites. Here as- cast Al7075-T6 specimen S0 with maximum percentage porosity showed lower microhardness and tensile strength while hybrid composite specimen S8 with higher reinforcement contents, longer stirring time and lesser percentage porosity demonstrated higher microhardness and tensile strength. In exceptional case, ultimate tensile strength of a composite specimen S1 was observed to be lesser than that of base metal (specimen S0) and it may be as a result of formation of loosely bound reinforcement particle micro-clusters due to agglomeration and porosity. In case of hybrid composites specimen S7, reduced ductility may be due to infusion of hard SiC and Al_2O_3 particles concentrating stress at metal matrix-reinforcement interface and localizing crack initiation resulting into brittleness. In some of the SEM micrographs of fractured specimens shown in figure 24, detached reinforcement particles were found due to the breakage of bonds between metal matrix and reinforcements. The fractured surfaces were observed to exhibit cup-cone mode of fracture, which substantiated that the fracture occurred was somewhat ductile in nature and necking of tensile test specimen under axial load eventuated before the metal matrix failure took place [35, 36].

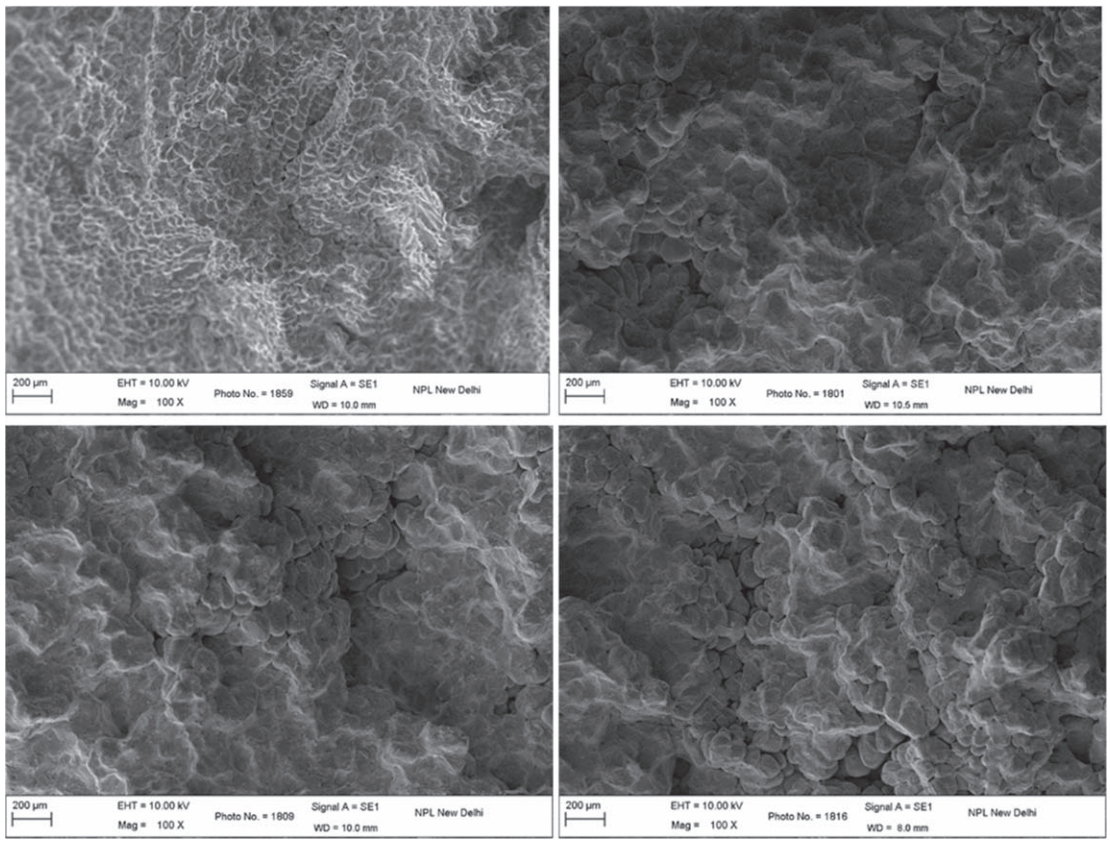


Figure 24. SEM micrographs of fracture surfaces of composite specimen after tensile test.

4. Conclusion

Al 7075-T6/Eggshell/SiC/Al_2O_3 hybrid composites with variable reinforcement's content and mechanical stirring time were developed successfully as per the design matrix by electromagnetic stir casting technique. Use of hazardous eggshell waste as reinforcement resulted into synthesis of ecodesigned and economical hybrid composites with augmented physical and mechanical attributes. Each composite specimen exhibited distinctive enhanced property, hence to be considered as viable alternate material for potential engineering applications.

- No significant change in density of composites was observed as compared to the base metal (only upto 2.2%).
- The maximum decrease in percentage porosity of synthesized hybrid composites was upto 75% as compared to as-cast Al 7075-T6 with optimum levels of significant factors (Eggshell wt%:1.5 and mechanical stirring time: 4 min). Predicted optimum value of percentage porosity for 95% confidence interval was $0.121 < PP < 0.5$ with mean value of percentage porosity $= 0.39$ from confirmation experiment corresponding to optimum conditions, which fell within the predicted confidence interval as per Taguchi's parameter design technique predictions.
- A maximum decrease in residual stress in composites was observed to be 76% as compared to as-cast Al 7075-T6 specimen. Eggshell wt%: 1.5, SiC wt%: 1 and Al_2O_3 wt% 1.5 were the optimum levels of significant process parameters. Predicted optimum value of residual stress for 95% confidence interval was $23.57 <$ RS (Mpa) < 35.83 with mean value of residual stress $= 31.5$ Mpa obtained from confirmation experiment corresponding to optimum conditions according to Taguchi's parameter design technique predictions.
- An enhancement of maximum 83% in microhardness of prepared hybrid composites was witnessed as compared to its unreinforced counterpart. The optimum levels of dominant process parameters were observed to be as eggshell wt%: 1.5, SiC wt%: 2 and Al_2O_3 wt%: 1.5. Predicted optimum value of microhardness for 95% confidence interval was $310.36 <$ H (VHN) < 320.04 with mean value of microhardness $= 312.28$ from confirmation experiment corresponding to optimum conditions of process parameters, establishing a good agreement between Taguchi's parameter design technique predictions and confirmation experiment outcomes.

- There is an increase of maximum 107% in tensile strength of fabricated hybrid composites specimen as compared to the as-cast Al 7075-T6 specimen. The significant process parameters have optimum levels as eggshell wt%: 1.5, SiC wt%: 1.5 and Al_2O_3 wt%: 1.5. Predicted optimum value of tensile strength for 95% confidence interval was 58.68 $<$ TS (Mpa) $<$ 89.32 with mean value of tensile strength $=$ 67.94 Mpa from confirmation experiment corresponding to optimum conditions of process parameters as per Taguchi's parameter design technique predictions.

Acknowledgments

Authors are thankful to DNPL for his constant support and encouragement. Authors would also like express their sincere thanks to IUAC, Delhi for providing characterization facilities.

ORCID iDs

Girija Moona https://orcid.org/0000-0001-9804-499X

References

[1] Yan C, Lifeng W and Jianyue R 2008 *CJA* **21** 578 (https://www.sciencedirect.com/science/article/pii/S1000936108601776)
[2] Christy T V, Murugan N and Kumar S 2010 *JMMCE* **9** 57
[3] Moona G, Walia R S, Rastogi V and Sharma R 2018 *IJPAP* **56** 164 (http://op.niscair.res.in/index.php/IJPAP/article/viewFile/17513/1465)
[4] Singla M, Dwivedi D D, Singh L and Chawla V 2009 *JMMCE* **8** 455
[5] Bhushan R K, Kumar S and Das S 2013 *Int J Adv Manuf. Technol.* **65** 611
[6] Poovazhagan L, Kalaichelvan K and Rajadurai A 2013 *Procedia. Eng.* **64** 681
[7] Pitchayyapillai G, Seenikannan P, Balasundar P and Narayanasamy P 2017 *Trans Nonferrous Met Soc China* **27** 2137
[8] Adeosun S O, Osoba L O and Taiwo O O 2014 *Int J Chem, Mol., Nucl. Mat. Metall. Eng.* **8** 731 (https://publications.waset.org/10000007/characteristics-of-aluminum-hybrid-composites)
[9] Balasivanandha S P, Karunamoorthy L, Kathiresan S and Mohan B 2006 *J. Mater. Process Technol.* **171** 268
[10] Li M J, Tamura T, Omura N and Miwa K 2010 *Trans. Nonferrous Met. Soc. China* **20** 1192
[11] Ravindran R, Manisekar K, Narayanasamy P, Selvakumar N and Narayanasamy R 2012 *Mater Des.* **39** 42
[12] Clark R Jr, Coughran B, Traina I, Hernandez A, Scheck T, Etuk C, Peters J, Lee E W, Ogren J and Es-Said O S 2009 *Eng. Fail. Anal.* **12** 520
[13] Gan Y X 2009 *Int. J. Mol. Sci.* **10** 5115
[14] Veeresh Kumar G B, Rao C S P, Selvaraj N and Bhagyashekar M S 2010 *JMMCE* **9** 43
[15] Buntan R, Phuenchomphu D, Sukmoung P, Doomao K, Anunapiwat O and Patcharawit T 2011 *JMMM* **21** 73 (http://ojs.materialsconnex.com/index.php/jmmm/article/view/188/215)
[16] Lashgari H R, Emamy M, Razaghian A and Najimi A A 2009 *Mater. Sci. Eng.* A **517** 170
[17] Parlevliet P, Bersee H and Beukers A 2006 *Composites Part* A **37** 1847
[18] Kok M 2005 *J. Mater. Process Techno.* **161** 381
[19] http://asm.matweb.com/search/SpecificMaterial.asp?bassnum=ma7075t6 (accessed in January 2019)
[20] Walia R S, Shan H S and Kumar P 2006 *Mater. Manuf. processes* **21** 375
[21] Walia R S, Shan h S and Kumar P 2006 *Mach. Sci. Technol.* **10** 341
[22] Ahmad S N, Hashim J and Ghazali M I 2005 *J. Compos. Mater.* **39** 451
[23] Selvakumar N and Narayanasamy P 2016 *Tribol. T.* **59** 733
[24] Brar B S, Walia R S and Singh V P 2015 *Int. J. Adv. Manuf. Tech.* **79** 329
[25] Narayanasamy P and Selvakumar N 2017 *J. Tribol.-ASME* **139** 051301
[26] Ravindran P, Manisekar K, Narayanasamy R and Narayanasamy P 2013 *Ceram. Int.* **39** 1169–82
[27] Singh H and Kumar P 2004 *Indian. J. Eng. Mater. Sci.* **11** 19 (http://nopr.niscair.res.in/bitstream/123456789/9256/1/IJEMS%2011%281%29%2019-24.pdf)
[28] Goyal T, Walia R S and Sidhu T S 2013 *Int J Adv Manuf Tech* **64** 903
[29] Withers P J and Bhadeshia H K D H 2000 *Mater. Sci. Tech* **17** 355
[30] Centea T and Hubert P 2012 *Composites Part* A **43** 1505
[31] Guzmán R E and Hernández Arroyo E 2016 *J. Phys.: Conference Series* **687** 012060
[32] Liu H T and Sun L Z 2004 *Int. J. Solid. Struct.* **41** 2189
[33] Suresh K R, Niranjan H B, Martin Jabraj P and Chowdaiah M P 2003 *Wear* **255** 638
[34] Wong W L E, Gupta M and Lim C Y H 2006 *Mater. Sci. Eng.* A **423** 148
[35] Huang H, Tsutsumi S, Wang J, Li L and Murakawa H 2017 *Finite. Elem. Anal. Des.* **135**
[36] Su H, Gao W, Feng Z and Lu Z 2012 *Mater. Des.* **36** 590

Performance Analysis of Different Modulating Techniques for Multilevel Inverter

Allu Bhargav
Dept. of Electrical Engineering
Delhi Technological University
Delhi, India
allubhargav@gmail.com

Alka Singh
Dept. of Electrical Engineering
Delhi Technological University
Delhi, India
alkasingh.dr@gmail.ac.in

Ankita arora
Dept. of Electrical Engineering
Delhi Technological University
Delhi, India
arora.ankita09@gmail.com

***Abstract*—Multilevel converters are getting increasingly popular these days due to their high-power capability under medium voltage applications. In this paper, the modelling and analysis of a seven-level cascaded H-bridge multilevel inverter connected with photovoltaic (PV) cells is presented. Conventional modulating techniques give large total harmonic distortion (THD), so the focus of this paper is on the analysis and study of different modulating techniques. The presented techniques viz. phase disposition (PD) carrier based PWM, phase opposition disposition (POD) carrier based PWM, alternate phase opposition disposition (APOD) carrier based PWM and phase shifting (PS) carrier based PWM are discussed and compared in terms of total harmonic distortion (THD). It is observed that phase shifting modulating technique results in lowest THD as compared to other techniques.**

Keywords— Photovoltaic, P&O, Boost, phase disposition, phase shifting, THD

I. INTRODUCTION

Focus on renewable energy sources in place of conventional sources has increased even in developing nations of the world. Limited resources and environmental pollution due to high emissions has led scientists and engineers search for new and reliable energy sources. Many non-conventional energy sources are available today, but solar photovoltaic (PV) and wind energy capture the market today. The installation of solar energy has been increasing at a fast pace and there is a growth potential of 20-25% over the last 10 years. PV source is pollution free and continuous energy supply during day light adds to its advantages [1].

Maximum power point tracking (MPPT) control plays an vital role to extract the maximum available power from the PV array. Different MPPT techniques are presented in the literature [2]. Integration of PV to the grid can be achieved using a boost converter. It is implemented to boost the input voltage and its duty cycle is regulated by MPPT control [3]. In general, to transform DC to AC, we use a conventional two level inverter, which gives high THD. Decreasing the THD to permissible levels as per IEEE standards requires the use of additional AC filters which have large size and cost.

The use of multilevel inverters is preferred to get high power from medium voltages. Though it has been introduced lately, it has gained a lot of attention nowadays. Many advantages result with multilevel converters such as low total harmonic distortion which decrease the size of filters, low switching losses, reduced electromagnetic interference and lower voltage stresses. Multilevel configurations are broadly categorized into three types viz. Cascaded H-bridge, Neutral point clamped, Flying capacitor multilevel inverter [4]. In this paper, cascaded H-bridge multilevel inverter [5] is implemented because it is the easiest to implement as compared to others.

This paper discusses the design of seven level cascaded H-bridge multilevel inverter [6] with PV connected at the DC link of each H-bridge. For MPPT control, perturb and observe (P&O) algorithm is used and boost converter is used at the DC link in multilevel inverter. Different modulation techniques [7]- [11] used in multilevel inverter are discussed in further sections.

II. SYSTEM DESCRIPTION

Seven level Cascaded H-bridge multilevel inverter connected with PV modules is illustrated in Fig. 1. Each H-bridge is a single-phase converter with four IGBTs and diode connected in reverse polarity. Three such bridges are connected in cascade configuration as illustrated in Fig.1.

A PV array is integrated at the DC link of each H-bridge. The design and modelling of PV array, MPPT and design of boost converter are discussed briefly.

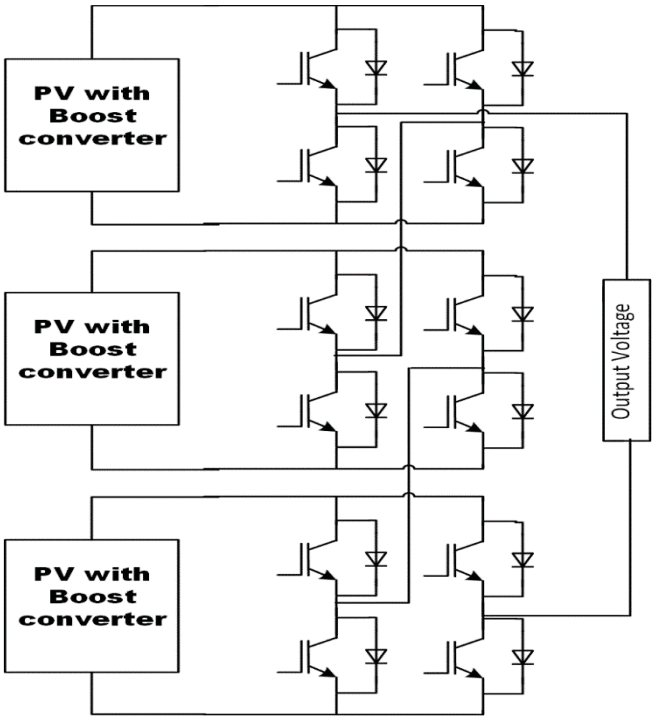


Fig. 1. Seven level Cascaded H-bridge based multilevel inverter connected with three PV modules

978-1-5386-6625-8/18/$31.00 ©2018 IEEE

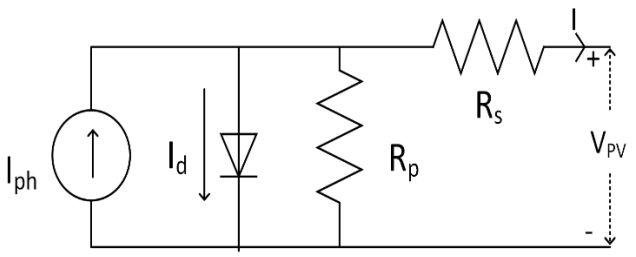


Fig. 2. Electrical equivalent network of PV cell

A. Modelling of PV Module

The equivalent circuit of PV cell is shown in Fig. 2. It shows that a solar cell can be modelled by current source and a diode in parallel with it and having a shunt (R_p) and series resistance (R_s) due to leakage current.

The modelling design of PV module is described below [12]:

The output PV module current is given in Eq. (1)

$$I = N_p I_{ph} - N_p I_d - I_p \quad (1)$$

where I_{ph}= photo current in Amperes

I_d = diode current in Amperes

I_p = leakage current in Amperes in shunt resistance R_p

The Photo current (I_{ph}) can be computed from Eq. (2)

$$I_{ph} = [I_s + K_s(T_e - 298)] \times I_r/1000 \quad (2)$$

where I_s = short circuit current in Amperes

K_s = short circuit current constant

T_e= operating temperature in kelvin

I_r = solar irradiation in W/m^2

The diode current (I_d) is computed from Eq. (3)

$$I_d = I_O \left[\exp\left(\frac{V_{OC}}{A.NV_T}\right) - 1\right] \quad (3)$$

where I_O = saturation current

V_{oc} = open circuit voltage in volts

A = ideality factor

N = Number of series connected solar cells

V_T = thermal voltage

The thermal voltage V_T is given in eq. (4)

$$V_T = \frac{kT_e}{q} \quad (4)$$

where k = Boltzmann's constant

q = charge of electron in coulombs

The saturation current (I_o) is given in eq. (5) below

$$I_O = I_{rs}\left(\frac{T_e}{T_r}\right)^3 \times exp\left[\frac{qE_g}{Ak}\left(\frac{1}{T_r} - \frac{1}{T_e}\right)\right] \quad (5)$$

where I_{rs} = reverse saturation current

T_r = nominal temperature in kelvin

E_g= band gap energy in eV

The reverse saturation current (I_{rs}) is given in eq. (6) below

$$I_{rs} = \frac{I_s}{\exp\left(\frac{qV_{oc}}{NkAT_e}\right) - 1} \quad (6)$$

The leakage current (Ip) is given in eq. (7) below

$$I_p = \frac{V \times \frac{N_p}{N_s} + I \times R_s}{R_p} \quad (7)$$

where N_p = number of parallel connected modules

N_s = number of series connected modules

TABLE I. PV CHARACTERISTICS

Parameters	Value
V_{oc}	32.9 V
I_s	8.21 A
P_{max}	200 W
A	1.3417
N	54
N_s	1
N_p	1
R_{sh}	951.9317 Ω
R_s	0.2127 Ω
I_r	1000 W/m^2
K_s	0.387×10^{-3}
E_g	1.1 Ev
V_{mp}	27.2 V
I_{mp}	7.35 A

The P-V characteristics and I-V characteristics of PV array is illustrated in Fig. 3 and Fig. 4.

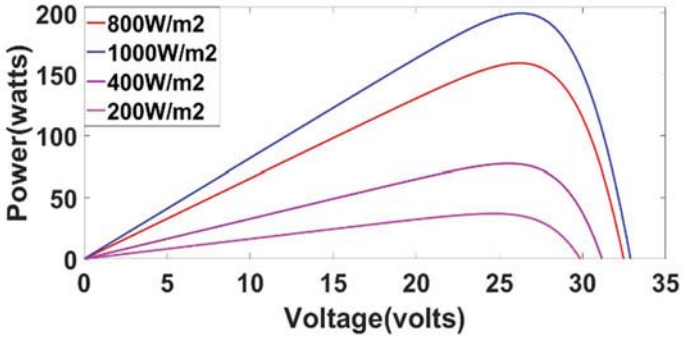
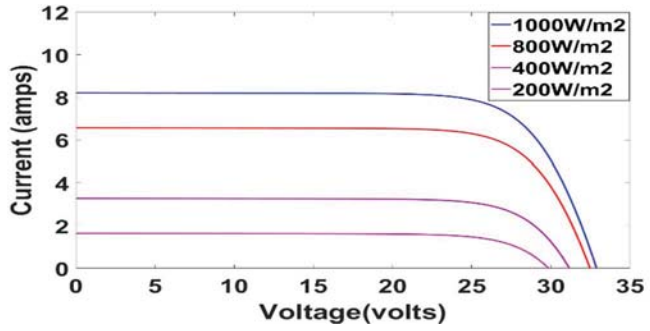
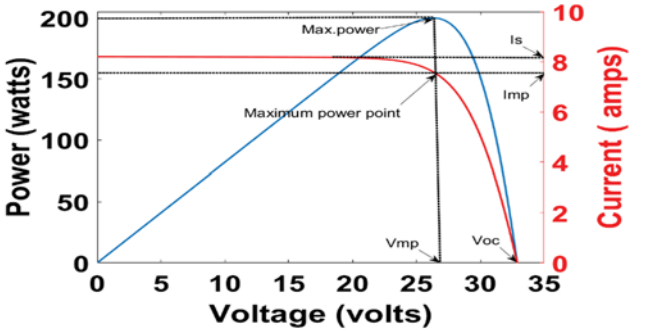


Fig. 3. P-V Characteristics of PV array



(a) I-V characteristics



(b) Characteristics showing maximum power point

Fig. 4. Characteristics of PV array (a) I-V (b) showing maximum power point

B. *Maximum power point tracking(MPPT)*

Maximum power point tracking control is used to obtain maximum power from solar PV module. It is also used to generate the duty cycle required for DC-DC converter. In this paper, Perturb and Observe algorithm has been used. It is a conventional algorithm which is easy to implement in real time as compared to other methods and gives fairly accurate results. The P&O algorithm can be mathematically represented by

$$\frac{dP}{dV_{pv}}(i) = \frac{P(i)-P(i-1)}{V_{pv}(i)-V_{pv}(i-1)} \tag{8}$$

where P(i), P(i-1) are present and previous power and $V_{pv}(i), V_{pv}(i-1)$ are present and previous voltage.

When $\frac{dP}{dV_{pv}}$ >0 then direction moves forward towards maximum power point, voltage must be incremented or increased. If $\frac{dP}{dV_{pv}}$ <0 then direction moves backward towards maximum power point, voltage must be decremented.

C. *Boost converter*

A boost converter is a step-up converter and plays a vital role in PV applications because low voltage is obtained from PV module which is not sufficient to drive the load. Boost converter is used to step-up the PV voltage and then connected to the DC link of each of the H-bridge inverter. The required duty cycle is generated by MPPT controller. The illustrative figure of boost converter is drawn below in Fig. 5.

The designing of boost converter and its parameters are calculated with the help of equations 9-11.

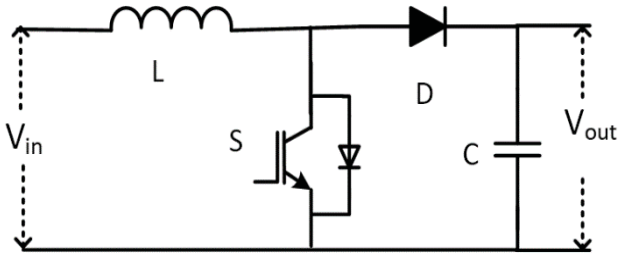


Fig. 5. Diagram of Boost Converter

$$\text{Duty cycle (D)} = \frac{V_o - V_i}{V_o} \tag{9}$$

where V_o = output voltage

V_i = input voltage

$$\text{Inductor (L)} = \frac{V_i \times D \times T}{\Delta i_l} \tag{10}$$

where T = time period of switching

Δi_l = inductor ripple current

$$\text{Capacitor (C)} = \frac{V_o \times D \times T}{R \times \Delta V_o} \tag{11}$$

where R = resistance

ΔV_o = capacitor ripple voltage

Where the Δi_l is the 3-5% of output current and ΔV_o is the 3-5% of output voltage. The values of inductor and capacitor and duty cycle and resistance are values are given in Table II.

Table II. Design values of boost converter

Parameters	Value
L	2.4mH
C	87.77μF
D	0.395
R	10Ω

D. *Seven level Cascaded H-bridge based multilevel inverter*

A cascaded H- bridge multilevel inverter is a popular configuration used in medium voltage applications. In this topology, cascade connection of three H-bridges is carried out so that the output voltage of whole system will be combination of the output of each H-bridge to form different level voltages. If we cascade 'n' number of H-bridges, then we get 2n+1 level of voltages in output voltage wave form. Each H bridge requires separate dc source which can be provided by either battery or PV cell. Cascaded H-bridge can be operated in symmetric as well as asymmetric conditions. Under symmetric condition, all the dc level voltages are the same and under asymmetric condition, different dc level voltages are used. In this paper, seven level cascaded H-bridge multilevel inverter has been realized in symmetric condition so that all the dc voltages are equal as V_{dc1}=V_{dc2}=V_{dc3}=V_{dc} and output voltage will be in form of V_o=V_{dc1}+V_{dc2} + V_{dc3}.

III. MODULATING TECHNIQUES

Several modulation techniques have been developed for multilevel inverter. As described in Fig. 6, modulating techniques can be broadly categorized into two viz. operation at fundamental switching frequency and high switching frequency PWM. The main focus of this paper is on multilevel carrier based PWM. The principle of carrier based PWM method is to use the i-1 carrier signals with reference signal for i level inverter. Difference of carriers will be as follows

- carrier frequency
- carrier amplitude
- carrier phase
- carrier dc offset

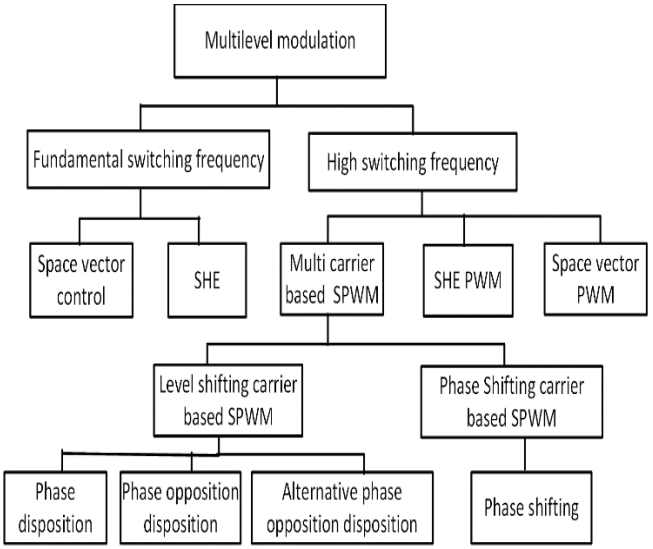


Fig. 6. Classification of multilevel modulation techniques

Multilevel carrier based PWM are classified as follows

- phase disposition (PD) carrier-based PWM
- phase opposition disposition (POD) carrier based PWM
- alternate phase opposition disposition (APOD) carrier based PWM
- phase shifting (PS) carrier based PWM

These techniques are discussed below and developed for the system represented in Fig.1.

A. Phase disposition carrier-based PWM

In phase disposition (PD) carrier-based PWM, all the carriers will be in same phase angle, same frequency and equal magnitude, but the difference will be in dc offsets so as to occupy contiguous bands. This is illustrated in Fig.7. In this, maximum harmonic energy is found at the carrier wave frequency and all other harmonic components are centered as side band harmonics on carrier wave frequency. In cascaded H-bridge seven level multilevel inverter, six carrier waveforms (of frequency 1KHz) have been used along with a sinusoidal reference waveform of 50Hz. The gate control is obtained when each of carrier waveforms with sinusoidal reference signal are compared, which in turn controls respective gate.

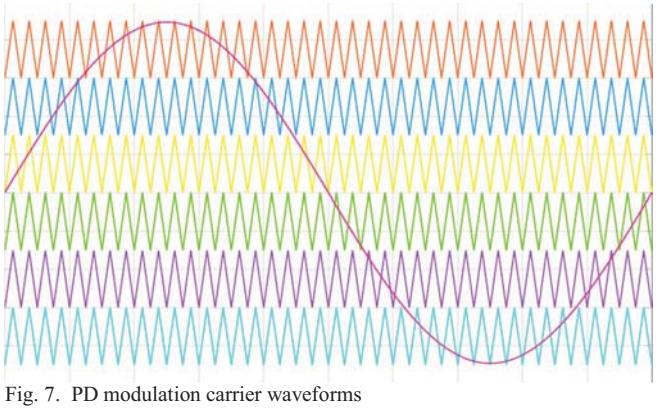


Fig. 7. PD modulation carrier waveforms

B. Phase opposition disposition carrier-based PWM

In this modulating technique as shown in Fig.8, phase opposition disposition (POD) carrier-based PWM, the carriers are having equal magnitude and same frequency, but the carriers have difference in dc offset and the carriers just above the zero reference will be in same phase angle and just below the zero reference carriers are in same phase angle and the phase angle difference between the above zero reference carriers and below zero reference carriers will have the 180 degrees phase shift. The maximum harmonic energy is found around the carrier wave frequency as side band harmonics

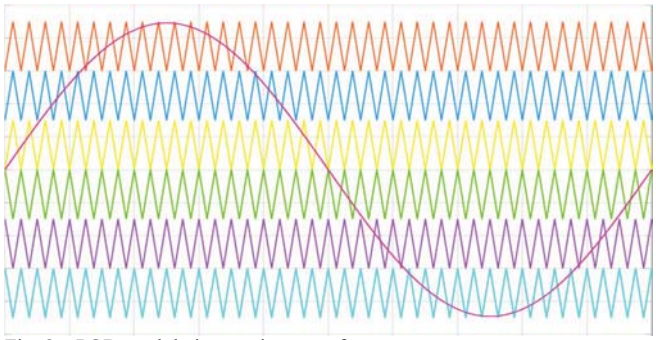


Fig. 8. POD modulation carrier wave forms

C. Alternate phase opposition disposition carrier-based PWM

In alternate phase opposition disposition (APOD) carrier-based PWM, all the carriers will have equal magnitude and same frequency, but the carriers have difference in dc offset and phase shifted by 180˚ alternately. The maximum harmonic energy is centered around carrier wave frequency as side band harmonics and no harmonics at carrier wave frequency. This is represented in Fig.9.

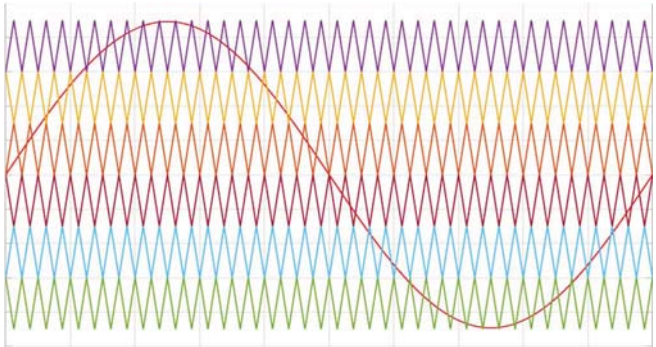


Fig. 9. APOD modulation carrier wave forms

D. Phase shifting carrier-based PWM

In phase shifting (PS) carrier-based PWM, all the carriers will have equal magnitude and same frequency and dc offset but the difference is that, each carrier will have certain phase shift angle π/m where, m= number of cascaded H bridges that are connected in series. This technique gives rise to cancellation of all the carrier and associated sideband harmonics. In cascaded H bridge seven level inverter, the phase shifting angle is 60˚.

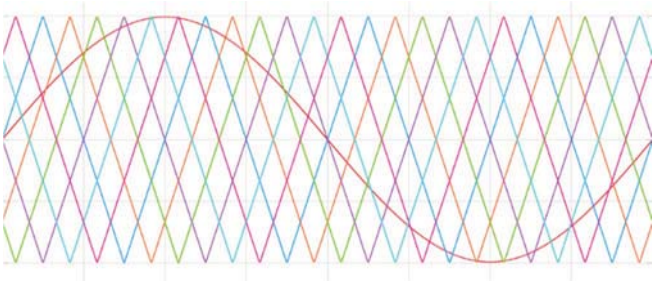


Fig. 10. PS modulation carrier wave forms

IV. SIMULATION RESULTS

Fig. 11. gives the output voltage results for the PV integrated with boost converter at the DC link of three H bridges. All PV modules are identical and operated under same irradiance and same temperature condition. For an input voltage of 27.2 V, the output voltage is boosted to 45V.

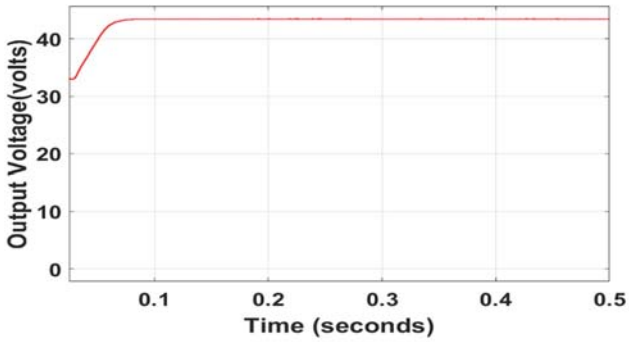
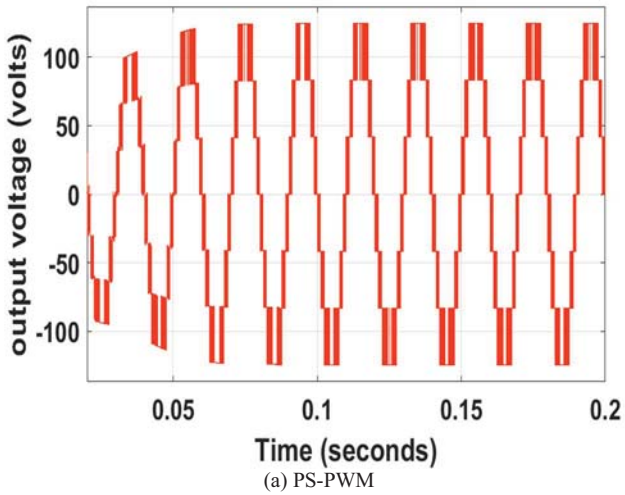
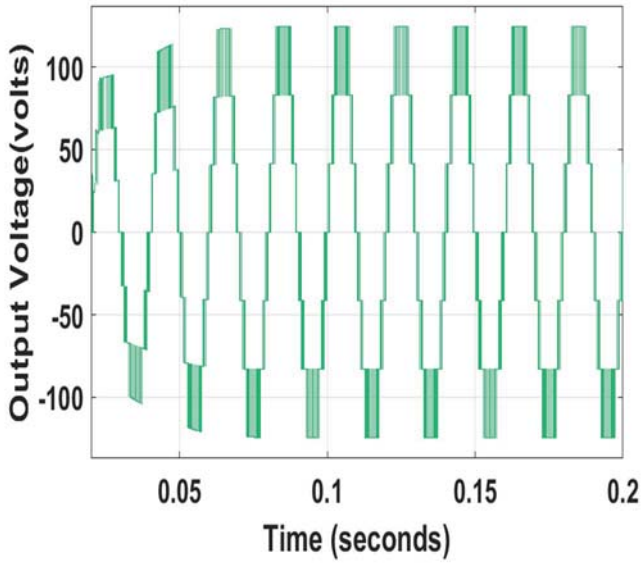


Fig. 11. output voltage of PV with boost converter and MPPT

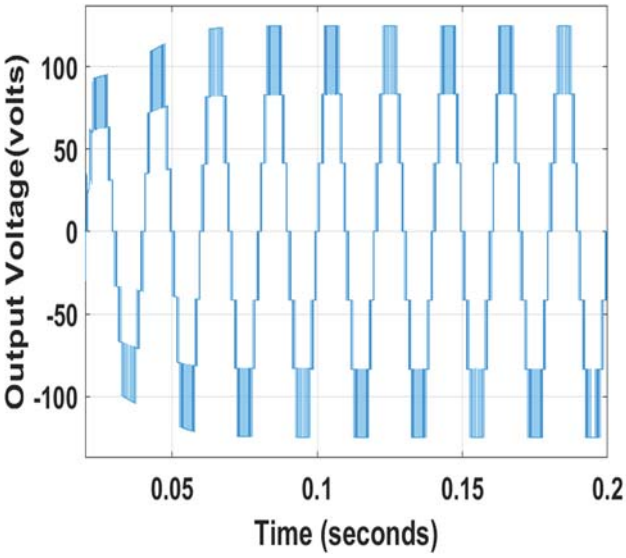
Fig. 12. gives the output voltages with three cascaded H - bridge multilevel inverter. It can be observed that with each of the modulating techniques, the levels are obtained as follows +45, +90, +135, 0, -45, -90, -135.



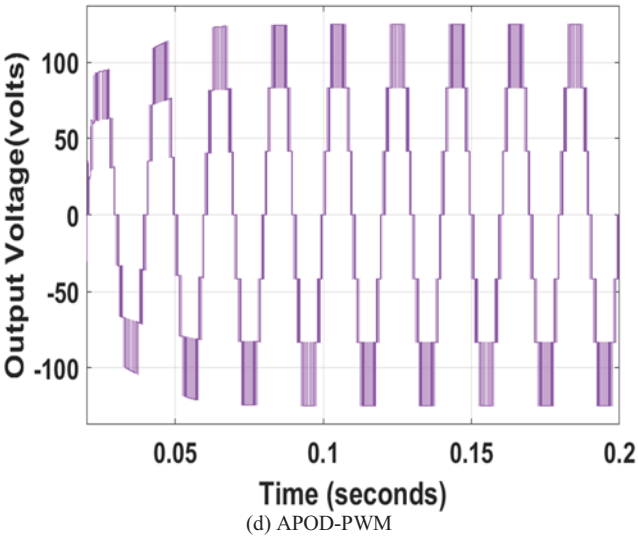
(a) PS-PWM



(b) PD-PWM



(c) POD-PWM



(d) APOD-PWM

Fig. 12. Output voltage waveforms of cascaded H bridge inverter with different modulating techniques

TABLE III. Comparison of different Modulating Techniques

Modulation technique	Output Voltage(rms)	%THD
PD	88.83	18.73
POD	88.73	18.93
APOD	88.72	19.22
PS	89.24	17.98

V. CONCLUSION

This paper has discussed the design of PV modules which are integrated at each of the H-bridge of the multilevel converter. The three H-bridges are connected in cascade configuration. Simulation model has been developed using MATLAB and Simpower system. Performance results with four different PWM techniques like PD, POD, APOD and PS techniques have been discussed. It can be inferred from the results of Table III, that Phase Shifting technique gives less percentage THD as compared to the other techniques. It is preferable to use PS-PWM technique for seven level cascaded H bridge multilevel inverter when integrated with PV modules.

ACKNOWLEDGMENT

The authors are thankful to the DST, SERB for the Sponsored project (EMR/2016/001874).

REFERENCES

[1] G. Eas Kannan N, Vakeesan D. Solar energy for future world: – a review. renew sustain energy rev,vol. 62,pp. 1092–105,2016.

[2] Liu L, Meng X, Liu C. “A review of maximum power point tracking methods of PVpower system at uniform and partial shading”Renew Sustain Energy Rev,vol. 53,pp. 1500–1507,2016.

[3] N. prabaharan, K. palanisamy, “Analysis and integration of multilevel inverter configuration with boost converters in photovoltaic system” Energy conversion and management, vol. 128, pp. 327-342, 2016.

[4] Jose´ Rodrı´guez, Leopoldo G. Franquelo, Samir Kouro, Ramo´n C. Portillo, Ma A´ ngeles Martı´n Prats, Marcelo A. Pe´rez” Multilevel converters: an enabling technology for high-power applications” Proc. IEEE,Vol. 97,pp. 1786-1817, 2009.

[5] Natarajan Prabaharan, Kaliannan Palanisamy, “Analysis of cascaded H-bridge multilevel inverter configuration with double level circuit”, IET power electron., vol. 10, no. 9, pp. 1023-1033, 2017.

[6] Prachi Salodkar, Sandeep. N, P. S. Kulkarni, Udaykumar R. Y” A comparison of seven-level inverter topologies for multilevel DC-AC power conversion” IEEE Int. Conf. on Power Electronics, Drives and Energy Systems (PEDES), 2014.

[7] Jose I. Leon, Sergio Vazquez, Leopoldo G. Franquelo” Multilevel converters: control and modulation techniques for their operation and industrial applications” Proc. IEEE,Vol. 105, pp. 2066-2081, 2017.

[8] Abuzaid Saeed Gadalla, Xiangwu Yan, Sara Yahia Altahir, Hashim Hasabelrasul” Evaluating the capacity of power and energy balance for cascaded H-bridge multilevel inverter using different PWM techniques" The sixth IEEE Int. Conf. on Renewable Power Generation (RPG) ,2017.

[9] P. Palanivel, S.S. Dash, "Analysis of THD and output voltage performance for cascaded multilevelinverter using carrier pulse width modulation technique", IET Power Electron., vol. 4, no. 8, pp. 951-958, 2010.

[10] Christopher D. Townsend, Terrence J. Summers, Robert E. Betz” Phase-shifted carrier modulation techniques for cascaded H-bridge multilevel converters” IEEE Trans. Ind. Electron.,vol. 62, pp. 6684-6696, 2015.

[11] R. Naderi, A. Rahmati, "Phase-shifted carrier PWM technique for general cascaded inverters", IEEE Trans. Power Electron.,vol. 23, no. 3, pp. 1257-1269, 2008.

[12] Xaun Hieu Nyuyen, Minh Phuong Nguyen “Mathematical modelling of photovoltaic cell/module/arrays withs tags in Matlab/simulink” a springer open journal , environmental system research,vol. 4, no. 24,2015.

[13] Janardhan Kavali, Arvind Mittal “Analysis of various control schemes for minimal total harmonic distortion in cascaded H-bridge multilevel inverters” Journal of Electrical Systems and Information Technology ,vol. 3 , pp. 428–441,2016.

Performance Analysis of FIS and ANFIS based MPPT for Solar PV System with Boost, SEPIC and CUK Converter Topologies

Mohak Jain
Department of Electrical Engineering
Delhi Technological University

Bharat Bhushan
Department of Electrical Engineering
Delhi Technological University

ABSTRACT
This paper works on the performance comparison of PV system implemented with three different DC/DC converter topologies named Boost, Cuk and SEPIC converters. Along with these three converters the MPPT techniques used for maximum power point tracking are FIS and ANFIS. The whole PV system is incorporated with these two soft computing techniques and three converters and voltage variation results have been obtained accordingly, then these results are compared simultaneously to evaluate the overall performance of the PV system in each case

Keywords
PV panel, MPPT techniques, FIS, ANFIS, Boost converter, cuk converter, SEPIC converter

1. INTRODUCTION
Solar PV system is a very broad and very relevant topic. Many research papers have already been published in the field of MPPT algorithms such as comparison of classical MPPT approaches such as Perturb and Observe Technique and Incremental conductance, or Fuzzy logic and neural network, some of the research has also be completed in suggesting the new algorithms for MPPT, also work has been done in the field of converters related to PV system and grid connected PV array. In paper[1] the study of battery charge controller used in standalone photovoltaic system has been done as it is a major component of standalone PV system. In [2] a soft computing technique that is adaptive neuro fuzzy inference system has been studied, in [3] also same soft computing technique ANFIS has been covered whereas [4] presents the application of ANFIS on the intelligent systems however [5] talks about the MPPT techniques when implemented on solar vehicle the complete simulation with analysis has been covered in this research work, now [6] covers the controlling of induction motor drives used in various types of applications, in [7] MPPT tracking using fuzzy logic controller when applied to a grid connected PV system has been discussed, however [8] works on the designing and proper selection of parameters of PV system for the production of electricity in Malaysia, in [9] application of large number of PV modules for distribution of energy in urban areas has been covered whereas in [10] a complete case study on the renewable power of malyasia has been studied, in next [11] neural based MPPT for PV system connected with boost converter was studied

2. MAXIMUM POWER POINT
Maximum Power Point Tracking, generally referred to as MPPT, drives solar PV array to operate in such a manner that maximum power which can be generated by PV module or array can be extracted fully to transfer it further. MPPT is not any mechanical device or mechanical technique to extract power but it works on control algorithm specially designed for a particular task. MPPT can be used along with with a mechanical tracking system, but both the systems act differently in case of power tracking. MPPT algorithms use the variation of irradiance and temperature to obtain or extract the maximum power from solar PV array. The voltage at which PV array can gives maximum power is called 'maximum power point' (or peak power voltage). Maximum power depends on solar radiation, ambient temperature and varies accordingly to the changes of these parameters. A characteristic PV module generates power having maximum power voltage of around 17 V measured when temperature of the cell is 25 degree Celsius, it can go down up to 15 V on a very hot day and it can also elevate to 18 V on a very cold day. The first and foremost principle of MPPT is to extract maximum power from the PV module by the application of suitable algorithm. MPPT Algorithm operates on the simple logic that, MPPT calculates the output of PV module, then compares it to voltage of battery then fix the optimum power which can be generated by PV module which helps in charging of battery and then converts it to the suitable voltage to obtain maximum current into battery. It can also use to supply power to a DC load, which is connected directly to the battery. MPPT is generally used to charge the deep discharged batteries mostly on cloudy days or time of faults

3. MPPT TECHNIQUES

3.1 Fuzzy Inference System
Fuzzy logic controller is generally composed of three independent processes which are: fuzzification, second is the rule base operation, and finally defuzzification as we have to convert fuzzy data again into crisp form. In whole fuzzification process, crisp or numerical data that is input variables are transformed into linguistic variables with the help of a membership function. Some of the linguistic variable used in this project are: NB (Negative Big), ZE (Zero) and PB (Positive Big). In Figures 1, 2, 3 given below we can clearly observe the membership functions for two inputs and output. The inputs to a Fuzzy system used as MPPT are generally an error E and the second one is change in error CE.. As dP/dV diminish at the maximum power point, the following approximation can be made.

$$E(n)=P(n)-P(n-1)/V(n)-V(n-1) \quad (1)$$

$$CE(n)=E(n)-E(n-1) \quad (2)$$

Once the value of E and CE are evaluated the rules can be applied to these linguistic variable according to the form stated in rule base the value of output which is usually a duty cycle that is provided to converter can be obtained. The inference system used in this case is mamdani. The selection of linguistic variables that are used to represent dD for the

different combinations of E and CE is totally depends on the data collected or analysed by the user. In the final defuzzification process, the fuzzy controller output which is obtained from linguistic variable is converted again to numerical value or crisp data with the help of membership functions. The defuzzification process generates an analog function in the form of output which is given to the converter in the form of duty cycle to drive the system. MPPT implemented using fuzzy logic controller gives best results when operate under atmospheric conditions. But their overall efficiency depends majorly on the data of controller or engineer or the user by correct computation of error using the rule base as shown in figure 4.

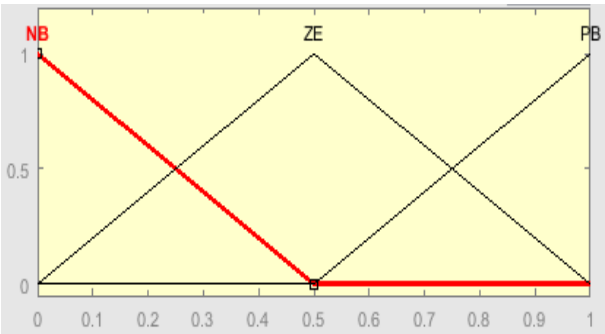


Figure 1: Membership functions for input variable (E)

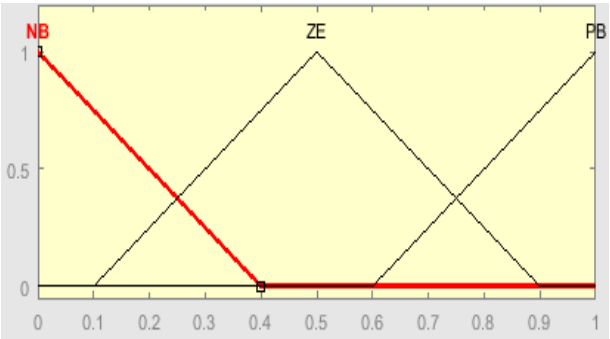


Figure 2: Membership function of input variable (CE)

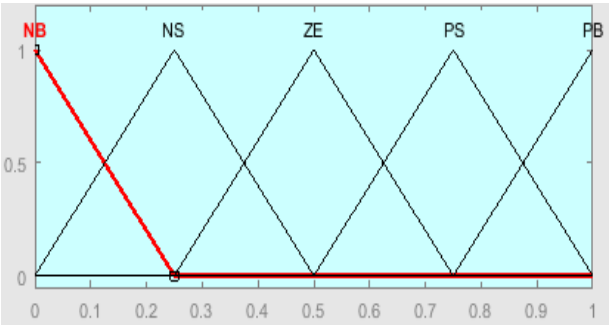


Figure 3: membership function of output variable (dD)

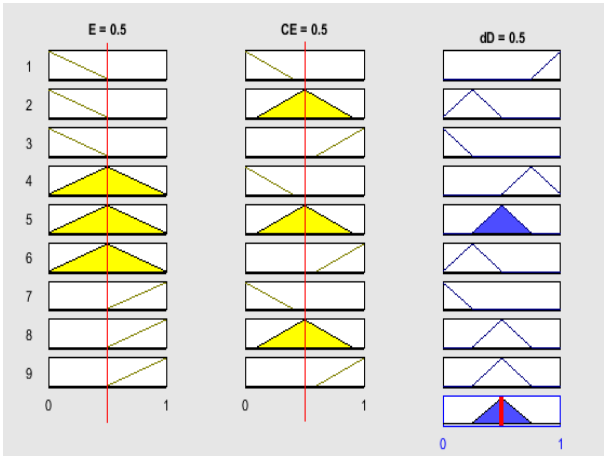


Figure 4: Rule viewer of rule base

3.2 ANFIS based MPPT

Over the past few years there has been a great development in the field of information based on non-linear network. These complex and broad systems cannot be explained or made to work with only one of the controlling techniques hence we require some more efficient way to complete this. One of the algorithm to manage these complex issues is combination of two or more system to accomplish a pre define goal and to overcome the shortcomings of previous controlling methodology. Fuzzy logic is a good tool for displaying uncertainties and approximate reasoning, on the other hand neural network is the best machine in field of learning. Adaptive neuro fuzzy inference system combines the point of interests of fuzzy logic and neural network in one and produce enhanced fuzzy framework which is incorporated with learning mechanism of neural network and hence more efficient. For PV cells also we can create a cross breed system that joins fuzzy logic and neural network to detect the maximum power point.

In this firstly we collect the data of different values of irradiance and temperature and output of panel accordingly which is fed into neuro fuzzy designer and with then help of this data sugeno inference system type fuzzy logic is designed with neural network incorporated in that. We can clearly see the trained rule viewer of FIS in figure 5.

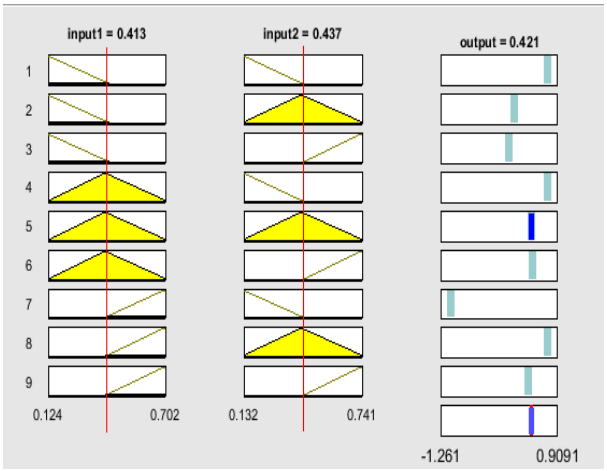


Figure 5: Rule Viewer of trained FIS

The trained ANFIS model is shown in figure 6 along with the final ANFIS system shown in figure 7.

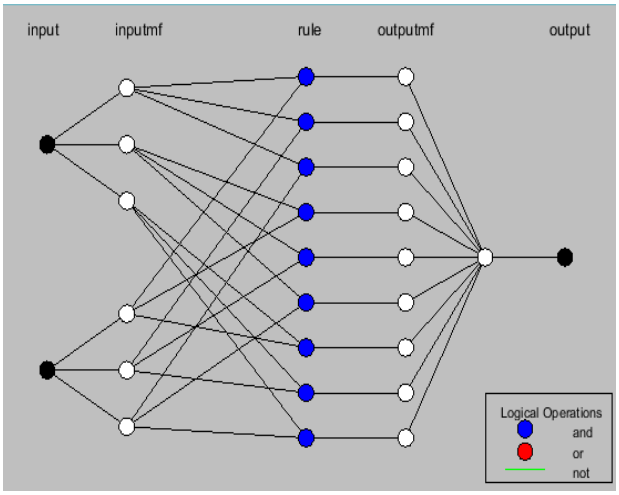


Figure 6: ANFIS model structure



Figure 7: Final Tested ANFIS system

4. DC/DC Converters

A DC to DC converter takes the voltage from a DC source and converts the voltage of supply into another DC voltage level. They are used to increase or decrease the voltage level. The DC/DC converter is mostly used in portable DVD players, automobiles and portable chargers. As most of the equipments need certain range or level of voltage to operate as very high voltage can damage that device and very low voltage cannot make it to run so for such cases a converter is used as it can takes power from the PV panel and varied the voltage by stepping up or stepping down it to a certain level.

4.1 Boost Converter

A boost converter as shown in figure 8 is used to convert the unregulated direct current input voltage, generated by a PV module to a controlled DC voltage with value higher than the input as required by the load that is it boost the voltage value of input and hence named as boost converter. This conversion of voltage is generally perform by applying a DC voltage across an inductor, for a period of time (usually in range of 20kHz to 5MHz) that produces current which flow through it and stores energy magnetically, and then we switch OFF this voltage which results in the transfer of stored energy to the output voltage in controlled way. This voltage is regulated by adjusting the duty cycle. To achieve this fast switching power electronics component like IGBT or MOSFET is used as they dissipate least power. Pulse width modulation (PWM) technique is use to control and regulate total output voltage. The ideal boost converter possess 100% efficiency but in general 70% to 90% of efficiency is obtained.

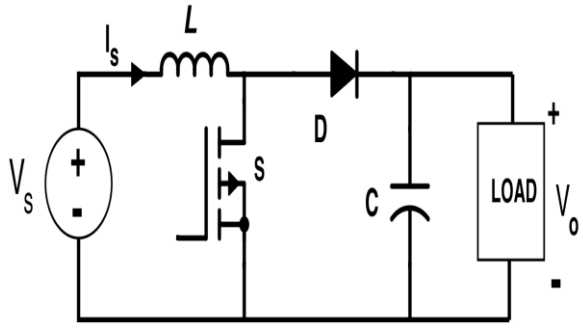


Figure 8: Boost converter

The boost converter as shown in the figure has a constant DC input voltage source Vs, boost inductor L, controlled switch S, diode D, filter capacitor C and a load.

DC voltage gain of converter is given as:

$$G = \frac{V_0}{V_s} = \frac{1}{1-\alpha} \quad (3)$$

Selection of inductor—Inductor with large value increases the startup time slightly whereas low inductance value allow the coil current to increase up to very high values before the switch turns OFF. It is selected on the basis of the maximum allowed ripple current at minimum duty cycle and maximum supply voltage. Boost converter works in continuous conduction mode for inductor value $L>L_c$ where L_c is a critical inductance value and is given by

$$L_c = \frac{(1-\alpha^2)*\alpha*R}{2f_s} \quad (4)$$

where R is the load resistance and f_s is the switching frequency of converter.

Selection of capacitor—the current supplied to the RC circuit is discontinuous that's why a larger filter capacitor is required to decrease the ripples in output voltage. The primary way to select filter capacitor is its capacitance and it's series resistance as this series resistance affects efficiency, low ESR-capacitors is used for best performance. The filter capacitor is use to decrease the ripples in output voltage. Minimum value of filter capacitor that allow current to flow through load when diode is OFF is given by

$$C_{min} = \frac{V_o*\alpha}{f_s*\Delta V_o*R} \quad (5)$$

Where ΔV_o is the ripple in output voltage which is generally 5% of output voltage

4.2 Cuk Converter

A CUK converter as shown in figure 9 is an another type of DC/DC converter which produce output voltage either greater or lesser than the input voltage. It is actually a boost converter which is followed by a buck converter. The main difference is that it consists of an additional capacitor to store energy. As the buck-boost converter produces an inverted output similarly cuk converter also produces an inverted output which can be either higher or lower than the input. As most of

the converters use inductor as their main energy storage element it uses an additional capacitor to store energy

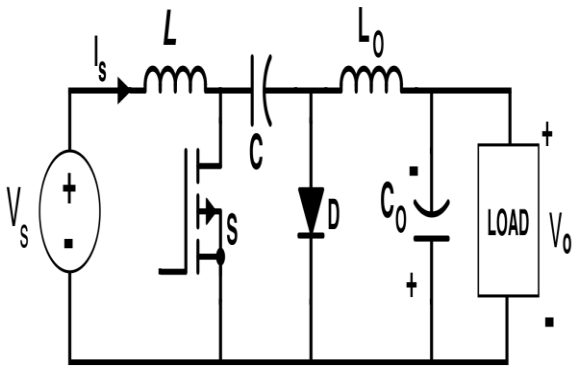


Figure 9: Cuk converter

A cuk converter basically consist of two capacitor, two inductors, one switch and one diode. The transfer of energy is done with the help of capacitor C and two inductors L and L_0 are used to convert input voltage source and output voltage source respectively into current source. The conversion of voltage source into current source is necessary because if capacitor is directly connected to resistance then it will cause high energy loss in the system

Now if we apply voltage sec balance across L

$$V_s\alpha T + (V_s - V_c)(1-\alpha)T = 0 \quad (6)$$

$$\therefore \quad V_s(1-\alpha)V_c = 0 \quad (7)$$

Or $$V_c = \frac{V_s}{1-\alpha} \quad (8)$$

Applying voltage sec balance across L_0 $(V_0 + V_c)\alpha T + V_0(1-\alpha)T = 0$ (9)

$$V_0 + \alpha V_c = 0 \quad (10)$$

$$V_0 = -\alpha V_c = -\frac{\alpha V_s}{1-\alpha} \quad (11)$$

Similarly current through two inductors L and L_0 are stated as follow

$$I = \frac{\alpha^2}{(1-\alpha)^2}\frac{V_s}{R} \ , \ I_0 = \frac{\alpha}{1-\alpha}\frac{V_s}{R} \quad (12)$$

So basically cuk converter combines the features of both boost and buck-boost converter hence it has following advantages

1. It provide continuous input current

2. It provide continuous output current

3. Output voltage obtained can be higher or lower than input voltage.

4.3 SEPIC Converter

A SEPIC converter or single-ended-primary-inductor-converter is also a DC/DC converter that gives output voltage either higher, lower or equal to the input voltage. It is actually a boost converter followed by a buck-boost converter. The major advantage of SEPIC converter over buck boost converter that unlikely buck boost converter it produces a non-inverting voltage output. It uses a series capacitor for energy coupling from input to output and hence can give better results when used in short circuit condition. Unlike cuk converter it has pulsating output which is one of the disadvantage of SEPIC converter, also its fourth order nature make it suitable for slow varying systems only. A detailed circuit diagram of SEPIC converter is shown in figure 10.

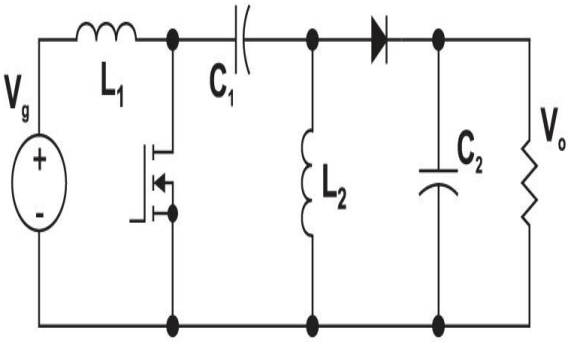


Figure 10: SEPIC converter

During the turn ON time the diode gets reverse biased and coupling capacitor has negative polarity which helps in charging of inductor L_1 and L_2 via source and coupling capacitor gets discharge on the other hand in case of turn OFF time the diode gets forward biased and inductor L_1 helps in the charging of coupling capacitor whereas inductor L_2 transfer its stored energy to the output and this is how an SEPIC converter works.

Duty cycle selection-for continuous mode operation duty cycle is given by

Output of a SEPIC converter is given by

$$V_0 = \frac{\alpha * V_g}{1-\alpha} \quad (13)$$

If we consider losses due to voltage drop across diode then output can be stated as-

$$V_0 + V_D = V_0 = \frac{\alpha * V_g}{1-\alpha} \quad (14)$$

Due to this final expression of duty cycle becomes

$$\alpha = \frac{V_0 + V_D}{V_g + V_0 + V_D} \quad (15)$$

Inductor calculation- inductors are basically used in converters to produce a ripple free output.

The ripple current flowing through L_1 and L_2 is given by

$$\Delta I_L = I_{in} * 40\% = I_0 * \frac{V_0}{V_g} * 40\% \quad (16)$$

The value of two inductors can be calculated as-$L_1 = L_2 = L = \frac{V_{g,min}}{\Delta I_L * f_s} * \alpha_{max}$ (17)

Coupling capacitor calculation- The value of capacitor depends on RMS current whose expression is given as-

$$I_{c1,rms} = I_0 * \sqrt{\frac{V_0 + V_D}{V_{g,min}}} \quad (18)$$

Peak to peak ripple voltage can be given as

$$\Delta V_{cs} = \frac{I_0 * \alpha_{max}}{C * f_s} \quad (19)$$

5. SIMULATION AND RESULTS

The basic Block Diagram of whole system on which analysis is done is shown in figure 11 below, it is divided into three parts the first one is PV array then the second art is DC/DC converter which is getting the gate pulse through the MPPT technique which has been applied to extract maximum power from the PV panel and the third segment is conversion of converter output into AC supply through which is supplied to the grid.

Table 1. Technical Specifications of PV array

TECHNICAL SPECIFICATIONS	VALUE
Cells Per Module	60
Open circuit voltage (V_{oc})	36.96 V
Short circuit current (I_{sc})	8.49 A
Maximum power	240.694 W
Voltage at MPP (V_{mp})	30.2 V
Current at MPP(I_{mp})	7.97 A

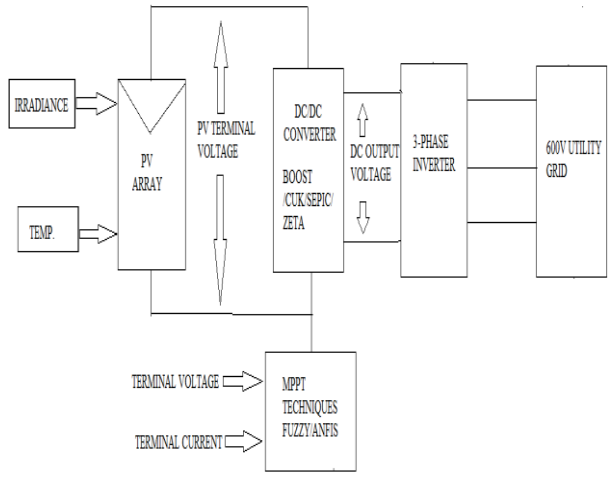


Figure 11: Schematic block diagram of system

The Panel which is selected for analysis is one of the specified panels of MATLAB/SIMULINK library and that is Neo Solar Power D6P240B3A, in this project five parallel string with four panel in series connected in each string is taken into consideration for analysis. Hence we have an array of 20 such modules. Technical specifications of this panel is shown below:

The two major inputs to PV array are irradiance and temperature. In this project analysis is done for three different values of irradiance and temperature. For the daytime the value of irradiance is 600W/m^2 and temperature is 25˚C. For noontime the irradiance value is taken as 1000 W/m^2 and temperature is 45˚C and for evening time the value of irradiance is set at 400 W/m^2 and temperature is taken as 32˚C.These values are plot using signal builder in MATLAB as shown in figure 12 and 13.

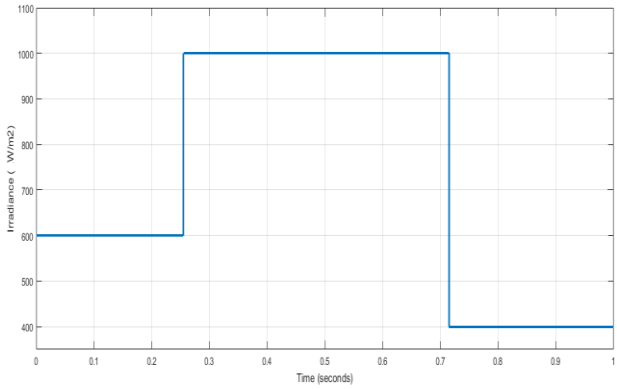


Figure 12: Irradiance plot for three different values

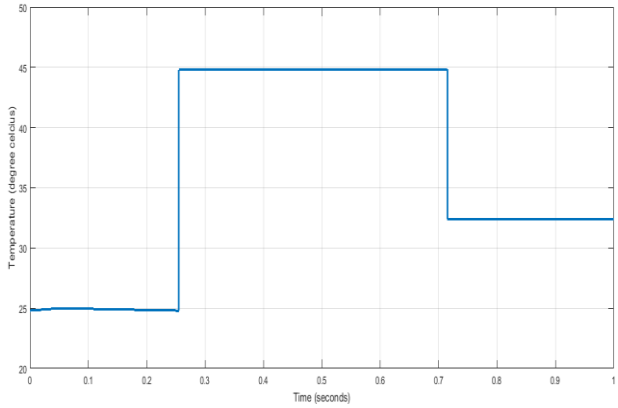


Figure 13: Temperature variation

5.1 PV system with boost converter

The voltage variation of PV output and output of converter is shown in figure 14 for FIS and figure 15 for ANFIS

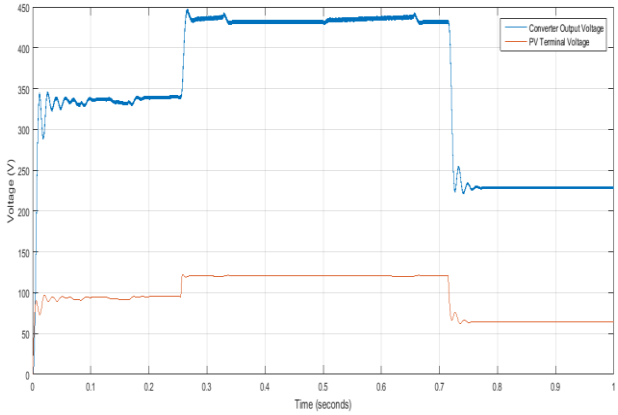


Figure 14: Voltage variation for FIS based MPPT

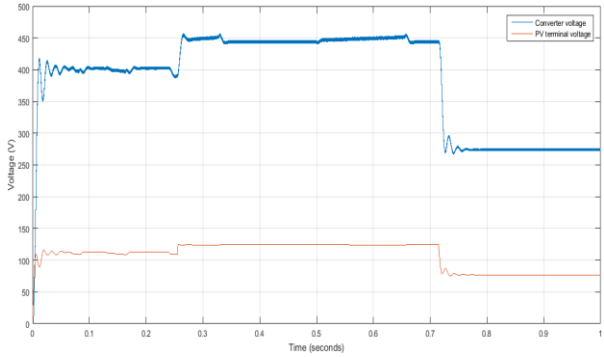


Figure 15: Voltage variation for ANFIS based MPPT

Table 2. Boost converter performance comparison

MPPT TECHNIQUES	IRRADIANCE/TEMP.	PV TERMINAL VOLTAGE (V)	CONVERTER OUTPUT VOLTAGE
FUZZY LOGIC	600/25	99.8	356.42
	1000/45	109.9	392.5
	400/32	80.2	286.42
ANFIS	600/25	108.2	386.42
	1000/45	110	392.85
	400/32	98.6	352.14

5.2 PV system with Cuk converter

Voltage output for cuk converter is shown in figures 16 and 17 for FIS and ANFIS based MPPT respectively

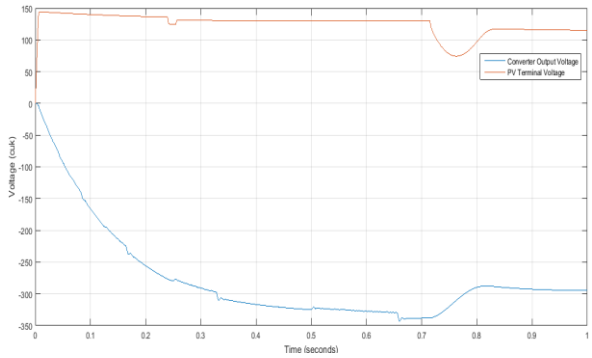


Figure 16: Voltage variation for FIS based MPPT

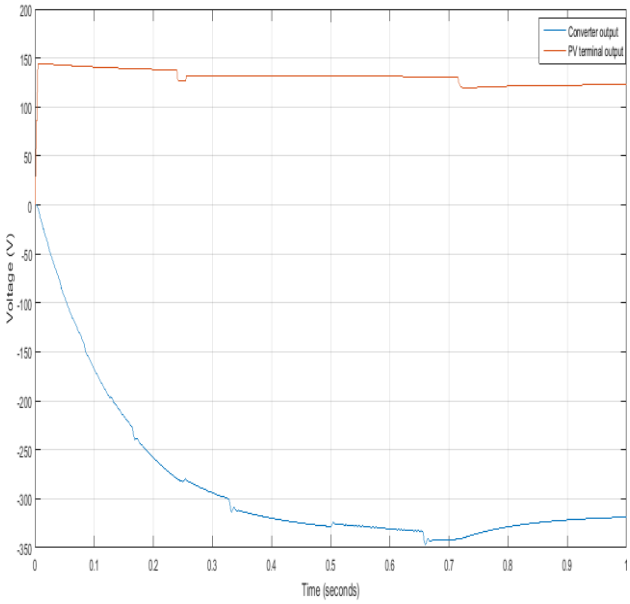


Figure 17: Voltage variation for ANFIS based MPPT

Table 3.Cuk converter performance comparison

MPPT TECHNIQUES	IRRADIANCE/TEMP.	PV TERMINAL VOLTAGE (V)	CONVERTER OUTPUT VOLTAGE
FUZZY LOGIC	600/25	119.1	-338.24
	1000/45	108.2	-307.28
	400/32	105.6	-299.90
ANFIS	600/25	120	-340.8
	1000/45	109.4	310.69
	400/32	107.4	-305.01

5.3 PV system with SEPIC converter

The output waveforms for FIS and ANFIS based MPPT is shown in figure 18 and 19 respectively

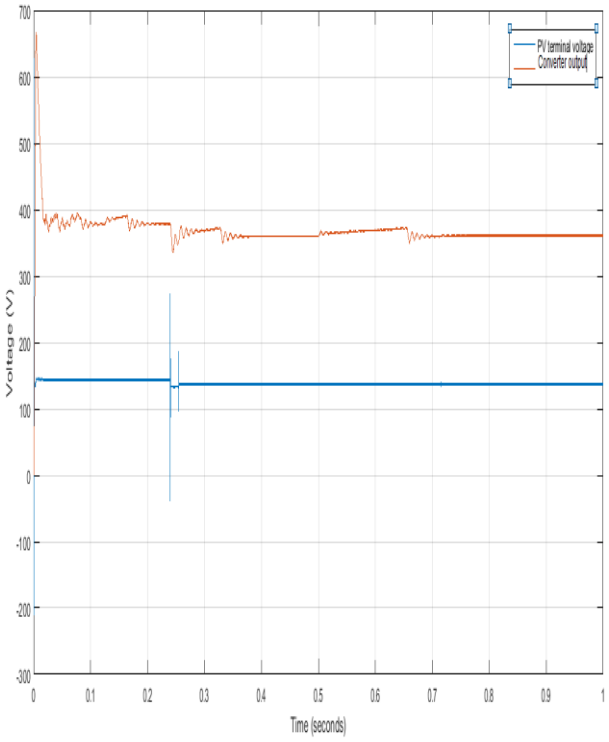


Figure 18: Voltage variation for FIS based MPPT

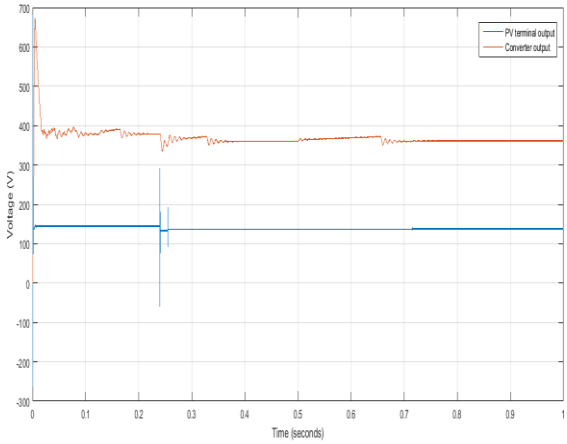


Figure 19: Voltage variation for ANFIS based MPPT

Table 4. SEPIC converter performance comparison

MPPT TECHNIQUES	IRRADIANCE /TEMP.	PV TERMINAL VOLTAGE (V)	CONVERTER OUTPUT VOLTAGE
FUZZY LOGIC	600/25	109.6	356.3
	1000/45	109.7	358.2
	400/32	108.3	349.1
ANFIS	600/25	110	358.4
	1000/45	109.7	370.9
	400/32	109	352.5

6. CONCLUSIONS

From the above work it can be concluded that the performance of ANFIS based MPPT is slightly better than FIS based MPPT in achieving the maximum power point. Also if we talk about the converters then each configuration boost up the voltage according to the parameters of its components and duty cycle but the variations in voltage are more in case of boost converter due to change in values of temperature and irradiance whereas voltage is almost constant in case of cuk and SEPIC converter.in case of cuk converter the output generated is inverted one whereas in case of SEPIC the ripple content is very high hence for stable output we can use cuk converter or SEPIC Converter whereas for ripple free voltage boost converter can be used.

7. REFERENCES

[1] Harrington S, Dunlop J (1992) Battery charge controller characteristics in photovoltaic systems. In: Proceedings of the 7th annual battery conference on advances and applications. Long Beach, California, 21 Jan 1992

[2] Jang, J.-S.R. (1993). "ANFIS: adaptive-network-based fuzzy inference system". IEEE Transactions on Systems, Man and Cybernetics 23 (3). doi:10.1109/21.256541, 1993.

[3] Borowy BS, Salameh ZM (1996) Methodology for optimally sizing the combination of a battery bank and PV array in a wind/PV hybrid system. IEEE Trans Energy Conv 11(2):367–375

[4] Lin C-T, Lee CSG (1996) Neural fuzzy systems: a neuro-fuzzy synergism to intelligent systems. Prentice-Hall, Upper Saddle River

[5] H. Knopf, "Analysis, Simulation, And Evaluation of Maximum Power Point Tracking (MPPT) Methods for a solar power vehicle," in Electrical and Computer Engineering, vol. Master of Science in Electrical and Computer Engineering: Portland State University 1999, pp. 177.

[6] A.M. Khambadkone, and J. Holtz, "Current Control in Over-modulation Range for Space Vector Modulation based Vector Controlled Induction Motor Drives," IEEE Industrial Electronics Society, Vol.2, pp. 1134- 1339, 2000.

[7] N. Patcharaprakitia, and al. "Maximum power point tracking using adaptive fuzzy logic control for grid-connected photovoltaic system", in IEEE Power Eng. SocietyWinter Meeting,2002, pp. 372-377.

[8] Ahmed MM, Sulaiman M (2003) Design and proper sizing of solar energy schemes for electricity production in Malaysia. National Power and Energy Conference 2003, pp 268–271

[9] Conti S, Raiti S, Tina G, Vagliasindi U (2003) Integration of multiple PV units in urban power distribution systems. Sol Energy 75:87–94

[10] A. Zain-Ahmed, K. Sopian, Z. Zainol Abidin and M. Y. H. Othman, "The Availability of Daylight from Tropical Skies – A Case Study of Malaysia", Renewable Energy, Vol.28, Issue 15, pp. 2355-2365, December 2003.

[11] M. Veerachary, T. Senjyu, and K. Uezato, ―Neural-network-based maximum- power-point tracking of coupled-inductor interleaved boost converter-supplied

International Journal of Mechanical and Production Engineering Research and Development (IJMPERD)
ISSN (P): 2249–6890; ISSN (E): 2249–8001
Vol. 9, Issue 5, Oct 2019, 961–972
© TJPRC Pvt. Ltd.

TRANS STELLAR
•Journal Publications •Research Consultancy

PERFORMANCE EVALUATION OF ABSORPTION REFRIGERATION SYSTEMS USING INTELLIGENT OPTIMIZATION TECHNIQUES: A REVIEW

RAVINDRA KANNOJIYA[1] & RAJESH KUMAR[2]

[1]*Research Scholar, Department of Mechanical Engineering, Delhi Technological University, Delhi, India*

[2]*Professor, Department of Mechanical Engineering, Delhi Technological University, Delhi, India*

ABSTRACT

Absorption refrigeration technologies have developed to provide enormous contribution to the industrial as well as residential applications. Providing cooling by utilization of renewable energy mediums as low grade heat and many others, are of utmost importance to the sustainable energy needs and surrounding preserving approach. This study provides an approach of different absorption refrigerating methods and the course of their development from the perspective of thermodynamics and economics. Theoretical and actual use for refrigerating machines with various pairs of working substances assisted by limited as well as new energy with recent advances are included in the present work. Thermally powered refrigeration technologies are not only dependent on nature of energy source but also on cost of the components during their operation and maintenance. Exergetic efficiency, exergy destruction, COP, ECOP and such other characteristics are the essential parameters which need to be synchronized with cost. To deal with these multiple objectives, optimization of the refrigeration systems becomes significant for better utilization of the sources. Many researchers have presented the ways for analyzing the performance through evolutionary algorithms as well as thermo-economic methodologies. The use of cumbersome mathematical and numerical techniques is always not feasible to provide better performance. The work presented here attempts to encourage the use of intelligent optimization techniques for analysis of performance characteristics.

KEYWORDS: Absorption Refrigeration, Evolutionary Algorithms, Exergy, Optimization & Renewable Energy

Received: Jul 12, 2019; **Accepted**: Aug 06, 2019; **Published**: Sep 25, 2019; **Paper Id.**: IJMPERDOCT201985

Original Article

1. INTRODUCTION

The modern trends of global world energy consumption imply that dependency on the conventional resources of energy is not enduring and also require environmental control from contaminating elements. The utilization of other sources of energy like wind, energy from Sun, from bio-degradable substances, geothermal and other non-conventional sources can be of utmost importance in the development of advanced machines that may fulfill the energy needs globally. The absorption refrigeration systems work on the heat-driven input. The heat can be given to the system either by conventional sources or renewable energy sources. The encouragement provided by the effort to protect atmosphere and ozone layer, researchers are trying to reduce the pollution effects. Global warming takes place when emissions from the combustion of oil, natural gas, coal and other gases, and other conventional sources chlorofluorocarbons, hydro-chlorofluorocarbons and water vapor, gets accommodated in the ecosystem. Refrigeration industry is taking care of the adverse effect on the environment. In Europe, the protocol is followed for the air conditioning systems in vehicles. Checking and remedies are needed for all refrigerating machines and other thermal systems if the protocol gets violated. Less consumption of energy for refrigeration cannot only be achieved only relying on efficient use of working fluids which are vital for solar refrigerating setup. Taking into

consideration that cooling requirements are very high with the rise in intensity of radiation, solar refrigeration has been of importance which gives an option for cooling. Solar operated absorption refrigerating systems have various configurations with different refrigerant-absorbent elements. The modern scenario requires energy sustainability of the thermal systems for all major applications. For rural areas, an NH_3-H_2O system was observed experimentally using sun as source of input but problem of leakage occurred in various components [1]. This situation required improvement in design as well as analysis for further research. The performance of the system was poor and it needed to be improved at the prototype stage. In the commercial spectrum of refrigeration systems, experimentation has been conducted with natural gas as energy input [2]. In the various components with respect to temperature of water, responses have been collected and heat interactions in the entire cycle provided the improvements which can be kept in the design. The major finding of this work was that for a low energy input the required cooling will also be less. The changes in absorbent configuration can provide better cooling effect as compared to conventional system of absorbents in absorption refrigeration. It was observed that mixture of LiBr and potassium formate provided better results [3]. The comparison has been made with the help of a program and also that less energy input required in the generator. Cost was another parameter which can be considered here for fabrication purpose. Heat source temperature has significant effect on COP and energy utilization. Study on single effect LiBr-H_2O absorption refrigeration provided that when temperature of source increases it affects the heating and cooling performance in a better way [4]. The effect of component temperature has not been taken into account for analysis. Energy utilization capacity shows slightly decreasing performance characteristics in this study for both applications. Energy analysis approach for absorption refrigeration uses the effect of temperature of components and circulation rate for measuring a desired COP [5]. Single effect as well as double effect systems have been analysed, and it was found that COP of both decides different application for their use in industry. Observation suggested that COP of double-effect absorption system has higher value. While exergy approach shows that thermal systems by variation of few parameters produced some different aspect of energy sustainability. Computational model of a single-effect LiBr-H_2O system has been developed with exergy calculations [6]. The relation between temperatures of components been determined and it was found that generator produces high exergy loss on certain situations. Performance of the said arrangement dependent on value sets of component temperatures. The other observation was that the generator deals with energy input and is most vital part of the system. Air-conditioning systems can also be analysed by exergy methods. An exergy approach implemented on air-conditioning system provided the optimization [7]. Decision making multi-objective techniques has been used in this research which works on an algorithm. The results of this process help with economic as well as product output optimal solution. In addition to this, emphasis on intelligent optimization techniques also increased showing reliability. Entropy generation method is also another way to provide user friendly design of the system. A single effect system has been taken for cooling load calculations where the evaporator and condenser temperatures are 4^oC and 38^oC and the generator temperature is 90^oC [8]. The values of effectiveness and efficiency for heat exchanger and pump are also of importance. The results show that entropy generation within the components regulates the behavior of system. The addition in exergy method provides the avoidable and unavoidable parts of exergy. An absorption system has been taken by using this concept which deals with exergy destruction [9]. The segregation of exergy components provides that there can be improvement in each component of the machine. This information was not available earlier in the analysis. A double effect machine taken for analysis based on exergy using LiBr and water as working fluids [10]. The performance show that both the generators have temperature dependency on each other and the exergy loss is highest in absorber and high pressure generator. This designates generator significant component of absorption cycle. Comparison has been made between systems on the basis of energy balances and thermodynamic properties investigated by developing a program [11]. The results of the analysis show

that condenser and evaporator works for an optimum value set of generator condition as well as provide the exergy relation of both systems. The results also show that exergetic efficiency has very less margin between them. This study further provides the way for optimization of the thermal systems. Irreversibility is one of the major causes of exergy losses in thermal system. Parametric study of absorption cycle shows that exergetic performance of the multi-effect systems depends on temperature setting of the components [12]. The research shows irreversibility is appreciable in absorber for both the systems. COP of both the systems gets affected by losses in all the components. A Mathematical model has been developed for NH_3 and sodium thiocynate using laws of thermodynamics for cooling as well as heating [13]. Exergy analysis conducted for the system and it was concluded that heat rejection and input in various parts of the system give performance variation with respect to temperature levels. Performance in both applications provides different aspect as well. Crystallization problem in the absorption cycle has been investigated by developing a computational method in various configurations [14]. The capacity of these systems has been kept same throughout the cycle. The observation has been made that risk of crystallization is less in series flow network. On the other hand, parallel and reverse pattern has more chance of this problem taking place. EES code has been developed for diffusion absorption cycle using NH3-H2O configuration [15]. The findings of this simulation provide that the concentration of 0.35 of ammonia rich solution is best. Exergy losses were also observed in different components and validation has been done. Simulation results also provide the scope for optimizing the working conditions. Temperature relations among components establish that findings help in more structured design. Use of waste heat in combined cycle for absorption systems has been carried out for other working fluids as well [16]. Measurement of irreversibilities in various components has been determined in their work. It was estimated that cogeneration cycle provides better performance characteristics. The useful energy output potential is less as compared to exergy destruction taking place within the system. This on the other hand provides that optimization need is there for thermal behavior of the system.

2. ABSORPTION REFRIGERATION

Absorption refrigeration frequently provides for solar refrigeration. It requires low grade energy input and, providing the same capacity, the size of an absorption chiller is relatively smaller than adsorption refrigerating machines due to higher value of transfer of heat rates of absorbent in the chemical process [17]. The systems that have been used are having LiBr-H_2O and aqua-ammonia as working fluids. They can be made to work as multi-effect systems with the wide range of temperature varying gradually. Other organic fluids as well as refrigerants also have vital roles depending upon their implication to the industry and households. Observations on design and optimization of LiBr-H_2O cycle has been carried out for thermal system considerations providing sustainable energy methods [18]. The finding was that generator governs the capacity of cooling and heating applications. Cost is also one of the parameter which needs to be considered. The problem of crystallization should also be taken care of while it is in operation. This factor requires special attention from the design point of view. For resolving this problem concentration range should be set accordingly.

3. LIBR-H_2O ABSORPTION WITHOUT EJECTOR

Few researchers have conducted analysis taking into consideration the part which cannot be avoided for various cycles in this configuration [19]. They have observed various performance characteristics and the effect of temperature. The performance of triple effect is better than double lift systems. It has been studied that various chillers with combination of collectors of different configuration provide simulation of systems, with single or multi-effect and collectors [20]. Comparison has been made to double lift machines, appreciable savings observed to be appreciable as 39% results as for the combination of single lift machine and the collector. It is observed that double effect system with the thermodynamic as

well as thermo-economic analysis and also performed the optimization of it [21]. They have the heat source as steam which comes from energy resource. A cost minimization methodology based on the thermodynamics and economics combination concept is applied for calculating cost factors of input and output of system using cost reduction criteria. The system is again checked to find the significance of several variables on component costs and other important components. Researchers have performed the exergetic analysis technique on a solar operated double-effect absorption LiBr-H_2O system [22]. The analysis has been done to form the rational basis of the potential that a system possesses. Also, they have shown that better evaporator quality give better performance. Analysis have the coupling of single lift LiBr-H_2O cycle and CO_2 operated compression cycle for high electronics applications and for space conditioning [23]. A thermodynamic model has also observed the cascade system characteristics, and analysis was carried out to find out the system performance under various operating conditions. Availability analysis carried out for determination of irreversibility within system components providing condenser and absorber temperature 87.8^oC and 140.6^oC respectively in both the systems. [24]. Investigation on the system components in cooling mode through cycle simulation has been carried out by researchers. They described the system behavior characteristics in relation with inlet temperature of air to the absorber, concentration, the solution distribution ratio[25]. Observed critical value of the thermodynamic aspects can be maximized. This observation provides the required criteria for the design of future thermal systems.

4. LIBR-H_2O ABSORPTION WITH EJECTOR ASSEMBLY

It is observed that combining the LiBr-H_2O system with combined power and ejector based cycle having R141b as working fluid provides different aspect [26]. They have performed the exergy analysis to observe the cycle efficiency. It is shown that the at a particular temperature range single and double effect cycles operates and temperature range is higher for double-effect systems [27]. They have also shown a 30% increase of performance in terms of COP in comparison to conventional cycle. It has been analyzed that thermal system having micro-turbine as power source on the basis of balance equations has different nature [28]. It is provided from results that integrated system is efficient and less energy consumer than other conventional systems. For energy saving the favorable system is that which uses two stage compression chiller providing intercooling and sub-cooling as well.

5. AQUA-AMMONIA ABSORPTION SYSTEMS

Researchers have taken the case of Saudi Arabia, where electricity consumption is much higher for the purpose of refrigeration and air-conditioning [29]. It is tested and found that their work by consuming solar energy to provide energy for such systems will conserve large amount of energy that can be used for other influential sector. The design is for 24 hr operation of absorption refrigerating systems. Study on thermal system show that coefficient of performance, mass flow rates behaves according to heat interactions taking place within the system. It is shown that COP and work done are dependent on component temperature values and on chemical nature of the solution [30]. Aqua-ammonia absorption refrigeration system has been studied on the basis of second law and exergy loss of each component, ECOP, COP and other parameters have been found. Exergy losses change in the system components [31].

6. AQUA-AMMONIA ABSORPTION WITHOUT EJECTOR

Comparison of the results with experimental and some manufacturer data reported in the literature [32]. They have analyzed performance characteristics of various components on the basis of energy and mass conservation. They have found appreciable closeness in the results. Results obtained for this analysis shows deviation. Efficient performance of the

separating component is of importance. Work have been conducted for the analysis on an intermittent operation of refrigerating system and evaluated with various other mixtures [33]. It was mentioned that while using ternary mixture the performance rating can be much higher. It has been proposed for a different system for modelling and its simulation and considered the role of gravity in it [34]. The pump was specially designed to deal with the certain parameters. The flow conditions also improved by researchers using valves configuration. The leakage issue also taken care of for better results in various capacities. It has been proposed that a novel cycle using combination of expansion and compression has value for thermal systems [35]. Performance of this cycle is much higher than that of the usual cycle providing higher efficiency. Pump can provide work for advancement of the cycle in other ways also. Research work have provided the work on ammonia-water system and also provided the costing analysis of the system [36]. They have also emphasized on the optimization of various parameters. The variables were selected to provide cooling capacity at the economic scale. A detailed mathematical analysis was carried out in their work. Scientists have taken large scale heat-driven absorption cooling system that is available in the marketplace for industrial applications but the concept of a solar driven absorption chiller for air-conditioning applications is relatively new [37]. Absorption chillers have a lower efficiency than compression refrigeration systems, when used for small scale applications and this restrains the absorption cooling system from air conditioning applications in residential buildings. They have emphasize on the potential of a solar driven ammonia-water absorption chiller for residential air conditioning application. They have developed a thermodynamic model based on a 10 kW air cooled ammonia-water absorption chiller driven by solar thermal energy. They have conducted both energy and exergy analyses to observe the performance of this residential scale cooling system. The analyses shows that absorber is where the most exergy loss occurs (63%) followed by the generator (13%) and the condenser (11%).

7. AQUA-AMMONIA ABSORPTION WITH EJECTOR

It is observed that energy input can be provided by using solar energy but there is a limitation on the source temperature criteria which can affect the overall performance of the cycle [38]. The condensation part can also be controlled by using these considerations. The solar components can give better and efficient results through this and the COP will increase due to this. The modifications in the design provided the combination of absorber and ejector. This change in design has also improved the cooling in the setup where flash tank and other components were installed. They have developed a simulation program to evaluate the modified combined cycle using aqua-ammonia refrigerant. The comparison of the proposed combined cycle with conventional cycle shows improvement in the performance.

8. AQUA-AMMONIA IN CASCADE & SPACE CONDITIONING

Recent works have provided a different approach using hybrid refrigerator running on waste heat with a binary mixture as working fluid [39]. It consists of heat-driven compression refrigeration and an absorption refrigeration subsystem. They share the same condenser and evaporator. Mid-temperature waste heat is used in the power and compression refrigeration subsystem to compress ammonia vapor. The low-temperature waste heat is used in the absorption refrigeration subsystem to preheat the strong solution before entering the rectifier. The exhaust vapor from the ammonia–steam turbine is introduced into the rectifier of the absorption refrigeration subsystem to generate pure ammonia. The new system exhibits superior performance because of the cascade use of waste heat in the two subsystems. Few studies show that a triple effect cycle with ammonia-water as working fluids has other potential [40]. They have investigated a triple effect absorption heat pump using simulation. Ammonia-water solution used as the working fluid for the high pressure cycle, ammonia-water and ammonia-sodium thiocyanate solutions investigated for the lower pressure cycle. The overall system is so configured that

the absorber, condenser and rectifier heat duty from the high pressure cycle is rejected to the generator of the low pressure cycle. The complete absorption system has been analyzed. Cycle performance was modeled over a wide range of cooling and heating mode to determine the overall advantages. It can provide better opportunities for future aspects.

9. HYBRID REFRIGERATION SYSTEMS

These systems works on compression as well as absorption technique. Mechanical work and solution circuit both play a vital role here. The solution cycle performs absorption and desorption of the refrigerant present in the system. These systems provide a bridge between traditional compression and absorption cycles. The hybrid cycle uses mixture of refrigerants as absorbent and other as desorbent. This arrangement provides wide range of temperatures available for the system to perform for a mixture. The volatile nature of the refrigerants plays a vital role for the analysis. The irreversibility associated with the system also gets reduced in the heat interaction process among components. Analysis on heat pump cycle as well as on solution cycle has been performed in two stages of each [41]. The results show that there is a significant increase in the COP as compared to R-22 only. The other aspect of the analysis emphasized on energy saving and balance in pressure conditions in a traditional way of refrigeration cycle. Another work on successive substitution approach investigated that heat interaction among components provides COP measure [42]. The results show that COP has been increased and also the pressure balance condition restored in comparison to earlier traditional systems. Analysis of overall heat interaction and its behavior in all components has been performed by simulation model [43]. The observations were made for the mass flow of ammonia and water pair using experimentation. The design and analysis of the system provided the better criteria for future optimization approach in terms of energy saving. Application of internal combustion engines to run the combined cycle has its observations. A study on hybrid cycle working on traditional fluids using compressor has been performed [44]. The drawback of this analysis is from the economic point of view. The system worked on pressure balance in all the components. The input parameters have not been considered in terms of temperature of external components. The internal behavior reflects the cycle performance and provides the way for further clarity towards optimization. Study on ammonia water absorption cycle in combination with compressor assembly provided optimization [45]. The process has been achieved by temperature gradient in the internal and external factors. Again the pressure balance and constant values for heat interaction process were assumed for equilibrium condition. The optima was found controlling the heat interaction among the components and it is observed that hybrid system is better for cooling applications considering external and internal relation. Ternary working fluid condition provides the relation among properties in a hybrid system [46]. The analysis on the basis of working fluid configuration is uncertain about property calculations of the solution. The intermittent operation of the hybrid systems provide higher COP [47]. The study shows that each and every system works better in terms of COP if the combined intermittent operation is to be carried out.

10. INTELLIGENT TECHNIQUES

It has been proposed that few techniques such as ANN model, fuzzy logic, fuzzy inference systems and other ways can be adopted for the simulation of various thermodynamic systems. The new formulation has been done to determine the COP and circulation factor. The other components have been used to create the network. Apart from that MATLAB and EES are the other simulation and solver methods respectively, which can provide complex relations to be solved easily. A refrigeration machine for optimization requires objective function which considers all the necessary parameters satisfying

multiple criteria as well. A machine assisted by cooling tower in a refrigeration method considered for optimization using cost and exergy destruction as objectives of analysis [48]. The criteria set taken as thermodynamic and economic condition. This has energy and exergy approach for thermodynamic part and total revenue requirement for economic part. In their analysis, comparison has been made for optimized systems. It was also observed that multi-objective design satisfy the general approach of engineering applications.

11. TLBO ALGORITHM IN THERMAL SYSTEMS

In recent works in the field of thermal engineering, optimization of different thermodynamic parameters by the meta-heuristic algorithms has been proposed by researchers. But, many of these algorithms can perform effectively when a set of tuning parameters is there and can be adjusted as per the requirements [49]. For these algorithms to perform best, optimized values of the tuning parameters are required which is more sophisticated in nature. Teaching-learning based optimization is less time consuming and provide better results. This is a parameter-less algorthim-specific technique to perform simulation. It can be tested for refrigeration systems considering cost and exergy parameters. The variety of applications has been considered in decision making problems using this algorthim.

12. GENETIC ALGORITHM

For the performance evaluation thermal systems, this algorithm can be used. The convergence rate of this is slow because it considers several parameters which control the algorithm. Due to this it can sometimes behave abruptly. However few researchers have conducted its application and found that the proper tuning of parameters can help in controlling the better results. This algorithm has been used by few researchers to optimize the system and has shown significant performance in this way.

13. TLBO FOR OPTIMIZATION OF SYSTEMS

Optimization of thermal as well as other systems require strategy to achieve certain set of values of different components for better results. Global optimization still remains one of the challenges due to the fact that it takes set of mathematical configurations for any system [50]. The benchmark functions were taken for the analysis, and results were drawn for the thermal system. Figure 1 shows that the algorithm works for decision makers for teacher-learner phase.

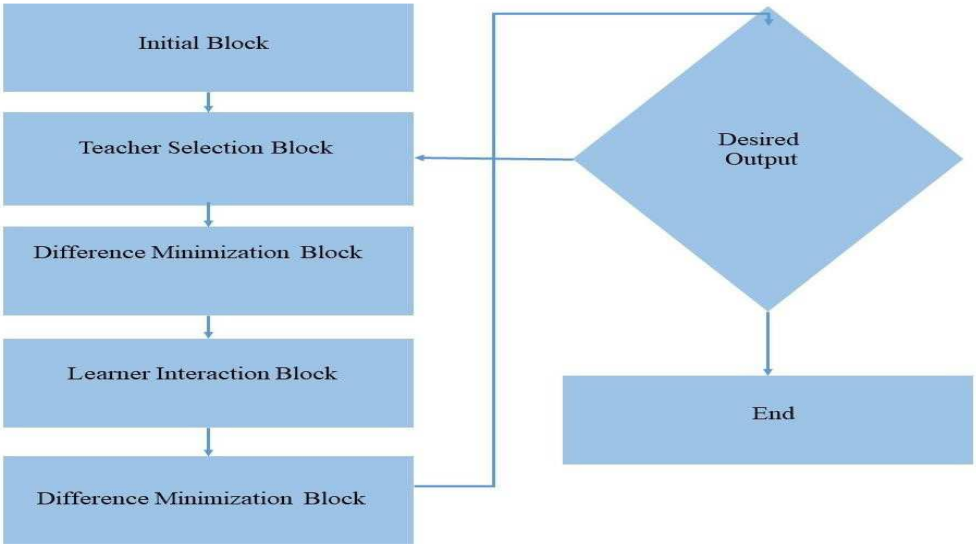


Figure 1: TLBO Flow Process[50].

There is also classification according to level of complexity for solving the multi-objective problem. The working of algorithm provides the idea about the simulation process and its progress step by step.

14. FUZZY INFERENCE SYSTEMS

Fuzzy logic is applicable to wide range of fields including artificial intelligence and smart controllers. It is a three-stage process, firstly all the input values are fuzzified, next fuzzy output is calculated using these inputs and finally the output is de-fuzzified in crisp output. Researchers have applied this technique for speed regulation of compressor in a refrigeration plant [51]. Fuzzy analysis for thermal systems has shown variety of results, which can be considered for further optimization process.

15. ARTIFICIAL NEURAL NETWORK

Neural network has certain layers which connect the various components of the refrigeration system, and then it is trained to provide necessary analysis [52]. It is performed on ammonia water refrigeration systems. There are various learning techniques for training different neural networks. The back-propagation algorithm is a technique which provides variants in a way that network can be trained according to the problem. Standard back-propagation is another way to train the network. It is dependent on the user's decision that which training algorithm will be suitable for his problem and the selection is done by checking the behavior of variants in each training technique. The simple analysis of thermodynamic system can be done by artificial neural network technique for regulation of frequency of different components. Neural networks provide the approach which simulates the various parameters and the results emphasize the use of the tool for optimization of complex problems. The mathematical model of complex thermal systems can be developed for better understanding of intelligent techniques. The relation can be built for the artificial intelligent atmosphere where control can be achieved for the system properties.

16. COMBINATION OF TECHNIQUES

It can be observed that few researchers have used Adaptive Neuro-fuzzy inference systems on thermal systems [53] and Fuzzy-TLBO on electrical systems [54]. The results of the combination techniques show promising approach. It can be observed that convergence time, tuning of parameters and achieving global optima form these techniques are of a better possibility.

17. CONCLUSIONS

- The solar assisted absorption refrigeration and cooling systems are the keys to supply the energy needs of the world. Renewable sources, waste heat etc. are the heat input while LiBr-H2O, aqua-ammonia, organic refrigerants etc. are the working fluid pairs with different combinations.
- In various countries which are having high requirement of energy cooling, solar operated absorption refrigeration machines with combined-ejector cycle or cascaded cycle may provide sound supply.
- The temperature range for single, double and triple-effect cycles vary because the temperature conditions at single-effect cannot drive double-effect cycle.
- The cost minimization methodology using thermo-economic concept helps to reduce the cost of the overall system. Further, optimization of the system or hybrid systems can be done by using various techniques.

- The simulation part of the absorption refrigeration and cooling systems can provide the way to solve the complex relations.
- The future energy needs will be fulfilled by the renewable energy sources using combined power for cooling and heating purposes.
- Economic point of view provides better understanding of thermal aspects as well for energy saving potential in a thermal system. It is of prime importance to deal with the cost factors.
- All the energy and exergy methods for determining the performance in addition to conventional losses is more vital thermodynamically.
- The main objective of the study is to understand the concept of avoidable and unavoidable losses in a thermal system.
- The environment of artificial intelligent techniques may provide better way to regulate the system behavior and the real time values can be obtained.
- The range of optimization can lead to global optima while training from local optima for thermal systems.

REFERENCES

1. *De Francisco, A., Illanes, R., Torres, J. L., Castillo, M., De Blas, M., Prieto, E., Garcia, A., 2002, Development and testing of a prototype of low-power water-ammonia absorption equipment for solar energy applications, Renewable Energy, 25 (2002)537–544.*
2. *Horuz, I. and Callander, T. M. S, 2004, Experimental investigation of a vapor absorption refrigeration system, International Journal of Refrigeration, 27(2004)10–16.*
3. *De Lucas, Antonio., Donate, Marina., Molero, Carolina., Villasenor, Jose., Rodriguez, Juan F., 2004, Performance evaluation and simulation of a new absorbent for an absorption refrigeration system, International Journal of Refrigeration, 27(2004)324–330.*
4. *Sencan, A., Yakut, K. A., Kalogirou, S. A., 2005, Exergy analysis of lithium bromide/water absorption systems, Renewable Energy, 30(2005)645–657.*
5. *Kilic, M. and Kaynakli, O., 2007, Second law-based thermodynamic analysis of water-lithium bromide absorption refrigeration system, Energy, 32 (2007)1505–1512.*
6. *Kilic, M. and Kaynakli, O., 2007, Theoretical study on the effect of operating conditions on performance of absorption refrigeration system, Energy Conversion and Management, 48 (2007)599–607.*
7. *Gong, G., Zeng, W., Chang, S., He, J., Li, K., 2007, Scheme-selection optimization of cooling and heating sources based on exergy analysis, Applied Thermal Engineering, 27 (2007) 942–950.*
8. *Kaynakli, O., Yamankaradeniz, R., 2007, Thermodynamic analysis of absorption refrigeration system based on entropy generation, Current Science, 92(4)(2007) 472–479.*
9. *Morosuk, T., Tsatsaronis, G., 2008, A new approach to the exergy analysis of absorption refrigeration machines, Energy, 33(2008) 890–907.*
10. *Gomri, R., Hakimi, R., 2008, Second law analysis of double effect vapour absorption cooler system, Energy Conversion and Management, 49(11) (2008) 3343–3348.*

11. *Gomri, R., 2009, Second law comparison of single effect and double effect vapour absorption refrigeration systems, Energy Conversion and Management, 50(2009) 1279–1287.*
12. *Kaushik, S. C., Arora, A., 2009, Energy and Exergy analysis of single effect and series flow double effect water-lithium bromide absorption refrigeration systems, International Journal of Refrigeration, 32 (2009)1247–1258.*
13. *Zhu, L., Gu, J., 2010, Second law-based thermodynamic analysis of ammonia/sodium thiocyanate absorption system, Renewable Energy, 35(2010) 1940–1946.*
14. *Garousi Farshi, L., Mahmoudi, S. M. S., Rosen, M. A., 2011, Analysis of crystallization risk in double effect absorption refrigeration systems, Applied Thermal Engineering, 31(10) (2011) 1712–1717.*
15. *Behrooz, M., Ziapour, M. T., 2011, Performance study on a diffusion absorption refrigeration heat pipe cycle, International Journal of Thermal Sciences, 50(4) (2011)592–598.*
16. *Majhi, B. P., & Sahu, S. H. A. T. E. N. D. R. A. (2015). A review on Application of Bio-geography based Algorithm and other Optimization Techniques. International Journal of Management, Information Technology and Engineering, 3(6), 19–28.*
17. *Khaliq, A., Agrawal, B. K., Kumar, R., 2012, First and second law investigation of waste heat based combined power and ejector-absorption refrigeration cycle, International Journal of Refrigeration, 35(1) (2012)88–97.*
18. *Kim D. S., Infante Ferreira C. A., 2008, Solar refrigeration options – a state-of-the-art review, International Journal of Refrigeration, 31(2008) 3–15.*
19. *Alizadeh, S., Bahar, F., Geoola, F., 1997, Design and optimization of an absorption refrigeration system operated by solar energy, Solar Energy, 22(1997) 149–154.*
20. *Gebreslassie Berhane H., Medrano Marc, Boer Dieter, 2010, Exergy analysis of multi-effect water–LiBr absorption systems: From half to triple effect, Renewable Energy, 35(2010) 1773–1782.*
21. *Tierney M. J., 2007, Options for solar-assisted refrigeration-Trough collectors and double-effect chillers, Renewable Energy, 32(2007) 183–199.*
22. *Misra R. D., Sahoo P. K., Gupta A., 2005, Thermo economic evaluation and optimization of a double-effect H_2O/LiBr vapour-absorption refrigeration, International Journal of Refrigeration, 28(2005) 331–343.*
23. *Ravikumar T. S., Suganthi L. and Anand A. Samuel, 1998, Exergy analysis of solar assisted double effect absorption refrigeration system, Renewable Energy, 14(1998) 55–59.*
24. *Garimella Srinivas, Brown Ashlie M., Nagavarapu Ananda Krishna, 2011, Waste heat driven absorption/vapor-compression cascade refrigeration system for megawatts cale, high-flux, low-temperature cooling", International Journal of Refrigeration, 34(2011) 1776–1785.*
25. *Anand, D. K., Kumar, B., 1987, Absorption machine irreversibility using new entropy calculations, Solar Energy, Vol.39, (1987), pp. 243–256.*
26. *Khaliq Abdul, Agrawal Basant K., Kumar Rajesh, 2012, First and second law investigation of waste heat based combined power and ejector-absorption refrigeration cycle, International Journal of Refrigeration, 35(2012) 88–97.*
27. *Daliang Hong, Guangming Chen, Limin Tang, Yijian He, 2011, A novel ejector-absorption combined refrigeration cycle, International Journal of Refrigeration, 34(2011) 1596–1603.*
28. *Seyfouri Z., Ameri M., 2012, Analysis of integrated compression-absorption refrigeration systems powered by a microturbine", International Journal of Refrigeration, 35(2012) 1639–1646.*

29. *Tyagi, K. P., 1988, Design parameters of an aqua-ammonia vapour absorption refrigeration system, Heat recovery systems & CHP, 8(4) (1988)375–377.*

30. *Ercan Ataer. O, Gogus, Yalcin., 1991, Comparative study of irreversibilities in an aqua-ammonia absorption refrigeration system, International Journal of Refrigeration, 14(1991) 86–92.*

31. *Said Syed A. M., El-Shaarawi Maged A. I., Siddiqui Muhammad U., 2012, Alternative designs for a 24-h operating solar-powered absorption refrigeration technology, International Journal of Refrigeration, 35(2012) 1967–1977.*

32. *Darwish N. A., Al-Hashimi S. H., Al-Mansoori A. S., 2008, Performance analysis and evaluation of a commercial absorption–refrigeration water–ammonia (ARWA) system, International Journal of Refrigeration, 31(2008) 1214–1223.*

33. *Moreno-Quintanar G., Rivera W., Best R., 2012, Comparison of the experimental evaluation of a solar intermittent refrigeration system for ice production operating with the mixtures NH3/LiNO3 and NH3/LiNO3/H2O, Renewable Energy, 28(2012) 62–68.*

34. *Sohel M. Imroz and Dawoud B., 2006, Dynamic modelling and simulation of a gravity-assisted solution pump of a novel ammonia–water absorption refrigeration unit, Applied Thermal Engineering, 26(2006) 688–699.*

35. *Hong Daliang, Tang Limin, He Yijian, Chen Guangming, 2010, A novel absorption refrigeration cycle, Applied Thermal Engineering, 30(2010) 2045–2050.*

36. *Misra R. D., Sahoo P. K., Gupta A., 2006, Thermo economic evaluation and optimization of an aqua-ammonia vapour-absorption refrigeration system, International Journal of Refrigeration, 29(2006) 47–59.*

37. *Aman J., Ting D. S-K, Henshaw P., 2014, Residentialsolar air conditioning: Energy and Exergy analyses of an ammonia-water absorption cooling system, Applied Thermal Engineering, 62(2014) 424–432.*

38. *Sirwan Ranj, Alghoul M. A., Sopian K., Ali Yusoff, Abdulateef Jasim, 2013, Evaluation of adding flash tank to solar combined ejector–absorption refrigeration systems, Solar Energy, 91(2013) 283–296.*

39. *Han Wei, Sun Liuli, Zheng Danxing, Jin Hongguang, Ma Sijun, Jing Xuye, 2013, New hybrid absorption–compression refrigeration system based on cascade use of mid-temperature waste heat, Applied Energy, 106(2013) 383–390.*

40. *Garimella Srinivas, Lacy Daryl and Stout Roger E., 1997, Space-conditioning using triple-effect absorption heat pumps, Applied Thermal Engineering, 17(1997) 1183–1197.*

41. *Kumar, G. N., & Kalavathi, M. S. Static Load Modeling For Voltage Stability Studies With Optimal Placement Of Upfc Using Cat Swarm Optimization.*

42. *Shivam Rajak, Ravindra Kannojiya and Shubham Kumar, 2017, "A Review Paper on Optimization Techniques of Thermal System", 4(2017) 84–87.*

43. *Pourreza-Djourshari, S. and Radermacher, R., 1996, Calculation of the performance of vapour compression heat pumps with solution circuits using the mixture R-22-DEGDME, International Journal of Refrigeration, 9(1996) 245–250.*

44. *Radermacher, R., 1987, Vapour compression heat pumps with desorber/absorber heat exchange, Proc. Of XVIIth, International Congress of Refrigeration, (1987)1061–1066.*

45. *Agarana, M. C., Bishop, S. A., & Odetunmibi, O. (2014). Optimization of banks loan portfolio management using goal programming technique. International Journal of Research in Applied Natural and Social Sciences (IMPACT: IJRANSS), 2(8), 43–52.*

46. *Stokar, M. and Trepp, C., 1987, Compression heat pump with solution circuit part-1: design and experimental results, International Journal of Refrigeration, 10(1987)87–96.*

47. *Nath, M. Optimization Of Sll Of Apcp Antenna Array.*

48. *Herold, K. E., Howe, L. A and Radermacher, R., 1991, Analysis of hybrid compression-absorption cycle using lithium bromide and water as the working fluid, International Journal of refrigeration, 14(1991) 264–272.*

49. *Ahlby, L., Hodgett, D. and Berntsson, T., 1991, Optimization study of the compression/absorption cycle, International Journal of Refrigeration, 14(1991) 16–23.*

50. *Ahlby, L., Hodgett, D. and Radermacher, R., 1993, NH3/H2O/LiBr as working fluid for the compression/absorption cycle, International Journal of Refrigeration, 16(4)(1993) 265–273.*

51. *Riffat, S. B and Shankland, N., 1993, Integration of absorption and vapour-compression systems, Applied Energy, 46(4) (1993) 306–316.*

52. *Sayyaadi, H., Nejatolahi, M., 2011, Multi-objective optimization of a cooling tower assisted vapor compression refrigeration system, International Journal of Refrigeration, 34(1) (2011)243–256.*

53. *C. Aprea, R. Mastrullo, C. Renno, 2004, Fuzzycontrol of the compressor speed in a refrigeration plant, International Journal of Refrigeration, 27(2004) 639–648.*

54. *Ravindra Kannojiya, Mohnish Dulwani, Kartikey Sharma, 2018, Proposed Algorithm (P. E. A) for Optimization, 8th International Conference on Cloud Computing, Data Science & Engineering, 2018, 849–852.*

55. *Arzu Sencan, 2007, Performance of ammonia–water refrigeration systems using artificial neural networks, Renewable Energy 32 (2007) 314–328.*

56. *Onder Kizilkan, 2011, Thermodynamic analysis of variable speed refrigeration system using artificial neural networks, Expert Systems with Applications, 38(2011) 11686–11692.*

57. *M. Hosoz, H. M. Ertunc, H. Bulgurcu, 2011, An adaptive neuro-fuzzy inference system model for predicting the performance of a refrigeration system with a cooling tower, Expert Systems with Applications, 38(2011) 14148–14155.*

58. *Ahmad Moghadam, Ali Reza Seifi, 2014, Fuzzy-TLBO optimal reactive power control variables planning for energy loss minimization, Energy Conversion and management, 77(2014) 208–215.*

International Journal of Research in Engineering and Innovation (IJREI)
journal home page: http://www.ijrei.com
ISSN (Online): 2456-6934

Performance evaluation of half effect LiBr-H_2O vapour absorption systems using multi cascading of vapour compression cycles for low temperature applications

Radhey Shyam Mishra

Department of Mechanical, Production, Industrial and Automobiles Engineering, Delhi technological University, Delhi, India

Abstract

Most of the absorption cooling system use either LiBr-H_2O or NH_3-H_2O solutions. The LiBr-H_2O system can operate at a low generator temperature with better coefficient of performance than NH_3-H_2O system. However, COP of absorption system is relatively less as compared to the compression system. To improve its performances, several modifications have been made in the cycle. Therefore, this paper mainly deals with performance evaluations of half effect LiBr-H_2O vapour Absorption Systems using multi cascading of vapour compression cycles for low temperature applications (at -100^{o}C) used for cryogenics applications and comparison at -50^{o}C evaporator temperature in the low temperature circuit using HFO refrigerants in the intermediate temperature circuit and found that half effect LiBr-H_2O vapour Absorption Systems using multi cascading of vapour compression cycles for low temperature applications using HFC152a in intermediate temperature cycle and HFC-134a in LTC gives better thermodynamic performances than by using HFO refrigerants in intermediate temperature cycle & HFC-134a in low temperature cycle. The thermodynamic performances using HFO-1234ze in intermediate temperature cycle is better than using HFO-1234yf in intermediate temperature cycle.
© 2019 ijrei.com. All rights reserved
Keywords: Multi-Cascade systems, Half effect LiBr-H_2O integrated absorption systems, HFO refrigerants

1. Introduction

Vapour absorption cooling systems are environmental, clean and economically driven refrigerating cycles. By consuming very small electric power, they can use waste heat or solar energy for cooling. The half effect absorption systems have the advantage of using low temperature heat energy for cooling. The first law & second law performances (i.e. coefficient performance (COP) and the exergetic efficiency) of the half effect absorption systems are found as 0.45 and 0.24, respectively. Arivazhagan R, et.al [1] computed component's irreversibilities and also are found most of the exergy destruction occurred in the evaporator and in the absorbers and concluded that the half effect absorption systems is the best for cooling driven by low temperature heat energy and the performance of the evaporator and the absorbers is very important for the cycle. In recent years, the fourth generation Hydrofluoro-olefins (HFOs)-R1234yf and R1234ze are being considered as alternative to R134a. A number of studies have been carried out using HFO 1234yf and HFO 1234ze. Although, R134a is a wide spread used refrigerant due to its commercial availability, similar properties to R12, less ODP value, excellent thermal stability, non toxic and non-flammability etc has high GWP value is more than 1300.

The European Union (EU) regulation is phasing out the current generation HFCs like R134a due to its high GWP and environment consequences. The thermodynamic and environmental characteristics of refrigerants HFC 134a, HFO 1234yf & HFO 1234ze are shown in Table-1.

The European Union (EU) regulation is phasing out the current generation HFCs like R134a due to its high GWP and environment consequences. A number of studies have been carried out using R1234yf and R1234ze [2]. In the notable studies [3-8], Yataganbaba et al. [3] performed exergy analysis on a two evaporator vapour compression refrigeration system using R1234yf, R1234ze and R134a as refrigerants. The two refrigerants R1234yf and R1234ze were good alternatives to R134a regarding their environment friendly properties.

Sanchez et al. [8] compared five low GWP refrigerants R152a, R1234yf, R1234ze, R290 and R600a for the replacement of R134a using hermetic compressor in the experimental test rig and

Corresponding author: R.S. Mishra
Email Address: hod.mechanical.rsm@dtu.ac.in
http://doi.org/10.36037/IJREI.2019.3506

found that the R1234yf and R152a can be considered suitable drop-in alternative to R134a by considering the energy consumption and the cooling refrigerating capacity of facility. Arora and Kaushik [9-10] developed then energy and exergy analysis of single effect and series flow double effect water–lithium bromide absorption system and found that the irreversibility is highest in the absorber in both systems as compared to other systems. Gomri [11] carried out thermodynamic analysis of single effect & double effect absorption refrigeration systems and found the COP of double effect system is approximately twice the COP of single effect system. S.B. Riffat N. Shankland [12] studied different types of absorption systems integrated with vapour-compression systems. Kilic and Kaynakli [13] carried out thermodynamic analysis for finding the performance of a single stage water lithium bromide absorption refrigeration system by varying inputs parameters and found that that the maximum energy loss occurs in generator of the system. Chinnappa et al. [14] proposed a compression-absorption cascaded refrigeration system which consist a conventional refrigerants with a solar operated, NH3-H_2O, VARS for air conditioning application. The above investigators have not carried out the performance evaluation for low temperature applications in cryogenics and the effect of performance parameters using HFO-1234yf in intermediate temperature circuit and HFC/134a in low temperature circuit. Therefore, this paper mainly deals with performance evaluations at -100ºC used for cryogenics applications and comparison at -50ºC evaporator temperature in the low temperature circuit using HFO refrigerants in the intermediate temperature circuit.

Table 1. Thermodynamic and environmental characteristics of refrigerants HFC 134a, HFO 1234yf & HFO 1234ze

Refrigerant	HFC 134a	HFO 1234yf	HFO 1234ze
Chemical Name	1,1,1,2-Tetrafluoroethane	2,3,3,3-Tetrafluoro-propene	trans-1,3,3,3-Tetrafluoro-prop-1-ene
Molecular formula	CH_2CF_4 (CF_3-CH_2F)	$C_3H_2F_4$ (CH_2=CF$C F_3$)	$C_3H_2F_4$ (CF_3CH=CHF)
Molecular mass (kg/kmol)	102.03	114.04	114.04
Boiling Point (^{0}C) at 1 atm	-26.07	-29.45	-18.95
Freezing Point (^{0}C) at one atm	-103.3	-150	-156
GWP Rating	1430	4	<1
ODP Rating	0	0	0
Appearance	Colourless	Colourless	Colourless
Combustibility	No	Yes (Low)	No
Critical Temperature (^{0}C)	101.06	94.69	109.37
Critical Pressure (MPa)	4.0593	3.3822	3.6363
Thermal stability	Excellent	Very good	Very good
Flammability	Non flammable	Mild flammable	Mild flammable

2. Results and Discussion

Following systems were chosen for numerical computation of integrated half effect LiBr-H_2O VARS multi cascaded VCRS for low temperature applications.

System-1

Half effect LiBr-H_2O vapour absorption refrigeration system using cascaded HFC-152a in Intermediate/Medium temperature vapour compression cycle and HFC-134a in cascaded vapour compression low temperature cycle

System-2

Half effect LiBr-H_2O vapour absorption refrigeration system using cascaded HFC-152a in Intermediate/Medium temperature vapour compression cycle and HFC-404a in cascaded vapour compression

System-3

Half effect LiBr-H_2O vapour absorption refrigeration system using cascaded HFC-152a in Intermediate/Medium temperature vapour compression cycle and HC-290 in cascaded vapour compression low temperature cycle

System-4

Half effect LiBr-H_2O vapour absorption refrigeration system using cascaded HFC-152a in Intermediate/Medium temperature vapour compression cycle and HC-600a in cascaded vapour compression low temperature cycle

System-5

Half effect LiBr-H_2O vapour absorption refrigeration system using cascaded HFC-152a in Intermediate/Medium temperature vapour compression cycle and HC-600 in cascaded vapour compression low temperature cycle

System-6

Half effect LiBr-H_2O vapour absorption refrigeration system using cascaded HFC-152a in Intermediate/Medium temperature vapour compression cycle and ethylene in cascaded vapour compression low temperature cycle

System-7

Half effect LiBr-H_2O vapour absorption refrigeration system using cascaded HFO-1234ze in Intermediate/Medium temperature vapour compression cycle and HFC-134a in cascaded vapour compression low temperature cycle

System-8

Half effect LiBr-H_2O vapour absorption refrigeration system using cascaded HFO-1234ze in Intermediate/Medium temperature vapour compression cycle and HFC-404a in cascaded vapour compression low temperature cycle.

System-9

Half effect LiBr-H_2O vapour absorption refrigeration system using cascaded HFO-1234ze in Intermediate/Medium temperature vapour compression cycle and HC-290 in cascaded vapour compression low temperature cycle

System-10

Half effect LiBr-H_2O vapour absorption refrigeration system using cascaded HFO-1234ze in Intermediate/Medium temperature vapour compression cycle and HC-600a in cascaded vapour compression low temperature cycle

System-11

Half effect LiBr-H_2O vapour absorption refrigeration system using cascaded HFO-1234ze in Intermediate/Medium temperature vapour compression cycle and HC-600 in cascaded vapour compression low temperature cycle

System-12

Half effect LiBr-H_2O vapour absorption refrigeration system using cascaded HFO-1234ze in Intermediate/Medium temperature vapour compression cycle and ethylene in cascaded vapour compression low temperature cyclcle.

System-13

Half effect LiBr-H_2O vapour absorption refrigeration system using cascaded HFO-1234yf in Intermediate/Medium temperature vapour compression cycle and HFC-134a in cascaded vapour compression low temperature cycle

System-14

Half effect LiBr-H_2O vapour absorption refrigeration system using cascaded HFO-1234yf in Intermediate/Medium temperature vapour compression cycle and HFC-404a in cascaded vapour compression low temperature cycle.

System-15

Half effect LiBr-H_2O vapour absorption refrigeration system using cascaded HFO-1234yf in Intermediate/Medium temperature vapour compression cycle and HC-290 in cascaded vapour compression low temperature cycle.

System-16

Half effect LiBr-H_2O vapour absorption refrigeration system using cascaded HFO-1234yf in Intermediate/Medium temperature vapour compression cycle and HC-600a in cascaded vapour compression low temperature cycle

System-17

Half effect LiBr-H_2O vapour absorption refrigeration system using cascaded HFO-1234yf in Intermediate/Medium temperature vapour compression cycle and HC-600 in cascaded vapour compression low temperature cycle

System-18

Half effect LiBr-H_2O vapour absorption refrigeration system using cascaded HFO-1234yf in Intermediate/Medium temperature vapour compression cycle and ethylene in cascaded vapour compression low temperature cycle

The following numerical values have been used for numerical computations.

(i) Generator temperature is 80oC (although it varying from 60^0C to 90^0C
(ii) Half effect vapour absorption refrigeration system evaporator temperature is 5^0C (although it varying from 1^0C to 10^0C).
(iii) Heat exchanger effectiveness is 0.5 (although it varying from 0.50 to 0.80).
(iv) Condenser temperature of half effect vapour absorption refrigeration system is 30^0C (although it varying from 30^0C to 40^0C.
(v) Temperature overlapping between HFO condenser and LiBr-H2O evaporator is 10 oC (although it varying from 0^0C to 15^0C)
(vi) Temperature overlapping between HC/HFC condenser and HFC/HFO evaporator is 10 ^{0}C (although it varying from 0^0C to 15^0C)

Table-2 (a) shows the effect of LTC refrigerants on thermodynamic performance of cascaded integrated vapour compression half effect LiBr H_2O absorption systems for ITC evaporator temperature of -50^{o}C using HFC 152a and R134a in low temperature cycle (LTC) of -100^{o}C (system-1 to System-6) and found that HFO refrigerants of low GWP gives better thermodynamic performances than HFC refrigerants and also gives better improvement in the thermodynamic performances. The lowest thermodynamic performances were observed by using ethylene in the low temperature application as shown in table-2(b).

Table-3 (a) shows the effect of LTC refrigerants on performance of cascaded integrated vapour compression half effect LiBr H_2O absorption systems for ITC evaporator temperature of -50^{o}C using HFO1234ze and R134a in low temperature cycle (LTC) of -100^{o}C (system-7 to System-12) and found that HFO refrigerants of low GWP gives better thermodynamic performances than HFC refrigerants and also gives better improvement in the

thermodynamic performances. The lowest thermodynamic performances were observed by using ethylene in the low temperature application as shown in table-3(b).

Table-4 (a) shows the effect of LTC refrigerants on performance of cascaded integrated vapour compression half effect LiBr H_2O absorption systems for ITC evaporator temperature of -50°C using HFO1234yf and R134a in low temperature cycle (LTC) of -100°C (system-13 to System-18) and found that HFO refrigerants of low GWP gives better thermodynamic performances than HFC refrigerants and also gives better improvement in the thermodynamic performances. The lowest thermodynamic performances were observed by using ethylene in the low temperature application as shown in table-4(b).

Table-5, shows the comparison of thermodynamic performance of cascaded integrated vapour compression half effect LiBr H_2O absorption systems HFC-152a and HFO refrigerants in the intermediate temperature cycle for ITC evaporator temperature of -50°C and R134a in low temperature cycle(LTC) of -100°C (system-1, system-7 & System-13) and found that HFO refrigerants of low GWP gives lower thermodynamic performances than HFC-152a refrigerant and also gives better improvement in the thermodynamic performances.

Table-2(a): Performance Parameters of Integrated half effect LiBr-H_2O VARS multi cascaded VCRS using HFC-152a in Intermediate temperature circuit and following systems for low temperature applications

Parameters	System_1 LTC_R134a	System_2 LTC_R404a	System_3 LTC_R290	System_4 LTC_R600a	System_5 LTC_R600	System_6 LTC_Ethylene
Cascade COP	0.7675	0.7606	0.7691	0.7693	0.7720	0.7443
$EDR_{_Cascade}$	0.975	1.046	0.9598	0.9578	0.9314	1.230
Exergetic $Efficiency_{_Cascade}$	0.5063	0.4887	0.5016	0.5108	0.5178	0.4484

Table-2(b) : % improvement in Performance Parameters of Integrated half effect LiBr-H_2O VARS multi cascaded VCRS using HFC-152a in Intermediate temperature circuit and following systems for low temperature applications

Performance Parameters	System_1 LTC_R134a	System_2 LTC_R404a	System_3 LTC_R290	System_4 LTC_R600a	System_5 LTC_R600	System_6 LTC_Ethylene
% improvement in cascade COP	76.06	74.47	76.41	76.46	77.08	70.72
% decreasement $EDR_{_Cascade}$	-77.46	-75.81	-77.81	-77.85	-78.47	-71.56
% improvement in $ExergeticEfficiency_{_Cascade}$	169.6	160.3	171.7	172.0	175.7	138.8

Table-3(a): Performance Parameters of Integrated half effect LiBr-H_2O VARS multi cascaded VCRS using HFO-1234ze in Intermediate temperature circuit and following systems for low temperature applications,

Parameters	System_7 LTC_R134a	System_8 LTC_R404a	System_9 LTC_R290	System_10 LTC_R600a	System_11 LTC_R600	System_12 LTC_Ethylene
Cascade COP	0.7637	0.7569	0.7652	0.7654	0.7681	0.7407
$EDR_{_Cascade}$	0.9379	1.065	0.9785	0.9764	0.9499	1.25
Exergetic $Efficiency_{_Cascade}$	0.5016	0.4842	0.5054	0.5060	0.5128	0.4444

Table-3(b): % improvement in Performance Parameters of Integrated half effect LiBr-H_2O VARS multi cascaded VCRS using HFO-1234ze in Intermediate temperature circuit and following systems for low temperature applications,

Performance Parameters	System_7 LTC_R134a	System_8 LTC_R404a	System_9 LTC_R290	System_10 LTC_R600a	System_11 LTC_R600	System_12 LTC_Ethylene
% improvement in cascade COP	75.18	73.61	75.53	75.57	76.19	69.9
% decreasement $EDR_{_Cascade}$	-77.02	-75.37	-77.38	-77.42	-78.04	-71.09
% improvement in Exergetic $Efficiency_{_Cascade}$	167.10	157.8	169.2	169.4	173.1	136.6

Table-4(a): Performance Parameters of Integrated half effect LiBr-H_2O VARS multi cascaded VCRS using HFO-1234yf in Intermediate temperature circuit and following systems for low temperature applications,

Parameters	System_13 LTC_R134a	System_14 LTC_R404a	System_15 LTC_R290	System_16 LTC_R600a	System_17 LTC_R600	System_18 LTC_Ethylene
Cascade COP	0.7607	0.7539	0.7622	0.7624	0.7650	0.7378
$EDR_{_Cascade}$	1.009	1.061	0.9935	0.9915	0.9648	1.266
Exergetic $Efficiency_{_Cascade}$	0.4978	0.4806	0.5016	0.5021	0.5090	0.4412

Table-4(b): % improvement in Performance Parameters of Integrated half effect LiBr-H_2O VARS multi cascaded VCRS using HFO-1234yf in Intermediate temperature circuit and following systems for low temperature applications

Performance Parameters	System_13 LTC_R134a	System_14 LTC_R404a	System_15 LTC_R290	System_16 LTC_R600a	System_17 LTC_R600	System_18 LTC_Ethylene
% improvement in cascade COP	74.48	72.92	74.83	74.87	75.48	69.25
% decreasement $EDR_{_Cascade}$	-76.68	-75.02	-77.03	-77.08	-77.69	-70.72
% improvement in Exergetic $Efficiency_{_Cascade}$	165.1	155.9	167.1	167.4	171.0	135.0

Table-5: Comparison of Performance Parameters of three integrated half effect LiBr-H_2O VARS multi cascaded VCRS in Intermediate temperature circuit and following systems for low temperature applications using HFC-134a in LTC

Parameters	System_1 MTC_R152a	% improvement	System_7 MTC_R1234ze	% improvement	System_13 MTC_R1234yf	% improvement
MTC_COP	0.7116	63.22	0.7077	62.34	0.7047	61.64
$EDR_{_Cascade}$	1.337	69.08	1.373	- 68.26	1.402	-67.60
$Exergetic\ Efficiency_{_Cascade}$	0.4278	-127.8	167.1	124.4	0.4164	121.7

3. Conclusions

Following conclusions were drawn from present investigations.

(i) Thermodynamic performance of cascaded integrated vapour compression half effect LiBr H_2O absorption systems HFC-152a and HFO refrigerants in the intermediate temperature cycle for ITC evaporator temperature of -50ºC and R134a in low temperature cycle (LTC) of -100ºC (system-1, system-7 & System-13) and found that HFO refrigerants of low GWP gives lower thermodynamic performances than HFC-152a refrigerant and also gives better improvement in the thermodynamic performances.

(ii) Half effect LiBr-H2O vapour Absorption Systems using multi cascading of vapour compression cycles for low temperature applications using HFC152a in intermediate temperature cycle and HFC-134a in LTC gives better thermodynamic performances than by using HFO refrigerants in intermediate temperature cycle & HFC-134a in low temperature cycle.

(iii) The thermodynamic performances using HFO-1234ze in intermediate temperature cycle is better than using HFO-1234yf in intermediate temperature cycle.

(iv) The first law efficiency (COP_Cascade) of multi-cascade system increases with an increase with increasing evaporator temperature of vapour absorption refrigeration cycle.

(v) The second law efficiency (exergetic efficiency) of multi-cascade system decreases with an increase with increasing generator temperature of vapour absorption refrigeration cycle.

(vi) The second law efficiency (exergetic efficiency) of multi-cascade system decreases with an increase with increasing evaporator temperature of vapour absorption refrigeration cycle.

References

[1] S. arivazhagan ,R Saravanan & S[2006] Renganarayanan Experimental studies on HFC based two-stage half effect vapour absorption cooling system Applied Thermal Eng, Vol-26, Issue-14-15, Page 1455-1462,

[2] Yataganbaba, A., Kilicarslan, A., Kurtbas, I.[2015]: Energy analysis of R1234yf and R1234ze as R134a replacements in two evaporator vapour compression refrigeration system, Int. J. Refrigeration, 60, page-26-37.

[3] Regulation (EU) No 517/2014 of the European Parliament and of the Council of Fluorinated Greenhouse Gases and Repealing Regulation (EC), No 842/2006 (2014)

[4] Mota-Babiloni, A., Navarro-Esbrı, J., Barragan-Cervera, A., Moles, F., Peris, B., Verdu, G.: Commercial refrigeration- An overview of current status, Int. J. Refrigeration, 57, 186-196 (2015)

[5] Mota-Babiloni, A., Navarro-Esbrí, J., Barragan, A., Moles, F., Peris, B.: Drop-in energy performance evaluation of R1234yf and R1234ze(E) in a vapor compression system as R134a replacements, Appl. Therm. Eng., 71, 259-265 (2014)

[6] Mota-Babiloni, A., Navarro-Esbrı, J., Barragan-Cervera, A., Moles, F., Peris, B.: Experimental study of an R1234ze(E)/R134a mixture (R450A) as R134a replacement, Int. J. Refrigeration, 51, 52-58 (2015)

[7] Mota-Babiloni, A., Navarro-Esbrı, J., Barragan-Cervera, A., Moles, F., Peris, B.: Analysis based on EU Regulation No 517/2014 of new HFC/HFO mixtures as alternatives of high GWP refrigerants in refrigeration and HVAC systems, Int. J. Refrigeration, 52, 21-31(2015)

[8] Sanchez, D., Cabello, R., Llopis, R., Araguzo, I., Catalan-Gil, J., Torrella, E.,[2017] Energy performance evaluation of R1234yf, R1234ze(E), R600a, R290 and R152a as low-GWP R134a alternatives, Int. J. Refrigeration, Vol-74, page-269-282;

[9] Arora, A., Dixit, M., Kaushik, S. C.: Computation of optimum parameters of a half effect water-lithium bromide vapour absorption refrigeration system, J. Thermal Eng., 2(2), 683-692 (2016)

[10] Arora, A., Dixit, M., Kaushik, S. C.: Energy and exergy analysis of a double effect parallel flow LiBr/H_2O absorption refrigeration system, J. Thermal Eng., 2(2), 541-549 (2016)

[11] Gomri R. Second law comparison of single effect and double effect vapour absorption refrigeration systems, Energy Conversion and Management 2009; 50: 1279-1287.

[12] Riffat SB, Shankland N. Integration of absorption and vapour compression systems. Applied Energy 1993; 46 (4): 303-316

[13] Kilic M, Kaynakli O. Theoretical study on the effect of operating conditions on performance of absorption refrigeration system, Energy Conversion and Management 2007; 48: 599-607.

[14] Chinnappa J, Crees M, Murthy SS, Srinivasan K. Solar-assisted vapor compression/absorption cascaded air-conditioning systems. Solar Energy 1993; 50(5): 453-458.

Cite this article as: R.S. Mishra, Performance evaluation of half effect LiBr-H_2O Vapour Absorption Systems using Multi cascading of Vapour Compression Cycles for low temperature applications, International Journal of Research in Engineering and Innovation Vol-3, Issue-5 (2019), 321-325

International Journal of Research in Engineering and Innovation (IJREI)
journal home page: http://www.ijrei.com
ISSN (Online): 2456-6934

Performance measurement of flexible manufacturing system: A case study

R.S. Mishra, Himani Saxena, A.K. Madan

Department of Mechanical Production Industrial and Automobiles Engineering, Delhi Technological University Delhi, India

Abstract

A flexible manufacturing system (FMS) is a manufacturing system in which there is flexibility that allows the system to react to changes, whether predicted or unpredicted. It is a highly integrated manufacturing system. The relation between its components is very complex. The mathematical programming approaches are very difficult to solve for very complex system so the simulation of FMS is widely used to analyze its performance measures. Also the FMS components are very sophisticated and costly. If FMS has to be implemented then it is better to analyze its results using simulation which involves no loss of money, resource and labor time. FMS have been studied in aspects as modeling and performance analysis. In this paper, a concept and implementation of the measuring and analysis of performance measures of FMS is applied. Also the system has been modeled. Later the mathematical technique has also been applied for the purpose of comparison and verification of the simulation results. The dispatching problem of FMS is that the performance depends on the state the system is in at each moment, and no single rule exists that is better than the rest in all the possible states that the system may be in. It would therefore be interesting to use the most appropriate dispatching rule at each moment. To achieve this goal, a scheduling approach which uses machine learning can be used. ©2019 ijrei.com. All rights reserved

Keywords: nanotechnology, photochemistry, Spectroscopic methods, Synthesis of materials

1. Introduction

In the present market scenario, the customer demand and specifications of any product changes very rapidly so it is very important for a manufacturing system to accommodate these changes as quickly as possible to be able to compete in the market. This evolution induces often a conflict for a manufacturing system because as the variety is increased the productivity decreases. So the flexible manufacturing system (FMS) is a good combination between variety and productivity. In this system, the main focus is on flexibility rather than the system efficiencies. A competitive FMS is expected to be flexible enough to respond to small batches of customer demand and due to the fact that the construction of any new production line is a large investment so the current production line is reconfigured to keep up with the increased frequency of new product design. The optimal design of FMS is a critical issue and it is a complex problem. There are various modeling techniques for FMS; the most common one are based on mathematical programming. FMS is a highly integrated manufacturing system and the inter-relationships between its various components are not well understood for a very complex system. Due to this complexity, it is difficult to accurately calculate the performance measures of the FMS which leads to its design through mathematical techniques. Therefore, computer simulation is an extensively used numeric modeling technique for the analysis of highly complex flexible manufacturing systems.

2. Literature survey

Browne et al., 1984 defines FMS as an integrated computer controlled system with automated material handling devices and CNC machine-tools and which can be used to simultaneously process a medium-sized volume of a variety of parts. Chan et al. (2007) presented a simulation study using Taguchi's method analysis of physical and operating parameters of the flexible manufacturing system along with flexibility. An approach is developed to study the impact of variations in the physical and operating parameters of an FMS and to identify the level of these variations. The physical and operating parameters of alternative resources may influence the system's performance with the changing levels of flexibility and operational control parameters such as scheduling rules. The results of simulation study shows that expected benefits may not be present when routing flexibility (RF) levels are increased with presence of the variations in physical and operating parameters. The increase in RF level

Corresponding author: R.S. Mishra
Email Address: hod.mechanical.rsm@dtu.ac.in

becomes counterproductive under such environment when variations are above certain limits. It may be useful for decision maker to distinguish the level of flexibility up to which it can be gainfully increased under the presence of variations. Sarker et al. (1994) have presented a detailed classification for the types of manufacturing related flexibility as follows: routing flexibility (RF), machine, flexibility, process flexibility, expansion flexibility, job flexibility, design flexibility, material handling flexibility, setup time flexibility, and volume flexibility. Buitenhek et al. (2002) described that the design of these systems is an important issue of the expensive components of FMS. The design of FMS requires both the physical and the control aspects. Physical aspects includes the issues such as types and numbers of machines, material handling systems, processing times on a machine, machine setting time, tool changing time, transportation time, loading, unloading time, etc. and for the control aspects, the design involves defining the scheduling rules or algorithms that defines the way the system is to be operated. Gupta and Buzacott (1989) explained that the flexibility does not come from the abilities of machine alone; in fact flexibility is the result of a combination of factors like physical characteristics, operating decisions, information integration, and management practice.

3. Overview of flexible manufacturing system

There are three capabilities that a manufacturing system must possess in order to be flexible:

- The ability to identify and distinguish among different incoming part or product styles processed by the system.
- Quick changeover of operating instructions.
- Quick changeover of physical setup.
- To qualify as being flexible the automated system should pass these four tests:
- Part variety test.
- Schedule change test.
- Error recovery test.
- New part test.

The FMS has emerged as one of the revolutions in the manufacturing industries in recent years. It has made it possible to produce a variety of parts in less time and cost. The application of FMS in the current market scenario can satisfy the growing demands of variety, quantity and speed at the same time. The components of the FMS can be classified into two categories:

3.1 Hardware

Machine tools, handling systems, guided vehicles, inspection center, robots, etc.

3.2 Software

Software for FMS can further be classified into extrinsic and intrinsic functions.

The different levels of manufacturing flexibility can be defined as follows:

3.2.1 Basic flexibilities

- Machine flexibility: machine's ability to adapt to a variety of products.
- Material handling flexibility: it is a measure of the system's ability with which different part types can be transported and properly positioned at the various machine tools.
- Operation flexibility: it measures adaptability to alternative operation sequences for processing a part type.

4. System flexibilities

4.1 Volume flexibility

It measures system's capability to operate efficiently at different volumes of the part types.

4.2 Routing flexibility

It is the system's ability to use multiple machines to perform the same operation on a part. It is a measure of the alternative paths that a part can effectively follow through a system for a given process plan.

4.3 Process flexibility

It is a measure of the volume of the set of part types that a system can produce without changing any setup.

4.4 Product flexibility

The volume of the set of part types that can be manufactured in a system with minor setup.

4.5 Aggregate flexibilities

4.5.1 Program flexibility

The ability of a system to run for long periods.

4.5.2 Production flexibility

The volume of the set of part types that a system can produce without major investment in capital equipment.

4.5.3 Market flexibility

The ability of a system to efficiently adapt to changing market conditions.

The case study presented in the paper mainly consists of two kinds of flexibilities machine flexibility and routine flexibility. A key issue in the FMS is the performance evaluation of the system.

The better performance of the FMS results in reduced labor costs, increased output, decreased manufacturing costs, increased flexibility, and reduced production lead time. The major performance measures used in the study were machine utilization and overall productivity. Machine utilization increases as the jobs to be processed on the machine increases and a bottleneck machine has 100% utilization in the system. The machine utilization is measured by the number of hours it operates in the system to the total available hours in the system. The design and performance evaluation of the FMS system is a complex process and requires a thorough investigation. Three different methods have been proposed and compared in the presented case studies to evaluate the different cases of different FMS systems. The feasibility of the different techniques has also been reviewed in order to determine their successful application in the evaluation of FMS system.

5. Petri net

Petri nets are a class of modeling tools, which is well-defined mathematical foundation and easy to understand graphical feature. It is a powerful design tool which facilitates visual communication between people who are engaged in the design process. A Petri net is a directed graph consisting of three structural components – places, transitions, and arcs. Places which are drawn as circles represent possible states or conditions of the system while transition, which are shown by bars or boxes, describe events that may modify the system states. Manufacturing system is a discrete system. Hence any modeling has to be based on the concepts of events and activities. An event corresponds to a state change. When using Petri nets, events are associated with transitions. Activities are associated to the firing of transitions or/and to the marking of places. Queuing models can also be used for handling events and activities but synchronizations are difficult in these models. Hence Petri net is preferred. Analysis of the Petri net reveals important information about the structure and dynamic behavior of the modeled system. This information is used to evaluate the modeled system and suggest improvements of changes. Petri nets are used to model the occurrence of various events and activities in a system.

6. Modeling in Petri net

The system consists of loading and unloading station, two process stations, inspection center and two AVGs. To start a cycle, raw parts and the AVGs must be available. Then only firing will take place. The AVG carries a raw part from loading station to the process station according to the given sequence for the different parts. After the completion of an operation in one station the part is again carried by AVG to its next required station. At the end the part is carried to the unloading station. Place representing the stations have tokens according to the number of machines they have. The Petri net model is simulated to get the overall productivity of the given system.

7. System description for a case study

The system shown in the Fig. 1 consists of three robots, two machines, i.e. a drilling machine and a milling machine and an inspection center. The system also consists of two conveyors, conveyor in and conveyor out. The system has operational flexibility in the sense that two types of products are produced in the system using two different process operations. Type A product undergoes milling operation only whereas Type B product undergoes drilling and then milling. Both the parts are inspected before moving to conveyor out. Robot 2 loads the milling and drilling machine from conveyor in, and Robot 1 loads the part B onto the milling machine after it completes the drilling operation. It also unloads the milling machine. Robot 3 loads the inspection center. Material handling system consists of three robots, one conveyor and three work carriers with mean transport time =5 min (see Table 1)

8. Solution methodology

Three types of techniques are applied to find the parameters of the given FMS; the two are simulation techniques and the one is mathematical technique. The simulation technique is Petri net. The system is modeled in this.

8.1 System modeling

The network is shown below. The system is using different kinds of nodes such as create node, assign node, await node, free node, collect node, terminate node, goon node, etc. to describe the given system. The system starts with creating entities at an interval of 2 min. A goon node is used to divide in different sequence according to their operational requirements. In the await node, entities wait for the resources to be available. The system is using three resources of robots, one resource of milling machine and one resource of drilling machine each having a capacity of three. An inspection system is also present in the system. The system runs for 1 week working hours. The system consists of loading and unloading station, two process stations, inspection center and two AVGs.

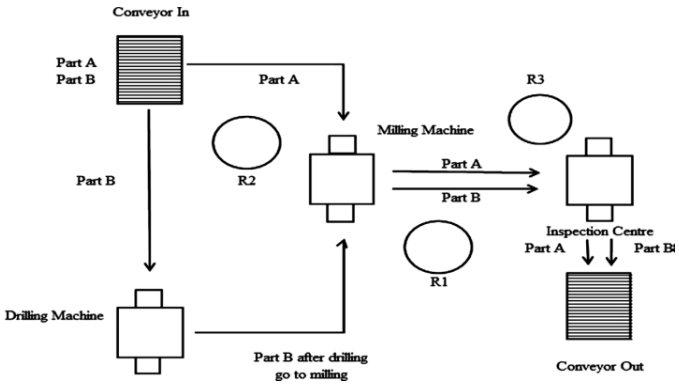


Figure 1: Block diagram of considered FMS in case study

9. Results and Discussions

The following operations and processes have been listed on different machining centers in Table-1.

Table 1: List of operations and process time on different machining centers

Part	Part mix	Operation	Process time (min)	No. of servers	Frequency
A	0.4	Load	4	1	1
		Mill	25	3	1
		lisped	6	1	1
		Unload	2	1	1
B	0.6	Load	4	1	1
		Drill	20	3	1
		Mill	30	3	1
		Inspect	8	1	1
		Unload	2	1	1

Table 2. List of operations and process time on different stations.

Part	Weekly demand	Process sequence	Load	Process station		Inspection station	Unload station
			A	B	C	D	A
1	250	A –> C –> D –> A	5		21	14	3
2	350	A –>B –> D –> A	5	22		14	3
3	150	A –> B –> C –> D –> A	5	20	22	15	3
4	250	A –> C –> B –> C –> D	5	15	20	14	3

To start a cycle, raw parts and the AVGs must be available. The AVG carries a raw part from loading station to the process station according to the given sequence for the different parts. After the completion of an operation in one station the part is again carried by AVG to its next required station. At the end the part is carried to the unloading station. The utilization and overall productivity is then compared .There are large numbers of techniques such as simulation techniques, modeling techniques, mathematical programming which can be used to evaluate the performance of any FMS

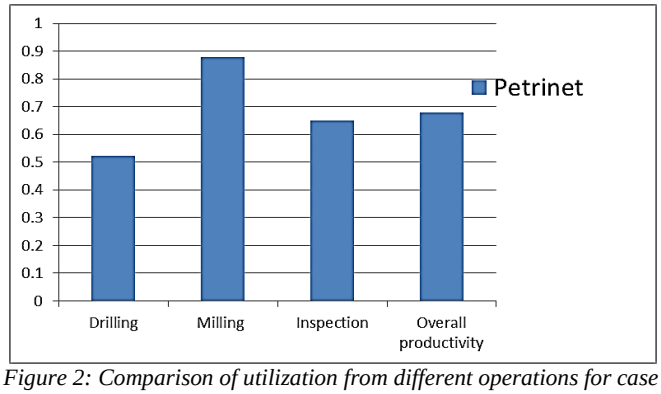


Figure 2: Comparison of utilization from different operations for case study

10. Conclusion

From the results it can be concluded that the performance obtained for a given system from the techniques is very clear and precise. Hence it can be said that these techniques are applicable to any FMS system to evaluate and confirms its performance.

References

[1] Browne, J., Dubois, D., Rathmill, K., Sethi, P., Steke, KE., 1984. Classification of flexible manufacturing systems. FMS Mag., 14–27.

[2] Bruccoleri, M., Sergio, NL.,Perrone, G., 2003. An object-oriented approach for flexible manufacturing controls systems analysis and design using the unified modeling language. Int. J. Flexible Manuf. Syst. 15 (3), 195–216.

[3] Buitenhek, R., Baynat, B., Dallery, Y., 2002. Production capacity of flexible manufacturing systems with fixed production ratios. Int. J. Flexible Manuf. Syst. 14 (3), 203–226.

[4] Chan, FTS., 2001. Effects of routing flexibility on a flexible manufacturing system. Int. J. Comput. Integrat. Manuf. 14 (5), 431–445.

[5] Chan, F.T.S., Bhagwat, R., Wadhwa, S., 2007. Flexibility performance: Taguchi's method study of physical system and operating control parameters of FMS. Rob. Comput. Integr. Manuf. 23, 25–37.

[6] Chen, S.C., Ke, Y.L., Wu, J.S., 2001. Coloured petri-nets approach for solving distribution system contingency. Proc. IEEE 148 (5), 463–470.

[7] Cheng, T.C.E., 1985. Simulation of flexible manufacturing system. Simulation 45 (6), 299–302.

[8] Chin-Jung, T., Li-Chen, F., Yung Jen, H., (1992). Modeling and simulation for flexible manufacturing system using Petri net. Second Int. Conf. Autom. Technol. 4, 31–36.

[9] Crockett, D., Dearochers, A., DiCesare, F., Ward, T. (1987). Implementation of a Petri net controller for machine workstations. Proc. of IEEE Robotics Automat. Conf. 1861–1867.

[10] Cuninghame, Green R.A., (1979). Minimax Algebra, Vol. 166 of Lecture Notes in Economics and Mathematical Systems. Springer- Verlag, Berlin, Germany. Delgadillo,

[11] G.M., Llano, S.B., 2006. Scheduling application using petri nets: a case study: intergra´ficass.a.'. In: Proceedings of 19th international conference on production research, Valparaiso, Chile. Diaz, M., 1982. Modeling and analysis of communication and cooperation protocols using Petri net based models. Comput. Networks 6.

[12] Ezpeleta, S.D., Colom, J.M., Martinez, J.A., 1995. Petri net based deadlock prevention policy for flexible manufacturing systems. IEEE Trans. Rob. Autom. 11 (2), 173–184.
[13] Ge, S.S., Lee, T.H., Gu, D.L., Woon, L.C., 2000. A one stop solution in robotic control system design. IEEE Rob. Autom. Mag. 7, 42–55.
[14] Gertz, M. W., Khosla, P. K., (1994). Onika: A multilevel human– machine interface for real-time sensor-based robotics systems. In: Proceedings of SPACE 94: The Fourth International Conference and Expo. on Engineering Construction, Albuquerque. Gupta, D., Buzacott, JA. 1989. A framework for understanding flexibility of manufacturing systems. J. Manuf. Syst. 8 (2), 89–97.
[15] Gurel, A., Bogdan, S., Lewis, F.L., Huff, B., (2000). Matrix approach to deadlock-free dispatching in multi-class finite buffer flowlines. IEEE Trans. Autom. Control 45(11), 2086–2090.
[16] Huang, Y-M., Chen, J-N., Huang, T-C., Jeng, Y-L., Kuo, Y-H., 2008. Standardized course generation process using dynamic fuzzy petrinets. Expert Syst. Appl. 34, 72–86.
[17] Jain, S., Foley, W.J., (1986). Basis for development of a generic fms simulator. Proc. Second ORSA/TIMS Conf. Flexible Manuf. Syst.: Oper. Res. Models Appl., 393–403.
[18] Kalkunte, M.V., Sarin, S.C., Wilhelm, W.E., 1986. Flexible Manufacturing Systems: A Review of Modeling Approaches to Design, Justification and Operations. Flexible Manuf. Syst.: Methods Stud.. Springer, Berlin, pp. 3-25.
[19] Kimon, P.V., 1990. On the hierarchical modeling analysis and simulation of flexible manufacturing system with extended Petrinets. IEEE Trans. Syst. Manuf. Cybernatics 20 (1), 94–109.
[20] Kovac˘ ic, Z., Bogdan, S., Reichenbach, T., Smolic´-Roc˘ak, N., Birgmajer, B., (2001). FlexMan – A computer-integrated tool for design and simulation of flexible manufacturing systems. In: Proceedings of the Ninth Mediterranean Conference on Control and Automation Control, Dubrovnik

Cite this article as: R.S. Mishra, Himani Saxena, A.K. Madan, Performance measurement of flexible manufacturing system: A case study, International Journal of Research in Engineering and Innovation Vol-3, Issue-4 (2019), 230-234.

This article has been accepted for publication in a future issue of this journal, but has not been fully edited. Content may change prior to final publication. Citation information: DOI 10.1109/TIFS.2019.2950134, IEEE Transactions on Information Forensics and Security

PermPair: Android Malware Detection using Permission Pairs

Anshul Arora, Sateesh K Peddoju, *Senior Member, IEEE*, Mauro Conti, *Senior Member, IEEE*

***Abstract*—The Android smartphones are highly prone to spreading the malware due to intrinsic feebleness that permits an application to access the internal resources when the user grants the permissions knowingly or unknowingly. Hence, the researchers have focused on identifying the conspicuous permissions that lead to malware detection. Most of these permissions, common to malware and normal applications present themselves in different patterns and contribute to attacks. Therefore, it is essential to find the significant combinations of the permissions that can be dangerous.**

Hence, this paper aims to identify the pairs of permissions that can be dangerous. To the best of our knowledge, none of the existing works have used the permission pairs to detect malware. In this paper, we proposed an innovative detection model, named *PermPair*, that constructs and compares the *graphs* for malware and normal samples by extracting the permission pairs from the *manifest* file of an application. The evaluation results indicate that the proposed scheme is successful in detecting malicious samples with an accuracy of 95.44% when compared to other similar approaches and favorite mobile anti-malware apps. Further, we also proposed an efficient edge elimination algorithm that removed 7% of the unnecessary edges from the malware graph and 41% from the normal graph. This lead to minimum space utility and also 28% decrease in the detection time.

***Index Terms*—Android Malware, Android Security, Malware Detection, Permissions Pair Graph, Smartphone Security.**

I. Introduction

SMARTPHONES have gained popularity with the presence of feature-rich apps which provide services like social networking, online banking, online gaming, and location-based services, in addition to the conventional services like phone calls and messaging. A report [1] shows that there is tremendous growth in smartphone sales, with 82% Android smartphone users. Rising popularity has made them susceptible to malware attacks. The year 2013 recorded 1,45,000 new malware samples, with 97% of them targeted towards Android platform [2]. This indicates that Android is evidently the major target, with nearly 5000-6000 malware samples attacking them every 14 seconds, and the figure touched 3.5 million malicious samples in 2017 and is expected to rise to 25 million by 2019 [3]. This trend shows how malware attackers are relentlessly developing new malware samples targeting smartphones, especially Android. Apart from the traditional drive-by-downloads way of infecting the system, malware is also injected into smartphones through repackaging and update attacks. The threats posed by mobile malware include financial loss to users, information leakage, system damage, and mobile bots [4].

The increase in the number of Android malware attacks is mainly from three major sources: (a) App markets, an easy distribution gateway for malware developers; (b) Users, drive-by-downloads, and (c) Developers, weak code.

The design of the Android platform secures the system by restricting the access to local resources by the applications (apps) using the permission constraints. A user is prompted with the list of permissions during the installation of an application. This list is supposed to alert the users about the resources that the application accesses. Most of the users ignore them and grant the permissions liberally. They do not have adequate expertise to understand the significance of these permissions, and the harm caused by them if any [10]. This weakness of the users drew the attention of the attackers. Consequently, the researchers aim to analyze the permissions for detecting malicious behavior.

Several related works such as [5], [8], [14]–[16], [22], [23], [25] have used permissions to detect Android malware. They have analyzed the permissions in malicious apps, detected during the period, 2010-2012. These studies have examined the permissions of normal and malicious samples, and have reported that most of the top permissions in malware and normal apps are quite similar, and hence not distinguishable. For instance, the authors in [14] reported that the top five permissions in both the categories are exactly the same. Therefore, it is important to find the vital combinations of the permissions present in malware and normal samples. None of the previous works, except the one proposed in [22], have aimed at finding the permission patterns that can launch any malicious activity. They have also identified risky permission patterns in malware samples. However, they did not find the permission patterns that occur prominently in normal apps. Moreover, they did not propose any detection model.

Motivation: We believe that the pairing of dangerous permissions together can be effective in detecting malicious apps. For instance, to leak device-specific information to the server, an application requires only two permissions: INTERNET and READ_PHONE_STATE. This permission pair, alone, is dangerous and can launch a malicious activity. However, to evade the detection, malware developers may supplement some additional permissions [11]. The presence of such dangerous permission pairs can help detect malicious behavior. Therefore, this work aims to analyze permissions in a group of two

A. Arora is with the Discipline of Mathematics and Computing, Delhi Technological University Delhi, India. Email: anshul15arora@gmail.com

S.K.Peddoju is with the Department of Computer Science and Engineering, Indian Institute of Technology Roorkee, India. Email: sateesh@ieee.org

M.Conti is with the Department of Mathematics, University of Padua, Italy, and with the Department of Electrical Engineering, University of Washington, Seattle, USA. Email: conti@math.unipd.it

1556-6013 (c) 2019 IEEE. Personal use is permitted, but republication/redistribution requires IEEE permission. See http://www.ieee.org/publications_standards/publications/rights/index.html for more information.

This article has been accepted for publication in a future issue of this journal, but has not been fully edited. Content may change prior to final publication. Citation information: DOI 10.1109/TIFS.2019.2950134, IEEE Transactions on Information Forensics and Security

and proposes a new methodology to find such pairs that can distinguish normal and malicious samples. The following research questions emerge in the light of permission pair analysis:

1) How to represent the permission pairs extracted from the applications?
2) How to build a detection model using permission pairs?
3) Is there any change in the permission pairs of malware samples over a period of time?
4) What are the top dangerous permission pairs present in malicious samples but not in benign ones?
5) What are the top permission pairs present in normal apps and how are they different from malicious samples?

We are motivated to answer these questions with a vision to develop an Android malware detector based on permission pairs. We present *PermPair*: Permission Pair Based Android Malware Detection model, based upon permissions extracted from the manifest file of the applications. We use the graph data structure to represent these permission pairs. Our detection results are relatively better than the mobile anti-malware apps which we evaluate against the same dataset of malicious apps. The work proposed in this paper employs a mix of old and recent datasets for evaluation.

Contributions: The contributions of this research are highlighted below:

- Built the permission pair graphs for different malware datasets and analyzed the impact of the permission pairs on both, old and recent, malicious apps.
- Proposed a novel algorithm to merge graphs of different malware datasets to construct a single final malware graph of permission pairs (named as Malicious-Graph (G_M)). Similarly, a separate permission pair graph of normal apps known as Normal-Graph (G_N) was also established.
- Designed an algorithm to detect malicious apps by comparing both malicious (G_M) and normal (G_N) graphs.
- Compared the detection results with that of widely used mobile anti-malware apps and other similar defense mechanisms proposed in the literature. Concluded that the proposed approach is more effective in detecting malicious apps.
- Performed edge elimination to remove insignificant permission pairs from both the graphs, to reduce the size of the graphs and the detection time.

Organization: The rest of the paper is organized as follows: Section II provides the background knowledge of Android permissions, and related work proposed in the literature for Android malware detection. The discussion of the proposed *PermPair* model is in section III. A report of results and findings of the proposed work is presented in section IV. Finally, section V concludes with the scope of future work.

II. Background and Related Work

This section, initially, presents a brief description of Android permission system followed by a critical review of the studies that have been proposed for Android malware detection. In the end, a summary of the important takeouts from the review of the literature is presented.

A. Background

Every Android application[1] consists of *AndroidManifest.xml* file having permissions and other parameters required by the application. The user receives this list of permissions for additional resources at the time of installation. Once the user grants all the permissions, the app gets installed. The Java code of the application houses, possibly, the malicious component of the malware samples. If the manifest file has the required permissions, it invokes the API calls in the code. This is the primary reason why permissions have been the most used static feature in Android malware detection.

B. Related Work

Android malware detection is broadly categorized into three types: Static, Dynamic, and Hybrid Detection. This section reviews all these detection types published in the literature in the following subsections.

1) Static Detection: Static solutions aim to analyze the app's manifest file components, Java code or the sequence of API calls within the code. These related works can further be sub-divided into six categories: Permissions Analysis, Permissions Based Malware Detection, Permission Pattern Analysis of Android Malware, Manifest File-Based Detection, Permission Graph Analysis, and API Calls Based Detection.

Permissions Analysis: Some of the earlier works like [8], [9] analyzed permissions to detect malicious behavior within the normal apps. Grace et al. [8] evaluated potential risks associated with in-app advertisement libraries by analyzing permissions and API calls. *Kirin* [9] model developed the security rules to identify the risky applications based upon permission combinations.

Holavanalli et al. [12] analyzed the cross-app, i.e., colluding apps, flow permissions to identify the interaction of apps with each other. Grace et al. [13] identified the permission leaks, i.e., several permissions that protect access to sensitive user data are unsafely exposed to other apps.

In all of these studies, the authors have analyzed permissions within the normal apps to look for any signs of dangerous behavior. They did not consider the malware samples in their analysis. However, we aim to find the dangerous permission pairs found in malware samples by analyzing different malware datasets.

Permissions Based Malware Detection: Sanz et al. [14] extracted top permissions in malicious and normal apps using machine learning classifiers. *MAMA* model [15] extracted not only the permissions but also other features of the manifest file. In both these works, the authors focused on extracting the widely used permissions by malware and normal apps.

Talha et al. [16] extracted permissions from the apps. For each permission, they calculated the score based upon the number of malware containing the permission, to the total number of malware. Tao et al. [17] analyzed permissions, APIs, and the correlation between them to detect malware.

Cen et al. [18] applied the probabilistic discriminative model on decompiled source code and the permissions for

[1]https://developer.android.com/guide/topics/manifest/manifest-intro

1556-6013 (c) 2019 IEEE. Personal use is permitted, but republication/redistribution requires IEEE permission. See http://www.ieee.org/publications_standards/publications/rights/index.html for more information.

This article has been accepted for publication in a future issue of this journal, but has not been fully edited. Content may change prior to final publication. Citation information: DOI 10.1109/TIFS.2019.2950134, IEEE Transactions on Information Forensics and Security

detecting malicious samples. In similar lines, Peng et al. [19] applied probabilistic generative models like Naïve Bayes for evaluating risks of the Android apps based upon the permissions requested. Few recent studies like [20], [21] applied permissions to detect Android malware.

However, none of these works discussed the significant presence of permission patterns in malware samples that can launch any malicious activity. In comparison to these studies, our work focuses on analyzing which permission patterns, in pairs, are significantly present in normal and malicious apps.

Permission Patterns of Android Malware: Few studies like [22]–[24] have focused on the analysis of the permission patterns found in Android malware. In [22], permission patterns mining algorithm is applied to identify dangerous permission patterns. However, the model did not consider the normal apps and did not present any model for detection. Similarly, the model presented in [23] used the feature ranking methods to rank the risky permissions. It is identified that SVM gives high accuracy when the model uses a set of 40 permissions, and Random Forest gives better results with ten permissions.

DroidRanger [24] model identified that a few permission combinations like ⟨SEND_SMS,RECEIVE_SMS⟩, and ⟨INTERNET,RECEIVE_SMS⟩ help in detecting malware. However, it does not discuss in detail which specific permission pairs are prominently present in normal or malicious apps.

Having realized that a large permission set is too complex to analyze, the proposed model selects permission pairs for analysis and detection. Unlike the results reported in [23] and [24], in our study, a thorough examination of which permission pairs exist in normal and malicious apps is made, and a detection model that was missing in [22] is proposed.

Manifest File Based Malware Detection: Few studies like [5], [25]–[27] analyzed manifest file components in addition to the permissions. *DroidMat* [25] model analyzed permissions, intents, components, and API calls, and applied K-means clustering for detection. Arp et al. [5] used features like permissions, hardware components, API calls, and network addresses to detect malware. The work proposed in [26] used permissions and intents to detect malware. Kim et al. [27] formed a vector of the apps consisting of static features such as manifest file components, strings, and API calls.

The proposed work in this paper employs only significant permission pairs, instead of extracting all the components from the manifest file, to reduce the substantial computation overhead. It is also observed in our studies that many recent malware samples like Koodous dataset include only the permissions, not the other components from their manifest files.

TABLE I: Comparison of Proposed Work with State-of-the-art Static Mobile Malware Detection Models

Tech.	Features	Perm. Pattrn Analy.	#	Source	Period	Unknown Detection
[14]	P	No	4301	VT	2010-2012	-
[15]	M	No	2808	VT	2010-2012	-
[16]	P	No	6909	G, D, C	2010-2011	-
[17]	P, APIs	No	15336	VS, C	2010-2016	-
[25]	M	No	238	C	2011-2012	-
[5]	M	No	5560	D	2010-2013	-
[30]	APIs	No	8407	G, C, VS	2010-2014	-
[31]	APIs	No	2200	G, MF	2010-2015	-
Prop.	**P**	**Pairs**	**6208**	**G, D, K, C, PZ**	**2010 - 2018**	**84.48%**

Prop. : Proposed Work; P: Permissions; M: Manifest File Components; VT: VirusTotal; G: Genome; D: Drebin; C: Contagio; VS: VirusShare; MF: Mcafee; PZ: Pwnzen Infotech

Permission Graph Analysis: Solokova et al. [28] used graphs to represent the correlation between the permissions of normal apps. They grouped the apps of the same category and calculated metrics like node degree, weighted degree, and page rank score for each graph. However, they considered only the categorized normal apps and not the malicious samples. The proposed work in this paper considers both malware and normal apps to construct separate permission pair graphs.

Zhu et al. [29] built a system to evaluate the risks involved in an app based on the permissions. They created a bipartite graph, where one set of vertices constitute the apps and the other set constitute the permissions. There was no relation between the permissions, unlike in our proposed work.

API Calls Based Detection: Fan et al. [30] formed API calls based frequent subgraphs to classify Android malware into their corresponding families. Zhang et al. [31] built dependency graphs of the API calls and applied similarity metrics to classify malware into their families. The *Stowaway* model in [32] determined the set of API calls used by an app and mapped them with the permissions. *Apposcopy* [33] model aimed to detect the apps that steal the user information, by analyzing control-flow and data-flow properties of the apps. Elish et al. [34] focused on user-trigger dependence and sensitive APIs to detect malware.

Often, if the APIs used are not related to any manifest file component, they act as noise in the detection process.

Table I compares the existing static works with the proposed work. Most of the works have used outdated malware samples for their experiments and have not analyzed dangerous permission patterns in malware apps. They have also not analyzed the detection rate of their proposed model on unknown samples.

2) Dynamic Detection: Dynamic solutions intend to analyze the run-time behavior of the applications. Related works in this field mainly fall into two aspects: OS-level Detection and Network-level detection.

OS-Level Detection: TaintDroid [35] model, based on dynamic taint analysis, tracked the flow of privacy-sensitive information through third-party apps. Many systems such as [36] are built on TaintDroid. *TaintART* [37] detected the privacy leakage from the apps on the Android Run Time (ART). Yang et al. [38] extended the TaintDroid model to detect the data leaks from the apps and also determine whether the leak is due to user intention or not. All these works focused on analyzing data-leaks from the apps, rather than detecting malicious apps.

Shabtai et al. [39] analyzed dynamic features such as the CPU usage, number of running processes, and the number of packets sent through Wi-Fi to detect malware. *CopperDroid* [40] model analyzed system calls of malware samples and described whether the malicious behavior is initiated from Java, JNI or native code execution. Afonso et al. [41] analyzed dynamic API calls and system calls to detect malicious apps.

All these solutions have relatively high computational overheads compared to static solutions. Moreover, stealthy malware samples try to evade such detection by gaining awareness

1556-6013 (c) 2019 IEEE. Personal use is permitted, but republication/redistribution requires IEEE permission. See http://www.ieee.org/publications_standards/publications/rights/index.html for more information.

This article has been accepted for publication in a future issue of this journal, but has not been fully edited. Content may change prior to final publication. Citation information: DOI 10.1109/TIFS.2019.2950134, IEEE Transactions on Information Forensics and Security

about the simulation environment. Hence, we focus on static permissions based detection.

Network-Level Detection: Wang et al. [42] applied Natural Language Processing methods on the HTTP headers to detect malicious apps. Shabtai et al. [43] applied machine learning algorithms on traffic features to generate the patterns of normal traffic and used those patterns to detect malicious apps. Chen et al. [44] analyzed network traffic of malicious samples and found that the majority of those samples generated their malicious traffic within the first five minutes.

In one of our previous works [45], we deployed Android emulator to capture the network traffic of malicious and normal apps. Out of 16 network traffic features, 7 of them were found to distinguish normal and malicious traffic. In our other work [46], we used smartphones rather than emulators to capture the traffic. We did not observe any distinguishable features. Therefore, we minimized the number of features required to detect Android malware by ranking them.

All such network traffic based solutions detect only those samples that have network connectivity. For instance, any malware that only sends SMS in the background, will not generate any network traffic. The proposed approach in this paper, however, can be used to detect such type of malware.

Table II compares the existing dynamic models with the proposed work. All the dynamic solutions have feature extraction overheads, and none of them except one has evaluated their model on unknown samples. Moreover, the malware dataset used by other works is relatively older, whereas we have used recent malware samples for our experiments.

3) Hybrid Detection: Hybrid solutions aim to combine static and dynamic components to detect malware. Saracino et al. [47] analyzed various dynamic and static features such as system calls, API calls, user activity logs, and permissions. Sun et al. [48] proposed a hybrid model by generating static and dynamic graphs from manifest file components, and system calls respectively.

Xia et al. [49] performed static APIs analysis and dynamic bytecode analysis to detect the data leaks from the apps. *Riskranker* [50] analyzed dynamic features like run-time Dalvik code loading, and static features like permissions to detect malware. Arora et al. [51] [52] presented two different hybrid models by combining traffic features and permissions.

Table III compares the existing hybrid models with the proposed work. All these approaches also suffer from the drawbacks of the dynamic solutions, i.e., high computational overheads. Hence, the proposed work aims to analyze static permission pairs to detect Android malware. Additionally, it also analyzes and detects the recent unknown malware samples.

TABLE II: Comparison of Proposed Work with State-of-the-art Dynamic Mobile Malware Detection Models.

Tech.	Features	Features Overhead	#	Source	Period	Unknown Detection
[35]	DL	Yes	-	-	-	-
[36]	SE, APIs, KL	Yes	3	G	2010-2011	-
[37]	APIs, SC, KL	Yes	-	-	-	-
[43]	TCP	Yes	2267	G, D	2010-2014	-
[44]	HTTP	Yes	725	G	2010-2012	-
[46]	TCP	Yes	889	G	2010-2012	92%
Prop.	**P**	**No**	**6208**	**G, D, K, C, PZ**	**2010 - 2018**	**84.48%**

Prop. : Proposed Work; DL: Dynamic Logs; SE: System Events; KL: Kernel Logs; SC: System Calls; TCP: TCP Traffic; HTTP: HTTP Traffic; P: Permissions; G: Genome; D: Drebin; K: Koodous; C: Contagio; PZ: Pwnzen

TABLE III: Comparison of Proposed Work with State-of-the-art Hybrid Mobile Malware Detection Models

Tech.	Features	Features Overhead	#	Source	Period	Unknown Detection
[47]	SC, APIs, AC	Yes	2784	G, C, VS	2010-2015	-
[48]	M, SC	Yes	3273	G, DA, C	2010-2016	-
[49]	API-S, API-D	Yes	1061	G, DB	2010-2015	-
[50]	P, J, DC	Yes	718	G	2010-2012	-
[51]	P, N	Yes	985	G	2010-2012	-
[52]	P, N	Yes	363	G	2010-2012	-
Prop.	**P**	**No**	**6208**	**G, D, K, C, PZ**	**2010-2018**	**84.48%**

Prop. : Proposed Work; SC: System Calls; AC: App Components; M: Manifest File; API-S: Static APIs ; API-D: Dynamic APIs; P: Permissions; J: Java Code; DC: Dalvik Code; N: Network Traffic; G: Genome; C: Contagio VS: VirusShare; DA: DroidAnalytics; DB: DroidBench; D: Drebin; K: Koodous; PZ: Pwnzen

III. Proposed PermPair Detection

Analyzing permissions in a group of more than two can be complex, as it can lead to a high number of permission patterns. If an application contains N number of permissions, and we want to analyze permission patterns in the group of R, then the total number of permission patterns will be ${}^{N}C_{R}$, i.e., $\frac{N!}{R!(N-R)!}$. Increasing the value of R from two will result in more number of permission patterns or will be complex to represent. Therefore, we focus on analyzing permission pairs.

In this section, we present our proposed novel *PermPair* model for detecting malicious Android apps.

A. System Design

In order to conduct extensive analysis on permission pairs, we considered malware samples from three different sources: Genome [4], Drebin [5], and Koodous [6]. Besides, we downloaded normal Android apps from the Google Play Store.

The proposed model consists of three phases as shown in Figure 1. The first phase, *Graph Construction phase*, extracts permission pairs from each application to form a graph. Four different permission pair graphs: Genome Graph (G_G), Drebin Graph (G_D), Koodous Graph (G_K) and Normal Graph (G_N) are built during this phase. Typically, every new dataset used in the analysis and detection needs the construction of the graph.

The next phase, *Graph Merge phase*, deals with the merging of all malicious graphs into a single malicious graph (G_M). Hence, the final model consists of two graphs: a normal

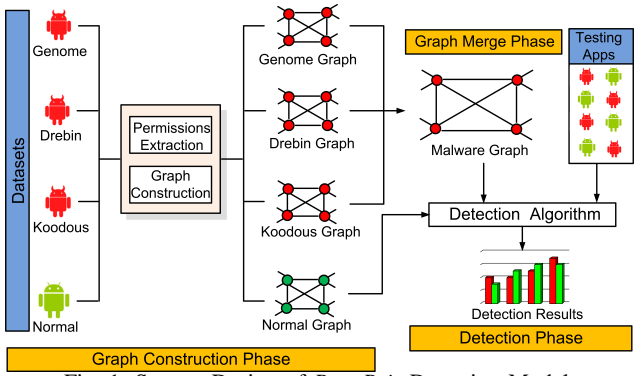


Fig. 1: System Design of *PermPair* Detection Model.

1556-6013 (c) 2019 IEEE. Personal use is permitted, but republication/redistribution requires IEEE permission. See http://www.ieee.org/publications_standards/publications/rights/index.html for more information.

This article has been accepted for publication in a future issue of this journal, but has not been fully edited. Content may change prior to final publication. Citation information: DOI 10.1109/TIFS.2019.2950134, IEEE Transactions on Information Forensics and Security

Algorithm 1 Graph Construction Algorithm

Input: Set of Applications (*N*) in a dataset (*D*)
Output: Permission Pair Graph *G(V,E)*
Initially $V \leftarrow \emptyset$ and $E \leftarrow \emptyset$
for $\forall\ N \in D$ **do**
  Extract its Manifest File *M* using apktool
  Let P = (P_1, P_2, P_3...P_m) be set of permissions in M
  if ($|P| == 0$ or $|P| == 1$) **then**
    $V \leftarrow V + \emptyset$ and $E \leftarrow E + \emptyset$ ▷ zero or single permission
  else
    For every permission $P_i \in M$, create a node V_i if $V_i \notin V$
    Add an edge between every permission pair (P_i,P_j) derived from *M*
    if (P_i, P_j) $\notin E$ **then**
      $W_{(P_i, P_j)} = 1$
    else
      $W_{(P_i, P_j)}$ ++
    end if
  end if
end for
Divide each edge weight by *N*
Return Graph *G(V,E)*

graph (G_N) and a malicious graph (G_M). The subsequent phase proposes a detection algorithm to distinguish normal and malicious apps. Finally, the model eliminates the irrelevant edges, that do not affect the detection results, from both G_M and G_N, to optimize it.

1) Graph Construction Algorithm: The proposed model uses graphs to represent the relationship between various permissions in each application. The model applies the *Algorithm* 1 to construct a graph *G(V, E)*, by representing a unique permission at vertex *V* and a pair of permissions connected by a weighted edge *E*. Each edge weight increases with the occurrence of the same permission pair from different applications. An application with single or no permission does not contribute to any analysis or detection.

The algorithm extracts the permissions from each application and generates all the permission pairs. If an app has *N* number of unique permissions, then the algorithm creates *N* number of vertices, one for each permission. The number of possible permission pairs added to the graph among all is $\binom{N}{2}$. For instance, in an app, if there are two permissions P_1 and P_2, then, an edge, with an edge weight of one is created between them if it did not exist earlier. Otherwise, edge weight is incremented by one, as presented in Algorithm 1.

Once we process all the apps in a dataset, we divide each edge weight by the total number of apps in that dataset to normalize weights of permission pairs between different graphs. This phase answers our research question 1, describing how to represent the permission pairs extracted from the apps.

After generating separate Genome(G_G), Drebin(G_D) and Koodous(G_K) graphs, they are merged into a single graph (G_M) to represent a common malicious graph.

2) Graph Merge Algorithm: Graph Merge Algorithm, Algorithm 2, merges three malware graphs (G_G, G_D, G_K) to form a common malware graph (G_M) by combining their edges. There are two types of edges: common and disjoint.

Inserting all disjoint edges along with their edge weights to G_M is straightforward. The challenge lies in deciding the weights of the common edges. Consider a common edge *e*, with weights e_{w1}, e_{w2}, and e_{w3} in G_G, G_D, and G_K respectively. There are different possible ways the weight of edge *e* can be considered in the final graph G_M such as taking their average, minimum or maximum. However, we have adapted the multi-objective optimization approach for the reasons explained below.

The important merge criteria, to find the weights for common edges are (i) a high number of true positives, and (ii) a low number of false positives. This is similar to a multi-objective optimization where objectives are conflicting, i.e., no single solution can give optimum value for all the objectives. Weighted sum method is the most suited classical solution for solving such problems in which we assign weights to all the objectives, as shown in Equation 1.

$$\begin{aligned} &\underset{x}{\text{minimize}}/\underset{x}{\text{maximize}} \quad F(x) = [f_0(x), f_1(x), \ldots, f_k(x)], \\ &\text{subject to} \qquad\qquad g_i(x) \leq b_i,\ i = 1, \ldots, m. \end{aligned} \tag{1}$$

where f_0 , f_1 , . . . , f_k are *k* objective functions to be optimized, with *m* constraints. Weighted sum method applies scalar weights α_i for each objective such that the sum of all weights is one. Then, each objective is multiplied with its corresponding weight and all of them are added to form a single objective function which is to be optimized, as shown in Equation 2.

$$\begin{aligned} &\underset{x}{\text{minimize}} \quad Z, \quad \text{where } Z = \sum_{j=1}^{k} \alpha_j f_j \ \text{ and } \sum_{j=1}^{k} \alpha_j = 1, \\ &\text{subject to} \quad g_i(x) \leq b_i,\ i = 1, \ldots, m. \end{aligned} \tag{2}$$

Graph merging problem has two objective functions: one for maximizing true positives, say F_1, and other for minimizing false positives, say F_2. The weighted sum method requires weights for both the objectives. Consider an edge *e* having weights e_{w1} (from G_G), e_{w2} (from G_D), e_{w3} (from G_K), and e_{wn} (from G_N) respectively. The weight assigned to function F_1, say α_1, is the ratio of the percentage of malware samples containing that edge *e* to the percentage of the total number of samples containing *e*, as mentioned in Equation 3.

$$\alpha_1 = \frac{\sum_i e_{wi}}{\sum_i e_{wi} + e_{wn}}. \tag{3}$$

Here $\sum_i e_{wi}$ is the sum of edge weights of any edge *e* in all the malicious graphs and e_{wn} represents its edge weight in the normal graph.

Similarly, the weight assigned to function F_2, say α_2, is the ratio of the percentage of normal samples containing that edge *e* to the percentage of the total number of samples containing the edge *e*.

Algorithm 2 describes the method to merge three malware graphs. We divide the complete edge set into disjoint and collectively exhaustive sets called $Common_{edge-set}$ and $Disjoint_{edge-set}$. We place the edges common in two or three graphs in $Common_{edge-set}$. We place the remaining edges in $Disjoint_{edge-set}$ and then add them forthwith to G_M.

We apply the weighted sum method to find the weight for the common edges. Let m_i be the weight of a common edge e_i in G_M. The Equation 4 denotes functions F_1 and F_2.

1556-6013 (c) 2019 IEEE. Personal use is permitted, but republication/redistribution requires IEEE permission. See http://www.ieee.org/publications_standards/publications/rights/index.html for more information.

This article has been accepted for publication in a future issue of this journal, but has not been fully edited. Content may change prior to final publication. Citation information: DOI 10.1109/TIFS.2019.2950134, IEEE Transactions on Information Forensics and Security

$$F_1 = (m_i - w_n)(w_1 + w_2 + w_3),\ F_2 = (w_n - m_i)(w_n). \quad (4)$$

where w_1, w_2, w_3, and w_n denotes the weights for e_i in G_G, G_D, G_K, and G_N respectively. The probability of a sample to be classified as malware increases when the weight of any permission pair in G_M is higher than G_N. If m_i is greater than w_n, then the probability of $(w_1 + w_2 + w_3)$ percentage of samples to be classified as malware increases by $(m_i - w_n)$. If w_n is more than m_i, the probability of w_n percentage of samples to be classified as normal increases by $(w_n - m_i)$. Hence, we choose m_i such that both F_1 and F_2 are optimized. No single value of m_i can optimize both the objectives. Therefore, the weighted sum method is opted to solve, which reduces this to single-objective optimization as:

$$Maximize \quad Z = \alpha_1(m_i - w_n)(w_1 + w_2 + w_3) + \alpha_2(w_n - m_i)(w_n), \quad (5)$$

subject to the three constraints:

$$\{\alpha_1 + \alpha_2 = 1, \qquad m_i <= max(w_1, w_2, w_3), \quad and \quad m_i >= min(w_1, w_2, w_3)\}. \quad (6)$$

For every edge e_i in $Common_{edge-set}$, we calculate its weight m_i using equations 5 and 6. Then we add e_i and its weight m_i to the final malware graph G_M.

Let us consider an example where there is a common edge, say E_C, in all the three malware graphs and the normal graph. Suppose E_C has weights w_1, w_2, and w_3 in the three malware graphs and w_n in the normal graph respectively. We apply Algorithm 2 to find the weight of E_C in G_M. There can be three possibilities:

Algorithm 2 Graph Merge Algorithm

1: **Input**: Three separate malware graphs: $G_G(V_g,E_g)$, $G_D(V_d,E_d)$ and $G_K(V_k,E_k)$
2: **Output**: Final Malware Graph $G_M(V_m,E_m)$
3: Distribute edge set of all three graphs in two subsets: $Common_{edge-set}$ and $Disjoint_{edge-set}$.
4: **for** each edge $e_i \in Disjoint_{edge-set}$ **do**
5: $E_m \leftarrow (e_i, W(e_i))$
6: **end for**
7: **for** each edge $e_j \in Common_{edge-set}$ **do**
8: $w_1 \leftarrow$ weight of $e_j \in G_G$
9: $w_2 \leftarrow$ weight of $e_j \in G_D$
10: $w_3 \leftarrow$ weight of $e_j \in G_K$
11: $w_n \leftarrow$ weight of $e_j \in G_N$
12: **if** *minimum*$\{w_1,w_2,w_3\} > w_n$ **then**
13: $W(e_j) \leftarrow$ *minimum*$\{w_1,w_2,w_3\}$
14: $E_m \leftarrow (e_j, W(e_j))$
15: **else if** *maximum*$\{w_1,w_2,w_3\} < w_n$ **then**
16: $W(e_j) \leftarrow$ *maximum*$\{w_1,w_2,w_3\}$
17: $E_m \leftarrow (e_j, W(e_j))$
18: **else**
19: Let m_j be weight of edge e_j in final graph G_M
20: Solve for m_j the following optimization problem:
21: Maximize $Z = \alpha_1(m_j - w_n)(w_1 + w_2 + w_3) + \alpha_2(w_n - m_j)(w_n)$; Subject to constraints: $\alpha_1 + \alpha_2 = 1$ and $m_j <= max(w_1, w_2, w_3)$ and $m_j >= min(w_1, w_2, w_3)$
22: $W(e_j) \leftarrow m_j$
23: $E_m \leftarrow (e_j, W(e_j))$
24: **end if**
25: **end for**
26: Return $G_M(V_m,E_m)$

- If the edge weight of E_C in all the three malware graphs is higher than that in the normal graph, Algorithm 2 (Steps 12-14) gives *Minimum*(w_1, w_2, w_3) as the weight for the edge E_C in G_M.
- If the edge weight of E_C in all the three malware graphs is lower than that in the normal graph, Algorithm 2 (Steps 15-17) gives *Maximum*(w_1, w_2, w_3) as the weight for the edge E_C in G_M.
- Let w_1, w_2, w_3, and w_n be 0.6, 0.7, 0.9, and 0.8 respectively, i.e., edge weight of E_C in G_N lies between *Minimum*(w_1, w_2, w_3) and *Maximum*(w_1, w_2, w_3). Algorithm 2 (Steps 18-23), formulates the following multi-objective optimization problem:

$$Maximize \quad Z = \alpha_1(m_i - 0.8)(0.6 + 0.7 + 0.9) + \alpha_2(0.8 - m_i)(0.8), \quad (7)$$

where m_i is the required weight of edge E_C in G_M,

$$\alpha_1 = \frac{0.6 + 0.7 + 0.9}{0.6 + 0.7 + 0.9 + 0.8} = 0.73, \quad (8)$$

and

$$\alpha_2 = 1 - 0.73 = 0.27. \quad (9)$$

Hence, multi-objective optimization problem becomes:

$$Maximize \quad Z = 0.73(m_i - 0.8)(2.2) + 0.27(0.8 - m_i)(0.8), \quad (10)$$

Solving the above equation, keeping the Equation 6 in mind, gives the value of m_i as 0.9. Therefore, the weight of the edge E_C in G_M turns out to be 0.9.

This graph merge procedure is not required for G_N because we get only one normal graph from the Algorithm 1.

3) Malicious App Detection Algorithm: Algorithm 3 describes the procedure that determines whether the app is malicious or not. For every testing app, the algorithm extracts its permission pairs using Algorithm 1. The procedure uses two scores $Normal_{score}$ and $Malicious_{score}$ for the testing apps. These scores can be calculated by searching every permission pair of the testing app in both G_M and G_N and adding the corresponding weights. If $Malicious_{score}$ is greater than $Normal_{score}$ then the procedure declares the app as malicious. This technique is based on the fact that *higher the weight of a permission pair in the malicious graph, higher is the chance of any app containing that permission pair to be malicious*. This phase answers our research question 2, describing the detection model using permission pairs.

4) Edge Elimination: The graphs, G_M and G_N, may contain several edges that do not contribute to the detection such as the edges that have similar weights in both G_M and G_N. We believe the removal of such edges may not alter the detection results. Consider an edge e_1 that has weight 0.1 in both the graphs. It is probable that the deletion of e_1 from both the graphs may not alter the accuracy because e_1 contributes equally to $Malicious_{score}$ and $Normal_{score}$. If on the removal of such edges, *True Positive Rate (TPR)* and *True Negative Rate (TNR)* do not decrease, then we can delete

1556-6013 (c) 2019 IEEE. Personal use is permitted, but republication/redistribution requires IEEE permission. See http://www.ieee.org/publications_standards/publications/rights/index.html for more information.

This article has been accepted for publication in a future issue of this journal, but has not been fully edited. Content may change prior to final publication. Citation information: DOI 10.1109/TIFS.2019.2950134, IEEE Transactions on Information Forensics and Security

Algorithm 3 Detection Algorithm

Input: Set of Applications (A_1, A_2,.....,A_N) to be Tested
Output: Outputs each application as Malware or Normal
for each A_i **do**
  Extract its Manifest File *M* using apktool
  Let P = (P_1, P_2, P_3...P_m) be set of permissions in *M*
  if ($|P|$ == 0 or $|P|$ ==1) **then**
    Return ▷ zero or single permission
  else
    Mal_{score} =0 ; $Norm_{score}$=0
    for Every permission pair (P_i, P_j) $\in$ *M* **do**
      Mal_{score} + = $W_{(P_i, P_j)} \in G_M$
      $Norm_{score}$ + = $W_{(P_i, P_j)} \in G_N$
    end for
    if $Malicious_{score} > Normal_{score}$ **then**
      Return A_i as malware
    else
      Return A_i as normal
    end if
  end if
end for

the aforesaid edges from the graphs. We call this procedure as *Edge Elimination*.

Figure 2 describes the Edge Elimination mechanism that generates Reduced Malicious and Normal graphs. The procedure consists of two phases: 1) Irrelevant Edges Identification, 2) Finding Maximal Set of Irrelevant Edges (M_S).

Irrelevant Edges Identification: For each unique edge existing in the union of G_M and G_N, we delete one edge, common or disjoint, at a time from both the graphs and apply Algorithm 3 to check the detection accuracy. Only if both *TPR* and *TNR* do not decrease, then the edge is considered to be inappropriate, and it is added to the set say $E_{reduced}$. Suppose an irrelevant edge has weight λ and μ in G_M and G_N respectively, then its weight difference from both the graphs comes out to be $\mid \lambda - \mu \mid$. We define the *Sum of Weight Differences (SWD)* of all these irrelevant edges as β. We insert all such weight differences for every irrelevant edge of $E_{reduced}$ in a separate list say E_{list}, sorted in increasing order. Now, we need to find the maximal possible set of edges, which is the subset of E_{list}, which we can remove from the graphs that do not lower the *TPR* or *TNR*.

Find Maximal Set of Irrelevant Edges: We aim to find the maximal set of irrelevant edges that can be eliminated from the graphs. To begin with, we delete all the irrelevant edges, i.e., we delete the edges whose *SWD* is β and check the detection rate. If both *TPR* and *TNR* do not decrease, then we eliminate all the irrelevant edges and the algorithm ends. However, if it results in lowering of *TPR* or *TNR*, then we need to find the maximum possible set of edges that is a subset of E_{list}, which we can remove from the graphs.

We apply a technique similar to the Bisection method [53] to find the maximum possible subset. We set a lower limit, say $\delta 1$, initialized to zero, and an upper limit, say $\delta 2$, equal to β. Our objective is to find δmax, between $\delta 1$ and $\delta 2$, such that *TPR* and *TNR* remain same or higher on deleting all the edges whose weight differences summed up to δmax.

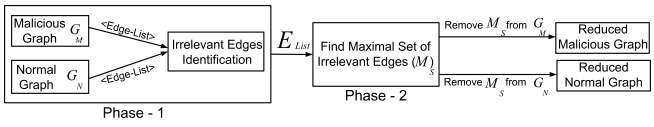


Fig. 2: Phases of Edge Elimination.

Initially, we set δmax equal to $\delta 2$. If, on deleting all the edges of set E_{list} from the graphs, either *TPR* or *TNR* decreases, we half the upper limit, i.e. $\delta 2$ = $\frac{\beta}{2}$ whereas the lower limit $\delta 1$ remains zero. The procedure terminates when both $\delta 1$ and $\delta 2$ converge to the same value, which we call as δmax. We delete the edges from the graphs whose *SWD* sums up to $\delta 2$ and test the detection results. Two cases may arise:

- If the detection rate does not decrease, then $\frac{\beta}{2}$ is the new lower limit and the previous value of $\delta 2$ becomes the new upper limit.
- If the detection rate decreases, then zero remains the lower limit and $\frac{\beta}{4}$ is the new upper limit.

The above steps repeat until $\delta 1 = \delta 2$ and we name that point as δmax. We finally remove those set of edges, whose weight difference sums up to the δmax, from G_M and G_N.

The following example, along with Figure 3, demonstrates the working of edge elimination. For simplicity, we consider four irrelevant edges, found at the end of phase 1. Let these edges between the permission pairs be E_1, E_2, E_3, and E_4. Let E_1 has a weight of 0.6 in G_M and 0.5 in G_N respectively. Hence, its weight Difference from both the graphs is: $\mid 0.6 - 0.5 \mid = 0.1$. Similarly, let us assume weight difference for the edges E_2, E_3, and E_4 is 0.2, 0.3 and 0.4 respectively. We arrange these irrelevant edges in increasing order of weight difference.

Deletion of these edges, individually, from G_M and G_N, does not decrease the detection rate. We assume that the deletion of all the four irrelevant edges from the graphs decreases the detection rate. Hence, phase 2 of the procedure is required to find the maximal set of irrelevant edges.

Sum of Weight Differences (SWD) from the E_{list} comes out to be $\beta = 0.1 + 0.2 + 0.3 + 0.4 = 1.0$. According to the procedure, the lower limit $\delta 1$ is set to zero, the upper limit $\delta 2 = \beta = 1.0$, and $\delta max = \delta 2 = 1.0$. Since it was assumed that deletion of all the four edges decreases the detection rate, in the next iteration, we decrease the upper limit $\delta 2$ from β to $\frac{\beta}{2}$, i.e., new $\delta 2$ is 0.5. Then we delete all the irrelevant edges whose SWD does not exceed $\delta 2$, i.e., 0.5. In this example, *SWD* for the edges E_1 and E_2 is $0.1 + 0.2 = 0.3$. Therefore, we delete only the edges E_1 and E_2 from both the graphs, and check for detection results. Further two cases may arise:

- If the detection rate decreases, then we further lower the upper limit from $\frac{\beta}{2}$ to $\frac{\beta}{4}$, i.e., new $\delta 2$ is 0.25. The lower limit remains as zero. Then we find the irrelevant edges whose SWD does not exceed 0.25. In this case only edge E_1 is selected for deletion from graphs.
- If the detection rate does not decrease, then $\delta 1$ is increased from zero to $\frac{\beta}{2}$, $\delta 1 = 0.5$ and $\delta 2$ is increased from $\frac{\beta}{2}$ to β, i.e., $\delta 2 = 1.0$. All the irrelevant edges whose SWD lie in the range from $\delta 1$ to $\delta 2$ are selected for deletion. We further test the detection rate by deleting the corresponding edges from both the graphs.

At every iteration, we check for the detection results after deleting some edges from the graphs, and we repeat the steps to decide for the values of $\delta 1$ and $\delta 2$. The procedure terminates

1556-6013 (c) 2019 IEEE. Personal use is permitted, but republication/redistribution requires IEEE permission. See http://www.ieee.org/publications_standards/publications/rights/index.html for more information.

This article has been accepted for publication in a future issue of this journal, but has not been fully edited. Content may change prior to final publication. Citation information: DOI 10.1109/TIFS.2019.2950134, IEEE Transactions on Information Forensics and Security

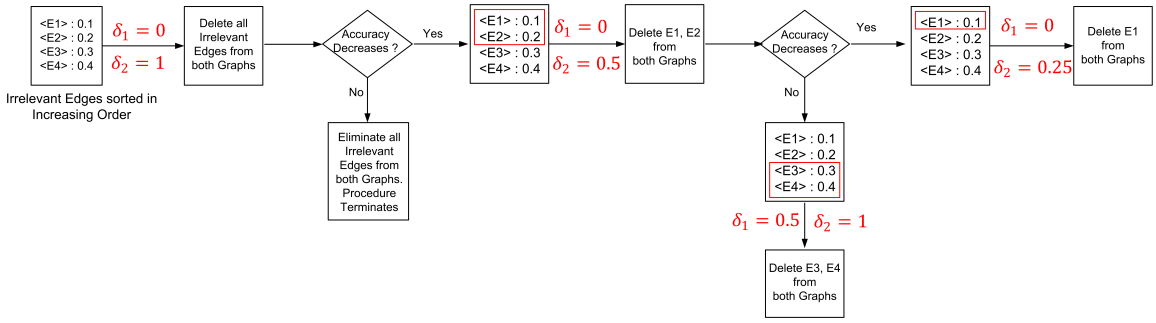


Fig. 3: Example of Edge Elimination from the Graphs

when $\delta 1 = \delta 2$. Finally, we eliminate all the edges whose SWD does not exceed $\delta 2$ and return the reduced graphs.

IV. Results and Discussion

This section reports the results of each phase of the *PermPair* model. We performed all the experiments on a desktop system with Ubuntu 12.04 OS and 8 GM RAM and used *apktool* to extract manifest files of the applications. We wrote *shell* scripts to analyze all the phases.

Datasets: In order to perform extensive analysis, we considered a total of 7533 malware apps from three different sources. We used 2944 samples for training during the Graph Construction phase and 3264 samples for testing the accuracy of the proposed model, as shown in Table IV. For the detection phase, we divided the malware samples into two types: *Known* and *Unknown* samples. Consider a typical malware family AnserverBot, say with a total of 180 samples. We used 100 of its samples in the training phase and remaining in the testing phase. Though the malware family is the same, the samples are different in the detection phase. Hence, we named them as *Known* samples. Table IV summarizes the number of *Known* samples from each dataset used for detection. Similarly, the *Unknown* samples are the ones whose family has not been considered in the graph construction phase. We used 1325 *Unknown* samples to test the detection accuracy of our proposed model. All such unknown samples were in the year 2018. We collected the diverse malware samples covering various attack categories as summarized in Table V.

Additionally, we downloaded 1493 normal apps for training and 4500 for testing. We manually downloaded the normal apps on the same desktop machine via a freely available interface[2]. We selected 15 prominent categories from the Google Play Store having the highest number of apps, as summarized in Table VI. In each category, we selected the freely available apps having the rating of at least 4 in the Google Play Store. We have considered only those normal apps which pass the VirusTotal[3] test. The complete dataset of benign apps used in our experiments is made available at "www.iitr.ac.in/media/facspace/drpskfec/Dataset".

TABLE IV: Android Malware Dataset

Dataset Name	Detection Period	Number of Samples Used in		
		Graph Construction Phase	Detection Phase(Known Samples)	Detection Phase(Unknown Samples)
Genome [4]	2010-11	900	364	-
Drebin [5]	2010-12	1244	1500	-
Koodous [6]	2014-18	800	1400	775
Contagio [54]	2018	-	-	250
PwnZen [55]	2018	-	-	300
TOTAL	-	**2944**	**3264**	**1325**

TABLE V: Various Attack Categories of Android Malware

Spyware	Adware
Phishing Apps	Mobile Bots
System Damage	Information Leak
Financial Loss	Ransomware

TABLE VI: Number of Normal Apps used (Category-wise)

Category	Number of Apps used in	
	Training Phase	Detection Phase
Education	65	180
Entertainment & Books	94	200
Food & Drink	28	50
Health & Fitness	65	156
Lifestyle	52	96
Music & Video	124	372
Creativity	184	600
Shopping	65	120
Beauty	95	360
Photography	60	150
Social & Communication	88	250
News & Magazines	48	120
Medical	90	300
Business	65	156
Games	370	1390
TOTAL	1493	4500

A. Phase-1: Permission Pair Graphs Analysis

First, we defined short notations for permissions as shown in Table VII for easy reference. We highlighted the top ten

[2]https://www.apkpure.com
[3]https://www.virustotal.com/

TABLE VII: Notations used for Top Permissions

Permission	Notation
INTERNET	INT
WRITE_EXTERNAL_STORAGE	WES
ACCESS_NETWORK_STATE	ANS
WAKE_LOCK	WAKE
READ_PHONE_STATE	RPS
ACCESS_WIFI_STATE	AWS
RECEIVE_BOOT_COMPLETED	RBC
READ_SMS	READ
SEND_SMS	SEND
GET_ACCOUNTS	GA
GET_TASKS	GT
SYSTEM_ALERT_WINDOW	SAW

1556-6013 (c) 2019 IEEE. Personal use is permitted, but republication/redistribution requires IEEE permission. See http://www.ieee.org/publications_standards/publications/rights/index.html for more information.

This article has been accepted for publication in a future issue of this journal, but has not been fully edited. Content may change prior to final publication. Citation information: DOI 10.1109/TIFS.2019.2950134, IEEE Transactions on Information Forensics and Security

TABLE VIII: Top ten permission pairs along with edge weights in malware and normal graphs

Genome (G_G)		Drebin (G_D)		Koodous (G_K)		Normal (G_N)	
Permission Pair	Edge Weight	Permission Pair	Edge Weight	Permission Pair	Edge Weight	Permission Pair	Edge Weight
INT:RPS	0.9574	INT:RPS	0.9153	ANS:INT	0.9378	ANS:INT	0.9538
ANS:INT	0.8314	INT:WES	0.6677	INT:WES	0.8261	INT:WES	0.7842
ANS:RPS	0.8062	RPS:WES	0.6530	INT:RPS	0.8210	ANS:WES	0.7670
INT:WES	0.6746	ANS:INT	0.6465	ANS:WES	0.7868	INT:WAKE	0.6457
RPS:WES	0.6702	ANS:RPS	0.6172	ANS:RPS	0.7753	ANS:WAKE	0.6381
AWS:INT	0.6454	INT:SEND	0.5472	RPS:WES	0.7449	WAKE:WES	0.5782
AWS:RPS	0.6412	RPS:SEND	0.5211	AWS:INT	0.6751	GA:INT	0.5320
INT:READ	0.6328	INT:RBC	0.5097	INT:RBC	0.6713	ANS:GA	0.5272
RPS:READ	0.6174	RPS:RBC	0.4934	ANS:AWS	0.6687	INT:RPS	0.4838
ANS:AWS	0.6134	ANS:WES	0.4934	RPS:RBC	0.6649	AWS:INT	0.4803

TABLE IX: Different Merging Schemes to get G_M and their Comparison of Detection Results

Notation	Description	TPR(%)	FPR(%)	Accuracy(%)
Graph-1	*Minimum*$\{e_{w1}, e_{w2}, e_{w3}\}$	54.88	3.12	75.88
Graph-2	*Maximum*$\{e_{w1}, e_{w2}, e_{w3}\}$	99.31	41.35	78.98
Graph-3	*Average*$\{e_{w1}, e_{w2}, e_{w3}\}$	90.49	25.24	82.62
Graph-4	*Average*{*Graph-1, Graph-2*}	93.42	21.27	86.07
Graph-5	*Average*{*Graph-3, Graph-2*}	95.25	30.47	82.39
Graph-6	*Weighted Sum Approach*	95.13	4.25	**95.44**

TABLE X: Top ten permission pairs in final malicious graph taken from different combinations

Minimum (Graph-1)		Maximum (Graph-2)		Average (Graph-3)		Weighted Sum	
Permission Pair	Edge Weight	Permission Pair	Edge Weight	Permission Pair	Edge Weight	Permission Pair	Edge Weight
INT:RPS	0.83	INT:RPS	0.95	INT:RPS	0.88	ANS:INT	0.92
INT:WES	0.67	ANS:INT	0.92	ANS:INT	0.79	INT:RPS	0.81
RPS:WES	0.64	INT:WES	0.83	ANS:RPS	0.74	INT:WES	0.80
ANS:INT	0.63	ANS:RPS	0.81	INT:WES	0.71	ANS:WES	0.78
ANS:RPS	0.61	ANS:WES	0.79	RPS:WES	0.69	ANS:AWS	0.68
INT:RBC	0.52	RPS:WES	0.75	ANS:WES	0.62	RPS:WES	0.66
RPS:RBC	0.48	AWS:INT	0.68	AWS:INT	0.59	AWS:INT	0.62
ANS:WES	0.47	INT:RBC	0.67	INT:RBC	0.58	ANS:RPS	0.61
AWS:INT	0.43	ANS:AWS	0.66	RPS:RBC	0.56	INT:WAKE	0.58
INT:SEND	0.42	RPS:RBC	0.66	ANS:AWS	0.55	ANS:WAKE	0.56

TABLE XI: Comparison of Detection Results

Graph used as G_M for Testing	Detection Accuracy (%)				
	Genome Samples	Drebin Samples	Koodous Samples	Normal Apps	Overall Accuracy
Genome Graph (G_G)	90.65	87.86	58.92	83.88	80.32
Drebin Graph (G_D)	85.16	91.86	34.92	93.95	76.47
Koodous Graph (G_K)	99.17	99.13	94.71	31.08	81.02
Graph Merge of G_G and G_D	90.93	92.13	58.57	95.31	84.23
Graph Merge of G_G and G_K	98.35	97.80	88.35	61.55	86.50
Graph Merge of G_D and G_K	96.70	98.60	84.64	76.62	89.14
Graph Merge G_G, G_D and G_K	98.07	98.06	89.28	95.75	**95.44**

permission pairs found in G_G, G_D, G_K, and G_N datasets in decreasing order of weights in Table VIII. Permission pair of *INT : RPS* with a weight of 0.9574 in G_G (Table VIII) indicate that the permissions *INTERNET* and *READ_PHONE_STATE* occur together in 95.74% of the Genome samples. Similarly, one can infer the other pairs and their weights.

It can be observed that the top five permission pairs of all three malware graphs are quite similar. Pair $\{\text{INT} : \text{RPS}\}$ has a high weight in all the malware graphs compared to that of G_N, indicating the leakage of private information of the device to a server. Permissions patterns consisting of ANS, INT, AWS, and WES are more prominent in recent malware compared to the older ones. This leads to the conclusion that the recent malware samples try to evade detection by retaining similar permission patterns as that of normal apps. It is also observed that some pairs containing permissions *WAKE_LOCK* and *GET_ACCOUNT* existed in the top ten pairs of normal apps but were missing in top pairs of malicious apps. Similarly, the pairs like $\{ANS : RPS\}$, $\{RPS : WES\}$ appeared in the top ten pairs of malware samples but were not found in normal ones.

On closely analyzing the pairs, we found that *Koodous* samples have similarity not only with *Genome* and *Drebin*, but also with the normal apps. This answers our research question 3 that recent malware not only contains permission patterns of the yesteryears but also integrate permission patterns which match largely with the normal apps to evade detection.

B. Phase-2: Graph Merge

For every common edge e with weights e_{w1}, e_{w2} and e_{w3} in three malware graphs, we considered different merging schemes as shown in Table IX. Note that Graph-4 and 5 are different from Graph-3. In Graph-3, the final weight of an edge is the average of weights from G_G, G_D, and G_K; whereas in Graph-4, the final weight of an edge is the average of its minimum and its maximum weight.

Table X presented the top ten pairs found from three merging possibilities: taking the *minimum* (Graph-1), *maximum* (Graph-2) and *average* (Graph-3) of the edge weights. Similarly, Table X showed the top permission pairs found from the weighted sum approach (Graph-6). It is observed that there is some similarity between the top pairs of G_D and Graph-1, and G_K and Graph-2; because G_K and G_D have the highest and the lowest weights for most of the common edges.

Table IX summarized the *TPR* and False Positives Rate (*FPR*) for different malware graphs. G_N remained the same in all the experiments. A least *TPR* and *FPR* is observed in Graph-1 because of assignment of minimum weights to the edges in the G_M; the normal score is likely to beat the malware score. Graph-2, on the other hand, displayed the highest *TPR* and *FPR*. We noted that with an increase in the weights of the edges in G_M, both *TPR* and *FPR* increased.

To calculate the accuracy, we considered the average of *TPR* and *True Negative Rate (TNR)*. As can be seen from Table IX, the weighted sum method gave relatively better accuracy of 95.44%. Hence, our proposed graph merge algorithm is better than other possibilities to merge the malicious graphs.

C. Phase-3: Detection

In this section, we analyzed the detection results obtained from the proposed *PermPair* approach for two cases: (i) **Individual Detection** in which we do not perform any graph merge, and every individual malicious graph is taken as G_M for detection, and (ii) **Graph Merge based Detection** in which we apply graph merging to get the G_M for detection.

1) Individual Detection: As an outcome from Section III(1), three malware graphs G_G, G_D, and G_K were produced. These graphs individually were considered as G_M to observe the detection results. We tested all the datasets with all these malware graphs. Note that, we considered different samples for the graph construction and detection phases. Table XI summarized the detection results.

Detection of Genome and Drebin Samples: Table XI indicates that G_K detected the malware samples with high accuracy because the permission pairs in G_K had a high similarity to G_G and G_D (Table VIII). Figure 4 showed the detection rate of Genome and Drebin samples. Figure 4(b)

1556-6013 (c) 2019 IEEE. Personal use is permitted, but republication/redistribution requires IEEE permission. See http://www.ieee.org/publications_standards/publications/rights/index.html for more information.

This article has been accepted for publication in a future issue of this journal, but has not been fully edited. Content may change prior to final publication. Citation information: DOI 10.1109/TIFS.2019.2950134, IEEE Transactions on Information Forensics and Security

showed that among the top ten pairs in G_G, G_K scored more than G_N for nine pairs. Similarly, Figure 4(d) demonstrated that for top pairs in G_D, G_K scored more than G_N for nine pairs. Therefore G_K detected 99.17% and 99.13% of Genome and Drebin samples respectively. On the contrary, G_G and G_D detected the malware samples with relatively lower accuracy. This is because G_N scored higher for a few of the top permission pairs, as Figures 4(a) and 4(c) depicted it.

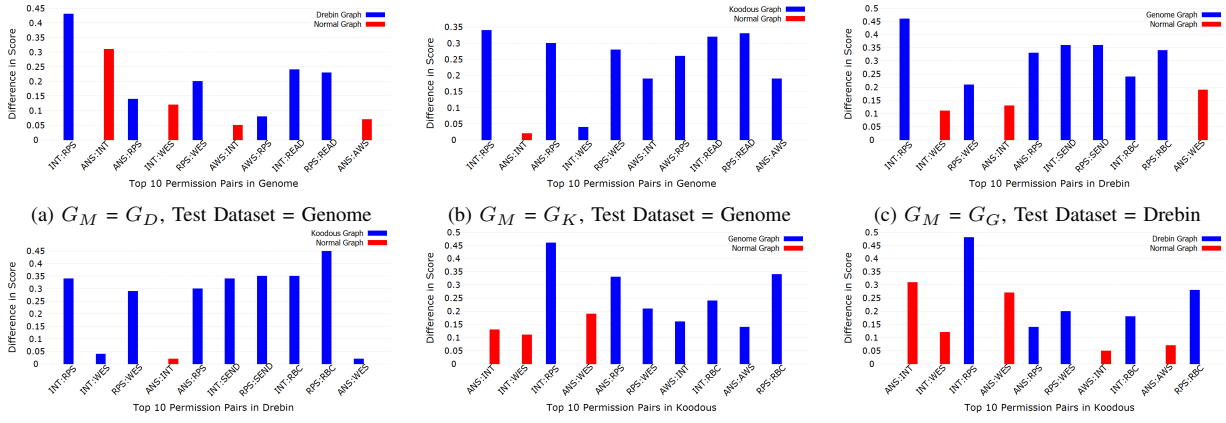
Detection of Koodous Samples: Figures 4(e) and 4(f) showed that G_N scored higher than G_G and G_D for three and five permission pairs respectively out of the top ten pairs of G_K. As a result, G_G and G_D detected a low accuracy, 58.92%, and 34.92% respectively, of the Koodous samples.

Detection of Normal Samples: Figure 5(c) showed that many top permission pairs of normal apps scored high in G_K than G_N. Hence G_K generated a high false positives rate as compared to G_G and G_D. There were some of the permissions which existed only in one or two of the malicious datasets. Consider a case where some permission pairs existed only in G_G and G_D. Even on adding such pairs to G_K, the detection results did not alter. Similarly, some pairs existed only in G_K. Even on adding these pairs to G_G and G_D, the results did not improve because such pairs existed in very few samples as they were having a very low edge weight and therefore did not contribute to the detection results. Hence, the overall detection accuracy from individual malware graphs was relatively low.

2) Graph Merge based Detection: Refer to Tables IX and XI, as discussed in the previous subsection, the overall accuracy achieved by merging of malware graphs using weighted sum approach is 95.44%, which is better than the accuracy achieved by any of the individual malware graphs. We merged two malware graphs at a time, using the same Weighted Sum approach, and checked for detection accuracy, as summarized in Table XI. None of the two-graphs merge approaches yielded better accuracy than the three-graph merge approach. Hence, we focused our discussion on three-graphs merge approach. This subsection deals with the analysis of false positives and false negatives when we merge all three graphs to get G_M.

False Positives Analysis: Graph-6, from Table IX, when used as G_M, identified 4.25% False Positives (FPs). Table XII, having top ten *dangerous permission pairs*, presented the reason behind these results. A pair is said to be *dangerous* if it has more weight in G_M than in G_N. As big as 35% of the total *FPs* recorded high malware score. Table XII summarized many of such apps. We observed that apps like *Fonetastic*, *Block SMS and Call*, *Android Assistant*, etc. had all top ten *dangerous permission pairs*. Hence, they are detected as malicious with a high score. Besides, most of these normal apps indicated the signs of suspicious behavior. For instance, they can block calls/SMS, kill apps, delete files, and disable features like Wi-Fi. Though our model detected such apps as malware, we observed that the majority of the *FPs* belong to the *Social and Communication* category of the normal apps.

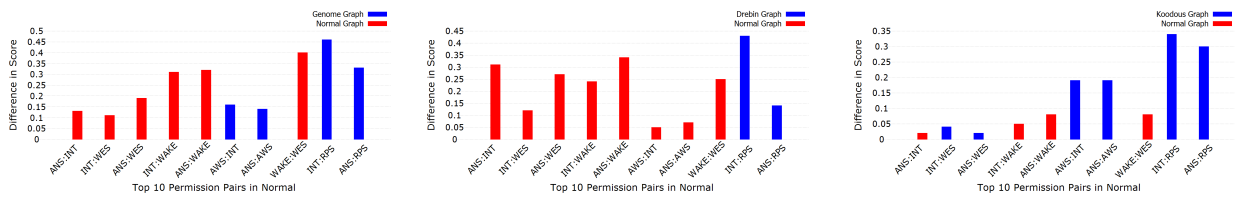
Interestingly, normal chat apps like *TextPlus* and *Chaton*, too had the dangerous permission pairs, but they did not pose any serious functionality. We tested other similar apps like *WhatsApp* and found that the proposed approach detected *WhatsApp* as malware with a low score difference of 0.04 in favor of G_M. On the contrary, *TextPlus* and *Chaton* scored a high difference of 21 and 10 respectively. *WhatsApp* also contained 6 of the top ten dangerous permission pairs, but it was the presence of permissions like *SYSTEM_ALERT_WINDOW*,



(a) $G_M = G_D$, Test Dataset = Genome (b) $G_M = G_K$, Test Dataset = Genome (c) $G_M = G_G$, Test Dataset = Drebin

(d) $G_M = G_K$, Test Dataset = Drebin (e) $G_M = G_G$, Test Dataset = Koodous (f) $G_M = G_D$, Test Dataset = Koodous

Fig. 4: Comparison of Top Permission Pairs for the detection of Malware Samples.

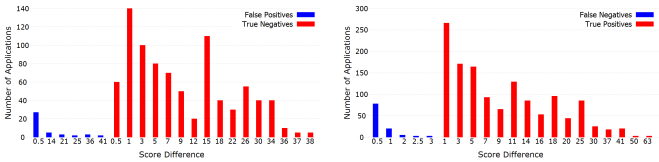


(a) $G_M = G_G$, Test Dataset = Normal (b) $G_M = G_D$, Test Dataset = Normal (c) $G_M = G_K$, Test Dataset = Normal

Fig. 5: Comparison of Top Permission Pairs for the detection of Normal Samples.

1556-6013 (c) 2019 IEEE. Personal use is permitted, but republication/redistribution requires IEEE permission. See http://www.ieee.org/publications_standards/publications/rights/index.html for more information.

This article has been accepted for publication in a future issue of this journal, but has not been fully edited. Content may change prior to final publication. Citation information: DOI 10.1109/TIFS.2019.2950134, IEEE Transactions on Information Forensics and Security



(a) For normal apps (b) For malware apps

Fig. 6: Difference in detection score.

RECEIVE_MMS, *BROADCAST_SMS*, *READ_CALL_LOG* and *WRITE_CALL_LOG* in *TextPlus* and *Chaton* which gave a high malicious score. The pairing of these permissions with *INTERNET* and *ACCESS_NETWORK_STATE* had a high weight in G_M than in G_N, hence giving a high malware score.

Remaining 65% of the FPs had a very low score difference, and they belonged to categories like online shopping apps, taxi booking apps, spy camera apps, and online games. Figure 6(a) showed the difference in the score of the testing set of normal apps. Most of the FPs had a score difference of as low as 0.05. Apps like *Fonetastic* and *Block SMS and call* had a high score difference of 41 in favor of G_M.

False Negatives Analysis: Table XIII and Figure 6(b) showed False Negatives (FNs) analysis. Analogous to *dangerous pairs*, we define the term *normal permission pairs*; i.e., pairs with the highest difference in favor of G_N. The proposed model detected samples of 19 malware families as FNs. Eight of them contained many of the top *normal pairs*. The remaining ones did not include any of the top *normal permission pair*, instead, they had a very less number of permissions (between two to five) as showed in Table XIII(b). Edge weight of these pairs was almost equivalent in both the graphs with very little difference in favor of G_N. 84% of the FNs had a score difference of less than or equal to one.

We conclude that our approach is effective in detecting Android malware with an accuracy of 95.44%, and the majority of the FPs (65%) and FNs (84%) had a very low score difference. Tables XII and XIII answered our research questions 4 and 5, highlighting the dangerous and normal permission pairs significantly present in malware and normal apps respectively.

Detection of Unknown Samples: We considered 775 recent samples from Koodous, 250 samples from Contagio, and 300 samples from Pwnzen Infotech [55] to test the detection rate of the proposed approach on the unknown samples. The results demonstrated that the proposed approach detected 714 of the Koodous, 205 of the Contagio, and 238 of the Pwnzen samples correctly with the detection rates of 92.12%, 82%, and 79.33% respectively. Hence, the overall detection rate on unknown samples was 84.48%. Many recent samples from Contagio and Pwnzen contained permissions similar to the normal apps, hence, gave a relatively lower detection rate of 82% and 79% respectively. This highlighted the fact that the proposed model should be continuously trained with the recent malware so that it can detect the unknown samples with high accuracy. While analyzing the false negatives for Koodous samples, we found similar permission patterns as in false negatives of known samples, i.e., containing less number of permissions such as *INT*, *ANS*, and *VIB*.

D. Phase-4: Edge Elimination

The number of edges in G_M and G_N is 7,658 and 10,661 respectively. We applied the Edge Elimination algorithm to eliminate the unnecessary edges. After the first phase, we found a total of 12,130 edges, i.e., deleting these edges from both the graphs, one at a time, did not decrease the detection accuracy. However, deleting all these edges together decreased the accuracy. Phase-2 of the algorithm aimed at finding the maximal subset of edges that can be deleted from the graphs and do not decrease the accuracy. We noticed that the accuracy of our model was 95.44%. Table XIV summarized the results of Phase-2. After a certain number of iterations, we got $\delta 1$ and $\delta 2$ nearly up to four decimal places. We observed that the algorithm could remove a maximum of 552 and 4382 edges from G_M and G_N respectively, thus, eliminating 7.2% edges in G_M and 41.1% edges in G_N. The detection time for testing 3264 malicious and 4500 normal apps was measured to be 2 minutes 45 seconds without edge elimination. This got reduced to 1 minute 58 seconds, i.e., a reduction of around 28% was possible. Even though this reduction is in seconds, this will have an impact if there are hundreds of thousands of files to be tested. Hence, the edge elimination algorithm reduces both, the number of edges in G_M & G_N, and the detection time, as shown in Table XV.

TABLE XII: False positives : Presence of top dangerous permission pairs in normal apps

Normal Apps	Type of App / Functionality	Top ten dangerous permission pairs sorted in decreasing order of edge weight									
		GT:RBC	ANS:GT	GT:WES	RPS:SND	INT:RPS	INT:SAW	INT:SND	GT:SAW	RPS:SAW	ANS:SAW
TextPlus	online SMS/calls	✓	✓	✓	✓	✓	✓	✓	✓	✓	✓
Fonetastic	blocks call/ SMS	✓	✓	✓	✓	✓	✓	✓	✓	✓	✓
Block sms call	blocks calls/SMS, deletes call history	✓	✓	✓	✓	✓	✓	✓	✓	✓	✓
Android Assistant	deletes files and browser history	✓	✓	✓	✓	✓	✓	✓	✓	✓	✓
Chaton	texting app	✓	✓	✓	✓	✓	✓	✓	✓	✓	✓
Golocker	changes wallpaper	✓	✓	✓		✓	✓		✓	✓	✓
Omni Swipe	changes user profile,disables Wi-Fi	✓	✓	✓		✓	✓		✓	✓	✓
All in one Tool	reboots device, deletes files	✓	✓	✓		✓	✓		✓	✓	✓
Passcode Lock	disables HOME keys and sound	✓	✓	✓		✓	✓		✓	✓	✓
UR Launcher	change wallpaper and user profiles	✓	✓				✓		✓		✓
Surefox Browser	locks browser, disables websites	✓	✓	✓		✓	✓		✓	✓	✓
Shutapp	shut-downs apps	✓	✓	✓		✓	✓		✓	✓	✓
Vpn Proxy	encrypts network communication	✓	✓	✓		✓	✓		✓	✓	✓

1556-6013 (c) 2019 IEEE. Personal use is permitted, but republication/redistribution requires IEEE permission. See http://www.ieee.org/publications_standards/publications/rights/index.html for more information.

This article has been accepted for publication in a future issue of this journal, but has not been fully edited. Content may change prior to final publication. Citation information: DOI 10.1109/TIFS.2019.2950134, IEEE Transactions on Information Forensics and Security

TABLE XIII: False Negatives Analysis

(a) Top normal permission pairs in malicious apps

Malicious Apps	Top ten normal permission pairs sorted in decreasing order of edge weight									
	ANS:GA	GA:INT	GA:WAKE	GA:WES	WAKE:WES	AWS:WES	GA:VIB	RES:WAKE	AWS:GA	GA:RES
DroidKungFu3	✓	✓		✓		✓	✓		✓	
Opfake		✓	✓	✓	✓					
Faketimer		✓	✓				✓			
SMSReg	✓	✓	✓	✓	✓		✓			
Airpush	✓	✓	✓	✓	✓	✓	✓		✓	
Banker	✓	✓	✓	✓	✓		✓	✓		✓
Clicker	✓	✓	✓	✓	✓		✓	✓		✓
Dendroid	✓	✓	✓				✓			

(b) Less number of permissions in malicious apps

Malware	Permissions
Basebridge	INT, ANS, VIB
Hamob	INT, ANS
Fakeinstaller	INT, WAKE, WES
Hacktool	INT, AWS, VIB, ANS, WAKE
Mobidash	INT, AWS, VIB, ANS, WAKE
Slembunk	INT, AWS, VIB, ANS, WAKE
SLocker	INT, AWS, VIB, ANS, WAKE
Ransomware	INT, AWS, ANS, WES
Viking Horde	INT, RES, WES

TABLE XIV: Number of edges removed in G_M and G_N after every iteration of Phase 2 of Edge Elimination

$\delta 1$	$\delta 2$	Number of edges removed		TPR (%)	FPR (%)	Accuracy (%)	Computation Time
		Malware Graph	Normal Graph				
0	97.1	6709	9665	90.46	2.9	93.78	0m 50 s
0	48.55	6164	9097	91.58	3.52	94.03	1m 8s
0	24.275	5145	8173	92.34	3.82	94.26	1m 17s
0	12.1375	3450	7044	93.26	3.98	94.64	1m 32s
0	6.06875	1909	5854	93.26	3.98	94.64	1m 48s
0	3.0343	684	4512	94.14	4.18	94.98	1m 59s
0	1.517	362	2347	95.13	4.25	95.44	2m 3s
1.517	3.0343	424	3500	95.13	4.25	95.44	1m 58s
2.275	3.0343	424	4046	95.13	4.25	95.44	1m 58s
2.6546	3.0343	464	4300	95.13	4.25	95.44	1m 58s
2.844	3.0343	595	4421	94.14	4.18	94.98	1m 58s
2.844	2.939	515	4352	95.13	4.25	95.44	1m 58s
2.891	2.939	569	4395	94.14	4.18	94.98	1m 58s
2.891	2.915	528	4366	95.13	4.25	95.44	1m 58s
2.903	2.915	563	4389	94.14	4.18	94.98	1m 58s
2.903	2.909	537	4371	95.13	4.25	95.44	1m 58s
2.906	2.909	545	4377	95.13	4.25	95.44	1m 58s
2.9075	2.909	552	4382	95.13	4.25	95.44	1m 58s
2.9082	2.909	563	4389	94.14	4.18	94.98	1m 58s
2.9082	2.9086	552	4382	95.13	4.25	95.44	1m 58s
2.9084	2.9086	563	4389	94.14	4.18	94.98	1m 58s
2.9084	2.9085	552	4382	95.13	4.25	95.44	1m 58s
2.90845	2.9085	563	4389	94.14	4.18	94.98	1m 58s
2.90845	2.908475	563	4389	94.14	4.18	94.98	1m 58s
2.90845	2.9084625	552	4382	95.13	4.25	95.44	1m 58s

TABLE XV: Comparison of Different Parameters With and Without Graph Reduction Algorithm

	Without Graph Reduction	With Graph Reduction	Efficiency
Number of Edges in G_M	7658	7106	7.2%
Number of Edges in G_N	10661	6279	41.1%
Detection Time	2m 45s	1m 58s	28%
TPR (%)	95.13	95.13	Same
FPR (%)	4.25	4.25	Same

E. Comparison with Anti-Malware Apps

To appraise the achieved results, we compared the malware detection rate of our model with 12 popular mobile anti-malware apps, taken from *VirusTotal* [4]. For comparison, we chose 275 random *unknown* malware from Koodous from a total of 775 *unknown* malicious samples to check manually for each sample through *VirusTotal*. Figure 7 compared the results of *PermPair* model with widely known anti-malware apps. We noticed that except *QuickHeal*, all of the anti-malware apps had a lower malware detection rate than *PermPair*. *Quickheal* detected 265 samples, three more than *PermPair*. Those three samples had single permission defined in their manifest file, hence those three samples went undetected by our model. We conclude that (a) our approach is relatively better than eleven of the mobile anti-malware apps, and (b) most of the anti-malware apps are unable to detect newer malicious samples.

[4]https://www.virustotal.com/

TABLE XVI: Comparison of the proposed approach with existing permissions-based malware detection techniques

(a) TPR and FPR

Detection Techniques	TPR (%)	FPR (%)	Permission Patterns
Sanz et al. [14]	91	19	All permissions together
Sanz et al. [15]	94	5	All permissions together
Arp et al. [5]	94	1	All permissions together
Wang et al. [23]	94.6	0.6	Set of 40
Proposed Approach	**95.13**	**4.25**	Set of 2

(b) Precision and Recall

Detection Techniques	Precision (%)	Recall (%)
Zhua et al. [21]	88.16	-
Milosevic et al. [20]	95.8	95.7
Wu et al. [25]	96.7	87.3
Proposed Approach	**96.3**	**95.13**

F. Comparison with Existing Approaches

In this subsection, we presented a comparative evaluation with other state-of-the-art permissions-based detection techniques, though they used different datasets for their experiments. To the best of our knowledge, no other work in the literature used the same datasets as ours. Some of the works reported their results in *TPR* and *FPR*, whereas others measured *Precision* and *Recall*. Table XVI compared the detection results of the proposed approach with other permissions-based solutions. The proposed approach gave nearly the same detection rate as that of other related works which used *Precision* and *Recall* for evaluation. Furthermore, the proposed approach outperformed all the works in terms of *TPR*. The better performance of our approach was due to the dangerous permission pairs analysis. Presence of such pairs contributed to detecting a high number of malicious samples.

Our model detected a few *FPs* with some malicious behavior. Few normal apps behaved maliciously such as blocking phone calls and deleting the files. Therefore, our model reported a little higher *FPR* than [5] and [23]. However, authors in [5] did not analyze the permission patterns of malicious samples. The authors in [23] reported dangerous permission patterns but in the set of 40. Representing and analyzing a large set of permissions can be complex. We analyzed permissions in a group of two and can be easily represented by graphs.

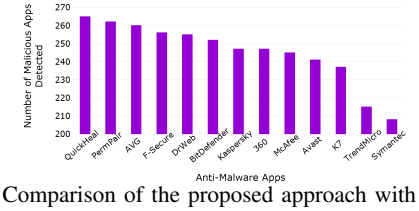


Fig. 7: Comparison of the proposed approach with different anti-malware apps

1556-6013 (c) 2019 IEEE. Personal use is permitted, but republication/redistribution requires IEEE permission. See http://www.ieee.org/publications_standards/publications/rights/index.html for more information.

This article has been accepted for publication in a future issue of this journal, but has not been fully edited. Content may change prior to final publication. Citation information: DOI 10.1109/TIFS.2019.2950134, IEEE Transactions on Information Forensics and Security

G. Limitations

The proposed approach has some gray areas which we intend to discuss in this subsection. The proposed model requires permission pairs to test the apps. Hence, the apps containing single or no permission cannot be analyzed. Some of the malware samples with few permissions evade the detection. Moreover, the proposed model gives relatively high *FPR* because many normal apps from *Social and Communication* category of the Google Play Store have been identified as malicious due to the presence of dangerous permission pairs. To evade detection, attackers may add widely used normal permissions in the malware samples, thus, generating more number of normal permission pairs. Besides, the proposed approach does not focus on detecting colluding apps [56] [57]. To overcome these limitations, in the future, we will analyze how efficiently other components such as intent filters, hardware components, and API call logs can be used for detection, in addition to the permissions. Since the proposed approach is static, malware with update capabilities (downloading of malicious components at update time) may evade the detection. To overcome this limitation, a dynamic detector can be deployed that could analyze the run time behavior of the apps. However, this will come at the cost of some computational overhead.

V. Conclusion and Future Work

In this paper, we proposed a novel approach for detecting malicious apps by using permission pairs extracted from the manifest files. We constructed the graphs to analyze permission pairs for both normal and malicious samples and assigned an edge weight to every pair depending upon the number of samples in which the pair is present. We subjected three malware datasets namely: Genome, Drebin, and Koodous to analysis. The datasets contained the newer samples detected in 2014-18 in addition to the older samples, detected in 2010-2014. Initially, we constructed three different graphs; one for each dataset and we observed certain deviations in permission pairs of newer samples compared to the older ones. We merged different malware graphs in a single graph using the weighted sum method. We further performed edge elimination to remove the unnecessary edges. Results showed that our proposed method is better than eleven of the popular mobile anti-malware apps. Our future work will focus on analyzing the other components of the manifest file like intent filters and hardware components to increase the detection accuracy.

Acknowledgment

We have taken the Genome dataset from the authors of [4], Drebin [5] dataset from Institute for System Security, Technische Universitat Braunschweig, Germany, and Koodous [6] dataset from their website that hosts a large number of malicious applications for analysis. We express deep gratitude to Genome, Drebin and Koodous projects for providing us the malware samples.

References

[1] Gartner, *Market Share Alert:Preliminary,Mobile Phones,Worldwide*,2017.
[2] Forbes Report, *97% Of Mobile Malware Is On Android. This Is The Easy Way You Stay Safe*, 2014.
[3] Security Report, *2018 Malware Forecast: the onward march of Android malware*, 2017.
[4] Y. Zhou, and X. Jiang, *Dissecting android malware: Characterization and evolution*, IEEE Symposium on Security and Privacy, 2012.
[5] D. Arp, M. Spreitzenbarth, M. Hubner, H. Gascon, and K. Rieck, *DREBIN: Effective and Explainable Detection of Android Malware in Your Pocket*. NDSS, 2014.
[6] Koodous Malware Dataset, *"www.koodous.com"*.
[7] Android Developers Guide, *https://developer.android.com/guide/index*.
[8] M. C. Grace, W. Zhou, X. Jiang, and A.'R. Sadeghi, *Unsafe exposure analysis of mobile in-app advertisements*, 5th ACM WiSec, 2012.
[9] W. Enck, M. Ongtang, and P. McDaniel, *On Lightweight Mobile Phone Application Certification*, 16th ACM CCS, 2009.
[10] A. Felt et al., *Android Permissions: User Attention, Comprehension, and Behavior*, 8th Symposium on Usable Privacy and Security, 2012.
[11] K. Au, Y. Zhou, Z. Huang, and D. Lie, *PScout: Analyzing the Android Permission Specification* , 19th ACM CCS, 2012.
[12] S. Holavanalli et al. *Flow Permissions for Android*, 28th IEEE/ACM International Conference on Automated Software Engineering, 2013.
[13] M. Grace, Y. Zhou, Z. Wang, and X. Jiang, *Systematic Detection of Capability Leaks in Stock Android Smartphones*, NDSS, 2012.
[14] B. Sanz, I. Santos, C. Laorden, X. Ugarte-Pedrero, P. G. Bringas, and G. Álvarez, *Puma: Permission usage to detect malware in android*, International Joint Conference CISIS'12-ICEUTE 12-SOCO 12 Special Sessions, Springer Berlin Heidelberg, 2013.
[15] B. Sanz, I. Santos, C. Laorden, X. Ugarte-Pedrero, J. Nieves, P. G. Bringas, and G. Álvarez Marañón, *MAMA: manifest analysis for malware detection in android*, Cybernetics and Systems, 44(6-7), 469-488, 2013.
[16] K. A. Talha,D. I. Alper, and C. Aydin, *APK Auditor: Permission-based Android malware detection system*, Digital Investigation, 13, 1-14, 2015.
[17] G. Tao, Z. Zheng, Z. Guo, and M. Lyu, *MalPat: Mining Patterns of Malicious and Benign Android Apps via Permission-Related APIs*, IEEE TRANSACTIONS ON RELIABILITY, 67(1), 355-369, 2018.
[18] L. Cen, C. Gates, L. Si, and N. Li, *A Probabilistic Discriminative Model for Android Malware Detection with Decompiled Source Code*, IEEE Transactions On Dependable And Secure Computing, 12(4), 400-412, 2015.
[19] Peng et al. *Using Probabilistic Generative Models for Ranking Risks of Android Apps*, ACM CCS 2012.
[20] N. Milosevic, A. Dehghantanha, and K.K. Choo, *Machine learning aided Android malware classification*, Computers and Electrical Engineering, 61, 266-274, 2017
[21] H. Zhua, Z. Youb, Z. Zhud, W. Shi, X. Chen, and L. Cheng, *DroidDet: Effective and robust detection of android malware using static analysis along with rotation forest model*, Neurocomputing, 272,638-646, 2018.
[22] V. Moonsamy, J. Rong, and S. Liu, *Mining permission patterns for contrasting clean and malicious android applications*, Future Generation Computer Systems, 36, 122-132, 2014
[23] W. Wang, X. Wang, D. Feng, J. Liu, Z. Han, and X. Zang, *Exploring Permission-Induced Risk in Android Applications for Malicious Application Detection*, IEEE Transactions on Information Forensics and Security, 9 , 1869-1882, 2014.
[24] Y. Zhou, Z. Wang, W. Zhou, and X. Jiang, *Hey, You, Get Off of My Market: Detecting Malicious Apps in Official and Alternative Android Markets*, NDSS, 2012.
[25] D. J. Wu, C. H. Mao, T. E. Wei, H. M. Lee, and K. P. Wu, *Droidmat: Android malware detection through manifest and api calls tracing*, Seventh Asia Joint Conference on Information Security (Asia JCIS), 2012
[26] F. Idrees, M. Rajarajan, M. Conti, T. Chen, and Y. Rahulamathavan, *PIndroid: A novel Android malware detection system using ensemble learning methods*, Computers & Security, 68, 36-46, 2017
[27] T. Kim, B. Kang, M. Rho, S. Sezer, and E. Im, *A Multimodal Deep Learning Method for Android Malware Detection Using Various Features*, IEEE Transactions on Information Forensics and Security, 14 (3), 2019.
[28] K. Sokolova, C. Perez, and M. Lemercier, *Android application classification and anomaly detection with graph-based permission patterns*, Decision Support Systems, 93, 62-76, 2017.
[29] H. Zhu, H. Xiong, Y. Ge, and E. Chen, *Mobile App Recommendations with Security and Privacy Awareness*, ACM KDD 2014.

1556-6013 (c) 2019 IEEE. Personal use is permitted, but republication/redistribution requires IEEE permission. See http://www.ieee.org/publications_standards/publications/rights/index.html for more information.

This article has been accepted for publication in a future issue of this journal, but has not been fully edited. Content may change prior to final publication. Citation information: DOI 10.1109/TIFS.2019.2950134, IEEE Transactions on Information Forensics and Security

[30] M. Fan et al. *Android Malware Familial Classification and Representative Sample Selection via Frequent Subgraph Analysis*, IEEE Transactions on Information Forensics and Security, 13 (8), 2018.

[31] M. Zhang, Y. Duan, H. Yin, and Z. Zhao, *Semantics-Aware Android Malware Classification Using Weighted Contextual API Dependency Graphs*, ACM CCS, 2014.

[32] A. Felt, E. Chin, S. Hanna, D. Song, and D. Wagner, *Android Permissions Demystified*, ACM CCS, 2011.

[33] Y. Feng, S. Anand, S., I. Dillig, and A. Aiken, *Apposcopy: Semantics-based detection of android malware through static analysis*, 22nd ACM SIGSOFT Symposium on Foundations of Software Engineering, 2014.

[34] K. Elish et al., *Profiling user-trigger dependence for Android malware detection*, Computers & Security, 49, 255-273, 2015.

[35] W. Enck et al., *TaintDroid: An Information-Flow Tracking System for Realtime Privacy Monitoring on Smartphones*, ACM Transactions on Computer Systems, 32 (2), 2014.

[36] V. Rastogi, Y. Chen, and W. Enck, *AppsPlayground: Automatic Security Analysis of Smartphone Applications*, ACM CODASPY, 2013.

[37] M. Sun, T. Wei, and J. Lui, *TaintART: A Practical Multi-level Information-Flow Tracking System for Android RunTime*, ACM CCS, 2016.

[38] Z. Yang et al. *AppIntent: Analyzing Sensitive Data Transmission in Android for Privacy Leakage Detection*, ACM CCS, 2013.

[39] A. Shabtai, U. Kanonov, Y. Elovici, C. Glezer, and Y. Weiss, *Andromaly: a behavioral malware detection framework for android devices*, Journal of Intelligent Information Systems, 38(1), 161-190, 2011.

[40] A. Reina, A. Fattori, and L. Cavallaro, *A System Call-Centric Analysis and Stimulation Technique to Automatically Reconstruct Android Malware Behaviors*, 6th European Workshop on System Security, 2013.

[41] V.M. Afonso et al. *Identifying Android malware using dynamically obtained features*, Journal of Computer Virology and Hacking Techniques, 11(1), 9-17, 2015.

[42] S. Wang, et al.*Detecting Android Malware Leveraging Text Semantics of Network Flows*, IEEE Transactions On Information Forensics And Security, 13(5), 1096-1109, 2018.

[43] A. Shabtai et al. *Mobile malware detection through analysis of deviations in application network behavior*, Computers & Security, 43, 1-18, 2014.

[44] Z. Chen et al. *A First Look at Android Malware Traffic in First Few Minutes*, IEEE Trustcom, 2015.

[45] A. Arora, S. Garg, and S. K. Peddoju, *Malware detection using network traffic analysis in android based mobile devices*, 8th International Conference on Next Generation Next Generation Mobile Apps, Services and Technologies, 2014.

[46] A. Arora, and S. Peddoju, *Minimizing Network Traffic Features for Android Mobile Malware Detection*, 18th International Conference on Distributed Computing and Networking, 2017.

[47] A. Saracino, D. Sgandurra, G. Dini, and F. Martinelli, *MADAM: Effective and Efficient Behavior-based Android Malware Detection and Prevention*, IEEE Transactions on Dependable and Secure Computing, 15(1), 83-97, 2018.

[48] M. Sun at al. *Monet: A User-Oriented Behavior-Based Malware Variants Detection System for Android*, IEEE Transactions on Information Forensics and Security, 12(5), 2017.

[49] M. Xia, Lu. Gong, Y. Lyu, Z. Qi, and X. Liu, *Effective Real-Time Android Application Auditing*, IEEE Symposium on Security and Privacy, 2015.

[50] M. Grace, Y. Zhou, Q. Zhang, S. Zou, and X. Jiang, *Riskranker: scalable and accurate zero-day android malware detection*, 10th international conference on Mobile systems, applications, and services, 2012.

[51] A. Arora, and S. Peddoju, *NTPDroid: A Hybrid Android Malware Detector Using Network Traffic and System Permissions*, 17th IEEE TrustCom, 2018.

[52] A. Arora, S. Peddoju, V. Chauhan, and A. Chaudhary, *Poster: Hybrid Android Malware Detection by Combining Supervised and Unsupervised Learning*, 24th ACM MobiCom, 2018.

[53] K. Atkinson, *An Introduction to Numerical Analysis*, John Wiley & Sons, 2008.

[54] Contagio Mobile Malware Dump, *"www.contagiominidump.blogspot.com"*.

[55] S. Chen at al. *Automated poisoning attacks and defenses in malware detection systems: An adversarial machine learning approach*, Computers & Security, 73, 2018.

[56] S. Bugiel et al. *Towards Taming Privilege-Escalation Attacks on Android*, 19th Annual Network and Distributed System Security Symposium, 2012.

[57] K. Elish et al. *Identifying Mobile Inter-App Communication Risks*, IEEE Transactions on Mobile Computing, 73, 2018.



Anshul Arora is currently working as Assistant Professor in Discipline of Mathematics and Computing, Delhi Technological University Delhi, India. He is pursuing Ph.D. from Department of Computer Science and Engineering, Indian Institute of Technology Roorkee, India, working under the able guidance of Dr. Sateesh K Peddoju. His areas of research include Mobile Security, Mobile Malware Detection, and Network Traffic Analysis.



Sateesh K Peddoju is currently working with the Indian Institute of Technology Roorkee, India since 2010. His research interests include Cloud Computing, Ubiquitous Computing, High Performance Computing and Security. He has publications in reputed journals like IEEE Potentials, MTAP, WPC, and IJIS, and conferences like TrustCom, MASS, ICDCN, and ISC. He is the Secretary for IEEE Roorkee section, Vice-Chair for IEEE Computer Society, India council, and Founding Faculty Advisor for ACM Student Chapter-IIT Roorkee. He is reviewer of top-rated journals like IEEE TCC, IEEE TSC, MTAP, COSE, COMNET, and JNCA. He is the founding General Co-Chair for SLICE-2018 and General Chair for DSEA-2018. He is in several conferences like IEEE MASS, IEEE ATC, IEEE SmartComp, IEEE iNIS, and IoTSMS. He is the recipient of University Rank and scholarship, and also received several Best Paper awards and Best Teacher award. He is the Senior Member of ACM and IEEE.



Mauro Conti is Full Professor at the University of Padua, Italy, and Affiliate Professor at the University of Washington, Seattle, USA. He obtained his Ph.D. from Sapienza University of Rome, Italy, in 2009. After his Ph.D., he was a Post-Doc Researcher at Vrije Universiteit Amsterdam, The Netherlands. In 2011 he joined as Assistant Professor the University of Padua, where he became Associate Professor in 2015, and Full Professor in 2018. He has been Visiting Researcher at GMU (2008, 2016), UCLA (2010), UCI (2012, 2013, 2014, 2017), TU Darmstadt (2013), UF (2015), and FIU (2015, 2016). He has been awarded with a Marie Curie Fellowship (2012) by the European Commission, and with a Fellowship by the German DAAD (2013). His research is also funded by companies, including Cisco and Intel. His main research interest is in the area of security and privacy. In this area, he published more than 200 papers in topmost international peer-reviewed journals and conference. He is Area Editor-in-Chief for IEEE Communications Surveys & Tutorials, and Associate Editor for several journals, including IEEE Communications Surveys & Tutorials, IEEE Transactions on Information Forensics and Security, and IEEE Transactions on Network and Service Management. He was Program Chair for TRUST 2015, ICISS 2016, WiSec 2017, and General Chair for SecureComm 2012 and ACM SACMAT 2013. He is Senior Member of the IEEE.

1556-6013 (c) 2019 IEEE. Personal use is permitted, but republication/redistribution requires IEEE permission. See http://www.ieee.org/publications_standards/publications/rights/index.html for more information.

Power Factor Correction Using APFC Panel on Different Loads

Vinay Sehwag
Department of Electrical Engineering
Delhi Technological University
Delhi, India
vinaysehwag7@gmail.com

Vaibhav Dua
Department of Electrical Engineering
Delhi Technological University
Delhi, India
vaibhav3025@gmail.com

Ajendra Singh
Department of Electrical Engineering
Delhi Technological University
Delhi, India
ajendrasingh25@gmail.com

Jitendra Nath Rai
Department of Electrical Engineering
Delhi Technological University
Delhi, India
jnrai@dce.ac.in

Vineet Shekhar
Dept. of Electrical and Electronics Engineering
NIET
Greater Noida, India
vshekher2407@gmail.com

***Abstract*—A major chunk of losses in electrical power systems is constituted by losses incurred due to poor power factor. A plethora of ways have been implemented to deal with this problem for quite a long time now. The intention behind this paper was to address to this woe which may be used for correction of power factor in various power systems. Employment of Automatic Power Factor Correction panels or more commonly known as APFC panels in electrical distribution networks is gaining prominence owing to the superiority of APFC panels over fixed capacitor banks in maintaining the desired power factor with different loads therefore, improving overall efficiency of the power system. A power factor correction unit enables the system to attain power factor values close to unity for efficient operation. The merits of higher power factor values include increased efficiency, load carrying capacity, better voltage regulation etcetera. The APFC panel was implemented on various loads operating together three phase Induction motor connected in parallel to series combination of a variable resistive and variable inductive load. In accordance to the instantaneous recorded value of power factor, the apposite capacitors are injected into the circuit to improve the power factor values. Improvised instantaneous values of the power factor were observed**

***Keywords*—Automatic Power Factor Correction (APFC), Inductive Load, Resistive Load, Capacitive Load**

I. INTRODUCTION

In present world, disparity in electrical power transmission and utilization is a major concern. People are unaware about the amount of energy being wasted by being ignorant of minor factors. Say, to travel short distances, many people turn to private conveyance instead of using public transport being ignorant of the consequences leading to consumption of non-renewable sources of energy like fossil fuels at a disturbing rate plus leading to pollution, global warming and thinning of ozone layer. In an electrical network Power Factor is a clandestine factor, on which depends a great deal of electrical energy losses.

Power factor gives indication of real power presence in a power system [1, 2]. If in a system there is 100% power and the pf is 0.85, then it indicates that net power consists of 85% Active power & 15% Reactive power. Highest possible values of power factor is desired in a system, this leads to reduction in current demand. Hence, it is intended to maintain power factor close to unity in order to reduce the current demand therefore minimizing the size and the overall conductor costs in the network. Mathematically, power factor is defined as the ratio of the real power (in kW) and apparent load power (in kVA) consumed in a network [4].

$$P.F. = \cos\varphi = \frac{activepower}{reactivepower} \qquad (1)$$

Practical electrical loads are majorly inductive in nature which leads to lagging power factor [1][2]. The problem of lagging power factors can be addressed in a most practical and economical approach by injecting reactive compensation into the circuit by installing power capacitors of appropriate capacity and rating at key points in the electrical network. Power factor improvement holds more relevance in electrical distribution systems. In order to achieve this objective low voltage (LV) capacitors are being substantially used in both conventional fixed capacitor banks and in modern Automatic Power Factor Correction panels. APFC panels are now increasingly becoming more popular than ever due to a number of advantages they offer, namely (1) Capability of maintaining system power factor at the target high value (near unity) [6] and therefore circumvent penalties levied by electricity supply companies due to poor power factor, (2) A void over compensation during low load conditions [6][7] and (3) Enhanced overall efficiency of the power system attributable to reduction in losses due to low power factor [7]. With appropriate design and construction, the required features and rating of APFC panels can be decided, designed and implemented for a variety of loads and power system networks. Power factor correction is the technique of compensating where leading current compensates lagging current through employment of capacitances of suitable rating in the network.

Capacitors present in various power factor correction system extract current that leads voltage and hence produce a leading power factor. A suitable capacitance is introduced in the system to attain highest possible values of power factor i.e. close to unity. Hypothetically speaking, capacitors could provide 100% of the desired reactive power by our network

978-1-5386-6625-8/18/$31.00 ©2018 IEEE

[5], however, in real world conditions, overcorrecting power factor in extremely close proximity to unity may cause harmonic distortions. If the capacitors connected in a circuit that normally works at a lagging power factor help to reduce the circuit lags quite appreciably. This technique is applied to negate as much of the unwanted magnetizing current as possible in order to reduce losses in the distribution system thus improving operational frequency. The benefits on offer to the commercial electrical consumer include minimized electricity bills by removing charges on reactive power reduced losses making extra, KVA available from the present sources or supply. Hence, improving the system efficiency

A. Power factor improvement through capacitive switching

At No-Load operation the inductive load (3 phase IM, purely inductive load) has a very low pf of about 0.1 Lagging as it consumes a large value of magnetizing current component and relatively a meagre value of real current component to meet the no load losses [3][4] under loaded conditions the inductive load draws a large amount of real current to meet the increased load and losses while the magnetizing component of the current remains constant [3]. As a result, power factor of the system increases. The capacitors in the APFC unit provide required reactive power for the system. Power factor correction capacitors lead to reduction in net current drawn from the distribution system and as a consequence of this they raise the system's overall operational capacity by taking up the power factor values close to unity. [3][4]. By supplying the reactive power requirement at the load end, the industrial and domestic consumer emancipate the utility from having to supply it, hence resulting in reduction in the total amount of apparent power supplied by the utility thus leading to conservation of energy and reduction in energy cost [4].

B. Automatic power factor correction unit

Most of the real world and industrial load is inductive in nature which leads to lagging power factor and hence, there is loss and wastage of energy which further leads to heavy penalties from electricity board combined with large electricity consumption bills. It is a difficult task to maintain ideal unity power factor and to overcome this difficulty we have APFC panels which maintain power factor close to unity [6].

II. HARDWARE DESCRIPTION

A. Moulded Case Circuit Breaker (MCCB)

A moulded circuit breaker is a special kind of electrical protective instrument that can be used for a wide range of voltages and frequencies of both 50Hz and 60Hz. The MCCB is used to control electric energy in distribution network. This circuit Breaker is an electromechanical device which shields a circuit from short circuit and over current. Operational range of MCCB is around 63A for short circuit current and 3000A for overcurrent protection. The chief roles of MCCB are to provide a way to open a circuit both automatically and manually under short circuit or overload condition. Majorly MCCBs have three essential functions, protection against overload, protection against electric faults and lastly switching a circuit ON and OFF.

B. Contactor

It is a special electrical device utilized for isolating or opening and closing or connecting an electric power circuit. They are sometimes called special purpose relays which operate for high values of current. A contactor is controlled by a low power level circuit.

C. Miniature Circuit Breaker

MCB is an electromechanical protective electrical instrument which shields an electrical network from large values of over current, which may a consequence from short circuit, overload or imperfect design. MCBs are superior in operation to conventional fuses since they do not need an alternate once an overload is identified. An MCBs have the ability to be simply rearranged and thus providing improved operational protection and greater handiness without incurring large expenses.

D. Capacitor

A capacitor also known as condenser is a passive electrostatic device where applying a constant potential will gather a fixed amount of charge on both opposing parallel plates, with the magnitude of the charge induced on both ends being equal and opposite to each other. This ratio of the applied voltage to the gathered charge is known as capacitance. Electrical energy in a capacitor is stored in the form of electric field.

E. Power Factor Meter/Relay

It is a five-stage power factor relay which works in five stages as per the system requirement. It is one current transformer operated relay which is connected either in any phase, here we have connected this CT in R-phase of 3-phase supply system.

F. Rotary Switch

It is a special switch which is to be twisted or rotated for its application in an electrical circuit. They are employed in situations where more than two electrical states are desired. It has a rotating axis that has a contact arm or “spoke” which protrudes out from the body. The terminals are arranged like an array around the rotor in a circular fashion, each of which acts like a contact or position for the contact arm to connect various electrical sub circuits in the larger circuit.

G. Current Transformer

A current transformer is a transformer that is used to measure alternate current and shielding associated electrical instruments or devices. An alternate current in its secondary circuit directly proportional to the alternate current flowing in its primary circuit is produced in current transformer.

When the current to be measured has exceedingly large value to be measured directly or the system voltage of the circuit has large magnitude, a current transformer can be employed in such conditions.

H. Load Description

A three-phase load which includes three phase resistive and inductive loads in parallel with three phase Induction Motor.

III. DESIGN OF APFC PANEL

APFC unit used here is a five-stage automatic power factor corrections unit, here five condensers two 1 kVAR, one 2 kVAR and two 3 kVAR condensers signifying the five stages constitute the APFC unit. Each condenser is connected through a 32A MCB with 100A MCCB providing power supply to the system. The power factor relay is connected in any one terminal of three phase system and it is energized by single phase supply, S1 and S2 are the terminals of the current transformer connected to S1 and S2 points of power factor relay. There are five points on the power factor relay which are connected to condenser through rotary switch. Power factor correction panel operates in automatic mode when all rotary switches are in position-1 and when the relay does not work due to any reason the rotary switches are turned to position-2, that is in manual mode.

In general, a 440V APFC Panel shall be metal clad, indoor type floor mounted in Non-draw out execution. Fabricated from Sheet steel shall be CRCA of minimum 2.0 mm thickness. Incomer Circuit breaker (MCCB) shall be mounted in a separate compartment and Metering compartment along with APFC Relay etc. shall be separate. The position of various control switches, push buttons, louvers etc. requiring manual operation. The operational Height of Panel shall be at a height not less than 300mm and shall not exceed 1850mm from the finished floor level. Name plate for each incoming and outgoing feeder at front. All equipments of similar rating shall be interchangeable.

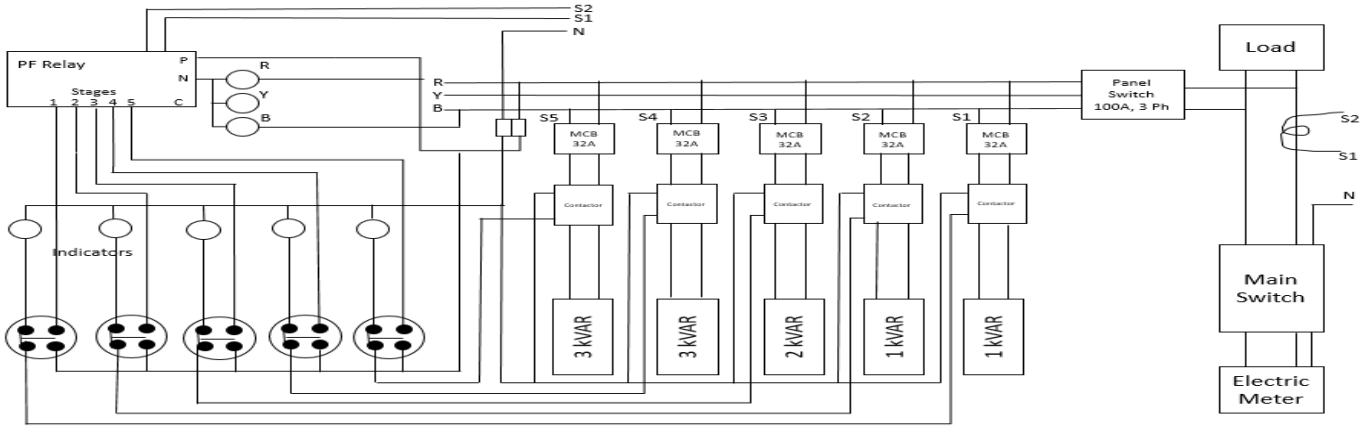


Fig. 1: Circuit Diagram of APFC Panel

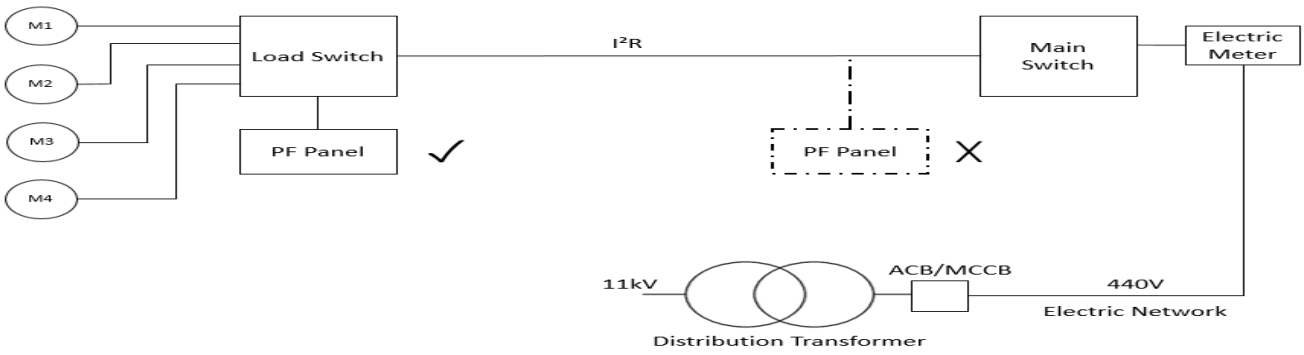


Fig. 2: Location of APFC panel in an electric network

Table 1: Components used in APFC panel

S.No.	Name of Equipments	Qty
1	MCCB	1
2	CONTACTOR LC1D123	2
3	CONTACTOR	3
4	MCB	2
5	MCB	15
6	CAPACITOR	2
7	CAPACITOR	1
8	CAPACITOR	2
9	P.F. METER/RELAY	1
10	ROTARY SWITCH	5
11	CURRENT TRANSFORMER	1
12	LED LIGHT	8
13	PANEL BODY	1



Fig. 3: Components of APFC Panel

IV. IMPLEMENTATION OF APFC PANEL

Presence of lagging power factor in a system is sensed by power factor relay (the relay of the power factor meter is set in between 0.5 to 0.98) and it switches ON the first stage of the unit. If the first stage is not able to correct the power factor value then second stage comes into play and further stages are engaged till the required value of the power factor is achieved but if the required power factor is maintained then further switching ON of the condenser will stop at that stage. APFC relay automatically switches OFF the stage when the required power factor is maintained. If there is a case of relay becoming faulty due to some reason then we have to manually turn the rotary switches in position-2. In small industries having highly inductive load and lagging power factor, here we have to maintain the pf up to 0.9.

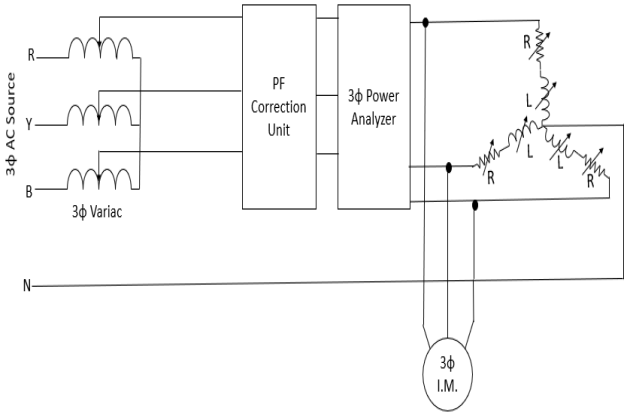


Fig. 4: 3-Phase load with 3-Phase resistance and inductance in parallel with 3-Phase Induction Motor

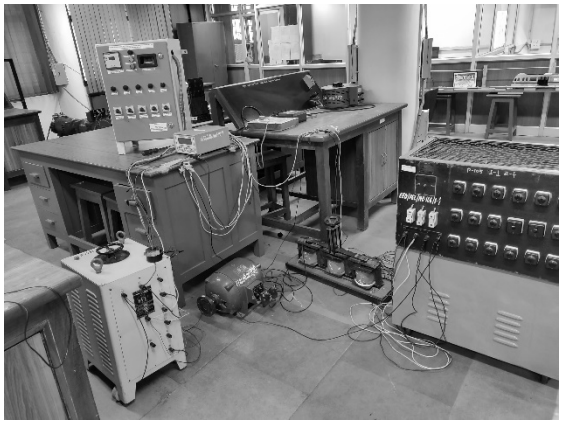


Fig. 5: Hardware Load Depiction

The use of a common motor controller for switching the motor and the capacitor as a unit has become increasingly popular because of the elimination of one switching device and because of the operational convenience [7]. The capacitor is switched in and out of service with its associated motor and therefore tends to eliminate overvoltage usually associated with light load conditions in a plant [7]. This unit switching arrangement is economically attractive when only a few motors are involved or when there is no diversity among motors [7].

Capacitors causes leading power factor as it shifts current ahead of voltage, so to correct lagging power factor, it is a convenient method for which this method is practiced worldwide vastly [5]. Though it has some limitations like the inability to absorb harmonics and doesn't provide step-less correction, it is a popular choice for PFC for its low cost of installation and maintenance [5].

VI. RESULT AND DISCUSSION

The APFC used was for a maximum of 16 kVA and 0.75pf, as we know kW=kVA*pf we can say the maximum real power in consideration was 12 kW, so as to achieve unity power factor we have to add 10 kVAR of reactive power to the circuit.

Table 2 gives the stepped correction of power factor of the system with the application of 5 kW load. Similarly, Table 3 gives the values of the corrected power factor after each stage with the application of 10kW load. A variable resistance connected in series with a variable inductance and this whole combination connected in parallel to a three-phase induction motor constitutes our electrical load.

VII. CONCLUSION

Automatic mode of the APFC swings into action when the power factor on the load side is low due to the inductive effect of the load but when the machine load is increased with the increase in resistive load the power factor shoots up to 0.98 from 0.75. When the power factor of the load is reached to the optimum value the APFC stops working in the automatic mode. The APFC panel drives out large current drawn by the electrical power system and it further leads to decrease in electricity consumption bills. Reduction in electrical energy use results in reduction in fossil fuel consumption by power stations which means protection of ozone layer from depletion and curbing the phenomenon of Green House influence leading to deceleration of global temperature rise. The most common application of these panels are in the small scale industries. The motivation and principle of operation of this paper may further be used in future endeavours involving design of power factor technologies for various loads.

REFERENCES

[1] John J. Grainger, William D. Stevenson, Jr., "Power System Analysis", McGraw-Hill International Editions, ISBN 0-07-113338-0.

[2] P.S. Bhimbra, "Electric Machinery", Khanna Publishers, 7th Edition, 2014, India.

[3] Rishabh Jain, Shashank Sharma, Mini Sreejeth, Madhusuadan Singh, "PLC based Power Factor Correction of 3-phase Induction Motor", 1st IEEE conference on Power Electronics, Intelligent Control and Energy Systems, 2016.

[4] Nagarajan. M, Kandasamy. k. v," Optimal Power Factor Correction for Inductive Load using PIC", International Conference on Modelling, Optimization and Computing, 2012.

[5] Yasin Kabir, Yusuf Mohammad Mohsin, Mohammad Monirujjaman Khan," Automated Power Factor Correction and Energy Monitoring System", IEEE, 2017.

[6] Muhammad Bilal Khan, Muhammad Owais," Automatic Power Factor Correction Unit", IEEE, 2016.

[7] W.C. Bloomquist, W.K. Boice," Application of Capacitors for Power Factor Improvement of Induction Motors", Transactions, Volume 64, May 1945.

IOP Conference Series: Materials Science and Engineering

PAPER • **OPEN ACCESS**

Prediction of residual stresses in biaxial stretching of tailor welded blanks by finite element analysis

To cite this article: Amit Kumar *et al* 2019 *IOP Conf. Ser.: Mater. Sci. Eng.* **651** 012039

View the article online for updates and enhancements.

This content was downloaded from IP address 14.139.251.100 on 02/12/2019 at 06:11

IOP Conf. Series: Materials Science and Engineering **651** (2019) 012039 doi:10.1088/1757-899X/651/1/012039

Prediction of residual stresses in biaxial stretching of tailor welded blanks by finite element analysis

Amit Kumar[1], **D Ravi Kumar**[1] and **Vijay Gautam**[2]
[1] Department of Mechanical Engineering, Indian Institute of Technology Delhi, New Delhi 110016, India
[2] Department of Mechanical Engineering, Delhi Technological University, Delhi 110042, India

E-mail: amitk3551@gmail.com, dravi@mech.iitd.ac.in, vijay.dce@gmail.com

Abstract. Residual stresses in sheet metal components play an important role in determining the life of parts especially in automotive industry. In this work, residual stresses have been predicted numerically in biaxial stretching of laser welded interstitial free (IF) steel blanks of different thickness combinations. The effective stress-effective strain curves of the parent sheets obtained from uniaxial tensile tests have been used as an input in finite element (FE) simulations to define the flow behavior of the materials. It has been found out that the residual stresses are tensile and similar on both sides of the weld zone in tailor welded blanks (TWB) of same thickness combination. In TWBs of different thickness combinations, the residual stresses on both sides are tensile and almost equal in the central region of the cup and they became compressive as the distance from the pole increases. The effect of thickness ratio on residual stresses has also been predicted in FE simulations of biaxial stretching of TWBs. It has been found out that with increase in the thickness ratio, the residual stress has slightly increased. Residual stresses have also been determined experimentally by using x-ray diffraction technique and it has been found out that the predicted values agreed well with the experimental results.

1. Introduction

Tailor welded blanks (TWBs) are being used in automotive industry for some sheet metal parts and they are generally prepared with the help of laser welding that generates residual stresses in the material due to the temperature gradient generated during joining process. Residual stresses also occur in the material due to non-homogeneous plastic deformation and structural changes [1]. Hariharan et al. [2] conducted stretch forming experiments using low carbon steel sheets of thickness 1 mm to determine residual stresses on the surface of the formed samples by using X-ray diffraction method. Residual stresses were also predicted by using Hill's 48 and Barlat's 89 yield criterion in commercially available LS-DYNA software. It was reported that the Barlat's 89 yield criterion was able to predict more accurately as compared to the other criterion. Bedan et al. [3] performed experiments on AA1050 alloy sheets using single point incremental forming process and studied the effect of rotational speed, feed rate and depth size on residual stresses in the part. It was found out that high forming depth lead to higher residual stresses in the part. It was also reported that the higher rotational speed of the tool caused more uniform distribution of the residual stresses. Arshpreet et al. [4] determined and compared the residual stresses on AA6063-T6 aluminium alloy of thickness 1 mm by using nanoindentation method in conventional bending, incremental sheet metal bending and deformation machining (DM) bending. It

Content from this work may be used under the terms of the Creative Commons Attribution 3.0 licence. Any further distribution of this work must maintain attribution to the author(s) and the title of the work, journal citation and DOI.
Published under licence by IOP Publishing Ltd

was reported that the residual stresses induced in DM bending mode were more uniform and comparable to the conventional bending. The residual stresses were reported to be higher in incremental bending process. Bruni et al. [5] determined springback and residual stresses by conducting experiments using double sheet hydroforming process under free expansion as well as under constrained expansion conditions at the die corners. The materials considered for the experiments are TRIP800 steel and FeP04 steel with 1.5 mm thickness. It was observed that high pressure, low corner radius and high friction allowed more equivalent plastic strain with a reduction in springback. Krux et al. [5] conducted deep drawing experiments using hydroforming process on low carbon steel (DC04) and austenitic high strength steel (X5 CrNi 1810) sheets of 1 mm thickness. The residual stresses were determined at the bottom of the cups and it was found out that high compressive stresses were present at the outer layer of bottom of the cup.

A few publications [7-10] have been found on determination of residual stresses in welded blanks. Clapham et al. [7] determined the residual stresses in same gauge and differential gauge laser welded TWBs by using neutron diffraction technique. The stresses were measured in as-welded condition and also after giving the uniaxial tensile strains of 0.5%, 3% and 7%. It was reported that residual stresses are lower on thinner side when compared to thicker side of the TWB. This was due to the less constraint applied by the thinner side of TWB during cooling of the molten pool. Peel et al. [8] studied the effect of welding speed on residual stresses present in the friction stir welded AA5083 sheets of 3 mm thickness. It was observed that with increase in the welding speed, the peak residual stress has been found closer to the weld line with higher magnitude. Staron et al. [9] used neutron diffraction technique to measure the residual stresses in two friction stir welded aluminium (AA2024-T31) sheets of thickness 6.3 mm or 3.2 mm. It was found out that the tensile residual stresses can be reduced by mechanical tensioning during welding. It was also reported that the maximum compressive stress in the weld zone was found to be -150 MPa in 3.2 mm thick sheet and -200 MPa in 6.3 mm thick sheet. Compressive residual stresses delay fracture in the material by increasing the required amount of stress to deform the material [10]. No literature has been found on prediction or determination of residual stresses due to forming of TWBs.

In this work, the residual stresses have been predicted in finite element (FE) simulations of biaxial stretching of TWBs of interstitial free (IF) steel sheets of same and different thickness combinations. The effect of thickness ratio on residual stresses in TWBs has been studied. Experiments were also conducted to determine residual stresses by using x-ray diffraction technique to validate the predictions.

2. Preparation of tailor welded blanks and properties

The thickness of the IF steel sheets (0.7 mm, 0.8 mm, 1.2 mm and 1.4 mm) have been chosen taking into consideration their usage in the automobile industry for manufacturing sheet metal parts. The tensile properties and anisotropic parameters of all the thicknesses were determined [11, 12] and they have been used in FE simulation of TWBs in the present research. Engineering stress-strain and true stress-strain curves of the parent sheets of thicknesses 0.7 mm and 1.4 mm are shown in Figures 1(a) and (b). TWBs of same as well as different thickness combinations (0.8 mm-0.8 mm, 0.8 mm-1.2 mm and 0.7 mm-1.4 mm) were made by laser welding the blanks in butt configuration. Initially the plain sheets were cut with the help of laser such that there was minimum burr on the edges of the sheets. After various trial runs, the sheets were welded in such a way that the alignment of the weld line was perpendicular to the rolling direction of both the parent sheets. Nd:YAG laser of power 4 kW was used to weld the blanks with a welding speed of 4 m/min. The weld zone properties of TWBs of thickness combinations 0.8 mm-0.8 mm and 0.8 mm-1.2 mm were already reported [11] earlier using minitiarised tensile specimens and the tensile properties of the weld zone of TWB 0.7 mm-1.4 mm were determined using the same geometry of the tensile specimen as shown in Figure 1(c). The uniaxial tensile tests were conducted on a universal testing machine (UTM) with a capacity of 100 kN at a constant crosshead speed of 2.5 mm/min. To make sure that the results are repeatable, 3 specimens were tested. The small pieces of steel (or thin strips) were placed on the thinner side of the tensile specimen of the weld zone to avoid the problem with the gripping. The flow curves of the weld zone of TWB 0.7 mm-1.4 mm are

shown in Figure 1(d). The tensile properties of the parent sheets and weld zone of TWB 0.7 mm-1.4 mm are given in Table 1. To represent the flow curves of the parent sheets and weld zone, Swift law of strain hardening $\sigma = K(\varepsilon_0 + \varepsilon_p)^n$ (where ε_0 is the strain at the yield point and ε_p is the plastic strain) and power law of strain hardening $\sigma = K\epsilon^n$ (where n is the strain hardening exponent and K is the strength coefficient) were used as input to define the material model in FE simulations respectively.

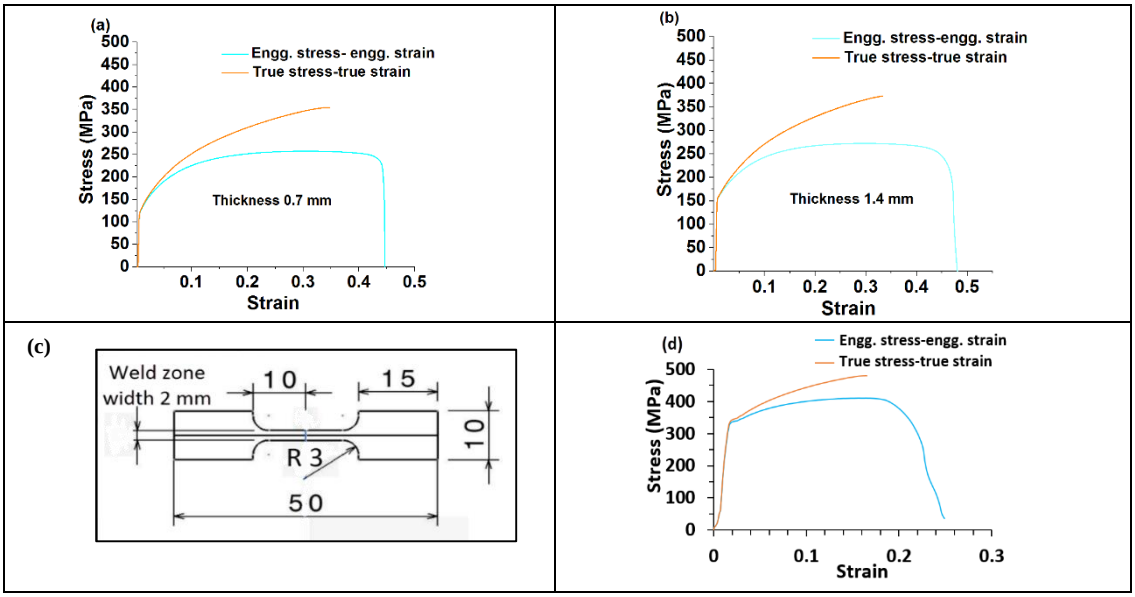


Figure 1. Engineering stress-engineering strain and true stress-true strain curves of the parent sheets of thickness (a) 0.7 mm [11] and (b) 1.4 mm [11], (c) Dimensions of a tensile specimen for the weld zone used in uniaxial tensile tests [12] and (d) Engineering stress-engineering strain and true stress-true strain curves of the weld zone of TWB of thickness combination 0.7 mm-1.4 mm.

Table 1. Tensile properties of parent sheets and weld zone of TWB 0.7 mm-1.4 mm of IF steel.

Thickness/Thickness combination (mm/mm-mm)	YS (MPa)	UTS (MPa)	Total elongation (%)	Strain hardening exponent (n)	Strength coefficient (K) (MPa)
0.7 [11]	125	256	44.2	0.29	503
1.4 [11]	140	270	48.3	0.28	520
0.7-1.4	340	411	24.9	0.18	661

3. Finite element (FE) simulation

3.1. Biaxial stretching of TWBs

The FE simulations of biaxial stretching of TWBs were carried to predict the dome height using a dynamic-explicit FE software, DYNAFORM with solver LSDYNA. The tools (die and blank holder) were modelled in the pre-processor such that the elastic deformation will not play any role during FE simulations and also the computational time will be reduced. The blank holder was modelled with a step to make sure that it makes contact with the TWB on both sides of the weld. A hemispherical bottom punch of diameter 50 mm was modelled. TWBs of dimensions 110 mm x 110 mm were modelled as surfaces followed by meshing with the triangular and rectangular Belytschko-Tsay thin shell elements of size 2 mm. Thickness of the thin shell elements was considered to be equal to the thickness of the blanks. The through thickness integration points were taken to be 9. Thickness of the weld zone was considered to be average of the thicknesses of the parent blanks. The nodes of the blanks and the weld zone were joined to make TWBs in such a way that one side of the TWB has a flat surface. The friction

coefficient between the punch and the blank was assumed to be 0.04 [13]. The simulations have been performed up to a constant dome height of 12.50 mm in all the simulations. A constant clamping force to avoid material flow from the flange region was defined to be 100 kN. The yielding behavior of the material was defined by using Barlat's 3-parameter material model [14] to incorporate the effect of anisotropy. Simulations were carried out by using the stress-strain curves obtained from the uniaxial tensile tests to define the flow behavior during the plastic deformation of the welded blanks.

3.2. Springback in biaxial stretching of TWBs

The springback simulations of formed TWBs were carried to predict the residual stresses in transverse direction (across the weld line) over the surface of the dome. The x-component and y-component of the residual stress was predicted at various points across the weld zone at different intervals. The output file of the forming simulation was imported into the springback simulation model. A FE model of the formed sample of TWB is shown in Figure 2(a). The material model was defined as in the case of forming simulations. The Barlat's 3-parameter material model (Barlat's 89) was used [14]. The nodal constraints of 8 were defined on the flange region. From the simulations, the residual stresses after springback were predicted.

4. Experimental work

4.1. Limiting dome height tests

The stretch forming experiments were carried out on TWBs of same as well as different thickness combinations. The experimental setup used for carrying out experiments consists of die, blank holder and a cylindrical punch of diameter 50 mm with hemispherical bottom. A thin shim was placed on the thinner side of the TWBs of different thickness combinations so that the blank holder makes uniform contact on both sides of the welded blanks. To reduce friction between the punch and the blank, teflon sheet of 0.5 mm thickness was used. In the experiments, a constant punch speed of 2 mm/sec was used. A schematic representation of biaxial stretching is given in Figure 2(b). After a few trial experiments, the tests on all the TWBs were stopped at the predetermined dome height and the dome height was measured using a vernier height gauge with a least count of 0.01 mm.

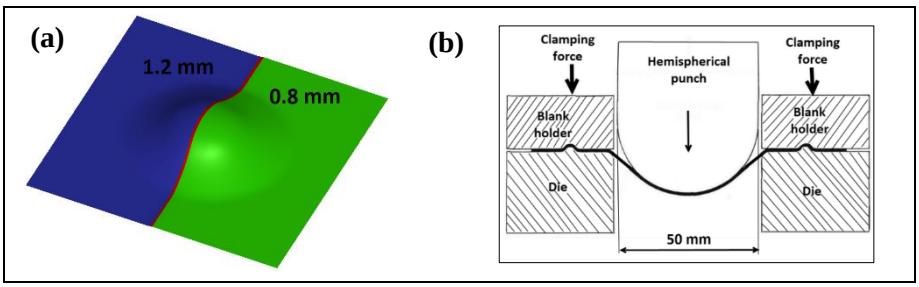


Figure 2. (a) A FE model of the formed sample of TWB and (b) Schematic representation of biaxial stretching with hemispherical punch of diameter 50 mm.

4.2. Residual stress measurement

The residual stress measurements were carried out after biaxial stretching of the TWBs to validate the predicted results. The residual stresses were also determined before forming of the TWBs. The experimental setup used for conducting the measurements consists of a sensor unit, power supply unit and a small adjustable table to keep the specimen as shown in Figure 3(a). A formed TWB sample are also shown in Figure 3(b) and the residual stresses were measured in the transverse direction. The sensor unit includes the x-ray tube (target material: chromium) that generates x-rays by using voltage and current of 30kV and 1 mA respectively. The beam wavelength was 2.29 A^0 and a collimator of 1 mm diameter size was used. The measurement time for each reading at a point was 90 seconds. In this work, $cos\alpha$ technique was used for the residual stress measurement due to its ability to measure an entire Debye ring at once from the two-dimensional detector, thus not requiring multiple sample tilts [15].

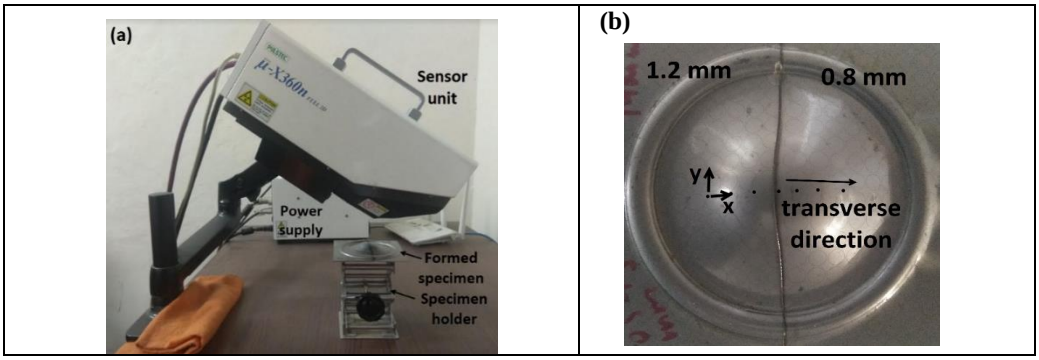


Figure 3. (a) Experimental setup for determination of residual stresses for TWBs and (b) transverse direction in which residual stresses were measured on deformed specimen along with x and y components.

The residual stress (in MPa) along the transverse direction was determined by using equation (1) [16].

$$\sigma_x = -\left(\frac{E}{1+\nu}\right)\left(\frac{1}{sin2\eta\, sin\psi_0}\right)\left(\frac{\partial \varepsilon_{\alpha 1}}{\partial cos\alpha}\right) \quad (1)$$

where E is the Young's modulus, ν is the Poisson's ratio, 2η is the angle between the incident ray and the diffracted ray, ψ_0 is the angle between the incident x-ray and the surface normal to the specimen, $\varepsilon_{\alpha 1}$ is the strain at azimuthal angle α and $\frac{\partial \varepsilon_{\alpha 1}}{\partial cos\alpha}$ is the slope of the linear relation between $\varepsilon_{\alpha 1}$ and $cos\alpha$.

5. Results and Discussion

5.1. Residual stress before forming

Residual stress patterns (before forming) in the welded blanks (are shown in Figure 4) as a function of distance from the weld zone on both sides of TWB for the all the thickness combinations. The x-component of the residual stresses for all the thickness combinations is shown in Figure 4. The presence of tensile residual stresses are observed close to the weld zone because of the high rate of heating and cooling during laser welding of the two blanks of same and different thicknesses in butt configuration. During solidification, the material in the weld zone shrinks towards the center and the material away from the weld zone tries to pull the half solidified weld zone away from the center and hence higher tensile residual stresses are observed close to the weld zone [8]. The tensile residual stress has been found to decrease with increasing distance from the center and it became compressive away from the weld zone as shown in Figure 4(a)-(c). It has also been observed that the residual stresses on thicker side are higher as compared to the stresses on thinner side of the TWB with different thickness combinations. This is due to higher constraint applied from the thicker side of the TWB, towards the shrinkage of the molten pool during its solidification [7].

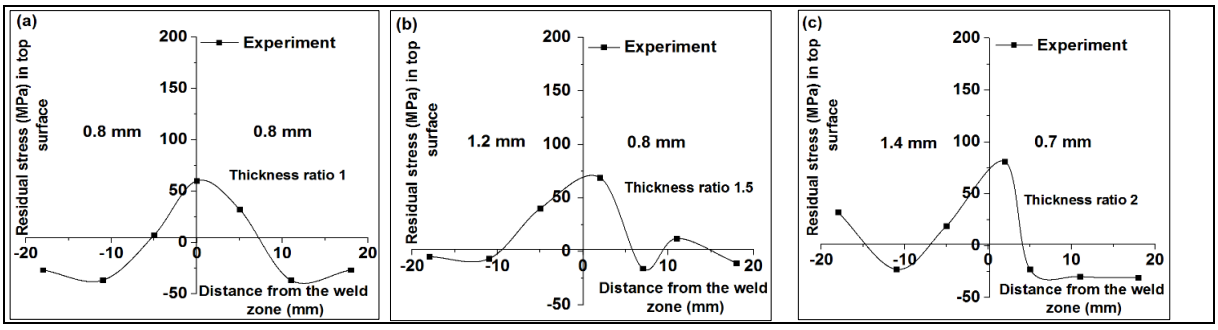


Figure 4. Residual stress patterns of the x-component (before forming) of the TWBs with thickness combination (a) 0.8 mm-0.8 mm, (b) 0.8 mm-1.2 mm and (c) 0.7 mm-1.4 mm.

5.2. Effect of the thickness ratio on residual stress

It has been observed that the forming stresses before springback in transverse direction (across the weld line) are same for TWB 0.8 mm-0.8 mm due to which equal amount of deformation on either side of the weld zone has been observed (Figure 5(a) and (b)). In TWB with thickness combinations 0.8 mm-1.2 mm and 0.7 mm-1.4 mm, the forming stresses before springback are higher on thinner side due to which larger plastic deformation has been observed on thinner side when compared to the thicker side of both the TWBs (as shown in Figures 5(c)-(f)). During springback, the elastic energy gets relieved [2], leaving behind residual stresses in the weld zone as well as on both sides of the weld zone. The residual stresses are also induced in the formed TWB due to the inhomogeneous plastic deformation on either side of the weld zone [17]. In TWB 0.8 mm-0.8 mm, it has been observed that the two components (x and y) of the residual stresses are low, tensile and similar on both sides of the weld zone. In TWBs of different thickness combinations, the components of the residual stresses are tensile and almost equal in the central region of the cup on both sides of the weld zone and they became compressive as the distance from the pole increases. Even though the springback is expected to be higher on the thinner side of the TWB but as it is welded to the thicker sheet, due to the constraint at the weld zone from the thicker sheet on the thinner side the residual stresses are observed to be almost equal on both sides of the weld zone. The above effect increases with increase in the thickness ratio and due to which the residual stresses have been observed to be higher in the central region of the formed specimen, in case of TWB with higher thickness ratio. Even though in the TWB 0.7 mm-1.4 mm (with thickness ratio 2) the thicknesses are different, the residual stresses are still observed to be slightly higher when compared to the TWB 0.8 mm-1.2 mm in the central region of the formed TWB. The residual stresses are also observed to be non-uniform in nature on either side of the weld zone as shown in Figures 5(c)-(f).

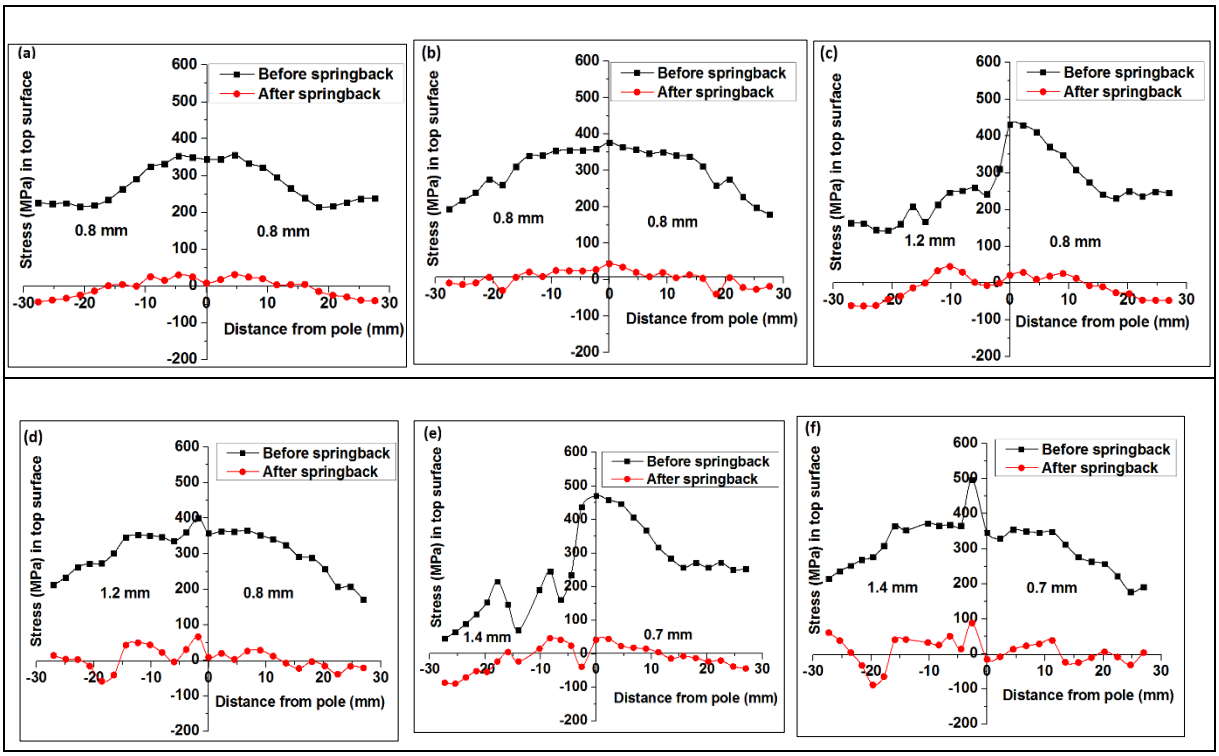


Figure 5. Predicted stress patterns over the top surface of the dome before and after springback (at the dome height of 12.50 mm) of TWBs with thickness combinations (a) 0.8 mm-0.8 mm (x-component), (b) 0.8 mm-0.8 mm (y-component), (c) 0.8 mm-1.2 mm (x-component), (d) 0.8 mm-1.2 mm (y-component), (e) 0.7 mm-1.4 mm (x-component) and (f) 0.7 mm-1.4 mm (y-component).

Experimentally, it has been observed that in all the three thickness combinations, the residual stresses (after forming) at the weld zone have reduced. However, in the TWBs with different thickness combinations, the weld zone did not undergo much deformation rather it has moved towards the thicker side of the TWBs due to which the residual stresses (after forming) are not induced but they have reduced. It has been observed that the residual stresses on thinner and thicker sides of TWBs has slightly increased after forming as compared to the undeformed TWBs (as shown in Figure 6). This could be due to the plastic deformation occurred on both the sides of the weld zone [1]. Overall, it has been observed that experimental values agreed well with the predicted results.

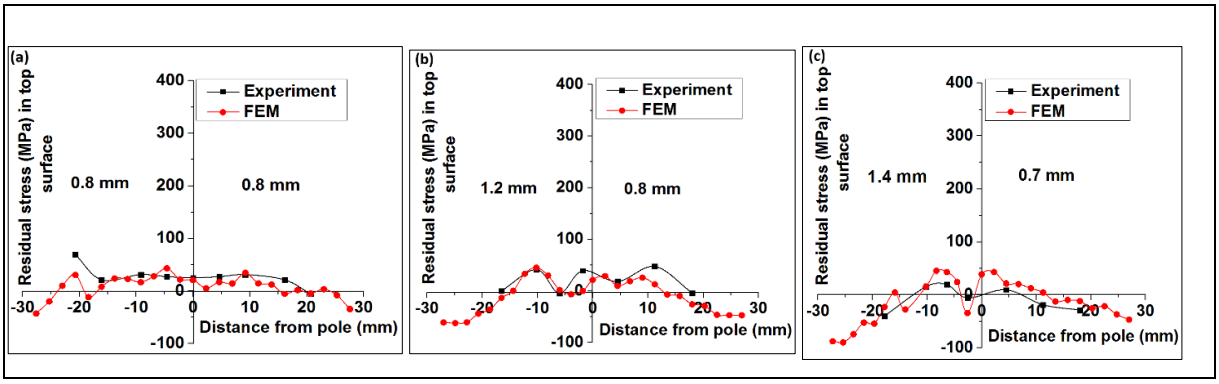


Figure 6. Residual stress patterns in transverse direction (only the x-component) over the top surface of the dome formed by biaxial stretching (at the dome height of 12.50 mm) with TWBs of thickness combination (a) 0.8 mm-0.8 mm, (b) 0.8 mm-1.2 mm and (c) 0.7 mm-1.4 mm.

6. Conclusion

It has been observed in FE simulations that the forming stresses are higher on thinner side of the biaxially stretch formed TWBs due to which larger plastic deformation occurred on the thinner side as compared to the thicker side of the TWBs. In TWB of same thickness combination, it has been observed that the two components (x and y) of the residual stresses are low, tensile and similar on both sides of the weld zone. However, in TWBs of different thickness combinations, the components of the residual stresses are tensile and almost equal in the central region of the cup and they became compressive as the distance from the pole increases. It is due to the constraint at the weld zone from the thicker side on the thinner side during the springback. It has been observed that with increase in the thickness ratio, the residual stresses slightly increased on both sides of the weld zone. Experimentally, it has been observed that the residual stresses on thinner and thicker sides of TWBs have slightly increased after forming as compared to the undeformed TWBs due to the plastic deformation occurred on both the sides of the weld zone. It has been observed that experimental values agreed well with the predicted results.

References

[1] Rossini N S, Dassisti M, Benyounis K Y and Olabi A G 2012 *Mater. & Des.* **35** 572–588
[2] Hariharan K, Prakash R V, Prasad M S and Reddy G M 2010 *Int. J. Mater. Form.* **3(4)** 291–297
[3] Bedan A S, Mohammed S and Kamal M 2017 *J. Eng. Technol.* **35**, 41-48
[4] Singh A and Agrawal A 2016 *J. Mater. Process. Technol*. **234**, 259-271
[5] Bruni C, Celeghini M, Geiger M and Gabrielli F 2006 *Int. J. Adv. Manuf. Technol.* **33(9-10)** 929–939
[6] Krux R, Kleiner M and Homberg W 2005 *Proc. 8th ESAFORM Conf. Mater. Form.* 459–462
[7] Clapham L, Abdullah K, Jeswiet J J, Wild P M and Rogge R 2004 *J. Mater. Process. Technol.* **148(2)** 177–185
[8] Peel M, Steuwer A, Preuss M and Withers P J 2003 *Acta Mater*. **51(16)** 4791–4801
[9] Staron P, Kocak M, Williams S and Wescott A 2004 *Phys. B: Condens. Matter* **350(1-3)** 491–493
[10] Withers P J and Bhadeshia H K D H 2001 *Mater. Sci. Technol.* **17** 355–365

[11] Kumar A, Gautam V and Kumar D R 2017 *J. Manuf. Sci. Eng.* **140** 031005 (1–14)
[12] Gautam V and Kumar D R 2017 *Proc. Inst. Mech. Eng. Part B* **232(12)** 2178–2191
[13] Anup SA and Shete MT 2012 *Int. J. Sci. Res.* **3(6)** 2153-2156
[14] Barlat F and Lian K 1989 *Int. J. Plast.* **5** 51–66
[15] Taira S, Tanaka K and Yamasaki 1978 *J. Soc. Mater. Sci.* **27(294)** 251-256
[16] Delbergue D, Texier D, Levesque M and Bocher P 2016 *Residual Stresses 2016: ICRS-10* **2** 55-60
[17] Schijve J (eds) 2009 *In: Fatigue of Structures and Materials* Springer Dordrecht

Energy Systems
https://doi.org/10.1007/s12667-019-00369-5

ORIGINAL PAPER

Scalable intelligent data-driven decision making for cognitive cities

Akshi Kumar[1] · **Arunima Jaiswal**[1]

Received: 6 August 2019 / Accepted: 9 November 2019
© Springer-Verlag GmbH Germany, part of Springer Nature 2019

Abstract

Advancement of Web 2.0 has completely revolutionized the way people communicate and exchange information among them using social media such as Twitter etc. People are using smart technology based solutions (including IoT's, sensors etc.) at an unprecedented scale for enhancing their quality of the life and building a smart city. These social sensors etc. are huge source of sentiment-rich data that needs to be processed and comprehended well in order to facilitate enhanced and smart decision making by the citizens of the smart city for any product, service or policy etc. The objective of this research is to leverage deeper insights of application of intelligent computation techniques for sentiment analysis of cognitive cities using user-generated data to improve the urban ecosystem. Sentiment analysis is quite imperative and serve as info-foundation for smart cities as they have the ability to harness the opinions or sentiments accurately based on the computation technology applied. The results are evaluated and analyzed on Twitter datasets that are constructed by the students of the Stanford University. It is observed that the alliance of big data and social media analytics using intelligent sentiment computation has helped in making citizens smart for taking smart decisions and eventually building a smart city.

Keywords Web 2.0 · Sentiment analysis · Social media · Crowd-sensing · Cognitive city · Smart decision making

1 Introduction

Digitalization plays an important role in building and developing smarter cities for enabling a better quality of urban life. It encapsulates various measures including enhancing the productivity of the city systems, creating innovative amenities for

✉ Arunima Jaiswal
arunimajaiswal@gmail.com

Akshi Kumar
akshikumar@dce.ac.in

[1] Department of Computer Science and Engineering, Delhi Technological University, Delhi, India

Published online: 19 November 2019

citizens, reducing the traffic and energy consumption in the city, safeguarding public security, evolving transportation etc. using advanced technologies. This facilitates constant interaction of the citizens with the evolving advanced technologies that in turns generates vast amount of data [1] that flows among its citizens and the systems. Such cities are called as cognitive cities [2] that are more sustainable, adaptable and technology driven [3]. The prime aspect of cognitive city is to provide and enhance the quality of life for its citizens. One of the edge of Internet [4] involves the integration and collision of sensing and embedded computing devises that formulate the generation of Internet of Things (IoT) and cognitive cities [5]. These incorporate the use of mobile sensing and computing devices that are favorable for crowd-sensing. It also involves harnessing vast amount of user generated big data [6] in order to improvise, analyze and evaluate effective plus efficient planning, governance and infrastructure of the city. Such cities that involve constant engagement of its citizens and the advanced technology driven services are called as cognitive cities. The cognition in a cognitive city occurs primarily due to the consumption and generation of data among the whole city i.e. from citizen to citizen and from citizen to the system. These days, open data initiatives have come in lead at a global level for providing public data that is available online to widespread audiences. For this, a lot of inventiveness has been made for capturing this humongous amount of user generated big data that could be further used for efficient and smart decision making as well. Nevertheless, social media [7] such as Twitter, Facebook, Instagram etc. are growing quite popular among the masses. Thus, these are becoming huge source of real time information that could be later on used for developing smarter city aspects. This data requires adequate data management and needs to be processed further for achieving the goals of building a smart city and understanding the trends and patterns in the data as well. We can say that, Internet has turned our existence upside down. It has revolutionized our way of communications such that there is exponentially increase in the use of smart technology based solutions including smart phones, tablets, phablets, ipods, gps etc. Comprehensive Internet connectivity via these devices is shaped predominantly by instant-mobile-communications. Enormous use of these devices for social media has changed our personal space and made us more cognitive [8]. These entire mobile, sensing and communicating devices that lead to crowd-sensing generates humongous amount of information about our recent environment that could further be used in the public interest for the benefit of the society. Adequate and proper usage of this sentiment-rich data [9] could be used for analysis purposes that would aid in solving social problems related to tourism, environment disaster management, meteorology, policy-making, feedbacks, gaming, entertainment, start-ups, business making, recommendations, tourism etc. The common thing amongst all is the real time big data that is being obtained from crowd-sensing, IoTs, smart phones etc. which is often associated with the public via social media as shown in Fig. 1.

Sentiment analysis [10] is a phenomenon that mines knowledge from user-generated online content and classifies them into various polarity-oriented classes such as positive/negative/neutral [11]. It also expresses the understanding of the opinions, sentiment prediction, polarity and strength of expressions and their consequent relationship for the subject taken [12]. Utilizing, gathering, processing and analyzing

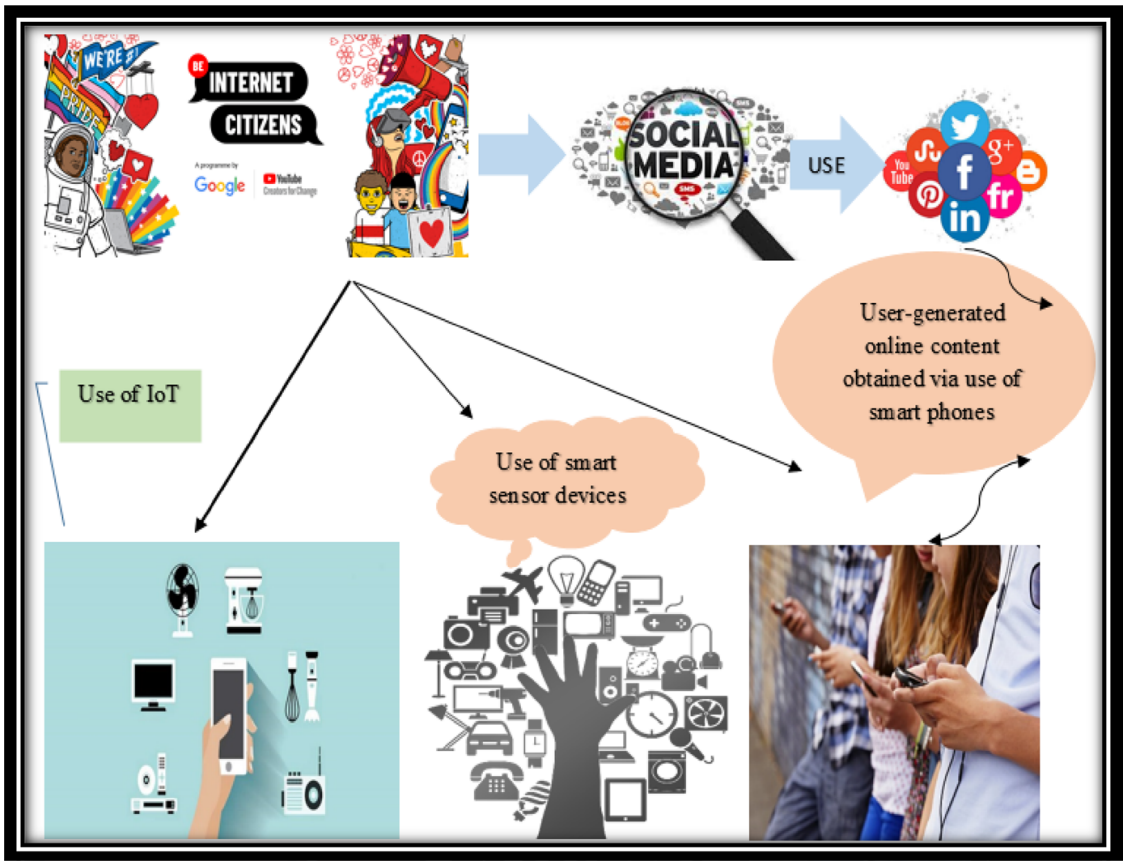


Fig. 1 Real time big data generation using IoT, smart phones and smart devices on social media

this big data from these sources often produce information that never existed and could further be used for the betterment of the citizens together with empowering and enhancing smart-city-governance [13]. Consequently, it can be eluded that increasing use of social media by the mass actually triggered the emergence of sentiment analysis [14]. It eventually led to the upcoming of possibly new and creative ideas that drives an easier way for building smart city and for developing potential strategies for efficient decision making [15] for the citizens of the smart city. In this era of digitization, handling big data [16] is of prime concern as it has its own difficulties and associated complexities. Smart city [17] data is often available in heterogeneous formats. User-generated online content obtained from various social media, humanoid robots, government open data, surveillance cameras, smart and multi-sensor devices including smart phones, smart watches, smart washing machines etc. produce data. This data is available in diverse forms including images, texts, videos, selfies, audios, heart beat rates, pulse rate, emotions, emojis, mood valence data, galvanic skin response etc. Intelligent and smart solutions are thus evidently required for sentiment analysis of such multi-modal data in order to gauge sentiments of the citizens of a smart city towards any subject of interest. For this, sentiment analysis is going to be a prime aspect for upgrading, augmenting and intensifying smart-city-governance [18] values in order to improve the urban ecosystem, as shown in Fig. 2.

Consequently, supervised learning techniques [19] that emerge to be an intelligent solution provider serve as a medium for implementation on such multi-modal data for sentiment analysis system designed for smart-city-governance.

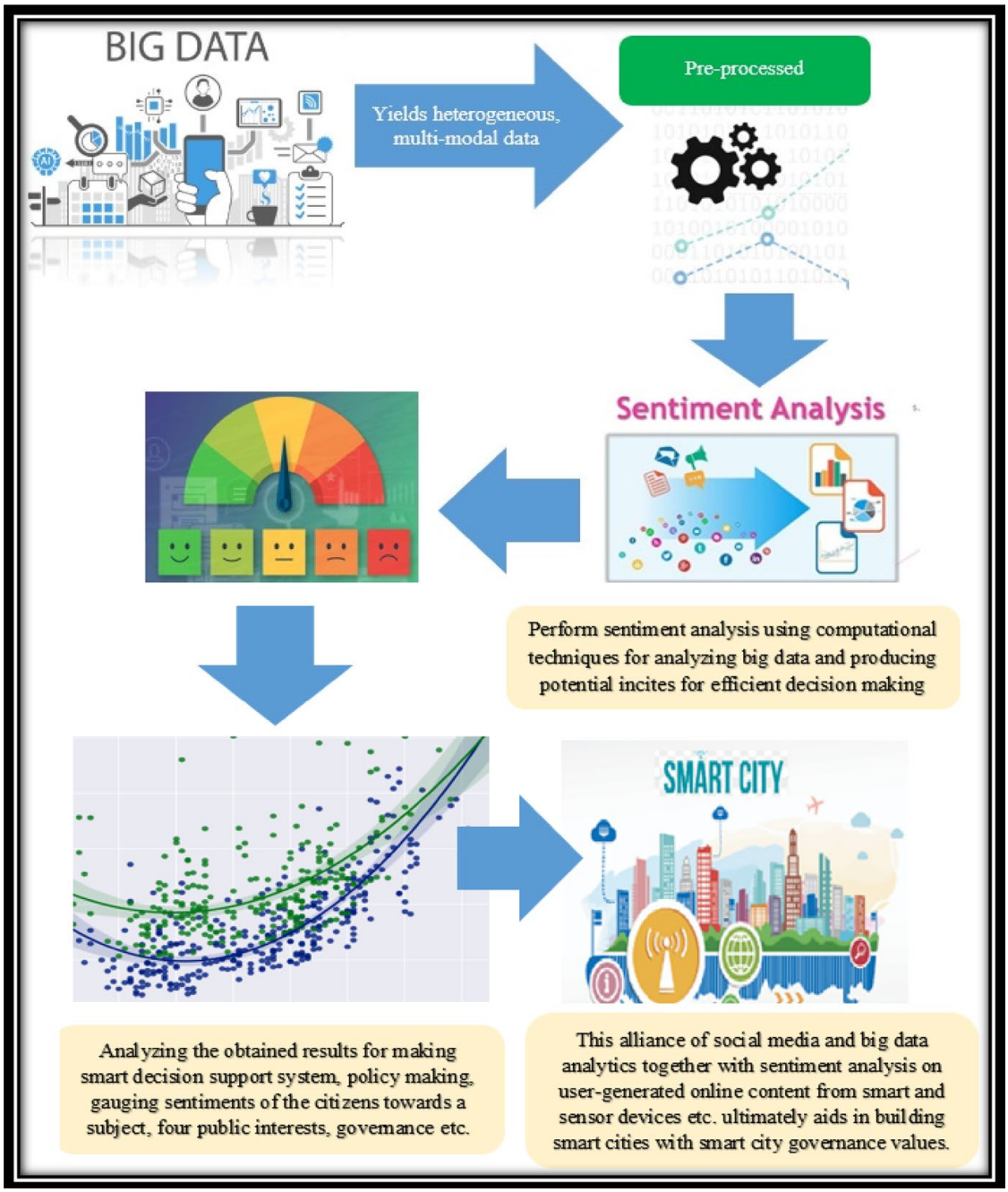


Fig. 2 Relevance of sentiment analysis in building smart city

This alliance of social media [9] and big data analytics [2] can be further used for the betterment of the masses and the society by meticulously analyzing the interest of the public. This could eventually be a major aid in competent and potential decision-making and thus ultimately amplifying smart-city-governance. It has altogether improved and presented a new way for expressing the opinions or sentiments of an individual for effective policy or decision-making. Individuals are expected to build up a system that can identify, distinguish, arrange and classify sentiments into different classes accurately. The system should derive the mood

and polarity of the sentiments efficiently, which is prime factor in crowd-sensing and making smarter informed decisions [20].

There is ongoing research prevailing in the field of sentiment analysis across our pertinent literature [21] in the past decade concentrating from transitional-passive content to highly dynamic-active user-generated online content from social media, IoT and from smart devices etc. These days, humongous amount of unstructured data, preferably opinions of people is available on Web pertaining to the highly dynamic usability of users on social media via crowd-sensing. Other individuals for any products or services or for any other knowledge gaining purposes and hence eventually generating a certain judgment or decision observe these views or opinions. All these opinions are then gathered together to serve as feedbacks for others, in order to yield some useful and purposeful information where we actually use sentiment analysis. Opinions or views available online are not structured and easily deducible for making any conclusion or decision based on them. Hence, for serving this purpose, we essentially require sentiment analysis that actually processes and classifies the online available information about any products or services etc. and provides its judicious views or opinions. This data driven decision-support based approach for classifying opinions or sentiments is used by marketers, firms, producers etc. for getting feedbacks about their products or services before acquiring them. This analysis aids in better understanding the market and the public opinions, which can finally be altered and offered as per the user's needs. This guarantees the wider publicity together with lesser range of failure and better utility of the launched item, product, services or any movies etc. We can say that, informed decision-making is the prime call of the hour and is of utmost importance. In this research, we present use of intelligent supervised learning techniques for understanding the phenomenon of sentiment analysis based on social media content during efficient policy or decision-making.

The main contributions of this research are as follows:

- Demonstrating the real life application of sentiment analysis towards building a smarter city.
- Analysis of opining mining on social media that could be utilized for potential decision-making.
- Application of supervised learning techniques using sentiment analysis on social media based on accuracy performance criteria.
- The evaluation is done on two different datasets of Twitter. One of the dataset is a benchmark corpus named 'sentiment140' and the other is real time dataset of imdb movie reviews.

The rest of the paper is organized as follows. Section 2 discusses in brief about the widespread use of sentiment analysis in varied domains for crowd sensing. Section 3 discusses about the approach we followed for sentiment analysis of online social media content and the results obtained. Followed by conclusion and future work discussion in the Sect. 4.

2 Application domain areas of sentiment analysis

It is an upcoming and recent area of research where user generated real time data obtained via crowd-sensing and smart devices is perpetually analyzed for getting proper visions leading to better performances. The usage of these social media platforms has observed an explosive growth in last decade [21] where people are connected to each other via links or connections etc. where they are allowed to share or posts without any geographical boundaries with the help of their computing devices such as mobiles, ipods, laptops etc. It has wide range of applications covering almost every domain [21] like social, political, business, management, finance, public, entertainment etc.

For *business domain*, sentiment analysis has proven to be a major advancement for the complete 'brand revitalization'. The prime concern for running an efficacious business with the sentiments rich data is the ability to exploit this data for actionable insights with various soft computing models etc. Relying on the reviews generated by the application of these models or tools, one can always adjust and adapt to the 'Recent and Dynamic' market needs which would eventually be indispensable for better understanding and effective decision making for analyzing the customer trends, estimating customer retention rates, predicting customer satisfaction, social campaigning, online marketing, customer oriented report services, consumers voice, online commerce, brand reputation etc. We can say that, sentiment analysis when applied to Business Intelligence can lead to a major breakthrough in identifying potential customers and developing market strategies for enabling quick transition to ever-changing market needs. It also captures brand reputation.

It has a high impact in *finance domain* as well. It has been observed that 'financial news reports' has a direct influence on the prices of the commodities, stocks and shares, trading, and fund investment etc. For financial leaders, their aim is to transform the sentiment rich information into enormous increase in the value of their funds, retail traders, products or services, stocks etc. This information is eventually required for building apt strategies prominently for trading purposes, management of their funds and risk control.

It has been extremely beneficial in *management* perspective for corporate groups also. For example, if we talk of a hotelier, he can any time have a glance of the hotel reviews, surveys, feedbacks etc. and could recognize the positive, negative and neutral sentiments of the people about his hotel. This information would thus be helpful to him in evaluating his hotel conditions and identifying his position among all his competitors as well. Based on this, he can also assess his brands value for further operational improvements or capital expenditures etc.

The proliferation of Web 2.0 has changed the way people express themselves by posting their thoughts, feelings, opinions etc. on any social media platform like Twitter etc. It has played a keen role in *political domain* as well. It majorly helps to provide substantial value to the political leaders or candidates running for varied positions and evaluating voting response to their political parties etc. It enables them to understand the public feelings, thoughts and opinions about

their leader's speeches, actions etc. For example, the administration of Obama had used SA in order to gauge the opinion of the public for their campaign in 2012 US presidential elections.

It has often been used by people to express and vent out their opinions, frustrations etc. via social media platforms like Facebook, Twitter etc. It has been widely used these days and people are becoming more aware about the current trending topics prevailing across the globe. Using this as a medium, almost every individual is getting involved in it by posting his views and concerns about the prevailing topic. For example, on the Supreme Court's verdict about "Teen Tallaak", the prime effect of public discourse could very well be understood from these social media platforms. We can say that, it has a powerful impact on the *public* concerning government policies, regulation proposals, legal matters, law amendments etc.

We can say that it is a domain specific concept. Likewise, it has wide range of applications in field of *entertainment* (sports, movies, gaming etc.). Entertainment is transforming into a science. Social media mining is enabling us to distinguish between positive, neutral or negative opinions. Hence, we can say that different domain-wise applicability of sentiment analysis plays an important role in providing scalable intelligent solutions for developing a sustainable smart city environment to the people.

When applied to entertainment, sentiment analysis thus helps us to evaluate and detect the polarities pertaining to the movies or songs reviews. Hence, in this paper, we focus on the use of Twitter, which is quite popular social media amongst users. The reasoning has been performed on two different datasets. One of the dataset is of online imdb movie reviews and the other is 'sentiment140', the students of Stanford University develop both of these. These contain the tweets from the popular social media named Twitter. These are applied for sentiment analysis that could be further beneficial for decision making about the views on the movies or brands or topics etc. based on supervised learning techniques. People often look for the genuine reviews of any movie they wish to see or any items they wish to purchase. Based on the reviews given by other people, they sort, select and make decision for the same. Hence, we can infer that predicting sensible and accurate sentiments is indispensable for coherent decision-support making as these have the power in altogether altering the way the mass thinks. Mining and classifying opinions from big data is a challenging task. There is a constant need to improve sentiment classification accuracy with the increase in practical use of sentiment analysis for various analytic domains (Market, Business, Government, Social, and Entertainment etc.). Based on the inferences obtained from the latest studies of our pertinent literature [21], we could deduce that tapping the dimensionality, complexity and fuzziness of sentiment-rich information on social media is the prime need of the hour. For achieving this, there is a continual need to employ new computational techniques for enhancing the sentiment classification accuracy. Thus, we can infer that the chief concern is to identify how sentiment analysis on social media facilitates decision support and delivers targeted information. This paper provides relevant support for proving the convergence of Web 2.0 technologies and sentiment analysis on social media via real-life application including movie, brand, and topic reviews etc. Overall, our study shows that the

obtained sentiments do contain valuable information for investing decision or policy making and supporting crowd-sensing.

3 Case study: analyzing sentiments in movie reviews

Sentiment analysis [10] is typically a multi-step process encompassing various sub-tasks such as Data collection; Feature Selection; Sentiment Classification and Sentiment Polarity detection as shown in Fig. 3. Effective feature selection [19] is a computationally hard task and has a significant role in determining the sentiment classification accuracy.

For accomplishing this, we have taken two datasets. One of the dataset is of Imdb movie reviews [DS1] and the other is 'sentiment140' [DS2]. DS1 determined the polarity in terms of positive, negative and neutral tweets whereas DS2 determines polarity in terms of positive and negative tweets. The datasets were pre-processed and cleaned. The details about the datasets are given in Tables 1 and 2.

Tf-idf vectorization [19] was used for feature selection. Post this, supervised learning techniques namely logistic regression [22, 23], multinomial naïve Bayesian [24], Bernoulli naïve Bayesian [25], ridge classifier [26, 27], adaboost [28], multi-layer perceptron [29, 30] and support vector machines [31, 32] were applied using python for determining the polarity. The results are depicted in Table 5. We had also

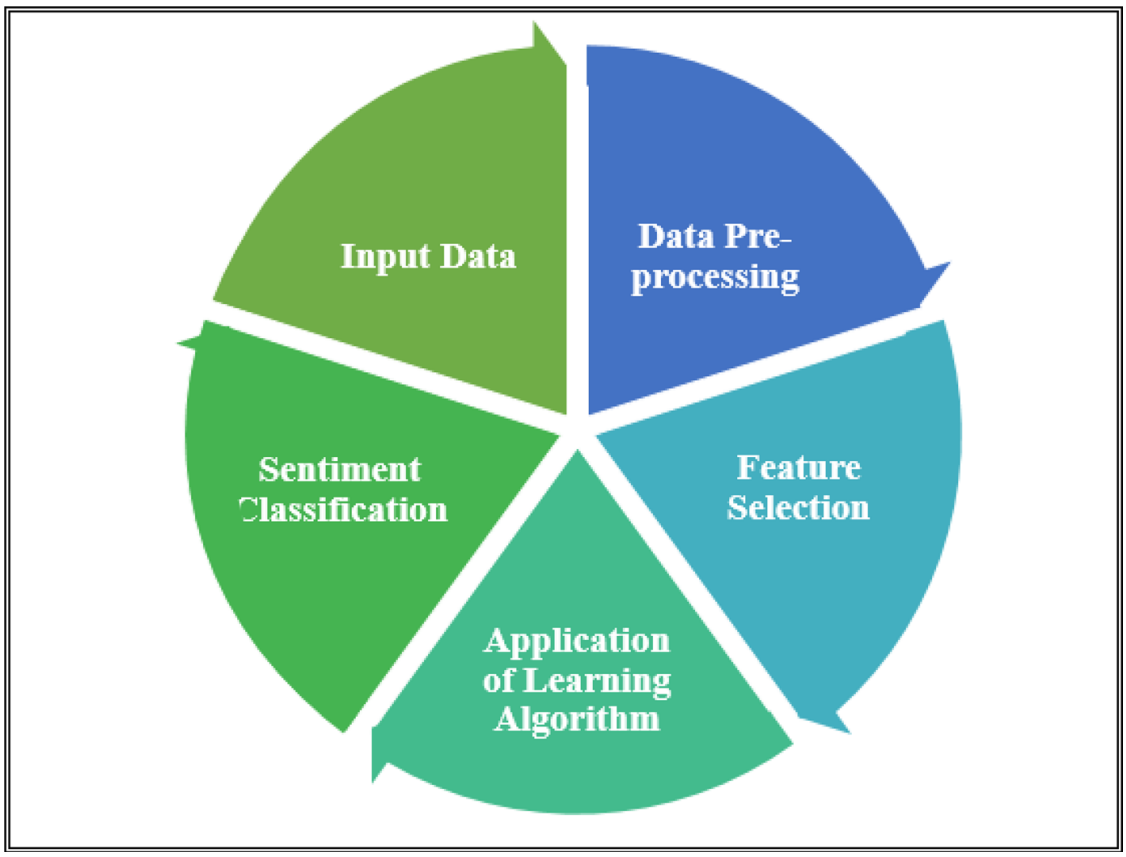


Fig. 3 Generic sentiment analysis process

Table 1 Details about Imdb movie reviews

Parameters	Details
Source	Stanford.edu
Number of tweets	25,000
Number of positive tweets	12,500
Number of negative tweets	12,500
Number of tweets after cleaning and pre-processing	25,000
Number of features (total words in corpus)	74,140

Table 2 Details about sentiment 140 dataset

Parameters	Details
Source	Stanford.edu
Number of tweets	1,600,000
Number of positive tweets	800,000
Number of negative tweets	800,000
Number of tweets after cleaning and pre-processing	1,596,753
Number of features (total words in corpus)	273,694



Fig. 4 Word cloud for negative tweets for DS1

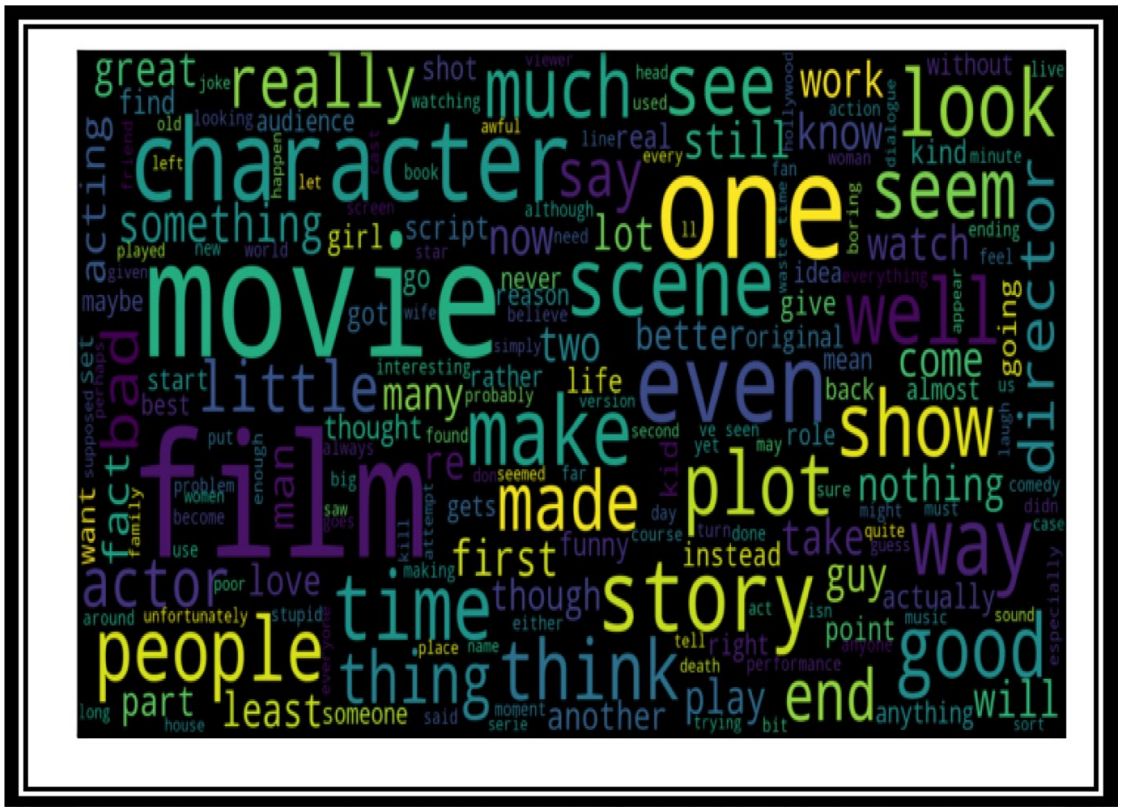


Fig. 5 Word cloud for positive tweets for DS1



Fig. 6 Word cloud for negative tweets for DS2

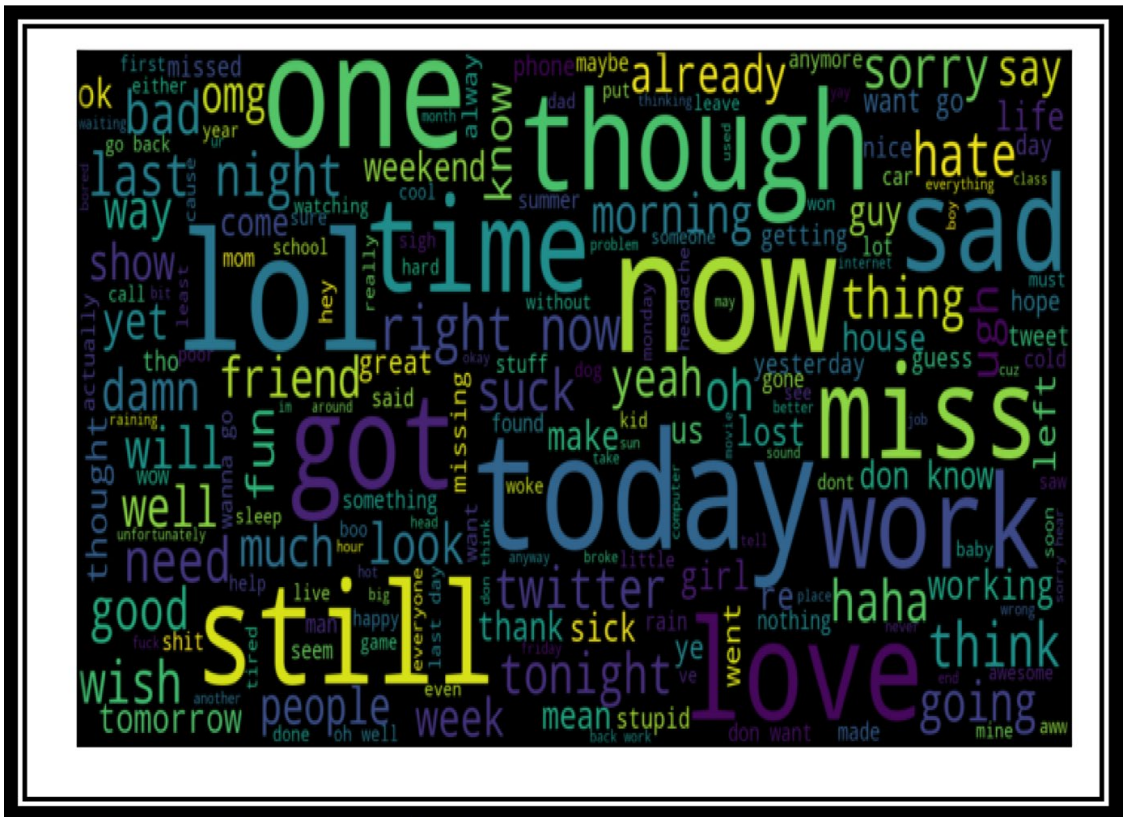


Fig. 7 Word cloud for positive tweets for DS2

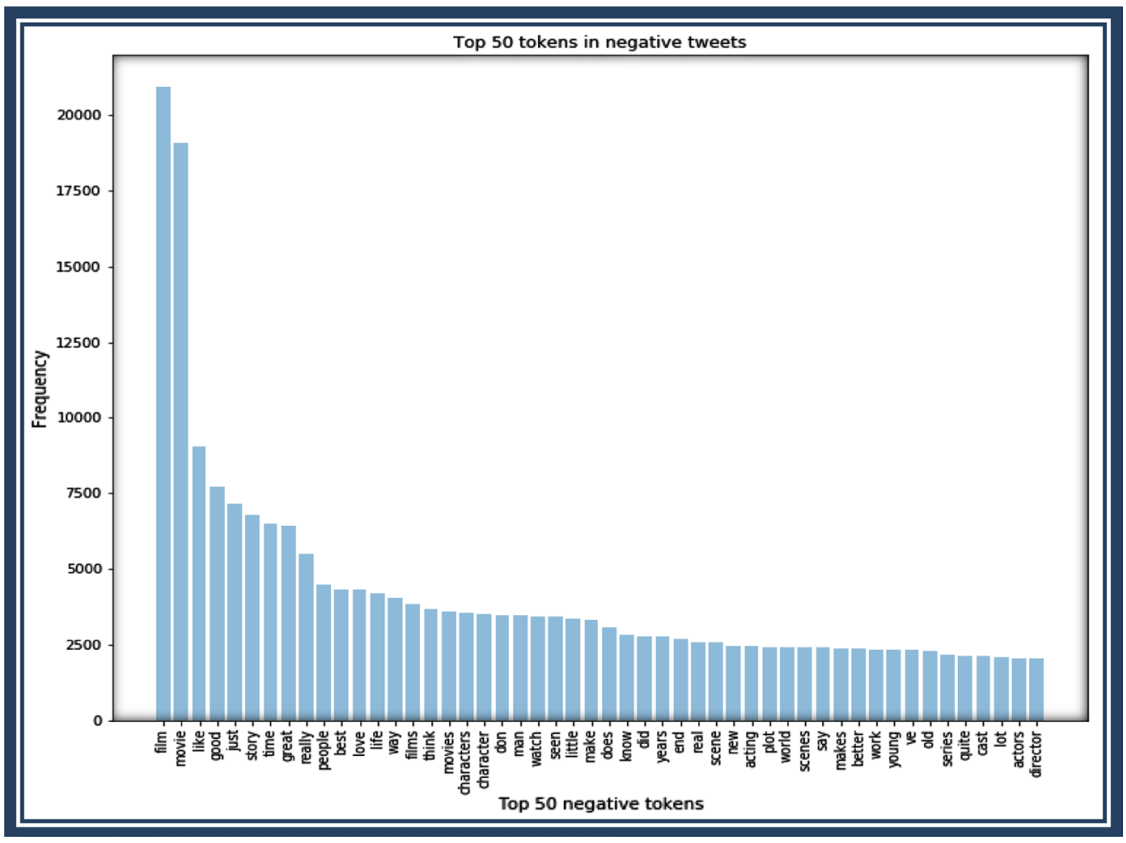


Fig. 8 Top 50 frequent tokens in negative tweets for DS1

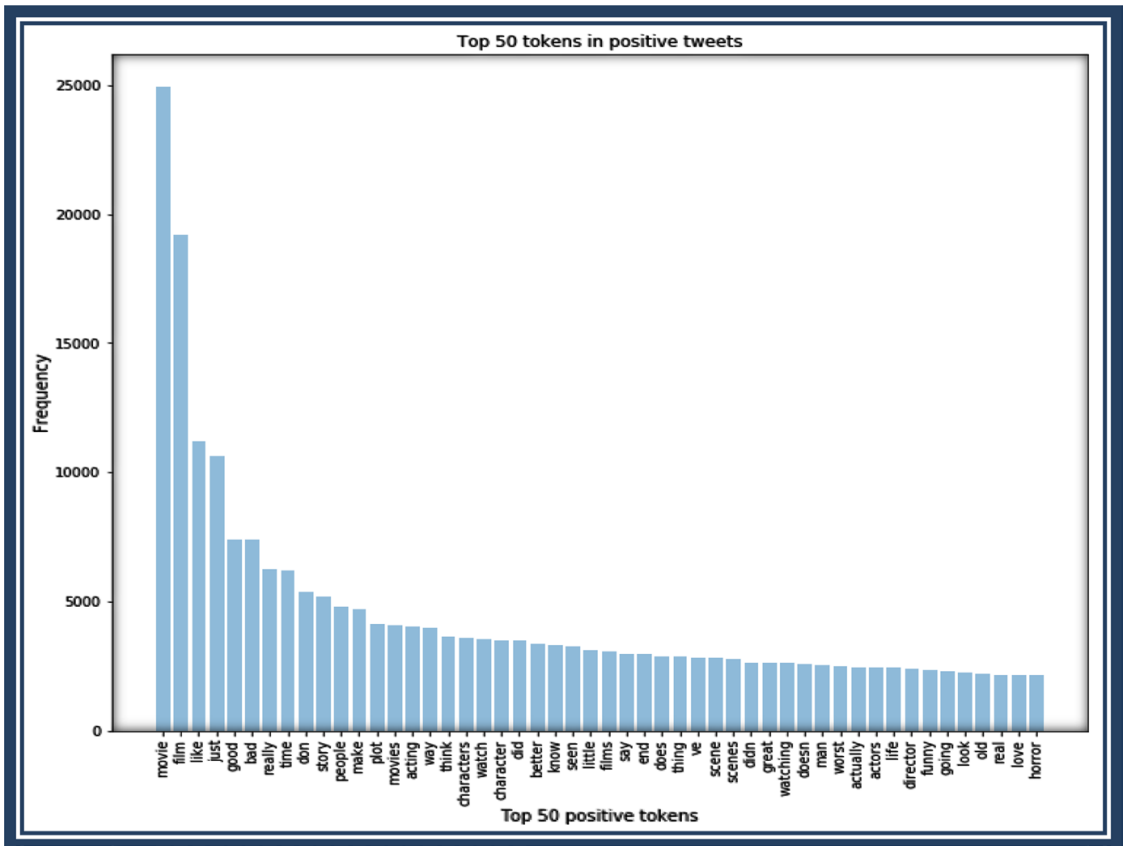


Fig. 9 Top 50 frequent tokens in positive tweets in DS1

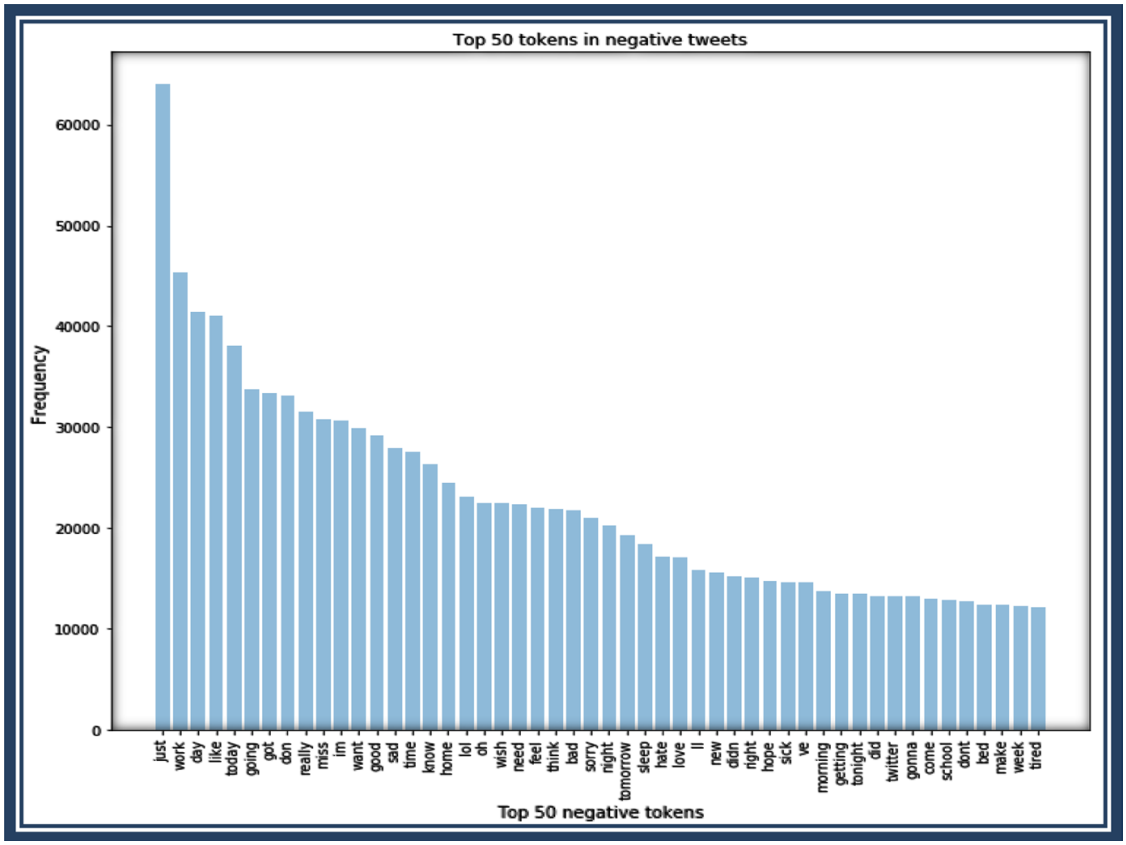


Fig. 10 Top 50 frequent tokens in negative tweets in DS2

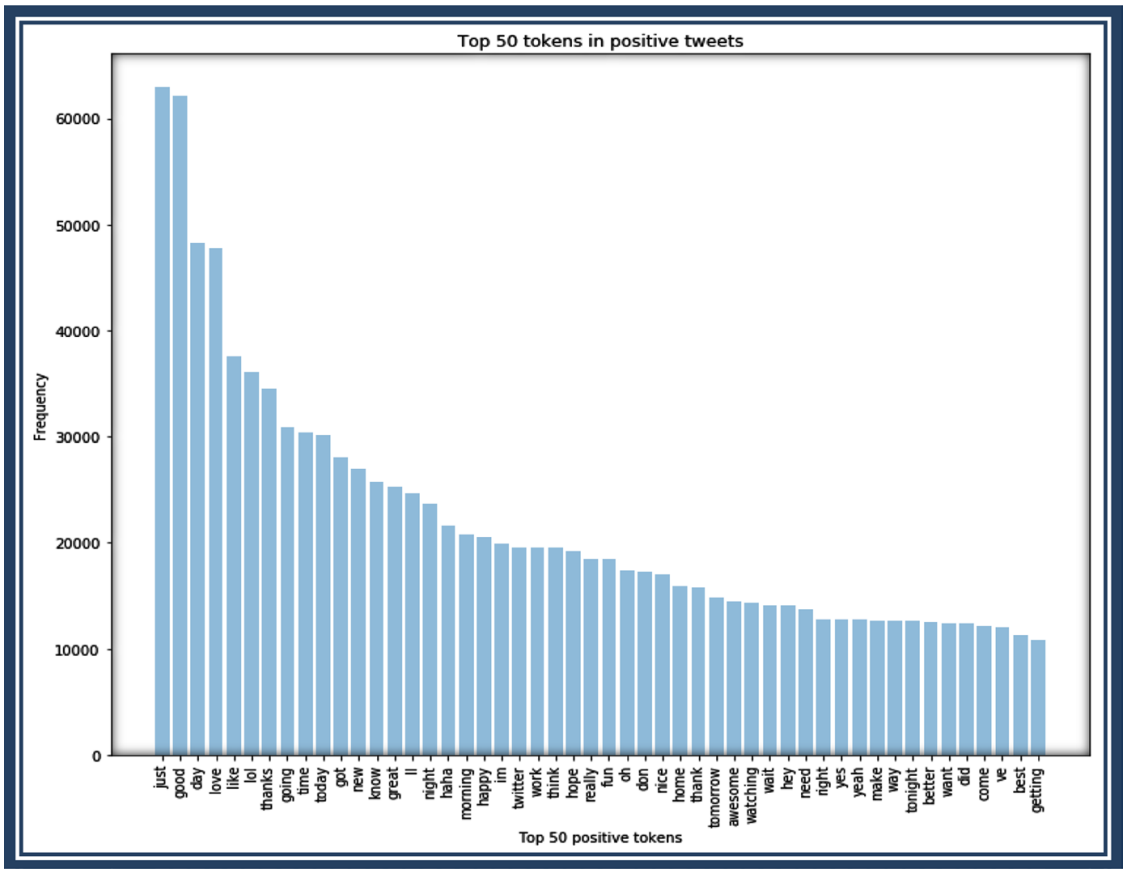


Fig. 11 Top 50 frequent tokens in positive tweets in DS2

employed data visualization concept by using word cloud for negative and positive tweets obtained as shown in Figs. 4, 5, 6 and 7 for both the datasets.

Figures 8, 9, 10 and 11 shows the top 50 frequent tokens in negative and positive tweets for both the datasets.

Table 3 depicts the comparative analysis of Logistic Regression (count vectorizer) for both the datasets via using unigram, bigram and trigrams.

From the above table, we observed that the best accuracy was obtained using trigrams. Hence, we implemented the supervised learning techniques using trigrams as shown in Table 5. Table 4 shows the implementation results of applying Logistic Regression on both the datasets for trigrams using different features with stop words (Table 5).

Figure 12 shows the diagrammatic illustration of the comparative analysis of these techniques for both the datasets.

Above results show that the final output of the processes yields purposeful information for these datasets. It also depicts that amongst all movie reviews for DS1, majority of the reviews were towards higher range of viewer satisfaction i.e. within the range of approximately 68–82%. This higher level shows these reviews were correct and absolute that could be utilized by the viewers for judicious decision making, whereas there were around 32–18% that happened to be quite inaccurate in sentiment prediction. It all depends on the technique employed. Different techniques yield different results based on their computational abilities.

Table 3 Comparative analysis of Logistic Regression on the datasets using unigram, bigram and trigrams

N-gram	Stop words	Number of features	DS2 accuracy (%)	DS1 accuracy (%)
Unigram	Without	10,000	77.28	87.6
Unigram	Without	20,000	77.54	87.2
Unigram	Without	30,000	77.63	87.6
Unigram	Without	40,000	77.72	88
Unigram	Without	50,000	77.78	88.4
Unigram	Without	60,000	77.79	88.4
Unigram	Without	70,000	77.78	88.4
Unigram	Without	80,000	77.83	88.4
Unigram	Without	90,000	77.83	88.4
Unigram	Without	100,000	77.77	88.4
Unigram	With	10,000	79.03	87.60
Unigram	With	20,000	79.18	88
Unigram	With	30,000	79.33	88.8
Unigram	With	40,000	79.39	88.4
Unigram	With	50,000	79.42	88
Unigram	With	60,000	79.41	88.4
Unigram	With	70,000	79.50	88.4
Unigram	With	80,000	79.48	88.4
Unigram	With	90,000	79.54	88.4
Unigram	With	100,000	79.49	88.4
Bigram	With	10,000	80.12	85.2
Bigram	With	20,000	80.85	87.2
Bigram	With	30,000	81.16	87.2
Bigram	With	40,000	81.16	88.8
Bigram	With	50,000	81.26	88.8
Bigram	With	60,000	81.26	88.8
Bigram	With	70,000	81.28	88.8
Bigram	With	80,000	81.24	88.4
Bigram	With	90,000	81.14	88.4
Bigram	With	100,000	81.12	88.4
Trigram	With	10,000	79.95	84
Trigram	With	20,000	80.72	87.2
Trigram	With	30,000	81.19	88.8
Trigram	With	40,000	81.21	88
Trigram	With	50,000	81.34	89.2
Trigram	With	60,000	81.26	89.2
Trigram	With	70,000	81.37	89.2
Trigram	With	80,000	81.51	89.2
Trigram	With	90,000	81.60	89.2
Trigram	With	100,000	81.66	89.2

Table 4 Comparative analysis of Logistic Regression on the datasets for trigrams using different features

Number of features	DS2	DS1
10,000	80.07	89.60
20,000	80.84	88.8
30,000	81.21	89.6
40,000	81.49	89.6
50,000	81.47	89.2
60,000	81.48	89.2
70,000	81.65	90
80,000	81.73	89.6
90,000	81.88	90
100,000	82.01	89.2

Table 5 Comparative analysis of supervised learning techniques for the datasets

Techniques (with trigrams)	DS1 accuracy (%)	DS2 accuracy (%)
Logistic regression (LR)	82.01	89.2
Support vector machines (SVM)	81.51	90.8
Multinomial Naïve Bayesian (MNB)	79.45	88.0
Bernoulli Naïve Bayesian (BNB)	78.78	87.2
Ridge classifier (RC)	81.34	91.2
Adaboost (Adb)	68.78	80.0
Multi-layer perceptron (MLP)	75.46	87.6

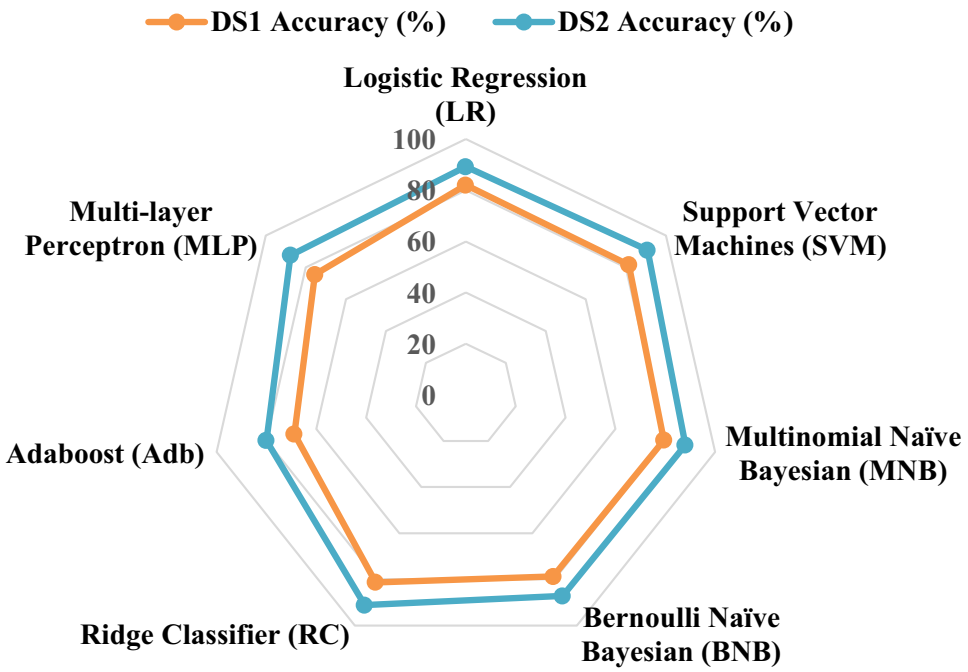


Fig. 12 Comparative analysis of supervised techniques for DS1 and DS2

Amongst all, LR predicted sentiments most aptly, i.e. it was able to accurately predict 82% of the sentiments as positive, negative or neutral and for rest of the cases, it failed to predict absolutely. Likewise, for DS2, different techniques gave different results for sentiment prediction about the opinions for any topics, brand etc. Highest accuracy of around 91% was obtained using support vector machines that mean that for 91% of the times, it was able to correctly classify the sentiment as either positive or negative about any brand or topic etc., and for rest of the cases, it went out inaccurate. Consequently, these techniques showed different sentiment prediction rate owing to their respective competence and ability. The techniques that are showing higher accuracy percentages offer better credibility to the users.

Higher precision rate means higher sentiment index that would aid in easy decision making by the masses. These results depict that using such learning techniques for sentiment analysis of real time big-data would actually pave to be an intelligent solution provider that would help guiding citizens to take 'smart and well-informed' decisions [33] towards any subject under interest. In our study, we observed sentiments for movies, products, topics, brands reviews etc. Determining sentiments for DS1 corpus helped in analyzing opinions about the movie reviews. Developing intelligent systems using these techniques could actually provide users ample amount of comprehensive reviews of movies without requiring them to go through numerous individual reviews. Thus, user would also be able to take decision based on the results provided by these intelligent systems. This would save time and resources of the people as well. Movie reviews would help user to find whether the released movie is worth watching or not. Moreover, this would probably give the movie-makers the taste about the likes and dislikes of the audience, so that this could be utilized in future for movie making concepts. Sentiment analysis of movie reviews also helps in getting an idea beforehand about the response of the people based on previous reviews and would be able to mark approximate profit gain from the movie. Likewise, considering the sentiments for DS2 dataset helped in analyzing opinions about the products, topics, brands etc. Sentiment analysis of such data using these learning techniques often results in improved brand monitoring, product analytics and market understanding. One is able to track the trends over the time, prioritize actions, monitor competitors in the market and analyze brand reputation. It would also help in augmenting the gauging of citizens for any of the decisions they wish to take for any public subject, i.e. it lessens the un-certainty associated with the consumer-decision-making. All this would certainly aid in assessing quality-oriented decision making that would make the citizen more confident and more reliable for such entities, thus manifesting a smarter, improved and intelligent city.

Applying other optimization learning paradigms such as evolutionary computation, meta-heuristics etc. would also help attain much more scalable intelligent solutions for driving smart data driven decision-making. Utilizing the collective intelligence of these computing techniques that happen to be an intelligent solution providers as well, the citizens of the city can become actually smart by taking smart and intellectual decisions and thus, eventually perpetuating towards building a smart city for its smart citizens.

4 Conclusion and future scope

In the recent years, due to enormous increase in the number of online movie reviews or be it reviews of any products, services or policies etc., it has become increasingly crucial to tap and analyze these reviews. Regular and automatic monitoring of these reviews could help the relevant industry for gaining useful information about the same based on viewer or customer satisfaction feedback. It would help the entrepreneurs, managers, government and marketers etc. to testify their products, services or policies in advance before actually launching them into the city for avoiding any future losses in case the product or service or policy failed to satisfy the citizen's needs. This will benefit in providing transparency and openness from the perspectives of a smart city, proper data and resource utilization and improved quality of living. It has various applications covering domains including health care, transportation, business, government policies, entertainment etc.

Deployment of such intelligent systems in the urban cities that could aptly cater the sentiments automatically would evidently aid in building smart education systems, smart schools, smart traffic lights, smart grids etc. and eventually a more efficient-sustainable-resilient cognitive city where the citizens are capable enough to take well-informed and dynamic decisions for any subject of interest. For this purpose, supervised learning techniques were used that are quite imperative to facilitate knowledge extraction for decision support, aid in policy making and deliver targeted information to analysts that span wide application domains. Amongst all, highest accuracy was obtained via ridge classifier, followed by support vector machines, logistic regression, Naïve Bayeisan, multi-layer perceptron and adaboost. The predicted accuracy percentages express the degree of sentiment index for these datasets. Based on these polarities, one can decide his or her opinion about the same. Thus, observing the obtained result pattern, we can infer that majority of the reviews belonged to the positive range. We can say that viewers and customers are subject to these sentiments before any intelligent decision making and crowd-sensing plays a key role for attaining this. This gained knowledge is highly beneficial and valuable for decision support as a part of any business etc. in order to provide proper insight to relevant perspective about the interest of the mass, be it favorable or un-favorable. Henceforth, the results of our research could be basis for further studies that relate to viewer or customer satisfaction using other supervised soft computing techniques such as fuzzy logic, nature inspired algorithms, evolutionary computing etc.

Different accuracy measurement of these techniques depicts the robustness and scalability of these techniques for varied datasets. These learning techniques could further be subject to optimization for yielding much enhanced and improved scalable intelligent solutions that would aid in driving more informed and smart decisions. Future implication of the work could be the development of a review data warehouse, which will then be further subjected to varied OLAP operations for data mining and analysis purposes along varied attributes, properties and dimensions.

Compliance with ethical standards

Conflict of interest There is no conflict of interests.

References

1. Somov, A., Dupont, C., Giaffreda, R.: Supporting smart-city mobility with cognitive Internet of Things. In: Future Network and Mobile Summit, IEEE, pp. 1–10 (2013)
2. Mohammadi, M., Al-Fuqaha, A.: Enabling cognitive smart cities using big data and machine learning: approaches and challenges. IEEE Commun Mag **56**(2), 94–101 (2018)
3. Wu, Q., Ding, G., Xu, Y., Feng, S., Du, Z., Wang, J., Long, K.: Cognitive internet of things: a new paradigm beyond connection. IEEE Internet of Things J. **1**(2), 129–143 (2014)
4. Kumar, A., Abraham, A.: Opinion mining to assist user acceptance testing for open-beta versions. J. Inf. Assur. Secur. **12**(4), 46–153 (2017)
5. Vlacheas, P., Giaffreda, R., Stavroulaki, V., Kelaidonis, D., Foteinos, V., Poulios, G., Moessner, K.: Enabling smart cities through a cognitive management framework for the internet of things. IEEE Commun Mag **51**(6), 102–111 (2013)
6. Khan, Z., Anjum, A., Soomro, K., Tahir, M.A.: Towards cloud based big data analytics for smart future cities. J. Cloud Comput. **4**, 1 (2015)
7. Kumar, A., Jaiswal, A., Garg, S., Verma, S., Kumar, S.: Sentiment analysis using cuckoo search for optimized feature selection on kaggle tweets. Int. J. Inf. Retriev. Res. **9**, 1–15 (2019)
8. Ahmed, K.B., Radenski, A., Bouhorma, M., Ahmed, M.B.: Sentiment analysis for smart cities: state of the art and opportunities. In: Proceedings on the International Conference on Internet Computing, pp. 55. ICOMP. The Steering Committee of The World Congress in Computer Science, Computer Engineering and Applied Computing (WorldComp) (2016)
9. Kumar, A. Joshi, A.: Ontology driven sentiment analysis on social web for government intelligence. In: Proceedings of the Special Collection on eGovernment Innovations in India, pp. 134–139. ACM (2017)
10. Pang, B., Lee, L.: Opinion mining and sentiment analysis. Found. Trends Inf. Retriev. **2**(1–2), 1–135 (2008)
11. Kumar, A., Dogra, P., Dabas, V.: Emotion analysis of Twitter using opinion mining. In: Contemporary Computing, 8th International Conference on IC3, pp. 285–290. IEEE (2015)
12. Kumar, A., Sebastian, T.M.: Machine learning assisted sentiment analysis. In: Proceedings of International Conference on Computer Science and Engineering, pp. 123–130. ICCSE (2012)
13. Massobrio, R., Nesmachnow, S., Tchernykh, A.N., Avetisyan, A.I., Radchenko, G.I.: Towards a cloud computing paradigm for big data analysis in smart cities. Proc. Inst. Syst. Program. RAS **28**(6), 121–140 (2012)
14. Kumar, A., Sebastian, T.M.: Sentiment analysis: a perspective on its past, present and future. Int. J. Intell. Syst. Appl. **4**(10), 1–14 (2012)
15. Reyes, A., Rosso, P.: Making objective decisions from subjective data: detecting irony in customer reviews. Decis. Support Syst. **53**(4), 754–760 (2012)
16. Xhafa, F., Barolli, L., Barolli, A., Papajorgji, P.: Modeling and Processing for Next-Generation Big-Data Technologies: With Applications and Case Studies, 4th edn. Springer, Berlin (2014)
17. Durán-Sánchez, A., del Río, M.D.L.C., Sereno-Ramírez, A., Bredis, K.: Sustainability and quality of life in smart cities: analysis of scientific production. Sustainable Smart Cities, pp. 159–181. Springer, Cham (2017)
18. Schaffers, H., Komninos, N., Pallot, M., Trousse, B., Nilsson, M., Oliveira, A.: Smart cities and the future internet: towards cooperation frameworks for open innovation. The Future Internet Assembly, pp. 431–446. Springer, Berlin (2011)
19. Kumar, A., Jaiswal, A.: Swarm intelligence based optimal feature selection for enhanced predictive sentiment accuracy on twitter. Multimed. Tools App;. **2019**, 1–25 (2019)
20. Lak, P., Turetken, O.: The impact of sentiment analysis output on decision outcomes: an empirical evaluation. AIS Trans. Hum. Comput. Interact. **9**(1), 1–22 (2017)

21. Kumar, A., Jaiswal, A.: Systematic Literature Review of Sentiment Analysis on Twitter Using Soft Computing Techniques. Concurrency and Computation Practice and Experience. Wiley, New York (2019). https://doi.org/10.1002/cpe.5107
22. Sulis, E., Farías, D.I.H., Rosso, P., Patti, V., Ruffo, G.: Figurative messages and affect in Twitter: differences between# irony,# sarcasm and# not. Knowl. Based Syst. **108**, 132–143 (2017)
23. Wu, F., Song, Y., Huang, Y.: Microblog sentiment classification with heterogeneous sentiment knowledge. Inf. Sci. (Ny) **373**, 149–164 (2016)
24. Xu, S.: Bayesian Naïve Bayes classifiers to text classification. J. Inf. Sci. **44**(1), 48–59 (2018)
25. Altheneyan, A.S., Menai, M.E.B.: Naïve Bayes classifiers for authorship attribution of Arabic texts. J. King Saud Univ. Comput. Inf. Sci. **26**(4), 473–484 (2014)
26. Grüning, M., Kropf, S.: A ridge classification method for high-dimensional observations. From Data and Information Analysis to Knowledge Engineering, pp. 684–691. Springer, Berlin (2006)
27. de Vlaming, R., Groenen, P.J.: The current and future use of ridge regression for prediction in quantitative genetics. BioMed Res. Int. (2015)
28. Wang, G., et al.: Sentiment classification: the contribution of ensemble learning. Decis. Support Syst. (2013). https://doi.org/10.1016/j.dss.2013.08.002
29. Wang, N, Varghese B, Donnelly, P.D.: A machine learning analysis of Twitter sentiment to the sandy hook shootings. In: Proceedings of 12th International IEEE Conference on e-Science, USA, pp. 3–312 (2016)
30. Kumar, A., Jaiswal, A.: Empirical study of Twitter and Tumblr for sentiment analysis using soft computing techniques. Proc. World Congr. Eng. Comput. Sci. **1**, 1–5 (2017)
31. Ghiassi, M., Lee, S.: A domain transferable lexicon set for Twitter sentiment analysis using a supervised machine learning approach. Expert Syst. Appl. **106**, 197–216 (2018)
32. Symeonidis, S., Effrosynidis, D., Arampatzis, A.: A comparative evaluation of pre-processing techniques and their interactions for twitter sentiment analysis. Expert Syst. Appl. **110**, 298–310 (2018)
33. Tan, W.K., Tan, C.H., Teo, H.H.: Consumer-based decision aid that explains which to buy: decision confirmation or overconfidence bias? Decis. Support Syst. **53**(1), 127–141 (2012)

Publisher's Note Springer Nature remains neutral with regard to jurisdictional claims in published maps and institutional affiliations.

ISSN: 2395-1680 (ONLINE)
DOI: 10.21917/ijme.2019.0138

SINUSOIDAL POWER CLOCK BASED PFAL

Sagar Jain[1], Shubham Garg[2], Neeta Pandey[3] and Kirti Gupta[4]
[1,2,3]*Department of Electronics and Communication Engineering, Delhi Technological University, India*
[4]*Department of Electronics and Communication Engineering, Bharti Vidyapeeth's College of Engineering, Delhi, India*

Abstract

The following manuscript proposes a modification to the existing PFAL based adiabatic structure called 2Phase PFAL for its operation on two phase sinusoidal power clocks and lower power dissipation. Sinusoidal shaped power clocks are easier to design and can be used to operate the adiabatic circuit in two phases. This proves to be advantageous as it reduces the on-chip routing complexity and density of the power-clock logic. Moreover usage of a two phase structure over a four phase structure for adiabatic operation reduces the phase consistency relationship requirement among the power clocks to realize the potential adiabatic gains. Conventional PFAL based approach requires the usage of buffers both at the input and output stages, increasing the buffer requirement. The proposed circuit is advantageous as it operates on two phases, reducing the buffer requirement leading to savings in area and power. Simulations using a standardized test bench have been performed for CMOS, PFAL and Proposed Logic based Inverter, Inverter Chain, NAND, NOR, XOR and XNOR structures. The results show that the proposed structure require less power as compared to its nearest competitors. Lower power dissipation with phase reduction, ease of power clock generation, reduced routing complexity and phase consistency relations among the power clocks make the proposed logic an suitable candidate for use in low power digital devices operating at low frequencies such as radio-frequency identifications (RFID`s), smart cards, and sensors.

Keywords:

PFAL, 2Phase PFAL, CMOS, Sinusoidal

1. INTRODUCTION

Evolution and demand of portable devices has led to the development of better display technologies and batteries with high energy storage densities [1]. Also, significant research efforts are made towards reducing power consumption of electronic circuits. The CMOS based circuit design has been used extensively in designing the digital circuits because of design ease and availability of extensive electronic design automation tools. However, the energy dissipated in these circuits is proportional to capacitive load and square of supply voltage. The charge flow occurs during charging when the load capacitance is charged to VDD via the pull-up network whereas this charge is discharged to the ground during the discharging event via the pull-down network [2]. In recent past, adiabatic logic style, which is based on adiabatic process of thermodynamics and characterized by no gain or loss of energy, has gained popularity [3]. The adiabatic logic finds its emergence and proliferation in Smart Cards and other security-centric technologies [4]. The supply voltage in adiabatic circuits is time varying clocks (sinusoidal, trapezoidal or triangular). In adiabatic logic charge recovery (i.e. energy supplied during charging is fed back to the source) while discharging takes place [5]. The guidelines for adiabatic circuit operation [6, 7] are; never switch transistor ON while a potential difference exists between the drain and source terminals; never turn transistor OFF when there is current flow through the circuit.

Positive Feedback Adiabatic Logic (PFAL), Efficient Charge Recovery Logic (ECRL) and Two NMOS-two NMOS- two PMOS (2N2N2P) are some of the most profound adiabatic families which have thoroughly been investigated by the researchers in adiabatic literature [8]-[10]. The PFAL logic outperforms these families in terms of power and hence it has been used for further exploration in this paper. The PFAL requires four phase trapezoidal shaped power clocks for its proper operation. Power clocks play the dual role of enforcing correct logic as well as charge recovery from the output node. The generation of trapezoidal clocks is more complex and would require much more area and power overhead than sinusoidal clocks [8]. Usage of such clocks (trapezoidal, sinusoidal) in adiabatic families calls for proper phase alignment between the clocks and inputs. Such requirement is important both for correct logic as well as to realize the theoretical adiabatic gains. When implemented on a chip alongside other components, the path parasitic will delay these clocks with varying degree leading to reduced power efficiency. PFAL uses buffers to ensure phase alignment among the inputs and clocks, but introduction of such buffers increases the area and power overhead. In particular for an n-bit RCA, the buffer size grows with the order of n^2 and for higher values of n the buffer number dominates the overall area and power of the structure reducing the theoretical power efficiency. For other cascaded designs, depending upon the circuit topology the buffer size grows.

Hence to overcome shortcomings of the trapezoidal clocks, sinusoidal clocks are employed for the operation, which are easier to produce vis-à-vis trapezoidal shaped counterpart. The sinusoidal power clocks are applied to PFAL structure as it presents most power saving and is energy efficient. The modification is named as 2PHASE-PFAL where the word 2PHASE indicates two phase operation. The proposed structure is differential in operation, similar to PFAL and uses full swing sinusoidal clocks VCLK and VCLKBAR for its operation.

The paper is divided into 5 sections. The rest of the paper is divided as follows Section 2 deals with Differential Adiabatic Logic Circuits [14-18], such as PFAL. Section 3 deals with our proposed circuit 2 Phase PFAL on similar lines. Results and Simulations are presented in Section 4 while further discussion and conclusion in Section 5.

2. BACKGROUND AND RELATED WORK

2.1 ADIABATIC LOGIC

Adiabatic logic represents a class of logic circuits that reduces the energy dissipation during the switching events, and improves the possibility of recycling, or reusing the energy drawn from the

power supply. Koller and Athas [1] introduced an adiabatic latch circuit that stores the information which node was charged. Without the need to keep and restore the input signals, the energy can be recovered from the output nodes through the use of powered/clocked/pulsed power supplies. To understand the adiabatic switching, a simple RC circuit with capacitor being charged by a voltage ramp is shown in Fig.1. Since a whole cycle consists of charging and recovery event, the overall dissipation in adiabatic logic is given as:

$$E_{Dissipation} = E_{Charging} + E_{Discharging} \quad (1)$$

$$E_{Dissipation} = I^2 R_{Charging} T + I^2 R_{Discharging} T \quad (2)$$

$$E_{Dissipation} = (R_{Charging} C_L + R_{Discharging} C_L) C_L V_{DD}^2 / T \quad (3)$$

where, time period of the supply is given by T, charging /discharging path resistances are $R_{Charging}/R_{Discharging}$ respectively, load capacitance is given C_L and Supply Voltage by V_{DD}. Using Eq.(3), $E_{Dissipation}$ tends to zero when $T >> (R_{Charging} + R_{Discharging})C_L$. This is referred to as adiabatic loss in the literature. The dissipated energy is smaller than the CMOS [1] if the charging time is larger than $2RC$. The energy dissipation can be made arbitrarily small by increasing the charging time. Reducing the resistance of the circuit will reduce the energy.

2.2 POSITIVE FEEDBACK ADIABATIC LOGIC

The PFAL (Positive Feedback Adiabatic Logic) family has been prevalent in the literature since two decades. The structure is a latch element formed by two cross-coupled inverters with the functionality implemented with an NMOS transistors connected in parallel to PMOS in latch structures. PFAL gates exhibit high immunity and lowest power consumption. However, the output node is kept floating when the magnitude of the power clock is less than the threshold voltage, leading to partial energy-recovery logic. Previously discussed logic families require multiphase trapezoidal clock which are difficult to generate. In contrast, sinusoidal waveform generators are simple and are efficient than the trapezoidal waveforms. In addition, the longer rise and fall time of sinusoidal power clock over trapezoidal power clock at the same frequency makes them more suited to the basic aim of low power adiabatic circuit design. The Fig.1 shows the design of PFAL inverter/buffer operating with four phase trapezoidal clock VCLK. The Fig.2 shows the waveform of PFAL based inverter/buffer.

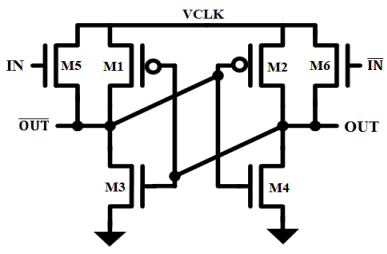


Fig.1. PFAL Inverter/Buffer

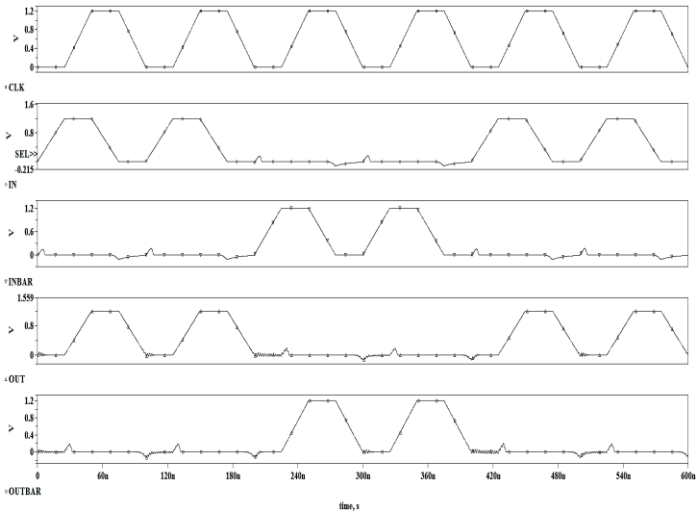


Fig.2. PFAL Inverter Waveform

2.3 SINUSOIDAL OERATION ON POSITIVE FEEDBACK ADIABATIC LOGIC

The advantages of sinusoidal clocks both in terms of generation and phase of operation, make them a viable alternative to the existing four phase trapezoidal families in differential adiabatic logic families. Hence, we first aim to operate the conventional PFAL structure with sinusoidal clocks to study and understand the operation.

For the operation we use the conventional PFAL Inverter Structure operating with the following power clock:

$$V_{CLK} = \frac{V_{DD}}{2} + \frac{V_{DD}}{2}\sin(wt) \quad (4)$$

Subsequent stages of the pipeline are fed with complementary clocks for proper operation. The complete circuit was operated on two phase which are as follows:

2.3.1 Evaluate Phase:

When the VCLK goes from 0 to VDD it is referred to as evaluate phase. Inputs are evaluated in this phase to decide the respective outputs.

2.3.2 Hold Phase:

When the V_{CLK} ramps down from V_{DD} to ground it is referred to as the hold phase. During this phase the output logic is kept constant and the output is used by subsequent stages for their evaluation.

Sinusoidal shaped power clocks are fed to the PFAL Inverter and the results are compared with those of conventional PFAL structure. The results of the comparison were far from being acceptable. The power dissipation in the new circuit increased manifolds from the conventional PFAL structure. Careful analysis of the circuit revealed that such losses were observed mainly due to inability of the circuit to provide complete isolation of the power clock and ground during its operation. This non-isolation leads to a short circuit between the power clock and ground leading to high power losses. When PFAL is operated on two phase clocks, the evaluation phase of one stage overlaps with the hold phase of the subsequent stage. For instance, assume that a two stage PFAL Inverter is available with IN , IN_{BAR} as the input

to the first stage, OUT_1, OUT_{BAR1} as the outputs of first stage and OUT_2, OUT_{BAR2} as the output of the second stage respectively. During the evaluation phase of second stage (i.e. when CLK_2 ramps towards V_{DD}), its complementary inputs (OUT_1 and OUT_{BAR1}) are HIGH (V_{DD}) and LOW (0V) respectively as shown in Fig.3. The second stage depending upon the input, evaluates the logic and the required output OUT_{BAR2} (for the above case) follows the clock. When the second stage enters the hold phase, the inputs from previous stage are no longer required for operation as the power clock is connected to the output node through one of the cross-coupled PMOS. During this time the first stage has entered into evaluate phase and its output logic can change depending upon the inputs applied. Towards the end of the hold phase, before the PMOS turns OFF, the output OUT_{BAR1} from first stage turns ON the complementary logic NMOS transistor of the second stage making a direct path between OUT_2 and the its power clock, which also turns ON the NMOS connected between ground and OUT_{BAR2}. This process occurs before the PMOS connected to OUT_{BAR2}, turns OFF. Due to this a direct path is formed between power clock and the ground, leading to short-circuit power losses. The Fig.6 also shows the current flow through the clock CLK_2 during various transitions. It shows that whenever the logic from first stage changes and towards the end of hold phase of second stage, a high amount of current flows from the power clock, indicating a short circuit.

3. PROPOSED - 2PHASE PFAL

3.1 OPERATION

To overcome the problem enshrined above and to take on the advantage of two phase sinusoidal clock operation, we propose a modification to the conventional PFAL structure. The structure is similar to basic PFAL with an addition of MT transistor as presented in Fig.4. The transistor is driven by true clock (V_{CLK}) while its source is connected to complementary clock (V_{CLKBAR}). So transistor MT turns OFF for V_{CLK}, V_{CLKBAR} and eliminates the direct path formation between power clock and ground.

The proposed logic shown in Fig.4 operates on full swing sinusoidal clocks, true V_{CLK} and complementary V_{CLKBAR}. The proposed logic operates on two phase evaluate and hold phase. During the evaluate phase V_{CLK} ramps up from 0 to V_{DD} whereas V_{CLKBAR} ramps down. During the hold phase, V_{CLK} ramps down from V_{DD} to ground and V_{CLKBAR} ramps up to V_{DD} from ground. V_{CLK} rises in the evaluate phase and supplies energy to the circuit, then during its fall, the energy flow back from the load capacitance to the power clock. For instance it is assumed that the input IN is in logic HIGH and the dual input IN_{BAR} is at logic LOW during the evaluation phase. Consequently, M5 is conducting and the output node OUT_{BAR} follows the power clock V_{CLK}. The hold phase starts with the enabling of latch when V_{CLK} reaches V_{DD}-V_{TN} and V_{CLKBAR} decays to V_{TN}, node OUT follows the V_{CLKBAR}. The input IN can ramp down since the latch is ON. In the hold phase since OUT and OUT_{BAR} hold valid logic levels which they can be used as input to the other cascaded stages. The recovery phase starts when the V_{CLK} ramps down to V_{DD}-V_{TN} and extends till it reaches V_{TP}. As the V_{CLK} falls, the resistance of M_1 increases until M_1 turns OFF and recovery stops. The charges are supplied back to the power clock V_{CLK} during this phase.

The Fig.5 shows simulation waveform for a two stage proposed inverter with IN, IN_{BAR} as the inputs of first stage, OUT and OUT_{BAR} first stage outputs and OUT_1 and OUT_{BAR1} the outputs of second stage. It also shows the Evaluate and Hold phases for the first power clock. The simulation waveforms show that whatever be the input (ideal or actual) the output remains same. In cascaded designs, the inputs and outputs are out of phase by 180, due to which we observe a delay of 0.5 clock cycle.

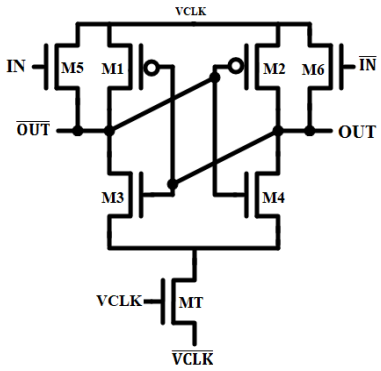


Fig.4. 2Phase-PFAL Inverter/Buffer

Table.1. Simulation Setup

Parameter	Value	
Process/MOS Model	90nm PTM	
Simulator	SYMICA Design Environment	
MOS dimensions	135/90 for NMOS	600/90 for PMOS
Supply Voltage	1.2V	
Clock Rate (F_{CLK})	Twice the Data Rate (F_{IN})	
Simulation Time	10 cycles of Charging and Discharging	
Threshold Voltages	PMOS = 0.243V, NMOS = 0.393V	

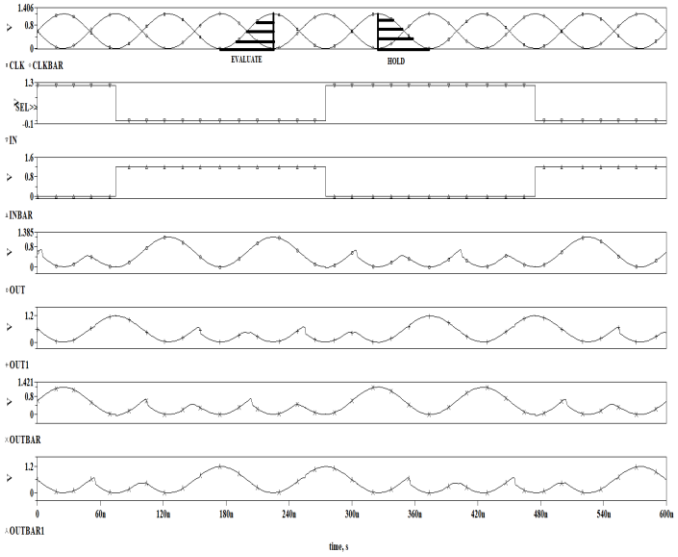


Fig.5. 2Phase-PFAL Inverter Waveform

4. SIMULATIVE INVESTIGATION

4.1 SIMULATION ENVIRONMENT

The Adiabatic Logic Circuits use time varying supplies called power clocks - trapezoidal or sinusoidal and inputs. Hence it becomes essential that that realistic supplies and inputs be used for simulating the Design Under Test (DUT) in order correctly observe circuit's behavior and the power estimate from the simulation tool be as much close to real scenario as possible. But developing these realistic inputs simulation tools is very difficult and not an effective solution. To solve this problem with view in mind for realistic analysis a standardized simulation setup [15] has been established as shown in Fig.11 wherein instead of using realistic load we have used capacitive load for simulations. It shows that the power measurements for any *N* input, *M*-output adiabatic circuit requires that any ideal signals be applied to the first stage, whereas the DUT is fed by outputs from the second stage. The Fig.11 shows the simulation setup for more accurate and realistic simulations.

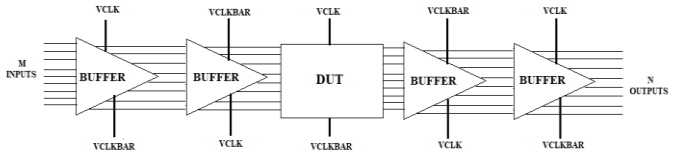


Fig.6. Standardized Simulation Setup

4.2 SINGLE STAGE CIRCUIT DESIGN USING PROPOSED LOGIC

4.2.1 Inverter - Power Dissipation with Frequency:

The Fig.7 shows the variation of Power Dissipation with Frequency for an Inverter circuit. The graph shows that proposed logic dissipate the least power among PFAL and CMOS from 10 MHz – 200 MHz. The graph shown below completely justifies our claim that the proposed logic saves on the non-adiabatic losses. Non-adiabatic losses are dominant losses for lower values of frequencies, hence our proposed logic which saves on non-adiabatic losses, shows higher savings at lower frequencies.

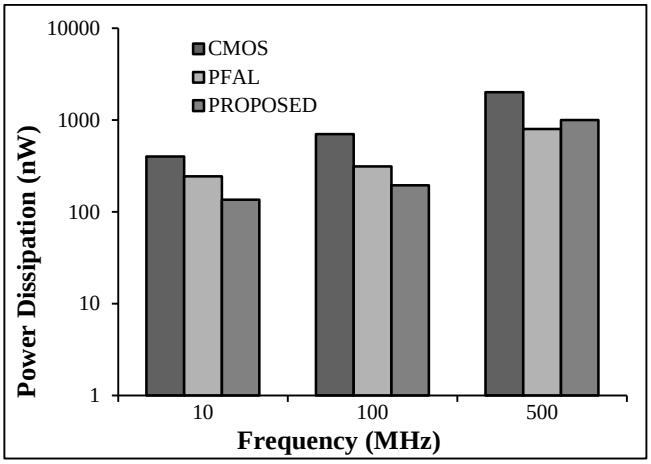


Fig.7. Power Dissipation vs. Frequency for an Inverter

The Fig.8 shows the variation of power dissipation with capacitance for an inverter circuit. The graph shows that proposed logic dissipate the least power among PFAL and CMOS from 1fF to 100fF. The graph shows that the proposed logic can work with load capacitances up to 100fF for lower power operation.

4.2.2 Power Dissipation with Capacitance:

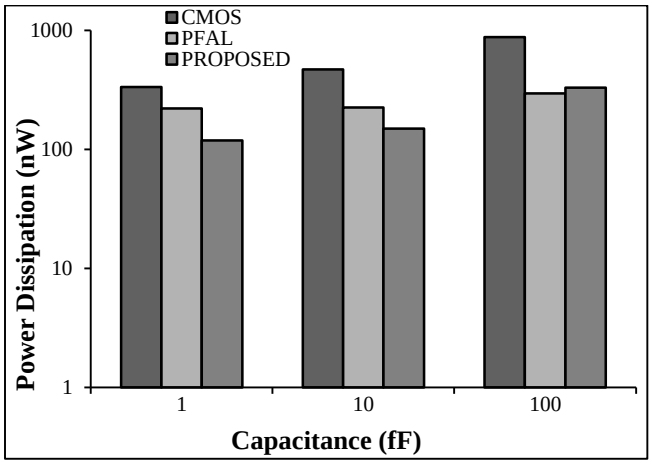


Fig.8. Power Dissipation vs. Capacitance for an Inverter

4.2.3 NAND/NOR Gate Topology:

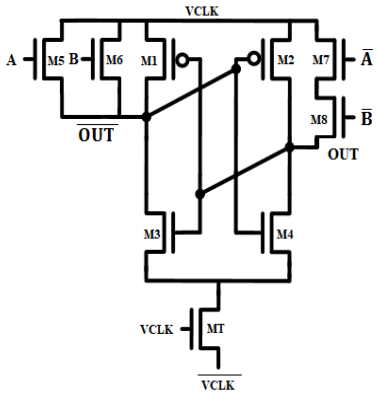


Fig.9. NOR/OR Gate

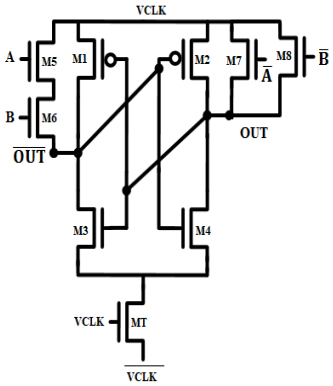


Fig.10. NAND/AND Gate

The Fig.11 shows the variation of Power Dissipation with Frequency for NAND/NOR gate topology. The graph shows that

the proposed logic dissipates low power for frequencies till 200MHz, due to complete charge recovery for reducing the non-adiabatic losses.

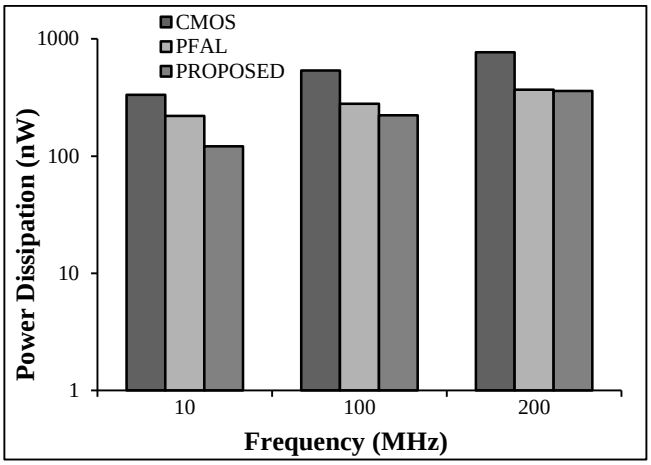


Fig.11. Power Dissipation vs. Frequency for NAND/NOR Topology

4.2.4 XOR-XNOR Gate Topology:

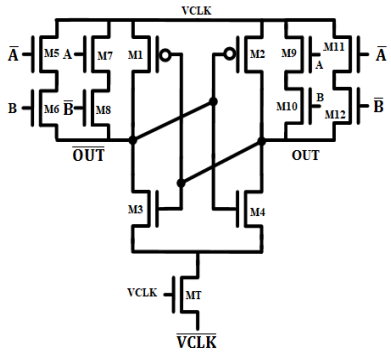


Fig.12. XOR /XNOR Gate

The Fig.13 shows the variation of Power Dissipation with Frequency for an XOR-XNOR gate topology. The graph shows that the proposed logic dissipates low power for frequencies till 200MHz, due to complete charge recovery for reducing the non-adiabatic losses.

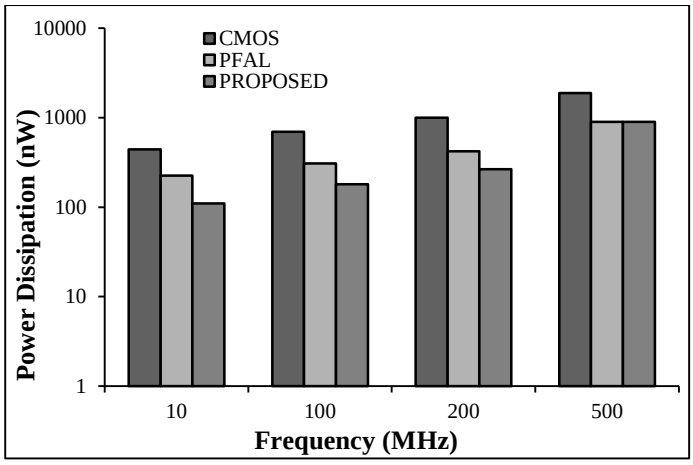


Fig.13. Power Dissipation vs. Frequency for an XOR-XNOR Gate

4.3 MULTI STAGE CIRCUIT DESIGN USING PROPOSED LOGIC - STAGE NAND OPERATIONS

The Table.2 shows Power-Transistor Product (i.e. Product of Power Dissipated and number of transistor) of a 4 Input NAND Operation, it shows that for a Multi Stage Circuit Design, the proposed logic saves both on Power and Area. The Fig.14 shows the gate level design for a 3 Stage NAND Operation

Table.2. Power-Transistor Product for a 3 Stage NAND Operation

Frequency	10	100	200
PFAL	99000	164400	300000
Proposed	21976	44690	108240
NT(PFAL) = 60	NT (Proposed) = 41		

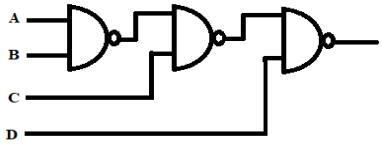


Fig. 14. Gate level Design for a 3 Stage NAND Operation

The Table.3 shows Power-Transistor Product (i.e. product of power dissipated and number of transistor) for the Maximum Length of Buffer with dissimilar phases. It shows that for a Multi Stage Circuit Design, the proposed logic saves both on Power and Area.

Table.3. Power-Transistor Product for Maximum Length of Buffer with dissimilar phases

Frequency	10	100	500
PFAL	12060	16200	37080
Proposed	952	1365	6965
NT(PFAL) = 18 (3 Buffers)		NT (Proposed) = 7 (1 Buffer)	

5. CONCLUSIONS

The Simulative Investigation shows that the proposed logic can efficiently replace PFAL based structures for lower power dissipation at low to medium frequencies. For higher frequencies, it indirectly saves power and area because of the reduced buffer requirement. In adiabatic logic circuits, to realize the theoretical gains, it is important that the power clocks, maintain their phase consistency relation throughout the operation, any deviation from these might lead to potentially higher power losses. For four phase logic circuits, this phase consistency requirement among the power clocks is manifested in form of delay of *T*/4 in each of the four consecutive power clocks. For two phase logic, this phase consistency requirement is somewhat relaxed to only two (rather than four) consecutive power clocks, separated by *T*/2 delay. Moreover, generating a sinusoidal shaped clock is much simpler and easier than generating a trapezoidal shaped clock. On-chip implementation of the four phase clock logic will require more area and increase its routing complexity and density as compared

to two phase logic clock logic. Moreover, in adiabatic logic, the external circuitry responsible for generating the power clock must be able to recover the charge through the output node during recovery phase to realize the adiabatic gains. Practically generated sinusoidal shaped clocks are similar to the sinusoidal clocks used for theoretical calculations, but the same is not true with trapezoidal shaped clocks [1]. Hence, usage of sinusoidal clocks provides us with more reliable and practically realizable gains. Hence, we can conclude that proposed logic can be used for adiabatic logic circuit designs for higher power and area savings which are realizable both theoretically and practically.

REFERENCES

[1] Philip Teichmann, "*Adiabatic Logic in Future Trend and System Level Perspective*", 1st Edition, Springer, 2012.

[2] A. Pal, "*Low-Power VLSI Circuits and Systems*", Springer, 2014.

[3] V.K. De and J.D. Meindl, "Opportunities for non-dissipative computation", *Proceedings of 9th Annual IEEE International ASIC Conference and Exhibit*, pp. 297-300, 1996.

[4] G. Indhumathi and G. Arunmani, "Implementation of 3t DRAM using Adiabatic Logic for Ultra Low Power Applications", *Proceedings of International Conference on Advanced Communication Control and Computing* Technologies, pp. 1-7, 2016.

[5] A.G. Dickinson, and J.S. Denker, "Adiabatic Dynamic Logic", *IEEE Journal of Solid State Circuits*, Vol. 30, No. 3, pp. 311-315, 1995.

[6] V. Bindal, "Adiabatic Logic Circuit Design", *International Journal of Innovative Science, Engineering and Technology*, Vol. 3, No. 3, pp. 688-694, 2016.

[7] S. Jain, N. Pandey and K. Gupta, "Complete Charge Recovery Diode Free Adiabatic Logic", *Proceedings of 5th International Conference on Signal Processing and Integrated Networks*, pp. 656-660, 2018.

[8] A. Vetuli, S.D. Pascoli and L.M. Reyneri, "Positive Feedback in Adiabatic Logic", *Electronics Letters*, Vol. 32, No. 20, pp. 1867-1869, 1996.

[9] Y. Moon and D.K. Jeong, "Efficient Charge Recovery Logic", *Proceedings of International Conference on VLSI Circuits*, pp. 129-130, 1995.

[10] A. Kramer, J.S. Denker, B. Flower and J. Moroney, "2nd Order Adiabatic Computation with 2N-2P and 2N-2N2P Logic Circuits", *Proceedings of International Symposium on Low Power Design*, pp. 191-196, 1995.

[11] V. Ponnusamy and K. Gunavathi, "Energy Efficient Charge Recovery for Positive Feedback Adiabatic Logic", *IETE Technical Review*, Vol. 24, No. 2, pp. 127-133, 2007.

[12] V.K. Bhaaskaran, "Asymmetrical Positive Feedback Adiabatic Logic for Low Power and Higher Frequency", *Proceedings of International Conference on Advances in Recent Technologies in Communication and* Computing, pp. 5-9, 2010.

[13] A. Agrawal, T.K. Gupta and A.K. Dadoria, "Ultra Low Power Adiabatic Logic using Diode Connected DC Biased PFAL Logic", *Advances in Electrical and Electronic Engineering*, Vol. 15, No. 1, pp. 46-54, 2017.

SLIDING MODE CRUISE CONTROL BASED ON HIGH GAIN OBSERVER

Ajit Kumar Sharma[1], Bharat Bhushan[2]
[1,2]Electrical Engineering Department, Delhi Technological University, Delhi, India

***Abstract*- Vehicular and highway automation has demonstrated superior safety performance, increased capacity, reduced fuel consumption and enhanced overall comfort and performance for drivers. This paper proposes an exponential high gain, sliding-mode observer (SMO) as a cruise control strategy for a longitudinal vehicle model. First, longitudinal model of vehicle is analysed and transfer function of model is obtained. Thereafter, sliding mode high gain observer is designed considering uncertainties and external disturbances. The model with integrated high gain observer is simulated on MATLAB environment. Numerical simulations on longitudinal vehicular model with designed Sliding mode controller demonstrate faster convergence, improved position and speed tracking.**

Index Terms- SMO (sliding mode observer), HGO (high gain observer), Estimation, Lyapunov function.

I. INTRODUCTION

Automatic vehicle speed control or cruise control is one of the widely researched topics in the automotive industry. [1]. Most of research in the literature embodies the objectives of range policy, string stability and human comfort & safety [2-8]. Few studies are mainly focused on reducing the model uncertainty and external disturbance, since the vehicle dynamics are highly nonlinear and uncertain [9]. Some researchers have tried to develop model based lower level controller which determines control inputs using the vehicle parameters and inverse dynamics [10]. Furthermore, linearized vehicle model has also been considered in literature to design gain scheduling linear quadratic controller for throttle and brake actuation [11]. The problem of cruise control system is to maintain the output speed of the system as set by input signal. This can be achieved by various control strategies such as proportional-integral derivatives (PID) controller, state-space controller and fuzzy logic based controllers. [12]. In modelling of a cruise control, it is vital that model takes into account all of the important parameters, which directly or indirectly affect the overall performance of the system. [13] Post modelling, the designing of appropriate controller along with stability analysis based on linear state-space model or transfer function is performed. [13]

Sliding-mode control is a well-established method for handling disturbances and modelling uncertainties through the concepts of sliding surface design and equivalent control. Based on the same concept, sliding-mode observers (SMOs) have been developed in literature for robust estimation of system states [14]– [22]. State estimation of nonlinear systems has been an active field of research in the last few decades. High-gain observers have received wide attention for uniformly observable single output systems [23]- [25]. A constant gain observer is a special class of nonlinear systems that does not require the nonlinear transformation [26]. Furthermore, there is significant improvement in the existing design of the HGO with incorporation of the nonlinear system into the gain design strategy [27]. The Lyapunov-based approach is followed to tackle the problems of state observation in the presence of bounded uncertainties/unknown inputs in HGO.

In this article, a high gain observer based SMC is designed and integrated to the vehicle dynamics on MATLAB Simulink Platform. The output of the system is controlled by the controller in order to provide the desired speed at which the car is to be maintained in the presence of uncertainties and external disturbance.

The remainder of this paper is organized as follows. Section II presents the cruise description and modelling. Section III presents the design of high gain observer that incorporates an SMO. In Section IV, design of sliding-mode controller is discussed. Section V presents the results of cruise control. Section VI embodies conclusion.

II. SYSTEM DISCRIPTION

The purpose of the cruise control system is to regulate the vehicle speed so that it follows the driver's command and maintains the speed. The Vehicle block represents a two-axle vehicle body in longitudinal motion as shown in fig (1). The vehicle can have the same or a different number of wheels on each axle. The vehicle wheels are assumed identical in size. The vehicle can have a canter of gravity (CG) positioned at or below the plane of travel.

The vehicle block accounts for body mass, aerodynamic drag, road incline, and weight distribution between axles due to acceleration and road profile. It may optionally include pitch and suspension dynamics. The vehicle does not move vertically relative to the ground.

The vehicle axles are parallel and form a plane. The longitudinal, x, direction lies in this plane and perpendicular to the axles. If the vehicle is traveling on an incline slope, β, the normal, z, direction is not parallel to gravity but is always perpendicular to the axle-longitudinal plane.

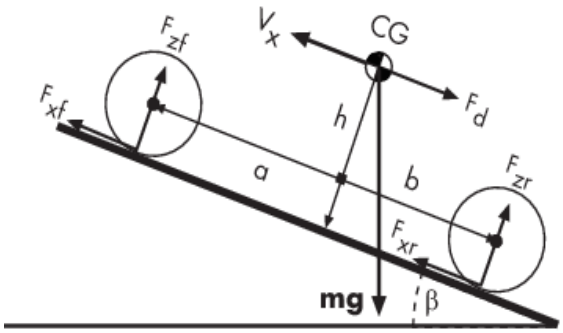


Fig. 1. Longitudinal vehicle model

TABLE I. PARAMETERS OF LONGITUDINAL VEHICLE

Parameters	Meaning	Unit
g	Gravitational acceleration	m/s^2
β	Incline Angle	rad
m	Mass of Vehicle	kg
h	Height of vehicle from CG	m
V_x	Velocity of the vehicle	m/s
V_w	Wind speed	m/s
F_{xf}, F_{xr}	Longitudinal forces on each wheel at the front and rear ground contact points, respectively	N
F_{zf}, F_{zr}	Normal load forces on each wheel at the front and rear ground contact points, respectively	N
A	Vehicle cross section area	m^2
C_d	Aerodynamic drag coefficient	
ρ	Mass density of air	Kg/m^3
F_d	Aerodynamic drag force	N
n	Number of wheels on each axle	

Case: When $V_x > 0$, the vehicle moves forward,

When $V_x < 0$, the vehicle moves backward,

When $V_w > 0$, the wind is headwind,

When $V_w < 0$, the wind is tailwind,

By applying newton's second law for z direction (i.e no vertical acceleration) ,[]

$$0 = w * Cos\beta - F_{zf} - F_{zr} + R_{hz}$$

$$m_{ax} = \frac{w}{g} a_x$$

$$= m\frac{du}{dt}$$

$$= F_{xr} + F_{xf} - w * Sin\beta - R_{xr} - R_{xf} - D_A - R_{hx} \quad (1)$$

The aerodynamic drag force depends on the relative velocity between vehicle and the surrounding air, given by-

$$D_A = 0.5 * \rho * C_d * A(V_x + V_w)^2$$

The rolling resistance arises due to work of deformation on the tire and road surface and is roughly proportional to the normal force on tire-

$$R_x = R_{xf} + R_{xr} = f(F_{zf} + F_{zr})$$

A simple model of the longitudinal motion of a vehicle can be used to determine changes in the vehicle forward motion due to grades, breaking, accelerating with, R_{hx} =0, F_{xr} = 0 & a_x= du/dt,

At equilibrium du/dt=0

$$F_{x0} = mgSin_{\beta 0} + \rho mgCos_{\beta 0} + 0.5 * \rho C_d A(V_x + V_w)^2 \quad (2)$$

The actuator and the vehicle propulsion system are modelled as cascaded of first order

$$\frac{C_1}{(1 + sT)}$$

However, a problem of non-linearity arises, one way to overcome this problem is to linearize all of the state-equations by differentiating both left and right hand sides of the equations.

The linearized model provides a transfer function can be obtained by solving the state-equations for the ratio of ΔV (s) / ΔU(s).

$$\frac{\Delta V(s)}{\Delta U(s)} = \frac{KC_1}{(\tau s + 1)(1 + sT)}$$

Where $\tau = {}^{m}/_{\rho C_d A(V_x + V_w)}$

$K = 1/\rho C_d A(V_x + V_w)$

$$\frac{\Delta V(s)}{\Delta U(s)} = \frac{0.0144}{(s^2 + 0.018s + 0.006)}$$

Which can be represented as

$$\left.\begin{array}{c} \dot{x_1} = \dot{\theta} \\ \dot{x_2} = -0.018x_2 - 0.006x_1 + 0.0144\,u(t) \\ y = x_1 \end{array}\right\} \quad (3)$$

II. DESIGN OF HIGH GAIN OBSERVER

Design a high gain observer as

$$\left.\begin{array}{c} \dot{\hat{x_1}} = \hat{x_2} + \frac{\alpha_1}{\epsilon}(y - \hat{x_1}) \\ \dot{\hat{x_2}} = -0.018x_2 - 0.006x_1 + 0.0144\,u + \frac{\alpha_2}{\epsilon^2}(y - \hat{x_1}) \end{array}\right\} (4)$$

Where α_1 & α_2 are the positive values, and $\epsilon \ll 1$.

Let $g_1 = \frac{\alpha_1}{\epsilon}$, $g_2 = \frac{\alpha_2}{\epsilon^2}$ then we have,

$$\dot{\hat{x_1}} = \hat{x_2} + g_1(y - \hat{x_1})$$

$$\dot{\hat{x_2}} = -0.018x_2 - 0.006x_1 + 0.0144\,u + g_2(y - \hat{x_1})$$

Where $\tilde{x} = x - \hat{x}$

Hence, from above equations,

$$\left.\begin{aligned}\dot{\tilde{x}_1} &= -g_1\tilde{x_1} + \tilde{x_2}\\ \dot{\tilde{x}_2} &= -g_2 - a\tilde{x_2}\\ y &= x_1\end{aligned}\right\} \quad (5)$$

i.e $\dot{\tilde{x}} = A\tilde{x}$

where $A = \begin{bmatrix}-g_1 & 1\\ -g_2 & -a\end{bmatrix}$, $\tilde{x} = \begin{bmatrix}\tilde{x_1}\\ \tilde{x_2}\end{bmatrix}$

It is assume that if A is Hurwitz, then $\tilde{x}$ will converge to zero exponentially, and can be expressed as

$$\|\tilde{x}(t)\| \le \emptyset_0\|\tilde{x}(t_0)\|e^{-\sigma_0(t-t_0)} \quad (6)$$

Where $\emptyset_0$ and σ_0 are positive constants.

Consider σ_0 is related to the minimum eigenvalue of A; the smaller the € value is, the bigger the h_i value is, and then the smaller the minimum eigenvalue of A is, the bigger the σ_0 value is.

Therefore, the convergence of $\|\tilde{x}(t)\|$ depends on €, and high gain observer will improve convergence precision of $\|\tilde{x}(t)\|$ greatly.

III. SLIDING MODE CONTROLLER DESIGN

The system is designed to drive and then constrain the system state to lie within a neighbourhood of the switching function. Trajectory of a system is designed by a sliding mode controller.

Let the sliding surface is represented by "s". The surface "s" is chosen to reduced order dynamics when constrained to plane.

The sliding mode function is-

$$s = ce + \dot{e}$$

where $c > 0$.

The tracking error and its derivative value is-

$\hat{s} = c\hat{e} + \dot{\hat{e}}$

where $\hat{e} = \theta_d - \hat{\theta}$ and $\dot{\hat{e}} = \dot{\theta_d} - \dot{\hat{\theta}}$

The sliding mode controller is

$$u(t) = \frac{1}{k}(\ddot{\theta_d} + a\dot{\hat{\theta}} + b\theta + \eta\hat{s} + c\dot{e}) \quad (7)$$

where $\eta>0$, $\hat{e} = \theta_d - \hat{\theta}$ and $\hat{s} = c\hat{e} + \dot{\hat{e}}$.

Let the Lyapunov funcion for the controller

$$V_S = \frac{1}{2}s^2$$

Since

$$\dot{e} = \ddot{\theta_d} - \ddot{\theta} = \ddot{\theta_d} + a\dot{\theta} + b\theta - ku$$

$$\dot{s} = c\dot{e} + \ddot{e} = c\dot{e} + \ddot{\theta_d} + a\dot{\theta} + b\theta - ku$$

then

$$\dot{s} = c\dot{e} + \ddot{\theta_d} + a\dot{\theta} + b - \left(\ddot{\theta_d} + a\dot{\hat{\theta}} + b\theta + \eta\hat{s} + c\dot{\hat{e}}\right)$$

$$= c\dot{\tilde{e}} + a\dot{\tilde{\theta}} - \eta\hat{s} = -\eta s + \eta\tilde{s} + c\dot{\tilde{e}} + a\dot{\tilde{\theta}}$$

$$= -\eta s + \eta\left(-c\tilde{\theta} - \dot{\tilde{\theta}}\right) + c\left(-\dot{\tilde{\theta}}\right) + a\dot{\tilde{\theta}}$$

$$= -\eta s + \eta\left(-c\tilde{\theta} - \dot{\tilde{\theta}}\right) + c\left(-\dot{\tilde{\theta}}\right) + a\dot{\tilde{\theta}}$$

$$= -\eta s - \eta c\tilde{\theta} + (a - \eta - c)\dot{\tilde{\theta}}$$

where $\tilde{\theta} = \theta - \hat{\theta}, \dot{\tilde{\theta}} = \dot{\theta} - \dot{\hat{\theta}}$,

$$\tilde{e} = e - \hat{e} = -\theta + \hat{\theta} = -\tilde{\theta},$$

$$\dot{\tilde{e}} = -\dot{\tilde{\theta}} \text{ and } \tilde{s} = s - \hat{s}$$

$$= c\tilde{e} + \dot{\tilde{e}} = -c\tilde{\theta} - \dot{\tilde{\theta}}$$

Then,

$$\dot{V_S} = -\eta s^2 + s\left(-\eta c\tilde{\theta} + (a - \eta - c)\dot{\tilde{\theta}}\right)$$

$$= -\eta s^2 + k_1 s\tilde{\theta} + k_2 s\dot{\tilde{\theta}},$$

where $k_1 = -\eta c$ and $k_2 = a - \eta - c$.

Since $k_1 s\tilde{\theta} \le \frac{1}{2}s^2 + \frac{1}{2}k_1^2\tilde{\theta}^2$

and $k_2 s\dot{\tilde{\theta}} \le \frac{1}{2}s^2 + \frac{1}{2}k_2^2\dot{\theta}^2$

$$\dot{V_S} \le -\eta s^2 + \frac{1}{2}s^2 + \frac{1}{2}k_1^2\tilde{\theta}^2 + \frac{1}{2}s^2 + \frac{1}{2}k_2^2\dot{\theta}^2$$

$$= -(\eta - 1)s^2 + \tfrac{1}{2}k_1^2\tilde{\theta}^2 + \tfrac{1}{2}k_2^2\dot{\tilde{\theta}}^2 \quad (8)$$

where $\eta > 1$.

As per the, Lyapunov function for the closed system is improved and designed as

$$V = V_S + V_O,$$

where $V_O = \frac{1}{2}\tilde{x}^T\tilde{x} = \frac{1}{2}\tilde{\theta}^2 + \frac{1}{2}\dot{\tilde{\theta}}^2$.

Since $\dot{V_O} = \tilde{x}^T\dot{\tilde{x}} = \tilde{x}^TA\tilde{x}$, and $\dot{V_O}$ converges to zero exponentially, i.e.,

$\tilde{x}^TA\tilde{x} \le \chi(\bullet)e^{-\sigma_O(t-t_O)}$,

where $\chi(\bullet)$ is a K-class function $\|\tilde{x}(t_O)\|$

Then

$\dot{V} \le -(\eta - 1)s^2 + \frac{1}{2}k_1^2\tilde{\theta}^2 + \frac{1}{2}k_2^2\dot{\tilde{\theta}}^2 + \tilde{x}^TA\tilde{x}$,

$= -\eta_1 V_S - \frac{1}{2}\eta_1\tilde{\theta}^2 - \frac{1}{2}\eta_1\dot{\tilde{\theta}}^2 + \frac{1}{2}(k_1^2 + \eta_1)\tilde{\theta}^2 + \frac{1}{2}(k_2^2 + \eta_1)\dot{\tilde{\theta}}^2 + \tilde{x}^TA\tilde{x}$

$$\le -\eta_1 V + \chi(\bullet)e^{-\sigma_O(t-t_O)}$$

where $\eta_1 = 2(n-1) > 0, \sigma_O > 0, x$

$$= [\theta \quad \dot{\theta}]^T$$

The solution of

$$\dot{V} \le -\eta_1 V\,\chi(\bullet)e^{-\sigma_O(t-t_O)}$$

$$V(t) \le e^{-\eta_1(t-t_O)}V(t_O) + \chi(\bullet)\int_{t_o}^{t} e^{-\eta_1(t-\tau)}e^{-\sigma_o(\tau-t_O)}d\tau$$

$$= e^{-\eta_1(t-t_O)}V(t_O)\,\chi(\bullet)e^{-\eta_1 t+\sigma_O t_O}\int_{t_o}^{t} e^{\eta_1\tau}e^{-\sigma_o\tau}d\tau$$

$$= e^{-\eta_1(t-t_o)}V(t_o)\frac{\chi(\bullet)}{\eta_1-\sigma_o}e^{-\eta_1 t+\sigma_o t_o}\, e^{(\eta_1-\sigma_o)\tau}\,|_{t_o}^{t}$$

$$= e^{-\eta_1(t-t_o)}V(t_o)\frac{\chi(\bullet)}{\eta_1-\sigma_o}e^{-\eta_1 t+\sigma_o t_o}\left(e^{(\eta_1-\sigma_o)t}-e^{(\eta_1-\sigma_o)t_o}\right)$$

$$= e^{-\eta_1(t-t_o)}V(t_o)+\frac{\chi(\bullet)}{\eta_1-\sigma_o}(e^{\sigma_o(t-t_o)}-e^{-\eta_1(t-t_o)}$$

i.e.,

$$\lim_{t\to\infty} V(t) \le \theta$$

Since, $V(t) \ge 0$, then we have$t \to \infty$, $V(t) = 0$ and $V(t)$ to zero exponentially, the convergence precision depends on $\eta_1, i.e. \eta$.

IV. RESULT & DISCUSSION

The system is modelled using Matlab/Simulink as shown in figure 2. The speed of cruise system, based on an exponential high gain observe is tracked. A closed system exponential convergence is also analysed.

The following parameters were chosen for simulation: k=.014; a=.018; b=.006; c=5; xite=10, k=.014; h1=400-a; h2=40000;

The initial states are $x_1(0) = 0.20, x_2(0) = 0$, and ideal position signal is set as θ_d = sint.

Fig. 2 shows the simulation model of controller and vehicle.

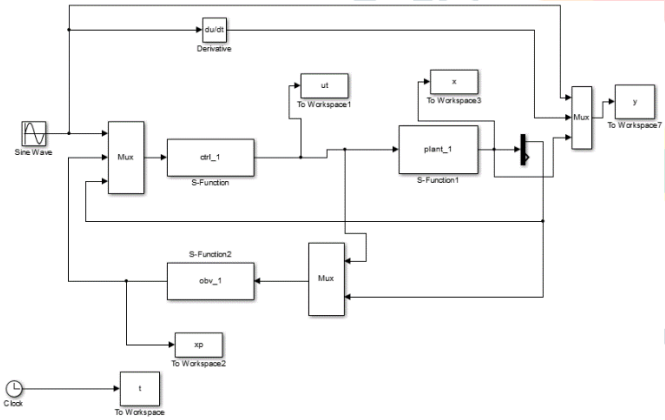


Fig 2. Block diagram of simulate cruise control with SMC

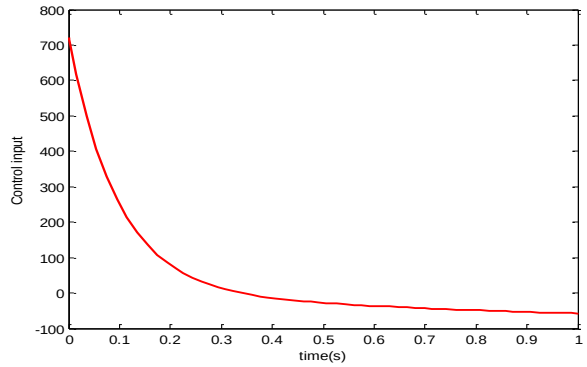


Fig 3. Control input for plant

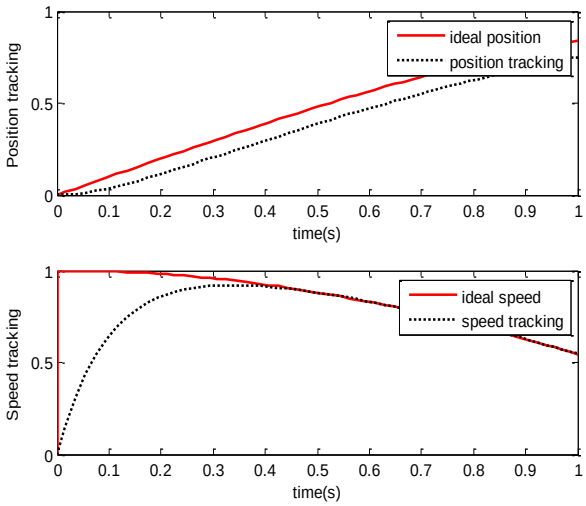


Fig 4. Speed & Position tracking

The simulation results of control input of vehicle is shown in Figures (3). Improved estimation performance can be clearly observed from control input. It is seen that the speed tracking and position of vehicle in fig. (4) shows a better results and gives small error which enhance the cruise trajectory.

V. CONCLUSIONS

The mathematical model for cruise control system has been derived. A robust HGO design is developed for a cruise system by incorporating a sliding-mode term into the nonlinear observer to improve estimation accuracy. Vehicle model along with Sliding mode observer is simulated in MATLAB Simulink environment. Simulation results obtained show superior cruise trajectory, speed tracking and minimised position error.

REFERENCES

[1] Kim, Hakgu, and Kyongsu Yi. "Combined throttle and brake control for vehicle cruise control: A model free approach." *Intelligent Vehicles Symposium (IV), 2013 IEEE*. IEEE, 2013.

[2] Choi, Sungwoo, et al. "Model-free control of automotive engine and brake for Stop-and-Go scenarios." *Control Conference (ECC), 2009 European*. IEEE, 2009.

[3] Naranjo, José Eugenio, et al. "ACC+ Stop&go maneuvers with throttle and brake fuzzy control." *IEEE Transactions on intelligent transportation systems* 7.2 (2006): 213-225.

[4] Martinez, J-J., and Carlos Canudas-de-Wit. "Model reference control approach for safe longitudinal control." *American Control Conference, 2004. Proceedings of the 2004*. Vol. 3. IEEE, 2004.

[5] Levine, W., and Michael Athans. "On the optimal error regulation of a string of moving vehicles." *IEEE Transactions on Automatic Control* 11.3 (1966): 355-361.

[6] Zhou, Jing, and Huei Peng. "Range policy of adaptive cruise control vehicles for improved flow stability and string stability." *IEEE Transactions on intelligent transportation systems* 6.2 (2005): 229-237.

[7] Wang, Junmin, and Rajesh Rajamani. "Should adaptive cruise-control systems be designed to maintain a constant time gap between vehicles?." *IEEE Transactions on Vehicular Technology* 53.5 (2004): 1480-1490.

[8] Fancher, P., Z. Bareket, and R. Ervin. "Human-centered design of an ACC-with-braking and forward-crash-warning system." *Vehicle System Dynamics* 36.2-3 (2001): 203-223.

[9] Moon, Seungwuk, Ilki Moon, and Kyongsu Yi. "Design, tuning, and evaluation of a full-range adaptive cruise control system

with collision avoidance." *Control Engineering Practice* 17.4 (2009): 442-455.

[10] Liang, Chi-Ying, and Huei Peng. "Optimal adaptive cruise control with guaranteed string stability." *Vehicle system dynamics* 32.4-5 (1999): 313-330.

[11] Goodrich, Michael A., and Erwin R. Boer. "Model-based human-centered task automation: a case study in ACC system design." *IEEE Transactions on Systems, Man, and Cybernetics-Part A: Systems and Humans* 33.3 (2003): 325-336.

[12] Shakouri, Payman, et al. "Adaptive cruise control system: comparing gain-scheduling PI and LQ controllers." *IFAC Proceedings Volumes* 44.1 (2011): 12964-12969.

[13] V. I. Utkin, Sliding Modes in Control and Optimizations. Berlin, Germany: Springer-Verlag, 1992.

[14] B. L. Walcott and S. H. Zak, "State observation of nonlinear uncertain dynamical systems," IEEE Trans. Autom. Control, vol. AC-32, no. 2, pp. 166–170, Feb. 1987.

[15] S. Drakunov and V. Utkin, "Sliding mode observers. Tutorial," in Proc. 34th IEEE Conf. Decision Control, New Orleans, LA, 1995, pp. 3376–3378.

[16] J. P. Barbot, T. Boukhobza, and M. Djemai, "Sliding mode observer for triangular input form," in Proc. 35th IEEE Conf. Decision Control, Kobe, Japan, 1996, pp. 1489–1490.

[17] C. Edwards, S. K. Spurgeon, and R. J. Patton, "Sliding mode observers for fault detection and isolation," Automatica, vol. 36, no. 4, pp. 541–553, Apr. 2000.

[18] Y. Xiong and M. Saif, "Sliding mode observer for nonlinear uncertain systems," IEEE Trans. Autom. Control, vol. 46, no. 12, pp. 2012–2017, Dec. 2001.

[19] A. J. Koshkouei and A. S. I. Zinober, "Sliding mode state observation for non-linearsystems," Int.J.Control,vol.77,no.2,pp.118–127,Jan.2004.

[20] K. C. Veluvolu, Y. C. Soh, and W. Cao, "Robust discrete-time nonlinear sliding mode state estimation of uncertain nonlinear systems," Int. J. Robust Nonlinear Control, vol. 17, no. 9, pp. 803–828, Jun. 2007.

[21] K. C. Veluvolu, Y. C. Soh, and W. Cao, "Robust observer with sliding mode estimation for nonlinear uncertain systems," IET Control Theory Appl., vol. 1, no. 5, pp. 1533–1540, Sep. 2007.

[22] J. P. Gauthier, H. Hammouri, and S. Othman, "A simple observer for nonlinear systems applications to bioreactors," IEEE Trans. Autom. Control, vol. 37, no. 6, pp. 875–880, Jun. 1992.

[23] J. P. Gauthier and I. A. K. Kupka, "Observability and observers for nonlinear systems," SIAM J. Control Optim., vol. 32, no. 4, pp. 975–994, Jul. 1994.

[24] F. Deza, E. Busvelle, J. P. Gauthier, and D. Rakotopara, "High gain estimation for nonlinear systems," Syst. Control Lett., vol. 18, no. 4, pp. 295–299, Apr. 1992.

[25] K. Busawon, M. Farza, and H. Hammouri, "Observer design for a special class of nonlinear systems," Int. J. Control, vol. 71, no. 3, pp. 405–418, Oct. 1998.

[26] K. Busawon and J. De León-Morales, "An observer design for uniformly observable non-linear systems," Int. J. Control, vol. 73, no. 15, pp. 1375–1381, 2000.

[27] A. N. Atassi and H. K. Khalil, "Separation results for the stabilization of nonlinear systems using different high-gain observer design," Syst. Control Lett., vol. 39, no. 3, pp. 183–191, Mar. 2000.

Source Scheduling for Power Matching of Clustered Induction Generators fed VSC supported Micro grid

Peeyush Pant
Department of Electrical Engineering
Delhi College of Engineering (Now DTU) Delhi 110 042, India
pantpeeyush@gmail.com

Vishal Verma
Department of Electrical Engineering
Delhi Technological University, Delhi 110 042, India vishalverma@dce.ac.in

***Abstract*—This paper proposes an autonomous off-grid generation system fed through clustered cage-rotor induction generators (IGs) acting in parallel and forming a micro-grid. The soul of the control for proposed generation system is rested in the selection of the capacity of participating generators in binary weighted IG unit. The arrangement provides optimal capacity utilization of each source, power matching during load perturbations acting together with very small capacity storage system and easy management of the source leading to regulated voltage and frequency at point of common coupling (PCC). The aforesaid system is supported with current-controlled voltage source converter (VSC) with smaller capacity battery energy storage (BES) to substantiate the deficit real power matching during disturbances. The VSC also supplies reactive power both for generator excitation and voltage regulation at PCC. The current control of VSC is actuated in tandem with source scheduling routine during perturbations of the load. The proposed scheme offers optimal head conversion opportunities for the micro-hydro turbines with improved efficiency and reduced cost. The performance of the system is evaluated in Matlab/ Simulink and its effectiveness is gauged through simulation results.**

Keywords— Induction generator, Dynamic excitation, Micro-grid, Source scheduling, Current control, Voltage source converter

I. INTRODUCTION

Fast depletion of fossil fuel has encouraged the researchers to investigate the possibilities of electricity generation using renewable energy resources [1]. Utilizing solar, wind and/or micro/pico-hydro resources seems attractive option to generate electricity effectively without carbon footprints [2]-[6]. Selecting micro-hydro system with cage rotor induction generators offers brushless, rugged, maintenance-free structure and fault immunity features for smaller capacity generation in remote locations since it experiences lesser perturbations on input power side, besides near constant head [7]-[11]. This arrangement of electricity generation utilizing micro hydro source integrated with small units of induction generator(IG) in parallel and forming a micro-grid advocates attainment of improved performance with efficient outcome and fault immune generation features utilizing near constant head siphon turbines[12],[13].

Parallel operation of induction generator for attaining improved reliability, stability and loading capacity is rarely investigated. The reported schemes do not addresses exact compensation of reactive power when dynamic reactive power consuming loads are connected at PCC making it unsuitable for off-grid application[14]-[16]. The deployment of fixed capacitors for IG excitation thus also takes short leading unregulated voltage/ fluctuations during load perturbations [17], [18]. Recently, IG fed micro-grid for optimal source utilization of the source is reported [19]-[20]. Since, IG is perceived as a weak source before PCC the issues of unregulated voltage and frequency amid reactive power consuming loads connected at PCC become prominent and is remediation is yet to be addressed. Hybrid combination of capacitors and VSC supported autonomous distribution system is also reported [21]-[25]. Large capacitor often provokes over excitation of generator during light load at PCC and even causes severe voltage spike during declutching of the source from the micro-grid and thus cannot confirm to capacity utilization of the source [26]. Dynamic excitation control of individual induction generator with current controlled VSC presents attractive option to attain precise voltage control even during declutching of generator [27]-[31]. Forming a micro-grid by integrating cluster of induction generators operating in parallel with dynamic excitation from a single VSC offers an attractive option. However, reported literature indicates large capacity battery storage source for maintaining frequency constant by matching the load. Thus investigation with small capacity battery storage acting with scheduling of IG source with constant head siphon turbine is yet to be explored for operations with optimal head converters.

In this paper a micro-grid fed through the binary weighted clustered parallel connected IGs with a current controlled VSC with storage is presented. Each CRIG is coupled to a separate micro-hydro siphon turbine of respective capacity. The capacity of each participating IG in the formation of the micro-grid is binary weighted so that rated capacity of next higher IG is nearly double of the former unit. This arrangement enables the capacity ratio as 2^n (for n=0 to 3) for optimal source scheduling amid harnessing the energy when generation system caters perturbing load in off-grid system. The micro-grid is supported by a VSC for adequate supply of reactive power both for IG excitation and reactive power hungry loads at PCC. The control action acts to regulate the voltage and frequency at PCC of micro-grid by source scheduling and battery storage support deployed at the dc-bus of VSC. The battery storage also emulates as a load controller when operating under battery charging mode and a real power source to releases the part/full real power demanded during load perturbations. The proposed current controlled scheme is demonstrated to present simple, cost-effective, efficient and responsive hardware. The scheme effectively and efficiently converts the head of micro-hydro system leading to improved reliability of the overall system. The proposed system is realized in Matlab/ Ps-Block set and the effectiveness of the system is gauged through simulation results.

II. SYSTEM CONFIGURATION

978-1-5386-6625-8/18/$31.00 ©2018 IEEE

The block diagram of the proposed system is shown in Fig.1. The system integrates clustered parallel connected induction generators along with a current controlled VSC forming a micro-grid. The capacity ratio of the generators are selected as 2^n (n=0 to 3) that of the former. The proposed system considers four IGs of rated power capacities 2.2kW, 5.5kW, 14kW and 30kW each of 415V, 50Hz rating. Small capacitors (600V, 1μF each) are connected at stator terminals of each IG for harmonics filtering. This IG and capacitor combination is hence forth considered as source. A current controlled VSC with a capacitor(3000μF, 1200V) at dc-bus is integrated at PCC which supplies adequate reactive power both for generators excitation and voltage regulation at PCC. The dc-bus of VSC is also supported by a small battery storage source of capacity 135Ah. The dc-bus voltage is maintained in self-support mode and transacts requisite amount of real-power by absorbing or delivering current from the battery source. This arrangement eliminates the necessity of installing costlier governor and/or complex load controllers.

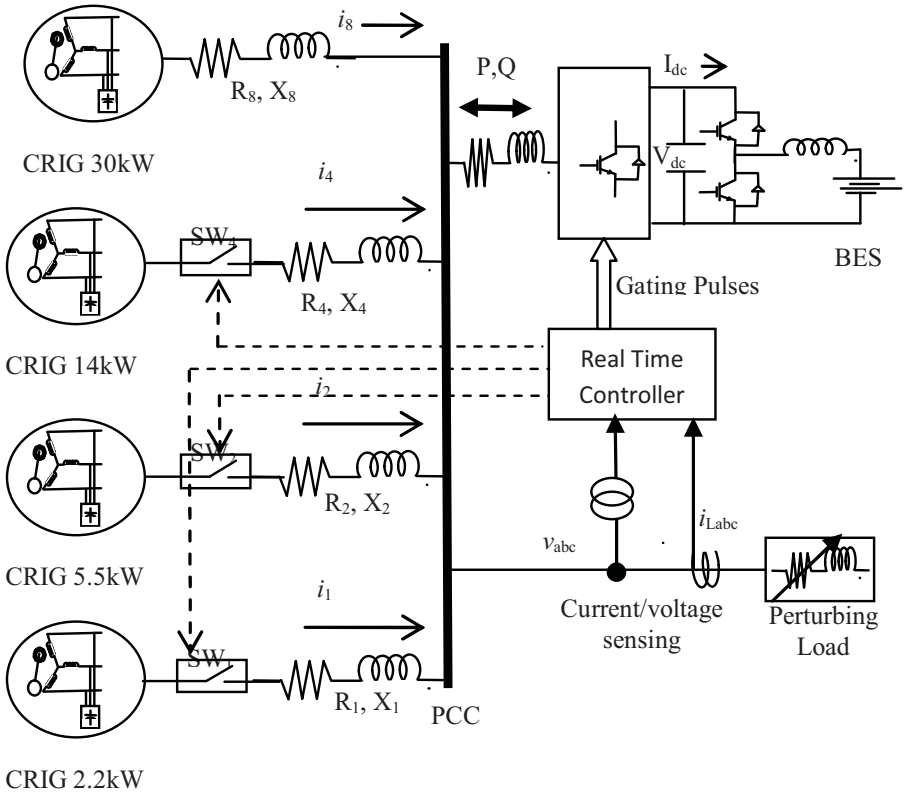


Fig.1 Block diagram of the proposed system depicting cluster of IGs operation in parallel and forming a micro-grid.

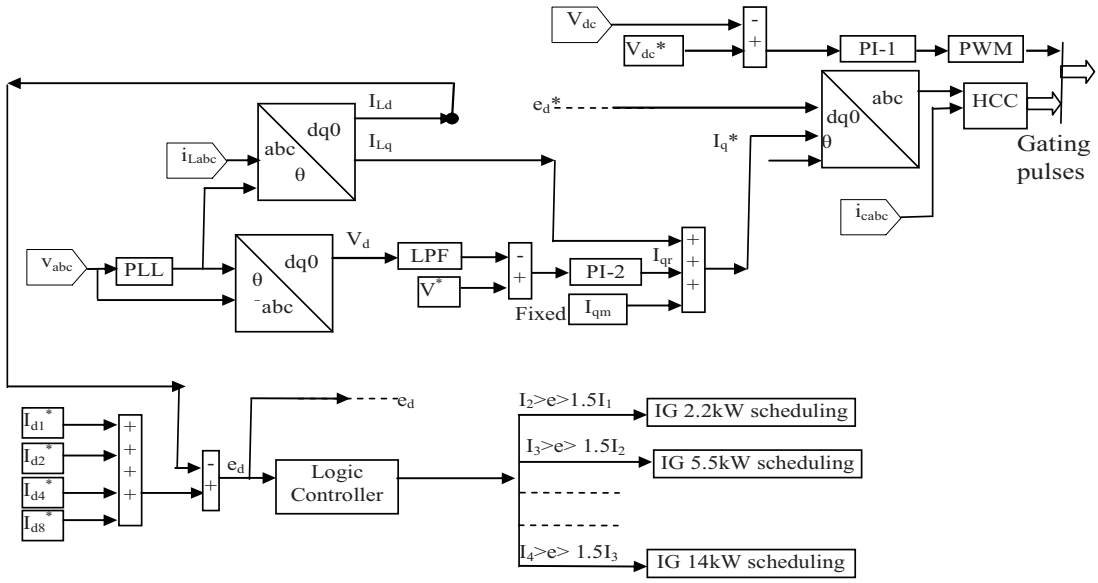


Fig.2 Control scheme pertaining dynamic excitation control of IG and source scheduling during load/ source disturbances.

Regulation of the input side potential energy utilization is made through adequate selection of binary weighted CRIGs providing the small power for load matching by the battery storage. A three-phase reactive power consuming load is connected at PCC to gauge the effectiveness of the control under adverse conditions. The loading perturbations enables battery charging/ discharging operation in tandem with source scheduling to offset the incremental load difference leading to the condition of load matching enabling near constant frequency operation. The system offers head conversion opportunities along with improved efficiency at reduced cost of electricity generation. An indirect current control of VSC is implemented in the synchronous reference frame and the same is explained in the next section.

III. Control Strategy

The block diagram of the control algorithm to regulate voltage and frequency at PCC of the clustered IGs fed micro-grid with current controlled VSC and a small battery energy storage support at dc-bus is depicted in Fig.2. The VSC supplies reactive power both for generator excitation and voltage regulation at PCC. The control algorithm is realized in synchronous reference frame. To implement the control action the load current (i_{Labc}), VSC current (i_{Cabc}), phase voltage (v_{abc}) and dc-bus voltage (V_{dc}) are sensed. The proposed control scheme is oriented in the following sub-sections.

A. Regulation of dc-bus voltage and estimation of reference current I_d

Source scheduling/ load perturbation at PCC of micro-grid may lead to mismatch in real power pertaining unregulated voltage at dc-bus of VSC. Eventually larger loading may lead to voltage sag at dc-bus of VSC. The control action pertaining dc-bus voltage regulation is realized by estimating the error between the sensed voltage in dc-bus and the reference voltage (V_{dc}*). The error is passed through PI controller (PI-1) which estimates the current corresponding to real power drawn from the battery storage for dc bus voltage regulation. Similarly during deficit load the deviation of loading from rated value on generator simultaneously affect the dc-bus voltage and the energy is transferred across the battery storage and maintaining dc-bus voltage regulated.

The current corresponding to real power drawn by the load (I_{Ld}) is compared with the cumulative current equal to the rated capacity of all integrated IG sources. The error estimates the reference current I_d for real power equalization by extracting rated capacity power from the IG sources connected at PCC.

B. Voltage regulation and estimation of reference current I_q

The estimation of reference current corresponding to reactive power (I_q) is made by accumulating the current required for IG magnetization (I_{qm}) along with the current corresponding to reactive power (I_{qr}) required for voltage regulation at PCC. The estimation of the former component is derived by comparing per unit rms value of the sensed phase voltage (v_{abc}) with the unit reference voltage (v*) through PI controller (PI-2). This estimates the requisite current (I_{qr}) for voltage regulation.

C. IG source scheduling

The current corresponding to real power drawn by the load (I_{Ld}) is compared with the current corresponding to cumulative rated capacity of all the sources (i.e. $I_{d1} + I_{d2} + I_{d4} + I_{d8}$). The estimated error($e_d$) is passed through the logic controller circuit which leads to the scheduling action of suitable capacity IG source. This presents real power matching of the source and load. The cumulative action of source scheduling and battery storage in turn pivots each IG source to contribute its rated capacity real power at PCC.

A digital PLL is implemented to realize the fast control action in turn producing synchronization signals via Park/Clark transformation. The estimated values of reference real and reactive currents in dq0 frame are reverse transformed and compared with the sensed VSC currents (i_{Cabc}). The error is fed through a hysteresis current controller (HCC) which forces the VSC currents to follow the reference currents and maintains requisite real and reactive power transaction at PCC. Matlab based simulations are performed and the system performance is presented in the forthcoming section of the paper. The attained results validate that the scheme offers fast, easy and efficient control for effective system operation.

IV. Simulation Scheme

The proposed system is simulated in Matlab/Simulink. The induction generator and the system parameters are kept close to the standard values enabling correct assessment of the modeling and control algorithms. The rated capacities of considered IGs are selected as 2.2kW, 5.5kW, 14kW and 30kW each of 415V, 50 Hz rating. The micro-grid is supported by a VSC and small battery storage at dc-bus. The three-phase reactive power hungry load perturbing in nature is connected at PCC. Each IG of the system is mechanically coupled to the respective low head constant power prime mover (siphon turbine). Three capacitors (each 1μF, 600V) are connected in star configuration across the stator terminals of each generator for harmonic filtering. A VSC with a tank capacitor at dc-bus has been used in tandem with a small battery at PCC and regulates the exchange of both real and reactive power. The tank capacitor voltage is maintained at 600V. A hysteresis band of 0.1A is considered to realize carrier-less PWM signals operating in current control mode. The system is operated at 12.8 kHz switching frequency. The simulation model of the system is executed with fixed-step solver using ode3 (Bogacki-Shampine) for estimating both dynamic and steady state simulation based performance of the system. The performance of the proposed system is evaluated by appropriate tuning of both simulation and control parameters of the system. The simulation scheme is realized by triggering the VSC when self-excitation of the IG is established leading stabilized voltage at PCC. During steady state operation the reactive power supplied by the VSC is sufficient to compensate the magnetization current of IG sources and also establishes voltage regulation at PCC. To demonstrate the potential of the scheme under adverse load condition load perturbations are made at PCC and the onus is transacted via battery source and source scheduling bringing the system to equilibrium again. The voltage across the dc-bus has been maintained by BES charging/ discharging action. This ensures compensation of real and

reactive powers through the VSC in controlled manner. The next section demonstrates the attained results and performance of the system for validating successful implementation of the proposed control algorithm.

V. PERFORMANCE OF THE SYSTEM

Matlab based simulations are performed to evaluate the performance of the proposed system. The performance is validated in terms of the following (Refer Table I) illustrations.

1) Steady-state operation of the system.

2) Dynamic operation of the system during load perturbation at PCC.

3) Power matching by source scheduling and small battery support.

The performance of the system based on simulation results validates the effectiveness of the proposed micro grid which integrates cluster of IGs in parallel with VSC support. The performance of system is evaluated during steady- state operation and dynamic load perturbations. The attained waveforms are depicted in Fig.3 which presents PCC voltage (v_{abc}), source currents (i_{abc}), VSC current (i_{cabc}), load current (i_{Labc}), and the dc bus voltage (V_{dc}). The results are analyzed in the following three time sections.

(i) t=0.5s-2.0s: Steady-state operation of system with VSC supplies reactive power in dynamic manner
(ii) t=2s - 4s: Load perturbation at PCC and
(iii) t=4.5s onwards: Re-insertion of IG source at PCC of micro grid.

At t=0.5s the VSC is connected at PCC of micro-grid.

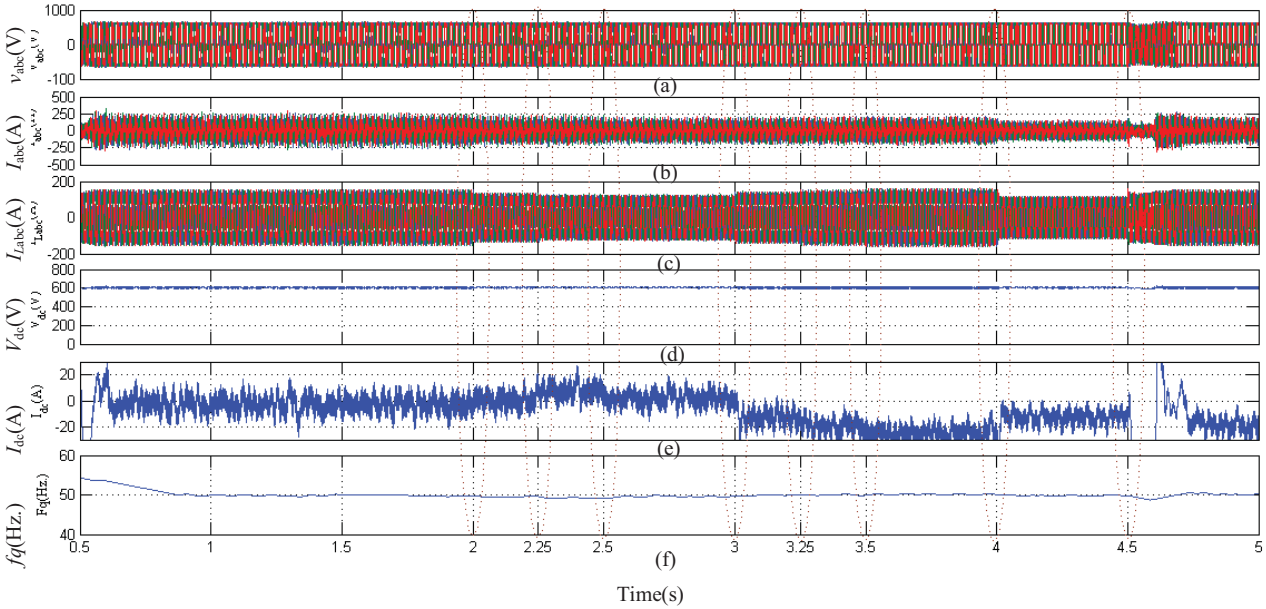


Fig.3 Performances of the proposed system during load perturbations at PCC of micro grid.

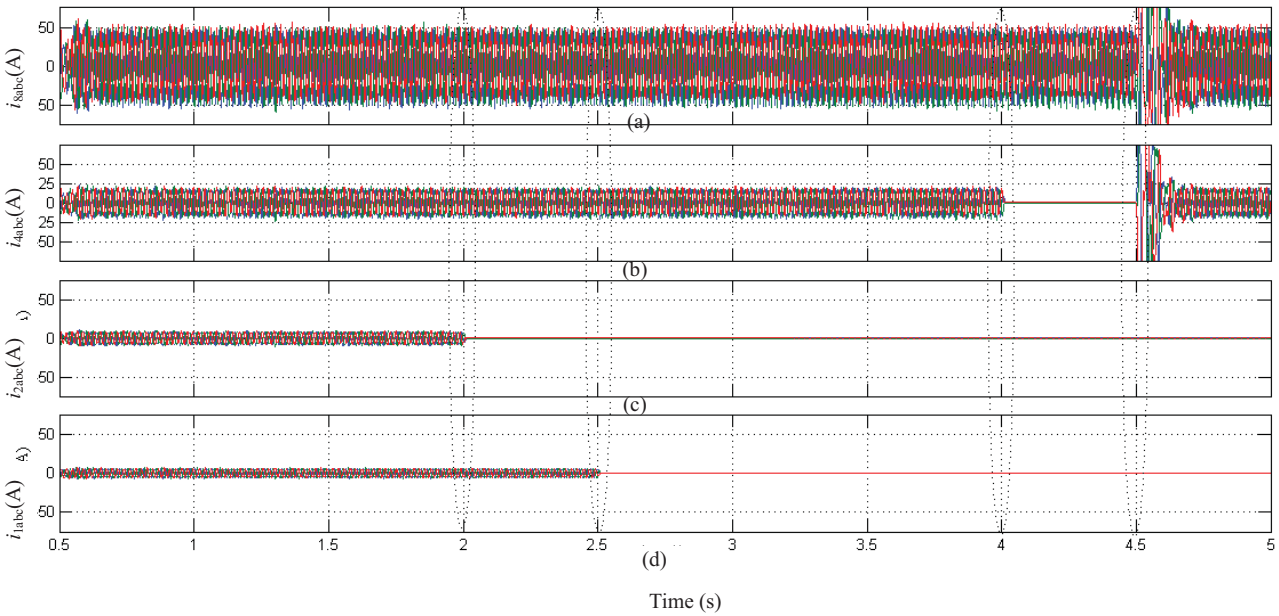


Fig.4. Simulation results depicting stator current of each IG sources connected at PCC

As shown in Fig.3(a,b) current transient and glitch in PCC voltage is observed. Small transient is also observed in the current transacted through dc-bus and is shown in Fig. 3(e). Further, the system comes to steady state within few cycles and no abnormal state is observed in the system.

At t=2s-5s the system experiences load perturbations in steps and are depicted in Fig.3(c). During perturbations the power matching is made fast by real power transaction to/from the battery and IG source scheduling and is presented in Table-I. At t=2.25s and 2.5s load at PCC is reduced to 46kW and 44kW respectively in steps. For real-power matching the logic controller schedules 5.5kW IG source from the system and is shown in Fig. 4(c). Effective power matching is maintained in the system vis-a- vis the VSC regulates reactive power and presents regulated voltage at PCC. The battery inacts in charging mode and the same may be observed in Fig.3(e). Further, as shown in Fig.3(c) at t=2.5s, 3s and 3.25s, the load changes to 43kW, 46kW and 48kW respectively. The logic controller matches the real-power by scheduling 2.2kW IG source from PCC and the same is shown in Fig. 4(d). Also it is observed at 2.5s-3s in Fig.3(e) that battery operates in charging mode and than inacts in discharging mode during t=3s-4s. At t=4s shown in Fig. 3(c) the loading at PCC changes to 32kW. To match the real power the 14kW IG is scheduled by the controller action (Refer Fig. 4(b)) and only 30kW IG source integrated in the system caters the load at PCC. Moreover the transient load matching is made by battery operation inacting in discharging mode and is clearly seen in Fig.3(e). At t= 4.5s - 5s the loading at PCC rises to 44kW. In this condition the real power matching is made by resynchronization action of 14kW IG source. As shown in Fig. 4(a, b) the synchronization of IG at PCC may results the current transients under acceptable limits. It is observed in Fig. 3(e) that requisite current is drawn by the battery storage to meet the loading perturbations. The battery turns idle at t=5s.

It may also be clearly observed in Fig.3 that controller action for dynamic compensation of reactive power and real-power matching operates the system well under synchronism. The PCC voltage and frequency are depicted in Fig.3 (a,f) are well regulated and pivoted under limits. Also the dc-bus voltage shown in Fig. 3(d) is well regulated at 600V throughout the system operation. This validates the effectiveness of the proposed control.

The results depicting the stator current of each IG is shown in Fig.4(a-d). It may be clearly demonstrated that the proposed scheme maintains rated extraction of real power from each IG source even under sudden load changes, scheduling and reinsertion of sources. The overall performance of the system presents fast compensation of both real and reactive power and effective load matching.

VI. Conclusion

The performance of the VSC supported autonomous generation system integrating cluster of IGs and small battery to cater reactive power consuming load at PCC is successfully demonstrated. The system successfully works well under load perturbations in steps and source scheduling operations. The PCC voltage and frequency is regulated by current controlled VSC by reactive power compensation and exact power matching. Employing VSC enables the scheme to respect dynamic excitation control of induction generator. It is successfully demonstrated that even under extreme load perturbation the voltage at dc-bus of VSC is maintained. The scheme involves lesser computation effort in deriving current capacity of IGs sources from their rated capacity. The scheme is simple, fast acting and maintains healthy voltage profile of the connected loads. The proposed system effectively fulfills the requirement of utilizing renewable energy resources for electricity generation and forming a micro-grid.

TABLE I. Source scheduling and battery operation during load perturbation

Time Range	Load at PCC of micro-grid	IGs delivering power at PCC	Scheduled IGs for real power matching	Battery operation
0-2s	52kW	2.2kW, 5.5kW, 14kW and 30kW (51.7kW)	nil	Discharge mode for real power topping
2s-2.25s	46 kW	2.2kW, 14kW and 30kW (46.2kW)	5.5kW	Charging mode (real power matching)
2.25s-2.5s	44kW	2.2kW, 14kW and 30kW (46.2kW)	5.5kW	Trigger charging (prior to source scheduling)
2.5s-3.0s	43kW	14kW and 30kW (44kW)	5.5kW and 2.2kW	Charging mode (Real power matching)
3s-3.25s	46 kW	14kW and 30kW (44kW)	5.5kW and 2.2kW	Discharging mode (real power supply)
3.25s-4.0s	48kW	14kW and 30kW (44kW)	5.5kW and 2.2kW	Discharge mode to compensate transient overloads
4.0s-4.5s	32kW	30kW (30kW)	14kW, 5.5kW, 2.2kW	Discharging mode
4.5s-5.0s	44kW	30kW and 14kW IG resynchronized at 4.5s (44kW)	5.5kW and 2.2kW	Battery idle after stabilization

References

[1] I.R. Pillai and R. Banerjee, "Renewable energy in India: status and potential," Energy, Vol.34, No. 8, pp.970-980, August 2009.

[2] M.A. Elhadidy and S. M.Shaahid, "Parametric study of hybrid (wind +solar+ diesel) power generating systems," Renewable Energy, vol. 21, no.2, pp.129-139, October 2000.

[3] Y.Jiang, L.Lu, H.Lu, "A novel model to estimate the cleaning frequency for dirty solar photovoltaic (PV) modules in desert environment," Solar Energy, vol. 140, pp. 236-40, December 2016.

[4] S.Adhikari, F. Li, "Coordinated V/f and PQ control of solar photovoltaic generators with MPPT and battery storage in micro-grids," IEEE Transactions on Smart Grid, vol.5, no.3, pp.1270-81, May 2014.

[5] M.Motevasel, A.R.Seifi, "Expert energy management of a micro-grid considering wind energy uncertainty," Energy Conversion and Management, Vol. 83, pp. 58-72, July 2014.

[6] Thomsen B, J.M.Guerrero, P.B.Thøgersen, "Faroe islands wind-powered space heating micro-grid using self-excited 220-kW induction generator," IEEE Transactions on Sustainable Energy, vol.5, no.4, pp.1361-66, October 2014.

[7] L.Wang, S.J.Chen, S.R.Jan, and H.W.Li, "Design and implementation of a prototype underwater turbine generator system for renewable microhydro power energy," IEEE Transactions on Industry Applications, vol. 49, no.6, pp.2753-2760, June 2013.

[8] A.S. Ridwan, S.Anjar, and I.Pudji, "Design and analysis of the prototype of pico hydro scale submersible type turbine-generator for flat flow river application," Teknologi Indonesia, vol. 35, no. 3, pp. 1–8, February 2015.

[9] A.O.Edeoja, J.S.Ibrahim, and E.I. Kucha, "Investigation of the Effect of Penstock Configuration on the Performance of a Simplified Pico-hydro System," British Journal of Applied Science & Technology, vol.14, no.5, pp. 1-11, January 2016.

[10] A.Alidai and I.W. Pothof, "Hydraulic performance of siphonic turbine in low head sites," Renewable Energy, vol. 75, pp. 505-511, March 2015.

[11] N. P. Smith, "Induction generator for stand-alone micro-hydro systems," in Institute of Electrical and Electronics Engineers, Inc., Piscataway, NJ (United States), 1995.

[12] D.Zhou, and Z. D. Deng, "Ultra-low-head hydroelectric technology: A review," Renewable and Sustainable Energy Reviews, vol.31, no.78, pp.23-30, October 2017.

[13] V.Z. Silva, A.J. Rezek, and R.D. Corrêa, "Analysis of synchronous and induction generators in parallel operation mode in an isolated electric system," IEEE 8th Intl Symposium on Power Electronics for Distributed Generation Systems (PEDG), 2017, Apr. 17, pp. 1-8.

[14] D.B.Watson, and I.P.Milner, "Autonomous and parallel operation of self-excited induction generators," International Journal of Electrical Engineering Education, vol.22, no.4, pp.365-374, Oct 1985.

[15] L.Wang, and C.H.Lee, "Dynamic analyses of parallel operated self-excited induction generators feeding an induction motor load," IEEE Transactions on Energy Conversion, vol. 14, no.3, pp. 479-485, September 1999.

[16] I.Tamrakar, L.B. Shilpakar, B.G.Fernandes, and R. Nilsen, "Voltage and frequency control of parallel operated synchronous generator and induction generator with STATCOM in micro hydro scheme," IET Generation, Transmission & Distribution, Voo.1, no.5, pp. 743-750, September 2007.

[17] Y.K. Chauhan, V.K.Yadav, and B. Singh, "Optimum utilisation of self-excited induction generator," IET Elect. Power Appl., vol. 7, no.9, pp.680-692, November 2013.

[18] Salimikordkandi and T. Surgevil, "Modeling and analysis of self-excited induction generator with fixed capacitor excitation and shunt voltage regulation," In IEEE 16th Power Electronics and Motion Control Conference and Exposition, September 21, 2014, pp. 149-155.

[19] M.Jain, S.Gupta, D.Masand, D.Agnihotri and S.Jain, "Real-Time Implementation of Islanded Micro-grid for Remote Areas. Journal of Control Science and Engineering," Journal of computer science and Engineering, April 2016.

[20] L.Che, X.Zhang, M.Shahidehpour, A.Alabdulwahab and A.Abusorrah, "Optimal interconnection planning of community micro-grids with renewable energy sources," IEEE Transactions on Smart Grid, vol.8, no.3, pp.1054-63, May 2017.

[21] N. Bottrell, M. Prodanovic, T.C. Green, "Dynamic stability of a micro-grid with an active load," IEEE Transactions on Power Electronics, vol. 28, no.11, pp.5107-19, November 2013.

[22] G. K. Kasal and Bhim Singh, "Decoupled voltage and frequency controller for isolated asynchronous generators feeding three-phase four-wire loads," IEEE Transactions on Power Delivery, vol. 23, no. 2, April 2008.

[23] L.G. Scherer, R.V. Tambara, and R.F. de Camargo, "Voltage and frequency regulation of standalone self-excited induction generator for micro-hydro power generation using discrete-time adaptive control," IET Renewable Power Generation, vol.10, no.4, pp. 531-540, January 2016.

[24] B.Singh and G.K.Kasal, "Neural network-based voltage regulator for an isolated asynchronous generator supplying three-phase four-wire loads," Electric Power Systems Research, vol.78, no. 6, pp. 985-994, June 2008.

[25] L.Wang and D.J. Lee, "Coordination control of an AC-to-DC converter and a switched excitation capacitor bank for an autonomous self-excited induction generator in renewable-energy systems," IEEE Transactions on Industry Applications, vol.50, no. 4, pp.2828-2836, July-August 2014.

[26] Li Wang, and Dong-Jing Lee, "Coordination Control of an AC-to-DC Converter and a switched excitation capacitor bank for an autonomous self-excited induction generator in renewable-energy systems," IEEE Trans. Ind. Appl., Vol.50, No. 4, pp.2828-2836, Aug. 2014.

[27] N. Bottrell, M. Prodanovic, T.C. Green, "Dynamic stability of a micro-grid with an active load," IEEE Transactions on Power Electronics, vol. 28, no.11, pp.5107-19, November 2013.

[28] M. Srinivasan and A.Kwasinski, "Autonomous hierarchical control of DC micro-grids with constant-power loads," IEEE Applied Power Electronics Conference and Exposition APEC, Charlotte NC, March 15, 2015, pp. 2808-2815.

[29] Alireza Kahrobaeian, and Yasser Abdel-Rady I. Mohamed, "Analysis and mitigation of low-frequency instabilities in autonomous medium-voltage converter-based micro-grids with dynamic loads," IEEE Transactions on Industrial Electronics, vol. 61, no. 4, pp. 1643- 1658, April 2014.

[30] R. Zhu, Z.Chen, X. Wu, and F.Deng, "Virtual damping flux-based LVRT control for DFIG-based wind turbine" IEEE Transactions on Energy Conversion, vol. 30, no. 2, pp.714-25, June 2015.

[31] P.T. Manditereza and R. Bansal, "Renewable distributed generation: The hidden challenges–A review from the protection perspective," Renewable and Sustainable Energy Reviews, vol.31, no.58, pp. 1457-65, May. 2016.

Study of Forced Oscillations in Two Area Power System

Vertika Jain
Post Graduate Student
Electrical Engineering Department
Delhi Technological University,
Delhi dvertikaj28@hotmail.com

S.T Nagarajan
Professor
Electrical Engineering Department
Delhi Technological University,
Delhi stnagarajan@dce.ac.in

Rachana Garg
Professor
Electrical Engineering Department
Delhi Technological University,
Delhi rachnagarg@dce.ac.in

***Abstract*— Low frequency oscillations in power systems is a potential threat to the power system as it can lead to blackout of the system. In today's scenario, oscillation analysis has become an area of great interest for the researchers in dealing with stability problems of the power grid. This paper simulates a recent event in western American power system which reported several instances of north-south inter area mode below 3% for several hours. The present work deals with the study of recently detected forced oscillations in power system with the popular Kundur two area test system simulated on Digsilent Power factory and the detection of forced oscillations by measurement based methods namely the Frequency Domain Decomposition (FDD) and Prony Analysis (PA) method.**

Keywords- Power System, Electromechanical modes, Interarea Oscillations, Resonance, Stability.

I. INTRODUCTION

Oscillations in power system is a potential threat to the power system, as oscillations can grow steadily over a period of time leading to blackout of the power system. Power system engineers are more concerned to low frequency oscillations in the system which are below the system nominal frequency which are caused various reasons like sub synchronous resonance and low damped electromechanical modes in the system. The main concern of these low frequency oscillations is the damping of these oscillations by the power system. More recently a new type of low frequency oscillation has been identified to be caused by Forced Oscillation (FO) in the power system. FOs are considered to be injected into the system by mal operation mechanical parts in the system or disoperation of controllers in the system.

For any power system operations and for its reliability it is necessary to have knowledge and estimation of electromechanical oscillation at low frequency. For reliable operation of such mode estimation we have two different methods:

- Using a power system model and linearization of equations about an equilibrium point of operation [1] or by
- Using mode estimation method by measurement techniques [2] [3].

Ring down and ambient data are the two different types of analysis form measurement data. Measurements from power system's response to sudden change or disturbance such as, tripping of line or outage of generator which consequentially results in excitation of oscillatory modes, is treated as ring-down data. Measurements from power system operating in quasi-steady state condition where the measurement system input is from small continuous random oscillations in loads and other system fluctuations which are assumed to be white noise, is treated as ambient data.

Apart from natural electromechanical modes which are excited from load variations, they can be excited from forced oscillations injected by external mechanism such as from cyclic loads or mechanical aspects of generators [4] [5]. They can have adverse effects on generators produced by resonance among forced oscillations. Also, due to widespread nature of power system, forced oscillations are more liable to occur with inter area modes of power system. When a forced oscillation frequency is close to system mode frequency or when inter area mode is poorly damped at a location where inter area mode is associated, oscillations at much higher value as compare to source can appear leading to resonance in system.

Concept of resonance in Physics states that system operating at natural frequencies of system for undamped or poorly damped modes will undergo resonance when subjected to external forced oscillation. The destructive behavior of resonance is strongly identified in power system in the conditions of sub synchronous resonance [5] that originate from opposing interactions from modes of electrical and mechanical torsional behavior. Further, it has been reported in literature that, natural modes of estimation are affected by the presence of forced oscillations by some methods based on measurement estimation [6].

This paper studies the nature of forced oscillations in popular Kundur's two are power system simulated on Digsilent Power factory software in time domain. The different shapes of forced oscillations were presented for different operation scenarios. This work also and analyses the results by measurement based techniques of ambient method, namely the Frequency Domain Decomposition (FDD) method and ring down method namely, Prony Analysis (PA) method.

978-1-5386-6625-8/18/$31.00 ©2018 IEEE

II. RESONANCE IN POWER SYSTEM FROM FORCED OSCILLATIONS

A brief overview on concept of resonance as per theory of physics is explained in this section. Resonance is a process in which the system oscillates with higher amplitude for specific frequencies for the vibrating system or for system which derives external force. When the amplitude of the response of the system is relatively maximum for a frequency then these types of frequencies are known as resonant frequencies. At these resonant frequencies, due to storage of vibrational energy small periodic force has the ability to generate large amplitude oscillations. The phenomenon of resonance occurs between two or more various modes have the capability to store and transfer energy easily. Although, there are various losses which varies from cycle to cycle and is known as damping. When there is no forced oscillation then these resonant frequencies is almost equal to natural frequencies then the damping of the system is small [7].

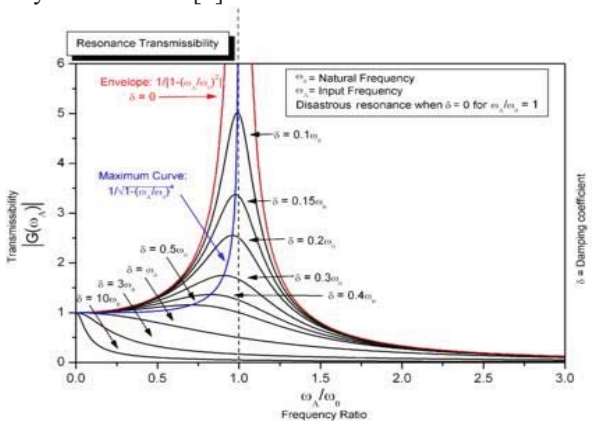


Fig 1: Concept of Resonance

According to the concept of physics in reference to resonance [8], let us consider a mass spring system as shown in Fig 2 for an undamped forced oscillation of $F_o\cos\omega t$. From Newton's law we get:

$$mX + bX + KX = F_o\cos\omega t \quad (1)$$

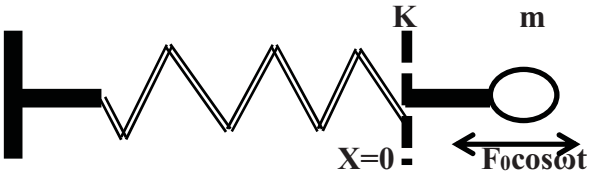


Fig 2: Mass Spring System with undamped Forced oscillation

whereas the system damping γ and system natural frequency ω_o are:

$$\omega_o^2 = \frac{K}{m}, \quad \gamma = \frac{b}{m} \quad (2)$$

Damping ratio is given by $\zeta = \frac{\gamma}{2\omega_o}$, rewrite equation (1) in complex plane and replacing equation (2) we get,

$$Z + \gamma Z + \omega_o^2 Z = \frac{F_o}{m} e^{j\omega t} \quad (3)$$

The solution of equation (3) is given as:

$$Z = Ae^{j(\omega t-\delta)} \quad (4)$$

Replacing equation (4) in (3) we solve the equations for A and δ and is given as:

$$\begin{cases} A = \dfrac{\frac{F_o}{m}}{\sqrt{(\omega_o^2-\omega^2)^2+(\omega\gamma)^2}} \\ \tan\delta = \dfrac{\omega\gamma}{(\omega_o^2-\omega^2)^2} \end{cases} \quad (5)$$

Where δ is the phase difference for the forced oscillation and A is the amplitude of oscillation. Resonance condition arises when amplitude A is at its peak value. From equation (5) for an undamped system i.e. $\gamma = 0$ while forced frequency equal to natural frequency i.e. $\omega = \omega_0$ then resonance occurs due to which amplitude of oscillation becomes infinity. Whereas for damped system i.e. $\gamma = 0$ then amplitude will have some finite value from equation (5) and the amplitude becomes maximum at a frequency ω_{max} which is smaller than ω_0.

There can be three possible conditions:

$$\begin{cases} \omega \to 0, A = \dfrac{F_0}{K} \delta \to 0 \\ \omega \to \omega_0, A = \dfrac{F_0}{K} \delta \to \dfrac{\pi}{2} \\ \omega \to \infty, A = 0 \ \delta \to \pi \end{cases} \quad (6)$$

Fig 1 shows the different damping level of forced oscillation which varies the amplitude A. The lowest damping system $\zeta = 2\%$ has the highest peak and with lowest damping system $\zeta = 27\%$ shows the lowest peak. Therefore the graph clearly shows that for poorly damped system the effect of resonance can be ignored.

III. STUDY OF FORCED OSCILLATIONS TEST SYSTEM

The study system of this work is the popular two area Kundur's test system [9] that provides a standard test case benchmark system. In this system a small mechanical sustained oscillation is induced by governor of generator G4 of Kundur test system which is connected at bus 4 of the system as shown in Fig 3. It is connected to the bus 10 of system through transformer between 4-10.The location of the forced oscillation can be changed to other buses as per requirement of the system or for analysis of the system.

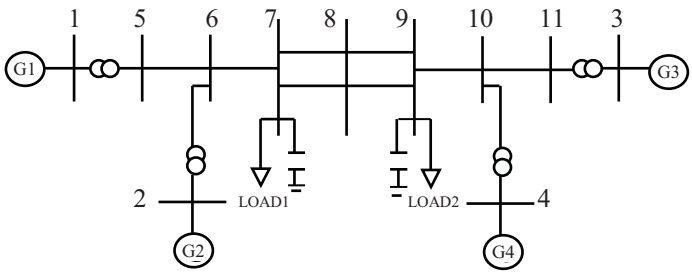


Fig 3: Two Area Kundur Power System

Load flow analysis was performed with Newton Raphson method with constant load on the system. Then modal analysis was performed to find the modal properties of the system. Two operation scenarios were created by varying the damping of the interarea modes of the system.

Scenario 1: Here the interarea modes of the system is at a frequency of 0.2 Hz. The details of the modal analysis are given in table 1.

Table 1: Modal Analysis at 0.2 Hz

Mode No.	Magnitude 1/s	Damped Freq Hz	Angle deg	Damping Ratio
1	0	0	0	0
2	46.90635	7.29357109	102.31599	0.213303
3	46.90635	7.29357109	-102.31599	0.213303
4	37.94158	0	180	1
5	37.94158	0	180	1
6	35.47603	0	180	1
7	34.39755	0	180	1
8	32.9964	0	180	1
9	32.65079	0	180	1
10	26.42154	0	180	1
11	25.93187	0	180	1
12	6.07404	0.96372978	94.50362	0.078522
13	6.07404	0.96372978	-94.50362	0.078522
14	6.10888	0.96413627	97.41143	0.128993
15	6.10888	0.96413627	-97.41143	0.128993
16	5.7795	0	180	1
17	5.29859	0	180	1
18	3.8406	0.07370135	173.07473	0.992704
19	3.8406	0.07370135	-173.07473	0.992704
20	**1.39946**	**0.22270722**	**90.86023**	**0.01501327**
21	**1.39946**	**0.22270722**	**90.86023**	**0.01501327**
22	1.9457	0	180	1
23	0.60331	0	180	1
24	0.26124	0.00191032	177.36658	0.998943
25	0.26124	0.00191032	-177.36658	0.998943
26	0.0498	0.0034	154.59948	0.903331
27	0.0498	0.0034	-154.59948	0.903331
28	0.0003	0	180	1

Scenario 2: Here the interarea modes of the system is at a frequency of 0.3 Hz. The details of the modal analysis are given in table 2, with only relevant mode ie interarea mode.

Table2: Modal Analysis at 0.3 Hz

Mode No.	Magnitude 1/s	Damped Freq Hz	Angle deg	Damping Ratio
20	1.11946	0.34583	90.86022	0.051015
21	1.11946	0.34583	90.86022	0.051015

The interarea mode can be identified with the phasor plot of the mode given below, with pair of generators oscillating opposite to each other in two clusters

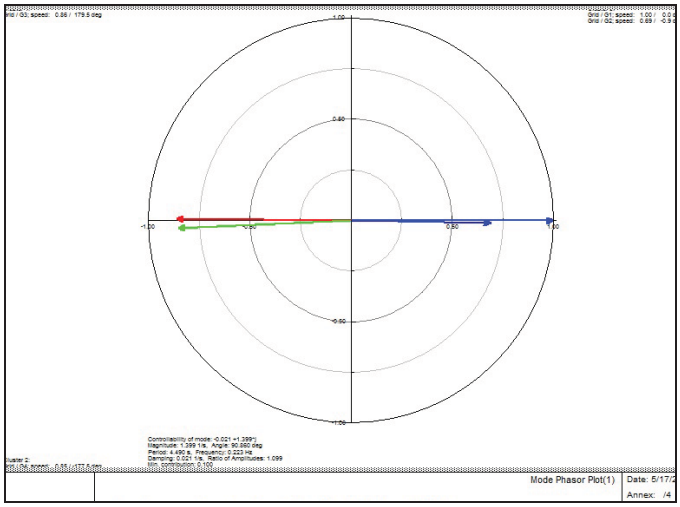


Fig 4: Modal Analysis at 0.2 Hz

IV. DYNAMIC ANALYSIS

Forced oscillations were simulated in governor of generator 4 as explained below.

A. Controller Description:

For the analysis of the dynamic behavior of the system controllers have been implemented in simulation. PowerFactory offers global library for the use of variety of different predefined controllers such as IEEE standard models of power plants i.e. providing a wide range of dynamic regulators like governors, voltage controllers and power system stabilizers.

Power Factory control modes design concept can be summarize as follows. For a control mode designing the fundamental element is 'Model/Block definition' as it constitute specified preconfigured units or controller

definition such as generators. Excitation systems, PSS and Hydro Governor are examples of Model/Block Definition described in Fig 6. A composite frame is a general control model which is used to define inputs and outputs of these control models. Hydro power plant schematic diagram of 'composite frame' is shown in Fig 5. Where the forced oscillation is injected.

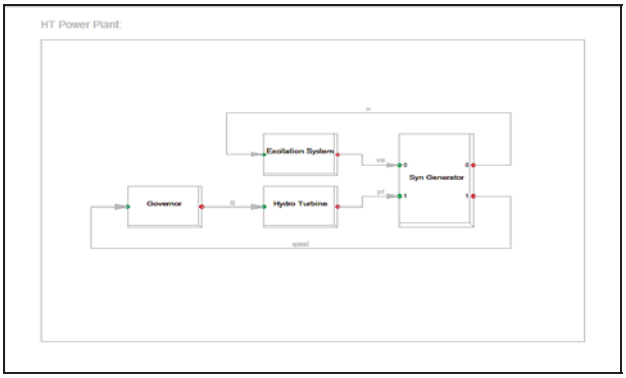


Fig 5: Schematic diagram of a 'Composite Frame' for a hydro power plant

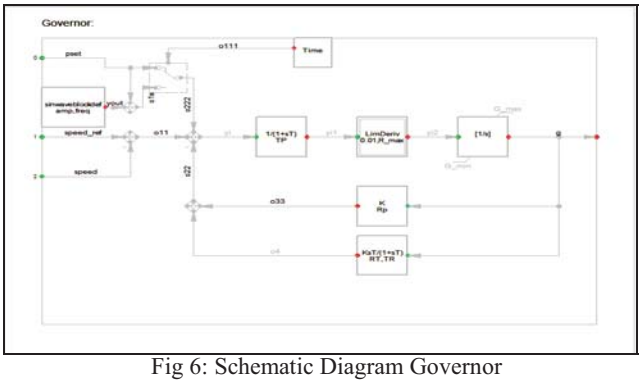


Fig 6: Schematic Diagram Governor

B. Resonance With Inter Area Mode Forced Oscillation Output Graphs

A forced oscillation at bus4 from synchronous generator G4 is injected into the bus 10 with small magnitude of generator governor oscillations at time 5 secs. Now two scenarios were studied in each case we have two cases as case 1 and case 2.

Scenario 1: The interarea mode details is given below for this scenario.



Fig 7: Mode 20 Eigen Value at 0.2Hz interarea mode

Case 1: Resulting oscillations due to forced oscillations in tie line 5 are shown in Fig 8.

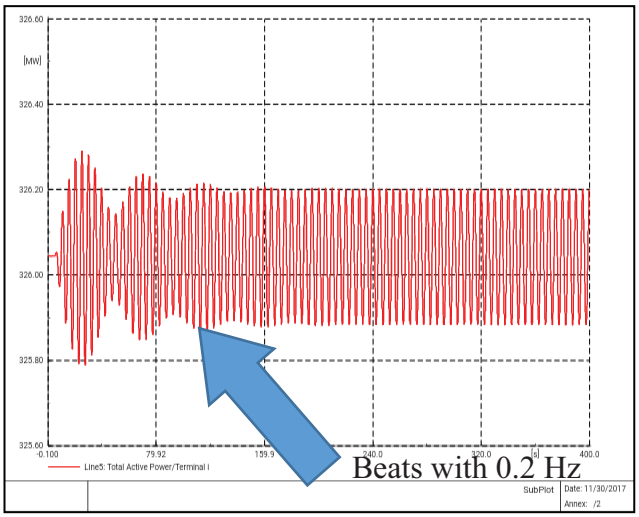


Fig 8: Tie Line Active Power At 0.2Hz FO

Observation: It can be seen form figure above that the beats are visible along with strong oscillations in the tie line power as the forced oscillation frequency of 0.2 Hz is close to the Interarea mode frequency of 0.2227072 Hz. This resembles to the beats in the resonance concept under physics.

Case2: A forced oscillation at G4 is applied with frequency 0.2227072 Hz and the resulting oscillations in tie line 5 are shown in Fig 9.

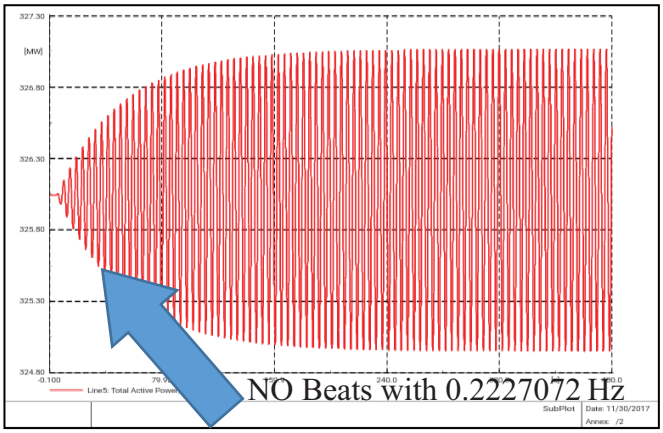


Fig 9: Tie Line Active Power At 0.2227072 Hz FO

Observation: In this case no beats are observed and the envelope is smooth as expected since there is no difference in frequencies of the interarea mode and FO. Further in both cases the amplitude of oscillation is very high which can cause the lines to trip or inflict damage to the system equipment.

Scenario 2: Interarea mode of the two area system as shown in Fig 9 below for this scenario. Also it can be noted from Fig 10 that the Interarea mode is having a frequency of 0.3458351Hz.

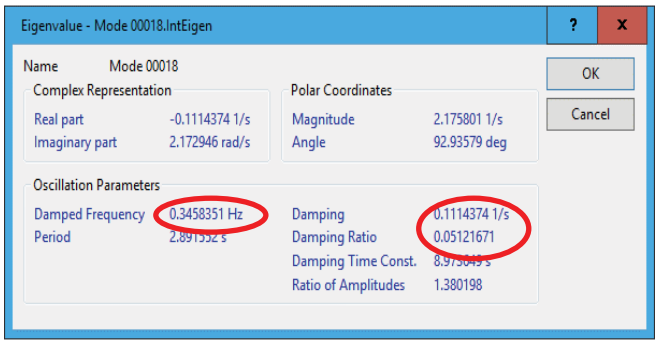


Fig 10: Mode 20 Eigen Value with 0.3Hz interarea mode

Case 1: A forced oscillation at G4 is applied with frequency 0.3 Hz and the resulting oscillations in tie line 5 are shown in Fig 11.

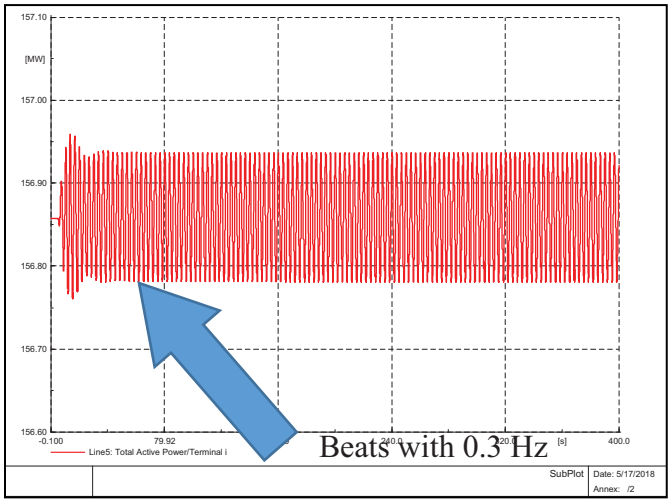


Fig 11: Tie Line Active Power At 0.3Hz FO

Observation: It can be seen form Fig 11 that the beats are visible but subdued due to higher damping along with strong oscillations in the tie line power as the forced oscillation frequency of 0.3 Hz is close to the Interarea mode frequency of 0.3458351 Hz. Compared with scenario1 these beats are subdued due to higher damping of the system.

Case 2: A forced oscillation at G4 is applied with frequency 0. 3458351 Hz and the resulting oscillations in tie line 5 are shown in Fig 12.

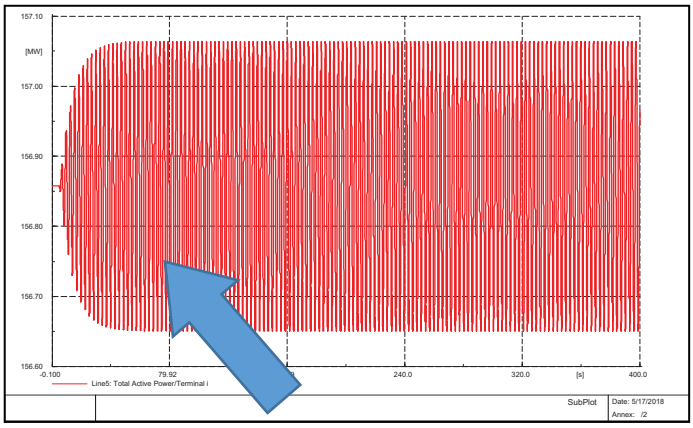


Fig 12: Tie Line Active Power At 0.3458351Hz

Observation: There are no beats as in scenario 1. Further, the envelope shape for forced oscillation can be compared. For resonances in scenario 1 and 2 their upper envelopes without overshoot are convex in nature whereas beats are negligible as the forced component dies out rapidly the overshoots are very small in the envelope.

V. MEASUREMENT BASED STUDIES

Measurement based studies are carried out to identify the method which can detect the presence of forced oscillations in the system. The main target is to identify a method which can detect the zero damping of the modal frequency due to forced oscillations. Two methods are tested as given below.

1) FDD Analysis

FDD method has been executed by exporting the line oscillation values from Digsilent Power Factory to comma separated value (CSV) file and importing these results in MATLAB. Fig 13 shows the Power spectral density (PSD) at 0.2Hz of frequency. The identified results related to the FDD method is as follows:
Identified frequencies
Mode: 1; Modal Frequency: 0.2 (Hz)
Damping Factor: 0.99
So the system is found estimated to be critically stable at 0.2Hz of frequency of forced oscillations. However, the expected results for forced oscillations has to be undamped or zero damping. Therefore FDD method is found not suitable for detecting forced oscillations.

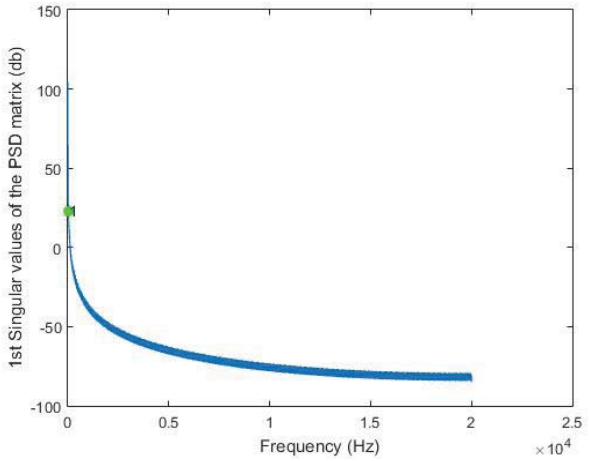


Fig 13: FDD Graph

2) Prony Analysis:

As second method Prony analysis technique has been applied to forced oscillation response data to find an inter-area mode forced oscillation near 0.2Hz case. Power factory has inbuilt Prony analysis engine which was used in this study. By using prony analysis damping ratio was found to be near zero as shown in Table 3, which satisfies the condition for undamped system.

Table 3: Prony Analysis

Line5	
Estimated Prony Frequency in Hz	**Prony Damping Ratio**
-50.000001	13.690756
-41.246751	13.418404
-32.342931	12.575557
-22.941919	10.934012
-0.400688	0.012539
-0.19938	-0.001903
0	0.000001
0.19938	**-0.001903**
0.400688	0.012539
22.941919	10.934012
32.342931	12.575557
41.246751	13.418404

VI. CONCLUSION

In this paper, measurement based oscillation monitoring techniques namely FDD and PA were studied to make use of the PMU data available for small signal stability monitoring with respect to forced oscillations in power system. The objective is to detect the presence of forced oscillations of poorly damped modes that occur in system by making use of Synchrophasor data from PMUs. Modal estimation such as frequency, mode shapes, damping ratio and energy level were estimated for forced oscillations. This work also studies the components, amplitude and envelope of forced oscillation in Two Area Kundur power system. The nature of the forced oscillations has been studied for Interarea modes, and also how the conditions of resonance occur. Some important conclusions for forced oscillations in power system are:

- Forced oscillations can occur in power system due a malfunctioning of mechanical components in power system as well as power electronic components in the system. If the frequency of the forced oscillations injected in the power system is close to that of the system electromechanical modes, then there is a possibility of resonance in the system.
- The forced one is of the same frequency with zero damping as forced disturbance. Another one is similar as system mode modal properties.
- Forced oscillation shapes are identical as envelope.

It has been found that PA method gives better estimate of forced oscillations than FDD method of estimation. Further research in this area is necessary.

REFERENCES

[1] Pal, Bikash, Chaudhuri, Balarko, "Robust Control in Power Systems", Springer, 2005 [ISBN NO- 9780387259505].

[2] P.Kundur, Power System Stability and Control, New York: McGraw-Hill, Inc., 1994.

[3] J.W.Pierre, D.J.Trudnowskiand, M.K.Donnely, "Initial Results in Electromechanical Mode Identification from Ambient Data", IEEE trans. On Power System, Vol. 12, no.3, pp. 1245-1250, Aug. 1997.

[4] https://en.wikipedia.org/wiki/Resonance#Theory.

[5] Van Ness, "Response of large power systems to cyclic load variations," IEEE trans. On power apparatus and systems, vol.PAS-85, no.7, pp. 723-727, July. 1966.

[6] K.R. Rao and L. Jenkins, "Studies on Power Systems That Are Subjected to Cyclic Loads," IEEE trans. on power syst., vol.3, no.1, pp. 31-37, Feb. 1988.

[7] P.Kundur, "A Survey of Utility Experiences with Power Plant Response During Partial Load Rejections and System Disturbances," IEEE TransPower Apparatus and Systems, vol. PAS-100, pp. 2471–2475, May1981.

[8] J.Follum, and W. Pierre, "Initial Results in the Detection and Estimation of Forced Oscillations in Power Systems," Proc. North American Power Symposium NAPS, Sep 2013, pp. 1-6.

[9] G.Liu, J.Quintero and V.Venkatasubramanian, "Oscillation Monitoring System Based On Wide Area Synchrophasors in Power Systems", Proc. IREP Bulk Power System Dynamics and Control-VII, August 19-24,2007.

[10] S.Arash Nezam Sarmadi, Student Member, IEEE, and Vaithianathan Venkatasbramanian, Fellow IEEE, "Inter-Area Resonance in Power System From Forced Oscillations", January 2016.

[11] W.Lewin, Physics III: Vibration and Waves, Fall 2004, MIT Open Course Ware, http:// ocw.mit.edu (Accessed June 1, 2014). License: Creative Commons BY-NC-SA.

[12] L.Vanfretti, S.Bengtsson, V.Peric and J.Gjerde, "Effects of Forced Oscillations in Power Damping Estimation", In Proc. IEEE International Applied Measurements for Power Systems (AMPS), 2012.

[13] N.Zhou, D.J.Trudnowski, J.W.Pierre and R.T.Guttromoson, "Electromechanical Modes Online Estimation Using Regularized Robust RLS Methods", IEEE trans. On Power System, Vol. 23, No.4, pp. 1670-1680, Nov. 2008.

Available online at www.pelagiaresearchlibrary.com

Pelagia Research Library

Der Chemica Sinica, 2018, 9(3):708-715

ISSN : 0976-8505
CODEN (USA): CSHIA5

Synthesis and Structural Characterization of Meso-tetrakis(3,4-dimethoxyphenyl)Porphyrin

Anil K *, Omprakash Y

Department of Applied Chemistry, Delhi Technological University, Delhi-42, India.

ABSTRACT

Sterically hindered and electron releasing group attached on meso phenyl containing porphyrin are of great interest in the scientific community. This report emphasize on the synthetic as well as structural characterization of meso-tetrakis(3,4-dimethoxyphenyl)porphyrin.

Keywords: porphyrin, crystal, methoxy, synthesis

INTRODUCTION

Porphyrins and their analogues materials serve different applications. Metalloporphyrins assemblies has been used as building block for tailored materials properties during the past decades the [1]. These fascinating molecules have broad applications as field responsive materials, particularly for optoelectronic applications [2-4]. The facile substitution of the periphery of various porphyrins has generated a series of unusual liquid crystalline materials [5-8]. The porphyrins ligand serves as a platform on which one can erect desirable molecular and materials properties, including very large dipole moments [9], polarizabilities [10], and hyperpolarizibilities [11-13]. The nonlinear optical properties of these materials can be explored in optical communications, data storage, and electro-optical signal processing [14-18]. The porphyrin π-radical makes these systems especially interesting for photoionization processes [19-25], closely related to the so-called ion pair reaction centre of photosynthesis and the photo-generation of electron transfer [26]. Porphyrins can interact with chemical species (chemo-responsive) also in contrast to their interaction with applied electric [27], magnetic or electromagnetic fields. The materials based on chemo-responsive are less advanced e.g. porphyrins solids, being highly porous, are involved in the current development of molecular based molecular sieves or shape- selective solid catalysts and in sensor applications [28-31]. In this paper, we have reported the single crystal structure of sterically hindered porphyrin for future applications.

EXPERIMENTAL

Materials and methods

The synthesis of 3, 4-dimethoxytetraphenylporphyrin was carried using reported method [22] and details are as 1.0 g (6.0 mmol) of 3, 4-dimethoxybenzaldehyde was dissolved in 50 ml of argon-purged dimethylformamide. 0.5 mL conc. HCl was added into it followed by drop wise addition of 0.42 mL (6.0 mmol) of freshly distilled pyrrole. The mixture was stirred under argon for a 1 hour. The final reaction mixture was refluxed for 8 hour in air. The solvent was evaporated on water bath and washed with hot water. The crude product was extracted by flash chromatography over silica gel using 10% ethyl acetate-chloroform mixture. The desired porphyrin was finally purified by column chromatography over silica gel using 7% ethyl acetate-chloroform mixture. The yield of the purple crystal compound was calculated to 25%.

Analytical data

^{1}H ($CDCl_3$, 400MHz); δ-2.81 (br s, -NH, pyrrole), 3.93 (s, 12H, m-OCH_3), 4.11 (s, 12H, p-OCH_3), 7.17 (d, 4H, phenyl), 7.67 (d, 4H, phenyl), 7.70 (s, 4H, phenyl), 8.83 (s, 8H, pyrrole); 13C ($CDCl_3$, 400MHz); 56.2 (m-OCH_3),

56.3 (p-OCH_3), 127.46 (meso-carbon), 134.85 (β-C, pyrrole), 147.1 (α-C, pyrrole), 109.51, 118.3, 119.9, 148.95; λ_{max} ($CHCl_3$: logε); 425 (5.63), 464 (4.17), 519 (4.28), 559 (4.04), 593 (3.78), 649 (3.14); FAB mass (m/z): 856.

RESULTS AND DISCUSSION

The diffraction quality single crystals of meso-tetrakis(3,4-dimethoxyphenyl)porphyrin were grown by direct solvent diffusion of n-hexane in a saturated solution of porphyrin in chloroform in a long cylindrical tube standing on several days at room temperature. A dark purple rectangular block shaped single crystal of meso-tetrakis(3,4-dimethoxyphenyl) porphyrin having approximate dimensions of crystal size 0.20 × 0.10 × 0.07 mm was mounted for data collection. A total no. of 17352 reflections ($2.20<Q<28.33^o$) were collected of which 6395 no. of unique reflections (R (int) 0.0612) were used. This crystal was solved under the space group of I-4 in tetragonal system. Final R=0.0634 for 6395 no of unique reflections with I>2σ Max/min residual density 0.470 and -0.268 e $Å^{-3}$. The asymmetric unit (Z=4) contains two one fourth of two structurally different porphyrin molecules which are separated by each other and one disordered chloroform solvent molecule. The two Cl atoms of chloroform are disordered over four positions (Cl1A, Cl1B, Cl2A and Cl2B) and were refined using free part variable, due the disorderness of the solvent we are unable to put the hydrogen atom in chloroform. The ORTEP and DIAMOND views of free base porphyrin are shown in **Figures 1 and 2** respectively where hydrogen atoms are omitted due to clarity. The anisotropic parameters for all non-hydrogen atoms are listed below in **Table 1**. The selected bond lengths and bond angles are summarized in **Table 2**. A crystallographic data is tabulated in the **Table 3**.

In the crystal structure of meso-tetrakis(3,4-dimethoxyphenyl)porphyrin, asymmetric unit contains ¼ of the two porphyrin molecule that is why we are unable to fix the hydrogen atom on the nitrogen of pyrrole ring. Out of the two molecule, one porphyrin molecule is almost planar and other is saddle in shape as compared with the structure of H_2TPP [23]. The porphyrin core of the planar molecule consisting of 24 atoms which is non planar and the deviation from the mean plane does not exceed 0.1 Å but in the case of saddle molecule the deviation from the mean plane does not exceed 0.4 Å. The meso phenyl ring in the saddle porphyrin attached to the carbon atoms C17 are not perpendicular to the mean plane of the porphyrin ring and make a dihedral angle of 47.8o with the core as compared to the angles 61.1 and 63.1o in H_2TPP. The torsion angles of C18-C17-C19-C24=126.2, C16-C17-C19-C24=52.9^o were observed in the saddle molecule. The meso phenyl groups in the saddle porphyrin are more tilted in the case of meso-tetrakis(3, 4-dimethoxyphenyl)porphyrin as compared to the H_2TPP. But in the case of planar porphyrin the phenyl rings are almost planar and are oriented almost perpendicular to the porphyrin ring at an angle of 75.4-91.1^o as compared to that for meso-tetrakis(3,5-dihydroxyphenyl)porphyrin and meso-tetrakis(3,5-dinitrophenyl)porphyrin 56.0^o-68-5^o [24]. The observed bond lengths and bond angles of porphyrin macrocycles are not significantly different from those of H_2TPP [23] as observed in the present case of meso-tetrakis(3,4-dimethoxyphenyl)porphyrin. The

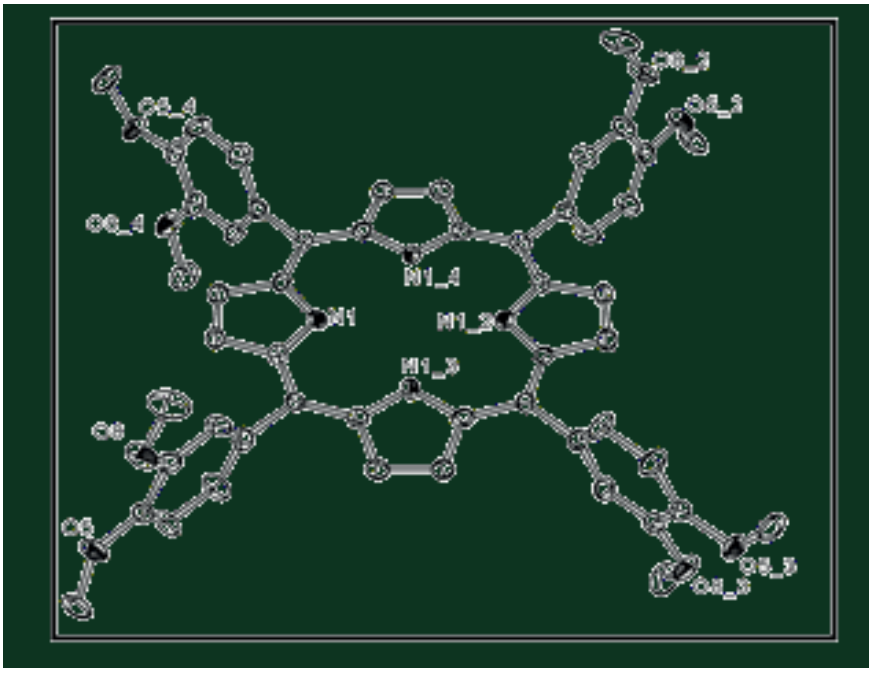


Figure 1: ORTEP view of meso-tetrakis(3, 4-dimethoxyphenyl)porphyrin.

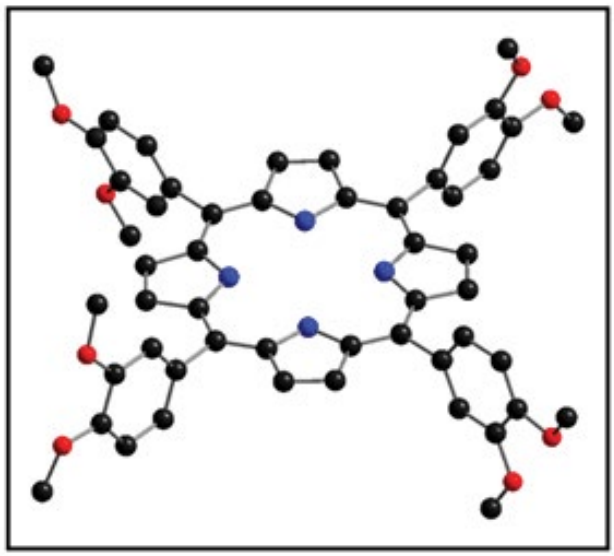


Figure 2: A DIAMOND view of meso-tetrakis(3, 4-dimethoxyphenyl)porphyrin.

Table 1: Atomic coordinates (X 104) and equivalent isotropic displacements parameters (Å2 × 103) for meso-tetrakis(3, 4-dimethoxyphenyl)porphyrin. U(eq) is defined as one third of the trace of the orthogonolized Uij tensor.

	X	Y	Z	U(eq)
O(2)	892 (1)	2589 (1)	6794 (1)	23 (1)
O(3)	-85 (1)	1962 (1)	7696 (1)	25 (1)
N(1)	5655 (2)	3966 (2)	4998 (2)	18 (1)
O(5)	3712 (2)	-286 (1)	4971 (1)	27 (1)
O(8)	3735 (2)	493 (2)	3763 (1)	30 (1)
C(5)	4546 (2)	2991 (2)	5002 (2)	17 (1)
C(17)	3076 (2)	757 (2)	7551 (2)	15 (1)
C(21)	1208 (2)	1986 (2)	7204 (2)	18 (1)
N(10)	3872 (2)	-491 (2)	7504 (1)	16 (1)
C(4)	5353 (2)	3206 (2)	4978 (2)	19 (1)
C(11)	4170 (2)	1719 (2)	4360 (2)	23 (1)
C(19)	2240 (2)	1079 (2)	7613 (2)	17 (1)
C(22)	671 (2)	1648 (2)	7703 (2)	19 (1)
C(3)	6004 (2)	2648 (2)	4935 (2)	21 (1)
C(23)	932 (2)	1051 (2)	8160 (2)	20 (1)
C(6)	4348 (2)	2116 (2)	5005 (2)	20 (1)
C(24)	1714 (2)	770 (2)	8109 (2)	21 (1)
C(10)	3966 (2)	925 (2)	4363 (2)	23 (1)
C(14)	2854 (2)	-1356 (2)	7261 (2)	20 (1)
C(20)	1980 (2)	1693 (2)	7152 (2)	17 (1)
C(1)	6473 (2)	3909 (2)	4976 (2)	17 (1)
C(16)	3164 (2)	-71 (2)	7460 (2)	15 (1)
C(25)	1421 (2)	2965 (2)	6290 (2)	31 (1)
C(15)	2533 (2)	-617 (2)	7297 (2)	17 (1)
C(12)	3554 (3)	-680 (2)	5635 (2)	33 (1)
C(18)	3719 (2)	1304 (2)	7599 (2)	14 (1)
C(9)	3953 (2)	498 (2)	5018 (2)	21 (1)
C(8)	4148 (2)	879 (2)	5648 (2)	27 (1)
C(2)	6694 (2)	3074 (2)	4941 (2)	23 (1)
C(7)	4343 (2)	1691 (2)	5646 (2)	27 (1)

C(26)	-692 (2)	1513 (3)	8061 (2)	29 (1)
C(13)	3705 (3)	902 (3)	3095 (2)	43 (1)
Cl(3A)	8520 (7)	1834 (6)	5964 (10)	91 (3)
Cl(3B)	8429 (4)	1895 (3)	5811 (6)	37 (3)
Cl(2A)	9254 (2)	1960 (2)	4593 (1)	57 (1)
Cl(2B)	9849 (3)	1748 (2)	4959 (3)	98 (2)
Cl(1A)	9640 (2)	824 (2)	6241 (2)	68 (1)
Cl(1B)	10095 (2)	1127 (2)	5709 (2)	69 (2)
C(27A)	9445 (3)	1829 (3)	5668 (4)	85 (2)

Table 2: Selected bond distance (Å) and bond angles (deg) for meso-tetrakis(3, 4-dimethoxyphenyl)porphyrin.

Bond distance			
O(2)-C(21)	1.367 (4)	N(10)-C(18)#2	1.366 (4)
O(2)-C(25)	1.432 (4)	N(10)-C(16)	1.378 (4)
O(3)-C(22)	1.369 (4)	N(1)-C(4)	1.367 (4)
O(3)-C(26)	1.432 (4)	N(1)-C(1)	1.371 (4)
O(5)-C(9)	1.372 (4)	O(8)-C(10)	1.380 (4)
O(5)-C(12)	1.419 (4)	O(8)-C(13)	1.415 (5)
C(17)-C(18)	1.413 (5)	C(17)-C(16)	1.402 (4)
C(18)-N(10)#4	1.366 (4)	Cl(3A)-C(27A)	1.640 (9)
Cl(3B)-C(27A)	1.722 (8)	Cl(2A)-C(27A)	2.026 (8)
Cl(2B)-C(27A)	1.482 (7)	Cl(2B)-Cl(1B)	1.781 (7)
Cl(1A)-C(27A)	2.014 (7)	Cl(1B)-C(27A)	1.599 (6)
C(27A)-H(27A)	0.98	C(18)-C(14)#4	1.438 (4)
Bond angles			
C(21)-O(2)-C(25)	116.5 (3)	C(22)-O(3)-C(26)	116.7 (3)
C(4)-N(1)-C(1)	107.6 (3)	C(9)-O(5)-C(12)	116.2 (3)
C(10)-O(8)-C(13)	117.4 (3)	C(18)#2-N(10)-C(16)	107.4 (2)
N(1)-C(4)-C(5)	126.5 (3)	N(1)-C(4)-C(3)	109.0 (3)
N(1)-C(1)-C(5)#3	126.0 (3)	N(1)-C(1)-C(2)	108.8 (3)
N(10)#4-C(18)-C(17)	126.0 (3)	N(10)#4-C(18)-C(14)#4	108.7 (3)
C(8)-C(9)-O(5)	124.6 (3)	O(5)-C(9)-C(10)	115.8 (3)

Table 3: Summary of X-ray crystallographic data for complexes meso-tetrakis(3, 4-dimethoxyphenyl)porphyrin.

Parameters	**Compound**
Empirical formula	$C_{54}H_{46}C_{l6}N_4O_8$
Formula weight	1091.65
Temperature	100(2) K
Wavelength	0.71069 Å
Crystal system	Tetragonal
Space group	I-4
a	16.713(5) Å
b	16.713(5) Å
c	18.507(5) Å
α	90.000(5)o
β	90.000(5)o
γ	90.000(5)o
Volume	5169(3) Å3
Z	4
Density (calculated)	1.403 Mg/m3
Absorption coefficient	0.391 mm-1
F (000)	2256
Refinement method	Full-matrix least-squares on F2
Goodness-of-fit on F2	1.042
Final R indices [I>2σ(I)]	R1 = 0.0634, wR2 = 0.1240
R indices (all data0	R1 = 0.0932, wR2 = 0.1365

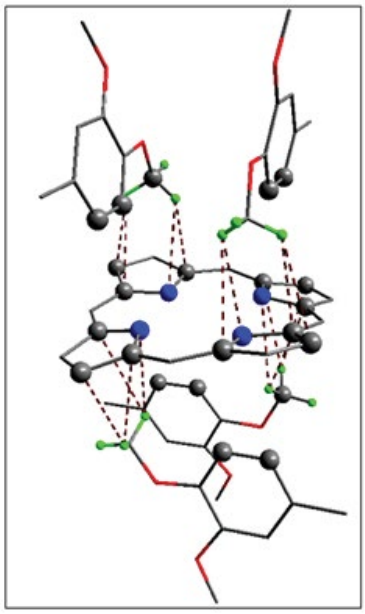


Figure 3: H-bonding between the methoxy groups of planar porphyrin molecule with the pyrrole ring of non-planar porphyrin, meso phenyl rings and hydrogen atoms are omitted for clarity.

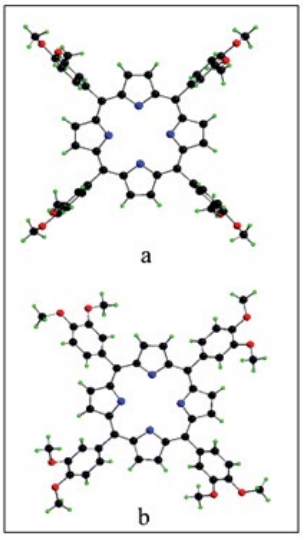


Figure 4a: A DIAMOND view of the planar (a) and saddle (b) conformation.

torsion angles of C1-C5-C6-C11=85.05 and C4-C5-C6-C7=84.84^o were observed. The meso phenyl group attached to the C5 carbon atom of the planar ring makes a dihedral angle of 82.7^o to the porphyrin core, a slight deviation occurs from the perpendicular position. Interesting feature observed in this porphyrin is the mixture of ruffled and planar molecule in the unit cell packed one after one. This may be explained on the basis of the fact observed in the structure that main cause for this type of behavior of this porphyrin is hydrogen bonding between the hydrogen of the methoxy group of planar molecule to the nitrogen as well as carbon of the pyrrole ring of another molecule which turns into the saddle shape which has been shown in the **Figure 3**. 1,3 pyrrole of the ring are making hydrogen bond from top side from the mean plane while 2,4 pyrrole make hydrogen bond with bottom side from the mean plane. This type of hydrogen bonding is C – H …….π type interaction. The distance between the C-H of methoxy group making hydrogen bond with π-orbital of the pyrrole is 2.96 Å. A DIAMOND view of planar and saddle conformation of free base porphyrin has been presented in the **Figure 4a** (insight **Figure 4a**, a= planar, b= saddle). The angle between the two opposite pyrrole formed by the plane passing through the pyrrole was found to be 23.72^o and the views through

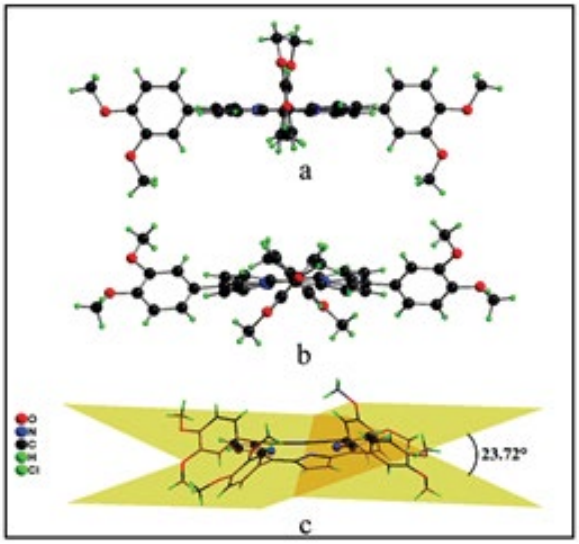


Figure 4b: Views through different positions (insight Figure 4b a= view through 1, 2 nitrogen atoms of saddle porphyrin, b= view through 1, 2 nitrogen atoms of planar porphyrin and c= showing two plane through 1, 3 pyrroles rings and angle between the two opposite pyrrole).

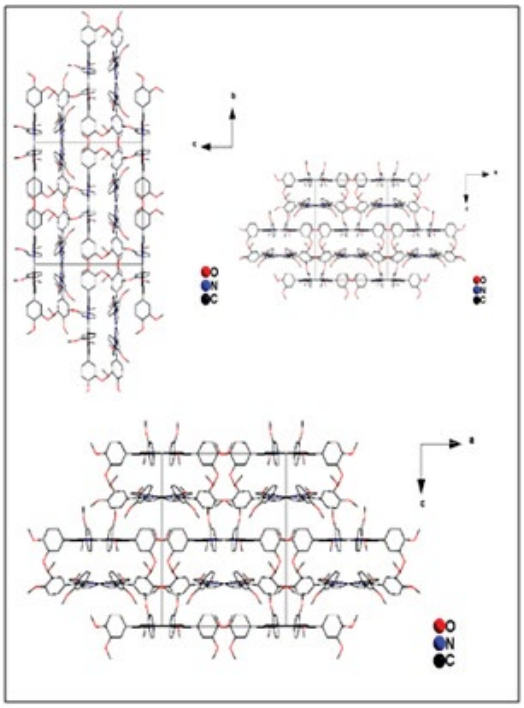


Figure 5: Unit cell packing diagram in compound and hydrogen atoms are omitted for clarity.

the different positions have been presented in the **Figure 4b**. The unit cell packing diagram is shown in the **Figure 5** where hydrogen atoms are omitted for clarity. The porphyrins rings are arranged in one dimension only with CH – π interaction and π- π staking interaction among the porphyrin rings. The distance between the oxygen atoms of para methoxy group of planar molecule to that of two neighboring methoxy group of ruffled porphyrin in one dimensional array is 5.204 Å while that of oxygen atoms of meta position is 4.893 Å with the methoxy group of para positions. The intermolecular closest distance between the aryl group carbon and methoxy group oxygen is 2.38 Å. The distance between the nuclear least square plane of planar molecule and ruffled molecule is 4.627 Å.

CONCLUSION

In this paper, we have shown that crystal structure of 3,4-dimethoxyphenylporhyrin show unique hydrogen bonding interaction and have potential to be used in several porphyrin based materials in different applications.

REFERENCES

[1] Suslick KS **(1996)**, Comprehensive Supramolecular Reactivity and Transport: Bioinorganic Systems. Elsevier,USA.

[2] Robison GW, Brookhaven **(1967)** On the theory of trapping of excitation in the photosynthetic *Unit Symp Biol* 19: 16-21.

[3] Yadav O, Varshney A, Kumar A **(2017)** Manganese(III) mediated synthesis of A_2B Mn(III) corroles: A new general and green synthetic approach and characterization. *Inorg Chem Commun* 86: 168–171.

[4] [4] Fleming GR, Martin J L, Breton J **(1988)**, Rate of primary electron transfer in photosynthetic reaction centers and their mechanistic applications *Nature* 333: 190-192.

[5] Paddock ML, Rongey SH, Feher G, Okamura MY **(1989)** Pathway of proton transfer in bacterial reaction centers: Replacement of glutamic acid 212 in the L subunit by glutamic inhibits quinone (secondary acceptor) turnover. *Proc Natl Acad Sci* USA 86: 6602-6606.

[6] Feher G, Allen JP, Okamura MY, Rees DC **(1989)** Structure and function of bacterial photosynthetic reaction centres. *Nature* 339: 111-116.

[7] Holten D, Kirmarier C **(1987)** Primary photochemistry of reaction centers from photosynthetic purple bacteria. *Photosynth Res* 13: 225-260.

[8] Girolami GS, Hein CL, Suslick KS **(1996**), A Zirconium BisBis(porphyrin) sandwich complex with an appended Quinone. Angew. *Chem Intl Edn* 35: 1223-1225.

[9] Kong JL, Loach PA **(1978)** Model reactions in photosynthesis. *Frontier Biol Energ* I: 73-78.

[10] Neil MP, Niemczyk MP, Svec WA, Gosztola D, Gaines GL, et al. **(1992)** Picosecond optical switching based on biphotonic excitation of an electron donor-acceptor-donor molecule. *Science* 257: 63-5.

[11] Wanger R, Lindsey JS **(1994)** A molecular photonic wire. *J Am Chem Soc* 116: 9759-9760.

[12] Wanger R, Lindsey JS, Seth J, Palaniappan V, Bocian DF **(1996)** Molecular Optoelectronic Gates. *J Am Chem Soc* 118: 3996-3997.

[13] Shimidzu T **(1995)** Terminology for membranes and membrane processes. *Pure Appl Chem* 67: 11193.

[14] Shimidzu T, Iyoda T, Koide Y **(1985)** An advanced visible-light-induced water reduction with dye-sensitized semiconductor powder catalyst. *J Am Chem Soc* 107: 35-41.

[15] Gau D, Li J, Ru- Qin Y, Zheng G **(1978)** Selective extraction and enrichment of multiphosphorylated peptides using polyarginine-coated diamond nanoparticles. *Anal Chem Soc* 100: 5075-5079.

[16] Yoo IJ, Shin JH, Paeng IR, Nam H, Cha GS, et al. **(1998)** Current status of modern analytical luminescence methods. *Anal Chim Acta* 367: 175-178.

[17] Sessler JL, Kral V, Genge JW, Thomas RE, Iverson BL **(1998)** Anion selectivity of a sapphyrin-modified silica gel HPLC support, *Anal Chem* 70: 2516-2522.

[18] Malinski T, Ciszewski A, Fish JR, Czuchajowski L **(1990)** Conductive polymeric tetrakis(3-methoxy-4-hydroxyphenyl)porphyrin film electrode for trace determination of nickel. *Anal Chem* 62: 909-914.

[19] Gupta VK, Ajay KJ, Singh LP, Khurana U **(1997)** Porphyrins as carrier in PVC based membrane potentiometric sensors for Nickel (II). *Anal Chim Acta* 355: 33-45.

[20] Dobson DJ, Saini S **(1997)** Porphyrin-modified electrodes as biomimetic sensors for the determination of organohalide pollutants in aqueous samples. *Anal Chem* 69: 3532-3538.

[21] Priyantha N, Weerabahu D **(1996)** Amperometric sensor for propanil. *Anal Chim Acta* 320: 263-268.

[22] Kumar A, Maji S, Dubey P, Abhilash GJ, Pandey S, et al. **(2007)** One-pot general synthesis of metalloporphyrins. *Tett Lett* 48: 7287-7290.

[23] Silvers SJ, Tulinsky A **(1967),** The crystal and molecular structure of triclinic tetraphenylporphyrin. *J Am Chem Soc* 89: 3331-3337.

[24] Bhyrappa P, Suslick, KS **(1998)** Synthesis and crystal structure of 5,10,15,20-Tetrakis (3,5-dinitrophenyl) porphyrin *JPP* 2: 391-396

[25] Vlascici D, Cosma E, Pica EM, Cosma V, Bizerea O, et al. **(2008)** Free base porphyrins as ionophores for heavy metal sensors sensors (Basel). 8: 4995-5004.

[26] Fadda A, Mekawy RE, El-Shafei A, Freeman HS, Hinks D et al. **(2012)** Design, synthesis, and pharmacological screening of novel porphyrin derivatives. *JOC* 2013: 11.

[27] Antonangelo AR, Westrup KCM, Burtb LA, Grazia BC, Malewschika T et al. **(2017),** Synthesis, crystallographic characterization and homogeneous catalytic activity of novel unsymmetric porphyrins. *RSC Adv* 7: 50610-50618.

[28] Cosma EF, Vlascici D, Cosma GF, Palade A, Lascu A, et al. **(2014)**, A Sensitive A_3B Porphyrin Nanomaterial for CO_2 Detection. *Molecules* 19: 21239-21252.

[29] Ding K, Yewei ZZ, Si W, Zhong X, Cai Y et al. **(2018)** Zinc(II) metalated porphyrins as photothermogenic photosensitizers for cancer photodynamic/photothermal synergistic therapy. *ACS Appl Mater Interfaces* 10: 238-247.

[30] Cosma EF, Badea V, Cosma GF, Palade A, Lascu A et al**. (2017)** Trace oxygen sensitive material based on two porphyrin derivatives in a heterodimeric complex. *Molecules* 22: 1787.

[31] Antonangelo AR, Westrup KCM, Burt LA, Grazia Bezzu C, Malewschik TGS, et al. **(2017)** Synthesis, crystallographic characterization and homogeneous catalytic activity of novel unsymmetric porphyrins. *RSC*

Journal of Engg. Research Vol. 7 No. (4) December 2019 pp. 115-137

Taylor series based compressive approach and Firefly support vector neural network for tracking and anomaly detection in crowded videos

Avinash Ratre

Department of Electronics and Communication Engineering,
Delhi Technological University, India
avinashratre14@gmail.com

ABSTRACT

The application areas of multimedia content and computer vision analysis gains remarkable attention towards the motive to recognize the actions of the humans present in the video. Accordingly, crowd behavior analysis is an important topic owing to the significance of video surveillance in the public localities. This work introduces an anomaly detection (AD) model by introducing a tracking model and the optimization based classifier for the crowd video. The objects present in the video require tracking since the anomaly depends on the action of the object. This work proposes a hybrid tracking (HT) model by combining the Taylor series based predictive (TSP) tracking and the compressive tracking (CT) approach. The features are extracted from the tracked objects, and a feature vector is formed. Moreover, this work proposes the Firefly based support vector neural network (FSVNN) for the classification purpose. The weights of the proposed FSVNN classifier are trained with the genetic and the firefly algorithm. The performance of the proposed model is analyzed using three videos from the standard databases and is compared with the existing methods, such as self-organizing map (SOM), deep belief network (DBN), neural network (NN), and Firefly-based deep belief network (FDBN). The simulation results reveal that the proposed AD model with the FSVNN classifier attains overall better performance with the values of 0.97035, 1, and 0.96, for sensitivity, specificity, and accuracy, respectively than the comparative methods.

Keywords: Anomaly detection; crowd video; taylor series based predictive tracking; compressive tracking approach; firefly algorithm.

INTRODUCTION

Due to the increase in the video surveillance system, a large number of researchers in computer vision focus on excavating the valuable information from the monitored video data for public security. Problems, like representing the human behaviour in crowded scenes, recognizing the various human actions and, determining the associations of various events have more importance in research. Among them, anomaly detection (AD) from the crowded scenes has captured the interest of the researchers due to the advent of various technologies available in the multimedia applications (Arora & Singh, 2013 ; Ratre & Pankajakshan, V. 2018a,b). The aim of AD is to differentiate uncertain abnormal behaviours from certain normal ones accurately in real-time. Depending on the locality of anomaly, crowd behaviours are categorized into two groups, namely, local anomaly and global anomaly. In local anomaly, an abnormal behaviour is present in a local region of a frame and its surroundings are normal ones. In global anomaly, an abnormal behaviour is present in an entire frame; i.e., the frame contains several local anomalies. The different surveillance scenes contain different abnormal behaviours. Hence, the tasks of AD always vary for different surveillance scenes. As a result, several AD techniques have been introduced for various surveillance tasks. The study of the crowd behavior in the public places, such as parks, marathon race, movie theatres, mall, etc., is considered important to ensure the

safety of the public (Fradi *et al.,* 2017). Owners of the private and the public firms install a video surveillance system to monitor the activities of the persons (Laptev *et al.,* 2008; Narasimhan & Kamath, 2017). Public places have many persons moving in a group, and they are mentioned as the crowd (Du *et al.,* 2007). The people moving as a crowd in the video have different speeds and trajectories and do varying actions (Natarajan & Nevatia, 2008). To ensure the safety of the persons in the public, it is necessary to monitor the action of the public at each frame of the video (Sempena *et al.,* 2011; Soma & Gupta, 2017). The presence of the anomaly in the video can be monitored manually or automatically. The video obtained through the public monitoring of the persons is lengthy and, hence, requires constant manual monitoring for the detection of the anomaly. The manual processing requires more time and also leads to human errors (Narasimhan & Kamath, 2017). Hence, the AD model opts for the automation. The automation of the AD alerts the security while detecting the anomaly in the video (Chen *et al.,* 2017).

The persons moving in the crowd do actions, as walking, cycling, etc. The anomaly represents the abnormal behavior, such as intrusion, and fault of the person (Bensch *et al.,* 2017). Differentiation of the anomaly from the normal behavior acts as a prime concern of the AD model. Another challenge involved in the AD is the selection of the features for the detection. Traditional models have used trajectory-based algorithms and spatiotemporal domain-based algorithms (Zhou *et al.,* 2016) for the AD (Yuan *et al.,* 2017). Detection of the anomaly in the video is majorly classified as object based model and holistic based model (Fradi *et al.,* 2017). In the object based model, the crowds are segmented for the detection, while in the second approach, the crowd is considered as a whole. The use of the object based models is more suitable for the video with a small number of persons. The holistic based model analyzes the system as a whole, and thus, it is suitable to analyze the dynamics of the video frame than the action of the person.

The features representing the anomalies of the video have a complex structure, and hence suitable features need to be used (Narasimhan & Kamath, 2017). Literature works have included optimization based procedures for the AD. The literature works have used the Kernel-based classifiers (Sempena *et al.,* 2011), Support vector machines (SVM) (Natarajan & Nevatia, 2008) for the AD. Some works have included the classification algorithms based on the temporal approaches, namely, the Dynamic Time Warping (DTW) (Du *et al.,* 2007). The temporal based algorithms detect the anomalies in the video by analyzing the time or speed. Some of the works have performed the classification based on the Hidden Markov Models (HMM) (Laptev *et al.,* 2008) and Dynamic Bayesian Networks (DBN) (Foroughi *et al.,* 2008). The use of the SVM (Natarajan & Nevatia, 2008), Relevant Vector Machine (RVM) (Tipping, 2000), and Artificial Neural Networks (ANN) (Jun & Kim, 2012) has proved efficient in classifying the anomaly in the video. The K-nearest neighbor (K-NN) (Herbrich, R. 2002) based models also perform well in the crowded scenarios. Other NN based networks such as deep learning (Revathi & Kumar, 2017) and deep neural network (DNN) (Sabokrou *et al.,* 2017) provide better AD in the video.

This research work provides an innovative approach to the AD scheme. The proposed model performs the AD in three steps. These are 1) object detection, 2) object tracking, and 3) feature extraction. The proposed AD scheme primarily detects the presence of various objects in the crowded videos. Then, based on the proposed object tracking model, the movement of objects from one frame to another is detected. The proposed object tracking model uses the Taylor series based predictive (TSP) model (Yang *et al.*, 2001) and the compressive tracking (CT) model (Zhang *et al*., 2012). For tracking the objects in the frame, the proposed object tracking model uses the average results from both the TSP model and the CT model. The physical parameters, such as, mean and variance of the frame to frame distance traveled, speed, motion deviation, and frame occupancy, are extracted as quantitative values from the tracked objects. Along with that, the histogram based appearance features are also extracted from the tracked objects. Finally, the proposed FSVNN classifier detects the normal and the abnormal behavior of the crowds with the extracted features as its input. The metrics, sensitivity, specificity, accuracy, and the receiver operating characteristics (ROC) curve determine the performance of the proposed FSVNN classifier. The proposed model of AD has applications in various domains, like event detection in sensor networks, system health monitoring, fault detection, fraud detection, intrusion detection, and so on.

The major contribution of this work towards the AD is briefed below:

- Design of a novel hybrid approach for the object tracking. Here, the proposed Taylor series based compressive (TSC) approach finds the average of the results obtained from the Taylor series and the CT algorithm to track the objects in the video.
- Design of the FSVNN classifier by modifying the conventional support vector neural network (SVNN) classifier with the genetic algorithm (GA) and the Firefly algorithm (FF).

The rest of the paper is structured as follows: Section 1 introduces the AD scheme. Section 2 surveys various literary works dealing with the AD and different challenges involved in the AD purpose. Section 3 details about the proposed object tracking approach and the proposed FSVNN classifier. Section 4 contains the collection of simulation results of the proposed AD scheme. Section 5 concludes the work.

MOTIVATION

Literature survey

This section comes up with a survey of eight literature works compiling the AD in the crowd videos.

A. E. Gunduz *et al.* (2016) had proposed the density aware approach with the sparse features for the AD. The proposed model was trained with the sparse features as a separate HMM. Then, from each model AD was done. The proposed model detected the low-velocity and high-velocity anomalies without the training process. Besides, it does not detect the textural anomalies in the videos. H. Fradi *et al.* (2017) had proposed the AD model with the use of a set of visual descriptors. The proposed model used the spatio-temporal model for finding the visual descriptor set. The neighborhood interaction was based on the Delaunay triangulation. However, the work has utilized Crow Search Algorithm (CSA) for the optimal estimation, but only less concentration is given on the dynamic behavior of the crows.

C. Chen *et al.* (2015) had presented the AD algorithm with the acceleration feature. The acceleration feature had the gray-scale invariance properties for the three adjacent frames. A foreground extraction step used by the detection algorithm was designed by acceleration computation. The proposed detection approach utilized higher time for the computation. Soma & Gupta (2017) presented an approach for the abnormality detection with the input video image to be represented as feature matrices. The feature matrices are provided as the input maintains the spatial and temporal structure of the crowd video. The decomposition of the feature vectors was based on the low-rank and sparse components for the AD. The temporal and the spatial correlations between the components were not considered for evaluation. T. Chen *et al.* (2018) proposed the AD model with the low-level feature from the video. The motion energy model considered the Sum of Squared Differences (SSD) for the AD in the video. Sabokrou *et al.* (2017) had presented the fast AD model based on the localization of the video. They had proposed the cubic-patch-based model with the series of classifiers. The proposed model depends on the low likelihood of the video features and thus, performed the AD. The proposed model contains both the local and the global descriptors.

Narasimhan & Kamath (2017) presented the dynamic anomaly detection and localization system with the deep learning classifiers. The proposed model detected the local and the global anomalies present in the video by representing the frames in the video as the cubic patches. Sparse denoising autoencoder was employed in the model for reducing the computation speed of the model. S. Amraee *et al.* (2017) presented the AD system for the surveillance systems. The model had not considered the object detection and the object tracking for the feature extraction purpose. Besides, the training of the model was based on the HOG descriptors and a multivariate Gaussian model. The model assumed the background of an intended scene of the video as time invariant sequence.

Challenges

Various challenges pertained to the AD from the crowded video are briefed below:

- The major challenge involved in the AD scheme is the finding of the suitable features for the detection purpose (Gunduz *et al.,* 2016). Besides, the crowded videos have increased crowd density. Hence, for the improved accuracy, the detection scheme needs to overlook more crowd scenes/frames to detect the anomaly.
- The features representing the anomaly activity within the video have a complex structure and hence, training the classifier with the large sized features increases the complexity of the algorithm (Narasimhan & Kamath, 2017).

The proposed method extracts the histogram based features, which avoid hard decisions compared to edge based features. The integration of GA and the firefly algorithm with the SVNN classifier yields good results and decreases the complexity.

- The other factors affecting the AD in the crowded scenes are inter-object occlusion and the low resolution of the video frame (Soma & Gupta, 2017).
- Availability of training samples for the detection of the anomaly in each scenario is very scarce. The anomalies change frequently based on the video environment (Chen *et al.,* 2015).

The proposed model of AD works well even if the video has objects occlusion and low resolution frames.

- The crowd video with the varying actions, such as cycling, driving, and walking objects, has varying speed of movement within the frames. The proposed scheme needs to clearly distinguish the actions of the objects from the anomaly.

The proposed AD model clearly distinguishes the actions of the objects from the anomaly.

PROPOSED METHOD: TAYLOR SERIES BASED COMPRESSIVE APPROACH AND FIREFLY SUPPORT VECTOR NEURAL NETWORK FOR ANOMALY DETECTION

This work introduces the AD approach using the proposed FSVNN classifier from the crowd videos. Figure 1 shows the proposed AD model with the proposed object tracking model and the FSVNN classifier. Initially, the AD in the crowd video represents the abnormal activities. The proposed AD model gets each frame of the crowd video as the input. Then, the objects present in the video are detected by finding the center pixel location of the object. Tracking of the movement of objects from one frame to another is necessary to detect the activities of the objects in the video. This can be done through the proposed object tracking model. This model uses both the TSP and the compressive approach for the tracking of the movement of the objects from frame to frame. In the next step, the features of the tracking model for the training purpose are extracted. Various features, such as mean and variance of the frame to frame distance traveled, speed, motion deviation, frame occupancy and the histogram based features, are extracted from the tracking model. The proposed FSVNN classifier gets the features for the training phase and detects the presence of the anomaly in each frame of the video.

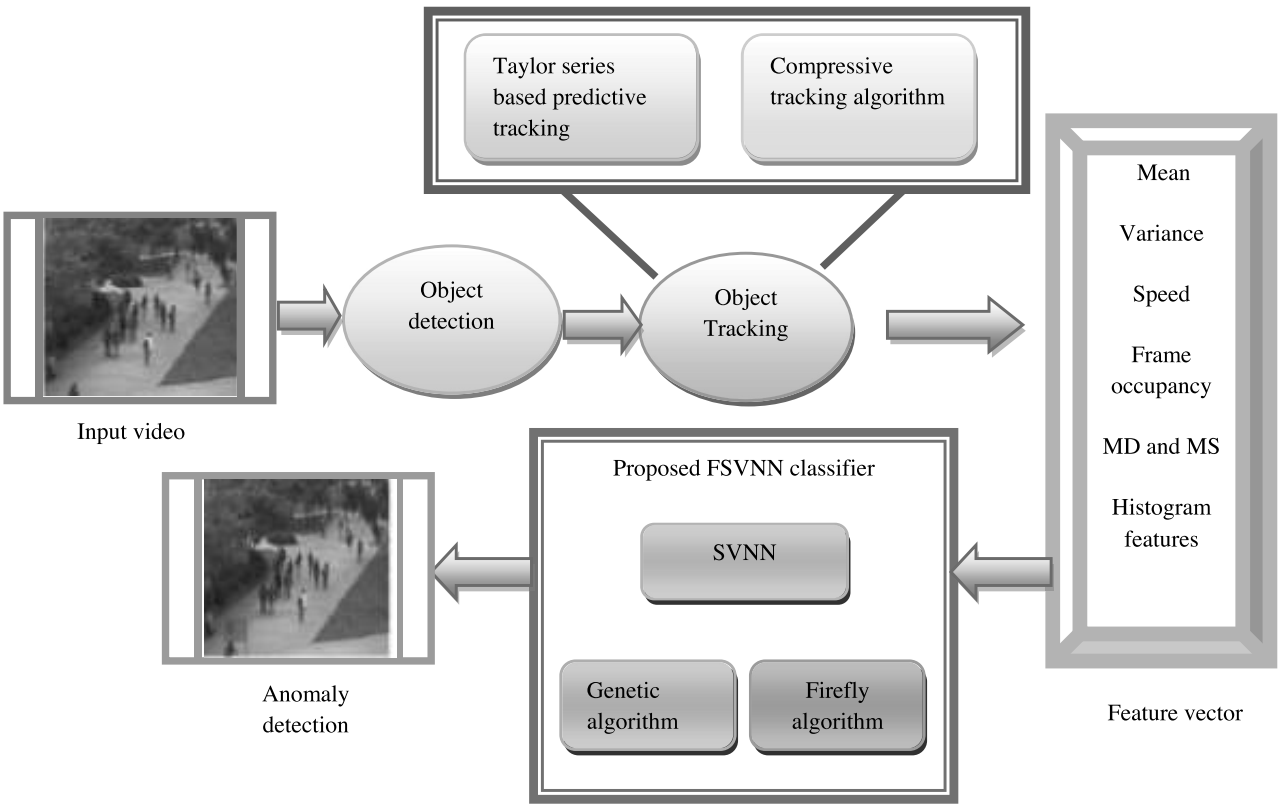


Figure 1. The proposed AD model in the crowd video based on the FSVNN classifier

Object detection

The initial step in the detection of the presence of the anomaly in the crowd video, is the detection of the objects in each frame of the video. The objects in the video indicate that the persons in the video are doing different activities. This work utilizes the video taken from the crowded environment. The crowded video contains many objects doing different activities, as walking, running, cycling, and so on. One object in the frame may overlap over the other object in the subsequent frames. Hence, the position of the objects in each frame needs to be detected for identifying the abnormal activities in the video. Consider the crowded video A with N frames. Equation (1) presents each frame present in the video A.

$$A = \{A_1, A_2, ..., A_a, ..., A_N\}; \quad 1 \le a \le N \tag{1}$$

where, the term A_a represents the a^{th} frame of the video A. The value, a varies between 1 and N. Consider the a^{th} frame of the video having M objects. Then, the objects of the a^{th} frame in the video are represented by the following expression,

$$O_a = \{O_a^1, O_a^2, ..., O_a^o, ..., O_a^M\}; 1 \le a \le N \ \ and \ \ 1 \le o \le M \tag{2}$$

where, the term O_a expresses the objects in the a^{th} frame. The term O_a^o indicates the o^{th} object in the a^{th} frame of the video A. The object's position in the frame is detected through the unsheathing of the object from the background of the video frame. The object detection uses a preset threshold for defining the presence of the object in the frame. The object's center position in the frame is located, and the difference between the positions of the object from one frame to another frame is found. Consider the object's center position in the a^{th} frame of the video as (x_a, y_a) and the object's position in the $(a+1)^{th}$ frame as (x_{a+1}, y_{a+1}). The difference in position of the object in the a^{th} and the $(a+1)^{th}$ frame is

expressed as $D(x,y)$. The presence of the object in the pixel location (x,y) depends on the preset threshold ξ and it is expressed by the following equation:

$$\begin{Bmatrix} if \quad D(x,y) \geq \xi \;\; ; \quad Location\ defines\ an\ object \\ else \;\; D(x,y) < \xi \;\; ; \quad Location\ is\ not\ an\ object \end{Bmatrix} \tag{3}$$

Object tracking based on the proposed Taylor series based compressive approach

The next step in the AD process is the tracking of the objects from one frame to another. In this paper, a hybrid object tracking model is proposed based on the predictive tracking model using the Taylor series (Yang *et al.,* 2001) and the spatial model that uses the compressive approach (Zhang *et al.,* 2012). The predictive tracking based on the Taylor series uses the second degree Taylor polynomial so that the accuracy in tracking can be improved. Meanwhile, the compressive approach utilized can track the object such that the image structure of objects is preserved.

Object tracking with the predictive approach: Taylor series

The TSP model predicts the motion of the object from one frame to another. The TSP model uses the second-degree polynomial for the prediction purpose. The position change of the object from the a^{th} frame to the $(a+1)^{th}$ frame based on the TSP model is indicated in the following equation:

$$T(a+1) \approx T(a) + \frac{T'(a)}{1!} + \frac{T''(a)}{2!} \tag{4}$$

where, the terms $T'(a)$ and $T''(a)$ express the first degree and the second degree polynomials. Equations (5) and (6) define the expression for $T'(a)$ and $T''(a)$ as

$$T'(a) = \frac{T(a) - T(a-Z)}{Z} \tag{5}$$

$$T''(a) = \frac{T'(a) - T'(a-Z)}{Z} = \frac{T(a) - 2T(a-Z) + T(a-2Z)}{Z^2} \tag{6}$$

where, the term Z represents the constant for the predictive approach. By applying the TSP approach, the position of the object o in each video frame is found. Equation (7) expresses the object's position in the video frames based on the TSP approach.

$$B_T = \left\{ \left(x^o_{T(1)}, y^o_{T(1)}\right), \left(x^o_{T(2)}, y^o_{T(2)}\right), ..., \left(x^o_{T(a)}, y^o_{T(a)}\right), ..., \left(x^o_{T(N)}, y^o_{T(N)}\right) \right\} \tag{7}$$

Where the term $\left(x^o_{T(a)}, y^o_{T(a)}\right)$ represents the o^{th} object's position in the a^{th} frame of the video based on the TSP model.

Object tracking with the compressive algorithm

The other model used in the proposed object tracking model is the CT algorithm. The CT algorithm considers both the low and the high dimensional features present in the frame. The object in the frame is tracked by applying the random matrix over the frame of the video. The random matrix involved in the tracking process is provided in Equation (8):

$$l = G.h \tag{8}$$

where, the term l represents the low dimensional space, $l \in \mathbb{R}^x$ in the video frame and the term h represents the

high dimensional space, $h \in \mathbb{R}^{y}$ in the video frame where $x \ll y$. The random matrix used for the CT is represented as $G \in \mathbb{R}^{x \times y}$. The algorithmic steps involved in the CT algorithm are briefed below:

1) The a[th] frame of the video is provided as the input to the algorithm.

2) The low dimensionality features of the a[th] frame is extracted with the use of the set of image patches. The image patches are represented as $P_{\varsigma} = \left\{ r \middle\| B_C(r) - B_C(a-1) \right\| < \varsigma \right\}$ where, the term $B_C(a-1)$ represents the required tracking location of the $(a-1)^{th}$ frame.

3) The low dimensionality features are assigned as the input to the naive Bayes classifier (NBC). The NBC transforms each image patch into the log-likelihood ratio map which indicates chances that patches belong to object or non-object. The NBC, $C(l)$ provides the required tracking location B_C and it is represented as the sum of log-likelihood ratios of independent Gaussian distributed conditional distributions, $p(l_l | u = 1)$ and $p(l_l | u = 0)$ with their respective mean and variance parameters:

$$C(l) = \sum_{l=1}^{l1} \log\left(\frac{p(l_l | u = 1)}{p(l_l | u = 0)}\right) \tag{9}$$

where, the likelihood pdf are estimated directly/independently from the image patches, the term *u* represents the variable between 0 and 1, and *l*1 is the number of features.

4) In the next step, two sets of image patches are used for finding the tracking location, $B_C(a)$. The image patches are represented as, $P_{\psi} = \left\{ r \middle\| B_C(r) - B_C(a) \right\| < \psi \right\}$, and $P_{\zeta} = \left\{ r \middle| \varphi < \left\| B_C(r) - B_C(a) \right\| < \zeta \right\}$ with $\psi < \varphi < \zeta$.

5) Finally, the parameters of the classifier equation are updated based on the features obtained from the two image patches of previous step. The tracked location based on the CT algorithm is given as follows:

$$B_C = \left\{ \left(x^o_{C(1)}, y^o_{C(1)} \right), \left(x^o_{C(2)}, y^o_{C(2)} \right), ..., \left(x^o_{C(a)}, y^o_{C(a)} \right), ..., \left(x^o_{C(N)}, y^o_{C(N)} \right) \right\} \tag{10}$$

Tracking model based on the proposed Taylor series based compressive approach

The proposed TSC approach provides the final equation for the object tracking. The proposed TSC approach depends on the value of the tracking location obtained from both the TSP model and the CT algorithm. Equation (11) presents the equation for the object tracking by the proposed TSC approach. The proposed tracking model provides the accurate object's location in the video frame.

$$B = \frac{B_T + B_C}{2} \tag{11}$$

where, the term *B* presents the accurate object's location in the frame. The terms B_T and B_C are the tracked results obtained using Taylor series and compressive approaches.

Feature extraction

The feature extraction process extracts the necessary features from the objects tracked through the tracking model. In this work, features, such as mean, variance, speed, motion deviation, motion stopping, and frame occupancy, and relevant histogram based features as mean, variance, and color, are extracted from the tracked objects. The features extracted forms the feature vector. The features involved in the feature extraction procedure is explained as follows:

Mean of the frame to frame distance travelled

As the position of the object changes from frame to frame in the video, the distance between the object's location from one frame to another is computed. Then, the mean value of the distance travelled by each object between

two frames is measured and considered as a feature. The mean determining the frame to frame distance travelled is expressed as follows:

$$\rho(A_a, A_{a+1}) = \frac{\sum_{a=1}^{N} D}{N} \tag{12}$$

where, the term D represents the distance travelled by the object between the a^{th} and the $(a + 1)^{th}$ frame. The term N represents the total number of video frames.

Variance of the frame to frame distance travelled

Similarly, the variance of the distance measured is obtained for the object in each video frame. The variance of the frame to frame distance travelled by the object is given as follows:

$$\vartheta(A_a, A_{a+1}) = \frac{\sum_{a=1}^{N} (D - \rho)^2}{N} \tag{13}$$

where ρ is the mean.

Speed

The next feature involved in the feature extraction process is the speed. In the video, the objects move at varying speeds between the successive frames. The speed allows the researcher to determine the activity of the object. The speed of the movement by the object defines the ratio of the distance to the time. Equation (14) expresses the mathematical form of the speed.

$$Speed = \frac{D}{\delta} \tag{14}$$

where, the term D expresses the distance moved by the object from a frame to another, and the term δ represents the time utilized by the object to cover the distance D.

Motion deviation and motion stopping

The motion deviation (MD) and the motion stopping (MS) criteria features determine the change in the position of the object between the frames. MD defines the difference in the position of the object from the a^{th} and the $(a + 1)^{th}$ frame. Expression (15) defines the MD feature.

$$I = \sum_{a=1}^{N-1} \left\| (x_{a+1}, y_{a+1}) - (x_a, y_a) \right\| \tag{15}$$

where, the term (x_a, y_a) represents the center object's position in the a^{th} frame. The MS feature determine the position variation of the object from the previous frame, identifying the final object's location. Equation (16) gives the MS feature,

$$J = \sum_{a=1}^{N-1} \left\| (x_a, y_a) - (x_{a-1}, y_{a-1}) \right\| \tag{16}$$

where, (x_a, y_a) and (x_{a-1}, y_{a-1}) are the positions of the object in the a^{th} and $(a - 1)^{th}$ frame.

Frame occupancy

The frame occupancy feature defines the area occupied by the object in each frame. Since the objects move from one frame to another, the area occupied by the object in the frame differs from others. Measuring the area, the shape of

the object can be identified and thus, the object can be recognized easily. Hence, it is necessary to determine the area occupied by each object in the frame.

$$F^{O} = \sum_{b=1}^{K} \sum_{c=1}^{L} R_{bc} \tag{17}$$

$$R_{bc} = \begin{cases} 1 & ;if\ object \\ 0 & ;otherwise \end{cases} \tag{18}$$

Histogram based features

The histogram based features (Sergyan, 2008) like color, mean, and variance, are also extracted from the object. The histogram based features are briefed below.

i) Color

Color of an object is an important feature to be extracted, as it helps to determine whether the object is anomaly or not. Application of the probability histogram over the frame yields the required color histogram. Equation (19) presents the color histogram feature,

$$H(A_a) = \left[H^{Q} \quad H^{R} \quad H^{S} \right] \tag{19}$$

where, the term $H(A_a)$ indicates the color histogram of the frame A_a. The terms H^{Q}, H^{R} and H^{S} define the probability histogram of the red, the green, and the blue band, respectively.

ii) Mean

The brightness feature of the object in the frame is determined through the mean feature. The brightness of each pixel location of the object is determined through the calculation of the probability histogram and the gray level of the object. The mean of the object is represented as follows:

$$\bar{\mu}(A_a) = \sum_{k=0}^{i-1} k\, P(k) = \sum_{v=1}^{s} \sum_{w=1}^{s} \frac{A_a(v,w)}{s * s} \tag{20}$$

where, the term $A_a(v, w)$ represents the gray level of pixel position of the object in the a^{th} frame of the video and s is the size of the object in the frame. The term $P(k)$ represents the probability histogram.

iii) Variance

The contrast of the object is found through the variance measure. Equation (21) expresses the variance measure of the object.

$$\sigma^{2}(A_a) = \sum_{k=0}^{i-1} (\mu - \bar{\mu})^{2}\, P(k) \tag{21}$$

where, μ is gray level and $\bar{\mu}$ is the mean corresponding to the histogram features.

Construction of the feature vector

The feature vector is constructed with each features derived above. The feature vector is constituted by mean, variance, speed, frame occupancy, motion deviation and stopping criteria, and various histogram based features. The feature vector constructed with all the features is expressed below:

$$F = \left\{ F_1, F_2, ..., F_f, ..., F_m \right\} \tag{22}$$

where, the term F_f means the f^{th} feature in the feature vector. The features present in the feature vector vary between 1 and m.

Anomaly detection with the proposed FSVNN classifier

The next major step in the proposed work is design of the FSVNN classifier for the AD. The proposed FSVNN classifier uses the firefly algorithm (FF) (Arora & Singh, 2013) and Genetic Algorithm (GA) (Ludwig, *et al.,* 2014), in the SVNN classifier. The FF performs efficiently for the nonlinear and the multimodal problems. The FF has the flexible nature to be integrated with the other optimization algorithms. GA has better convergence for the solution with the larger space. Thus, the integration of GA and the FF for the optimization of the weights present in the SVNN classifier yields good results. The conventional SVNN classifier acts like a binary classifier. In the proposed FSVNN classifier, the weights for the optimization procedure are trained with the use of GA and the FF. The proposed FSVNN classifier utilizes a fitness function for the optimization process.

Fitness evaluation of the proposed FSVNN classifier

The proposed FSVNN classifier uses the maximization of fitness function for declaring the anomaly in the video frame. The fitness function depends on the Eigen value obtained from the weights of the proposed classifier. Equation (23) expresses the necessary maximisation fitness function of the proposed FSVNN classifier.

$$Fitness = \rho_{\max} + \rho_{\min} + \frac{\Gamma}{N}\sum_{a=1}^{N}\left|X_a - X_a^*\right| \tag{23}$$

where, the term X_a^* indicates the value of the ground truth information, the term X_a represents the classifier's output, the term Γ refers to the regularization factor and the term N represents the total video frames. The value of the $\rho_{\max}$ and $\rho_{\min}$ indicate the maximized and the minimized value of the Eigen function. The Eigen value for the fitness function is expressed by the following equation:

$$\rho = Eigen\left(W \times W^T\right) \tag{24}$$

$$\rho_{\max} = \max\left(\rho\right); \rho_{\min} = \min\left(\rho\right) \tag{25}$$

Where the term W represents the weight vector comprising of each weight in the proposed FSVNN classifier.

Architecture of the proposed FSVNN classifier

This section provides the architecture of the proposed FSVNN classifier in Figure 2. The Proposed FSVNN classifier has three layers. These are input layer, hidden layer and the output layer. The features of each object in the frame are fed into the input to the proposed FSVNN classifier. Since there are m features, the proposed FSVNN has m input layers. The features provided as the input are trained with the weights provided in the hidden layer. The proposed FSVNN classifier provides weights at both the input and the hidden layer. The input layer provides m weights for each feature input and the hidden layer provides a single hidden layer weight. The output provided in the hidden and the output layer is modified with the addition of biases. The final equation to the proposed FSVNN classifier is expressed in the Equation (26).

$$\mathrm{X_a} = \mathrm{W}_\chi \times \log\mathrm{sig}\left[\left(\sum_{\mathrm{f=1}}^{\mathrm{m}} \mathrm{F_f} * \mathrm{W_f}\right) + \mathrm{q_1}\right] + \mathrm{q_2} \tag{26}$$

where, the term X_a refers to the output to be classified under the FSVNN classifier. The term W_χ represents the weight provided by the hidden layer and the term W_f represents the f^{th} weight of the input layer. The terms q_1 and q_2 indicate the bias present in the FSVNN classifier. The term F_f represents the input feature given to the classifier.

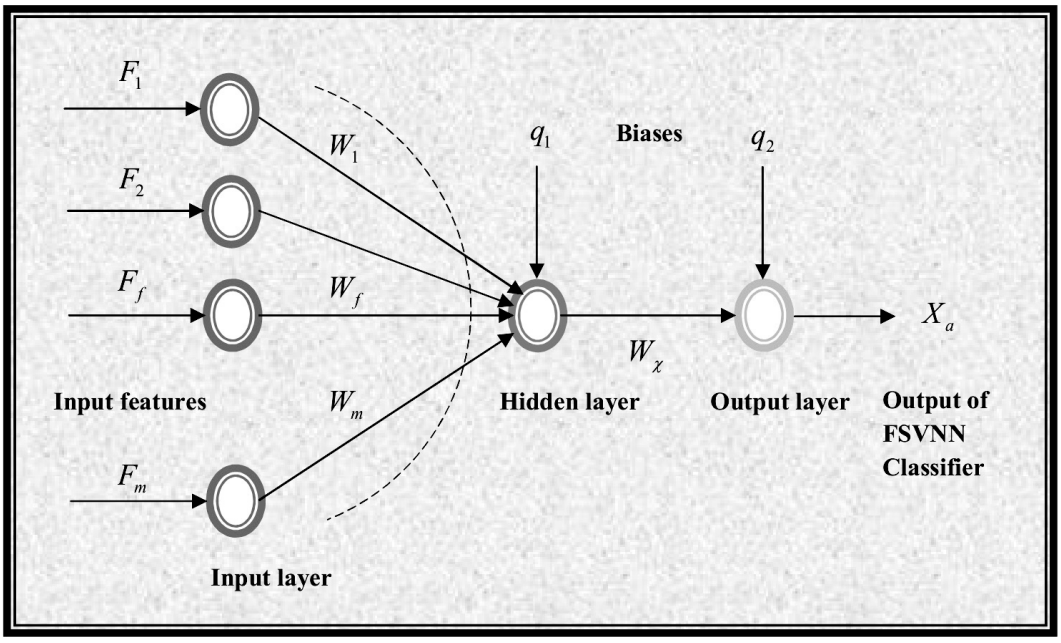


Figure 2. Architecture of the FSVNN classifier

3.4.3 Training phase: Training of the proposed FSVNN classifier with the features

The weights present in the proposed FSVNN classifier are trained with the features extracted from the tracked objects in the video frame. The *m* features extracted from the tracked objects in each video frame are fed into the input to the proposed FSVNN classifier. The weights at the input of the proposed classifier are trained with GA and the FF.

Algorithmic procedure of the FSVNN:

The general steps pertained to the training of the proposed FSVNN classifier to find the required input weights are explained as follows:

Step 1: Initialization: Initially, the weights present in the FSVNN classifier are randomly initialized. For the a^{th} video frame, *m* features are extracted. This requires *m* input weights for the AD. The randomly initialized weights are expressed as follows:

$$W^a = \left\{ W_f^a \quad ; 1 \le f \le m \right\} \tag{27}$$

where, W_f^a represents f^{th} weight for the a^{th} frame. The weights for the training process are initialized as the chromosomes.

Step 2: Evaluation of the fitness function: In this step, the fitness of the initialized weights is calculated. The fitness as the maximization function is expressed in the Equation (23).

Step 3: GA based weight update: GA finds the optimized weight based on three steps, such as selection, crossover, and mutation. The weight update based on the GA is expressed as follows:

$$W_a^{crossover}\left(t+1\right) = \alpha\, W_p\left(t\right) + \left(1-\alpha\right) W_q\left(t\right) \tag{28}$$

$$p = round\left[\left(E-1\right) \times \frac{e^{\eta\gamma_1} - 1}{e^{\eta} - 1} + 1 \right] \tag{29}$$

$$q = round\left[\left(E-1\right)\times\frac{e^{\eta\gamma_2}-1}{e^{\eta}-1}+1\right] \tag{30}$$

Where the terms p and q represent the indices of chromosomes. The term η refers to the selective pressure. The term α represents the constant for the weight update and E is the size of the population. γ_1 and γ_2 are random numbers in the range [0,1].

Step 4: FF based weight update: In this step, the weight of the proposed FSVNN classifier is updated based on the FF. The FF performs the updatation based on the attractiveness to another parameter. Equation (31) presents the weight update based on the Firefly.

$$\mathrm{W_a^{FF}(t+1)} = \mathrm{W_a^{FF}(t)} + \mathrm{Y_a(t+1)} \tag{31}$$

$$Y_a(t+1) = Y_a(t) + \delta_0 \times e^{-\beta d_{a,a1}^2}\left(Y_{a1}(t) - Y_a(t)\right) + \gamma K_a(t) \tag{32}$$

where, the term $W_a^{FF}\left(t+1\right)$ represents the updated weight at time $\left(t+1\right)$ based on the FF. The term $\mathrm{Y_a(t+1)}$ represents the required updated position based on the attractiveness of the fireflies. The term δ_0 represents the attractiveness parameter at $d_{a,a1}=0$ and $K_a(t)$ represents the vector of the Gaussian distributed random numbers drawn at time t. The terms γ and β are randomization parameter and light absorption parameter, respectively.

Step 5: Weight update for the proposed FSVNN classifier: The proposed FSVNN classifier takes the weight update from both the GA and the FF on the basis of their fitness function. In this step, the fitness of the weights is computed for both algorithms. If the fitness of GA is better than the FF, then the weight of the GA is used for the next iteration. Otherwise, the weight of the FF is utilized. Equation (33) expresses the weight update equation of the proposed FSVNN algorithm.

$$W_a\left(t+1\right) = \begin{cases} W_a^{crossover}\left(t+1\right) & ;if\ Fitness\left[W_a^{crossover}\left(t+1\right)\right] > Fitness\left[W_a^{FF}\left(t+1\right)\right] \\ W_a^{FF}\left(t+1\right) & ;Otherwise \end{cases} \tag{33}$$

where, the term $Fitness\left[W_a^{crossover}\left(t+1\right)\right]$ represents the fitness of the weights obtained by the GA, and the term $Fitness\left[W_a^{FF}\left(t+1\right)\right]$ indicates the fitness of the weights obtained through the FF.

Testing phase: Detection of the anomaly in the video from the trained data

Based on the optimal weights provided by the training phase, the AD is done in the testing phase. Here, the features of the test frame are fed into the input of the trained FSVNN classifier. The proposed FSVNN classifier provides the information about the presence of the anomaly in the frame. The output of the proposed FSVNN classifier is represented as follows:

$$X_a^{test} = \begin{cases} 1 & ; \quad Anomaly \\ 0 & ; \quad no\ anomaly \end{cases} \tag{34}$$

Pseudo code of the proposed FSVNN classifier

Figure 3 exhibits the pseudo code of the proposed FSVNN classifier employed in the AD system. The proposed FSVNN classifier is initially trained with the extracted features of the tracked objects. Then, the weights of the classifier are trained with GA and the FF. Then the proposed FSVNN classifier provides the required classified output for the test video at the testing phase.

Sl. no	Algorithm: Pseudo code of the proposed FSVNN classifier
1	**Input: F= Feature vector**
2	**Output:** X_a^{test} = Output of the classifier
3	**Begin**
4	**//Training phase**
5	**For (t=0: t= max)**
6	**Initialize** the weights of the FSVNN classifier
7	$W^a = \{W_f^a \quad ; 1 \le f \le m\}$
8	Find the fitness of the weights using the fitness equation (23)
9	Update the weight $W_a^{crossover}(t+1)$ using GA
10	Update the weight $W_a^{FF}(t+1)$ using the FF
11	Find the fitness for the updated weights
12	**If** $\left(Fitness\left[W_a^{crossover}(t+1)\right] > Fitness\left[W_a^{FF}(t+1)\right]\right)$
13	Update the weight of the FSVNN using the $W_a^{crossover}(t+1)$
14	$W_a(t+1) = W_a^{crossover}(t+1)$
15	**Else**
16	Update the weight of the FSVNN using the $W_a^{FF}(t+1)$
17	**End if**
18	$W_a(t+1) = W_a^{FF}(t+1)$
19	Train the classifier with the updated weight $W_a(t+1)$
20	Find the output of the classifier based on the equation (26)
21	**End for**
22	**End**
23	**// Testing phase**
24	Provide the features of the test video
25	Find X_a^{test} based on the equation (34)
26	**End**

Figure 3. Pseudo code of the proposed FSVNN classifier for the AD from the crowded videos

RESULTS AND DISCUSSION

The simulation results of the proposed TSC based tracking and proposed FSVNN classifier are briefed in this section. The metrics, such as sensitivity (SEN), specificity (SPE), and accuracy (ACC), MOTP, and ROC curve, measure the performance of the FSVNN model.

Experimental setup

The experimentation of the proposed FSVNN model requires a PC with Windows 10 OS, 4 GB memory, and Intel i3 processor. The simulation work is completed using the MATLAB tool, and various simulation results are obtained.

Database description

The experimentation of the proposed AD model with the FSVNN classifier, uses three videos from the standard databases. Video 1 for the experimentation is utilized from the UCSD-Peds1 dataset (Dataset, 2017a). Video 1 contains the moving of the pedestrians, bicycles, carts, etc. along the walkway. Video 2 is obtained from the dataset (Dataset, 2017b), which comprises persons running a marathon race. Video 3 (Dataset, 2017c) provides the moving persons, vehicles along the road, obtained from the publicly available resource.

	Initial AD duration in seconds	Ground truth object number of anomalous activities
Video 1	2.00	9
Video 2	1.07	7
Video 3	0.90	12

Evaluation metrics

The evaluation metrics, such as SEN, SPE, and the ACC analyze the quantitative performance of the proposed FSVNN classifier involved in the AD. The mathematical expression of each metric involved in the performance analysis is briefed below,

Sensitivity: SEN metric measures the true positives provided by the AD model. The expression for the SEN regarding the true positive and the false negative is expressed below:

$$Sensitivity = \frac{True^{+}}{True^{+} + False^{-}} \tag{35}$$

where, $True^{+}$ is the true positives, and $False^{-}$ is the false negatives.

Specificity: The SPE measure provides the evaluation of the true negatives achieved by the AD model. The expression for the SPE is expressed as follows:

$$Specificity = \frac{True^{-}}{True^{-} + False^{+}} \tag{36}$$

where, $True^{-}$ is the true negatives, and $False^{+}$ is the false positives.

Accuracy: The ACC metric measures the closeness of the model to achieve the true value. Equation (37) expresses the ACC metric.

$$Accuracy = \frac{True^{+} + True^{-}}{True^{+} + True^{-} + False^{+} + False^{-}} \tag{37}$$

Multiple Object Tracking Precision (MOTP): The MOTP metric for the AD scheme defines the ratio of the total number of matched object hypothesis in the video frame to the total number of matches created in the frame.

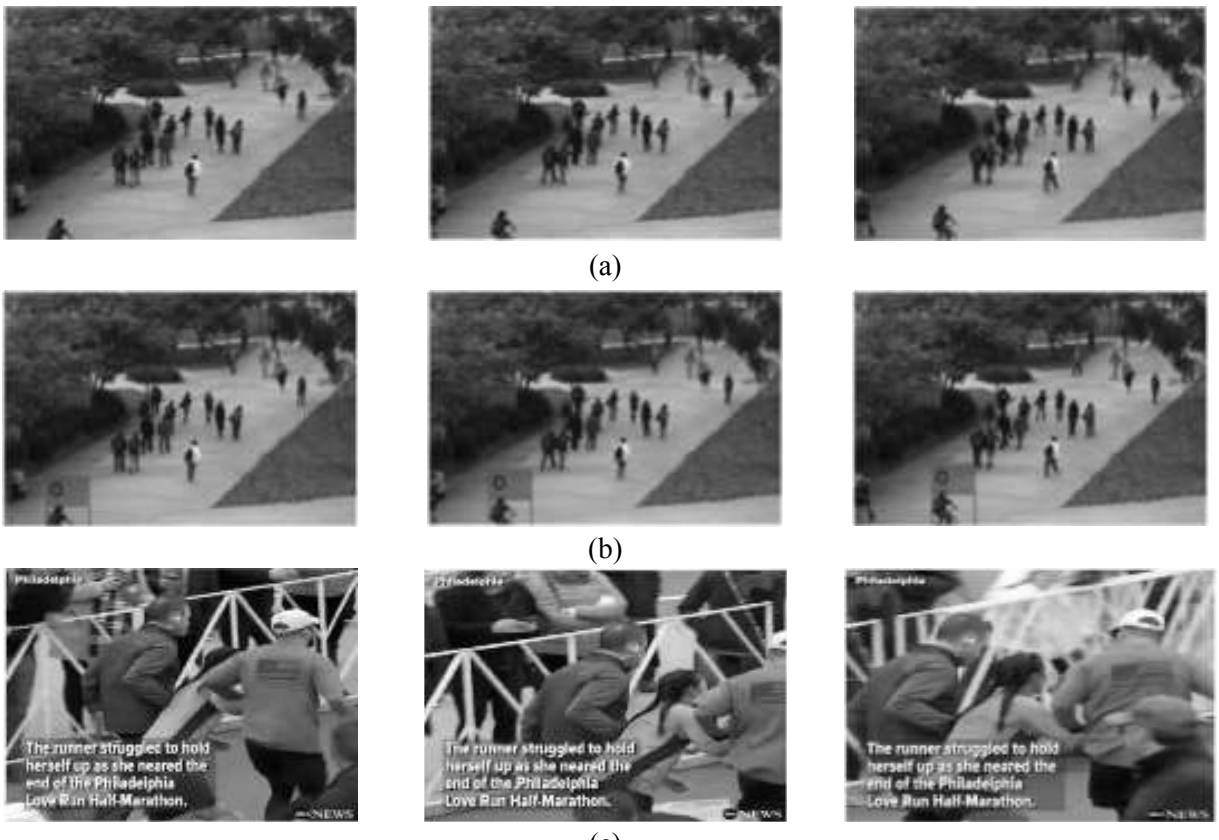
$$MOTP = \frac{\sum_a Hypothesis^N}{\sum_a Matches^N} \tag{38}$$

Comparative models

The proposed AD model with the FSVNN classifier is compared with the conventional models, such as Self-organizing Map (SOM) (Giovanis, 2010), Deep Belief Network (DBN) (Hu, *et al.,* 2016), Neural network (NN) (Giovanis, 2010), and Firefly based DBN (FDBN) (Applied FF to train DBN). The comparative models are analyzed using the performance metrics. The comparative models have the same experimental settings as the proposed model while obtaining the experimental results.

Experimental results of the proposed FSVNN classifier

Figure 4 shows various experimental AD results of the proposed FSVNN classifier based AD system. The experimentation of the proposed work is done with the use of three videos, i.e., video 1, video 2, and video 3. Video 1 presents the video of the several pedestrians walking on the sideways. Video 2 presents the persons running the marathon. Video 3 presents cyclists, pedestrians moving on the road. Figures 4.a, 4.c, and 4.e show the input sample provided to the proposed AD scheme from video 1, video 2, and video 3, respectively. Figure 4.b presents the AD in the video 1. The movement of the cyclist on the walkway is detected as the anomaly by the proposed scheme for the video 1. Figure 4.d provides the various anomalies present in video 2. Similarly, Figure 4.f provides the anomalies of video 3.



(a)

(b)

(c)

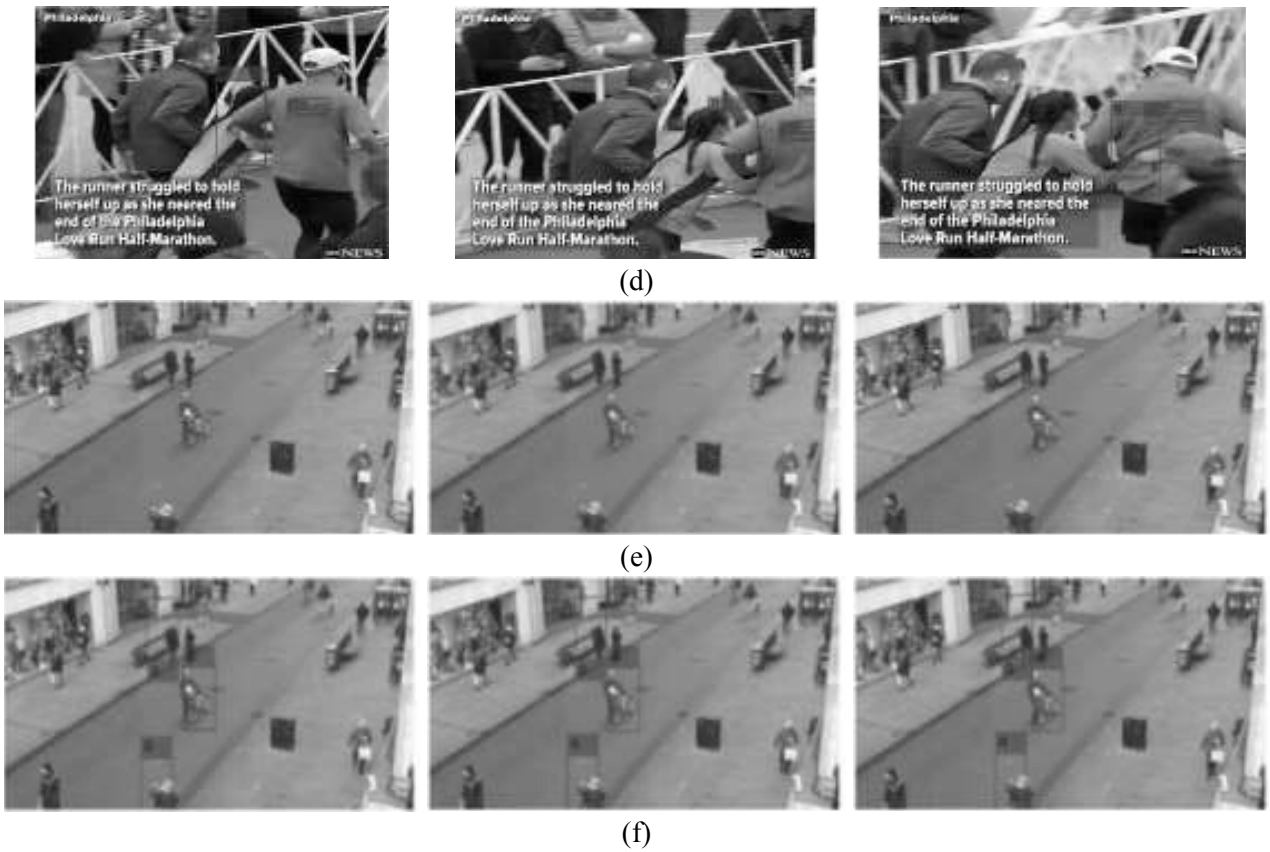


Figure 4. Experimental AD results of the proposed FSVNN classifier (a) Sample input images of the video 1, (b) Results of AD of (a), (c) Sample input images of the video 2, (d) Results of AD of (b), (e) Sample input images of the video 3, (f) Results of AD of (e)

Performance analysis of the proposed TSC based tracking approach and proposed FSVNN classifier

This section provides the performance analysis of the proposed TSC based approach for tracking in terms of MOTP and proposed FSVNN classifier for the AD in terms of metrics such as, SEN, SPE, and ACC. The performance of the proposed FSVNN classifier is also done through ROC curve analysis.

MOTP Analysis for TSC based tracking approach

The MOTP analysis is done between the varying number of objects in the video and the MOTP metric. In this work, the proposed hybrid tracking (HT) model is based on the Taylor series model and the CT model. The proposed HT model is analyzed by comparing the results with the compressed sensing (CS) approach (Zhang *et al.*, 2012) and the moving average (MA) model (Ratre *et al*., 2018b). Figure 5 shows the performance of the proposed HT Model in terms of MOTP curve. Figure 5.a presents the MOTP analysis for the video 1. For video 1 with two objects, the existing CS and the MA algorithms attain the MOTP value of 0.96954 and 0.8959. The proposed HT model attains the MOTP value of 0.98223 for video 1 with two objects. When video 1 has ten objects, the existing CS and the MA model attain the MOTP value of 0.9741 and 0.95228. The proposed HT model attains the MOTP value of 0.98934 for video 1 with ten objects.

Figure 5.b presents the performance analysis of the proposed HT model for video 2. For video 2 with two objects, the existing CS and the MA algorithm attain the MOTP value of 0.97 and 0.907. The proposed HT model attains the MOTP value of 0.98 for video 2 with two objects. When video 2 has 20 objects, the existing CS and the MA model attain the MOTP value of 0.97 and 0.980097. The proposed HT model attains the MOTP value of 0.98 for video 2

with 20 objects. Figure 5.c presents the performance analysis of the proposed HT model for video 3. For video 3 with ten objects, the existing CS and the MA algorithm attain the MOTP value of 0.98832 and 0.96371. The proposed HT model attains the MOTP value of 0.99353 for video 3 with ten objects. When video 3 has 20 objects, the existing CS and the MA model attain the MOTP value of 0.97749 and 0.95674. The proposed HT model attains the MOTP value of 0.98854 for video 3 with 20 objects. Here, the proposed HT model attains the maximum MOTP value more than that of the existing methods, since it takes the advantages of both TSP tracking and the CT approach. Also, the proposed HT model extracts the histogram based features, which avoid hard decisions compared to edge based features.

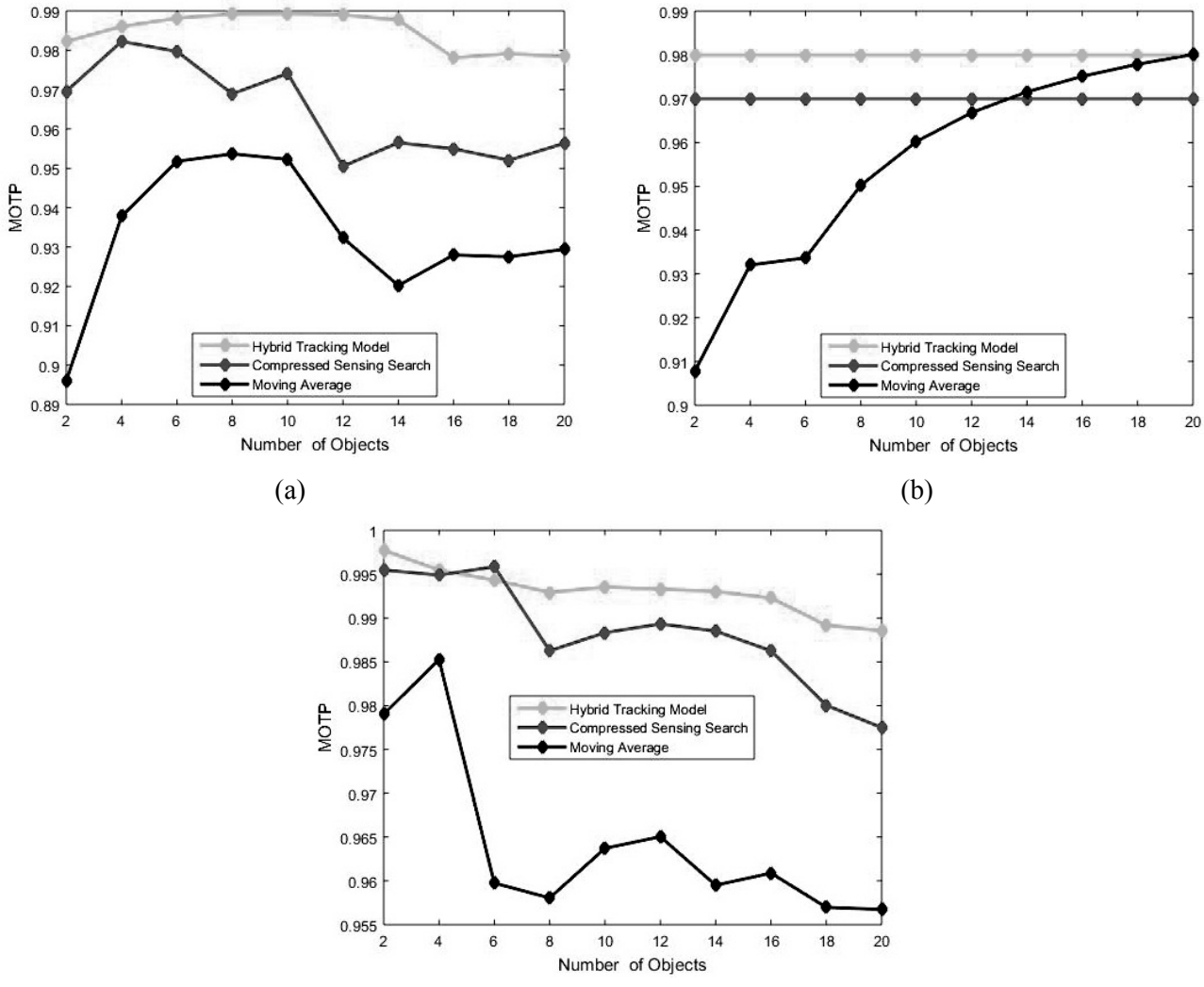


Figure 5. Performance of the proposed HT Model based on the MOTP curve for (a) video 1, (b) video 2, and (c) video 3.

Comparative Analysis

Here, the performance of the proposed FSVNN method is analyzed and compared with the existing methods, such as SOM, DBN, NN, and FDBN.

ROC curve Analysis

The performance of the proposed FSVNN classifier used for the AD is analyzed using the ROC curve. The ROC curve analysis is done between the True Positive Rate (TPR) and the False Positive Rate (FPR). Figure 6.a presents

the ROC curve for video 1. For the FPR value of 0.1, the conventional SOM, DBN, NN, and FDBN models attain the TPR value of 0.38764, 0.4256, 0.6025, 0.6525, and 0.7025. For the proposed FSVNN model, TPR is increased to 0.7025. When the FPR value is 0.5, the TPR value of the conventional SOM, DBN, NN, and FDBN models is 0.5805, 0.61822, 0.8025, and 0.8525. The proposed FSVNN model attains the improved TPR value of 0.9025 for the FPR value of 0.5. Figure 6.b presents the ROC curve for video 2. For the FPR value of 0.5, the conventional SOM, DBN, NN, and FDBN models attain the TPR value of 0.52675, 0.56175, 0.6878, and 0.8525. For the FPR value of 0.5, the proposed FSVNN classifier attains TPR of 0.9025. Figure 6.c presents the ROC curve analysis of the proposed model for video 3. For the FPR value of 0.5, the conventional SOM, DBN, NN, and FDBN models attain the TPR value of 0.602, 0.642, 0.8025, and 0.8525, respectively. Here, FSVNN classifier performs better than competing classifiers.

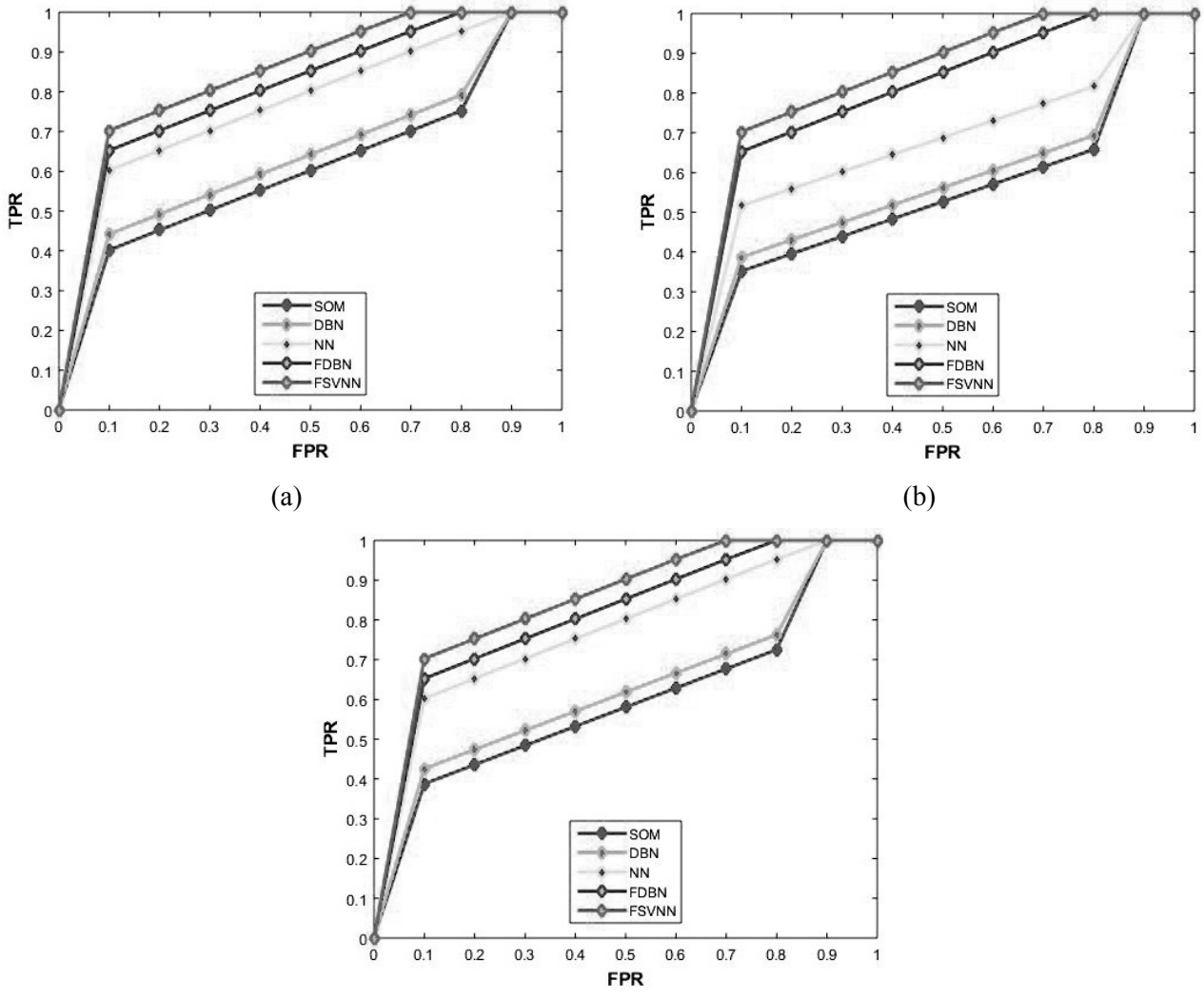


Figure 6. Performance of the proposed FSVNN classifier based on the ROC curve for (a) video 1, (b) video 2, and (c) video 3.

Analysis for 80 % training data

Figure 7 shows the performance analysis and comparative evaluation of the proposed FSVNN classifier for 80 % training data. Figure 7.a shows the SEN analysis for the proposed FSVNN classifier. The conventional SOM, DBN, NN, and FDBN models attain the SEN value of 0.93103, 0.89655, 0.89655, and 0.93103, respectively, for video 1. The proposed FSVNN classifier attains the overall improved value of SEN value of 0.97034 for video 1. Figure 7.b

shows the SPE analysis of the proposed FSVNN classifier. For video 1, the conventional SOM, DBN, NN, and FDBN models attain the SPE value of 0.5, 0.5, 0.5, and 1, respectively, for video 1. The proposed FSVNN model attains the SPE value of 1 for the three videos. Figure 7.c presents the performance analysis of the proposed model based on the ACC metric. For video 1, the conventional SOM, DBN, NN, and FDBN models attain the ACC value of 0.90322, 0.8709, 0.87096, and 0.93548, respectively. The proposed FSVNN model attains ACC value of 0.96 for the 80 % training data for video 1.

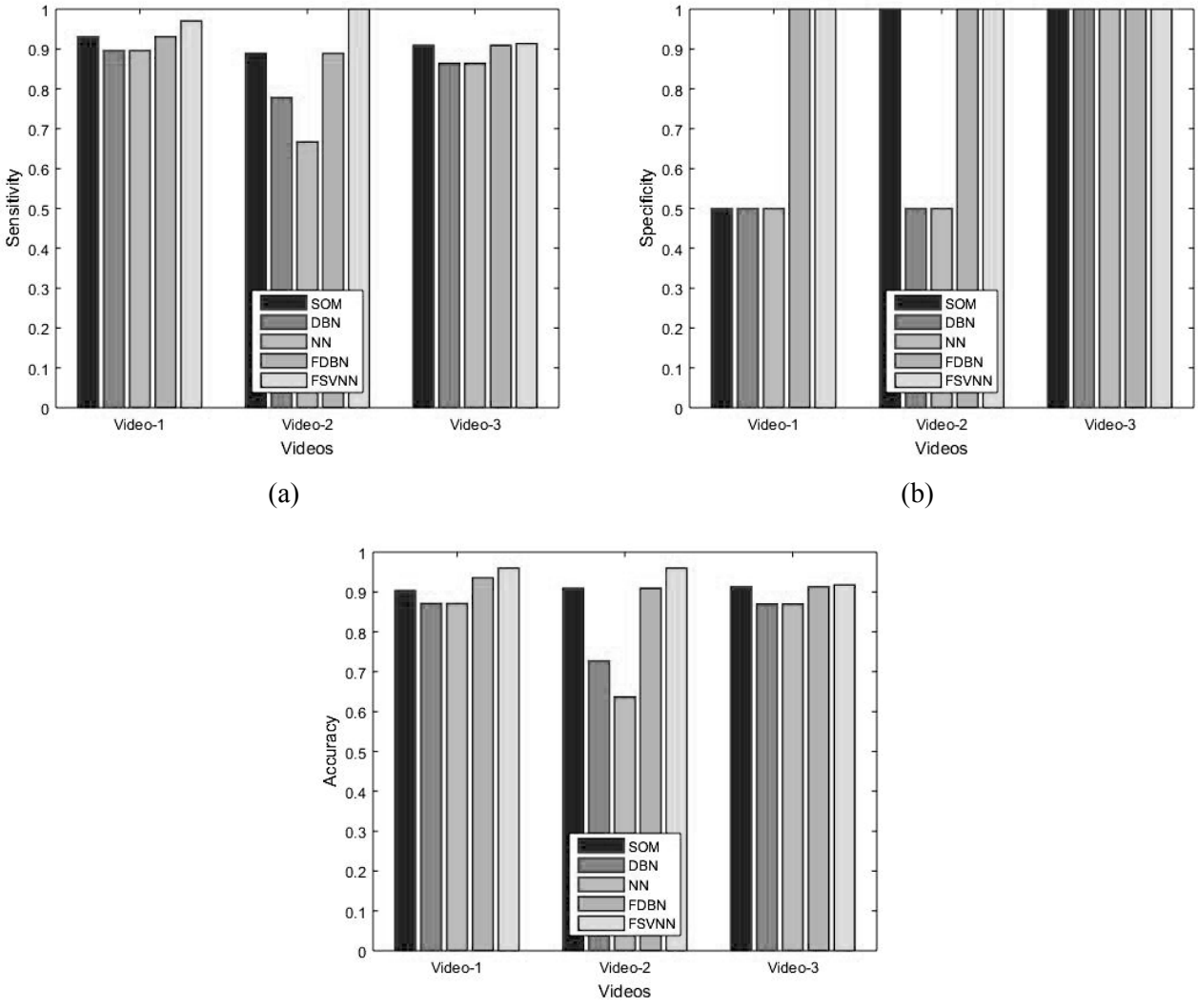


Figure 7. Performance of the proposed FSVNN classifier for 80 % training data (a) SEN, (b) SPE, and (c) ACC.

Analysis for 90 % training data

Figure 8 shows the performance analysis and comparative evaluation of the proposed FSVNN classifier for 90% training data. Figure 8.a shows the SEN analysis for the proposed FSVNN classifier. The conventional SOM, DBN, NN, and FDBN models attain the SEN value of 0.93103, 0.89655, 0.89655, and 0.93103, respectively, for video 1. The proposed FSVNN classifier attains the overall improved value of SEN value of 0.93568 for video 1. Figure 8.b shows the SPE analysis of the proposed FSVNN classifier for 90 % training data. Increasing the training to 90 % shows that the proposed model attains negligible changes in the SPE analysis for each input video. The proposed

FSVNN model achieved overall high SPE value of 1 for video 1, video 2, and video 3, respectively. Figure 8.c presents the performance analysis of the proposed model based on the ACC metric for 90 % training data. For video 3, the conventional SOM, DBN, NN, and FDBN models attain the ACC value of 0.913043, 0.86956, 0.86956, and 0.91304, respectively. The proposed FSVNN model attains ACC value of 0.917608 for 90 % training of video 3.

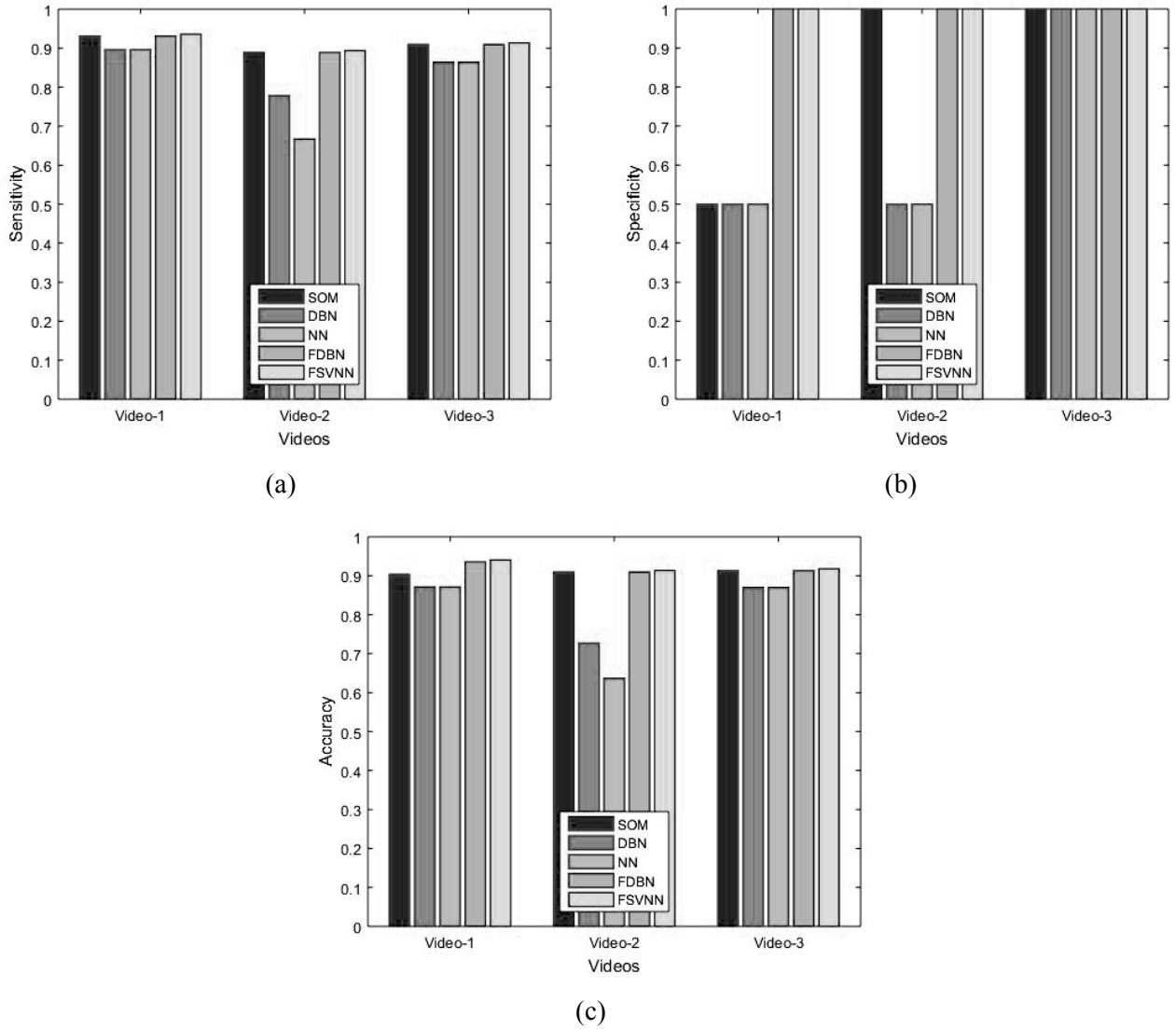


Figure 8. Performance of the proposed FSVNN classifier for 90 % training data
(a) SEN, (b) SPE, and (c) ACC.

Discussion

The performance of the proposed AD scheme with the FSVNN classifier and the HT model is analyzed and compared with that of the various comparative models. From Table 1, it is demonstrated that the proposed AD with the FSVNN classifier performs better than the other comparative models. Table 1 contains the values of metrics obtained by the comparative models for the 80 % training of the video 1. The proposed AD scheme with the FSVNN classifier attains SEN, SPE, and ACC values of 0.97035, 1, and 0.96, respectively.

Table 1. Comparative evaluation of the proposed AD with the FSVNN

Performance metrics	Comparative models for the video 1				
	SOM	**DBN**	**NN**	**FDBN**	**Proposed FSVNN**
SEN	0.931034	0.896552	0.896552	0.931034	**0.970345**
SPE	0.5	0.5	0.5	1	**1**
ACC	0.903226	0.870968	0.870968	0.935484	**0.96**

CONCLUSION

This paper presents the AD model by proposing the HT model and the FSVNN classifier. The proposed AD model primarily develops a HT model based on the TSP model and CT approach for tracking the objects in the video. Then, various features, such as speed, mean, variance, motion deviation and stopping, frame occupancy and several histogram based features, are extracted from tracked objects in the frames. Then the features are fed to the input layers of the proposed FSVNN classifier for the training purpose. The proposed FSVNN classifier modifies the existing SVNN classifier with the GA and the FF. The simulation of the proposed AD model based on the FSVNN classifier utilizes three videos from the standard datasets. The performance of the proposed model is analyzed and compared with the conventional models, such as SOM, DBN, NN, and FDBN, respectively. The MATLAB simulation results demonstrate that the proposed AD model with the FSVNN classifier attains the effective performance with the values of 0.97035, 1, and 0.96, for SEN, SPE, and ACC, respectively.

REFERENCES

Amraee, S., Vafaei, A., Jamshidi, K. & Adibi, P. 2018. Anomaly detection and localization in crowded scenes using connected component analysis, *Multimedia Tools and Applications,* **77**(12): 14767-14782.

Arora, S. & Singh, S. 2013. The Firefly optimization algorithm: convergence analysis and parameter selection, *International Journal of Computer Applications*, **69**(3): 48-52.

Bensch, R., Scherf, N., Huisken, J., Brox, T. & Ronneberger, O. 2017. Spatiotemporal deformable prototypes for motion anomaly detection, *International Journal of Computer Vision,* **122**(3): 502-523.

Chen, C., Shao, Y. & Bi, X. 2015. Detection of anomalous crowd behavior based on the acceleration feature, *IEEE Sensors Journal,* **15**(12): 7252-7261.

Chen, T., Hou, C., Wang, Z. & Chen, H. 2018. Anomaly detection in crowded scenes using motion energy model, *Multimedia Tools and Applications*, **77**(11): 14137-14152.

Dataset., 2017a. Dataset 1 (UCSD ped1) from "http://www.svcl.ucsd.edu/projects/anomaly/dataset.htm".

Dataset., 2017b. Dataset 2 (Philadelphia Love Run Half Marathon) from "https://youtu.be/TvViJO7Pt44".

Dataset., 2017c. Dataset 3 (Town centre dataset-Univ. of Oxford) from "https://medium.com/@madhawavidanapathirana/real-time-human-detection-in-computer-vision-part-2-c7eda27115c6"

Du, Y., Chen, F. & Xu, W. 2007. Human interaction representation and recognition through motion decomposition, *IEEE Signal Processing Letters,* **14**: 952-955.

Foroughi, H., Naseri, A., Saberi, A. & Yazdi, H.S. 2008. An Eigen space-based approach for human fall detection using integrated time motion image and neural network, *In Proceedings of the IEEE 9th International Conference on Signal Processing (ICSP),* 1499– 1503, Beijing, China.

Fradi, H., Luvison, B. & Pham, Q.C. 2017. Crowd behavior analysis using local mid-level visual descriptors, *IEEE Transactions on Circuits and Systems for Video Technology,* **27**(3): 589-602.

Giovanis, E. 2010. Application of logit model and self organizing maps (SOMs) for the prediction of financial crisis periods in US economy, *Journal of Financial Economic Policy.* **2**(2): 98-125.

Gunduz, A.E., Ongun, C., Temizel, T.T. & Temizel, A. 2016. Density aware anomaly detection in crowded scenes, *IET Computer Vision,* **10**(5): 374-381.

Herbrich, R. 2002. Learning Kernel Classifier: Theory and Algorithm, *The MIT Press, Cambridge,* 384 pages, ISBN: 9780262256339.

Hu, X., Hu, S., Huang, Y., Zhang, H. & Wu, H. 2016. Video anomaly detection using deep incremental slow feature analysis network, *IET Computer Vision* **10**(4): 258-265.

Jun, B. & Kim, D. 2012. Robust face detection using local gradient patterns and evidence accumulation, *Pattern Recognition,* **45**(9): 3304-3316.

Laptev, L., Marszalek, M., Schmid, C. & Rozenfeld, B. 2008. Learning realistic human actions from movies, *In Proceedings of the IEEE Conference on Computer Vision and Pattern Recognition (CVPR),* 1–8, Anchorage, AK, USA.

Ludwig, O., Nunes, U. & Araujo, R. 2014. Eigen value decay: A new method for neural network regularization, *Neurocomputing*, **124**: 33-42.

Narasimhan, M.G. & Kamath, S. 2018. Dynamic video anomaly detection and localization using sparse denoising autoencoders, *Multimedia Tools and Applications*, **77**(11): 13173-13195.

Natarajan, P. & Nevatia, R. 2008. Online, real-time tracking and recognition of human actions, *In Proceedings of IEEE Workshop on Motion and Video Computing (WMVC), Copper Mountain,* 1– 8, Copper Mountain, CO, USA.

Ratre, A. & Pankajakshan, V. 2018a. Tucker tensor decomposition based tracking and Gaussian mixture model for anomaly localization and detection in surveillance videos, *IET Computer Vision,* **12**(6): 933-940.

Ratre, A. & Pankajakshan, V. 2018b. Tucker visual search-based hybrid tracking model and fractional Kohonen self-organizing map for anomaly localization and detection in surveillance videos, *The Imaging Science Journal,* **66**(4): 195-210.

Revathi, A.R. & Kumar, D. 2017. An efficient system for anomaly detection using deep learning classifier, *Signal, Image and Video Processing,* **11**(2): 291-299.

Sabokrou, M., Fathy, M., Moayed, Z. & Klette, R. 2017a. Fast and accurate detection and localization of abnormal behavior in crowded scenes, *Machine Vision and Applications,* **28**(8): 965-985.

Sabokrou, M., Fayyaz, M., Fathy, M. & Klette, R. 2017b. Deep-Cascade: Cascading 3D deep neural networks for fast anomaly detection and localization in crowded scenes, *IEEE Transactions on Image Processing*, **26**(4): 1992-2004.

Sempena, S., Maulidevi, N. & Aryan, P.R. 2011. Human action recognition using dynamic time warping, *In Proceedings of the IEEE International Conference on Electrical Engineering and Informatics (ICEEI),* 1–5, Bandung, Indonesia.

Sergyan, S. 2008. Color histogram features based image classification in content-based image retrieval systems, *2008 6th International Symposium on Applied Machine Intelligence and Informatics,* 221-224, Herlany, Slovakia.

Soma, B. & Gupta, V. 2017. Abnormality detection in crowd videos by tracking sparse components, *Machine Vision and Applications,* **28**(1-2): 35-48.

Tipping, M.E. 1999. The relevance vector machine, *Advanced Neural Information Processing System,* 652–658.

Yang, Q., Zhang, H.H. & Zhang, H. 2001. Taylor series prediction: a cache replacement policy based on second-order trend analysis, *Proceedings of the 34th Annual Hawaii International Conference on System Sciences, Maui, HI, USA,* 7.

Yuan, Y., Wang, D. & Wang, Q. 2017. Anomaly detection in traffic scenes via spatial-aware motion reconstruction, *IEEE Transactions on Intelligent Transportation Systems,* **18**(5): 1198-1209.

Zhang, K., Zhang, L. & Yang, M. 2012. Real-time compressive tracking, *In Proceeding ECCV'12 Proceedings of the 12th European Conference on Computer Vision, Florence,* Italy, 864-877.

Zhou, S., Shen, W., Zeng, D., Fang, M., Wei, Y. & Zhang, Z. 2016. Spatial–temporal convolutional neural networks for anomaly detection and localization in crowded scenes, *Signal Processing: Image Communication*, 47: 358-368.

Submitted: 20/11/2017
Revised: 02/07/2018
Accepted: 03/07/2018

سلسلة تايلور القائمة على نهج التتبع الضاغط والشبكة العصبية لمتجهات الدعم المعتمدة على خوارزمية اليراعات المضيئة لتتبع والكشف عن الخلل في أشرطة الفيديو الجماهيرية

أفيناش راتر
قسم هندسة الإلكترونيات والاتصالات، جامعة دلهي التكنولوجية، طريق باوانا، دلهي، الهند

الخلاصة

تحظى مجالات تطبيق محتوى الوسائط المتعددة وتحليل مشاهد الكمبيوتر باهتمام ملحوظ نحو التعرف على حركات الأشخاص الموجودين داخل الفيديو. وفقاً لذلك، يُعد تحليل سلوك الجماهير موضوعاً مهماً نظراً لأهمية المراقبة بالفيديو في الأماكن العامة. يقدم هذا العمل نموذجاً للكشف عن الخلل من خلال تقديم نموذج تتبع ومُصَنِف يرتكز على تحسين مقاطع الفيديو الجماهيرية. تتطلب الأجسام الموجودة في الفيديو تتبعاً لأن الخلل يعتمد على حركة تلك الأجسام. يقترح هذا العمل نموذج تتبع هجين من خلال الجمع بين سلسلة تايلور القائمة على التتبع التنبئي ونهج التتبع الضاغط. تم استخراج السمات من الأجسام التي تم تتبعها، وتم تشكيل متجه الخصائص. علاوة على ذلك، يقترح هذا العمل الشبكة العصبية لمتجهات الدعم المعتمدة على خوارزمية اليراعات المضيئة (FSVNN) بغرض التصنيف. تم تجريب أوزان مصنف FSVNN المُقترح على الخوارزمية الجينية وخوارزمية اليراعات المضيئة. تم تحليل أداء النموذج المُقترح باستخدام ثلاثة مقاطع فيديو من قواعد البيانات القياسية ومقارنتها بالطرق الحالية، مثل SOM وDBN وNN وFDBN. من نتائج المحاكاة، تبين أن النموذج المُقترح للكشف عن الخلل مع مصنف FSVNN قد حققا أداءً أفضل بشكل عام من الطرق المقارنة بقيم 0.97035 و1 و0.96 للحساسية والنوعية والدقة على التوالي.

ResearchGate

See discussions, stats, and author profiles for this publication at: https://www.researchgate.net/publication/337136765

The fourth industrial revolution, women engineers and SDGs: an exploratory study with special reference to India

Conference Paper · September 2019

CITATIONS
0

READS
2

1 author:



Seema Singh
Delhi Technological University
40 PUBLICATIONS **35** CITATIONS

SEE PROFILE

Some of the authors of this publication are also working on these related projects:

Women in Engineering View project

Women in Engineering Education in Ethiopia View project

All content following this page was uploaded by Seema Singh on 09 November 2019.

The user has requested enhancement of the downloaded file.

The fourth industrial revolution, women engineers and SDGs: an exploratory study with special reference to India



Professor Seema Singh

INWES Vice-President (Education & Research) & Professor of Economics, Delhi Technological University, INDIA

September 20' 2019

Abstract

Under the UN's SDGs and Fourth Industrial Revolution, engineers have come to the core of the developmental framework. Here, gender differentiation, cannot be ignored as women are unique and the technology is also not gender-neutral. In this background, the paper on the basis of existing literature and an ethnographic study of twenty women engineers has been able to bring out emerging features of the labour market. First is changing employer-employee relation under 4th Industrial relation and the second is discrimination and bullying of women engineers at the workplace. There is a need for a strong legal framework to take care of both issues. Again, women in significant numbers leave the labour market during the age of childbearing and rearing. Once they leave the labour market and as technology changes very fast, it is difficult for them to re-join. The onus comes on the Continuing Engineering Education (CEE) programme to design modules on emerging technologies. At the same time, emphasis must be given on innovation and entrepreneurship also.

Key words

Sustainable Development Goals, Fourth Industrial Revolution, Women engineer, Discrimination, Bullying

Acronyms, Units and Currenciesused

AICTE	All India Council for Technical Education
APNN	Asia Pacific National Network
DST	Department of Science and Technology
ICT	Information and Communication Technology
INWES	International Network of Women in Engineering and Science
IR	Industrial Revolution
IT	Information Technology
MBA	Masters of Business Administration
M2M	Machine-to-Machine
M.Tech.	Master of Technology
NSO	National Statistical Office
NGO	Non-Governmental Organisation
Ph.D.	Doctor of Philosophy
PSU	Public Sector Undertaking
Rs.	Indian Currency
SDGs	Sustainable Development Goals
UGC	University Grants Commission
UN	United Nations
UNESCO	United Nations Educational Scientific and Cultural Organisations
US	United States
VET	Vocational Education and Training
WEF	World Economic Forum

Contents

	Abstract		2
	Key words		2
	Acronyms, Units and Currencies		3
1	Executive summary		5
2	Background		6
4	Review of Literature		7-10
	4.1	Fourth Industrial Revolution (4^{th} IR) and its impact on employment	7-8
	4.2	Sustainable Development Goals	8-9
	4.3	Emerging World of Work and Women Engineers	9-10
5	Research Objective and Methodology		11
6	Discussion and Findings		11-16
	6.1	Ethnographic study of twenty women engineer	11-15
	6.2	Preparedness to face 4^{th} IR and SDGs	15
	6.3	Legal framework to safeguard women employees at the workplace	15-16
7	Management Approach		16
8	Technical Inputs		16
9	Conclusion and Recommendation		16-17
10	References		17-19
11	Annexure-A;		20

Table1: Sustainable Development Goals and Branches of Engineering

1. Executive Summary

Out of seventeen Sustainable Development Goals of the UN, majority of them needs involvement of engineers for their achievement to ultimately, achieve rest of the SDGs. At the same time, the world is experiencing the Fourth Industrial Revolution, stemming from automation. The technological intensity of the products and production process has increased. Engineers are required to contribute even in non-technical sectors. In a nutshell, engineers have come to the core of the developmental framework. Here, gender differentiation, cannot be ignored as women are unique and the technology is also not gender-neutral. Lately, the corporate sector has realised it; they are emphasising on an inclusive employee base. However, it is yet to be accepted by all stakeholders. The INWES has taken initiative in that direction. During the APNN 2018 at Hanoi, Vietnam, the participants through its declaration urged the governments, corporate sector and the society at large to work towards creating a legal framework to ensure favourable mechanism and sensitive resource allocation for women scientists and engineers, as well as intellectuals. So, they could contribute to the sustainable development of the region in the context of the Fourth Industrial Revolution.

Significant features of women participation in the engineering labour market have been discussed as follow:

1. Women engineers in large number are at junior level but their presence decreases as the rise- up to the professional ladder. There are different types of discrimination and bullying which works against their growth as a professional.

2. Women in significant numbers leave the labour market during the age of childbearing and rearing. Once they leave the labour market and as technology changes very fast, it is difficult for them to re-join the labour market. During the 4th IR, the rate of change of knowledge has intensified. The onus comes on the Continuing Engineering Education (CEE) programme to design modules on emerging technologies. At the same time, emphasis must be given on innovation and entrepreneurship also.

During the 4th IR, the nature of employment and employee-employer relation is also going to change a lot. There is a need for formulation of a legal framework which takes care of all emerging nature of employment and employee-employer relation and corresponding social security measures. The framework needs to protect women engineers from the harassment at the workplace also. Associations like INWES are playing a very crucial role in this direction by raising issues concerning women engineers at different platforms.

2. Introduction

Basic activity data including:



- ***India***

  Though the study deals with Indian labour market but it may be applicable to other countries of the region.

- Professor Seema Singh
- 29.8.2019 (On going project)

3. Background

The UN's seventeen Sustainable Development Goals are going to be the governing criterion for countries. Out of those seventeen, at least ten (Table-1 given as annexure p. 20) need major involvement of engineers for their achievement which will ultimately, help in achieving others as SDG -1: no poverty; SDG-8- Decent Work and Economic Growth and to reduce inequality (SDG-10). At the same time, the world is experiencing the Fourth Industrial Revolution, stemming from automation. The technological intensity of the products and production process have increased. Engineers are required to contribute even in non-technical sectors. In a nutshell, engineers have come to the core of the developmental framework. Here, gender differentiation, cannot be ignored as women are unique and the technology is also not gender-neutral. Lately, the corporate sector has realised it; they are emphasising on an inclusive employee base. However, it is yet to be accepted by all stakeholders. The INWES has taken initiative in that direction. During the APNN 2018 at Hanoi, Vietnam, the participants through its declaration urged the governments, corporate sector and the society at large to work towards creating a legal framework to ensure favourable mechanism and sensitive resource allocation for women scientists and engineers, as well as intellectuals. So, they could also contribute to the sustainable development of the region in the context of the Fourth Industrial Revolution.

In this background, the paper does an exploratory study on the basis of review of literature complemented with an ethnographic study of twenty female engineers. The second section details the literature review. The third section discusses the objective and methodology. The discussion and findings have been given in the fourth and fifth section, respectively. The last section concludes the discussion and provides a recommendation.

4. Review of literature

Professor Joseph. A. Schumpeter in his famous book, Capitalism, Socialism and Democracy, has discussed technology as the tool of creative destruction which is developed due to insatiable search of the human being for improvement of technology. It destroys the existing production process and gives way to a new one. In the process of such transformation, job losses also occur as a cleansing process (Schumpeter, 1944). "It brings cultural and social changes eventually but slowly" said Professor Thorstein B.Veblen (Veblen, 1898). The present change, known as the Fourth Industrial Revolution (4^{th} IR) fuelled by automation, artificial intelligence, blockchain, sensors etc. has started during the twenty-first century (Singh et. al., 2018). It is also termed as Second Information Technology (IT) Revolution. The main difference between the first and second IT Revolution is of nature. While during the first one, there was a distinct relationship between technology and the market as the IT was related to the Electronics industry and mechanics was related to the automobile industry. There was no connection between mechanics and IT and at the same time, there was no connection between the automobile and electronics industry but during the 2^{nd} IT revolution highlights the combinations of technologies so all technologies are being combined with others and thus, companies are also redesigned their operation models, (MinHwa et. al., 2018). The review has been done in three sub-sections as Fourth Industrial Revolution and its impact on employment, ii. Sustainable Development Goals and iii. The emerging world of work and women engineers as follows:

4.1 Fourth Industrial Revolution (4^{th} IR) and its impact on employment

The first industrial revolution marks with steam-power; the second one with the electrical machine; the beginning of the computer age marked the third Industrial revolution. The fourth – which is also called as 2^{nd} Information Technology (IT) Revolution, may be marked with the era of wearable gadgets, 3D printing, machine intelligence and networked devices full of electronic sensors (Schwab, 2016). Sensors are being entrenched and integrated with the IT network and the domain of operations which ultimately, adds value to the product and services. The artificial intelligence has taken the interaction level beyond human –to- machine and has made Machine-to-Machine (M2M) interaction possible (Bloem, 2014). Obviously, the 4^{th} IR will be impacting on all aspects of life. From the customer point of view, it will make our life easy as the fridge will remind owner what needs to be brought from the market and also may reduce the cost of production as robots will be working along on the floor without taking break, will not ask for leave and definitely, not indulge in any rowdy activity as protest. However, a plethora of studies starting from Autor (2003), Frey and Osborne (2013) and Arntz et. al. (2016) highlights the impact of the fourth industrial revolution on jobs. While the ideological basis is laid by Piva and Vivarelli, Pianta, these studies explain the analytical approaches to the 4^{th} IR. But the approaches followed by each are different. While some overestimate the job losses, others underestimate the impact. But a common thread that runs through these studies is the emphasis over the fact that jobs—whether more or less—will be lost. In the words of Acemoglu and Restrepo, "new technology will render labour redundant

in a static framework if capital is fixed and technology is exogenous and the task earlier was performed by labour, is automated. Even the wages may be reduced. However, in a dynamic framework, a new version of existing tasks, in which labour has a comparative advantage, can be created. They have developed a model by considering capital accumulation as endogenous and the direction of research towards automation of existing job and the creation of new tasks. If the long-run rental rate of capital relative to the wage is sufficiently low, the long-run equilibrium involves automation of all tasks. Otherwise, there exists a stable balanced growth path in which the two types of innovations go together" (Acemoglu and Restrepo, 2018). The recent Indian experience substantiated the model as per the National Statistical Office's (NSO's) Periodic Labour Force Survey 2017-18, the unemployment rate is highest among male since 1977-78 and among female since 1982-83. However, a joint study conducted by Talent Edge and Centre for Economic Policy Research (CEPR) on one million young professionals reveals that 68% of the Indian feel that the job market has improved during the last 5 years. It is good for all professional but better for higher degree holders (IANS, 2019). Thus, professional and engineers will have to continuously hone their skills. Hence, continuing education has become very crucial (Singh at.el., 2018). Findings of a study conducted in the United States of America reveals that 70% of training content is forgotten within 24 hours. As per the recent advances in neuroscience, adults learn best at the point of need on the job. It has been substantiated by the experimental learning experience of the apprenticeships, such as Switzerland's Vocational Education and Training (VET). It has been proved and justified that the future generation of workers will learn on the job and not during time off. The educational tools as virtual and augmented reality and Artificial Intelligence have also effectively blurred the lines between working and learning (WEF, 2019).

4.2. Sustainable Development Goals

Bigger and broader than Millennium Development Goals (MDGs) that focused on eight goals, 18 targets, and 48 indicators, the Sustainable Development Goals (SDGs) include 17 goals, 169 targets, and 230 indicators. Among the earliest sceptics of the SDGs was the Bill & Melinda Gates Foundation, which suggested that any new goals must be easy to communicate, specific, attainable, relevant, measurable, and time-bound (Sridhar 2016). Though sustainable development was interpreted differently by different countries in the beginning, most countries have agreed now that it advocates about environmental protection, gender equality and promotes prosperity and economic opportunity along with greater social well-being (Rahimifard&Trollman, 2018). Rahimifard and Trollman (2017) has discussed the adoption of a net-positive approach in the manufacturing sector to achieve SDGs. Traditionally, engineers have focused on the uni-directional production process which 'converts raw materials into products and services, often in large volumes' or in other words, development of a set of methods with specific tools and technologies that aim to optimise production which ultimately based on cost reduction in order to maximise profit. More recently, increased consumption has been aggressively promoted to increase profit. Conversely, "the proposed

net-positive manufacturing adopts a distinctly different approach based on the concept of 'borrowing resources to satisfy needs' so that these resources are returned for further use. This circularity in the use of resources may be referred to as immortal use of resources" (Rahimifard, 2015), and to being net-positive is the ability to up-cycle resources or at least recycle (but not down-cycle) them (Rahimifard and Trollman, 2017).

4.3 Emerging World of Work and Women Engineers

Traditionally, engineering is considered a male bastion throughout the world (Wyer, 2003; Küskü *et al.*, 2007; Singh 2013). Not only economic but social and cultural factors also affect women decision of not joining engineering. Again, even if one thinks of joining she has to be good in mathematics and science is her school grades which are a challenge (Singh and Fenton, 2014). However, the need for gender diversity has been realized during past fifteen-twenty years and efforts are being taken by the Governments and other stakeholders to increase women participation (Singh 2014; Singh and Peers, 2019). Singh (2013) has given a detailed discussion of affirmative action taken by State Governments in India, regulatory bodies like All India Council for Technical Education, University Grants Commission (UGC), Department of Science and Technology and academia have shown a keen interest in ensuring higher participation of women in engineering education. In the national capital of Delhi, Indira Gandhi Institute of Technology (IGIT) was an only for women college under GGSIP University. The University Grants Commission (UGC) in the 12th Plan has upgraded the institute to a Women Technological University as Indira Gandhi Delhi Technological University for Women. The Delhi Technological University (DTU) and PEC University of Technology, Chandigarh provides reservation of one and two seats respectively for only girl child among all branches of engineering. At the state level, there are 33 per cent reservation girls students in all engineering colleges of Madhya Pradesh and Rajasthan and 30 per cent reservation in all engineering colleges of Maharashtra. The regulatory bodies as UGC, AICTE and DST have also several programmes to hone R&D skills of women engineers and scientists who may not be in regular employment. Even the industries have realised the advantage of gender balance even for engineers. It was evident from the hiring trend as Auto giants, Maruti and Yamaha as they are hiring more women B.Tech. of Mechanical engineers branch for aesthetic input in the design and better productivity. Engineering firms are coming forward to accommodate the work-life balance of women engineers. Microsoft has a programme of re-employment of women engineers who have taken a break from their regular career. Women First Council is a new chapter in HCL's employee-first philosophy. It's a council by the women, of the women, for the women, that provides an organized platform to address unique and special needs of the women which give women empowerment a new meaning at HCL Technologies. The council gives its members ample opportunities to make a difference in their lives and those of their women colleagues. Wipro EcoEnergy has partnered with UN Women to Strengthen Women's Role in Business**.** Most of the firms are organising seminars for their staff for gender sensitising (Singh, 2013). Though companies are adopting affirmative policies to encourage women engineers but at the implementation level, how much flexibility will be given depends on the decision of the project manager and no one likes to compromise with the profit criteria as not including a pregnant lady in his or her project and so, even though she can work for next sex seven months, she stays without work which is called 'on the bench' on the corporate terminology and lose some perks which she could have earned otherwise. Many leave the job and even though there are programmes of re-employment as the shelf-life of technology is small and they need to hone their skills (Singh, 2014).

Women participation in engineering has increased substantially in all countries of South Asia (data for Afghanistan is not available). Even those who join, find the problem in home-work

balance and always live with a guilty feeling due to self-perception about care work (Singh and Fenton, 2014). The regional share of female researchers in R&D is lowest in South Asia (16.9 %) than other blocks of the world. In West Asia, the share is 22.4%. Even the Sub Saharan Africa and the Arab States are having a share of 30% and 36.8% respectively. As per UNESCO data, South East Europe leads among all groups with 48.5% (Singh, 2018) even though, women researchers in engineering are less noticed. A study of nearly 1 million engineering papers from the web of science reveals that even though, female engineers publish, on an average, in slightly more prestigious journals than their male counterpart, but their research is getting less attention (Bohannon, 2016).

When technology entering another dimension and Capitalism entering its fourth revolution, it is imperative that there will be a change in the nature of work as well as a change in the nature of the workforce as well. Claudia Goldin (2017) has discussed that flexibility and choice in where, when and how to work can be beneficial to women and, in particular, may boost their employment rates. For example, countries with the highest shares of women working from home also have the highest maternal employment rates - while no such relationship emerges for men. Moreover, evidence from the United States shows that gender pay gaps tend to be lower in industries where working arrangements are more flexible (Goldin, 2014).

The APNN18 declaration is about making strong legal framework so that female engineer can contribute in a better way. In India, there is an elaborate legal framework to protect working women and there is a paucity of data on women engineers also but whatever data and its analysis are available to reveal that they are discriminated. On the basis of a study of 377 engineering graduates' campus placement experience, Choudhury has been able to suggest that female graduate s are discriminated in both employment and earning offered to them (Choudhury, 2015). The findings of a study of 423 women and 270 men engineers which has been carried out by the Society of Women Engineers and the Centre for Worklife Law (WLL) shows that 76% of women engineers expressed their concern for proving themselves repeatedly to get the same level of respect as their male counterpart. Almost two-fifths of the women respondents expressed concern against mothers at the workplace. Again, the incidence of sexual harassment at the workplace is also shocking. Around 11% reported as a victim of unwanted sexual attention (BI Indian Bureau, 2019).

5. Research Objective and Methodology

5.1 Research Objective

In this background, the objective of paper to discusses

5.1.1 Preparedness of women engineers to face 4th IR and SDGs.

5.1.2 Type of discrimination faced by women engineers

5.1.3 Action taken by the, the Government, the corporate sector and the society at large towards creating strong legal network in order to create an environment where women engineers can work optimally.

5.2 Research Methodology

The research has been mainly based on the secondary sources which has been supplemented by an ethnographic study of twenty Indian women engineers. Ethnographic studies helps in bring out the cultural and social aspect of the respondent and well as of the environment where she is working. Questions were also asked about their perception and preparedness for the 4th IR and about SDGs. How they are preparing for the 4th IR and whether they have ever experienced suppression. Salient points from the discussion with all respondents have been given in section 6.1.

6 Discussion and Findings

The need for gender diversity has been realized during the past fifteen-twenty years and efforts are being taken by the Governments and other stakeholders to increase women participation (Singh 2014; Singh and Peers, 2019).

6.1 Ethnographic study of twenty women engineer

An ethnographic study has been carried out on twenty women engineers. The salient points of discussion are as follow:

1. Respondent-1

In the late twenties, she is computer engineer from a private engineering college in Delhi. She is quite optimistic about the future of computer engineers in the 4th IR. Being a consultant with a private consulting firm, she is working with many clients. To facilitate her work, she wants to learn a few more programmes. However, she wants to pursue MBA course also. Admits that whatever was taught in the college was not enough and has upgraded her knowledge through joining online courses. However, there is lack of good programmes too and good courses are costly too.

About gender justice, the company has a policy of zero tolerance and there is an anti-harassment cell. However, it is difficult to prove and then, off the record you will be advised to settle down. His intention was not to sexually harass you.

2. Respondent-2

Working as a Research Associate in a government research laboratory, she is in her late early thirties. She knows about 4th IR and has heard about SDGs. Regarding discrimination, there is no clear discrimination but subtle. In the meeting, proper notice is not given to the suggestion given by her and she will perceive that she may be wrong. As it happens continuously after sometimes, she will start feeling that she is inferior and knows less than their male counterpart.

3. Respondent-3

A civil engineer in her late forties has progressed in the professional ladder in a private construction company. Now a saturation point has come in her career and if she has to accept the next level she will have to go to Dubai for which she is not prepared. She is thinking of leaving the job and to start her own consultancy firm.

4. Respondent-4

An electrical engineer who is working in a multinational company. Joining an organisation is easy but after that for getting all type of opportunity you have to network and please the superior. She does not want to do all these and just performing whatever comes to her way. So, she is prepared never to get an opportunity to go abroad.

5. Respondent-5

A civil engineer in her early thirties is working at a Multinational company in Delhi. As her husband has got a job in Canada, she is also planning to leave the job to join her husband. Eventually, she will try for a job in Canada. As her in-laws can accompany them so she does not have any issue regarding her very young son. Her office in Delhi has also assured that she can join again when she comes back. In the meantime, she can do some work of the Delhi office through net and phone.

6. Respondent-6

In her late 40's and mother of three sons, respondent-6 is working at a senior position with an established Public Sector Undertaking (PSU). She remembers her father as very abusive. Her mother who was married at a very young age but was able to continue her higher studies and ultimately, joined as a college teacher after obtaining post-graduate degree and was able to raise her three children with dignity. So, from the very beginning respondent-6 was very sure of doing a job. She took engineering as a sense of masculinity attached to it. For raising her three sons, she hired three maids so that she can continue working smoothly.

She does not see any threat for her job under 4th IR but she continuously upgrades knowledge. In fact, after joining the PSU, she acquired Post Graduate degree through Face-2-Face method of continuing engineering education.

7. Respondent-7

Working with a private consulting firm and a civil engineer by training, she is in her mid 30's. As per the demand of the client, one has to read but with 4th IR, she thinks technology is becoming more complex. One has to spend a lot of time for learning. Her husband who is also an engineer works with a manufacturing firm. They have married five years ago but they do not have any child so far. Once she conceived but due to some problem, miscarried. Now she is planning to take a break. So that she can take rest and plan her family. Later on, she will think of joining again.

8. Respondent-8

A young computer engineer in her late twenties looks 4th IR as great opportunity. At present, she is bored with her present job. Planning to leave the job and go on a long holiday to Leh and Laddakh. After that, she will think about what to do. May be joining again. Before joining, she wants to do some advance courses of programming.

9. Respondent-9

A chemical engineer in her mid-thirties is working with a private company. She has two young kids who need their care. Her husband is also an engineer and working in another company. His job is also quite demanding. She is thinking of switching to a teaching job which is less demanding. So, she will be able to take care of her kids.

10. Respondent- 10

An electronics engineers in her early thirties, she wants to be tech. writers on the net. She graduated from a private engineering college. The situation of campus placement was disastrous due to recession. Ultimately she got a job for Rs. 3,60,000/ annum which she carried on for some time. Eventually, she was married and left the job. Now, she is in search of a job, has met few and discussed but nothing has materialised yet but she is optimistic.

11. Respondent- 11

A computer engineer from a good engineering institution, she is in her mid twenties. During the last year of her B.Tech., she along with her three classmates did an innovation. No one from the team tried for the campus placement. Now, they want to give a try to entrepreneurship. They have taken a loan but finding a problem in marketing.

12. Respondent- 12

An environmental engineer, she was interested in social work since the beginning. After graduation, she has joined an NGO which works on waste management at Pune. She know about 4th IR and SDGs. In fact, through waste management they are contributing towards SDG11.

13. Respondent- 13

Teaches electronics engineering in a college, she is in her late twenties. Knowledge management has become a big issue and she wants to do Ph.D. in that area. At the same time, she is also planning to get married.

14. Respondent- 14

An electrical engineer, she was campus placed in a software company. She is working there since three years. Now she wants to do M.Tech from a good foreign university. For the forthcoming academic year, she has applied to seven –eight university of the US and Europe and waiting for the result.

15. Respondent- 15

An electronics engineer from a private engineering college of Uttar Pradesh. Now, she has joined an event management company. Though work is not technical but being engineer it is easier for her to manage data. She enjoys her work.

16. Respondent- 16

An electrical engineer by training, she is in her early forties. initially she could not get a job but instead, got a fellowship from the University Grants Commission. She took the second fellowship also from the Department of Science and Technology. Later on, she joined a college in her city. In a college, though you have to spend so much time on raking classes and other administrative work, but there is a feeling of continuity. Have heard about SDGs and 4th IR. Though both are being discussed in the college but more should be done.

17. Respondent- 17

In her early fifties Acquired B.Tech. degree from a government college in Hyderabad and had to migrate to Delhi due to marriage. Husband is a Charted Accountant. After that she did not join any organisation due to care work for her only son. During those days there were not so many opportunities. As her son has also joined engineering, now she is thinking to start doing something out of her engineering knowledge. She is trying for some opportunity at the internet but so far, nothing has been finalised.

She knows about 4th IR but not decided to join a course but if required, will read more about it on the net.

18. Respondent- 18

A mechanical engineer who is working in a very renowned automobile company, Maruti. Enjoying her bachelorhood but there is pressure for marriage in the family. She is in her early thirties and does not have any boyfriend but friends are there. Knows about 4th IR. The lower level worker is already being affected due to automation but higher-level workers are not affected. However, she has already started reading about the 4th IR. Few training programmes were conducted by the organisation and she is also planning to join a course on artificial intelligence.

19. Respondent- 19

Mother of a two-year boy and in her early thirties, she works in a multinational company. Had to go abroad once when the child was very young. She felt very bad. Now, she has decided not to go ever. At least, until her son needs her time.

20. Respondent- 20

An electrical engineer in her late twenties, she is working in a Multi-National Company. There is pressure from family to get married. But she is planning to try to the USA for higher education.

So, due to affirmative action taken by various stakeholders, women are going to be in the engineering labour market. From the pen sketch of twenty women engineers, they are participating in a type of jobs. But the difficulty in vertical growth progression and

maintaining balance between personal and professional life. The ICT has not only given an opportunity to balance the work-life in a better way but also helps in the safety and security of women. Again, as in the Fourth Industrial Revolution, engineers are not supposed to work with voluminous machine but the work has become more mind game. So, the chances are that more women engineers will be in the helm of affair. However, the nature of employment and employer-employee will significantly change. Here the role of the regulatory bodies will be to strengthen a legal framework which captures all emerging forms of employment and related social security measures.

6.2 Preparedness to face 4th IR and SDGs

The rapidly changing market has placed a premium on the innovation and entrepreneurship which has made the need for upgrading skills in general and technological skills in particular continuously which will ultimately, help in wealth creation along with maintaining long term cultural and environmentally sustainable practices (Dima et.al. 2018). Through continuing education is crucial for all disciplines of higher education but it is more for engineers as the engineering profession requires 'rigorous professional knowledge' (Schön, 1987, p. 3; Baukal Jr. 2012) which changes with time but the rate of change has intensified in the era of 4th IR. Engineers need to constantly update their skills through CEE with sufficient opportunity for innovations. Today, there are several channels of CEE as academic organisations, professional association of engineers and industries. The regulatory bodies as Department of Science and Technology, University Grants Commission and All India Council for Technical Education have several programmes for women candidates only. However, not only formal training but informal and non-formal learning opportunities need to be provided to women engineers and scientist (Singh, 2019) for their effective contribution.

6.3 Legal framework to safeguard women employees at the workplace

The preamble of the Indian Constitution provides all citizens of India "equality of status and opportunity' which is guaranteed by Article 14 of the Indian constitution. So, irrespective of gender, it is a legal obligation to give equal treatment. No women what to talk of engineers can be denied and discriminated. The Prevention of Workplace Sexual Harassment Act has been enacted since December 2013 as an outcome of Supreme Court's guideline for effective enforcement of the fundamental right of women. Basis of the act is the landmark case of "Vishakha and others vs. State of Rajasthan". The case was filed against the State of Rajasthan and Union of India for the brutal rape of a state government employee, a social worker for impeding child marriage which was very prevalent in the society at that time. Now, all employers, both in public and private, are obliged to provide a two-tier- internal and external redressal mechanism against sexual harassment (legal Council' 2017).

However, on the basis of review and ethnographic study of twenty engineers, it can be said that women engineers are also subject to the following type of discrimination at the workplace (the whole network with whom work professionally):

Table2: Type of Discrimination at the Work Place

SN	Discrimination	Detail

1	Discrimination at the time of joining	Considering male candidate first.
2	More work is given	Though salary may be same but more additional work is given
3	Fault Finding	To criticise works, to give less importance to suggestions
4.	Not considering at the time of promotion	Saying not-qualified for promotion.
5.	Lower salary	In the private sector where salary is negotiated,

Sourse: Ethnographic study by author

Except for the salary, all other discrimination given in the table, are very difficult to prove, but they have a disastrous effect on the self-esteem of the women employee.

At the society level, # Me too movement against sexual harassment of the women employees has got a lot of support.

7 Management Approach

The research is basically done on the basis of secondary sources which were searched and information collected through net. The twenty engineers who have been considered for ethnographic study are my friend. I tried to include a representative sample for the study.

8 Technical Inputs

I. am teaching in one of India's oldest engineering college since 1999 and was warden of the girls student for ten years. I know many women engineers of different age groups.
2. Women engineer is one of my research areas since 2000.

9 Conclusions and recommendations

There are two significant features of women participation in the engineering labour market. They have been discussed as follow:

1. Women engineers in large number are at junior level but their presence decreases as the rise- up to the professional ladder. There are different types of discrimination and bullying which works against her growth as a professional.

2. Women in significant numbers leave the labour market during the age of childbearing and rearing. Once they leave the labour market and as technology changes very fast, it is difficult for them to re-join the labour market. During the 4th IR, the rate of change of knowledge has intensified.

The onus comes on the Continuing Engineering Education (CEE) programme to design modules on emerging technologies. At the same time, emphasis must be given on innovation and entrepreneurship also.

During the 4th IR, the nature of employment and employee-employer relation is also going to change a lot. There is a need for formulation of a legal framework which takes care of all emerging nature of employment and employee-employer relation and corresponding social security measures. The framework needs to protect them from the harassment at the workplace also.Associations like INWES are playing a very crucial role in this direction by raising issues concerning women engineers at different platforms.

References:

1. Acemoglu Daron and RestropoPascual . 2018. The race between Man and Machine: implications of technology for growth , factors share and employment, American Economic Review, 108(6), 1488-1542, available at:https://economictimes.indiatimes.com/jobs/68-indians-feel-job-market-has-improved-in-5-years/articleshow/69431738.cms.
2. Aotor David H. 2003. Outsourcing at will: the contribution of unjust dismissal dotrine to the growth of employment outsourcing, Journal of Labour Economics, 21(01), pp. 1-42.
3. Arntz, M., T. Gregory and U. Zierahn. 2016. The risk of automation for jobs in OECD countries: a comparative analysis", OECD Social, Employment and Migration Working Papers, No. 189, OECD Publishing, Paris. Available at: http://dx.doi.org/10.1787/5jlz9h56dvq7-en
4. Baukal Jr. Charles E. 2012. A strategy for sourcing continuing engineering education", International Journal of Training and Development, 16:4, pp- 284-299.
5. Bohannon John . 2016. Female engineers publish in better journals but receive fewer citations. Science AAAs, Jan07, available at: http://www.sciencemag.org/news/2016/01/female-engineers-publish-better-journals-receive-fewer-citationsretrived on 20/8/2016
6. BI Indian Bureau, 2019. A whopping 40% of Indian women engineers do not have jobs because of' rampant' sexism at the work place. Business Insider, January 11, available at: https://www.businessinsider.in/a-whopping-40-of-indias-women-engineers-dont-have-jobs-because-of-rampant-sexism-at-workplace/articleshow/67486684.cms 26.8.2019
7. Choudhury Pradeep Kumar (2015), Explaning Geder Discrimintaion at the Employment and Earning of Engineering Graduatesin India, Journal of Educational Planning and Administration XXIX(03), July, pp. 225- 246.
8. Dima Alina Mihaela, LiviuBegu, Maria DenisaVasilescu and Maria Alexandra Maassen (2018), "The Relationship between the Knowledge Economy and Global Competitiveness in the European Union", Sustainability, 10, 1706; doi:10.3390/su10061706.
9. Frey Carl Benedikt and Osborne Michael A. 2013. THE FUTURE OF EMPLOYMENT: HOW SUSCEPTIBLE ARE JOBS TO COMPUTERISATION?. workshop on 'Machine and Employment", organised by Engineering Science department and the Oxford Martin Programme on Future Technology, Universty of Oxford, UK, pp. 1-72.
10. **IANS. 2019. 68 per cent Indian feel job market has improved in the 5 years, Economic Times, May 21 Available at:** https://economictimes.indiatimes.com/jobs/68-indians-feel-job-market-has-improved-in-5-years/articleshow/69431738.cms

11. Legal Councel (2017. Indian Law on Protecting Women Right at the Workplace. Available at http://www.dandreapartners.com/india-law-on-protection-of-women-rights-at-workplace/ 26.8.2019

12. **MinHwa Lee et.al. (2012)** How to Respond to the Fourth Industrial Revolution, or the Second Information Technology Revolution? Dynamic New Combinations between Technology, Market, and Society through Open Innovation, *Journal of Open Innovation: Technology, Market, and Complexit, y* MDPI, 04 (21); doi:10.3390/joitmc4030021, pp. 1-24.

13. Pianta Mario (2004), Innovation and Emplymen. in Fegerberg J., Morey D. And Nelson R. (eds) Hand Book of Innovation, Oxford University Press, the USA ISBN: 9780199264551

14. **Piva, Mariacristina; Santarelli, Enrico; Vivarelli, Marco.** 2003, The Skill Base Effect of Technological and Organisational Change: Evidence and Policy Implication, IZA DP No. 93, November. https://www.econstor.eu/bitstream/10419/20171/1/dp934.pdf

15. **Reese Hope . 2018. Why women work in gig economy. The gig economy: An insider's guide, TechRepublic, CBS INTERACTIVE INC.available at: http://b2b.cbsimg.net/downloads/Gilbert/TR_EB_gig.pdf**

16. Schumpeter, Joseph A., Capitalism, Socialism, and Democracy (1942). pp. 431, ISBN: 0061330086

17. Schwab Klaus. 2016. The Fourth Industrial Revolution, World Economic Forum, https://www.weforum.org/about/the-fourth-industrial-revolution-by-klaus-schwab 27.8.2019

18. Schön, D. A. (1987), *Educating the Reflective Practitioner: Toward a New Design for Teaching and Learning in the Professions,* San Francisco, CA: Jossey-Bass.

19. Rahimifard Shahin &Trollman Hana (2018) UN Sustainable Development Goals: an engineering perspective, International Journal of Sustainable Engineering, 11:1, 1-3, DOI: 10.1080/19397038.2018.1434985

20. **UN Women. 2019. Women in STEAM and STEAM for Women. Available at: https://www.empowerwomen.org/en/who-we-are/initiatives/ict-for-development**

21. ICLG 2019 India Employment and Labour Laws 03/04https://iclg.com/practice-areas/employment-and-labour-laws-and-regulations/india

22. Singh Seema, 2019, Indian Continuing Engineering Education in context of Globalisation, All India Council for Technical Education, New Delhi.

23. Singh Seema. 2018. Challenges and Opportunities before Women Engineers under Fourth Industrial Revolution: An Inquiry with special reference to SAARC region. AONN18 held at Vietnam during October 18-20' 2018

24. Singh Seema, 2013. "Women in Engineering Education in India"(2013) in Dr Ravi Prakash Yadav (eds.) Women Workers in Informal Sector, AavishkarPublishers&Distributers,Jaipur, pp. 115-125ISBN no. 978-81-7910-431-6.

25. Singh Seema and Fenton Susan Lee. 2014. Women Engineers: A Comparative Study between India and Australia. International Journal of Advancements in Research & Technology, Volume 3, Issue 7, July, pp. 108-122.

26. Sridhar Devi, 2016. Making the SDGs useful : A herculean task, The Lancet, September 21, available at https://www.thelancet.com/journals/lancet/article/PIIS0140-6736(16)31635-X/fulltext#gbd-linkback-header

27. *Veblen Thorstein, 1898. Why Economics not an Evalutionary Science. The Quarterly Journal of Economics,* Vol. 12, No. 4 (Jul., 1898), pp. 373-397 (25 pages) DOI: 10.2307/1882952

28. Wyer, M. (2003, January). Intending to stay: Images of scientists, attitudes toward women, and gender as influences on persistence among science and engineering majors. *Journal of Women and Minorities in Science and Engineering*, *9*(1), 1–16. DOI: 10.1615/JWomenMinorScienEng.v9.i1.10

Annexes Table1: Sustainable Development Goals and Branches of Engineering

SN	SDG	Description	Related to Branch of Engineering
1	Goal-2	Zero Hunger	Agricultural Engineering
			Bio Technology
			Genetic Engineering
2	Goal-3	Good Health and Well Being	Bio-medical Engineering
			Genetic Engineering
			Bio-technology
3	Goal-6	Clean Water and Sanitation	Mechanical engineering
			Architecture
			Civil
4	Goal-7	Affordable and Clean Energy	Electrical
			Electronics
			Information Technology
5	Goal-9	Industry, Innovation and Infrastructure	Mechanical Engineering
			Civil Engineering
			Production Engineering
			For innovation- all branches of engineering
6.	Goal-11	Sustainable Cities	Information Technology
			Computer and Software Engineering
			Architecture
			Civil and Environmental Engineering
7	Goal-12	Responsible Consumption and Production	Production Engineering
			Mechanical Engineering
			Mechatronics Engineering
			Nanotechnology
8	Goal-13	Climate Action	Environmental Engineering
			Civil Engineering
9	Goal-14	Life Below Water	Bio-Technology
			Genetic Engineering
10	Goal-15	Life on Land	Bio Technology

			Genetic Engineering

View publication stats

International Journal of Research in Engineering and Innovation (IJREI)
journal home page: http://www.ijrei.com
ISSN (Online): 2456-6934

Thermal modelling and optimization of four stages cascade vapor compression refrigeration systems for ultra-low temperature applications

R.S. Mishra

Department of Mechanical, Production, Industrial and Automobiles Engineering, Delhi technological University, Delhi, India

Abstract

Exergy analysis is a useful way for determining the real thermodynamic losses in terms of exergy destruction in each components and optimizing environmental and economic performances of the four stages vapour compression cascade refrigeration systems using HFO refrigerant in high temperature cycle (HTC) and also HFO-1234yf in medium temperature cycle (MTC) along with HFC-134a in intermediate temperature (ITC) and HFC-404a / Ethylene/ hydrocarbons in ultra-low temperature cycle (LTC). The present study deals with the exergy analysis on a four stages cascade vapour compression refrigeration system using R1234yf, R1234ze, HFC-134a and R404a/Ethylene/HC refrigerants. A computer code is developed by using Engineering Equation Solver (EES-V9.172-3D) software package program. The numerical comparison were made using hydrocarbons / ethylene /HFC-404a in ultra-low temperature cycle. The effects of the temperature overlapping in LTC, ITC, MTC cascade condensers and HTC condenser temperatures have been carried out. The effect of LTC, ITC, MTC & HTC evaporator temperatures on the exergy destruction ratio and first law efficiency (COP_Over_all) and second law efficiency (exergy efficiency) of the system were computed and the optimum values were obtained for such combinations. It was also found that R1234yf and R1234ze, are good alternatives to R12, R22 in view of their environmentally friendly properties for high temperature and medium temperature cycles. Furthermore HFC-404a / ethylene/ hydrocarbons can be used in place of R13 for similar reasons.
© 2019 ijrei.com. All rights reserved

Keywords: Thermodynamic Analysis, Energy, Exergy Analysis, Irreversibility Evaluation

1. Introduction

The During World War II, low temperatures were found useful in aeronautical instrument testing, steel alloy treatment, blood plasma desiccation and similar purposes; and these war needs stimulated the development on ultra-low temperatures refrigeration systems, with evaporators from -29^{0}C down to as low as (-140^{0}C). There are many ultra-low temperature cascade refrigeration systems in use today with evaporator temperatures from 5^{0}C to -100^{0}C. In research laboratories. Ultra-low temperature applications require refrigeration in the range of -80°C to -140°C. Single stage vapour compression refrigeration system is not capable to achieve such low temperatures with the use of reciprocating compressor, due to a very high pressure ratios across the compressor. Higher pressure ratios and volumetric efficiency give you an idea about to higher condenser temperatures and for this reason the capacity of the reciprocating compressor drastically reduces. Though multistage or screw compressors can assist excluding the use of single refrigerant at low temperature is limited by solidification temperature of the refrigerant, extremely low pressures in the evaporator, large suction volumes in the evaporator for a high boiling point refrigerant and high condenser pressure for a low boiling refrigerant. This necessitates integrating for other viable options to partially or fully overcome the above shortcomings. The characteristics of any refrigerant to exhibit best performance, when operating in a certain range of temperature and pressure, provide cascade refrigeration systems an edge over single stage and multistage refrigeration systems for low temperature applications. Cascade refrigeration cycles are commonly used in the liquefaction of natural gas, which consists basically of hydrocarbons of the paraffin series, of which methane has the lowest boiling point at atmospheric pressure. Refrigeration down to that temperature can be provided by a ternary cascade

Corresponding author: R.S. Mishra
Email Address: hod.mechanical.rsm@dtu.ac.in
https://doi.org/10.36037/IJREI.2019.3609

refrigeration cycle using propane, ethane and methane, whose boiling points at standard atmospheric pressure are 231.1 K, 184.5 K and 111.7 K. Cascade refrigeration systems employ series of single stage units which are thermally coupled with evaporator/condenser cascades. In 1974, CFC's were tentatively identified as destructive to the ozone layer. For the next decade, this relationship was investigated and a quantitative statement that tied CFC's to the depletion of ozone was released by the World Meteorological Organization (WMO) and the United Nations Environment Program (UNEP) in 1985. The Montreal Protocol (1987) which was agreed by nearly one hundred and fifty countries froze CFC consumption in 1989 and pledged to cut it in half by 1998. In 1992, the Copenhagen amendments went even farther and halted the production of CFCs in developed countries by 1996.CFCs scheduled to be phased out, hydro chlorofluorocarbons (most notably HCFC22) gained in popularity, while their production levels were controlled by 1992, and they were not scheduled for complete elimination. HCFCs were still damaging to the ozone layer, but much lesser than CFCs. Their average stratospheric lifespan was much shorter and not many of them penetrated into the upper atmosphere. CFC-12 has a stratospheric lifetime of 102 years compared to a lifetime of 13.3 years for HCFC22. Furthermore the ozone depletion potential (ODP) of R22 is only 5.5% of the ODP of R12. To improve the performance of the system and to protect the nature with advanced and increased low temperature application, it is important to go with the cascade systems which handle the low temperature demand with the two different and costlier operations. Zubair [1] simulated thermodynamic performance of an actual single stage vapour compression system using a thermal model to study the performance of a variable-speed refrigeration system in which the evaporator capacity was varied by changing the mass-flow rate of the refrigerant for the constant inlet chilled-water temperature. Cabell et al. [2] developed steady-state model to predict the energy performance of a single stage vapour compression system. Kilicarslan [3] carried out the theoretical and experimental investigation of a two-stage vapor compression cascade refrigeration system using R-134a as the refrigerant. Bhattacharya et al. [4] carried out thermodynamic analysis of an endo-reversible two-stage cascade cycle and obtained optimum intermediate temperature for maximum exergy and refrigeration effect. By developing numerical model of a trans-critical CO_2-C3H8 cascade system to validate the theoretical results. Getu and Bansal [5] carried out the thermodynamic analysis of carbon dioxide–ammonia (R744–R717) cascade refrigeration system to optimize the design and operating parameters of the system by using multi-linear regression analysis in terms of operating for maximum COP, optimum evaporating temperature and optimum mass flow ratio of R717 to that of R744 in the cascade system. Lee et al.[6] did thermodynamically a cascade refrigeration system that uses carbon dioxide and ammonia as refrigerants, to determine the optimal condensing temperature of the cascade condenser to maximize the COP and minimize the exergy destruction of the system. Bhattacharyya et al. [7] carried out the performance of a cascade refrigeration–heat pump system based on a model incorporating both internal and external irreversibilities. Calm [8] examines the outlook for current options in the contexts of existing international agreements, including the Montreal and Kyoto Protocols to avert stratospheric ozone depletion and global climate change, respectively. Literature shows that several refrigerants have emerged to substitute R12, the most widely used fluorocarbon refrigerant in the world. These include the environmental friendly refrigerants i.e. R717, R290, R744, R404A and R1270. Mishra [9] focused on alternative ecofriendly refrigerants for replacing CFC-12 which contains global warming (GWP=1500) and ozone depleting potential (GWP=0055) containing chlorine sustenance. The main critical issue in the field of green technologies is to develop the relationship between ODP and GWP and suggest new and alternative refrigerants which do not damage ozone layer and not to increase global warming. Different ecofriendly HFOs, HFCs and HCs refrigerants are used in each of the circuit depending on the optimum characteristics shown by the refrigerant for a particular application and also carried out using first and second law thermodynamic analysis (i.e. energy and exergy analysis) of two and three stages cascade vapor refrigeration system of 10 ton capacity for seven eco-friendly refrigerants such as R-1234yf and R-1234ze in high temperature circuit, and R134a ,R-404a, R-407C, R-502, propane(R-290), isobutene(R-600a), butane (R-600)) in lower temperature circuit in two stage and above refrigerants in intermediate circuit in three stage system. The performance parameters such as COP, EDR .Therefore four stage cascade refrigeration systems employ four circuits namely a high temperature circuit (HTC), medium temperature circuit (MTC), intermediate temperature circuit (ITC) and a low temperature circuit (LTC). The high temperature circuit serves to extract heat from the medium temperature circuit and medium temperature circuit serves to extract heat from the intermediate temperature circuit and intermediate temperature circuit serves to extract heat from the low temperature circuit and the desired cooling is achieved at the evaporator of the low temperature circuit. The four circuits are coupled together by a heat exchangers called the cascade condensers, where the refrigerant vapours of LTC are condensed by rejecting heat to the refrigerant in the ITC and similarly the refrigerant vapours of ITC are condensed by rejecting heat to the refrigerant in the MTC. Also the refrigerant vapours of MTC are condensed by rejecting heat to the refrigerant in the HTC. The intermediate temperature between the four circuits is an important design parameters that decide the COP of the entire system. The thermodynamic analysis is carried out to evaluate thermodynamic performances of four stages cascade systems at varying design parameters using a HFO and HFC and HC refrigerants. For this study, HFO-1234ze is selected in the high temperature cycle and other alternatives are R152a and R717 .Similarly HFO-1234yf and other HFC were chosen of medium temperature circuit and also HFC were chosen of intermediate temperature cycle. As the low-temperature refrigerant due to its many inherent advantages. Propane, propylene, R404A, and hydrocarbons are selected as ultra-low temperature refrigerants and comparisons were made. In the present research work, energy and exergy analysis is performed on four stages cascade vapour compression refrigeration system in which high temperature circuit ecofriendly refrigerants (R1234ze/R152a/R717) have been used. In the medium temperature ranges HFO-1234yf and

other HFC were used. Similarly In intermediate temperature circuit, HFC are used and in low temperature circuit, HFC-404a, Ethylene, and R600a, R290, R600 were used. The objective of the present study mainly deals with the utility of ecofriendly refrigerants particularly in the intermediate temperature circuit and R1234ze and R1234yf refrigerants. The expressions for the exergy losses (lost works) for the individual processes of the cycle as well as the coefficient of performance (COP) and second law efficiency for the entire cycle has been obtained. Effect of variation of condensing and evaporating temperatures on exergy losses, second law efficiency and COP has been investigated.

2. Results and Discussions

Following five systems of four stages cascade refrigeration systems have been chosen for numerical computations using HFO and HFC refrigerants

System-1: R1234ze in HTC, R1234yf in MTC, R134a in ITC & R404a in LTC
System-2: R1234ze in HTC, R1234yf in MTC, R134a in ITC & R290 in LTC
System-3: R1234ze in HTC, R1234yf in MTC, R134a in ITC & R600a in LTC
System-4: R1234ze in HTC, R1234yf in MTC, R134a in ITC & R600 in LTC
System-5: R1234ze in HTC, R1234yf in MTC, R134a in ITC & Ethylene in LTC

For above five systems, the following input data have been assumed

- Efficiency of HTC compressor = 0.80,
- Efficiency of MTC compressor = 0.80,
- Efficiency of ITC compressor = 0.80,
- Efficiency of LTC compressor = 0.80,
- Temperature of HTC condenser= 50^{o}C
- Temperature of HTC Evaporator= 10^{o}C
- Temperature of MTC Evaporator= -30^{o}C
- Temperature of ITC Evaporator= -80^{o}C
- Temperature of LTC Evaporator= -135^{o}C
- Temperature overlapping of MTC cascade Condenser =10^{o}C
- Temperature overlapping of ITC cascade Condenser =10^{o}C
- Temperature overlapping of LTC cascade Condenser =10^{o}C
- Load of LTC Evaporator= 175 “kW”

Tables-1, show the variations of HTC condenser temperature with thermal performances of four stages cascade vapour compression refrigeration system. As HTC condenser temperature is increases the overall first law efficiency, exergetic efficiency and high temperature circuit first law efficiency is decreases while exergy destruction ratio of whole system and power required to run whole system (i.e. running of four compressors) is also increases. Tables-2 show the variations of HTC evaporator temperature with thermal performances of four stages cascade vapour compression refrigeration system. As HTC evaporator temperature is increases the overall first law efficiency, exergetic efficiency and high temperature circuit first law efficiency is increases and reached to an optimum value and then decreases while exergy destruction ratio of whole system and power required to run whole system (i.e. running of four compressors) is also decreases and reached to an optimum value and then increases. Tables-3 show the variations of MTC evaporator temperature with thermal performances of four stages cascade vapour compression refrigeration system. As MTC evaporator temperature is increases, the overall first law efficiency, exergetic efficiency and high temperature circuit first law efficiency is increases while exergy destruction ratio of whole system and power required to run whole system (i.e. running of four compressors) is also decreases. Table-5 shows, the variations of ITC evaporator temperature with thermal performances of four stages cascade vapour compression refrigeration system. As ITC evaporator temperature is increases the overall first law efficiency, exergetic efficiency and high temperature circuit first law efficiency is decreases while exergy destruction ratio of whole system and power required to run whole system (i.e. running of four compressors) is also increases. Tables-5 shows, the variations of LTC evaporator temperature with thermal performances of four stages cascade vapour compression refrigeration system. As LTC evaporator temperature is increases the overall first law efficiency, exergetic efficiency and high temperature circuit first law efficiency is increases while exergy destruction ratio of whole system and power required to run whole system (i.e. running of four compressors) is also decreases. Tables-6 show the variations of Temperature Overlapping (^{0}C) in MTC condenser and HTC evaporator with thermal performances of four stages cascade vapour compression refrigeration system. As temperature Overlapping (^{0}C) in MTC condenser and HTC evaporator is increases the overall first law efficiency, exergetic efficiency and high temperature circuit first law efficiency is decreases while exergy destruction ratio of whole system and power required to run whole system (i.e. running of four compressors) is also increases. Tables-7 shows the variations of temperature overlapping (^{0}C) in ITC condenser and MTC evaporator with thermal performances of four stages cascade vapour compression refrigeration system. As temperature Overlapping (^{0}C) in ITC condenser and MTC evaporator is increases the overall first law efficiency, exergetic efficiency and high temperature circuit first law efficiency is decreases while exergy destruction ratio of whole system and power required to run whole system (i.e. running of four compressors) is also increases.Tables-9 show the variations of temperature overlapping (^{o}C) in LTC condenser and ITC evaporator with thermal performances of four stages cascade vapour compression refrigeration system. As temperature overlapping (^{o}C) in LTC condenser and ITC evaporator is increases the overall first law efficiency, exergetic efficiency and high temperature circuit first law efficiency is decreases while exergy destruction ratio of whole system and power required to run whole system (i.e. running of four compressors) is also increases. Table-9(a) shows the effect of ecofriendly Refrigerants in low temperature circuit (LTC) with thermal performances of four stages cascade vapour compression refrigeration system. It

is seen, that the overall first law efficiency and exergetc efficiency, is highest and lowest power required to drive four compressors (whole system) by using R600a and lowest by using ethylene. Table-10(a): shows the effect of ecofriendly Refrigerants in low temperature circuit (MTC) with thermal performances of four stages cascade vapour compression refrigeration system. It is seen, that the overall first law efficiency and exergetc efficiency, is highest and lowest power required to drive four compressors (whole system) by using R1234yf and lowest by using R407C. Tables-11 show the variations of Temperature Overlapping (^oC) in LTC condenser and ITC evaporator with thermal performances of four stages cascade vapour compression refrigeration system. As temperature overlapping(^oC) in LTC condenser and ITC evaporator is increases the overall first law efficiency, exergetic efficiency and high temperature circuit first law efficiency is decreases while exergy destruction ratio of whole system and power required to run whole system (i.e. running of four compressors) is also increases. Tables- 12 shows the variations of Effect of ecofriendly refrigerants in the HTC condenser with thermal performances of four stages cascade vapour compression refrigeration system. And found that using R152a in HTC condenser, the overall first law efficiency, exergetic efficiency and high temperature circuit first law efficiency is maximum while exergy destruction ratio of whole system and power required to run whole system (i.e. running of four compressors) is minimum as compared to R1234ze in high temperature circuit. The highest thermodynamic performances were achieved by using R717 in high temperature condenser as compared to R152a and R1234ze. Similarly power required by using R717 is lowest. The comparison were made for various systems by using R1234yf in high temperature circuit and HFC in MTC and ITC circuit and results are shown in table-13(a) to table-13(d) respectively. Tables- 12 shows the variations of effect of ecofriendly refrigerants in the MTC condenser with thermal performances of four stages cascade vapour compression refrigeration system and found that using R245a in MTC condenser gives maximum the overall first law efficiency ,exergetic efficiency and high temperature circuit first law efficiency is while exergy destruction ratio of whole system and power required to run whole system (i.e. running of four compressors) is minimum as compared to R227 ea in medium temperature circuit (MTC). The thermodynamic performances were slightly less by using R236fa in medium temperature condenser as compared to R245fa. Similarly power required by using R245fa is lowest. It was also observed that thermal performances of four stages cascade refrigeration system is for better than using HFO-1234yf in high temperature circuit and R134a in ITC and R404a in LTC.

Table 1: Effect of HTC condenser temperature on the first and second law thermal Performance of four stages cascade vapour compression refrigeration using eco-friendly refrigerants (System-1: R1234ze in HTC, R1234yf in MTC, R134a in ITC & R404a in LTC)

HTC Condenser Temp (^0C)	COP_{Over_all}	Exergy Destruction Ratio (EDR_{System})	Exergetc Efficiency	COP_{HTC}	COP_{MTC}	COP_{ITC}	COP_{LTC}	Exergy of Fuel (kW)	Exergy of Product (kW)
35	0.3144	4.847	0.1710	7.911	2.983	2.021	1.163	556.7	95.21
40	0.3036	5.055	0.1652	6.374	2.983	2.021	1.163	576.5	95.21
42	0.2992	5.140	0.1628	5.890	2.983	2.021	1.163	588.8	95.21
44	0.2949	5.234	0.1604	5.461	2.983	2.021	1.163	593.5	95.21
45	0.2927	5.181	0.1592	5.264	2.983	2.021	1.163	598.6	95.21
50	0.2816	5.528	0.1532	4.421	2.983	2.021	1.163	621.5	95.21
55	0.2702	5.802	0.1470	3.758	2.983	2.021	1.163	647.6	95.21
60	0.2585	6.111	0.1406	3.209	2.983	2.021	1.163	677.0	95.21

Table 2: Effect of HTC evaporator temperature on the first and second law thermal Performance of four stages cascade vapour compression refrigeration using eco-friendly refrigerants(System-1: R1234ze in HTC, R1234yf in MTC, R134a in ITC & R404a in LTC)

HTC Evaporator Temp (^oC)	COP_{Over_all}	Exergy Destruction Ratio (EDR_{System})	Exergetc Efficiency	COP_{HTC}	COP_{MTC}	COP_{ITC}	COP_{LTC}	Exergy of Fuel (kW)	Exergy of Product (kW)
-20	0.2666	5.896	0.1450	1.86	8.961	2.021	1.163	656.5	95.21
-15	0.2719	5.760	0.1479	2.117	6.998	2.021	1.163	643.6	95.21
-10	0.2762	5.654	0.1503	2.42	5.681	2.021	1.163	633.5	95.21
-5	0.2794	5.578	0.1520	2.78	4.731	2.021	1.163	626.3	95.21
0	0.2814	5.531	0.1531	3.215	4.011	2.021	1.163	621.8	95.21
5	0.2822	5.514	0.1535	3.750	3.444	2.021	1.163	620.2	95.21
10	0.2816	5.528	0.1532	4.421	2.983	2.021	1.163	621.5	95.21
15	0.2795	5.576	0.1521	5.287	2.60	2.021	1.163	326.1	95.21
20	0.2759	5.661	0.1501	6.446	2.273	2.021	1.163	634.2	95.21

Table 3: Effect of MTC evaporator temperature on the first and second law thermal Performance of four stages cascade vapour compression refrigeration using eco-friendly refrigerants (System-1: R1234ze in HTC, R1234yf in MTC, R134a in ITC & R404a in LTC)

MTC Evaporator Temp (^oC)	COP_{Over_all}	Exergy Destruction Ratio (EDR_{System})	Exergetc Efficiency	COP_{HTC}	COP_{MTC}	COP_{ITC}	COP_{LTC}	Exergy of Fuel (kW)	Exergy of Product (kW)
-20	0.2806	5.552	0.1526	4.421	4.103	1.641	1.163	623.8	95.21
-25	0.2816	5.528	0.1532	4.421	3.479	1.818	1.163	621.5	95.21
-26	0.2817	5.525	0.1532	4.421	3.371	1.856	1.163	621.3	95.21

-27	0.2817	5.525	0.1533	4.421	3.268	1.895	1.163	621.2	95.21
-28	0.2817	5.525	0.1533	4.421	3.144	1.936	1.163	621.2	95.21
-29	0.2817	5.526	0.1532	4.421	3.014	1.978	1.163	621.3	95.21
-30	0.2816	5.528	0.1532	4.421	2.983	2.021	1.163	621.5	95.21
-31	0.2814	5.531	0.1531	4.421	2.896	2.066	1.163	621.8	95.21
-32	0.2813	5.535	0.1530	4.421	2.812	2.112	1.163	622.2	95.21
-33	0.2811	5.54	0.1529	4.421	2.732	2.160	1.163	622.6	95.21
-34	0.2808	5.545	0.1528	4.421	2.654	2.209	1.163	623.2	95.21
-35	0.2805	5.552	0.1526	4.421	2.580	2.260	1.163	623.8	95.21
-40	0.2785	5.60	0.1515	4.421	2.247	2.545	1.163	628.4	95.21
-45	0.2755	5.672	0.1499	4.421	1.967	2.891	1.163	635.2	95.21
-50	0.2715	5.769	0.1477	4.421	1.729	3.323	1.163	644.5	95.21

Table 4: Effect of ITC evaporator temperature on the first and second law thermal Performance of four stages cascade vapour compression refrigeration using eco-friendly refrigerants(System-1: R1234ze in HTC, R1234yf in MTC, R134a in ITC & R404a in LTC)

ITC Evaporator Temp (^oC)	COP_{Over_all}	Exergy Destruction Ratio (EDR_{System})	Exergetc Efficiency	COP_{HTC}	COP_{MTC}	COP_{ITC}	COP_{LTC}	Exergy of Fuel (kW)	Exergy of Product (kW)
-70	0.2657	7.041	0.1244	4.421	1.729	4.867	0.9601	658.5	81.90
-75	0.2691	6.359	0.1359	4.421	1.729	3.984	1.055	650.4	88.38
-80	0.2715	5.769	0.1477	4.421	1.729	3.323	1.163	644.5	95.21
-85	0.2732	5.256	0.1598	4.421	1.729	2.810	1.289	640.6	102.4
-86	0.2734	5.162	0.1623	4.421	1.729	2.721	1.316	640.1	103.9
-87	0.2736	5.07	0.1647	4.421	1.729	2.635	1.345	639.6	105.4
-88	0.2738	4.98	0.1672	4.421	1.729	2.554	1.374	639.3	106.9
-89	0.2739	4.898	0.1697	4.421	1.729	2.476	1.405	639.0	108.4
-90	0.2739	4.809	0.1722	4.421	1.729	2.40	1.436	638.8	110.0
-95	0.2738	4.418	0.1846	4.421	1.729	2.067	1.613	639.2	118.0
-100	0.2737	4.076	0.1970	4.421	1.729	1.790	1.828	641.8	126.4

Table 5: Effect of LTC evaporator temperature on the first and second law thermal Performance of four stages cascade vapour compression refrigeration using eco-friendly refrigerants (System-1: R1234ze in HTC, R1234yf in MTC, R134a in ITC & R404a in LTC)

LTC Evaporator Temp (^oC)	COP_{Over_all}	Exergy Destruction Ratio (EDR_{System})	Exergetc Efficiency	COP_{MTC}	COP_{MTC}	COP_{ITC}	COP_{LTC}	Exergy of Fuel (kW)	Exergy of Product (kW)
-120	0.3490	4.267	0.1893	4.421	1.729	3.323	1.868	501.5	95.21
-125	0.3224	4.702	0.1754	4.421	1.729	3.323	1.589	542.8	95.21
-130	0.2966	5.198	0.1613	4.421	1.729	3.323	1.358	590.1	95.21
-1355	0.2715	5.769	0.1477	4.421	1.729	3.323	1.163	644.5	95.21
-140	0.2474	6.431	0.1346	4.421	1.729	3.323	0.9972	707.5	95.21

Table 6: Effect of temperature overlapping between MTC condenser and HTC cascade evaporator on the first and second law thermal Performance of four stages cascade vapour compression refrigeration using eco-friendly refrigerants(System-1: R1234ze in HTC, R1234yf in MTC, R134a in ITC & R404a in LTC)

Temp Overlapping (^oC) in MTC	COP_{Over_all}	Exergy Destruction Ratio (EDR_{System})	Exergetc Efficiency	COP_{MTC}	COP_{MTC}	COP_{ITC}	COP_{LTC}	Exergy of Fuel (kW)	Exergy of Product (kW)
0	0.3018	5.09	0.1642	4.421	2.204	3.323	1.163	579.8	95.21
2	0.2928	5.214	0.1609	4.421	2.098	3.323	1.163	591.6	95.21
4	0.2897	5.344	0.1576	4.421	1.998	3.323	1.163	604.0	95.21
5	0.2867	5.411	0.1560	4.421	1.951	3.323	1.163	610.4	95.21
6	0.2837	5.479	0.1543	4.421	1.904	3.323	1.163	616.9	95.21
8	0.2776	5.621	0.1510	4.421	1.814	3.323	1.163	630.3	95.21
10	0.2715	5.769	0.1477	4.421	1.729	3.323	1.163	644.5	95.21
12	0.2654	5.925	0.1444	4.421	1.648	3.323	1.163	659.3	95.21
14	0.2593	6.088	0.1411	4.421	1.57	3.323	1.163	674.9	95.21
15	0.2562	6.173	0.1394	4.421	1.533	3.323	1.163	683.0	95.21

Table 7: Effect of temperature overlapping between ITC condenser and MTC cascade evaporator on the first and second law thermal Performance of four stages cascade vapour compression refrigeration using eco-friendly refrigerants(System-1: R1234ze in HTC, R1234yf in MTC, R134a in ITC & R404a in LTC)

Temp Overlapping (°C) in ITC	$COP_{_Over_all}$	Exergy Destruction Ratio ($EDR_{_System}$)	Exergetc Efficiency	$COP_{_HTC}$	$COP_{_MTC}$	$COP_{_ITC}$	$COP_{_LTC}$	Exergy of Fuel (kW)	Exergy of Product (kW)
0	0.2959	5.212	0.1610	4.421	1.729	4.613	1.163	591.4	95.21
2	0.2908	5.32	0.1582	4.421	1.729	4.291	1.163	601.7	95.21
4	0.2859	5.429	0.1555	4.421	1.729	4.006	1.163	612.1	95.21
5	0.2834	5.485	0.1542	4.421	1.729	3.876	1.163	617.4	95.21
6	0.2810	5.541	0.1529	4.421	1.729	3.753	1.163	622.7	95.21
8	0.2762	5.654	0.1503	4.421	1.729	3.527	1.163	633.5	95.21
10	0.2715	5.769	0.1477	4.421	1.729	3.323	1.163	644.5	95.21
12	0.2669	5.886	0.1452	4.421	1.729	3.138	1.163	655.6	95.21
14	0.2624	6.006	0.1427	4.421	1.729	2.97	1.163	667.0	95.21
15	0.2601	6.066	0.1415	4.421	1.729	2.891	1.163	672.8	95.21

Table 8: Effect of temperature overlapping between LTC condenser and ITC cascade evaporator on the first and second law thermal Performance of four stages cascade vapour compression refrigeration using eco-friendly refrigerants(System-1: R1234ze in HTC, R1234yf in MTC, R134a in ITC & R404a in LTC)

Temp Overlapping (°C) in LTC condenser & ITC evap	$COP_{_Over_all}$	Exergy Destruction Ratio ($EDR_{_System}$)	Exergetc Efficiency	$COP_{_HTC}$	$COP_{_MTC}$	$COP_{_ITC}$	$COP_{_LTC}$	Exergy of Fuel (kW)	Exergy of Product (kW)
0	0.3057	5.012	0.1663	4.421	1.729	3.323	1.446	572.4	95.21
2	0.2985	5.158	0.1624	4.421	1.729	3.323	1.374	586.2	95.21
4	0.2915	5.306	0.1586	4.421	1.729	3.323	1.316	600.4	95.21
5	0.288	5.381	0.1557	4.421	1.729	3.323	1.289	607.5	95.21
6	0.2847	5.457	0.1549	4.421	1.729	3.323	1.262	614.8	95.21
8	0.2780	5.612	0.1513	4.421	1.729	3.323	1.211	629.5	95.21
10	0.2715	5.769	0.1477	4.421	1.729	3.323	1.163	644.5	95.21
12	0.2552	5.930	0.1443	4.421	1.729	3.323	1.118	659.8	95.21
14	0.2591	6.094	0.1410	4.421	1.729	3.323	1.075	675.4	95.21
15	0.2561	6.178	0.1393	4.421	1.729	3.323	1.055	683.4	95.21

Table 9(a): Effect of ecofriendly refrigerants in low temperature circuit (LTC) on the first and second law thermal Performance of four stages cascade vapour compression refrigeration using eco-friendly refrigerants

Ecofriendly Refrigerants in LTC	$COP_{_Over_all}$	Exergy Destruction Ratio ($EDR_{_System}$)	Exergetc Efficiency	$COP_{_HTC}$	$COP_{_MTC}$	$COP_{_ITC}$	$COP_{_LTC}$	Exergy of Fuel (kW)	Exergy of Product (kW)
R404a	0.2715	5.679	0.1477	4.421	2.204	3.323	1.163	644.9	95.21
R290	0.2761	5.658	0.1502	4.421	2.098	3.323	1.196	633.9	95.21
R600a	0.2811	5.539	0.1529	4.421	1.998	3.323	1.234	622.6	95.21
R600	0.2802	5.559	0.1525	4.421	1.951	3.323	1.228	624.6	95.21
Ethylene	0.2651	5.935	0.1442	4.421	1.904	3.323	1.117	660.2	95.21

Table 9(b): Effect of ecofriendly refrigerants in low temperature circuit (LTC) on the power consumed by the compressors and total power consumed by whole system using four stages cascading vapour compression refrigeration cycle.

Ecofriendly Refrigerants in LTC	Total power consumed by whole system (kW)	Work done by HTC compressor $W_{_Comp}$ (kW)	Work done by MTC compressor $W_{_Comp}$ (kW)	Work done by ITC compressor $W_{_Comp}$ (kW)	Work done by LTC compressor $W_{_Comp}$ (kW)	Exergy of Fuel (kW)	Exergy of Product (kW)
R404a	644.9	151.2	244.9	97.95	150.5	644.9	95.21
R290	633.9	149.2	241.7	96.69	146.3	633.9	95.21
R600a	622.6	147.1	238.3	95.33	141.8	622.6	95.21
R600	624.6	147.5	238.9	95.56	142.5	624.6	95.21
Ethylene	660.2	154.1	249.6	99.83	156.7	660.2	95.21

Table 10(a): Ecofriendly Refrigerants in *medium temperature circuit (*MTC) on *the first and second law thermal Performance of four stages cascade vapour compression refrigeration using eco-friendly refrigerants*

Ecofriendly Refrigerants in MTC	$COP_{_Over_all}$	Exergy Destruction Ratio ($EDR_{_System}$)	Exergetc Efficiency	$COP_{_HTC}$	$COP_{_MTC}$	$COP_{_ITC}$	$COP_{_LTC}$	Exergy of Fuel (kW)	Exergy of Product (kW)
R1234yf	0.2959	5.212	0.1610	4.421	1.729	4.613	1.163	591.4	95.21
R32	0.2908	5.32	0.1582	4.421	1.729	4.291	1.163	601.7	95.21
R152a	0.2859	5.429	0.1555	4.421	1.729	4.006	1.163	612.1	95.21
R410a	0.2834	5.485	0.1542	4.421	1.729	3.876	1.163	617.4	95.21
R407c	0.2810	5.541	0.1529	4.421	1.729	3.753	1.163	622.7	95.21

Table 10(b): Effect of Ecofriendly Refrigerants in medium temperature circuit (MTC) on the power consumed by the compressors and total power consumed by whole system using four stages cascading vapour compression refrigeration cycle

Ecofriendly Refrigerants in MTC	Total power consumed by whole system (kW)	Work done by HTC compressor $W_{_Comp}$ (kW)	Work done by MTC compressor $W_{_Comp}$ (kW)	Work done by ITC compressor $W_{_Comp}$ (kW)	Work done by LTC compressor $W_{_Comp}$ (kW)	Exergy of Fuel (kW)	Exergy of Product (kW)
R1234yf	624.5	147.5	238.9	95.56	142.5	624.5	95.21
R32	609.9	144.8	227.1	95.56	142.5	609.9	95.21
R152a	594.0	141.9	214.1	95.56	142.5	594.0	95.21
R410a	610.0	144.8	227.2	95.56	142.5	610.0	95.21
R407c	649.9	152.2	259.6	95.56	142.5	649.9	95.21

Table 11(a): Effect of Ecofriendly Refrigerants in ITC on the first and second law thermal Performance of four stages cascade vapour compression refrigeration using eco-friendly refrigerants

Ecofriendly Refrigerants in ITC	$COP_{_Over_all}$	Exergy Destruction Ratio ($EDR_{_System}$)	Exergetc Efficiency	$COP_{_HTC}$	$COP_{_MTC}$	$COP_{_ITC}$	$COP_{_LTC}$	Exergy of Fuel (kW)	Exergy of Product (kW)
R134a	0.2802	5.559	0.1525	4.421	1.729	3.323	1.228	624.5	95.21
R410a	0.280	5.585	0.1523	4.421	1.729	3.313	1.228	625.0	95.21
R407c	0.2568	6.158	0.1397	4.421	1.729	3.539	1.228	681.5	95.21
R125	0.2787	5.595	0.1516	4.421	1.729	3.262	1.228	627.9	95.21
R507a	0.2793	5.581	0.1520	4.421	1.729	3.286	1.228	626.6	95.21
R236fa	0.2803	5.559	0.1525	4.421	1.729	3.323	1.228	624.4	95.21
R245fa	0.2805	5.553	0.1526	4.421	1.729	3.333	1.228	623.9	95.21

Table 11(b): Effect of Ecofriendly Refrigerants in intermediate temperature circuit (ITC) on the power consumed by the compressors and total power consumed by whole system using four stages cascading vapour compression refrigeration cycle.

Ecofriendly Refrigerants in ITC	Total power consumed by whole system (kW)	Work done by HTC compressor $W_{_Comp}$ (kW)	Work done by MTC compressor $W_{_Comp}$ (kW)	Work done by ITC compressor $W_{_Comp}$ (kW)	Work done by LTC compressor $W_{_Comp}$ (kW)	Exergy of Fuel (kW)	Exergy of Product (kW)
R134a	624.5	147.5	238.9	95.95	142.5	624.5	95.21
R410a	625.0	147.6	239.1	95.85	142.5	625.0	95.21
R407c	681.5	158.0	256.0	125.0	142.5	681.5	95.21
R125	627.9	148.1	239.9	97.33	142.5	627.9	95.21
R507a	626.6	147.9	239.5	96.64	142.5	626.6	95.21
R236fa	624.4	147.5	238.9	95.54	142.5	624.4	95.21
R245fa	623.9	147.4	238.7	95.26	142.5	623.9	95.21

Table 12(a) : Effect of HTC condenser ecofriendly refrigerants on the first and second law thermal performance of four stages cascade vapour compression refrigeration using eco-friendly refrigerants

Ecofriendly Refrigerants in HTC	$COP_{_Over_all}$	Exergy Destruction Ratio ($EDR_{_System}$)	Exergetc Efficiency	$COP_{_HTC}$	$COP_{_MTC}$	$COP_{_ITC}$	$COP_{_LTC}$	Exergy of Fuel (kW)	Exergy of Product (kW)
R1234ze	0.2715	5.769	0.1477	4.421	1.729	3.323	1.228	644.5	95.21
R152a	0.2749	5.687	0.1494	4.661	1.729	3.313	1.228	636.7	95.21
R717	0.2764	5.649	0.1504	4.782	1.729	3.539	1.228	633.0	95.21

.

Table 12(b): Effect of Ecofriendly Refrigerants in high temperature circuit (HTC) on the power consumed by the compressors and total power consumed by whole system using four stages cascading vapour compression refrigeration cycle

Ecofriendly Refrigerants in HTC	Total power consumed by whole system (kW)	Work done by HTC compressor $W_{_Comp}$ (kW)	Work done by MTC compressor $W_{_Comp}$ (kW)	Work done by ITC compressor $W_{_Comp}$ (kW)	Work done by LTC compressor $W_{_Comp}$ (kW)	Exergy of Fuel (kW)	Exergy of Product (kW)
R1234ze	644.5	151.2	244.9	97.95	150.5	644.5	95.21
R152a	636.7	143.4	244.9	97.95	150.5	636.7	95.21
R717	633.0	139.8	244.9	244.9	150.5	633.0	95.21

Table 13: Thermal performance of four stages cascade vapour compression refrigeration using eco-friendly refrigerants HFO-1234yf in HTC ecofriendly refrigerants in MTC & R134a in ITC and R404a in LTC for evaporator temperature of -135°C

Eco Friendly Refrigerants	$COP_{_Over_all}$	Exergy Destruction Ratio ($EDR_{_System}$)	Exergetc Efficiency	$COP_{_HTC}$	$COP_{_MTC}$	$COP_{_ITC}$	$COP_{_LTC}$	Exergy of Fuel (kW)	Exergy of Product (kW)
R227ea	0.2563	6.171	0.1395	4.2019	1.572	3.323	1.163	682.7	95.21
R236fa	0.2688	5.837	0.1463	4.2019	1.737	3.323	1.163	650.9	95.21
R245fa	0.2798	5.569	0.1522	4.2019	1.898	3.323	1.163	625.4	95.21

Table 13(b): Thermal performance of four stages cascade vapour compression refrigeration using eco-friendly refrigerants R1234yf in HTC-Eco friendly Ref in MTC –R134a in ITC –R404a in LTC

Eco Friendly Refrigerants	Total power consumed by whole system (kW)	Work done by HTC compressor $W_{_Comp}$ (kW)	Work done by MTC compressor $W_{_Comp}$ (kW)	Work done by ITC compressor $W_{_Comp}$ (kW)	Work done by LTC compressor $W_{_Comp}$ (kW)	Exergy of Fuel (kW)	Exergy of Product (kW)
R227ea	682.7	164.9	269.4	97.95	150.5	682.7	95.21
R236fa	650.9	158.8	243.7	97.95	150.5	650.9	95.21
R245fa	625.4	158.9	223.1	97.95	150.5	625.4	95.21

Table 13(c): Thermal performance of four stages cascade vapour compression refrigeration using eco-friendly refrigerants HFO-1234ze in HTC-Eco friendly Ref in MTC –R134a in ITC –R404a in LTC

Eco Friendly Refrigerants	$COP_{_Over_all}$	Exergy Destruction Ratio ($EDR_{_System}$)	Exergetc Efficiency	$COP_{_HTC}$	$COP_{_MTC}$	$COP_{_ITC}$	$COP_{_LTC}$	Exergy of Fuel (kW)	Exergy of Product (kW)
R227ea	0.2594	6.085	0.1412	4.421	1.572	3.323	1.163	682.7	95.21
R236fa	0.2721	5.754	0.1481	4.421	1.737	3.323	1.163	650.9	95.21
R245fa	0.2833	5.489	0.1541	4.421	1.898	3.323	1.163	625.4	95.21

Table 13(d): Thermal performance of four stages cascade vapour compression refrigeration using eco-friendly refrigerants R1234ze in HTC-Eco friendly Ref in MTC –R134a in ITC –R404a in LTC

Eco Friendly Refrigerants	Total power consumed by whole system (kW)	Work done by HTC compressor $W_{_Comp}$ (kW)	Work done by MTC compressor $W_{_Comp}$ (kW)	Work done by ITC compressor $W_{_Comp}$ (kW)	Work done by LTC compressor $W_{_Comp}$ (kW)	Exergy of Fuel (kW)	Exergy of Product (kW)
R227ea	674.5	156.7	269.4	97.95	150.5	682.7	95.21
R236fa	674.5	150.9	243.7	97.95	150.5	650.9	95.21
R245fa	617.8	146.3	223.1	97.95	150.5	625.4	95.21

Table 14: First and second law thermal Performance of four stages cascade vapour compression refrigeration using eco-friendly refrigerants

Systems	COP_{Over_all}	Exergy Destruction Ratio ($EDR_{_System}$)	Exergetc Efficiency	$COP_{_HTC}$	$COP_{_MTC}$	$COP_{_ITC}$	$COP_{_LTC}$	Exergy of Fuel (kW)	Exergy of Product (kW)
System-1	0.2816	5.528	0.1532	4.421	2.983	2.021	1.163	621.5	95.21
System-2	0.2863	5.420	0.1558	4.421	2.983	2.021	1.196	611.2	95.21
System-3	0.2916	5.304	0.1586	4.421	2.983	2.021	1.234	600.2	95.21
System-4	0.2907	5.324	0.1581	4.421	2.983	2.021	1.228	602.1	95.21
System-5	0.2748	5.689	0.1495	4.421	2.983	2.021	1.117	636.8	95.21

Table-14: shows the First and second law thermal Performance of four stages cascade vapor compression refrigeration using eco-friendly refrigerants and found that system-3 is better systems than system-5.

3. Conclusions

The following conclusions were drawn from present investigations.

- The system-3 (using R1234ze in HTC, R1234yf in MTC, R134a in ITC & R600a in LTC) gives better first law efficiency and system-5 gives lowest thermodynamic performance system -5 using R1234ze in HTC, R1234yf in MTC, R134a in ITC & ethylene in LTC.
- Thermodynamic performances of system-1 using R1234ze in HTC, R1234yf in MTC, R134a in ITC &R404a in LTC is slightly less than the system-3 (using R1234ze in HTC, R1234yf in MTC, and R134a in ITC &R600a in LTC).
- Thermodynamic performances using HFO-1234yf in HTC is lower than using HFO-1234ze in high temperature condenser and HFC in MTC & ITC circuits.
- R245fa gives better thermodynamic performance as compared to HFC-134a and HFO-1234yf.

References

[1] S. M. Zubair [1999] "Performance Evaluation of Vapour Compression System", International Journal of Refrigeration, vol. 22, pp. 235-243,

[2] R. Cabello, J. Navarro, E. Torrella , [2005]" Simplified Steady-State Modelling of a Single Stage Vapour Compression Plant. Model Development and Validation", Applied Thermal Engineering, vol. 25, pp. 1740–1752, 2005

[3] A. Kilicarslan, [2004] "An Experimental Investigation of a Different Type Vapor Compression Cascade Refrigeration System", Applied Thermal Engineering, vol. 24, pp. 2611–2626..

[4] S. Bhattacharyya, S. Bose, J. Sarkar, [20087] "Exergy Maximization of Cascade Refrigeration Cycles and Its Numerical Verification for a Transcritical CO2-C3H8 System", International Journal of Refrigeration, vol. 30, pp. 624-632,

[5] H.M. Getu, P.K. Bansal, [2008] "Thermodynamic Analysis of an R744–R717 Cascade Refrigeration System", International Journal of Refrigeration, vol. 31, pp. 45-54,

[6] T.S. Lee, C.H. Liu, T.W. Chen, [2006] "Thermodynamic Analysis of Optimal Condensing Temperature of Cascade-Condenser in CO2/NH3 cascadeRefrigeration Systems", International Journal of Refrigeration, vol. 29, pp. 1100-1108,

[7] S. Bhattacharyya, S. Mukhopadhyay, J. Sarkar, [2008] "CO2–C3H8 Cascade Refrigeration–Heat Pump System: Heat Exchanger Inventory Optimization and Its Numerical Verification", International Journal of Refrigeration, vol. 31, pp. 1207-1213,

[8] J. M. Calm, (2008) "The Next Generation of Refrigerants – Historical Review, Considerations, and Outlook", International Journal of Refrigeration, vol. 31, pp. 1123-1133.

[9] R.S. Mishra [2013] Thermodynamic analysis of three stages cascade vapour compression refrigeration system for biomedical applications, Journal of Multi Disciplinary Engineering Technologies Volume 7 No.1, page-27-35.

Cite this article as: R.S.Mishra, Thermal modelling and optimization of four stages cascade vapor compression refrigeration systems for ultra-low temperature applications, International Journal of Research in Engineering and Innovation Vol-3, Issue-6 (2019), 408-416. *https://doi.org/10.36037/IJREI.2019.3609*.

International Journal of Research in Engineering and Innovation (IJREI)
journal home page: http://www.ijrei.com
ISSN (Online): 2456-6934

Thermal performance of cascaded vapour compression absorption systems

R.S. Mishra

Department of Mechanical & Production Engineering, Delhi Technological University Delhi, India

Abstract

In this paper, we propose four cascaded half effect, single effect, double effect and triple effect Lithium/Bromide vapour absorption–compression refrigeration systems using fifteen ecofriendly refrigerants such as hydrocarbons, HFC and HFO refrigerants and natural refrigerants to produce cooling capacity at -30 °C. The comparison of four cascaded systems were also carried out at -55ºC using HFC refrigerants with R717 refrigerant. It is found that cascaded vapour compression absorption systems significantly improve first and second law performances as compared to simple vapour absorption refrigeration system.

© 2019 ijrei.com. All rights reserved

Keywords: Cascaded Vapour Absorption Compression Refrigeration Systems, Performance Evaluation.

1. Introduction

The use of vapour absorption refrigeration system is a talented way towards utilizing waste heat from industrial processes. LiBr absorption refrigeration system and ammonia–water absorption refrigeration systems are commonly used for low temperature applications. Even though ammonia–water absorption refrigeration system is commonly used for freezing applications with temperatures lower than 0 °C [10-11].

The performance of NH_3H_2O system has low first law efficiency. When the refrigeration temperature is lower than -25 °C, the thermal performance dramatically decreases. We proposed cascaded half effect, single effect, double effect and triple effect Lithium/Bromide vapour absorption–compression refrigeration systems using fifteen ecofriendly refrigerants such as hydrocarbons, HFC and HFO refrigerants and natural refrigerants to produce cooling capacity at -30 °C.

The comparison of four cascaded systems were also carried out at -55ºC using HFC refrigerants with R717 refrigerant. It is found that cascaded vapour compression absorption systems significantly improve first and second law performances as compared to simple vapour absorption refrigeration systems.

2. Literature Review

A number of research work is devoted to thermodynamic, analyses of vapour absorption refrigeration systems

S.B. Riffat N. Shankland [1] described the integration of different types of absorption systems with vapour-compression systems. The performances of the single-effect and double-effect series and the double-effect parallel continuous absorption systems and their integration with vapour-compression systems have been carried out.

Kaushik and Arora [2-3] carried out the energy and energy analysis of single effect and series flow double effect water–lithium bromide absorption system and developed thermal computational model for parametric investigation. Their analysis involves the effect of generator, absorber and evaporator temperatures on the energetic and energetic performance. They concluded that the irreversibility is highest in the absorber in both systems as compared to other systems

Gomri [4] carried out comparative thermodynamic analysis between single effect and double effect absorption refrigeration systems and developed the computer program using thermodynamic properties based on energy balance equations and found that for each condenser and evaporator temperature, there is an optimum generator temperature where change in energy of single effect and double effect absorption refrigeration system is minimum. They also found that the COP of double effect system is approximately twice the COP of single effect system but there is marginal difference between the energetic efficiency of the system.

Yi Chena, et.al. [5] proposed a new absorption–compression refrigeration system to produce cooling energy at -30 °C to -

Corresponding author: R. S. Mishra
Email Address: hod.mechanical.rsm@dtu.ac.in

40 °C and showed that the coefficient of performance of 0.277, which was approximately 50% higher than that of a conventional two-stage absorption refrigeration system. Fernández–Seara et al. [6] studied a cascade refrigeration system with a CO_2 compression vapour refrigeration system and an NH_3/H_2O absorption system at an evaporation temperature of -45°C. and found its first law efficiency in terms of COP. Garimella and Brown [7] developed a novel cascaded absorption–compression system that coupled a single-effect $LiBr/H_2O$ absorption cycle and a subcritical CO_2 vapor–compression cycle to generate low-temperature refrigerant (-40 °C). Rogdakis and Antonopoulos [8] studied a NH_3/H_2O absorption refrigeration system driven by waste heat and predicted the theoretical COP below 0.40 when the lowest temperature is in the range of -64 °C to -30 °C.

Kilic and Kaynakli [9] carried out first and second law thermodynamic analysis to analyze the performance of a single stage water lithium bromide absorption refrigeration system by varying some working parameters and developed a mathematical model based on energy method and found that the performance of the ARS increases with increasing generator and evaporator temperatures but decreases with increasing condenser and absorber temperatures. Also concluded that the highest energy loss occurs in generator regardless of operating conditions and therefore it is most important component of the system. R.S. Mishra [12] compared three cascade vapour compression systems cascaded with evaporator of LiBr-H_2O vapour absorption refrigeration system cascaded by condenser of vapour compression refrigeration system using ecofriendly refrigerants (i.e. R1234yf, R134a, R-32, R507a, R227ea, R236fa, R245fa , R717) carried out energy and exergy analysis of all three systems and found 122% first law efficiency enhancement using triple effect VARS cascaded with VCRS and 79.45% enhancement in second law efficiency using triple effect VARS cascaded with VCRS. Similarly exergy destruction is 56.60% using triple effect VARS cascaded with VCRS and 25.9% reduction using double effect VARS cascaded with VCRS as compared with single effect. R.S. Mishra [2019] carried out Thermal performances (first law efficiency, exergy destruction ratio & exergetic efficiency) of cascade single effect ammonia-water (NH3-H_20) vapour absorption refrigeration system coupled with vapour compression refrigeration using ecofriendly refrigerants in the low temperature cycle of VCRS system, The combined thermodynamic first law efficiency in terms of coefficient of performance ($COP_{_Overall}$), second law efficiency in terms of exergetic efficiency and exergy destruction ratio working with each of the following refrigerants in the cascaded vapour compression cycle R1234yf, R227ea, R236fa, R245fa, R143a,R134a, R32, R507 operating at (- 223 K) of evaporator temperature with temperature overlapping and evaporator temperature of vapour absorption refrigeration cycle working at 13.5 bar of highest generator pressure and 1.75 bar as lowest evaporator pressure have been presented and it is found thatR141b and R245fa gives better performance.

R.S. Mishra [13] found that the thermodynamic performances in the case of cascaded half effect vapour absorption refrigeration system coupled with vapour compression cycle is improved by 44.6% increment of first law efficiency (i.e. over all COP), 172.87% increment of second law efficiency (i.e. exergetic efficiency) of the half effect vapour absorption refrigeration cascaded with vapour compression cycle using HFC-134a, 42.87% enhancement in first law efficiency (COP) of 142.73% increment of second law efficiency using HFO-1234yf for -50^{o}C of evaporator temperature of VCRS. Similarly 72% reduction in exergy destruction ratio based on exergy of output of the half effect vapour absorption refrigeration cascaded with vapour compression cycle using HFC-134a and 70.4% reduction in exergy destruction ratio using HFO-1234yf ecofriendly refrigerant for -50^{o}C of evaporator temperature of VCRS. The performances of single effect cascaded vapour absorption refrigeration system coupled with vapour compression cycle significantly higher than cascaded half effect vapour absorption refrigeration coupled with vapour compression cycle.

3. Results and Discussions

Performance of four cascaded vapour compression-absorption refrigeration systems have been carried out using following input data.

Table-1(a) shows the thermal performances of simple half effect vapour absorption system with half effect cascade vapour absorption system using R134a,and it was found that Cascaded half effect gives better first law thermodynamic performance (COP) and second law thermodynamic performance in terms of exergetic efficiency than simple half effect vapour absorption refrigeration system. Table-1(b) shows the thermal performances of simple single effect vapour absorption system with single effect cascade vapour absorption system using R134a,and it was found that Cascade single effect gives better first law thermodynamic performance (COP) and second law thermodynamic performance in terms of exergetic efficiency than simple single effect vapour absorption refrigeration system. Table-1(c) shows the thermal performances of simple double effect vapour absorption system with double effect cascade vapour absorption system using R134a,and it was found that Cascade double effect gives better first law thermodynamic performance (COP) and second law thermodynamic performance in terms of exergetic efficiency than simple double effect vapour absorption refrigeration system

Table-1(a): Comparison between performance parameters of simple half effect VARS and half effect VARS with cascading.

Performance Parameters	Simple Half Effect VARS	Half Effect VARS with VCRS cascade using R134a
COP	0.4255	0.7152
EDR	5.419	1.257
Exergetic Efficiency	0.1558	0.4439

Table-1(b): Comparison between performance parameters of simple single effect VARS and single effect VARS with cascading

Performance Parameters	Simple Single Effect VARS	Single Effect VARS with VCRS cascade using R134a
COP	0.7496	1.193
EDR	4.19	1.862
Exergetic Efficiency	0.3628	0.3494

Table-1(c): Comparison between performance parameters of simple double effect VARS and double effect VARS with cascading.

Performance Parameters	Simple Double Effect VARS	Double Effect VARS with VCRS cascade using R134a
COP	1.201	1.781
$EDR_{_Rational}$	2.802	0.4243
Exergetic Efficiency	0.263	0.5757

Table-2: Comparison between performance Parameters of Simple tripple effect VARS and tripple effect VARS with Cascading.

Refrigerants	Simple Tripple Effect VARS	Tripple Effect VARS with VCRS cascade using R134a
COP	1.786	2.432
EDR	2.166	1.05
Exergetic Efficiency	0.3158	0.4879

Table-2 shows the thermal performances of triple effect vapour absorption system. it was found that triple effect gives better first law thermodynamic performance (COP) and second law thermodynamic performance in terms of exergetic efficiency than double effect and single effect & half effect vapour absorption refrigeration systems. Table-3(a) shows the thermal performances of simple half effect vapour absorption system with half effect cascade vapour absorption system using following eco-friendly refrigerants ,and it was found that cascade half effect gives better first law thermodynamic performance (COP) and second law thermodynamic performance in terms of exergetic efficiency than simple half effect vapour absorption refrigeration system the thermodynamic performances (i.e. coefficient of performance (COP) and exergetic efficiency (second law efficiency) using R245fa gives better thermodynamic performances as compared to R134a and R236fa used in cascade vapour compression-absorption refrigeration systems.

The thermodynamic performance performances using R227ea is found to be lowest in vapour -compression-absorption LiBr refrigeration system. Table-3(b) shows the thermal performances of simple single effect vapour absorption system with single effect cascade vapour absorption system using following eco-friendly refrigerants ,and it was found that cascade single effect gives better first law thermodynamic exergetic efficiency of cascaded triple effect vapour absorption-vapour compression refrigeration system is decreasing along with increasing exergy destruction ratio. Similarly the first law efficiency in terms of coefficient of performance (COP_VARS) is decreasing and second law efficiency in terms of exergetic efficiency of the triple effect performance (COP) and second law thermodynamic performance in terms of exergetic efficiency than simple single effect vapour absorption refrigeration system. The thermodynamic performances (i.e. coefficient of performance (COP) and exergetic efficiency (second law efficiency) using R245fa gives better thermodynamic performances as compared to R134a and R236fa used in single effect cascade vapour compression-absorption refrigeration systems. The thermodynamic performance performances using R227ea is found to be lowest in single effect vapour -compression-absorption LiBr refrigeration system. Table-3(c) shows the thermal performances of simple double effect vapour absorption system with double effect cascade vapour absorption system using following eco-friendly refrigerants ,and it was found that cascade double effect gives better first law thermodynamic performance (COP) and second law thermodynamic performance in terms of exergetic efficiency than simple double effect vapour absorption refrigeration system. The thermodynamic performances (i.e. coefficient of performance (COP) and exergetic efficiency (second law efficiency) using R245fa gives better thermodynamic performances as compared to R134a and R236fa used in double effect cascade vapour compression-absorption refrigeration systems. The thermodynamic performance performances using R227ea is found to be lowest in double effect vapour compression-absorption LiBr refrigeration system. Table-3(d) to Table-3(g) show the thermal performances of simple triple effect vapour absorption system with triple effect cascade vapour absorption system using twenty eco-friendly refrigerants ,and it was found that cascade triple effect gives better first law thermodynamic performance (COP) and second law thermodynamic performance in terms of exergetic efficiency than simple triple effect vapour absorption refrigeration system. The thermodynamic performances (i.e. coefficient of performance (COP) and exergetic efficiency (second law efficiency) using R245fa gives better thermodynamic performances as compared to R134a and R236fa used in double effect cascade vapour compression-absorption refrigeration systems. The thermodynamic performance performances using R407c is found to be lowest in triple effect vapour -compression-absorption LiBr refrigeration system. Table-4 shows the effect of condenser/absorber/ temperatures on thermal performances of cascaded vapour compression – triple effect vapour absorption refrigeration system using R134a eco-friendly refrigerants and simple triple effect LiBr vapour absorption refrigeration system and it is found that as condenser/absorber/ temperatures of triple effect vapour absorption is increasing, the first law efficiency in terms of coefficient of performance (COP) is decreasing and second law efficiency in terms of vapour absorption refrigeration system is decreasing along with increasing exergy destruction ratio of triple effect VARS as increasing generator temperature of vapour compression – triple effect vapour absorption refrigeration systemTable-5 shows the effect of generator temperature on thermal performances of cascaded vapour compression – triple effect

vapour absorption refrigeration system using R134a eco-friendly refrigerants and simple triple effect LiBr vapour absorption refrigeration system and it is found that as generator temperature of triple effect vapour absorption is increasing, the first law efficiency in terms of coefficient of performance (COP) is increasing and second law efficiency in terms of exergetic efficiency of cascaded triple effect vapour absorption-vapour compression refrigeration system is decreasing along with increasing exergy destruction ratio. Similarly the first law efficiency in terms of coefficient of performance (COP_VARS) is increasing and second law efficiency in terms of exergetic efficiency of the triple effect vapour absorption refrigeration system is increasing along with increasing exergy destruction ratio of triple effect vapour compression triple effect vapour absorption refrigeration system as increasing generator temperature of vapour compression triple effect vapour absorption refrigeration system. Table-6 shows the effect of evaporator temperature on thermal performances of cascaded vapour compression – triple effect vapour absorption refrigeration system using R134a eco-friendly refrigerants and simple triple effect LiBr vapour absorption refrigeration system and it is found that as evaporator temperature of triple effect vapour absorption is increasing, the first law efficiency in terms of coefficient of performance (COP) and second law efficiency in terms of exergetic efficiency of cascaded triple effect vapour absorption-vapour compression refrigeration system are increasing with increasing exergy destruction ratio . Similarly the first law efficiency in terms of coefficient of performance (COP_VARS) and second law efficiency in terms of exergetic efficiency of the triple effect vapour absorption refrigeration system are increasing with decreasing exergy destruction ratio of triple effect VARS as increasing evaporator temperature of vapour compression triple effect vapour absorption refrigeration system. The optimum exergetic efficiency of triple effect vapour absorption refrigeration system is to be found as 35.4% at 3^{o}C evaporator temperature while optimum exergetic efficiency of cascaded triple effect vapour absorption-compression refrigeration system is to be found as 35.4% at 4^{o}C evaporator temperature while the first law efficiency in terms of coefficient of performance (COP) cascaded system is found at 5^{0} evaporator temperature. Table-7 shows the variation of effectiveness of heat exchanger with first law efficiency, second law efficiency and exergy destruction ratio of triple effect vapour absorption refrigeration system and cascaded vapour compression - triple effect absorption refrigeration system, and it is found that first law efficiency in terms of coefficient of performance (COP) and second law efficiency in terms of exergetic efficiency of vapour absorption refrigeration system are increasing with increasing effectiveness of heat exchanger and exergy destruction ratio of vapour absorption refrigeration system is decreasing with increasing effectiveness of heat exchanger. Similarly that first law efficiency in terms of coefficient of performance (COP) and second law efficiency in terms of exergetic efficiency of cascaded-vapour compression triple stage vapour absorption refrigeration system are increasing with increasing effectiveness of heat exchanger and exergy destruction ratio of cascaded-vapour compression triple stage vapour absorption refrigeration system is decreasing with increasing effectiveness of heat exchanger. Table-8 shows the variation of temperature overlapping (Approach) with first law efficiency, second law efficiency and exergy destruction ratio of triple effect vapour absorption refrigeration system and cascaded vapour compression triple effect absorption refrigeration system, and it is found that first law efficiency in terms of coefficient of performance (COP) and second law efficiency in terms of exergetic efficiency of vapour absorption refrigeration system are decreasing with increasing temperature overlapping (Approach) and exergy destruction ratio of vapour absorption refrigeration system is increasing with increasing temperature overlapping (Approach).

Table-3(a): Comparison between thermal performances various eco-friendly refrigerants in half effect LiBr cascade vapour absorption refrigeration system.

Performance parameters	Simple Half Effect VARS	Half Effect VARS with VCRS cascade using R134a	Half Effect VARS with VCRS cascade using R1234ze	Half Effect VARS with VCRS cascade using R227ea	Half Effect VARS with VCRS cascade using R236fa	Half Effect VARS with VCRS cascade using R245fa
COP	0.4255	0.7152	0.7150	0.7133	0.7173	0.7175
EDR	5.419	1.257	1.291	1.306	1.274	1.237
Exergetic Efficiency	0.1558	0.4439	0.4366	0.4336	0.4398	0.4407

Table-3(b): Comparison between thermal performances various eco-friendly refrigerants in Single effect LiBr cascade vapour absorption refrigeration system.

Performance parameters	Simple Single Effect VARS	Single Effect VARS with VCRS cascade using R134a	Single Effect VARS with VCRS cascade using R1234ze	Single Effect VARS with VCRS cascade using R227ea	Single Effect VARS with VCRS cascade using R236fa	Single Effect VARS with VCRS cascade using R245fa
COP	0.7496	1.193	1.193	1.18	1.189	1.198
EDR	4.19	1.862	1.865	1.972	1.896	1.824
Exergetic Efficiency	0.3628	0.3494	0.3490	0.3378	0.3454	0.3541

Table-3(c): Comparison between thermal performances various eco-friendly refrigerants in Double effect LiBr cascaded vapour absorption refrigeration system.

Performance parameters	Simple Double Effect VARS	Double Effect VARS with VCRS cascade using R134a	Double Effect VARS with VCRS cascade using R1234ze	Double Effect VARS with VCRS cascade using R236fa	Double Effect VARS with VCRS cascade using R245fa
COP	1.201	1.781	1.780	1.773	1.79
$EDR_{_Rational}$	2.802	0.4243	0.4248	0.4294	0.1182
Exergetic Efficiency	0.263	0.5757	0.5752	0.5706	0.5818

Table-3(d): Comparison between thermal performances various eco-friendly refrigerants in triple effect LiBr cascaded vapour absorption refrigeration system

Performance parameters	Simple Tripple Effect VARS	Tripple Effect VARS with VCRS cascade using R134a	Tripple Effect VARS with VCRS cascade using R1234ze	Tripple Effect VARS with VCRS cascade using R245fa	Tripple Effect VARS with VCRS cascade using R236fa	Tripple Effect VARS with VCRS cascade using R227ea
COP	1.786	2.432	2.431	2.447	2.419	2.391
EDR	2.166	1.05	1.052	1.025	1.071	1.122
Exergetic Efficiency	0.3158	0.4879	0.4874	0.4939	0.4827	0.4718

Table-3(e): Comparison between thermal performances various eco-friendly refrigerants in triple effect LiBr cascade vapour absorption refrigeration system.

Performance parameters	R404a	R410a	R407c	R290	R600a	R600	R507a
COP	2.384	2.425	2.291	2.428	2.431	2.445	2.401
EDR	1.135	1.061	1.315	1.056	1.051	1.027	1.105
Exergetic Efficiency	0.4684	0.4851	0.4320	0.4863	0.4875	0.4933	0.4751

Table-3(f): Comparison between thermal performances various eco-friendly refrigerants in triple effect LiBr cascade vapour absorption refrigeration system.

Performance parameters	R123	R143a	R141b	R744	R717	R125	R1234yf
COP	2.455	2.406	2.469	2.299	2.429	2.381	2.420
EDR	1.01	1.096	0.9864	1.297	1.055	1.141	1.055
Exergetic Efficiency	0.4975	0.4773	0.4034	0.4353	0.4856	0.4670	0.4870

Table-3(g): Comparison between thermal performances various eco-friendly refrigerants in triple effect LiBr cascade vapour absorption refrigeration system.

Performance parameters	R134a	R1234ze	R245fa	R236fa	R227ea	R152a	R32
COP	2.432	2.431	2.447	2.419	2.391	2.446	2.418
EDR	1.05	1.052	1.025	1.071	1.122	1.026	1.073
Exergetic Efficiency	0.4879	0.4874	0.4939	0.4827	0.4718	0.4936	0.4823

Table-4: Effect of condenser/Absorber on thermal performances using R134a eco-friendly refrigerants in triple effect LiBr cascade vapour absorption refrigeration system.

Effect of condenser/Absorber Temperature	$COP_{_VARS}$	$EDR_{_VARS}$	Exergetic Efficiency	$COP_{_Cascade}$	$EDR_{Cascade}$	Exergetic $Efficiency_{_Cascade}$	$COP_{_VCRS}$
30	1.786	2.160	0.3158	1.998	1.044	0.4892	2.402
35	1.479	2.825	0.2614	1.758	1.212	0.4521	2.402

Table-5: Effect of generator temperature on thermal performances using R134a eco-friendly refrigerants in triple effect LiBr cascaded vapour absorption refrigeration system.

Effect of Generator Temperature	$COP_{_VARS}$	$EDR_{_VARS}$	Exergetic Efficiency	$COP_{_Cascade}$	$EDR_{Cascade}$	Exergetic efficiency_ Cascade	COP VCRS
170	1.769	2.058	0.3270	1.986	1.017	0.4958	2.402
175	1.780	2.110	0.3215	1.993	1.030	0.4926	2.402
180	1.786	2.166	0.3158	1.998	1.044	0.4892	2.402
185	1.790	2.225	0.3101	2.011	1.059	0.4856	2.402
190	1.792	2.286	0.3043	2.003	1.075	0.4820	2.402
195	1.793	2.349	0.2986	2.003	1.091	0.4783	2.402
200	1.792	2.413	0.293	2.003	1.107	0.4746	2.402

Table-6: Effect of evaporator temperature on thermal performances using R134a eco-friendly refrigerants in triple effect LiBr cascaded vapour absorption refrigeration system.

Effect of evaporator Temperature	COP_{VARS}	EDR_{VARS}	Exergetic Efficiency	$COP_{Cascade}$	$EDR_{Cascade}$	Exergetic Efficiency_Cascade	COP VCRS Decreasing
0	1.233	2.081	0.3299	1.636	1.128	0.470	2.916
1	1.348	1.898	0.3451	1.736	1.066	0.4841	2.844
2	1.442	1.838	0.3524	1.810	1.032	0.4921	2.774
3	1.520	1.825	0.3540	1.865	1.015	0.4962	2.706
4	1.586	1.845	0.3515	1.908	1.01	0.4976	2.641
5	1.644	1.892	0.3458	1.989	1.012	0.4971	2.579
6	1.696	1.962	0.3376	1.964	1.019	0.4953	2.518
7	1.743	2.053	0.3275	1.983	1.030	0.4926	2.459
8	1.786	2.166	0.3158	1.998	1.044	0.4892	2.402
9	1.826	2.302	0.3028	2.010	1.061	0.4852	2.347
10	1.864	2.464	0.2887	2.019	1.08	0.4808	2.294
15	2.028	3.86	0.2058	2.037	1.197	0.4553	2.050

Table-7: Effect of Heat Exchanger Effectiveness on thermal performances using R134a eco-friendly refrigerants in triple effect LiBr cascaded vapour absorption refrigeration system.

Effect of Heat Exchanger Effectiveness	COP_{VARS}	EDR_{VARS}	Exergetic Efficiency	$COP_{Cascade}$	$EDR_{Cascade}$	Exergetic $Efficiency_{Cascade}$	COP_{VCRS}
0.40	1.719	2.291	0.3039	1.948	1.076	0.4817	2.402
0.45	1.752	2.228	0.3097	1.973	1.060	0.4854	2.402
0.50	1.786	2.166	0.3158	1.998	1.044	0.4892	2.402
0.55	1.822	2.104	0.3222	2.025	1.028	0.4930	2.402
0.60	1.86	2.041	0.3288	2.051	1.012	0.4969	2.402
0.65	1.818	1.979	0.3356	2.079	0.9966	0.5008	2.402

Table-8: Effect of temperature overlapping (Approach) on thermal performances using R134a eco-friendly refrigerant in triple effect LiBr cascaded vapour absorption refrigeration system.

Approach	COP_{VARS}	EDR_{VARS}	Exergetic Efficiency	$COP_{Cascade}$ Decreasing	$EDR_{Cascade}$ increasing	Exergetic $Efficiency_{Cascade}$ Decreasing	COP VCRS Decreasing
0	1.786	2.166	0.3158	1.998	1.044	0.4892	2.402
2.5	1.786	2.166	0.3158	1.957	1.132	0.4691	2.268
5.0	1.786	2.166	0.3158	1.916	1.222	0.450	2.144
7.5	1.786	2.166	0.3158	1.876	1.317	0.4317	2.028
10	1.786	2.166	0.3158	1.837	1.815	0.4141	1.920
12.5	1.786	2.166	0.3158	1.799	1.518	0.3972	1.819
15	1.786	2.166	0.3158	1.762	1.625	0.3810	1.724

4. Conclusion

The following conclusions were drawn from present investigations.

(i) Triple effect gives better first law thermodynamic performance (COP) and second law thermodynamic performance in terms of exergetic efficiency than double effect and single effect & half effect vapour absorption refrigeration systems.

(ii) Cascaded half effect gives better first law thermodynamic performance (COP) and second law thermodynamic performance in terms of exergetic efficiency than simple half effect vapour absorption refrigeration system.

(iii) Cascaded single effect gives better first law thermodynamic performance (COP) and second law thermodynamic performance in terms of exergetic efficiency than simple single effect vapour absorption refrigeration system. the thermodynamic performances (i.e. coefficient of performance (COP) and exergetic efficiency (second law efficiency) using R245fa gives better thermodynamic performances as compared to R134a and R236fa used in single effect cascade vapour compression-absorption refrigeration systems.

(iv) The thermodynamic performance performances using R227ea is found to be lowest in single effect vapour - compression-absorption LiBr refrigeration system.

(v) Cascaded half effect gives better first law thermodynamic performance (COP) and second law thermodynamic performance in terms of exergetic efficiency than simple half effect vapour absorption refrigeration system.

(vi) Cascade single effect gives better first law thermodynamic performance (COP) and second law

thermodynamic performance in terms of exergetic efficiency than simple single effect vapour absorption refrigeration system.

(vii) Cascade double effect gives better first law thermodynamic performance (COP) and second law thermodynamic performance in terms of exergetic efficiency than simple double effect vapour absorption refrigeration system.

(viii) Cascade triple effect gives better first law thermodynamic performance (COP) and second law thermodynamic performance in terms of exergetic efficiency than simple triple effect vapour absorption refrigeration system.

(ix) The first law efficiency in terms of coefficient of performance (COP_VARS) is increasing and second law efficiency in terms of exergetic efficiency of the triple effect vapour absorption refrigeration system is increasing along with increasing exergy destruction ratio of triple effect vapour compression – triple effect vapour absorption refrigeration system as increasing generator temperature of vapour compression – triple effect vapour absorption refrigeration.

(x) The optimum exergetic efficiency of triple effect vapour absorption refrigeration system is to be found as 35.4% at 3^{o}C evaporator temperature while optimum exergetic efficiency of cascaded triple effect vapour absorption-compression refrigeration system is to be found as 35.4% at 4^{0}C evaporator temperature while the first law efficiency in terms of coefficient of performance (COP) cascaded system is found at 5^{o}C evaporator temperature.

(xi) The first law efficiency in terms of coefficient of performance (COP) and second law efficiency in terms of exergetic efficiency of vapour absorption refrigeration system are increasing with increasing effectiveness of heat exchanger and exergy destruction ratio of vapour absorption refrigeration system is decreasing with increasing effectiveness of heat exchanger.

(xii) The first law efficiency in terms of coefficient of performance (COP) and second law efficiency in terms of exergetic efficiency of cascaded-vapour compression triple stage vapour absorption refrigeration system are increasing with increasing effectiveness of heat exchanger and exergy destruction ratio of cascaded-vapour compression triple stage vapour absorption refrigeration system is decreasing with increasing effectiveness of heat exchanger.

(xiii) The first law efficiency in terms of coefficient of performance (COP) and second law efficiency in terms of exergetic efficiency of cascaded vapour compression-tripple effect absorption refrigeration system are decreasing with increasing temperature overlapping (Approach) and exergy destruction ratio of cascaded vapour absorption-compression refrigeration system is increasing with increasing temperature overlapping.

References

[1] S.B. Riffat N. Shankland [1993] Integration of absorption and vapour-compression systems**,** Applied Energy**,** Vol-46, Issue-4**,**1993, Pages 303-316.

[2] Kaushik, S.C., Arora, A., Energy and Exergy analysis of single effect and series flow double effect waterlithium bromide absorption refrigeration systems, International Journal of Refrigeration, Vol. 32, (2009), pp. (1247-1258)

[3] A Arora and S.C. Kaushik [2009]Theoretical analysis of LiBr/H2O absorption refrigeration system, International Journal of Energy Research, 33(15), page-1321 - 1340

[4] Gomri, R., Second law comparison of single effect and double effect vapour absorption refrigeration systems, Energy Conversion and Management,Vol. 50, (2009), pp.1279-1287).

[5] Yi Chena,b, Wei Hana, Liuli Sunc , Hongguang Jina A new absorption–compression refrigeration system using a mid-temperature heat source for freezing application , The 7th International Conference on Applied Energy – ICAE2015, Energy Procedia 75 (2015) 560 – 565

[6] Fernández-Seara J, Sieres J, Vázquez M. Compression–absorption cascade refrigeration system. Applied Thermal Engineering. 2006;26:502-12.

[7] Garimella S, Brown AM, Nagavarapu AK. Waste heat driven absorption/vapor-compression cascade refrigeration system for megawatt scale, high-flux, low-temperature cooling. International Journal of Refrigeration. 2011;34:1776-85

[8] Rogdakis ED, Antonopoulos KA. Performance of a low- temperature NH_3H_2O absorption-refrigeration system. Energy. 1992;17:477-84.

[9] Kilic, M. and Kaynakli, O., Theoretical study on the effect of operating conditions on performance of absorption refrigeration system, Energy Conversion and Management, Vol. 48, (2007), pp.(599-607).

[10] Lee T-S, Liu C-H, Chen T-W. Thermodynamic analysis of optimal condensing temperature of cascade-condenser in CO_2/NH_3 cascade refrigeration systems. International Journal of Refrigeration. 2006;29:1100-8.

[11] Wu W, Wang B, Shi W, Li X. An overview of ammonia-based absorption chillers and heat pumps. Renewable and Sustainable Energy Reviews. 2014; 31:681-707.

[12] R.S. Mishra (2018) Comparison of thermal performances of single effect, double effect and triple effect LiBr-H2O absorption system cascaded with vapour compression refrigeration systems using ecofriendly refrigerants, International Journal of Research in Engineering and Innovation Vol-2, Issue-6 (2018), 610-621.

[13] R.S. Mishra (2019) Thermal performances (first law efficiency, exergy destruction ratio & exergetic efficiency) of cascade single effect ammonia-water (NH3-H20) vapour absorption refrigeration system coupled with vapour compression refrigeration using ecofriendly refrigerants in the low temperature cycle of VCRS system, International Journal of Research in Engineering and Innovation Vol-3, Issue-1 (2019), 1-5

[14] R.S. Mishra (2019) Comparison of half effect absorption-compression cascaded refrigeration system using thermodynamic (energy-exergy) analysis. International Journal of Research in Engineering and Innovation Vol-3, Issue-1 (2019), 6-11.

Cite this article as: R.S. Mishra, Thermal Performance of Cascaded Vapour Compression Absorption Systems, International journal of research in engineering and innovation (IJREI), vol 3, issue 1 (2019), 48-56.

International Journal of Research in Engineering and Innovation (IJREI)
journal home page: http://www.ijrei.com
ISSN (Online): 2456-6934

Thermal performances (first law efficiency, exergy destruction ratio & exergetic efficiency) of cascade single effect ammonia-water (NH_3-H_20) vapour absorption refrigeration system coupled with vapour compression refrigeration using ecofriendly refrigerants in the low temperature cycle of VCRS system

R.S. Mishra

Department of Mechanical & Production Engineering, Delhi Technological University Delhi, India

Abstract

Solar thermal power energy and waste heat from different power plants have immense application potential for production of refrigeration through combined vapour compression–absorption refrigeration systems. The aim of this work is to develop an integrated solar refrigeration system where waste heat from different energy resources assists a combined vapour absorption compression system, and to analyze feasibility & practicality of that system of thermodynamically for improving its COP and exergetic efficiency by reduction of irreversibilities in terms of exergy destruction /losses occurred in the system components. The combined thermodynamic first law efficiency in terms of coefficient of performance (COP_Overall), second law efficiency in terms of exergetic efficiency and exergy destruction ratio based on exergy of product of a combined vapour absorption-compression system working with each of the following refrigerants in the cascaded vapour compression cycle R1234yf, R227ea, R236fa, R245fa, R143a,R134a, R32, R507 operating at - 223 K evaporator temperature with temperature overlapping (Approach means the difference between cascaded condenser temperature of vapour compression cycle and evaporator temperature of vapour absorption refrigeration cycle working at 13.5 bar of highest generator pressure and 1.75 bar as lowest evaporator pressure have been presented and it is found thatR141b and R245fa gives better performance
© 2019 ijrei.com. All rights reserved

Keywords: Low GWP Refrigerants, Energy-Exergy Analysis, Single effect VAR-Cascade VCR System,

1. Introduction

Vapor compression refrigeration system (VCRS) is widely used refrigeration system (about 80%) and requires a large amount of electrical energy for its operation. The advancement in refrigeration sector has a major impact on energy demand which approximates to 15% of the total energy consumption in the world. Many developing countries like India currently suffer from a major shortage of electricity. Around 55% of the total electrical capacity is generated using coal in India [1].
Solar thermal power energy and waste heat from different power plants have immense application potential for production of refrigeration through combined vapour compression absorption refrigeration systems. The aim of this work is to develop an integrated solar refrigeration system where waste heat from different energy resources assists a combined vapour absorption -compression system, and to analyze feasibility & practicality of that system of thermodynamically for improving its COP and exergetic efficiency by reduction of irreversibilities in terms of exergy destruction /losses occurred in the system components [2].
The combined refrigeration system consists of a conventional vapour compression refrigeration system cascaded with vapour absorption system. The LiBr–H_2O couples is used for the absorption refrigeration system and nine different refrigerants (i.e.R1234yf, R227ea, R236fa, R245fa , R141b,R134a, R32, R507, R717, are evaluated to find the best suitable ecofriendly) for cascaded vapour compression system and found that first law efficiency of combined cycle cascaded of evaporator of vapour absorption cycle with

Corresponding author: R. S. Mishra
Email Address: hod.mechanical.rsm@dtu.ac.in

condenser of vapour compression cycle found 55.36% enhancement in overall COP of combined cycle using double effect vapour absorption LiBr-H2O system and 80% enhancement in overall COP of combined cycle using double effect vapour absorption LiBr-H_2O system as compared to single effect LIBr-H_2O) system for -323 K of evaporator VCR temperature using R134a while 16% improvement in COP using triple effect VARS as compared to double effect VARS cascaded with VCRS. Similarly Second law efficiency of combined cycle cascaded of evaporator of vapour absorption cycle with condenser of vapour compression cycle found 11.29% enhancement in overall COP of combined cycle using double effect vapour absorption LiBr-H_2O system and 21.8% enhancement in overall COP of combined cycle using double effect vapour absorption LiBr-H_2O system as compared to single feect LIBr-H_2O) system for -323 K of evaporator VCR temperature using R134a while 9.44% improvement in COP using triple effect VARS as compared to double effect VARS cascaded with VCRS [3]

The present paper provided the best refrigerant for the novel combined vapour absorption refrigeration cycle/cascaded with vapour compression cycle to provide the highest thermodynamic efficiency for lowest degree of environmental damage.

2. Literature Review

Jain et al. [1] studied various integrated refrigeration systems and concluded that these systems are promising energy efficient and decarbonizing cooling technology in near future. Riiffit S.B., Shankland N [4] thermo-dynamically analyzed different types of integrated single-effect, double-effect series and the double-effect parallel continuous absorption systems and their integration with vapour-compression systems using various refrigerant/absorbent pairs and intermittent absorption system, the intermittent absorption/vapour recompression system and the combined intermittent absorption/vapour compression system.L. Kairouani, E. Nehdi [5] carried out thermodynamic analysis of novel combined refrigeration system using geothermal energy temperature source in the range 343–349 K supplied to a generator operating at 335 K.to supply vapour absorption system cascaded with conventional compression system using three working fluids (i.e.R717, R22, and R134a) and found that the COP can be improved by 37–54%, as compared with the conventional cycle, under the same operating conditions, (i.e. Vaporization temperature of 263 K and a condensation temperature of 308 K). Results of this studied show that the COP of a combined system is significantly higher than that of a single stage refrigeration system. For industrial refrigeration, the proposed system constitutes an alternative solution for reducing energy consumption and greenhouse gas emissions

3. Results and Discussions

Table-1 shows the variation of thermal performance parameters of single effect cascade vapour absorption refrigeration system using lithium bromide -water solution coupled with vapour compression refrigeration system. The evaporator of VARS is cascaded with condenser of vapour compression refrigeration systems using nine ecofriendly refrigerants. It is found that overall first law efficiency in terms of coefficient of performance (COP) of cascade refrigeration system using R245fa refrigerant is highest and lowest by using R227ea as shown in fig-1 .while exergy destruction of cascade system is lowest by using R141b and highest while using R227ea as shown in Fig-2. The cascade system exergetic efficiency is highest by using R141b and lowest by using R227ea as shown in Fig-3. The thermal performances using ecofriendly refrigerants in the low temperature circuit of vapour compression refrigeration system is shown in Table-1 and it is found that maximum coefficient of performance (COP)of vapour compression refrigeration system by using R141b and lower COP by using R227ea respectively as shown in Fig-4. Similarly exergy destruction of vapour compression refrigeration system is lowest by using R141b and highest while using R227ea as shown in Fig-5. The exergetic efficiency of vapour compression of refrigeration system is highest by using R141b and lowest by using R227ea as shown in Fig-6

Table 1: Thermal performances of single effect (NH_3-H_20) vapour absorption refrigeration system using vapour compression refrigeration system (T_Eva_VARS= -20°C, approach_VCRS=10°C, T_Eva_Ref= -50°C, compressor efficiency=0.80, generator heat exchanger effectiveness= 0.6894

Refrigerant	COP (Overall)	Overall Exergy Destruction ratio (EDR)	Overall Exergetic Efficiency	COP (VCRS)	VCRS Exergy destruction Ratio (EDR)	VCRS Exergetic Efficiency
R134a	0.4554	1.998	0.3335	1.485	1.002	0.4995
R1234yf	0.4463	2.152	0.3173	1.356	1.192	0.4561
R141b	0.4699	1.773	0.3607	1.719	0.7301	0.5780
R227ea	0.4331	2.394	0.2947	1.188	1.503	0.3996
R236fa	0.4474	2.133	0.3192	1.371	1.169	0.4610
R245fa	0.4596	1.930	0.3413	1.55	0.9188	0.5212
R32	0.4558	1.992	0.3342	1.491	0.9947	0.5013
R507a	0.4426	2.217	0.3109	1.387	1.275	0.4396

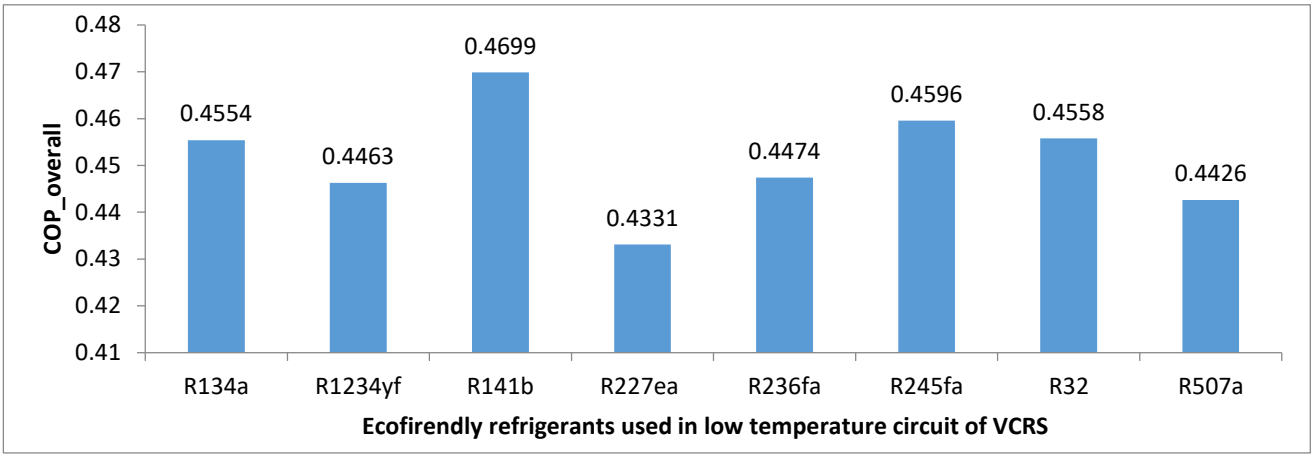


Figure 1: *Thermal performances in terms of first law efficiency (overall COP_Cascade) of cascade single effect ammonia-water(NH_3-H_20) vapour absorption refrigeration system coupled with vapour compression refrigeration using ecofriendly refrigerants in the low temperature cycle of VCRS system*

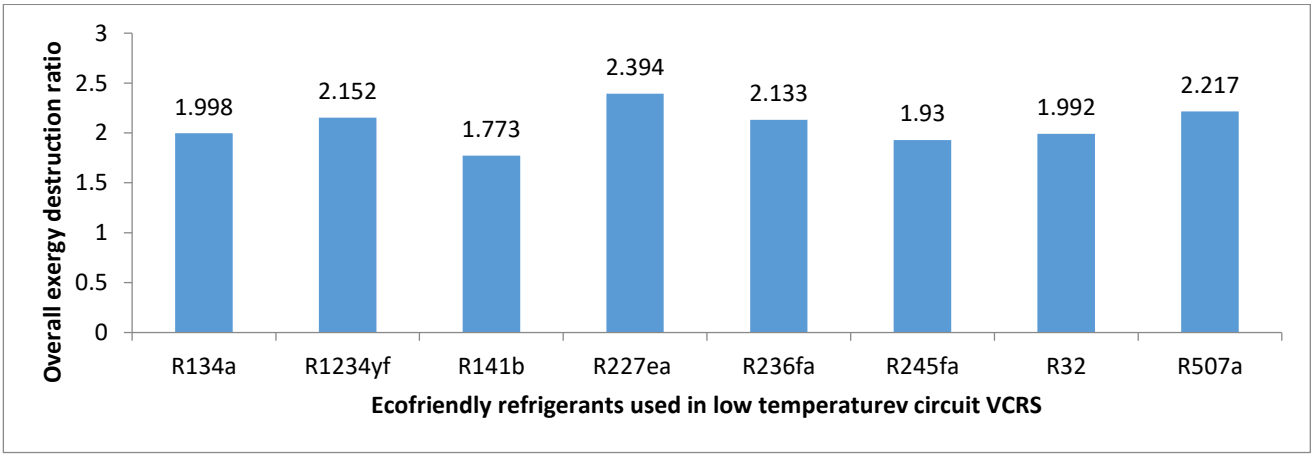


Figure 2: Thermal performances in terms of overall exergy destruction ratio (EDR_Overall) of cascade single effect ammonia-water (NH_3-H_20) with vapour absorption refrigeration system coupled with vapour compression refrigeration using ecofriendly refrigerants in the low temperature cycle of VCRS system

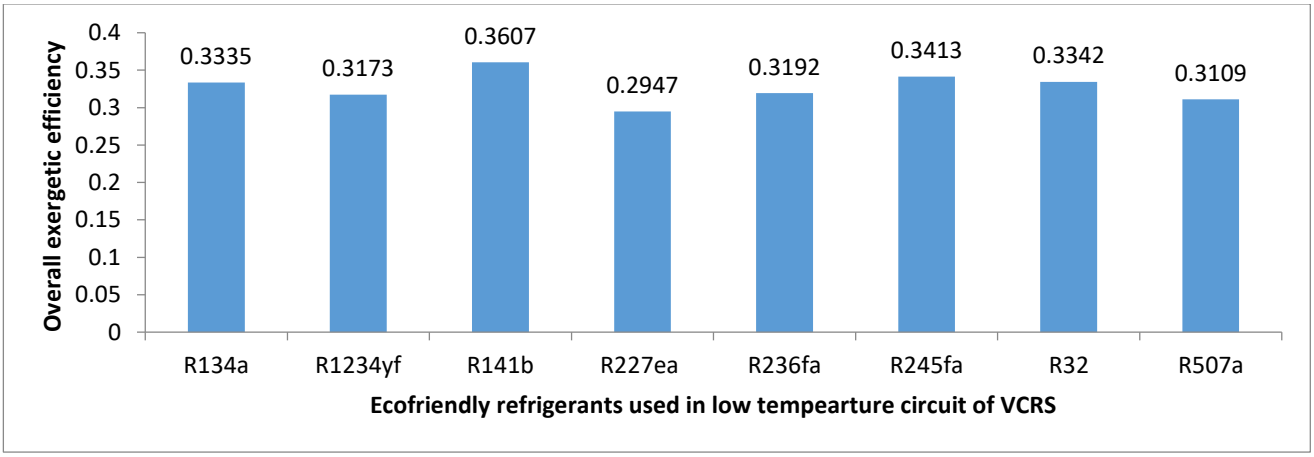


Figure 3: *Thermal performances in terms of overall exergetic efficiency of cascaded single effect ammonia-water (NH_3-H_20) with vapour absorption refrigeration system coupled with vapour compression refrigeration using ecofriendly refrigerants in the low temperature cycle of VCRS system*

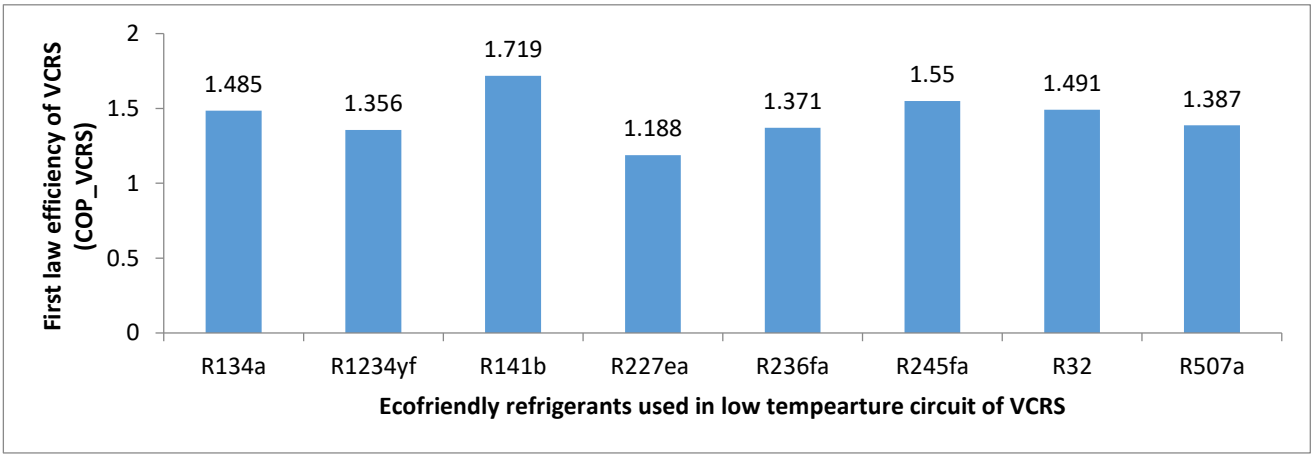


Figure 4: *Thermal performances in terms of first law efficiency of vapour compression refrigeration system (COP_VCRS) of cascaded with single effect ammonia-water (NH_3-H_20) vapour absorption refrigeration system coupled with vapour compression refrigeration using ecofriendly refrigerants in the low temperature cycle of VCRS system*

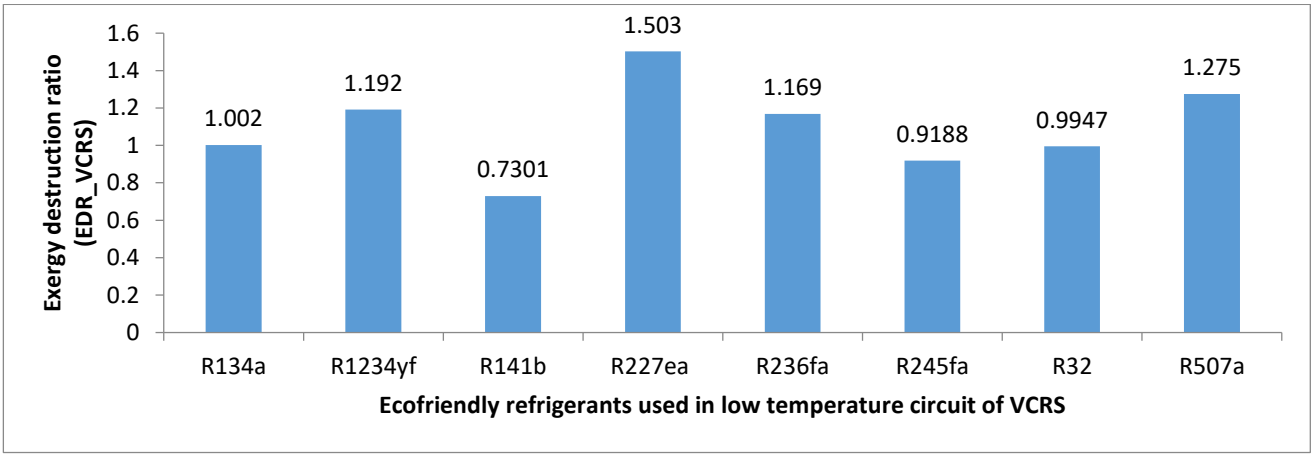


Figure 5: Thermal performances in terms of exergy destruction ratio (EDR_VCRS) of vapour compression system of vapour compression refrigeration system (COP_VCRS), of cascaded with single effect ammonia-water (NH_3-H_20) vapour absorption refrigeration system coupled with vapour compression refrigeration using ecofriendly refrigerants in the low temperature cycle of VCRS system

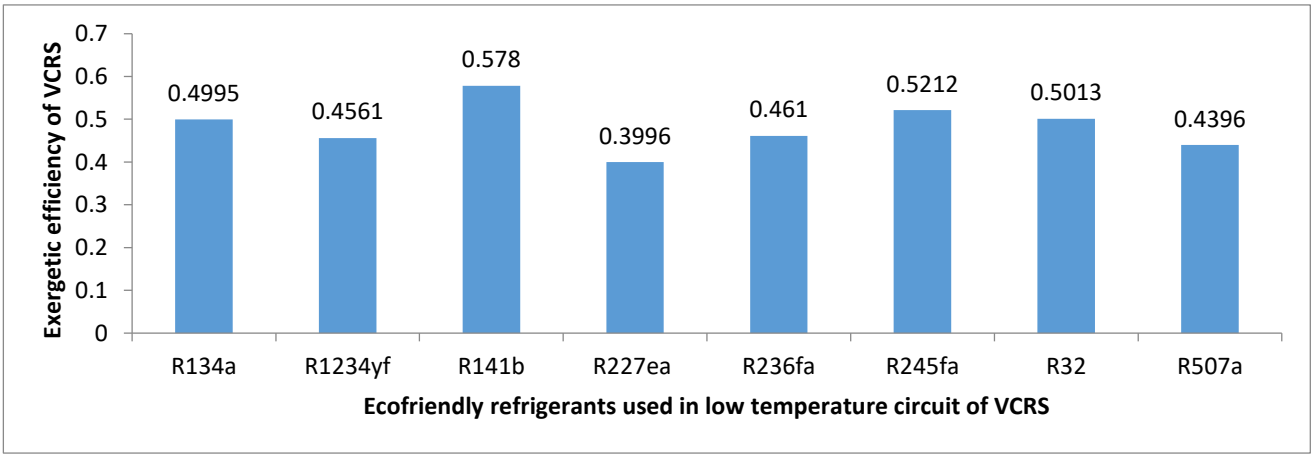


Figure 6: Thermal performances in terms of exergetic efficiency of vapour compression system of vapour compression refrigeration system (COP_VCRS), of cascaded with single effect ammonia-water(NH_3-H_20) vapour absorption refrigeration system coupled with vapour compression refrigeration using ecofriendly refrigerants in the low temperature cycle of VCRS system

The percentage improvement in thermal performance of combined novel vapour absorption refrigeration system coupled with vapour compression refrigeration system is shown in Table-2. It is found that this system combined single effect NH_3-H_2O vapour absorption system combined with vapour compression system using R141b ecofriendly refrigerant gives best first law performance(COP_Overall) improvement around 45.65% along with 45.73% improvement second law performance in terms of exergetic efficiency. However minimum exergy destruction ratio by using R227ea

Table-2: Percentage improvements in thermal performances of single effect NH_3_H_2O vapour absorption system cascaded with vapour compression refrigeration system using ecofriendly refrigerants

Performance Parameters	% First law Performance improvement (COP)	% II law Performance improvement (Exergetic)	% Reduction in Irreversibility (EDR)
R134a	41.428	34.34	34.29
R1234yf	38.60	28.20	29.0
R227ea	34.50	19.07	21.30
R236fa	38.912	28.96	29.88
R245fa	42.7	37.89	36.55
R32	41.55	35.03	34.51
R141b	45.65	45.73	41.71
R507a	37.45	25.61	27.12

4. Conclusions

The following conclusions were drawn.

(i) The thermodynamic performance in terms of first law efficiency and second law efficiency improved significantly by using vapour absorption system cascaded with vapour compression refrigeration system.

(ii) The 45.65% improvement in first law efficiency (i.e. over all COP) of combined single effect vapour absorption refrigeration cascade system using R141b refrigerant in the vapour compression cycle is found as compared to single effect NH_3H_2O vapour absorption refrigeration system

(iii) 45.73% increment of second law efficiency (i.e. exergetic efficiency) of the single effect NH_3H_2O vapour absorption refrigeration system cascaded with vapour compression refrigeration system is found as compared to single effect NH_3H_2O vapour absorption-refrigeration system

(iv) Minimum exergy destruction ratio in the single effect NH_3H_2O vapour absorption refrigeration system cascaded with vapour compression refrigeration system by using R227ea is found as compared to single effect NH_3H_2O vapour absorption- refrigeration system.

References

[1] Vaibhav Jain, S.S. Kachhwaha , Gulshan Sachdeva, Thermodynamic performance analysis of a vapour compression–absorption cascadedrefrigeration system, Energy conversion & Management, 2013, 685- 700.

[2] A Arora, Energy and exergy analyses of compression, absorption, and combined cycle cooling systems (Ph.D. Thesis), Centre for Energy Studies, IIT Delhi, India, 2009.

[3] Mishra R.S., Comparison of thermal performances of single effect, double effect and tripple effect LiBr-H2O absorption system cascaded with vapour compression refrigeration systems using ecofriendly refrigerants, International Journal of research in engineering and innovation , Vol-2, No-6 (2018), 610-621. .

[4] Riiffit S.B. , Shankland N, Integration of absorption and vapour-compression systems,Applied Energy, Volume-46, issue-4, 1993, 303-316.

[5] L. Kairouani, E. Nehdi, Cooling performance and energy saving of a compression–absorption refrigeration system assisted by geothermal energy, Applied Thermal Engineering, Vol- 26, 2006, 288–294.

Cite this article as: R.S. Mishra, Thermal performances (first law efficiency, exergy destruction ratio & exergetic efficiency) of cascade single effect ammonia-water (NH_3-H_20) vapour absorption refrigeration system coupled with vapour compression refrigeration using ecofriendly refrigerants in the low temperature cycle of VCRS system, *International journal of research in engineering and innovation (IJREI)*, vol 3, issue 1 (2019), 1-5.

International Journal of Research in Engineering and Innovation (IJREI)
journal home page: http://www.ijrei.com
ISSN (Online): 2456-6934

Thermodynamic analysis of brayton cycle for power generation

R.S. Mishra, Manish Kumar

Department of Mechanical, Production, Industrial and Automobiles Engineering, Delhi technological University, Delhi, India

Abstract

This paper mainly deals with the thermodynamic performances of Brayton Cycle in detail. The performance equation are developed which includes the effect of intercooling and reheating using three operating fluids R123, R245fa and R134a for improving its thermodynamic performances. It was observed the Brayton cycle working on R123 gives better thermodynamic performances then R245fa & R134a. Since R123 containing chlorine content therefore R245fa is recommended which has better thermodynamic performance then HFC-134a. The effect of various performance parameters such as pressure ratio, maximum temperature in cycle, inlet temperature of compressor the change in Net efficiency and net-work of the Brayton cycle is investigated.

©2019 ijrei.com. All rights reserved

Keywords: Joule cycle thermodynamic performance, ecofriendly fluids, gas turbines cycle

1. Introduction

Energy security, economic development and atmosphere protection are not very well balanced these days which has put further pressure on energy demand which is closely connected to the economic process. At the same time, the over-consumption of fossil fuels has led to a lot of surroundings issues like heating, ozone depletion and atmosphere pollution. Fossil fuels are still the dominant form of energy resources worldwide, accounting for 77 of the increasing energy demand 2007-2030 (IEA 2009). When combined with the quick development of business, a significant increase in energy shortages and blackouts has been noticed a lot frequently everywhere around the globe. Due to of those reasons, utilizing inferior waste heat for energy consumption. The most ordinarily investigated in inferior heat supply and waste heat utilizations these days are Organic Rankine Cycle (ORCs) and Kalina Cycle (binary fluids and fluid mixtures). When low grade heat is used, the conventional steam Rankine cycle does not offer acceptable performance as a result of its poor thermal efficiency and big volume flows, and so therefore known as Organic Rankine Cycle (ORCs) are projected. These cycle use organic substances as operating fluid system comprises a minimum of 4 major comparisons, a regenerator is additionally enclosed within the current calculation.

In this study the Combined Organic Cycle focuses the performance of three fluids R123, R134a and R245fa. Though earlier studies hold innumerable options, this work provides a much clearer statement on IHE in subcritical ORC system setting a new model taking pressure drop by loops and pinch point into thought. The common operating fluids R123, R134a and R245fa have been chosen for subcritical cases.

2. Literature review

The theoretical investigation and has instructed the feasibleness of introducing a waste heat recovery system in 2 stage turbocharged HDD engine.The waste heat recovery (WHR) is earned by introducing a Rankine cycle that uses an organic substance or directly water as operating fluid looking on energetic performance concerns.They additionally instructed an alternate for rising the general thermal efficiency of internal-combustion engine consists of recovering the energy lost by suggests that of a waste heat recovery (WHR) system. These solutions are supported adapting one among the turbochargers by removing its rotary engine and making an attempt to recover the energy by Rankine cycle. Finally, the rotary engine of the Rankine cycle provides the recovered energy on to the compressor of this turbocharger [1]. The strategy for customizing an organic Rankine cycle to a fancy heat supply for economical energy conversion, demonstrated on a Fischer Tropsch plant. Organic Rankine Cycle offer an alternate to ancient steam temperature unit cycle for the conversion of low grade heat supply into power, wherever typical steam power cycle is thought to be inefficient. A large process plant typically has multiple low temperatures waste heat supply obtainable for conversion to electricity by a low temperature cycle, leading to composite heat supply with a

Corresponding author: R.S. Mishra
Email Address: hod.mechanical.rsm@dtu.ac.in

complex temperature-enthalpy profile. Organic fluids are sculptured employing a pure substance information. The pinch analysis technique of forming composite curve is applied to research the impact of every building block on the temperature-enthalpy profile of the ORC heat demand [2]. The performance analysis of double organic Rankine cycle for discontinuous temperature waste heat recovery. The optimum operation of many operating fluids are calculated by a procedure using MATLAB and REPROP. The influence of outlet temperature of warmth supply on internet power output, thermal efficiency, power consumption, mass rate of flow, expander outlet temperature, cycle irreversibility and exergy potency at a given pinch temperature difference has been used to get a thermodynamically understanding of the ORC performance [4]. Electricity from industrial waste heat exploitation high speed organic Rankine cycle. Within the conversion of cold heat into electricity the best efficiency is obtained in several cases by using AN Organic Rankine Cycle. The ORC method additionally be possible also in warm temperature applications. This paper deals with an ORC style, during which a high speed oil free turbo generator feed pump is employed [5].

Analysis of external heat loss from a little scale expander employed in organic Rankine cycle. With the lowering of the ORC, the engine shaft power isn't solely determined by the enthalpy drop by the expansion method however additionally the external heat loss from the expander. On paper and by experimentation support in evaluating tiny scale expander heat loss is rare. They give a quantitative study on the convection, radiation and conductivity heat transfer from a kw-scale expander. A mathematical model is constructed and valid [6]. Recent interests in little scale solar thermal combined heat and installation has coincided with the demand growth for distributed electricity providers in space poorly served by centralized power stations. One potential technical approach to fulfill this demand is parabolic trough solar thermal collector including Organic Rankine Cycle engine. He additionally describes the planning of solar organic Rankine cycle being put in in Kingdom of Lesotho for rural electrification purpose. The system carries with it parabolic trough collectors, a tank, atiny low scale ORC engine scroll expanders. A model of every part is developed that permits sizing the various parts of cycle and evaluates the performance of system [7].

Energy primarily based fluid choice for a geothermic Organic Rankine Cycle for combined heat power generation. During this study the choice of combined heat and power generation was thought-about for geothermic resources at a temperature level below 450k. Series and parallel circuits of an organic Rankine cycle and extra heat generation was organized by second law analysis. The result shows that the second law efficiency of energy station will be considerably enlarged compared to power generation [8]. The investigation of 2 stage Rankine cycle for power plant. A 2 stage Rankine cycle for power generation is given during this paper. It's product of water steam Rankine Cycle and Organic Rankine bottoming Cycle. By using an organic fluid with density over water. The performance of 2 stage Rankine cycle operative with those completely different operating fluids is evaluated. System efficiency may be increased by introducing a regenerator for a few of operating fluids [9]. Pumping within Rankine cycle and created calculation based mostly result for the pumping work on ORC. Analysis has been administrated for eighteen completely different organic fluids that may be used an operating fluids within the subcritical ORC system. A trial was created to search out correlations between numerous thermo-physical properties of operating fluids, specific work and power of cycle [10].

The energy potency analysis of organic Rankine cycle with scroll expanders for co-generative applications. The model of scroll machine is applicable to calculate the performance of each a compressor and expander, as perform of pure mathematics of device and dealing fluid [11]. Solar power-driven Rankine cycle for water production. He additionally centered that on the analysis of distributed solar power-driven generation systems for driving a reverse diffusion method process. Results signifies the desalinization system coupled to solar power-driven organic Rankine cycle exhibit lower specific consumption of solar power than solar distillation [12]. The review of temperature unit Cycle for combustion engine exhaust waste heat recovery. This paper review the history of combustion engine exhaust waste heat recovery specializing in organic Rankine cycle since this thermodynamically cycle works well with medium grade energy of exhaust. Choice of cycle expander and dealing fluid are primary focus of the review. Results demonstrate a possible fuel economy improvement around ten [13]. Exergy based mostly fluid choice for a geothermic Organic Rankine Cycle for combined heat and power generation [14]. The comparative energetic analysis of hot temperature subcritical and trans critical Organic temperature unit cycle during a biomass application within the Sibari district. The current work aims to research the energetic performance of ORC's for tiny scale applications [15]. The improvement of temperature exhaust gas waste heat fueled organic Rankine cycle. Cycle parametric analysis was performed to look at the consequences of thermodynamically parameters on the cycle [16]. The constant theoretical study of a 2 stage solar Rankine cycle for Ro distillation. The current work issues the constant study of an autonomous 2 stage solar ORC for Ro desalinization. The most aim is to estimate the efficiency similarly on calculate annual energy out there for desalinization [17]. An analysis of regenerative Organic Rankine Cycle (ORC), supported constant quantity optimization using R-123 and R-134a throughout superheating at a continuing pressure of 2.50 MPa underneath realistic conditions. The aim was to pick a much better operating fluid on the idea of obtained system efficiency, turbine work output, irreversibility rate and second law efficiency underneath applied fastened and variable heat supply temperature conditions, R-123 has been found a more robust operating fluid than R-134 for changing low grade heat to power. A computer program has been developed to parametrically optimize and compare the system and irreversibility ratio with will increase in rotary engine water temperature (TIT) underneath completely different heat supply temperature conditions to get the optimum operative conditions whereas using R-123 as the operating fluid throughout superheating at varied rotary engine water pressures for the use of the waste heat sources of temperatures higher than 150ºC. The calculated results reveal that an water pressure of 2.70 MPa offers the most system efficiency, rotary engine work output and second law efficiency with minimum irreversibility rate,

irreversibility magnitude relation and system mass rate of flow up to a TIT within the vary of 165ºC-250ºC [18].

Some initial conditions, boundary conditions, and hypothesis for a mathematical model. 3 types of pure fluid and one mixture were hand-picked as operating fluids and their constant quantity changes were calculated below totally different evaporating temperatures. Once organic Rankine cycle (ORC) is supplied with internal device (IHE), its parameters varies whereas using totally different operating fluids [19]. Constant optimization and comparative study of Organic Rankine Cycle for low grade waste heat recovery in saturated cycle [20].

A subcritical cycle and stimulated it beneath constant operation conditions as superheated cycle, however, the pumping pressure is unbroken above the pressure used for superheated cycle however slightly less than the critical pressure for operating fluids [21]. The results of an experimental study administered on a model of an open-drive oil-free scroll expander integrated into an ORC operating with refrigerant HCFC-123. By exploiting the expander performance measurements, the eight parameters of a scroll expander semi-empirical model are then known. The model is ready to calculate variables of 1st importance like the mass rate, the delivered shaft power and also the discharge temperature, and secondary variables like the availability heating-up, the exhaust cooling-down, the close losses, the interior escape and also the mechanical losses. The utmost deviation between the predictions by the model and also the measurements is two hundredth for the mass rate, 5-hitter for the shaft power and 3K for the discharge temperature. The valid model of the expander is finally wont to quantify the various losses and to point how the planning of the expander can be altered to realize higher performances. This analysis detected that the internal leakages and, to a lesser extent, the availability pressure drop and also the mechanical losses are the most losses moving the performance of the expander [22]. The use of organic operating fluids for the conclusion of the thus known as Organic Rankine Cycle (ORC) has been established to be a promising resolution for decentralized combined heat and power production (CHP). The method permits the employment of low temperature heat sources, giving an advantageous efficiency in tiny scale applications. This is often the explanation why the quantity of energy and biomass fired power plants supported this technology are enhanced among the last years. The favorable characteristics of ORC build them appropriate for being integrated in applications like solar desalinization with reverse diffusion system, waste heat recovery from biogas digestion plants or micro-CHP systems. During this paper, the state of the art of ORC applications are going to be given beside innovative systems that are simulated in an exceedingly method simulation setting using experimental data. The results of the simulations like efficiencies, water production rates or possible electricity cost are given and mentioned [23]. The choice of combined heat and power generation was thought of for energy resources at a temperature level below 450 K. Series and parallel circuits of an Organic Rankine Cycle (ORC) and a further heat generation were compared by second law analysis. Looking on operative parameters criteria for the selection of the operating fluid were known. The results show that because of a combined heat and power generation, the second law efficiency of an energy station will be considerably enhanced as compared to a power generation, the second law efficiency of an energy station will be considerably enhanced as compared to a power generation. The foremost economical conception may be a series circuit with an organic operating fluid that shows high critical temperatures like iso-pentane. For parallel circuits and for power generation, fluids like R227ea with low critical temperatures are to be most well-liked [24]. Parametric optimization and performance analysis of a waste heat recovery system supported Organic temperature unit Cycle, using R-12, R-123 and R-134a as operating fluids for power generation are studied. The cycles are compared with heat supply as waste heat of flue gas at 140ºC and 312 Kg/s/unit mass rate of flow at the exhaust of ID fans for 4×210 MW, NTPC Ltd. Kahalgaon, India. Optimization of rotary engine inlet pressure for max work and efficiencies of the system on the saturated vapor line and isobaric superheating at completely different pressures has been carried out for the chosen fluids. The results show that R-123 at corrected pressure evaluated among all the chosen fluids. The Carnot efficiency for R-123 at corrected pressure evaluated underneath similar conditions is near to the particular potency. It will generate 19.09 MW with a mass rate of flow of 341.16 Kg/s having a pinch point of 5ºC, 1st law efficiency of 25.30% and also the second law efficiency of 64.40%. Therefore choice of an Organic Rankine Cycle with R-123 as operating fluid seems to be an alternative system for utilizing inferior heat sources for power generation [25].

The reducing of the Organic Rankine Cycle (ORC), the engine shaft power isn't solely determined by the enthalpy drop by the expansion method however additionally the external heat loss from the expander. Theoretical and experimental support in evaluating tiny scale expander heat loss is rare. This paper presents a quantitative study on the convection, radiation and conductivity heat transfer from a kW-scale expander. A mathematical model is constructed and valid. The results show that the external radiative or convective heat loss constant was regarding 3.2 or 7.0 W/m2K once the ORC operated around 100ºC. Radiative and convective heat loss coefficients enhanced because the expander operation temperature enhanced. Conductive heat loss because of the affiliation between the expander and also the support accounted for an oversized proportion of the warmth loss. The fitting relationships between heat loss and mean temperature distinction were established. It's recommended that low conduction material be embodied within the support of expander. Mattress insulation for compact expander may be eliminated once the operation temperature is around 100ºC [26]. Recent interests in little scale solar thermal combined heat and installation has coincided with the demand growth for distributed electricity providers in space poorly served by centralized power stations. One potential technical approach to fulfill this demand is parabolic trough solar thermal collector including Organic Rankine Cycle engine. He additionally describes the planning of solar organic Rankine cycle being put in in Kingdom of Lesotho for rural electrification purpose. The system carries with it parabolic trough collectors, a tank, a tiny low scale ORC engine scroll expanders. A model of every part is developed that permits sizing the various parts of cycle and evaluates the performance of system. Totally different operating fluids area unit compared, and 2 totally different growth machine configurations area unit simulated (single and double stage) [27].

HFO-1234yf could be a new refrigerant with a virtually zero warming potential (GWP) and gas depletion potential (ODP); it exhibits thermodynamically properties just like HFC-134a. The potential if HFO-1234yf as an operating fluid for organic Rankine cycle (ORC) is elucidated through a primary order simulation. A basic thermodynamically model of ORC with 5 forms of cycles trilateral, saturated, superheated, sub-critical, and critical wont to compare the thermal efficiency of HFO-124yf thereupon of different operating fluids. HFO-1234yf was found to supply a thermal efficiency that was like that of HFC-134a. This paper provides a helpful clearly shows the simplest attainable thermal efficiency among the 5 forms of cycle for numerous expander recess and condensation temperatures. the best thermal potency vary (8.8%- 11.4%) was obtained once the critical ORC was used at an expander inlet temperature of 170ºC and condensation temperature vary of 20-40ºC for the given pump and expander potency. it's concluded that HFO-1234yf could be a potential operating fluid for ORC applications, particularly for those with low to medium temperature heat sources [28].

The study presents the thermo economic improvement formulations of 3 new tri-generation systems using organic Rankine Cycle (ORC): SOFC-tri-generation, biomass-tri-generation, and solar-tri-generation systems. A thermoeconomic modeling is used using the precise exergy costing (SPECO) methodology whereas the improvement performed using the Powell's methodology to reduce the product value of tri-generation (combined cooling, heating, and power) [29]. This study reveals that the utmost tri-generation-exergy efficiencies are regarding thirty eighth for the SOFC-tri-generation system, twenty eighth for the biomass-tri-generation system and eighteen for the solar-tri-generation system. Moreover, the most price per exergy unit for the SOFC-tri-generation system is about 38$/GJ, for the biomass-tri-generation system is 26$/GJ and for the solar-tri-generation system is 24 $/GJ. This study reveals that the solar tri-generation system offers the simplest thermoeconomic performance among the 3 systems. This is often as a result of the solar-tri-generation system has the lowest price per exergy unit. Moreover, the solar tri-generation system has zero carbon dioxide emissions and it's supported a free renewable energy supply [30].

2.1 Simple Brayton Cycle

The Brayton cycle highlights the standard model for a gas turbine power cycle. According to the principle, the compressor compresses the air, which is then mixed with fuel and burned in the combustor under a consistent pressure. This air can also be heated by a waste heat flow. The resultant high pressure and temperature gas is then allowed to expand through a turbine to perform work. The majority work produced in the turbine is used to support the compressor while the remaining is available for further applications. This is commonly used for stationary power generation plants (electric utilities) and mobile power generation engines (ships and aircraft). For power plant applications, the turbine output is used to provide shaft power to drive a generator. A jet engine aircraft is propelled by the reaction thrust of the exiting gas stream. The turbine provides enough power to run the compressor and deliver auxiliary power.

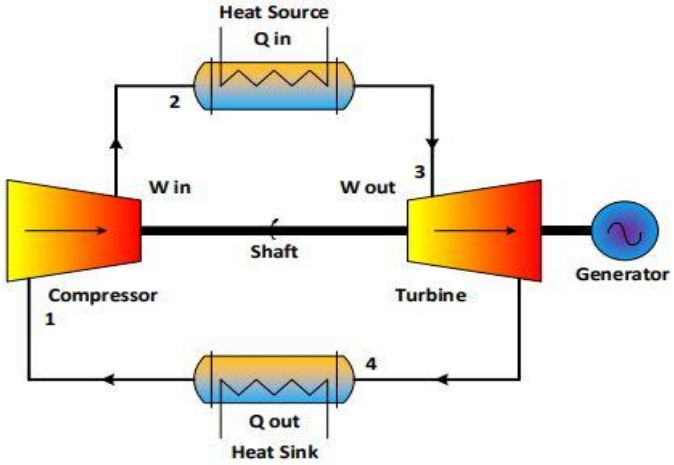


Figure 1: Schematic Diagram of Simple Brayton cycle

Working fluids such as R123, R134a and R245fa have been used in the present investigation. Several researchers investigated these operating fluids and are representative operating fluids that are employed in ORC, Not solely HFC-134a is employed however additionally HFC-245fa and iso-pentane are employed in an Organic Rankine Cycle to collect low heat from the industrial plants. Ethanol performs fine at medium temperature level i.e. 200-300ºC hence, it is also a common as an automotive ORC operating fluid. The evaporation temperature for organic substances is comparatively lower as compare to steam, this being the most reason and advantage of exploitation them as operating fluid in ORC. The low evaporation temperature makes it attainable for them to vaporize or superheat with just low or medium heat sources. Additionally, the expander life are often extended by using the organic substances which are classified as dry or isentropic fluids. Under the saturated or superheated tends to be dry. The particular performance needs to be verified by playing elaborate simulations for the model that employs heat exchanger. The major focus these days is kept on the subcritical cycle, however a number of the research on critical cycle using heat exchanger has also been done. The aim of the study is to identify the impact of internal heat exchanger on the sub-critical, as well as super-critical Organic Rankine Cycle. Net power output, thermal and exergy efficiency are the key performance analysis parameters observed in this study.

In the Brayton cycle, following processes are used

1-2: Isentropic compression of the compressor
2-3: Constant pressure heat inclusion in the combustion chamber
3-4: Isentropic Expansion of the turbine
4-1: Constant pressure heat rejection of the cooler.

For thermodynamic analysis of Brayton cycle the following assumptions are taken:

- The turbine's isentropic efficiency is taken to be 90% and pump's isentropic efficiency is taken to be 89%.
- The cycle is working at steady state conditions.
- Dropping of pressure in the heat exchangers can neglected.
- Minimum temperature of cycle is set as 25ºC.

2.2 Brayton Cycle with Intercooling

In this cycle multi compression is done in intercooler. The low-pressure stream is firstly made to enter a heat exchanger (pre-cooler) and was allowed to cool thereafter. The cooled flow was then made to go along the pre-compressor, from where it is made to compress to a halfway pressure. Then, the fluid enters the intercooler and is cooled down there again before entering the main compressor. Fig.2 shows the layout of Brayton cycle with Intercooling.

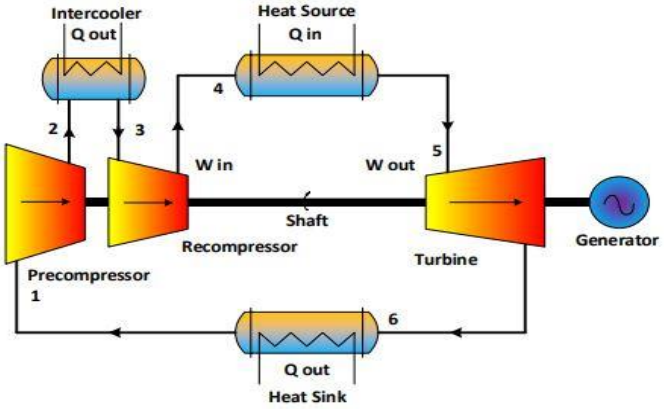


Figure 2: Brayton cycle with intercooling

The inlet temperature in the compressors does not need to be equal, but since only 1 cold sink is need to be used, the temperature should be equal. Hence, the compressor inlet temperature is alike in this above study.

2.3 Brayton cycle with Reheating

The third cycle is with reheating. Fig. 3 shows the layout of Brayton cycle with reheating. It is similar to simple Brayton cycle i.e. after compression process the gas goes to combustion chamber and then to the turbine for expansion, the only difference is that the expansion process is done in multiple stages i.e. first the gas will expand in High pressure turbine and after reheating it expands in low pressure turbine.

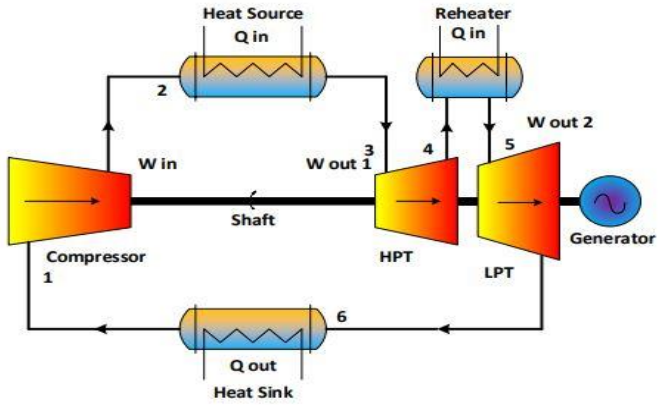


Figure 3: Layout of Brayton cycle with Reheating

The reheating resulted in the improvement of the cycle efficiency by raising the Carnot temperature of the cycle. The fluid at high pressure leaves the compressor and passes into the gas heater or heat exchanger as the cold stream (2). The stream at high temperature and pressure pass on to the HP turbine (3) and faces energy loss in the HP turbine door (4). Low- pressure stream has gained energy in the re-heater and made to exit through the LP turbine (5). It is possible to initiate more than one reheat stage where two reheat stages being used. In the case of 3 stages of reheat, there occurs an inclusion of another turbine body into the working system. At the end, the heat is rejected in the pre-cooler (6), where the working fluid is allowed to cool to the temperature according to the temperature of the compressor inlet

2.4 Brayton cycle with Intercooling and Reheating

In this given cycle, there is multistage compression and expansion. The stream, which exits from pre-cooler, enters into the pre-compressor (1) shown in Fig.4. After the stage of compression, the fluid passes on to an intercooler to dissipate heat (2). After the intercooler, stream enters to the main compressor (re-compressor) where its pressure and temperature increased (3).

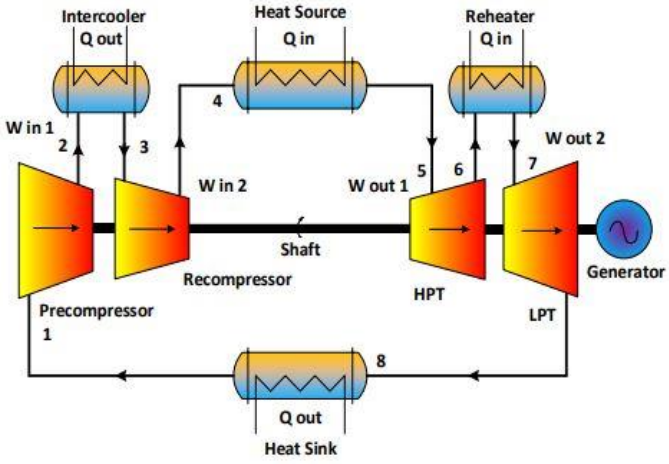


Figure 4: Layout of Brayton cycle with Intercooler and Re-heater

After this procedure, stream absorbs the heat from the heat exchanger (gas heater) (4 to 5) and made to move to HP turbine. The outlet fluid from HP turbine is hot in the re-heater at constant pressure (6). The low-pressure hot fluid (7) moves the LP turbine and allowed to expand there (8).After the generation of electricity, the fluid was made to go through heat sink where the remaining heat is dissipated and thereafter enters to a pre-compressor and the complete process starts all over again.

Thermal modelling

This chapter deals with the set of equations that are used for the different steps of analysis to be performed. They are presented in order of the showed system performance.

The equation of work of 1st compressor is

$$W_{in,precompressor} = h_2 - h_1 \quad (1)$$

The equation of work of 2nd compressor is

$W_{in,recompressor} = h_4 - h_3$ (2)

The equation for net compressor work is

$W_{in} = W_{in,precompressor} + W_{in,recompressor}$ (3)

The equation for high pressure turbine is

$W_{out,HPturbine} = h_6 - h_5$ (4)

The equation for low pressure turbine is

$W_{out,LPturbine} = h_8 - h_7$ (5)

The equation for net turbine work is

$W_{out} = W_{out,HPturbine} + W_{out,LPturbine}$ (6)

The equation for net work of the cycle is

$W_{net} = W_{out} - W_{in}$ (7)

The equation for heat input in combustor is

$q_{in,combustor} = h_5 - h_4$ (8)

The equation for heat input in reheater is

$q_{in,reheater} = h_7 - h_6$ (9)

The equation for net heat input is

$q_{in} = q_{in,combustor} + q_{in,reheater}$ (10)

The equation for heat output in intercooler is

$q_{out,intercooler} = h_2 - h_3$ (11)

The equation for heat output in heat exchanger is

$q_{out,hex} = h_8 - h_1$ (12)

The equation for net heat output in cycle is

$q_{out} = q_{out,intercooler} + q_{out,hex}$ (13)

The equation for thermal efficiency of the cycle is

$\eta = \frac{Wnet}{Qin}$ (14)

3. Results and Discussions

A steady temperature of 200ºC is used for warmth supply while maintaining a constant mass flow rate of 1 kg/sec. The Engineering Equation solver (EES) software package is utilized for analysis. A different approach to calculation of most heat exchange in Internal Heat Exchanger (IHE) is use when modelling a supercritical cycle, due to large dynamic heat component close to the critical point. Also, an alternative approach is required to compute the outlet temperature of the warmth source and identify the point of the pinch in supercritical cases. The results prove that IHE is useful in a subcritical case, but will improve system performance only partially for the low pressure stage in a supercritical scenario. In subcritical cycle it's discovered that power obtained is 27.33 kilowatt and cycle efficiency is 12.03% at an evaporator pressure of 1326 kPa and therefore the second law efficiency is 40.41% at an evaporator pressure of 1326 kPa using fluid R123. The cycle efficiency is coming out to be 11.27%, the second law efficiency is coming out to be 38.67% and net-work is 28.38 kW using fluid R245fa. Analysis is done on combined Organic Rankine cycle in which the exhaust coming out of heat exchanger of Brayton cycle is supplied to the Organic Rankine cycle. The analysis is done on both fluids R123 and R245fa.

In combined cycle the combined efficiency, Rankine efficiency, Brayton efficiency is 12.43%, 11.79%, 10.72% respectively at heater pressure 2600 kPa for fluid R245fa and 12.43%, 14.04%, 10.99% respectively for fluid R123. Also, in this study various cases of Brayton cycle is analyzed such as simple Brayton cycle, with intercooling, with reheating and with both intercooler and re-heater. The study is done on fluids R123 and R245fa.

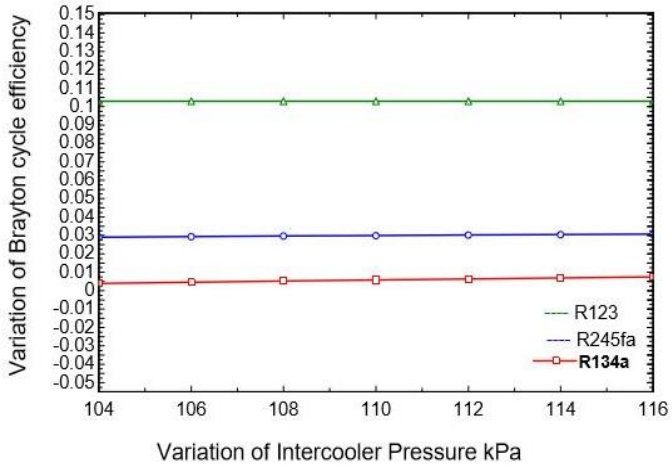


Figure 5: variation of cycle efficiency with intercooler pressure

Fig 5 shows the outcome of cycle efficiency by varying the intercooler pressure. As per the figure by increasing the intercooler pressure the cycle efficiency is also increasing. In this study analysis is done on three fluids i.e. R123, R245fa and R134a. From fig.5 the Brayton cycle efficiency at intercooler pressure 106kPa is 10.29%, 2.939% and 0.454% for fluid R123, R245fa and R134a respectively. Fig 6 shows the outcome of Brayton cycle efficiency by varying the maximum temperature of cycle. As per the figure by increasing the maximum cycle temperature the cycle efficiency is also increasing. In this study analysis is done on three fluids i.e. R123, R245fa and R134a. From fig.6 the Brayton cycle efficiency at temperature165 ºC is 10.29%, 3.023% and 0.6376% for fluid R123, R245fa and R134a respectively.

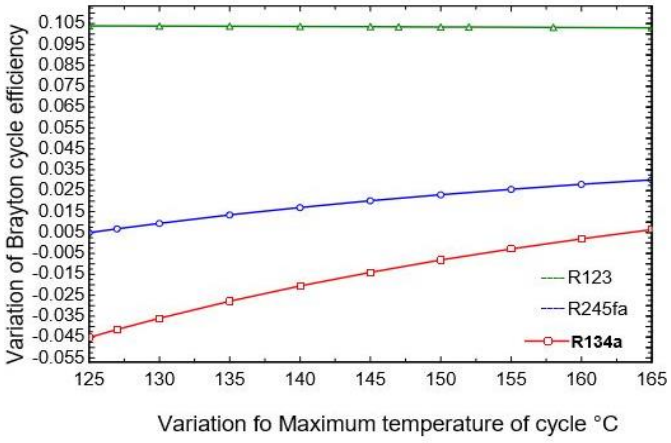


Fig 6 variation of cycle efficiency with maximum inlet temperature of turbine

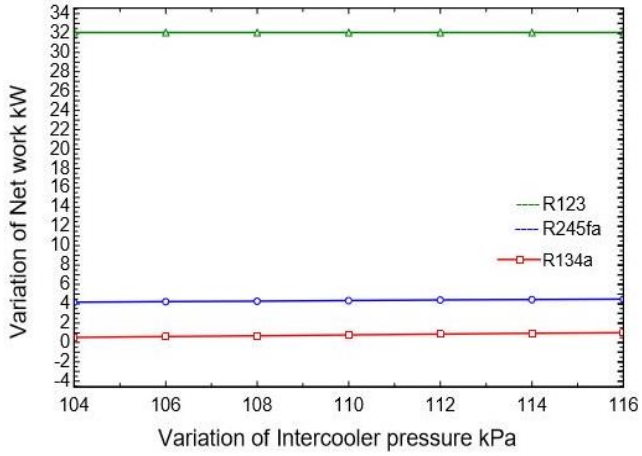


Fig 7 variation of net work of cycle with intercooler pressure

Fig 7 shows the outcome of net work by varying the intercooler pressure. As per the figure by increasing the intercooler pressure the net work is also increasing for R245fa and R134a but it is constant for R123. From fig.7 the Brayton cycle net work at intercooler pressure 106kPa is 32.04 kW, 4.217 kW and 0.6055 kW for fluid R123, R245fa and R134a respectively.

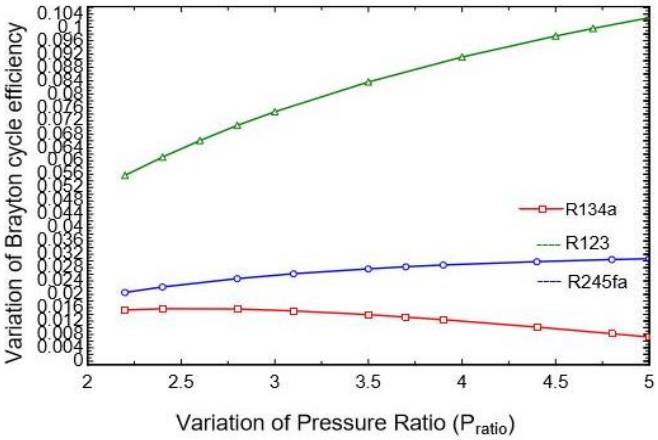


Fig 8 variation of cycle efficiency with pressure ratio

Fig 8 shows the outcome of cycle efficiency by varying the pressure ratio. As per the figure by increasing the intercooler pressure the cycle efficiency is increasing up to pressure ratio 3 and after thet it starts decreasing for R245fa while for R134a after pressure ratio 3 it decreases rapidly as compared to R245fa. It can be seen from the fig-8, on increasing of the pressure ratio efficiency is also increasing for R123.

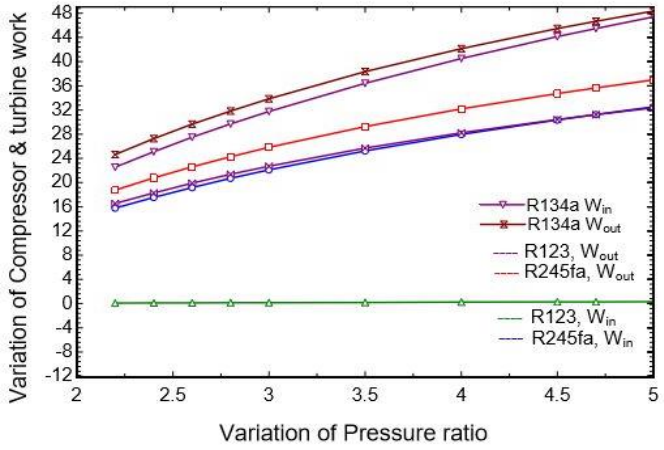


Fig 9 variation of compressor and turbine works with pressure ratio

Fig 9 shows the outcome of compressor and turbine work by varying the pressure ratio. As per the fig-9, by increasing the pressure ratio both compressor and turbine work is increasing for R123, R245fa and R134a.

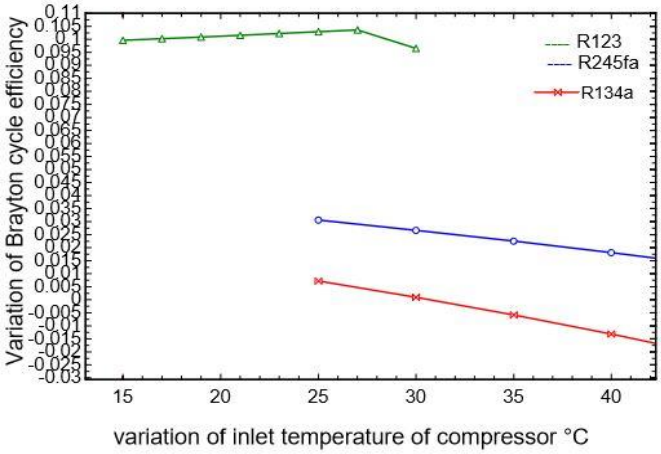


Fig 10 variation of Brayton cycle efficiency with inlet temperature of compressor

Fig 10 shows the outcome of cycle efficiency by varying the inlet temperature of compressor. As per the figure by increasing the inlet temperature of compressor the cycle efficiency is decreasing for R245fa and R134a while it is increasing for R123 upto 27ºC and after that it starts decreasing. From fig.10, the Brayton cycle efficiency at inlet temperature of compressor25ºC is 10.29%, 3.064% and 0.721% for fluid R123, R245fa and R134a respectively.

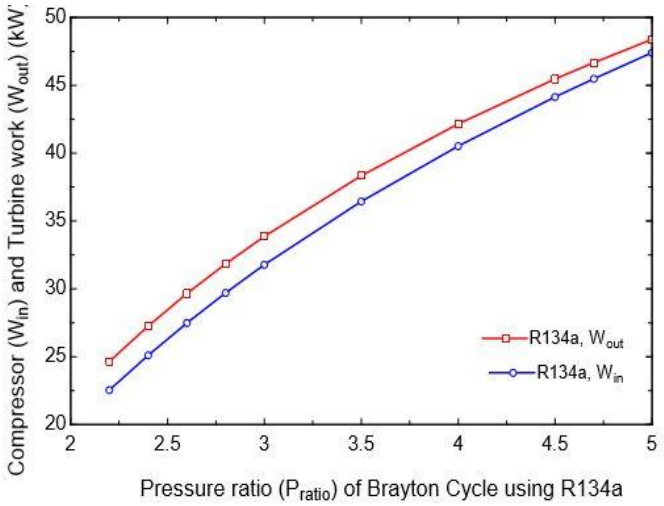


Fig 11 variation of compressor and turbine works with pressure ratio using R134a

Fig 11 shows the outcome of compressor and turbine work by varying the pressure ratio. As per the figure by increasing the pressure ratio the compressor and turbine work is also increasing for R134a. From fig.11, compressor and turbine work is 31.77 kW and 33.87 kW respectively at pressure ratio 3.

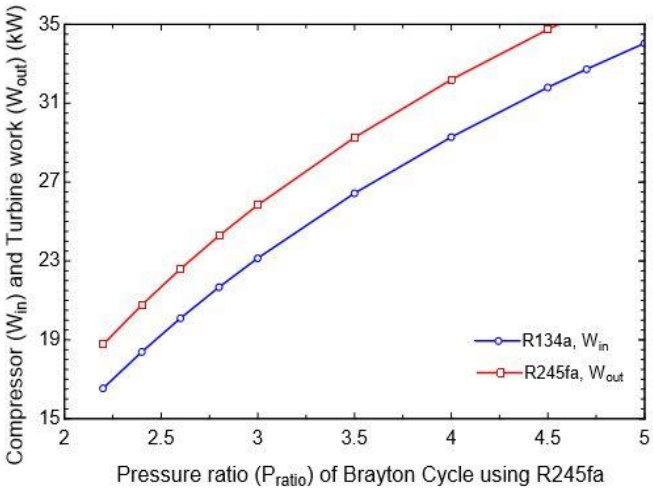


Fig 12 variation of compressor and turbine works with pressure ratio using R245fa

Fig 12 shows the outcome of compressor and turbine work by varying the pressure ratio. As per the figure by increasing the pressure ratio the compressor and turbine work is also increasing for R245fa. From fig.12, compressor and turbine work is 23.14 kW and 25.83 kW respectively at pressure ratio 3.

Fig 13, shows the outcome of compressor and turbine work by varying the pressure ratio. As per the figure by increasing the pressure ratio the compressor and turbine work is also increasing for R123. From fig.13, compressor and turbine work is 40.51 kW and 42.15 kW respectively at pressure ratio 4.

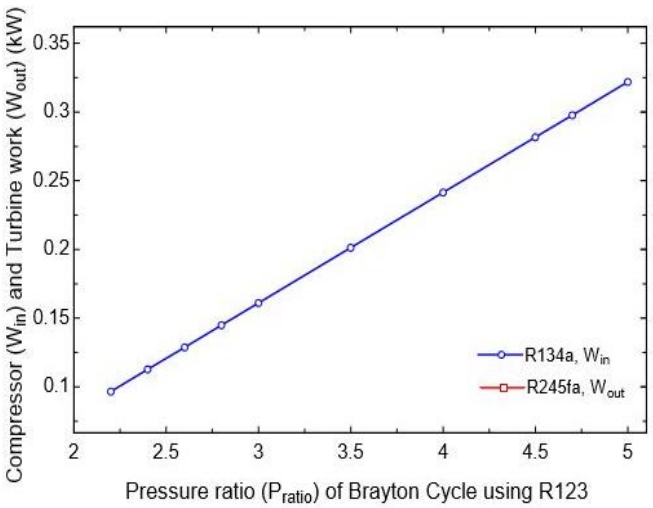


Fig 13 variation of compressor and turbine works with pressure ratio using R123

4. Conclusions

The following conclusion has been made from the above results

(i) As pressure ratio increases, the turbine & compressor work are increasing.

(ii) As intercooler pressure increases the cycle efficiency increases.

(iii) R123 is giving better performance than R245fa and R134a

References

[1] Serrano J.R., Dolz V., Novella R., Garcia A., 2011. HD Diesel engine equipped with a bottoming Rankine cycle as a waste heat recovery system. Applied Thermal Kevinj Engineering 36(2011), 279-287.

[2] Wang X. D., Zhao L., Wang J.L., Zhang W.Z., Zhao X.Z., W.Wu. 2009, Performance evaluation of low temperature Solar Rankine Cycle System utilizing R245fa. Solar Energy 84(2010), 353-364.

[3] Di GenovaKevinj., Botros Barbara B, Brisson J.G., 2012 Method for customizing on Organic Rankine cycle to a complex heat source for efficient energy conversion, demonstrated on Fischer Tropsch Plant. Applied Energy 102(2013) 746-754.

[4] Wang Dongxiang, Ling Xiang, PengHao, 2012. Performance Analysis of double organic Rankine cycle for discontinuous low temperature waste heat recovery. Applied thermal Engineering 48(2012) 63-71.

[5] Larjola J., 1994. Electricity from industrial waste heat using high speed organic Rankine cycle. International journal of Production Economics 41(1995) 227-235.

[6] Li Jing., Pei Gang, Li Yumhuli, JiJie., 2012. Evaluation of External heat loss from small scale expander used in organic Rankine cycle. Applied Thermal Engineering 31(2011) 2694-2701.

[7] Quilin S., Orosz M.,Hemond H., Lemort V., 2012. Performance and design optimization of Low cost solar organic Rankine cycle for remote power generation. Solar Energy 85(2011) 955-966.

[8] Herberle Florian, Bruggemann Dieter, 2010. Exergy based fluid selection for geothermal organic Rankine cycle for combined heat and power generation. Applied Thermal Engineering 30(2010) 820-880.

[9] Liu Bo., Riviere Philippe, Coquelet Christopher, Gicquel Renaud, David Frank, 2012. Investigation of a two stage Rankine cycle for Electric power Plants. Applied energy 100(2012) 285-294.

[10] Borsukiewiz- Gozdur Aleksandra, 2012. Pumping work in organic Rankine cycle. Applied thermal engineering 51(2013)781-786.

[11] Clemente Stefno, Michel Diego, Mauro Reini, TaccaoniRodolf, 2012. Energy Efficiency analysis of organic Rankine cycle with scroll expander. Appplied energy 97(2012) 792-801.

[12] Garcia Lourdes Rodriguez, Austin M.Delgado-Torres, 2006. Solar powered Rankine cycle for fresh water production. Desalination 212(2007) 319-327.

[13] Sprousell Charles, Depicl Christopher, 2012. Review of organic Rankine cycle for internal combustion engine Exhaust waste heat recovery. Applied Thermal Engineering 51(2013) 711-722.
[14] Herberle Florian, Bruggemann Dieter, 2010. Exergy based fluid selection for Geothermal Organic Rankine cycle for combined heat and power generation. Applied Thermal Engineering 30(2010) 1326-1332.
[15] Algieri Angelo, MorronePietropaolo, 2011. Comparative energetic analysis of high temperature sub-critical and transcritical organic Rankine cycle. Applied Thermal Engineering 36(2012) 236-244.
[16] Hui-tao Wang, Hu Wang, Zhu-ming Zhang, 2011. Optimization of low temperature exhaust gas waste heat fuelled organic Rankine cycle. Journal of Iron and Steel Research, International 2012,19(6), 30-36.
[17] Kosmadakis G, Manolakos D, Papadakis G, 2009. Parametric Theoretical study of a two stage solar organic Rankine cycle for RO desalination 2009, Renewable Energy 35(2010) 989-996.
[18] P.J. Mago, K.K. Srinivasan, L.M. Chamra, C. Simayaji, An examination of exergy destruction in organic Rankine cycles, Int. J.Energy Res 32(2008) 926-938.
[19] W. Li, X. Feng, L.J. Yu, J. Xu, Effects of evaporating temperature and internal heat exchanger on organic Rankine cycle, Appl. Therm. Eng. 31(2011) 4014-4023.
[20] Y.P. Dai, J.f. Wang, L. Gao, Parametric optimization and comparative study of organic Rankine cycle (ORC) for low grade waste heat recovery, Energy Convers, Manag. 50(2009) 576-582.
[21] Karellas S, Schuster A., Supercritical fluid parameter in organic Rankine cycle Applications. International Journal of Thermodynamics, 2008. 11(3), 1018.
[22] V. Lemort, S. Quoilin, C. Cuevas, J. Lebrun, Testing and modeling a scroll expander integrated into an organic Rankine cycle, Appl. Therm. Engg. 29(2009) 3094-3102.
[23] A. Schuster, S. Karellas, E. Kakaras, H. Spliethoff, Energetic and economic investigation of organic Rankine cycle applications, Appl. Therm. Eng. 29(2009) 1809-1817.
[24] F. Heberle, D. Bruggemann, Exergy based fluid selection for a geothermal organic Rankine cycle for combined heat and power generation, Appl. Therm. Eng. 30(2010) 1326-1332.
[25] J.P. Roy, M.K. Mishra, A. Mishra, Parametric optimization and performance analysis of a waste heat recovery system using organic Rankine cycle, Energy 35(2010) 5049-5062.
[26] J. Li, G. Pei, Y.Z. Li, J. Ji, Evaluation of external heat loss from a small-scale expander used in organic Rankine cycle, Appl. Therm. Eng. 31(2011) 2694-2701.
[27] S. Quoilin, R. Aumann, A. Grill, A. Schuster, V. Lemort, H. Spliethoff, Dynamic modeling and optimal control strategy of waste heat recovery organic Rankine cycle, Appl. Energy. 88(2011) 2183-2190.
[28] N. Yamada, M.N.A. Mohammad, T.T. Kien, Study on thermal efficiency of low to medium temperature organic Rankine cycles using HFO-1234yf, Renew. Energy 41(2012) 368-375.
[29] F.A. Al-Sulaiman, I. Dincer, F. Hamdullahpur, Thermo-economic optimization of three tri-generation systems using organic Rankine cycles: part 1 – formulations, Energy Convers. Manag. 69(2013) 199-208.
[30] F.A. Al-Sulaiman, I. Dincer, F. Hamdullahpur, Thermo-economic optimization of three tri-generation systems using organic Rankine cycles: part II – applications, Energy Convers. Manag. 69(2013) 209-216.
[31] World Energy Outlook 2013. 2013; International Energy Agency]. Available from: http://www.iea.org/.
[32] Horuz, I. and B. Kurt, Absorption heat transformers and an industrialapplication. Renewable Energy, 2010. 35(10): p. 2175-2181.
[33] Klein, S.A. and F. Alvarado, Engineering Equation Solver, version 9.237, FChartSoftware. Middleton 2012.
[34] Kim, Y.M., C.G. Kim, and D. Favrat, Transcritical or supercritical CO2 cyclesusing both low- and high-temperature heat sources. Energy, 2012. 43(1): p.402-415.
[35] Institute, P. Energy Source: Solar Energy. Renewable Energy. . 2011;Available from: http://www.pembina.org/re/sources/solar.
[36] Chen, H., The Conversion of Low-Grade Heat into Power Using SupercriticalRankine Cycles, in Chemical and Biomedical Engineering. 2010, Universityof South Florida.
[37] Stijepovic, M.Z. and P. Linke, Optimal waste heat recovery and reuse inindustrial zones. Energy, 2011. 36(7): p. 4019-4031.
[38] R.S. Mishra &Manish Kumar [2018] Thermodynamic models for combined cycle power plants used in organic Rankine&Brayton Cycles, International Journal of research in Engineering and innovation (IJREI) e-ISSN: 2456 - 6934 , Vol: 02, Issue: 04 ,2018, 449-463
[39] R.S. Mishra &Manish Kumar [2018]Thermodynamic analysis of modified rankine cycle used for power generation, International Journal of research in Engineering and innovation (IJREI) e-ISSN: 2456 -6934, Vol: 02, Issue: 01, 2018, 33-40.
[40] R.S. Mishra &AakashBehl [2018]Thermodynamic analysis of combined cycle power plant with trans-critical cycle integrated with solar system for power generation for space heating and cooling, International Journal of research in Engineering and innovation (IJREI) e-ISSN: 2456 -6934, Vol: 02, Issue: 04, 2018, 423-441

Cite this article as: R.S. Mishra, Manish Kumar, Thermodynamic analysis of brayton cycle for power generation, International Journal of Research in Engineering and Innovation Vol-3, Issue-4 (2019), 282-290.

Transformer Health Monitoring System Using Internet of Things

Divyank Srivastava
Electrical Engineering Department
Delhi Technological University
New Delhi, India
divyanksri.srivastava@gmail.com

M. M. Tripathi
Electrical Engineering Department
Delhi Technological University
New Delhi, India
mmmtripathi@gmail.com

***Abstract*— Health monitoring of electrical equipment using IOT may help to replace the equipment before failure and continuity of the power will not be disturbed. This paper presents an implementation of this concept which acquires the real-time condition of the distribution transformer remotely with the use of internet implementing IOT. The proposed health monitoring system works in real time and uses temperature-sensor, potential transformer and current transformer for monitoring temperature, voltage and current of the distribution transformer and send these information to a remote server where it can be monitored and necessary action may be taken to avoid the outage of the electricity supply. The proposed system has been implemented in Laboratory and tested. The data collected are validated and it has been found that the proposed system is working satisfactorily.**

Keywords—Internet of things, Health monitoring system, Distribution transformer,GSM, Microcontroller, Sensor.

I. INTRODUCTION

A distribution transformer is a step down transformer which delivers power to the users which can be used in houses or industries, etc. Various predicaments can be faced by distribution transformers if their health is not monitored periodically[1]. The operating parameters such as temperature, voltage and current of a distribution transformer are vital measurement criterion which can tell about the health of the transformer. The operating condition depends on several factors such as overloading, loss of supply etc. Life of a transformer is proportional to its health. Better the health of a transformer, longer the life. Issues such as overburden and inadequate heating of a transformer are the main reasons of deterioration of a transformer's health[2]-[3]. Earlier the health monitoring system was not much prevalent in the distribution network and the faults could only be detected after a complete blackout. It caused major penalties for the distribution system as large amount of losses were incurred. Therefore, there was a foremost need for a reliable health monitoring system which would help in creating preventive measures beforehand. The present health monitoring systems pose a few concerns which are listed below: (i) Common systems for transformer measurements merely identify a single transformer parameter. Even if some systems are able to detect multiple parameters, the time consumed in the testing is too lengthy and hence slow speed is attained. (ii) Detection system is erratic. The performance of the detection system is less accurate[4]-[8]. Slower detection of the faults is present and it is unreliable and unstable (iii) The monitoring system is unable to observe all the user data of transformers to decrease costs.

As per the abovementioned requirements, we need a monitoring system to analyze real time data associated with the distribution transformer to characterize various operating parameters and further provide the information to the monitoring centre in requisite time [9]. This is when Internet of Things(IOT) comes into picture. It helps to invigilate the data online of the key functional factors of the distribution transformers which grants constructive data about the health of distribution-transformers which in turn will facilitate the services to use their transformers in a best possible way and increase the life of a transformer. IOT helps in identifying the problems beforehand i.e. Before the occurrence of any failed mechanism which facilitates cost effective solutions and hence less penalty. IOT serves greater reliability and stability than other conventional systems[10].

II. BLOCK DIAGRAM

The fig.1 represented by a block diagram suggests it is essential that the device being used for invigilating (monitoring) be housed nearby the transformer itself. The blocks represented in the block diagram evaluate different parameters communicating the health of the transformer. Furthermore, the proposed system provides us with a health monitoring system of the distribution transformer which presents us with the data regarding various parameters of the transformer. Additionally, three sensors have been used in the proposed system, namely, voltage sensor, a current sensor, and temperature sensor. For the use of PIC microcontroller, a power supply for supplying power has been used, a Wi-fi modem for internet connectivity has been used and several sensors has been used. Fig.1 shows the different modules used in the proposed model. The data received by the IOT is sensed by the sensors incorporated and displayed on the LCD screen. Furthermore, at the same time, data is also being sent to the user on a given server or on the cellphone via Wi-fi connection. The advantage of having such a system is that if estimation of an unprotected system is made by IOT, system failure can be prevented. The proposed system comprises the following module:

978-1-5386-6625-8/18/$31.00 ©2018 IEEE

A. Power Supply

As per the standard process we need 5V power supply for our proposed model, in which we have used a bridge rectifier, capacitors and a 7805 voltage regulator. Here we have used a 230/12V transformer to convert the power supply to its desirable value, i.e 12V [11]. A bridge rectifier is connected after a 230/12V transformer which convert the 12V AC to DC, then a 1000µf capacitor is connected in parallel to filter out the ripples from there we give a connection to our GSM module then a 7805 regulator is connected after that two 100µf capacitors are connected which gives a pure 5V dc to give in whole circuit.

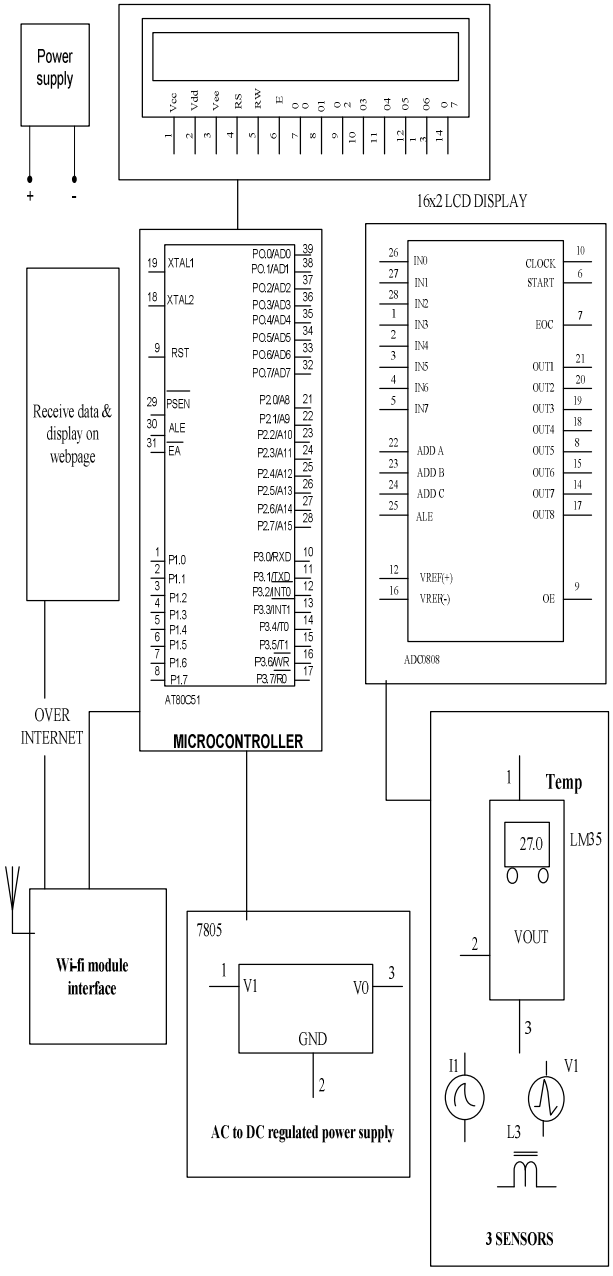


Fig.1: Block Diagram of proposed model

B. LCD Module

One of the commonly used devices connected to a PIC microcontroller is an LCD module. Some common LCDs which can be used with the PIC microcontroller for implementation of any kind of hardware projects are 16x2 type and 20x2 type display LCD, means it can show 16 characters in each line, and 20 characters in each line (both can show output in two line).

C. PIC-Microcontroller 18F4520

PIC-microcontroller was made by Microchip-Technology in 1993.Acronym of PIC is Peripheral Interface Controller. The performance of these microcontrollers are steadfast and they can implement a program very easily compared with other microcontroller of same categories. PIC-microcontrollers are widely used because of their effortless programming, wide obtainability, easily connection with other peripherals, cheapness, large client network and serial-programming ability (reprogramming along with flash-memory), etc. In 2000, Microchip-technology present the PIC18 microcontroller which is distinct from the 17 series, which become very popular and fast selling microcontroller in the market, with a huge number of PIC-microcontroller-17 deviations presently in production. In compare to earlier microcontroller, which mainly used assembly language for programming, Now C has become the major programming language [12].

D. GSM Module

In the village areas, GSM delivers an ultimate communication network by using the web of mobile communication network. With the use of GSM technology we can transmit data with high efficiency, suitability and with low cost. Through GSM the monitoring of distribution-transformer health can be done easily. We used 2.4 GHz GSM module which is a very precise, accurate and high speed data transfer can be achieved .It works with the baud rates 9600, 19200.etc. It is a transceiver part through which information can be simultaneously transmitted and received. It should be connected to any TTL/CMOS logic serial RXD and TXD lines and can support Baud-rate of 9600bps, 19200bps, 38400bps and 57600bps. It can also works with 4 different RF [13].

E. Regulator

The used voltage regulator L7800 series is a three-terminal regulator(+), which is available in D^2PAK packages and multiple no of output voltage, because of that we can used it in different and wide number of application. With these regulators local-on card regulation can be achieved, removing the error occur due to single-point regulation.[14] Each regulator type can used in internal current limiting, thermal shut-down and protection of the network, making it fundamentally enduring. If suitable heat-sinking is offered, they can gives over 1A output current. While these devices used as primarily voltage regulator, these can also be used with external hardware circuit for getting constant voltage and desirable current.

F. LM 35 Temperature Sensor

LM35 sensors are used for sensing the temperature and an IC ADC0808 is used to convert the data into digital form. LM35 sensor consist of 3 pin's i.e., VCC, GND and output pin. When LM35 is heated the voltage at output pin increases, it is connected to the analog to digital convertor IC (ADC). This LM35 series sensors are more accurate integrated-circuit temperature sensors, because there output voltage is directly proportional (linear) to Celsius temperature scale. Thus LM35 are more advantageous than other standard linear temperature sensors which are calibrated in kelvin, due to this there is no need to minus a large voltage value from its output to convert in centigrade value. The LM35 don't entail any external regulation to deliver distinctive precision of ±1⁄4˚C at room temperature and ±3⁄4˚Cover a full(−55 to +150˚C) temperature range.

G. Voltage Sensor

A voltage sensor is nothing but a potential transformer. Voltage sensors sense the voltage of an output terminal and gives a signa1 directly proportional to it. The sent signal can be in the form of analog current or voltage, which can be converted into a digital output using ADC [15]. The output produced is employed to exhibit the precise voltage by a suitable measuring device or it can be saved for further analytical purpose in the database for controlling of different variables.

H. Current Sensor

A current sensor is equivalent to a current transformer. Current sensors sense the current in an external load and gives a signal directly proportional to it. The produced output could be analog voltage or current which can be converted into digital form using ADC. The produced signal is utilized to display the measured current using a suitable measuring device [15]. Value obtain from current sensors can be saved for further analytical purpose in the database for controlling of different variables. The output of current sensor can be in the form of various quantities such as:

DC input, a tripping output like in a relay, which replicates the value of the sensed current digital output, which tripped when the sensed current surpasses a certain pickup value.

III. CONNECTIONS AND DESIGNING

The connection of LCD , microcontroller , temeperature sensor, current transformer and potential transformer are as follows:

We connect a 16x2 LCD which is having 16 pin , 1st pin is connected to ground , 2nd to 5v supply, 3rd is connected with 2 resistors value 1kΩ and 10kΩ through 5v supply , this pin is used to adjust the contrast, 4th pin is Rs pin, 5th is data read/write, 6th is data enable pin and these 3 goes to 27,28,29th pin of microcontroller. 7th to 14th pins are data pins and connected to 33th to 40th pins of microcontroller, 15th pin is again used for brightness adjustment, connected to 5v supply and the last 16th pin is grounded.

33th to 40th pins are data pins which is connected to 7th to 14th pin of 16x2 LCD , 27th 28th 29th pins are Rs , RD/WR , En pins connected to 4th 5th 6th pin of 16x2 LCD , 11th and 32th pins are power pin connected to 5v supply and 12th and 31th pins are used for grounding. There is a .1µf capacitor is connected between pin 12 and 32. 1st pin is used to reset the microcontroller connected to 5v supply through a 10kµ resistor and a switch. 13th and 14th pins are used to connect the crystal oscillator of 11.0592MHZ frequency, 22pf capacitor are connected to both the pins. 15th 16th 17th 18th pins are used to enter the mobile no on which we have to send the transformer health data, each is connected to 5v supply through a 10kΩ ladder resistor network and a switch. Pins 19th 20th 21th and 22nd are connected to 4 LED to send some data from the remote center to our GSM module and the LED glow according to the message, pins 25th and 26th are transmitter and receiver pins connected to 11th and 12th pins of max 232, microcontroller works on RS232 level, 5V TTL logic.

MAX 232 is used for level conversion because as all the system works on 5V supply but our GSM module works on +10V, +12V, +18V supply so MAX 232 convert +5V to +12V , its 11th and 12th pins are connected to 25th and 26th pins of microcontroller. 16th pin is connected to +5V supply and 15th pin to ground, there is .1µf capacitor connected between these two pins. There is 10µf capacitor connected between 1st -3th pin and 4th – 5th pin, similarly pin 2 is connected to 5v supply through 10µf capacitor and pin 6th to ground through 10µf capacitor.

GSM module (SIM 900) also works on RS232 level its pin 3 is receiver pin which receive the signals from 14th pin of MAX 232 and its 2 pin is transmitter pin which transmit data to pin 13th of MAX 232.

The 12V ac coming from 220/12V transformer is converted to 12V DC through 4 diode (1N4007) bridge converter then a 100µf capacitor is connected in parallel to eliminate the ripple content then 3, 10kΩ resistors are connected in series with a 6.5kΩ resistor and 4.7kΩ variable resistor in parallel. This variable resistance is connected to limit the output to 5V, than this circuit output goes to pin 3rd of ADC.

A phase and neutral wire goes to load from which a C.T is connected to load wire from which a diode (1N4148) is connected , a 10kΩ resistor and a 100µf capacitor are connected in parallel, one 83kΩ resistor is connected in series then a 6.8kΩ resistor along with 4.7kΩ variable resistor is connected in parallel to limit the output current, than this circuit output is goes to pin 4 of ADC.

There is an analog temperature sensor i.e LM35 which can sense 10mV/o , its 1st pin is connected to 5V supply and 3rd pin to ground. 2nd pin is goes to pin 2 of ADC.

For designing a PCB layout we use DIP TRACE software. In this software, for creating a 16, 32 or 40 DIP pin we use pattern template. The toolbox is used to select various components. The selected component is held and dragged into the workspace. The wired network of desired width is used to connect the components in the workspace. We can use pin manager for

connection of microcontroller pins with other components. We have Design manager on the left side of our workspace from which properties of selected object or function can be modified. Parameters in this panel change, depending on the selection (component, net, bus etc.). If several objects are chosen, we will see only common parameters for all of them. The schematic diagram of our PCB layout is shown in fig.2.

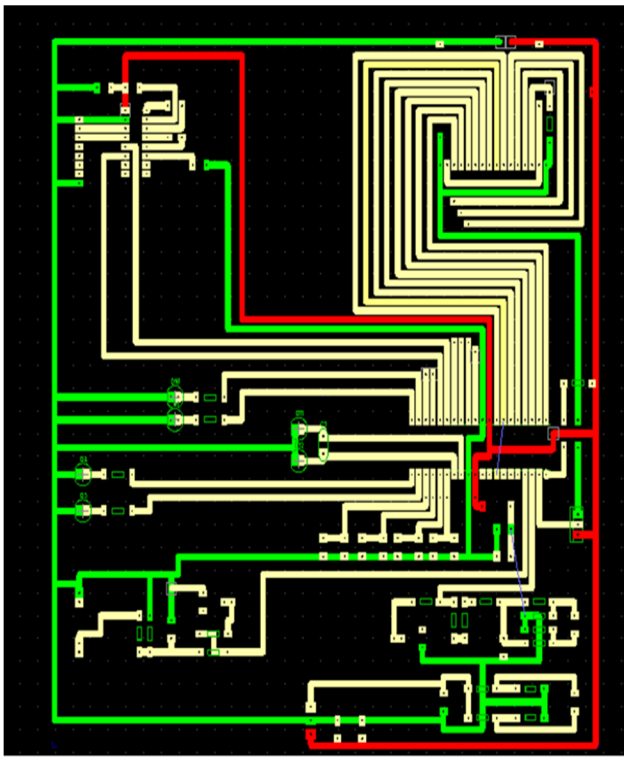


Fig.2: PCB Layout

When we switch on the circuit it takes 7 initialization pulses to display the current, voltage and temperature at the 16x2 LCD and after 9 initialization pulses the data is send to IOT server on which we can see the health data of transformer. There is 199 count counter using which we can see a new response after 199 count, as we increase the load the load current increases in the monitor, and we can vary the transformer voltage with the help of variable resistor. The hardware model is shown in fig.3.



Fig: 3 Actual hardware Model

IV. RESULTS

On the 16x2 LCD, transformer current, voltage and temperature were observed after 7 initialization pulses. After the next 9 pulses the data was sent to the IOT servers on which the health was monitored and necessary actions were taken.

On the IOT servers, three parameters can be viewed i.e. temperature, voltage and current as seen in fig.3, fig.4 and fig.5 respectively. The data entries can also be viewed on the IOT server on JSON file type as shown in fig.6.

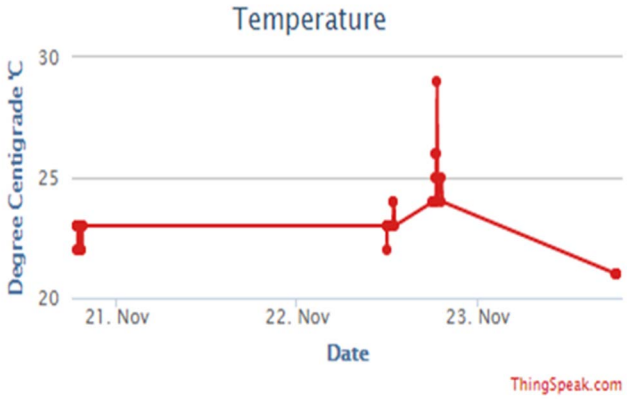


Fig.3: Transformer Temperature

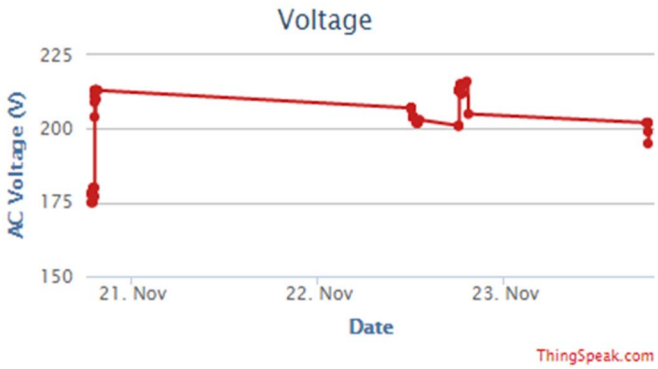


Fig.4: Transformer Voltage

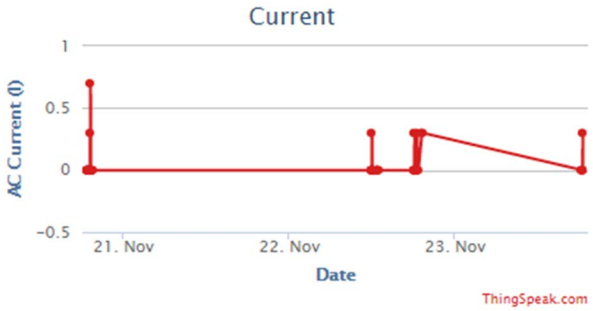


Fig.5: Load current

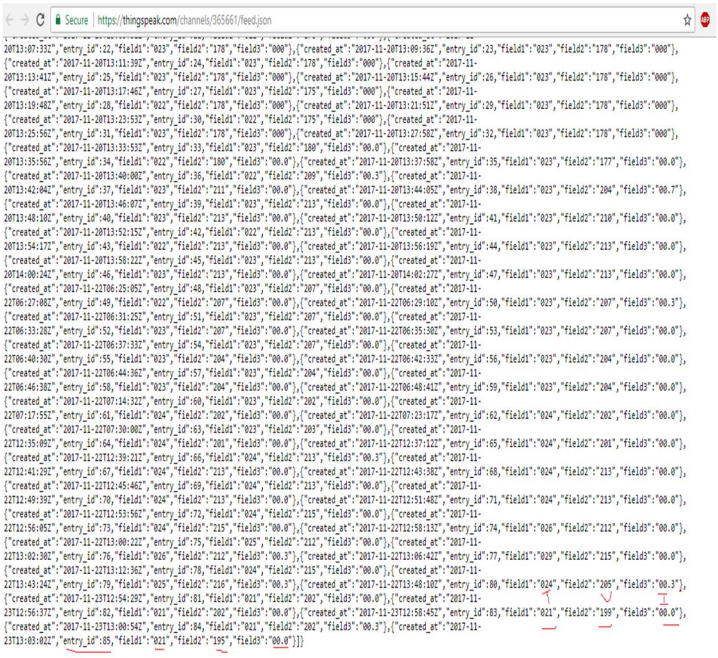


Fig: 6 Real Time Data on IOT Server

V. CONCLUSIONS

The IOT wireless open typical technology is being designated in this paper as the energy management and efficiency technology of choice. Employing the system for real time monitoring of power line with an open standard such as IOT helps to keep costs down and condensed power consumption. We can observe from this project that sensors can be employed to conventional as well as smart grid for monitoring of different parameter of the grid. It can be concluded that our model showing results on internet through GSM module as well as on the on-board LCD. Using IOT for monitoring different parameter of distribution transformer, human labour will be minimised and we can also save the data for forecasting as well as for any electricity theft. With the use of IOT our power system would become more accurate and reliable. The advantage of using GSM based monitoring over manual monitoring is that there is no need for an operator to note down the variables after every minute because with the use of IOT the data can be stored with every 90 second After we found out any abnormality in the system, necessary action can be taken instantly and any catastrophic failure can be prevented.

In the same way we can implement wireless sensors on relays of transmission line, RTD of generators and different power system component, and send their data through GSM on internet making our power system network healthy and reliable.

REFERENCES

[1] Chan, W. L, So, A.T.P. and Lai, L., L.; "Interment Based Transmission Substation Monitoring", IEEE Transaction on Power Systems, Vol. 14, No. 1, February 2014, pp. 293-298.

[2] Performance Monitoring of Transformer Parameters in (IJIREEICE) Vol. 3, Issue 8, August 2015.

[3] Gsm based transformer monitoring" in "International Journal of Advance Research in Computer and Communication Engineering", Vol.2, Issue3, JAN 3.

[4] "Distributed Transformer Monitoring System" International Journal of Engineering Trends and Technology (IJETT) - Volume4 issue5- May 2013.

[5] Microcontroller Based Substation Monitoring and Control System with Gsm Modem'' IOSR Journal of Electrical and Electronics Engineering (IOSRJEEE) ISSN: 2278-1676 Volume 1, Issue 6 (July-Aug. 2012).

[6] Ravishankar Tularam Zanzad, Prof. Nikita Umare, and Prof Gajanan Patle "ZIGBEE Wireless Transformer Monitoring, Protection and Control System",International Journal of Innovative Research in Computer and Communication Engineering (An ISO 3297: 2007 Certified Organization), Vol. 4, Issue 2, February 2016.

[7] N Maheswara Rao, Narayanan R, B R Vasudevamurthy, and Swaraj Kumar Das, ''Performance Requirements of Present-Day Distribution Transformers for Smart Grid'', IEEE ISGT Asia 2013 1569815481.

[8] Mohamed Ahmed Eltayeb Ahmed Elmustafa Hayati, and Sherief F. Babiker, ''Design and Implementation of Low-Cost SMS Based Monitoring System of Distribution Transformers'', 2016 Conference of Basic Sciences and Engineering Studies (SGCAC).

[9] Leibfried, T, "Online monitors keep transformers in service", Computer Applications in Power, IEEE, Volume: 11 Issue: 3, July 1998 Page(s): 36 -42.

[10] http://www.microchip.com/wwwproducts/en /PIC18F4520.

[11] Xiao-hui Cheng, and Yang Wang, ‘‘The remote monitoring system of transformer fault based on The internet of Things’’, 2011 International Conference on Computer Science and Network Technology.

[12] Leib fried, T, ‘‘Online monitors keep Transformers in service’’, Computer Applications in Power, IEEE, Volume: 11 Issue: 3, July 1998 Page(s):36-42.

[13] Chan, W. L, So, A.T.P. and Lai, L., L., ‘‘Interment Based Transmission Substation Monitoring’’, IEEE Transaction on Power Systems, Vol. 14,No. 1, February 1999, pp.293 – 298.

[14] Abdul-Rahman AI-Ali, Abdul Khaliq & Muhammad Arshad,” GSM-Based Distribution Transformer Monitoring System”, IEEE MELECON 2004, May 12-5,2004, Vol 3 Pages-9991002, Croatia.

[15] Muhammad Ali Mazidi , Janice Gillispie Mazidi, Rolin D.Mckinlay, The 8051 Microcontroller And Embedded Systems Using Assembly And C,Second Edition, Pearson Education, 2008, India.

Transmission Congestion Management Considering Modeling of Solar Photovoltaic Distributed Generator in Deregulated Power System

Anu Singla, Kanwardeep Singh,Vinod Kumar Yadav

Abstract*: This paper presents an effective methodology for transmission congestion management (TCM) in deregulated power system considering random nature of solar photovoltaic distributed generator (SPVDG). Solar photovoltaic power generation has gained popularity worldwide. Its' optimal sitting in the grid can provide congestion relief and reduce line losses etc. However, to maximize the potential benefits of this renewable energy source, its' stochastic power output which mainly depends on solar irradiance needs due consideration. In this paper, seasonal variations of solar irradiance have been modeled using beta probability density function to determine expected power output of SPVDG over various seasons of one year. TCM problem has been formulated as a non-linear programming with the objective of social welfare maximization of electricity market subject to equality and inequality constraints incorporating seasonal load demand variations. The optimal siting of SPVDG integration in the grid has been discussed. The proposed methodology has been simulated by incorporating practical data of a real-life SPVDG in standard IEEE 30-bus, IEEE 118-bus and practical Indian Utility 62-bus systems. Simulation results show the benefits of proposed methodology on market indices. The effectiveness of proposed approach is also discussed in comparison with existing methodology of distributed generation modeling

Keywords*: Beta probability density function, locational marginal pricing, solar photovoltaic distributed generator, transmission congestion.

I. INTRODUCTION

Transmission congestion management (TCM) plays an important role in the deregulated environment of power sector [1]. Congestion in transmission network creates market inefficiency, increases power losses and cost of energy. The various TCM schemes have been adopted in different electricity market models worldwide which can be briefly summed as pricing methods [2]-[4], re-dispatch [5]-[6], counter-trading [7], load auctions [8], reactive power support [9]-[10], load curtailment [11], deploying flexible AC transmission system (FACTS) devices [12]-[13], demand management [13]-[14], and distributed generation (DG) [15]-[19]. Nodal pricing/locational marginal pricing (LMP) mechanism [1], [10], [15] is adopted in several United States (U.S). Zonal pricing, a variant of nodal pricing is implemented by Australian and Scandinavian electricity markets for market clearing [1]-[2]. Nodal/LMP and zonal pricing methods indicate the location for installation of new generators and/or transmission expansion to manage congestion in the network. These financial tools act as deterrent for market constituents to re-schedule their generation/demand schedules but network congestion still exists posing threat to system security. Re-dispatching of hydro-thermal combination and all-thermal generators for alleviation of TCM in a pool based electricity market is used in [5]-[6]. References [12]-[14] have used FACTS devices and employed demand response technique for cost effective congestion management. However, the cost of reactive power and the impact of load variations have not been included in [5]-[6],[12]-[14]. The reactive power management is an integral component of transmission management [9]-[10].

The load side management has emerged as quite effective technique for congestion management. Distributed generation (DG) technology is one of the most effective tools of load management [15]-[21]. DG constitutes harnessing small and medium amount of power (few kW ~ few MW) from renewable energy resources like solar, wind, biomass and small/mini hydro plants etc. In this work, solar photovoltaic distributed power generator (SPVDG) is explored as DG technology for TCM for pool based market. The operating cost of solar power plants mainly comprises small operation & maintenance cost while fuel cost is zero [15]-[19]. Numerous literatures are available on the optimal siting and sizing of DG in power system with different objective functions. In deregulated electricity markets, the optimal placement and sizing of DG is important for TCM and social welfare (SW) maximization [17]-[18], [20]. Singh et al. [18] have used Z-bus based contribution factors for optimal placement of DG in the network to maximize SW. However, authors have used DC modeling and considered only real power generation cost for load instance in the optimization problem. LMP is widely used tool for DG integration in system for TCM [3]-[4], [15], [18]. Kumar and Gao [4] have used real power nodal price based

Revised Manuscript Received on September 15, 2019
***** Correspondence Author
Anu Singla*, [1]Research Scholar, I.K. Gujral PTU, Kapurthala, [2]Department of Electrical Engineering, Chitkara University Institute of Engineering and Technology, Punjab, India. Email: anusingla04@gmail.com.
Kanwardeep Singh, Department of Electrical Engineering, Guru Nanak Dev Engineering College, Ludhiana, (I.K. Gujral PTU, Kapurthala), Punjab, India. Email: kds97dee@gmail.com
Vinod Kumar Yadav, Department of Electrical Engineering, Delhi Technological University, Delhi, India. Email: vinodkumar@dtu.ac.in

zonal approach for optimal siting of DG in pool and hybrid electricity markets. Ramesh and Kumar [21] have used transmission line relief sensitivity index as tool for optimal placement of DG. Peesapati et al. [19] have presented a multi-objective TCM approach with solar, biomass and wind based DGs. But, the variability of the DG outputs has not been taken onto account in [15]-[16], [18]-[19] and the authors have committed the rated capacities of DGs in market dispatch.

However the power production of renewable DGs like wind and solar power is stochastic due to their dependence on random variables such as temperature, irradiance level and wind speed [20]. Hence analysis of such DGs requires probabilistic approach before committing their generation in electricity markets. Solar generation is mainly function of irradiance falling on photovoltaic (PV) panels. In this paper, seasonal variations in solar irradiance over the span of one year have been modeled using beta probability density function (PDF). Randomness of solar irradiance can be best modeled with beta PDF than other probability distribution functions like lognormal, weibull, gamma and logistics functions [22]-[24]. The problem has been formulated as non-linear optimization of TCM with an objective to maximize the SW of electricity market over the year incorporating the probabilistic seasonal output of SPVDG. The proposed approach has been applied for IEEE 30-bus, IEEE 118-bus and practical Indian Utility 62-bus systems. The results show the benefits of proposed methodology on SW, its components, merchandising surplus (MS) and losses.

The novelty of the present paper lies in the fact that the effects of seasonal variations of solar generation output using beta pdf, and seasonal variations in load demand changes have been incorporated in the TCM problem. Moreover, full AC modeling of power system is used which includes the reactive power generation cost in addition to real power generation cost and demand benefit in the objective function. The mechanism for optimal placement of SPVDG in the system based on market operations over the year has been discussed in the present work and contributes to the planning part of power system.

The rest of paper is organized as follows: Modeling of SPVDG is detailed in Section II. Section III provides formulation of TCM problem in electricity market. Results and discussion are presented in Section IV. Conclusions are drawn in Section V.

II. MODELING OF SPVDG

Solar PV power generation depends on site climatic conditions like irradiance, ambient temperature, dust, humidity and wind speed, characteristics of PV modules, regular cleaning and maintenance of plant [24]-[25]. Therefore it is vital to analyze the output of solar power plant apropos site conditions. In order to simplify the SPVDG modeling equations, the variation of site irradiance, temperature and characteristics of PV modules are considered only to determine the expected power output of plant. Thus modeling of SPVDG consists of two parts: solar irradiance modeling and power generation function for PV array.

A. Solar irradiance modeling

Solar irradiance and hence power output varies with the time of day and season of a year. In this work, one year is divided into four seasons as per prevailing conditions of Indian subcontinent. During any t th season, for i th time interval the solar irradiance is modeled by beta pdf, $f_b^t\left(s^t\right)$ as given below [20], [26].

$$f_b^t(s^t)=\begin{cases}\dfrac{\Gamma(\alpha^t+\beta^t)}{\Gamma(\alpha^t)\,\Gamma(\beta^t)}*(s^t)^{(\alpha^t-1)}*(1-s^t)^{(\beta^t-1)}, \\ for\ 0\le s^t\le 1,\ \alpha^t\ge 0,\ \beta^t\ge 0 \\ 0, \qquad otherwise\end{cases} \tag{1}$$

Where $\Gamma(.)$ is gamma function, β^t and α^t are parameters of beta distribution function and s^t is solar irradiance in kW/m^2 during t th season. β^t and α^t are calculated from mean (μ^t) and standard deviation (σ^t) of random variable solar irradiance, s^t from [20], [26].

B. Power generation function for PV array

The power $P_o^t\left(s^t\right)$ generated by PV array corresponding to solar irradiance s^t during t th season is calculated as [20], [24], [26]:

$$P_O^t(s^t)=N*FF*V^t(s^t)*I^t(s^t) \tag{2}$$

Where N is total number of PV modules in array forming SPVDG and F is the fill factor. $I^t(s^t)/V^t(s^t)$ are current/voltage of solar PV module during t th season and can be obtained from the characteristic parameters of PV modules and equations given in [20], [24], [26]. Once the beta pdfs of solar irradiance are generated for specified time intervals, the expected power output, $P_{pvi}^t(s^t)$ of SPVDG for any i th time interval during t th season can be obtained from the integration of product of $P_o^t(s^t)$ and $f_b^t(s^t)$ over $s_{\min}^t$ to $s_{\max}^t$ as:

$$P_{pvi}^t(s^t)=\int_{s_{\min}^t}^{s_{\max}^t}P_o^t(s^t)*f_b^t(s^t)\,ds \tag{3}$$

C. Algorithm for calculation of SPVDG output

The methodology adopted to determine the expected power output of SPVDG as function of site climatic conditions is summarized in following steps:

step 1. The hourly historical data of irradiance of SPVDG site under study is taken for one year.

step 2. The year is divided into four seasons as per prevalent site conditions. Then mean irradiance for each hour of the season is calculated and plotted versus time (7:00 to 18:00 hours). Observing the variation of irradiance with

time, the time intervals are specified from the plot, such that one mean value of irradiance pertains for each specified time interval. The mean μ^t and standard deviation σ^t of irradiance are calculated using Microsoft Excel.

step 3. Beta probability density function is applied to model stochastic solar irradiance using (1). The parameters β^t and α^t of beta distribution function are obtained from [20], [26].

step 4. The power outputs of SPVDG are calculated for each specified time interval (3).

step 5. The weights w_i^t of each time interval of a day for each season are calculated. The expected SPVDG power outputs, P_{PV}^t (MW) during any t th season is obtained from (4).

Seasonal expected power output of SPVDG,

$$P_{PV}^t = \left(w_i^t * P_{pvi}^t\right) / \sum_i w_i^t \quad \forall i \in time\ intervals, t \in T \tag{4}$$

Where T is set of seasons.

Steps 3-5 are coded with MATLAB programming.

step 6. Repeat steps 1-5 to determine expected power outputs for all seasons of the year.

III. TCM PROBLEM FORMULATION IN ELECTRICITY MARKET WITH SPVDG PLACEMENT IN SYSTEM

In this work, a double auction pool based electricity market followed by Pennsylvania-New Jersey-Maryland (PJM) has been considered for analysis. GENCOs and DISCOs submit their supply and demand bids to ISO. The seasonal variations in load demand and SPVDG power output affect the generation and demand schedules; as a result SW changes in each season. In the proposed approach, ISO prepares a generation and demand schedules with an objective of social welfare maximization over the year considering non-linear load flows as equality constraints and transmission line loadings as inequality constraints. SW function as given in [18] is multiplied with fractional weight of respective season to maximize SW over a set of seasons of the year. The sum of weights equals to one. Hence mathematically TCM problem has been formulated as non-linear optimization problem with the objective of maximization of SW over the year.

A. Objective function

$$Max\ SSW = \sum_{t=1}^{T} ws^t * \left[\sum_{i=1}^{N,t} \left\{ B_i^t\left(P_{di}^t\right) \right\} - \sum_{i=1}^{N,t} \left\{ C_i^t\left(P_{gi}^t\right) + C_{qi}^t\left(Q_{gi}^t\right) \right\} - C(SPVDG) \right] \tag{5}$$

Where SSW is annualized value of SW in \$, $B_i^t(P_{di}^t) / C_i^t(P_{gi}^t)$ are demand benefit function of DISCO/ cost function of GENCO for real power demand (P_{di}^t) /generation (P_{gi}^t) at i th bus during t th season in \$/hr and can be obtained from their demand bids and supply bids respectively [18]. $C_{qi}^t(Q_{gi}^t)$ is cost of reactive power generation of GENCO at i th bus during t th season in \$/hr and can be obtained from reactive power capability curve of generator [9-10]. The cost of SPVDG, $C(SPVDG)$ can be obtained from its supply bid as:

$$C(SPVDG) = a_{PVk}^t (P_{PVk}^t)^2 + b_{PVk}^t P_{PVk}^t \qquad \$/hr \tag{6}$$

a_{PVk}^t, b_{PVk}^t are coefficients of cost function of SPVDG in \$/MWh^2, \$/MWh respectively during t th season.

The non-linear load flows as equality constraints, transmission line loadings as inequality constraints, bounds on variables and capability curve constraints are referred from [9]-[10], [18]. But with placement of SPVDG at k th bus in system, real power equation gets modified. Real power constraints at i th bus during t th season are given in (7) – (8).

$$P_{gi}^t - P_{di}^t = V_i^t \sum_{j=1}^{N} V_j^t \{G_{ij} \cos(\delta_i^t - \delta_j^t) + B_{ij} \sin(\delta_i^t - \delta_j^t)\} \quad \forall i = 1,2,\ldots N; i \neq k, t \in T \tag{7}$$

$$P_{gk}^t + P_{PVk}^t - P_{dk}^t = V_k^t \sum_{j=1}^{N} V_j^t \{G_{kj} \cos(\delta_k^t - \delta_j^t) + B_{kj} \sin(\delta_k^t - \delta_j^t)\}; \quad t \in T, k \text{ is SPVDG bus} \tag{8}$$

Where $G_{ij} + j\,B_{ij}$ is bus admittance matrix element for i th row and j th column, N is set of system buses, and V_i^t / δ_i^t are bus voltage magnitude / angle at i th bus during t th season.

SPVDG power output constraint is

$$0 \le P_{PVk}^t \le P_{pv\max}^t \quad \forall k \in N, t \in T \tag{9}$$

Where $P_{PVk}^t / P_{pv\max}^t$ is solar power generation at k th bus during t th season/rated capacity of SPVDG.

B. Locational marginal price (LMP)

LMPs are by-products of market dispatch solution, determined as Lagrangian multipliers of real and reactive power constraints [9]-[10], [15]. The difference of LMPs between two nodes of transmission line gives a measure of its congestion.

C. Consumer payment (CP)

Consumer payment, at any node i, during t th season is the amount to be paid by the consumer for purchase of electricity at that node [15] and is calculated as:

$$CP_i^t = \lambda_{pi}^t * P_{gi}^t + \lambda_{qi}^t * Q_{gi}^t \qquad \$/hr \tag{10}$$

λ_{pi}^t, λ_{qi}^t are Lagrangian multipliers of real power and reactive power constraints respectively at i th bus. CP is one of the selection criterions for optimal placement of DG in the system [15], [18]. DG supplies the loads locally thereby relieving the transmission line from hitting any of its limits.

D. Congestion rent (CR) and Merchandising surplus (MS)

Congestion rent (CR) is calculated as difference in SW value of TCM problem without and with taking into account congestion constraints [18]. CR in $/hr can be determined as

$$SW_5^{wo,t} - SW_5^t \quad (11)$$

$SW_5^{wo,t}$, SW_5^t are the values of SW of the TCM problem as given by (5), without and with taking into account line flow limit constraints.

Merchandising surplus (MS) is defined as the difference of buyer payments and seller revenues and the annualized value can be calculated in $/hr as:

$$MS = \sum_{t=1}^{T} ws^t * \begin{pmatrix} \sum_{i=1}^{N,t} \left(\lambda_{pi}^t * P_{di}^t + \lambda_{qi}^t * Q_{di}^t\right) \\ -\sum_{j=1}^{N,t} \left(\lambda_{pj}^t * P_{gj}^t + \lambda_{qj}^t * Q_{gj}^t\right) \end{pmatrix} \forall i \in N, t \in T \quad (12)$$

It occurs due to congestion in the network. The annualized values of SW and MS in $/hr are multiplied with 8760 (number of hours in a year) to obtain the annual values of SW and MS in $.

IV. RESULTS AND DISCUSSION

The proposed methodology has been simulated on IEEE 30-bus, IEEE 118-bus and a practical Indian utility 62-bus systems. The TCM problem has been solved with "A Modeling Language for Mathematical Programming" (AMPL) software employing KNITRO solver [27]. Interior/Direct algorithm has been used for solving non-linear optimization TCM problem and implemented on computer with configuration OS-WIN7, CPU i3@2.30 GHz (4CPUs), 2 cores, RAM-4GB.

A. IEEE 30-bus system

IEEE-30 bus system consists of 6 GENCOs, 21 DISCOs and 41 transmission lines. The cost coefficients of SPVDG bid, supply and demand bids of GENCOs and DISCOs respectively are as given in [18]. The generation power limits are taken from [18], [28]. Minimum real power generation limit is assumed to be zero. The annual seasonal variations can be divided into four seasons namely winter (December-February), summer (March-June), rainy (July-September) and post-monsoon (October-November). Seasonal load demands on various buses of IEEE-30 bus system assumed in this work are shown in Fig. 1. Load demands are assumed to be constant during a particular season.

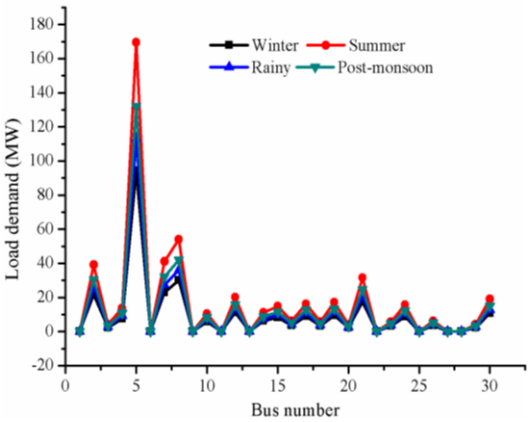


Fig. 1. Seasonal load demands on IEEE-30 bus system

B. Expected power output of SPVDG

For the present work, a SPVDG of capacity 24 MWp (228600 modules of 105 kWp each made of thin film CdTe type) situated at Sri Muktsar Sahib (Punjab State), India is considered for analysis. The site latitude and longitude are 30.47°N and 74.37°E, respectively, which has average annual horizontal solar insulation of 4.73 kWh/m^2/day. The data sources for analysis are taken from Meteonorm [29]. Solar irradiance data of one year is used for analysis. Following the algorithm given in sub-section C of Section II, the time intervals of one day during summer and rainy seasons are specified as 7:00-9:00, 9:00-11:00, 11:00-14:00, 14:00-16:00 and 16:00-18:00 hours while for winter and post-monsoon seasons are specified as 8:00-11:00, 11:00-14:00 and 14:00-17:00 hours. The beta pdfs are obtained during each specified time interval of each season using (1). As an example, beta pdf of solar irradiance during interval 11:00-14:00 hours in summer season is shown in Fig. 2. The mean ambient temperatures during winter, summer, rainy and post-monsoon are 13.43°C, 28.13 °C, 29.67 °C and 21.6 °C respectively as calculated from historic data.

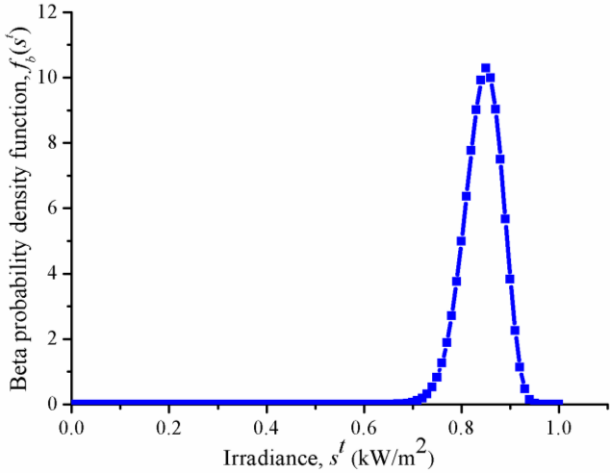


Fig. 2. Beta PDF of irradiance during 11am-2pm in summer season

The expected power outputs of SPVDG during specified time intervals of four seasons of one year are calculated using (2) – (3) and are given in Table-I.

Table-I: Expected power output (MW) of SPVDG during specified time intervals

of four seasons of one year.

Time interval (hours)					
Season	**7:00-9:00**	**9:00-11:00**	**11:00-14:00**	**14:00-16:00**	**16:00-18:00**
Summer	6.0484	13.4518	17.2443	13.9811	6.6248
Rainy	5.4938	12.4798	15.5051	12.8334	5.8047
Time interval (hours)					
Season	**8:00-11:00**	**11:00-14:00**	**14:00-17:00**	**-**	**-**
Winter	6.1776	11.1324	6.2872	-	-
Post-monsoon	8.6952	13.4669	7.2334	-	-

The variation of expected power output corresponding to expected value of irradiance in summer season during sunshine hours is shown in Fig. 3.

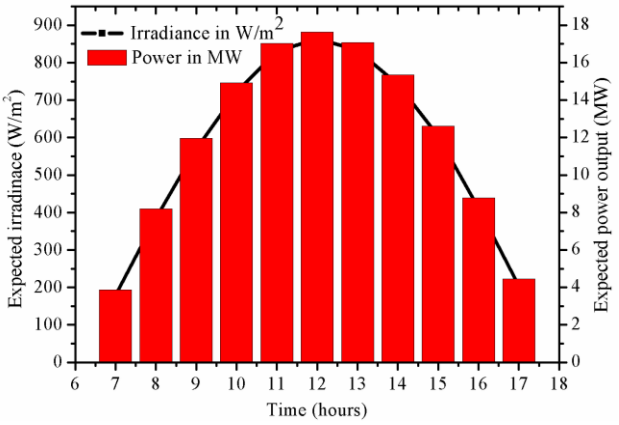


Fig. 3.Variation of expected irradiance and expected power output during 7:00-17:00 hours in summer

The expected power outputs of SPVDG obtained from (4) for winter, summer, rainy and post-monsoon seasons are 7.866MW, 11.995MW, 10.8853MW and 9.7985MW, respectively.

C. TCM with SPVDG

For base case analysis, TCM problem is solved without SPVDG. The weights taken for winter, summer, rainy and post-monsoon seasons are 25%, 33.3%, 25% and 16.7%, respectively. The system becomes congested in all the seasons except summer season, due to the line number 2 connecting bus 1 and bus 3 hitting its line loading limit. SW, demand benefits, GENCO costs of real and reactive powers, congestion rent, during various seasons, and Annual SW and MS are obtained for base case, as shown in Table-III. The various annualized values are obtained by taking weighted sum of corresponding seasonal values. The congestion rent in summer season is nil (Table-III). This is due to the reason that, high demand in summer season requires more power to be purchased from costlier generators (for example generator at bus number 5), which causes change in pattern of power flow over the transmission lines. Hence, line 1-3 operates within the rated capacity in this season.

The optimal location for SPVDG placement in system is decided based on weighted LMPs and weighted CPs of real power. The highest priority locations obtained by weighted LMPs is bus 30, whereas by weighted CPs is bus 5. Three top locations obtained by these methods for SPVDG placement in system are tabulated in Table-II.

Table-II: Ranking of buses for SPVDG placement based on weighted LMPs and weighted CP.

Ranking	**Bus No.**	**LMP method ($/MWh)**	**Bus No.**	**CP method ($/hr)**
1	30	48.83	5	5864.92
2	29	45.88	8	1704.99
3	26	44.43	7	1490.10

The proposed TCM problem is solved with SPVDG placed at bus 30 (optimal location given by weighted LMP) and bus 5 (given by weighted CPs). The expected power outputs of SPVDG as determined in sub-section B of Section IV for each season are committed in electricity market. The various indices of electricity market obtained for each season and calculated for the year are tabulated in Table-III.

Table-III: Social welfare, its components and congestion rent without SPVDG and with SPVDG placed at bus 30 and bus 5.

Parameters		**Base Case (without SPVDG)**	**SPVDG placed at bus 30 (weighted LMP-based approach)**	**SPVDG placed at bus 5 (weighted CP-based approach)**
Social welfare ($/hr)	Winter	7978.74	8075.72	8061.09
	Summer	11260.33	11543.42	11452.70
	Rainy	9038.38	9182.30	9156.55
	Post-monsoon	10004.14	10200.64	10112.49
	Annualized value	9674.66	9861.97	9806.94
Demand benefit ($/hr)	Winter	17004	17004	17004
	Summer	27741.75	28195.13	27902.01
	Rainy	20404.80	20404.80	20404.80
	Post-monsoon	23636.66	23805.6	23638.74
	Annualized value	22537.52	22716.72	22591.24
GENCO cost of real power ($/hr)	Winter	8994.89	8662.53	8676.76
	Summer	16393.75	16203.78	16001.39
	Rainy	11319.81	10851.20	10875.65
	Post-monsoon	13560.55	13240.99	13160.89
	Annualized value	12802.4	12485.54	12414.43
GENCO cost of reactive power ($/hr)	Winter	30.36	29.77	30.18
	Summer	87.68	88.07	88.07
	Rainy	46.61	44.75	46.04
	Post-monsoon	71.98	70.02	71.41
Congestion Rent ($/hr)	Winter	71.96	66.36	73.24
	Summer	0.0	0.0	0.0
	Rainy	75.51	68.53	77.74
	Post-monsoon	52.67	62.90	56.49
	Annualized value	45.66	44.23	47.18

Annual SW (k$)	-	84750.02	86390.86	85908.82
Annual MS (k$)	-	15161.79	13790.06	14913.5

D. Effectiveness of Proposed Methodology

The results in Table-III show that annual SW of value 86390.86 k$ is maximum with SPVDG placed at bus 30. Also, annual MS of market participants decreases significantly to value 13790.06 k$ from 15161.79 k$ in base case indicating overall reduction in transmission congestion. Moreover, the results obtained in Table-III show that demand benefits have been improved and GENCO costs of real and reactive power and congestion rent have been reduced by the placement of SPVDG in the system. The percentage improvement in SW is highest in summer season. This is due to the reason that summer season witness more sunny hours and load demand. This means the SPVDG brings maximum improvement in the market, when it was desperately needed. This depicts self-healing feature of SPVDG integrated electricity market.

The availability of solar power output varies from season to season and is definitely less than the rated capacity of SPVDG. Although, modeling SPVDG by its rated capacity (as projected in some earlier approaches [15]-[16], [18]-[19]) would give apparently improved results, but the same are not practically attainable. In this regard, the proposed methodology of modeling SPVDG gives more accurate results. Hence, the ISO and utilities can be benefited from the proposed approach of TCM of electricity markets.

The improvement in these market indices is more prevalent for SPVDG location at bus 30 (LMP method) than bus 5 (CP method). It shows that CP method is not able to provide the optimal location for SPVDG placement, as CP at any bus is proportional to load demand at that bus, which is not a correct economic signal for congestion management. Fig.4 show the variation in annual SW and annual MS due to SPVDG placement at optimal (bus 30) and sub-optimal locations (bus 29 and bus 26) determined from LMPs. Similarly, Fig.5 shows the variation of line power flow losses during different seasons with SPVDG placement at different locations. Highest improvement is obtained by placing SPVDG at bus 30, which proves the importance of placing SPVDG at optimal location given by LMP method.

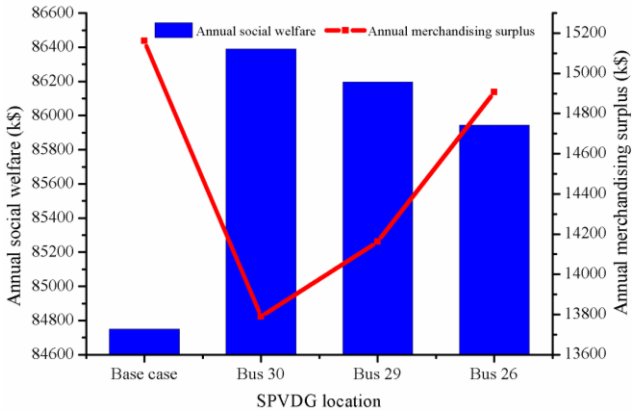


Fig.4. Variation of annual SW and MS with SPVDG placement at optimal and sub-optimal locations

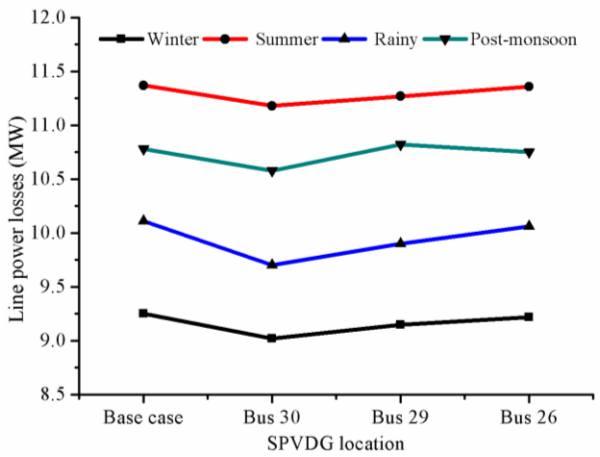


Fig.5. Seasonal variation in line power losses with different SPVDG locations

In the nutshell, it can be concluded that the improvement in market indices are governed by weight assigned to each season (which in turn depends upon the duration of a particular season), availability of power from SPVDG, and location of SPVDG.

The proposed TCM methodology is compared with an existing TCM approach [18], as given in Table-IV. The optimal location of SPVDG placement by proposed approach is bus 30, but by [18] is bus 3. This is due to the incorporation of AC modeling, reactive power cost and seasonal variations of load in the proposed approach. The optimal location in proposed approach is decided based on performance of market operations over the year.

In Table-IV, the SW, demand benefit, GENCO costs of real and reactive power, DG cost and CR obtained in proposed TCM approach are compared with that of [18].

Table -IV: Comparison of results of proposed approach with [18]

	Base Cases		**After DG Placement**	
	Without DG placement [18]	**Proposed approach-Base case**	**With DG placed [18]**	**Proposed approach-SPVDG placed at optimal location**
Social welfare ($/hr)	8438.4	9674.66	9073.5	9861.97
Demand benefit ($/hr)	17,004.0	22,537.52	17,004.0	22716.72
GENCO cost of real power ($/hr)	8565.6	12802.4	6130.5	12485.54
GENCO cost of reactive power ($/hr)	-	60.46	-	59.65
DG cost ($/hr)	-	-	1800.0	309.56
Congestion rent ($/hr)	222.2	45.66	-	44.23

The comparison of results given in Table-IV shows that value of SW with proposed approach has increased to 9861.97 $/hr from 9073.50 $/hr

in [18], and demand benefit with proposed approach has increased to 22,716.72 $/hr from 17004.0 $/hr in [18] with SPVDG placement at optimal location. The cost of generation has gone higher and CR is not completely eliminated in proposed approach due to reason that only expected power output of SPVDG for various seasons are committed in proposed approach. Expected power output is quite lower than DG capacity of 60 MW taken in [18]. CR in proposed approach has decreased significantly from 222.2 $/hr [18] to 45.66 $/hr in the base case itself due to AC modeling as reactive power support in system helps in reducing network congestion.

E. IEEE 118-bus system and Indian Utility 62-bus system

The proposed approach is also implemented on IEEE 118-bus system [28] and Indian Utility 62-bus system [30]. In IEEE 118-bus system, the congested system conditions are simulated by considering maximum line loadability limit of 125MVA. In Indian utility 62-bus system, the number of lines which hit the limits during winter, summer, rainy and post-monsoon seasons are 16, 30, 20 and 25, respectively, out of the total 89 transmission lines. Due to increase in scale of these systems, the maximum capacity of SPVDG is taken as 50MWp, which provides 16.385 MW (32.77%), 24.985MW (49.97%), 22.675 MW (45.35%), and 20.415MW (40.83%) power output during winter, summer, rainy and post-monsoon seasons, respectively. The optimal locations obtained for SPVDG placement based on weighted LMP method are bus 59 and bus 53respectively for IEEE 118-bus and Indian utility 62-bus systems. The results obtained in these systems also demonstrate the effectiveness of proposed methodology, as discussed in sub-section D of Section IV. The reductions in seasonal CR obtained in these systems are shown in Fig.6 and Fig.7, respectively.

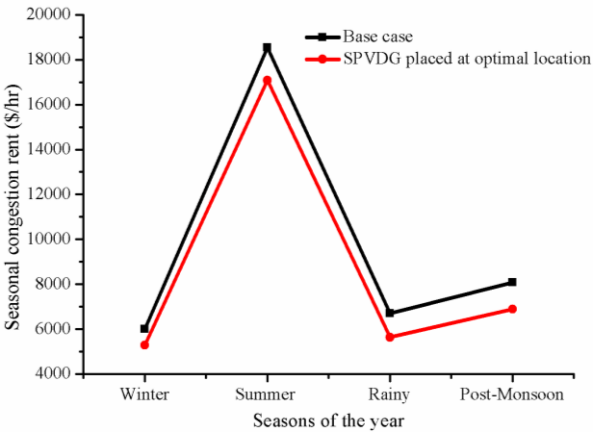


Fig.6. Seasonal variation of CR with and without SPVDG placement in IEEE 118-bus system

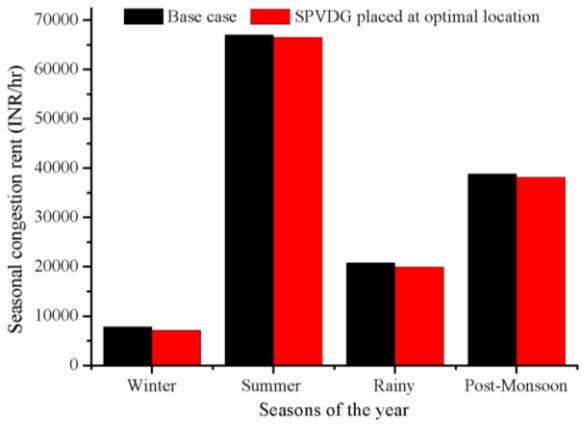


Fig.7. Seasonal variation of CR with and without SPVDG placement in Indian Utility 62-bus system

V. CONCLUSION

In this paper, an effective TCM methodology for pool based electricity market integrated with SPVDG in deregulated environment is presented. In the proposed methodology, the problem of stochastic power output of SPVDG due to its dependence on solar irradiance is addressed by modeling the randomness of irradiance with beta pdf. TCM incorporates seasonal variations of expected power outputs as determined from beta pdf as well as seasonal variations of load demands. Simulation of proposed methodology on IEEE 30-bus, IEEE 118-bus and practical Indian utility 62-bus system and comparison with existing TCM approach give following concluding points:

1) Due to the dependency of solar power output on irradiance, the expected power output available during various seasons is much less than the rated capacity of SPVDG. Hence, modeling of SPVDG by its rated capacity (as done in some earlier approaches) in TCM problem, cannot give accurate results. This proves the effectiveness of proposed methodology.
2) TCM results are largely influenced by the location of SPVDG placement and availability of its power output. SW of electricity market increases whereas MS and CR decrease with optimal location of SPVDG in the system.
3) Due to incorporation of the effect of reactive power and losses (AC modeling of power system), the TCM results are quite different than the DC approach.

ACKNOWLEDGMENT

Anu Singla is thankful to I. K. Gujral Punjab Technical University, Kapurthala, India for providing her an opportunity to pursue Ph.D programme in Electrical Engineering. Authors are grateful to the authorities of Punjab Energy Development Agency, Chandigarh, India for sharing technical detail of SPVDG incorporated in the present work.

REFERENCES

1. A.Pillay, S. Prabhakar Karthikeyan and D.P. Kothari, “Congestion management in power systems—a review,” International Journal of Electrical Power and Energy Systems, vol.70, Sept.2015, pp. 83– 90.

2. T. Krause, "Congestion management in liberalized electricity markets – theoretical concepts and international application," EEH Power Syst. Lab. 1-4. Available: http://www.eeh.ee.ethz.ch/downloads/psl/publications/krause_congestion_management.pdf.
3. D. Gautam, and M. Nadarajah, "Influence of distributed generation on congestion and LMP in competitive electricity market," International Journal of Energy and Power Engineering, vol. 3(4), Jan. 2010, pp. 228-235.
4. A. Kumar, and W. Gao, "New price area zonal-based approach for optimal location of distributed generation in hybrid electricity markets," Electric Power Components and Systems, vol.37 (6), 2013, pp.672-692.
5. Y.P. Verma, and A. K. Sharma, "Congestion management solution under secure bilateral transactions in hybrid electricity market for hydro-thermal combination," International Journal of Electrical Power and Energy Systems, vol.64,2015, pp. 398-407.
6. S.Verma, and V. Mukherjee, "Firefly algorithm for congestion management in deregulated environment," International Journal of Engineering Science and Technology, vol.19, 2016,pp. 1254–1265.
7. J.Dijk, and B. Willems, "The effect of counter-trading on competition in electricity markets," Energy Policy, vol. 39 (3), March 2011, pp.1764-1773.
8. R.Philipsen, M. de Weerdt, and L.de Vries, "Auctions for congestion management in distribution grids,"13th International Conference on the European Energy Market (EEM 2016), Porto, Portugal, 2016, pp. 1-5.
9. Dai, Y., Ni, Y. X., Shen, C. M., Wen, F. S., Han, Z. X., and Wu, F. F. ,"A study of reactive power marginal price in electricity market," Electric Power Systems Research, vol. 57, 2001,pp. 41–48.
10. K.Singh, N. P. Padhy, and J. D. Sharma, "Social welfare maximization considering reactive power and congestion management in the deregulated environment," Electric Power Components and Systems, vol. 38 (1), 2010, pp. 50–71.
11. B. K. Talukdar, A. K. Sinha, S. Mukhopadhyay, and A. Bose, "A computationally simple method for cost-efficient generation rescheduling and load shedding for congestion management," International Journal of Electrical Power and Energy Systems, vol. 27(5-6), 2005, pp. 379–388.
12. J. G. Singh, S. N. Singh, and S. C. Srivastava,"Congestion management by using FACTS controller in power system," Proceedings of IEEE Region 10 Humanitarian Tech. Conference, Agra India,2016, pp. 1-7.
13. A. Yousefi, T.T. Nguyen, H. Zareipour, and O.P. Malik, "Congestion management using demand response and FACTS devices,"International Journal of Electrical Power and Energy Systems,vol. 37 (1), 2012, pp.78–85.
14. J. Hazra, K. Das, and D. P. Seetharam, "Smart grid congestion management through demand response," IEEE Third International Conference on Smart Grid Communications, Tainan, Taiwan, 2012, pp. 109-114.
15. D. Gautam, and N. Mithulananthan, "Locating distributed generator in the LMP-based electricity market for social welfare maximization,"Electric Power Components and Systems, vol. 35, 2007pp. 489-503.
16. M. Khanabadi, M. Doostizadeh, A. Esmaeilian, and M. Mohseninezhad, "Transmission congestion management through optimal distributed generation's sizing and placement," International Conference on Environment & Electrical Engineering, Rome, Italy, 2011,pp. 1-4.
17. M.Shahidehpour ,"Distributed resources for transmission congestion and expansion management," Proceedings of PES Summer Meeting, Chicago, USA,2002, pp. 1045-1048.
18. K.Singh, V. K. Yadav, N. P. Padhy, and J. D. Sharma, "Congestion management considering optimal placement of distributed generator in deregulated power system networks," Electric Power Components and Systems, vol. 42, 2014, pp. 13-22.
19. R. Peesapati, V.K. Yadav,and N.Kumar, "Transmission congestion management considering multiple and optimal capacity DGs," Journal of Modern Power Systems and Clean Energy, vol.5(5), 2017, pp.713–724.
20. Y. M. Atwa, E. F. El-Saadany, M. M. A. Salama, and R. Seethapathy, "Optimal renewable resources mix for distribution system energy loss minimization," IEEE Transactions on Power Systems, vol. 25(1),2010, pp. 360-370.
21. G. Ramesh, and T. K. S. Kumar, "Congestion management in a deregulated power system with micro grid," International Journal of Electrical, Computer, Energetic, Electronic and Communication Engineering, vol. 7 (11), 2013, pp. 1460-64.
22. A. Abdulkarim, S. M. Abdelkader, and D. J. Morrow, "Statistical analyses of wind and solar energy resources for the development of hybrid microgrid," International Congress on Energy Efficiency and Energy Related Materials, Springer proceedings in Energy, 2015, pp.9-14.
23. S.Liu, F. Liu, T. Ding, and Z. Bie, "Optimal allocation of reactive power compensators and energy storages in microgrids considering uncertainty of photovoltaics," Energy Procedia, vol. 103, Dec. 2016, pp. 165-170.
24. S. Alireza, A. Morteza, and E.Mehdi, "A probabilistic modeling of photo voltaic modules and wind power generation impact on distribution networks," IEEE Systems Journal, vol. 6 (2), 2012,pp. 254-259.
25. S.Ghosh, V. K. Yadav, V. Mukherjee, and P. Yadav,"Evaluation of relative impact of aerosols on photovoltaic cells through combined Shannon's Entropy and Data Envelopment Analysis (DEA),"Renewable Energy, vol.105, 2017, pp. 344-353.
26. K N Maya, and E. A. Jasmin., "Optimal integration of distributed generation (DG) resources in unbalanced distribution system considering uncertainty modelling,"International Transactions on Electrical Energy Systems, vol.27 (1), 2017.
27. R. A. Waltz, and T. D. Plantenga, Knitro User's Manual: Version 6.0, Ziena Optimization 2009.
28. R.D. Zimmerman, C.E. Murillo-Sanchez, and D. Gan, "MATPOWER—A MATLABTM power system simulation package," 2005. Available: http://www.pserc.cornell.edu/matpower/.
29. Version, Meteonorm. "6, software version 6.1. 0.20 of April 2010." Meteotest, Switzerland.
30. R. Gnanadass, N.P. Padhy, and K. Manivannan, "Assessment of available transfer capability for practical power systems with combined economic emission dispatch," Electric Power Systems Research,vol.69(2-3), 2004,pp. 267-276.

AUTHORS PROFILE



Anu Singla received B.E. in Electrical Engineering from Thapar Institute of Engineering & Technology (Now Thapar University), Patiala in 1993, M.Tech (Electrical Engg.) from I.K. Gujral Punjab Technical University, Kapurthala in 2007 and is pursuing Ph.D programme in Electrical Engineering from I.K. Gujral Punjab Technical University, Kapurthala, India. She is Chartered Engineer (India), The Institution of Engineers (India). She is serving as an Associate Professor, Department of Electrical Engineering, Chitkara University Institute of Engineering and Technology, Punjab, India. Her research interests include power system restructuring and operation, renewable energy systems and solar cells.



Kanwardeep Singh has obtained B.E. in Electrical Engineering from GZSCET, Bathinda in 1996 and M.Tech. (Electrical Engg. With specialization in Power Systems) from Regional Engg.College, Kurukshetra (Presently NIT, Kurukshetra) in 2000. He has obtained Ph.D. from Indian Institute of Technology, Roorkee in 2010. He has published many papers in International Journals of repute including IEEE Transactions on Power Systems, Electrical Power and Energy Systems, Electric Power Components and Systems, Sustainable Energy Grids and Network, and presented many research papers in International and National Conferences. His research areas are Transmission Open Access, Reactive Power Management, DG Placement, Transmission Expansion Planning and Demand Response based electricity pricing systems. Presently, he is serving as an Associate Professor and Head of Department of Electrical Engineering, Guru Nanak Dev Engineering College, Ludhiana, India.



Vinod Kumar Yadav (M'09) received B.Tech. degree in Electrical Engineering from Institute of Engineering and Technology (IET), Bareilly, India in 2003, M.Tech. degree in power system engineering from National Institute of Technology (NIT), Jamshedpur, India in 2005 and Ph. D. degree in power system engineering from Indian Institute of Technology (IIT), Rookee, India in 2011. Since 2011, he is associated with various technical universities and involved in teaching electrical engineering. Currently he is Associate Professor of Electrical Engineering in Delhi Technological University (previously Delhi College of Engineering), Delhi, India. His research interests include optimization of renewable energy systems, power system policy and restructuring, distributed generation and smart grid.

Materials Research Express

ACCEPTED MANUSCRIPT

Tribological behavior of sustainable Carbon based composite coating for wear resistance applications

To cite this article before publication: Ankit Tyagi *et al* 2019 *Mater. Res. Express* in press https://doi.org/10.1088/2053-1591/ab52b4

Manuscript version: Accepted Manuscript

Accepted Manuscript is "the version of the article accepted for publication including all changes made as a result of the peer review process, and which may also include the addition to the article by IOP Publishing of a header, an article ID, a cover sheet and/or an 'Accepted Manuscript' watermark, but excluding any other editing, typesetting or other changes made by IOP Publishing and/or its licensors"

This Accepted Manuscript is **© 2019 IOP Publishing Ltd**.

During the embargo period (the 12 month period from the publication of the Version of Record of this article), the Accepted Manuscript is fully protected by copyright and cannot be reused or reposted elsewhere.
As the Version of Record of this article is going to be / has been published on a subscription basis, this Accepted Manuscript is available for reuse under a CC BY-NC-ND 3.0 licence after the 12 month embargo period.

After the embargo period, everyone is permitted to use copy and redistribute this article for non-commercial purposes only, provided that they adhere to all the terms of the licence https://creativecommons.org/licences/by-nc-nd/3.0

Although reasonable endeavours have been taken to obtain all necessary permissions from third parties to include their copyrighted content within this article, their full citation and copyright line may not be present in this Accepted Manuscript version. Before using any content from this article, please refer to the Version of Record on IOPscience once published for full citation and copyright details, as permissions will likely be required. All third party content is fully copyright protected, unless specifically stated otherwise in the figure caption in the Version of Record.

View the article online for updates and enhancements.

This content was downloaded from IP address 14.139.251.100 on 06/11/2019 at 04:52

Tribological behavior of sustainable Carbon based composite coating for wear resistance applications

Ankit Tyagi [a], S M Pandey[a*], Kalpna Gupta[a], R.S. Walia [a], Qasim Murtaza[a], Kumar Krishen[b]

[a] Department of Mechanical Engineering, Delhi Technological University, Delhi 110042, India.

[b] NASA Johnson Space Center Houston, TX, USA

Abstract

The principal aim of the present study is to develop carbon based composite coating for wear resistance, having excellent tribological properties and enhanced mechanical properties using atmospheric plasma spray coating technique. FESEM, and HRXRD results confirms the presence of Cr_3C_2, MoO_2 and Mo_2C along with Cr_2C_2, hard phased in the carbon based composite coating. The carbon based composite coating was wear tested at variable temperature, the hardness and residual stress of the coating increases with increase in wear temperature, due to the formation of oxides and carbide in the coating. The experimental result shows that carbon based composite coating was temperature dependent and at 350^{o}C temperature; lowest COF (0.08), wear (105 micron) and frictional force (3N) was obtained.

Keywords: Carbon based composite coating; Residual stress; Micro-hardness; Wear test.

*Corresponding author.

E-mail address: shalieshmanipandey@dce.ac.in

1. Introduction

Over the years, automobile manufacturers, have realized their responsibility to prevent environment from emission of harmful gases and improve fuel efficiency. A research study shows that frictional losses in piston-cylinder assembly contributes almost 45% to the overall frictional losses in engine components [1]. Researchers reveals that reduction in tribological properties, can considerably reduce economic costs [2, 3]. Generally, Chrome coated [4], thermal spray Mo_2C, NiCrBSi, $MoSi_2$, MoO, CrC, Al-Si alloy and NiCr with molybdenum (Mo) powder [5-13], Cr3C2-WC-NiCoCrMo [7], WC-CoCr [12], and Fe based coating [13], coatings were developed on piston-cylinder, in order to increase service life, and to reduce friction. A comparative study shows that W-DLC (0.10) coating will exhibit lowest COF value owning to the presence of carbon rich film on the substrate, while COF of nitrogen-based film is greater than 0.45 [16]. DLC coatings using CVD process can be used in piston cylinder arrangement in order to enhance COF and wear and to improve piston ring life [17]. However, there are certain limitation in the application of DLC coating in the piston-cylinder arrangement. The use of DLC coating in the piston cylinder arrangement is limited due to

Accepted Manuscript

higher cost, low deposition rate (coating deposition on the substrate material is low), high porosity, and less coating thickness on the substrate material. CVD diamond coating possesses unique physical characteristics which include low COF (<0.1) and high hardness (>40 GPa) [18]. So, the microstructure of CVD diamond possesses significant coating thickness in order to achieve long service life, low friction, good adhesion strength, lubricant compatibility, good thermal stability [19].

The principal aim of the present study is concerned with development of wear resistance having excellent tribological properties (COF, wear) and enhanced mechanical properties (micro-hardness, residual stress) using atmospheric plasma spray coating technique.

2. Materials and method

The substrate material of dimension 80x240x2mm has been used to develop carbon based composite coating. Table 1 represent the chemical composition of steel substrate. The coating materials used were carbon powder, NiCr, Mo and Cr_3C_2powders. Initially 40 wt.% carbon, 20 wt.% NiCr, 20 wt.% Mo and 20 wt.% Cr_3C_2 powders were blend together using ball milling process, in order to get composite powder for coating deposition. The particle size distribution of carbon powder, NiCr, Mo and Cr_3C_2 were in the range of 40-75±5µm. The high quality carbon based composite coating (CC1, CC2, and CC3) using atmospheric plasma spray process were deposited on the steel substrate for wear resistance applications. The chemical composition CC1, CC2, and CC3 is same as that of carbon based composite coating (CC) is 40wt.% C-20 wt.% NiCr-20 wt.% Mo-20 wt.% Cr_3C_2. In the present work CC is carbon based composite coating and 1, 2 and 3 are suffix of carbon based coating used to differentiate operating condition i.e. CC1 at 150^{o}C, CC2 at 250^{o}C, and CC3 at 350^{o}C temperature respectively of carbon coating during tribological testing. Table 2 shows the eexperimental conditions for carbon based composite coating (CC1, CC2, and CC3) deposition.

Table 1 Chemical composition of steel substrate

Element	C	Mn	Si	S	P	Cr	Ni	Mo	Cu
% Composition	0.16	1.07	0.24	0.01	0.01	0.10	0.02	0.02	0.17

Accepted Manuscript

Table 2: Deposition conditions of carbon based composite coating.

Sr. no.	Parameters used	Values
1.	Substrate material	Steel
2.	Coating material (CC1, CC2, and CC3)	carbon powder, NiCr, Mo and Cr_3C_2 powders
3.	Particle size of powders	60±10 µm
4.	Carrier Gases	Argon/Hydrogen
5.	Ar (m_3/min)	120
6.	Deposition rate	50±5 gram/min
7.	H_2 (m_3/min)	15
8.	Coating thickness	380±14 µm

2.1 Carbon based composite coating characterization

The FESEM attached with EDS, were used to characterize and analyze the microstructure and surface morphology of developed carbon based composite coating. PANalytical X'Pert PRO MRD systems made HRXRD was used to confirm the carbon based composite coating deposition on the steel substrate.

The Vickers micro hardness was evaluated using Fischer make micro hardness tester, available at Delhi Technological University, New Delhi. The hardness test was carried out with a load of 300mN ($3.05915*10^{-2}$Kgf), indentation time of the 20s and dwell time of 5s. The residual stresses developed on the coated surfaces were measured with the help of residual stress analyzer based, having LED marker, CCD camera support, power and sensor unit, available at precision manufacturing laboratory, DTU, Delhi.

2.2 Wear test

The wear behavior of carbon based composite coating, was performed rotary tribometer, with data acquisition card. The disc speed (counter-body) having range upto 3000rpm, and accuracy 1±1 of measured speed in rpm can be measured using proximity sensor. The high temperature rotary tribometer can measured wear range 0-2000µm±1 and least count 1micron can be measured using LVDT sensor. The magnified view of wear track along with counterbody, pin holder and wear sensor. Fig. 1 shows the schematic diagram of the tribometer showing the contact pair.

Accepted Manuscript

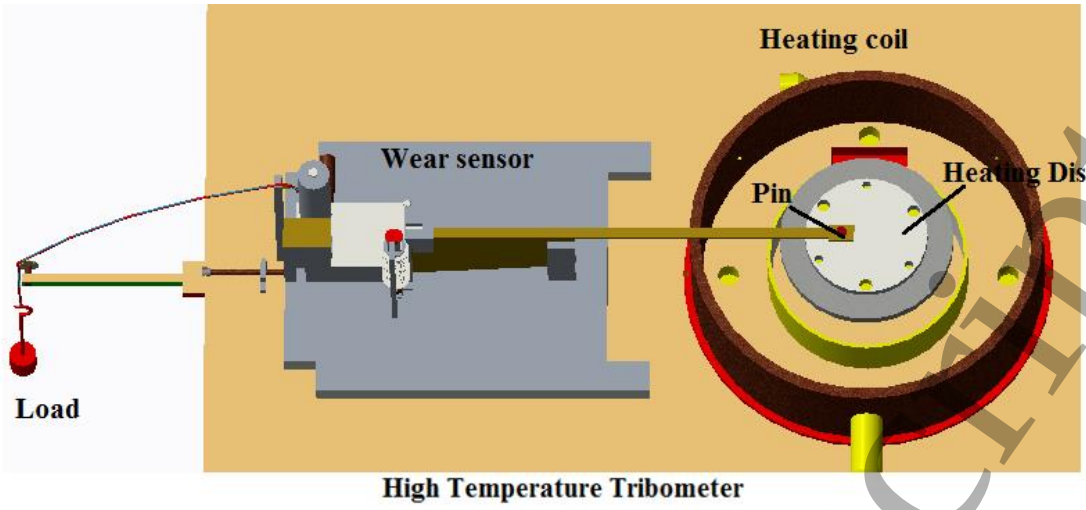


Fig. 1 Schematic diagram of the wear test showing the contact pair.

Table 3 shows the experimental conditions for wear test used in the present research work. In the present research, author was aiming to test the wear mechanism and behavior of carbon based composite coating on extreme condition where piston ring and cylinder liner are running without lubrication and has maximum working temperature is around 300-350$_o$C. This is the reason, author has opted for maximum operating temperature as 350$_o$C. Author was also aiming to enhance wear rate, COF and mechanical properties that ultimately results in enhancement of piston- cylinder life as working of piston is continuous sliding process and in this process maximum load acting on piston cylinder liner is low [8].

The main advantage of the coating is:

1. To study wear mechanism and behavior of carbon based composite coating.
2. To enhance wear rate, COF and mechanical properties that ultimately results in enhancement of piston- cylinder life.
3. To study on extreme condition where piston ring and cylinder liner are running without lubrication.
4. High deposition rate with low cost.
5. Higher coating thickness with less porosity and voids.

Table 3 Experimental conditions of carbon based composite coating for wear test

Sr. No.	Process Parameter	CC1	CC2	CC3
1	Temperature($_o$C)	150	250	350
2	Load (N)	20	20	20
3	S V (m/s)	0.3	0.3	0.3

Accepted Manuscript

3. Results and discussion

3.1 Carbon based composite coating characterization

Fig. 2(a-d) shows the cross-sectional morphology of different types of splats with complete melting, and bonding conformity using FESEM. Presence of splats confirmed homogeneous coating and uniform bonding of sprayed material. It was also noted that FESEM shows different types of splat (a) Flash & splash splat (b) As – sprayed splat (c) Splash splat (d) Melting & bonding of splat (e) Disc splat (f) Flattened & solidified droplet. FESEM images shows uniform melting of powder expects very few partially melted powder, formation of lamellae with molten, partially molten & non-melted particles was also observed. In addition, flattened, solidified droplet and crack formed during tensile quenching stress may be initiated due to increase in temperature during thermally sprayed coating deposition.

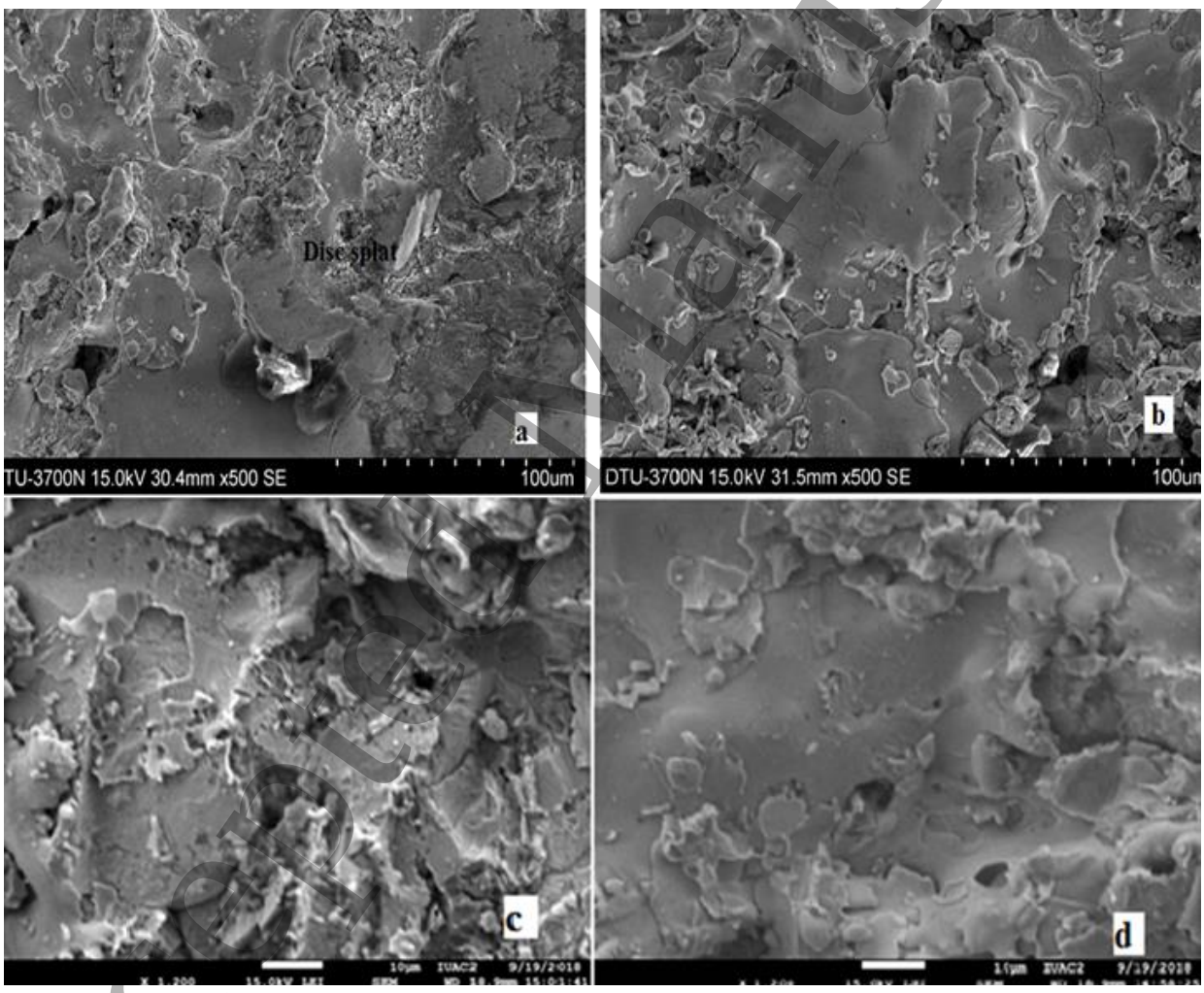


Figure 2 (a-d) SEM images of composite coating

Figure 3 (a) EDS (b) HRXRD analysis of composite coating. EDS results confirm homogeneous mixing of composite powders as shown in fig. 3(a). Presence of Mo, Cr, S, O and C confirms formation of carbide, sulphide and oxide layers. HRXRD patterns

Accepted Manuscript

corresponding to Mo-C composite coatings are shown in fig 3(b). It can be observed that the 2theta angle peak of composite coating was at 40.4o and 73.6o. The HRXRD peaks also confirms the presence of hard phases such as MoO_2 and Mo_2C in the composite coating. The hard phase in the composite coating have positive impact on hardness and tribological properties.

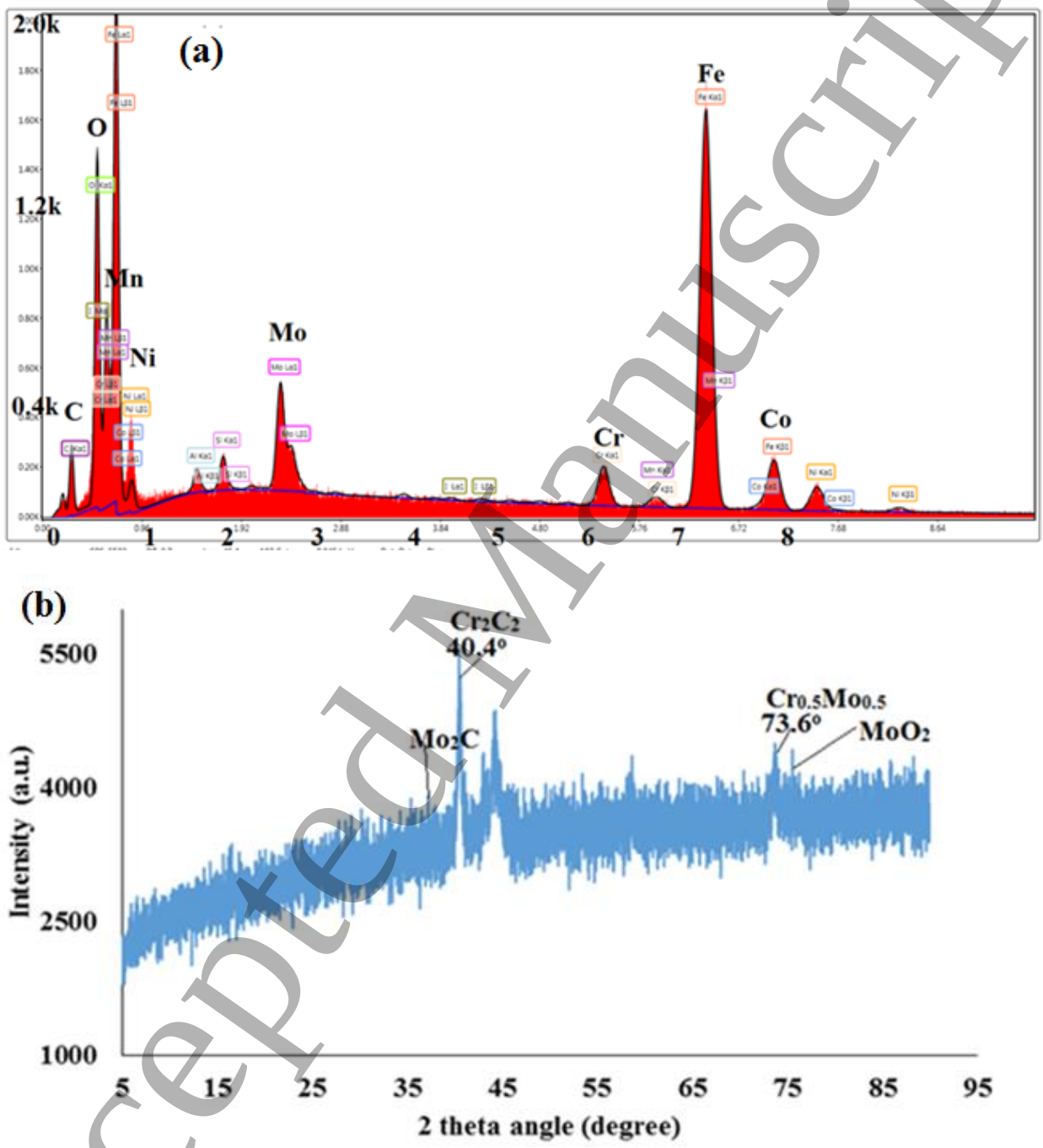


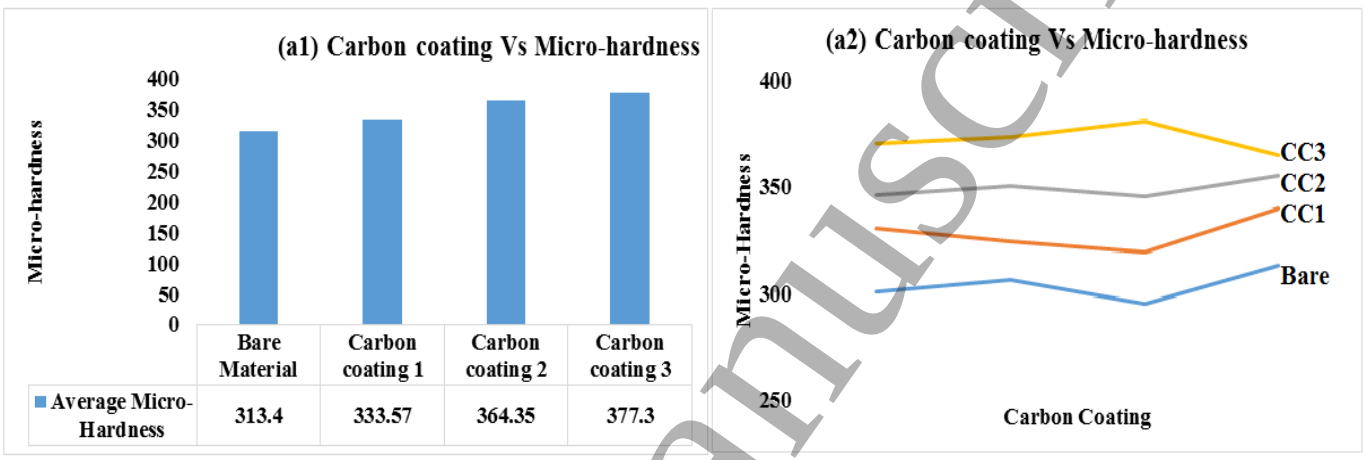
Figure 3 (a) EDS (b) HRXRD analysis of composite coating

3.2 Micro hardness and residual stress of carbon coating

Fig. 4(a1-a2) shows the experimental results of Vickers micro hardness, on carbon based composite coating at different locations. The carbon based composite coating (CC1, CC2, CC3)

Accepted Manuscript

displayed the hardness value of 333.57, 364.35, 377.32 HV respectively, while hardness of bare sample was 313.4 HV. The hardness value of CC3 coating was higher than CC2 and CC1. Presence of micron size hard structured coating particles and also due to presence of Cr_3C_2, MoO_2 and Mo_2C along with Cr_2C_2, hard phased works as a barrier and finally results increase in micro-hardness of carbon coating 3 on comparing with other developed carbon coatings. The interfacial strength between coated particles also increases, when the particle size of coating is increased [20-21]], which finally results in higher hardness.



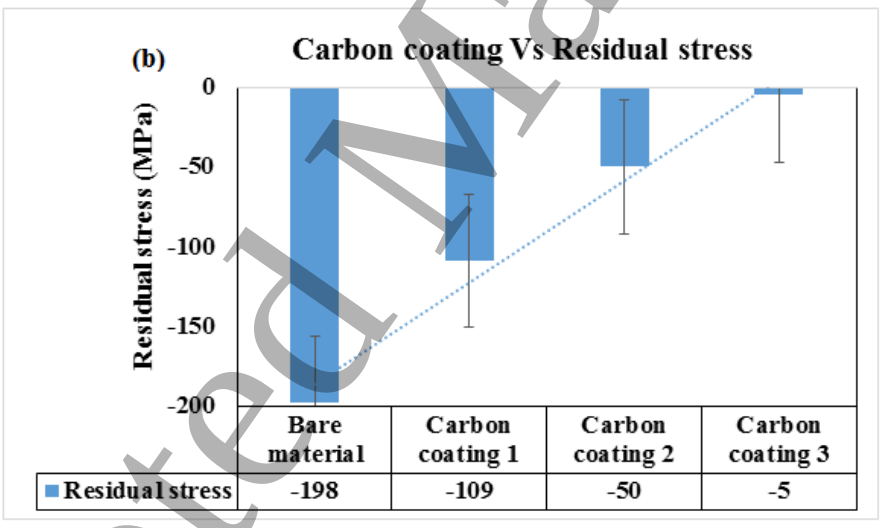


Fig. 4 Experimental results of carbon coating Vs (a1-a2) Vickers microhardness (b) Residual stress

Fig. 4(b) and fig. 5 shows the experimental results of XRD residual stress, developed on carbon based composite coating. Residual stress of carbon coating (CC1, CC2, and CC3) were found to be -109, -50, and -5 respectively as shown in fig. 4(b)-5. The compressive stresses were developed, due to bombardment of high-velocity carbon particles and good adhesive bonding between substrate materials and the coating film [21, 22]. The decrease in residual

Accepted Manuscript

stress may be attributed due to the increase in tensile stresses, stress relief and change in grain orientation of coated samples.

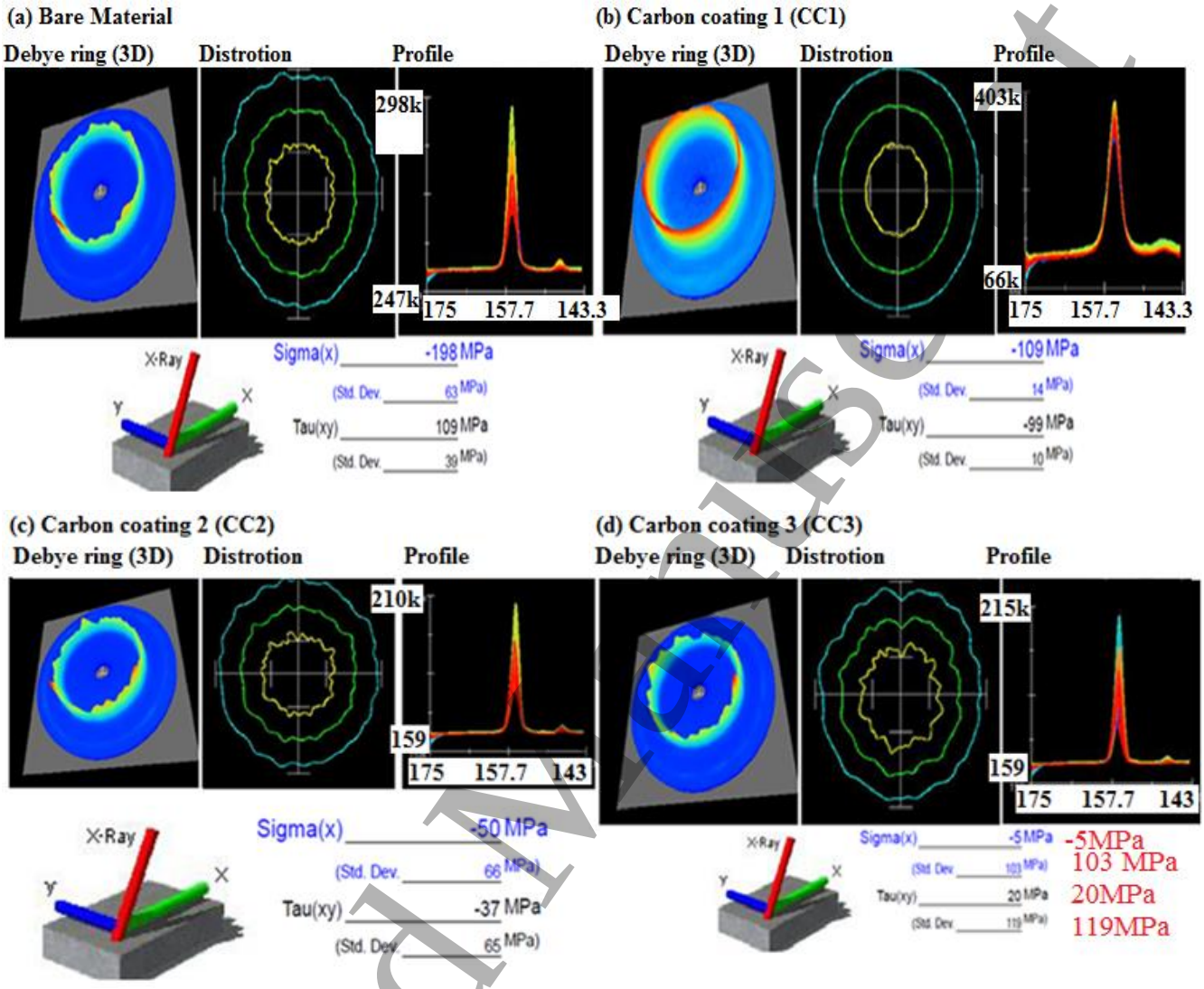


Fig. 5 Residual stress testing of (a) Bare material (b) Carbon coating 1 (c) Carbon coating 2 (d) Carbon coating 3

3.3.Tribological performance

The coefficient of friction is one of the vital parameters to discuss the wear resistance property of coating. The fig. 6(a) shows a variation of friction coefficient value of carbon based composite coatings with the counter body in dry condition. Friction coefficient average values are 0.28, 0.16, and 0.08 of CC1, CC2 and CC3 respectively under dry condition. Coefficient of friction decreases from 3.4 to 0.08 from carbon coating (CC) 1 to carbon coating 3. The fig. 6(b) shows variation in wear values of carbon based composite coating under test condition. The average wear values of coating is 380, 280, and 105 micron of CC1, CC2 and CC3 respectively under dry condition. The friction coefficient, wear and frictional force values

Accepted Manuscript

increase in running process, then become stable [21-23] due to highly adhesive contact produced between the coated and counter body. The decrease in friction coefficient, wear and frictional force values may be accredited due to increase in carbon content, presence of Cr_3C_2, MoO_2 and Mo_2C along with Cr_2C_2, hard phased, strong adhesion strength and formation of the tribo oxidative film on the developed carbon coatings

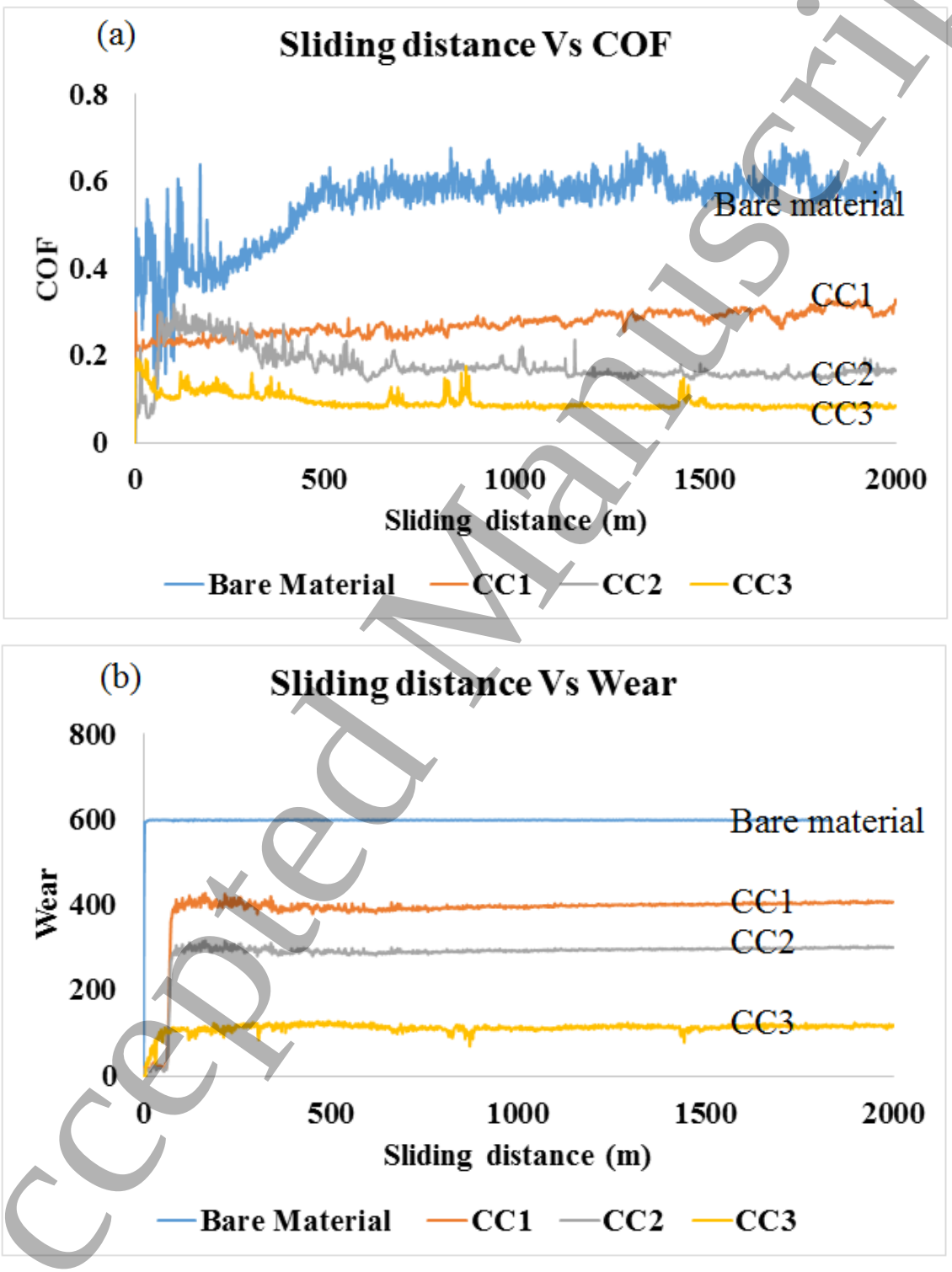
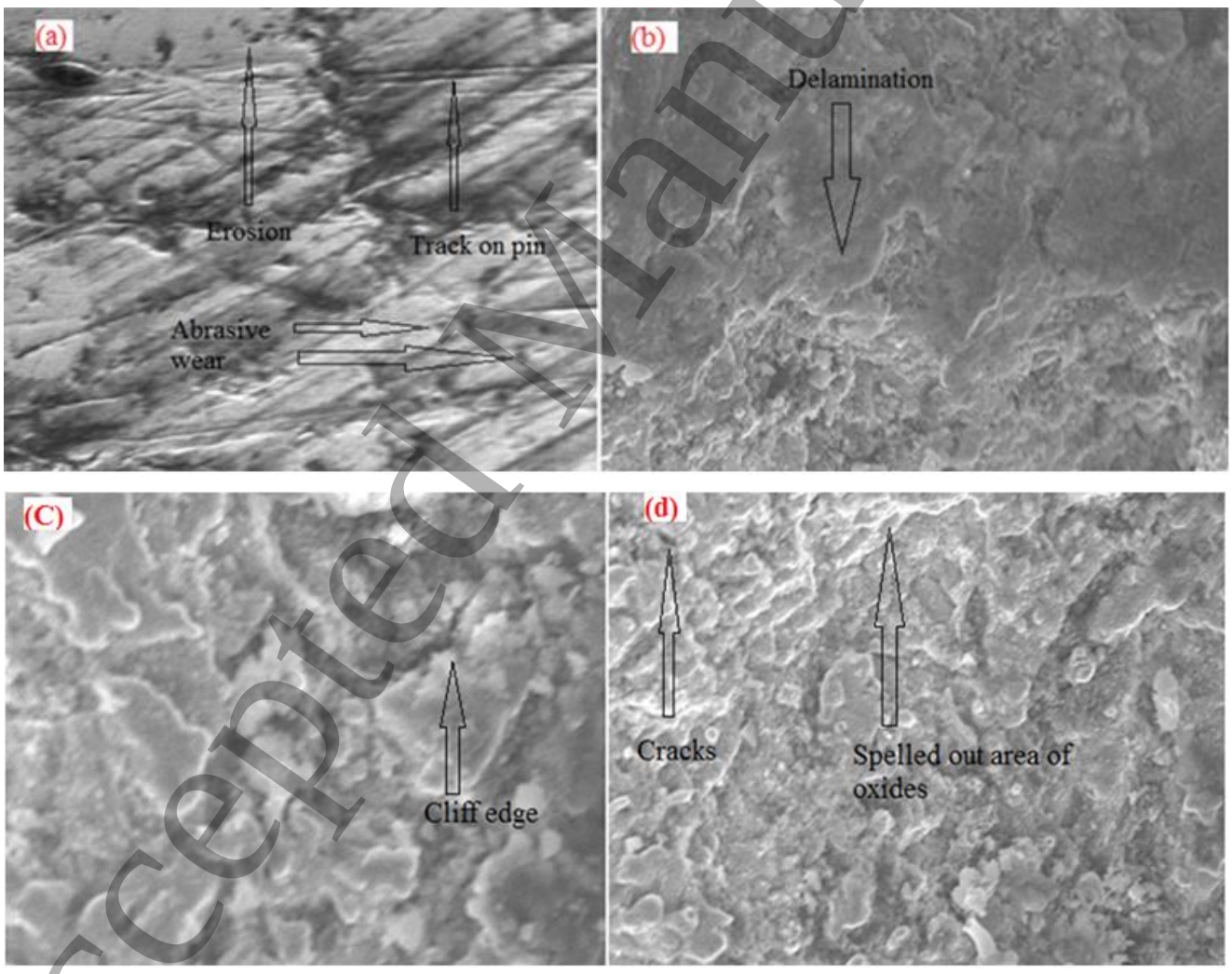


Fig. 6 (a) Sliding distance Vs COF (b) Sliding distance Vs Wear of composite coating

Accepted Manuscript

3.3 Wear mechanism of worn out surfaces during wear test

Fig. 7 shows FESEM-EDS images of worn surfaces in order to examine the wear behavior of coated samples. Fig. 7 (a) illustrate surface morphology of wear track on pin. FESEM image shows erosion of material with presence of abrasive wear. Wear mechanism of worn surfaces and delamination, oxide formation, cracks, cliff edges, coarse grain and debris formation confirms abrasive marks and erosion, indicates that abrasive wear was dominant wear mechanism. EDS result also confirms the formation of oxides and tribo films, due to the increase in content of oxygen (O), Chromium (Cr), Mo, and Carbon (C) as shown in Fig. 7 (e). Fig. 7 (b, c) showing delamination at variable temperature, load and sliding velocity at 20N and 0.3m/s respectively. The increase in carbon content, presence of Cr_3C_2, MoO_2 and Mo_2C along with Cr_2C_2, hard phased, strong adhesion strength and formation of the tribo oxidative film on the developed carbon coatings and results in abrasive wear resistance [24].



Accepted Manuscript

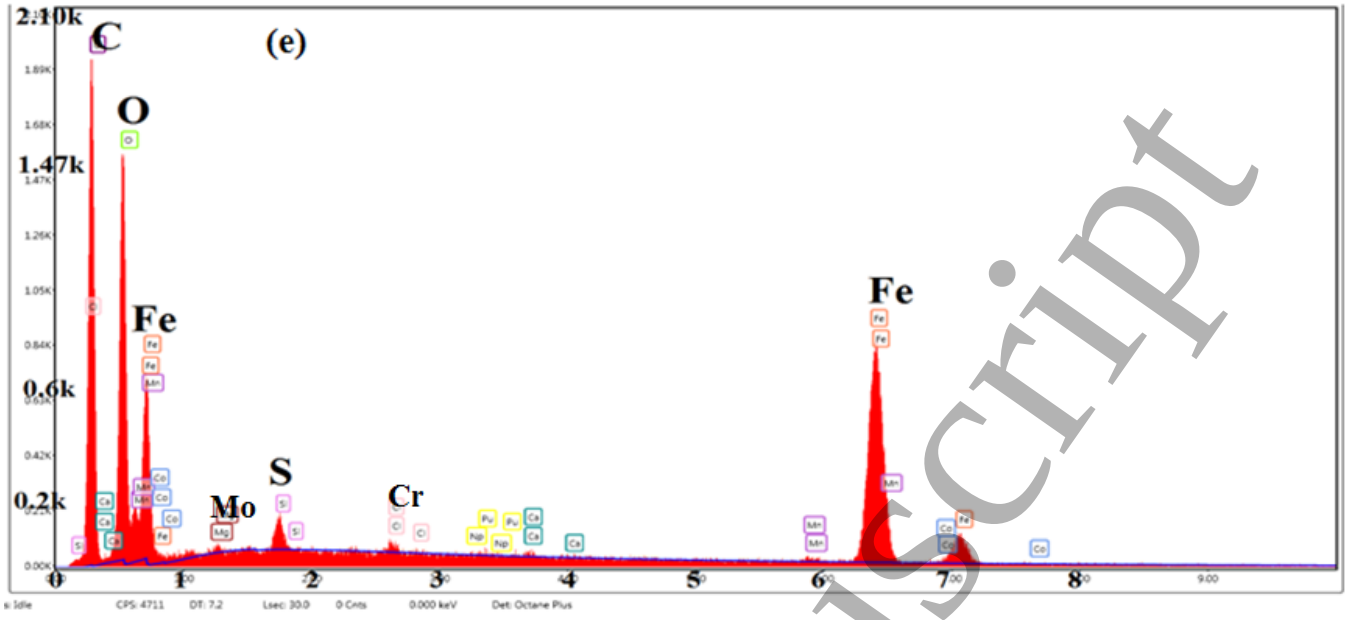


Fig. 7 (a)-(d) FESEM (e) EDS images of worn surfaces during wear test

4. Conclusions

The present work, successfully demonstrated carbon based composite coating developed with carbon powder, Mo, NiCr and CrC powders (40wt.% C-20 wt.% NiCr-20 wt.% Mo-20 wt.% Cr_3C_2) using atmospheric plasma spray process for wear resistance applications. The FESEM, and HRXRD confirms the presence of homogenous Carbon based composite coating, which depicts good mechanical properties (micro-hardness, residual stress) and excellent tribological performance (COF and wear). The major results are drawn as follows:

1. FESEM, and HRXRD results confirms the presence of Cr_3C_2, MoO_2 and Mo_2C along with Cr_2C_2, hard phased in the Carbon based composite coating.
2. The carbon based composite coating was wear tested at variable temperature, the hardness and residual stress of the coating increases with increase in wear temperature, due to the formation of oxides and carbide in the coating.
3. The experimental result shows that carbon based composite coating was temperature dependent and at 350^{o}C temperature, lowest COF (0.08), wear (105 micron) and frictional force (3N) was obtained.

References

1. M. Nakada, Trends in engine technology and tribology, Tribolgy International, 1994; 27 (1):3–8.
2. A.Z. Szeri, “Tribology: Friction, lubrication, and wear,” McGraw-Hill, 1980.

Accepted Manuscript

3. M. Kennedy, S. Hoppe, J. Esser, Lower Friction Losses with New Piston Ring Coating, MTZ World Wide,2014; 75 (4):24–29.
4. Kapsiz M, Durat M, Ficici F (2011) Friction and wear studies between cylinder liner and piston ring pair using Taguchi design method. Adv Eng Softw, 2011; 42; 595–603.
5. Yan J, He Z, Wang Y, et al. Microstructure and wear resistance of plasma-sprayed molybdenum coating reinforced by MoSi2 particles. J Therm Spray Technol. 2016; 25; 1322–1329.
6. Matikainena V, Bolelli G, Koivuluoto H, et al. Sliding wear behaviour of HVOF and HVAF sprayed Cr3C2-based coatings. Wear. 2017. doi:10.1016/j.wear.2017.04.001
7. Zhou W, Zhou K, Deng C, et al. Hot corrosion behavior of HVOF-sprayed Cr3C2-WC-NiCoCrMo coating. Ceram Int. 2017. doi:10.1016/j.ceramint.2017.04.109
8. Shailesh Mani Pandey, Qasim Murtaza, R. S. Walia, Study of dry wear behavior and morphological characteristic of 60%Mo-20%NiCr-10%CrC-10%Mo+Fe based alloy coating by atmospheric plasmaspray technique, Advances in Materials and Processing Technologies, DOI: 10.1080/2374068X.2017.1334997.
9. Liu Z, Hua M. Wear transitions and mechanisms in lubricated sliding of a molybdenum coating. Tribol Int. 1999; 32; 499–506.
10. Obert P, Muller T, Fu.er HJ, et al. The influence of oil supply and cylinder liner temperature on friction, wear and scuffing behavior of piston ring cylinder liner contacts – a new model test. Tribol Int. 2016; 94; 306–314.
11. Liu X, Liu H, Liu Y, et al. Effects of temperature and normal load on tribological behavior of nickel-based high-temperature self-lubricating wear-resistant composite coating. Compos B Eng. 2013; 53; 347–354.
12. Hong S, Wu Y, Wang B, et al. The effect of temperature on the dry sliding wear behavior of HVOF sprayed nanostructured WC-CoCr coatings. Ceram Int. 2017; 43; 458–462.
13. Priyan MS, Hariharan P. Wear and corrosion resistance of Fe-based coatings by HVOF sprayed on gray cast-iron for automotive application. Tribol Ind. 2014; 36; 394–405.
14. Z. Sun, P. Zhang, L. Zhai, X. Xu, A. Han, W. Zhang, Multi-layer compound coating on cast iron piston ring by multi-arc and magnetron sputtering ion compound plating technique, Surf. Coat. Technol. 2000; 131; 422–427.

Accepted Manuscript

15. C. Friedrich, G. Berg, E. Broszeit, F. Rick, J. Holland, PVD CrxN coatings for tribological application on piston rings, Surf. Coat. Technol.1997; 97; 661–668.
16. A. Banerji, S. Bhowmick, A. T. Alpas. High temperature tribological behavior of W containing diamond like carbon (DLC) coating against titanium alloys. Surf. Coatings Technol. 2014; 241; 93–104.
17. Ankit Tyagi, R.S. Walia, Qasim Murtaza, Shailesh Mani Pandey, Pawan Tyagi, Bharat Bajaj, A critical review of Diamond like Carbon Coating for Wear Resistance Applications, International Journal of Refractory Metals & Hard Materials, 2019; 78; 107–122.
18. Dumpala R, Kumar N, Kumaran CR, Dash S, Ramamoorthy B, Ramachandra Rao MS. Adhesion characteristics of nano- and micro-crystalline diamond coatings: Raman stress mapping of the scratch tracks. Diamond Relat Mater 2014; 44; 71–7.
19. Dumpala R, Ramamoorthy B, Rao MSR. Graded composite diamond coatings with top-layer nanocrystallinity and interfacial integrity: cross-sectional Raman mapping. Appl Surf Sci 2014; 289:545–50.
20. S. Alirezaei, S.M. Monirvaghefi, M. Salehi, A. Saatchi, Wear behavior of Ni-P and Ni-P-Al2O3 electroless coatings, Wear, 2007; 262 (7–8) ; 978–985
21. Tyagi A., Murtaza Q., Walia, RS., Pandey SM., Characterization and parametric optimization of tribological properties of Mo blend composite coating, Material Research Express, (Accepted, 2019).
22. Tyagi A., Walia, RS., Murtaza Q., Tribological behavior of temperature dependent environment friendly thermal CVD diamond coating, Diamonds and Related Materials, 96 (2019) 148–159.
23. H. Wu, X.D. Lan, Y. Liu, F. Li, W.D. Zhang, Z.J. Chen, X.F. Zai, H. Zeng, Fabrication, tribological and corrosion behaviors of detonation gun sprayed Fe-based metallic glass coating, Trans. Nonferrous Metals Soc. China, 2016; 26 (6); 1629–1637.
24. Jian Wang, Feng-Lin Zhang, Teng Zhang, Wen-Guang Liu, Wei-Xiong Li, Yu-Mei Zhou, Preparation of Ni-P-diamond coatings with dry friction characteristics and abrasive wear resistance, International Journal of Refractory Metals & Hard Materials, 2018; 70; 32–38.

Accepted Manuscript

Wavelet Based Control of Shunt Compensator for Power Quality Enhancement

Masood Anzar
Department of Electrical Engineering
Delhi Technological University
New Delhi, India
masoodanzar@gmail.com

Narendra Kumar
Department of Electrical Engineering
Delhi Technological University
New Delhi, India
dnk_1963@yahoo.com

M. Rizwan
Department of Electrical Engineering
Delhi Technological University
New Delhi, India
rizwan@dce.ac.in

Abstract— **Wavelet based control is proposed in the paper for the removal of harmonics and power factor improvement. The non-linear balanced or unbalanced load current is divided into direct and quadrature axis. The active and reactive current weights are extracted by the wavelet transform. The technique is capable to eliminate of harmonics, compensate reactive power and load balancing. The approach is finds to be among the fastest weight learning approach.**

Keywords—***Harmonics Elimination, Reactive Power Compensation, Wavelets Control, Shunt Compensator***

I. INTRODUCTION

The disturbances in the power system are increasing with the increase in the usage of electronic equipment. As a result, many researchers are focused to find the possible solution on the enhancement of reliability and power quality of distribution system.

Non-linear reactive and unbalanced loads have adversely affected power quality supplied by the source. Some of the problems include the temperature rise of electrical equipments, neutral current, voltage between ground and neutral and supply rating. Compensators are proposed as a solution of these power quality (PQ) issues. The shunt compensator provides possible solution for harmonics current, low power factor and load unbalancing, which are the major issues of power quality.

There are two operational process of a shunt compensator. One includes the identifying current harmonics while the other governs the injection of the compensated current into power network. The algorithms based on accuracy, the speed, stability, computation complexity and implementation cost are proposed in due time. The authors have proposed various solutions based on time domain like IRP, SRF, and symmetrical component theory [1]. But such time domain techniques have some limitations of their own. The performance is degraded in case of unequal power disturbances in all the phases.

Periodic signals are required for frequency domain techniques [2]. Fourier transform estimates the frequencies present in the signal over the entire time. It fails to find the time of the transient. Also, the Fourier analysis fails to consider non stationary signals where frequencies evolve with time [3]. Fourier techniques also have some additional issues like aliasing with non-stationary signals and Gibbs' phenomena. STFT (Short Time Fourier Transform) was also proposed [3] but it does not provide good resolution both in time and frequency due to fixed window size. Due to this the signal transient analysis was still a hindrance in the STFT.

Wavelet Transform based method provides an optimized resolution of frequency and time, overcoming the above discussed drawbacks. Thus wavelets transform is a proper tool to deal with real life signals, i.e., low duration, high frequency disturbances and signals of low frequencies with longer time duration [4]. Thus wavelets are best suited for the power system signals analysis. As wavelet transform based method extract a band of frequency, the technique is also found to be less sensitive for frequency oscillation in power system. The time domain based algorithm for the estimation of phase-angle and amplitude can also be synchronously applied with other frequency estimation algorithms for frequency variation detection [5]. But these techniques are complex and not as fast as wavelet transform based algorithm in harmonic conditions. *Musab.A et al* [6] used wavelet transform for active component estimation from the load current. The computation complexity increases because it requires wavelet transform analysis of the currents of all the three phases. Also, the absence reactive power compensation and ZVR mode provided us a research gap. The paper introduces the wavelet control for the removal of harmonics and compensation of reactive power and load unbalancing.

II. WAVELET TRANSFORM

The signal is decomposed into oscillatory mathematical functions called as wavelets in wavelet transforms. It provides "variable time frequency" resolution in comparison to Fourier transform which provide only frequency resolution. The wavelets oscillations make it highly useful in non-stationary signals. It is classified into continuous and discrete form

A. Continuous Wavelet Transform

The time and scale parameters are continuous in continuous wavelet transform (CWT). The transform of a time function $X(t)$ is given as:

$$F(s,\tau)=\frac{1}{\sqrt{s}}\int X(t)\Phi^{*}(\frac{t-\tau}{s})dt \quad (1)$$

Where, "s" and "τ" are the scale and translation of the wavelet with $\Phi(t)$ as a mother wavelet of zero mean value.

$$\int_{-\infty}^{\infty}\Phi(t)\,dt=0 \quad (2)$$

978-1-5386-6625-8/18/$31.00 ©2018 IEEE

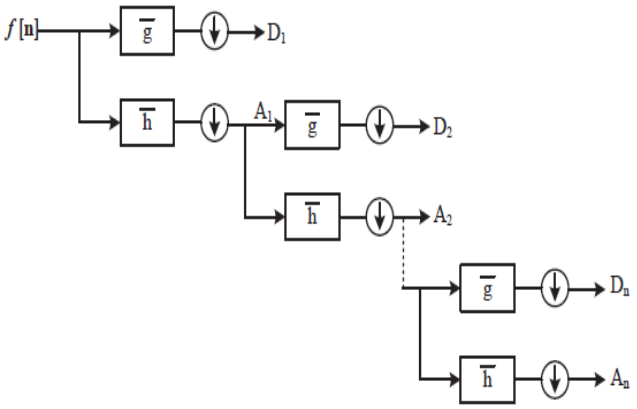


Fig (1): Multi Resolution Analysis of a Signal

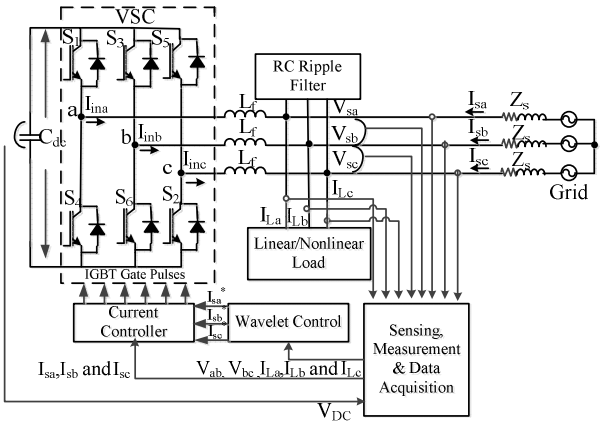


Fig (2): Schematic of Shunt Compensator

B. Discrete Wavelet Transform

In Discrete Wavelet Transform (DWT) scale and translation is incorporated in the wavelet function by providing binary dilations (2j) and dyadic translations (k/2j). The DWT of a signal is defined as:

$$DWT(m,k)=\frac{1}{\sqrt{s_0^j}}\sum_{n=0}^{N-1}X[n]\Phi(\frac{k-na_o^j}{s_o^j}) \quad (3)$$

where, j,k are integers

The multi-resolution decomposition of the signal is very useful in signal analysis of the real world. The signal is converted into a series of $[A_1,D_1,A_2,D_2,...,A_n,D_n]$ of coefficients at different level, where n is the number of level. The low pass coefficients $[A_1,A_2,...,A_n]$ are known as approximations and high pass coefficient $[D_1,D_2,...,D_n]$ are known as details.

Various discrete wavelets available to us are Haar, Daubechies, and Symlet etc. Daubechies wavelets represent the wavelet with adjoin, i.e. orthogonal, wavelet and inverse wavelet transform. The vanishing moments are maximum in Daubechies wavelets and hence represent polynomial functions of higher degree. It results in progressively finer discrete samplings. We have used Daubechies wavelet (db1) to filter a high frequency component from the direct axis current (I_d).

III. CONTROL SCHEME

The wavelet based proposed control scheme requires the source voltages (V_s), source current (I_s), load currents (I_L) and dc link voltage (V_{dc}) for the generation of reference currents $(Ia_{ref}, Ib_{ref}, Ic_{ref})$ as shown in Figure 2and 3. The generated reference current are compared with the source current (I_s) and produce the proper firing sequence for the voltage source converter (VSC) to produce compensating currents (I_c). These compensating currents are able to eliminate harmonics, maintaining the unity power factor under different load.

A. Unit Template Estimation of Load Voltages

The amplitude (V_m) of three phase voltages at PCC is estimated by the instantaneous value (V_{sa},V_{sb},V_{sc}) of the three sensed phases.

$$V_m=\sqrt{\frac{2(V_{sa}^2+V_{sb}^2+V_{sc}^2)}{3}} \quad (4)$$

The unit templates in phase (v_{pa},v_{pb},v_{pc}) and quadrature vectors (v_{qa},v_{qb},v_{qc}) with voltages are calculated as given in [8-10].

$$v_{pa}=\frac{V_{sa}}{V_m},\ v_{pb}=\frac{V_{sb}}{V_m},\ v_{pc}=\frac{V_{sc}}{V_m} \quad (5)$$

$$v_{qa}=\frac{1}{\sqrt{3}}(v_{pc}-v_{pb}),v_{qb}=\frac{\sqrt{3}v_{pa}}{2}+\frac{(v_{pb}-v_{pc})}{2\sqrt{3}}$$

$$v_{qc}=-\frac{\sqrt{3}v_{pa}}{2}+\frac{(v_{pb}-v_{pc})}{2\sqrt{3}} \quad (6)$$

B. Average Active Power Weights Estimation

To control the dc link voltage, a proportional-integral controller based (PI) is used in the shunt compensator. The measured dc link voltage (V_c) is first passed through a low with the reference value of dc link voltage (V_c^{ref}) to calculate an error (V_{ce}). This error gives us the loss component when passed through a proportional integral (PI) controller. The controller output (w_{dc}^p) meets the compensator losses and regulates the dc link capacitor voltages. The output is given by:

$$w_{dc}^p(n)=w_{dc}^p(n-1)+k_p^p[V_c(n)-V_c(n-1)]+k_i^pV_c(n) \quad (7)$$

where, the proportional and integral constants are k_p^p and k_i^p of controller.

Load currents are passed through Clark's transformation to obtain I_α *and* I_β

.

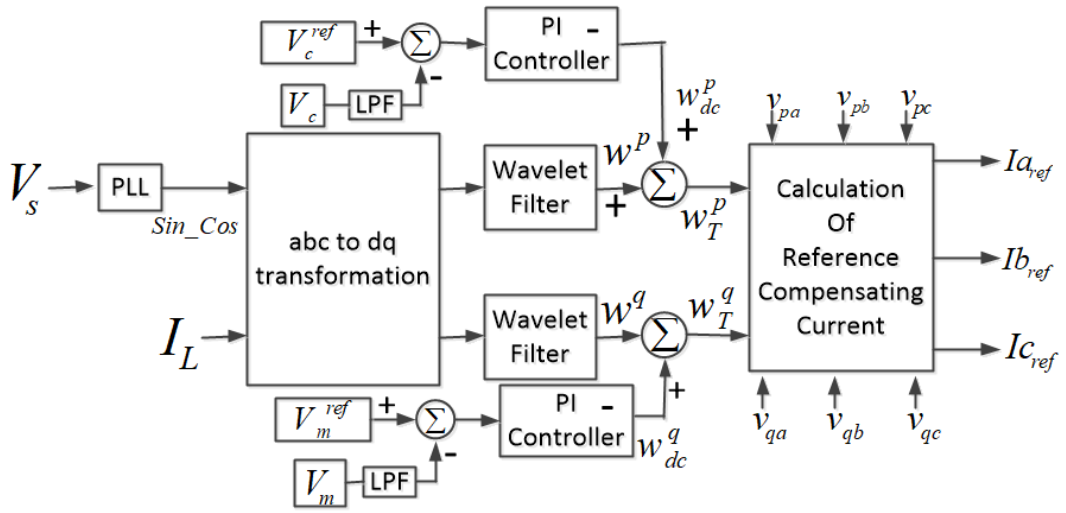


Figure (3): Block Diagram of Wavelet Based Algorithm

$$\begin{bmatrix} I_\alpha \\ I_\beta \end{bmatrix} = \sqrt{\frac{2}{3}} \begin{bmatrix} 1 & -1/2 & -1/2 \\ 0 & \sqrt{3}/2 & -\sqrt{3}/2 \end{bmatrix} \begin{bmatrix} iL_a \\ iL_b \\ iL_c \end{bmatrix} \quad (8)$$

The obtained I_α *and* I_β are passed through Park's Transformation to get I_d *and* I_q.

$$\begin{bmatrix} I_d \\ I_q \end{bmatrix} = \begin{bmatrix} \cos\theta & \sin\theta \\ -\sin\theta & \cos\theta \end{bmatrix} \begin{bmatrix} I_\alpha \\ I_\beta \end{bmatrix} \quad (9)$$

The direct axis current (I_d) is processed with DWT for the fundamental current component estimation. The direct axis current (I_d) is buffered and passed through the MATLAB function to calculate the wavelet decomposition of the signal. The signal is subdivided into two coefficients as approximation and detail with wavelets "db1" at level 10. The approximate coefficient (A_{10}) is our filtered signal which is further smoothed out by taking the windowing-mean some of the samples of A_{10} to find the fundamental active weight (w_{lpav}). The total active power weight (w_T^p) is calculated by adding the loss component (w_{dc}^p) to the average fundamental active power weight (w^p)

$$w_T^p = w^p + w_{dc}^p \quad (10)$$

C. Estimation of Average Reactive Power Weights

The amplitude of sensed voltage (V_m) is compared with the reference value (V_m^{ref}) and the output is passed through PI controller. The PI controller output (w_{dc}^q) regulates the magnitude of phase voltage at its reference value and is:

$$w_{dc}^q(n) = w_{dc}^q(n-1) + k_p^q[V_m(n) - V_m(n-1)] + k_i^q V_m(n) \quad (11)$$

where, k_p^q and k_i^q are proportional and integral constants of ac bus controller.

This reactive power component (w^q) compensates the change in load current and the drop in voltage because of the impedance of the source. The reference reactive power (w_T^q) is obtained by subtraction of the average reactive weight (w_{dc}^q) from (w^q)

$$w_T^q = w^q - w_{dc}^q \quad (12)$$

D. Estimation of Reference Currents

The active current component can be calculated by multiplying the active power unit templates with the active power weights. Similarly, reactive power current component can be obtained by multiplying reactive power unit templates with the reactive power weights. The active and reactive currents are combined to estimate the total reference current as:

$$Ia_{ref} = (w_T^p \times v_{pa}) + (w_T^q \times v_{qa})$$
$$Ib_{ref} = (w_T^p \times v_{pb}) + (w_T^q \times v_{qb})$$
$$Ic_{ref} = (w_T^p \times v_{pc}) + (w_T^q \times v_{qc}) \quad (13)$$

IV. Simulation Results

Simulation model based on wavelet control for the shunt compensator is developed in MATLAB/Simulink environment. Simulated results are presented to verify the wavelet control for power factor correction (PFC) and voltage regulation (VR) mode with nonlinear balanced/unbalanced loads.

A. Performance under load change for PFC

The dynamic performance of shunt compensator connected across the nonlinear load for PFC (power factor correction) mode can be seen in Figure 4. The waveforms of supply voltages (V_s), supply currents (I_s), load currents (I_L), compensator currents (I_f) and dc link voltages (V_{dc}) are shown in this figure. For time t < 0.2 sec the dc link voltage is maintained at its reference value and the source is delivering balanced sinusoidal currents in steady state.

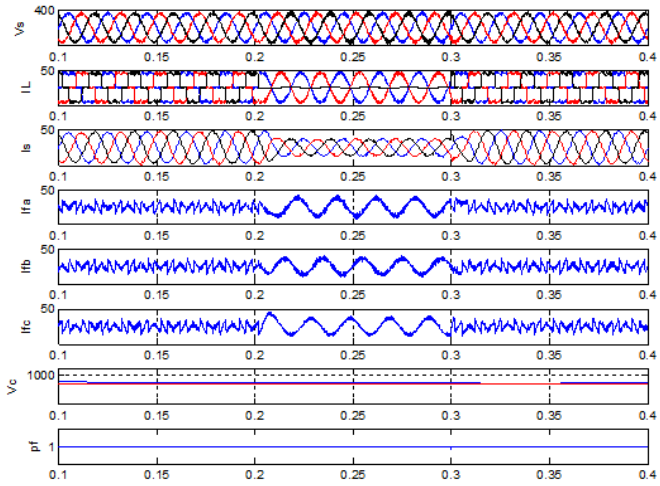


Figure (4): Shunt Compensator Performance in PFC mode

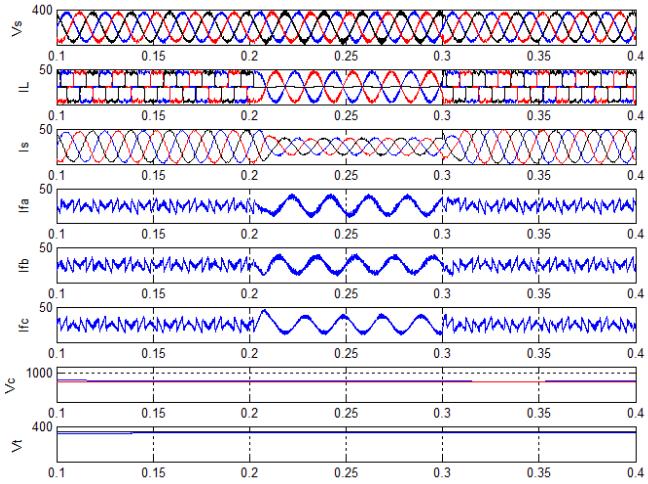


Figure (6): Shunt Compensator Performance in VR mode

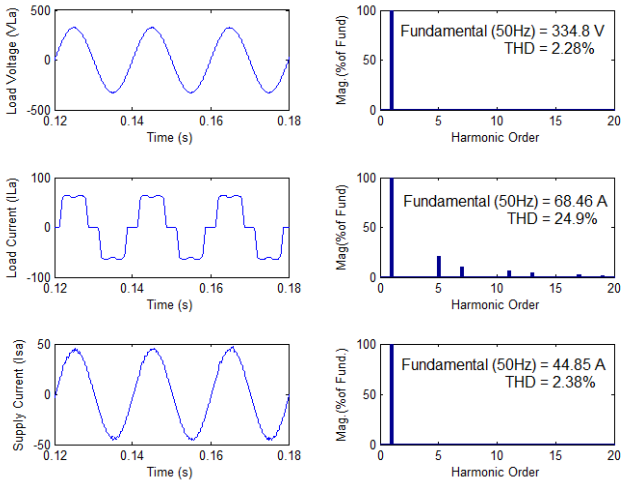


Figure (5): Supply Voltage, supply current and Load Current Harmonics in PFC Mode.

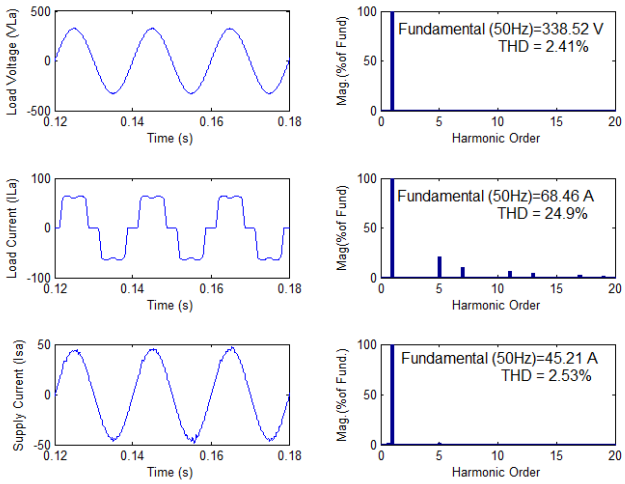


Figure (7): Supply Voltage, supply current, Load Current in VR Mode.

During time 0.2 < t < 0.3 sec, phase "c" is switched disconnected to create unbalancing in the load currents. It can be observed that the control continues to provide balanced supply currents during load unbalance.

The harmonic analysis of phase "a" for source voltage (V_s), source current (I_s) and load current is shown in figure 5. The total harmonic distortions (THD) observed are 2.28% in supply voltage (V_s), 2.38% in supply current (I_s) and 24.9% in load current (I_L). The satisfactory performance of compensator with wavelet control can be observed from the fact that the supply current THD is reduced to 2.28% even if the load requires the current of THD 24.95%. The obtained THD values of supply voltage (V_s) and supply current (I_s) fulfills the IEEE-519 standard.

B. Performance under load change for VR

The shunt compensator performances are shown in Figure 6. The supply voltages (V_s), supply currents (I_s), load currents (I_L), compensator currents (I_c), dc link capacitor voltage (V_c) and Voltage amplitude (V_m) are plotted in the figure 6.

The steady state condition results are observed for time $t \le 0.2\,\text{sec}$. The source is providing sinusoidal balanced currents, with the dc link capacitor voltages and terminal voltage maintained at their reference values, i.e., $V_{dc}^* = 700V$, $V_t^* = 338.8V$.

The dynamic performance of control is also tested with load unbalancing by disconnecting phase "c" during $0.2 \le t \le 0.3\,\text{sec}$. The harmonic content of supply voltage (V_{sa}), supply current (I_{sa}) and non linear load current (I_{La}) for phase-A in voltage regulation are shown in Figure 7. The total harmonic distortions (THDs) for V_{sa}, I_{sa} *and* I_{La} are 2.41%, 2.53% and 24.9% respectively.

. The THD values of V_{sa} and I_{sa} are satisfying the permitted IEEE-519 standards [7]. It can be observed that the control is able to provide balanced sinusoidal supply currents under maintained values of dc link voltages and PCC voltages for harmonics PFC and VR.

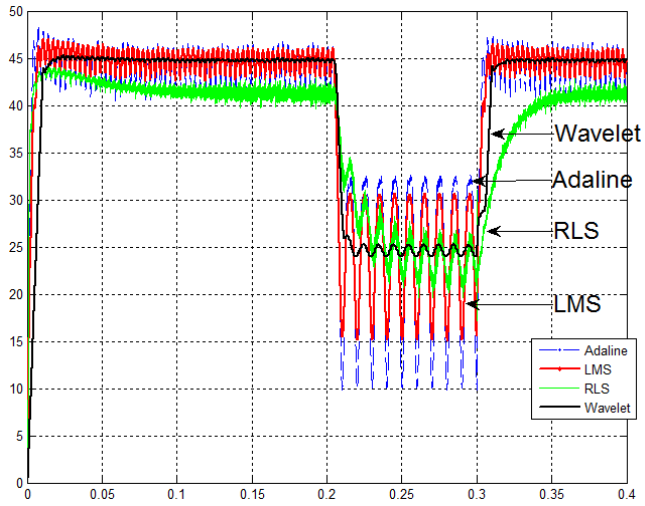


Figure (8): Comparison of Adaline, LMS, RLS and Wavelet Control

C. *Comparative Analysis of Wavelet Based Control*

The parameters of wavelet based control are compared with Adaline, LMS and RLS algorithm. The convergence of active weight of load current is compared with all the four algorithms in Figure 8. Result shows that wavelet control converge the weight faster in few cycles as compared to other controls algorithms. The estimated weight fluctuates around the mean value with Adaline, LMS and RLS control algorithm. But wavelet control provides more stable and fast weight update as compared with RLS algorithm. Adaline, LMS and RLS algorithm when implemented need a low pass filter after the weigh extraction, adding more delay into the system. But with wavelet control, no such low pass filter is required.

It can be also observed from these results that wavelet control provides best convergence of active weights under unbalanced load also. The wavelet control is seen to perform better in weight estimation and system delays.

TABLE I. PARAMETERS IN DIFFERENT MODES

Modes	Parameters	Magnitude	THD (%)
Power Factor Correction	Load Voltage	334.8 V	2.28
	Source Current	44.85A	2.38
	Load Current	68.46 A	24.9
Voltage Regulation	Load Voltage	338.52 V	2.41
	Source Current	45.21 A	2.53
	Load Current	68.46 A,	24.9

a.)

V. CONCLUSION

The proposed wavelet control is applied for reference current determination from non-linear load currents. The control is also compared with other algorithms such as Adaline, LMS and RLS. The proposed wavelet based control algorithm is found to offer fast convergence and robustness as compared to other algorithms. The working is found satisfactory in both power factor correction (PFC) and voltage regulation modes under balanced and unbalanced loading conditions. The elimination of harmonic, compensation of reactive power and balance source currents are achieved with dc link voltage regulation. The supply current THD is reduced from 24.9% to 2.38% and 2.53% in PFC and VR mode respectively, satisfying IEEE-519 standards

APPENDIX

3-ph, 50Hz, 415V AC Supply with source resistance $R_s = 0.01\Omega$ and source inductance $L_s = 2mH$, DC link voltage $V_c = 700V$, Interfacing Inductor: $L_f = 2.7mH$, Passive filter: Resistance $R_f = 5\Omega$, capacitance .DC Link Controller: $k_p^p = 0.1, k_i^p = 0.001$ Terminal Voltage PI controller: $k_p^q = 0.05, k_i^q = 0.001$, Nonlinear load: 3-phase bridge rectifier (uncontrolled) with $R = 13\Omega$.

REFERENCES

[1] U. Rao, Mahesh. K. Mishra, and A. Ghosh, Control strategies for load compensation using instantaneous symmetrical component theory under different supply voltages, IEEE Transactions on Power Delivery, vol. 23, no. 4, pp. 23102317, 2008.

[2] L. Asiminoaei, F. Blaabjerg, S. Hansen, Evaluation of harmonic detection methods for active power filter applications, in: Proceedings of APEC'05, vol. 1, March 2005, pp. 635–641.

[3] A. Galli, G. Heydt, and P. Ribeiro, Exploring the power of wavelet analysis, Computer Applications in Power, IEEE, vol. 9, no. 4, pp. 3741, Oct 1996.

[4] Shyh-Jier Huang and Cheng-Tao Hsieh, "Computation of continuous wavelet transform via a new wavelet function for visualization of power system disturbances," 2000 Power Engineering Society Summer Meeting (Cat. No.00CH37134), Seattle, WA, 2000, pp. 951-955 vol. 2.

[5] C. H. Kim and R. Aggarwal, Wavelet transforms in power systems. i. general introduction to the wavelet transforms, Power Engineering Journal, vol. 14, no. 2, pp. 8187, April 2000.

[6] Mus-ab.A, Mahesh K. Mishra, "Wavelet Transform Based Algorithms for Load Compensation Using DSTATCOM", IEEE PES Asia-Pacific Power and Energy Engineering Conference (APPEEC) 8-10 Nov. 2017

[7] A. Mus-ab and M. K. Mishra, "Wavelet transform based algorithms for load compensation using DSTATCOM," *2017 IEEE PES Asia-Pacific Power and Energy Engineering Conference (APPEEC)*, Bangalore, 2017, pp. 1-6.

[8] R. Kumar, B. Singh, D. T. Shahani and C. Jain, "Dual-Tree Complex Wavelet Transform-Based Control Algorithm for Power Quality Improvement in a Distribution System," in *IEEE Transactions on Industrial Electronics*, vol. 64, no. 1, pp. 764-772, Jan. 2017.

[9] W. Li, B. Rahmani and G. Liu, "A Wavelet-Based Shunt Active Power Filter to Integrate a Photovoltaic System to Power Grid," *2016 Sixth International Conference on Instrumentation & Measurement, Computer, Communication and Control (IMCCC)*, Harbin, 2016, pp. 482-485.

[10] B. Singh and S. Arya, "Composite observer-based control algorithm for distribution static compensator in four-wire supply system," IET Power Electron., vol. 6, Iss. 2, pp. 251–260, 2013.

[11] B. Singh and S. Arya, "Implementation of single-phase enhanced phase-locked loop-based control algorithm for three-phase DSTATCOM," IEEE Trans. Power Del., vol. 28, no. 3, pp. 1516-1524, July 2013.

[12] I. D. Landau, R. Lozano, M. M"Saad, and A. Karimi, Adaptive Control: Algorithms, Analysis and Applications. New York, NY, USA: Springer- Verlag, 2011.

[13] M. I. M. Montero, E. R. Cadaval, and F. B. Gonzalez, ''Comparison of control strategies for shunt active power filters in three phase four wire systems,'' IEEE Trans. Power Electron., vol. 22, no. 1, pp. 229–236, Jan. 2007

[14] M. Forghani and S. Afsharnia, ''Online wavelet transform-based control strategy for UPQC control system,'' IEEE Trans. Power Delivery, vol. 22, pp. 481–491, Jan. 2007.

[15] J. Barros and R. I. Diego, ‘‘Analysis of harmonics in power systems using the wavelet-packet transform,’’ IEEE Trans. Instrum Meas., vol. 57, pp. 63–69, Jan. 2008.

[16] G. Escobar, P. R. Martinez, J. Leyva Ramos, and P. Mattavelli, ‘‘A negative feedback repetitive control scheme for harmonic compensation,’’ IEEE Trans. Ind. Electron., vol. 53, no. 4, pp. 1383–1386, 2006.

[17] B. Singh, V. Verma, and J. Solanki, ‘‘Neural network-based selective compensation of current quality problems in distribution system,’’ IEEE Trans. Ind. Electron., vol. 54, no. 1, pp. 53–60, Feb. 2007.

[18] D. O. Abdeslam, P. Wira, J. Merckle, D. Flieller, and Y.-A. Chapuis, ‘‘A unified artificial neural network architecture for active power filters,’’ IEEE Trans. Ind. Electron., vol. 54, no. 1, pp. 61–75, Feb. 2007.

ResearchGate

See discussions, stats, and author profiles for this publication at: https://www.researchgate.net/publication/336825255

Wear Behaviour of Al/B4C Surface Composite Fabricated by Friction Stir Processing

Article *in* The ISME Journal · January 2018

CITATIONS
0

READS
6

1 author:



Yuvaraj N.
Delhi Technological University
12 PUBLICATIONS **84** CITATIONS

SEE PROFILE

Some of the authors of this publication are also working on these related projects:

Surface composites View project

All content following this page was uploaded by Yuvaraj N. on 26 October 2019.

The user has requested enhancement of the downloaded file.

ISME Journal of Manufacturing Sciences

Vol. 07, No. 01, 2018 pp. 38-50

Wear Behaviour of Al/B_4C Surface Composite Fabricated by Friction Stir Processing

Yuvaraj N

[1] Department of Mechanical Engineering, Delhi Technological University, Delhi 110 042, India.

*corresponding author: yuvraj@dce.ac.in

Abstract

Friction Stir Processing (FSP) technique improves the hardness and wear resistance of the surface layer. This technique finds in a different industrial application due to improvement of service life of components. FSP Technique was used to produce Al5083/B_4C nano composite surface layer. The processed regions were examined by SEM and XRD studies. The micro hardness and tensile strength were measured. Wear performance of the surface was evaluated through a pin on disc test. The sliding load range was varied from 20 to 80N, whereas sliding velocity was in the range of 1 to 5 m/s. Worn out surfaces were analysed through SEM for analyzing the different wear mechanisms. The tribological studies showed that FSPed surface composite was beneficial concerning the improvement of wear resistance and reduced friction coefficient. With increase in sliding load increases the wear rate of the base metal as well as the composite. The wear rate decreases marginally up to the sliding velocity up to 3 m/s and beyond that velocity, wear increases for composites for all loads. The wear mechanisms for composites at lower loads and sliding velocities are oxidation, plastic deformation and abrasive. With the higher loads and sliding velocities the wear mechanisms are delamination, severe plastic deformation and seizure wear.

Keywords: Aluminium, Nanocomposite, Friction Stir, Boron Carbide, Wear, Tensile Microhardness

1. Introduction

The aluminum composites are replacing the aluminum alloys due to their excellent engineering properties like high hardness, wear resistance, high strength, stability at elevated temperature, low thermal expansion and enhanced creep resistance. The Aluminum based composites are find in automobile, aerospace and marine applications. Many of these applications are based on the surface property for the longer life of the mechanical components [1]. Recently, significant recognition has given to FSP technique. FSP is also a used to produce the surface composites and useful to obtain a refined grained microstructure and property enhancement in cast aluminum alloys with enhanced hardness, tensile, wear and corrosion properties [2]. The production of surface composite through FSP technique is explained elsewhere [3]. Recently various nano particulates such as SiC [4], Al_2O_3 [5], ZrO_2 [6], TiO_2 [7], Si_3N_4 [8], CNT [9] and B_4C [10] were used to fabricate the Aluminum surface composite surface by FSP Technique. B_4C is a ceramic material, high hardness, low density, high melting point and high magnitude for neutron absorption [11]. B_4C based Aluminum composite can be processed by economically by casting. But in the casting route, B_4C is difficult to be mixed into the liquid phase due to poor wetting characteristics, and also, the interfacial reactions are difficult to control with the combination. FSP Technique is an economical method to produce

surface composite and beneficial. Since the undesirable intermetallic materials formed between reinforcement and matrix are avoided [2-3]. Only limited studies on FSP of Al5083/B_4C nano composites are available. In this present work FSP Technique is used to an incorporation of B_4C nano particles in 5083 aluminum substrate to fabricate surface composite. The hardness, tensile and wear properties of the surface modified region were evaluated. The effects of various sliding speed (1-5 m/s) and the effect of various sliding load (20N-80N) on the composite and base material under dry sliding conditions are also examined.

2. Materials and Methods

Commercial Al 5083-O plate with a size of 200mm x 80mm and a thickness of 8mm were used. The composition of the as received aluminum alloy was 4.1%Mg, 0.5%Mn, 00.19%Fe, .06%Cr, 0.02%Zn, 0.2%Si, 0.04%Ti (all in weight %) and rest aluminum. In the middle of the aluminium plate 1mm width and 3mm depth size of groove was machined, and the groove was filled with 30-60nm sized B_4C particles. A threaded cylindrical H-13 tool with a shoulder of 18mm diameter was used for FSP. The FSP tool dimensions and experimental set up is shown in Figure1. FSW machine capacity of 11 kW, 40kN was used to produce the surface composite. Initially pinless tool with shoulder diameter of 18mm only used to close the groove for preventing the escape of the ceramic particles during FSP. All the samples were produced with four passes. After number of preliminary trials, the tool rotational speed of 1000 rpm and transverse speed of 40mm/min were fixed. The tool direction was changed after each FSP pass. After FSP, the stir cross section stir zone samples were examined through SEM and XRD. The micro hardness values of the processed sample were measured at the load of 100g with 10s of dwell time. The tensile tests of specimens were carried out computerized tensile testing machine at 1mm/min speed. The longitudinal tensile specimens of 4 mm thickness were sliced from the processed region as per ASTM: E8/E8M-011 standard.

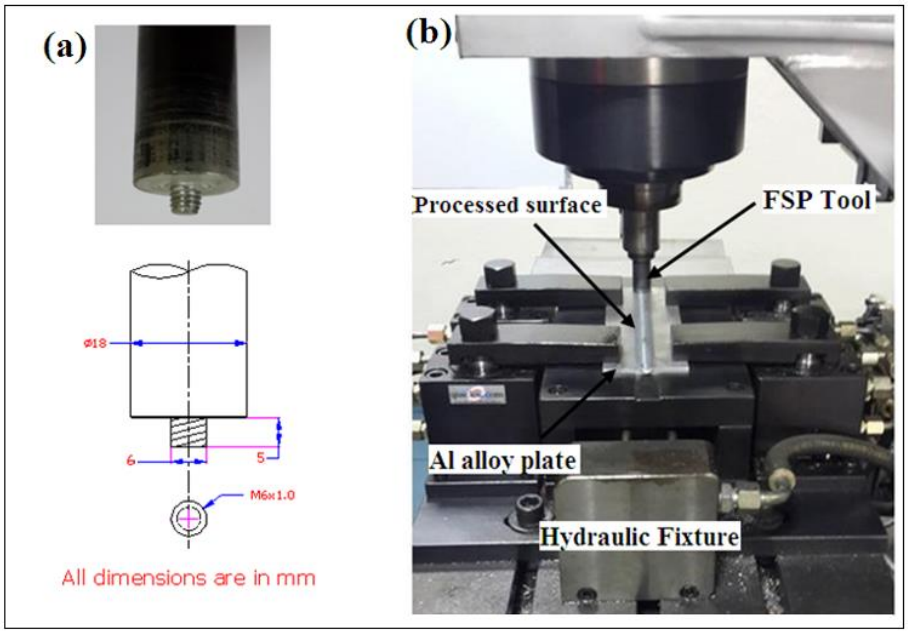


Figure 1: (a) FSP Tool (b) Experimental setup

The dry sliding wear performance of the composite surface was examined through a pin on disc (make DUCOM) and the tests were performed as per ASTM G99-04 Standard. The wear test pin specimens of 10mm diameter were extracted from the processed surface, and the counter disc was made of EN-24 hardened steel with 55-58 HRC. The surface of the wear test specimen grounds on the 1600 grit emery sheet before the test. The wear tests were performed at sliding speeds of 1, 2, 3, 4 and 5 m/s under normal sliding loads of 20, 40, 60 and 80N for distance up to 3000m. Prior to weighing of the wear tested samples and disc were cleaned with acetone. Thee wear test pins were weighed to an accuracy of ±0.01mg. The worn surfaces of specimens were analyzed through SEM with Energy Dispersive Spectrometer (EDS).

3. Results and Discussions

3.1 Microstructure

Figure 2(a) exhibits the SEM of a cross section of the composite surface. The base material average grain size is 49.5µm. The grain size of the composite surface is reduced about 3µm. During FSP, the drastic rise of heat occurs in the stir zone due to friction between tool shoulder and aluminum plate. Severe plastic deformation takes place in the stir zone due to dynamic recrystallization and presence of uniformly distributed B_4C nano reinforcement's lead to extreme grain refinement. The presence of nano particles induces pinning effect and also it restraints the grain boundary migration. Previous studies indicated that that the increase in FSP passes decreases the grain size of the Aluminum matrix [12]. With increase in the number of passes and changing the of tool rotation direction in the second pass leads to more uniform homogeneous distribution of reinforcements in the. Typical XRD pattern of the cross-section composite specimen is shown in Fig. 2(b). The XRD results confirm the presence of B_4C particles and no intermetallics formed during FSP. The melting temperature of Al alloys during FSP in the range of 400-500^oC [13], and it is inadequate to melt the hard B_4C nano ceramic particles, as a result of no intermetallics phases was present in the composite.

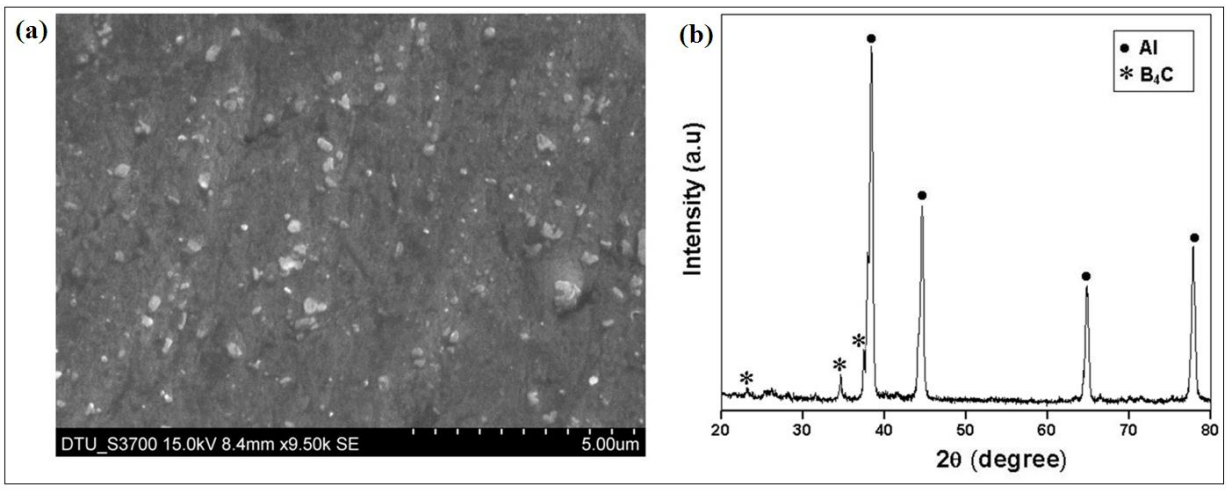


Figure 2: Surface composite cross section (a) SEM image (b) Typical XRD profile

3.2 Hardness

The typical macrograph of the stir zone of the processed composite specimen and microhardness values are shown in Figure 3(a). The micro hardness of base material and cross section of the processed composite surface are shown in Figure 3(b). The three-microhardness average value was taken for the experimental purpose. During the FSP process, the heat produced during processing softens the Aluminum base alloy, the hard reinforcement particles are uniformly dispersed in the base alloy due to intensive stirring of the hard FSP tool. The material processed with hard ceramic reinforcements increases the hardness of the base alloy by the promotion of grain refinement. According to Hall-Petch relation the finer grain size material has higher hardness [14]. The enhancement of hardness in the FSPed composite surface is due to finer grains in the stir zone and individual hardness of Boron carbide particles. Several mechanisms are involved in the improvement of the properties of metal matrix material during FSP [15-18].

(i) Fine grains are formed by recrystallization during FSP.
(ii) Dislocation occurs due to pinning of hard reinforcement particles.
(iii) Orowan strengthening, since the fine dispersion of nano reinforcements in the base alloy.
(iv) The bonding of hard nano reinforcements and Aluminum matrix can effectively transfer the load from Aluminum matrix to hard nano reinforcements. (shear lag or load transfer strengthening)
(v) The distinction in thermal contraction of Al substrate and reinforcements. (Quench hardening effect)
(vi) Elastic strain in matrix reinforcements.

(vii) Work hardening due to misfit in elastic and thermal expansion coefficients between the Al substrate and the reinforcement.

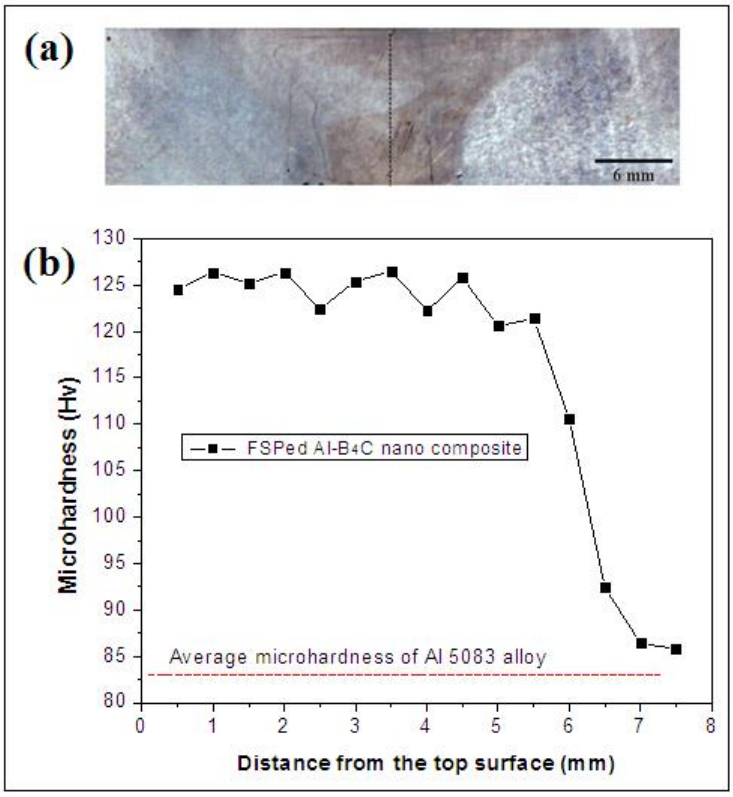


Figure 3: (a) Micro hardness measurement line across the cross section of Al-B_4C composite specimen (b) Micro hardness profile

3.3 Tensile Properties

Figure 4 exhibits the tensile results of base alloy and processed surface composite. Tensile properties of composite depend on the grain size, density of density, bonding of reinforcement particles with matrix and generation of intermetallic phases [19]. The tensile properties of the FSP samples increase with the decrease in grain size as per Hall-petch relationship. Table 1 shows tensile test data of base material and Al-B_4C composite specimen.

Figure 5 shows the fractography of tensile tested fracture surfaces. In the base alloy and processed samples ductile in fracture were observed. However, different fracture morphologies were observed between in both the samples. In the base material big size with cragged dimples were observed, in the composite specimen finer dimples in large numbers were observed. These finer dimples were created by the micro-void nucleation and finer grain size of the matrix in the location of the interface of second phase particles and reinforcements. The composite specimen improves the tensile strength and a slight reduction in elongation.

Table 1: Tensile test data of base alloy and composite specimen

Specimen	Micro hardness (Hv)	Tensile strength (Mpa)	Yield strength (Mpa)	Elongation (%)
Al 5083 alloy	82.5±2	305	139	27.2
Al-B_4C composite	126.5±2	364	145	16.2

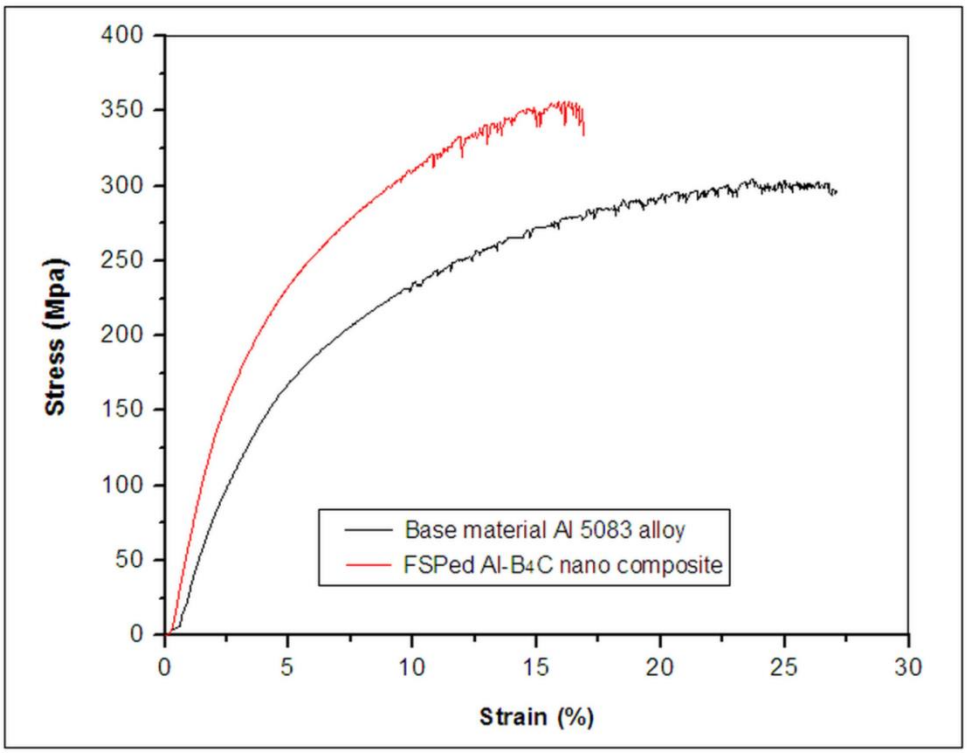


Figure 4 Typical Stress-strain curve

3.4 Wear Testing

3.4.1 Effect of sliding load and sliding velocity on wear rate

The macro image of composite conducted at different sliding velocities and different load wear test specimens are shown in Figure 6. The better wear resistance of composite surface is obtained when to compare to the base material. The composite layer attributed to higher hardness. The hard nano reinforcement has more significant wear resistance. The wear rate of the FSPed composite specimen is greatly influenced by inter-particle spacing, particle/matrix interfacial bond strength, matrix grain size and various strengthening mechanisms discussed in the previous section.

The wear rates obtained for the base material and composite at 1, 2, 3, 4 and 5 m/s sliding velocities at varies normal loads of 20N, 40N, 60N, and 80N are shown in Figure 7 (a) and (b). From the figure it is understood that the surface composite layer has better wear resistance compared to the base material in all sliding velocities and at all loads. The presence of hard B_4C nano particles act as a load carrying element and increase the wear resistance of the composite. The hard reinforcement withstands the cutting action of the wear and reduces the elimination of material from the wear specimen. The maximum wear rate happened at larger normal sliding load, and it decreases with decreases in the sliding load values for both base material and composite. The existence of hard B_4C nano reinforcements in the specimen and FSP enhances the strength and hardness of the processed composite surface. The wear rate of the base alloy and composite sample is increasing with increase in load. These results are reported by various researchers [20-22]. The wear rate of base alloy and composites decreased with increasing sliding speed up to certain speed, then the wear rate is increased. This sliding speed is relying on the load and hardness of the contact surfaces. At the higher speeds the wear specimen got softened due to increase in heat, as a result of higher wear rate occurred [23-24].

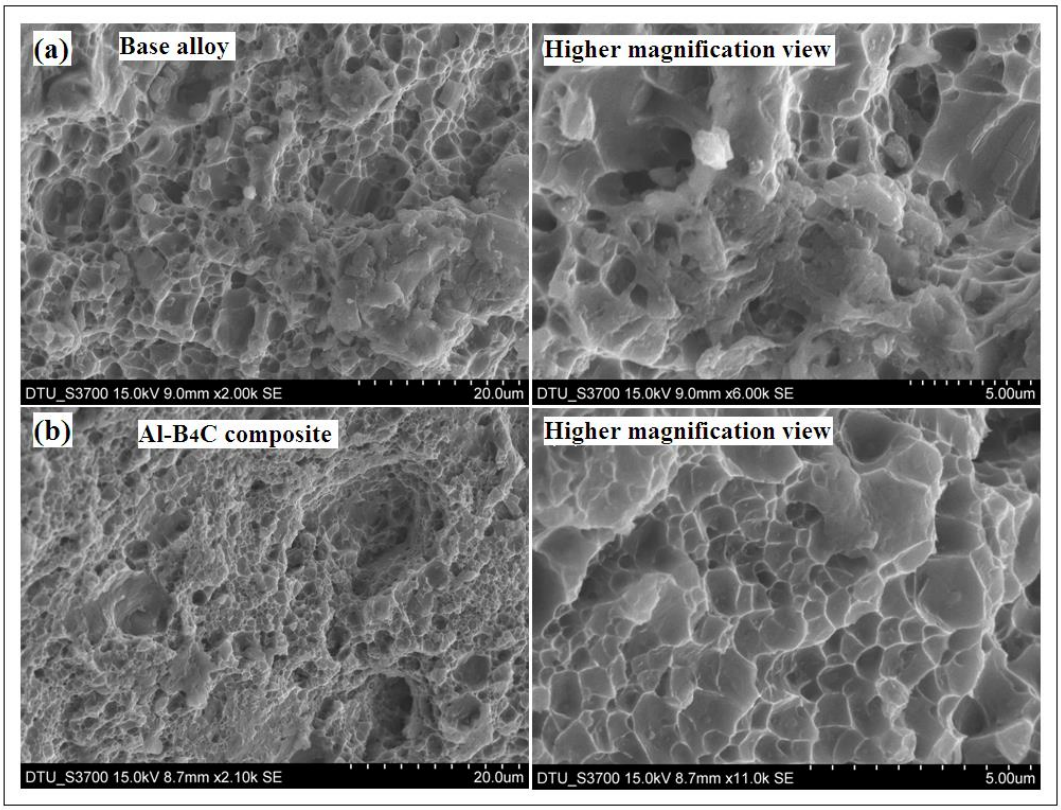


Figure 5: SEM images of tensile fractured surfaces



Figure 6 The composite wear test specimens showing after the wear test

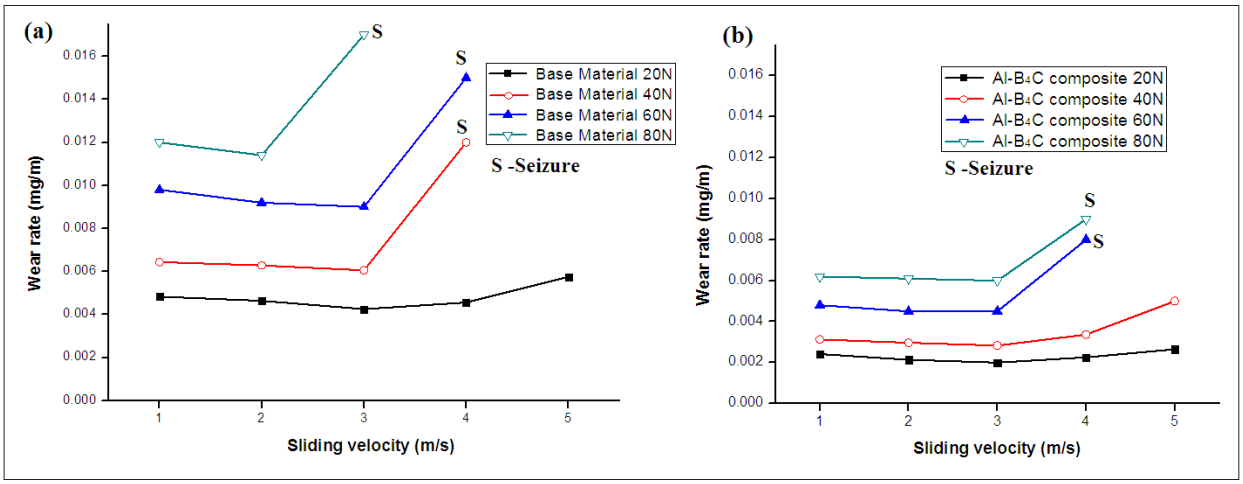


Figure 7: Wear rate of normal sliding load at different sliding velocities

At a lower sliding speeds of 1 & 2 m/s base alloy and composite specimens have completed the 3000m run without failure for the entire range of 20N to 80N. When sliding speed is increased to 3 m/s at 80N the composite specimen only could complete the 3000m run without failure. On the other hand, in the case of base alloy after 2800m of the sliding distance, the material got sticking with the disc, with an abnormal sound and material got the seizure and approached towards the failure. In the case of composite specimens, there is no such seizure occurs even at the higher load of 80N and velocity of 3m/s due to the increased hardness of the composite. The wear rate is observed to be marginally decreased for the both base material and composite specimen with an increase in sliding velocity up to 3 m/s at the lower load of 20N and 40N. At the higher loads of 60N & 80N and higher the speeds of 4 & 5 m/s, it was difficult to complete the 3000m of sliding distance. Fig. 8 shows the worn surfaces of the base material and composite specimen after sliding at the normal load of 20N load reveals oxidation, delamination wear, and abrasive wear as responsible for material loss. At 40N and 60N, coarser pits containing wear debris with abrasive grooves and surface cracks, delamination, and oxidation of wear are observed in all sliding velocities of the base material.

The worn surfaces of base alloy and composite specimens at different sliding velocities of 60N load is shown in Figure 9. With increase in load, the wear rate of base material is showing a growing tendency of wear due to direct contact between base material and disc material. At lower sliding speed (1m/s) of the composite specimen, the taking away of material from the matrix due to high frictional forces, and at intermediate speeds (2 & 3 m/s) the wear occurs in the form of micro grooves in the matrix. At lower and intermediate sliding speeds the superior wear mechanisms are oxidation and abrasive wear. At higher sliding speeds of 4 & 5 m/s and loads of 60N & 80N the main wear mechanism observed by abrasive, adhesive and seizure wear due to localized melting on the wearing surface at higher loads and higher speeds. At larger load and velocity, the type of wear mode is dominated by the seizure.

The EDS profile of a selective region of the worn specimen of base alloy and the processed composite at 80N at 3 m/s sliding velocity are shown in Figure 10 (a) & (b) respectively. The primary peaks of aluminum with Iron & Oxygen peaks are detected. However, at higher loads with higher sliding velocity, the degree of oxidation was reduced, and the surface of the base alloy was found to be having deeper and larger pits. Different wear mechanisms at under different sliding conditions is shown in Figure 11.

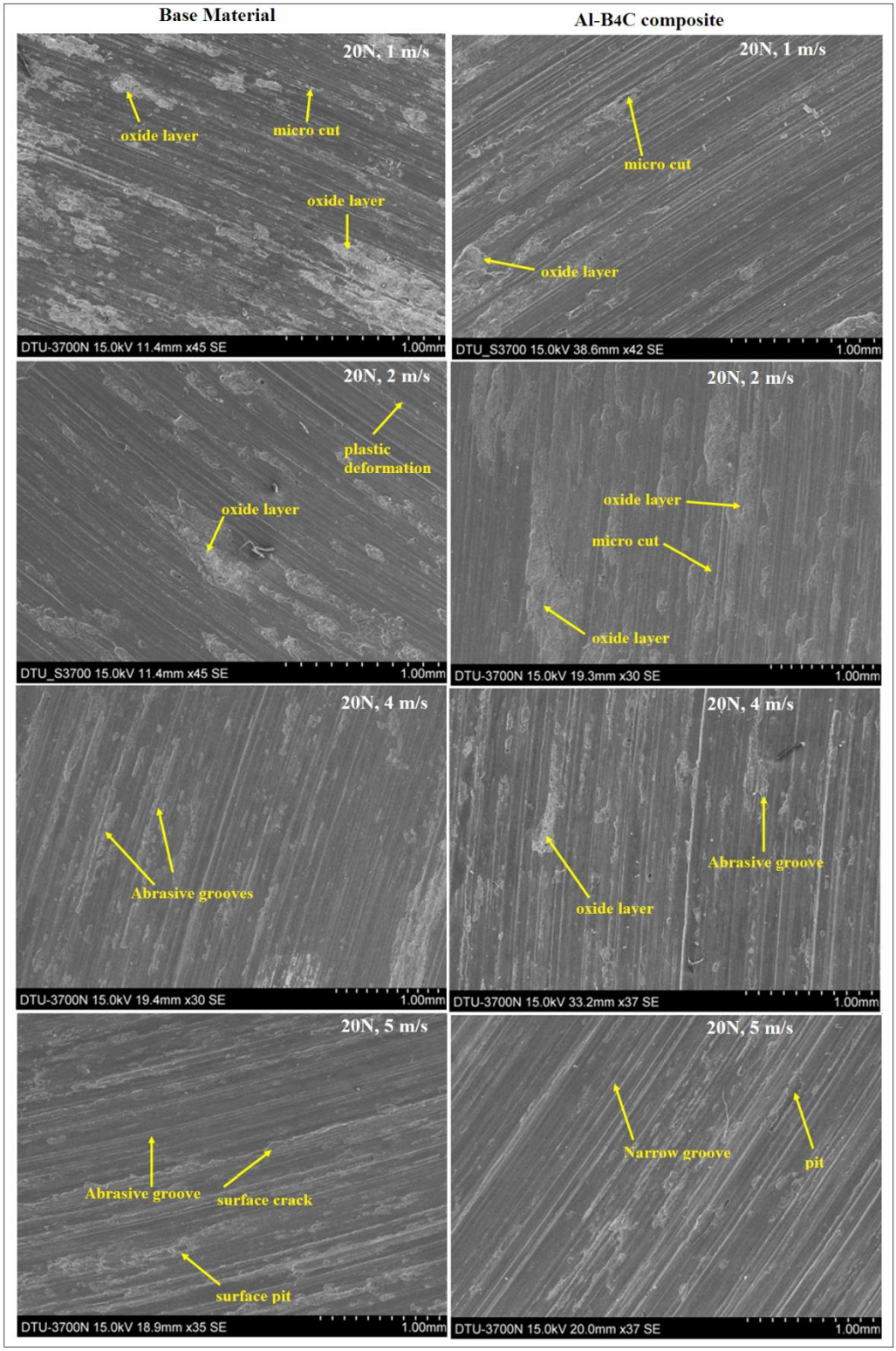


Figure 8 Worn surface of Base material and Al-B_4C surface composite at 20N

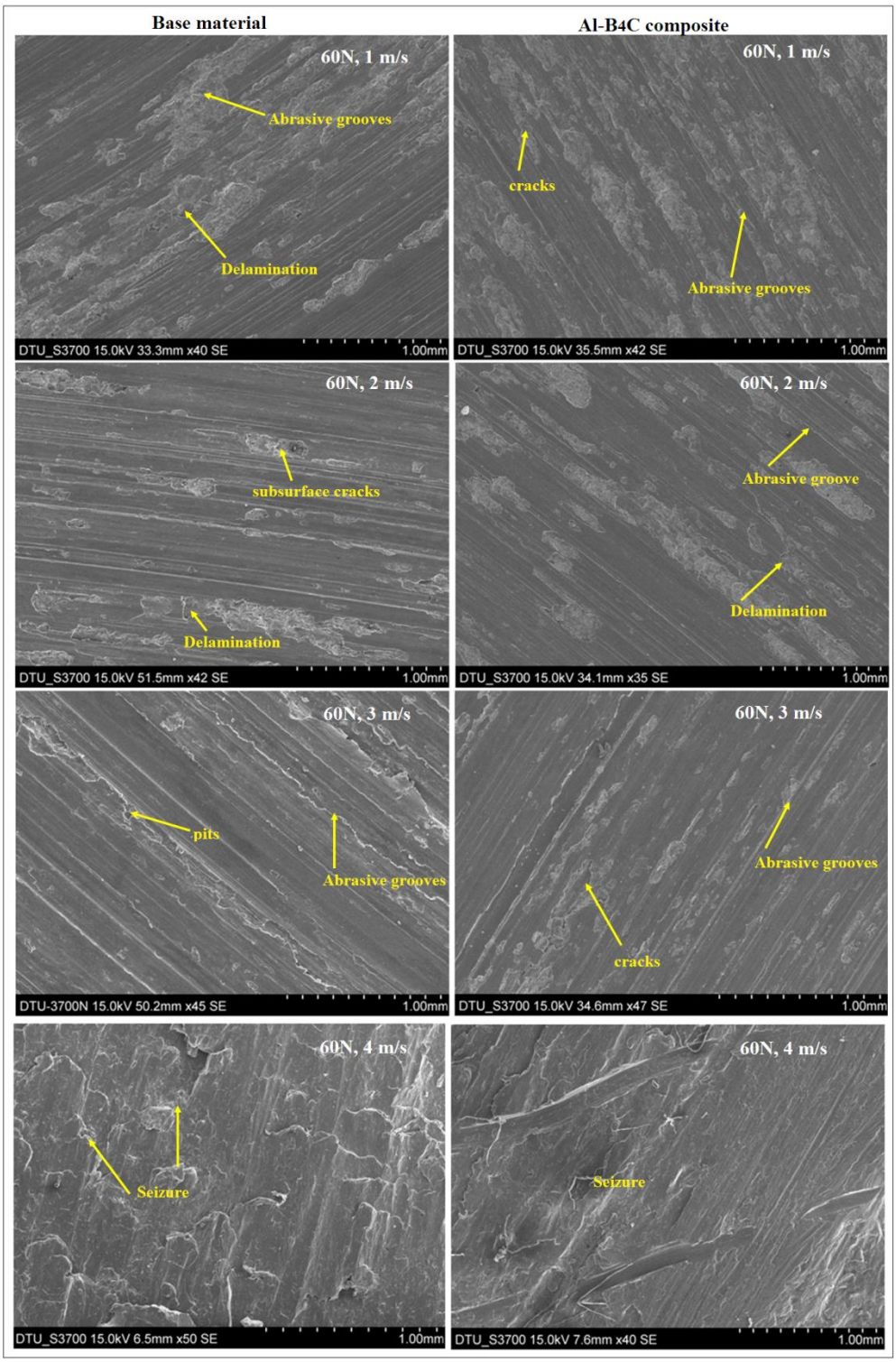


Figure 9 Worn surface of Base material and Al-B_4C surface composite at 60N

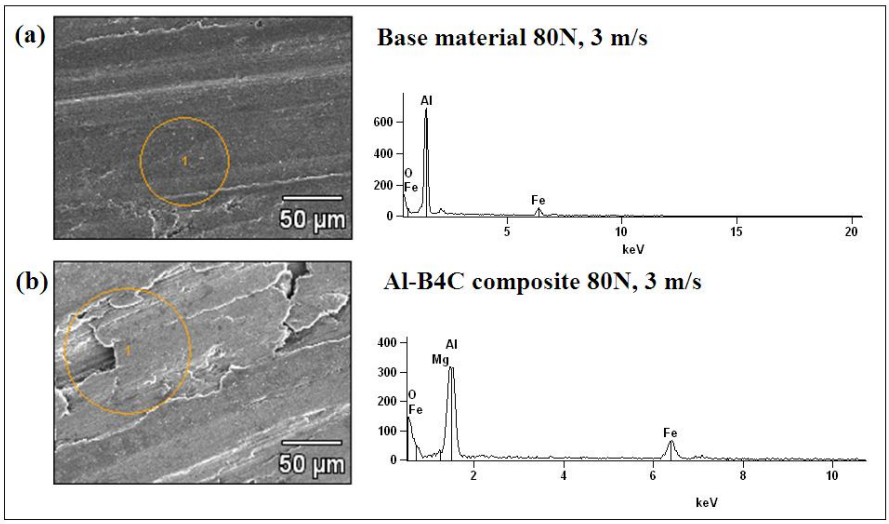


Figure 10 EDS of selective region of worn surface

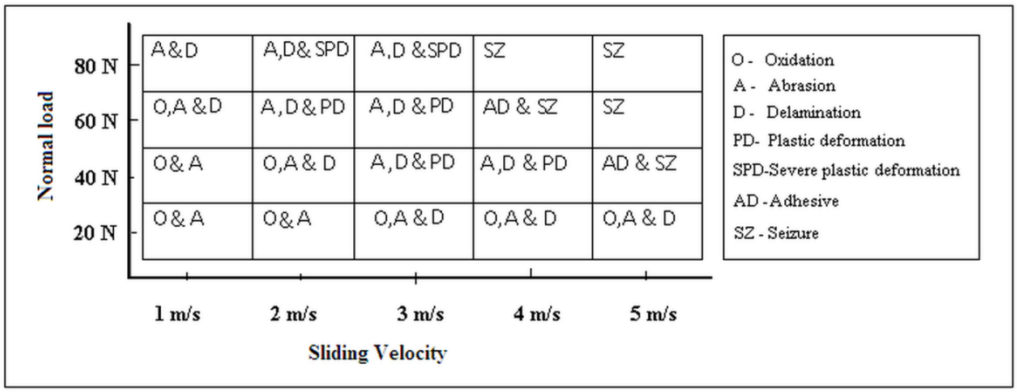


Figure 11 Wear mechanisms for composite under all investigated sliding conditions

3.4.2 Friction coefficient

The change in the friction coefficient of base alloy and composite with a load is shown in Figure 12. Friction coefficient is higher for base material in comparison with composite specimen in all sliding velocity. The higher friction coefficient is attributed to localizing adhering of the worn debris to the surface. The base alloy is considerable softer than the disc material, and the material disc cut's the surface of wear test specimen due to excessive plastic deformation as a result of excessive loss of material occurs.

The friction coefficient of surface composite is lower than base alloy due to a uniform dispersion of nano reinforcements in the matrix. The lower friction coefficient of composite specimen is due to lower in adhesive wear and abrasive wear because of higher hardness. The composite specimen's wear rate is less and reduction in friction coefficient is due to the formation of an oxide surface on the contact zone, which acts as the lubricant. With the increase in load, the coefficient of friction increases marginally up to 40N for 1 to 3 m/s sliding velocities and then that it remains constant.

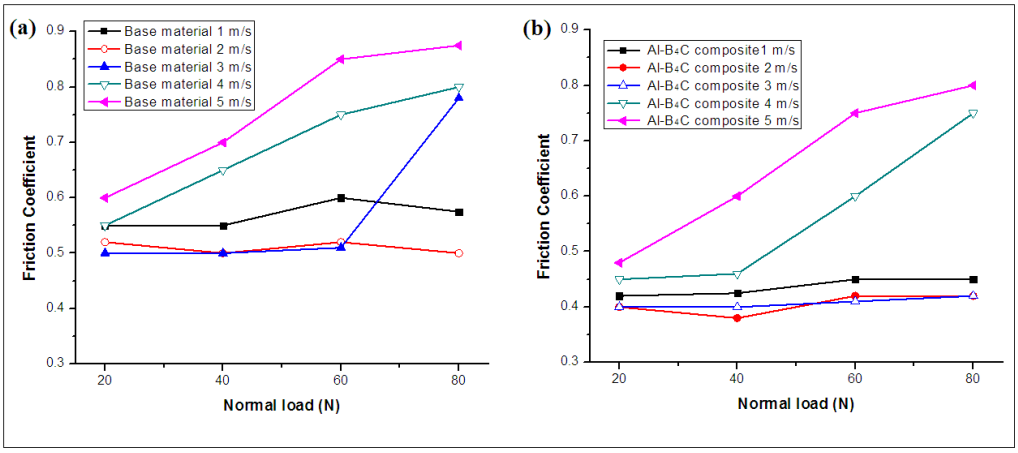


Figure 12 Friction coefficient with Normal load at different sliding velocities

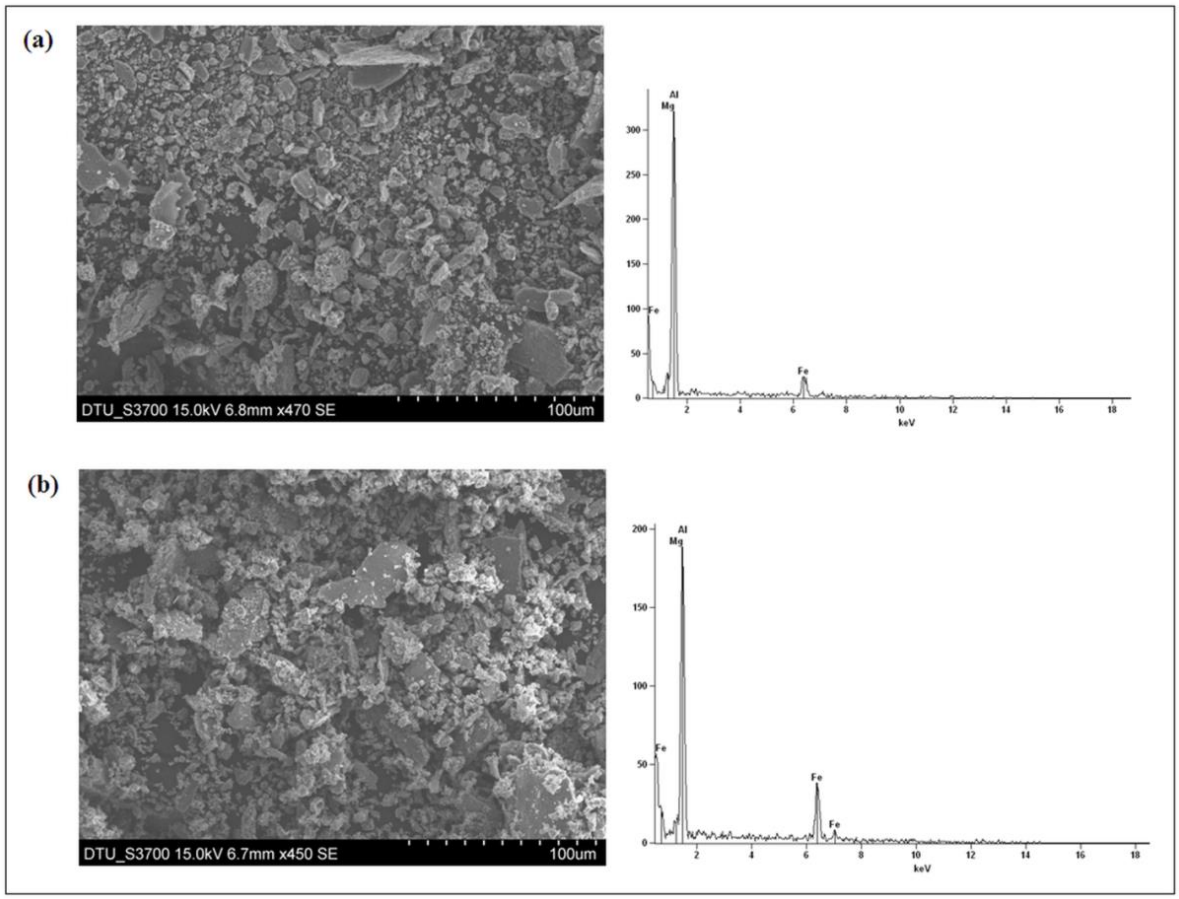


Figure 13 SEM and EDS analysis of wear debris of specimen tested at 80N & 1 m/s (a) Base alloy (b) Al-B_4C composite specimen.

3.4.3 Wear debris analysis

Figure 13 shows shape of wear debris, EDS pattern and iron content in the debris of the base alloy and processed specimen. The composite specimen contains higher amount of iron content in the wear debris than the base material, which indicates the higher amount of material is transferred from the steel disc. The hard reinforcement present in the composite specimen resists the wear loss, and more material is removed from the counter face due increase in surface hardness of the specimen. The pull-out wear debris act as the solid lubricant which leads to reduction of the wear rate. The wear debris of the composite specimen forms tribo layer and reduced the wear rate of the composite specimen.

4. Conclusions

Aluminum matrix reinforced with B_4C nano particles were prepared by FSP. The mechanical properties and wear behavior of the surface composites were investigated.

The following conclusions can be drawn from the experimental results.

- FSPed Al-B_4C composite specimen's exhibits higher hardness, better tensile properties, and enhanced wear properties than base Al5083 alloy. The microhardness and tensile strength of the base material were 82.5±2Hv and 305Mpa respectively, and the maximum microhardness and tensile strength values of the surface composite produced by four passes were achieved 126.5±2Hv and 364Mpa respectively.
- The composite specimens retain the wear resistance properties in the range of (20N- 80N) and sliding speed ranges 1–3m/s. whereas in the base material the wear test could not complete for the sliding distance of 3000m at the load of 80N and sliding speed of 3 m/s and the material got heated and approached towards to failure due to the seizure of the material.
- At 40N & 4 m/s sliding speed, the composite could complete the sliding distance without failure, on the other hand, the base alloy got the seizure. At higher sliding speeds with higher loads (4 m/s with 60N and above) both matrix material and composite specimen got seizure.
- The friction coefficient and wear rate are increased with load increased load in both the base alloy and composite specimen.

5. References

[1] Miracle, D. B. (2005). Metal matrix composites–from science to technological significance. *Comp Sci Technol,* 65:2526–2540. Doi.org/10.1016/j.compscitech.2005.05.027

[2] Mishra, R. S., Ma, Z. Y. (2005). Friction stir welding and processing. *Mater Sci Eng R* 50: 1-78. Doi.org/10.1016/j.mser.2005.07.001

[3] Sharma, V., Prakash, U., Kumar, B. V. M. (2015). Surface composites by friction stir processing: A review. *J Mater Proc Technol,* 224:117-134. Doi.org/10.1016/j.jmatprotec.2015.04.019

[4] Khorrami, M. S., Kazeminezhad, M., Kokabi, A. H. (2014). The effect of SiC nanoparticles on the friction stir processing of severely deformed aluminium. *Mater Sci Eng A,* 602: 110-118. Doi.org/10.1016/j.msea.2014.02.067

[5] Sharifitabar, M., Sarani, A., Khorshahian, S., Afarani, M. S. (2011). Fabrication of 5052Al/Al_2O_3 nanoceramic particle reinforced composite via friction stir processing route. *Mater Des,* 32: 4164-4172. Doi.org/10.1016/j.matdes.2011.04.048

[6] Shahraki, S., Khorasani, S., Behnagh, A. B., Fotouhi, Y., Bisadi, H. (2013). Producing of AA5083/ZrO_2 Nanocomposite by Friction Stir Processing (FSP). *Metall Mater Trans B,* 44: 1546-1553. DOI: 10.1007/s11663-013-9914-9

[7] Khodabakhshi, F., Simchi, A., Kokabi, A. H., Nosko, M., Simancik, F., Svec, P. (2014). Microstructure and texture development during friction stir processing of Al-Mg alloy sheets with TiO_2 nano particles. *Mater Sci Eng A,* 605: 108-118. Doi.org/10.1016/j.msea.2014.03.008

[8] Moghaddas, M. A., Kashani-Bozorg, S. F. (2013). Effects of thermal conditions on microstructure in nanocomposite of Al/Si_3N_4 produced by friction stir processing. *Mater Sci Eng A,* 559: 187–193. Doi.org/10.1016/j.msea.2012.08.073

[9] Izadi, H., Gerlich, A. P. (2012). Distribution and stability of carbon nanotubes during multi-pass friction stir processing of carbon nanotube/aluminum composites. *Carbon,* 50:4744-4749. Doi.org/10.1016/j.carbon.2012.06.012

[10] Sahraeinejad, S., Izadi, H., Haghshenas, M., Gerlich, A. P. (2015). Fabrication of metal matrix composites by friction stir processing. *Mater Sci Eng A,* 626:505–513. Doi.org/10.1016/j.msea.2014.12.077

[11] Khakbiz, M., Akhlaghi, F. (2009). Synthesis and structural characterization of Al–B_4C nano-composite powders by mechanical alloying. *J Alloys Comp,* 479:334–341. Doi.org/10.1016/j.jallcom.2008.12.076

[12] Yuvaraj, N., Aravindan, S., Vipin. (2015). Fabrication of Al5083/B_4C surface composite by friction stir processing and its tribological characterization. *J Mater Res Technol,* 4:398-410. Doi.org/10.1016/j.jmrt.2015.02.006

[13] Shabani, M., O., Mazahery, A. (2011). Modeling of the wear behavior in A356–B_4 C composites. *J Mater Sci,* 46:6700-6708. DOI 10.1007/s10853-011-5623-4

[14] Izadi, H., Sandstrom, R., Gerlich, A. P. (2014). Grain Growth Behavior and Hall–Petch Strengthening in Friction Stir Processed Al 5059. *Metall Mater Trans A,* 45A:5635-5644. DOI: 10.1007/s11661-014-2492-x

[15] Zhang, Z., Chen, D. L. (2008). Contribution of Orowan strengthening effect in particulate-reinforced metal matrix nano composites. *Mater Sci Eng A,* 483–484:148–152. Doi.org/10.1016/j.msea.2006.10.184

[16] Hosseini, S. A., Ranjbar, K., Dehmolaei, R., Amirani, A. R. (2015). Fabrication of Al5083 surface composites reinforced by CNT sandcerium oxide nano particles via friction stir processing. *J Alloys Comp,* 622:725–733. Doi.org/10.1016/j.jallcom.2014.10.158

[17] Mazaheri, Y., Karimzadeh, F., Enayati, M. H. (2011). A novel technique for development of A356/Al_2O_3 surface nanocomposite by friction stir processing. *J Mater Process Technol,* 211:1614– 1619. Doi.org/10.1016/j.jmatprotec.2011.04.015

[18] Rejil, M., Dinaharan, C. I., Vijay, S. J., Murugan, N. (2012). Microstructure and sliding wear behavior of AA6360/(TiC + B_4C) hybrid surface composite layer synthesized by friction stir processing on aluminum substrate. *Mater Sci Eng A,* 552:336-344. Doi.org/10.1016/j.msea.2012.05.049

[19] Barmouz, M., Besharati Givi, M. K., Seyfi, J. (2011). On the role of processing parameters in Producing Cu/SiC metal matrix composites via friction stir processing: Investigating microstructure, microhardness, wear and tensile behavior. *Mater character* 62:08–117. Doi.org/10.1016/j.matchar.2010.11.005

[20] Alidokht, S. A., Abdollah-Zadeh, A., Assadi, H. (2013). Effect of applied load on the dry sliding wear behavior and the subsurface deformation on hybrid metal matrix composite. *Wear,* 305:291-298. Doi.org/10.1016/j.wear.2012.11.043

[21] Kumaran, S. T., Uthayakumar, M. (2014). Investigation on the dry sliding friction and wear behavior of AA6351-SiC-B_4C hybrid metal matrix composites. *Proc IMechE Part J: J Eng Tribology, 228*:332-338. Doi.org/10.1177/1350650113508103

[22] Ekka, K. K., Chauhan, S. R., Varun. (2014). Study on the effects of micro size ceramic particulates (SiC, Al_2O_3 and cenosphere) on mechanical, friction and sliding wear behaviour of aluminium matrix composites under dry sliding condition. *Proc IMechE Part J: J Eng Tribology,* 228:682-691. Doi.org/10.1177/1350650114526581

[23] Yuvaraj, N., Aravindan, S., Vipin, (2017). Comparison studies on Mechanical and Wear behavior of fabricated Aluminum surface nano composites by fusion and solid-state processing. Surface & Coat Technol, 309:309-319. Doi.org/10.1016/j.surfcoat.2016.11.076

[24] Dwivedi, D.K. (2010). Adhesive wear behavior of cast aluminium–silicon alloys:Overview. *Mater Design,* 31:2517–253. Doi.org/10.1016/j.matdes.2009.11.038

View publication stats